frontiers | Research Topics

Quantitative characterization and engineering application of pores and fractures of different scales in unconventional reservoirs – volume II

Edited by
Wenlong Ding, Hu Li and Shuai Yin

Published in
Frontiers in Earth Science

ISSN 1664-8714
ISBN 978-2-83251-812-0
DOI 10.3389/978-2-83251-812-0

About Frontiers

Frontiers is more than just an open access publisher of scholarly articles: it is a pioneering approach to the world of academia, radically improving the way scholarly research is managed. The grand vision of Frontiers is a world where all people have an equal opportunity to seek, share and generate knowledge. Frontiers provides immediate and permanent online open access to all its publications, but this alone is not enough to realize our grand goals.

Frontiers journal series

The Frontiers journal series is a multi-tier and interdisciplinary set of open-access, online journals, promising a paradigm shift from the current review, selection and dissemination processes in academic publishing. All Frontiers journals are driven by researchers for researchers; therefore, they constitute a service to the scholarly community. At the same time, the *Frontiers journal series* operates on a revolutionary invention, the tiered publishing system, initially addressing specific communities of scholars, and gradually climbing up to broader public understanding, thus serving the interests of the lay society, too.

Dedication to quality

Each Frontiers article is a landmark of the highest quality, thanks to genuinely collaborative interactions between authors and review editors, who include some of the world's best academicians. Research must be certified by peers before entering a stream of knowledge that may eventually reach the public - and shape society; therefore, Frontiers only applies the most rigorous and unbiased reviews. Frontiers revolutionizes research publishing by freely delivering the most outstanding research, evaluated with no bias from both the academic and social point of view. By applying the most advanced information technologies, Frontiers is catapulting scholarly publishing into a new generation.

What are Frontiers Research Topics?

Frontiers Research Topics are very popular trademarks of the *Frontiers journals series*: they are collections of at least ten articles, all centered on a particular subject. With their unique mix of varied contributions from Original Research to Review Articles, Frontiers Research Topics unify the most influential researchers, the latest key findings and historical advances in a hot research area.

Find out more on how to host your own Frontiers Research Topic or contribute to one as an author by contacting the Frontiers editorial office: frontiersin.org/about/contact

Quantitative characterization and engineering application of pores and fractures of different scales in unconventional reservoirs – volume II

Topic editors

Wenlong Ding — China University of Geosciences, China

Shuai Yin — Xi'an Shiyou University, China

Hu Li — Southwest Petroleum University, China

Citation

Ding, W., Yin, S., Li, H., eds. (2023). *Quantitative characterization and engineering application of pores and fractures of different scales in unconventional reservoirs – volume II*. Lausanne: Frontiers Media SA.

doi: 10.3389/978-2-83251-812-0

Table of contents

frontiers | Frontiers in Earth Science

TYPE Editorial
PUBLISHED 17 February 2023
DOI 10.3389/feart.2023.1133707

OPEN ACCESS

EDITED AND REVIEWED BY
Derek Keir,
University of Southampton,
United Kingdom

*CORRESPONDENCE
Hu Li,
lihu860628@126.com

SPECIALTY SECTION
This article was submitted to Structural Geology and Tectonics, a section of the journal Frontiers in Earth Science.

RECEIVED 29 December 2022
ACCEPTED 03 January 2023
PUBLISHED 17 February 2023

CITATION
Li H, Yin S and Ding W (2023), Editorial: Quantitative characterization and engineering application of pores and fractures of different scales in unconventional reservoirs—Volume II. *Front. Earth Sci.* 11:1133707. doi: 10.3389/feart.2023.1133707

Editorial: Quantitative characterization and engineering application of pores and fractures of different scales in unconventional reservoirs—Volume II

Hu Li[1,2,3]*, Shuai Yin[4] and Wenlong Ding[5]

[1]Sichuan College of Architectural Technology, Chengdu, China, [2]School of Geoscience and Technology, Southwest Petroleum University, Chengdu, China, [3]Natural Gas Geology Key Laboratory of Sichuan Province, Chengdu, China, [4]School of Earth Science and Engineering, Xi'an Shiyou University, Xi'an, China, [5]School of Energy Resources, China University of Geosciences, Beijing, China

KEYWORDS

unconventional reservoirs, tight sandstone, shale, multi-scale pore, fracture, quantitative characterization, engineering application

Editorial on the Research Topic
Quantitative characterization and engineering application of pores and fractures of different scales in unconventional reservoirs—Volume II

Introduction

With the depletion of conventional oil and gas resources in the world, unconventional oil and gas resources have become the focus and hotspot of exploration and development (Li et al., 2019; Yin et al., 2020a; Fan et al., 2020; Li, 2022a). In recent years, a series of unconventional oil and gas resources (e.g., tight sandstone gas, shale gas, coalbed methane, and gas hydrate) have been explored and developed in China, among which tight sandstone gas and shale gas have been commercially exploited (Wu et al., 2022; Xie et al., 2022). Tight sandstone gas is the earliest unconventional gas developed in China, which plays an important role in China's total natural gas reserves and production, with a total resource of about 17.4×10^{12}–25.1×10^{12} m^3, and its recoverable resource is about 8.8×10^{12}–12.1×10^{12} m^3 (Zou et al., 2018).

In the past decade, China has achieved significant exploration and development achievements in shale gas. Eight shale gas fields have been built in and around the Sichuan Basin (e.g., Fuling, Luzhou, Changning, Weiyuan, and Zhaotong). In 2021, China's shale gas production reached 230 $m^3 \times 10^8$ m^3, mainly from shale formations shallower than 3,500 m. Deep shale gas resources (more than 3,500 m) will be long-term exploration and development targets for more than 80% of the total resources (Li J. et al., 2022a). Both tight sandstone and shale reservoirs have the characteristics of ultra-low porosity and permeability, and shale reservoirs have the worst physical properties (Li J. et al., 2022b; Fan et al., 2022). Therefore, quantitatively characterization of such reservoirs' multi-scale pore and fracture characteristics is of profound significance for tight oil and gas.

This Research Topic is Volume II of a series "*Quantitative characterization and engineering application of pores and fractures of different scales in unconventional reservoirs*." The set of 39 studies in this Research Topic aimed to understand multiple methods for quantitative characterization of the pore and fracture systems, as well as provide a general framework for future research efforts.

Quantitative characterization of multi-scale pores in unconventional reservoirs

Tight sandstone reservoirs

The results of qualitative and quantitative characterization of multi-scale pores are abundant, and systematic theoretical methods and characterization techniques have been formed. Guo et al. (ID: 959796) take the Chang 6 Member of the Yanchang Formation in the Huaqing area of the Ordos Basin as an example. The pore-throat heterogeneity of tight sandstone reservoirs and its influence on the fluid occurrence state were studied using thin sections, scanning electron microscope (SEM), X-ray diffraction (XRD), constant velocity Mercury intrusion, and nuclear magnetic resonance (NMR) tests. Luan et al. (ID: 963316) take the Chang 8 Member of the Yanchang Formation in the Shuimogou area in the southern Ordos Basin as an example, the sedimentary facies types, microscopic pore structures, diagenesis, influencing factors of physical properties, and hydrocarbon enrichment of tight oil reservoirs were studied. Wang et al. (ID: 996167) take the Paleogene reservoirs in the Gaoshangpu area of the Nanpu saga as an example, it shows that compaction is the main cause of reservoir densification, argillaceous and calcareous cementation is the secondary cause, and later dissolution is another main cause of reservoir enhancement. Wei et al. (ID: 1011219) identified macro-micro characteristics of glutenite reservoirs in the Dinan 15 well area in the Junggar Basin and established criteria for identifying favorable reservoir studies. How to accurately predict hydrocarbon enrichment and high-yield areas in ultra-low permeability sandstone reservoirs is a hot spot in petroleum geology. Liao et al. (ID: 1013776) take the Chang 6 Member of the Yanchang Formation in the Huaqing area as an example, the analysis of dominant facies, lithologic assemblages and electrical properties formulated the evaluation criteria for hydrocarbon enrichment. Through observations under an optical microscope and SEM, casting thin sections, and plane porosity measurements, Yang et al. (ID: 1016973) investigated the diagenesis differences in the third member of the Shahejie Formation in the root and central portions of a fan deltan the eastern Laizhou Bay Sag. Evaluating tight oil reservoir properties is significant to exploring tight oil and gas. The reservoir characteristics of the Chang 1 Member in the Wanhua area and the effects of superimposed sand bodies, structures, and paleogeomorphology on hydrocarbon accumulation were studied by Ji et al. (ID: 1023844). Tan et al. (ID: 1028439) studied the controlling effect of source-reservoir assemblage on the gas accumulation in the Xujiahe Formation, and they think the type of source-reservoir combination mainly controls the development scale of natural gas, and the areas with close source-reservoir contact and high hydrocarbon generation intensity are high-quality reservoir development areas. Kuang and Liu (ID: 1033344) think the controlling factors of the petrophysical properties of the conglomerate reservoirs in the Baikouquan Formation in the northwestern margin of the Junggar Basin include sedimentation, diagenesis, and tectonic movements, while that of the sandstone reservoirs mainly include sedimentation and diagenesis. Si et al. (ID: 1042927) considered that compaction, calcite and siliceous cementation, and illite packing are primarily responsible for reservoir densification of the Gaotaizi oil layer in the Qijia area. Qiu et al. (ID: 1046489) evaluated the reservoir quality of tight oil sandstones in Chang 7 Member of Ordos Basin by NMR, clay mineral analysis, high-pressure Mercury injection analysis, and logging interpretation technology. Based on petrographic observations, micro–Raman spectroscopy, and fluorescent spectrometry, petroleum inclusions, CH_4-bearing inclusions, and CO_2-bearing inclusions were discovered in quartz-hosted minerals. Tang et al. (ID: 1059909) investigated two types of sandstone reservoirs with different pressure states and fluid evolution of the Shahejie Formation in the Western slope belt, Dongpu sag.

Shale reservoirs

Shale is a kind of fine-grained sedimentary rock denser than conventional sandstone and conglomerate reservoirs. The conventional reservoir characterization techniques are difficult to apply to shale. Multiple methods are generally used to realize the qualitative and quantitative characterization of shale pore characteristics (Li H. et al., 2022; Li J. et al., 2022a; Li J. et al., 2022b). Scholars have made extensive studies on marine, transitional and continental shales. Based on the results of high-pressure Mercury intrusion, low-pressure N_2, and CO_2 adsorption and organic geochemical experiments, XRD and SEM observations, Xiao et al. (ID: 981037) investigated the effects of organic and inorganic compositions on the development of pore structures of the Upper Permian Shanxi shale in the southern Yan'an area. Han et al. (ID: 981127) take the black shale from the Upper Ordovician and Lower Silurian in the Southern Sichuan Basin as an example, and discussed the effectiveness of shale pore detection by multiple methods. Peng et al. (ID: 985302) studied the geological conditions of shale gas accumulation in the marine-continental transitional facies sediments in the South North China Basin using sedimentary, logging, seismic, core, geochemical, physical property, and SEM data. Wang et al. (ID: 1012607) take the Chang 7 Member shale in the Yan'an area as an example, the results show that it has complete gas-generating conditions. Shale gas accumulation requires three necessary accumulation elements, i.e., gas source, reservoir, and good preservation conditions. Integrating SEM, NMR, LTNA, MICP experiments, and other basic measurements, Zhou et al. (ID: 1055541) studied the nano-scale pore category, structure, and corresponding controlling factors of Dongyuemiao lacustrine shale in the Eastern Sichuan Basin. The quartz has no significant effect on the formation of nano-scale pores. The intraparticle pores within calcite particles constitute part of mesopore-macropore but not micropores. Clay minerals are conducive to the formation of micropores but play a negative role in mesopore-macropores. The Lower Permian Shanxi Formation in the Eastern Ordos Basin is a set of transitional shale, Cai et al. (ID: 1061211) evaluated the pore fluid based on a series of NMR experiments, and they believe the total content of movable pores and bound pores in the Lower shale is the highest, while that in the Upper shale is lower. Zhang et al. (ID: 1052734) divided the lithofacies types of the Da'anzhai Member in the

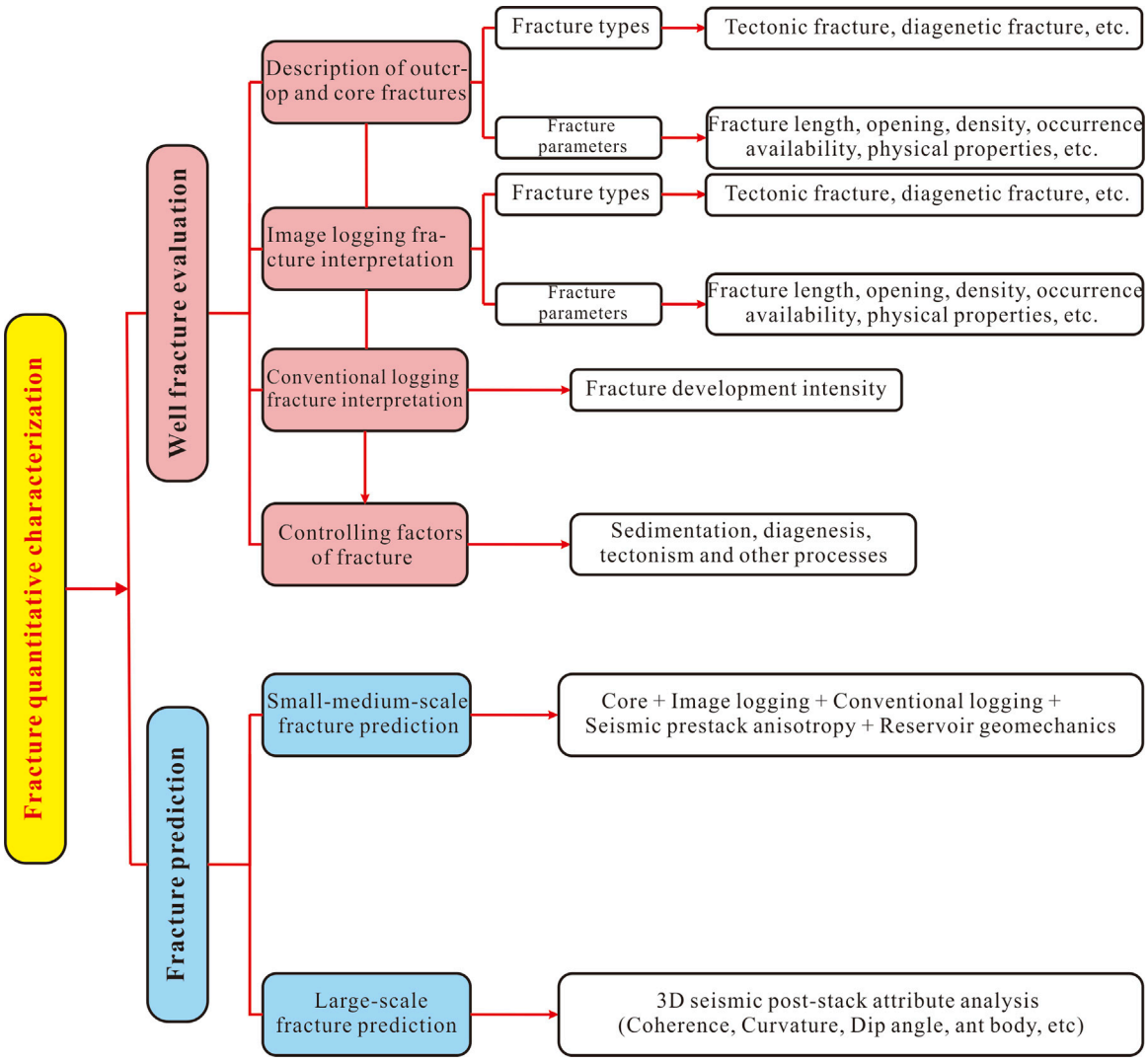

FIGURE 1
Characterization method of natural fracture (Lv et al., 2021; Li, 2022c).

Well Ren'an 1 into six types. The thick clay shale lithofacies have the highest TOC content and are mainly developed in the depositional environment of warm and humid, deep water, quiet, low salinity, and abundant terrigenous clasts.

In addition, there are also many researches related to volcanic and carbonate reservoirs. Fu et al. (ID: 983572) studied the relation of the "four properties" and fluid identification of the carboniferous weathering crust volcanic reservoir in the Shixi Oilfield. The cross-plot method determines lower limits of the reservoir's physical properties and oil saturation, yielding porosity >9%, permeability >.2 MD, and oil saturation >45%. Ren et al. (ID: 984463) studied the effects of diagenesis on the quality of deep dolomite reservoirs of the Upper Cambrian Xixiangchi Formation. Hu et al. (ID:1022911) believe that the key factors affecting hydrocarbon accumulation in the Xixiangchi Formation are sufficient oil and gas supply, development of inherited paleo-uplift, effective transportation system, and favorable reservoir-forming combination. Zhang et al. (ID:1015460) selected 11 carbonate samples from three deep reservoirs in Tarim Basin. The carbonate reservoir dissolution process was simulated using an advanced continuous flow reaction system at high temperature and high pressure. The dissolution rate of the dolomite reservoir has a trend of increasing and then decreasing under the deeply buried environment, which proves that there is an optimal dissolution range of dolomite in the deeply buried environment. Gu et al. (ID: 1041164) studied the effects of diagenesis on the quality of the Dengying Formation deep dolomite reservoir by the petrology, geochemistry, and *in situ* U-Pb dating. Qu et al. (ID: 1043148) also made quantitative characterization and origin of differences in pore parameter distribution of the Lower Cambrian Longwangmiao Formation in the Gaoshiti area of the central Sichuan Basin.

In general, since the pores of shale reservoirs are mainly nano-scale, the pore size is composed of nano- and micron-scale. Therefore, it is impossible to rely on a single method to characterize shale pores. Generally, the combination of multiple methods is used to achieve qualitative and quantitative characterization. Almost all of the above studies have adopted this method. In addition, it applies to shale

reservoirs and tight sandstone, carbonate, volcanic, and other tight reservoirs.

Quantitative characterization of multi-scale fractures in unconventional reservoirs

Natural fractures can improve the porosity of tight reservoirs and control the seepage system of such reservoirs. The fracture development is the key to the high and stable production of tight oil and gas (Yin et al., 2020b; Yin and Wu, 2020). However, they may also communicate with the upper strata, which is not conducive to preserving tight reservoirs. In recent years, quantitative characterization of natural fractures has been established based on the outcrop, core, multi-type thin sections, image/conventional logging, and seismic data (Figure 1) (Yin and Ding, 2019; Yin and Gao, 2019; Li et al., 2020; Li et al., 2021; Forstner and Laubach, 2022; Wang et al., 2021; Wang and Wang, 2021). According to this research method, scholars have done many studies.

The paleo-tectonic stress field controls tectonic fractures. Zhang et al. (ID: 1024748) used the finite element numerical simulation technology to analyze the distribution of the paleo-tectonic stress field of the Longmaxi Formation in the Lintanchang area. Then they predicted the fracture development areas under the superposition of two stages of tectonic stress. It is found that the comprehensive fracture coefficients of the anticline core and fault areas are both greater than 1.1, which are the areas with the most developed tectonic fractures, and these areas have poor shale gas preservation conditions. The shale is in a state of "breaking without cracking," and shale gas can be well preserved. The preservation of shale gas is closely related to tectonic fractures, the structural preservation conditions are the key factors in controlling the rich and integrated shale gas reservoirs in the Wuxi area of Chongqing City. Li et al. (ID: 1032597) found that there are three structural preservation modes of shale gas in the study area, i.e., lost destruction type, lost residual type, and trap preservation type. The trap preservation type is more conducive to the preservation of shale gas, which is the most favorable structural mode for shale gas exploration. Frackability is of great significance to shale gas development, Guo et al. (ID: 993829) take the Longmaxi Formation shale in the Changning and Luzhou Blocks in the southern Sichuan Basin as an example, and the Analytic Hierarchy Process (AHP) method was adopted to establish a comprehensive evaluation index of shale fracturability. The modulus brittleness index, mechanical brittleness index, *in-situ* stress difference coefficient, rock compressive strength, and TOC content are the most important evaluation indexs.

For the engineering application, Yang et al. (ID: 970719) carried out the experimental evaluation and numerical simulation research on the adaptability of CO_2 flooding in beach-bar sand reservoirs of the Shahejie Formation in the Dongying Sag. Yang et al. (ID: 1029309) also conducted indoor water flooding experiments after polymer gel injection using artificial cores, and a set of criteria for determining reservoir-matched polymer gel profile control agents was proposed. Liu et al. (ID: 1037532) put forward a coupled CFD-DEM method to simulate the particle plugging process of propagating fracture, and the effects of positive pressure difference, fracture roughness, particle concentration, and particle shape on the plugging mechanism were examined.

Among these 39 studies, we received a paper about the Lunpola Basin and the southern East China sea shelf. Zhang et al. (ID: 1034069) summarized the oil and gas accumulation conditions of the Lunpola Basin and pointed out the favorable zones with the most exploration potential. Wang et al. (ID: 1015832) analyzed the burial history of wells and simulation wells in SECS by the data of drilling, seismic, and source rocks. Moreover, favorable oil-gas accumulation modes in Lower-Middle Jurassic were proposed by combining them with studies on oil-gas accumulation elements and conditions.

Summary

In summary, the 39 high-quality papers on this Research Topic represent a step forward in understanding the quantitative characterization and engineering application of pores and fractures of different scales in unconventional reservoirs. We appreciate the opportunity to present this hot Research Topic and hope that readers will benefit from the breadth and scope of the research. More importantly, we hope these studies offer new directions for future research that will guide future scientific community efforts. Many researchers have contributed to the hot Research Topic, and we have applied for Volume III. We hope more scholars will be involved in the Research Topic, especially on the quantitative characterization of multi-scale fractures. It will offer new directions for future research that guide the quantitative characterization of multi-scale pores and fractures of unconventional reservoirs in the future.

Author contributions

HL, SY, and WD, edited the Research Topic of quantitative characterization and engineering application of pores and fractures of different scales in unconventional reservoirs—Volume II. HL and SY wrote and revised the manuscript.

Funding

This work was supported by the Key R&D Projects of the Deyang Science and Technology Plan (Nos. 2022SZ049 and 2021SZ002), the Open funds of Natural Gas Geology Key Laboratory of Sichuan Province (No. 2021trqdz05), and Shale Gas Evaluation and Exploitation of the Key Laboratory of Sichuan Province (No. YSK2022002), and China National Scientific and Technical Support Program (No. 2018YFC0406402).

Conflict of interest

The authors declare that the research was conducted in the absence of any commercial or financial relationships that could be construed as a potential conflict of interest.

Publisher's note

All claims expressed in this article are solely those of the authors and do not necessarily represent those of their affiliated

organizations, or those of the publisher, the editors and the reviewers. Any product that may be evaluated in this article, or claim that may be made by its manufacturer, is not guaranteed or endorsed by the publisher.

References

Fan, C. H., Li, H., Qin, Q. R., He, S., and Zhong, C. (2020). Geological conditions and exploration potential of shale gas reservoir in Wufeng and Longmaxi Formation of southeastern Sichuan Basin, China. *J. Pet. Sci. Eng.* 191, 107138. doi:10.1016/j.petrol.2020.107138

Fan, C. H., Xie, H. B., Li, H., Zhao, S. X., Shi, X. C., Liu, J. F., et al. (2022). Complicated fault characterization and its influence on shale gas preservation in the southern margin of the Sichuan basin, China. *Lithosphere* 2022, 8035106. doi:10.2113/2022/8035106

Forstner, S. R., and Laubach, S. E. (2022). Scale-dependent fracture networks. *J. Struct. Geol.* 165, 104748. doi:10.1016/j.jsg.2022.104748

Li, H. (2022a). Research progress on evaluation methods and factors influencing shale brittleness: A review. *Energy Rep.* 8, 4344–4358. doi:10.1016/j.egyr.2022.03.120

Li, H. (2022b). A review of mechanical mechanism and prediction of natural fracture in shale. *Arab. J. Geosci.* 15 (6), 474. doi:10.1007/s12517-022-09786-w

Li, H., Tang, H. M., Qin, Q. R., Zhou, J. L., Qin, Z. J., Fan, C. H., et al. (2019). Characteristics, formation periods and genetic mechanisms of tectonic fractures in the tight gas sandstones reservoir: A case study of Xujiahe Formation in YB area, Sichuan Basin, China. *J. Pet. Sci. Eng.* 178, 723–735. doi:10.1016/j.petrol.2019.04.007

Li, H., Qin, Q. R., Zhang, B. J., Ge, X. Y., Hu, X., Fan, C. H., et al. (2020). Tectonic fracture formation and distribution in ultradeep marine carbonate gas reservoirs: A case study of the maokou Formation in the jiulongshan gas field, Sichuan Basin, southwest China. *Energy Fuel* 34 (11), 14132–14146. doi:10.1021/acs.energyfuels.0c03327

Li, H., Wang, Q., Qin, Q. R., and Ge, X. Y. (2022b). Characteristics of natural fractures in an ultradeepmarine carbonate gas reservoir and their impact on the reservoir: A case study of the maokou formation of the jls structure in the Sichuan Basin, China. *Energy Fuel* 35 (16), 13098–13108. doi:10.1021/acs.energyfuels.1c01581

Li, H., Zhou, J. L., Mou, X. Y., Guo, H. X., Wang, X. X., An, H. Y., et al. (2022c). Pore structure and fractal characteristics of the marine shale of the Longmaxi Formation in the Changning area, southern Sichuan basin, China. *Front. Earth Sci.* 10, 1018274. doi:10.3389/feart.2022.1018274

Li, J., Li, H., Xu, J. L., Wu, Y. J., and Gao, Z. (2022a). Effects of fracture formation stage on shale gas preservation conditions and enrichment in complex structural areas in the southern Sichuan Basin, China. *Front. Earth Sci.* 9, 823855. doi:10.3389/feart.2022.921988

Li, J., Li, H., Yang, C., Wu, Y. J., Gao, Z., and Jiang, S. L. (2022b). Geological characteristics and controlling factors of deep shale gas enrichment of the Wufeng-Longmaxi Formation in the southern Sichuan basin, China. *Lithosphere* 2022, 4737801. doi:10.2113/2022/4737801

Lv, W. Y., Zeng, L. B., Chen, S. Q., Lv, P., Dong, S. Q., Hui, C., et al. (2021). Characterization methods of multi-scale natural fractures in tight and low-permeability sandstone reservoirs. *Geol. Rev.* 67 (2), 543–556. doi:10.16509/j.georeview.2021.02.020

Wang, B., Lu, C. L., Huang, Z. K., and Hu, S. Y. (2021). Experimental study on damage evolution characteristics of rock under triaxial rheological disturbance. *J. Min. Strata Control Eng.* 3 (4), 043028. doi:10.13532/j.jmsce.cn10-1638/td.20210525.001

Wang, J., and Wang, X. L. (2021). Seepage characteristic and fracture development of protected seam caused by mining protecting strata. *J. Min. Strata Control Eng.* 3 (3), 033511. doi:10.13532/j.jmsce.cn10-1638/td.20201215.001

Wu, Z. H., Tang, M. T., Zuo, Y. J., Lou, Y. L., Wang, W. T., Liu, H., et al. (2022). Acoustic emission-based numerical simulation of tectonic stress field for tectoclase prediction in shale reservoirs of the northern Guizhou area, China. *Energy Geosci.* 3 (4), 436–443. doi:10.1016/j.engeos.2021.10.005

Xie, R. C., Luo, Z. W., Zhang, M. Y., Wang, Y. F., Chen, J., and Zhu, M. (2022). Factors controlling tight oil and gas reservoir development in the Jurassic siliciclastic-carbonate rocks in Sichuan Basin, China. *Energy Geosci.* 3 (4), 453–464. doi:10.1016/j.engeos.2021.08.001

Yin, S., and Ding, W. (2019). Evaluation indexes of coalbed methane accumulation in the strong deformed strike-slip fault zone considering tectonics and fractures: A 3D geomechanical simulation study. *Geol. Mag.* 156 (6), 1052–1068. doi:10.1017/s0016756818000456

Yin, S., Dong, Li., Yang, Xia., and Wang, R. (2020). Experimental investigation of the petrophysical properties, minerals, elements and pore structures in tight sandstones. *J. Nat. Gas. Sci. Eng.* 76 (1), 103189–103214. doi:10.1016/j.jngse.2020.103189

Yin, S., and Gao, Z. (2019). Numerical study on the prediction of "sweet spots" in a low efficiency-tight gas sandstone reservoir based on a 3D strain energy model. *IEEE Access* 7, 117391–117402. doi:10.1109/access.2019.2933450

Yin, S., Tian, T., Wu, Z., and Li, Q. (2020). Developmental characteristics and distribution law of fractures in a tight sandstone reservoir in a low-amplitude tectonic zone, eastern Ordos Basin, China. *Geol. J.* 55, 1546–1562. doi:10.1002/gj.3521

Yin, S., and Wu, Z. (2020). Geomechanical simulation of low-order fracture of tight sandstone. *Mar. Pet. Geol.* 100, 104359. doi:10.1016/j.marpetgeo.2020.104359

Zou, C. N., Tao, S. Z., Han, W. X., Zhao, Z. Y., Ma, W. J., Li, C. W., et al. (2018). Geological and geochemical characteristics and exploration prospect of coal-derived tight sandstone gas in China: Case study of the Ordos, sichuan, and Tarim basins. *Acta Geol. Sin.* 92 (4), 1609–1626. doi:10.1111/1755-6724.13647

frontiers | Frontiers in Earth Science

TYPE Original Research
PUBLISHED 25 July 2022
DOI 10.3389/feart.2022.963316

OPEN ACCESS

EDITED BY
Hu Li,
Southwest Petroleum University, China

REVIEWED BY
Cunhui Fan,
Southwest Petroleum University, China
Shun He,
Southwest Petroleum University, China

*CORRESPONDENCE
Bo Zhang,
zhangbo1934@163.com

SPECIALTY SECTION
This article was submitted to Structural Geology and Tectonics, a section of the journal Frontiers in Earth Science

RECEIVED 07 June 2022
ACCEPTED 06 July 2022
PUBLISHED 25 July 2022

CITATION
Luan B, Zhang B, Wang D, Deng C and Wang F (2022), Quantitative evaluation of tight oil reservoirs in the Chang 8 Member of the Yanchang Formation in southern Ordos Basin.
Front. Earth Sci. 10:963316.
doi: 10.3389/feart.2022.963316

Quantitative evaluation of tight oil reservoirs in the Chang 8 Member of the Yanchang Formation in southern Ordos Basin

Beibei Luan[1], Bo Zhang[2]*, Didong Wang[1], Chao Deng[3] and Feng Wang[4]

[1]Development Department, Yanchang Oifield Co., Ltd., Yan'an, Shaanxi, China, [2]Zhidan Oil Production Plant, Yanchang Oilfield Co., Ltd., Zhidan, Shaanxi, China, [3]Yulin Refinery, Yanchang Petroleum (Group) Co., Ltd., Jingbian, Shaanxi, China, [4]Jingbian Oil Production Plant, Yanchang Oilfield Co., Ltd., Jingbian, Shaanxi, China

The precise and quantitative characterization of reservoir properties is the key to efficient development of tight oil reservoirs. In this paper, taking the Chang 8 Member of the Yanchang Formation in the Shuimogou area in the southern Ordos Basin as an example, the sedimentary facies types, microscopic pore structures, diagenesis, influencing factors of physical properties, and hydrocarbon enrichment law of tight oil reservoirs are systematically studied. The research results show that the Chang 8 Member in the study area is a typical delta front subfacies deposit, including distributary channel and inter-distributary bay microfacies. The constructive diagenesis of the Chang 8 Member include dissolution, metasomatism and rupture; while the destructive diagenesis include mechanical compaction and cementation. The Chang 8 reservoir has entered the middle diagenetic stage A. The factors affecting the physical properties of tight oil reservoirs include deposition, compaction, cementation and dissolution. The secondary pores formed by dissolution account for 10–40% of the total surface porosity, with an average value of 24%. Local structures and sediments have significant control over hydrocarbon accumulation. The westward dipping tectonic setting of the northern Shaanxi Slope provides the basic conditions for the migration of oil and gas to the eastern updip areas. The changes of lithology and physical properties in the updip direction of the structure form the blocking conditions for the continued migration of oil and gas, which is conducive to the accumulation of oil and gas. In addition, the main oil reservoirs are mainly distributed along the distributary channel of the delta front, and most of the distributary channel sandstone is more than 20 m thick. The areas of thick sand body with multiple layers in the lateral direction is the main part of oil and gas accumulation. However, the reservoirs formed on the flanks of underwater distributary channels are generally thin and poorly sorted, which is not conducive to the accumulation of hydrocarbons.

KEYWORDS

reservoir evaluation, tight oil reservoirs, pore type, diagenesis, physical properties

Introduction

After more than a decade of exploration and research on tight oil exploration in China, rich areas of tight oil have been found in the Qingshankou Formation of the Songliao Basin, the Yanchang Formation of the Ordos Basin, and the Jurassic of the Sichuan Basin. Since 2010, based on the theory of "continuous hydrocarbon accumulation", the exploration thinking of tight oil in China has changed from "oil traps" to "entering oil sources". Later, the Changqing Oilfield has built China's first industrially produced tight oil area in the Ordos Basin. In 2013, a demonstration base for efficient development of tight oil in Xinjiang Oilfield was built. In 2015, the Xinanbian Oilfield, the first large-scale tight oil field of 100 million tons, was discovered in the Ordos Basin. In 2019, the one billion ton Gyeongseong Oil Field was discovered. At present, the Ordos Basin has the largest demonstration base for tight oil development in China (Yan, 2020).

With the decrease of conventional oil and gas resources, the exploration and development of tight oil and gas resources has attracted more and more attention (Cai, 2020; Curtis et al., 2012; Hong et al., 2020). There are abundant tight sandstone oil resources in the Upper Triassic Yanchang Formation in the Ordos Basin in the central China. The large-scale accumulation of oil and gas resources in the Yanchang Formation did not undergo long-distance migration. In recent years, with the developments of horizontal wells and fracturing technology, tight oil reservoirs of the Yanchang Formation has achieved great process (Houben et al., 2013; Li., 2022; Liu et al., 2021a). Evaluation of resource potential of tight oil depends on the accurate evaluation of various reservoir parameters (Li et al., 2019; Nie et al., 2020; Lan et al., 2021). Fine and quantitative characterization of reservoirs combining various advanced experimental and interpretation techniques is the key to efficient development of tight oil reservoirs (Anovitz et al., 2013; Cao et al., 2020; Chalmers et al., 2009).

In this paper, taking the Chang 8 Member of the Yanchang Formation in the Shuimogou area in the southern Ordos Basin as an example, the sedimentary facies types, microscopic pore structures, diagenesis, influencing factors of physical properties, and hydrocarbon enrichment law of tight oil reservoirs are systematically studied using the data of core, thin section, scanning electron microscope, X-ray diffraction, physical properties, oil testing and well logging. This study can provide a scientific basis for the rational and effective development of tight oil reservoirs.

Geological background

The study area is located in the Shuimogou Block of the Fuxian exploration area in the Ordos Basin (Figure 1A). The entire Upper Triassic Yanchang Formation in the study area is a west-dipping monocline, on which a series of low-amplitude uplifts developed (Figure 1B). The marker layers of the Chang 8 Member include K0, K1 and the middle mudstone (Figure 1C):

(1) Lijiapan Shale K0

The top interface of the K0 mark layer is the boundary between the Chang 8 and Chang 9 Members, and its thickness is generally 4–8 m. The lithology include black mudstone and shale, and the electrical characteristics are characterized by high natural gamma, high spontaneous potential, blocky high value of acoustic time difference, and relatively high resistivity (Figure 1C).

(2) Zhangjiatan Shale K1

The Zhangjiatan Shale is a thick oil shale segment. Its electrical characteristics are characterized by high acoustic time difference, high natural gamma, and high resistivity. It is an extremely important source rock marker layer distributed in the Ordos Basin (Figure 1C).

(3) Middle mudstone marker layer

The main lithology is gray-black mudstone, and its electrical properties are characterized by high acoustic time difference, high natural gamma, and high resistivity, and are widely developed in this area (Figure 1C).

From the statistical results, the burial depth of the Chang 8 Member in the study area is mainly between 1,300 and 1700 m, with an average burial depth of 1,500 m. The thickness of the Chang 8_1 sub-member is mainly between 40 and 60 m, with an average thickness of 53.4 m; and the thickness of the Chang 8_2 sub-member is mainly between 30 and 50 m, with an average thickness of 45.7 m.

On the basis of the identification of marker layers, wells with different positions, appropriate locations, and complete logging data are selected as comparison standard wells, and stratigraphic division is carried out in combination with rock debris, cores, gas logging and logging data (Li et al., 2012; Chen et al., 2021). The stratigraphic division adheres to the principle of "sedimentary cycle comparison". In this study, the stratigraphic division and comparison of 267 wells in the whole area have been completed, and a stratigraphic division and comparison database has been formed.

Materials and methods

Experimental test items include thin section, scanning electron microscope, X-ray diffraction, physical properties tests. Thin sections and scanning electron microscopy were used to analyze mineral composition, pore structures, and

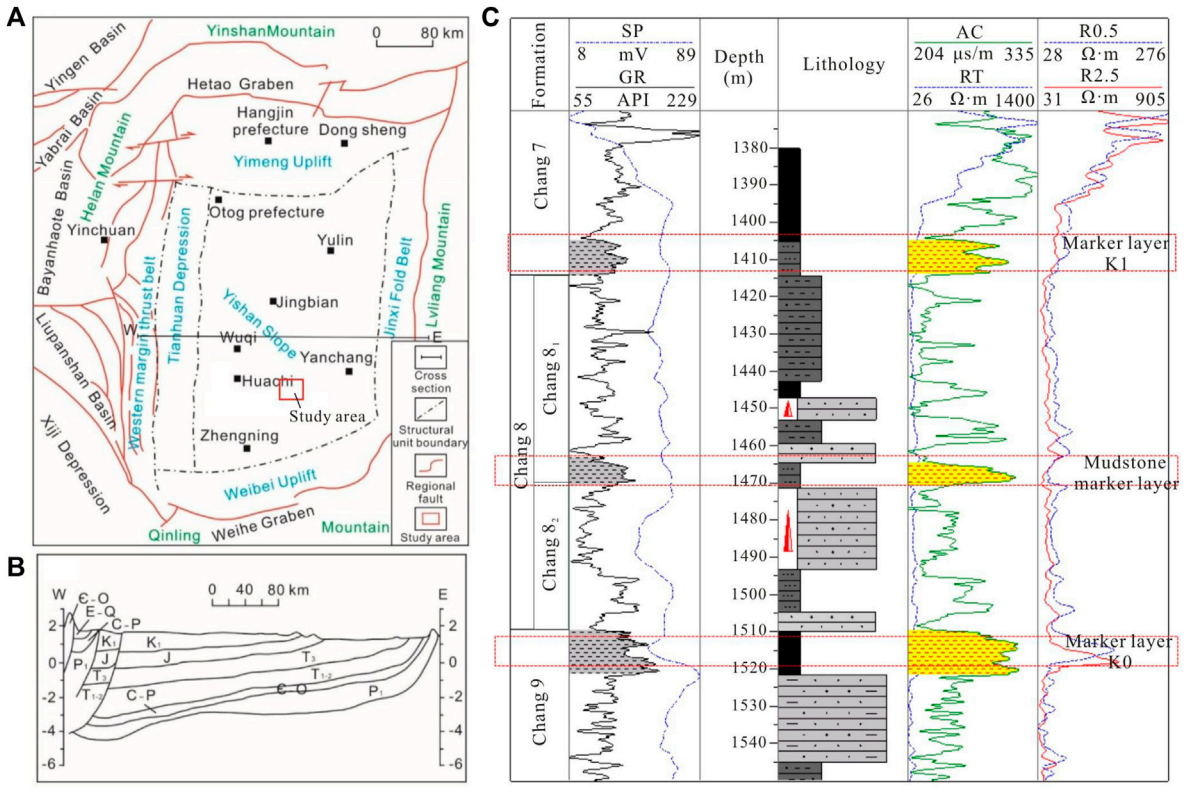

FIGURE 1
Location of the study area and division of the stratigraphic units of the Chang seven to Chang nine Members. **(A)** Location of the study area (Modified after Xiao et al., 2019); **(B)** East-west stratigraphic profile through the central part of the Ordos Basin; **(C)** Stratigraphic unit division of Chang seven to Chang nine Members.

surface porosity. X-ray diffraction experiments were used to determine the composition, crystal structure and content of various minerals and clays in the samples. The X-diffraction experimental instrument is a DMAX2500X diffractometer. Its 2θ angle measurement range: 10° ~ +154°; scanning step: 0.002°–90° (2θ/θ scan); 0.001°–90° (2θ scan); scanning speed: 0.002–100°/min (2θ/θ scan); 0.001°–100°/min (2θ scan). The instrument for physical property testing is a physical property testing system.

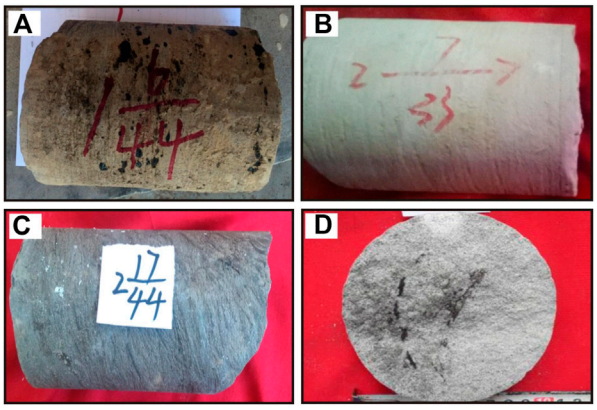

FIGURE 2
Sedimentary structures of the Chang 8 Member of Yanchang Formation in the study area. Notes: **(A)** Oil trace fine sandstone, Well L144, 1195.81 m; **(B)** Parallel bedding, Well L149, 1535.15 m; **(C)** Deformation bedding, Well L143, 1526.98 m; **(D)** Plant carbon fractions, Well L96, 1,526.98 m.

Results

Sedimentary facies type

The sedimentary facies markers should have special lithology in the vertical direction, and the electrical measurement curves should reflect clearly the special sedimentary environment (Bieniawski., 1967; Chalmers and Bustin., 2007; Chen et al., 2016). Therefore, it should have the characteristics of stable thickness and extensive development in the lateral direction.

That is to say, as a sedimentary facies marker of a sedimentary basin, it should not only be regionally extensive, but also have easy-to-identify characteristics (Lorenz and Finley., 1991; Lai and Wang., 2015; Lai et al., 2018; Mahmud et al., 2020).

(1) Color

Core observations show that the medium-fine sandstone and siltstone in the Yanchang Formation in the study area are gray-white and dark gray, and the mudstone is gray, gray-black, and black (Figure 2). It reflects that the target layer was a weak reduction-reduction depositional environment at that time (Liu et al., 2015; Mahmoodi et al., 2019; Liu B et al., 2020; Radwan., 2022).

(2) Special sedimentary structures

Parallel bedding, wavy bedding, sand-mud rhythmic bedding, and trough-like cross bedding can be seen widely in the cores of the target layer; however, contemporaneous deformation structures, carbonized plant debris, and thin coal seams can be seen in very few cores (Figure 2).

(3) Authigenic minerals

Although authigenic minerals are usually low in terrigenous clastic rocks. However, authigenic pyrite crystals are common in the mudstone of the Chang 8 Member in the study area, reflecting a strong reduction environment in deeper water.

The Chang 8 Member in the study area developed delta front subfacies, including underwater distributary channel and interdistributary bay microfacies. The delta front is located between the lake surface and the wave base, and is not only the main part of the delta deposition, but also the areas where the sandy sediments in the delta depositional facies are concentrated (Xiao et al., 2019; Liu J et al., 2020; Santosh and Feng., 2020; Radwan et al., 2021; Liu et al., 2022). According to different sedimentary characteristics and sedimentary facies markers, two microfacies of underwater distributary channel and inter-distributary bay were identified in Chang 8 Member of the study area. Among them, the underwater distributary channel has deposited large-scale sand bodies, which are the "main body" of the delta front.

The underwater distributary channel is the continuous extension of the distributary channel on the delta plain to the underwater, and the bottom of the channel is washed by water (Shuai et al., 2013; Shanley and Cluff 2015; Xu et al., 2021; Yin et al., 2018). Relatively coarse-grained fine-siltstone is found near the main channel, and relatively fine-grained siltstone, argillaceous siltstone, and mudstone are deposited along the underwater distributary channel farther out. Drilling coring observation shows that there are many parallel- and cross-beddings in the cores, and the grain size curve shows a common two-stage type (Figure 3). Curves such as natural gamma, resistivity, and sonic time difference show box- or bell-shaped features, indicating that the channel water flow has a strong sorting effect on sand bodies and bringing out and reforming fine-grained materials.

The inter-distributary bay is formed by the deposition of fine-grained silt mudstone and mudstone in a relatively quiet still water environment (Zhang et al., 2006; Wang and Wang., 2021; Xue et al., 2021; Yang et al., 2021). Drilling and coring observation of cores can show the development of horizontal bedding, lenticular bedding, and a few waves forming ripples. At the same time, plant debris and thin coal seams can be seen in the cores. The natural gamma and sonic time difference curves are all zigzag or small peaks with small fluctuations, reflecting the sedimentary characteristics of argillaceous components (Zeng et al., 2007; Yin and Wu., 2020; Zhang et al., 2020).

Sand body distribution characteristics

The sand bodies of the Chang 8 Member in the study area are relatively developed, and the continuity of sand bodies along the strike of the provenance is good (Figure 4). The thickness of the Chang 8_1 sand body is distributed between 5 and 45 m, with an average thickness of 20.5 m. The hydrocarbons are distributed in the upper, middle and lower parts of the Chang 8_1 oil group. The thickness of the Chang 8_2 sand body is distributed between 5 and 40 m, with an average thickness of 23.1 m. A set of relatively thick sand bodies developed in the upper part with good continuity, which is one of the main oil-rich sand layers in this area. Due to the frequent oscillation of the paleochannel, the multi-layered sand bodies develop vertically, and the sand bodies are not well connected in the lateral direction (Figure 4).

Petrological features

The underwater distributary channel of the delta front controls the scale of the reservoir sand bodies in the Chang 8 Member, and the formed sandstones are relatively simple in composition and micro-structures. The reservoirs are dominated by fine sandstone, silty sandstone and siltstone, and are generally characterized by low porosity, low permeability, low oil saturation, and low oil and gas production.

(1) Composition and content of debris components

The main mineral component in the sandstone clastic component is feldspar, accounting for 37–61%, with an average of 51.3%, followed by quartz, accounting for 15–37%, with an average of 23.5%, mainly single crystal quartz. The debris content is 1–16%, with an average of 5.5%. The rock debris are mainly metamorphic debris, the content is generally 1–8%, and

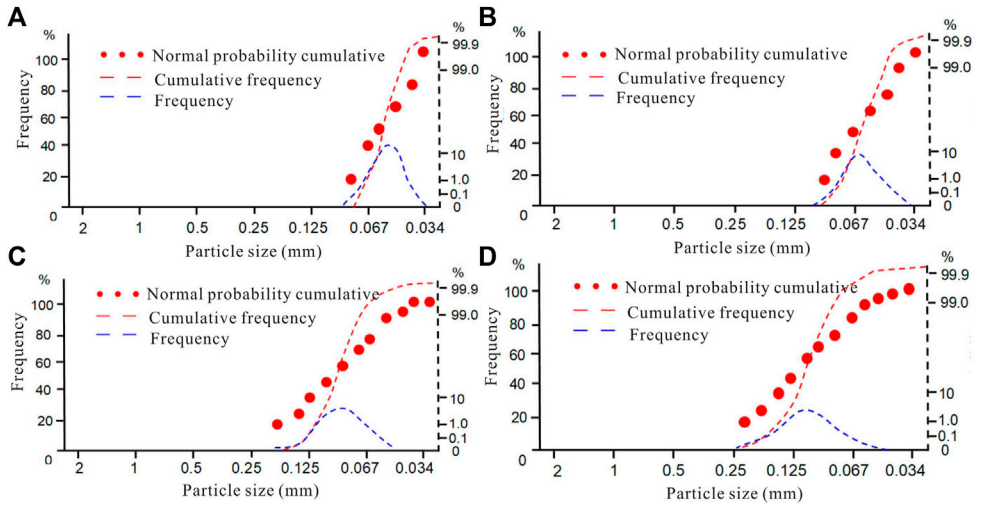

FIGURE 3
Probability accumulation curve of sandstone grain size in the Chang 8 Member of the study area. Notes: **(A)** Well L141, 1,534.2 m; **(B)** Well L143, 1,527.91 m; **(C)** Well L147, 1,449.12 m; **(D)** Well F100, 1,426.52 m.

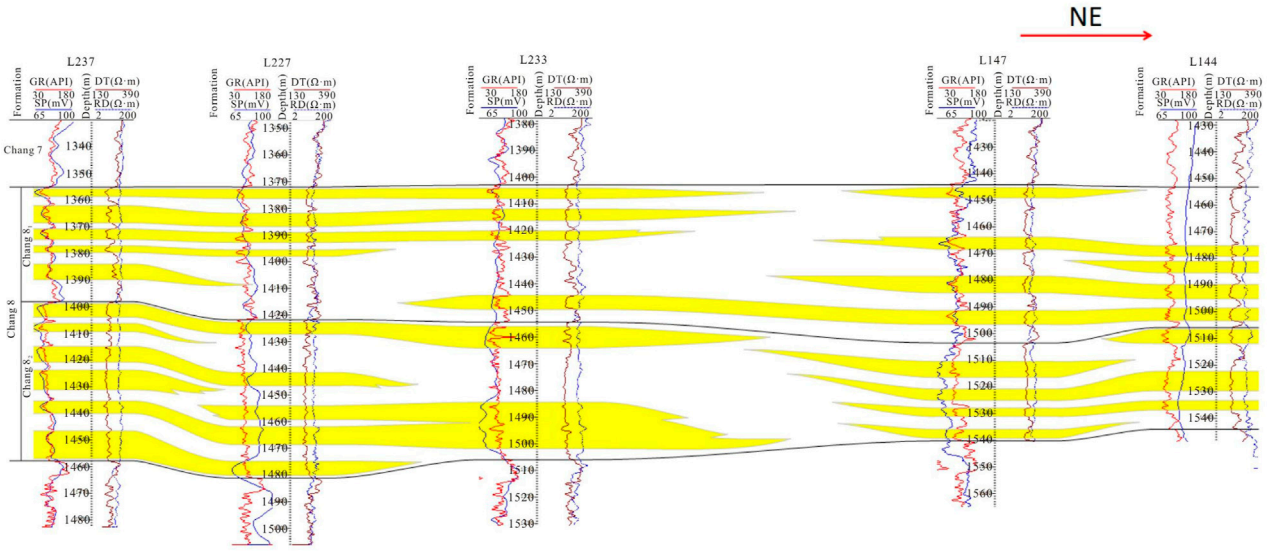

FIGURE 4
Profile of the sand layers (yellow) passing through Wells L237~L144.

the average is 3.4%. Followed by sedimentary rock debris, the content is generally 1–16%, with an average of 1.6%. Magmatic rock debris is the least, and the content is generally 2–5%, with an average of 0.5%; in addition, the content of mica varies greatly, with a content of 1–6%, with an average of 3.6%. The sandstone of the Chang 8 Member in the study area is mainly feldspar sandstone, followed by lithic feldspar sandstone (Figure 5).

(2) Composition and content of interstitials components

The content of cement was distributed between 4.1 and 26%, with an average of 14.91%. The matrix components are mainly mud, and the cements are mainly siderite, calcite, authigenic clay minerals (chlorite, illite, illite/smectite, etc.) and hydromica, followed by secondary growth of quartz and feldspar.

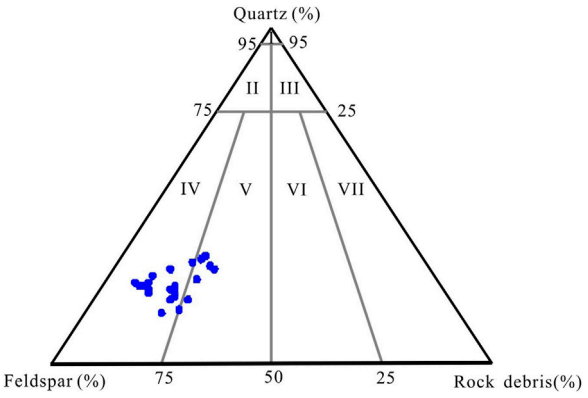

FIGURE 5
Classification triangular map of the Chang 8 sandstone in the study area. Notes: I-quartz sandstone; II-feldspar quartz sandstone; III-lithic quartz sandstone; IV- feldspar sandstone; V-lithic feldspar sandstone; VI- feldspar lithic sandstone; VII-lithic sandstone.

(3) Structural features

According to the identification of a large number of cast thin sections and the results of image particle size analysis, the clastic particles of the Chang 8 reservoir sandstone in the study area are mostly sub-angular-sub-circular, with moderate-to-good sorting, particle support, and line or point-line contacts. The local particles are in concave-convex contact, and the long axes are arranged in a slightly fixed direction.

The main types of cementation are pore-type and membrane-pore type cementation, followed by membrane type and pore-regenerative type cementation, and vitiated cementation can be seen locally. The particle size of most clastic particles is between 0.0625 and 0.25 mm, accounting for 82.14% of the statistical samples, and the median particle size is between 0.05 and 0.15 mm, which is dominated by fine sandstone, followed by silt-fine sandstone.

Discussion

Evaluation of diagenesis

From the perspective of the contribution of diagenesis to reservoir pores, it can be divided into: constructive and destructive diagenesis (Corbett et al., 1987; Chen et al., 1988).

(1) Constructive diagenesis

Constructive diagenesis is the diagenesis that increases the porosity and permeability of the reservoir, which include dissolution, metasomatism, and rupture (Gai et al., 2016; Li et al., 2018; Dong et al., 2020; Liu et al., 2021b).

① Dissolution

The Chang 8 sandstone reservoir in the study area contains a large amount of feldspar, zeolite, calcite and other easily soluble components, which can lead to the dissolution of sandstone components under certain circumstances. Due to the various changes in the environment of the rock, when the fluid in the pore medium has moderate organic acid content and geothermal conditions, some feldspars will be dissolved, resulting in secondary dissolution pores (Figure 6a~b). When the burial depth of the reservoir exceeds 2 km, the strong compaction also aggravates the dissolution. Mechanical dissolution will produce a large amount of H_2SO_4, which can promote the dissolution of quartz and feldspar components.

② metasomatism

Metasomatism is common in the Chang 8 reservoir sandstone in this area, including the alteration of clastic particles and the replacement of clastic particles by cement. The metasomatism of calcite to feldspar can be observed in the target layer, and it can also be seen that the edges of quartz grains are replaced by chlorite. During the metasomatism process, no new substances are produced, and no loss of mineral components occurs, so it has little effect on the quality of the reservoir (Figures 6C, D).

③ rupture

During core observation and thin section identification, various fractures formed by rock instability and fracture can be seen, including structural fractures and interlayer tension fractures (Figure 6E). The production scale of fractures varies, including obvious fractures that can be clearly observed with the naked eye, micro-fractures that can only be described under a microscope, and even hidden fractures or ultra-fine fractures that are difficult to observe under a microscope. The development of fractures can improve the porosity and permeability of the reservoir sandstone to a certain extent, and is also one of the important factors causing the strong heterogeneity of the Chang 8 reservoir in this area.

(2) Destructive diagenesis

Destructive diagenesis can increase the diagenesis of reservoir porosity and permeability, which includes mechanical compaction and cementation (Lima and Deros., 2003; Lommatzsch et al., 2015; Li et al., 2020).

① Mechanical compaction

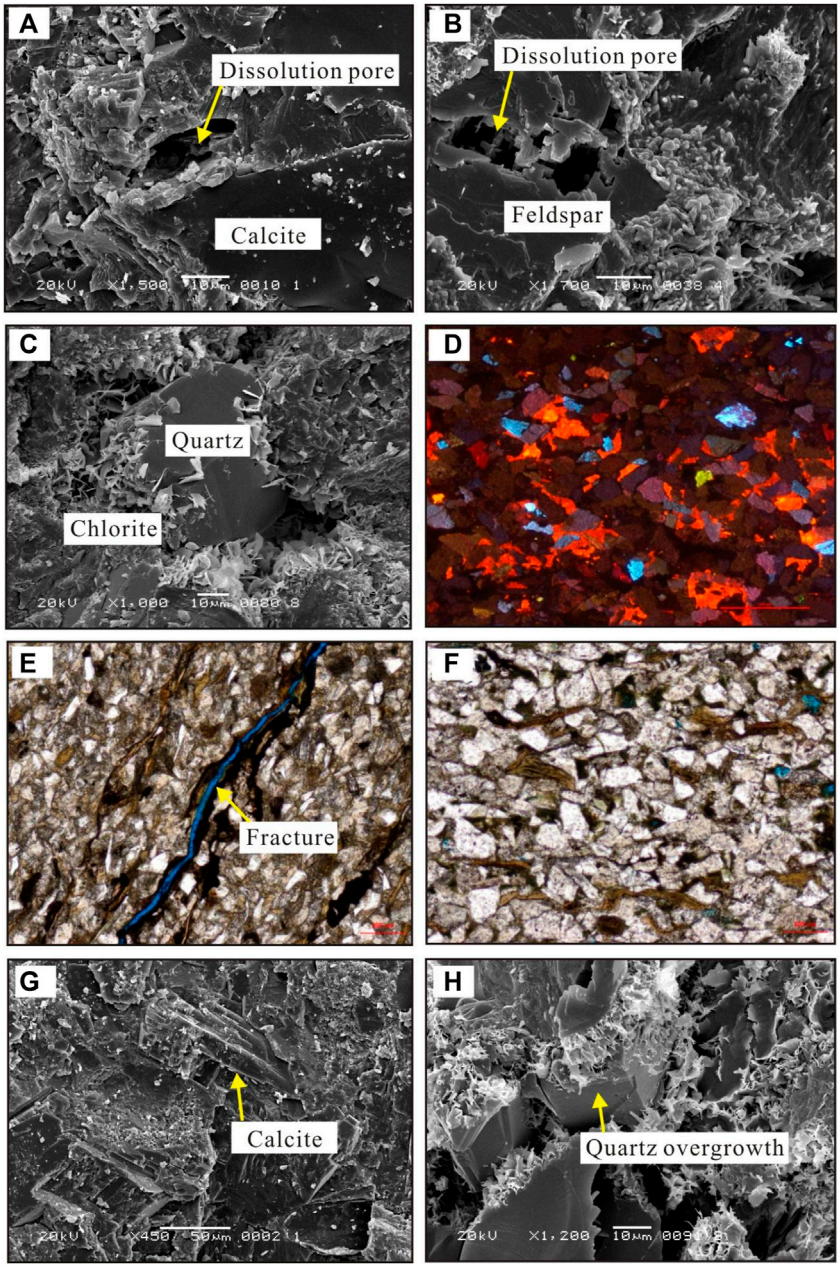

FIGURE 6
Images of microscopic features of different types of pores in the Chang 8 Member. Notes: **(A)** Calcite crystals are dissolved to form dissolution pores (Well L227, 1,429.41 m); **(B)** Feldspar particles were dissolved to form intragranular dissolution pores (Well L237, 1,412.67 m); **(C)** The edge of quartz crystal is replaced by chlorite, (Well L236, 1,412.68 m); **(D)** Feldspar particles were replaced by calcite, (Well L237, 1,412.17 m); **(E)** There are micro-fractures along the bedding direction (Well L227, 1,429.15 m); **(F)** Mica was compacted and deformed, (Well L237, 1,412.59 m); **(G)** Calcite crystals are filled between the detrital grains (Well L227, 1,429.15 m); **(H)** The secondary increase of quartz particles tends to be euhedral (Well L236, 1,415.85 m).

Mechanical compaction runs through the entire process of the burial diagenetic stage, and is one of the main reasons for the reduction of sandstone porosity (McBride., 1989; Moos and Zoback., 1990; Muhammad et al., 2014; Mirzaei-Paiaman and Ghanbarian., 2021). The main manifestations of compaction are: I-plastic deformation, distortion and pseudo-hybridization of I-plastic particles (mica, mudstone, epimetamorphic rock, and volcanic rock debris) (Figure 6F); II-brittle micro-cracks on the surface of rigid particles (quartz, feldspar, etc.) and their displacement and rearrangement; III-compacted directional

fabric, feldspar and mica are often oriented along the long axis direction; Ⅳ-tight packing of debris particles.

② cementation

There are three types of cementation in the Chang 8 clastic rock reservoir in the study area: carbonate, clay mineral and siliceous cementations (Qie et al., 2021; Tong et al., 2012; Zhao et al., 2020; Zeng et al., 2013). Calcite cementation is the most common in the Chang 8 sandstone reservoirs, and is widely distributed in sandstone. The content of carbonate cement in the sandstone of the oil interval is relatively low, generally 0.5–3%. It is usually partially filled with pores or flaky or continuously distributed in flaky shape, which has little effect on porosity loss. The carbonate content in the poor reservoir and tight sandstone is higher, and its content can reach 10–20%. The carbonates with large conjoined crystals fill most or even all of the intergranular pores and replace the clastic particles and interstitials such as feldspar and debris components. Furthermore, the primary intergranular pores are almost completely lost and become a dense barrier (Figure 6G).

The clay minerals include chlorite, illite/smectite, illite, and kaolinite in the clastic reservoirs of the Chang 8 Member in the study area. Among them, the most common one under scanning electron microscope is chlorite, whose content is generally 4–6%, with an average content of 5.55% and a maximum of more than 10%. Among the clay minerals, the average relative content of chlorite can reach 44.3%, followed by illite/smectite mixed layer and illite, with an average content of 2.27 and 2.25%, respectively; the content of kaolinite is the least, with an average content of 1.1%.

The siliceous cement is also widely distributed in the Chang 8 sandstone in this area, and the content is generally 0.5–2%, with an average of 1.0%. Under the scanning electron microscope, secondary enlarged siliceous cementation of quartz can be seen in the clastic rock reservoirs in the study area (Figure 6H), and the secondary enlarged edges of quartz show different colors. Overall, the development of siliceous cementation in the Yanchang Formation sandstone is relatively weak, and the average primary intergranular pores lost by siliceous cementation is 1.0%. However, siliceous cement will cause permanent damage to the pores.

(3) Diagenetic stage

According to previous studies, R_o<0.5% represents early diagenetic stage, R_o = 0.5–1.3% represents middle diagenetic stage A, R_o = 1.3–2.0% represents middle diagenetic stage B. Combined with the diagenetic mineral type and formation sequence of the I/S mixed layer clay in the Chang 8 sandstone in the study area, the vitrinite reflectance (R_o) in the mudstone in the study area is between 0.5 and 1.3%. Therefore, it can be determined that the Chang 8 reservoir in this area has entered the middle diagenetic stage A.

Microscopic pore structures of reservoir

(1) Pore types

The pore types of the target tight sandstone reservoir include intergranular pores, intragranular pores, interstitial pores and fractured pores. According to its origin, it can be divided into three categories: primary pores, secondary pores and fractures.

① Primary pores

Primary pores are the pores formed during the deposition of rocks, including primary intergranular pores and remaining intergranular pores (Price., 1966; Nelson., 1985; Qiao et al., 2020; Radwan and Sen., 2021a; Radwan and Sen., 2021b). Analysis and tests show that the primary pores in the Chang 8 reservoir in the study area mainly develop residual intergranular pores. This type of pore refers to a kind of pore that is not subject to obvious dissolution between skeleton particles due to normal compaction and cementation in the process of diagenetic evolution. Under the microscope, the particles around the pores have no obvious corrosion marks. Its shape is a triangular or irregular polygonal gap (Figures 7A, B).

② Secondary pores

Secondary pores include pores formed by diagenesis such as leaching, dissolution, and metasomatism.

Intergranular dissolution pores are secondary pores formed between particles after the dissolution of rock particles or cements (Shi et al., 2004; Xia et al., 2020; Yoshida and Santosh., 2020; Wang et al., 2021). They are mostly irregular under the microscope, with serrated or harbour-shaped edges. Intragranular dissolution pores are mainly secondary pores generated by local dissolution of feldspar or debris particles, that is, the particles themselves are partially dissolved. Through the observation of cast thin sections and scanning electron microscope, secondary pores generated by local dissolution of feldspar and cement particles are mainly seen in the Chang 8 sandstone in the area (Figures 7C, D). Under the microscope, the dissolution of feldspar particles is more common to form dissolved intergranular pores, and the pores are usually filled with various clay and crystalline minerals, resulting in finer pores in the reservoir and poor pore throat structures.

Intercrystalline pores mainly include intercrystalline micropores formed by the recrystallization of clay minerals,

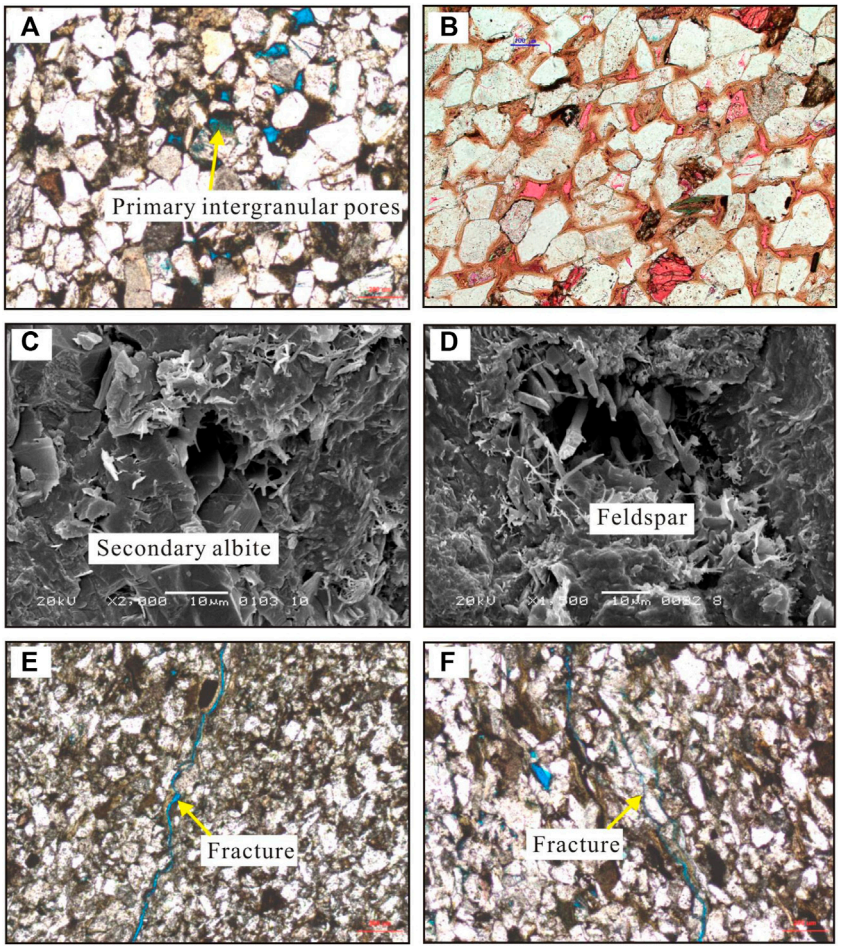

FIGURE 7
Microscopic characteristics of different types of pores in the Chang 8 reservoirs in the study area. Notes: **(A)** Well L227, residual intergranular pores, 1,429.48 m; **(B)** Well L136, residual intergranular pores, 1,527.54 m; **(C)** Well L236, secondary albite crystals in dissolution pores, 1,420.39 m; **(D)** Well L237, hair-like illite is attached to the feldspar dissolution pores, 1,417.91 m; **(E)** Well L237, micro-fractures developed between rock grains, 1,414.25 m; **(F)** Well L236, micro-fractures formed between rock grains, 1,420.46 m.

such as leaf-shaped chlorite intercrystalline micropores, irregular flaky or silky illite intercrystalline micropores, and illite intercrystalline micropores. . Such pores are generally small and poorly connected, and are of little significance for hydrocarbon accumulation.

③ fractures

Fractured pores include rock fissures and grain fissures, which are long and narrow pores and fissures formed by tectonic, mechanical compaction and shrinkage transformation of rocks. Such kind of pores are only developed in local sandstones, and are mainly interlayer horizontal fractures. Fractures develop along layers enriched with biotite or plant debris, and a small number of compression and tensional fractures of oblique bedding can be seen. The opening of microscopic cracks is generally less than 10–20 μm. Statistics show that the opening of the filling crack is relatively large and irregular, and the opening value of the same crack does not change much. The mesh-like micro-cracks are curved, and the opening value is also small. Generally, micro-fractures with an opening greater than 0.1 μm can become effective fractures for oil and gas migration. The opening of micro-fractures in this area is more than 0.1 μm, which can be used as oil and gas storage spaces and oil and gas seepage channels, and become effective fractures (Figures 7E, F).

The development of fractures can improve the porosity and permeability of the reservoir sandstone to a certain extent, and is also one of the important factors causing the strong heterogeneity of the Chang 8 reservoir in this area.

(2) Pore structure features

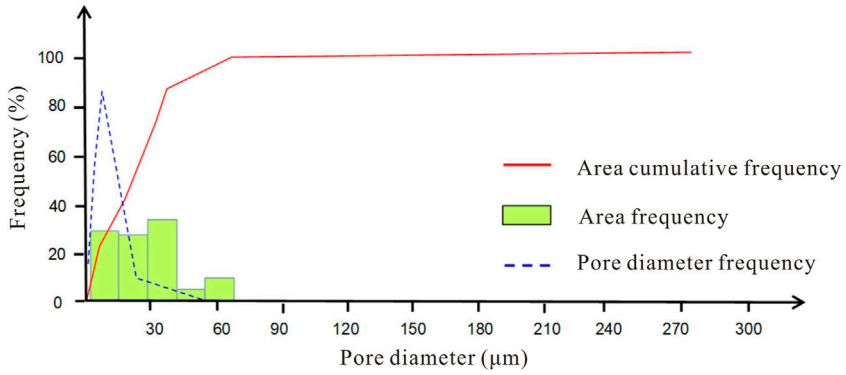

FIGURE 8
Statistical histogram of reservoir pores in the Chang 8 Member in the study area. Well L227, 1,429.15 m.

TABLE 1 Classification standard for pore and throat size of the Chang 8 reservoir in the study area (after Tang et al., 2014).

Pore level	Average pore diameter (μm)	Throat level	Average throat radius (μm)
Macropores	>80	Coarse throats	>3.0
Mesopores	80–50	Medium thin throats	3.0–1.0
Small pores	50–10	Thin throats	1.0–0.5
Thin pores	10–0.5	Micro - thin throats	0.5–0.2
Micropores	<0.5	Micro throats	<0.2

The pore structures of the reservoir rock refer to the geometry, size, distribution and interconnection of the pores and throats of the rock. The properties of the pore structure directly affect the storage performance of the reservoir rock.

Pore analysis of cast images shows that the pores in the Chang 8 reservoir in the study area are poorly developed, and the surface porosity is generally 0.3–2.0%, with an average of 1.33%. Pore shapes are mostly triangular, quadrilateral and irregular. The pore size distribution in a single sample ranges from 5 μm to more than 60 μm, the average pore size is generally 10–30 μm, and the arithmetic mean is 27.45 μm. Therefore, the pores belong to medium to small pores (Figure 8).

Based on the data of rock casting thin section, image pores and scanning electron microscope, the pore structures of the reservoir sandstone of the Chang 8 oil layer group in this area are divided into five types (Table 1).

Influencing factors of physical properties

The Chang 8 Member in the study area developed low-porosity-ultra-low permeability reservoirs. The reasons for their formation are complex and the result of the coupling of various geological factors.

(1) Sedimentation

Sedimentation is the basis for reservoir formation. The regional structure of this area is relatively gentle, and the distribution of oil reservoirs is mainly controlled by the delta front subfacies. The underwater distributary channel sand bodies of the delta front are good oil and gas reservoirs. Usually in the main channel area with good contiguousness and large thickness, the sand body is well sorted and the grain size is coarse. These areas are also blocks with high values of reservoir porosity and permeability, and the oil-bearing properties of the reservoirs are generally good (Figure 9).

(2) Burial compaction

As the overlying sediment thickens, the burial depth increases and the original porosity decreases. Besides being related to the burial depth, there are a lot of mica and epimetamorphic rock debris in the Chang 8 sandstone. During the compaction process, these plastic particles are easily deformed to form pseudo-hetero-bases to fill the original intergranular pores and reduce the physical properties of the reservoir. The analysis shows that there

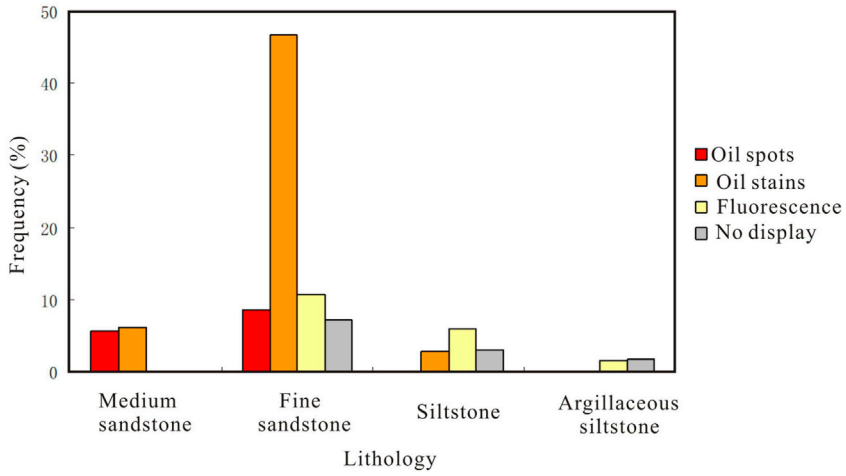

FIGURE 9
Coupling relationship between physical properties and lithology of the Chang 8 Member of Yanchang Formation.

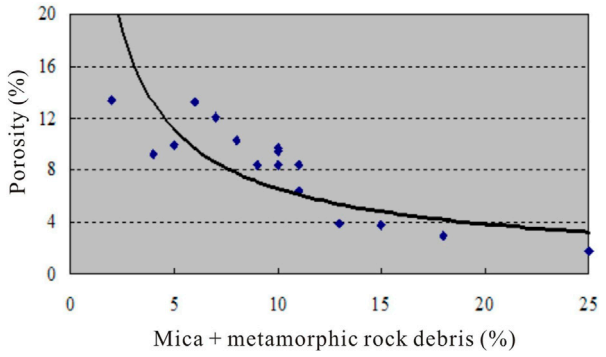

FIGURE 10
Relationship between the content of mica + metamorphic rock debris and porosity in the Chang 8 Member.

is a negative correlation between the content of detrital mica and porosity (Figure 10).

(3) Cementation

Cementation is the main reason affecting the physical properties of the Chang 8 reservoir, and the reduction in porosity can reach about 10% on average. Among all kinds of cementation, the effect of carbonate cementation (calcite, dolomite) is the most obvious. The carbonate cement content in the Chang 8 reservoir in the study area is 1–30%, with an average of 6.5%. The core analysis results show that the carbonate content has a negative relationship with the physical properties of the reservoir, and the higher the carbonate content, the worse the reservoir physical properties (Figure 11).

(4) Dissolution

Dissolution is the main constructive diagenesis. It mainly occurs in the middle-late diagenesis. During the thermal maturation of organic matter, a large amount of organic acid is produced, which dissolves aluminosilicate minerals such as feldspar and debris components. The secondary pores formed by dissolution account for 10–40% of the total surface porosity, with an average of 24%.

Controlling factors for hydrocarbon distribution

The Chang seven and Chang nine source rocks in the study area have wide distribution, large thickness and high hydrocarbon abundance. The sedimentary thickness of the underwater distributary channel sand in the Chang 8 delta front is relatively large, and it is in direct contact with the Chang nine and Chang seven source rocks. Therefore, the Chang 8 Member has the “innate advantageous conditions” for hydrocarbon accumulation.

(1) Controlling effect of local structures on hydrocarbon distribution

The westward dipping tectonic setting of the northern Shaanxi Slope provides the basic conditions for the migration of oil and gas to the eastern updip direction. The regional

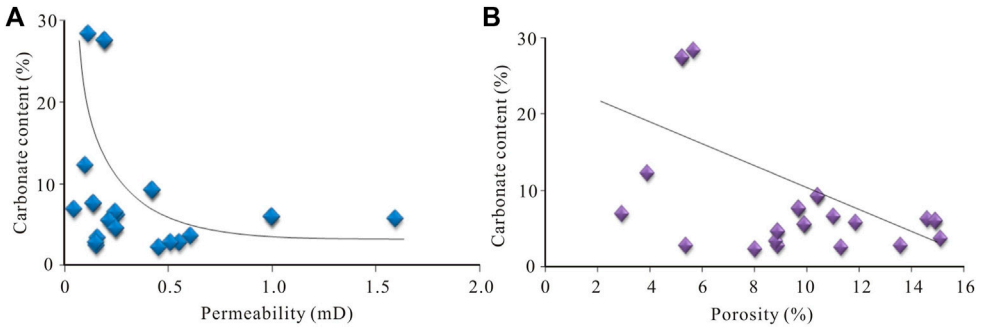

FIGURE 11
Relationship between physical parameters and carbonate content in the target layer. Noets: **(A)** Relationship between permeability and carbonate content; **(B)** Relationship between porosity and carbonate content.

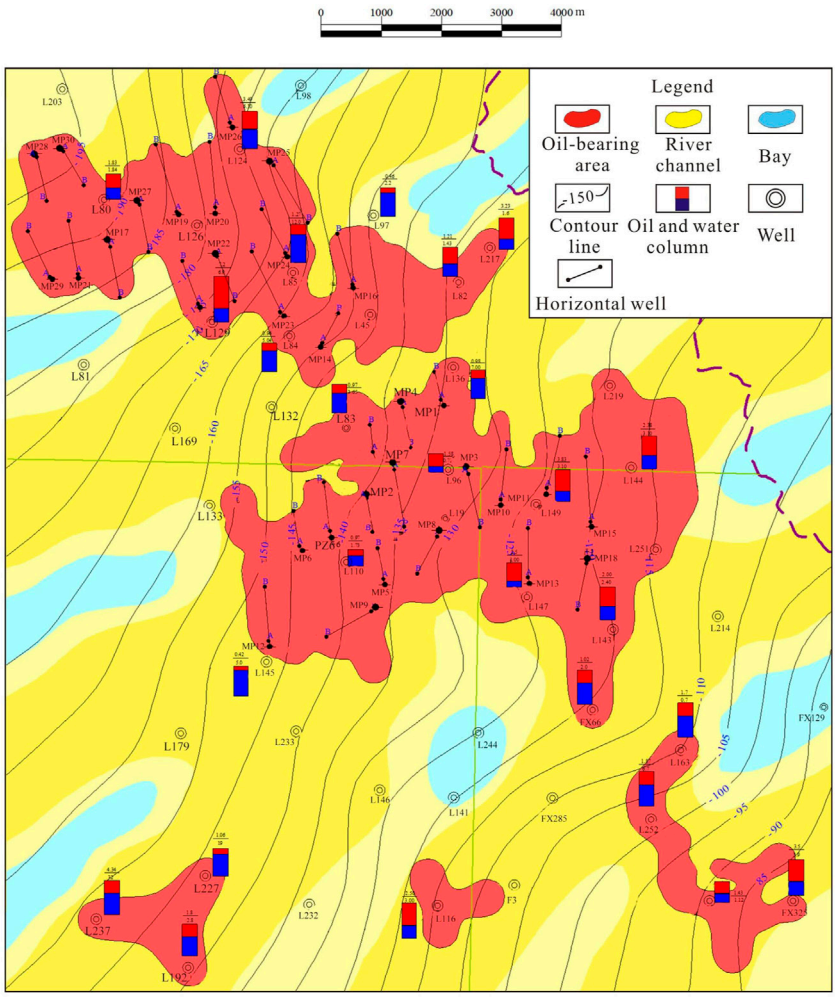

FIGURE 12
Superimposed relationship between the distribution of oil-bearing areas and structures and sedimentary facies (top of the Chang 8_2 sub-member).

structure of this area is a gentle west-dipping monocline, which slopes slightly to the northwest direction and develops a series of nose-shaped uplifts. In addition, the changes of lithology and physical properties in the updip direction of the structure form the blocking conditions for the continued migration of oil and gas, so the oil and gas can form various lithologic reservoirs in the updip direction of the structure. It can be seen from Figure 12 that the central and southern oil reservoirs are mainly distributed in the structural high parts; while some oil reservoirs in the northern part are distributed in relatively low parts. The production capacity of the central and southern reservoirs is significantly higher than the northern one. Therefore, the oil and gas enrichment degree is higher in the high structural parts.

(2) Controlling effect of sedimentary on hydrocarbon distribution

The Chang 8 Member in the study area is a delta front deposit, and mainly develops two microfacies of underwater distributary channel and underwater interdistributary bay. The oil reservoirs are mainly enriched in the main channel area, and the distribution of the oil reservoirs is obviously controlled by the change of the sedimentary facies belt (Figure 12). In addition, the main body of the reservoir is mainly distributed along the distributary channel of the delta front, and most of the distributary channel sandstone is more than 20 m thick. Horizontally, the multi-layer thick sand body distribution area is the main part of oil and gas accumulation. However, the reservoirs formed on the flanks of underwater distributary channels are thin and poorly sorted, which is not conducive to hydrocarbon accumulation.

Conclusion

1) The Chang 8 Member in the study area is a typical delta front subfacies deposit, including distributary channel and inter-distributary bay microfacies. The constructive diagenesis of the Chang 8 Member include dissolution, metasomatism and rupture; while the destructive diagenesis include mechanical compaction and cementation. The Chang 8 reservoir has entered the middle diagenetic stage A.

2) The factors affecting the physical properties of tight oil reservoirs include deposition, compaction, cementation and dissolution. The secondary pores formed by dissolution account for 10–40% of the total surface porosity, with an average value of 24%.

3) Local structures and sediments have significant control over hydrocarbon accumulation. The westward dipping tectonic setting of the northern Shaanxi Slope provides the basic conditions for the migration of oil and gas to the eastern updip direction. The changes of lithology and physical properties in the updip direction of the structure form the blocking conditions for the continued migration of oil and gas, which is conducive to the accumulation of oil and gas.

4) The main oil reservoirs are mainly distributed along the distributary channel of the delta front, and most of the distributary channel sandstone is more than 20 m thick. The distribution area of thick sand body with multiple layers in the lateral direction is the main part of oil and gas accumulation. However, the reservoirs formed on the flanks of underwater distributary channels are thin and poorly sorted, which is not conducive to the accumulation of hydrocarbons.

Data availability statement

The original contributions presented in the study are included in the article/supplementary material further inquiries can be directed to the corresponding author.

Author contributions

BL is responsible for the idea and writing of this paper and BZ, DW, CD, and FW are responsible for the logging interpretation and the experiments.

Conflict of interest

Authors BL and DW were employed by the Development Department, Yanchang Oifield Co., Ltd., author BZ was employed by the Zhidan Oil Production Plant, Yanchang Oilfield Co., LTD., author CD was employed by the Yulin Refinery, Yanchang Petroleum (Group) Co. LTD., and author FW was employed by the Jingbian Oil Production Plant, Yanchang Oilfield Co., LTD.

Publisher's note

References

Anovitz, L. M., Cole, D. R., Rother, G., Allard, L. F., Jackson, A. J., Littrell, K. C., et al. (2013). Diagenetic changes in macro- to nano-scale porosity in the st. Peter sandstone: an (ultra) small angle neutron scattering and backscattered electron imaging analysis. *Geochim. Cosmochim. Acta* 102, 280–305. doi:10.1016/j.gca.2012.07.035

Bieniawski, Z. T. (1967). Mechanism of brittle fracture of rock. *Int. J. Rock Mech. Min. Sci. Geomechanics Abstr.* 4, 407–423. doi:10.1016/0148-9062(67)90031-9

Cai, M. F. (2020). Key theories and technologies for surrounding rock stability and ground control in deep mining. *J. Min. Strata Control. Eng.* 2 (3), 033037. doi:10.13532/j.jmsce.cn10-1638/td.20200506.001

Cao, L., Yao, Y., Cui, C., and Sun, Q. (2020). Characteristics of *in-situ* stress and its controls on coalbed methane development in the southeastern qinshui basin, north china. *Energy Geosci.* 1 (1–2), 69–80. doi:10.1016/j.engeos.2020.05.003

Chalmers, G., Bustin, R. M., and Powers, I. (2009). *A pore by any other name would be as small: The importance of meso-and microporosity in shale gas capacity/*. Denver, Colorado: AAPG Annual Convention and Exhibition, 7–10.

Chalmers, G., and Bustin, R. M. (2007). The organic matter distribution and methane capacity of the lower cretaceous strata of northeastern british columbia, canada. *Int. J. Coal Geol.* 70 (1-3), 223–239. doi:10.1016/j.coal.2006.05.001

Chen, G. B., Li, T., Yang, L., Zhang, G. H., Li, J. W., and Dong, H. J. (2021). Mechanical properties and failure mechanism of combined bodies with different coal-rock ratios and combinations. *J. Min. Strata Control Eng.* 3 (2), 023522. doi:10.13532/j.jmsce.cn10-1638/td.20210108.001

Chen, Q., Zhang, J., Tang, X., Li, W., and Li, Z. (2016). Relationship between pore type and pore size of marine shale: an example from the sinian - cambrian formation, upper yangtze region, south china. *Int. J. Coal Geol.* 158, 13–28. doi:10.1016/j.coal.2016.03.001

Chen, Z. M., Zhang, S. L., and Wan, L. G. (1988). Gulong qingshankou mudstone north of structural cracks and reservoir distribution and prediction. *Pet. Technol.* 9, 5

Corbett, K. P., Friedman, M., and Spang, J. (1987). Fracture development and mechanical stratigraphy of Austin Chalk, Texas. *Am. Assoc. Pet. Geol.* 71, 17

Curtis, M. E., Cardott, B. J., Sondergeld, C. H., and Rai, C. (2012). Development of organic porosity in the woodford Shale with increasing thermal maturity. *Int. J. Coal Geol.* 103, 26–31. doi:10.1016/j.coal.2012.08.004

Dong, S., Zeng, L., Lyu, W., Xia, D., Liu, G., Wu, Y., et al. (2020). Fracture identification and evaluation using conventional logs in tight sandstones: a case study in the Ordos Basin, china. *Energy Geosci.* 1 (3–4), 115–123. doi:10.1016/j.engeos.2020.06.003

Gai, S., Liu, H., He, S., Mo, S., Chen, S., Liu, R., et al. (2016). Shale reservoir characteristics and exploration potential in the target: a case study in the longmaxi formation from the southern sichuan basin of China. *J. Nat. Gas Sci. Eng.* 31, 86–97. doi:10.1016/j.jngse.2016.02.060

Hong, D., Cao, J., Wu, T., Dang, S., Hu, W., Yao, S., et al. (2020). Authigenic clay minerals and calcite dissolution influence reservoir quality in tight sandstones: insights from the central junggar basin, NW China. *Energy Geosci.* 1 (1–2), 8–19. doi:10.1016/j.engeos.2020.03.001

Houben, M. E., Desbois, G., and Urai, J. L. (2013). Pore morphology and distribution in the shaly facies of opalinus clay(mont terri, Switzerland): insights from representative 2D BIB-sem investigations on mm to nm scale. *Appl. Clay Sci.* 71, 82–97. doi:10.1016/j.clay.2012.11.006

Lai, J., and Wang, G. (2015). Fractal analysis of tight gas sandstones using high-pressure mercury intrusion techniques. *J. Nat. Gas Sci. Eng.* 24, 185–196. doi:10.1016/j.jngse.2015.03.027

Lai, J., Wang, G. W., Wang, Z. Y., Chen, J., Pang, X. J., Wang, S. C., et al. (2018). A review on pore structure characterization in tight sandstones. *Earth-Science Rev.* 177, 436–457. doi:10.1016/j.earscirev.2017.12.003

Lan, S. R., Song, D. Z., Li, Z. L., and Liu, Y. (2021). Experimental study on acoustic emission characteristics of fault slip process based on damage factor. *J. Min. Strata Control Eng.* 3 (3), 033024. doi:10.13532/j.jmsce.cn10-1638/td.20210510.002

Li, D. Y., Wong, L. N. Y., Liu, G., and Zhang, X. P. (2012). Influence of water content and anisotropy on the strength and deformability of low porosity meta-sedimentary rocks under triaxial compression. *Eng. Geol.* 126, 46––66. doi:10.1016/j.enggeo.2011.12.009

Li, H. (2022). Research progress on evaluation methods and factors influencing shale brittleness: a review. *Energy Rep.* 8, 4344–4358. doi:10.1016/j.egyr.2022.03.120

Li, L., Huang, B., Li, Y., Hu, R., and Li, X. (2018). Multi-scale modeling of shale laminas and fracture networks in the Yanchang Formation, southern Ordos Basin, China. *Eng. Geol.* 243, 231–240. doi:10.1016/j.enggeo.2018.07.010

Li, X., He, Y., Huo, M., Yang, Z., Wang, H., Song, R., et al. (2019). Simulation of coupled thermal-hydro-mechanical processes in fracture propagation of carbon dioxide fracturing in oil shale reservoirs. *Energy Sources Part A Recovery Util. Environ. Eff.* 23, 1–20. doi:10.1080/15567036.2019.1676329

Li, Y., Zhou, D., Wang, W., Jiang, T., and Xue, Z. (2020). Development of unconventional gas and technologies adopted in China. *Energy Geosci.* 1 (1–2), 55–68. doi:10.1016/j.engeos.2020.04.004

Lima, R. D., and Deros, L. F. (2003). The role of depositional setting and diagenesis on the reservoir quality of devonian sandstones from the solimões basin, brazilian amazonia. *Mar. Petroleum Geol.* 19, 1047. doi:10.1016/s0264-8172(03)00002-3

Liu, B., He, S., Meng, L., Fu, X., Gong, L., Wang, H., et al. (2021a). Sealing mechanisms in volcanic faulted reservoirs in xujiaweizi extension, northern songliao basin, northeastern china. *Am. Assoc. Pet. Geol. Bull.* 105, 1721–1743. doi:10.1306/03122119048

Liu, B., Sun, J., Zhang, Y., He, J., Fu, X., Yang, L., et al. (2021b). Reservoir space and enrichment model of shale oil in the first member of Cretaceous qingshankou formation in the changling sag, southern Songliao Basin, NE China. *Petroleum Explor. Dev.* 48 (3), 608–624. doi:10.1016/S1876-3804(21)60049-6

Liu, Y., Chen, L., Tang, Y., Zhang, X., and Qiu, Z. (2022). Synthesis and characterization of nano-SiO_2@octadecylbisimidazoline quaternary ammonium salt used as acidizing corrosion inhibitor. *Rev. Adv. Mater. Sci.* 61 (1), 186–194. doi:10.1515/rams-2022-0006

Liu, Z. L., Fan, A. P., Li, Y. J., Du, Z. W., Zhao, Z. J., and Zhang, T. (2015). Constraints of clastic component difference on diagenesis: a case study of sandstone reservoirs in dong-2 block of the sulige gasfield, Ordos Basin. *Nat. Gas. Ind.* 35, 30–38.

Liu, B, B., Yang, Y., Li, J., Chi, Y., Li, J., Fu, X., et al. (2020). Stress sensitivity of tight reservoirs and its effect on oil saturation: a case study of lower cretaceous tight clastic reservoirs in the hailar basin, northeast China. *J. Petroleum Sci. Eng.* 184, 106484. doi:10.1016/j.petrol.2019.106484

Liu, J, J., Yang, H., Bai, J., Wu, K., Zhang, G., Liu, Y., et al. (2020). Numerical simulation to determine the fracture aperture in a typical basin of China. *Fuel* 283, 118952. doi:10.1016/j.fuel.2020.118952

Lommatzsch, M., Exner, U., Gier, S., and Grasemann, B. (2015). Dilatant shear band formation and diagenesis in calcareous, arkosic sandstones, Vienna Basin (Austria). *Mar. Petroleum Geol.* 62, 144–160. doi:10.1016/j.marpetgeo.2015.02.002

Lorenz, J. C., and Finley, S. J. (1991). Regional fractures: fracturing of mesaverde reservoirs in the piceance basin, Colorado. *Am. Assoc. Pet. Geol. Bull.* 75, 1738–1757.

Mahmoodi, S., Abbasi, M., and Sharifi, M. (2019). New fluid flow model for hydraulic fractured wells with non-uniform fracture geometry and permeability. *J. Nat. Gas Sci. Eng.* 68, 102914. doi:10.1016/j.jngse.2019.102914

Mahmud, H., Hisham, M., Mahmud, M., Leong, V., and Shafiq, M. (2020). Petrophysical interpretations of subsurface stratigraphic correlations, baram delta, sarawak, malaysia. *Energy Geosci.* 1 (3–4), 100–114. doi:10.1016/j.engeos.2020.04.005

McBride, E. F. (1989). Quartz cement in sandstones: a review. *Earth. Sci. Rev.* 26, 69–112. doi:10.1016/0012-8252(89)90019-6

Mirzaei-Paiaman, A., and Ghanbarian, B. (2021). A new methodology for grouping and averaging capillary pressure curves for reservoir models. *Energy Geosci.* 2 (1), 52–62. doi:10.1016/j.engeos.2020.09.001

Moos, D., and Zoback, M. D. (1990). Utilization of observations of well bore failure to constrain the orientation and magnitude of crustal stresses: application to continental, deep sea drilling project, and ocean drilling program boreholes. *J. Geophys. Res.* 95, 9305. doi:10.1029/jb095ib06p09305

Muhammad, A., Hammerschmidt, U., and Köhler, J. (2014). Thermophysical properties of a fluid- saturated sandstone. *Int. J. Therm. Sci.* 76, 43–50. doi:10.1016/j.ijthermalsci.2013.08.017

Nelson, R. A. (1985). *Geologic analysis of naturally fractured reservoirs: contributions in petroleum geology and engineering*. Houston: Gulf Publishing Company, 320–321.

Nie, H., Li, D., Liu, G., Lu, Z., Hu, W., Wang, Ru., et al. (2020). An overview of the geology and production of the Fuling shale gas field, Sichuan Basin, China. *Energy Geosci.* 1 (3–4), 147–164. doi:10.1016/j.engeos.2020.06.005

Price, N. J. (1966). *Fault and joint development in brittle and semi-brittle rock*. Oxford, England: Pergamon Press, 221–240.

Qiao, J., Zeng, J., Jiang, S., and Wang, Y. (2020). Impacts of sedimentology and diagenesis on pore structure and reservoir quality in tight oil sandstone reservoirs: implications for macroscopic and microscopic heterogeneities. *Mar. Petroleum Geol.* 111, 279–300. doi:10.1016/j.marpetgeo.2019.08.008

Qie, L., Shi, Y. N., and Liu, J. S. (2021). Experimental study on grouting diffusion of gangue solid filling bulk materials. *J. Min. Strata Control Eng.* 3 (2), 023011. doi:10.13532/j.jmsce.cn10-1638/td.20201111.001

Radwan, A. E., Abdelghany, W. K., and Elkhawaga, M. A. (2021). Present-day *in-situ* stresses in southern gulf of suez, egypt: insights for stress rotation in an extensional rift basin. *J. Struct. Geol.* 147. doi:10.1016/j.jsg.2021.104334

Radwan, A. E. (2022). "Chapter Two - three-dimensional gas property geological modeling and simulation," in *Sustainable geoscience for natural gas sub-surface systems*. Editors D. A. Wood and J. Cai (Elsevier), 29–45. Chapter 2 in. doi:10.1016/B978-0-323-85465-8.00011-X

Radwan, A. E., and Sen, S. (2021b). Characterization of *in-situ* stresses and its implications for production and reservoir stability in the depleted El Morgan hydrocarbon field, gulf of suez rift basin, egypt. *J. Struct. Geol.* 148. doi:10.1016/j.jsg.2021.104355

Radwan, A., and Sen, S. (2021a). Stress path analysis for characterization of *in situ* stress state and effect of reservoir depletion on present-day stress magnitudes: reservoir geomechanical modeling in the gulf of suez rift basin, Egypt. *Nat. Resour. Res.* 30, 463–478. doi:10.1007/s11053-020-09731-2

Santosh, M., and Feng, Z. Q. (2020). New horizons in energy geoscience. *Energy Geosci.* 1 (1–2), 1. doi:10.1016/j.engeos.2020.05.005

Shanley, K. W., and Cluff, R. M. (2015). The evolution of pore-scale fluid-saturation in low permeability sandstone reservoirs. *Am. Assoc. Pet. Geol. Bull.* 99, 1957–1990. doi:10.1306/03041411168

Shi, D. S., Li, M. W., Pang, X. Q., Chen, D. X., Zhang, S. W., Wang, Y. S., et al. (2004). Fault-fracture mesh petroleum plays in the zhanhua depressio, bohai bay basin: Part2. Oil-source correlation and secondary migration mechanisms. *Org. Geochem.* 36, 203–223.

Shuai, Y., Zhang, S., Mi, J., Gong, S., Yuan, X., Yang, Z., et al. (2013). Charging time of tight gas in the upper paleozoic of the Ordos Basin, central china. *Org. Geochem.* 64, 38–46. doi:10.1016/j.orggeochem.2013.09.001

Tang, Y., Song, Z., and Zhao, K. (2014). Characteristics and influencing factors of Chang 8 reservoir of Yanchang Formation in western Ordos Basin. *J. Lanzhou Univ. Sci.* 50 (6), 779–785+794. doi:10.13885/j.issn.0455-2059.2014.06.003

Tong, K. J., Zhao, C. M., Lu, Z. B., Zhang, Y. C., Zheng, H., Xu, S. N., et al. (2012). Reservoir evaluation and fracture chracterization of the metamorphicburied hill reservoir in bohai bay basin. *Petroleum Explor. Dev.* 39, 62–69. doi:10.1016/s1876-3804(12)60015-9

Wang, D. L., Hao, B. Y., and Liang, X. M. (2021). Slurry diffusion of singlefracture based on fluid-solid coupling. *J. Min. Strata Control. Eng.* 3 (1), 013038. doi:10.101638/td.20200429.001

Wang, J., and Wang, X. L. (2021). Seepage characteristic and fracture development of protected seam caused by mining protecting strata. *J. Min. Strata Control Eng.* 3 (3), 033511. doi:10.13532/j.jmsce.cn10-1638/td.20201215.001

Xia, Y. X., Lu, C., Yang, G. Y., Su, S. J., Pang, L. N., Ding, G. L., et al. (2020). Experimental study on axial fracture cutting and fracturing of abrasive jet in hard roof hole. *J. Min. Strata Control Eng.* 2, 033522.

Xiao, Z., Ding, W., Liu, J., Tian, M., Yin, S., Zhou, X., et al. (2019). A fracture identification method for low-permeability sandstone based on R/S analysis and the finite difference method: a case study from the Chang 6 reservoir in huaqing oilfield, Ordos Basin. *J. Petroleum Sci. Eng.* 174, 1169–1178. doi:10.1016/j.petrol.2018.12.017

Xu, Y., Zhang, H., and Guan, Z. (2021). Dynamic characteristics of downhole bit load and analysis of conversion efficiency of drill string vibration energy. *Energies* 14, 229. doi:10.3390/en14010229

Xue, F., Liu, X. X., and Wang, T. Z. (2021). Research on anchoring effect of jointed rock mass based on 3D printing and digital speckle technology. *J. Min. Strata Control Eng.* 3 (2), 023013. doi:10.13532/j.jmsce.cn10-1638/td.20201020.001

Yan, D. (2020). *Identification and evaluation of source rock and reservoir in tight oil from the 7th member of Yanchang Formation in the center of Lake basin, Ordos Bain*. Northwest University, 45–48. doi:10.27405/d.cnki.gxbdu.2020.002273

Yang, J. X., Luo, M. K., Zhang, X. W., Huang, N., and Hou, S. J. (2021). Mechanical properties and fatigue damage evolution of granite under cyclic loading and unloading conditions. *J. Min. Strata Control Eng.* 3 (3), 033016. doi:10.13532/j.jmsce.cn10-1638/td.20210510.001

Yin, S., Lv, D. W., and Ding, W. L. (2018). New method for assessing microfracture stress sensitivity in tight sandstone reservoirs based on acoustic experiments. *Int. J. Geomech.* 18 (4), 1–16. doi:10.1061/(asce)gm.1943-5622.0001100

Yin, S., and Wu, Z. (2020). Geomechanical simulation of low-order fracture of tight sandstone. *Mar. Petroleum Geol.* 100, 104359. doi:10.1016/j.marpetgeo.2020.104359

Yoshida, M., and Santosh, M. (2020). Energetics of the solid Earth: an integrated perspective. *Energy Geosci.* 1 (1–2), 28–35. doi:10.1016/j.engeos.2020.04.001

Zeng, L. B., Qi, J. F., and Li, Y. G. (2007). The relationship between fractures and tectonic stress field in the extra low-permeability sandstone reservoir at the south of western sichuan depression. *J. China Univ. Geosciences* 18, 223–231. doi:10.1016/s1002-0705(08)60003-5

Zeng, W. T., Zhang, J. C., Ding, W. L., Zhao, S., Zhang, Y. Q., Liu, Z. J., et al. (2013). Fracture development in paleozoic shale of chongqing area (South China). part one: fracture characteristics and comparative analysis of main controlling factors. *J. Asian Earth Sci.* 75, 251–266. doi:10.1016/j.jseaes.2013.07.014

Zhang, B., Shen, B., and Zhang, J. (2020). Experimental study of edge-opened cracks propagation in rock-like materials. *J. Min. Strata Control Eng.* 2 (3), 033035. doi:10.13532/j.jmsce.cn10-1638/td.20200313.001

Zhang, T., Switzer, P., and Journel, A. (2006). Filter-based classification of training image patterns for spatial simulation. *Math. Geol.* 38 (1), 63–80. doi:10.1007/s11004-005-9004-x

Zhao, Z., Wu, K., Fan, Y., Guo, J., Zeng, B., Yue, W., et al. (2020). An optimization model for conductivity of hydraulic fracture networks in the longmaxi shale, sichuan basin, southwest china. *Energy Geosci.* 1 (1–2), 47–54. doi:10.1016/j.engeos.2020.05.001

frontiers | Frontiers in Earth Science

ORIGINAL RESEARCH
published: 08 August 2022
doi: 10.3389/feart.2022.959796

Micro-Scale Pore-Throat Heterogeneity of Tight Oil Sandstone Reservoirs and Its Influence on Fluid Occurrence State

Qing Guo[1,2]*, *Mancang Dong*[3], *Hengbo Mao*[4] and *Jiangtao Ju*[5]

[1]Bailie School of Petroleum Engineering, Lanzhou City University, Lanzhou, China, [2]State Key Laboratory of Continental Dynamics, Northwest University, Xi'an, China, [3]Fuxian Oil Production Plant, Yanchang Petroleum (Group). Ltd., Fuxian, China, [4]No.12 Oil Production Plant, Changqing Oilfield Company, PetroChina, Qingyang, China, [5]No.5 Oil Production Plant, Changqing Oilfield Company, PetroChina, Xi'an, China

OPEN ACCESS

Edited by:
Wenlong Ding,
China University of Geosciences, China

Reviewed by:
Xiaowei Lv,
Chengdu University of Technology, China
Ying Tang,
Xi'an Shiyou University, China

***Correspondence:**
Qing Guo
qingguo133@126.com

Specialty section:
This article was submitted to Structural Geology and Tectonics, a section of the journal Frontiers in Earth Science

Received: 02 June 2022
Accepted: 15 June 2022
Published: 08 August 2022

Citation:
Guo Q, Dong M, Mao H and Ju J (2022) Micro-Scale Pore-Throat Heterogeneity of Tight Oil Sandstone Reservoirs and Its Influence on Fluid Occurrence State. Front. Earth Sci. 10:959796. doi: 10.3389/feart.2022.959796

Quantitatively characterizing the micro-scale heterogeneity of pore throats in tight sandstone reservoirs is the key to accurately describing the influence of pore structures on fluid occurrence characteristics. In this study, taking the Chang 6 Member of the Yanchang Formation in the Huaqing area of the Ordos Basin as an example, the pore-throat heterogeneity of tight sandstone reservoirs and its influence on the fluid occurrence state have been systematically studied using cast thin section, scanning electron microscope, X-ray diffraction, constant velocity mercury intrusion, and nuclear magnetic resonance tests. The main types of pores developed in the target layer were intergranular pores, followed by feldspar dissolution pores. The radius distribution of the intergranular pores is between 5.0 and 210 μm, with an average value of 50.27 μm. In addition, the pore combination types with the best petrophysical properties are the intergranular pore type, the intergranular-dissolution pore type, and the dissolution-intergranular pore type; the average permeability and porosity are 0.62 mD, 0.40 mD, 0.44 mD, and 12.0, 12.3, 12.3%, respectively. The target sandstones contain four typical T_2 relaxation time types. The large-pore-fine-throat combination reservoir has the best petrophysical properties. The larger the pore-throat uniformity value, the more uniform the pore-throat radius, and the greater the reservoir permeability. Therefore, the uniformity of throat development controls the seepage capacity of the tight reservoirs. The movable fluid saturation of different pore types has obvious differences. The movable fluid saturations at the 0.1 and 0.5 μm pore diameters of the macro-pore-fine-throat and macro-pore-micro-throat reservoirs both show an obvious inflection point, and the movable water saturation is higher with a larger throat radius.

Keywords: pore-throat heterogeneity, tight oil sandstone, fluid occurrence state, physical properties, permeability

1 INTRODUCTION

Tight oil reservoirs refer to oil layers such as sandstones and carbonate rocks with an overburden matrix permeability less than 0.2 mD or an air permeability less than 2 mD (Zou et al., 2012; Anovitz et al., 2013; Anovitz and Cole., 2015; Lai et al., 2018a; Cao et al., 2020). Tight sandstone reservoirs have the characteristics of small pore-throat size, strong heterogeneity, and complex pore structures (Lai and Wang., 2015; Cai, 2020; Hong et al., 2020; Bukar et al., 2021). The occurrence states and the final recoverability of oil and gas in tight reservoirs are the most concerning issues in the exploration and production of oil and gas (Gier et al., 2008; Desbois et al., 2011; Chen et al., 2014; Ghanizadeh et al., 2015; Lai et al., 2018b).

Reservoir heterogeneity is the inhomogeneous changes of the internal properties of reservoirs caused by the influence of depositional environment, diagenesis, and tectonic action during the deposition and burial processes (Kwak et al., 2017; Meng et al., 2017; Li et al., 2019; Hower and Groppo., 2021; Huang et al., 2021). Obviously, the sorting coefficients of pores and throats cannot accurately reflect the heterogeneity of the microscopic pore structures of tight sandstone reservoirs. In fact, in the reservoir storage of tight sandstone reservoirs, there are certain differences in the distribution of pore throats in different pore-throat intervals (Ma, 2005; Jiang et al., 2017; Pang et al., 2019; Liu et al., 2020; Kang, 2021). Therefore, quantitatively characterizing the micro-scale heterogeneity of pore-throats in tight sandstone reservoirs is the key to accurately describing the influence of pore structures on fluid occurrence characteristics (Lei et al., 2012; Sun et al., 2014; Li et al., 2019; Luo et al., 2019; Ren et al., 2019; Liu J et al., 2022). Pore-throat heterogeneity has a significant effect on tight reservoir permeability. The configuration of pores and roars determines the path of fluid flow and the resistance they need to overcome, which ultimately affects fluid flowability or reservoir permeability. Permeability is a core factor in determining reservoir productivity (Sun et al., 2014; Luo et al., 2019; Ren et al., 2019).

At present, the main problem in the efficient development of the Chang 6 Member of Yanchang Formation in the Ordos Basin is that the influence mechanism of microscopic pore structures on oil productivity is not clear. In this study, taking the Chang 6 Member of the Yanchang Formation in the Huaqing area of the Ordos Basin as an example, the pore-throat heterogeneity of tight sandstone reservoirs and its influence on the fluid occurrence state have been systematically studied using cast thin section, scanning electron microscope, X-ray diffraction, constant velocity mercury intrusion, and nuclear magnetic resonance tests. This study can provide scientific guidance for the scientific formulation of tight oil reservoir recovery programs.

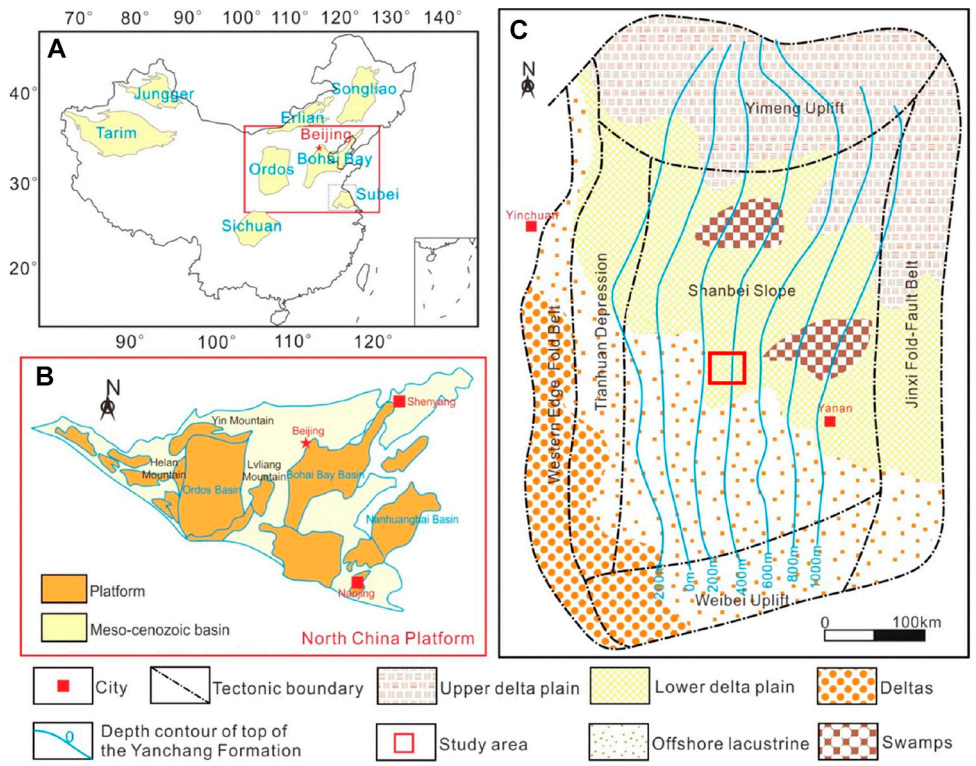

FIGURE 1 | Location of the study area (modified after Liu Y et al., 2022). **(A)** The study area is located in the Ordos Basin of the North China Plate; **(B)** The distribution of sedimentary basins in the North China Plate; **(C)** The study area is located in the central part of the Ordos Basin.

2 MATERIALS AND METHODS

2.1 Study Area

The study area is located in the Huaqing area of the Ordos Basin (**Figure 1**). The area is adjacent to the Changguan Temple in the north, the Resettlement Farm in the south, Yuancheng city in the west and Majiabian city in the east, with an area of about 6,150 km^2. Its tectonic location is located in the southern part of the Yishan Slope. The target layer is the Chang 6 Member of the Upper Triassic Yanchang Formation, and it belongs to the delta front facies deposits.

2.2 Constant-Rate Mercury Intrusion Technology

Constant-rate mercury intrusion technology can provide detailed information on pore structures by monitoring the pressure fluctuations during mercury injection. Constant-rate mercury intrusion can measure the number of throats during the experiments; it has overcome the shortcomings of conventional mercury intrusion. In this study, the mercury was injected into the core at a low injection rate (0.00005 ml/min). During the mercury injection process, the pressure drops and rises periodically, and the experiment ends when the pressure reaches 900 psi (6.2055 MPa).

An ASPE-730 constant-speed mercury intrusion device was used to conduct the constant-speed mercury intrusion experiments. The specific steps taken in the experiments are as follows:

(1) First, drilling a standard core with a diameter of 2.5 cm from a full-diameter core, then drying it at an experimental temperature of 23°C.
(2) Then, measuring the porosity of the standard core after drying via the gas measurement method.
(3) Using the gas measurement method to measure the permeability of the standard core after drying.
(4) Selecting representative standard cores for constant-rate mercury intrusion experiments.
(5) Evacuating the rock samples and immersing them in the mercury solution.
(6) Adjusting the experimental temperature to 25°C, the humidity to 65–75%, and the mercury injection rate to 0.000001 ml/s~1 ml/min. The contact angle was 140° and the surface tension was 485 dyne/cm. Real-time monitoring and automated data acquisition were output through computer systems.

2.3 Nuclear Magnetic Resonance Technology

The interior of the reservoir is saturated with three-phase fluids of oil, gas, and water. The occurrence states of these fluids in the reservoir can be divided into two categories: one is bound fluid state; the other is free fluid state. When the fluid-contained rock sample is in a static magnetic field, the hydrogen nuclei contained in the fluid are easily polarized by the magnetic field. NMR technology uses the inverse relationship between the hydrogen nuclear relaxation rate and the pore size of the reservoir rock to study the pore structures of rocks, and to determine the movable fluid saturation and the occurrence states of fluids of the reservoir. When the pore radius of the rock is too small, the fluid in it cannot flow due to the large capillary force and the specific surface binding effect. NMR experiments were used to determine the occurrence characteristics of movable fluids and the distribution of pore throats based on the T_2 spectral relaxation time and different spectral peak characteristics. The calculation relationship between the movable fluid porosity (Φ_m, %), the movable fluid saturation (S_m, %), and the water-measured porosity (Φ, %) is: $\Phi_m=S_m\times\Phi/100$.

A Magnet 2000 instrument was used to perform NMR T_2 measurements at a constant temperature of 20°C. The specific experimental steps are as follows:

(1) Selecting a representative standard core with a diameter of 2.5 cm.
(2) Drying the standard core.
(3) Measuring the porosity and air permeability of the samples.
(4) Saturating the samples with the simulated formation water (total salinity is 25,000 mg/L).
(5) Calculating the porosity of cores using the difference between the wet weight and the dry weight.
(6) Performing nuclear magnetic resonance T_2 measurements on the standard core saturated with simulated formation water.

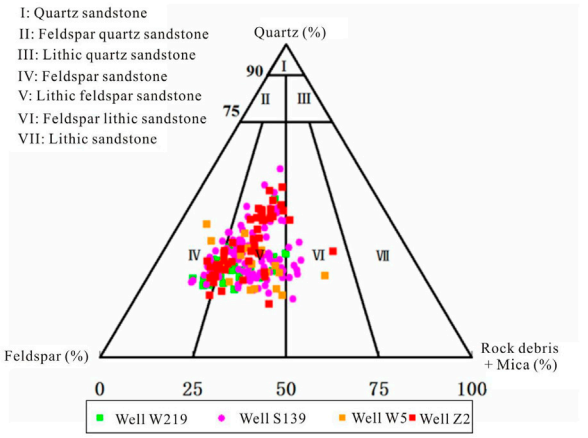

FIGURE 2 | Classification of sandstone lithology of the Chang 6 Member in the study area.

3 RESULTS

3.1 Rock Type and Mineral Composition

According to the observation results of cast thin sections, the sandstones of the Chang 6 oil layer group in this area have the characteristics of "low quartz and high feldspar content." The main lithologies of the Chang 6 Member include feldspar sandstone and lithic feldspar sandstone. The quartz content

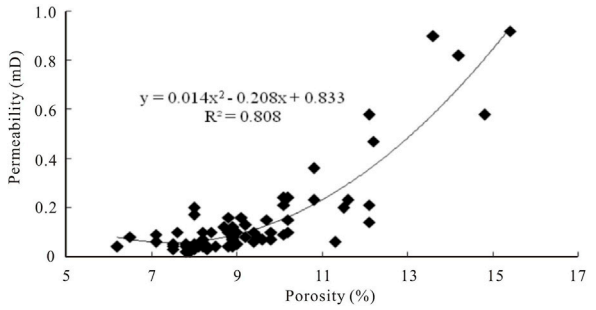

FIGURE 3 | Relationship between porosity and permeability of the samples in the target layer.

ranges from 28 to 30%, the feldspar content ranges from 34 to 40%, and the debris content ranges from 10 to 12% (**Figure 2**). The debris components are mainly composed of metamorphic rocks with a content of 5.5–7.5%, followed by the sedimentary rocks, with a content of 2.5–3.2%, and the igneous rocks, with a relatively small content of 1.2–2.5%. In addition, there are detrital minerals such as mica and chlorite.

According to the results of the cast thin sections of the rock samples, the maximum particle size distribution of the Chang 6 reservoir sandstone in the study area is 0.10–0.90 mm, and the main particle size is 0.01–0.50 mm. The cements of the Chang 6 sandstone mainly include hydromica, chlorite, iron calcite, iron dolomite, calcite, and siliceous components.

3.2 Reservoir Petrophysical Properties

The porosity of the Chang 6 reservoir in the study area is between 8 and 20.9%, the main interval is between 8 and 12%, and the average porosity is 11.6%; the permeability is between 0.08 and 17.49 mD, the main interval is between 0.1 and 0.5 mD, and the average permeability is 0.355 mD. Therefore, the Chang 6 Member belongs to the low-porosity-ultra-low-porosity, low-permeability-ultra-low permeability reservoir.

It can be seen from **Figure 3** that the correlation between the porosity and permeability of the samples satisfies the quadratic polynomial relationship, and the correlation coefficient is 0.808.

3.3 Pore Type

The main types of pores developed in the Chang 6 reservoir in the study area are intergranular pores, intergranular dissolution pores, feldspar dissolution pores, debris dissolution pores, and intercrystalline pores, among which intergranular pores and feldspar dissolution pores are the main ones.

Residual intergranular pores refer to the remaining part of the initial intergranular pores during deposition and filled with cements (**Figures 4A,B**). These pores are further subdivided into compacted intergranular pores, interstitial intergranular pores, and dissolution intergranular pores according to the degree of filling, dissolution, and compaction. The shapes of these pores are mostly polygonal, triangular, and irregular (Li and Zhang., 2011; Li et al., 2017). The samples mainly developed cement-type and dissolution-type intergranular pores. These pores generally exist between framework minerals, and the surface of the pores are often coated with chlorite, while secondary quartz is occasionally to be seen; the other kind of pores exists between the framework minerals and clay minerals, which are the products of clay minerals under compression and bending, and the pores are mostly triangular or meniscus. The absolute content of the intergranular pores is between 0.2 and 12.0%, with an average value of 3.81% and a relative average content of 71.06%. Statistics show that the radii of different types of pores vary greatly, and the pore radii of the target layer are mainly between 5.0 and 210 μm, with an average value of 50.27 μm. Intergranular pores are the main oil and gas storage space in the target layer.

The dissolution pores developed in the target layer are mainly feldspar dissolution pores, followed by the debris dissolution pores and the cement dissolution pores. Feldspar dissolution pores are the most important type of dissolution pores. It undergoes selective grain boundary and intragranular dissolution along the soluble part and cleavage of feldspar grains, and presents various pore morphologies, such as cleavage dissolution, mold dissolution, and irregular grain boundary dissolution (**Figures 4C,D**). The dissolution pores and intergranular pores of feldspar particles can be connected together to form super-large pores, and the pore sizes vary widely (15–200 μm). The absolute content of feldspar dissolution pores is between 0.1 and 2.0%, with an average content of 0.65%.

Intercrystalline micro-pores are also an important type of pore, which includes primary and secondary cement intercrystalline micro-pores (Luo et al., 2018; Mirzaei-Paiaman and Ghanbarian., 2021). It can be seen that the radius of such pores is generally less than 5 μm under the scanning electron microscope (**Figures 4E,F**). The primary intercrystalline micro-pores in the samples are mainly cleavage intercrystalline micro-pores of mica. The intercrystalline pores of framework minerals are generally formed by the dissolution of feldspar minerals. The intercrystalline micro-pores mainly include authigenic chlorite, illite, and micro-pores between secondary quartz. Statistics show that the absolute content of the intergranular micro-pores is between 0.01 and 0.6%, with an average value of 0.12%.

The final statistical results show that the pore combination types with the best petrophysical properties are the intergranular pore type, the intergranular-dissolution pore type, and the dissolution-intergranular pore type; their average permeability and porosity are 0.62 mD, 0.40 mD, 0.44 mD, and 12.0, 12.3, 12.3%, respectively. The micro-pore type has a small average pore size, low surface porosity, and the lowest seepage capacity.

3.4 Occurrence Characteristics of Movable Fluids

In this experiment, 13.895 ms was taken as the limit value of T_2 relaxation time of movable and bound fluids. Movable fluid saturation is the percentage of the amplitude of each point, with T_2 relaxation time greater than 13.895 ms on the T_2 spectrum. Conversely, the bound fluid saturation is the percentage of the amplitudes of the points where the T_2 relaxation time is less than 13.895 ms on the T_2 spectrum.

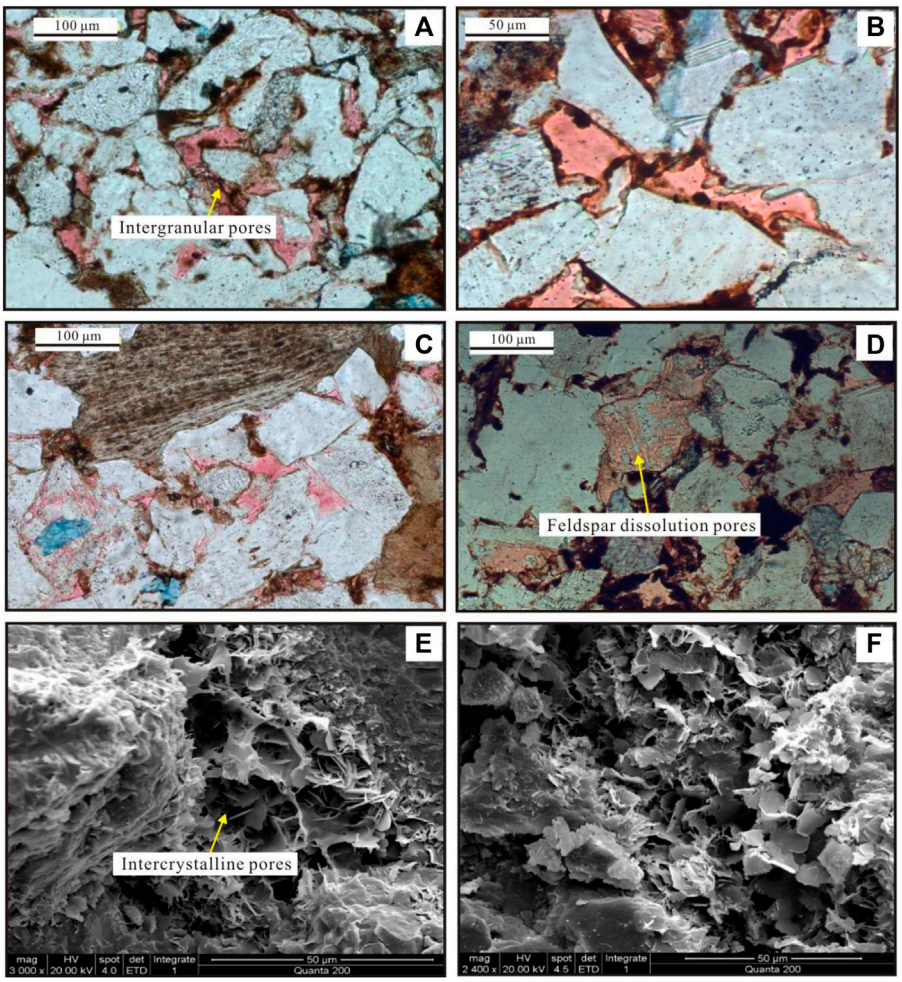

FIGURE 4 | Development characteristics of different types of pores in the target layer. **(A)** Intergranular pores, Well H259, 2,191.00 m; **(B)** Intergranular pores, Well H470, 2,140.8 m; **(C)** Feldspar dissolution pores, Well H408, 1,960.95 m; **(D)** Feldspar dissolution pores, Well H284, 2,181.95 m; **I** Illite and chlorite intercrystalline pores, Well H156, 2,084.28 m; **(F)** Illite and chlorite intercrystalline pores, Well H72, 2,069.00 m.

In order to achieve the comparative analysis of samples with different pore-throat matching relationships and different permeability levels, the screening of experimental samples has comprehensively considered the results of casting thin sections, scanning electron microscopy, and petrophysical property tests. On the basis of fully considering the characteristics of sedimentation and diagenesis, four groups of samples with different permeability levels were selected, respectively. Furthermore, in each group, one sample was selected for comparison of the microscopic pore structures.

The target sandstones contain four typical T_2 spectral relaxation time types (**Figure 5**):

(1) Bimodal type (the left peak is lower than right peak). For the first type, the H208 rock sample in **Figure 5A** is taken as an example, and its T_2 spectral distribution is bimodal type. The areas on both sides of the 13.895 ms time limit are basically equal, the movable fluid saturation is 45.55%, and the irreducible water saturation is 54.45%. It shows that the movable fluid saturation is slightly larger than the irreducible water saturation.

(2) Asymmetric unimodal type. The T_2 spectrum distribution of the H470 rock sample showed an asymmetric single peak type (**Figure 5B**). Its single peak is almost on the left side of the time limit of 13.895 ms, the movable fluid saturation is 11.37%, and the irreducible water saturation is 88.63%. This means that there are few movable fluids and a lot of bound water inside the rock;

(3) Bimodal type (the left peak higher than right peak). The T_2 spectrum distribution of the H518 rock sample is bimodal (**Figure 5C**). The area on the left side of the time limit of 13.895 ms is much larger than the area on the right side. The movable fluid saturation is 29.04%, and the irreducible water saturation is 70.96%. This means that the movable fluid saturation is less than the irreducible water saturation;

(4) Narrow single peak type. The T_2 spectrum of the H141 rock sample is a narrow single peak type (**Figure 5D**). The single-peak body is to the left of the 13.895 ms time limit. The

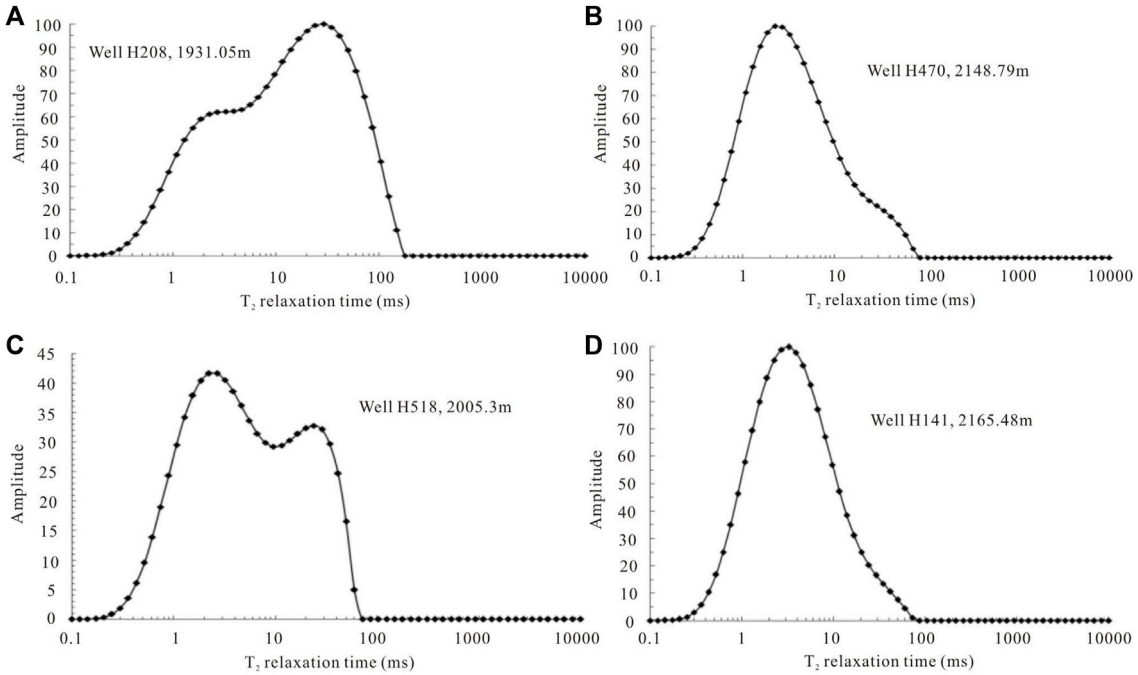

FIGURE 5 | Distribution characteristics of different types of T_2 relaxation times. **(A)** Well H208, 1931.05 m; **(B)** Well H470, 2148.79 m; **(C)** Well H518, 2005.3 m; **(D)** Well H141, 2165.48 m.

movable fluid saturation is 9.09%, and the irreducible water saturation is 90.91%.

This study shows that the T_2 spectral cutoff value of the low-permeability movable fluid is low, that the movable fluid saturation in the pores is low, and that the movable fluid saturation value and the movable fluid porosity value fluctuate greatly.

4 DISCUSSION

4.1 Correlation Between Pore Structure Parameters and Petrophysical Property Parameters

The pore-throat characteristic parameters of the capillary pressure curves of 28 samples were statistically analyzed, and the correlations between each pore-throat characteristic parameter and reservoir porosity and permeability were analyzed. The results show that the permeability has a good correlation with the displacement pressure and the maximum pore-throat radius, and the correlation coefficients are both 0.56 (**Figures 6A,B**). Moreover, the correlation between the porosity and the maximum mercury inflow saturation is also good, and it has a correlation coefficient of 0.51 (**Figure 6C**). However, the petrophysical parameters have poor or no correlation with other pore-throat characteristic parameters.

4.2 Influence of Pore-Throat Heterogeneity on Reservoir Physical Parameters and Permeability Contribution

Reservoir heterogeneity is the inhomogeneous change of internal properties caused by the influence of depositional environment, diagenesis, and tectonic action (Sebacher et al., 2017; Wang A. et al., 2018; Malatesta et al., 2018; Lan et al., 2021; Yang et al., 2021). Under the guidance of information entropy theory, this study takes different types of pore-throat assemblages and classifications as the starting point to construct a quantitative characterization model of pore-throat micro-scale heterogeneity in tight oil reservoirs.

(1) First, under the guidance of the information entropy theory, the information entropy of different pore and throat distributions is calculated using the MATLAB programming language:

$$H = -\sum_{i=1}^{m} z_i \ln z_i \quad (1)$$

where z_i is the percentage of the ith pore radius and throat radius, which is obtained from the frequency spectrum of the pore radius and throat radius distribution. When the travel frequency of different pores and throat sizes is the same, i.e. when $z_1=I...=z_n=1/N$, the entropy value reaches the maximum value of ln$N$, indicating that the size distribution of pores and throats has reached a uniform state.

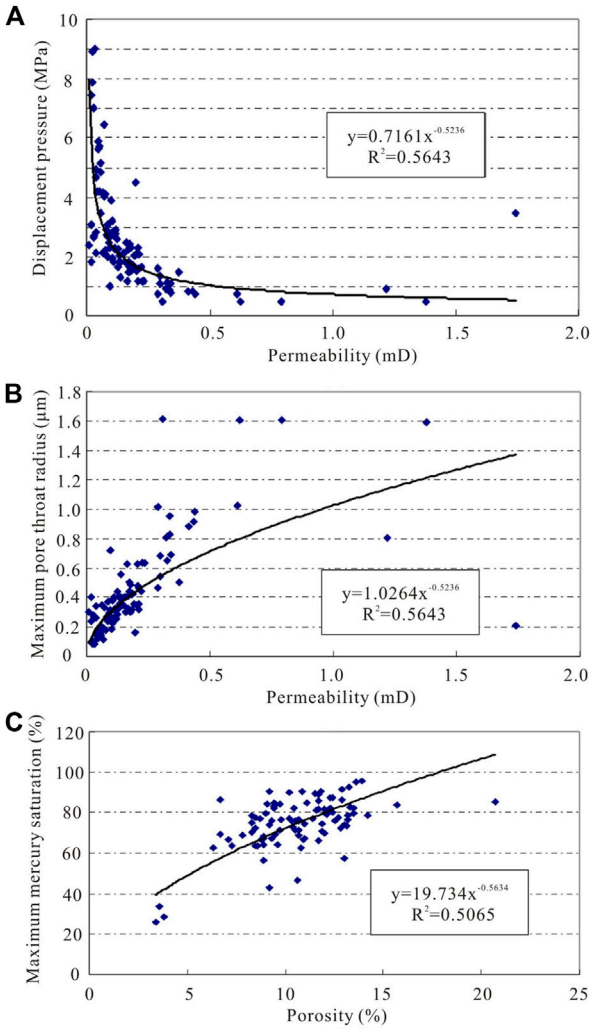

FIGURE 6 | Relationship between petrophysical property parameters and pore structure parameters. **(A)** Relationship between displacement pressure and permeability; **(B)** Relationship between maximum pore-throat radius and permeability; **(C)** Relationship between maximum mercury saturation and porosity.

In the same way, the information entropy can be used to analyze the relative uniformity of the size distribution of pore radii and throat radii within the interval of different pore radii and throat radii.

(2) In practical applications, there are differences in the size distribution characteristics of pores and throats of different types of pore-throat combination reservoirs (Meng et al., 2017; Huang et al., 2021). Therefore, the uniformity M (the ratio of the actual entropy value to the maximum entropy value) of the size distribution of pore radius and throat radius is introduced to characterize the uniformity of the size distribution of pores and throats in different types of pore-throat combination reservoirs, namely:

$$M = \frac{-\sum_{i=1}^{n}(z_i \ln z_i)}{\ln N} \tag{2}$$

The greater the uniformity, the more uniform the distribution of the parameter.

(3) In order to use the information entropy to determine the weight of pores and throats, and to solve the joint uniformity of pores and throats, the degree of dispersion of pores and throats is calculated first (Sebacher et al., 2017; Malatesta et al., 2018). Generally, the degree of dispersion of the jth index (pores, throats) depends on M_j:

$$h_j = 1 - M_j \tag{3}$$

The more dispersed the value of the jth index (pores, throats), the higher the importance of the jth index (pores, throats). Among all n indexes (pores, throats), the weight of the jth index (pores, throats) can be determined using **Eq. 4**.

$$w_j = \frac{h_j}{\sum_{i=1}^{n} h_j} \tag{4}$$

where j=1,2.

$$I = W_1 M_1 + W_2 M_2 \tag{5}$$

(4) Combining the uniformity information entropy of pores and throats, the generated joint uniformity information entropy I is:

Based on steps (3) and (4), combined with steps (1) and (2), the uniformity of pore radius and throat radius of six rock samples from the Chang 6 reservoir in the study area is obtained. The results are shown in **Table 1**.

It can be seen from **Table 1** that, for the reservoirs with macro-pore-micro-throat combination (rock samples H269, H470, and H141), the information entropy of the combined pore-throat uniformity ranges from 0.1240 to 0.0.5078, with an average value of 0.2593. For reservoirs with macro-pore-micro-throat combination (rock samples H518 and H259), the information entropy of the combined pore-throat uniformity ranges from 0.7301 to 0.0.7708, with an average value of 0.0.7504. The information entropy of the pore-throat uniformity of the H208 rock sample is 0.7693. The above results show that the pore-throat distribution of the reservoir with the macro-pore-fine-throat combination is the best, followed by the macro-pore-micro-throat combination, and the reservoir with the macro-pore-micro-throat combination has the worst pore-throat uniformity. This shows that the microscopic heterogeneity of the Chang 6 reservoir in the study area is mainly controlled by the uniformity of throat distribution.

The study found that the smaller the permeability of the sample, the more concentrated the distribution of the contribution of the throat to the rock permeability, and the larger the contribution peaks. With the gradual increase of rock permeability, the distribution interval of throats becomes

TABLE 1 | Pore-throat uniformity of reservoirs with different types of pore-throat combinations.

Number	Depth (m)	Porosity (%)	Permeability (mD)	Pore Uniformity	Throat Uniformity	Pore-throat Uniformity
H259	2,187.30	12.51	0.288	0.7249	0.8629	0.7708
H269	1,943.90	8.44	0.021	0.8224	0	0.1241
H470	2,148.79	9.77	0.031	0.7639	0	0.1460
H518	2,005.56	11.28	0.454	0.7269	0.7332	0.7301
H141	2,165.48	8.98	0.106	0.7304	0.4067	0.5078
H208	1,931.05	11.00	0.310	0.7324	0.8260	0.7693
H169	2,109.75	10.92	0.345	0.7295	0.7631	0.7409
H489	2,017.93	9.11	0.238	0.7345	0.6235	0.6792
H307	2,201.20	8.63	0.207	0.7296	0.5960	0.6537

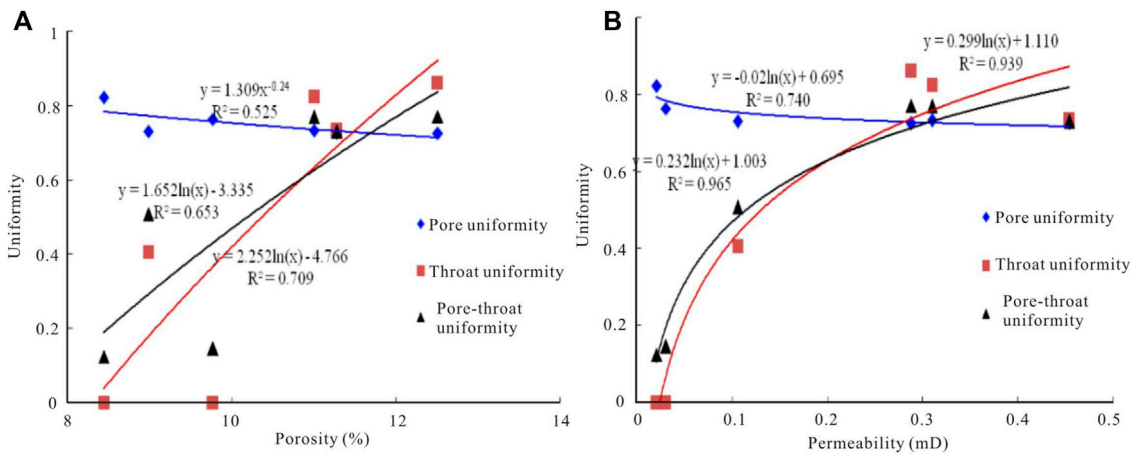

FIGURE 7 | Relationship between reservoir physical parameters and uniformity of pores and throats. **(A)** Relationship between porosity and uniformity; **(B)** Relationship between permeability and uniformity.

wider, the number of large throats increases, and the contribution of small throats to permeability decreases significantly. Then, the contribution of the large throats to the rock permeability increases, and the throat radius corresponds to the contribution peaks moves to the side of large throats. For example, the throat radii corresponding to the contribution peaks of the two samples of H208 and H518 are 1.1 and 0.6 μm, respectively. At this time, the number of large throats that mainly contribute to the rock permeability increases, and the peak value of the contribution decreases significantly. The fundamental reason for the poor petrophysical properties (especially permeability) of the low-permeability tight sandstones lies in the large proportion of small throats.

Statistics show that the H208 sample with a large-pore-fine-throat reservoir (permeability >0.3 mD, low permeability) has a peak throat radius of 1.1 μm, and the cumulative contribution to the rock permeability is 60.19%. For the H259 sample with macro-pore-micro-throat (permeability of 0.3 mD<K<0.1 mD, ultra-low permeability), the cumulative contribution of the permeability corresponding to the peak throat radius of 0.4 μm is 87.6%. In addition, the cumulative contribution of the permeability corresponding to the peak throat radius of 0.2 μm for the H141 sample with macro-pore-micro-throat (permeability K<0.1 mD) is 96.39%, and the main peak is in the micro-throat grade range.

It can be seen from **Figure 7** that the relationship between the permeability and uniformity of pore-throats is better than that of porosity. This is because permeability is the most direct factor determining the pore structures of tight reservoirs, while porosity is an indirect factor.

The pore uniformity is negatively correlated with the porosity, and the correlation coefficient R^2 is 0.525. This shows that the larger the value of the pore uniformity, the more uniform the development degree of pores, but the reservoir porosity will decrease; the throat uniformity is positively correlated with porosity, and the correlation coefficient R^2 is 0.653, indicating that the larger the throat uniformity value, the more uniform the development degree of throats, and the greater the reservoir porosity; in addition, the pore-throat uniformity is positively correlated with porosity, and the correlation coefficient R^2 is 0.709, indicating that the larger the pore-throat uniformity value, the more uniform the pore-throat boundary, and the greater the reservoir porosity (Rezaee et al., 2012; Mahmud et al., 2020; Mohammed et al., 2021).

The comparative results show that the uniformity of the throat development controls the effectiveness of the reservoir space

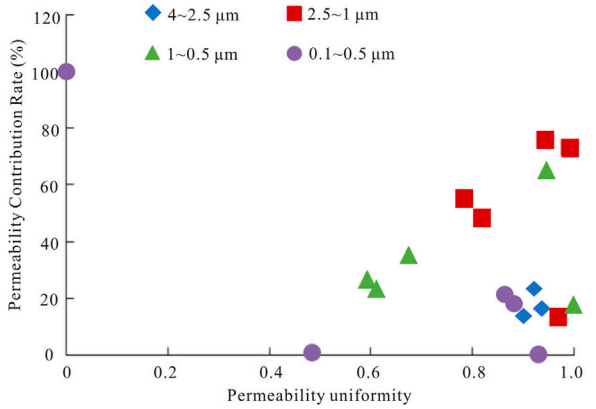

FIGURE 8 | Relationship between uniformity at different scales and permeability contribution of throats.

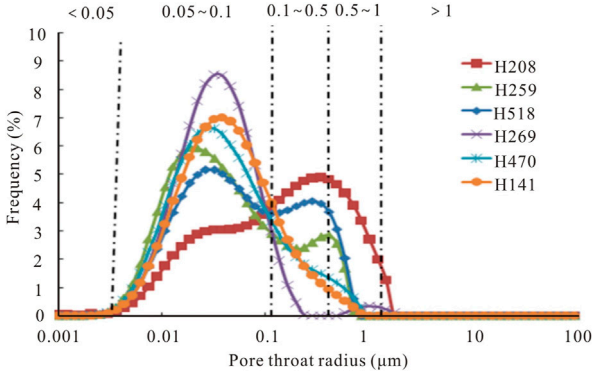

FIGURE 9 | Distribution frequencies of the pore-throat radius of the samples.

(Shanley and Cluff., 2015; Xi et al., 2016; Qiao et al., 2020; Qie et al., 2021). The pore uniformity is negatively correlated with permeability, and the correlation coefficient R^2 is 0.749, indicating that the larger the pore uniformity value, the more uniform the pores, but the reservoir permeability will decrease; the throat uniformity is positively correlated with porosity, and the correlation coefficient R^2 is 0.939, indicating that the larger the throat uniformity value, the more uniform the throats, and the greater the reservoir permeability; the pore-throat uniformity is positively correlated with rock permeability, and the correlation coefficient R^2 is 0.978, indicating that the larger the pore-throat uniformity value, the more uniform the pore-throat radius, and the greater the reservoir permeability. Therefore, the uniformity of throat development controls the seepage capacity of the reservoir (Zhao et al., 2015; Saein and Riahi., 2017; Yin et al., 2018; Santosh and Feng., 2020; Zhang et al., 2020).

It can be seen from **Figure 8** that the throat radius between 2.5 and 4.0 μm is only developed in the macro-pore-micro-throat combination type reservoir (H518 rock sample), but the contribution to permeability is relatively small (only 16.61%). This shows that the throats of 2.5–4.0 μm are less developed in this type of reservoir, thus it has little effect on the seepage capacity of the reservoir. When the throat radius is between 1.0 and 2.5 μm, the reservoirs of the large-pore-fine-throat (H208 rock sample) and the large-pore-micro-throat combination (H259, H518 rock samples) are uniformly developed. However, the reservoirs with macro-pore-micro-throat combination do not develop such kind of throats. The distribution of the uniformity (0.9917) and the permeability contribution (73.26%) of the throats of the large-pore-fine throat (rock sample H208) in this interval are better than those of the large-pore-micro-throat combination (rock samples H259 and H518). This shows that the throats of the 1.0–2.5 μm interval control the seepage capacity of the large-pore-fine-throat combination reservoirs. However, its effect on the seepage capacity of the reservoir with large pores and fine throats (the average permeability contribution is 34.02%) is relatively small. When the throat radius is between 0.5 and 1.0 μm, the reservoirs of the large-pore-fine-throat (H208 rock sample) and the large-pore-micro-throat combination (H259, H518 rock samples) are uniformly developed. However, reservoirs with macro-pore-micro-throat combination do not develop such kind of throats. The average value of throat uniformity (0.9718) and the average value of permeability contribution (41.455%) in the large-pore-micro-throat combination (rock samples H259 and H518) in this interval are better than those of the macro-pore-fine-throat (H208 rock sample). This shows that the throat radius of 0.5–1.0 μm can control the seepage capacity of the reservoir with the macro-pore-micro-throat combination better than the reservoir of the macro-pore-fine-throat combination (the uniformity of throat is 0.5931, and the permeability contribution is 26.73%). When the throat radius is between 0.1 and 0.5 μm, all kinds of reservoirs develop such throats. Among them, the throat uniformity (0.9308) of the large pores and fine throats (H208 rock sample) in this interval is better than that of other reservoirs. However, in terms of contribution to the seepage capacity of the reservoir, this type of throat is the most developed in the macro-pore-micro-throat reservoir, and the permeability contribution value (100%) is the largest. The second is the reservoir with macro-pore-micro-throat combination (the average permeability contribution is 11.13%). However, in the reservoir with large-pore-fine-throat combination, this type of throat contributes the least to the seepage capacity of the reservoir (the contribution value of permeability is 0.001%).

4.3 Influence of Pore-Throat Heterogeneity on Fluid Occurrence

Statistical results show that, when the throat radius is greater than 0.1 μm, the corresponding movable fluid percentages in the macro-pore-fine-throat, macro-pore-micro-/fine-throat, and macro-pore-micro-throat reservoirs are 45.55%, 24.45%, and 7.54%, respectively. When the throat radius is in the range of 0.1–0.5 μm, the corresponding movable fluid saturations of the macro-pore-fine-throat, macro-pore-micro-/fine-throat, and macro-pore-micro-throat reservoirs are 34.19, 24.11%, and 7.02%, respectively. When the throat radius is in the range of 0.5–1.0 μm, the corresponding movable fluid saturations of the macro-pore-fine-throat, macro-pore-micro-/fine-throat, and macro-pore-micro-throat reservoirs are 8.24, 0.34, and 0.43%, respectively. When the throat radius is

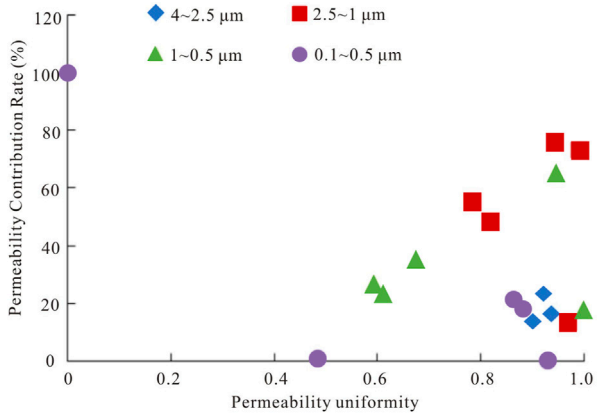

FIGURE 10 | Relationship between pore-throat heterogeneity at different scales and movable fluid saturation.

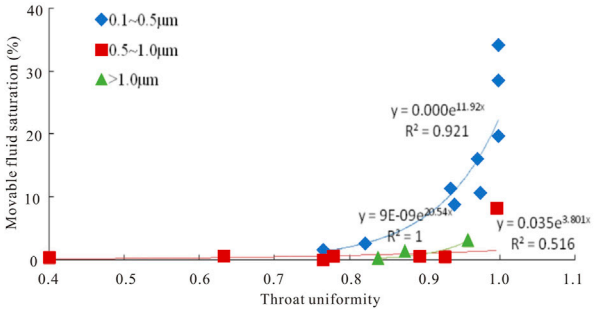

FIGURE 11 | Relationship between throat heterogeneity at different scales and movable fluid saturation.

greater than 1.0 μm, the corresponding movable fluid saturations of the macro-pore-fine-throat, macro-pore-micro-/fine-throat, and macro-pore-micro-throat reservoirs are 3.12%, 0, and 0.09%, respectively.

The movable fluids of different pore types have obvious differences (Wang L. et al., 2018; Shi et al., 2019; Yin and Wu, 2020; Zhou et al., 2021). Among them, the macro-pore-fine-throat reservoirs have the highest movable fluid saturation, followed by the macro-pore-micro-/fine-throat reservoirs, while the macro-pore-micro-throat reservoirs have the lowest movable fluid saturation. The macro-pore-fine-throat and macro-pore-micro/-fine-throat types show obvious inflection points at 0.1 and 0.5 μm, and the larger the throat radius, the higher the movable water saturation (**Figure 9**).

It can also be seen from **Figure 8** that the crude oil in the pore throat corresponding to the pore-throat radius >1.0 μm is preferentially produced and the remaining oil is less. However, most of the crude oil in the pore throats within the pore-throat radius of 0.1–1.0 μm is recovered. The distribution of the residual fluid is closely related to its existing pore structures (Zhang et al., 2019; Yoshida and Santosh., 2020; Wang et al., 2021; Xue et al., 2021). The distribution of the T_2 spectrum is different, and the remaining fluid volume and the states are different. Large-pore-fine-throat reservoirs have developed intergranular and dissolution pores, with large effective pore space and high residual movable fluid content. However, the remaining movable fluid is the least in the macro-pore-micro-throat type reservoirs.

4.4 Relationship Between Pore-Throat Heterogeneity at Different Scales and Movable Fluid Saturation

It can be seen from **Figure 10** that with the increase of core permeability, the movable oil saturation increases. The change trend of the movable oil controlled by different pore-throat radius is different. When the pore-throat radius is between 0.1 and 0.5 μm and with the peak point of permeability (0.03 and 0.3 mD) as the boundary, there is a good correspondence between the permeability and the change of movable oil saturation. Especially when the permeability is less than 0.10 mD and greater than 0.3 mD, the movable oil first increases and then decreases with the permeability and pore development degree. When the pore-throat radius is between 0.5 and 1.0 μm, the movable oil saturation first increases and then decreases with the permeability and pore development degree. When the permeability is greater than 0.3 mD and the intergranular and dissolution pores are relatively developed, the movable oil saturation tends to be opposite, with the development degree of pores due to the small throat radius. When the pore-throat radius is greater than 1.0 μm, the combination types of intergranular and dissolution pores develop, and the permeability boundary is 0.3 mD, but the movable oil changes little with the permeability and the degree of pore development. The above analysis shows that the change trend of movable oil is the largest in the range of pore-throat radius of 0.1–0.5 μm; however, when the permeability is larger and the intergranular pores are developed, the movable oil saturation shows a decreasing trend and fluctuates greatly (Zhang et al., 2006; Zhao et al., 2017; Zhong, 2017).

The relationship between pore-throat uniformity and movable fluid saturation at different scales is shown in **Figure 11**. It can be seen from **Figure 11** that there is a good exponential relationship between the pore-throat heterogeneity of different scales and the movable fluid saturation in the macro-pore-fine-throat, macro-pore-micro-/fine-throat, and macro-pore-micro-throat reservoirs. In the pore-throat range of 0.1–0.5 μm, 0.5–1.0 μm, and greater than 1.0 μm, the greater the uniformity of the pore throat, the greater the saturation of the movable fluids. Intergranular and dissolution pores are mainly developed in the pore-throat interval larger than 1.0 μm, and the relationship between pore-throat uniformity and movable fluid saturation is the best, followed by the 0.1–0.5 μm pore-throat interval. This is mainly because only a small amount of intergranular and dissolution pores are retained in this pore-throat interval, and intercrystalline and micro-pores are mainly developed (Zou et al., 2012; Zhu et al., 2013). In the pore-throat range of 0.5–1.0 μm, the relationship between the pore-throat uniformity and the movable fluid saturation is the worst. This is mainly due to the development of intergranular and dissolution pores, as well as intercrystalline pores and micro-pores.

5 CONCLUSION

(1) The main types of pores developed in the target layer are intergranular pores, followed by feldspar dissolution pores. The radius distribution of the intergranular pores is between 5.0 and 210 μm, with an average value of 50.27 μm. In addition, the pore combination types with the best petrophysical properties are the intergranular pore type, the intergranular-dissolution pore type, and the dissolution-intergranular pore type; their average permeability is 0.62 mD, 0.40 mD, 0.44 mD, and their average porosity is 12.0, 12.3, 12.3%, respectively.

(2) The target sandstones contain four typical T_2 relaxation time types. The large-pore-fine-throat combination reservoir has the best petrophysical properties. The larger the pore-throat uniformity value, the more uniform the pore-throat radius, and the greater the reservoir permeability. Therefore, the uniformity of throat development controls the seepage capacity of the tight reservoirs.

(3) The movable fluid saturation of different pore types has obvious differences. The movable fluid saturations at the 0.1 and 0.5 μm pore diameters of the macro-pore-fine-throat and macro-pore-micro-throat reservoirs both show an obvious inflection point, and the movable water saturation is higher with a larger throat radius.

DATA AVAILABILITY STATEMENT

The original contributions presented in the study are included in the article/Supplementary Material; further inquiries can be directed to the corresponding author.

AUTHOR CONTRIBUTIONS

The first author (QG) is responsible for the technical idea and the remaining authors (MD, HM, and JJ) are responsible for the experimental part of this study.

FUNDING

This research was supported by the Opening Foundation of State Key Laboratory of Continental Dynamics, Northwest University, "Quantitative characterization and evaluation of micro nano pore structure of tight reservoir based on multifractal theory (No. 21LCD05)" and Doctoral Research Fund of Lanzhou City University, "Study on micro pore structure and seepage mechanism of unconventional tight reservoir in Ordos Basin (No. LZCU-BS2021-01)."

REFERENCES

Anovitz, L. M., and Cole, D. R. (2015). 4. Characterization and Analysis of Porosity and Pore Structures. *Rev. Mineral. Geochem.* 80 (1), 61–164. doi:10.1515/9781501502071-004

Anovitz, L. M., Cole, D. R., Rother, G., Allard, L. F., Jackson, A. J., and Littrell, K. C. (2013). Diagenetic Changes in Macro- to Nano-Scale Porosity in the St. Peter Sandstone: an (Ultra) Small Angle Neutron Scattering and Backscattered Electron Imaging Analysis. *Geochimica Cosmochimica Acta* 102, 280–305. doi:10.1016/j.gca.2012.07.035

Bukar, M., Worden, R. H., Bukar, S., and Shell, P. (2021). Diagenesis and its Controls on Reservoir Quality of the Tambar Oil Field, Norwegian North Sea. *Energy Geosci.* 2 (1), 10–31. doi:10.1016/j.engeos.2020.07.002

Cai, M. F. (2020). Key Theories and Technologies for Surrounding Rock Stability and Ground Control in Deep Mining. *J. Min. Strata Control. Eng.* 2 (3), 033037. doi:10.13532/j.jmsce.cn10-1638/td.20200506.001

Cao, L., Yao, Y., Cui, C., and Sun, Q. (2020). Characteristics of *In-Situ* Stress and its Controls on Coalbed Methane Development in the Southeastern Qinshui Basin, North China. *Energy Geosci.* 1 (1–2), 69–80. doi:10.1016/j.engeos.2020.05.003

Chen, D., Pang, X., Xiong, L., Wang, L., and Xie, M. (2014). Porosity Evolution in Tight Gas Sands of the Upper Triassic Xujiahe Formation, Western Sichuan Basin, China. *Rev. Mex. Ciencias Geol.* 31, 361–375.

Desbois, G., Urai, J. L., Kukla, P. A., Konstanty, J., and Baerle, C. (2011). High-resolution 3D Fabric and Porosity Model in a Tight Gas Sandstone Reservoir: A New Approach to Investigate Microstructures from Mm- to Nm-Scale Combining Argon Beam Cross-Sectioning and SEM Imaging. *J. Petroleum Sci. Eng.* 78, 243–257. doi:10.1016/j.petrol.2011.06.004

Ghanizadeh, A., Clarkson, C. R., Aquino, S., Ardakani, O. H., and Sanei, H. (2015). Petrophysical and Geomechanical Characteristics of Canadian Tight Oil and Liquid-Rich Gas Reservoirs: I. Pore Network and Permeability Characterization. *Fuel* 153, 664–681. doi:10.1016/j.fuel.2015.03.020

Gier, S., Worden, R. H., Johns, W. D., and Kurzweil, H. (2008). Diagenesis and Reservoir Quality of Miocene Sandstones in the Vienna Basin, Austria. *Mar. Petroleum Geol.* 25 (8), 681–695. doi:10.1016/j.marpetgeo.2008.06.001

Hong, D., Cao, J., Wu, T., Dang, S., Hu, W., and Yao, S. (2020). Authigenic Clay Minerals an Calcite Dissolution Influence Reservoir Quality in Tight Sandstones: Insights from the Central Junggar Basin, NW China. *Energy Geosci.* 1 (1–2), 8–19. doi:10.1016/j.engeos.2020.03.001

Hower, J. C., and Groppo, J. G. (2021). Rare Earth-Bearing Particles in Fly Ash Carbons: Examples from the Combustion of Eastern Kentucky Coals. *Energy Geosci.* 2 (2), 90–98. doi:10.1016/j.engeos.2020.09.003

Huang, F. R., Yan, S. X., Wang, X. L., Jiang, P. C., and Zhan, S. B. (2021). Experimental Study on Infrared Radiation Characteristics of Gneiss under Uniaxial Compression. *J. Min. Strata Control. Eng.* 3 (1), 013011. doi:10.13532/j.jmsce.cn10-1638/td.20200730.001

Jiang, T., Zhang, J., and Wu, H. (2017). Effects of Fractures on the Well Production in a Coalbed Methane Reservoir. *Arab. J. Geosci.* 10 (22), 494. doi:10.1007/s12517-017-3283-7

Kang, H. P. (2021). Temporal Scale Analysis on Coal Mining and Strata Control Technologies. *J. Min. Strata Control. Eng.* 3 (1), 013538. doi:10.13532/j.jmsce.cn10-1638/td.20200814.001

Kwak, D., Han, S., Han, J., Wang, J., Lee, J., and Lee, Y. (2018). An Experimental Study on the Pore Characteristics Alteration of Carbonate during Waterflooding. *J. Petroleum Sci. Eng.* 161, 349–358. doi:10.1016/j.petrol.2017.11.051

Lai, J., and Wang, G. (2015). Fractal Analysis of Tight Gas Sandstones Using High-Pressure Mercury Intrusion Techniques. *J. Nat. Gas Sci. Eng.* 24, 185–196. doi:10.1016/j.jngse.2015.03.027

Lai, J., Wang, G., Wang, S., Cao, J., Li, M., Pang, X., et al. (2018b). Review of Diagenetic Facies in Tight Sandstones: Diagenesis, Diagenetic Minerals, and Prediction via Well Logs. *Earth-Science Rev.* 185, 234–258. doi:10.1016/j.earscirev.2018.06.009

Lai, J., Wang, G., Wang, Z., Chen, J., Pang, X., Wang, S., et al. (2018a). A Review on Pore Structure Characterization in Tight Sandstones. *Earth-Science Rev.* 177, 436–457. doi:10.1016/j.earscirev.2017.12.003

Lan, S. R., Song, D. Z., Li, Z. L., and Liu, Y. (2021). Experimental Study on Acoustic Emission Characteristics of Fault Slip Process Based on Damage Factor. *J. Min. Strata Control Eng.* 3 (3), 023038. doi:10.13532/j.jmsce.cn10-1638/td.20210510.002

Lei, T., Bikash, K. S., and Michael, S. (2012). Estimation of Horizontal Stress Magnitudes and Stress Coefficients of Velocities Using Borehole Sonic Data. *Geophysics* 77 (3), 181–196. doi:10.1190/geo2011-0277.1

Li, G., Qin, Y., Shen, J., Wu, M., Li, C., Wei, K., et al. (2019). Geochemical Characteristics of Tight Sandstone Gas and Hydrocarbon Charging History of Linxing Area in Ordos Basin, China. *J. Petroleum Sci. Eng.* 177, 198–207. doi:10.1016/j.petrol.2019.02.023

Li, H., and Zhang, J. (2011). Elastic Moduli of Dry Rocks Containing Spheroidal Pores Based on Differential Effective Medium Theory. *J. Appl. Geophys.* 75, 671–678. doi:10.1016/j.jappgeo.2011.09.012

Li, Z., Wu, S., Xia, D., Zhang, X., and Huang, M. (2017). Diagenetic Alterations and Reservoir Heterogeneity within the Depositional Facies: a Case Study from Distributary-Channel Belt Sandstone of Upper Triassic Yanchang Formation Reservoirs (Ordos Basin, China). *Mar. Petroleum Geol.* 86, 950–971. doi:10.1016/j.marpetgeo.2017.07.002

Liu, J., Zhang, G., Bai, J., Ding, W., Yang, H., and Liu, Y. (2022). Quantitative Prediction of the Drilling Azimuth of Horizontal Wells in Fractured Tight Sandstone Based on Reservoir Geomechanics in the Ordos Basin, Central China. *Mar. Petroleum Geol.* 136, 105439. doi:10.1016/j.marpetgeo.2021.105439

Liu Y, Y., Chen, L., Tang, Y., Zhang, X., and Qiu, Z. (2022). Synthesis and Characterization of Nano-SiO2@octadecylbisimidazoline Quaternary Ammonium Salt Used as Acidizing Corrosion Inhibitor. *Rev. Adv. Mater. Sci.* 61 (1), 186–194. doi:10.1515/rams-2022-0006

Liu, Y., Gao, M., and Zhao, H. (2020). Detection of Overlying Rock Structure and Identification of Key Stratum by Drilling and Logging Technology. *J. Min. Strata Control Eng.* 2 (2), 81–89. doi:10.13532/j.jmsce.cn10-1638/td.2020.02.004

Luo, Y., Huang, H., Jakobsen, M., Yang, Y., Zhang, J., and Cai, Y. (2019). Prediction of Porosity and Gas Saturation for Deep-Buried Sandstone Reservoirs from Seismic Data Using an Improved Rock-Physics Model. *Acta Geophys.* 67, 557–575. doi:10.1007/s11600-019-00274-6

Luo, Y., Huang, H., Yang, Y., Hao, Y., Zhang, S., and Li, Q. (2018). Integrated Prediction of Deepwater Gas Reservoirs Using Bayesian Seismic Inversion and Fluid Mobility Attribute in the South China Sea. *J. Nat. Gas Sci. Eng.* 59, 56–66. doi:10.1016/j.jngse.2018.08.019

Ma, R. H. (2005). Fracture Prediction of Tight Sandstone Reservoir. *Nat. Gas. Ind.* 25 (10), 36–37.

Mahmud, H. B., Bin Muhammad Hisham, M. H., Mahmud, W. M., Leong, V. H., and Shafiq, M. U. (2020). Petrophysical Interpretations of Subsurface Stratigraphic Correlations, Baram Delta, Sarawak, Malaysia. *Energy Geosci.* 1 (3–4), 100–114. doi:10.1016/j.engeos.2020.04.005

Malatesta, C., Federico, L., Crispini, L., and Capponi, G. (2018). Fluid-controlled Deformation in Blueschist-Facies Conditions: Plastic vs Brittle Behaviour in a Brecciated Mylonite (Voltri Massif, Western Alps, Italy). *Geol. Mag.* 155 (2), 335–355. doi:10.1017/s0016756816001163

Meng, Q., Hooker, J., and Cartwright, J. (2017). Lithological Control on Fracture Cementation in the Keuper Marl (Triassic), North Somerset, UK. *Geol. Mag.* 154, 1–15. doi:10.1017/s001675681700070x

Mirzaei-Paiaman, A., and Ghanbarian, B. (2021). A New Methodology for Grouping and Averaging Capillary Pressure Curves for Reservoir Models. *Energy Geosci.* 2 (1), 52–62. doi:10.1016/j.engeos.2020.09.001

Pang, Y.-M., Guo, X.-W., Han, Z.-Z., Zhang, X.-H., Zhu, X.-Q., Hou, F.-H., et al. (2019). Mesozoic-Cenozoic Denudation and Thermal History in the Central Uplift of the South Yellow Sea Basin and the Implications for Hydrocarbon Systems: Constraints from the CSDP-2 Borehole. *Mar. Petroleum Geol.* 99, 355–369. doi:10.1016/j.marpetgeo.2018.10.027

Qiao, J., Zeng, J., Jiang, S., and Wang, Y. (2020). Impacts of Sedimentology and Diagenesis on Pore Structure and Reservoir Quality in Tight Oil Sandstone Reservoirs: Implications for Macroscopic and Microscopic Heterogeneities. *Mar. Petroleum Geol.* 111, 279–300. doi:10.1016/j.marpetgeo.2019.08.008

Qie, L., Shi, Y. N., and Liu, J. S. (2021). Experimental Study on Grouting Diffusion of Gangue Solid Filling Bulk Materials. *J. Min. Strata Control Eng.* 3 (2), 023011. doi:10.13532/j.jmsce.cn10-1638/td.20201111.001

Ren, D., Zhou, D., Liu, D., Dong, F., Ma, S., and Huang, H. (2019). Formation Mechanism of the Upper Triassic Yanchang Formation Tight Sandstone Reservoir in Ordos Basin-Take Chang 6 Reservoir in Jiyuan Oil Field as an Example. *J. Petroleum Sci. Eng.* 178, 497–505. doi:10.1016/j.petrol.2019.03.021

Rezaee, R., Saeedi, A., and Clennell, B. (2012). Tight Gas Sands Permeability Estimation from Mercury Injection Capillary Pressure and Nuclear Magnetic Resonance Data. *J. Petroleum Sci. Eng.* 88-89, 92–99. doi:10.1016/j.petrol.2011.12.014

Saein, A., and Riahi, Z. (2017). Controls on Fracture Distribution in Cretaceous Sedimentary Rocks from the Isfahan Region, Iran. *Geol. Mag.* 154, 1–13. doi:10.1017/s0016756817000346

Santosh, M., and Feng, Z. Q. (2020). New Horizons in Energy Geoscience. *Energy Geosci.* 1 (1–2), A1. doi:10.1016/j.engeos.2020.05.005

Sebacher, B., Hanea, R., and Stordal, A. S. (2017). An Adaptive Pluri-Gaussian Simulation Model for Geological Uncertainty Quantification. *J. Petroleum Sci. Eng.* 158, 494–508. doi:10.1016/j.petrol.2017.08.038

Shanley, K. W., and Cluff, R. M. (2015). The Evolution of Pore-Scale Fluid-Saturation in Low-Permeability Sandstone Reservoirs. *Bulletin* 99, 1957–1990. doi:10.1306/03041411168

Shi, B., Chang, X., Yin, W., Li, Y., and Mao, L. (2019). Quantitative Evaluation Model for Tight Sandstone Reservoirs Based on Statistical Methods - A Case Study of the Triassic Chang 8 Tight Sandstones, Zhenjing Area, Ordos Basin, China. *J. Petroleum Sci. Eng.* 173, 601–616. doi:10.1016/j.petrol.2018.10.035

Sun, W., Li, Y. F., Fu, J. W., and Li, T. Y. (2014). Review of Fracture Identification with Well Logs and Seismic Data. *Prog. Geophys.* 29 (3), 1231–1242. doi:10.6038/pg20140332

Wang, A., Zhong, D., Zhu, H., Guo, L., Li, Z., Jiang, Y., et al. (2018a). Depositional and Diagenetic Controls on the Reservoir Quality of Upper Triassic Chang-7 Tight Oil Sandstones, Southwestern Ordos Basin, China. *Geosci. J.* 23 (3), 471–488. doi:10.1007/s12303-018-0042-z

Wang, D. L., Hao, B. Y., and Liang, X. M. (2021). Slurry Diffusion of Singlefracture Based on Fluid-Solid Coupling. *J. Min. Strata Control. Eng.* 3 (1), 013038. doi:10.13532/j.jmsce.cn10-1638/td.20200429.001

Wang, L., Zhao, N., Sima, L., Meng, F., and Guo, Y. (2018b). Pore Structure Characterization of the Tight Reservoir: Systematic Integration of Mercury Injection and Nuclear Magnetic Resonance. *Energy fuels.* 32 (7), 7471–7484. doi:10.1021/acs.energyfuels.8b01369

Xi, K., Cao, Y., Haile, B. G., Zhu, R., Jahren, J., Bjørlykke, K., et al. (2016). How Does the Pore-Throat Size Control the Reservoir Quality and Oiliness of Tight Sandstones? the Case of the Lower Cretaceous Quantou Formation in the Southern Songliao Basin, China. *Mar. Petroleum Geol.* 76, 1–15. doi:10.1016/j.marpetgeo.2016.05.001

Xue, F., Liu, X. X., and Wang, T. Z. (2021). Research on Anchoring Effect of Jointed Rock Mass Based on 3D Printing and Digital Speckle Technology. *J. Min. Strata Control Eng.* 3 (2), 023013. doi:10.13532/j.jmsce.cn10-1638/td.20201020.001

Yang, J. X., Luo, M. K., Zhang, X. W., Huang, N., and Hou, S. J. (2021). Mechanical Properties and Fatigue Damage Evolution of Granite under Cyclic Loading and Unloading Conditions. *J. Min. Strata Control Eng.* 3 (3), 033016. doi:10.13532/j.jmsce.cn10-1638/td.20210510.001

Yin, S., Lv, D., and Ding, W. (2018). New Method for Assessing Microfracture Stress Sensitivity in Tight Sandstone Reservoirs Based on Acoustic Experiments. *Int. J. Geomechanics* 18 (4), 1–11. doi:10.1061/(ASCE)GM.1943-5622.0001100

Yin, S., and Wu, Z. (2020). Geomechanical Simulation of Low-Order Fracture of Tight Sandstone. *Mar. Petroleum Geol.* 117, 1–10. doi:10.1016/j.marpetgeo.2020.104359

Yoshida, M., and Santosh, M. (2020). Energetics of the Solid Earth: An Integrated Perspective. *Energy Geosci.* 1 (1–2), 28–35. doi:10.1016/j.engeos.2020.04.001

Zhang, B., Shen, B., and Zhang, J. (2020). Experimental Study of Edge-Opened Cracks Propagation in Rock-like Materials. *J. Min. Strata Control Eng.* 2 (3), 033035. doi:10.13532/j.jmsce.cn10-1638/td.20200313.001

Zhang, J., Ju, Y., and Zhang, Q. (2019). Low Ecological Environment Damage Technology and Method in Coal Mines. *J. Min. Strata Control Eng.* 1 (1), 013515. doi:10.13532/j.jmsce.cn10-1638/td.2019.02.005

Zhang, T., Switzer, P., and Journel, A. (2006). Filter-Based Classification of Training Image Patterns for Spatial Simulation. *Math. Geol.* 38 (1), 63–80. doi:10.1007/s11004-005-9004-x

Zhao, H., Ning, Z., Wang, Q., Zhang, R., Zhao, T., Niu, T., et al. (2015). Petrophysical Characterization of Tight Oil Reservoirs Using Pressure-Controlled Porosimetry Combined with Rate-Controlled Porosimetry. *Fuel* 154, 233–242. doi:10.1016/j.fuel.2015.03.085

Zhao, J. L., Liu, J. J., Zhang, Q. H., and Qu, X. R. (2017). Overview of Geophysical Exploration Methods and Technical of Tight Sandstone Gas Reservoirs. *Prog. Geophys.* 32 (2), 840–848. doi:10.6038/pg20170253

Zhong, D. (2017). Micro-petrology, Pore Throat Characteristics and Genetic Mechanism of Tight Oil Reservoirs – A Case from the 6th and 7th

Members of Triassic Yanchang Formation in the Ordos Basin. *Oil Gas Geol.* 38 (1), 49–61. doi:10.11743/ogg20170106

Zhou, N., Lu, S., Wang, M., Huang, W., Xiao, D., Jiao, C., et al. (2021). Limits and Grading Evaluation Criteria of Tight Oil Reservoirs in Typical Continental Basins of China. *Petroleum Explor. Dev.* 48 (5), 1089–1100. doi:10.1016/S1876-3804(21)60093-9

Zhu, R., Bai, B., Cui, J., Wang, T., Niu, L., and Li, T. (2013). Research Advances of Microstructure in Unconventional Tight Oil and Gas Reservoirs. *J. Palaeogeogr.* 15, 615–623.

Zou, C., Zhu, R., Liu, K., Su, L., Bai, B., Zhang, X., et al. (2012). Tight Gas Sandstone Reservoirs in China: Characteristics and Recognition Criteria. *J. Petroleum Sci. Eng.* 88-89, 82–91. doi:10.1016/j.petrol.2012.02.001

Conflict of Interest: MD was employed by the Fuxian Oil Production Plant, Yanchang Petroleum (Group).Ltd., HM was employed by the Oil Production Plant, Changqing Oilfield Company, and JJ was employed by the Oil Production Plant, Changqing Oilfield Company.

The remaining authors declare that the research was conducted in the absence of any commercial or financial relationships that could be construed as a potential conflict of interest.

Publisher's Note: All claims expressed in this article are solely those of the authors and do not necessarily represent those of their affiliated organizations, or those of the publisher, the editors and the reviewers. Any product that may be evaluated in this article, or claim that may be made by its manufacturer, is not guaranteed or endorsed by the publisher.

frontiers | Frontiers in Earth Science

TYPE Original Research
PUBLISHED 10 August 2022
DOI 10.3389/feart.2022.983572

OPEN ACCESS

EDITED BY
Wenlong Ding,
China University of Geosciences, China

REVIEWED BY
Zhu Baiyu,
Yangtze University, China
Huigui Li,
Guizhou University of Engineering Science, China

*CORRESPONDENCE
Qirong Qin,
qqrong@126.com

SPECIALTY SECTION
This article was submitted to Structural Geology and Tectonics, a section of the journal Frontiers in Earth Science

RECEIVED 01 July 2022
ACCEPTED 18 July 2022
PUBLISHED 10 August 2022

CITATION
Fu L, Qin Z, Xie A, Chen L, Li J, Wang N, Qin Q and Mao K (2022), The relation of the "four properties" and fluid identification of the carboniferous weathering crust volcanic reservoir in the Shixi Oilfield, Junggar Basin, China. *Front. Earth Sci.* 10:983572. doi: 10.3389/feart.2022.983572

The relation of the "four properties" and fluid identification of the carboniferous weathering crust volcanic reservoir in the Shixi Oilfield, Junggar Basin, China

Lei Fu[1], Zhangjin Qin[2], An Xie[3], Liang Chen[4], Junfei Li[1], Nan Wang[1], Qirong Qin[5]* and Kailan Mao[5]

[1]Shixi Field Operation District, Xinjiang Oilfield Company, CNPC, Karamay, China, [2]Exploration Division, Petro China Southwest Oil and Gasfield Company, Chengdu, China, [3]Evaluation Department of Xinjiang Oilfield Company, CNPC, Karamay, China, [4]Development Department of Xinjiang Oilfield Company, CNPC, Karamay, China, [5]School of Geosciences and Technology, Southwest Petroleum University, Chengdu, China

This study addresses the poorly understood physical properties of the Shixi Oilfield reservoir, which consists of a weathered Carboniferous volcanic rocks with strong heterogeneity and in which logging identification and evaluation are difficult. Using the lithology, lithofacies, and reservoir space characteristics of volcanic materials, this comprehensive study uses core, well logging, mud logging, and production testing data to analyze the relationship among the lithology, physical properties, electrical properties, and oil-bearing properties (referred to as the "four properties") of weathered Carboniferous volcanic crust in addition to fluid identification. 1) The lithology of Carboniferous volcanic crust is dominated by breccia lava, agglomerate, banded lava, and compact tuff, and the lithofacies are mainly effusive facies. Secondary pores and tectonic fissures are important reservoir spaces, and the corrosion-fracture pores are significant for reservoir properties. 2) The "four properties" of volcanic reservoirs in the study area have clear relationships. On this basis, data on the electrical properties of the material, such as interval transit time, density, and neutron, were used to establish a logging interpretation model of the properties and oil saturation of the volcanic rock. 3) Using the resistivity-porosity cross-plot method, normal probability distribution method, and Rt/Rxo-Rt cross-plot method, volcanic reservoir fluids were identified with coincidence rates of 80%, 63.63%, and 63.63%, respectively. The cross-plot method determines lower limits of the reservoir's physical properties and oil saturation, yielding porosity>9%, permeability>0.2 mD, and oil saturation>45%.

KEYWORDS

"four properties" relation, fluid identification, lower limits of physical properties, logging interpretation model, weathering crust volcanic crust, carboniferous, Shixi Oilfield

1 Introduction

Volcanic oil and gas reservoirs provide important avenues for oil and gas exploration and are widely distributed in more than 40 basins in 13 countries around the world. Compared with primary volcanic deposits, the reservoirs of weathered secondary volcanic rock have significantly better reservoir property and oil-gas productivity than primary volcanic reservoirs. This major new understanding has promoted the exploration and discovery of many of these reservoirs (Feng 2008; Fan et al., 2020a; Weng et al., 2020; Li, 2022; Li, 2018; Liu et al., 2022). The weathered volcanic crust reservoirs in the Junggar Basin of China are widely distributed. More than 40 such oil and gas reservoirs have been discovered successively in Hongshanzui, District 5, District 8, District 7, Chepaizi, Shixi, Huwan District, and other areas. In recent years, researchers have devoted themselves to studying volcanic eruption, reservoir characteristics, and the controlling factors and have achieved rich research results (Zou et al., 2012; Hou et al., 2013; Yang et al., 2017; Li et al., 2017).

Since the discovery of well Shixi 1 (hereafter SX1) in 1992, the Carboniferous volcanic reservoir in the Shixi Oilfield, a typical reservoir of weathered volcanic crust, has been built up as a modern desert oil and gas field. The Carboniferous stratigraphic structure in this area is complex, including small faults that developed with rapidly changing occurrences. The lithology is also complex, as the effective thickness is highly heterogeneous, and the oil-water transition zone is nonuniform, resulting in many oil-bearing well sections and large changes in oil layer thickness and testing effects. The development degree of the reservoir (on a plane) is uneven, influenced by many factors, such as anomalously high pressure, fracture development, and active bottom water, which seriously restrict the efficient development of the reservoir (Li et al., 2019, Li et al., 2020; Zhang et al., 2020; Li et al., 2021; Qie et al., 2021; Shan et al., 2021). Recently, relevant studies have been conducted on the geological characteristics of oil reservoirs in this area, mainly including the characteristics of single-well volcanic reservoirs, primary gas pores, and tectonic styles (Chen et al., 1999; Hou et al., 2012; Li et al., 2017). However, studies of the relationship among the four properties (including lithology, physical properties, electrical properties, and oil/gas properties) and fluid identification of the volcanic reservoirs in this area are sparse. Limited research is not conducive to understanding the distribution of remaining oil reserves or to oil and gas development and expansion. In general, the fluid identification of volcanic reservoirs is based on elementary methods, such as the three-porosity combination, ratio, cross-plot identification, standard stratum superposition, and others. In addition, some scholars also use statistical techniques, such as neural networks, to identify fluids. Since the lithology and lithofacies of volcanic deposits have a great influence on the logging response of fluid identification, starting with lithology and lithofacies, this study investigates the relations of the four properties in this region and conducts research on fluid identification of volcanic reservoirs.

2 Geological setting

Geographically, the Shixi Oilfield is in Karamay City, Xinjiang, China, and is structurally located in the Shixi uplift in the interior of the Junggar Basin. It is adjacent to the West Depression of well Pen 1, Sannan Depression, and Dishuiquan Depression to the south, north, and east, respectively, showing favorable geological conditions of being "Adjacent to the West Depression in three directions" (Figure 1A). The study area can be divided into three uplifts, two Depressions, and five structural units. From west to east, these units are well SX1 Uplift, well SX1 South Depression, well SX4 South Uplift, well Shimo 1 (hereafter SM1) West Depression, and well SM1 Uplift. Among them, the Carboniferous system in well SX1 Uplift has been entirely explored, of which oil and gas are the most abundant resources. The overall shape is a triangular horst bordering the north fault of well SX2, the west fault of well S002, and the south fault of well SM1. Its interior can be further divided into three secondary tectonic units, i.e., the east horst-block, the west fall-block, and the north fault stage (Figure 1B).

The strata encountered by drilling from the bottom to the top in the Shixi area are Carboniferous (C), Permian Jiamuhe Formation (P_1j), Wuerhe Formation (P_2w), Triassic Baikouquan Formation (T_1b), Ke Xia Formation (T_2k^1), Ke Shang Formation (T_2k^2), Baijiantan Formation (T_3b), Jurassic Badaowan Formation (J_1b), San Gonghe Formation (J_1s), Xi Shanyao Formation (J_2x), Cretaceous Tu Gulu Formation (K_1t), Tertiary (R) and Quaternary (Q) (Figure 1C) (Li et al., 2017; Li X. et al., 2022). The Carboniferous structure in Shixi is an ancient buried hill with an amplitude variation in the hill surface that gradually decreases from south to north. The structural high points are in the region of well SH1025-well SX1 in the east area and the region of well SH1120-well SH1059 in the west area. Ten reverse faults are developed in the region, of which the fault of northern well SX2 and the fault of southern well SX1 are reservoir-controlling faults. They clamp each other to form a fault-block buried hill structure of the Carboniferous in the Shixi area. On the seismic section, the fault characteristics are clear, and the fault displacement is large; the rest of the faults in the study area have small extension lengths without reservoir-controlling features (Table 1), and the vertical fault displacement is within 20 m, which further complicates the structure.

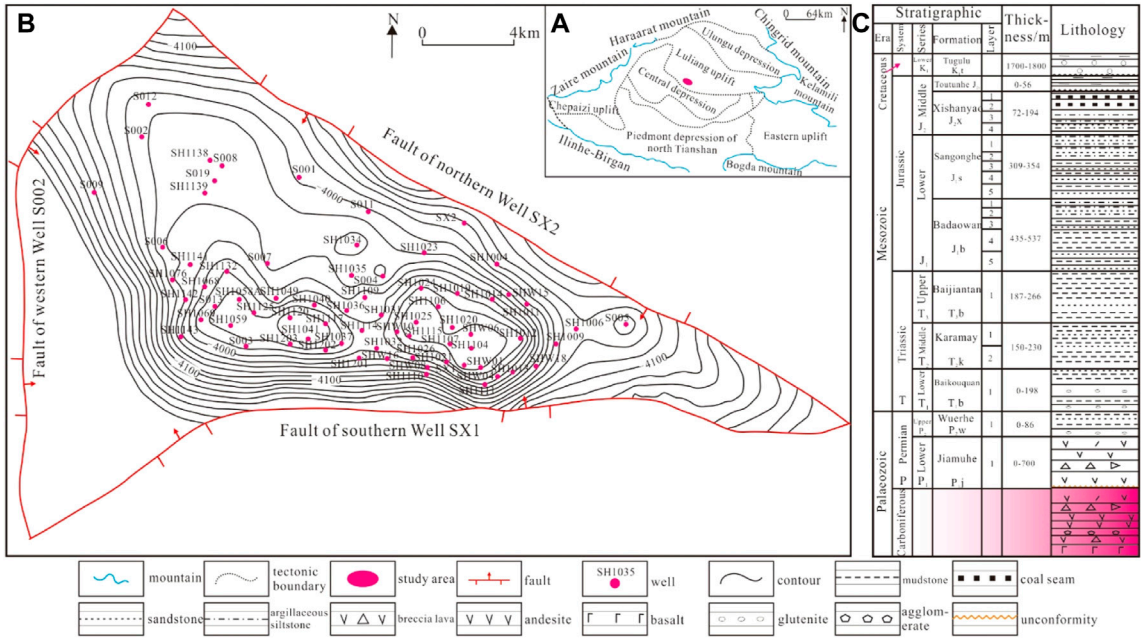

FIGURE 1
Geological survey of the study area. **(A)** Tectonic position; **(B)** The top surface structure of carboniferous; **(C)** Comprehensive stratigraphic histogram.

TABLE 1 Reservoir controlling fault (Type I fault) elements of Carboniferous volcanic rocks in Shixi Oilfield.

Number	Fault	Fault properties	Length (km)	Disconnected horizon	Strike	Inclination	Dip (°)	Fault distance(m)
1	Fault of northern well SX2	Reverse fault	19	T ~ C	NW	SW	30–45	150
2	Fault of southern well SX1		23	T ~ C	EW	N	40–50	200
3	Fault of western well S002		14	T ~ C	NS	E	40–50	150

3 Samples and methods

3.1 Samples

The samples and data used in this study mainly include field measurements, cores, and thin-section observation. Analysis of the physical properties of the cores was also conducted. Field measurements include the conventional logging and production data for 15 wells. The conventional logging data were chiefly collected through natural Gamma-ray (GR), spontaneous potential (SP), borehole diameter (CAL), deep lateral resistivity (Rt), acoustic (AC), density (DEN), and neutron (CNL) methods, among others. The production materials mainly include testing, perforation, and production dynamics. Observed cores from 10 wells (e.g., SX1, SX2, S001, S002, S003, S004) of length 152.0 m, and 212 photos of cores and fractures were obtained. Ten such samples were obtained.

3.2 Methods

Laboratory experiments were carried out on core samples to obtain porosity and permeability data, and thin-section observations were conducted to study the lithology and lithofacies characteristics of Carboniferous volcanic reservoirs in combination with regional sedimentary and tectonic backgrounds. Combined with conventional logging and production test data, the four-property relationship, logging interpretation model, and fluid identification of reservoirs are studied. Three main methods were adopted for reservoir fluid

identification: the resistivity-porosity cross-plot method, the normal probability distribution method, and the Rt/Rxo-Rt cross-plot method. The second method is more complex and will be explained here. Parameter $P^{1/2}$ was adopted for drawing a map on the probability paper to identify oil and water strata and estimate Sw, a method called the "normal probability distribution method". Let P=Rt × Φm, where Rt is replaced by deep detection resistivity, Φ is obtained from porosity logging, and cementation index *m* can be estimated by using a statistical method (Pan et al., 2019; He et al., 2020; Ajaz et al., 2021). *p* values were calculated for each reservoir, and $P^{1/2}$ was plotted against the cumulative frequency on a probability paper. This method can convert an arc-shaped normal probability curve into a straight line. The larger the slope (k) of the straight line is, the smoother the normal probability distribution curve; in contrast, the normal probability distribution curve is more vertical and steeper. Therefore, the fluid identification of the method generally applies to the following rules: the slope of the oil and gas stratum is relatively large, while the slope of the water stratum is relatively small.

4 Results

4.1 Basic characteristics of the reservoir

4.1.1 Lithology and lithofacies characteristics

Combined with core, conventional logging, thin-section authentication, and other data, the Carboniferous volcanic materials in this area are divided into three sections, from bottom to top: basic-intermediate basic rocks (Section 1), intermediate rocks (Section 2), and intermediate-acid rocks (Section 3). These sections form a complete eruption cycle and include three categories: lava, ordinary pyroclastic rock, and transitional rock. Among these categories, lava is the most developed stratum and mainly includes andesite, rhyolite, dacite, and basalt, which is dominated by banded lava (Chen et al., 1999; Hou et al., 2012; Hou et al., 2013). Ordinary pyroclastic rocks mainly include agglomerate, agglomerate breccia, volcanic breccia, and breccia tuff. The agglomerate and agglomerate breccia are the most widely developed, and the breccia composition is mainly andesite. The transition rocks are mainly dacite and andesite transition rocks. On the whole, the lithology of the reservoir is primarily banded lava, agglomerate, breccia, compact tuff, and similar minerals, accounting for more than 84% of the deposits. The lithofacies include explosion facies and effusive facies, dominated by the effusive facies. Andesite and dacite of effusive facies are widely distributed, mainly in the west and east of the study area. In contrast, the andesite tuff breccia and dacite breccia of the explosion facies are mainly distributed in the area, such as well S008-well S013-well S004 (Figure 2).

4.1.2 Reservoir space types and characteristics

Pores and fractures are the most important reservoir space types in Carboniferous volcanic reservoirs (Fan et al., 2020b; He et al., 2021; Li J. et al., 2022). Pores include primary and secondary pores, with the secondary pores being more meaningful for oil and gas reservoirs. Primary blow holes and intercrystalline pores dominate the primary pores, but such pores often appear alone. Although these structures increase the porosity of the reservoir, the migration of oil and gas is hindered. Primary pores refer to the pores left by the loss of the volatile components after the magma is ejected and condensed on the surface. Most are circular or elliptical and mainly developed at the bottom and top of the lava flow (Figures 3A,B); the intercrystalline pores mainly refer to the pores inside the crystal grains of minerals, such as quartz and feldspar. These have irregular shapes, and the size of the pores is mainly positively correlated with the size of the particles (Figures 3C,D). The secondary pores are dominated by various dissolution pores, such as matrix dissolution pores, intergravel dissolution pores, intercrystalline dissolution pores, intragravel dissolution pores, and others. Such pores are the products of the dissolution minerals, often with unclear boundaries and extremely irregular shapes (Figures 3E,F).

Fractures can not only provide reservoir space but also connect those isolated pores, thereby effectively improving the seepage capacity of the reservoir. According to the observation of cores and thin sections, the fractures of Carboniferous reservoirs mainly include tectonic fractures, condensation shrinkage fractures, intergravel fractures, dissolution fractures, and others. Among these, tectonic fractures are the most developed. The tectonic fractures are formed under the action of tectonic stress, and their distribution range is wide and regular. Tectonic fractures can be divided into shear and tensile fractures based on their mechanical characteristics. Shear fractures are dominant, and their characteristics are different from those of tensile fractures (Figure 3K) (Kang 2021; Li et al., 2019a; Smeraglia et al., 2021; Wang and Wang 2021). They are characterized by strong distribution regularity, long extension length, obvious directionality, strong stratum penetration, and straight fracture surface (Figures 3G–J). Weathering fractures are formed by weathering and leeching and are affected by lithology, climate, terrain, and other factors. In general, they are short in length and lie within the stratum. Their fracture surfaces are slightly corroded, forming irregular shapes (Figure 3L). Condensation shrinkage fractures refer to the primary pores and shrinkage fractures formed during the formation of volcanic deposits and magma condensation diagenesis due to the change in facies and the decrease in volume, whereas intergravel (crystal) fractures refer to the small irregular fractures developed in the process of diagenesis, which cut through the gravel or only develop within the gravel. These fractures of different origins can connect the primary and

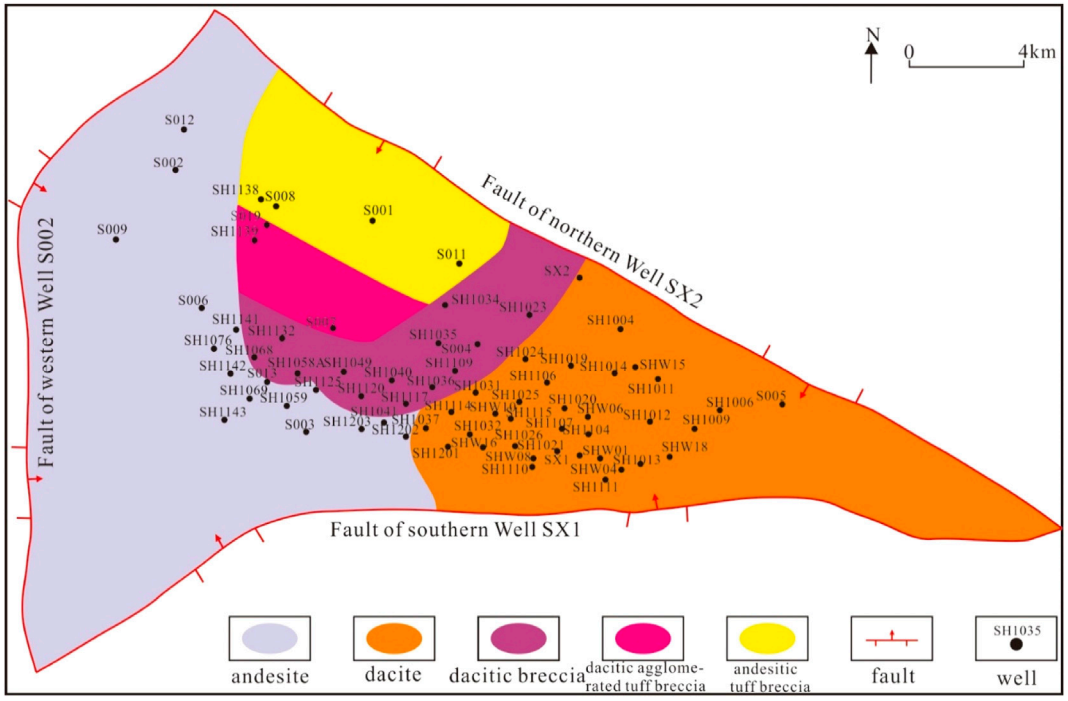

FIGURE 2
Lithology and lithofacies distribution of the Carboniferous volcanic top surface in the Shixi Oilfield.

secondary pores, which are more obvious under a microscope. The volcanic reservoir space in the study area often combines with microcracks to form dissolution-fracture pores (Li J. J. et al., 2022; Fan et al., 2022; Li, 2022; ; Wang et al., 2022).

4.2 The "four properties" relations of the reservoir

The "four properties" of the reservoir refer to the reservoir's lithology, physical properties, electrical properties, and oil and gas properties. Among them, the electrical properties constitute the comprehensive response to reservoir lithology, physical properties, and oil and gas properties; of these, lithology is dominant, and the particle size, sorting, cementation type, and argillaceous content directly affect the physical properties of the reservoir (Li et al., 2019b; Mollajan et al., 2013; Zhou et al., 2020; Zhao et al., 2022). Therefore, studying the relationship between these can determine the lower limit of the effective thickness and provide a basis for the final and accurate judgment of the oil and gas stratum.

4.2.1 Relationship between lithology and physical properties

The physical properties of different lithologies have obvious differences. Lithologies with relatively ideal physical properties in the study area include breccia lava, banded lava, agglomerate, and compact tuff. The maximum porosity is distributed between 20% and 30%, with an average of approximately 10%. The permeability variation range is between 0.02 and 500 mD, and the average is generally lower than 10 mD. The development of reservoir fractures greatly influences the permeability of different lithologies. In addition, the physical properties of the weathering crust after weathering and leaching are also ideal. At the same time, other lithologies, such as basalt and andesite, have poor physical properties, making it difficult to form effective reservoirs.

The correlation between the lithology and physical properties of the reservoirs in the study area is obvious. The correlation between agglomerate and breccia lava is relatively good, showing the characteristics of high porosity and high permeability, and the banded lava is characterized by high porosity and low permeability. This finding indicates, to some extent, that the degree of development of different lithologic fractures varies greatly. Generally, the correlation between porosity and permeability of the different lithologies in the study area is moderate (Figure 4).

4.2.2 Relationship between lithology and oil-bearing properties

The oil-bearing property grade of the core is an important indicator for judging the presence of oil and gas. According to the

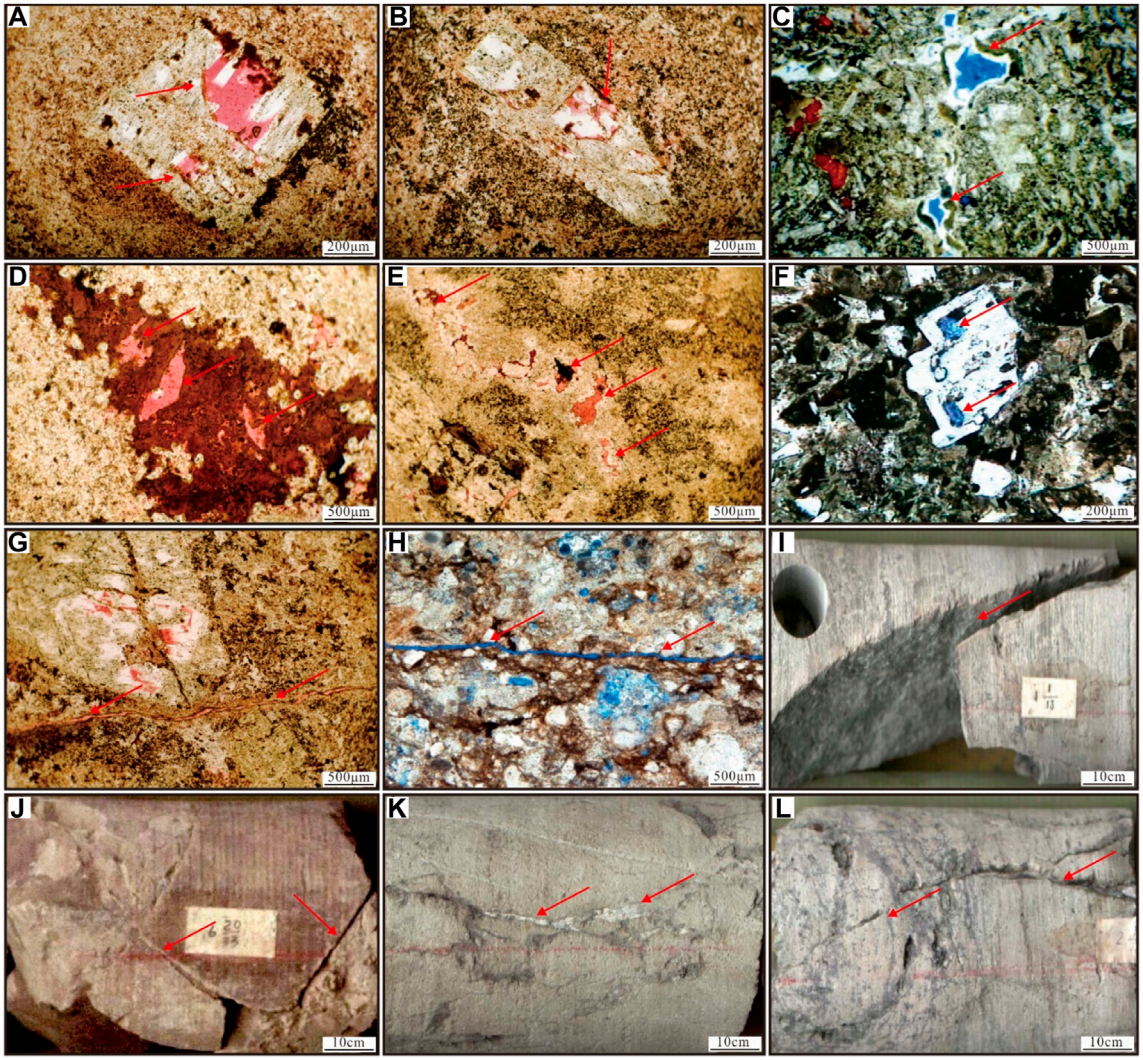

FIGURE 3
Types and characteristics of Carboniferous volcanic rocks reservoir space in Shixi Oilfield. **(A)** Primary pore, S001, 4502.90 m; **(B)** Primary pore, S001, 4501.75 m; **(C)** Intercrystalline pore, S004, 4382.00 m; **(D)** Intercrystalline pore, S001, 4519.97 m; **(E)** Dissolution pore, S001, 4524.50 m; **(F)** Dissolution pore, S004, 4368.70 m; **(G)** Micro shear fracture, S001, 4513.25 m; **(H)** Micro shear fracture, S004, 4392.16 m; **(I)** Shear fracture, S013, 4421.00–4421.10 m; **(J)** Shear fracture, S007, 4352.50 m; **(K)** Tensile fracture, S002, 4412.90 m; **(L)**. Weathering fracture, S013, 4421.10 m.

oil-bearing property analysis of 74 blocks of different lithologies in the study area, the oil- and gas-bearing properties of the cores constitute multiple levels, e.g., gas-bearing, fluorescence (dominant, accounting for 81.1%), oil spot, and oil-rich, while oil-rich samples are rare, accounting for only 1.3% (Figure 5), indicating that the oil-bearing property of Carboniferous reservoirs is average to poor.

4.2.3 Relationship between the electrical property and oil-bearing property

This study analyses the electrical properties of the tested oil and gas sections of the main Carboniferous exploration wells (S013, S004, S012, and S002) and clarifies the corresponding relationship between the electrical properties and oil-bearing properties of the reservoir. The research shows that the oil, gas, and water stratum can be explained well by the electrical measurement data (Rt, GR, AC, and DEN) (Table 2), and the test results correspond well to the interpreted electrical properties.

4.2.4 Relationship among lithology, physical properties, electrical properties, and oil-bearing property

Based on the above analysis, Carboniferous volcanic reservoirs' agglomerates and breccia lava have good physical properties. The physical properties of the agglomerate change greatly, and fluorescence display is more common; the resistivity

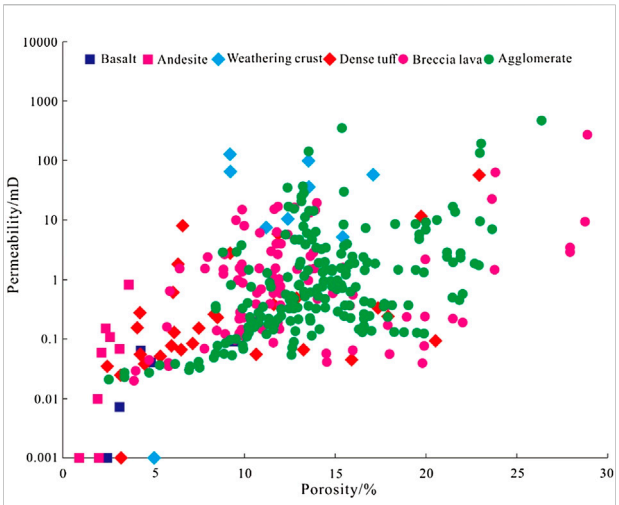

FIGURE 4
Cross plot of porosity and permeability of different lithologies of the Carboniferous system in the Shixi Oilfield.

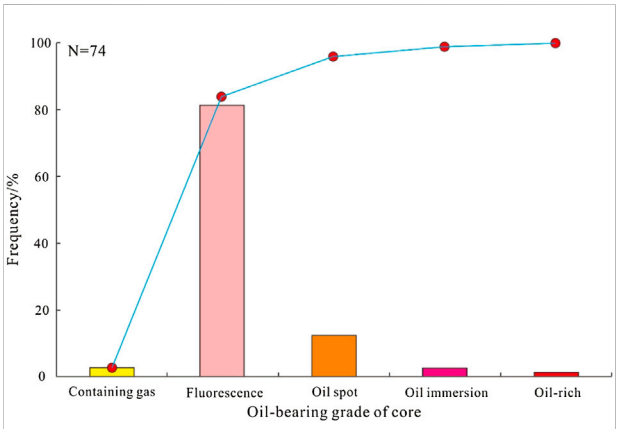

FIGURE 5
Oil-bearing property frequency distribution of the Carboniferous reservoir in the Shixi Oilfield.

shows obvious changes, and the resistivity increases with the increase in oil-bearing properties; when oil and gas are located, the spontaneous potential shows a positive anomaly. The spontaneous potential of the weathering crust is a negative anomaly, with low resistivity, and no oil and gas are found. In general, the lithology, electrical properties, physical properties, and gas-bearing properties of the volcanic reservoirs in the study area have obvious relationships. Lithology affects the physical properties, while physical properties control oil- and gas-bearing properties, and electrical properties respond to the differences and changes in lithology, physical properties, and gas-bearing properties.

4.3 Reservoir parameter logging interpretation model

The porosity, permeability, and saturation logging interpretation models are established based on the principle of "core scale logging" and combined with the analysis of the cross-plot and logging curve characteristics (Radwan 2021; He et al., 2021).

4.3.1 Physical property parameter logging interpretation model

Physical property parameters include porosity and permeability. In general, calculating porosity using logging parameters, such as acoustic waves, density, and neutrons (Saeid et al., 2022). According to the physical property analysis data for the 12 wells in the study area, the porosity value at each depth corresponds to the logging parameter value, and the acoustic wave-porosity, neutron-porosity, and density-porosity models of Carboniferous volcanic reservoirs are established (Figure 6). The corresponding relationships are illustrated as follows:

$$\varphi = 0.476\mathrm{AC} - 19.121, R^2 = 0.2826 \quad (1)$$

$$\varphi = -38.795DEN + 107.24, R^2 = 0.66 \quad (2)$$

$$\varphi = 0.1056\mathrm{CNL} + 11.55, R^2 = 0.0411 \quad (3)$$

The correlation coefficient R of the acoustic wave-porosity and neutron-porosity models is small, indicating a poor correlation, while the density-porosity model has a good correlation. Therefore, the density-porosity is selected to establish a porosity logging interpretation model. To verify the model's accuracy, well S001 and well S003 were selected for porosity calculation. The calculated results agree with the actual core analysis porosity, and the correlation coefficient exceeded 0.8, indicating that the model is accurate (Figure 7).

Carboniferous volcanic reservoir fractures have developed, making the fracture permeability hundreds of times higher than the matrix permeability. The correlation between rock porosity and the permeability of the fractured reservoir is poor. An effective method to calculate the permeability of fractured reservoirs is still lacking (Jarvie et al., 2007; Ibrahim et al., 2017; Hooker et al., 2018; Hou et al., 2020). Therefore, using conventional logging models to calculate permeability is of little significance.

4.3.2 Saturation calculation model

Oil-bearing saturation is the main basis for quantitatively evaluating the oil-bearing property of a reservoir. This parameter is important in describing the reservoir characteristics and is the key to identifying the oil layer. Comprehensively considering the geological properties, rock-electrical experimental parameters, formation water salinity, and other data, the Archie formula was used as the water saturation calculation formula (Eq. 5), establishing the oil saturation formula (Eq. 4).

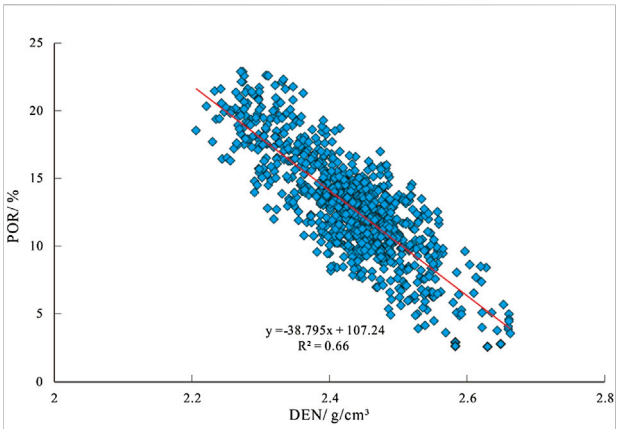

FIGURE 6
Density-porosity model of the Carboniferous volcanic in the Shixi Oilfield.

$$S_w^n = \frac{abR_w}{\varphi^m \times R_t} \quad (4)$$

$$So = 1 - Sw \quad (5)$$

where Sw—water saturation (%); Rt—stratum resistivity (Ω·m); Rw—stratum water resistivity (Ω·m); ф—porosity. The m, n, a, and b values of the study area were obtained from the comprehensive analysis of rock-electrical experiments and previous research results, m=2.13, *n*=1.7, a=0.85, b=1.06, and Rw=0.12 Ω m.

4.4 Reservoir fluid identification

Many methods are available for identifying reservoir fluids, including the porosity curve overlapping, cross-plot, and normal probability distribution methods. Regarding volcanic reservoirs,

TABLE 2 Relationship between the electrical property and oil-bearing property of the main exploration well.

Well	Depth (m)	Rt (Ω.m)	GR (API)	AC (μs/ft)	DEN (g/cm³)	Test	Logging interpretation	Remark
S013	4408–4425	14.66–40.08 25.73	86.38–131.14 112.36	61.51–71.85 65.53	2.33–25.0 2.42	Oil layer	Oil and gas production	A significantly negative difference in spontaneous potential
S004	4410–4420	17.57–51.81 28.31	76.42–142.54 109.5	55.41–68.71 62.08	2.39–2.57 2.5	Oil-water layer	Oil, gas, and water production	
S012	4460–4474	383.70–1025.82 650.3	114.26–126.14 120.27	51.90–55.71 53.85	2.53–2.60 2.57	Oil-bearing water layer	Oil-bearing water layer	
S002	4416–4428	7.30–23.65 13.44	85.40–134.59 116.3	62.65–86.89 70.82		Water layer	Water layer	Low resistivity, large interval transit time, and water saturation of 76.55%
	4483–4495							
	4508–4520							

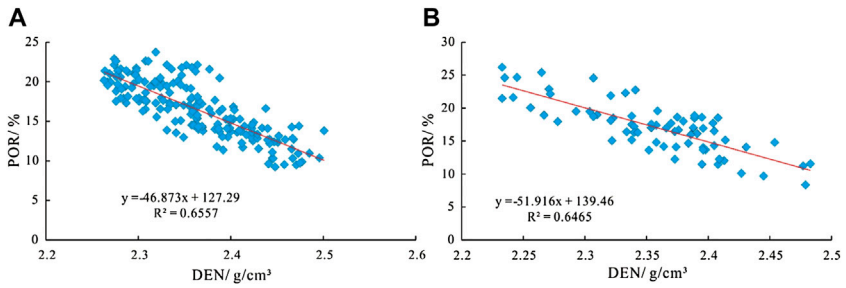

FIGURE 7
The relationship between porosity and density in the study area. **(A)** well S001; **(B)** well S005.

TABLE 3 Accuracy comparison of different fluid identification methods in Carboniferous volcanic reservoirs.

Well	Depth (m)	Test	Conclusion of explanation		
			Resistivity-porosity cross-plot	Normal probability distribution	Rt/Rxo-Rt cross-plot
S001	4442–4454	Water layer	Oil layer	Water layer	Water layer
S002	4416–4428	Water layer	Oil layer	Water layer	Water layer
S003	4415–4440	Oil-bearing water layer	Oil-bearing water layer	Oil-bearing water layer	Oil-bearing water layer
S004	4410–4420	Oil-water layer	Oil-water layer	Oil layer	Oil-water layer
S005	4536–4540	Water layer	Water layer	Oil layer	Oil-water layer
S006	4437–4443	Oil-water layer	Oil layer	Oil-bearing water layer	Water layer
S007	4497–4420	Oil-water layer	Oil-water layer	Oil-water layer	Water layer
S012	4460–4474	Oil-bearing water layer	Oil-bearing water layer	Oil-water layer	Oil layer + Oil-water layer
SX2	4552–4560	Dry layer	Dry layer	Water layer	Dry layer
S019	4420–4440	Oil layer	Oil layer	Oil layer	Oil-water layer

the cross-plot and normal probability distribution methods are often used for fluid identification.

4.4.1 Resistivity-porosity cross-plot method

Combined with the study on the relations of the "four properties" of the reservoir, the deep lateral resistivity (Rt) of the Carboniferous in the study area corresponds well to the oil-bearing property, and deep lateral logging has a large detection depth and high reliability. When the difference between lithology and physical properties of the reservoir is small, the resistivity increases, indicating the possible presence of an oil and gas stratum, though possibly a water stratum instead. In the meantime, the deep lateral resistivity and porosity cross-plot can also be used to judge the quality of physical properties to a certain extent. The porosity of the dry stratum is smaller than that of the oil and water strata. In addition, the dry and oil strata are easily distinguished, and the limit value between them is Φ=10% (Figure 8). The fluid properties of the reservoir are identified by the resistivity-porosity log cross-plot method, with the coincidence rate reaching 80% (Table 3).

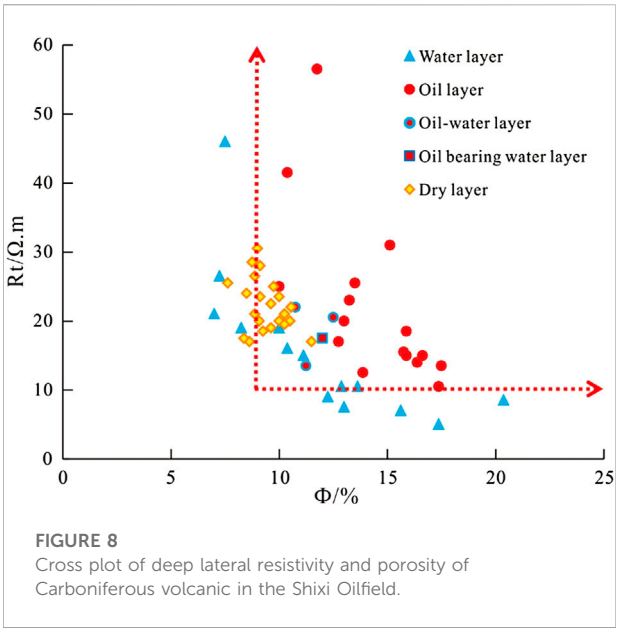

FIGURE 8
Cross plot of deep lateral resistivity and porosity of Carboniferous volcanic in the Shixi Oilfield.

4.4.2 Normal probability distribution method ($P^{1/2}$ method)

Normal probability distribution method is a mathematical statistical method for reservoir fluid identification. A normal probability distribution map was drawn to analyze the fluid properties using the test data for the main single well in the study area (Figure 9). The oil stratum k>0.009; the water stratum k<0.004; the electrical properties of the oil-water and oil-bearing water strata were very similar, with k ranging from 0.004 to 0.009; making it difficult to distinguish such fluid types using the normal probability distribution method. Similarly, using the single-well test data and interpretation results to compare, the coincidence rate of the normal probability distribution method for judging fluid properties is approximately 65% (Table 3).

4.4.3 Rt/Rxo-Rt cross-plot method

The cross-plot of Rt/Rxo and Rt can better identify the fluid properties of different reservoir types (Das and Chatterjee, 2018). Different fluids in the study area mainly show the following rules in the cross-plot of Rt/Rxo and Rt (Figure 10): 1) Oil stratum: resistivity is greater than 37 Ω m, and the ratio is greater than 1.6; 2) Oil-water and oil-bearing water strata: resistivity is 19–35 Ω m, and the ratio is between 0.7 and 2.2; water stratum: resistivity is lower than 30 Ω m, and the ratio is

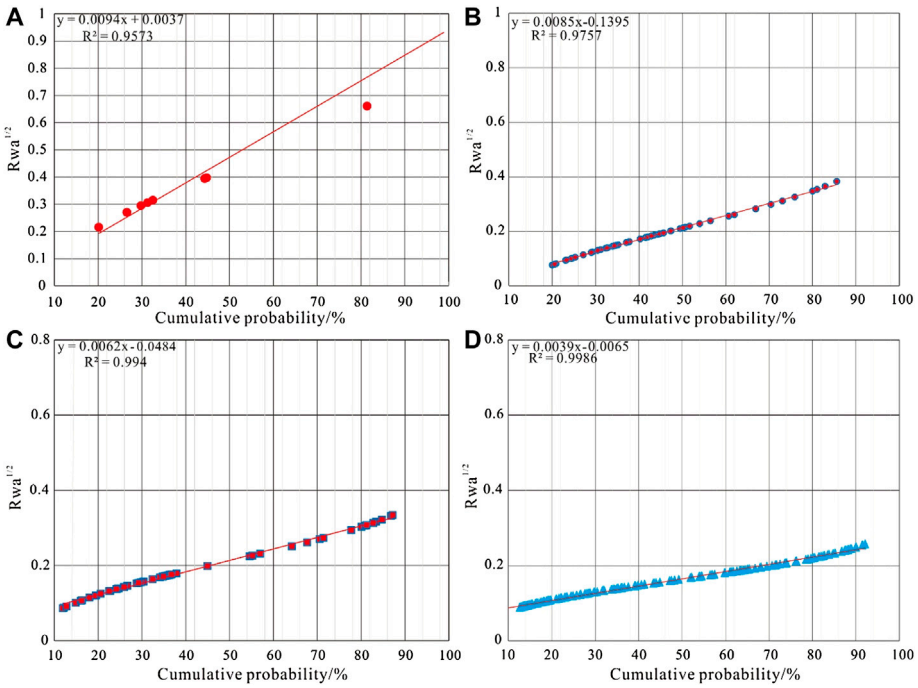

FIGURE 9
Normal probability distribution of the study area. **(A)** oil layer; **(B)** oil-water layer; **(C)** oil-bearing water layer; **(D)** water layer.

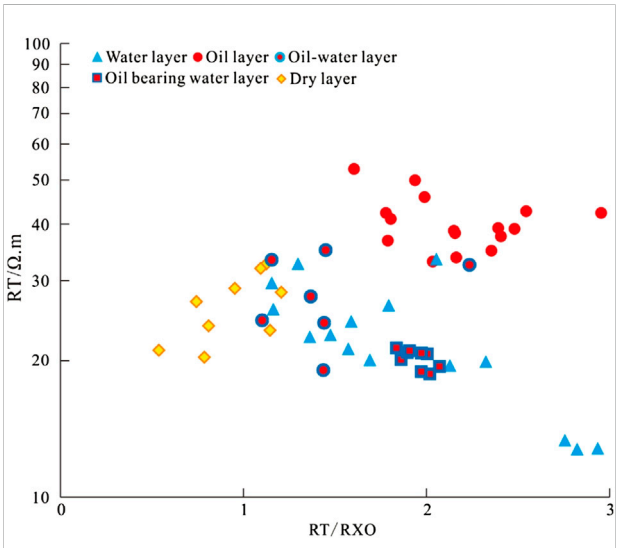

FIGURE 10
Rt/Rxo and Rt cross-plot of the Carboniferous volcanic in the Shixi Oilfield.

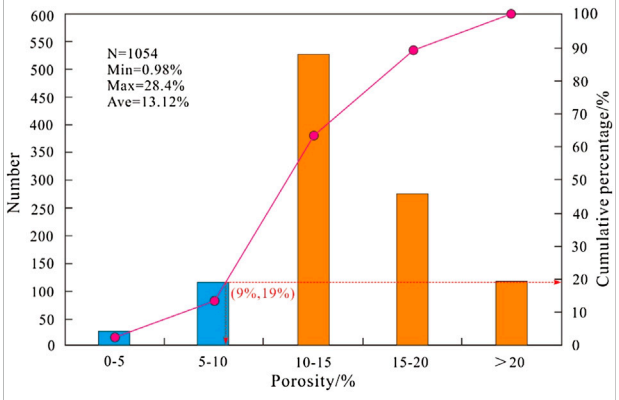

FIGURE 11
The lower limit of porosity of the Carboniferous volcanic in the Shixi Oilfield.

between 1.0 and 3.0; dry stratum: resistivity is 19–35 Ω m, and the ratio is between 0.5 and 1.2. Since the oil-water stratum and the oil-water stratum have similar electrical properties, they are combined for analysis. This method can better identify oil, water, and dry strata; however, distinguishing between oil-water and oil-bearing water strata is difficult. Similarly, using the single-well test data and interpretation results as a comparison, the coincidence rate of this method for judging fluid properties is approximately 63.63% (Table 3).

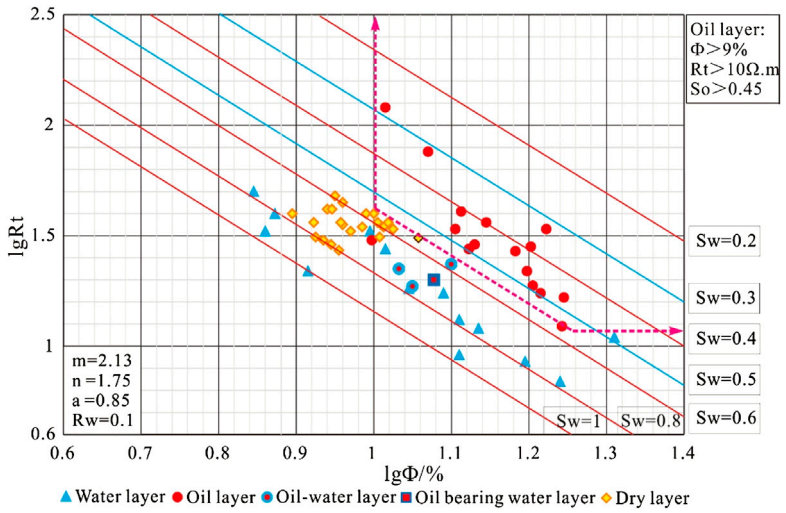

FIGURE 12
The cross plot of resistivity-porosity of the Carboniferous volcanic in the Shixi Oilfield.

TABLE 4 Statistics of oil and water stratum interpretation criteria.

Description	Oil layer	Oil-water layer (oil-bearing water layer)	Water layer	Dry layer
Rt (Ω.m)	>10	(12,24)	>4	(13,32)
POR (%)	>9	>10	>9	<10
So (%)	>45	(20,45)	<40	—

5 Discussion

5.1 Determination of the lower limits of the reservoirs

In general, the lower limits of the reservoir include two types such as that of physical properties and oil/gas saturation. This study determines the lower limit of physical properties based on the core physical property analysis data, combined with the oil and gas display. According to the oil and gas display and measured physical property data for the 12 wells, such as S005, S013, and S019, the porosity of 9% and the permeability of 0.2 mD have been determined as the lower limits of the physical properties of Carboniferous reservoirs (Figure 11).

The lower limit of oil saturation is also the upper limit of water saturation. Using the oil test, perforation, and logging data for the Carboniferous oil strata, a resistivity-porosity cross-plot is drawn, and the oil strata, oil-water strata, oil-bearing water strata, and water strata boundaries are demarcated based on the different distributions of them on the plate. Therefore, the lower limit of oil saturation of Carboniferous reservoirs in the study area is 45% (Figure 12).

5.2 Reservoir fluid identification criteria

In this study, three commonly used methods were selected to identify the fluid properties of Carboniferous volcanic reservoirs, and the coincidence rates of resistivity-porosity cross-plot, normal probability distribution, and Rt/Rxo-Rt cross-plot method were 80%, 63.63%, and 63.63%, respectively. The identification accuracy of different methods differs due to the particularity of volcanic reservoirs and the adaptability of the methods. The resistivity-porosity cross-plot method is suitable for areas where drilling fluid does not intrude deeply into the stratum, and the reservoir porosity is relatively high, and it can better divide dry, oil, and water strata. The normal probability distribution method identifies fluids using the combination of apparent stratum water resistivity and mathematical theory. This method applies to pore-type and

fracture-pore-type reservoirs, provided that the difference in stratum water resistivity is small. The Rt/Rxo-Rt cross-plot method is mainly suitable for the division of oil and water strata according to the different fluid properties corresponding to different reservoir types, while the applicability to oil-water and oil-containing water strata is poor. Therefore, the resistivity-porosity cross-plot method is used for fluid identification in the study area with high accuracy, but it is still necessary to combine multiple methods for mutual verification to better identify the fluid properties of volcanic reservoirs. Based on the above analysis, this study summarizes the oil-water stratum identification criteria for volcanic reservoirs in the study area based on the research on oil and gas displays, test data, conventional logging response characteristics, fluid identification methods, and reservoir lower limits (Table 4).

6 Conclusion

1) The lithofacies of Carboniferous volcanic in the Shixi Oilfield include explosive and effusive facies, with the latter dominating. The lithology is mainly breccia lava, agglomerate, banded lava, and compact tuff. The main types of reservoir space are secondary pores and tectonic fissures. The tectonic fissures are of great significance to the improvement of reservoir properties. The corrosion-fracture pores that connect with primary and secondary pores are important reservoir spaces. The physical properties of the reservoir matrix are characterized by medium-high porosity and low permeability and belong to the fracture-pore reservoir with medium-high porosity and low permeability overall.
2) The lithology, electrical properties, physical properties, and gas-bearing properties of the volcanic reservoirs in the study area have obvious relationships. Lithology affects physical properties, which control oil- and gas-bearing and electrical properties, all of which have obvious responses to the differences and changes in lithology, physical properties and gas-bearing properties. Thus, a logging interpretation model applicable to the volcanic reservoir's physical parameters and oil saturation in the study area has been established.
3) The fluid identification criteria for volcanic reservoirs were established based on three methods, among which the resistivity-porosity cross-plot method has the best identification effect, with a coincidence rate of 80%. Given the shortcomings of the different methods, mutual verification based on multiple methods is the key to accurately identifying reservoir fluids. Using the reservoir parameter logging interpretation model and fluid identification plate, the lower porosity, permeability, and oil saturation limits are 9%, 0.2 mD, and 45%, respectively. Based on the characteristics of volcanic rock lithology and lithofacies, this paper comprehensively applied various fluid identification methods to improve the identification accuracy, and effectively guided the exploration and development of volcanic oil and gas in this area.

Data availability statement

The original contributions presented in the study are included in the article/supplementary material, further inquiries can be directed to the corresponding author.

Author contributions

LF, ZQ, AX, LC, Junfei Li, NW contributed in writing, reviewing, and editing, datacuration, writing—original draft preparation; QQ, KM contributed in formal analysis, validation, and reviewing.

Acknowledgments

We thank all editors and reviewers for their helpful comments and suggestions.

Conflicts of interest

LF, JL, NW were employed by the Shixi Field Operation District, Xinjiang Oilfield Company, CNPC, ZQ was employed by the Exploration Division, Petro China Southwest Oil and Gasfield Company, AX was employed by the Evaluation Department of Xinjiang Oilfield Company, CNPC, and LC was employed by Development Department of Xinjiang Oilfield Company, CNPC.

The remaining authors declare that the research was conducted in the absence of any commercial or financial relationships that could be construed as a potential conflict of interest.

Publisher's note

References

Ajaz, M., Ouyang, F., Wang, G. H., Liu, S. L., Wang, L. X., and Zhao, J. G. (2021). Fluid identification and effective fracture prediction based on frequency-dependent AVOAz inversion for fractured reservoirs. *Pet. Sci.* 18 (4), 1069–1085. doi:10.1016/j.petsci.2021.07.011

Chen, Z. Y., Yan, H., Li, J. S., Zhang, G., Zhang, Z. W., and Liu, B. Z. (1999). Relationship between Tertiary volcanic rocks and hydrocarbons in the Liaohe basin, People's Republic of China. *AAPG Bull.* 83 (6), 1004–1014. doi:10.1306/E4FD2E51-1732-11D7-8645000102C1865D

Das, B., and Chatterjee, R. (2018). Well log data analysis for lithology and fluid identification in Krishna-Godavari Basin, India. *Arab. J. Geosci.* 11 (10), 231. doi:10.1007/s12517-018-3587-2

Fan, C. H., Xie, H. B., Li, H., Zhao, S. X., Shi, X. C., Liu, J. F., et al. (2022). Complicated fault characterization and its influence on shale gas preservation in the southern margin of the Sichuan Basin, China. *Lithosphere*, 2022 8035106. doi:10.2113/2022/8035106

Fan, C. H., Li, H., Qin, Q. R., He, S., and Zhong, C. (2020b). Geological conditions and exploration potential of shale gas reservoir in Wufeng and Longmaxi Formation of southeastern Sichuan Basin, China. *J. Pet. Sci. Eng.* 191, 107138. doi:10.1016/j.petrol.2020.107138

Fan, C. H., Li, H., Qin, Q. R., Shang, L., Yuan, Y. F., and Li, Z. (2020a). Formation mechanisms and distribution of weathered volcanic reservoirs: A case study of the carboniferous volcanic rocks in northwest Junggar Basin, China. *Energy Sci. Eng.* 8 (8), 2841–2858. doi:10.1002/ese3.702

Feng, Z. Q. (2008). Volcanic rocks as prolific gas reservoir: A case study from the qingshen gas field in the songliao basin, NE China. *Mar. Pet. Geol.* 25 (4/5), 416–432. doi:10.1016/j.marpetgeo.2008.01.008

He, M., Gu, H. M., and Wan, H. (2020). Log interpretation for lithology and fluid identification using deep neural network combined with MAHAKIL in a tight sandstone reservoir. *J. Pet. Sci. Eng.* 194, 107498. doi:10.1016/j.petrol.2020.107498

He, S., Li, H., Qin, Q. R., and Long, S. X. (2021). Influence of mineral compositions on shale pore development of longmaxi formation in the dingshan area, southeastern sichuan basin. China. *Energy fuels* 35 (13), 10551–10561. doi:10.1021/acs.energyfuels.1c01026

Hooker, J. N., Abu-Mahfouz, I. S., Meng, Q., and Cartwright, J. (2018). Fractures in mudrocks: Advances in constraining timing and understanding mechanisms. *J. Struct. Geol.* 125, 166–173. doi:10.1016/j.jsg.2018.04.020

Hou, E. K., Cong, T., Xie, X. S., and Wei, J. B. (2020). Ground surface fracture development characteristics of shallow double coal seam staggered mining based on particle flow. *J. Min. Strata Control Eng.* 2 (1), 013521. doi:10.13532/j.jmsce.cn10-1638/td.2020.01.002

Hou, L. H., Luo, X., Wang, J. H., Yang, F., Zhao, X., and Mao, Z. G. (2013). Weathered volcanic crust and its petroleum geologic significance: A case study of the carboniferous volcanic crust in northern Xinjiang, NW China. *Pet. explor. Dev.* 40 (3), 277–286. doi:10.1016/S1876-3804(13)60034-8

Hou, L. H., Zou, C. N., Liu, L., Wen, B. H., Wu, X. Z., Wei, Y. Z., et al. (2012). Geologic essential elements for hydrocarbon accumulation within Carboniferous volcanic weathered crusts in northern Xinjiang, China. *Acta Pet. Sin.* 33 (4), 533–540. doi:10.7623/syxb201204001

Ibrahim, M. I. M., Hariri, M. M., Abdullatif, O. M., Makkawi, M. H., and Elzain, H. (2017). Fractures system within Qusaiba shale outcrop and its relationship to the lithological properties, Qasim area, Central Saudi Arabia. *J. Afr. Earth Sci.* 133, 104–122. doi:10.1016/j.jafrearsci.2017.05.011

Jarvie, D. M., Hill, R. J., Ruble, T. E., and Pollastro, R. M. (2007). Unconventional shale-gas systems: The Mississippian Barnett Shale of north-central Texas as one model for thermogenic shale-gas assessment. *Am. Assoc. Pet. Geol. Bull.* 91 (4), 475–499. doi:10.1306/12190606068

Kang, H. P. (2021). Temporal scale analysis on coal mining and strata control technologies. *J. Min. Strata Control Eng.* 3 (1), 013538. doi:10.13532/j.jmsce.cn10-1638/td.20200814.001

Li, H., Qin, Q. R., Li, Z. J., Fan, C. H., Zhong, K., Li, Z., et al. (2017). Characteristics and distribution of cracks in Carboniferous buried volcanic reservoirs of the Shixi Oilfield. *Geol. Expl.* 53 (6), 1219–1228. doi:10.13712/j.cnki.dzykt.2017.06.018

Li, H., Tang, H. M., Qin, Q. R., Fan, C. H, Han, S., Yang, C., et al. (2018). Reservoir characteristics and hydrocarbon accumulation of Carboniferous volcanic weathered crust of Zhongguai high area in the western Junggar Basin, China. *J. Cent. South Univ.* 25 (11), 2785–2801. doi:10.1007/s11771-018-3953-y

Li, H., Tang, H. M., Qin, Q. R., Wang, Q., and Zhong, C. (2019a). Effectiveness evaluation of natural fractures in Xujiahe Formation of Yuanba area, Sichuan basin, China. *Arab. J. Geosci.* 12 (6), 194. doi:10.1007/s12517-019-4292-5

Li, H., Tang, H. M., and Zheng, M. J. (2019b). Micropore structural heterogeneity of siliceous shale reservoir of the Longmaxi Formation in the southern Sichuan Basin, China. *Minerals* 9, 548. doi:10.3390/min9090548

Li, H., Qin, Q. R., Zhang, B. J., Ge, X. Y., Hu, X., Fan, C. H., et al. (2020). Tectonic fracture formation and distribution in ultradeep marine carbonate gas reservoirs: A case study of the maokou formation in the jiulongshan gas field, sichuan basin, southwest China. *Energy fuels* 34 (11), 14132–14146. doi:10.1021/acs.energyfuels.0c03327

Li, H. (2022). Research progress on evaluation methods and factors influencing shale brittleness: A review. *Energy Rep.* 8, 4344–4358. doi:10.1016/j.egyr.2022.03.120

Li, H., Tang, H. M., Qin, Q. R., Zhou, J. L., Qin, Z. J., Fan, C. H., et al. (2019). Characteristics, formation periods and genetic mechanisms of tectonic fractures in the tight gas sandstones reservoir: A case study of xujiahe formation in YB area, sichuan basin, China. *J. Pet. Sci. Eng.* 178, 723–735. doi:10.1016/j.petrol.2019.04.007

Li, H., Wang, Q., Qin, Q. R., and Ge, X. Y. (2021). Characteristics of natural fractures in an ultradeep marine carbonate gas reservoir and their impact on the reservoir: A case study of the maokou formation of the jls structure in the sichuan basin, China. *Energy fuels* 35 (16), 13098–13108. doi:10.1021/acs.energyfuels.1c01581

Li, J. J., Qin, Q. R., Li, H., Zhao, S. X., and Wan, Y. F. (2022). Numerical simulation of the stress field and fault sealing of complex fault combinations in Changning area, Southern Sichuan Basin, China. *Energy Sci. Eng.* 10 (2), 278–291. doi:10.1002/ese3.1044

Li, J., Li, H., Yang, C., Wu, Y. J., Gao, Z., and Jiang, S. L. (2022). Geological characteristics and controlling factors of deep shale gas enrichment of the Wufeng-Longmaxi Formation in the southern Sichuan Basin, China. *Lithosphere* 2022, 4737801. doi:10.2113/1970/4737801

Li, X., Fu, L., Ji, J. Q., Xie, L., Zhang, J. L., Li, H., et al. (2022). Reservoir characteristics and accumulation analysis of carboniferous volcanic rocks in Shixi Oilfield, Junggar Basin, China. *Chin. J. Geol.* 57 (3), 704–719. doi:10.12017/dzkx.2022.041

Liu, Z. Y., Pan, Z. J., Li, S. B., Zhang, L. G., Wang, F. S., Wang, C. H., et al. (2022). Fracturing optimization design of fractured volcanic rock in songliao basin based on numerical research and orthogonal test. *Lithosphere* 2022, 3325935. doi:10.2113/2022/3325935

Mollajan, A., Memarian, H., and Tokhmechi, B. (2013). Proposing a new integral method for fluid type identification from petrophysical logs in a carbonate reservoir. *Energy Explor. Exploitation* 31 (6), 895–908. doi:10.1260/0144-5987.31.6.895

Pan, X. P., Zhang, G. Z., and Yin, X. Y. (2019). Linearized amplitude variation with offset and azimuth and anisotropic poroelasticity. *Geophys. Prospect.* 67 (7), 1882–1897. doi:10.1111/1365-2478.12778

Qie, L., Shi, Y. N., and Liu, J. G. (2021). Experimental study on grouting diffusion of gangue solid filling bulk materials. *J. Min. Strata Control Eng.* 3 (2), 023011. doi:10.13532/j.jmsce.cn10-1638/td.20201111.001

Radwan, A. E. (2021). Modeling pore pressure and fracture pressure using integrated well logging, drilling based interpretations and reservoir data in the giant El Morgan oil field, Gulf of Suez, Egypt. *J. Afr. Earth Sci.* 178, 104165. doi:10.1016/j.jafrearsci.2021.104165

Saeid, E., Kendall, C., Kellogg, J., De Keyser, T., Hafiz, I., Albesher, Z., et al. (2022). A depositional model for the Carbonera Formation, Llanos Foothills, Colombia, from workflow of a sequence stratigraphic framework and interpretation from well-log stacking patterns, well cuttings, and three-dimensional seismic spectral decomposition. *Am. Assoc. Pet. Geol. Bull.* 106 (2), 321–353. doi:10.1306/08092118015

Shan, S. C., Wu, Y. Z., Fu, Y. K., and Zhou, P. H. (2021). Shear mechanical properties of anchored rock mass under impact load. *J. Min. Strata Control Eng.* 3 (4), 043034. doi:10.13532/j.jmsce.cn10-1638/td.20211014.001

Smeraglia, L., Mercuri, M., Tavani, S., Pignalosa, A., Kettermann, M., Billi, A., et al. (2021). 3D Discrete Fracture Network (DFN) models of damage zone fluid corridors within a reservoir-scale normal fault in carbonates: Multiscale approach using field data and UAV imagery. *Mar. Pet. Geol.* 126, 104902. doi:10.1016/j.marpetgeo.2021.104902

Wang, J., and Wang, X. L. (2021). Seepage characteristic and fracture development of protected seam caused by mining protecting strata. *J. Min. Strata Control Eng.* 3 (3), 033511. doi:10.13532/j.jmsce.cn10-1638/td.20201215.001

Wang, S. L., Li, H., Lin, L. F., and Yin, S. (2022). Development characteristics and finite element simulation of fractures in tight oil sandstone reservoirs of Yanchang Formation in western Ordos Basin. *Front. Earth Sci.* 9, 823855. doi:10.3389/feart.2021.823855

Weng, K., Ma, Z. P., Cao, K., Dong, Y. P., Chen, B., and Zhao, X. J. (2020). Petrogenesis and tectonic implications of the early Carboniferous volcanic rocks in West Junggar, NW China. *Geol. J.* 55 (3), 1826–1848. doi:10.1002/gj.3604

Yang, Y. Q., Qiu, L. W., Cao, Y. C., Chen, C., Lei, D. W., and Wan, M. (2017). Reservoir quality and diagenesis of the permian lucaogou formation tight carbonates in jimsar sag, Junggar Basin, west China. *J. Earth Sci.* 28, 1032–1046. doi:10.1007/s12583-016-0931-6

Zhang, H., Ni, H. J., Wang, Z. Z., Liu, S. B., and Liang, H. J. (2020). Optimization and application study on targeted formation ROP enhancement with impact drilling modes based on clustering characteristics of logging. *Energy Rep.* 6, 2903–2912. doi:10.1016/j.egyr.2020.10.020

Zhao, B., Li, Z. P., Gao, C. Q., and Tang, Y. (2022). Identification of complex fluid properties in condensate gas reservoirs based on gas-oil ratio parameters calculated by optimization mathematical model. *Front. Energy Res.* 10, 863776. doi:10.3389/fenrg.2022.863776

Zhou, Y. H., Hu, Q. X., Liu, W. T., Wu, Z. Q., Yan, Y. L., and Ma, J. L. (2020). Study on the origin and fluid identification of low-resistance gas reservoirs. *Geofluids* 2020, 1–12. doi:10.1155/2020/8859309

Zou, C. N., Hou, L. H., Tao, S. Z., Yuan, X. J., Zhu, R. K., Zhang, X. X., et al. (2012). Hydrocarbon accumulation mechanism and structure of large-scale volcanic weathering crust of the Carboniferous in Northern Xinjiang, China. *Sci. China Earth Sci.* 55, 221–235. doi:10.1007/s11430-011-4297-8

frontiers | Frontiers in Earth Science

TYPE Original Research
PUBLISHED 15 August 2022
DOI 10.3389/feart.2022.970719

OPEN ACCESS

EDITED BY
Wenlong Ding,
China University of Geosciences, China

REVIEWED BY
Jun Liu,
Sichuan University, China
Wang Wei,
Jilin University, China

*CORRESPONDENCE
Qunshuang Zhang,
zqs_ha123@163.com

SPECIALTY SECTION
This article was submitted to Structural Geology and Tectonics, a section of the journal Frontiers in Earth Science

RECEIVED 16 June 2022
ACCEPTED 15 July 2022
PUBLISHED 15 August 2022

CITATION
Yang S, Xu Y, Huang Z, Zhang Q, Liu T and Li X (2022), Application of CO_2 miscible flooding in ultra-low permeability beach-bar sand reservoir. *Front. Earth Sci.* 10:970719. doi: 10.3389/feart.2022.970719

Application of CO_2 miscible flooding in ultra-low permeability beach-bar sand reservoir

Sen Yang[1,2], Yangmengzhe Xu[3], Zhiwei Huang[4], Qunshuang Zhang[5]*, Ting Liu[6] and Xuelei Li[6]

[1]Petroleum Engineering School, South West Petroleum University, Chengdu, China, [2]International Business Center, Sinopec Huadong Oilfield Service Corporation, Nanjing, China, [3]Changqing Oilfield Branch of Petrochina, Xi'an, China, [4]Shengli OilProduction Plant, Shengli Oilfield Company, SINOPEC, Dongying, China, [5]Gepetto Oil Technology Group Co Ltd., Chengdu, China, [6]Fracturing Company, Great Wall Drilling Corp, CNPC, Panjin, China

The beach-bar sand reservoir of the Sha 4 Member of the Shahejie Formation in the Dongying Sag is the main oil-bearing formation in this area. In recent years, its proven reserves have been getting lower and lower, and the poor petrophysical properties of the reservoir have made water injection development difficult. In turn, it results in a rapid decline in elastic development productivity and low oil recovery. In this study, the experimental evaluation and numerical simulation research on the adaptability of CO_2 flooding in beach-bar sand reservoirs are carried out on the basis of fully investigating the successful examples of CO_2 flooding conducted by the previous. According to the geological characteristics of the reservoir in the CL area of the Dongying Sag, the reasonable reservoir engineering parameters and surface injection procedures for the CO_2 flooding have been formulated. Experiments show that after the completion of water flooding, the recovery factor of the CO_2 continuous flooding is 85.64%. It proves that the recovery factor of the CO_2 flooding is higher than that of the water flooding. Field tests have shown that CO_2 molecules in beach-bar sand reservoirs behave in a supercritical state underground, which is easier to being injected into the reservoir than water. In addition, the displacement distance of the CO_2 is obviously larger than that of the water injection development. The gas-oil ratio variation of different flooding types is different, and CO_2 flooding can effectively increase the formation energy, and improve the oil recovery and economic benefits of this type of reservoir.

KEYWORDS

CO2 flooding technology, beach-bar sand reservoir, CO2 miscible flooding, recovery factor, field study

Introduction

The average recovery factor of water-flooding reservoirs is usually only 30.0%, and its remaining oil saturation is high, so the potential of tertiary oil recovery is great (Dicharry et al., 1973; Al-Abri et al., 2009; Al-Bayati et al., 2019; Gao and Pu., 2021; Li et al., 2021). CO_2 miscible flooding belongs to tertiary oil recovery technology. By injecting CO_2 into the reservoir, the interfacial tension, viscosity and fluidity of the crude oil can be improved, and the ultimate recovery of the crude oil is enhanced. Because CO_2 miscible flooding has good oil-increasing effect and wide adaptability, it has become the main measure for tertiary oil recovery in different oilfields (Al-Abri and Amin, 2010; Hu et al., 2015; Yongle et al., 2019; Chen et al., 2020; Qin et al., 2021). In the past 20 years, laboratory and field experiments of CO_2 miscible flooding have been carried out in the Daqing, Jilin, Zhongyuan and Huadong Oilfields in China. However, there are few reports on field trials of CO_2 miscible flooding in ultra-high water-cut reservoirs (Stalkup., 1978; Desch et al., 1984; Akbarabadi and Piri., 2013; Wang et al., 2019; Jia et al., 2021; Huang et al., 2022).

The CO_2 injection development of low permeability sandstone reservoirs is a reliable and effective method to enhance oil recovery. The main mechanisms include the reduction of interfacial tension, the reduction of crude oil viscosity, the swelling effect of crude oil, and the extraction of light hydrocarbons (Song et al., 2012; Chen et al., 2017; Zhang et al., 2018; Chen et al., 2019; Hou et al., 2020). Under miscible conditions, CO_2 and crude oil can be mixed in any ratio, thereby eliminating interfacial tension and obtaining high CO_2 flooding efficiency. However, CO_2 immiscible flooding is likely to cause early CO_2 breakthrough. Crude oil is considered a colloidal system, the dispersion medium is saturated and aromatic hydrocarbons, and the asphaltenes are in a dispersed phase (Paxton et al., 2002; Golkari and Riazi., 2017; Fakher and Imqam., 2020). When CO_2 is injected into the reservoir, it will dissolve into the crude oil, and its extraction of the light components of the crude oil will lead to changes in the composition of the crude oil system. Furthermore, the asphaltene molecules in the crude oil cannot continue to be stably dispersed in the crude oil. At this point, the asphaltene molecules collide with each other and flocculate into aggregates that eventually precipitate out of the crude oil and then solid precipitates are formed. The size of these precipitated particles will gradually increase as the fluid migrates in the rock pores (Lashkarbolooki et al., 2016; Ding et al., 2019; Du et al., 2021; Liu et al., 2022). When the size of the asphaltene precipitation particles approaches or exceeds the size of the pore throats, the particles can become trapped and form blockages at the narrow throats, and the pore throat connectivity of the rock will be reduced. At the same time, asphaltene precipitation is also continuously adsorbed on the surface of rock minerals, resulting in a gradual decrease in the size of pores and throats. Asphaltene precipitation particles are much more likely to block pore throats. In addition, the adsorption of these asphaltene precipitates on the pore surface can also cause changes in rock wettability. Therefore, asphaltene precipitation can change the pore-throat structures of the rock by forming plugging and adsorption, thereby impairing the reservoir permeability and increasing the water cut and residual oil ratio (Lv et al., 2015; Wang et al., 2018; Hong et al., 2020; Hu et al., 2020).

Typical beach-bar sand reservoirs are developed in the Sha 4 Member of the Shahejie Formation in the CL area of the Dongying Sag, China. In recent years, the quality of the newly added proven reserves in the Sha 4 Member of the Shahejie Formation has been getting worse and worse. This is because the burial depth of the reservoir is relatively deep (between 2,700–3,500 m), and the permeability of the reservoir drops sharply from 10 to 0.3 mD. Due to the inability to achieve high-efficiency water injection development, oilfield engineers can only select some units with relatively good petrophysical properties to carry out large-scale fracturing (Kazemzadeh et al., 2015; Qiao et al., 2019; Xu and Gao., 2020; Yoshida and Santosh., 2020; Lan et al., 2021). From the perspective of development status, for low-permeability reservoirs developed only by natural energy, the average monthly decline rate of their productivity reaches 4%. Therefore, many newly discovered low-permeability reserves are poorly developed, resulting in a huge potential of remaining reserves in unproduced beach-bar sand reservoirs. For ultra-low permeability beach-bar sand reservoirs, water flooding development is greatly restricted (Li et al., 2020; Mahmud et al., 2020; Wang et al., 2020; Li., 2022; Wang et al., 2022). The development method that relies solely on elastic energy results in rapid decline in production and low recovery of crude oil. Therefore, it is necessary to find new energy supplement methods to improve the development level and production degree of low-permeability reservoirs.

In this study, the experimental evaluation and numerical simulation research on the adaptability of CO_2 flooding in beach-bar sand reservoirs are carried out on the basis of fully investigating the successful examples of CO_2 flooding conducted by the previous. According to the geological characteristics of the reservoir in the CL area of the Dongying Sag, the reasonable reservoir engineering parameters and surface injection procedures for CO_2 flooding have been formulated. The research results have important reference value for formulating an efficient development plan for beach-bar sand reservoirs in similar areas.

Materials and methods

The target layer of this study is the beach-bar sand body in the upper part of the Sha 4 Member of the Shahejie Formation, which is widely distributed in the Dongying Sag. This set of sand bodies is located in the interlayer of the source rocks, and the thickness of the single layer is generally between 2 and 5 m, and it

has the characteristics of large-area oil-bearing properties. The residual amount of original formation water in the sand body is extremely low, so the CO_2 flooding technology is suitable for improving the oil recovery of this set of reservoirs.

Feasibility of CO_2 flooding development

Usually, the waterflooding development effect of low-permeability and ultra-low- permeability beach-bar sand reservoirs is not ideal. When the petrophysical properties of the sandstone reservoirs are less than 3 mD, the development benefit of water flooding is quite poor, and the permeability of the Sha 4 Formation reservoir in the study area is between 0.3–10 mD, so it is not suitable for water flooding development. For the XX-1 Block with relatively good petrophysical properties of the target layer in the study area, the large-scale anti-swelling method is adopted, and the initial oil pressure via water injection is between 20–30 MPa. In a short period of time, the water injection pressure can be increased to more than 35 MPa, and the wellhead can meet the injection requirements after the booster pump is used. However, with the deepening of development, the excessive water injection pressure caused serious damage to the casing of the water injection well, and the reservoir began to suffer from under-injection and under-production in a large area (Mahmi et al., 2018; Wang et al., 2021; Li et al., 2022). Therefore, it is urgent to explore the development method of CO_2 flooding for ultra-low permeability beach-bar sand reservoirs.

In this study, the reasons for the ultra-low permeability beach-bar sand reservoirs suitable for CO_2 miscible flooding in the Sha 4 Member of the Shahejie Formation in the CL area are as follows:

(1) The research block is in the early stage of crude oil development, and the degree of crude oil recovery is high. Moreover, its crude oil basically does not contain water, which is conductive to the development of CO_2 flooding technology.
(2) The connectivity of the beach-bar sand reservoirs in the study area is good, and the connectivity rate of the main sand bodies is 93%. At the same time, the beach-bar sand reservoir has no edge and interlayer water, which is conducive to reducing the corrosion of equipments, so it is suitable for CO_2 injection.
(3) The main reservoir of the ultra-low permeability beach-bar sand reservoir in the Sha 4 Member of the Shahejie Formation in the study area is buried between 2,700–3,400 m, and its original formation pressure is 32–45 MPa. Its ground saturation pressure difference is large, so it is easy to form miscible phase after CO_2 injection into the formation. Therefore, it is beneficial to carry out CO_2 miscible flooding.

Design of minimum CO_2 miscible pressure experiment

(1) Model parameters

The experimental model adopts a thin tube model with a length of 16 m and a diameter of 6.34 mm. The air permeability was maintained at <9.9 mD, the porosity was 32.25%, the experimental temperature was 126°C, and the displacement speed was 0.873 m/h.

(2) Criteria for determining the minimum miscible pressure for CO_2 flooding

When 1.2 times the pore volume of CO_2 was injected, there was a sudden change in the slope between the pressure curve and the displacement efficiency. Moreover, the final recovery factor is >95%, and the breakthrough value is later than 0.74 PV. In addition, a transition zone formed by immiscible gas and liquid phases can be seen in the observation port, which gradually diffuses to form a single phase after complete miscibility.

Design of long core flooding tests

The long core displacement test adopts a long core displacement device, which is mainly composed of a displacement system, a constant temperature device, a long core holder system, a back pressure controller and an oil measurement and gas measurement device. The maximum working pressure is 50 MPa and the temperature is 150°C.

The displacement tests of long cores were carried out under the conditions of simulated formation temperature of 125°C and pressure of 30 MPa. A total of three different long core flooding experiments were carried out. The experiments were used to evaluate the effect of injection timing and injection method on the enhanced oil recovery effect of miscible flooding.

A total of 3 sets of plans have been designed:

(a) After the water is flooded to 100% water content, CO_2 is continuously injected until no oil is produced;
(b) First, continuous injection of CO_2 large slug initially, when no oil is produced, it is transferred to water flooding;
(c) Initially, alternate injection of CO_2 and water is carried out, and when no oil is produced, it is transferred to the subsequent water flooding.

Numerical simulation of CO_2 flooding scheme

The numerical simulation in this study was completed using the PVT analysis results of laboratory experimental fluids and the CMG

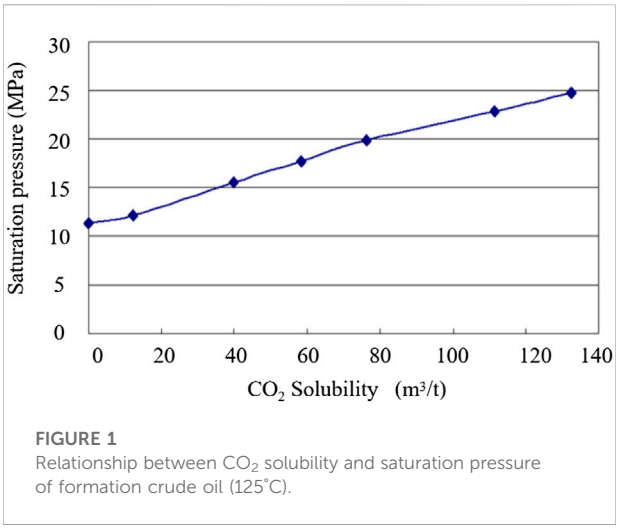

FIGURE 1
Relationship between CO_2 solubility and saturation pressure of formation crude oil (125°C).

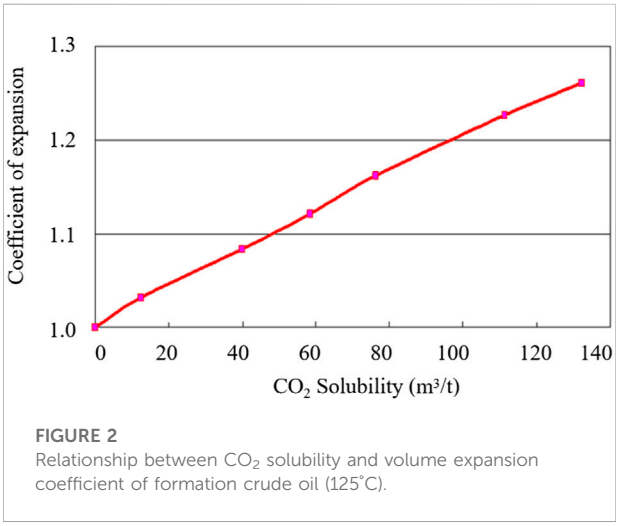

FIGURE 2
Relationship between CO_2 solubility and volume expansion coefficient of formation crude oil (125°C).

reservoir numerical simulation software. The construction of the equation of state for the CMG reservoir is based on the phase equilibrium software package Winprop. Furthermore, it is used for fluid characterization, compositional fitting, regression fitting of PVT experimental data, and simulation of multiple contact processes. It generates the data required by the component simulator GEM by establishing the equation of state of the crude oil in the target layer.

Results

Properties of CO_2 and formation crude oil

(1) Variation of saturation pressure of formation crude oil

Indoor CO_2 miscible flooding experiments show that the saturation pressure of formation crude oil will gradually increase after increasing the injection amount of CO_2. Therefore, CO_2 has strong mutual solubility in the formation crude oil in this block (Figure 1).

(2) Variation of volume expansion coefficient of formation crude oil

Through laboratory experiments, the relationship between CO_2 solubility and formation oil volume expansion coefficient (Figure 2) was plotted. The expansion coefficient is basically positively correlated with the solubility of CO_2, indicating that CO_2 has a better expansion ability of the crude oil in the formation.

(2) Changes in the viscosity of formation crude oil

In general, the greater the dissolved amount of CO_2 contained in crude oil, the lower its viscosity (Paul et al., 1984; Santosh and Feng., 2020; Yin and Wu., 2020; Mirzaei-Paiaman and Ghanbarian., 2021).

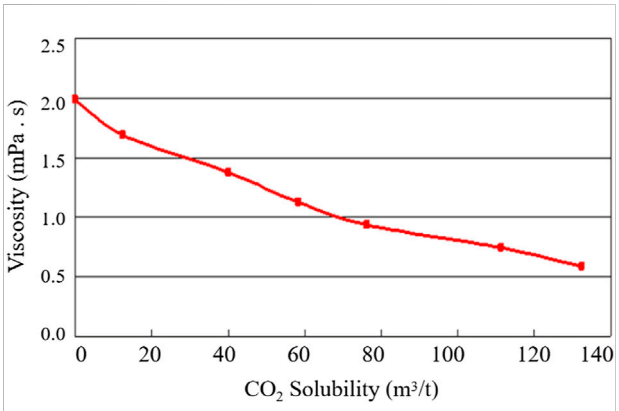

FIGURE 3
Relationship between CO_2 solubility and viscosity of formation crude oil (125°C).

The relationship between the viscosity of crude oil and the solubility of CO_2 in the study area shows that (Figure 3), the viscosity and solubility of crude oil are negatively correlated. Therefore, CO_2 can improve the flowability of formation crude oil.

According to this study, the crude oil in the study area has a relatively strong dissolving ability to CO_2, and the volume expansion and viscosity reduction of the crude oil are caused by the injection of CO_2.

Experimental results of minimum CO_2 miscible pressure

When the experimental pressure was gradually increased, the oil displacement effect of CO_2 began to increase significantly. When the pressure was increased to 29.0 MPa, the oil displacement efficiency at 1.1 PV was over 97%, and it had reached complete miscibility

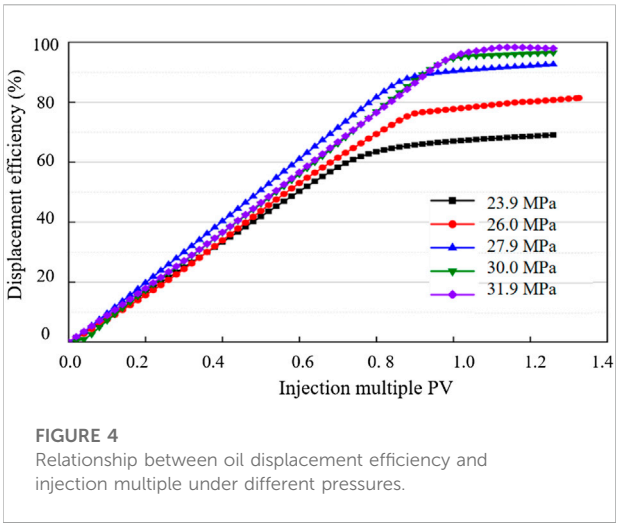

FIGURE 4
Relationship between oil displacement efficiency and injection multiple under different pressures.

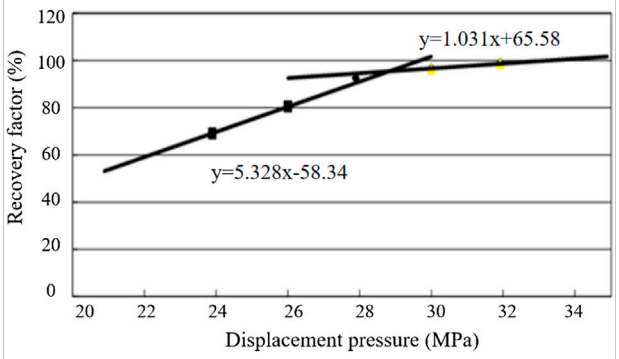

FIGURE 5
Determination of minimum miscible pressure.

(Figure 4). From the relationship between oil displacement efficiency and gas injection pressure at 1.1 PV, it can be concluded that the minimum miscible pressure in block XX is 28.94 MPa, and the corresponding oil displacement efficiency is 95.4% (Figure 5).

Therefore, it is easier to form a miscible state when the minimum miscible pressure is weaker than the original formation pressure.

Experimental results of CO_2 miscible oil displacement efficiency

The results of three long core flooding experiments show that (Figure 6), when the pressure and temperature are kept constant, the water flooding recovery factor is 33.50%; after the completion of water flooding, the recovery factor of the CO_2 continuous flooding is 85.64%; after CO_2 continuous flooding, the recovery factor when changed to water flooding is 79.58%; after the initial alternate injection of CO_2 and water, the recovery factor when changed to water flooding is 81.56%. The test results fully demonstrate that the

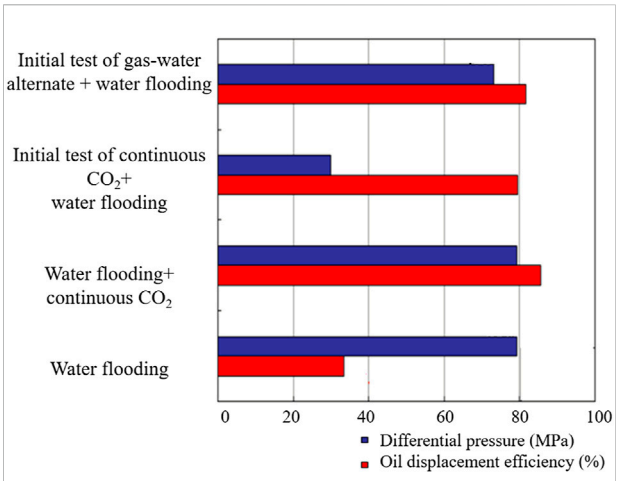

FIGURE 6
Oil displacement efficiency results for different injection methods.

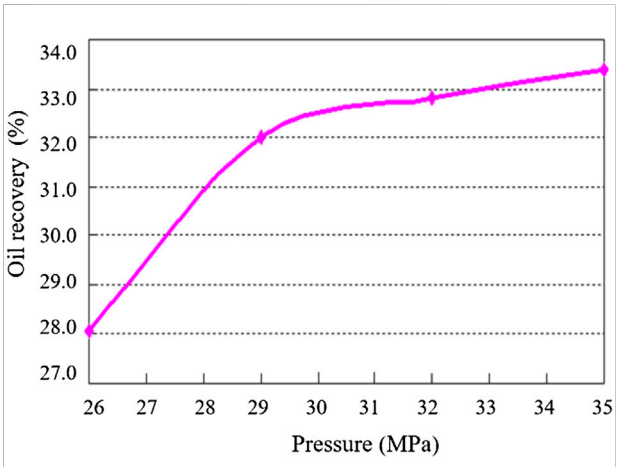

FIGURE 7
Variation characteristics of recovery factor with formation pressure.

oil recovery factor of the CO_2 flooding is much higher than1 that of water flooding. Considering the actual situation of the Block XX, the optimal injection method is continuous CO_2 flooding.

Discussion

Parameter optimization of CO_2 flooding scheme

For the simulation of the CO_2 flooding scheme in this study, the basic conditions of the production well are set as:

the minimum limit bottom-hole pressure: 12 MPa; the minimum limit oil production: 3 t/d; the limit gas-oil ratio: 2000 m^3/m^3. The basic conditions of the gas injection well are set as: the maximum injection pressure at the bottom of the well: 60 MPa.

(1) Optimization of pressure maintenance level

It can be clearly seen from the curve of recovery factor versus formation pressure (Figure 7) that when the miscible pressure is lower than 28.95 MPa, the pressure rises. And the recovery factor increases linearly and the growth rate is large, which is much higher than the recovery factor after miscible pressure. Therefore, the oil-reservoir pressure must be maintained above the miscible pressure (Trevisan et al., 2014; Qie et al., 2021; Wang and Wang., 2021).

(2) Optimization of CO_2 injection amount

According to the relationship among the PV value of CO_2 injection, the recovery factor and the daily oil production rate, it can be seen that the oil recovery factor increases with the increase of the injected PV value, and the daily oil production rate shows a slight downward trend. When the daily oil production rate dropped to 0.33, its changing trend began to stabilize, and the maximum value of the PV of injected CO_2 was 0.33.

(3) Optimization of gas injection and oil recovery rates

The optimization simulation results of different gas injection and oil recovery rates show that the oil recovery efficiency is the best when the oil recovery rate is maintained at 2% and the gas injection rate is maintained at 20 t/d.

Field application and effect analysis of CO_2 miscible flooding

In this study, we carried out the pilot experiment of CO_2 flooding and enhanced recovery in the study area. The three-stage test development mode of single well experiment-well group expansion-block implementation was adopted. The application uses procedures implemented from individual wells to groups of wells to blocks.

The first stage: single-well test injection of CO_2 in well A1.

Well A1 in the middle of Block XX is selected as the CO_2 injection test well. The well spacing between this well and the surrounding 6 production wells is 350–700 m, the daily gas injection volume is 30–60 m^3, and the gas injection pressure in the initial stage is low and maintained at 2–8 MPa. Except for the one well with the farthest distance of 700 m, which was not effective, the other five wells were all effective to varying degrees (Table 1).

The second and third stages: After the measure wells in the first stage are effective, the well group expansion will begin. 2 gas injection wells and 1 production well were newly drilled in Block XX, forming 4 central gas injection wells and 6 surrounding production wells. After that, the injection-production well pattern was gradually improved, and the overall development of the XX Block was realized.

(1) Gradual recovery of formation energy

The static pressure measured in Well A1 was 14.78 MPa at the time of transfer injection, and it changed to 25.628 MPa after 2 years, with an increase of 10.848 MPa and an average monthly increase of 0.638 MPa. For another gas injection well of Well A-16, the static pressure measured at the start-up stage was 26.03 MPa, and the static pressure measured after 2 years of gas injection was 28.3 MPa. It can be seen from the pressure tests of a single well that the formation pressure in the block is gradually recovered. According to the numerical simulation results, the formation pressure recovers faster near the bottom of the injection hole (Zekri et al., 2009; Zhang et al., 2020; Zhao et al., 2021).

In the design scheme, when the designed oil production rate of the central well group scheme is 2% and the injection-production ratio is 2.0, the time for the pressure to recover to miscibility is 1.25 years. At present, the oil production rate in the central well area is 1.76%, and the injection-production ratio is 1.23. The estimated time to start pressure recovery to miscibility at current production rates is 1.5 years. If the injection-production ratio is 2.0 according to the design, the pressure recovery time is 1 year (Figure 8).

(2) Analysis of oil-increasing effect

Judging from the effective time of a single well of the gas injection well group in the Block XX, the effective time is 2–8 months, the average effective time is 4.4 months, and the effective time is positively correlated with the well spacing. In addition, the decline of gas injection well groups is 15% slower than that of elastic development well groups. According to the production status and monitoring results of the oil wells, the surrounding wells have seen very significant oil increases. According to the calculation results of the exponential decreasing method, the cumulative oil increase of the well group is 10,200 t. Comparing the effects of water injection and gas injection, the first-line well with gas injection effect has a stable daily production of 10 t, and the single well with water injection effect has a stable daily production of 3–5 t. After the gas injection took effect, the liquid volume increased by an average of 2 times; and after the water injection took effect, the liquid volume increased by 0.5 times.

TABLE 1 Statistical results of productivity effectiveness of A1 well group.

Well	Production situation before measures				Production situation after measures				Daily oil production change (t)
	Daily liquid production (t)	Daily oil production (t)	Water content (%)	Liquid surface (m)	Daily liquid production (t)	Daily oil production (t)	Water content (%)	Liquid surface (m)	
A1	11.2	11	1.8	1,400	12.3	12.1	2.2	1,551	1.1
A2	2.6	2.6	0	2088	9.7	9.6	1.2	1814	7
A3	4.9	4.9	1.3	2,156	6.7	6.6	1.8	2,225	1.7
A4	6.8	5.9	13.5	2,660	4.6	4.5	1.5	/	−1.4
A5	6.8	6.7	1.5	1900	6	5.5	8.1	393	−1.2
A6	14.7	14.6	1.3	1,280	15.6	15.5	1.1	1,264	0.9
Total	47.5	46	3.2	1900	54.9	53.8	4.5	1,450	8.1

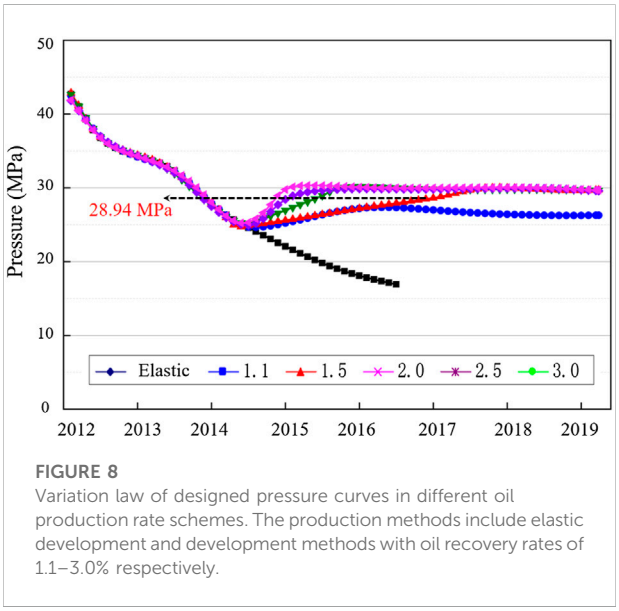

FIGURE 8
Variation law of designed pressure curves in different oil production rate schemes. The production methods include elastic development and development methods with oil recovery rates of 1.1–3.0% respectively.

(3) Analysis of economic benefit

Of the three development stages, the oil change ratio was 4.2: 1 in the first stage, 5.9:1 in the second stage, and 3.8:1 in the third stage. Currently, the block has an overall oil change ratio of 4.9:1. The second stage is mainly due to the reduction of oil change rate due to the phenomenon of gas channeling. With the increase of CO_2 injection amount, the formation energy gradually recovered and the oil change rate increased (Zhao et al., 2015; Xue et al., 2021; Yang et al., 2021).

Under the condition of production time of 6 years, the CO_2 gas injection in the XX block is compared with the water injection in the adjacent block. Under the same conditions of single well investment, the cost per 1 m^3 of water injection is 11 yuan, and the cost per 1 m^3 of gas injection is 300 yuan. There are 7 water injection wells corresponding to the 7 production wells in the adjacent block, while there are 7 CO_2 injection production wells in the XX Block, which corresponds to 4 gas injection wells. According to the current decreasing calculation of the block, the accumulated oil of water injection and gas injection after 6 years is 7.1736×10^4 t and 11.6916×10^4 t respectively, the income is 179.52 million yuan and 292.58 million yuan respectively, and the input-output ratio is 1:3.05 and 1: 2.95 respectively. It shows good economic benefits, and with the extension of time, the economic benefits of gas injection will be better than water injection.

Conclusion

(1) In this study, the experimental evaluation and numerical simulation research on the adaptability of CO_2 flooding in beach-bar sand reservoirs are carried out on the basis of fully investigating the successful examples of CO_2 flooding conducted by the previous. According to the geological characteristics of the reservoir in the CL area of the Dongying Sag, the reasonable reservoir engineering parameters and surface injection procedures for CO_2 flooding have been formulated.

(2) Experiments show that after the completion of water flooding, the recovery factor of the CO_2 continuous flooding is 85.64%. It proves that the recovery factor of the CO_2 flooding is higher than that of water flooding. Field tests have shown that CO_2 molecules in beach-bar sand reservoirs behave in a supercritical state underground, which is easier to being injected into the reservoir than water.

(3) The displacement distance of the CO_2 is obviously larger than that of the water injection development. The gas-oil ratio variation of different flooding types is different, and CO_2 flooding can effectively increase the formation energy,

and improve the oil recovery and economic benefits of this type of reservoir.

Data availability statement

The original contributions presented in the study are included in the article/Supplementary Material, further inquiries can be directed to the corresponding author.

Author contributions

SY and QZ are responsible for the idea and writing of this paper and YX, ZH, TL, and XL are responsible for the data interpretation.

Funding

We gratefully acknowledge National Science and Technology of China (2016ZX05070) financial support.

Conflict of interest

Author SY was employed by the Sinopec Huadong Oilfield Service Corporation, author YX was employed by the Changqing Oilfield Branch, author ZH was employed by the Shengli Oilfield Company, author QZ was employed by the Gepetto Oil Technology Group Co. Ltd., and authors TL and XL were employed by the Great Wall Drilling Corp, CNPC.

The remaining authors declare that the research was conducted in the absence of any commercial or financial relationships that could be construed as a potential conflict of interest.

Publisher's note

References

Akbarabadi, M., and Piri, M. (2013). Relative permeability hysteresis and capillary trapping characteristics of supercritical CO_2/brine systems: An experimental study at reservoir conditions. *Adv. Water Resour.* 52, 190–206. doi:10.1016/j.advwatres.2012.06.014

Al-Abri, A., and Amin, R. (2010). Phase behaviour, fluid properties and recovery efficiency of immiscible and miscible condensate displacements by $SCCO_2$ injection: Experimental investigation. *Transp. Porous Media* 85 (3), 743–756. doi:10.1007/s11242-010-9589-5

Al-Abri, A., Hiwa, S., and Robert, A. (2009). Experimental investigation of the velocity-dependent relative permeability and sweep efficiency of supercritical CO_2 injection into gas condensate reservoirs. *J. Nat. Gas Sci. Eng.* 1 (4-5), 158–164. doi:10.1016/j.jngse.2009.10.002

Al-Bayati, D., Saeedi, A., Myers, M., White, C., and Xie, Q. (2019). An experimental investigation of immiscible-CO_2-flooding efficiency in sandstone reservoirs: Influence of permeability heterogeneity. *SPE Reserv. Eval. Eng.* 22 (3), 990–997. doi:10.2118/190876-pa

Chen, H., Li, B., Duncan, I., Elkhider, M., and Liu, X. (2020). Empirical correlations for prediction of minimum miscible pressure and near-miscible pressure interval for oil and CO_2 systems. *Fuel* 278, 118272. doi:10.1016/j.fuel.2020.118272

Chen, H., Li, B., Zhang, X., Wang, Q., Wang, X., Yang, S., et al. (2019). Effect of gas contamination and well depth on pressure interval of CO_2 near-miscible flooding. *J. Petroleum Sci. Eng.* 176, 43–50. doi:10.1016/j.petrol.2019.01.062

Chen, H., Zhang, X., Chen, Y., Tang, H., Mei, Y., Li, B., et al. (2017). Study on pressure interval of near-miscible flooding by production gas Re-injection in QHD offshore oilfield. *J. Petroleum Sci. Eng.* 157, 340–348. doi:10.1016/j.petrol.2017.07.045

Desch, J. B., Larsen, W. K., Lindsay, R. F., and Nettle, R. L. (1984). Enhanced oil recovery by CO2 miscible displacement in the little knife field, billings county, north Dakota. *J. petroleum Technol.* 36 (09), 1592–1602. doi:10.2118/10696-pa

Dicharry, R. M., Perryman, T. L., and Ronquille, J. D. (1973). Evaluation and design of a CO2 miscible flood project-SACROC unit, Kelly-Snyder field. *J. Petroleum Technol.* 25 (11), 1309–1318. doi:10.2118/4083-pa

Ding, M., Gao, M., Wang, Y., Qu, Z., and Chen, X. (2019). Experimental study on CO2-EOR in fractured reservoirs: Influence of fracture density, miscibility and production scheme. *J. Petroleum Sci. Eng.* 174, 476–485. doi:10.1016/j.petrol.2018.11.039

Du, D., Li, C., Song, X., Liu, Q., Ma, N., Wang, X., et al. (2021). Experimental study on residue oil distribution after the supercritical CO2 huff-n-puff process in low permeability cores with Nuclear Magnetic Resonance (NMR). *Arabian J. Chem.* 14 (10), 103355. doi:10.1016/j.arabjc.2021.103355

Fakher, S., and Imqam, A. (2020). An experimental investigation of immiscible carbon dioxide interactions with crude oil: Oil swelling and asphaltene agitation. *Fuel* 269, 117380. doi:10.1016/j.fuel.2020.117380

Gao, H., and Pu, W. (2021). Experimental study on supercritical CO2 huff and puff in tight conglomerate reservoirs. *ACS omega* 6 (38), 24545–24552. doi:10.1021/acsomega.1c03130

Golkari, A., and Riazi, M. (2017). Experimental investigation of miscibility conditions of dead and live asphaltenic crude oil–CO2 systems. *J. Pet. Explor. Prod. Technol.* 7 (2), 597–609. doi:10.1007/s13202-016-0280-4

Hong, D., Cao, J., Wu, T., Dang, S., Hu, W., and Yao, S. (2020). Authigenic clay minerals and calcite dissolution influence reservoir quality in tight sandstones: Insights from the central Junggar Basin, NW China. *Energy Geosci.* 1 (1–2), 8–19. doi:10.1016/j.engeos.2020.03.001

Hou, E., Cong, T., and Xie, X. (2020). Ground surface fracture development characteristics of shallow double coal seam staggered mining based on particle flow. *J. Min. Strata Control Eng.* 2 (1), 013521. doi:10.13532/j.jmsce.cn10-1638/td.2020.01.002

Hu, Y., Guo, C., and Xu, X. (2015). Pore throat structure and flow characteristics of sandstone reservoirs. *Petroleum Geol. Exp.* 37 (3), 390–393.

Hu, Y., Patmonoaji, A., Zhang, C., and Suekane, T. (2020). Experimental study on the displacement patterns and the phase diagram of immiscible fluid displacement in three-dimensional porous media. *Adv. Water Resour.* 140, 103584. doi:10.1016/j.advwatres.2020.103584

Huang, X., Zhang, Y., He, M., Li, X., Yang, W., Lu, J., et al. (2022). Asphaltene precipitation and reservoir damage characteristics of CO2 flooding in different microscopic structure types in tight light oil reservoirs. *Fuel* 312, 122943. doi:10.1016/j.fuel.2021.122943

Jia, Z., Ning, Z., Gao, X., Wang, Q., Zhang, W., Cheng, Z., et al. (2021). Experimental investigation on molecular-scale mechanism of wettability alteration induced by supercritical carbon dioxide-water-rock reaction. *J. Petroleum Sci. Eng.* 205, 108798. doi:10.1016/j.petrol.2021.108798

Kazemzadeh, Y., Parsaei, R., and Riazi, M. (2015). Experimental study of asphaltene precipitation prediction during gas injection to oil reservoirs by interfacial tension measurement. *Colloids Surfaces A Physicochem. Eng. Aspects* 466, 138–146. doi:10.1016/j.colsurfa.2014.10.053

Lan, S. R., Song, D. Z., Li, Z. L., and Liu, Y. (2021). Experimental study on acoustic emission characteristics of fault slip process based on damage factor. *J. Min. Strata Control Eng.* 3 (3), 033024. doi:10.13532/j.jmsce.cn10-1638/td.20210510.002

Lashkarbolooki, M., Vaezian, A., Hezave, A. Z., Ayatollahi, S., and Riazi, M. (2016). Experimental investigation of the influence of supercritical carbon dioxide and supercritical nitrogen injection on tertiary live-oil recovery. *J. Supercrit. Fluids* 117, 260–269. doi:10.1016/j.supflu.2016.07.004

Li, H. (2022). Research progress on evaluation methods and factors influencing shale brittleness: A review. *Energy Rep.* 8, 4344–4358. doi:10.1016/j.egyr.2022.03.120

Li, L., Chen, Z., Su, Y. L., Fan, L. Y., Tang, M. R., Tu, J. W., et al. (2021). Experimental investigation on enhanced-oil-recovery mechanisms of using supercritical carbon dioxide as prefracturing energized fluid in tight oil reservoir. *SPE J.* 26 (05), 3300–3315. doi:10.2118/202279-pa

Li, X., Xue, J., Wang, Y., Yang, W., and Lu, J. (2022). Experimental study of oil recovery from pore of different sizes in tight sandstone reservoirs during CO2 flooding. *J. Petroleum Sci. Eng.* 208, 109740. doi:10.1016/j.petrol.2021.109740

Li, Y., Zhou, D., Wang, W., Jiang, T. X., and Xue, Z. J. (2020). Development of unconventional gas and technologies adopted in China. *Energy Geosci.* 1 (1–2), 55–68. doi:10.1016/j.engeos.2020.04.004

Liu, Y., Chen, L., Tang, Y., Zhang, X., and Qiu, Z. (2022). Synthesis and characterization of nano-SiO2@octadecylbisimidazoline quaternary ammonium salt used as acidizing corrosion inhibitor. *Rev. Adv. Mater. Sci.* 61 (1), 186–194. doi:10.1515/rams-2022-0006

Lv, G., Li, Q., Wang, S., and Li, X. (2015). Key techniques of reservoir engineering and injection–production process for CO2 flooding in China's SINOPEC Shengli Oilfield. *J. CO2 Util.* 11, 31–40. doi:10.1016/j.jcou.2014.12.007

Mahmi, O., Dypvik, H., and Hammer, E. (2018). Diagenetic influence on reservoir quality evolution, examples from Triassic conglomerates/arenites in the Edvard Grieg field, Norwegian North Sea. *Mar. Petroleum Geol.* 93, 247–271. doi:10.1016/j.marpetgeo.2018.03.006

Mahmud, H., Hisham, M., Mahmud, M., Leong, V. H., and Shafiq, M. U. (2020). Petrophysical interpretations of subsurface stratigraphic correlations, Baram Delta, Sarawak, Malaysia. *Energy Geosci.* 1 (3–4), 100–114. doi:10.1016/j.engeos.2020.04.005

Mirzaei-Paiaman, A., and Ghanbarian, B. (2021). A new methodology for grouping and averaging capillary pressure curves for reservoir models. *Energy Geosci.* 2 (1), 52–62. doi:10.1016/j.engeos.2020.09.001

Paul, G. W., Lake, L. W., and Gould, T. L. (1984). "A simplified predictive model for CO2 miscible flooding," in *SPE annual technical conference and exhibition* (Houston: OnePetro).

Paxton, S. T., Szzbo, J. O., Ajdukiewicz, J. M., and Klimentidis, P. E. (2002). Construction of an intergranular volume compaction curve for evaluating and predicting compaction and porosity loss in rigid-rain sandstone reservoirs. *AAPG Bull.* 86 (12), 2047–2067. doi:10.1306/61EEDDFA-173E-11D7-8645000102C1865D

Qiao, J. C., Zeng, J. H., Jiang, S., Feng, S., Feng, X., Guo, Z., et al. (2019). Heterogeneity of reservoir quality and gas accumulation in tight sandstone reservoirs revealed by pore structure characterization and physical simulation. *Fuel* 253, 1300–1316. doi:10.1016/j.fuel.2019.05.112

Qie, L., Shi, Y. N., and Liu, J. S. (2021). Experimental study on grouting diffusion of gangue solid filling bulk materials. *J. Min. Strata Control Eng.* 3 (2), 023011. doi:10.13532/j.jmsce.cn10-1638/td.20201111.001

Qin, Z., Arshadi, M., and Piri, M. (2021). Near-miscible supercritical CO2 injection in oil-wet carbonate: A pore-scale experimental investigation of wettability state and three-phase flow behavior. *Adv. Water Resour.* 158, 104057. doi:10.1016/j.advwatres.2021.104057

Santosh, M., and Feng, Z. Q. (2020). New horizons in energy geoscience. *Energy Geosci.* 1 (1–2), 1. doi:10.1016/j.engeos.2020.05.005

Song, Y., Jiang, L., Liu, Y., Yang, M., Zhao, Y., Zhu, N., et al. (2012). An experimental study on CO2/water displacement in porous media using high-resolution Magnetic Resonance Imaging. *Int. J. Greenh. Gas Control* 10, 501–509. doi:10.1016/j.ijggc.2012.07.017

Stalkup, F. I. (1978). Carbon dioxide miscible flooding: Past, present, and outlook for the future. *J. Petroleum Technol.* 30 (08), 1102–1112. doi:10.2118/7042-pa

Trevisan, L., Pini, R., Cihan, A., Birkholzer, J. T., Zhou, Q., Illangasekare, T. H., et al. (2014). Experimental investigation of supercritical CO2 trapping mechanisms at the intermediate laboratory scale in well-defined heterogeneous porous media. *Energy Procedia* 63, 5646–5653. doi:10.1016/j.egypro.2014.11.597

Wang, H., Tian, L., Huo, M., Xu, S., Liu, Z., Zhang, K., et al. (2022). Dynamic track model of miscible CO2 geological utilizations with complex microscopic pore-throat structures. *Fuel* 322, 124192. doi:10.1016/j.fuel.2022.124192

Wang, J., and Wang, X. L. (2021). Seepage characteristic and fracture development of protected seam caused by mining protecting strata. *J. Min. Strata Control Eng.* 3 (3), 033511. doi:10.13532/j.jmsce.cn10-1638/td.20201215.001

Wang, J., Zhang, Y., and Xie, J. (2020). Influencing factors and application prospects of CO2 flooding in heterogeneous glutenite reservoirs. *Sci. Rep.* 10 (1), 1839. doi:10.1038/s41598-020-58792-z

Wang, Q., Yang, S., Lorinczi, P., Glover, P. W., and Lei, H. (2019). Experimental investigation of oil recovery performance and permeability damage in multilayer reservoirs after CO2 and water–alternating-CO2 (CO2–WAG) flooding at miscible pressures. *Energy fuels.* 34 (1), 624–636. doi:10.1021/acs.energyfuels.9b02786

Wang, S., Jiang, L., Cheng, Z., Liu, Y., Zhao, J., Song, Y., et al. (2021). Experimental study on the CO2-decane displacement front behavior in high permeability sand evaluated by magnetic resonance imaging. *Energy* 217, 119433. doi:10.1016/j.energy.2020.119433

Wang, Y., Wei, N., Zhang, C., Wietsma, T. W., Bonneville, A., Li, X., et al. (2018). Experimental study of drying effects during supercritical CO2 displacement in a pore network. *Microfluid. Nanofluidics* 22 (9), 101. doi:10.1007/s10404-018-2122-9

Xu, N., and Gao, C. (2020). Study on the special rules of surface subsidence affected by normal faults. *J. Min. Strata Control Eng.* 2 (1), 011007. doi:10.13532/j.jmsce.cn10-1638/td.2020.01.011

Xue, F., Liu, X. X., and Wang, T. Z. (2021). Research on anchoring effect of jointed rock mass based on 3D printing and digital speckle technology. *J. Min. Strata Control Eng.* 3 (2), 023013. doi:10.13532/j.jmsce.cn10-1638/td.20201020.001

Yang, J. X., Luo, M. K., Zhang, X. W., and Huang, N. (2021). Mechanical properties and fatigue damage evolution of granite under cyclic loading and unloading conditions. *J. Min. Strata Control Eng.* 3 (3), 033016. doi:10.13532/j.jmsce.cn10-1638/td.20210510.001

Yin, S., and Wu, Z. (2020). Geomechanical simulation of low-order fracture of tight sandstone. *Mar. Petroleum Geol.* 100, 104359. doi:10.1016/j.marpetgeo.2020.104359

Yongle, H. U., Mingqiang, H. A. O., Guoli, C. H. E. N., Ruiyan, S. U. N., and Shi, L. I. (2019). Technologies and practice of CO2 flooding and sequestration in China. *Petroleum Explor. Dev.* 46 (4), 753–766. doi:10.1016/s1876-3804(19)60233-8

Yoshida, M., and Santosh, M. (2020). Energetics of the solid Earth: An integrated perspective. *Energy Geosci.* 1 (1–2), 28–35. doi:10.1016/j.engeos.2020.04.001

Zekri, A. Y., Shedid, S. A., and Almehaideb, R. A. (2009). Investigation of supercritical carbon dioxide, aspheltenic crude oil, and formation brine interactions in carbonate formations. *J. Petroleum Sci. Eng.* 69 (1-2), 63–70. doi:10.1016/j.petrol.2009.05.009

Zhang, B., Shen, B., and Zhang, J. (2020). Experimental study of edge-opened cracks propagation in rock-like materials. *J. Min. Strata Control Eng.* 2 (3), 033035. doi:10.13532/j.jmsce.cn10-1638/td.20200313.001

Zhang, N., Wei, M., and Bai, B. (2018). Statistical and analytical review of worldwide CO2 immiscible field applications. *Fuel* 220, 89–100. doi:10.1016/j.fuel.2018.01.140

Zhao, F., Hao, H., Hou, J., Hou, L., and Song, Z. (2015). CO2 mobility control and sweep efficiency improvement using starch gel or ethylenediamine in ultra-low permeability oil layers with different types of heterogeneity. *J. Petroleum Sci. Eng.* 133, 52–65. doi:10.1016/j.petrol.2015.05.014

Zhao, Y., Fan, G., Song, K., Li, Y., Chen, H., Sun, H., et al. (2021). The experimental research for reducing the minimum miscibility pressure of carbon dioxide miscible flooding. *Renew. Sustain. Energy Rev.* 145, 111091. doi:10.1016/j.rser.2021.111091

frontiers | Frontiers in Earth Science

TYPE Original Research
PUBLISHED 17 August 2022
DOI 10.3389/feart.2022.993829

OPEN ACCESS

EDITED BY
Wenlong Ding,
China University of Geosciences, China

REVIEWED BY
Qingan Zhou,
Changqing Oil Field Company, China
Wei Liao,
PetroChina Xinjiang Oilfield Company, China

*CORRESPONDENCE
Kaixun Zhang,
zhangkaixun@126.com

SPECIALTY SECTION
This article was submitted to Structural Geology and Tectonics, a section of the journal Frontiers in Earth Science

RECEIVED 14 July 2022
ACCEPTED 27 July 2022
PUBLISHED 17 August 2022

CITATION
Guo Y, Wang D, Han X, Zhang K, Shang X and Zhou S (2022), Evaluation of fracturability of shale reservoirs in the longmaxi formation in southern sichuan basin.
Front. Earth Sci. 10:993829.
doi: 10.3389/feart.2022.993829

Evaluation of fracturability of shale reservoirs in the longmaxi formation in southern sichuan basin

Ying Guo[1,2], Dapeng Wang[3], Xiaoying Han[4], Kaixun Zhang[5]*, Xiaofei Shang[3] and Song Zhou[6]

[1]Institute of Geology and Paleontology, Linyi University, Linyi, Shandong, China, [2]College of Geosciences, China University of Petroleum, Beijing, China, [3]Petroleum Exploration and Production Research Institute, SINOPEC, Beijing, China, [4]College of Mining Engineering, North China University of Science and Technology, Tangshan, China, [5]Institute of Geomechanics, Chinese Academy of Geological Sciences, Beijing, China, [6]Shandong Province Research Institute of Coal Geology Planning and Exploration, Jinan, Shandong, China

Major breakthroughs have been made in the exploration and development of shale gas in the Longmaxi Formation in the southern Sichuan Basin, China. The previous have adopted various methods to study the fracturability of shale, but the quantitative characterization of the comprehensive properties of shale during hydraulic fracturing is still difficult. For this reason, in this study, taking the Longmaxi Formation shale in the Changning and Luzhou Blocks in the southern Sichuan Basin as an example, the mineral composition, petrophysical properties, rock mechanical properties and *in-situ* stress of the shale were systematically studied using X-ray diffraction, pulsed porosity-permeability analysis, rock mechanics and *in-situ* stress tests. Furthermore, the brittle mineral content, elastic modulus, and *in -situ* stress parameters were calculated, and the Analytic Hierarchy Process (AHP) method was adopted to establish a comprehensive evaluation index of shale fracturability. The research results show that the shale of the Longmaxi Formation in southern Sichuan is dominated by mixed shale facies, and it has the characteristics of high content of brittle minerals, low porosity, large compressive strength and Young's modulus, and small value of *in-situ* stress difference coefficient. Therefore, the Longmaxi Formation shale has good fracturing conditions. TOC and quartz contents have important effects on the fracturability of the Longmaxi shale. The analytic hierarchy process was adopted to determine the weight coefficients of the modulus brittleness index, mechanical brittleness index, *in-situ* stress difference coefficient, rock compressive strength and TOC content. Furthermore, a comprehensive evaluation index of fracturability was constructed. Calculations show that the comprehensive fracability indices of shale in the Changning and Luzhou Blocks are 0.49 and 0.59, respectively. Moreover, the quality of shale in the Luzhou Block is better than that in the Changning Block, which is related to the organic matter and quartz content and the microscopic pore structures inside the shale.

KEYWORDS

mineral composition, rock mechanical properties, longmaxi formation, shale reservoir, fracturability, southern sichuan area

Introduction

In recent years, major breakthroughs have been made in the exploration and development of unconventional natural gas in China (Li, 2022). As an important unconventional oil and gas resource, shale gas has become the main resource for the increase of natural gas reserves and production capacity in China (Xu et al., 2019). After nearly a decade of development, China's shale gas production has also grown rapidly from 25 billion cubic meters in 2012 (Qiu et al., 2020) to 20 billion cubic meters in 2020 (Zhang et al., 2022). The Sichuan Basin, especially its southern region, has become the main battlefield for shale gas exploration and development in China (Fu et al., 2019). Different from conventional reservoirs, shale gas reservoirs are low-porosity and low-permeability tight reservoirs, which require hydraulic fracturing to achieve efficient development (Yu et al., 2019; Li et al., 2022). The fracturability of shale has become an important parameter for evaluating whether a complex fracture network can be effectively generated. Fracturability intuitively reflects the possibility of shale fracture and the improvement of reservoir seepage capacity (Wu et al., 2018). Generally, the evaluation indicators of shale fracturability mainly include: brittle mineral content (Mullen and Enderlin, 2012), Young's modulus and Poisson's ratio (Rickman et al., 2008), brittleness (Guo et al., 2015), and *in-situ* stress difference coefficient (Xiao et al., 2022). In recent years, more and more scholars have established a coupled multi-parameter comprehensive characterization model of shale fracturability by considering multiple geomechanical factors (Huang et al., 2019; Chen et al., 2021; Dou et al., 2021; Xiao et al., 2022).

At present, the quantitative characterization of the comprehensive properties of shale during hydraulic fracturing is still difficult. For this reason, in this study, taking the Longmaxi Formation shale in the Changning and Luzhou Blocks in the southern Sichuan Basin as an example, the mineral composition, petrophysical properties, rock mechanical properties and *in-situ* stress of the shale were systematically studied using X-ray diffraction, pulsed porosity-permeability analysis, rock mechanics and *in-situ* stress tests. Furthermore, the brittle mineral content, elastic modulus, and *in-situ* stress parameters were calculated, and the Analytic Hierarchy Process (AHP) method was adopted to establish a comprehensive evaluation index of shale fracturability.

Geological background

The Sichuan Basin is located in South China and belongs to the secondary structural unit of the Yangtze Platform (Shi et al., 2021). It is surrounded by mountains and has a NE-trending diamond shape as a whole (Shi et al., 2022). The east of the Sichuan Basin is the Daloushan Fold Belt, the south is the Emeishan Fold Belt, the west is the Longmenshan Fault Zone, and the north is the Qinling-Dabieshan Orogenic Belt. According to the regional tectonic characteristics, the interior of the Sichuan Basin is further divided into six secondary structural units, namely, the low-gentle structural belt in northern Sichuan, the low-steep structural belt in western Sichuan, the gentle structural belt in central Sichuan, the high-steep structural belt in eastern Sichuan, the low-fold structural belt in southwestern Sichuan, and the low-steep structural belt in southern Sichuan (Zhang, 2021; Zhang et al., 2021; Zou et al., 2022). The study area is located in the low-steep structural belt in southern Sichuan (Figure 1).

On the pre-Sinian metamorphic rock basement, the Sichuan Basin has experienced seven tectonic evolutions successively, including the Caledonian Movement, the Hercynian Movement, the Indosinian Movement, the Yanshan Movement and the Cenozoic Himalayan Movement. From bottom to top, it develops Paleozoic Cambrian, Ordovician, Silurian, Carboniferous and Permian, Mesozoic Triassic, Jurassic and Cretaceous strata (Liu et al., 2021). From the Late Ordovician to the Early Silurian, the Sichuan Basin was in a clastic shelf facies depositional environment. However, affected by the Caledonian Movement, the depth of the water body in the southern and northeastern parts of the Sichuan Basin is relatively large, and the sediments are in a deep-water shelf deposition environment (Xiong et al., 2021). Therefore, the energy of the water body is low, and the sediment as a whole is in an anoxic environment. Furthermore, the thick organic-rich shale deposits from the Ordovician Wufeng Formation to the Silurian Longmaxi Formation were formed (Tang et al., 2020; Liu et al., 2021; Shi et al., 2021). The buried depth of shale in the Longmaxi Formation in the southern Sichuan Basin varies widely. The buried depth of shale in the Longmaxi Formation in Changning Block rangs from 2000 to 3,500 m, while that in the Luzhou Block ranges from 3,500 m to 4,500 m (Chen et al., 2022).

Samples and experimental methods

The experimental samples were all taken from the Luzhou and Changning Blocks of the Longmaxi Formation shale in the southern Sichuan region, with a total of 24 samples. All samples are dark shales. Among them, the depth of samples in the Luzhou Block is 3,300–3500 m, and that in the Changning Block is 2,100–2500 m. In order to clarify the fracturability of the Longmaxi Formation shale in the study area, tests such as X-ray diffraction, pulsed porosity and permeability, rock mechanics, and *in-situ* stress were systematically carried out in this paper.

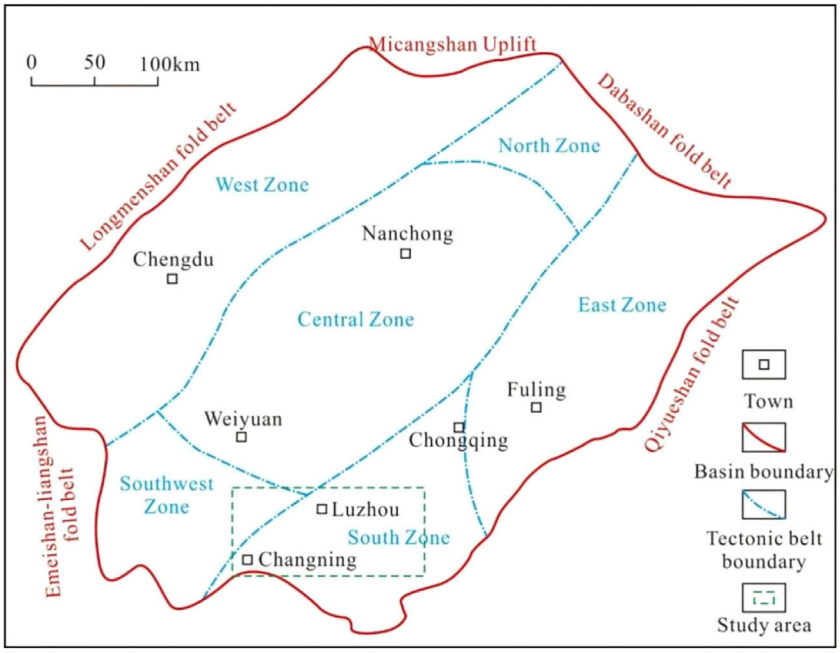

FIGURE 1
Location of the study area (Tang et al., 2020)

A SmartLab-9 X-ray diffractometer was used to carry out quantitative analysis of whole-rock minerals in shale samples. The shale samples were ground, dried and passed through a 200 mesh screen. The experimental operation process refers to SYT 5163–2010 "X-ray Diffraction Analysis Method of Clay Minerals and Common Non-Clay Minerals in Sedimentary Rocks".

The total organic carbon content (TOC) of shale is measured by a K35222 carbon sulfur analyzer. The experimental procedure was carried out with reference to the standard GB/T 19,145–2003 "Determination of total organic carbon in sedimentary rocks".

The storage properties of shale samples were tested by a TC-200 pulsed porosity and permeability tester. The experimental procedure was carried out with reference to the standard GB/T 29,172–2012 "Core Analysis Method". First, the shale samples were cut and machined into standard core columns with a diameter of 2.5 cm and a length of about 5.0 cm. Then, an S4800 scanning electron microscope was employed to observe the pore structures of the shale.

The MTS815 rock mechanics analysis system was adopted to complete the shale rock mechanics tests. The test item is a triaxial compression test. The maximum axial load of the compressor is 2,800 kN, the maximum confining pressure is 80 MPa, the maximum pore water pressure is 80 MPa, and the maximum temperature is 200°C. Similarly, the samples were cut into standard core columns 2.5 cm in diameter and 5.0 cm in length. For the five shale samples in the Changning Block, the burial depth is shallow (about 2300 m), and the experimental temperature is set at 75°C, the experimental confining pressure is 49 MPa, and the overlying rock pressure is 61 MPa. For the six shale samples in the Luzhou Block, the burial depth is about 3500 m, the experimental temperature is set at 121°C, the experimental confining pressure is 82 MPa, and the overlying rock pressure is 91 MPa. The rock mechanics parameters tested include the triaxial compressive strength, the young's modulus and the Poisson's ratio.

In addition, the *in-situ* stress tester was used to pressurize from 150 Psi to 10,000 Psi, and the *in-situ* stress test of shale was completed in three cycles. Changes in strain throughout the compression/decompression process are recorded.

Results

Mineral composition of shale reservoirs

Whole-rock mineral composition analysis of 24 shale samples in the study area shows that the mineral composition of the Longmaxi Formation shale is dominated by clay minerals and quartz, the sum of which is as high as 93.6%. Followed by feldspar and calcite content, in addition, there is a small amount of pyrite in the samples (Table 1). According to the shale facies classification standard (Liang et al., 2014; Xiao et al., 2022), the shale of the Longmaxi Formation in the study area is dominated by mixed shale facies (Figure 2).

Overall, the Longmaxi Formation shale in the southern Sichuan Basin has the highest clay mineral content, ranging

TABLE 1 Mineral components and contents in the longmaxi formation shale in the study area.

Area	Sample no.	Depth (m)	TOC (%)	Ro (%)	am	Mineral content (%)					
						Quartz	Feldspar	Calcite	Clay	Others	Pyrite
Changning (CN)	CN-1	2,100.5	0.16	2.19	2.36	17.2	12.5	24.1	33.7	11.3	1.2
	CN-2	2,156.8	0.22	2.28	2.42	20.3	4.5	31.2	37.3	5.8	0.9
	CN-3	2,208.1	0.36	2.37	2.53	14.5	6.3	35.8	33.1	8.9	1.4
	CN-4	2,243.5	3.08	2.31	4.15	28.3	1.8	56.4	10.7	0.5	2.3
	CN-5	2,270.1	1.13	2.26	3.12	17.5	3.6	36.2	32.4	8.6	1.7
	CN-6	2,291.6	0.78	2.35	4.45	19.3	4.5	10.8	44.7	20.1	0.6
	CN-7	2,317.3	1.01	2.24	4.6	23.8	7.1	13.9	42.9	10.8	1.5
	CN-8	2,332.1	4.05	2.26	6.29	34.6	5.2	10.7	44.6	0.7	4.2
	CN-9	2,341.5	1.42	2.38	6.37	30.1	8.7	11.7	40.8	5.4	3.3
	CN-10	2,346.7	8.89	2.41	5.12	66.5	2.8	7.8	19.1	0	3.8
	CN-11	2,362.6	1.51	2.45	6.89	27.1	6.9	13.5	41.5	8.9	2.1
	CN-12	2,380.8	4.36	2.43	6.91	29.1	4.3	17.2	29.7	15.6	4.1
Luzhou (LZ)	LZ-1	3,496.1	0.17	2.15	2.55	40.6	6.4	0	53	0	0
	LZ-2	3,505.2	0.25	2.2	1.96	34.8	8.4	0.8	54.3	0	1.7
	LZ-3	3,514.2	0.34	2.23	8.12	48.1	7.5	4	37.2	0	3.2
	LZ-4	3,524.8	1.31	2.27	4.41	45.1	5.5	1.3	45.9	0	2.2
	LZ-5	3,525.4	2.45	2.28	4.42	43.6	8.5	1.5	38.4	3.2	4.8
	LZ-6	3,526.3	4.06	2.26	5.53	35.7	10.2	1.5	43.1	4.1	5.4
	LZ-7	3,527.5	5.31	2.29	6.11	43.9	9.1	2.2	26.1	4.8	13.9
	LZ-8	3,530.9	5.14	2.21	5.51	56.3	6	3.8	21.1	9.8	3
	LZ-9	3,535.1	2.48	2.33	5.72	43.4	4.5	8.6	34.9	5.2	3.4
	LZ-10	3,535.7	6.34	2.59	3.71	43.1	10.8	10.1	24.6	6.3	5.1
	LZ-11	3,545	2.92	2.35	6.96	37.9	4.3	20.5	28.2	6.8	2.3
	LZ-12	3,554	2.39	2.4	4.89	41.2	6.1	4.3	31.2	13.1	4.1

from 10.7% to 54.3%, with an average of 35.35%; followed by quartz minerals, the content of which is between 14.5% and 66.5%, and the average value is 35.08%; the mineral content of feldspar ranges from 1.8% to 12.5%, with an average of 6.48%. Moreover, the content of calcite minerals varies widely, ranging from 0% to 56.4%, with an average value of 13.66%. In addition, the content of pyrite is relatively low, which generally does not exceed 5%. Statistics show that the content of pyrite ranges from 0% to 13.9%, with an average content of 3.18% (Figure 3).

In addition, there is a certain difference in the mineral content of the shale in the Changning and Luzhou Blocks. The content of quartz and feldspar in the shale in the Luzhou Block is significantly higher than that in the Changning area, while the calcite content in the shale is significantly lower than that in the Changning area, and the shale in the two blocks has comparable clay mineral content (Figure 4).

The difference in calcite content in shale in the two regions is mainly caused by the difference in depositional environment. The shale in the Luzhou Block has a relatively deep burial depth and is a product of deep-water shelf facies, while the shale in the Changning area has a relatively shallow burial depth and is a calcareous shallow-water shelf facies deposition (Zou et al., 2022). Statistics show that the clay mineral content of the shale in the Changning area is 10.7%–44.7%, with an average of 34.21%, and the clay mineral content of the shale in the Luzhou Block is 21.1%–54.3%, with an average of 36.50%.

Petrophysical properties of shale reservoirs

According to the analysis results of whole-rock mineral composition of the 24 shale samples in the study area, the porosity of shale is relatively low. The range of porosity is in the range of 1.96%–8.12%, with an average value of 4.80%. And with the increase of depth, the porosity of the shale in the Changning Block gradually increases, while the porosity of the shale in the Luzhou Block does not change significantly (Figure 5A). In comparison, the porosity of the Changning

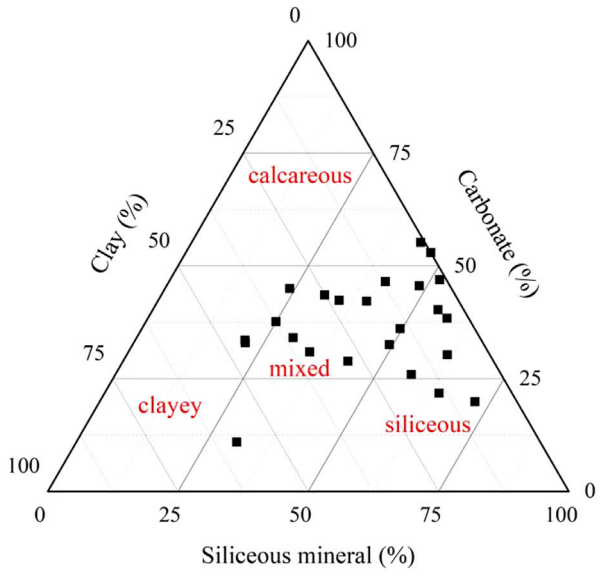

FIGURE 2
Ternary composition of shale mineral content in the Longmaxi Formation in the study area.

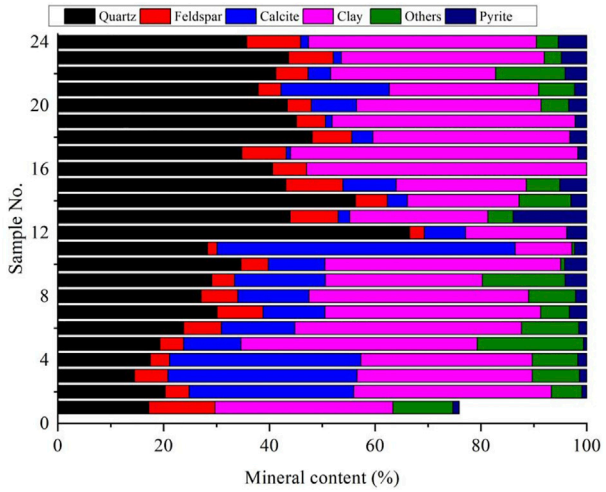

FIGURE 3
Distribution characteristics of whole-rock mineral content in the Longmaxi Formation shale in the study area.

Block shale ranges from 2.36% to 6.91%, with an average of 4.60%. More than 33% of the samples have a porosity greater than 4%, while more than 16.7% of the samples have a porosity greater than 6%; however, the porosity of the shale in the Luzhou Block varies widely, ranging from 1.96% to 8.12%, with an average value of 4.99%. Moreover, more than 37.5% of the samples have a porosity greater than 4%, while more than 12.5% of the samples have a porosity greater than 6% (Figures 5B,C).

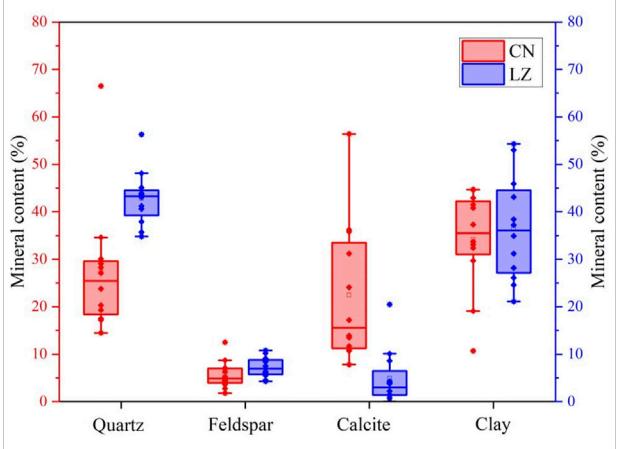

FIGURE 4
Box plot of mineral content in the Longmaxi Formation shale in the study area.

Microscopic pore structures of shale reservoirs

It can be seen from Figure 6 that the shale of the Longmaxi Formation in the southern Sichuan area mainly develops organic pores, mineral intergranular pores, intragranular pores, intercrystalline pores, clay mineral interlayer pores and micro-fractures. In comparison, due to the shallow burial depth of the shale of the Longmaxi Formation in the Changning Block, the shale mainly develops intergranular pores, organic pores and pyrite intercrystalline pores (Figures 6A–C), and micro-fractures are poorly developed. This can explain that the porosity of the shale in the Changning Block gradually increases with depth. However, the shale in the Luzhou Block has a larger burial depth. In addition to a large number of organic pores, the pore types of shale in this area also develop kaolinite interlayer pores and micro-fractures (Figures 6D–F). Therefore, the porosity of shale in this area is relatively high, and the porosity does not change significantly with the increase of burial depth.

Rock mechanical properties of shale reservoirs

Triaxial compression experiments were carried out on 11 samples of the Longmaxi Formation in southern Sichuan, and the test results are shown in Table 2.

It can be seen from Figure 7 that the compressive strength and Young's modulus of the Longmaxi Formation shale in the southern Sichuan area are relatively large. Among them, the compressive strength of shale is generally higher than 180 MPa, and the Young's modulus generally exceeds

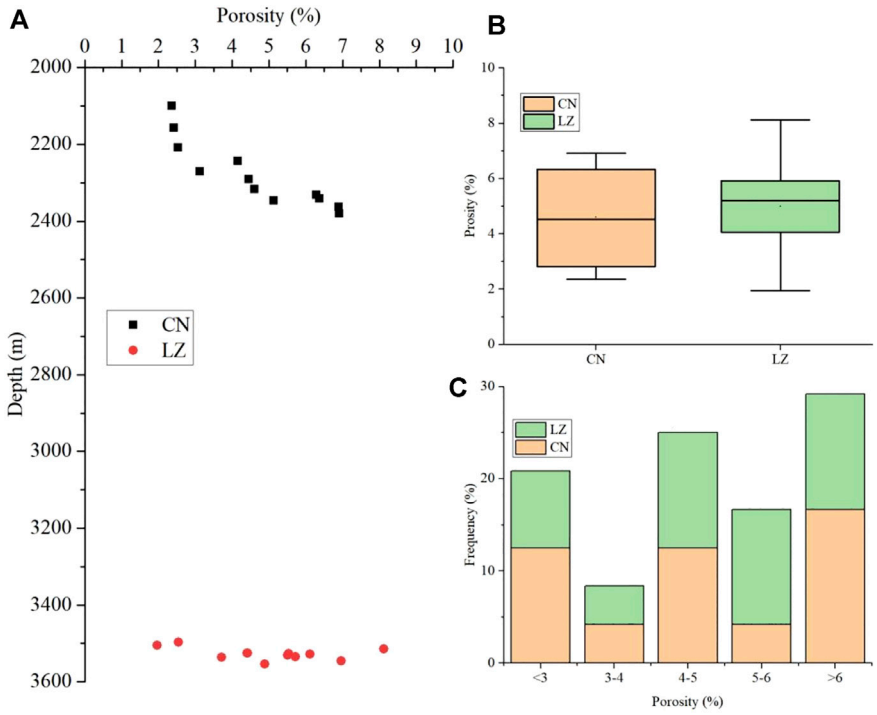

FIGURE 5
Porosity distribution of the Longmaxi Formation shale in the study area. **(A)** Porosity variation with depth, **(B)** Box plot of porosity in the Longmaxi Formation shale in Changning and Luzhou blocks, and **(C)** Cumulative distribution frequency of porosity.

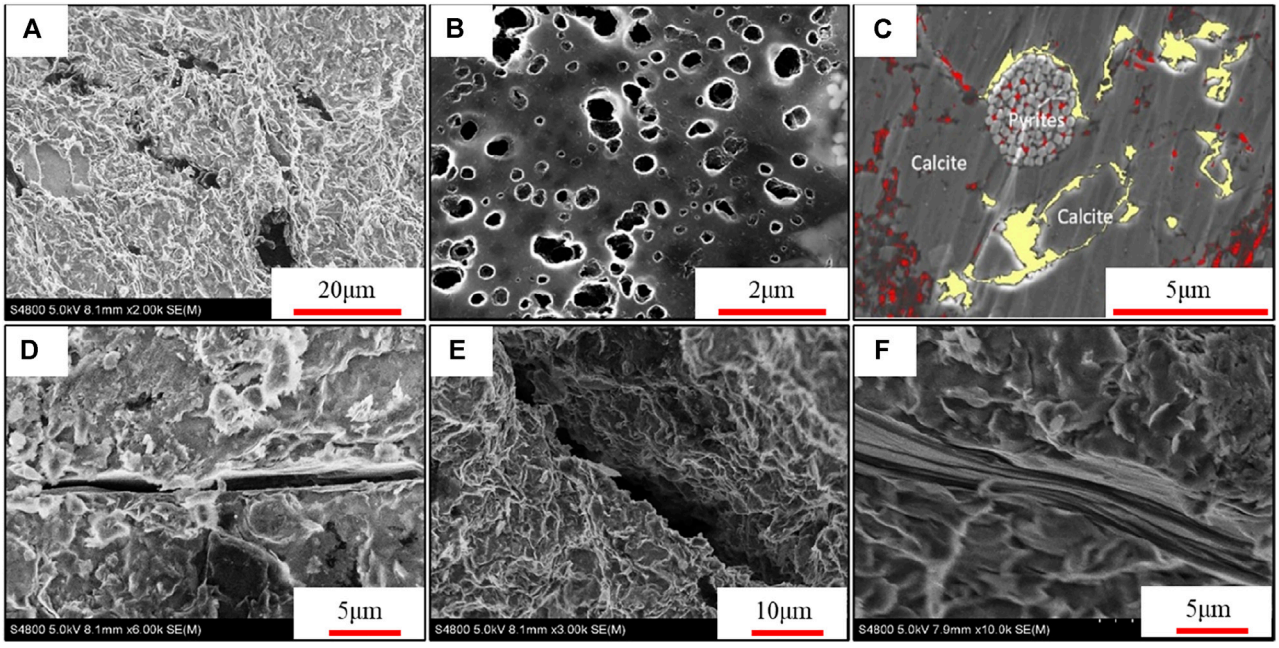

FIGURE 6
SEM images of the pore structure of the Longmaxi Formation shale in the study area. Notes: **(A–C)** are taken from the Changning Block, and **(D–F)** are taken from the Luzhou Block. **(B)** and **(C)** are from Shi et al., 2022.

TABLE 2 Test results of triaxial compression experiments of the longmaxi formation shale in the study area.

Area	Sample no.	Depth (m)	Compressive strength (MPa)	Young's modulus (GPa)	Poisson's ratio
Changning	CN-1	2,100.5	181.74	18.21	0.209
	CN-4	2,243.5	321.74	32.26	0.162
	CN-7	2,317.3	190.82	21.25	0.201
	CN-11	2,362.6	293.48	34.16	0.239
	CN-12	2,380.8	322.75	33.25	0.161
Luzhou	LZ-1	3,496.1	599.25	49.42	0.213
	LZ-3	3,514.2	294.92	32.45	0.273
	LZ-7	3,527.5	339.82	40.75	0.274
	LZ-9	3,535.1	191.14	16.94	0.288
	LZ-11	3,545	391.47	44.29	0.219
	LZ-12	3,554	554.6	48.95	0.251

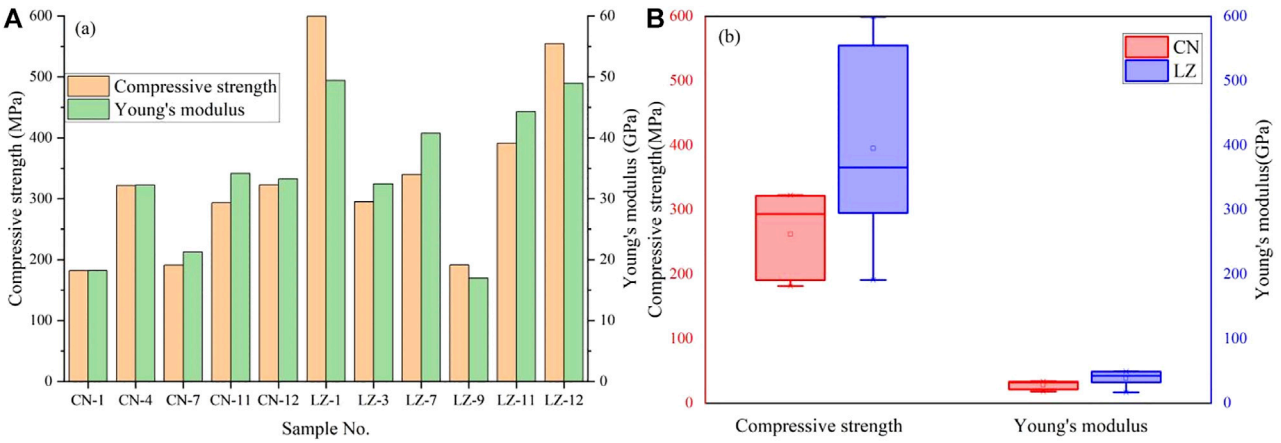

FIGURE 7
Distribution of compressive strength and Young's modulus of the Longmaxi Formation shale in the study area. Notes: **(A)** Test results of compressive strength of different samples; **(B)** Distribution intervals of compressive strength.

18 GPa (Figure 7A). In comparison, the compressive strength and Young's modulus of the shale in the Luzhou Block with a relatively large burial depth are significantly higher than those in the Changning Block. Among them, the compressive strength of shale ranges from 191.14 to 599.25 MPa with an average value of 395.20 MPa, and the Young's modulus ranges from 16.94 to 49.42 GPa with an average value of 38.80 GPa. However, the compressive strength of shale in the Changning Block generally does not exceed 350 MPa, which is between 181.74 MPa and 322.75 MPa, and the average is 262.11 MPa; the Young's modulus generally does not exceed 35 GPa, which is between 18.21 and 33.25 GPa, and the average value is 27.83 GPa (Figure 7B).

In-situ stress characteristics

The *in-situ* stress test results of the Longmaxi Formation in the study area are shown in Table 3. The results show that the three principal stresses in the Changning Block satisfy $\sigma_v>\sigma_H>\sigma_h$. The average value of the vertical principal stress is 60.65 MPa, and the average value of its stress gradient is 0.0257 MPa/m; the average value of the maximum horizontal principal stress is 21.15 MPa, and the average value of its stress gradient is 0.0090 MPa/m; the average value of the minimum horizontal principal stress is 20.9 MPa, and the average value of its stress gradient is 0.0089 MPa/m.

The three principal stresses in the Luzhou Block satisfy $\sigma_H>\sigma_v>\sigma_h$. The average value of the vertical principal stress is

TABLE 3 Test results of *in-situ* stress of the longmaxi formation in the study area.

Sample no.	Depth (m)	σH (MPa)	σh (MPa)	σv (MPa)	σH gradient (MPa/m)	σh gradient (MPa/m)	σv gradient (MPa/m)	*DF*
CN-8	2,332.1	19.4	19.2	61.5	0.0083	0.0082	0.0264	0.01
CN-12	2,380.8	22.9	22.6	59.8	0.0096	0.0095	0.0251	0.013
Average		21.15	20.9	60.65	0.009	0.0089	0.0257	0.0118
LZ-1	3,496.1	94.4	83.5	89.8	0.027	0.0239	0.0257	0.131
LZ-12	3,554	94.5	83.7	90.5	0.0266	0.0236	0.0255	0.129
Average		94.45	83.6	90.15	0.0268	0.0237	0.0256	0.1298

Notes: σ_H presents maximum horizontal stress; σ_h presents minimum horizontal stress; σ_v presents normal principal stress; *DF*, presents difference factor of crustal stress.

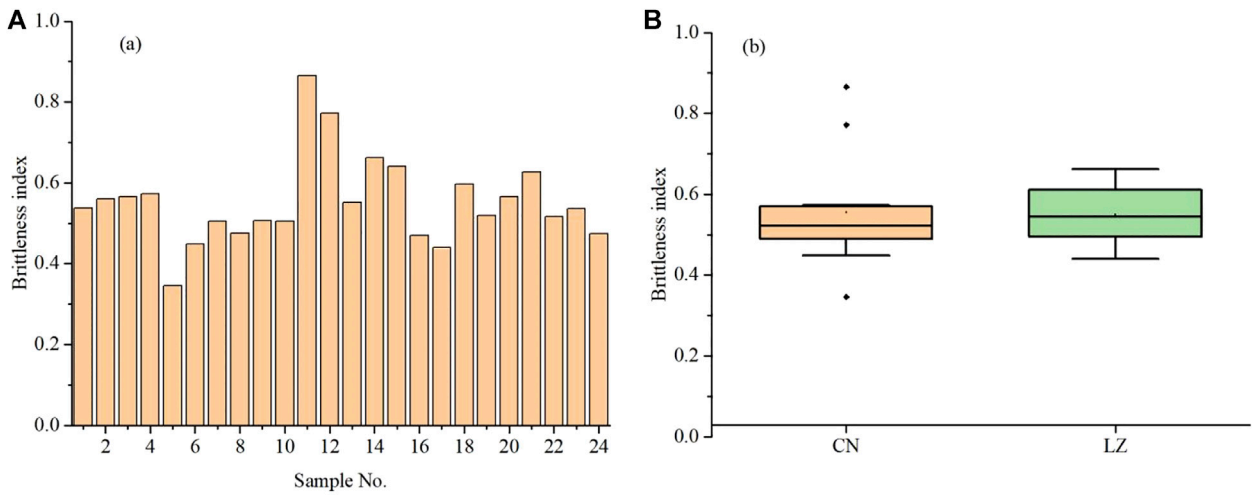

FIGURE 8
Distribution of the brittleness index of the Longmaxi Formation shale in the study area. Notes: **(A)** Brittleness index distribution for different samples; **(B)** Distribution range of brittleness index.

90.15 MPa, and the average value of its stress gradient is 0.0256 MPa/m; the average value of the maximum horizontal principal stress is 94.45 MPa, and the average value of its stress gradient is 0.0268 MPa/m; the average value of the minimum horizontal principal stress is 83.6 MPa, and the average value of its stress gradient is 0.0237 MPa/m.

Discussion

Fracturability analysis based on mineral composition

Brittle minerals in the mineral composition, such as quartz, feldspar, and calcite, are the main internal factors controlling the degree of fracture development, and directly affect the storage space and seepage channels of shale (Chen et al., 2012). Although pyrite is a brittle mineral, its content is generally low, and its contribution to the development of shale fractures is small. Therefore, in general, quartz, feldspar, and calcite are defined as brittle minerals (Xiao et al., 2022). Furthermore, the content of these three minerals as a percentage of the total mineral content is defined as the brittleness index:

$$B_1 = \frac{C_Q + C_F + C_C}{100\%} \quad (1)$$

In the formula, B_1 is the brittleness index, dimensionless; C_Q is the percentage of quartz minerals, %; C_F is the percentage of calcite minerals, %; C_C is the percentage of calcite minerals, %.

The calculation results are shown in Figure 8. The brittleness index of the Longmaxi Formation shale in the study area is generally higher than 0.4. Shales with a brittleness index higher than 0.4 generally have good fracturability (Xiao et al., 2022). Among them, the brittleness index of shale in Changning area is between 0.35 and 0.85, and its average is 0.55; while the

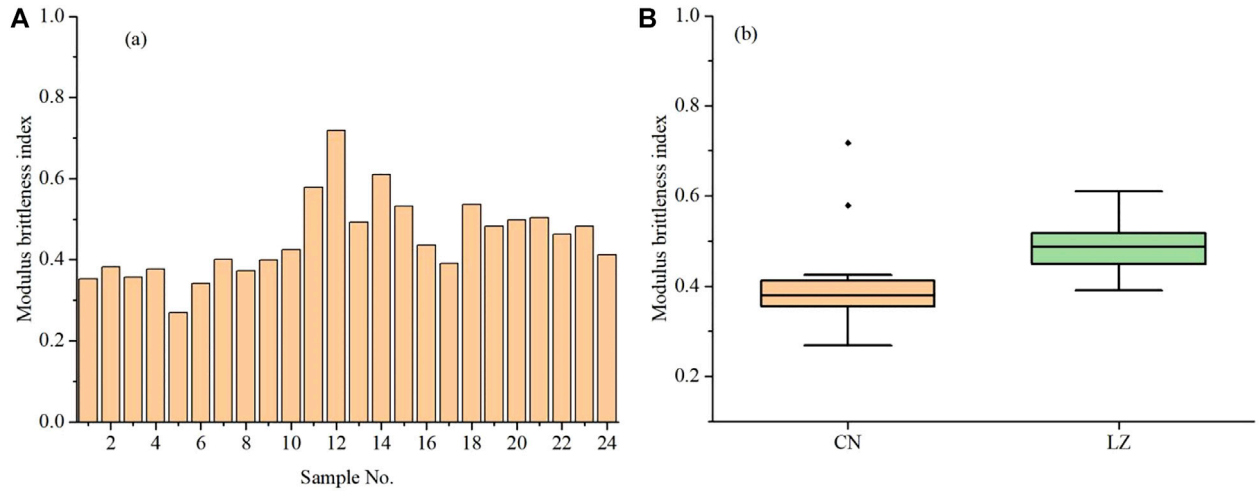

FIGURE 9
Distribution of the modulus brittleness index of the Longmaxi Formation shale in the study area. Notes: **(A)** Modulus brittleness index distribution for different samples; **(B)** Distribution range of modulus brittleness index.

brittleness index of shale in Luzhou area is between 0.44 and 0.66, and its average is 0.55. It reflects that the shale of the Longmaxi Formation in the southern Sichuan area has a high content of brittle minerals, and it has good fracturability.

However, brittle mineral content represents only one aspect of shale fracability. The final determination of fracturability also takes into account its mechanical properties, such as bulk modulus. The bulk modulus of a mineral represents the energy required for its deformation or rupture. The higher the bulk modulus, the smaller the capacity required to reflect the deformation or rupture of the mineral, and the stronger the fracturability; on the contrary, the weaker the fracturability of the mineral. According to Fjaer et al. (2008), the bulk moduli of quartz, feldspar, and calcite minerals are 37.5, 76, and 74 GPa, respectively. Quartz minerals have the smallest bulk modulus and contribute the most to shale fracturability. Therefore, the bulk modulus contributions of quartz, feldspar and calcite are defined as 1.0, 49, and 0.51, respectively. Furthermore, the modulus brittleness index is defined as:

$$B_M = M_Q \times C_Q + M_F \times C_F + M_C \times C_C$$
$$= C_Q + 0.49 \times C_F + 0.51 \times C_C \quad (2)$$

In the formula, B_M is the modulus brittleness index, dimensionless; C_Q is the percentage of quartz minerals, %; C_F is the percentage of calcite minerals, %; C_C is the percentage of calcite minerals, %; M_Q, M_F, and M_C are the bulk modulus contributions of quartz, feldspar, and calcite, respectively, dimensionless, which are defined as 1.0, 0.49, and 0.51, respectively.

The calculation results of the modulus brittleness index of the Longmaxi Formation shale in the study area are shown in Figure 9. The modulus brittleness index of the Longmaxi shale is generally higher than 0.30. Among them, the modulus brittleness index of shale in the Changning area is between 0.27 and 0.72, with an average value of 0.41; while that in the Luzhou Block is between 0.39 and 0.61, and its average value is 0.46. It reflects that the Longmaxi Formation in southern Sichuan area has good fracturability, and the shale fracturability in the Luzhou Block is significantly better than that in the Changning Block. This characteristic is not reflected by the brittle mineral content alone.

Previous studies have shown that the fracturability of shale is related to factors such as quartz content, natural fractures, and diagenesis (Tang et al., 2012). It can be seen from Figure 10 that the modulus brittleness index has a good positive correlation with shale TOC and quartz content, but has a poor correlation with shale maturity R_o and shale porosity. Among them, the shale R_o is between 2.1% and 2.6%, reflecting that the shale of the Longmaxi Formation in the study area is in the late diagenetic stage (Warpinki et al., 2009), so the diagenesis of the shale has little effect on its brittleness. The organic carbon content can reflect the hydrocarbon generation ability of shale. The higher the TOC, the lower the density of shale, the more developed fractures (Cui et al., 2019), and the higher the brittleness index of shale. Quartz has the smallest bulk modulus and requires the least amount of energy to deform or fracture. Therefore, the higher the quartz content in the shale, the higher the brittleness index of the shale, and the better the fracturability of the shale. However, the porosity has little effect on the shale fracturability. Because the porosity only represents the percentage of pore space or the size of reservoir space, and is related to the related to mineral arrangement instead of the mineral composition. The essence of shale fracturing is the ability to produce micro-fractures in

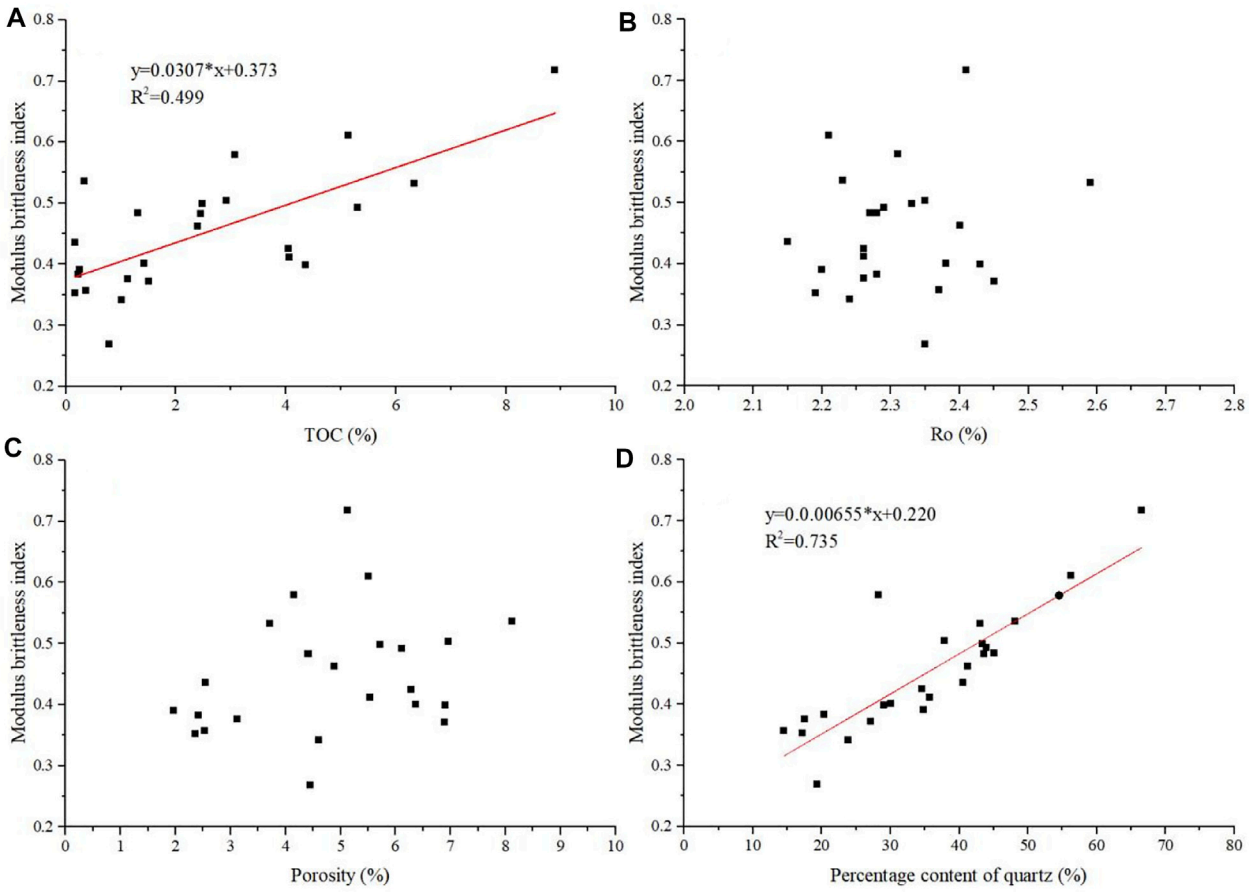

FIGURE 10
Relationship between the modulus brittleness index and TOC **(A)**, R_o **(B)**, porosity **(C)**, and quartz content **(D)** of the Longmaxi Formation shale in the study area, respectively.

shale, which is essentially related to shale mineral composition and rock mechanical properties, and has nothing to do with the size of its reservoir space.

Fracturability analysis based on rock mechanical properties

According to the theory of geomechanics, the fracturability of shale can also be quantitatively evaluated by parameters such as compressive strength, Young's modulus, and Poisson's ratio (Tan et al., 2019). Young's modulus and Poisson's ratio of rock can reflect the difficulty of deformation or rupture of rock after being stressed. The higher the Young's modulus and the larger the Poisson's ratio, the more likely the rock is to fracture (Rickman et al., 2008). The expressions of rock brittleness uses rock mechanical parameters are shown in Eqs (3–5):

$$B_D = 0.5E_n + 0.5\mu_n \tag{3}$$

$$E_n = \frac{E - E_{\min}}{E_{\max} - E_{\min}} \tag{4}$$

$$\mu_n = \frac{\mu - \mu_{\min}}{\mu_{\max} - \mu_{\min}} \tag{5}$$

where B_D is the mechanical brittleness index, E_n and μ_n are the normalized Young's modulus and Poisson's ratio, respectively, dimensionless; E is the Young's modulus, and E_{max} and E_{min} are the maximum and minimum Young's modulus of shale, respectively; μ is the Poisson's ratio, and μ_{max} and μ_{min} are the maximum and minimum Poisson's ratio of shale, respectively.

Because the rock mechanics parameters of the shale in the Luzhou and Changning Blocks are quite different, the maximum and minimum values are calculated respectively, and the calculation results are shown in Figure 11. It can be seen from Figure 11A that the mechanical brittleness index of shale in the southern Sichuan area is between 0.15 and 0.77, with an average value of 0.47, indicating that the shale fracturability is generally

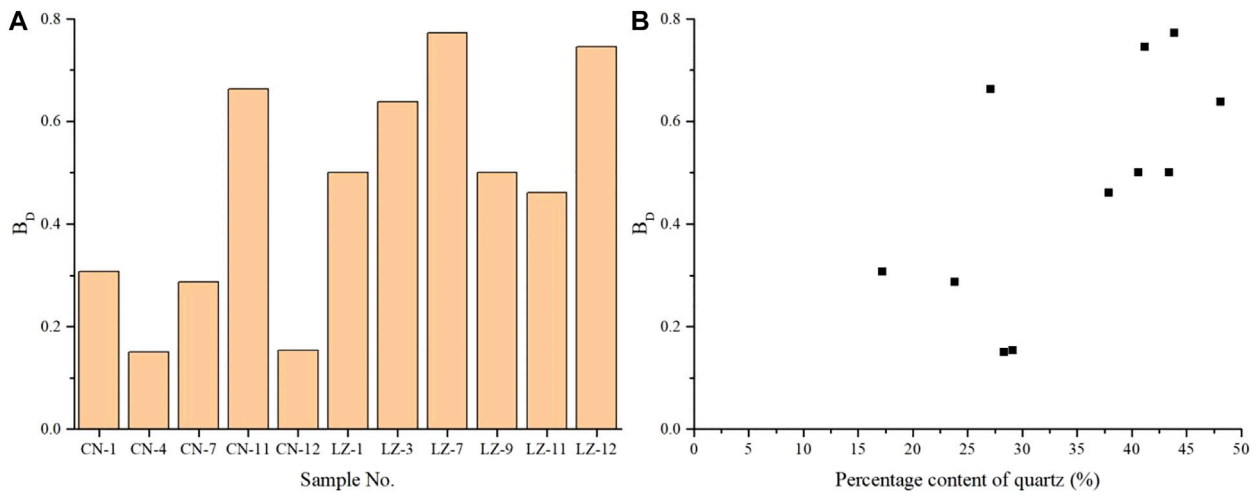

FIGURE 11
Distribution of the brittleness index of the Longmaxi Formation shale in the study area. **(A)** Brittleness index for different samples and **(B)** the relationship between the percentage content of quartz and brittleness index.

good. In addition, the mechanical brittleness index of shale in the Luzhou Block is significantly higher than that in the Changning Block. It shows that the shale fracturability in the Luzhou Block is better than that in the Changning Block. Moreover, the mechanical brittleness index of shale has a certain positive correlation with its quartz content (Figure 11B), indicating that quartz minerals have a great contribution to the fracturability of shale.

Fracturability analysis based on *in-situ* stress characteristics

The level of *in-situ* stress has an important influence on the distribution of fractures in shale and the difficulty of forming complex fracture networks. In general, the *in-situ* stress difference coefficient is adopted to characterize the *in-situ* stress:

$$DF = \frac{\sigma_H - \sigma_h}{\sigma_h} \quad (6)$$

In the formula, DF is the *in-situ* stress difference coefficient, dimensionless; σ_H is the maximum horizontal principal stress, MPa; σ_h is the minimum horizontal principal stress, MPa.

The calculation results are shown in Table 3. It can be seen that the *in-situ* stress difference coefficient of the Longmaxi Formation in the study area is between 0.010 and 0.131, with an average value of 0.071. The difference coefficient of *in-situ* stress is much less than 0.3, indicating that the shale in this area is prone to form a complex fracture network under the action of stress, and its fracturability is good.

Influence of shale microstructure on fracturability

The comparison indexes of the Longmaxi Formation shale in the two blocks are shown in Table 4. It can be found that the TOC, porosity, and quartz content of the shale in the Luzhou Block are significantly higher than those in the Changning Block, and the degree of microfracture development is higher, while the R_o difference is not significant. Therefore, it can be considered that the fracturability of the Longmaxi Formation shale is mainly controlled by the organic matter content, quartz content and pore structures of the shale reservoir. The higher the organic matter content, the lower the density of shale, and the more developed fractures. The higher the quartz content, the better the brittleness of the shale. However, the pore structures of the reservoir firstly control the petrophysical properties and micro-fracture development characteristics of the shale, and then controls the fracturability of the shale.

The microstructure of shale reservoir affects the occurrence state and storage characteristics of shale gas, and is the key factor controlling the fracturability of shale. The microstructure of the shale reservoir first controls the petrophysical properties of the shale reservoir. It can be seen from Figure 12 that there is a certain positive correlation between the porosity of the Longmaxi Formation shale in the southern Sichuan area and the content of siliceous minerals. With the increase of siliceous mineral content, the shale porosity increases significantly, but there are obvious differences between the Changning and Luzhou blocks. Among them, the porosity of the Changning Block shale

TABLE 4 Statistical results of the average value of factors affecting the fracturability of the longmaxi formation shale in the study area.

Area	*TOC* (%)	*Ro* (%)	Porosity (%)	Percentage content of quartz (%)	Development degree of microcracks	*B*
CN	2.25	2.33	4.6	27.36	Poor	0.49
LZ	2.76	2.3	4.99	42.81	Good	0.59

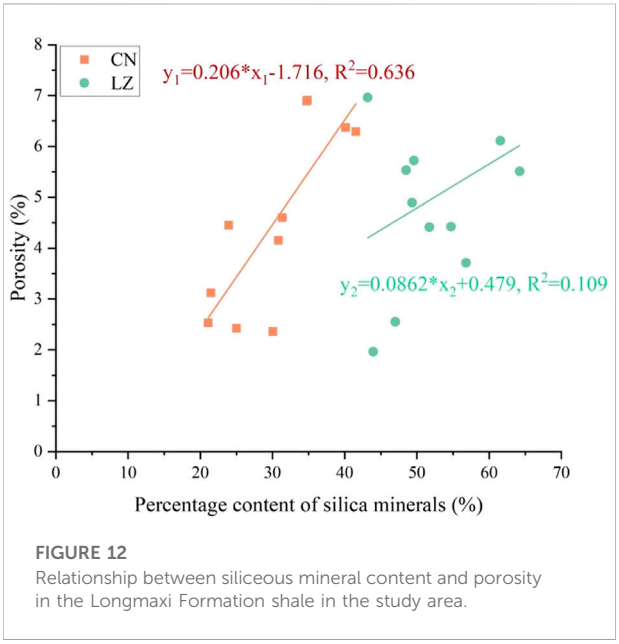

FIGURE 12
Relationship between siliceous mineral content and porosity in the Longmaxi Formation shale in the study area.

has a good positive correlation with the content of siliceous minerals. This is mainly because the shale in the Changning Block mainly develops intergranular pores (Figure 6A–C). The higher the content of siliceous minerals, the easier the formation of intergranular pores. However, the porosity of the shale in the Luzhou Block has a relatively poor positive correlation with the content of siliceous minerals. This is mainly due to the relatively developed micro-fractures in the shale of the Luzhou Block (Figures 6D–F). Furthermore, it leads to the contribution of micro-fractures in the shale pore space of this block in addition to the contribution of intergranular pores of siliceous minerals.

The influence of shale microscopic pore structure on the fracturability of shale is not only reflected in the control of reservoir characteristics, but also has an important influence on the characteristics of shale deformation or fracture after being stressed. Previous studies have shown that shale with natural fractures is more likely to develop micro-fractures along the fragile surface of the fracture after being stressed, and it is easier to connect to form a complex fracture network. However, shale without natural fractures will randomly generate micro-fractures after being stressed, and it requires large stress to form a connected fracture network. This is the fundamental reason why the fracturability of the shale in the Luzhou Block is significantly better than that in the Changning Block.

Comprehensive evaluation of shale fracturability

According to this study, the fracturability of shale can be evaluated from the aspects of mineral composition, rock mechanical properties and *in-situ* stress conditions. Moreover, the fracturability of shale is mainly controlled by multiple factors such as quartz content, TOC, mechanical properties of shale, and *in-situ* stress conditions, while R_o and petrophysical properties of shale have little effect on its fracturability. Therefore, the calculation formula of the comprehensive evaluation index of shale fracturability is defined as:

$$B = k_1 B_M + k_2 B_D + k_3 (1 - DF) + k_4 \left(1 - \frac{\sigma_c}{\sigma_{\max}}\right) + k_5 \left(\frac{TOC - TOC_{\min}}{TOC_{\max} - TOC_{\min}}\right) \quad (7)$$

In the formula, B is the comprehensive evaluation index of shale fracturability, B_M is the modulus brittleness index, dimensionless; B_D is the mechanical brittleness index, dimensionless; D_F is the *in-situ* stress difference coefficient, dimensionless; σ_c, σ_{max} are the compressive strength and maximum compressive strength, MPa, respectively; *TOC*, TOC_{max}, and TOC_{min} are the organic carbon content, the maximum and minimum values of the organic carbon content, respectively; k_1, k_2, k_3, k_4, and k_5 are the weight coefficients of the above five evaluation parameters, dimensionless, and $k_1+k_2+k_3+k_4+k_5=1$.

It can be seen from Eq. 7 that the comprehensive evaluation index of shale fracturability is calculated based on the weighting of mineral modulus components, elastic modulus, *in-situ* stress, compressive strength and TOC parameters. Finally, k_1, k_2, k_3, k_4, and k_5 are determined to be 0.3, 0.2, 0.2, 0.2, and 0.1, respectively. The comprehensive evaluation results are shown in Table 5, indicating that the

TABLE 5 Comprehensive evaluation results of fracturability of the longmaxi shale in the study area.

Area	*BM*	*BD*	1-*DF*	1-$\sigma c/\sigma max$	(*TOC*-*TOC*min)/(*TOC*max-*TOC*min)	*B*
CN	0.41	0.31	0.99	0.44	0.187	0.49
LZ	0.49	0.6	0.87	0.59	0.298	0.59

fracturability of the shale in the southern Sichuan area is better, and the fracturability of the shale in the Luzhou Block is significantly better than that in the Changning Block.

Conclusion

(1) In this study, taking the Longmaxi Formation shale in the Changning and Luzhou Blocks in the southern Sichuan Basin as an example, the mineral composition, petrophysical properties, rock mechanical properties and *in-situ* stress of the shale were systematically studied using X-ray diffraction, pulsed porosity-permeability analysis, rock mechanics and *in-situ* stress tests. Furthermore, the brittle mineral content, elastic modulus, and *in-situ* stress parameters were calculated, and the Analytic Hierarchy Process (AHP) method was adopted to establish a comprehensive evaluation index of shale fracturability.

(2) The shale of the Longmaxi Formation in southern Sichuan is dominated by mixed shale facies, and it has the characteristics of high content of brittle minerals, low porosity, large compressive strength and Young's modulus, and small value of *in-situ* stress difference coefficient. Therefore, the Longmaxi Formation shale has good fracturing conditions. TOC and quartz content have important effects on the fracturability of the Longmaxi shale.

(3) The analytic hierarchy process was adopted to determine the weight coefficients of the modulus brittleness index, mechanical brittleness index, *in-situ* stress difference coefficient, rock compressive strength and TOC. Furthermore, a comprehensive evaluation index of fracturability was constructed.

(4) The comprehensive fracability indices of shale in the Changning and Luzhou Blocks are 0.49 and 0.59, respectively. Moreover, the quality of shale in the Luzhou Block is better than that in the Changning Block, which is related to the organic matter and quartz content and the microscopic pore structures inside the shale.

Data availability statement

The original contributions presented in the study are included in the article/supplementary material, further inquiries can be directed to the corresponding author.

Author contributions

YG and KZ are responsible for the idea and writing of this paper and DW, XH, XS, and SZ are responsible for the experiments and calculation and simulation of the data.

Funding

This work was supported by the Scientific Research Foundation of the North China University of Science and Technology (BS201827), Science Foundation of Chinese Academy of Geological Sciences (DZLXJK20181201) and Linyi University (LYDX2017BS019).

Conflict of interest

Authors DW and XS were employed by the Petroleum Exploration and Production Research Institute, SINOPEC, and author SZ was employed by the Shandong Province Research Institute of Coal Geology Planning and Exploration

The remaining authors declare that the research was conducted in the absence of any commercial or financial relationships that could be construed as a potential conflict of interest.

Publisher's note

References

Chen, J., Wang, L., Wang, C., Yao, B., Tian, Y., and Wu, Y. S. (2021). Automatic fracture optimization for shale gas reservoirs based on gradient descent method and reservoir simulation. *Adv. Geo-Energy Res.* 5 (2), 191–201.

Chen, S. B., Zhu, Y. M., and Wang, H. Y. (2012). Structure characteristics and accumulation significance of nanopores in Longmaxi shale gas reservoir in the southern Sichuan Basin. *J. China Coal Soc.* 37 (3), 438–444. doi:10.13225/j.cnki.jccs.2012.03.007

Chen, Y., Tang, H. M., and Liao, J. J. (2022). Analysis of shale pore characteristics and controlling factors based on variation of buried depth in the Longmaxi Formation, Southern Sichuan Basin. *Geol. China* 49 (2), 472–484. doi:10.12029/gc20220209

Cui, C. L., Dong, Z. G., and Wu, D. S. (2019). Rock mechanics study and fracability evaluation for Longmaxi Formation of Baoj ing block in Hunan Province. *Nat. Gas. Geosci.* 30 (5), 626–634. doi:10.11764/j.issn.1672-1926.2018.12.021

Dou, L. B., Yang, H. J., and Xiao, Y. J. (2021). Probability study of formation brittleness and new quantitative evaluation of fracability for shale reservoirs. *Prog. Geophys.* 36 (2), 576–584. doi:10.6038/pg2021EE0460

Fjaer, E., Holt, R. M., and Horsrud, P. (2008). Petroleum related rock mechanics. *Dev. Petroleum Sci.* 53, 491–492. 2nd Edition. Elsevier.

Fu, Y., Jiang, Y., Wang, Z., Hu, Q., Xie, J., Ni, G., et al. (2019). Non-connected pores of the Longmaxi shale in southern Sichuan Basin of China. *Mar. Petroleum Geol.* 110, 420–433. doi:10.1016/j.marpetgeo.2019.07.014

Guo, J. C., Luo, B., Zhu, H. Y., Wang, Y. H., Lu, Q. L., and Zhao, X. (2015). Evaluation of fracability and screening of perforation interval for tight sandstone gas reservoir in Western Sichuan Basin. *J. Nat. Gas Sci. Eng.* 25, 77–87. doi:10.1016/j.jngse.2015.04.026

Huang, C., Xu, T., Ju, Y., Zhu, H., Ju, L., and Li, W. (2019). Fracability evaluation of shale of the Wufeng-Longmaxi Formation in the changning area, Sichuan Basin. *Acta Geol. sinica-. Engl. Ed.* 93 (4), 996–1004. doi:10.1111/1755-6724.13877

Li, L. (2022). Development of natural gas industry in China: Review and prospect. *Nat. Gas. Ind. B* 9 (2), 187–196. doi:10.1016/j.ngib.2022.03.001

Li, Z., Li, G., Yu, H., Jiang, Z., Li, H., and Gong, H. (2022). Fracability evaluation based on the three-dimensional geological numerical simulation of *in situ* stress: Case study of the Longmaxi Formation in the weirong shale gas field, southwestern China. *Math. Geosci.* 54, 1069–1096. doi:10.1007/s11004-022-10001-5

Liang, C., Jiang, Z. X., Zhang, C. M., Guo, L., Yang, Y., and Li, J. (2014). The shale characteristics and shale gas exploration prospects of the lower silurian Longmaxi shale, Sichuan Basin, south China,Sichuan Basin,south China. *J. Nat. Gas Sci. Eng.* 21, 636–648. doi:10.1016/j.jngse.2014.09.034

Liu, W., Wu, J., Jiang, H., Zhou, Z., Luo, C., Wu, W., et al. (2021). Cenozoic exhumation and shale-gas enrichment of the Wufeng-Longmaxi formation in the southern Sichuan basin, Western China. *Mar. Petroleum Geol.* 125, 104865. doi:10.1016/j.marpetgeo.2020.104865

Mullen, M., and Enderlin, M. (2012). Fracability index–more than just calculating rock properties//SPE Annual Technical Conference and Exhibition. doi:10.2118/159755-MS

Qiu, Z., Zou, C., Wang, H., Dong, D., Lu, B., Chen, Z., et al. (2020). Discussion on the characteristics and controlling factors of differential enrichment of shale gas in the Wufeng-Longmaxi formations in south China. *J. Nat. Gas Geoscience* 5 (3), 117–128. doi:10.1016/j.jnggs.2020.05.004

Rickman, R., Mullen, M. J., and Petre, J. E. (2008). A practical use of shale petrophysics for stimulation design optimization: All shale plays are not clones of the Barnett Shale//SPE annual technical conference and exhibition. doi:10.2118/115258-MS

Shi, X., Luo, C., Cao, G., He, Y., Li, Y., Zhong, K., et al. (2021). Differences of main enrichment factors of S1l11-1 sublayer shale gas in southern Sichuan Basin. *Energies* 14 (17), 5472. doi:10.3390/en14175472

Shi, Z., Zhou, T., Wang, H., and Sun, S. (2022). Depositional structures and their reservoir characteristics in the wufeng–longmaxi shale in southern Sichuan Basin, China. *Energies* 15 (5), 1618. doi:10.3390/en15051618

Tan, Y., Pan, Z., Feng, X. T., Zhang, D., Connell, L. D., and Li, S. (2019). Laboratory characterisation of fracture compressibility for coal and shale gas reservoir rocks: A review. *Int. J. Coal Geol.* 204, 1–17. doi:10.1016/j.coal.2019.01.010

Tang, L., Song, Y., Jiang, S., Li, L., Li, Z., Li, Q., et al. (2020). Sealing mechanism of the roof and floor for the Wufeng-Longmaxi shale gas in the southern Sichuan Basin. *Energy fuels.* 34 (6), 6999–7018. doi:10.1021/acs.energyfuels.0c00983

Tang, Y., Xing, Y., and Li, L. Z. (2012). Influence factors and evaluation methods of the gas shale fracability. *Earth Sci. Front.* 19 (5), 356–363.

Warpinki, N. R., Mayerhof, M. J., Vinct, M. C., Cipolla, C. L., and Lolon, E. P. (2009). Stimulating unconventional reservoirs: Maximizing network growth while optimizing fracture conductivity. *J. Can. Petroleum Technol.* 48 (10), 39–51. doi:10.2118/114173-MS

Wu, J., Zhang, S., Cao, H., Zheng, M., Sun, P., and Luo, X. (2018). Fracability evaluation of shale gas reservoir-A case study in the Lower Cambrian Niutitang formation, northwestern Hunan, China. *J. Petroleum Sci. Eng.* 164, 675–684. doi:10.1016/j.petrol.2017.11.055

Xiao, J. F., Hu, P. J., and Han, L. X. (2022). Mechanical properties and compressibility evaluation of Qiongzhusi shale in Weiyuan area in southern Sichuan. *Drill. Prod. Technol.* 45 (2), 61–66. doi:10.3969/J.ISSN.1006-768X.2022.02.11

Xiong, J., Liu, K., Shi, C., Liu, X., and Huang, L. (2021). Logging prediction and evaluation of fracture toughness for the shales in the Longmaxi Formation, southern Sichuan Basin. *Petroleum* 7 (3), 254–262. doi:10.1016/j.petlm.2020.10.003

Xu, H., Zhou, W., Zhang, R., Liu, S., and Zhou, Q. (2019). Characterizations of pore, mineral and petrographic properties of marine shale using multiple techniques and their implications on gas storage capability for Sichuan Longmaxi gas shale field in China. *Fuel* 241, 360–371. doi:10.1016/j.fuel.2018.12.035

Yu, H., Taleghani, A. D., and Lian, Z. (2019). On how pumping hesitations may improve complexity of hydraulic fractures, a simulation study. *Fuel* 249, 294–308. doi:10.1016/j.fuel.2019.02.105

Zhang, D. W. (2021). Development prospect of natural gas industry in the Sichuan Basin in the next decade. *Nat. Gas. Ind. B* 41 (8), 119–131. doi:10.1016/j.ngib.2021.08.025

Zhang, J., Shi, M., Wang, D., Tong, Z., Hou, X., Niu, J., et al. (2022). Fields and directions for shale gas exploration in China. *Nat. Gas. Ind. B* 9 (1), 20–32. doi:10.1016/j.ngib.2021.08.014

Zhang, L. H., He, X., and Li, X. G. (2021). Shale gas exploration and development in the Sichuan Basin: Progress, challenge and countermeasures. *Nat. Gas. Ind.* 41 (8), 143–152. doi:10.3787/j.issn.1000-0976.2021.08.013

Zou, X. Y., Li, X. Q., and Wang, Y. (2022). Reservoir characteristics and gas content of Wufeng-Longmaxi formations deep shale in southern Sichuan Basin. *Nat. Gas. Geosci.* 33 (4), 654–665. doi:10.11764/j.issn.1672-1926.2021.10.004

frontiers | Frontiers in Earth Science

TYPE Original Research
PUBLISHED 22 August 2022
DOI 10.3389/feart.2022.985302

OPEN ACCESS

EDITED BY
Hu Li,
Southwest Petroleum University, China

REVIEWED BY
Hui Xiao,
Xi'an Shiyou University, China
Peng Wang,
Yibin University, China

*CORRESPONDENCE
Jishun Pan,
jspan123@126.com

SPECIALTY SECTION
This article was submitted to Structural Geology and Tectonics, a section of the journal Frontiers in Earth Science

RECEIVED 03 July 2022
ACCEPTED 19 July 2022
PUBLISHED 22 August 2022

CITATION
Peng Y, Pan J and An X (2022), A preliminary study on the geological conditions and indexes for the accumulation of shale gas in the marine-continental transitional facies sediments in the South North China Basin.
Front. Earth Sci. 10:985302.
doi: 10.3389/feart.2022.985302

A preliminary study on the geological conditions and indexes for the accumulation of shale gas in the marine-continental transitional facies sediments in the South North China Basin

Yicong Peng[1], Jishun Pan[1]* and Xifeng An[2]

[1]College of Geosciences and Engineering, North China University of Water Resources and Electric Power, Zhengzhou, China, [2]Henan Yukuang Geological Exploration Investment Co., Ltd., Zhengzhou, China

At present, the Carboniferous-Permian shale gas in the South North China Basin is still in the exploration stage, and the understanding of the microscopic pore structures, mineral composition and hydrocarbon enrichment law of the marine-continental transitional shale gas reservoirs in this area is extremely limited. In this paper, taking the Carboniferous-Permian shale gas reservoir in the South North China Basin as an example, the geological conditions of shale gas accumulation have been systematically studied using a large amount of sedimentary, logging, seismic, core, geochemical, physical property, and scanning electron microscope data. The study shows that the transitional dark shale is stable and widely distributed in the South North China Basin. Among them, the average thickness of the high-quality shale in the Taiyuan Formation is 67 m, while that of the Shanxi Formation is 56 m. Carboniferous and Permian are the main strata for the distribution of shale gas resources. Among them, the dark shale developed in the Taiyuan and Shanxi Formations has the largest thickness and the highest organic matter abundance. In addition, the organic matter types of the Upper Paleozoic coal-measure source rocks in the South North China are mainly II_2-III types, and a small part of them belong to II_1 types. The brittle minerals in the target shale are mainly quartz, and the content of illite is the highest among the clay minerals. Porosity is negatively correlated with clay mineral content, and positively correlated with quartz and TOC content. In addition, the permeability is negatively correlated with the organic matter content. Finally, the criteria for key indicators of the transitional shale gas reservoirs in the South North China Basin were developed.

KEYWORDS

South North China Basin, marine-continental transitional facies, shale gas, organic matter, pore structure

Introduction

There are three types of sedimentary facies for organic-rich shales: marine, continental and marine-continental transitional facies (Bernard et al., 2012; Clarkson et al., 2013; Jiang et al., 2015; Li., 2022). Coal-measure shale is a typical marine-continental transitional facies deposit. At present, coal-measure shale gas in China is still in the exploratory stage (He et al., 2012; Zou et al., 2019). Compared with marine shale, it is generally believed that coal-measure shale gas reservoirs have the characteristics of rapid lithofacies change, thin single-layer thickness and high content of clay minerals (Chalmers and Bustin, 2007; Curtis et al., 2012; Wang et al., 2015; Kong et al., 2016). With the improvement of oil and gas development technology in tight reservoirs, the commercial development of coal-measure shale gas has gradually become possible. Shale gas will become one of the clean energy sources with the most development potential and prospects in China due to its huge resources, extensive gas-bearing areas and strong sustainable production (Yan et al., 2015; He et al., 2020; Li et al., 2020; Zheng et al., 2020).

The Carboniferous-Permian was a critical period for the transition of sedimentary systems from marine to continental in China. Transitional organic-rich shale is widely developed in China, for example, it is widely developed in the Tarim Basin, Ordos Basin, Qinshui Basin in the central and western China, and the Lower Yangtze and Yunnan-Guizhou areas in the southern China (Lu et al., 2015; Xi et al., 2017; Zou et al., 2019; Nie et al., 2020). Generally, the accumulation scale of transitional shale gas is limited, so its own shale gas reserves do not have high development and economic value. However, it is usually interbed with gas-bearing coal seams and tight sandstone layers, so the "multi-type-gas co-production" can be developed (Kruk and Jaroniec., 2001; Loucks et al., 2009; Fu et al., 2013; Fu et al., 2015). From this point of view, transitional shale gas still has good resource potential and economic benefits.

The main part of the South North China Basin is located in the central and eastern part of the Henan Province, and the Carboniferous-Permian is the main stratum for the distribution of shale gas resources (He et al., 2012). Shale gas in the Taiyuan and Shanxi Formations in the South North China Basin has great exploration potential. For example, the fracturing production of the Well MY1 is 1 200 m^3/d, and the production of the Well ZD2 after fracturing is 3 000 m^3/d. In addition, the current drilling in the Taikang Uplift, Luyi Depression and Zhoukou Depression have obtained good shale gas shows.

At present, there is insufficient understanding of the microscopic pore structures, mineral composition and hydrocarbon enrichment law of the Carboniferous-Permian shale gas reservoirs in the South China Basin. In this paper, taking the Carboniferous-Permian shale gas reservoir in the South North China Basin as an example, the geological conditions of the shale gas accumulation in the basin have been systematically studied using a large amount of sedimentary, logging, seismic, core, geochemical, physical property, and scanning electron microscope data. This study can provide scientific guidance for promoting the development of transitional shale gas in the South North China Basin and similar areas.

Geological background and methods

Structural and sedimentary background

The South North China Basin is located in the central and southern parts of the Henan Province, China, with a total area of about 150,000 km^2 (Figure 1). From north to south, the basin is divided into five sub-structural units: Kaifeng Depression, Taikang Uplift, Zhoukou Depression, Changshan Uplift and Xinyang-Hefei Depression. The ZM Block in the study area is located near the Kaifeng Depression, and the target layers are the Late Paleozoic Carboniferous and Permian strata.

The South North China Basin was part of the North China Craton Basin in the Late Paleozoic (He et al., 2012; Zou et al., 2019). Affected by the global sea level rise in the Late Carboniferous, extensive transgression gradually began to occur in the study area. During the depositional period of the Benxi Formation in the Late Carboniferous, the North China Plate was a gentle monoclinic paleotopography with high in the northwest and low in the southeast. At this time, seawater intruded from the northeast, and a set of marine-continental alternating strata was formed. In the early Permian, affected by the uplift of the Yinshan Ancient Land, the surface sea water of the North China continent retreated from the northwest to the southeast (He et al., 2012). Furthermore, a set of sedimentary strata dominated by marine and transitional facies developed in the Shanxi Formation of the South North China Basin. In the early stage, the tidal flat and peat swamp facies deposits formed on the basis of the gradual withdrawal of the surface sea water; in the late stage, the delta facies deposits under the action of rivers were formed (Wang et al., 2015; Yan et al., 2015). By the late Permian, the South North China Basin was uplifted as a whole, the paleotopography was higher in the north and lower in the south, the seawater completely retreated, and the basin entered the stage of continental sedimentary development. At this time, a set of red clastic deposits dominated by fluvial facies were deposited. The Carboniferous-Permian coal measure strata in the South North China Basin have experienced a complex evolution process of deposition→deep burial→uplifting and denudation transformation→second deep burial. It has the basic geological conditions for secondary hydrocarbon generation in the process of secondary deep burial.

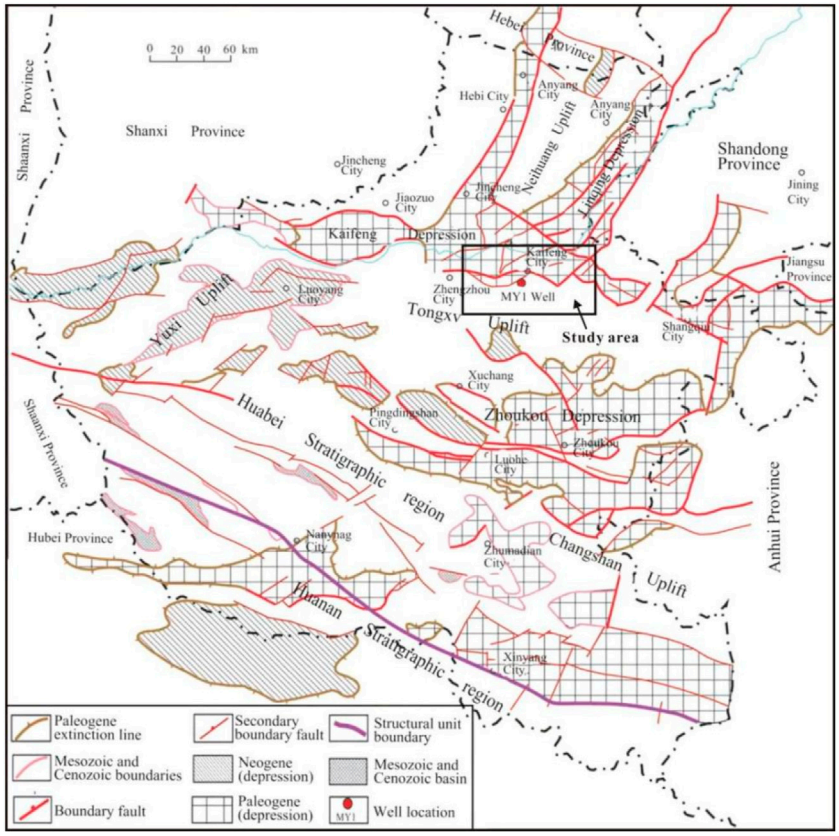

FIGURE 1
Structural unit division of the South-North China Basin and location of the study area.

Distribution characteristics of shale series in the taiyuan and shanxi formations

The Carboniferous and Permian in the southern part of the North China are widely distributed with diverse sedimentary types and rich biological fossils. Therefore, this area is one of the best areas to study the Carboniferous and Permian marine-continental transitional shale in China. Shales of the Taiyuan Formation is mainly distributed in the Taikang Uplift, Luyi Depression and Shenqiu Depression. Among them, the cumulative thickness of dark shales in the Taiyuan Formation in the Wells MY1 and ZX1 are 82 and 50 m, respectively. The burial depth of shale is mainly concentrated above 2000 m, and the maximum depth can reach 6,000 m. The shale with the maximum depth is mainly distributed in the Kaifeng and Zhoukou Depressions.

The thickness of the shale in the Shanxi Formation ranges from 5 to 100 m, and the deposition centers are concentrated in the northern part of the basin, such as the Taikang Uplift, Luyi Depression, Luoyang Basin and Xiangcheng Depression. In other areas, the average thickness of the shale is 30 m. Among them, the thickness of dark shale in the Wells MY1 and ZX1 are 91 and 70 m, respectively.

Experimental methods

The samples collected in this study were all from the lower Permian Taiyuan and Shanxi Formations of the Well MY1 in the Zhongmu Shale Gas Exploration Area, Henan Province. Organic carbon content testing and field emission scanning electron microscopy observations were carried out on all samples. Mineral composition analysis was carried out by X-ray diffraction (XRD) with the instrumental parameter of Cu Kα radiation (λ = 1.540 6 for CuKα_1) in a stepwise scan at a rate of 4°/min in the range of 3°–85° (2θ). The total organic carbon content (TOC) was measured using a LECO carbon-sulfur analyzer. Before the test, the samples were treated with hydrochloric acid to remove carbonate minerals. Vitrinite reflectance (R_o) testing was performed with a DM LPWITH MSP20 Vitrinite Reflectometer. In addition, the morphological features of the

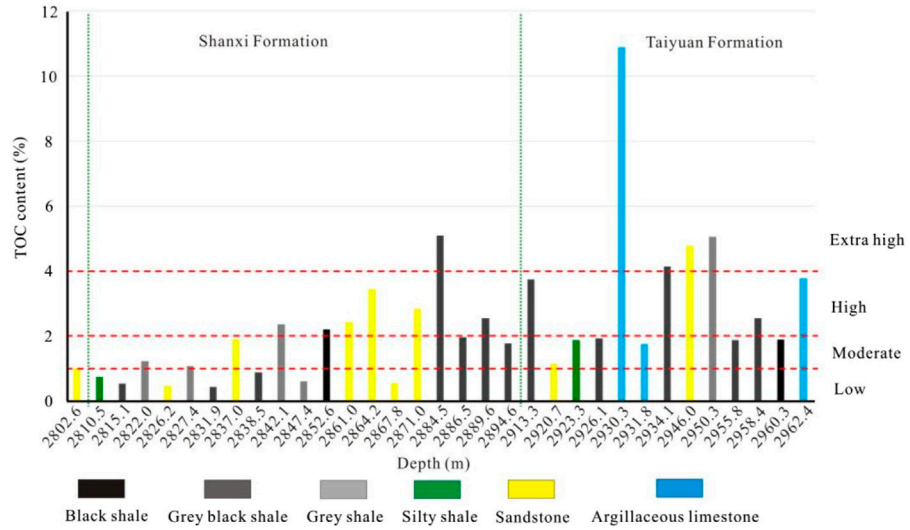

FIGURE 2
Total organic carbon content (TOC) distribution histograms for samples in well MY1.

pores of the samples were observed using a Quanta 250FEG SEM field emission scanning electron microscope. Before the experiment, an argon ion spectrometer was used to profile the sample surface to ensure smooth sample surface and improve imaging quality.

Results

Organic abundance of source rocks

The dark shale of the Upper Paleozoic is mainly distributed in the Taiyuan and Shanxi Formations of the Permian, with an average organic carbon content of 0.52%–3.21%. The abundance of organic matter gradually increased from top to bottom perpendicular to the bedding plane (Figure 2). The limestone and marl of the Upper Paleozoic are distributed in the Taiyuan Formation, with an average thickness of 30 m. Its organic carbon content is distributed between 0.07% and 4.54%, with an average value of 0.74%. The TOC content of 1.5%–3% represents medium source rocks, while that of 3%–6% represents good source rocks. Therefore, the target layer develop medium-good source rocks (Wang and Yin., 2019). On the whole, the organic matter abundance of the Upper Paleozoic coal-measure dark shale from bottom to top increases from high to low, and the source rock grade changes from good to poor. The dark shale of the Taiyuan Formation belongs to medium source rocks, while limestone and marl belong to the medium to good source rocks; in addition, the shale of the Shanxi Formation belongs to the poor to medium source rocks (Figure 3).

Types of organic matter in source rocks

For the organic matter types of the Upper Paleozoic coal-measure source rocks in the South North China Basin, dark shale is generally better than coal and carbonaceous shale. The microscopic composition of coal is mainly vitrinite, and the content is usually more than 60%; the second is inertite, its content is less than 30%; and the content of chitinite + sapropel group is generally less than 20%, and most of which are only 2%–15%. The organic matter component of coal is Type III kerogen.

Statistics show that the content of crustal group + sapropel group in the micro-component of dark shale is higher than that of coal and carbonaceous shale (generally more than 40%). It reflects that the organic matter type of dark shale is good. It is mainly Type II_2, and a small part is Type III. In addition, the H/C atomic ratios of the organic elements are between 0.51 and 0.91, and the O/C atomic ratios are between 0.06 and 0.14. It also reflects that the types of organic matter are mainly Type II_2-III.

On the whole, the organic matter types of the Upper Paleozoic coal measure source rocks in the South North China Basin are mainly Type II_2-III, and a small part is Type II_1. Moreover, the organic matter type of the black shale is better than that of the arbonaceous shale and coal.

Evolution of organic matter in source rocks

The thermal evolution of the Upper Paleozoic coal measure source rocks in the South North China Basin is uneven in different regions, which is caused by the superposition of the

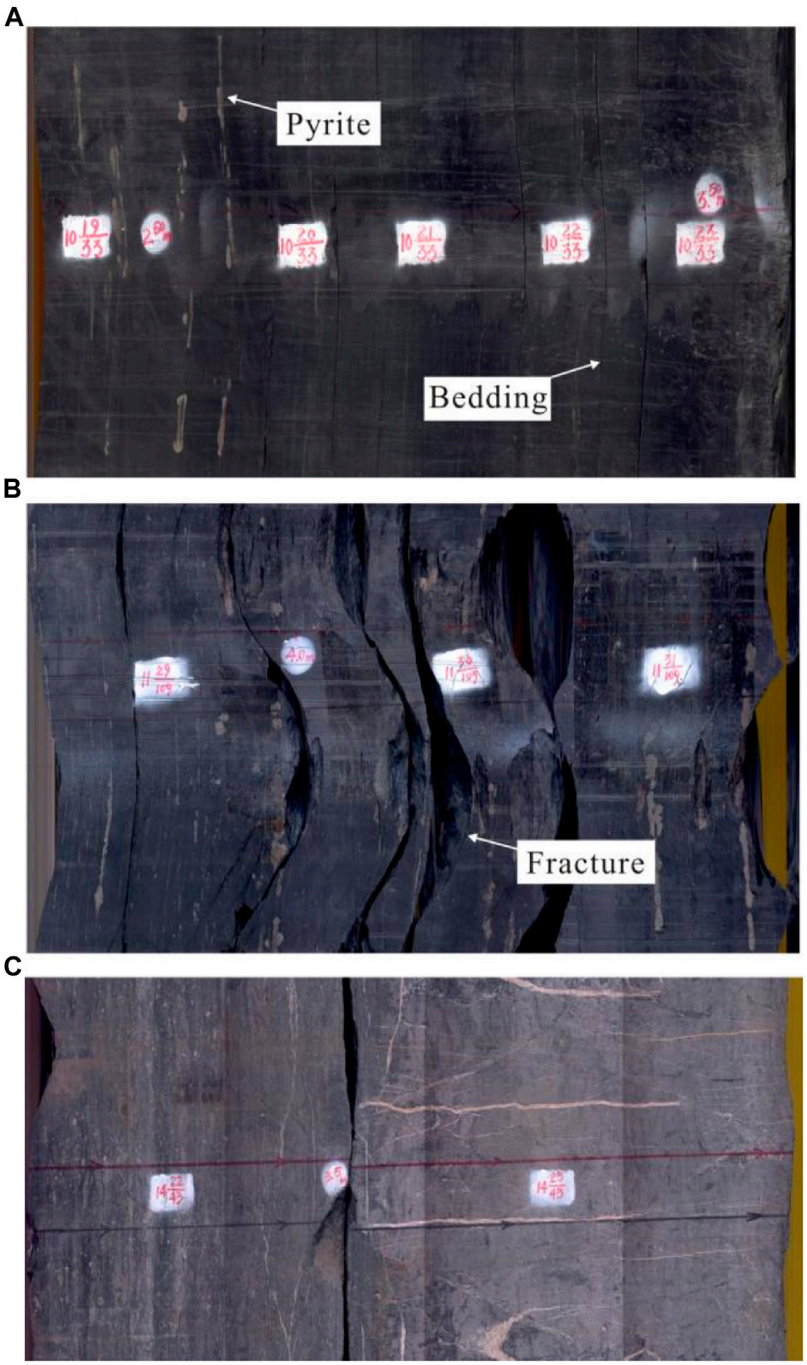

FIGURE 3
Development characteristics of different types of shale in Well MY1. **(A)** 2,895.25–2,895.91 m; **(B)** 2,916.6–2,917.4 m; **(C)** 2,959.24–2,969.13 m.

normal pleogenesis and various abnormal thermal evolutions. The R_o value in the Zhongmu-Taikang-Luyi areas is above 2%, and the source rocks are in the high-mature- overmature stage (Figure 4). It is mainly caused by the superposition of normal pleogenesis, mantle thermal uplift, and abnormal thermal evolution of igneous rock thermal contact metamorphism. The R_o value in the Xiangcheng-Tanzhuang-Shenqiu areas is 0.7%–1.5%, and the source rocks are mainly in the mature stage, which belongs to normal pleogenesis.

On the whole, the Upper Paleozoic coal measure source rocks in the South North China Basin are generally in the low-mature-over-mature stage. The general trend of maturity shows a ring-shaped

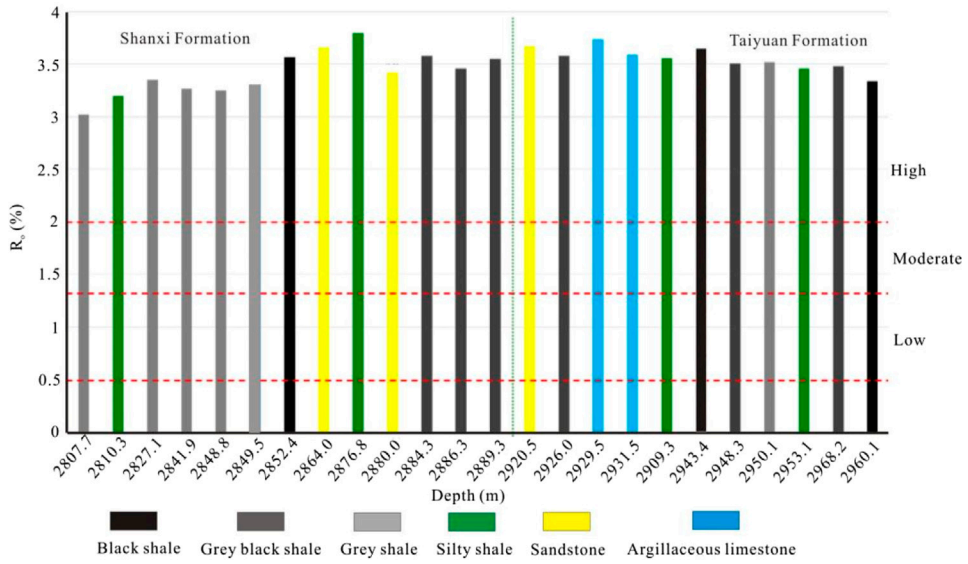

FIGURE 4
Histogram of vitrinite reflectance (R_o) distribution of rock samples from Well MY1.

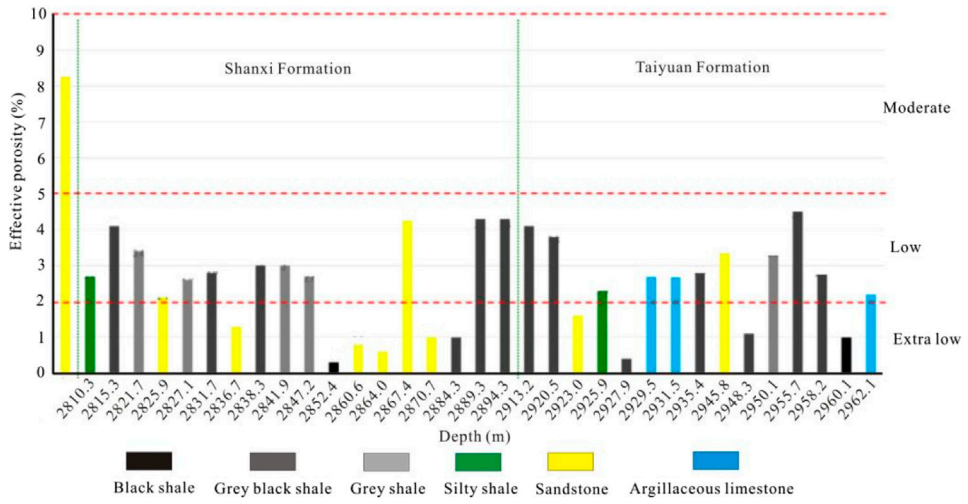

FIGURE 5
Histogram of effective porosity distribution of rock samples from Well MY1.

distribution along the Jiyuan-Jiaozuo-Taikang high evolution belt. It has the characteristics of high in the north and low in the south, and high in the west and low in the east. Among them, the high thermal evolution of the Zhongmu-Taikang-Luyi northern region is related to the thermal uplift caused by the thinning of the lithosphere and the upwelling of the asthenosphere. However, the high thermal evolution in the Tanzhuang-Shenqiu area is mainly related to the normal pleogenesis of the huge thick sediments in the Yanshanian-Himalayan period.

Physical properties

The porosity distribution of the Taiyuan Formation gas-bearing shale in Well MY1 ranges from 0.4% to 4.5%, with an average value of 2.1% (Figure 5); the permeability distribution ranges from 1.21×10^{-6} to 0.11 mD, with an average value of 7.48×10^{-3} mD (Figure 6). The porosity distribution of the gas-bearing shale intervals in the Shanxi Formation ranges from 0.3% to 8.8%, with an average value of 2.3% (Figure 5); the

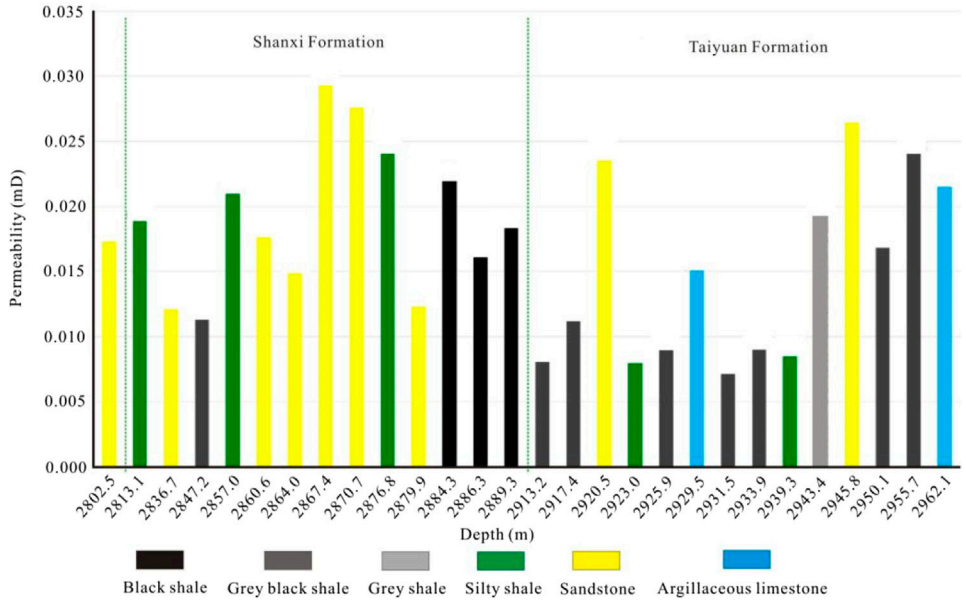

FIGURE 6
Histogram of permeability distribution of rock samples from Well MY1.

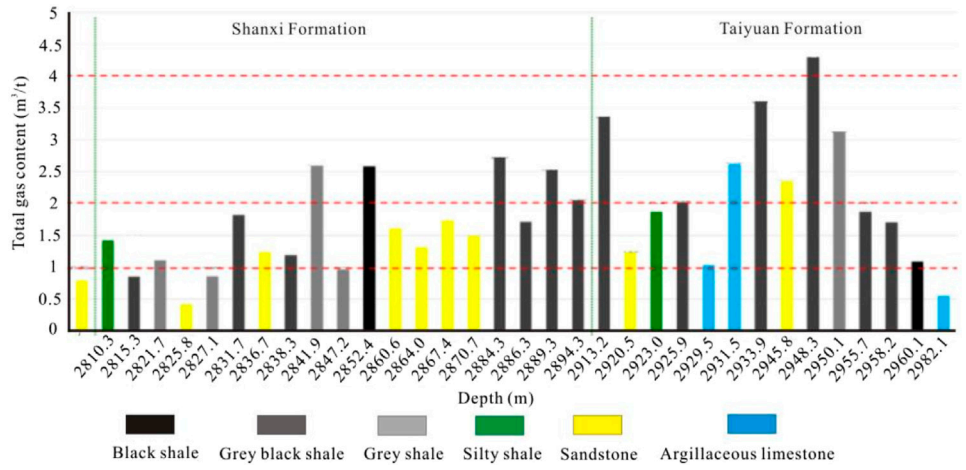

FIGURE 7
Histogram of field analytical total gas content distribution in Well MY1.

permeability distribution ranges from 23×10^{-6} to 0.92 mD, with an average value of 0.045 mD (Figure 6). The permeability of shale reservoirs in the area is usually less than 0.1 mD, which belongs to the ultra-low permeability type. On the whole, the porosity and permeability of the reservoirs in the area are low, and the shale reservoirs are low-porosity and low-permeability reservoirs.

Total desorption gas volume on site

Core observations in the Well MY1 revealed that the thickness of high-quality shale in the Taiyuan Formation is 77 m, and the thickness of high-quality shale gas in the Shanxi Formation is 67.5 m. The total gas content of high-quality shale ranges from 0.42 to 4.44 m^3/t, with an average of 1.93 m^3/t (Figure 7).

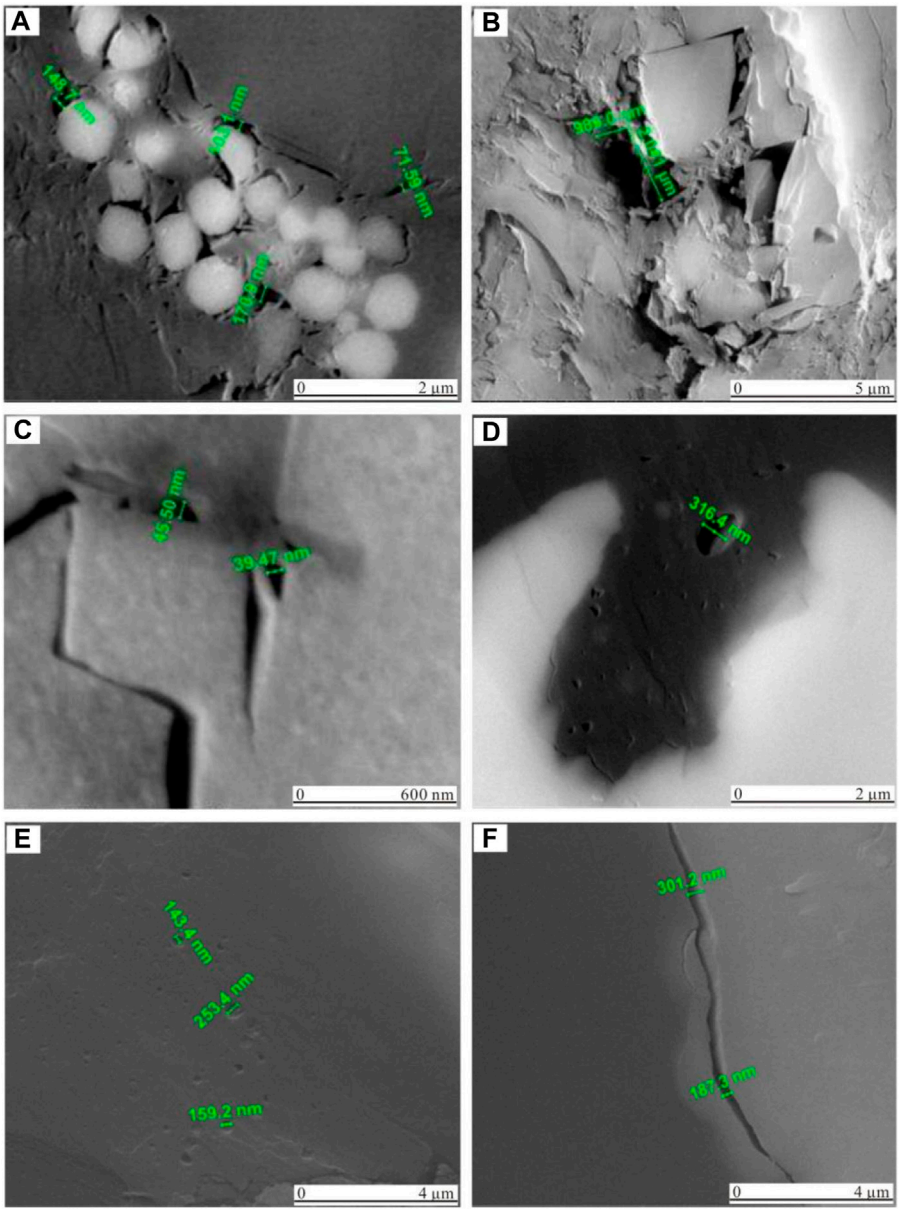

FIGURE 8
Microscopic images of pore characteristics of the Taiyuan and Shanxi Formation shales from Well MY1. **(A)** Pyrite intergranular pores, 2,934 m; **(B)** Intergranular pores, 2,937 m; **(C)** Calcite edge mold pores, 2,874 m; **(D)** Organic hydrocarbon generation pores, 2,944 m; **(E)** Organic hydrocarbon generation pores, 2,945 m; **(F)** Organic matter shrinkage crack, 2,948 m.

Discussion

Classification of pore types

The brittle minerals in the transitional shale of the target layer are mainly quartz, and the content of shale in the Taiyuan Formation in Well MY1 of the Zhongmu Block is 6%–55%; the content of clay minerals is 32%–64%. The content of clay minerals and quartz in the shale of the Shanxi Formation ranges from 35% to 89% and 3%–52%, respectively. The clay minerals in the Taiyuan Formation are dominated by illite, kaolinite, imonite mixed layers, and a small amount of chlorite. Among them, the average contents (volume fraction) of illite, kaolinite and imonite mixed layer are 28%, 22.17%, and 20.17%, respectively. For the Shanxi Formation, the clay minerals in the shale are mainly illite and kaolinite, and a small amount of chlorite and imonite mixed layers. Among them, the average volume fractions of illite, kaolinite and imonite mixed layer are 67.36%, 28.18%, and 25.09%, respectively.

Inorganic pores, organic pores and micro-fractures are the main storage spaces in the transitional shale gas reservoirs in the study area (Figure 8) (Zhang et al., 2021).

1) Inorganic pores: The minerals in the shale of the Taiyuan and Shanxi Formations are mainly composed of clay and quartz, which form a large number of micro-sedimentary structures. The incomplete cementation between various grains or the later diagenetic transformation will generate a large number of intergranular pores. Ductile minerals such as clay minerals, organic matter, and brittle minerals such as quartz, feldspar, and pyrite constitute the inorganic pores (Figures 8A–C).

2) Organic pores and micro-fractures: The shale samples of the Taiyuan and Shanxi Formations develope organic hydrocarbon-generating pores and a large number of organic shrinkage micro-fractures (Figure 8D–F). Organic micro-fractures are fractures formed by the shrinkage of organic matter in the process of hydrocarbon generation. It can not only provide space for the storage of shale gas, but also provide main channels for the seepage of gas (Tissot., 1978; Chalmers et al., 2009; Qi et al., 2019; Li., 2021).

Analysis of controlling factors of physical properties

Statistics show that the average volume fraction of quartz in the Shanxi Formation shale reservoirs in Well MY1 is 30%, while that in the Taiyuan Formation shale reservoirs is 37%. The clay minerals in the Shanxi Formation are dominated by illite and kaolinite, and the clay minerals in the Taiyuan Formation are dominated by illite, kaolinite and imon mixed layer. It fully shows that the shale reservoir in the area has strong brittleness and fracture-making ability, and is suitable for hydraulic fracturing.

Generally, clay minerals are favorable for the adsorption of shale gas (Yang et al., 2010; Yu et al., 2019). Montmorillonite has the strongest adsorption capacity, followed by illite, then chlorite and kaolinite. The composition of clay minerals in shale is relatively complex, with high content of quartz, which are mostly clay grade and often appear in the form of laminar structures (Yang et al., 2016; Xiong et al., 2017; Wang et al., 2018). However, shale with high organic matter and quartz content is highly brittle, and it is easy to form natural and induced fractures under the action of external force. In turn, it facilitates the percolation of natural gas.

There are many factors affecting the porosity of tight reservoirs, including framework particle size, organic matter content, clay mineral content, and dissolution diagenesis. The study found that the porosity of shale was negatively correlated with clay mineral content (Figure 9A), positively correlated with quartz content (Figure 9A) and TOC content (Figure 9B). During the original deposition of shale, the original porosity was very large, and during the later burial compaction and diagenesis, the porosity will continue to decrease. Quartz is a brittle mineral with strong compressive ability. Therefore, as the quartz content in the shale increases, the preservation of the original porosity is better.

Similarly, for permeability, interlayer pores with abundant clay minerals will greatly enhance the permeability of the reservoir. Therefore, the permeability increases continuously with the increase of authigenic clay content, and it tends to stabilize after reaching 50% (Figure 9C). There is a negative correlation between permeability and quartz content. The main reason is still the lack of connectivity between the intergranular pores. Therefore, in the process of deep burial, the intergranular pores are basically exhausted by compaction. In addition, the study also found that the permeability was negatively correlated with the organic matter content (Figure 9D). This is because the intercrystalline pores of clay minerals are mainly developed in the transitional shale, and the organic pores are not the main type of pores. When the degree of development of organic pores is high, it represents a strong reducing environment, and the degree of development of intercrystalline pores in clay minerals will decrease.

Accumulation conditions and indexes of shale gas

There is a good positive correlation between the maximum adsorbed gas volume and the desorption gas volume of the Taiyuan and Shanxi Formation shales in Well MY1 and the organic carbon content (Figure 10). This is caused by the presence of a large number of micropores and cracks in the organic matter. Moreover, with the increase of organic carbon content, the type of microscopic pores and fractures and the porosity will also increase, the specific surface area for natural gas adsorption increases sharply, and the maximum adsorbed gas content and desorption gas content of shale increase accordingly. Since the desorption gas volume includes adsorbed gas and free gas, the storage of free gas in pores is greatly affected by formation pressure (Guo et al., 2015; Gai et al., 2016; Ma et al., 2019; Xu et al., 2019). Therefore, the correlation between the desorption gas volume and the organic carbon content is weaker than that of the maximum adsorption gas volume.

The geological conditions required for the accumulation of shale gas include: large-scale development of dark shale, favorable structural and depositional background, good reservoir continuity, large thickness, and wide distribution areas. These geological conditions are the material basis for the large-scale accumulation of shale gas. At the same time, the good organic geochemistry, porosity and permeability properties, fracture development, and mineral composition

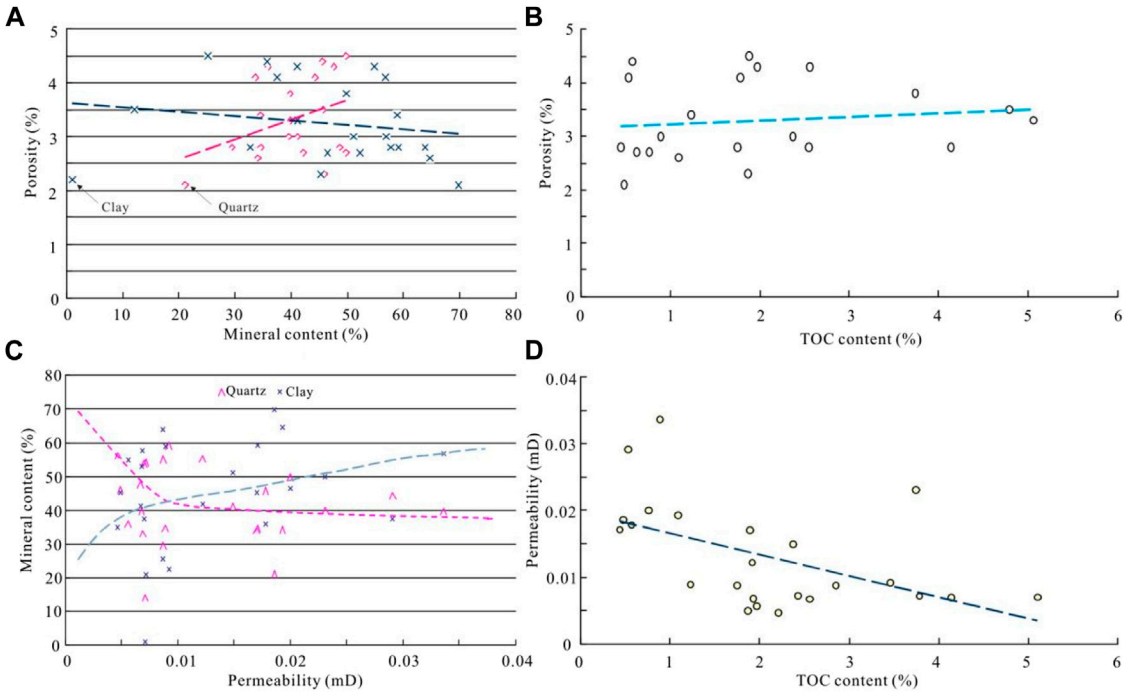

FIGURE 9
Characteristics of physical parameters, TOC content and mineral composition content of shale samples in the target layer. **(A)** Relationship between mineral composition content and porosity; **(B)** Relationship between TOC content and porosity; **(C)** Relationship between mineral composition content and permeability; **(D)** Relationship between TOC content and permeability.

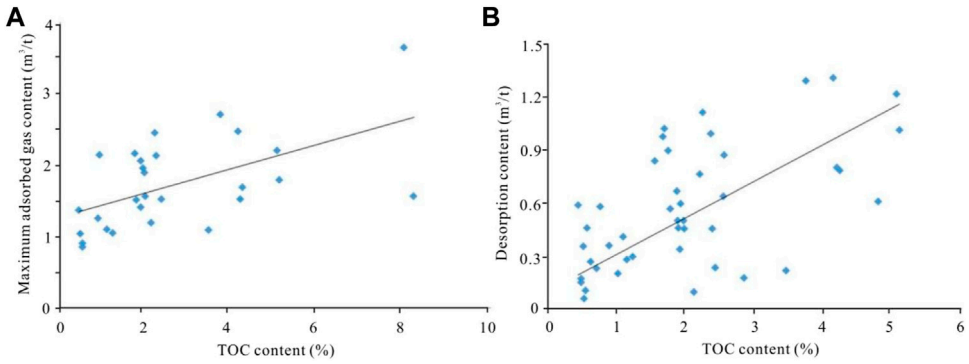

FIGURE 10
Effect of TOC content on the adsorption and desorption gas content of shale samples. **(A)** TOC content has a positive correlation with the maximum total adsorbed gas; **(B)** There is also a good positive correlation between TOC content and desorption gas volume.

are the key factors for the shale gas accumulation. They comprehensively control the hydrocarbon generation capacity, storage performance, oil and gas potential and production rate of shale, and determine the enrichment degree and exploration prospect of shale oil and gas. In addition, the burial depth, formation temperature, and pressure conditions of shale are also important factors that affect the accumulation of shale gas and determine whether it has industrial exploration and development value.

This study proposes that the key indicators of transitional shale gas include: 1) Organic matter abundance: organic carbon (TOC) content >1.0%, organic matter types are Type II_2 and Type III (these two types are the main types in the South North China Basin); 2) Organic matter maturity: vitrinite reflectance

R_o>0.9%, which is to ensure the quality of the gas source; 3) Brittle mineral content>40%, clay mineral content <40%, this is to ensure the quality of the reservoir; 4) Porosity>2%, permeability>100 nd, gas content>1.0 m^3/t, water saturation <45%, oil saturation <10%; in addition, shale gas resource abundance>2.0×10^8 m^3/km^2, which is to ensure the potential and prospects of shale gas resources; 5) Formation pressure: normal pressure to overpressure, continuous effective shale thickness >15 m, interlayer thickness <3.0 m; 6) Lithology and thickness of roof and floor: the thickness of impermeable rock layer is >10 m; 7) Preservation conditions: stable structure, low degree of transformation.

Conclusion

1) The transitional dark shale is stable and widely distributed in the South North China Basin. Among them, the average thickness of the high-quality shale of the Taiyuan Formation is 67 m, while that of the Shanxi Formation is 56 m. Carboniferous and Permian are the main strata for the distribution of shale gas resources. Among them, the dark shale developed in the Taiyuan and the Shanxi Formations has the largest thickness and the highest organic matter abundance.
2) The organic matter types of the Upper Paleozoic coal-measure source rocks in the South North China are mainly the II_2-III Types, and a small part of them belong to the II_1 Type.
3) The brittle minerals in the target shale are mainly quartz, and the content of illite is the highest among the clay minerals. Porosity is negatively correlated with clay mineral content, and positively correlated with the quartz content and TOC content. In addition, the permeability is negatively correlated with the organic matter content.
4) The criteria for key indicators of transitional shale gas reservoirs in the South North China Basin were developed. This study can provide scientific guidance for efficient exploration and development of transitional shales.

Data availability statement

The original contributions presented in the study are included in the article/supplementary material, further inquiries can be directed to the corresponding author.

Author contributions

YP and JP are responsible for the idea and writing of this paper and XA is responsible for the field investigation and experiments.

Acknowledgments

This research was funded by the Natural Science Foundation of Xinjiang Uygur Autonomous Region—Surface Project (2019D01A34) "Accumulation Mechanism, Occurrence Characteristics and Basin Dynamics Environment of Shale (Stratification) Gas Source-Reservoir Complex."

Conflict of interest

Author XA was employed by the Henan yukuang geological exploration investment Co., Ltd.

The remaining authors declare that the research was conducted in the absence of any commercial or financial relationships that could be construed as a potential conflict of interest.

Publisher's note

All claims expressed in this article are solely those of the authors and do not necessarily represent those of their affiliated organizations, or those of the publisher, the editors and the reviewers. Any product that may be evaluated in this article, or claim that may be made by its manufacturer, is not guaranteed or endorsed by the publisher.

References

Bernard, S., Wirth, R., Schreiber, A., Schulz, H. M., and Horsfield, B. (2012). Formation of nanoporous pyrobitumen residues during maturation of the barnett shale (fort worth basin). *Int. J. Coal Geol.* 103 (23), 3–11. doi:10.1016/j.coal.2012.04.010

Chalmers, G., Bustin, R. M., and Powers, I. (2009). A pore by any other name would be as small: the importance of meso-and microporosity in shale gas capacity," in AAPG annual convention and exhibition. Denver, Colorado, 7–10.

Chalmers, G., and Bustin, R. M. (2007). The organic matter distribution and methane capacity of the lower cretaceous strata of northeastern British Columbia, Canada. *Int. J. Coal Geol.* 70 (1-3), 223–239. doi:10.1016/j.coal.2006.05.001

Clarkson, C., Solano, N., Bustin, R., Bustin, A. M. M., Chalmers, G., He, L., et al. (2013). Pore structure characterization of North American shale gas reservoirs using USANS/SANS, gas adsorption, and mercury intrusion. *Fuel* 103, 606–616. doi:10.1016/j.fuel.2012.06.119

Curtis, M., Cardott, B., Sondergeld, C., and Rai, C. (2012). Development of organic porosity in the Woodford Shale with increasing thermal maturity. *Int. J. Coal Geol.* 103, 26–31. doi:10.1016/j.coal.2012.08.004

Fu, C. Q., Zhu, Y. M., and Chen, S. (2015). Diagenesis controlling mechanism of pore characteristics in the qiongzhusi Formation shale, east yunnan. *J. China Coal Soc.* 40, 439–448. doi:10.13225/j.cnki.jccs.2014.1588

Fu, J., Guo, S., Liu, X., and Wang, Y. (2013). Shale gas accumulation condition and exploration potential of the upper paleozoic Shanxi Formation in Ordos Basin. *J. Jilin Univ. (Earth Sci. Ed.* 43 (02), 382–389. doi:10.13278/j.cnki.jjuese.2013.02.001

Gai, S., Liu, H., He, S., Mo, S., Chen, S., Liu, R., et al. (2016). Shale reservoir characteristics and exploration potential in the target: A case study in the longmaxi formation from the southern sichuan basin of China. *J. Nat. Gas Sci. Eng.* 31, 86–97. doi:10.1016/j.jngse.2016.02.060

Guo, W., Liu, H., Xue, H., Lan, C., and Tang, X. (2015). Depositional facies of permian Shanxi formation gas shale in the Northern Ordos Basin and its impact on shale reservoir. *Acta Geol. Sin.* 89 (05), 931–941. doi:10.1108/WJE-06-2016-031

He, M., Wang, M., and Qiu, R. (2012). *Multi-stage composite superimposed basins in North South China and oil and gas*. Beijing: Geological Publishing House, 45–47.

He, X., Zhang, P., He, G., Gao, Y., Liu, M., Zhang, Y., et al. (2020). Evaluation of sweet spots and horizontal-well-design technology for shale gas in the basin-margin transition zone of southeastern Chongqing, SW China. *Energy Geosci.* 1 (3–4), 134–146. doi:10.1016/j.engeos.2020.06.004

Jiang, S., Xu, Z., Feng, Y., Zhang, J., Cai, D., Chen, L., et al. (2015). Geologic characteristics of hydrocarbon-bearing marine, transitional and lacustrine shales in China. *J. Asian Earth Sci.* 115, 404–418. doi:10.1016/j.jseaes.2015.10.016

Kong, L., Wan, M., Yan, Y., Zou, C., Liu, W., Tian, C., et al. (2016). Reservoir diagenesis research of silurian longmaxi Formation in sichuan basin, China. *J. Nat. Gas Geoscience* 23, 203–211. doi:10.1016/j.jnggs.2016.08.001

Kruk, M., and Jaroniec, M. (2001). Gas adsorption characterization of ordered Organic–Inorganic nanocomposite materials. *Chem. Mat.* 13, 3169–3183. doi:10.1021/cm0101069

Li, H. (2022). Research progress on evaluation methods and factors influencing shale brittleness: A review. *Energy Rep.* 8, 4344–4358. doi:10.1016/j.egyr.2022.03.120

Li, Y. (2021). Mechanics and fracturing techniques of deep shale from the Sichuan Basin, SW China. *Energy Geosci.* 2 (1), 1–9. doi:10.1016/j.engeos.2020.06.002

Li, Y., Zhou, D. H., Wang, W. H., Jiang, T. X., and Xue, Z. J. (2020). Development of unconventional gas and technologies adopted in China. *Energy Geosci.* 1 (1–2), 55–68. doi:10.1016/j.engeos.2020.04.004

Loucks, R., Reed, R., Ruppel, S., and Jarvie, D. (2009). Morphology, genesis, and distribution of nanometer-scale pores in siliceous mudstones of the mississippian barnett shale. *J. Sediment. Res.* 79, 848–861. doi:10.2110/jsr.2009.092

Lu, J., Ruppel, S. C., and Rowe, H. D. (2015). Organic matter pores and oil generation in the Tuscaloosa marine shale. *Am. Assoc. Pet. Geol. Bull.* 99, 333–357. doi:10.1306/08201414055

Ma, X., Guo, S., Shi, D., Zhou, Z., and Liu, G. (2019). Investigation of pore structure and fractal characteristics of marine-continental transitional shales from Longtan Formation using MICP, gas adsorption, and NMR (Guizhou, China). *Mar. Petroleum Geol.* 107, 555–571. doi:10.1016/j.marpetgeo.2019.05.018

Nie, H., Li, D., Liu, G., Lu, Z., Hu, W., Wang, R., et al. (2020). An overview of the geology and production of the Fuling shale gas field, Sichuan Basin, China. *Energy Geosci.* 1 (3–4), 147–164. doi:10.1016/j.engeos.2020.06.005

Qi, Y., Ju, Y., Huang, C., Zhu, H., Bao, Y., Wu, J., et al. (2019). Influences of organic matter and kaolinite on pore structures of transitional organic-rich mudstone with an emphasis on S2 controlling specific surface area. *Fuel* 237, 860–873. doi:10.1016/j.fuel.2018.10.048

Tissot, B. P. (1978). Petroleum formation and occurrence. *Eos Trans. AGU.* 55, 643–645. doi:10.1029/eo066i037p00643

Wang, F., and Yin, S. (2019). Hydrocarbon generation potential of the C-P continental source rocks in the Qinshui Basin. *Petroleum Sci. Technol.* 37 (2), 208–214. doi:10.1080/10916466.2018.1533865

Wang, G., Ju, Y., Yan, Z., and Li, Q. (2015). Pore structure characteristics of coal–bearing shale using fluid invasion methods: A case study in the huainan–huaibei coalfield in China. *Mar. Petrol. Geol.* 62, 1–13. doi:10.1016/j.marpetgeo.2015.01.001

Wang, P., Chen, Z., Jin, Z., Jiang, C., Jia, Z., Guo, Y., et al. (2018). Shale oil and gas resources in organic pores of the Devonian Duvernay Shale , Western Canada Sedimentary Basin based on petroleum system modeling. *J. Nat. Gas. Sci. Eng.* 50, 33–42. doi:10.1016/j.jngse.2017.10.027

Xi, Z., Tang, S., Zhang, S., and Li, J. (2017). Nano-scale pore structure of marine-continental transitional shale from liulin area, the eastern margin of Ordos Basin, China. *J. Nanosci. Nanotechnol.* 17, 6109–6123. doi:10.1166/jnn.2017.14501

Xiong, F., Jiang, Z., Li, P., Wang, X., Bi, H., Li, Y., et al. (2017). Pore structure of transitional shales in the Ordos Basin, NW China: Effects of composition on gas storage capacity. *Fuel* 206, 504–515. doi:10.1016/j.fuel.2017.05.083

Xu, H., Zhou, W., Zhang, R., Liu, S., and Zhou, Q. (2019). Characterizations of pore, mineral and petrographic properties of marine shale using multiple techniques and their implications on gas storage capability for Sichuan Longmaxi gas shale field in China. *Fuel* 241, 360–371. doi:10.1016/j.fuel.2018.12.035

Yan, D., Huang, W., and Zhang, J. (2015). Characteristics of marine continental transitional organic rich shale in the Ordos Basin and its shale gas significance. *Earth Sci. Froniters* 22 (6), 197–206. doi:10.13745/j.esf.2015.06.015

Yang, C., Zhang, J., Tang, X., Ding, J., Zhao, Q., Dang, W., et al. (2016). Comparative study on micro-pore structure of marine, terrestrial, and transitional shales in key areas, China. *Int. J. Coal Geol.* 171, 76–92. doi:10.1016/j.coal.2016.12.001

Yang, H., Li, S. X., and Liu, X. Y. (2010). Characteristics and resource prospects of tight oil and shale oil in Ordos Basin. *Acta Pet. Sin.* 34 (1), 1–11. doi:10.7623/syxb201301001

Yu, K., Shao, C., Ju, Y., and Qu, Z. (2019). The Genesis and controlling factors of micropore volume in transitional coal-bearing shale reservoirs under different sedimentary environments. *Mar. Petroleum Geol.* 102, 426–438. doi:10.1016/j.marpetgeo.2019.01.003

Zhang, Q., Liu, Z., Liu, C., Zhu, X., Steel, R., Tian, H., et al. (2021). Experimental study on the development characteristics and controlling factors of microscopic organic matter pore and fracture system in shale. *Front. Earth Sci. (Lausanne).* 7, 1–12. doi:10.3389/feart.2021.773960

Zheng, H., Zhang, J., and Qi, Y. (2020). Geology and geomechanics of hydraulic fracturing in the Marcellus shale gas play and their potential applications to the Fuling shale gas development. *Energy Geosci.* 1 (1–2), 36–46. doi:10.1016/j.engeos.2020.05.002

Zou, C. N., Zhu, R. K., Chen, Z. Q., Ogg, J. G., Wu, S. T., Dong, D. Z., et al. (2019). Organic-matter-rich shales of China. *Earth-Science Rev.* 189, 51–78. doi:10.1016/j.earscirev.2018.12.002

frontiers | Frontiers in Earth Science

TYPE Original Research
PUBLISHED 29 August 2022
DOI 10.3389/feart.2022.984463

OPEN ACCESS

EDITED BY
Shuai Yin,
Xi'an Shiyou University, China

REVIEWED BY
Meng Wang,
Chongqing University of Science and Technology, China
Fuhua Shang,
China University of Mining and Technology, China

*CORRESPONDENCE
Guanxiong Ren,
rgxxly1991@163.com

SPECIALTY SECTION
This article was submitted to Structural Geology and Tectonics, a section of the journal Frontiers in Earth Science

RECEIVED 02 July 2022
ACCEPTED 21 July 2022
PUBLISHED 29 August 2022

CITATION
Ren G, Qin Q, Qin Z, Guo Y and Ye Z (2022), Effects of diagenesis on quality of deep dolomite reservoirs: A case study of the Upper Cambrian Xixiangchi Formation in the eastern Sichuan Basin, China.
Front. Earth Sci. 10:984463.
doi: 10.3389/feart.2022.984463

Effects of diagenesis on quality of deep dolomite reservoirs: A case study of the Upper Cambrian Xixiangchi Formation in the eastern Sichuan Basin, China

Guanxiong Ren[1,2]*, Qirong Qin[1,2], Zhangjin Qin[3], Yanbo Guo[4] and Zhaoyang Ye[4]

[1]School of Geosciences and Technology, Southwest Petroleum University, Chengdu, China, [2]State Key Laboratory of Oil and Gas Reservoirs Geology and Development Engineering, Southwest Petroleum University, Chengdu, China, [3]Exploration Division, Southwest Oil and Gas Field Company, Petro China, Chengdu, China, [4]Chongqing Gas Field, Southwest Oil and Gas Field Company, Petro China, Chengdu, China

With the Upper Cambrian Xixiangchi Formation in the eastern Sichuan Basin as the target, this study investigates various diagenetic events during different diagenetic stages in deep dolomite reservoirs, accompanied by evaluations of their effects on the formation and evolution of the reservoir rock. A series of experiments are implemented on core and outcrop samples, including petrologic analysis, fluid inclusion analysis, rare earth and minor element investigation, and carbon and oxygen isotope test. During the syngenetic (syndepositional and penecontemporaneous) diagenesis stage, dolomitization is closely related to evaporation concentration and seepage reflux of high-salinity seawater, which facilitates the reservoir rock development by greatly enhancing the permeability of the reservoir. Meanwhile, a small number of secondary pores are generated in the sediments subjected to episodic atmospheric exposure and thus affected by meteoric water. During the early diagenesis stage, recrystallization transforms part of the granular dolomite into the crystalline dolomite with or without the phantom of the grain texture. It also alters the original rock's pore structure and improves the effective primary porosity. Thus, recrystallization is key in forming the crystalline dolomite reservoir rock. However, compaction, cementation, and filling lead to the loss of massive early-formed primary pores and some secondary pores. During the mesodiagenesis-late diagenesis stage, the burial karstification, related to organic matter maturation, is the most direct control factor of the effective reservoirs space formation, and its alteration effect on the reservoir rock is related to the early process. This research helps to better identify the impact of various diagenetic processes during different diagenetic stages upon the formation and evolution of the deep dolomite reservoir rock, and it also

helps analyze the relationships among these diagenetic processes. The findings of this research provide valuable references for investigating the formation mechanism of the deep dolomite reservoir rock in the Sichuan Basin.

KEYWORDS

Xixiangchi formation, east sichuan basin, deep dolomite reservoir, fluid inclusion, diagenesis 5 processes

1 Introduction

With continuous technological progress and ever-increasing demand for hydrocarbon resources, deep buried carbonate reservoirs have become an important target for hydrocarbon exploration and exploitation. In particular, the deep dolomite reservoirs are an important contributor to new commercial discoveries of oil and gas (Dyman et al., 2002; Zhai et al., 2012; Jiao et al., 2015; Liu et al., 2020; Liu L. H. et al., 2017; Li et al., 2021). At present, the known deepest oil and gas reservoirs in the world are in the Jack and St. Malo field of the Lower Tertiary Trend in the U.S.Gulf of Mexico, which has a burial depth of 8,839 m, a hydrocarbon reserve of $6,821 \times 10^4$ t oil equivalent, and a production rate up to 818 t/d during testing (Pang, 2010; Jiao et al., 2015; He et al., 2016; Li et al., 2021c). The deepest gas reservoir in the world is the Mills Ranch Field in the Anadarko Basin of Western Oklahoma, and its target layer is the Lower Ordovician dolomite at a depth interval of 7663–8103 m, with a maximum single-well gas production rate of 6×10^4 m^3/d and the recoverable gas initially in place of 365×10^8 m^3 (Bai and Cao, 2014; Jiao et al., 2015; Liu et al., 2020; Li et al., 2021). In China, a series of great progress has been made in the exploration of deep dolomite reservoirs, including those in the Ordovician–Cambrian of the Tarim Basin, Ordovician, and Cambrian in the Ordos Basin, as well as Permian, Sinian, and Cambrian in the Sichuan Basin (Qian et al., 2007; Zou et al., 2014; He et al., 2017; Zhang et al., 2017; Fu et al., 2019; Gao 2019). However, the deep dolomite reservoirs in China are formed in a way that is greatly different from that in other countries, as they are typically more ancient, deeper buried, and of longer formation processes (He et al., 2016; Zhang et al., 2017; Ma et al., 2019; Ma X. H. et al., 2019; Li et al., 2021). Correspondingly, the reservoir rock presents extremely complicated characteristics due to the superimposition of multiple diagenetic events during the burial process (Moor and Druckman, 1981; Yang et al., 2008; Shen et al., 2015). Therefore, understanding the relationship among different diagenetic events of different diagenetic stages and the effects of these events on the formation and evolution of the deep dolomite reservoirs is vital to exploring deep dolomite reservoirs.

Multiple wells drilled into the Upper Cambrian Xixiangchi Formation in the eastern Sichuan Basin have produced industrial gas streams, demonstrating high potential for natural gas exploration (Li et al., 2016; Jia et al., 2021). Exploration practice and data show that the reservoir rock in the Upper Cambrian Xixiangchi Formation in the eastern Sichuan Basin has the following features: First, the reservoir rock is highly heterogenous; second, the reservoir rock develops in the layered dolomite; third, the reservoir rock occurs not only in the frequently-seen granular dolomite but also in the crystalline dolomite; fourth, the reservoirs space is mostly attributed to secondary dissolution pores, with seldom primary pores. These features all imply the impacts of diagenesis upon the reservoir rock. Nonetheless, previous studies on diagenesis only focus on dolomitization and karstification, and they generally ignore the influences of other diagenetic processes on the reservoir rock and the relationship among different diagenetic processes. Moreover, it remains controversial when it comes to dolomitization and karstification.

This paper targets the Upper Cambrian Xixiangchi Formation in the eastern Sichuan Basin and performs analyses on drilling core samples and field outcrops, such as fluid inclusion, and geochemical tests.

(1) Reconstruct the diagenetic history of the deep dolomite reservoirs of the Xixiangchi Formation;
(2) Identify the specific diagenetic process and the corresponding diagenetic stage at which it occurs;
(3) Discuss the effects of various diagenetic processes on the formation and evolution of the deep dolomite reservoirs in the Xixiangchi Formation, and explore the relationships among these diagenetic processes.

2 Geological setting

The study area is located in the eastern Sichuan Basin of Southwest China Figure 1A. The Sichuan Basin lies on the relatively northwestern side of the Yangtze platform and is surrounded by the Daba and Micang Mountains in the north, the Longmen Mountain in the west, the Lou and Daliang Mountains in the south, and the Qiyue Mountain in the east (Zou et al., 2014; Wei et al., 2018; Jin et al., 2020). It is a subordinate structural unit of the Yangtze platform. The basin and basement are formed during the Yangtzeian, Caledonian, Hercynian, Indosinian, Yanshanian, and Himalayan (Deng, 1992; He et al., 2011; Li et al., 2011). The early basin is formed during the Indosinian stage, then affected by multi-

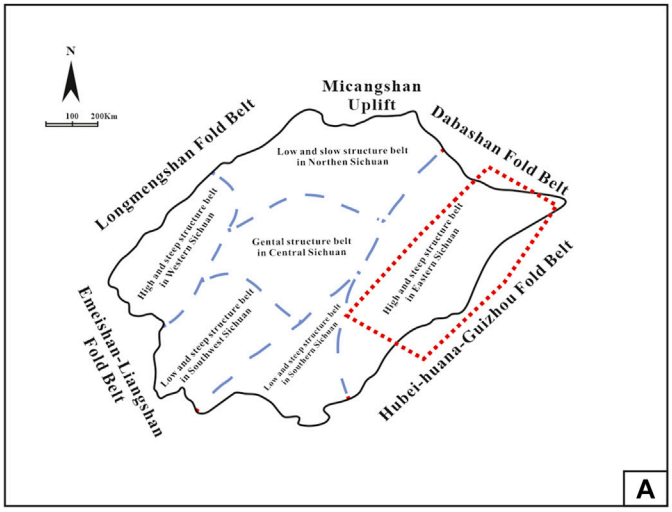

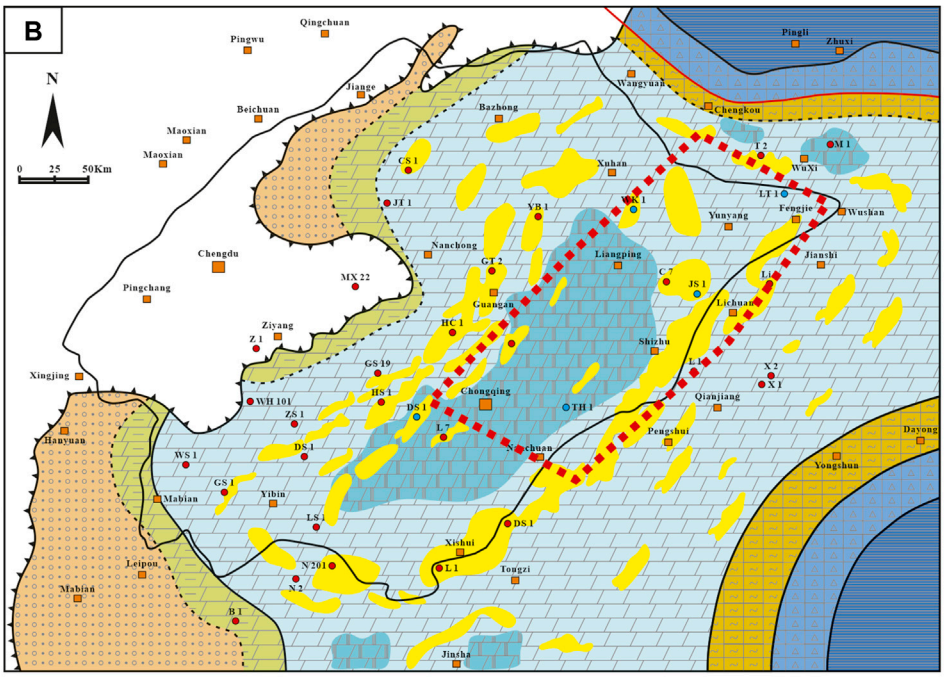

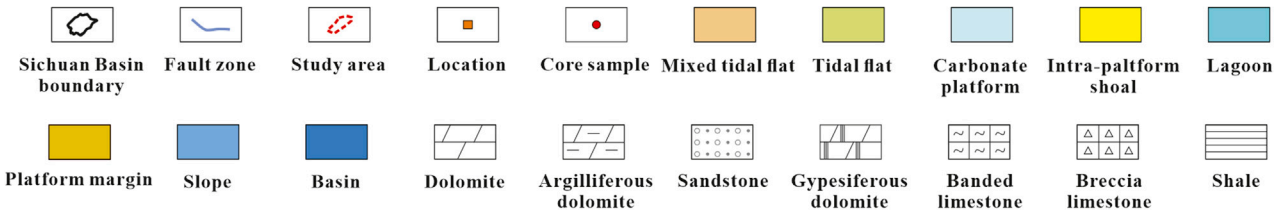

FIGURE 1
Geological survey of the study area. **(A)** Simplified map of the Sichuan Basin showing six subordinate structural belts. **(B)** The paleogeographic map of the Sichuan Basin and its adjacent areas during the Xixiangchi Formation (Modified from Li et al., 2016). The marked blue wells are sampling wells.

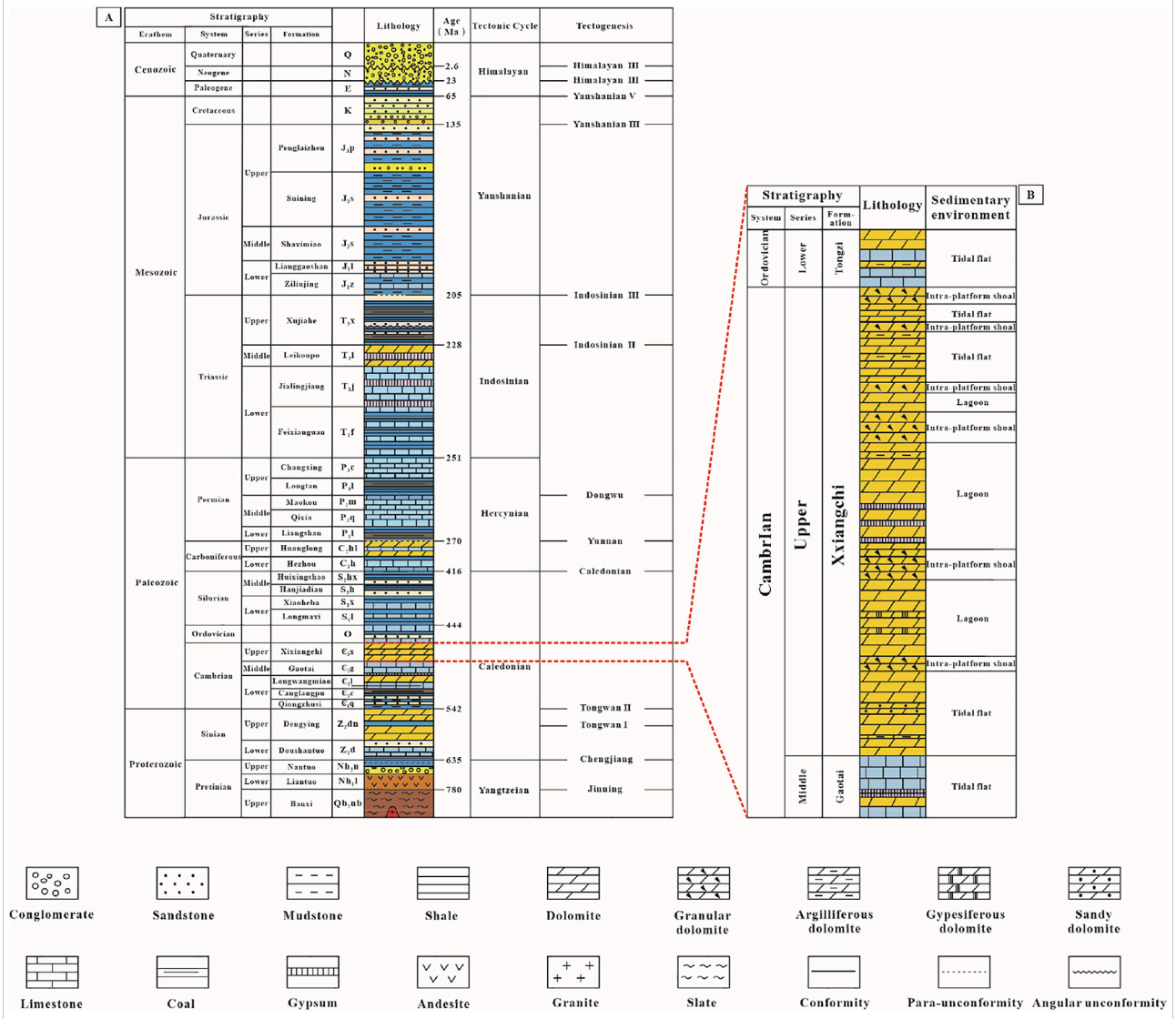

FIGURE 2
Comprehensive histogram of strata in the study area. **(A)**. Composite columnar section of the Presinian-Quaternary system of Sichuan Basin (Modified from Wei et al., 2018). **(B)**. Comprehensive stratigraphy of Xixiangchi Formation.

stage tectonic movement such as the Himalayan folding movement, and finally evolves into the current large multi-cycle-superimposed rhombic structural basin (Wang and Jin, 2002; Liu et al., 2011; Li et al., 2019). According to the regional tectonic characteristics, current tectonic features, and previous studies, the Sichuan basin is divided, by two major fault systems, namely the Huangyingshan and Longquanshan fault systems, into three structural zones, which are composed of six subordinate structural belts, namely high and steep structure belt in the Eastern Sichuan, Low and steep structure in Southern Sichuan, Low and steep structure belt in Southwest Sichuan, High and steep structure belt in Western Sichuan, Low and slow structure belt in Northern Sichuan, and Gental structure belt in Central Sichuan (Zhou et al., 2016; Li et al., 2019; Li H. K. et al., 2019, 2020, Li et al., 2021; Jia et al., 2021) Figure 1A. The study area lies within high and steep structure belt in the Eastern Sichuan.

As the top lithostratigraphic unit of the Cambrian in the Sichuan Basin, the Xixiangchi Formation continuously overlies the Middle Cambrian Gaotai Formation and underlies the Lower Ordovician Tongzi Formation (Figure 2A). During the Xixiangchi Period, the Sichuan Basin presents itself as a relatively stable cratonic deposition area, which almost completely inherits the paleogeographic pattern of the early and middle Cambrian, except for the further expansion of the Kangtien, Motianling, and Hannan ancient lands that are closely

adjacent to the western part of the basin (Feng et al., 2002; Zhang et al., 2010; Jia et al., 2021; Fan et al., 2022; Li et al., 2022).

The ancient land can provide terrigenous clasts, which results in the mixed tidal flat deposition dominated by fine-grained carbonate and clastic rocks. The middle and eastern parts of the basin are far from the ancient lands and thus mainly present the sedimentary formation of the carbonate platform facies. The Central Sichuan area, affected by the Leshan-Longnvsi paleo-uplift, is found with relatively thin deposition and shallow water depth. It mainly develops the tidal flat and intra-platform shoal deposits, mostly consisting of dolarenite, dolomicrite, and silty crystalline dolomite (Liu et al., 2017; Shi et al., 2020; Li et al., 2021c) Figure 1B. The deposition water depth of the study area is deeper than that of the Central Sichuan, and yet they share similar sedimentary environments. However, it should be noted that the restricted lagoon deposition, featuring interbedding of dolomicrite and silty crystalline dolomite, and gypsum-salt rock or gypsum salt-bearing dolomite, occurs around the intra-platform shoal deposition (Li et al., 2016; Shi et al., 2020) (Figure 2B).

3 Materials and methods

A total of 166 samples were obtained from 5 wells and 3 outcrop profiles in the Xixiangchi Formation in this study. To ensure the reliability of this study, samples should be collected and selected in accordance with the following principles:1) samples shall not be collected from the development parts such as structurally crushed and weathered zones; 2) fresh debris samples shall be selected. 3) Samples with obvious terrigenous matters and clay minerals shall be excluded.

210 thin sections were prepared for the study on petromineralogy and diagenesis. And petrologic observation and studied using the DM2500P Leica optical microscope. A thick double-face-polished thin section was prepared with 30 representative samples. On this basis, the homogenization temperatures (Th) of the fluid inclusions were tested using a Leica polarized light microscope carrying a THMSG600 geological cold-hot bench with the temperature measurement ranging from -196 to 600°C with a temperature accuracy of 0.2°C.

Geochemistry was analyzed based on the study of petrology. Besides, calcite veins and sparry calcite cements should be screened after a careful selection was performed on the sample for geochemical analysis to ensure the selected sample's reliability better. The sample was slowly ground to 74 μm in an agate mortar and was quartered. By retaining one for backup, the other three samples were applied for analyzing minor elements, carbon and oxygen isotopes, and rare earth elements. Orthophosphoric acid was adopted in the analytical test of carbon and oxygen isotopes. Specifically, powder samples are dissolved by phosphoric acid at 90°C to release carbon dioxide (CO_2). The generated CO_2 is converted into the MAT252 stable isotope mass spectrometer (Thermo Finnigan) via capillary tubes for analysis. The acquired data are converted to the PDB scale using the reference material NBS 19, and the standard deviations of $\delta^{13}C$ and $\delta^{18}O$ are 0.04 and 0.07%, respectively. The trace and rare earth elements are measured via the *in-situ* LA-ICP-MS analysis using the Agilent 7,700 Series Quadrupole ICP-MS (Agilent Technologies, United States) and the GeoLasPro 193 nm Excimer Laser Ablation System (Coherent, United States). The laser beam diameter is 25 μm, with a frequency of 8 Hz and an energy density of 10.61 J cm^{-2}, and the carrier gas is helium. The synthetic silicate glass of NIST SRM 610 is used as the external reference, while calcium (^{43}Ca) is used as the internal reference. Measurement of trace and rare earth elements is performed at Southwest Petroleum University.

4 Results

4.1 Petromineralogy

According to dolomite morphology, crystal size, and contact relation between minerals, the dolomite in the Xixiangchi Formation of the study area is mainly divided into three types: matrix, cement, and filling dolomite (MD, CD, and FD).

Matrix dolomite (MD) in the study area is divided into two types according to the preservation degree of the original rock texture (Zenger et al., 1980; Fang et al., 2003). One is the dolomite with the original rock texture, mainly including dolomicrite (MD 1) and granular dolomite (MD 2). The other is the crystalline dolomite (MD 3-1, MD 3-2, MD 3-3, and MD 3–4) with unidentifiable original rock texture.

Dolomicrite (MD 1) has extremely tiny crystallines, typically smaller than 0.005 mm, and thus it preserves a more original rock texture. The dolomite of this type is mainly subhedral–anhedral, with mosaic contact among crystallines. This type of dolomite is often seen with interbedding with gypsum-salt rock or an interlayer occurrence with gypsum-salt rock. Under the microscope, microalgae laminated texture and development of moldic pores in gypsum salt minerals are observed (Figure 3A), indicating that such dolomite is the product of early dolomitization under the arid climate.

Granular dolomite (MD 2) is the main reservoir rock type in the study area, with dominant sand-sized grains (Figure 3B), followed by oolith-sized and gravel-sized ones. The algal binding phenomenon is occasionally observed. The grain content reaches 60–80%. The gravel-sized grains typically have 2–15 mm diameters, while the others have diameters of 0.16–0.4 mm. Most grains have relatively regular shapes, typically sub-rounded to rounded, except for the sand-sized algae particles that are irregular in shape. Dolomitic cement is frequently observed among grains.

Crystalline dolomite (MD 3) in the study area can be divided into silty, fine, medium, and hetero-crystal crystalline dolomite

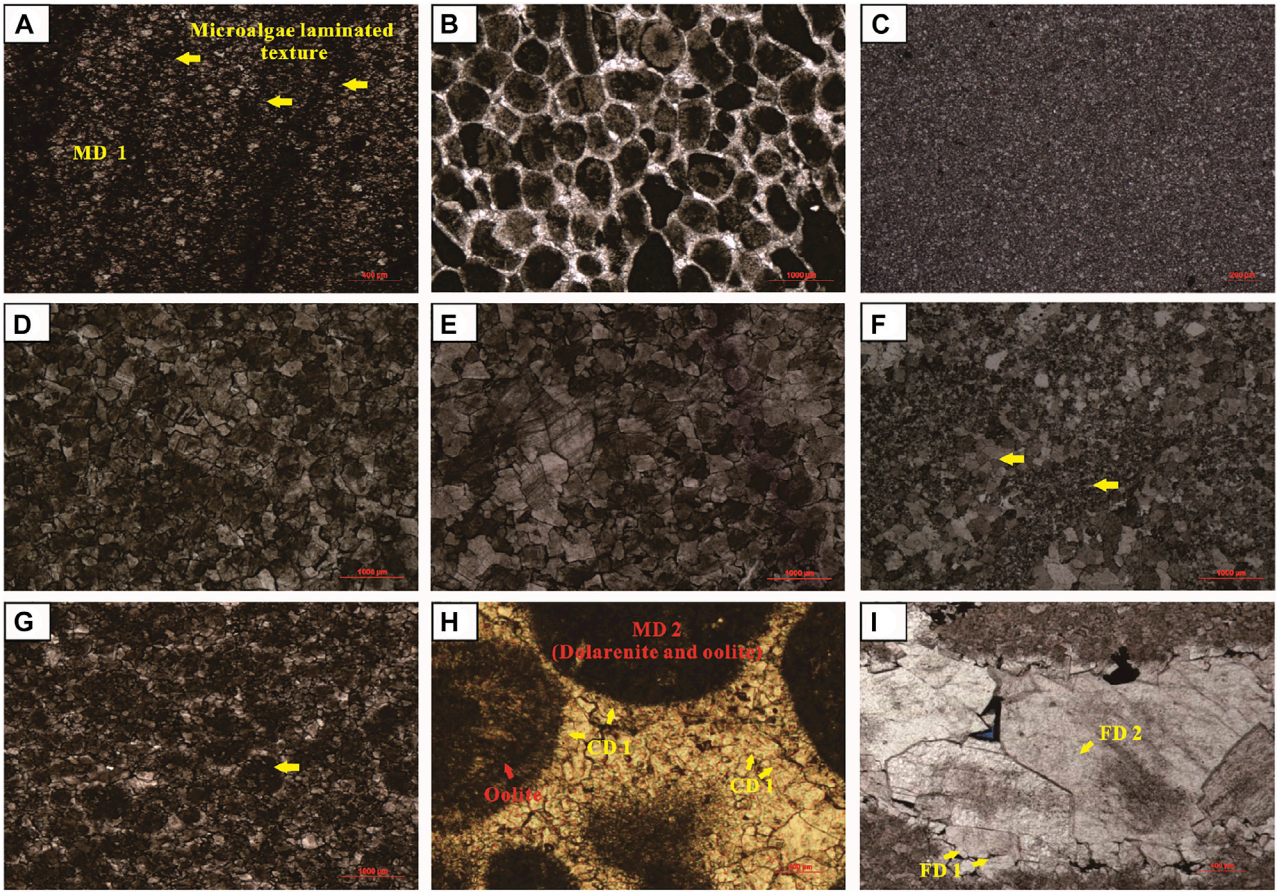

FIGURE 3
Petrographic characteristics of reservoirs. **(A)** A thin section micrograph shows the dolomicrite (MD 1) with microalgae laminated texture. **(B)** Micrograph of the thin section shows the granular (oolite) dolomite (MD 2). **(C)** Micrograph of the thin section shows the silty crystal dolomite (MD 3-1). **(D)** Micrograph of the thin section shows the fine crystal dolomite (MD 3-2) **(E)** Micrograph of the thin section shows the medium crystal dolomite (MD 3-3). **(F)** Micrograph of the thin section shows the hetero-crystal crystalline dolomite (MD 3–4). **(G)** Micrograph of the thin section shows the crystalline dolomite with the phantom of the grain texture. **(H)** The cement dolomite of the first stage (CD 1) and the dolomite cement of the second stage (CD 2). **(I)** The filling dolomite of the first stage (FD 1) and The filling dolomite of the second stage (FD 2).

(MD 3-1, MD 3-2, MD 3-3, and MD 3–4), according to the crystal sizes.

Silty crystalline dolomite (MD 3-1) is composed of tiny (0.03–0.05 mm) subhedral and euhedral crystals, with occasionally seen turbid core and bright rims (Figure 3C). Grains are tightly packed with mosaic contact among each other, and dissolution, and inter crystal pores well develop.

Fine crystalline dolomite (MD 3-2) has crystal diameters typically of 0.05–0.25 mm, with various (i.e., anhedral, subhedral, and euhedral) crystalline forms (Figure 3D). The subhedral–euhedral fine crystalline dolomite is abundant, with occasionally seen turbid core and bright rims accompanied by well-developed pores that are semi-filled to filled by bitumen. The less abundant anhedral–subhedral fine crystalline dolomite is associated with the dirty crystals surface, concave-convex contact among crystals, and limited development of pores.

Medium (MD 3-3) (Figure 3E)and hetero-crystal crystalline dolomite(MD 3-4) (Figure 3F) are mostly composed of anhedral–subhedral dolomite crystals with tight mosaic contact. In such dolomite, pores seldom develop, and thus the reservoir's capacity is low. In addition, the microscopy shows that some crystalline dolomite presents the granular phantom texture (Figure 3G) and is observed with the development of cross-bedding in the field outcrop, which suggests that part of the fine crystalline dolomite is attributed to the high-energy grain shoal deposition, and yet has its texture altered during diagenesis.

Fibrous cement dolomite (CD 1) presents itself as a circular belt with uniform thickness around the intergranular pores or the edge of grains (Figure 3H). The fibrous crystalline form is generally formed in a seawater environment. In most cases, aragonite and high-magnesium calcite are the initial carbonate sediments in seawater. The aragonite is mostly fibrous and

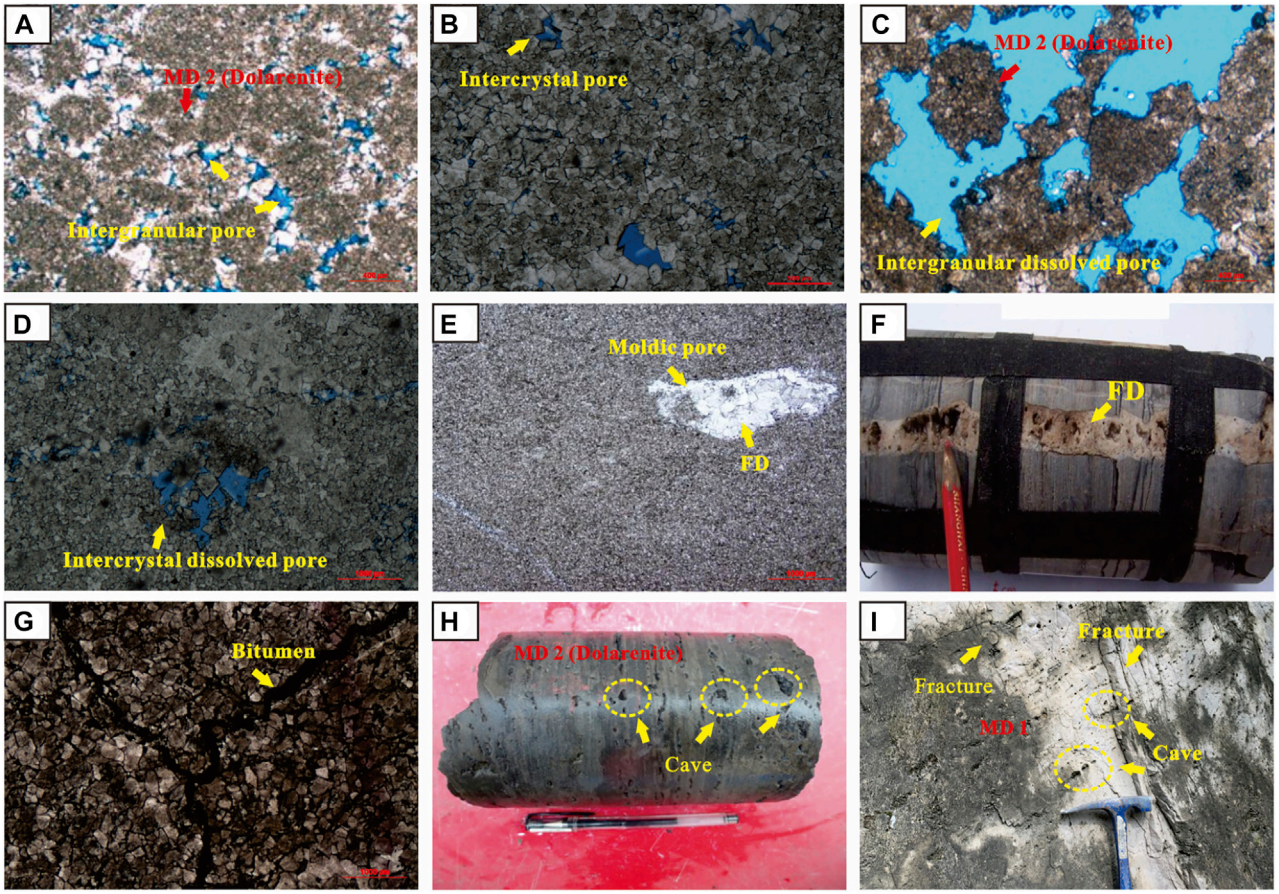

FIGURE 4
The reservoirs space type of Xixiangchi Formation. **(A)** Intergranular pores, granular (dolarenite)dolomite (MD 2).**(B)** Intercrystal pores **(C)** Intergranular dissolved pores. **(D)** Intercrystal dissolved pores, silty dolomite (MD 3-2) with dissolved crystals edge. **(E)** Moldic pores filled by dolomite. **(F)** Fractures are expanded by dissolution. **(G)** Fractures filled by bitumen. **(H)** Caves attributed to dissolution expansion of the residual intergranular pore in the granular dolomite. **(I)** Caves formed during the dissolution and alteration of the gypsum-salt moldic pore of the crystalline dolomite.

needle-like, while the high-magnesium calcite is the fiber with the uniform thickness or leaf-like crystals (Zenger et al., 1980; Fang et al., 2003; Zhang et al., 2014b). Hence, fibrous cement dolomite (CD 1) should be formed in a seabed diagenetic environment.

Granular cement dolomite (CD 2) is mostly anhedral crystals forms and tight mosaic contact among crystals (Figure 3H). Such cement generally occurs along the periphery of fibrous cement dolomite, and some are found with direct contact with grains.

Filling dolomite of the first stage (FD 1) normally occurs close to the secondary pores as well as caves and edges of fractures (Figure 3I). The dolomite crystals are mostly fine and medium-sized, with dominant subhedral and euhedral crystals forms and flat crystals surfaces.

Filling dolomite of the second stage (FD 2) presents crystals larger than those of the first stage-filling dolomite (FD 1), mostly medium and coarse sized, with some macro crystals (Figure 3I). The second stage-filling dolomite (FD 2) often develops above the first stage-filling dolomite (FD 1) and presents conformity or unconformity contact with the first stage-filling dolomite.

4.2 Types of reservoir space

According to its genesis, morphology, dimension, and distribution position, the reservoir space of the Xixiangchi Formation in the study area is divided into three types, namely pores, karst caves, and fractures. The pores include intergranular pores, inter crystal pores, intergranular dissolved pores, inter crystal dissolved pores, and moldic pores.

Intercrystal pores with regular shapes mainly occur in the dolomicrite (MD 1) and crystalline dolomite (MD 3) with relatively high euhedral degrees (Figure 4B). The size of the crystals controls the pore dimension. Intergranular pores primarily develop in the granular dolomite (MD 2), residual intergranular pores after multi-stage cementation and filling

TABLE 1 Na_2O, K_2O,BaO,FeO, MnO and FeO/MnO values of filling dolomite (FD) and cement dolomite (CD) in Xixiangchi Fm.

Sample	Lithology	Na_2O (ppm	K_2O (ppm)	BaO (ppm)	FeO (ppm)	MnO (ppm)	FeO/ MnO	Sample	Lithology	Na_2O (ppm)	K_2O (ppm)	BaO (ppm)	FeO (ppm)	MnO (ppm)	FeO/ MnO
JS-2-1	FD 1	12.82	20.18	333.06	328.69	1000.06	0.33	WK-3-1	CD 1	543.20	333.87	1123.84	798.44	837.79	0.95
JS-2-4	CD 1	512.85	435.28	927.36	445.28	464.08	0.96	WK-4-1	CD 1	555.28	367.82	1282.19	803.33	785.68	1.02
JS-4-1	CD 2	158.23	218.22	815.97	549.61	1125.08	0.49	DS-2-1	CD 2	181.62	141.22	743.65	156.36	572.99	0.27
JS-4-2	CD 2	145.22	194.59	1089.34	92.24	400.39	0.23	DS-2-2	CD 2	245.57	148.57	482.00	911.28	1008.38	0.90
JS-8-1	CD 1	684.72	281.23	3821.55	557.52	513.22	1.09	DS-3-1	CD 1	642.85	301.55	1063.85	925.09	1015.38	0.91
JS-8-2	FD 1	15.10	28.13	223.54	302.27	789.01	0.38	DS-4-4	FD 1	28.56	15.28	416.55	167.34	203.51	0.82
JS-8-3	FD 2	173.22	355.11	1238.38	133.02	1325.80	0.10	JFS-3	FD 2	65.81	128.30	894.33	278.25	1752.38	0.16
TH-1-2	CD 2	91.48	152.32	882.37	647.28	857.83	0.75	JFS-17	CD 1	700.55	318.46	2594.36	332.62	358.74	0.93
TH-1-3	FD 1	54.28	40.74	608.09	286.34	555.00	0.52	JFS-22	CD 2	108.38	200.48	545.81	468.75	763.44	0.61
TH-6-1	FD 1	44.67	37.35	141.23	105.49	294.73	0.36	JFS-27	FD 1	61.23	41.92	987.27	358.41	1334.56	0.27
TH-6-2	FD 2	158.94	380.54	91.28	48.44	854.27	0.06	JFS-28	FD 2	108.46	184.72	809.43	31.46	996.66	0.03
TH-6-5	FD 1	41.28	35.86	535.72	131.51	115.89	1.13	JSP-1	FD 2	25.66	99.17	448.56	202.67	2019.99	0.10
LT-5-1	FD 2	161.57	275.49	1526.73	58.49	154.26	0.38	JSP-8	CD 1	615.80	298.45	1845.88	765.81	801.66	0.96
LT-5-2	CD 2	204.29	172.28	687.51	644.00	825.77	0.78	JSP-9	CD 1	662.74	401.20	872.59	310.06	399.53	0.78
LT-7-6	CD 1	502.23	424.26	3044.18	923.82	1007.12	0.92	JSP-13	CD 2	213.77	163.85	1210.14	666.66	929.18	0.72
LT-10-3	FD 1	37.29	28.37	770.00	412.25	774.87	0.53	NC-1	CD 1	718.22	385.23	825.37	512.26	497.81	1.03
LT-10-4	FD 2	38.29	111.67	112.90	220.59	2282.18	0.10	NC-12	FD 2	188.14	378.24	1111.44	188.37	478.64	0.39
WK-1-1	FD 2	139.22	48.83	610.05	199.57	1932.21	0.10	NC-13	CD 2	151.84	130.71	777.29	428.03	388.59	1.10
WK-2-1	FD 1	48.34	34.19	567.64	88.47	165.26	0.54	NC-27	FD 1	57.89	38.62	1754.01	399.00	518.75	0.77
WK-2-2	CD 2	281.73	238.56	421.11	831.01	1350.24	0.62	NC-28	FD 2	99.38	185.31	708.28	250.04	1777.48	0.14

10.3389/feart.2022.984463

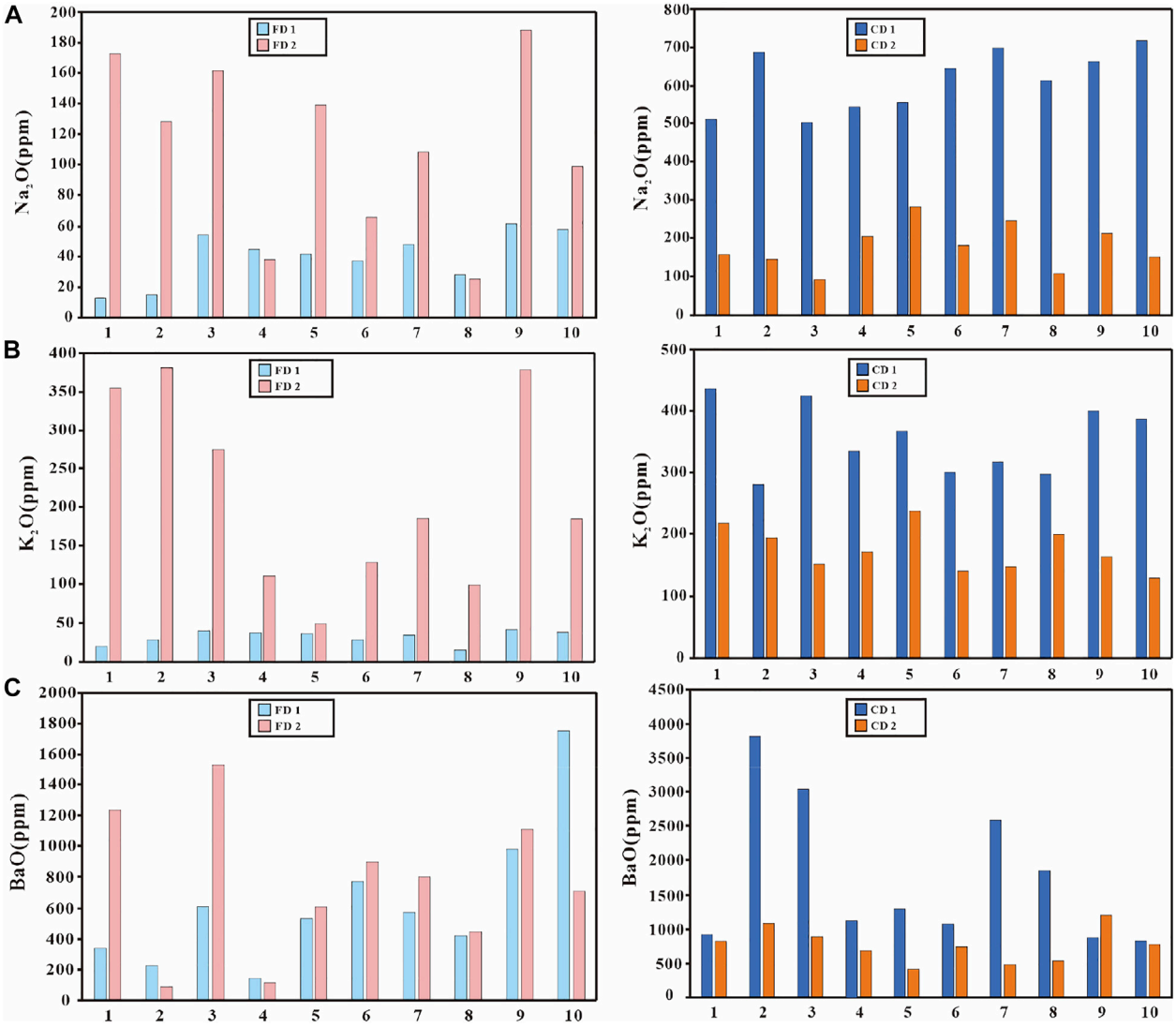

FIGURE 5
Histogram showing the variation of Na_2O, K_2O, and BaO contents of filling dolomite (FD) and cement dolomite (CD). **(A)** Variation in the Na_2O concentrations of the FD and CD. **(B)** Variation in the K_2O concentrations of the FD and CD. **(C)** Take in the BaO concentrations of the FD and CD.

among grains, and some framework pores among alga bindstones (Figure 4A). These pores are mostly oval and irregular. Intercrystal dissolved pores are most developed in the crystalline dolomite (MD 3) of the Xixiangchi Formation in the study area (Figure 4D). They derive from the expansion of inter crystal pores induced by dissolution. Intergranular dissolved pores are the main contributor to the reservoirs space of the granular dolomite in the Xixiangchi Formation of the study area (Figure 4C). The boundaries of the pores are smooth and, in most cases, harbor-like. Some pores are observed with undissolved residual cement. In the case of intensive dissolution, the residual sparry cement is unseen, and relatively large pores are formed. Moldic pores are often observed in the dolomicrit and silty crystalline dolomite that contains anhydrite nodules or rock salts (Figure 4E). The anhydrite nodule and rock salt are dissolved during the meteoric diagenetic environment, and the gypsum and salt moldic pores occur, which are mostly filled later by dolomite and bitumen.

Petrographic observations indicate that there are at least two stages of fractures. These fractures are mostly horizontal and high-angle ones, characterized by short extension, narrow opening, and filling or semi-filling of bitumen (Figure 4G). Nevertheless, some fractures are found with long extension, irregular fracture edges, and extremely coarse fracture surfaces, representing dissolution's effect. The structural suture

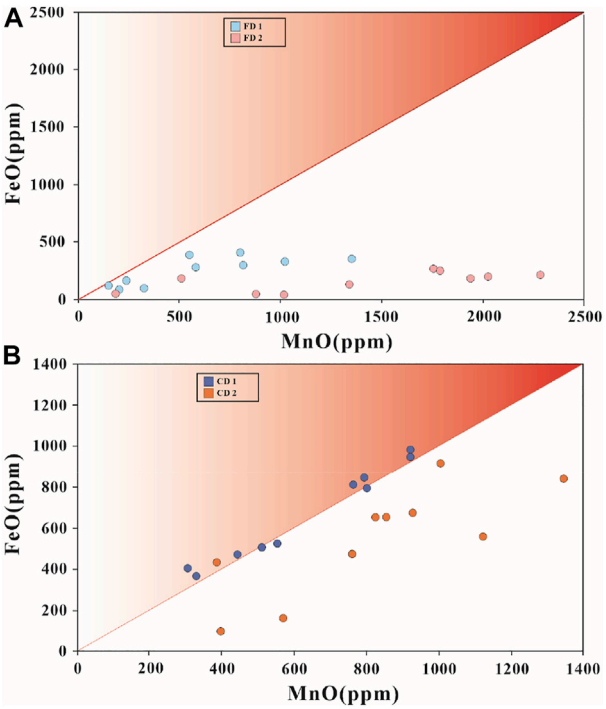

FIGURE 6
Relationship between FeO and MnO values of filling dolomite. **(A)**. FD1, **(B)**. FD2.

line is often high-angle or zigzagged and typically cuts the early structural fracture, which is considered the product of pressure solution along the vertical stress direction (Jiang et al., 2015; Liu et al., 2020).

The cave refers to pores with diameters larger than 2 mm. In other words, karst caves are formed due to the further expansion of various dissolved pores (Zhu et al., 2015; Li, 2002). Two types of karst caves occur in the Xixiangchi Formation of the study area. The first type is attributed to dissolution expansion of the residual intergranular pore in the granular dolomite, which, together with the intergranular pore, constituents good reservoirs space (Figure 4H). The other type is formed during the dissolution and alteration of the gypsum-salt moldic pore of the crystalline dolomite, which is often partially filled by bitumen and dolomite minerals. Such karst caves are found with limited contributions to reservoirs (Figure 4I).

4.3 Geochemistry

4.3.1 Minor elements

The minor element measurements of cement dolomite and filling dolomite (CD and FD) are summarized in Table 1. For the cement dolomite, the Na_2O content is 91.48–718.22 ppm; K_2O, 130.71–435.28 ppm; BaO, 421.11–3,821.55 ppm; FeO, 92.24–925.09 ppm; MnO, 358.74–1,350.24 ppm (Figures 5A–C). What's noteworthy is that the Na_2O, K_2O, and BaO contents of fibrous cement dolomite (CD 1) are higher than those of granular cement dolomite (CD 2). In addition, the FeO/MnO ratio of fibrous cement dolomite (approximately equal to about one) is higher than those of granular cement dolomite (obviously below one) (Figure 6B).

For the filling dolomite, the Na_2O content is 12.82–188.14 ppm; K_2O, 15.23–380.54 ppm; BaO, 91.28–1754.01 ppm; FeO, 31.46–412.25 ppm; MnO, 115.89–2282.18 ppm (Figures 5A–C). The Na_2O, K_2O, and BaO contents of the first stage-filling dolomite (FD 1) are relatively low, and the FeO/MnO ratio is below one. Compared with the first stage-filling dolomite (FD 1), the second stage-filling dolomite (FD 2) presents even lower Na_2O, K_2O, BaO contents, and lower FeO/MnO ratio (Figure 6A).

4.3.2 Rare earth elements

The rare earth element (REE) measurements of the matrix dolomite (MD) are presented in Table 2, which have been normalized against the Post-Archean Australian Shale (PAAS). Moreover, Ce and Eu anomalies are calculated respectively via the following equations: $Eu/Eu^* = Eu_{SN}/(0.67Sm_{SN} + 0.33Tb_{SN})$ and $Ce/Ce^* = Ce_{SN}/(0.5La_{SN} + 0.5Pr_{SN})$ (Hu et al., 2010; Liu et al., 2017; Lei et al., 2016). The total REE content (ΣREE) of the granular dolomite (MD 2) is 7.29–7.78 ppm (average 7.65 ppm); that of the dolomicrite (MD 1),9.78–10.04 ppm (average 9.86 ppm); that of the crystalline dolomite (MD 3-1, MD 3-2, MD3-3 and MD 3–4), 8.02–8.91 ppm (average 8.71 ppm). These three types of matrix dolomite (MD)are all observed with positive Ce anomaly, enrichment of light rare earth elements (LREE, from La to Nd), and loss of heavy rare earth elements (HREE, from Ho to Lu) (Figure 7).

4.3.3 Stable isotope

The carbon and oxygen isotope ratios of the matrix and filling dolomite (MD and FD) are included in Table 3. The distribution of matrix dolomite $\delta^{13}C$ is ranged from −1.46 to 0.40‰, with the $\delta^{18}O$ ranging from −11.33 % to −6.31%. The $\delta^{13}C$ values of hetero-crystal crystalline dolomite (MD 3-4) and dolomicrite (MD 1) are more negative than that of other matrix dolomites and other matrix dolomites share similar $\delta^{13}C$ values. $\delta^{18}O$ values of various matrix dolomite gradually become negative with the increase of crystal size. Besides, compared with the $\delta^{18}O$ of the seawater of the same period (during the Late Cambrian, the seawater presents $\delta^{18}O$ from -10‰ to -7%) (Veizer et al., 1999; Prokoph et al., 2008), most filling dolomite as well as fine, medium, and hetero-crystal crystalline dolomite (MD 3-2, MD3-3 and MD 3-4) have lower $\delta^{18}O$ values (Figure 8B).

$\delta^{13}C$ and $\delta^{18}O$ values of filling dolomite (FD) are ranged from −1.35% to −0.64% and from −10.98% to −8.77%, respectively. The $\delta^{13}C$ of the filling dolomite is more negative than that of the matrix dolomite. Also, the $\delta^{13}C$ and $\delta^{18}O$ values of varying filling dolomite are varied. The $\delta^{13}C$ and $\delta^{18}O$ values of filling dolomite of the second stage (FD 2) are more negative in

TABLE 2 Rare element data of the matrix dolomite (MD).

Sample	Lithology	La	Ce	Pr	Nd	Sm	Eu	Gd	Tb	Dy	Ho	Er	Tm	Yb	Lu	∑Ree	δCe	δEu	L/H
JS-2-1	MD 1	0.48	3.87	0.82	0.68	0.71	0.56	0.50	0.41	0.36	0.31	0.28	0.28	0.26	0.28	9.80	5.95	0.93	2.66
JS-4-2	MD 2	0.31	3.52	0.61	0.52	0.50	0.37	0.35	0.28	0.23	0.15	0.09	0.12	0.11	0.13	7.29	7.65	0.87	3.99
JS-7-3	MD 3-1	0.38	3.75	0.66	0.56	0.59	0.48	0.43	0.40	0.35	0.31	0.27	0.26	0.23	0.20	8.87	7.21	0.94	2.62
JS-7-4	MD 3-3	0.42	3.58	0.62	0.52	0.49	0.40	0.37	0.33	0.29	0.26	0.22	0.18	0.19	0.15	8.02	6.88	0.93	3.03
TH-1-4	MD 3-3	0.33	3.64	0.56	0.54	0.58	0.52	0.48	0.42	0.38	0.36	0.28	0.25	0.21	0.17	8.72	8.18	0.98	2.42
TH-1-5	MD 3-4	0.39	3.49	0.62	0.62	0.60	0.54	0.56	0.46	0.40	0.35	0.30	0.23	0.20	0.15	8.91	6.91	0.93	2.36
TH-6-5	MD 2	0.34	3.69	0.58	0.50	0.54	0.40	0.43	0.33	0.29	0.20	0.08	0.10	0.10	0.15	7.73	8.02	0.82	3.60
LT-5-1	MD 1	0.42	4.22	0.71	0.72	0.64	0.62	0.43	0.46	0.37	0.32	0.31	0.25	0.28	0.29	10.04	7.47	1.16	2.70
LT-5-2	MD 1	0.43	3.99	0.70	0.67	0.68	0.54	0.50	0.48	0.44	0.37	0.31	0.28	0.24	0.20	9.83	7.06	0.92	2.49
LT-7-6	MD 3-1	0.30	3.35	0.68	0.64	0.66	0.57	0.51	0.48	0.42	0.35	0.29	0.21	0.16	0.18	8.80	6.84	0.97	2.38
LT-10-1	MD 3-4	0.35	3.99	0.58	0.61	0.53	0.44	0.41	0.34	0.34	0.30	0.25	0.19	0.17	0.13	8.63	8.58	0.94	3.05
LT-11-5	MD 2	0.37	3.58	0.60	0.51	0.59	0.44	0.40	0.35	0.26	0.18	0.14	0.10	0.14	0.11	7.77	7.38	0.89	3.63
LT-11-6	MD 2	0.22	3.01	0.55	0.58	0.69	0.64	0.63	0.47	0.27	0.15	0.10	0.13	0.10	0.08	7.62	7.82	0.97	2.95
WK-1-1	MD 1	0.45	4.11	0.73	0.68	0.60	0.51	0.48	0.44	0.38	0.33	0.29	0.27	0.27	0.24	9.78	6.97	0.94	2.62
WK-4-2	MD 3-2	0.40	3.57	0.66	0.68	0.62	0.56	0.57	0.50	0.43	0.37	0.30	0.22	0.19	0.14	9.21	6.74	0.94	2.39
JSP-1	MD 2	0.33	3.37	0.56	0.50	0.72	0.52	0.44	0.38	0.25	0.18	0.15	0.09	0.13	0.10	7.72	7.57	0.90	3.49
JSP-8	MD 2	0.17	2.96	0.60	0.63	0.74	0.65	0.59	0.39	0.27	0.20	0.20	0.18	0.14	0.06	7.78	7.69	0.98	2.83
JSP-9	MD 3-2	0.37	4.01	0.61	0.58	0.55	0.42	0.35	0.31	0.31	0.29	0.24	0.18	0.15	0.11	8.48	8.18	0.93	3.37

[a]The data of Post-Archean Average Shale (PAAS) in normalized calculation were from Mclennan (1989). Eu and Ce, anomaly values were calculated by $Eu/Eu^* = Eu_{SN}/(0.67Sm_{SN} + 0.33Tb_{SN})$,$Ce/Ce^* = Ce_{SN}/(0.5La_{SN} + 0.5Pr_{SN})$ (Liu et al., 2017; Lei et al., 2016).

comparison to the filling dolomite of the first stage (FD 1) (Figure 8).

4.3.4 Fluid inclusions

This research finds gas-liquid two-phase fluid inclusions only in the filling dolomite (FD). The determined homogenization temperature of the fluid inclusion in the filling dolomite (FD) ranges from 70.8 to 178.6°C (Table 4). Specifically, the homogenization temperature of the fluid inclusion of filling dolomite of the first stage (FD 1) is 70.8–129.7°C, while that of the fluid inclusion of filling dolomite of the second stage (FD 2) is within 132.2–178.6°C (Figure 9).

5 Discussion

5.1 Destructive diagenesis and its impact on reservoir formation

The destructive diagenesis, unfavorable to reservoir rock development, is the main reason for the massive loss of primary pores and reduction of secondary pores. It includes compaction, pressure solution, cementation, and filling.

The Xixiangchi Formation in the study area is deeply buried and thus subjected to intensive compaction and pressure solution during its burial process (Zhao et al., 2012; Jiao et al., 2015; Li et al., 2022). However, due to the early formation of dolomite and cement in the study area, the corresponding detailed statement is presented below), these early-formed cement and grain textures of dolomite, to some extent, resist compaction. Therefore, the Xixiangchi Formation in the study area has relatively low degrees of compaction, mainly manifested as the dominance of floating contact among grains and rarely-observed grain crushing and deformation. Although the early-formed cement and dolomite, to some extent, support the framework and resist compaction, the primary porosity still declines by 20–30%.

The cement dolomite in the Xixiangchi Formation of the study area can be attributed to two stages. Fibrous cement dolomite (CD 1) was formed in a seabed diagenetic environment (Zenger et al., 1980; Fang et al., 2003). Compared with the cement of fibrous cement dolomite (CD 1), the Na_2O, K_2O, and BaO contents of the dolomite of granular cement dolomite (CD 2) are much lower, suggesting lower water salinity during this stage, possibly due to meteoric water invasion (Figures 5A–C) (Park and Schot, 1968; Lei et al., 2015; Lin et al., 2017). The FeO/MnO ratio of granular cement dolomite (CD 2) is obviously below one (Figure 6B), indicating a relatively closed diagenetic environment during the formation of such cement (Park and Schot, 1968; Lin et al., 2017). If such cement was formed in a deep burial environment, it would hardly be affected by meteoric water. Hence, it is speculated that the cement dolomite of granular cement dolomite (CD 2) should be formed in a shallow burial environment invaded by meteoric water. The cement of two-stage cementation occupies a large volume of space in the primary pores. The early-formed fibrous cement dolomite (CD 1) reduces the primary intergranular

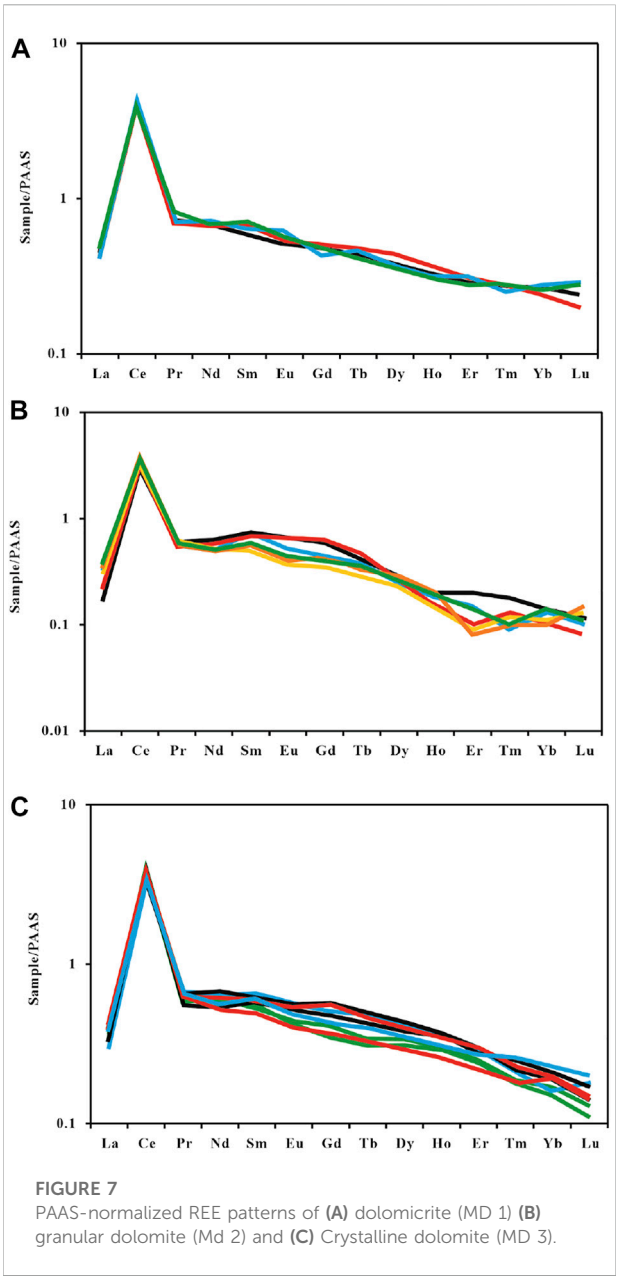

FIGURE 7
PAAS-normalized REE patterns of **(A)** dolomicrite (MD 1) **(B)** granular dolomite (Md 2) and **(C)** Crystalline dolomite (MD 3).

porosity by 5–10%, while granular cement dolomite (CD 2) with larger crystals, filling the remaining intergranular pores. Thus, the primary pores virtually completely vanish.

Dolomite also occurs in the study area's secondary pores and fractures of the Xixiangchi Formation. However, it is difficult to determine the genesis of such dolomite, and many claims that it should enter and fill the early pores and fractures in the later stage (Lin et al., 2015; Zhang et al., 2014b). Therefore, it is defined as the filling material instead of cement. There were two stages of filling in the Xixiangchi Formation. The first stage occurred in the middle-deep burial environment. The Na_2O, K_2O, and BaO contents of the first stage-filling dolomite (FD 1) are relatively low (Figures 5A–C), accompanied by the low negative $\delta^{13}C$ and the moderately negative $\delta^{18}O$ value. The FeO/MnO ratio of such filling dolomite is below one. According to the Th measurement of fluid inclusions, the burial depth should be 2000–3,500 m (Figure 9 and Figure 10). Compared with the first stage-filling dolomite (FD 1), the second stage-filling dolomite (FD 2) presents even lower $\delta^{13}C$ and $\delta^{18}O$ values (Table 3), lower Na_2O, K_2O, BaO contents (Figures 5A–C) and lower FeO/MnO ratio (Figure 6A), and considerably higher Th values of the fluid inclusions (Figure 9 and Figure 10), which suggest deeper burial depth during the formation of such filling dolomite. The second stage-filling dolomite (FD 2), should be formed in the deep burial. Besides dolomite, a small quantity of bitumen is also observed as the filling material in the Xixiangchi Formation of the study area. Filling dolomite and bitumen narrow the secondary pore and throat and reduce the reservoir rock's porosity and permeability.

5.2 Recrystallization and its impact on reservoir formation

The intensity of carbonate rock recrystallization grows with the increasing burial depth and elevated temperature (Mitchell et al., 1996; Zhao and Zheng, 2011). However, for the Xixiangchi Formation in the study area that features the same burial depth and diagenetic temperature, the difference in recrystallization intensity is mainly dependent on the composition characteristics during the deposition of the original rock. Recrystallization is suppressed in the dark dolomicrite (MD 1), dark granular dolomite (MD 2), and argilliferous dolomite that is enriched with insoluble residues such as organic and argillaceous matter because insoluble residues can effectively hinder the alteration of carbonate rock by diagenetic fluids (Veizer et al., 1999; Dyman et al., 2002; Ma et al., 2011; Qie et al., 2021). The pre- and post-crystalline structures are seen with slight differences. The dolomite crystals are still dominated by micritic crystals and are mostly anhedral–subhedral. The dolomite with uneven distribution of insoluble residues often evolves into hetero-crystal crystalline dolomite (MD 3–4) via recrystallization. The light-colored dolomicrite with only a few or no insoluble residues and other granular dolomite is found with high recrystallization intensity, which is manifested as the gradual expansion of the tiny crystal of the dolomicrite (MD 1) and destruction of the original granular texture of the granular dolomite that results in the silty and fine crystalline dolomite (MD 3-1 and MD 3-2) with or without granular phantom (Figure 11).

Recrystallization intensity can be directly revealed by the crystal size and structure of the rock, and the δ18O value can well indicate it (Li and He, 2014; Jiang et al., 2015; Li et al., 2021). With the increasing recrystallization intensity, the degree of order of crystals gradually increases, and meanwhile, the $\delta^{18}O$ value declines (Mitchell et al., 1996; Murray, 1960; Zhou et al.,

TABLE 3 δ13 C and δ18 O values of various types of dolomites in Xixiangchi Fm.

Sample	Lithology	$^{18}O_{PDB}$, ‰	$^{13}C_{PDB}$, ‰	Sample	Lithology	$\delta^{18}O_{PDB}$, ‰	$^{13}C_{PDB}$, ‰
JS-2-1	MD 1	−9.30	−0.78	WK-3-1	MD 3-1	−9.12	−0.41
JS-2-4	MD 2	−6.58	−0.40	WK-4-1	MD 3-2	−9.46	−1.28
JS-4-1	MD 1	−7.70	−0.31	WK-4-2	MD 3-2	−9.12	−0.70
JS-4-2	MD 2	−7.00	−0.62	DS-2-1	MD 3-2	−10.09	−0.42
JS-7-3	MD 3-1	−8.51	−1.21	DS-2-2	MD 3-3	−8.56	−0.90
JS-7-4	MD 3-3	−10.34	−0.89	DS-3-1	MD 3-3	−9.71	0.40
JS-8-1	MD 3-2	−10.03	−0.78	DS-4-4	FD 1	−9.43	−0.69
JS-8-2	FD 1	−9.56	−0.64	JFS-3	MD 1	−7.15	−0.72
JS-8-3	FD 2	−10.11	−0.83	JFS-14	MD 3-1	−8.61	−0.58
TH-1-2	MD 3-1	−8.31	−0.98	JFS-17	MD 3-3	−10.52	−1.13
TH-1-3	MD 3-2	−9.12	−1.46	JFS-22	MD 3-4	−10.76	−0.97
TH-1-4	MD 3-3	−10.28	−0.47	JFS-27	FD 1	−9.01	−1.33
TH-1-5	MD 3-4	−10.58	−0.61	JFS-28	FD 2	−9.67	−0.94
TH-6-1	MD 3-4	−10.23	−0.67	JSP-1	MD 2	−9.78	−1.00
TH-6-2	FD 2	−9.79	−0.92	JSP-8	MD 2	−7.22	−0.39
TH-6-5	MD 2	−9.12	−1.07	JSP-9	MD 3-2	−9.84	0.30
LT-5-1	MD 1	−8.12	−1.11	JSP-13	MD 3-3	−11.33	−0.81
LT-5-2	MD 1	−8.88	−0.74	JSP-15	MD 3-4	−11.25	−1.08
LT-7-5	MD 1	−9.64	−0.53	JSP-19	MD 3-2	−8.00	−0.70
LT-7-6	MD 3-1	−7.54	−0.53	JSP-25	MD 3-3	−9.99	−0.88
LT-7-7	MD 3-1	−9.24	−0.58	NC-1	MD 1	−6.31	−1.22
LT-10-1	MD 3-4	−10.98	−0.82	NC-12	MD 2	−7.33	−0.50
LT-10-3	FD 1	−8.77	−0.83	NC-13	MD 2	−8.01	−0.81
LT-10-4	FD 2	−10.98	−1.35	NC-18	MD 3-1	−8.37	−0.52
LT-11-3	MD 2	−6.92	−0.82	NC-19	MD 3-1	−9.92	−0.52
LT-11-4	MD 2	−8.22	−0.73	NC-20	MD 3-1	−9.03	−0.77
LT-11-5	MD 2	−8.73	−0.47	NC-23	MD 3-2	−11.02	−0.40
LT-11-6	MD 2	−7.62	−0.04	NC-24	MD 3-2	−10.87	−0.67
WK-1-1	MD 1	−8.89	−0.94	NC-27	FD 1	−9.60	−1.17
WK-2-2	MD 3-3	−10.12	−0.96	NC-28	FD 2	−9.54	−0.96

2014; Liu et al., 2018; Wang et al., 2022). This is attributed to the enhanced fractionation effect due to the improved recrystallization, which results in the loss of $\delta^{18}O$ of dolomite (Mitchell et al., 1996; Veizer et al., 1999).

During the gradual expansion of dolomite crystals, recrystallization also alters the reservoir pore, yet manifested as changes in the original pore structure instead of growth or reduction of total porosity. The inter crystal pore and crystal dissolved pore is the most developed pore types in the crystalline dolomite reservoir rock. The early-formed inter crystal pore mainly occurs in the dolomicrite (MD 1), which typically presents tiny pores and poor pore connectivity, although the pore is well developed. After recrystallization, dolomicrite (MD 1) gradually transforms into fine or silty crystalline dolomite (MD 3-1 and MD 3-2) with larger crystals, during which the early tiny intergranular pore is re-arranged and optimized. Consequently, the pore structure is altered, and the inner crystal pore with a larger storage space is formed. In addition, the euhedral degree of dolomite grows with the expansion of dolomite crystals, which tends to flatten the throats connecting pores. This, to some extent, improves the effective porosity and permeability of the reservoirs (Mitchell et al., 1996; Zhao et al., 2012) (Figure 11). To sum up, the formation of the crystalline dolomite reservoir rock is mainly attributed to recrystallization.

5.3 Dolomitization and its impact on reservoir formation

The dolomite in the Xixiangchi Formation of the study area mainly develops three types of dolo: matrixtrix, cement, and filling dolomite (MD, CD, and FD). The cement and filling dolomite (CD and FD)only occurs in the storage space, such as

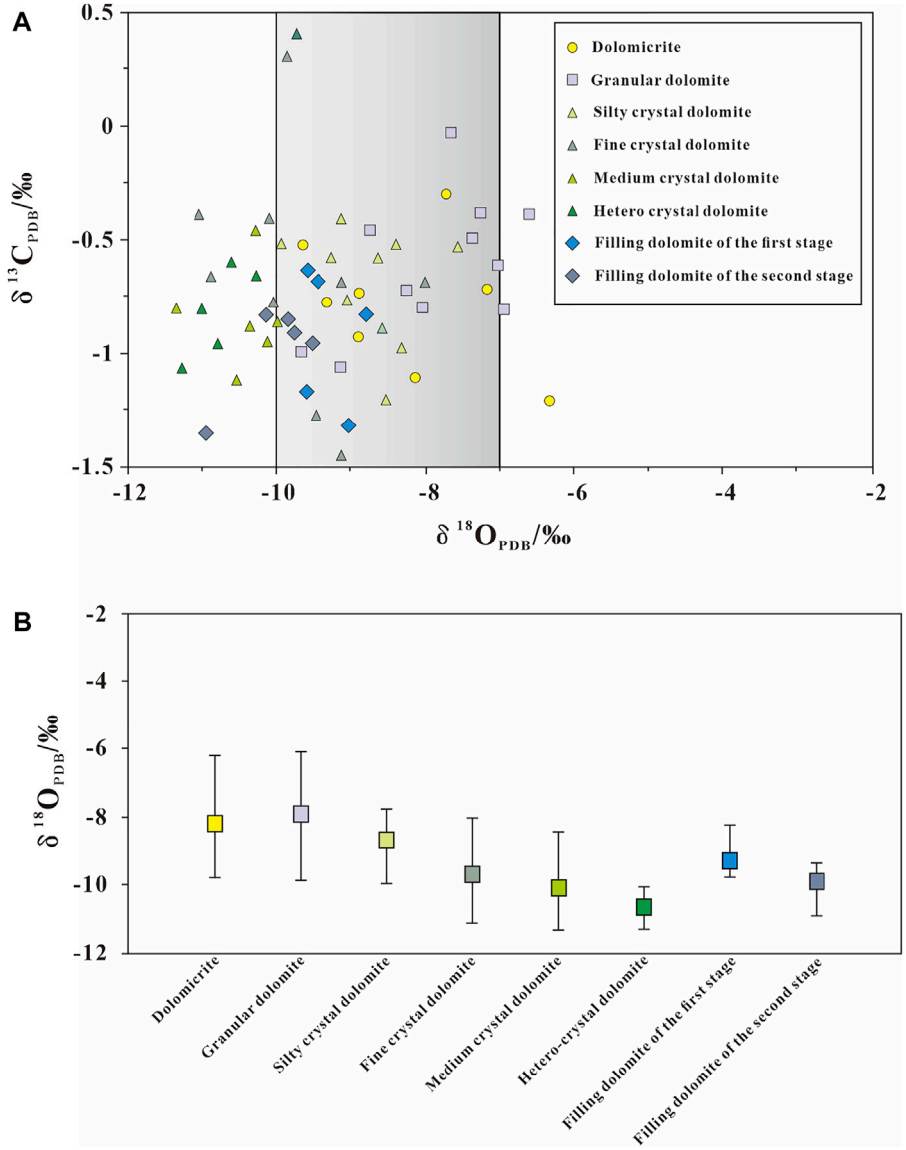

FIGURE 8
Characteristics of stable isotopes in deep dolomite reservoirs of Xixiangchi Formation in the eastern Sichuan Basin. **(A)** Cross-plot of $\delta^{13}C$ versus $\delta^{18}O$ values of various dolomite fabrics. **(B)** Variation of $\delta^{18}O$ contents of various type dolomites with the average values marked as square.

pores, karst caves, and fractures, and thus has no stratigraphic implications. Given this, the investigation of dolomitization in the study area focuses on the matrix dolomite (MD) that is stratigraphically meaningful.

The matrix dolomite (MD) in the study area has three characteristics. First, it is found with the common stratified occurrence and associated tiny crystals (dominant micritic–silty ones). Second, the vertical occurrence of dolomicrite (MD 1) is often observed as interbedding with evaporite or interlayers in evaporate. Third, the granular dolomite (MD 2), of which grains are mostly composed of dolomicrite (MD 1) and silty crystalline dolomite (MD 3-1), develops the fibrous or horse-tooth-like cement dolomite. These characteristics of the matrix dolomite (MD) eliminate the possibility of mixed-water dolomitization and highlight the possible early dolomitization closely related to evaporation concentration and seepage reflux of high-salinity seawater (Badiozamani, 1973; Li and He, 2014; Jia et al., 2021; Jia and Pang, 2015; Fan et al., 2020).

TABLE 4 Fluid inclusion data.

Sample	Lithology	TH (°C)	Sample	Lithology	TH (°C)
JS-2-1	FD 1	112.5	WK-1-1	FD 2	155.5
JS-2-1	FD 1	124.8	WK-1-1	FD 2	136.3
JS-2-1	FD 1	73.5	WK-1-1	FD 2	166.6
JS-8-2	FD 1	119.3	WK-2-1	FD 1	103.8
JS-8-2	FD 1	98.8	WK-2-1	FD 1	79.7
JS-8-2	FD 1	111.1	DS-4-4	FD 1	113.5
JS-8-2	FD 1	108.3	DS-4-4	FD 1	120.2
JS-8-3	FD 2	143.2	DS-4-4	FD 1	129.1
JS-8-3	FD 2	156.9	JFS-3	FD 2	147.3
JS-8-3	FD 2	178.6	JFS-3	FD 2	168.0
JS-8-3	FD 2	171.9	JFS-3	FD 2	173.4
TH-1-3	FD 1	77.7	JFS-3	FD 2	174.0
TH-1-3	FD 1	89.4	JFS-27	FD 1	76.1
TH-1-3	FD 1	124.6	JFS-27	FD 1	109.6
TH-1-3	FD 1	128.3	JFS-27	FD 1	122.9
TH-6-1	FD 1	82.8	JFS-28	FD 2	144.8
TH-6-1	FD 1	91.1	JFS-28	FD 2	148.0
TH-6-1	FD 1	129.7	JFS-28	FD 2	160.7
TH-6-2	FD 2	132.9	JFS-28	FD 2	175.2
TH-6-2	FD 2	136.8	JFS-27	FD 1	95.2
TH-6-2	FD 2	160.1	JFS-27	FD 1	118.7
TH-6-2	FD 2	158.6	JFS-27	FD 1	74.3
TH-6-5	FD 1	103.6	NC-27	FD 1	86.9
TH-6-5	FD 1	106.7	NC-27	FD 1	70.8
TH-6-5	FD 1	114.2	NC-27	FD 1	95.5
TH-6-5	FD 1	79.6	NC-27	FD 1	122.2
TH-6-5	FD 1	88.8	NC-27	FD 1	127.9
LT-5-1	FD 2	143.8	JS-1	FD 2	141.8
LT-5-1	FD 2	162.1	JS-1	FD 2	144.5
LT-5-1	FD 2	140.8	JS-1	FD 2	152.8
LT-5-1	FD 2	139.6	JS-1	FD 2	170.6
LT-10-3	FD 1	75.1	JS-1	FD 2	178.4
LT-10-3	FD 1	80.4	NC-12	FD 2	132.7
LT-10-3	FD 1	100.9	NC-12	FD 2	173.6
LT-10-3	FD 1	129.3	NC-12	FD 2	174.5
LT-10-4	FD 2	171.2	NC-12	FD 2	137.0
LT-10-4	FD 2	172.4	NC-28	FD 2	177.3
LT-10-4	FD 2	170.3	NC-28	FD 2	150.4
LT-10-4	FD 2	132.2	NC-28	FD 2	148.4

Besides, the geochemical evidence also proves that the matrix dolomite (MD) is not of mixed-water dolomitization. In most cases, the dolomite originating from mixed-water dolomitization presents extremely and yet greatly varied $\delta^{13}C$ values (from −10 to 20% PDB) and a narrow value range of $\delta^{18}O$(Badiozamani, 1973; Mckenzie, 1981). Clearly, the matrix dolomite (MD) in the Xixiangchi Formation of the study area shows no such characteristics concerning the $\delta^{13}C$ and $\delta^{18}O$ values. The $\delta^{18}O$ values of the fine, medium, and hetero-crystal crystalline dolomite (MD 3-2, MD 3-3, and MD 3–4) are lower than that of the contemporary seawater (during the Late Cambrian the seawater $\delta^{18}O$ ranges from -10‰ to -7%) (Veizer et al., 1999; Prokoph et al., 2008). This characteristic seems to indicate that the fine, medium and hetero-crystal

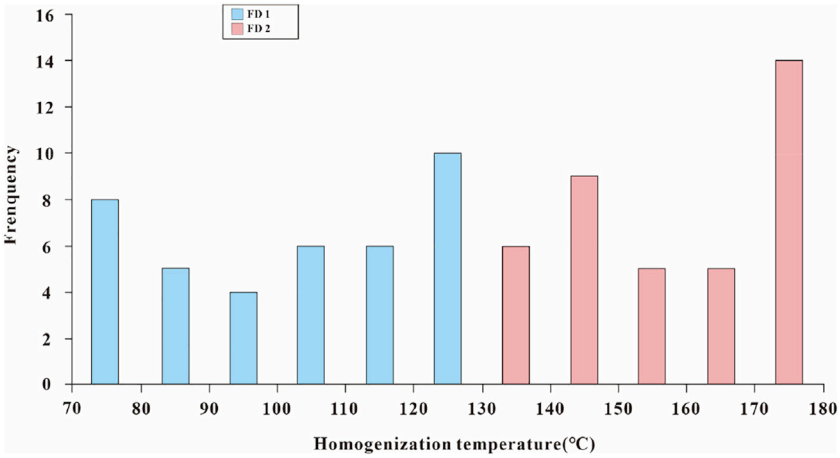

FIGURE 9
Histogram showing the ranges of homogenization temperatures of the fluid inclusions from filling dolomite (FD1 and FD2). Th=homogenization temperature.

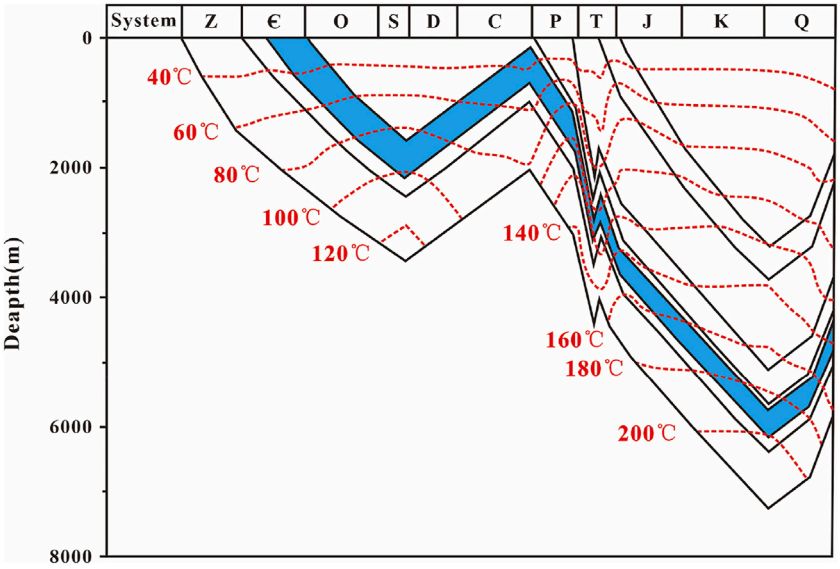

FIGURE 10
Typical burial and paleo-temperature history constructed from TH1 well from the eastern Sichuan Basin.

crystalline dolomite (MD 3-2, MD 3-3, MD 3–4) is later affected by hydrothermal fluids and thus should be attributed to burial dolomitization.

According to the above discussion, the genesis of the matrix dolomite in the Xixiangchi Formation of the study area seems to be the joint product of the early seepage reflux dolomitization and late burial dolomitization. Nonetheless, this research believes that the genesis of the matrix dolomite in the study area should be independent of burial dolomitization. Besides the evidence presented above, our opinion is also based on the following considerations:

To begin with, for almost all carbonate sediments, the burial process is associated with continuous diagenesis, which affects the carbon and oxygen isotopes of the matrix rock (Anderson and Arthur, 1983; Romanek et al., 1992; Prokoph et al., 2008). Determining the genesis of the ancient dolomite should not be completely based on the geochemical characteristics and instead should take other factors such as the geological setting and

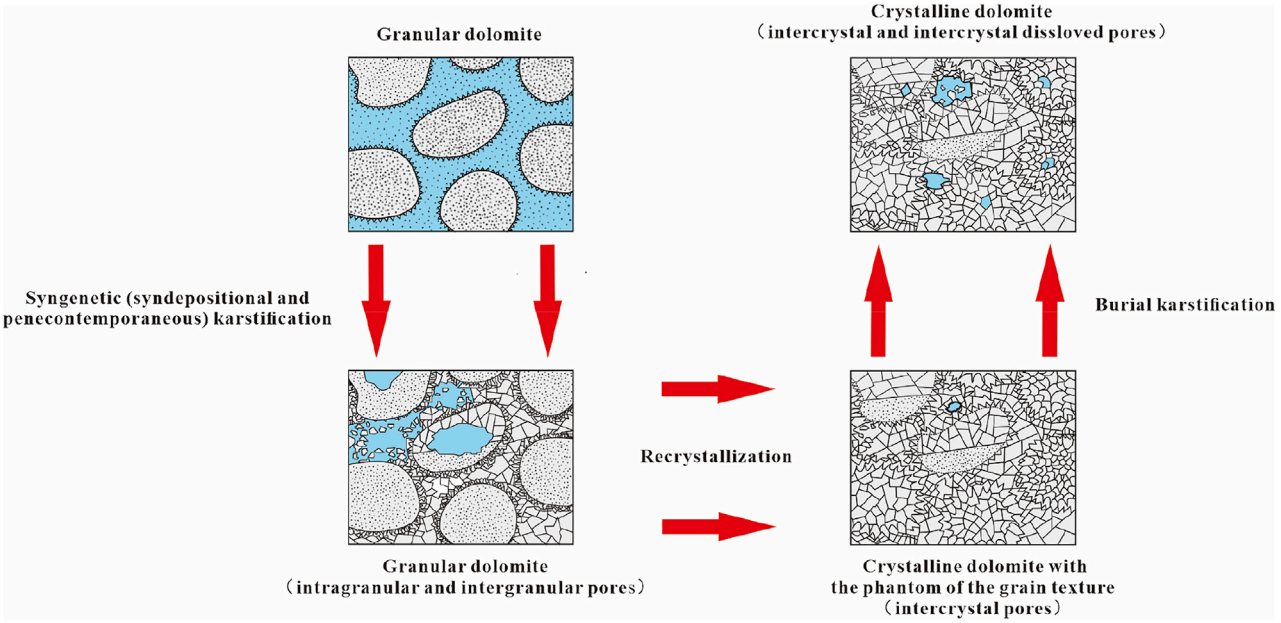

FIGURE 11
Formation and evolution model of the crystalline dolomite reservoirs in the Upper Cambrian Xixiangchi Formation in eastern Sichuan Basin (Modified from Yang et al., 2019).

principles of genesis into full consideration. Furthermore, the main mechanism behind burial dolomitization is that the mudstone in the basin produces Mg^{2+}-abundant fluids due to compaction, which flow into carbonate rock via the conduit such as faults and trigger dolomitization (Land, 1980; Kaufman and Knoll, 1995; Tang et al., 2006; Xu and Du, 2005). Assuming that the dolomite in the Xixiangchi Formation of the study area is affected by burial dolomitization, the key question lies in the source of the Mg^{2+} substance input that is sufficient to enable burial dolomitization. There is no development of extensive mudstone in the Xixiangchi Formation itself and the overlying Ordovician Tongzi Formation. The underlying Gaotai Formation, to some extent, develops mudstone, which, however, cannot facilitate the massive amount of Mg^{2+} required by the large-scale stratified dolomite occurring in the Xixiangchi Formation (Zhang X. F. et al., 2010; Jiang et al., 2015; Lei et al., 2015). Also, the gypsum-salt rock extensively develops in the Gaotai Formation (Jiang et al., 2015; Lei et al., 2015; Li et al., 2016). Consequently, it is safe to say that the source of Mg^{2+}-rich fluids in the Xixiangchi Formation in the study area is not the same as that of the Mg^{2+}-rich fluids required by burial dolomitization. At last, the REE evidence (∑REE) shows that in various matrix dolomite (MD) of the study area, the ∑REE values are below 100×10^{-6} and yet above 1×10^{-6}, with no positive anomaly of ∑REE. Previous studies conclude that the total REE content (∑REE) of the marine carbonate rock should be $(1–100) \times 10^{-6}$, and the carbonate rock affected by hydrothermal fluids should present a positive anomaly of the ∑REE value (Mclennan, 1989; Derry et al., 1994; Lei et al., 2016). Thus, the fluid source for dolomitization of the Xixiangchi Formation in the study area should be seawater (Hu et al., 2010; Lei et al., 2016; Liu et al., 2017). In addition, the various matrix dolomite (MD) in the Xixiangchi Formation of the study area is generally characterized by concentration of LREE and loss of HREE, associated with positive Ce anomaly (Figure 7). These also demonstrate that the diagenetic fluid for the matrix dolomite (MD) in the study water is seawater (Hu et al., 2010; Lei et al., 2016; Liu et al., 2017).

Based on the above discussion, this research believes that the mechanism behind dolomitization in the Xixiangchi Formation of the study area should be early evaporation concentration and seepage reflux, and the characteristics of burial dolomitization, presented by some matrix dolomite (MD), should be phantom induced by diagenesis (Figure 12).

For the dolomite reservoirs in the Xixiangchi Formation of the study area, dolomitization not only leads to the wide distribution of dolomite but also provides the bottommost basis for the formation and evolution of reservoir rock. It also significantly enhances the permeability of reservoir rock (Jardine and Wilshart, 1987; Ehrenberg, 2004; Ehrenberg et al., 2006). Dolomite is more brittle than limestone and thus more prone to cracking when externally loaded (Halley and Schmoker, 1983; Saller et al., 2004). In particular, with relatively deep burial depth, effective fractures in dolomite development are superior to that

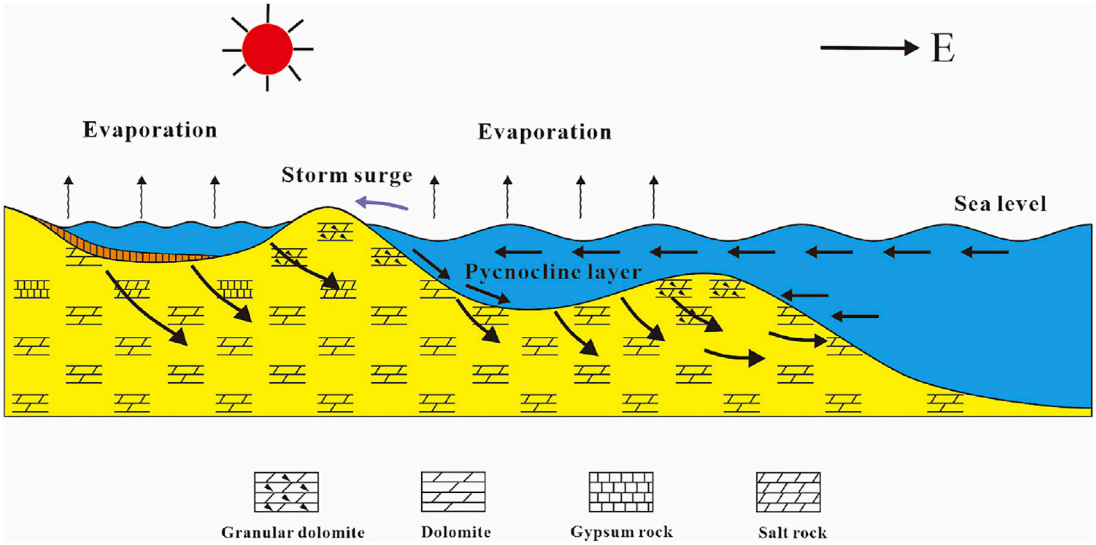

FIGURE 12
Dolomization model of Xixiangchi Formation (Modified from Yang et al., 2019). The mechanism behind dolomitization in the Xixiangchi Formation of the study area should be early evaporation concentration and seepage reflux, and the characteristics of burial dolomitization, presented by some matrix dolomite, should be phantom induced by diagenesis.

in limestone (Morrow, 1982; Murray, 1960; Warren, 2000; Ehrenberg et al., 2006). These fractures can serve as good flow channels and greatly enhance permeability (Jardine and Wilshart, 1987; Amthor et al., 1994; Sun, 1995; Li et al., 2019). Also, buried strata are all subjected to compaction, reducing porosity. Yet, dolomite presents relatively good compaction-resistant performance, which to some degrees offsets pore shrinkage and helps to maintain porosity and permeability. Therefore, it is considered that dolomitization is the essential diagenetic process for reservoir rock formation and evolution in the study area.

5.4 Karstificaiton and its impact on reservoir formation

During its deposition, the Xixiangchi Formation was subjected to multiple stages of karstification under paleogeomorphology, sedimentary environment, and tectonic movement. The karstification process in the Xixiangchi Formation of the study area is divided into the syngenetic (syndepositional and penecontemporaneous) and burial karstification stage based on the timing, product, and characteristics of karstification (Figure 13).

The fibrous cement in the granular dolomite is observed with partial dissolution and unconformity with the cement of the other stages. The fibrous cement is the product of early seabed cementation, and thus the dissolution of the fibrous cement and dissolution unconformity with the cement of other stages indicate that karstification occurs relatively early, supposedly between the first stage of seabed cementation and the second cementation stage (Hu et al., 2020; Shan et al., 2021; Fan et al., 2020; Li 2022). In other words, soon after deposition and short-term seabed cementation, the sediments experienced dissolution. The corresponding karstification is the syngenetic (syndepositional and penecontemporaneous) karstification.

Besides cement, pores and fractures are also affected by dissolution, which is mainly manifested in the following observations. First, some pores have harbor-like edges. Second, some pores are filled by bitumen, and they mostly present themselves as lining or streamer-like occurrence; the phenomenon of late granular cement dolomite (CD 2) dyed by bitumen is observed; some pores are seen with no filling of bitumen and thus clean pore space, and yet intensively dissolved dolomite crystals in the surrounding. Third, the structurally-induced fractures are expanded by dissolution (Figure 4F), and some fractures are bead-like. The above characteristics suggest that the study area is subjected to another karstification process, which should be later than the syngenetic one. We tend to interpret this later karstification as the burial karstification. Suppose the formation was subjected to supergene karstification. In that case, the study area should develop large-scale dissolution unconformity and the typical products of supergene karstification such as weathering crust, karst breccia, and grape-laced dolomite (Xu and Du, 2005; Yang et al., 2008; Hao et al., 2017; Yang et al., 2019; Yang X. F.

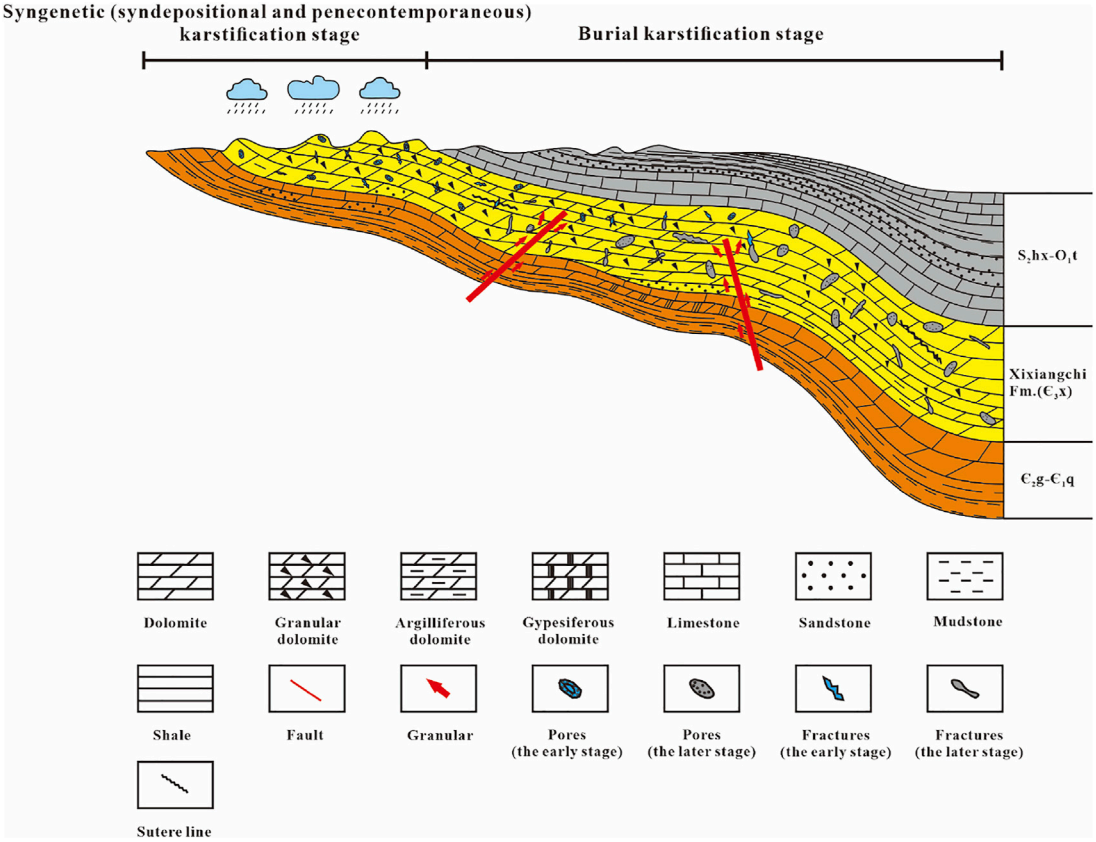

FIGURE 13
Karstification model of Xixiangchi Formation. Karstification results in new reservoirs space and re-adjustment of the early-formed reservoirs space and its position. Modified according to Li et al. (Li et al., 2020).

et al., 2019). However, such direct evidence is not found in the study area. Furthermore, the occurrence of bitumen demonstrates that the corresponding karstification is associated with the burial environment instead of the meteoric water environment.

The varied karstification stages are mainly dominated and differentiated by the different acid fluids (Sassen and Moore, 1988; Worden and Smalley, 1996; Xu and Du, 2005; Hao et al., 2017). On the one hand, the acid fluid of the syngenetic karstification originates from CO_2-rich meteoric water. On the other hand, the sources of the acid fluid for burial karstification are complicated—organic matter maturation, thermal sulfate reduction (TSR), and deep hydrothermal fluids can all generate acid fluids (Krouse et al., 1988; Sassen and Moore, 1988; Worden and Smalley, 1996; Davies and Smith, 2006; Zhu et al., 2006; Hu et al., 2009). We believe that the acid fluid for the burial karstification in the study area is derived from organic matter maturation, as directly implied by bitumen occurring in the dissolved pore. The organic matter at the maturation stage releases a large number of acid fluids containing corrosive components such as organic acid and CO_2, which enter and dissolve the reservoir rock before hydrocarbon charging (Krouse et al., 1988; Zhu et al., 2006; Hu et al., 2009) As the liquid hydrocarbon later flows into the pore and degrades, the resultant residual bitumen is preserved in the pore. With the increasing burial depth, crude oil cracking again generates acid fluids containing corrosive components, further dissolving the reservoir rock (Davies and Smith, 2006; Hu et al., 2009; Li et al., 2016; Li et al., 2019; He et al., 2021). The main product of crude oil cracking is natural gas; thus, no bitumen filling occurs in the dissolved pore. Nonetheless, in the case of deep burial, TSR, referring to the conversion of the sulfate into the acid fluids such as H_2S and CO_2 by hydrocarbons at high temperatures, can also generate acid fluids containing corrosive components. The onset of TSR requires three essential conditions, namely sufficient hydrocarbons, elevated temperatures (>120°C) and the development of thin gypsum rock (Worden and Smalley, 1996; Zhu et al., 2006). Although these three essential conditions are met in the study area, no direct evidence is found to support the onset of TSR, such as the development of secondary calcite in the gypsum moldic pore, pyrite crystals occurring at the interface between the gypsum, and secondary calcite, and presence of

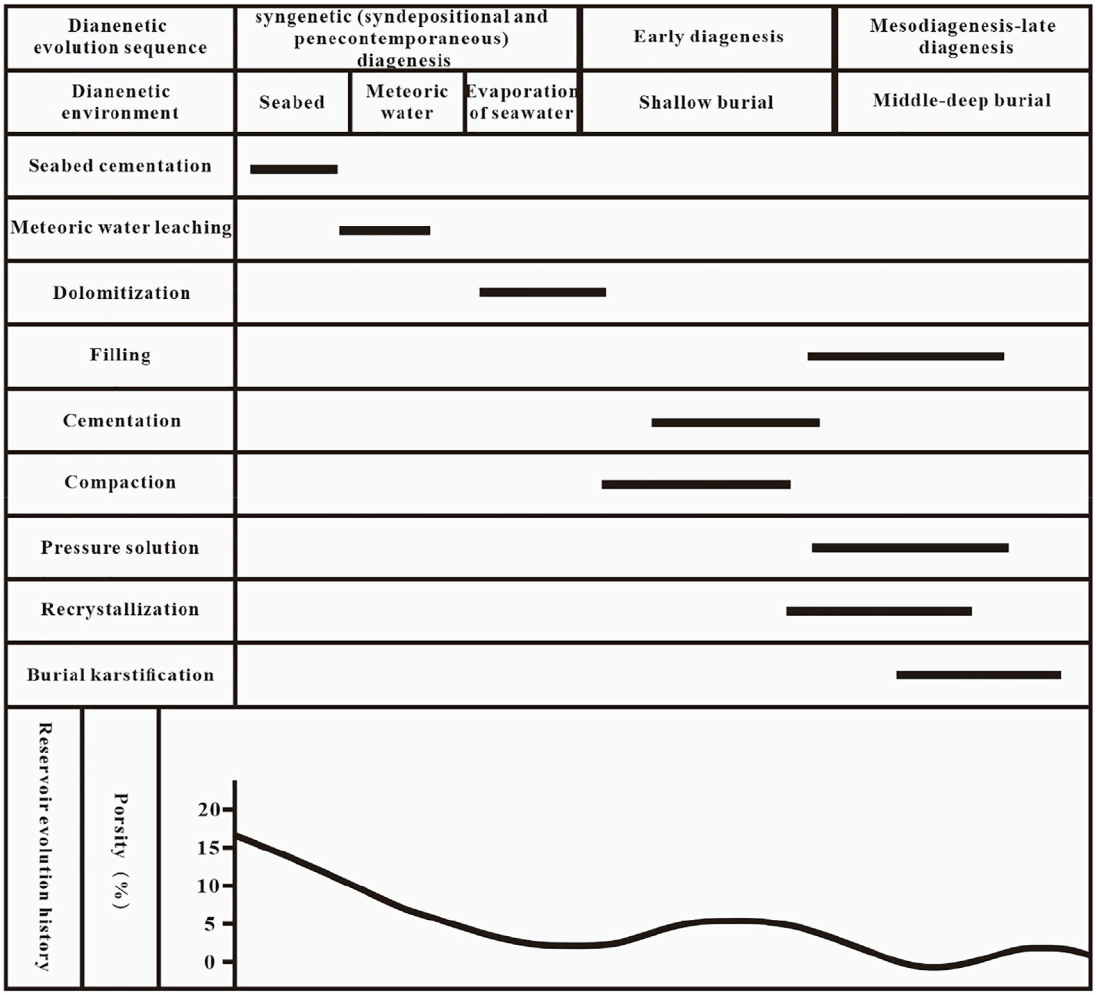

FIGURE 14
Evolution of diagenetic system in deep dolomite reservoirs of Xixiangchi Formation in the eastern Sichuan Basin.

high-H_2S natural gas (Krouse et al., 1988; Zhu et al., 2008). Dissolution by deep hydrothermal fluids typically occurs in fractures and dissolved pores and caves; thus, it is difficult to identify hydrothermal fluid dissolution traces from the resultant dissolution characteristic. Nonetheless, deep hydrothermal fluids may precipitate as they flow or due to variation in the formation temperatures, which produces typical hydrothermal minerals such as dolomite, quartz, fluorite, sphalerite, barite, and anhydrite (Davies and Smith, 2006; Zhu et al., 2008). The study area is seen with no development of such typical hydrothermal minerals, and thus the dissolution and alteration of the dolomite by hydrothermal fluids in the study area cannot be proved.

During the syngenetic (syndepositional and penecontemporaneous) stage, the sediments in the study area are subjected to cyclic exposure to the atmosphere due to sea level eustacy and also short-term leaching by meteoric water (Lin et al., 2017; Shi et al., 2020; Jia et al., 2021). During this stage, the sediments are in a semi-consolidated state (ductile–semi-ductile), and meteoric water leaching leads to selective dissolution, generating moldic pores, intragranular pores, and small dissolution fractures (Liu et al., 2017). However, meteoric water dissolution of this stage mainly occurs in the flat tidal deposition of relatively shallow water and intra-platform shoal deposition at the higher sedimentary terrain. Thus, the dissolution scale is small, and only a small quantity of dissolved pores are formed, mostly filled or damaged, due to later compaction, cementation, and filling. As the sediments reach a certain depth, burial dissolution leads to not only re-adjustment of the position of the reservoirs storage space but also occurrences of many new storage space types. As discussed above, burial karstification mainly occurs in the pore space of the early pores, caves, and fractures. In the granular and crystalline

dolomite, it primarily modifies the inner crystal and granular pores. The acid fluid migrates via fault and the early-formed pores, during which a large quantity of these pores are dissolved and re-adjusted to generate inter crystal dissolved pores, intergranular dissolved pores, and karst caves. Furthermore, such acid fluids may also flow through fractures or suture lines, dissolving the surrounding of the fracture wall and resulting in the bead-shaped dissolution-expanded fracture. Due to dissolution during the burial process, some isolated dissolved pores, karst caves, and dissolved fractures can also be effectively connected, which greatly enhances reservoir permeability.

In general, karstification results in new reservoirs space and re-adjustment of the early-formed reservoirs space and its position. It improves the porosity and permeability of the reservoir rock and thus enhances the reservoir's capacity. Therefore, karstification is considered a major factor affecting the reservoir's capacity.

5.5 Diagenetic evolution and its impact on reservoir formation

Based on the above analysis and the impact of diagenesis on the reservoirs, the diagenetic stages of the Xixiangchi Formation in the Sichuan Basin can be divided into the following stages (Figure 14).

During the syngenetic (syndepositional and penecontemporaneous) diagenesis stage, thick granular rocks featuring the highest deposit of water body energy and many developed intergranular pores normally accumulate in highland. A small number of secondary pores were formed easily under the syngenetic (syndepositional and penecontemporaneous) karstification. Also, the original intergranular porosity is low, with fine sediments on bottom lands between beaches. The primary porosity is reduced by 10–20% due to the deposited granular rock cemented by the early-formed fibrous cement under the sea. Meanwhile, micrite dolomite forms from the micrite calcite under the effect of dolomitization related to evaporation concentration and seepage reflux, of which the intercrystalline pores are highly developed, roughly above 50% (Figure 14).

During the early diagenesis stage, the sediments formed in the previous stage enter the shallow burial environment along with the deposition of the overlying formation. And porosities of intergranular and intercrystalline pores are reduced by 35–40% under the influence of compaction. Further, the cementation in the shallow burial stage promotes the disappearance of the storage space. Granular dolomite cement caused porosity loss of 20–25% and left some isolated intergranular pores and intercrystalline pores. In the meantime, dolomite crystals become thicker and form into powder-fine crystalline dolomite under the effect of recrystallization related to the buried depth. Also, the retained intercrystalline pores are readjusted and optimized. In effect, the recrystallization outcome increases the rock's effective porosity and permeability to a certain extent.

In the mesodiagenesis-late diagenesis stage, the recrystallization intensity grows with the rising burial depth, and the intercrystalline pores are constantly adjusted and optimized. Besides, pressure solution starts to occur and results in the suture line structure. When the burial depth reaches a certain value, the organic matter in the underlying Qiongzhusi Formation mudstone gradually transforms into liquid and gaseous hydrocarbons. And the occurrence of burial karstification is triggered by the large number of organic acids produced during the maturation of hydrocarbons. Buried karst can also form certain amounts of new pores to increase the porosity apart from modifying and adjusting the remaining intercrystalline and intergranular pores (Wang and Wang, 2021). What's more, some isolated dissolution pores, caves, and dissolution fractures can be effectively connected, greatly enhancing the permeability of the reservoir. The effective porosity can still reach 2–5%, although the porosity has decreased with the emergence of bitumen and dolomite fillings.

6 Conclusion

According to the petrographic characteristics, crystalline dolomite reservoirs dominated by crystalline dolomite and granular dolomite reservoirs dominated by granular dolomite are mainly developed in the Xixiangchi Formation. The formation was extremely vulnerable to various diagenesis during the geological history of deposition and burial for the long history of sedimentary time, and the dolomite was strongly sensitive to the diagenetic environment. The syngenetic (syndepositional and penecontemporaneous) diagenesis, the early diagenesis, and the mesodiagenesis-late diagenesis are three stages in the diagenetic process of deep dolomite reservoirs in the study area based on petrographic characteristics, geochemical characteristics, and burial history.

During the syngenetic (syndepositional and penecontemporaneous) diagenesis stage, dolomitization is closely related to evaporation concentration, and seepage reflux of high-salinity seawater facilitates the reservoir rock development by greatly enhancing the reservoir rock permeability. At the same time, Syngenetic karstification generates a small number of secondary pores in the sediments of the grain shoal facies via selective dissolution, and yet such primary pores are destructed by the cement early formed in the seabed diagenetic environment. In the early diagenesis stage, compaction and second-stage cementation further led to the disappearance of primary pores. Yet the dolomite and cement, to some extent, support the rock framework and thus resist compaction, which somewhat helps to preserve the primary

pores. The formation of the crystalline dolomite reservoir rock is mainly attributed to recrystallization, which to some degree alters the pore structure of the original rock and increases the effective porosity. In this regard, recrystallization facilitates the later modification of reservoir rock by karstification. A decrease in porosity is increased with the appearance of dolomite filling and bitumen in the mesodiagenesis-late diagenesis stage. Filling, cementation, and compaction are the main reasons for the decline of reservoir pores. The diagenetic system is in an enclosed environment with increasing burial depth. The burial karstification related to acidic fluids starts to appear. Then, the previously formed reservoir space and the reservoir position were re-adjusted, increasing the reservoir's porosity and permeability. It is a major contributor to enhancing reservoir capability and forming effective reservoir space.

According to the study of the Xixiangchi Formation of the study area, the influence of diagenesis on deep dolomite reservoirs is not caused by one or several types of diageneses. Instead, different diageneses in various diagenetic periods affect the reservoir. What's more, the strength of diagenesis also influences various reservoirs differently.

Data availability statement

The original contributions presented in the study are included in the article/supplementary material, further inquiries can be directed to the corresponding author.

Author contributions

GR, QQ, and ZQ contributed in writing, reviewing, and editing, datacuration, writing original draft preparation; YG and CY contributed in formal analysis, validation, and reviewing.

Funding

This study was financially supported by Comprehensive exploration research project of PetroChina Southwest Oil; Gas Field Company in 2020 (Grant No. XNS02J2020-0050), Project funded by Major Science and Technology Project of CNPC (Grant No. 2016E10-0611), "13th five year plan" National Science and Technology Major Project (Grant No. 2016ZX05062), and National Natural Science Foundation (Grant No. 41402126).

Acknowledgments

PetroChina Southwest Oil & Gas Field Company is thanked for providing basic data. Minglong Li in Southwest Petroleum University is thanked for helping analyze stable isotopes. Fei Li in Southwest Petroleum University assisted with situ LA-ICP-MS analysis.

Conflict of interest

The authors ZQ, YG and ZY are employed by Southwest Oil and Gas Field Company, Petro China.

The remaining authors declare that the research was conducted in the absence of any commercial or financial relationships that could be construed as a potential conflict of interest.

Publisher's note

References

Amthor, J. E., Mountjoy, E. W., and Machel, H. G. (1994). Regional-scale porosity and permeability variations in Upper Devonian Leducbuildups: Implications for reservoirs development and prediction in carbonates. *AAPG Bull.* 78 (10), 1541–1559. doi:10.1306/A25FF215-171B-11D7-8645000102C1865D

Anderson, T., and Arthur, M. A. (1983). Stable isotopes of oxygen and carbon and their application to sedimentologic and paleonvironmental problems. *SEPM Short. Course* 10, 1–151. doi:10.2110/scn.83.01.0000

Badiozamani, K. (1973). The dorag dolomitization model-application to the middle ordovician of sisconsin. *J. Sediment. Petrology* 43 (4), 965–984. doi:10.1306/74D728C9-2B21-11D7-8648000102C1865D

Bai, G. P., and Cao, B. F. (2014). Characteristics and distribution patterns of deep petroleum accumulations in the world. *Oil Gas Geol.* 35 (1), 19–25. doi:10.11743/ogg20140103

Davies, G. R., and Smith, L. B. (2006). Structurally controlled hydrothermal dolomite reservoir facies: An overview. *Am. Assoc. Pet. Geol. Bull.* 90 (11), 1641–1690. doi:10.1306/05220605164

Deng, K. L. (1992). Formation and evolution of Sichuan Basin and domains oil and gas exploration. *Nat. Gas. Ind.* 12 (5), 7–13.

Derry, L, A., Brasier, M. D., Corfield, R. M., Rozanov, A. Y., and Zhuravlev, A. Y. (1994). Sr and C isotopes in Lower Cambrian carbonates from the Siberian craton:A paleoenvironmental record during the 'Cambrian explosion. *Earth Planet. Sci. Lett.* 128 (3-4), 671–681. doi:10.1016/0012-821x(94)90178-3

Dyman, T. S., Crovelli, R. A., Bartberger, C. E., and Takahashi, K. I. (2002). Worldwide estimates of deep natural gas resources based on the U.S. *Nat. Resour. Res.* 11 (3), 207–218. doi:10.1023/a:1019860722244

Ehrenberg, S. N., Eberli, G. P., Keramati, M., and Moallemi, S. A. (2006). Porosity-permeability relationships in interlayered limestone-dolostone reservoirs. *Am. Assoc. Pet. Geol. Bull.* 90 (1), 91–114. doi:10.1306/08100505087

Ehrenberg, S. N. (2004). Factors controlling porosity in upper carboniferous–lower permian carbonate strata of the barents sea. *Am. Assoc. Pet. Geol. Bull.* 88 (12), 1653–1676. doi:10.1306/07190403124

Fan, C. H., Li, H., Qin, Q. R., He, S., and Zhong, C. (2020). Geological conditions and exploration potential of shale gas reservoir in Wufeng and Longmaxi

Formation of southeastern Sichuan Basin, China. *J. Petroleum Sci. Eng.* 191, 107138. doi:10.1016/j.petrol.2020.107138

Fan, C. H., Li, H., Zhao, S. X., Qin, Q. R., Fan, Y., Wu, J. F., et al. (2020). Formation stages and evolution patterns of structural fractures in marine shale: Case study of the Lower Silurian Longmaxi Formation in the Changning area of the Southern Sichuan Basin, China. *Energy Fuels* 34 (8), 9524–9539. doi:10.1021/acs.energyfuels.0c01748

Fan, C. H., Xie, H. B., Li, H., Zhao, S. X., Shi, X. C., Liu, J. F., et al. (2022). Complicated fault characterization and its influence on shale gas preservation in the southern margin of the Sichuan Basin, China. *Lithosphere* 2022, 8035106. doi:10.2113/2022/8035106

Fang, S. X., Hou, F. H., and Dong, Z. X. (2003). Non-stromatoltite ecologic system cyanobacteria dolostone in Dengying Formation of Upper-Sinian. *Acta Sedimentol. Sin.* 21 (1), 96–102.

Feng, Z. Z., Peng, Y. M., Jin, Z. K., and Bao, Z. D. (2002). Lithofacies palaeogeography of the late Cambrian in China. *J. Palaeogeogr.* 4 (3), 1–10. doi:10.7605/gdlxb.2004.02.001

Fu, J. H., Fan, L. Y., Liu, X., and Huang, D. J. (2019). Gas accumulation conditions and key exploration & development technologies in Yuanba gas field. *Acta Pet. Sin.* 40 (2), 748–760. doi:10.7623/syxb201902013

Gao, F. Q. (2019). Use of numerical modeling for analyzing rock mechanic problems in underground coal mine practices. *J. Min. Strata Control Eng.* 1 (1), 013004. doi:10.13532/j.jmsce.cn10-1638/td.2019.02.009

Halley, R. B., and Schmoker, J. W. (1983). High-porosity cenozoic carbonaterocks of South Florida: Progressive loss of porosity with depth. *AAPG Bull.* 67 (2), 191–200. doi:10.1306/03B5ACE6-16D1-11D7-8645000102C1865D

Hao, Y., Yang, X., Wang, Y. F., Chen, W., Gu, M. F., and Hou, G. F. (2017). Supergene karstification in the sinian dengying formation, Sichuan basin. *Sediment. Geol. Tethyan Geol.* 37 (1), 48–54.

He, D. F., Li, D. S., Zhang, G. W., Zhao, L. Z., Fang, C., Lu, R. Q., et al. (2011). Formation and evolution of multi-cycle superposed Sichuan Basin, China. *Chin. J. Geol.* 46 (3), 589–606.

He, S., Li, H., Qin, Q. R., and Long, S. X. (2021). Influence of mineral compositions on shale pore development of Longmaxi Formation in the Dingshan area, southeastern Sichuan Basin, China. *Energy Fuels* 35 (13), 10551–10561. doi:10.1021/acs.energyfuels.1c01026

He, Z. L., Jin, X. H., Wo, Y. J., Li, H. L., Bai, Z. R., Jiao, C. L., et al. (2016). Hydrocarbon accumulation characteristics and exploration domains of ultra-deep marine carbonates in China. *China Pet. Explor.* 21 (1), 3–14. doi:10.3969/j.issn.1672-7703.2016.01.001

He, Z. L., Zhang, J. T., Ding, Q., You, D. H., Peng, S. T., Zhu, D. Y., et al. (2017). Factors controlling the formation of high-quality deep to ultra-deep carbonate reservoirs. *Oil Gas Geol.* 38 (4), 633–644. doi:10.11743/ogg20170401

Hu, M. Y., Cai, X. Y., Hu, Z. G., Qian, Y., and Xiang, J. (2009). Deep buried dissolution of ordovician carbonates in tazhong area of Tarim Basin. *J. Oil Gas Technol. (JJPI)* 31 (6), 49–54.

Hu, W. X., Chen, Q., Wang, X. L., and Cao, J. (2010). REE models for the discrimination of fluids in the formation and evolution of dolomite reservoirs. *Oil Gas Geol.* 31 (6), 810–818. doi:10.11743/ogg20100614

Hu, Y. J., Cai, C. F., Liu, D. W., Chelsea, L. P., Jiang, L., Shen, J. A., et al. (2020). Formation, diagenesis and palaeoenvironmental significance of upper Ediacaran fibrous dolomite cements. *Sedimentology* 67, 1161–1187. doi:10.1111/sed.12683

Jardine, D., and Wilshart, J. W. (1987). Carbonate reservoirs description(in reservoirs sedimentology). *Soc. Econ. Paleontolo-gists Mineralogists* 40, 129–152. doi:10.2110/pec.87.40.0129

Jia, C. Z., and Pang, X. Q. (2015). Research process and development directions of deep hydrocarbon geological theories. *ACTA Pet. Sin.* 36 (12), 1457–1469. doi:10.7623/syxb201512001

Jia, P., Huang, F. X., Lin, S. G., Song, T., Gao, Y., Lv, W. N., et al. (2021). Sedimentary facies and model characteristics of middle upper cambrian Xixiangchi group in sichuang basin and its adjacent areas. *Geoscience* 35 (4), 1–12. doi:10.19657/j.geoscience.1000-8527.2021.026

Jiang, X. Q., Guan, H. L., Liu, G. X., Li, J. M., Luo, K. P., Yan, J. X., et al. (2015). Diagenesis of middle and upper cambrian loushanguan group reservoirs in nanchuan area, Sichuan basin. *Petroleum Geol. Experriment* 37 (3), 314–319. doi:10.11781/sysydz201503314

Jiao, F. Z., Feng, J. H., Yi, J. Z., Cai, X. Y., and He, F. Q. (2015). Direction, key factors and solution of marine natural gas exploration in Yangtze area. *China Pet. Explor.* 20 (2), 1–8. doi:10.3969/j.issn.1672-7703.2015.02.001

Jin, M. D., Li, B. S., Zhu, X., Dai, L. C., Jiang, Z. L., Wu, H., et al. (2020). Characteristics and main controlling factors of reservoirs in the fourth member of Sinian Dengying Formation in Yuanba and its peripheral area, northeastern Sichuan Basin, SW China. *Petroleum Explor. Dev.* 47 (6), 1172–1182. doi:10.1016/s1876-3804(20)60127-1

Kaufman, A. J., and Knoll, A. H. (1995). Neoproterozoic variations in the C-isotopic composition of seawater:stratigraphic and biogeochemical implications. *Precambrian Res.* 73 (1-4), 27–49. doi:10.1016/0301-9268(94)00070-8

Krouse, H. R., Viau, C. A., Eliuk, L. S., Ueda, A., and Halas, S. (1988). Chemical and isotopic evidence of thermochemical sulphate reduction by light hydrocarbon gases in deep carbonate reservoirs. *Nature* 33 (2), 415–419. doi:10.1038/333415a0

Land, L. S. (1980). "The isotopic and minor element geochemistry of dolomite: The state of the art," in *Concepts and models of dolomitization*. Editors D. H. Zenger, J. B. Dunham, and R. L. Ethington (Tulsa, Oklahoma: SEPM, Special publication) 28, 87–110.

Lei, H. J., Li, G. R., Gao, Y. W., Zhou, J. L., Feng, Y. Y., Fu, H., et al. (2016). Geochemical characteristics and generation mechanism of cambrian dolomite in the south of Sichuan basin. *Mar. Orig. Pet. Geol.* 21 (3), 39–47. doi:10.7623/syxb201609004

Lei, H. J., Li, G. R., Zhou, J. L., Gao, Y. W., Shen, T., Fu, H., et al. (2015). Carbonate diagenesis feature and controlling over reservoirs of Cambrian in south area of Sichuan Basin. *J. Northeast Petroleum Univ.* 39 (2), 59–68. doi:10.3969/j.issn.2095-4107.2015.02.008

Li, H. K., Li, Z. Q., Long, W., Wan, S. S., Ding, S., Wang, S. Z., et al. (2019a). Vertical configuration of Sichuan Basin and its superimposed characteristics of the prototype basin. *J. Chengdu Unniversity Technol. Technol. Ed.* 46 (3), 257–267. doi:10.3969/j.issn.1671-9727.2019.03.01

Li, H., Qin, Q. R., Zhang, B. J., Ge, X. Y., Hu, X., Fan, C. H., et al. (2020). Tectonic fracture Formation and distribution in ultradeep marine carbonate gas reservoirs: A case study of the maokou Formation in the jiulongshan gas field, Sichuan basin, southwest China. *Energy fuels.* 34 (11), 14132–14146. doi:10.1021/acs.energyfuels.0c03327

Li, H. (2022). Research progress on evaluation methods and factors influencing shale brittleness: A review. *Energy Rep.* 8, 4344–4358. doi:10.1016/j.egyr.2022.03.120

Li, H., Tang, H. M., Qin, Q. R., Zhou, J. L., Qin, Z. J., Fan, C. H., et al. (2019). Characteristics, formation periods and genetic mechanisms of tectonic fractures in the tight gas sandstones reservoir: A case study of xujiahe Formation in YB area, Sichuan basin, China. *J. Petroleum Sci. Eng.* 178, 723–735. doi:10.1016/j.petrol.2019.04.007

Li, H., Wang, Q., Qin, Q. R., and Ge, X. Y. (2021b). Characteristics of natural fractures in an ultradeep marine carbonate gas reservoir and their impact on the reservoir: A case study of the maokou formation of the jls structure in the Sichuan basin, China. *Energy fuels.* 35 (16), 13098–13108. doi:10.1021/acs.energyfuels.1c01581

Li, H., Tang, H. M., and Zheng, M. J. (2019). Micropore structural heterogeneity of siliceous shale reservoir of the Longmaxi Formation in the southern Sichuan Basin, China. *Minerals* 9, 548. doi:10.3390/min9090548

Li, H., Tang, H. M., Qin, Q. R., Wang, Q., and Zhong, C. (2019). Effectiveness evaluation of natural fractures in Xujiahe Formation of Yuanba area, Sichuan basin, China. *Arabian J. Geosci.* 12 (6), 194. doi:10.1007/s12517-019-4292-5

Li, H. T., Peng, R., Du, W. S., Li, X. P., and Zhang, N. B. (2021c). Experimental study on structural sensitivity and intervention mechanism of mechanical behavior of coal samples. *J. Min. Strata Control Eng.* 3(4), 043012. doi:10.1021/acsomega.1c05077

Li, J., He, D. F., Du, Y., Cui, J., Ma, Y., and Zhang, X. (2014). Electroacupuncture improves cerebral blood flow and attenuates moderate ischemic injury via Angiotensin II its receptors-mediated mechanism in rats. *BMC Complement. Altern. Med.* 16 (4), 441–460. doi:10.1186/1472-6882-14-441

Li, J., Li, H., Yang, C., Wu, Y. J., Gao, Z., and Jiang, S. L. (2022). Geological characteristics and controlling factors of deep shale gas enrichment of the Wufeng-Longmaxi Formation in the southern Sichuan Basin. *China. Lithosphere*, 2022. 4737801. doi:10.2113/1970/4737801

Li, J., Li, H., Xu, J. L., Wu, Y. J., and Gao, Z. (2022). Effects of fracture formation stage on shale gas preservation conditions and enrichment in complex structural areas in the southern Sichuan Basin, China. *Frontiers in Earth Sci.*, 9. 823855. doi:10.3389/feart.2022.921988

Li, J. Z., Tao, X. W., Bai, B., Huang, S. P., Jiang, Q. C., Zhao, Z. Y., et al. (2021). Geological conditions, reservoirs evolution and favorable exploration directions of marine ultra-deep oil and gas in China. *Petroleum Explor. Dev.* 48 (1), 52–67. doi:10.1016/S1876-3804(21)60005-8

Li, W. Z., Zhou, J. G., Zhang, J. Y., Hao, Y., Zeng, Y. Y., Wang, F., et al. (2016). Main controlling factors and favorable zone distribution of Xixiangchi Formation reservoirs in the Sichuan Basin. *Nat. Gas. Ind.* 36 (1), 52–60. doi:10.3787/j.issn.1000-0976.2016.01.006

Li, W. Z., Wen, L., Gu, M. F., Xia, M. L., Xie, W. R., Fu, X.D.,, et al. (2020). Development models of Xixiangchi Formation karst reservoirs in the Late Caledonian in the central Sichuan Basin and its oil-gas exploration implications. *Nat. Gas. Ind.* 40 (9), 30–38. doi:10.3787/j.issn.1000-0976.2020.10.004

Li, Z. Q., Ying, D. L., Li, H. K., Yang, G., Zeng, Q., Guo, X. Y., et al. (2011). Evolution of the Western Sichuan basin and its superimposed characteristics, China. *Acta Petrol. Sin.* 27 (8), 2362–2370.

Lin, X. X., Peng, J., Yan, J. P., and Hou, Z. J. (2015). A discussion about origin of botryoidal dolostone of the sinian dengying Formation in Sichuan Basin. *J. Palaeogeogr.* 17 (6), 755–770. doi:10.7605/gdlxb.2015.06.062

Lin, Y., Chen, C., Shan, S. J., Zeng, Y. Y., Liu, X., and Chen, Y. L. (2017). Reservoirs characteristics and main controlling factors of the cambrian Xixiangchi Formation in the Sichuan basin. *Petroleum Geol. Exp.* 39 (5), 610–616. doi:10.11781/sysydz201705610

Liu, C., Xie, Q. B., Wang, G. W., He, W. G., Song, Y. F., Tang, Y., et al. (2017). Rare Earth element characteristics of the carboniferous huanglong formation dolomites in eastern Sichuan basin, southwest China: Implications for origins of dolomitizing and diagenetic fluids. *Mar. Pet. Geol.* 81, 33–49. doi:10.1016/j.marpetgeo.2016.12.030

Liu, D. W., Cai, C. F., Hu, Y. J., Jang, L., Peng, Y. Y., Yu, R., et al. (2020). Multi-stage dolomitization process of deep burial dolostones and its influence on pore evolution: A case study of longwangmiao Formation in the lower cambrian of central Sichuan basin. *J. China Univ. Min. Technol.* 49 (6), 1150–1165. doi:10.1016/j.marpetgeo.2020.104752

Liu, L. H., Du, X. D., Xu, S. L., and Wen, H. G. (2017a). Characteristics and Formation of the cambrian dolomite in middle-south Sichuan basin, China. *J. Jilin Univ. Sci. Ed.* 47 (3), 775–784. doi:10.13278/j.cnki.jjuese.201703111

Liu, S. G., Deng, B., Sun, W., Zhong, Y., Li, Z. W., Li, J. X., et al. (2018). Sichuan Basin:A superimposed sedimentary basin mainly controlled by its peripheric tectonics. *Chin. J. Geol.* 53 (1), 308–326. doi:10.12017/dzkx.2018.018

Liu, S. G., Li, Z. B., Sun, W., Deng, B., Luo, Z. L., Wang, G. Z., et al. (2011). Basin geological features of superimposed basin and hydrocarbon accumulation in Sichuan Basin, China. *Chin. J. Geol.* 46 (1), 233–257. doi:10.3969/j.issn.0563-5020.2011.01.019

Ma, X. H., Yang, Y., Wen, L., and Luo, B. (2019a). Distribution and exploration direction of medium- and large-sized marine carbonate gas fields in Sichuan Basin, SW China. *Petroleum Explor. Dev.* 46 (1), 1–15. doi:10.1016/s1876-3804(19)30001-1

Ma, Y. S., Cai, X. Y., Zhao, P. R., and Zhu, H. Q. (2011). The research status and advances in porosity evolution and diagenesis of deep carbonate reservoirs. *Earth Sci. Front.* 18 (4), 181–192.

Ma, Y. S., He, Z. L., Zhao, P. R., Zhu, H. Q., Han, J., You, D. H., et al. (2019). A new progress in foumation mechanism of deep and ultra-deep carbonate reservoirs. *Acta Pet. Sin.* 40 (12), 1414–1425. doi:10.7623/syxb201912001

Mckenzie, J. A. (1981). Holocene dolomitization of calcium carbonate sediments from the coastal sabkhas of abu dhabi, U.A.E. A stable isotope study. *J. Geol.* 89 (2), 185–198. doi:10.1086/628579

Mclennan, S. M. (1989). Rare Earth elements in sedimentary rocks: Influence of provenance and sedimentary process. *Rev. Mineralogy* 21, 169–200. doi:10.1515/9781501509032-010

Mitchell, J. M., Paul, A. B., and Stephen, J. B. (1996). Recrystallization of dolomite: an experimental study from. *Geochimica Cosmochimica Acta* 60 (12), 2189–2207. doi:10.1016/0016-7037(96)00062-2

Moor, C. H., and Druckman, Y. (1981). Burial diagenesis and porosity evolution, upper jurassic smackover, Arkansas and lonisana. *AAPG Bull.* 65 (4), 597–628. doi:10.1306/2F919995-16CE-11D7-8645000102C1865D

Morrow, D. W. (1982). Diagenesis 1: Dolomite-part 1, the chemistry ofdolomitization and dolomite precipitation. *Geosci. Can.* 9 (1), 5–13.

Murray, R, C. (1960). Origin of porosity in carbonate rocks. *J. Sediment. Petrology* 30 (1), 59–84. doi:10.1306/74D709CA-2B21-11D7-8648000102C1865D

Pang, X. Q. (2010). Key challenges and research methods of petroleum exploration in the deep of super imposed basins in Western China. *Oil Gas Geol.* 31 (5), 517–534. doi:10.11743/ogg20100501

Park, W. C., and Schot, E. H. (1968). Styloites, their nature and origin. *J. Sediment. Petrology* 38 (1), 1–175.

Prokoph, A., Shields, G. A., and Veizer, J. (2008). Compilation and time-series analysis of a marine carbonate $\delta^{18}O$, $\delta^{13}C$, $^{87}Sr/^{86}Sr$ and $\delta^{34}S$ database through Earth history. *Earth. Sci. Rev.* 87, 113–133. doi:10.1016/j.earscirev.2007.12.003

Qian, Y. X., Taberner, C., Zou, S. L., You, D. H., and Wang, R. Y. (2007). Diagenesis comparison between epigenic karstification and burial dissolution in carbonate reservoirs:An instance of Ordovician carbonate reservoirs in Tabei and Tazhong regions, Tarim Basin. *Mar. Orig. Pet. Geol.* 12 (2), 1–7. doi:10.3969/j.issn.1672-9854.2007.02.001

Qie, L., Shi, Y. N., and Liu, J. G. (2021). Experimental study on grouting diffusion of gangue solid filling bulk materials. *J. Min. Strata Control Eng.* 3 (2), 023011. doi:10.13532/j.jmsce.cn10-1638/td.20201111.001

Romanek, C. S., Grossman, E. L., and Morse, J. W. (1992). Carbon isotopic fractionation in synthetic aragonite and calcite: Effects of temperature and precipitation rate. *Geochimica Cosmochimica Acta* 56 (1), 419–430. doi:10.1016/0016-7037(92)90142-6

Saller, A. H., Walden, S., Robertson, S., Nims, R., Schwab, J., Hagiwara, H., et al. (2004). *Three-dimensional seismic imaging of an Upper Paleozoic "reefal" buildup, Reinecke field, west Texas, United States.* Oklahoma, United States: AAPG Memoir, 107–122.

Sassen, R., and Moore, C. H. (1988). Framework of hydrocarbon generation and destruction in eastern Smackovertrend. *AAPG Bull.* 72 (6), 649–663.

Shan, S. C., Wu, Y. Z., Fu, Y. K., and Zhou, P. H. (2021). Shear mechanical properties of anchored rock mass under impact load. *J. Min. Strata Control Eng.* 3 (4), 043034. doi:10.13532/j.jmsce.cn10-1638/td.20211014.001

Shen, A. J., Zhao, W. Z., Hu, A. P., She, M., Chen, Y. N., and Wang, X. F. (2015). Major factors controlling the development of marine carbonate reservoirs. *Petroleum Explor. Dev.* 42 (5), 597–608. doi:10.1016/s1876-3804(15)30055-0

Shi, S. Y., Wang, T. S., Liu, W., Jiang, H., Li, Q. F., Liu, X., et al. (2020). Reservoirs characteristic and gas exploration potential in cambrian Xixiangchi Formation of Sichuan basin. *Nat. Gas. Geosci.* 31 (6), 773–785. doi:10.11764/j.issn.1672-1926.2020.03.007

Sun, S. Q. (1995). Dolomite reservoirs:Porosity evolution and reservoirs characteristics. *AAPG Bull.* 79 (2), 186–204.

Tang, C. Y., Wang, M., Yao, H. Z., Duan, Q. F., and Zhao, X. L. (2006). Current topics about dolomitization and the problem of dolostones. *Jouranal East China Inst. Technol.* 29 (3), 205–210. doi:10.3969/j.issn.1674-3504.2006.03.002

Veizer, J., Ala, D., Azmy, K., Bruckschen, P., Buhl, D., Bruhn, F., et al. (1999). $^{87}Sr/^{86}Sr$, $\delta^{13}C$ and$\delta^{18}O$ evolution of Phanerozoic seawater. *Chem. Geol.* 161 (1-3), 59–88. doi:10.1016/s0009-2541(99)00081-9

Wang, J., and Wang, X. L. (2021). Seepage characteristic and fracture development of protected seam caused by mining protecting strata. *J. Min. Strata Control Eng.* 3 (3), 033511. doi:10.13532/j.jmsce.cn10-1638/td.20201215.001

Wang, Q. C., and Jin, Z. Y. (2002). Superimposed basin and oil-gas formation and accumulation. *Chin. Basic Sci.* 6, 4–7. doi:10.3969/j.issn.1009-2412.2002.06.001

Wang, S. L., Li, H., Lin, L. F., and Yin, S. (2022). Development characteristics and finite element simulation of fractures in tight oil sandstone reservoirs of Yanchang Formation in western Ordos Basin. *Frontiers Earth Sci.* 9, 823855. doi:10.3389/feart.2021.823855

Warren, J. (2000). Dolomite:Occurrence, evolution and economically important associations. *Earth. Sci. Rev.* 52 (1-3), 1–81. doi:10.1016/s0012-8252(00)00022-2

Wei, G. Q., Yang, W., Xie, W. R., Jin, H., Su, N., Sun, A., et al. (2018). Accumulation modes and exploration domains of Sinian-Cambrian natural gas in Sichuan Basin. *Acta Pet. Sin.* 39 (12), 1317–1327. doi:10.7623/syxb201812001

Worden, R. H., and Smalley, P. C. (1996). H_2S-producing reactions in deep carbonate gas reservoirs:Khuff Formation, Abu Dhabi. *Chem. Geol.* 133 (1-4), 157–171. doi:10.1016/s0009-2541(96)00074-5

Xu, X. S., and Du, B. W. (2005). The palaeoweathering crust -type karst reservoir rocks in carbonate rocks. *Sediment. Geol. TethyanGeology* 25 (3), 1–7. doi:10.3969/j.issn.1009-3850.2005.03.001

Yang, F., Zhang, H. A., Wang, X. J., Peng, J., Mo, J. W., Zhuo, S. Q., et al. (2019). Characteristics and significance of supergene karst of the upper permian changxing Formation in puguang gasfield, Sichuan basin. *J. Palaeogeogr.* 21 (6), 901–912. doi:10.7605/gdlxb.2019.06.061

Yang, W., Hu, M. Y., Song, H. J., and Hu, Z. H. (2008). Diagenesis of middle and upper cambrian reservoirs in southern part of Sichuan basin. *Mar. Orig. Pet. Geol.* 13 (4), 29–36. doi:10.3969/j.issn.1672-9854.2008.04.005

Yang, X. F., Huang, X., Wang, X. Z., Wang, Y. P., Li, K., and Zeng, D. M. (2019a). Origin of crystal dolomite and its reservoir formation mechanism in the Xixiangchi Formation, upper cambrian in southeastern Sichuan Basin. *Carbonates Evaporites* 34, 1537–1549. doi:10.1007/s13146-019-00499-y

Zenger, D. H., Dunham, J. B., and Ethington, R. L. (1980). Concepts and moels of dolomitization. *Spec. Publ. -SEPM* 28, 1–320. doi:10.2110/pec.80.28

Zhai, G. M., Wang, S. H., and He, W. Y. (2012). Hotspot trend and enlightenment of global ten-year hydrocarbon exploration. *Acta Pet. Sin.* 33 (S1), 14–19.

Zhang, J., Shou, J. F., Zhang, T. F., Pan, L. Y., and Zhou, J. G. (2014b). New approach on the study of dolomite origin:the crystal structure analysis of dolomite. *Acta Sedimentol. Sin.* 32 (3), 550–559.

Zhang, J. Y., Ni, X. F., Wu, X. N., Li, W. Z., Hao, Y., Chen, Y. N., et al. (2017). Main controlling factors and distribution of high quality reservoirs of deep buried

dolomite in typical craton in China. *Nat. Gas. Geosci.* 28 (8), 1165–1175. doi:10.1016/j.jnggs.2018.04.003

Zhang, M. L., Xie, Z. Y., Li, X. Z., Gu, J. R., Yang, W., and Liu, M. Z. (2010). Characteristics of lithofacies paleogeography of cambrian in Sichuan basin. *Acta Sedimentol. Sin.* 28 (1), 128–139.

Zhang, X. F., Liu, B., Cai, Z. X., and Hu, W. X. (2010a). Dolomitization and carbonate reservoirs formation. *Geol. Sci. Technol. Inf.* 29 (3), 79–85. doi:10.3969/j.issn.1000-7849.2010.03.012

Zhao, W. Z., Shen, A. J., Hu, S. Y., Pan, W. Q., and Qiao, Z. F. (2012). Types and distributional features of Cambrian-Ordovician dolostone reservoirs in Tarim Basin, northwestern China. *Acta Petrol. Sin.* 28 (3), 758–768.

Zhao, Y. Y., and Zheng, Y. F. (2011). Diagenesis of carbonate sediments. *Acta Petrol. Sin.* 27 (2), 501–519.

Zhou, L., Kang, Z. H., Liu, Z., Kong, J. X., and Chen, Y. (2014). Characteristics of Xixiangchi group carbonate reservoirs space in leshan-longnvsi palaeouplift, Sichuan basin. *J. Central South University:Science Technol.* 45 (12), 4393–4402.

Zhou, Z., Wang, X. Z., Yin, G., Yuan, S. S., and Zeng, S. J. (2016). Characteristics and Genesis of the (sinian) dengying formation reservoir in central sichuan, China. *J. Nat. Gas Sci. Eng.* 29, 311–321. doi:10.1016/j.jngse.2015.12.005

Zhu, D. Y., Jin, Z. Y., Hu, W. X., and Zhang, X. F. (2008). Effects of deep fluid on carbonates reservoirs in Tarim Basin. *Geol. Rev.* 54 (3), 348–357. doi:10.3321/j.issn:0371-5736.2008.03.008

Zhu, D. Y., Meng, Q. Q., Jin, Z. J., Liu, Q. Y., and Hu, W. X. (2015). Formation mechanism of deep Cambrian dolomite reservoirs in the Tarim basin, northwestern China. *Mar. Petroleum Geol.* 59, 232–244. doi:10.1016/j.marpetgeo.2014.08.022

Zhu, Y. G., Zhang, S. C., Liang, Y. B., Ma, Y. S., Zhou, G. Y., and Dai, J. X. (2006). Characteristics of gas reservoirs with high content of H_2S in the Northeastern Sichuan Basin and the consumption of hydrocarbons due to TSR. *Acta Sedimentol. Sin.* 24 (2), 300–308. doi:10.3969/j.issn.1000-0550.2006.02.020

Zou, C. N., Du, J. H., Xu, C. C., Wang, Z. C., Zhang, B. M., Wei, G. Q., et al. (2014). Formation, distribution, resource potential and discovery of the Sinian-Cambrian giant gas field, Sichuan Basin, SW China. *Petroleum Explor. Dev.* 41 (3), 278–293. doi:10.1016/S1876-3804(14)60036-7

frontiers | Frontiers in Earth Science

TYPE Original Research
PUBLISHED 31 August 2022
DOI 10.3389/feart.2022.992013

OPEN ACCESS

EDITED BY
Hu Li,
Southwest Petroleum University, China

REVIEWED BY
Shun He,
Southwest Petroleum University, China
Shaoke Feng,
Chengdu University of Technology, China

*CORRESPONDENCE
Yaming Yao,
yaoyaming321@163.com

SPECIALTY SECTION
This article was submitted to Structural Geology and Tectonics, a section of the journal Frontiers in Earth Science

RECEIVED 12 July 2022
ACCEPTED 01 August 2022
PUBLISHED 31 August 2022

CITATION
Yao Y, Zhao F, Zhang J and Zhao J (2022), Evaluation of organic geochemical characteristics and experiments of thermal pressure simulation of Jurassic coal measure source rocks in the Yanqi Basin. *Front. Earth Sci.* 10:992013. doi: 10.3389/feart.2022.992013

Evaluation of organic geochemical characteristics and experiments of thermal pressure simulation of Jurassic coal measure source rocks in the Yanqi Basin

Yaming Yao[1]*, Fei Zhao[2], Junmin Zhang[2] and Juanjuan Zhao[2]

[1]College of Geosciences and Engineering, North China University of Water Resources and Electric Power, Zhengzhou, China, [2]School of Mining Engineering and Geology, Xinjiang Institute of Engineering, Wulumuqi, China

The Yanqi Basin is a coal-bearing basin in Western China. In order to determine the hydrocarbon generation potential of the Jurassic source rocks in this area, the organic matter composition of coal-measure mudstone, carbonaceous mudstone and coal rocks, the yields of liquid and gaseous hydrocarbons, and the comparison of hydrocarbon sources were studied by means of hydrocarbon-generating thermal simulation experiments. The results showed that the micro-composition of the Jurassic coal rocks in the Yanqi Basin showed the characteristics of rich vitrinite-inertinite and poor chitinite + saprolite components; however, the micro-composition of the mudstone showed the characteristics of poor inertinite and rich vitrinite–chitinite + saprolite components. The Jurassic mudstone has a wide distribution range of hydrogen and oxygen indexes, among which the hydrogen index is distributed between 2 and 266 mg/gTOC, and the oxygen index is distributed between 3 and 183 mg/g TOC. The organic matter in the mudstone belongs to Type II_2-III kerogen. The hydrogen index of coal is distributed in the range of 100–300 mg/gTOC, which is obviously larger than that of mudstone. The total liquid hydrocarbon yield of the coal rock is the highest (43.2 mg/gTOC), followed by mudstone (16.4–20.4 mg/gTOC), while that of the carbonaceous mudstone is the lowest (5.36 mg/gTOC). In addition, mudstone has the highest yield of gaseous hydrocarbons, followed by coal, while that of carbonaceous mudstone is the lowest. The oil-source comparison showed that the Jurassic crude oil has a certain affinity with its main source rocks (mudstone, carbonaceous mudstone, and coal). At the same time, the comparison results of steroid and terpene biomarker parameters with crude oil showed that the Middle and Lower Jurassic mudstone, carbonaceous mudstone, and coal rock in this area are all source rocks and the Badaowan Formation mudstone is the main hydrocarbon source.

KEYWORDS

Yanqi Basin, urassic source rock, hydrocarbon generation potential, organic carbon, oil-source correlation.

1 Introduction

The Yanqi Basin is a small coal-bearing basin in Western China. At present, certain breakthroughs in oil and gas exploration have been obtained in the Jurassic coal-measure strata in the Northern Sag. However, due to lack of research on the geochemical characteristics, organic petrological properties, and hydrocarbon generation mechanism of coal-measure source rocks, the prediction of Jurassic oil and gas resources and the evaluation of exploration prospects in the Yanqi Basin are restricted. The Yanqi Basin is located between the three major basins of Tarim, Junggar, and Tuha in China. It is a Mesozoic–Cenozoic sedimentary basin formed on the varixian folded basement (Cai et al., 2008; Guo et al., 2012). In addition to the good distribution of organic matter, there is a relatively high geothermal gradient inside the basin, which provides favorable conditions for the massive generation and accumulation of oil and gas (Li, 2000; He et al., 2013; Li et al., 2019).

The Yanqi Basin has experienced three large-scale lake transgressions since the Mesozoic. Furthermore, three sets of coal-bearing and carbonaceous mudstone lithologic assemblages were formed in the three coal accumulation stages. The three coal accumulation periods are the Triassic, Middle and Late Jurassic Badaowan Formation period, and Jurassic (Yao et al., 2003). Sedimentary facies studies show that the Jurassic is dominated by fluvial, delta, and shore-shallow lacustrine facies, especially the extensive development of shore-lake facies (Yao et al., 2003; Zhao et al., 2013). In order to explore the hydrocarbon generation potential of the Jurassic source rocks in this area, the organic matter composition of the coal-measure mudstone, carbonaceous mudstone and coal, the yields of liquid and gaseous hydrocarbons, and the comparison of hydrocarbon sources were studied by means of hydrocarbon-generating thermal simulation experiments. This study can provide a reference for similar studies worldwide.

2 Databases and methods

2.1 Geological background

The Yanqi Basin is located in the east of the South Tianshan Orogenic Belt and is a Mesozoic–Cenozoic sedimentary basin

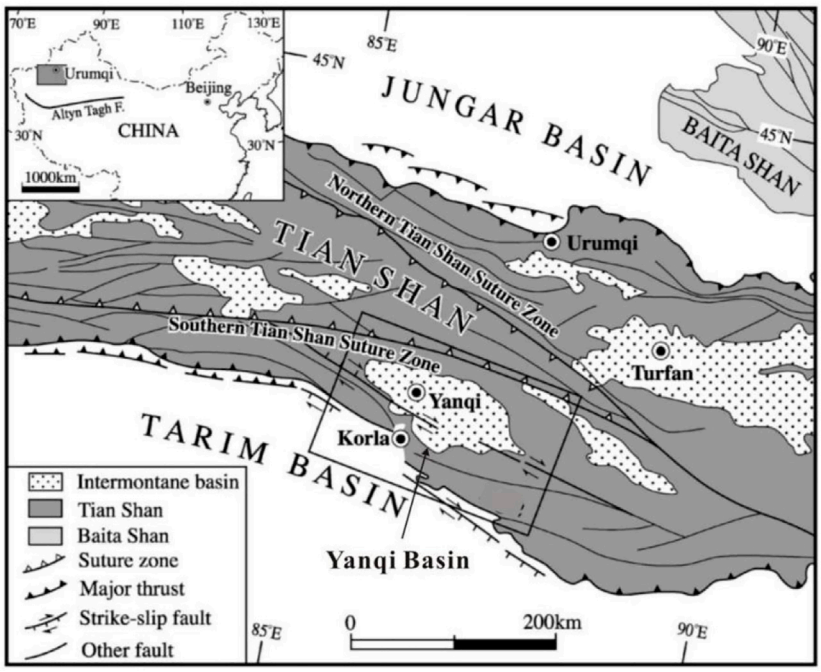

FIGURE 1
Location and regional structural characteristics of the Yanqi Basin, China (Lin et al., 2002).

TABLE 1 Basic information on the samples from the Jurassic in the Yanqi Basin.

Lithology	Formation	Well name	Depth (m)	R_o (%)	Organic carbon (%)	Type of organic matter
Dark gray mudstone	Badaowan Formation	Ma 1 well	1214.65	0.84	2.20	II_2
Dark gray mudstone	Xishanyao Formation	Bonan 1 well	2053.00	0.69	2.80	III
Coal	Xishanyao Formation	Hua'an Coal Mine	Downhole	0.59	77.21	II_2
Carbonaceous mudstone	Sangonghe Formation	Yan 2 well	2493.50	0.67	9.77	II_2

formed on the Hercynian folded basement. The Yanqi Basin covers an area of 1.3×10^4 km^2 (Figure 1). The sedimentary caprocks of the basin composed of Mesozoic Triassic, Jurassic, Cenozoic Tertiary and Quaternary, and Jurassic is the main exploration target layer (Yao et al., 2004; Zhang et al., 2011).

2.2 Thermal-pressure simulation experiments of coal-measure source rocks

In this study, the Jurassic low-maturity source rocks (dark gray mudstone, carbonaceous mudstone, and coal rock) (Table 1) were used for thermal-pressure simulation experiments under low temperature (360°C), long time (greater than 72 h), and water additions.

The thermal simulation experiment of hydrocarbon generation adopts the golden tube-autoclave thermal simulation system. The experimental conditions of the autoclave thermal simulation are as follows: the samples were heated from room temperature to 150°C within 10 h, and then they were heated to 450°C at 2°C/h. After thermal simulation, the gas in the gold tube was punctured and collected in a special glass vacuum device. The device is connected to an Agilent HP6890N chromatographic instrument, and gaseous products can be drawn into the chromatograph for analysis using an automatic control program. Gaseous hydrocarbon carbon isotopes were analyzed using a Delta V Advantage isotope mass spectrometer. The chromatographic column is a CP-Pora PLOT Q quartz column (30 m×0.32 mm×20 μm). For quantitative analysis of thermally simulated liquid hydrocarbons, an Agilent HP6890 was used as the chromatograph, and the chromatographic column was an HP-5 column (30 m×0.32 mm×0.25 μm).

3 Results

3.1 Organic micro-components of coal-measure source rocks

The micro-composition of the Jurassic coal rocks in the Yanqi Basin shows the characteristics of rich vitrinite–inertinite and poor chitinite + saprolite components; however, the micro-composition of the mudstone shows the characteristics of poor inertinite and rich vitrinite–chitinite + saprolite components (Figure 2). The average composition of micro-components in coal rock are as follows: vitrinite 72.0%, inertinite 19.4%, and chitinite + saprolite 8.6%; the average composition of micro-components in the mudstone are as follows: vitrinite 59.5%, inertinite 14.5%, and chitinite + saprolite 26.0%. In the distribution form of the micro components, the vitrinite–inertinite combination showed a distinct band-like distribution. The distribution of micro-components in mudstone is also relatively scattered, with no obvious center, reflecting the diversity of depositional environment and biogenic materials (Curtis et al., 2012; Jiang et al., 2015; Gai et al., 2016).

3.2 Organic geochemical characteristics of source rocks

3.2.1 Organic matter abundance

The organic carbon content of coal-measure mudstone is generally higher than that of lacustrine mudstone. Taking the Qinshui Basin as an example, the TOC of coal-measure mudstone in the Shanxi Formation is usually distributed in the range of 1%–6%, while the TOC of general lacustrine mudstone is usually distributed in the range of 0.1%–4%. However, the hydrocarbon generation potential, soluble organic matter, and total hydrocarbon contents of coal-measure mudstone are generally lower than those of lacustrine mudstone with the same organic carbon content. Therefore, when evaluating the organic carbon abundance of coal-measure mudstone, the evaluation standard of lacustrine mudstone cannot be used.

Tables 2, 3 show the statistical results of the organic matter abundance of the coal measure mudstones in the Badaowan, Sangonghe, and Xishanyao Formations and the coal rocks in the Bohu Depression.

Overall, the Jurassic coal-measure mudstones in the study area belong to medium–good source rocks, which account for 50%–60% of the total samples, while the poor-non-source rocks account for 40%–50% of the total samples. Carbonaceous

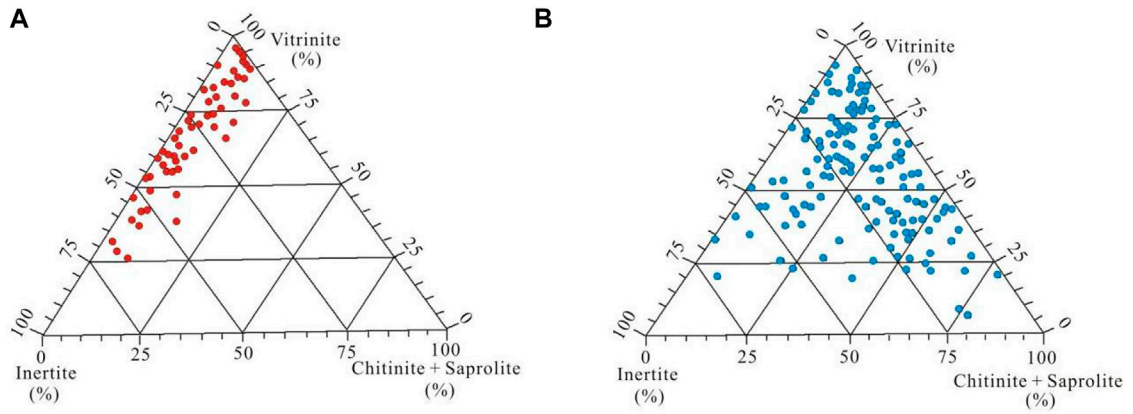

FIGURE 2
Microscopic composition of Jurassic coal **(A)** and mudstone **(B)** in the Yanqi Basin.

TABLE 2 Test results of organic carbon content and hydrocarbon generation potential of Jurassic source rocks in the Yanqi Basin.

Formation	Lithology	Organic carbon (%)				Hydrocarbon generation potential (mg/g)			
		Number of samples	Min	Max	Ave	Number of samples	Min	Max	Ave
Xishanyao Formation	Coal measure mudstone	7	0.36	5.68	2.31	7	0.42	12.6	4.46
	Carbonaceous mudstone	4	12.47	29.25	20.48	4	1.86	78.29	42.6
	Coal	10	44.86	74.02	57.85	10	87.79	144.98	92.24
Sangonghe Formation	Coal measure mudstone	42	0.22	5.21	1.78	42	0.17	15.23	3.54
Badaowan Formation	Coal measure mudstone	38	0.27	5.92	2.59	39	0.29	35.11	7.39
	Carbonaceous mudstone	19	6.02	68.86	18.09	19	5.66	170.77	55.44
	Coal	20	40.36	71.63	53.14	20	45.41	222.69	152

TABLE 3 Test results of chloroform bitumen "A" and total hydrocarbon content of Jurassic source rocks in the Yanqi Basin.

Formation	Lithology	Chloroform bitumen "a" (%)				Total hydrocarbons (ppm)			
		Number of samples	Min	Max	Ave	Number of samples	Min	Max	Ave
Xishanyao Formation	Coal measure mudstone	4	0.01	0.066	0.04	4	36	225	117
	Carbonaceous mudstone	2	0.02	0.22	0.12	2	77	783	430
	Coal	6	0.59	1.49	0.993	6	2850	4,556	3,773
Sangonghe Formation	Coal measure mudstone	20	0.005	0.09	0.034	20	19	246	98
Badaowan Formation	Coal measure mudstone	14	0.01	0.63	0.098	14	29	1630	329
	Carbonaceous mudstone	7	0.43	1.595	0.94	7	879	4,903	3,322
	Coal	10	0.721	2.845	1.97	10	2609	7,310	5,617

mudstones belong to medium source rocks, while they account for 45% of the total samples, and the poor source rocks account for 30% of the total samples. Moreover, 55%–65% of the coal rocks belong to poor source rocks, and only 30% are medium source rocks. Among the various Jurassic source rocks, the Lower Jurassic Badaowan Formation is the most important source rock in this area, with the best hydrocarbon generation conditions, followed by the Middle Jurassic Xishanyao Formation. However, the hydrocarbon generation conditions of the Lower Jurassic Sangonghe Formation are relatively poor. Therefore, the

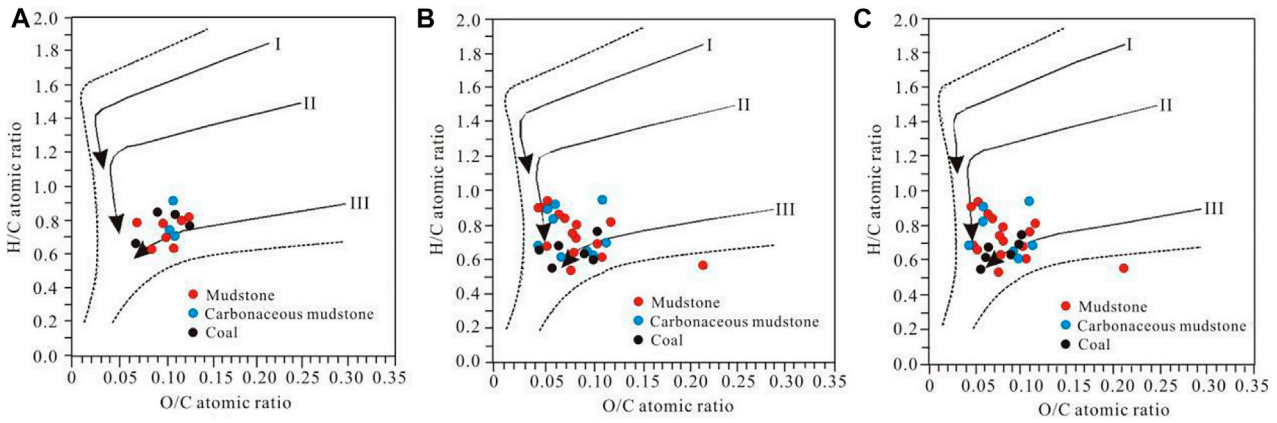

FIGURE 3
Relationship between H/C and O/C atomic ratios of Jurassic source rocks in the study area. Notes: **(A)** Xishanyao Formation; **(B)** Sangonghe Formation; **(C)** Badaowan Formation.

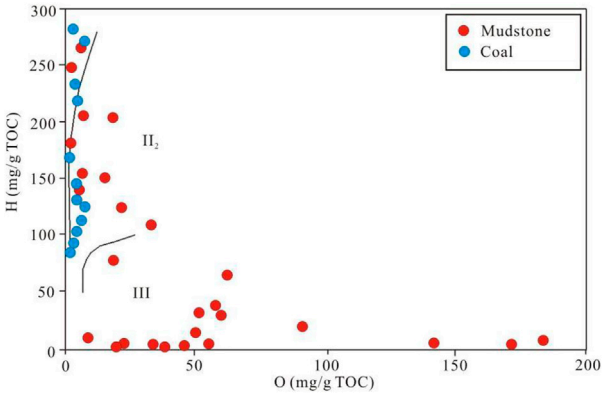

FIGURE 4
Correlation diagram of hydrogen and oxygen indexes of source rocks in Bohu Depression.

hydrocarbon-generating capacity of the coal-measure mudstone is better than that of the coal rock and carbonaceous mudstone. However, due to the high abundance of organic matter, the coal rocks and carbonaceous mudstones have great potential for hydrocarbon generation, and their contribution to oil and gas generation cannot be ignored (Guo et al., 2015; Wang et al., 2015; Yang et al., 2016; Li et al., 2020; Li, 2022).

3.2.2 Elemental composition of C, H, and O in kerogen

Figure 3 is the correlation diagram of H/C and O/C atomic ratios of various source rocks in the Jurassic Xishanyao, Sangonghe, and Badaowan Formations in the Bohu Depression. It reflects that most of the Jurassic source rocks in the Bohu Depression have a H/C atomic ratio of less than 0.8 and an O/C atomic ratio of less than 0.15, indicating that they are Type III parent materials. Only a few source rocks have H/C atomic ratios greater than 0.8, which belong to Type II_2 parent materials. By comparison, the Badaowan Formation source rocks are of the best quality, which may be related to the relatively high degree of the thermal evolution of the Badaowan Formation source rocks (Wang et al., 2015; Li et al., 2021).

3.2.3 Distribution characteristics of hydrogen and oxygen indexes

The Jurassic mudstone in the study area has a wide distribution range of hydrogen and oxygen indices, with the hydrogen index ranging from 2 to 266 mg/gTOC and the oxygen index ranging from 3 to 183 mg/gTOC (Figure 4). The degradation rate is less than 30%, which reflects that the type of organic matter in the mudstone belongs to Type II_2–III. The hydrogen index of coal is distributed in the range of 100–300 mg/gTOC, which is significantly higher than that of mudstone.

According to the abovementioned analysis, the organic matter type of the Jurassic source rocks in the Yanqi Basin is mainly Type III, followed by Type II_2. The quality of Jurassic source rocks from high to low is the Badaowan Formation, the Xishanyao Formation, and the Sangonghe Formation. In the same layer, the organic matter type of coal rock and carbonaceous mudstone is slightly better than that of the coal measure mudstone.

3.3 Carbon isotopic characteristics of crude oil

The stable carbon isotopic composition of crude oil is related to the type of parent material, so it can reflect the

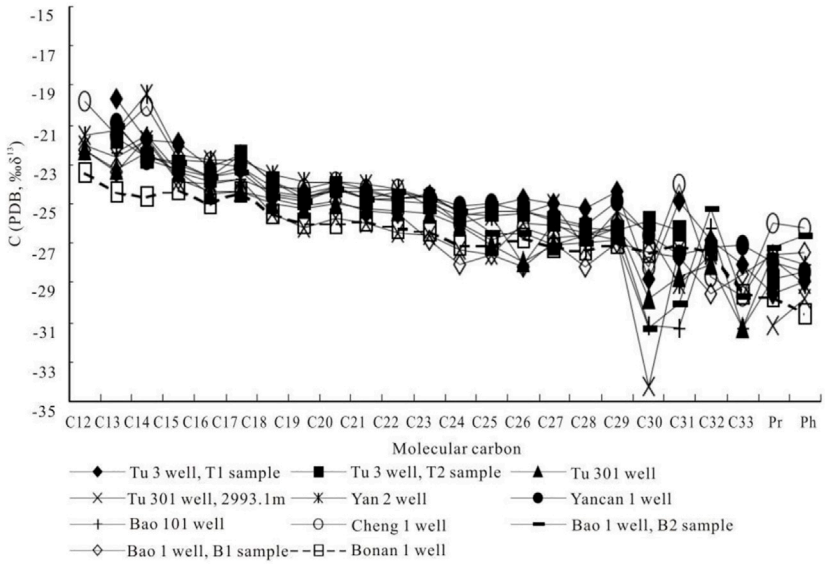

FIGURE 5
Distribution characteristics of carbon isotopes in the Lower Jurassic crude oil molecules in the study area.

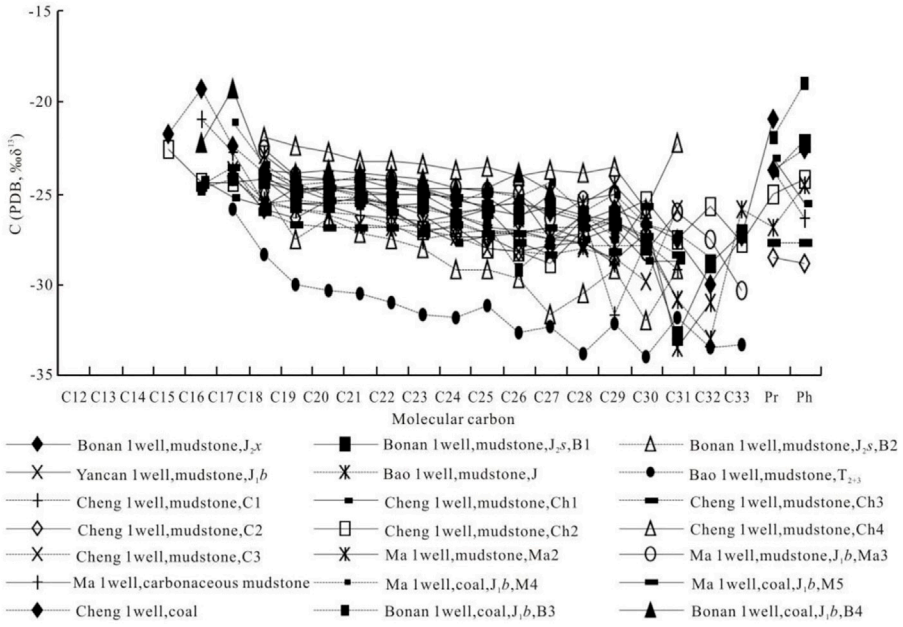

FIGURE 6
Distribution characteristics of molecular carbon isotopes in the J-T source rocks in the study area.

genetic type of crude oil. Generally, the $\delta^{13}C$ of crude oil related to sapropelic parent material is lighter than −27‰, the $\delta^{13}C$ of saturated hydrocarbons is lighter than −28.5‰, and the $\delta^{13}C$ of aromatic hydrocarbons is lighter than −26.5‰. However, the $\delta^{13}C$ of crude oil related to parent material is generally heavier than −27.0‰, and the $\delta^{13}C$ of saturated hydrocarbons is heavier than −28.5‰. In this study, only the $\delta^{13}C$ value in the crude oil from Well Bonan1 is lighter

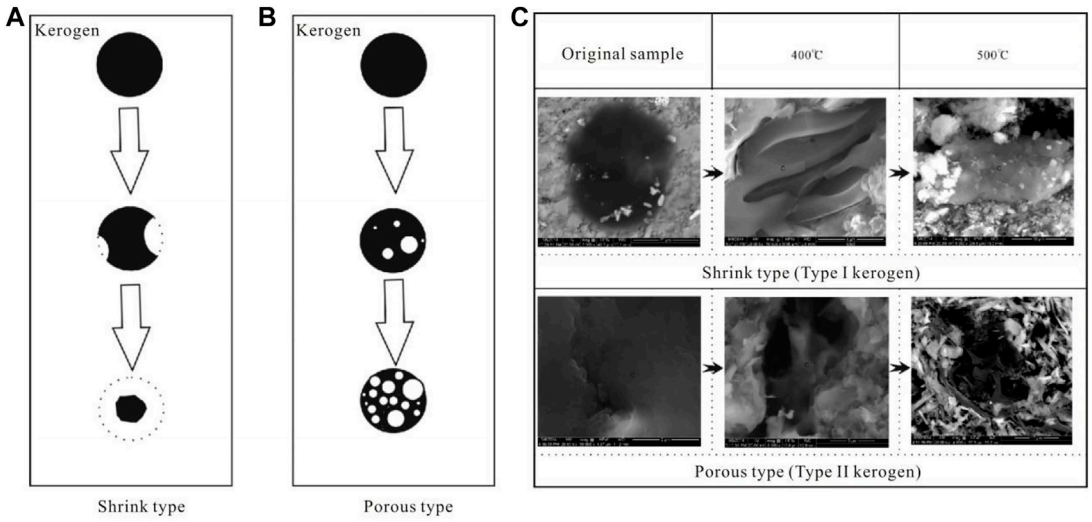

FIGURE 7
Evolution of organic matter morphology and organic matter pores (modified after Dong et al., 2015). Notes: **(A)** shrinkable organic matter; **(B)** porous organic matter; **(C)** thermal evolution mode of organic pores.

than −27‰, while that in the other crude oil samples are all heavier than −27.0‰. It reflects the characteristics that the crude oil in this area is dominated by higher plants and rich in heavy carbon isotopes (Loucks et al., 2009; Xiong et al., 2017; He et al., 2020).

3.3.1 Carbon isotopic characteristics of crude oil monomer hydrocarbons

Figure 5 shows the molecular isotopic distribution of 11 crude oils from the Middle and Lower Jurassic in the Yanqi Basin. It can be seen that the molecular isotope of C_{12}–C_{33} gradually becomes lighter with the increase of carbon number, and the $\delta^{13}C$ decreases from −20‰–23‰ to −27‰–34‰. Among them, the molecular isotope of one crude oil showed a slight difference in C_{30}, but the carbon isotope of the other molecules showed almost the same trend of decreasing isotopic mass with the increase of carbon number. The variation trend of the molecular carbon isotope of the crude oil further reveals a similar composition from the perspective of molecular composition (Lu et al., 2015; Wang et al., 2018; Yu et al., 2019; Li et al., 2022).

3.3.2 Distribution characteristics of carbon isotopes

Figure 6 is the molecular carbon isotope distribution of the possible source rocks (coal-measure mudstone, carbonaceous mudstone, and coal) in this area. The molecular carbon isotope distributions of the Triassic mudstones from Well Baonan1 are somewhat different from those of most samples, while the molecular carbon isotope distributions of most possible source rocks are basically the same. This fact indicates that the abovementioned possible source rocks share common original parental precursors (higher plants) and also reflects that they have common characteristics in carbon isotope fractionation and inheritance effects (Yang et al., 2010; Xu et al., 2019; Zou et al., 2019). Therefore, from the perspective of molecular isotope distribution, coal-measure mudstone, carbonaceous mudstone, and coal in this area have common source rocks for crude oil.

3.4 Biomarker composition characteristics of crude oil and various source rocks

3.4.1 Crude oil biomarkers

The tricyclic terpenes in the crude oil of the target layer are not developed, the pentacyclic triterpenes are generally $T_m > T_s$, and the 17α(H)-rearranged hopane is relatively developed, but the gammacerane is not developed. The sterane composition is generally dominated by C_{29} stigmasterane, and C_{29} sterane >> the sum of C_{27} sterane and C_{28} sterane, and rearranged sterane is not developed.

3.4.2 Biomarkers of coal-measure mudstone

The biological characteristics of the Middle–Lower Jurassic coal-measure mudstone in this area are relatively complex. The coal-measure mudstone biomarker is represented by Well Yancan1 (3,248.5 m, Badaowan Formation), and its main features are as follows: $T_m >> T_s$, gammacerane is extremely undeveloped. Both C_{29}

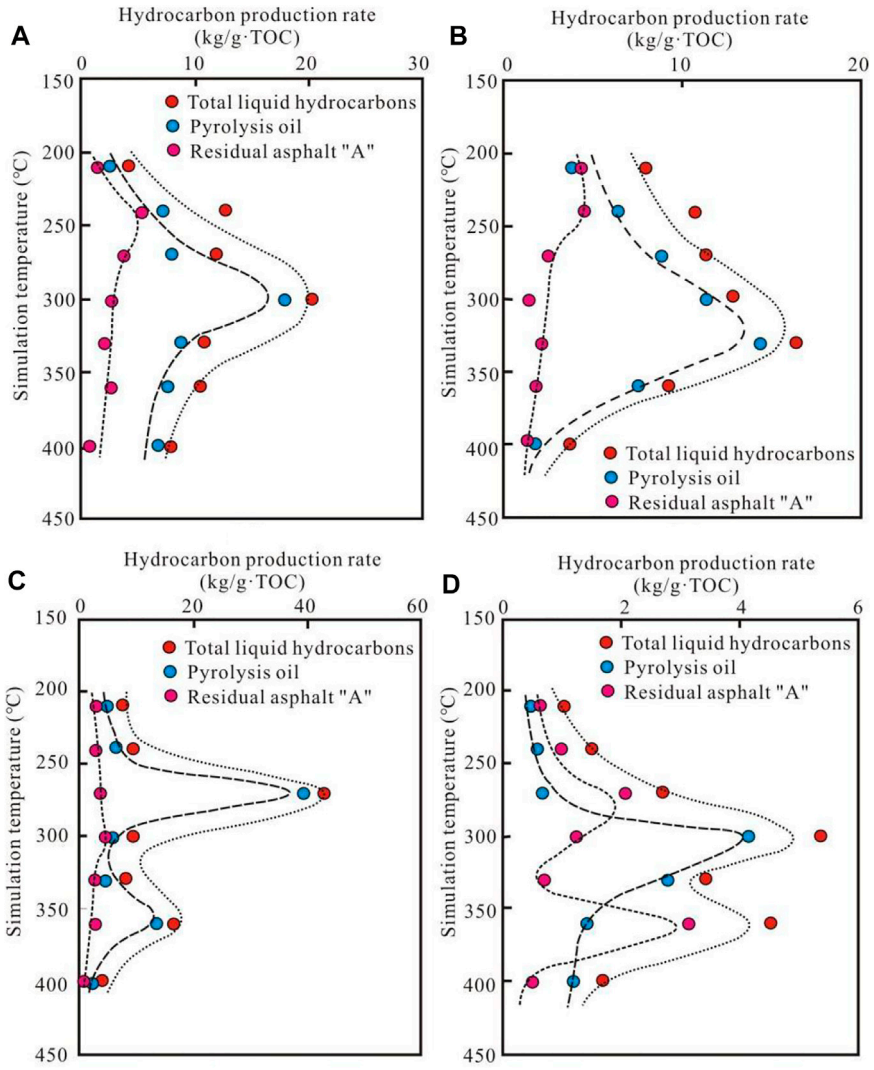

FIGURE 8
Yields of liquid hydrocarbons in thermal pressure simulations of coal rocks, carbonaceous mudstones, and coal-measure mudstones in the Middle and Lower Jurassic in the study area. Notes: **(A)** Well Ma 1, dark gray mudstone; **(B)** Well Yannan 1, dark gray mudstone; **(C)** Hua'an Coal Mine, coal; **(D)** Well Yan 2, carbonaceous mudstone.

nornehopanes ($C_{29}T_s$) and C_{30} rearranged hopanes are less developed, and C_{29} norhopanes are relatively developed. Due to the development of C_{29} normotane in this type of rock, its corresponding normotane is also relatively developed, which is also one of the biomarker characteristics of this type of coal-measure mudstone.

3.4.3 Biomarkers of carbonaceous mudstone

There are two biological characteristics of carbonaceous mudstone. One is that the C_{29} norhopane is larger than the C_{30} hopane, and the corresponding C_{29} hopane is also relatively developed. When T_m>>T_s, the gamma pole is not developed, reflecting the characteristics of freshwater deposition. Another characteristic is as follows: when C_{30} hopane>C_{29} norhopane, the corresponding C_{29} nornehopane (C_{29}Ts), and C30 rearranged hopane are relatively developed, and gammacerane is still very low.

3.4.4 Biomarkers of coal

The biomarker characteristics of coal are basically the same as those of carbonaceous mudstone, and there are also two types: one is C_{30} hopane>C_{29} hopane, T_m>>T_s, gammacerane is extremely undeveloped, such as the 2767 m (Badaowan Formation) coal of the Well Bonan 1; the other is C_{29} norhopane>C_{30} hopane, T_m>>T_s, gammacerane is also very

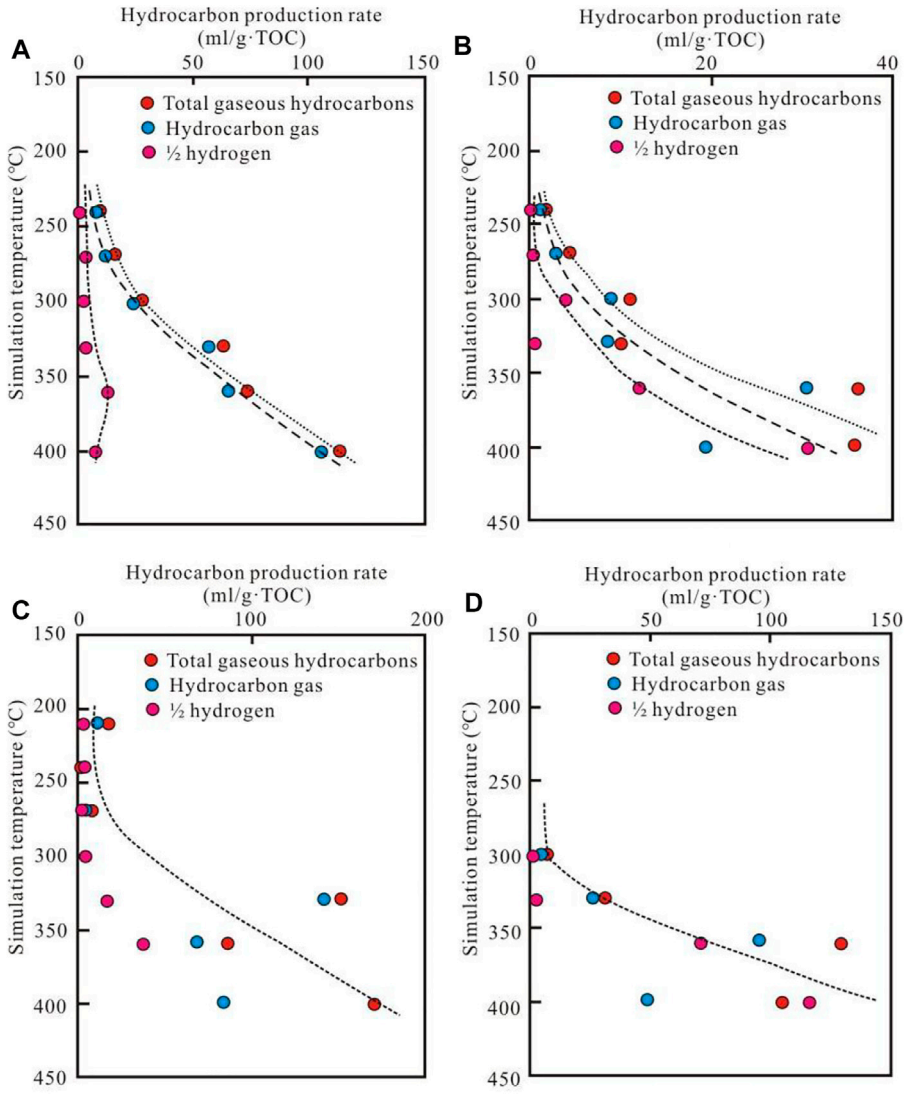

FIGURE 9
Test results of gaseous hydrocarbon yields from thermal pressure simulations of coal rocks, carbonaceous mudstones, and coal-measure mudstones in the study area in the Middle and Lower Jurassic. Notes: **(A)** Hua'an Coal Mine, coal; **(B)** Well Yan 2, carbonaceous mudstone; **(C)** Well Ma 1, dark gray mudstone; **(D)** Well Yannan 1, dark gray mudstone.

underdeveloped, such as the coal of 2392 m (Badaowan Formation) of the Well Cheng 1.

4 Discussion

4.1 Liquid hydrocarbon yields for thermal-pressure simulations

The thermal evolution of hydrocarbon generation is different for different types of kerogens (Dong et al., 2015). According to the previous research results, when the kerogen type is Type I, the organic matter is gnawed on the edge or inside, and the surface of the pores is smooth. When the volume of kerogen shrinks, then the marginal pores of organic matter will form. They belong to the shrinkage type (Figure 7A). When the kerogen is Type III, the total volume of the organic matter is basically unchanged. The interior of the samples is dominated by the formation of internal pores of organic matter (porous type) (Figure 7B). When the kerogen is Type II, the morphological evolution characteristics of organic matter are between Types I and III, and both marginal pores and internal pores of organic matter are developed. With

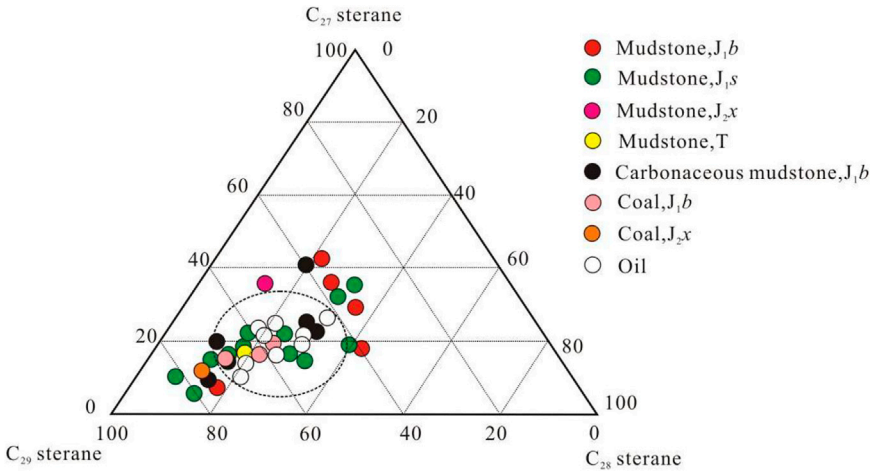

FIGURE 10
Triangular diagram of the composition of crude oil and related steranes in the Middle and Lower Jurassic in the study area.

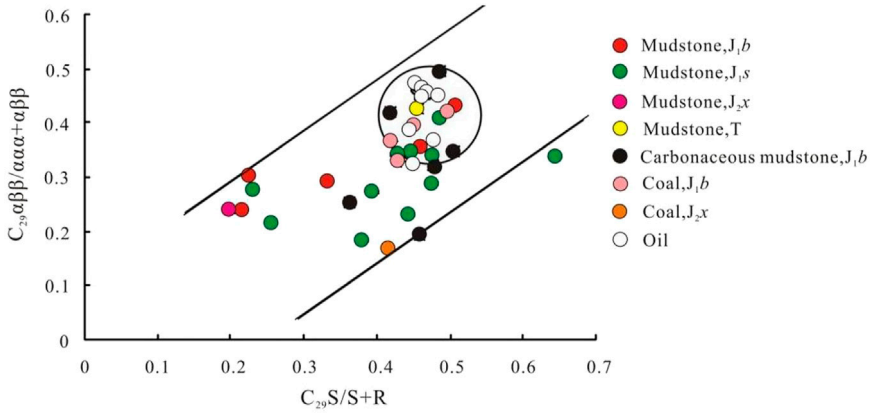

FIGURE 11
Relationship between crude oil and related sterane isomerization parameters in the Middle and Lower Jurassic in the study area.

the increase of the simulated temperature, the organic matter edge pores and the organic matter internal pores continue to increase (Figure 7C). The organic matter pores generated by the kerogen pyrolysis hydrocarbon generation are one of the main reasons for the increase in the internal storage space of mudstone (Cai et al., 2008).

4.1.1 Liquid hydrocarbon yield of coal-measure mudstone

The thermal-pressure simulation results of coal-measure mudstone in the Yanqi Basin show that the peak of liquid hydrocarbon generation occurs in the simulated temperature range of 300–340°C, and the R_o value is 0.89–1.22%. It is close to the peak of hydrocarbon generation in the natural evolution of organic matter, indicating that the simulation conditions of low temperature, water content, and long-term thermal pressure are close to the actual underground conditions (Guo et al., 2012). The peak value of chloroform bitumen "A" in the residue appears at the simulated temperature of 210–240°C, and the R_o value is 0.72%–0.78% at this time, which also indicates that there are some early hydrocarbon-generating substances in this type of source rocks. The appearance of the peak value indicates the existence of some early hydrocarbon-generating substances. These substances include resin and matrix vitrinite in the Jurassic coal-measure mudstone with higher plants as the main organic parent material.

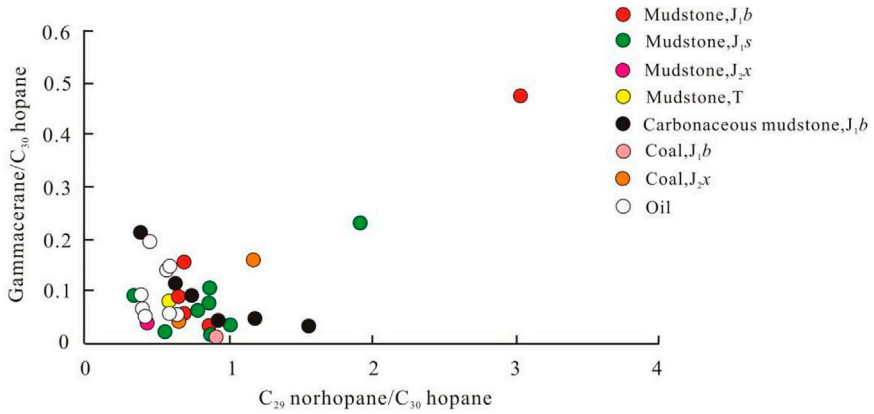

FIGURE 12
Relationship between gammacerane/C_{30} hopane and C_{29} norhopane/C_{30} hopane in Middle and Lower Jurassic crude oil and source rocks in the study area.

The highest liquid hydrocarbon production rate of the dark gray mudstone of the Badaowan Formation in Well Ma1 is 20.4 mg/gTOC, and the maximum liquid hydrocarbon production rate of dark gray mudstone of the Xishanyao Formation in Well Bonan 1 is 16.4 mg/gTOC. Compared with lacustrine mudstone, the liquid hydrocarbon yield in coal measure is not high. However, due to the high abundance of organic matter in coal-measure mudstone, its liquid hydrocarbon production rate is still considerable. On the other hand, it shows that the production rate of liquid hydrocarbons in the source rocks of the Xishanyao Formation in this area is generally lower than that of the mudstones of the Badaowan Formation (Figure 8).

4.1.2 Liquid hydrocarbon yield of carbonaceous mudstone

For the thermo-pressure simulations of carbonaceous mudstone, both total liquid hydrocarbons and residual chloroform "A" showed a distinct bimodal distribution, that is, there are two peaks of hydrocarbon generation between 240 and 300°C and 360°C, the R_o value of the former is 0.8%–0.9%, and the R_o value of the latter is 1.31%. It reflects that the parental composition of the source rock is relatively complex. However, from the change of the pyrolysis oil yield curve, the main peak is still at 300°C, and the R_o value is 0.9%. In the high evolution stage (R_o>1.3%) of carbonaceous mudstone, the residual bitumen "A" and total hydrocarbons still show a peak of hydrocarbon generation, which may be closely related to the adsorption of hydrocarbons by carbonaceous mudstone.

Although the change of the liquid hydrocarbon production curve of carbonaceous mudstone is complicated, the highest total liquid hydrocarbon production rate is only 5.36 mg/gTOC, which is much lower than that of mudstone and coal in this area. It shows that although the carbonaceous mudstone in this area has a high abundance of organic matter, its hydrocarbon generation rate is not high due to the poor type of parent material (Figure 8).

4.1.3 Liquid hydrocarbon yield of coal rock

The residual chloroform bitumen "A" and the total liquid hydrocarbon yield of the coal rock have bimodal distribution characteristics. The two peaks are located in 270°C and 360°C, respectively, and the corresponding R_o values are 0.68% and 1.70%, respectively. Obviously, the appearance of the peak of liquid hydrocarbons at 270°C is the contribution of early hydrocarbon-generating substances such as resin body, suberite, and matrix vitrinite in coal rock. The appearance of the peak of liquid hydrocarbon generation at 360°C may be due to the release of the adsorbed and encapsulated parts in the coal rock under high temperature conditions.

The yield of coal and rock pyrolysis oil is generally 2–3 mg/gTOC. The highest value appears at the temperature step of 300°C. At this time, the R_o value was 0.8%, and the pyrolysis oil yield was 5.2 mg/gTOC. It shows that the hydrocarbon generation potential of coal is equivalent to that of carbonaceous mudstone only by the yield of pyrolysis oil (Jiang et al., 2015).

It is worth mentioning that the total liquid hydrocarbon yield of the Xishanyao Formation coal rock in the Hua'an Coal Mine is as high as 43.2 mg/gTOC, which is double the total liquid hydrocarbon yield of the general Middle–Lower Jurassic coal measure mudstone in the Yanqi Basin. Moreover, the content of residual chloroform bitumen "A" in coal rock is also as high as 3%, which is close to the hydrocarbon expulsion threshold of coal. The total liquid hydrocarbon production rate of coal rocks

further supports that the Middle and Lower Jurassic coal rocks in this area can generate a certain quantity of liquid hydrocarbons, and some of them have approached or reached the threshold hydrocarbon concentration for coal rocks to expel liquid hydrocarbons (Figure 8).

The comparison results of the total liquid hydrocarbon production rate show that the Jurassic coal rock in the Yanqi Basin has the highest rate (43.2 mg/gTOC), followed by mudstone (16.4–20.4 mg/gTOC), and the carbonaceous mudstone has the lowest (the maximum liquid hydrocarbon production rate is only 5.36 mg/g TOC).

4.2 Gaseous hydrocarbon yield from thermal-pressure simulations

Figure 9 shows the gaseous hydrocarbon thermo-pressure simulation results of the four samples conducted in this study.

4.2.1 Gaseous hydrocarbon yield of coal rock

In Figure 9, the gaseous hydrocarbon yield chart of the coal rock of the Hua'an Coal Mine consists of three curves. One is the change in the yield of hydrocarbon gas with the increase of thermal maturity during the thermal evolution of organic matter. The other is that during the thermal evolution of organic matter, some free hydrogen can be generated due to thermal degradation of kerogen or thermal cracking of heavy hydrocarbons, condensation of aromatic hydrocarbons, or cyclization of paraffins. Since this part of hydrogen comes from organic matter, this study divides its volume by 2 and converts it into the hydrogen fraction of methane and calculates it as hydrocarbons. The third part is the sum of hydrocarbon gases and hydrogen.

The general trend of the change of gaseous hydrocarbon yield in the coal seam of the Hua'an Coal Mine is that it increases with the simulated temperature recovery. The highest gaseous yield in the high-maturity stage is 110.9 ml/g.TOC.

4.2.2 Gaseous hydrocarbon yield of carbonaceous mudstone

In Figure 9, the thermal pressure simulation gaseous hydrocarbon yield of the carbonaceous mudstone in the Sangonghe Formation in Well Yan2 shows that the gaseous hydrocarbon yield of the carbonaceous mudstone in this area is only 36.8 ml/gTOC in the wet gas-condensate stage (R_o is 1.31%). Its gas production is not high.

4.2.3 Gaseous hydrocarbon yield of coal measure mudstone

In Figure 9, the dark gray mudstone of the Badaowan Formation in Well Ma 1 has a gaseous hydrocarbon production rate of 171.6 ml/gTOC when R_o is 1.37%. Also, the dark gray mudstone of the Xishanyao Formation in Well Baoan1 has the highest gaseous hydrocarbon yield of 130.9 ml/gTOC when R_o reaches 1.42%.

In conclusion, the gaseous hydrocarbon yield per unit of organic carbon in source rocks is highest in mudstone, followed by coal rock, and lowest in carbonaceous mudstone.

4.3 Oil source comparison and analysis

Based on the comprehensive analysis of the carbon isotope, molecular carbon isotope, and biomarker characteristics of crude oil and various source rocks, this study focused on a direct oil/rock comparison using biomarkers such as steranes and terpenes.

4.3.1 Triangular diagram of C_{27}, C_{28}, and C_{29} regular sterane compositions

Figure 10 is a triangular diagram of regular sterane compositions of crude oil and various possible source rocks in this area. It can be seen from Figure 10 that in the affinity circle with crude oil as the core, there are coal-measure mudstone, carbonaceous mudstone, and coal together to form the affinity circle. There is also a considerable amount of mudstone, carbonaceous mudstone, and coal outside this phylogenetic circle. This result indicates that the Middle and Lower Jurassic crude oil series in the Yanqi Basin come from mudstone, carbonaceous mudstone, and coal in this area. The Middle and Lower Jurassic crude oil is not a single oil source but a mixed source oil of the abovementioned three lithologies. It should be noted that, according to the comparison results of the regular sterane composition triangle, coal-measure mudstone, carbonaceous mudstone, and coal all contribute to the source of oil and gas in this area. However, this does not mean that all coal-measure mudstone, carbonaceous mudstone, and coal are source rocks in this area. They are effective source rocks only when they reach the source rock standard in terms of organic matter abundance, hydrocarbon-forming parent material type, and thermal evolution degree.

4.3.2 Relationship between sterane C_{29}αββ/ααα+αββ and sterane C_{29}20S/20S+20R

It is generally believed that sterane C_{29}αββ/ααα+αββ should increase in a linear relationship with sterane C_{29}20S/20S+20R. In the case of self-generation and self-storage reservoirs, the abovementioned parameter distribution of oil/rock should follow a linear relationship. Conversely, in the case of secondary migration reservoirs, the abovementioned parameters do not follow a linear relationship but are far from the range of a linear relationship. From Figure 11, it can be seen that the Middle and Lower Jurassic reservoirs in this area should be self-generating and self-storing oil reservoirs. Also, it also shows that some coal-measure mudstone, carbonaceous mudstone, and coal should be its possible source rocks because, in the vicinity of crude oil, some coal-measure mudstone, carbonaceous mudstone, and coal together form a small-diameter affinity circle. From the

perspective of similarity comparison, some of these rocks should be the source rocks in this area.

4.3.3 Comparison of oil sources of terpanes

Figure 12 shows the relationship between gammacerane content and C_{29} norhopane content in representative crude oil and related coal-measure mudstone, carbonaceous mudstone, and coal in this area. The crude oil in the target layer is basically distributed in the range of C_{29} norhopane/C_{30} hopane<1.0 and Gammacerane/C_{30} hopane<0.2. It forms a small-diameter affinity circle with some coal-measure mudstone, carbonaceous mudstone, and coal in this area. Various kinds of rock in the circle are very likely to be the main source rocks in this area.

Overall, according to the molecular carbon isotopic characteristics of crude oil, the Jurassic crude oil in the coal measure of the study area has a certain affinity with its corresponding source rocks (mudstone, carbonaceous mudstone, and coal rock). At the same time, according to the comparison results of steroid and terpene biomarkers and crude oil, the Middle and Lower Jurassic mudstone, carbonaceous mudstone, and coal rock in this area are all source rocks. There is no doubt that the Badaowan Formation mudstone is the main source rock.

5 Conclusion

1) The micro-composition of the Jurassic coal rocks in the Yanqi Basin shows the characteristics of rich vitrinite–inertinite and poor chitinite + saprolite; however, the micro-composition of the mudstone shows the characteristics of poor inertinite and rich vitrinite–chitinite + saprolite.
2) The Jurassic mudstone has a wide distribution range of hydrogen and oxygen indexes, among which the hydrogen index is distributed between 2 and 266 mg/gTOC and the oxygen index is between 3 and 183 mg/gTOC. The organic matter in the mudstone belongs to Type II_2–III kerogen.
3) The hydrogen index of coal is distributed in the range of 100–300 mg/gTOC, which is obviously larger than that of mudstone. The total liquid hydrocarbon yield of the coal rock is the highest (43.2 mg/gTOC), followed by mudstone (16.4–20.4 mg/gTOC), and carbonaceous mudstone is the lowest (5.36 mg/gTOC). In addition, mudstone has the highest yield of gaseous hydrocarbons, followed by coal, while carbonaceous mudstone is the lowest.
4) The oil-source comparison shows that the Jurassic crude oil has a certain affinity with its main source rocks (mudstone, carbonaceous mudstone, and coal). At the same time, according to the comparison results of steroid and terpene biomarker parameters with crude oil, it shows that the Middle and Lower Jurassic mudstone, carbonaceous mudstone, and coal rock in this area are all source rocks and the Badaowan Formation mudstone is the main source rock.

Data availability statement

The original contributions presented in the study are included in the article/Supplementary Material; further inquiries can be directed to the corresponding authors.

Author contributions

YY is responsible for the idea of this paper. FZ, JZ, and JZ are responsible for the experiments.

Funding

This research was funded by the Natural Science Foundation of Xinjiang Uygur Autonomous Region—Surface Project (2019D01A34) “Accumulation Mechanism, Occurrence Characteristics and Basin Dynamics Environment of Shale (Stratification) Gas Source-Reservoir Complex”.

Conflict of interest

The authors declare that the research was conducted in the absence of any commercial or financial relationships that could be construed as a potential conflict of interest.

Publisher’s note

All claims expressed in this article are solely those of the authors and do not necessarily represent those of their affiliated organizations, or those of the publisher, the editors, and the reviewers. Any product that may be evaluated in this article, or claim that may be made by its manufacturer, is not guaranteed or endorsed by the publisher.

References

Cai, J., Wang, H., and Zhao, Z. (2008). Formation process and dynamic mechanism of Bohu depression in Yanqi Basin. *Earth Sci. J. China Univ. Geosciences* 33 (4), 555–563.

Curtis, M., Cardott, B., Sondergeld, C., and Rai, C. (2012). Development of organic porosity in the Woodford Shale with increasing thermal maturity. *Int. J. Coal Geol.* 103, 26–31. doi:10.1016/j.coal.2012.08.004

Dong, C., Ma, C., Luo, G., Lin, C., Zhang, X., and Ren, L. (2015). Late pyrolysis simulation experiment and diagenesis evolution pattern of shale. *ACTA SEDIMENTOL. SIN.* 33 (5), 1053–1061. doi:10.14027/j.cnki.cjxb.2015.05021

Gai, S., Liu, H., He, S., Mo, S., Chen, S., Liu, R., et al. (2016). Shale reservoir characteristics and exploration potential in the target: A case study in the longmaxi formation from the southern sichuan basin of China. *J. Nat. Gas Sci. Eng.* 31, 86–97. doi:10.1016/j.jngse.2016.02.060

Guo, J., Pang, X., and Liu, D. (2012). In the middle and lower Jurassic in Kuche depression, Jurassic coal measure hydrocarbon expulsion characteristics and resource potential evaluation. *Nat. Gas. Geosci.* 23 (2), 327–334.

Guo, W., Liu, H., Xue, H., Lan, C., and Tang, X. (2015). Depositional facies of permian Shanxi formation gas shale in the Northern Ordos Basin and its impact on shale reservoir. *Acta Geol. Sin.* 89 (5), 931–941.

He, D., Li, D., and He, J. (2013). Petroleum geology and exploration enlightenment analogy of kuche depression in Tarim basin and the southwest Tarim depression. *Acta Pet. sin.* 34 (2), 201–218.

He, X., Zhang, P., He, G., Gao, Y., Liu, M., Zhang, Y., et al. (2020). Evaluation of sweet spots and horizontal-well-design technology for shale gas in the basin-margin transition zone of southeastern Chongqing, SW China. *Energy Geosci.* 1 (3–4), 134–146. doi:10.1016/j.engeos.2020.06.004

Jiang, S., Xu, Z., Feng, Y., Zhang, J., Cai, D., Chen, L., et al. (2015). Geologic characteristics of hydrocarbon-bearing marine, transitional and lacustrine shales in China. *J. Asian Earth Sci.* 115, 404–418. doi:10.1016/j.jseaes.2015.10.016

Li, D. (2000). The progress in the petroleum geology of China towards new century. *Acta Pet. sin.* 21 (2), 1–8.

Li, H. (2022). Research progress on evaluation methods and factors influencing shale brittleness: A review. *Energy Rep.* 8, 4344–4358. doi:10.1016/j.egyr.2022.03.120

Li, H., Qin, Q. R., Zhang, B. J., Ge, X. Y., Hu, X., Fan, C. H., et al. (2020). Tectonic fracture formation and distribution in ultradeep marine carbonate gas reservoirs: A case study of the maokou Formation in the jiulongshan gas field, sichuan basin, southwest China. *Energy fuels.* 34 (11), 14132–14146. doi:10.1021/acs.energyfuels.0c03327

Li, H., Tang, H. M., Qin, Q. R., Zhou, J. L., Qin, Z. J., Fan, C. H., et al. (2019). Characteristics, formation periods and genetic mechanisms of tectonic fractures in the tight gas sandstones reservoir: A case study of xujiahe Formation in YB area, sichuan basin, China. *J. Petroleum Sci. Eng.* 178, 723–735. doi:10.1016/j.petrol.2019.04.007

Li, H., Wang, Q., Qin, Q. R., and Ge, X. Y. (2021). Characteristics of natural fractures in an ultradeep marine carbonate gas reservoir and their impact on the reservoir: A case study of the maokou formation of the JLS structure in the sichuan basin, China. *Energy fuels.* 35 (16), 13098–13108. doi:10.1021/acs.energyfuels.1c01581

Li, J., Li, H., Yang, C., Wu, Y. J., Gao, Z., and Jiang, S. L. (2022). Geological characteristics and controlling factors of deep shale gas enrichment of the Wufeng-Longmaxi Formation in the southern Sichuan Basin, China. *Lithosphere* 2022, 4737801. doi:10.2113/1970/4737801

Lin, A., Fu, B., Kano, K., Maruyama, T., and Guo, J. (2002). Late Quaternary right-lateral displacement along active faults in the Yanqi Basin, southeastern Tian Shan, northwest China. *Tectonophysics* 354, 157–178. doi:10.1016/s0040-1951(02)00288-3

Loucks, R., Reed, R., Ruppel, S., and Jarvie, D. (2009). Morphology, genesis, and distribution of nanometer-scale pores in siliceous mudstones of the mississippian barnett shale. *J. Sediment. Res.* 79, 848–861. doi:10.2110/jsr.2009.092

Lu, J., Ruppel, S. C., and Rowe, H. D. (2015). Organic matter pores and oil generation in the Tuscaloosa marine shale. *Am. Assoc. Pet. Geol. Bull.* 99, 333–357. doi:10.1306/08201414055

Wang, G., Ju, Y., Yan, Z., and Li, Q. (2015). Pore structure characteristics of coal–bearing shale using fluid invasion methods: A case study in the huainan–huaibei coalfield in China. *Mar. Petroleum Geol.* 62, 1–13. doi:10.1016/j.marpetgeo.2015.01.001

Wang, P., Chen, Z., Jin, Z., Jiang, C., Jia, Z., Guo, Y., et al. (2018). Shale oil and gas resources in organic pores of the Devonian Duvernay Shale , Western Canada Sedimentary Basin based on petroleum system modeling. *J. Nat. Gas. Sci. Eng.* 50, 33–42. doi:10.1016/j.jngse.2017.10.027

Xiong, F., Jiang, Z., Li, P., Wang, X., Bi, H., Li, Y., et al. (2017). Pore structure of transitional shales in the Ordos Basin, NW China: Effects of composition on gas storage capacity. *Fuel* 206, 504–515. doi:10.1016/j.fuel.2017.05.083

Xu, H., Zhou, W., Zhang, R., Liu, S., and Zhou, Q. (2019). Characterizations of pore, mineral and petrographic properties of marine shale using multiple techniques and their implications on gas storage capability for Sichuan Longmaxi gas shale field in China. *Fuel* 241, 360–371. doi:10.1016/j.fuel.2018.12.035

Yang, C., Zhang, J., Tang, X., Ding, J., Zhao, Q., Dang, W., et al. (2016). Comparative study on micro-pore structure of marine, terrestrial, and transitional shales in key areas, China. *Int. J. Coal Geol.* 171, 76–92. doi:10.1016/j.coal.2016.12.001

Yang, H., Li, S. X., and Liu, X. Y. (2010). Characteristics and resource prospects of tight oil and shale oil in Ordos Basin. *Acta Pet. Sin.* 34 (1), 1–11.

Yao, Y., Liu, C., and Zhao, Z. (2003). Tectonic evolution and hydrocarbon accumulation in Yanqi Basin. *Petroleum Geol. Xinjiang* 24 (2), 115–117.

Yao, Y., Zhang, Y., and Fu, D. (2004). Relationship between the formation of paleo geotemperature and oil and gas in Bohu depression of Yanqi Basin. *Petroleum Explor. Dev.* 31 (1), 24–27.

Yu, K., Shao, C., Ju, Y., and Qu, Z. (2019). The Genesis and controlling factors of micropore volume in transitional coal-bearing shale reservoirs under different sedimentary environments. *Mar. Petroleum Geol.* 102, 426–438. doi:10.1016/j.marpetgeo.2019.01.003

Zhang, H., Wang, R., and Jin, B. (2011). Jurassic hydrocarbon accumulation model in Bohu depression, Yanqi Basin, Xinjiang. *Petroleum Geol. Xinjiang* 32 (6), 613–615.

Zhao, W., Hu, S., Wang, H., Bian, C., Wang, Z., and Wang, Z. (2013). Large-scale accumulation and distribution of medium-low abundance hydrocarbon resources in China. *Petroleum Explor. Dev.* 40 (1), 1–14. doi:10.1016/s1876-3804(13)60001-4

Zou, C. N., Zhu, R. K., Chen, Z. Q., Ogg, J. G., Wu, S. T., Dong, D. Z., et al. (2019). Organic-matter-rich shales of China. *Earth-Science Rev.* 189, 51–78. doi:10.1016/j.earscirev.2018.12.002

frontiers | Frontiers in Earth Science

TYPE Original Research
PUBLISHED 06 September 2022
DOI 10.3389/feart.2022.1013776

OPEN ACCESS

EDITED BY
Wenlong Ding,
China University of Geosciences, China

REVIEWED BY
Peng Wang,
Yibin University, China
Liu Chang,
China National Offshore Oil Corporation, China

*CORRESPONDENCE
Jianbo Liao,
liao_jb@126.com

SPECIALTY SECTION
This article was submitted to Structural Geology and Tectonics, a section of the journal Frontiers in Earth Science

RECEIVED 07 August 2022
ACCEPTED 15 August 2022
PUBLISHED 06 September 2022

CITATION
Liao J, Hong L, Li Z, Tan K, Zhao L, Yang J and Yu P (2022), Characterization of ultra-low permeability tight sandstone reservoir properties and criteria for hydrocarbon accumulation in Chang 6 member, Huaqing area, Ordos basin. *Front. Earth Sci.* 10:1013776. doi: 10.3389/feart.2022.1013776

Characterization of ultra-low permeability tight sandstone reservoir properties and criteria for hydrocarbon accumulation in Chang 6 member, Huaqing area, Ordos basin

Jianbo Liao[1,2]*, Liang Hong[1], Zhiyong Li[1,2], Kaijun Tan[1], Leyi Zhao[3], Jun Yang[3] and Pinghui Yu[1]

[1]Research Institute of Petroleum Exploration and Development Northwest Branch, Lanzhou, China, [2]Key Laboratory of Reservoir Description, CNPC, Lanzhou, China, [3]Exploralion & Development, PetroChina Yunmen Oil field Company, Jiuquan, China

How to accurately predict hydrocarbon enrichment and high-yield areas in ultra-low permeability sandstone reservoirs is a hot spot in petroleum geology. Taking the Chang 6 Member of the Yanchang Formation in the Huaqing Area, Ordos Basin as an example, the quantitative characterization and classification criteria of ultra-low permeability sandstone reservoir properties are systematically studied. The research results show that the seismic reflection characteristics of the Chang 6 Member show multi-stage wedge progradation characteristics, reflecting the sedimentary characteristics of the end of the delta front. The maturity of the minerals in the Chang 6 Member sandstones in the study area is very low, it indicates a low degree of transformation of sediments. Three types of sand bodies, namely sandy debris flow, turbidite, and slump rock sand bodies, were identified in the Chang 6 Member of the Yanchang Formation. The pore types of the Chang 6 Member in the study area include intergranular pores, dissolution pores (feldspar, detrital dissolution pores), and intercrystalline pores. Among them, the intergranular pores and feldspar dissolution pores are the most important storage spaces. The study also found that the test oil production is highly correlated with the cumulative thickness of the massive sandstone segments. Therefore, massive sandstone (sand debris flow) is the main contributor to oil well production, and its distribution directly controls the accumulation of oil reservoirs and the high production of oil wells. In addition, geological parameters affecting reservoir enrichment evaluation were analyzed, which include permeability, oil layer thickness, resistivity, and reservoir penetration rate. Finally, the evaluation criteria for hydrocarbon enrichment in the Chang 6 Member were formulated by the analysis of dominant facies, lithologic assemblages and electrical properties.

KEYWORDS

ultra-low permeability sandstone, chang 6 member, yanchang formation, lithologic combination, evaluation index

1 Introduction

A large amount of tight sandstone oil resources are present in the Yanchang Formation in the Ordos Basin, China. With the deepening of oil and gas exploration and production, relatively high-quality reserves have been utilized to a high degree. Furthermore, the proportion of low-grade hydrocarbon-bearing blocks in untapped geological reserves is increasing. The exploration and development of ultra-low permeability reservoirs with permeability less than 1 millidarcy has become an important part of the rapid growth of reserves and production in the Yanchang Formation (He et al., 2008; Huang et al., 2019; Wang et al., 2022).

The permeability range of ultra-low permeability reservoirs is less than 1.0 mD (Yang et al., 2010; Li et al., 2013; Li, 2022). How to predict high-yield areas in ultra-low permeability sandstone reservoirs has become the focus of attention. In this paper, taking the Chang 6 Member of the Yanchang Formation in the Huaqing Area, Ordos Basin as an example, the quantitative characterization and classification criteria of ultra-low permeability sandstone reservoir properties are systematically studied. This study can provide a reference for formulating reasonable tight sandstone oil reservoir development strategies.

2 Geological background

The Huaqing Oilfield is located in the southwest part of the Ordos Basin (Figure 1). The surface of this area is covered by the Quaternary loess with a thickness of 100–200 m. The surface elevation is 1350–1660 m, and the relative height difference is about 310 m. The proven reserves of the Chang 6 reservoir in the Huaqing Oilfield have reached 500 million tons, with a total resource scale of nearly 1 billion tons. Therefore, the development prospect of its

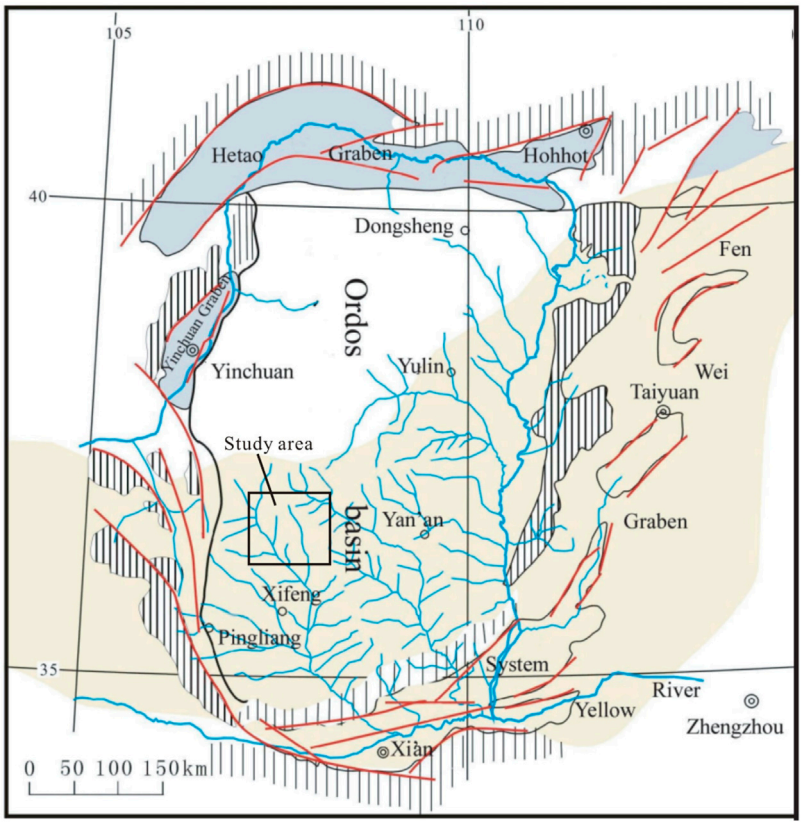

FIGURE 1
Geographical location of the Huaqing area (Liu et al., 2009).

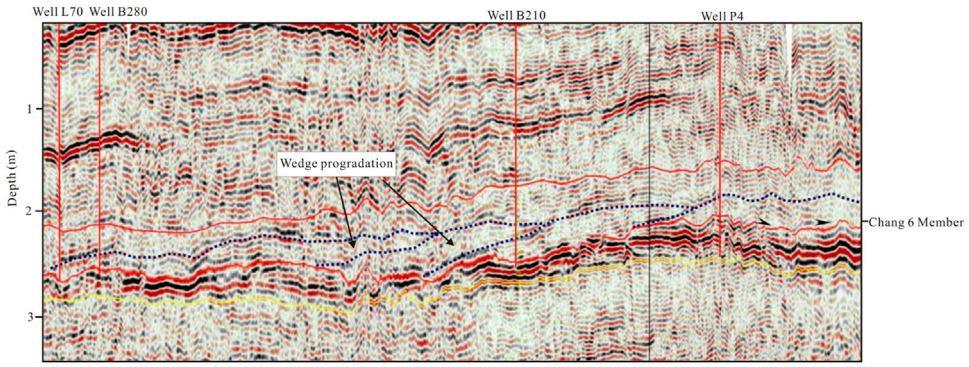

FIGURE 2
A seismic profile passing through Wells L70 and P4 of the study area.

petroleum resources is very broad. There are 121 industrial oil flow wells in the study area, the average oil layer thickness is 10.8 m, the average porosity is 11%, and the average permeability is 0.52 mD. In addition, the average oil test output of a single well is 11.8 t/d, and the daily oil production of the highest producing oil well can reach 119.85 t/d.

3 Databases and methods

Core observation was carried out on 50 drilling cores (about 1100 m in length) in the study area. Physical properties, X-ray diffraction and cast thin sections were tested on the collected samples. The physical property experiments were used to test the porosity and permeability of the samples. The X-diffraction experiments used a Japanese Rigaku DMAX2500X diffractometer. Its 2θ angle measurement range: 10° ~ +154°; scanning step: 0.002°–90° (2θ/θ scanning); 0.001°–90° (2θ scanning); scanning speed: 0.002–100°/min (2θ/θ scan); 0.001°–100°/min (2θ scan). The cast thin section experiments were done with polarized light microscopes, and they were then used to observe the mineral composition, contact relationship, and pore structures within the rock samples. In addition, the petroelectric data and oil testing data of the reservoir were used to analyze the influencing factors of hydrocarbon enrichment.

Based on the comprehensive study of the seismic, geology and well logging, we identified three types of sediment gravity flow and traction bottom flow for the first time in the Chang 6 Member of the Yanchang Formation in Huaqing area, namely, sandy clastic flow, classical turbidite and slump rock sandbodies. Among them, the massive sandy clastic flow is the main oil-bearing reservoir, and the multi-stage vertical superposition constitutes the skeleton sand body of the ultra-low permeability and thick reservoirs.

4 Results

4.1 Sedimentary characteristics of the chang 6 member

It can be seen from the seismic profile that the Yanchang Formation in the study area is relatively flat (Figure 2). For the area near the center of the basin, the Chang 6 Member show multi-stage wedge progradation characteristics, reflecting the sedimentary characteristics of the end of the delta front. The sedimentary slope formed by rapid accumulation provides a prerequisite for the formation of gravity flow slumps.

On the seismic profile, the superposition of the two wedges can be found, which is located at the junction of the end of the delta front and the tail of the gravity flow slump. The event axis reflection in the lower part of the transition zone is clear and continuous. It has a strong lithologic differentiation and can reflect the delta front facies (Liu et al., 2009; Asante-Okyere et al., 2021). However, the reflection of the upper event axis is relatively blurred and internally disordered, showing mixed lithology and strong heterogeneity. It represents the reflection characteristic of the gravitational flow slump facies (Katz et al., 2021; Vafaie et al., 2021; Jiang et al., 2022).

The approximate location of the slope break zone can be determined intuitively by observing the cores of the coring wells on both sides of the slope break. A total of 1100 m of cores were used for core observations. The sedimentary mechanisms of delta front and slump gravity flow are different, which leads to the great differences in the characteristics of their sedimentary structures. The scouring phenomenon of the delta front is obvious, and most of them have the characteristics of tractive flow deposits such as parallel and oblique beddings with coarse lithology (Figure 3). The color of the delta front deposits is mainly light gray or grayish white. However, the slump gravity flow has the characteristics of rapid deposition such as slump

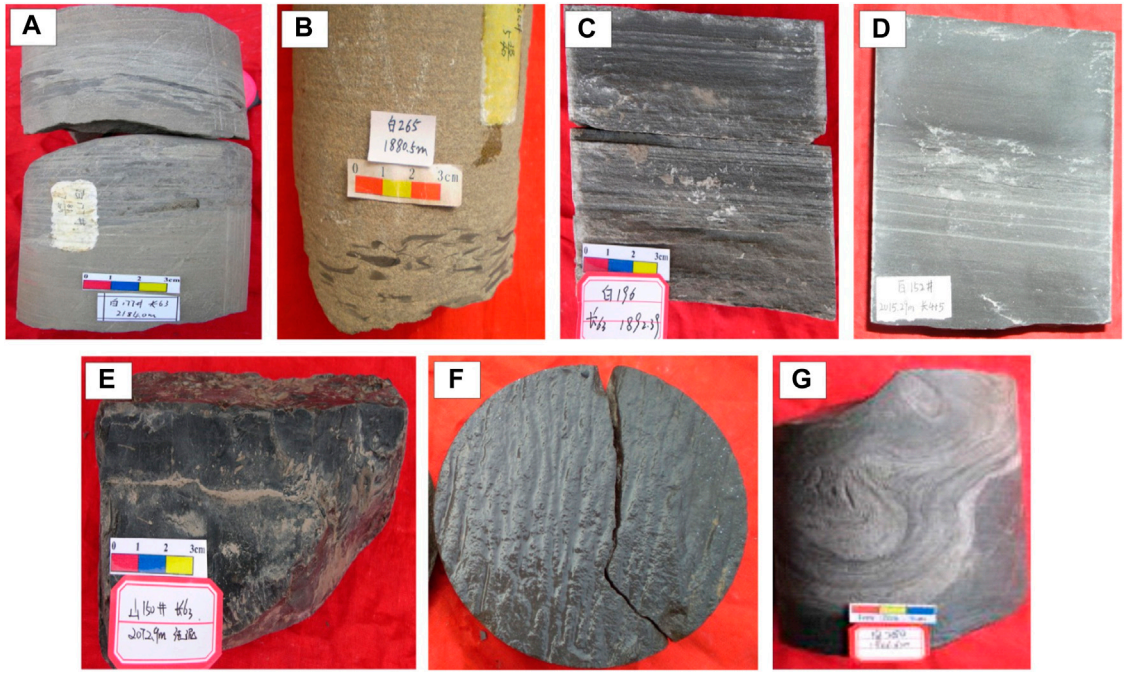

FIGURE 3
Sedimentary-structural characteristics of the Chang 6 Member in the study area. **(A)** Well B177, 2184 m, two-stage channel scour surface; **(B)** Well B265, 1880,5m, scour face contact; **(C)** Well B196, 1892, 39m, parallel bedding; **(D)** Well B152, 2015.29m, oblique bedding; **(E)** Well S150, 2072.9m, deep lake dark mudstone; **(F)** Well H12, 2003m, groove; **(G)** Well H14, 2013m, slump deformation bedding.

deformation, groove mold, slot mold, and heavy-duty mold. Dark mudstone is developed in the slump gravity flows. Meanwhile, the pyrite nodules are common, and it reflects a low-energy and still water depositional environment (Wang, 2005; Zhao et al., 2007; Wu et al., 2008).

Due to the control of paleotopography and sedimentary facies belts, the flow characteristics of the sedimentary medium above and below the slope change significantly. The end of the delta front on the slope belongs to the grain support, and it reflects the transport characteristics of the tractive flow; while the lower slope belongs to the semi-deep lake-deep lake environment, and it has the gravity flow transport characteristics of the matrix support (Figure 3).

4.2 Petrological characteristics of the chang 6 member

The color of rock, especially the primary color of mudstone, can be directly used as an identification marker for judging the climatic conditions, oxidation-reduction conditions of water media and the quality of source rocks during deposition (Tchistiakov, 2000; Zeng et al., 2003; Li et al., 2012). The deep-semi-deep lacustrine facies gray-black to black shales are widely developed in the Chang 6 Member of the study area. It reflects that in the Late Triassic, the study area had perennial water overburden and strong reducing environmental conditions.

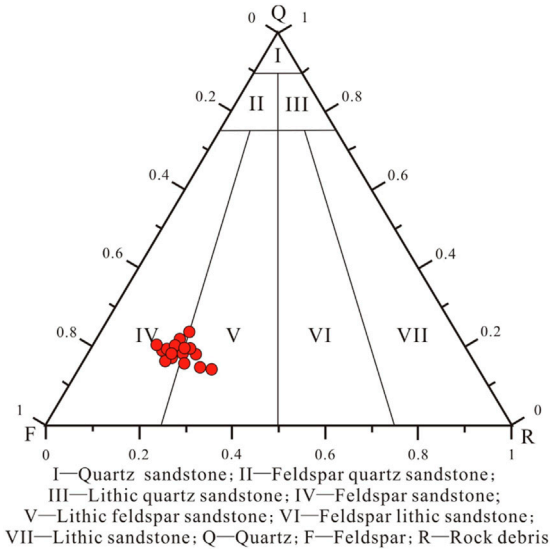

FIGURE 4
Distribution of three-unit components of the Chang 6 sandstone in the study area.

The Chang 6 Member of the study area is sandwiched by a large set of dark mudstones. Sandstones and mudstones are interbeded frequently. The clastic composition of sandstone is mainly feldspar and quartz, followed by lithic debris. Its lithology is dominated by powder to fine-grained feldspar sandstone, followed by lithic sandstone, and quartz sandstone is rare to be seen. The three-component distribution of the sandstones is shown in Figure 4. The compositional characteristics of the detrital skeleton components are as follows:

Quartz (Q): It is mainly composed of single crystal quartz, while polycrystalline quartz is occasionally seen, and siliceous debris is not seen. The content of quartz is between 18 and 40%, mainly 25–30%, and the average is 28%.

Feldspar (F): It is dominated by plagioclase, followed by striped feldspar, microplagioclase, and a small amount of albite and orthoclase. According to the identification results of thin sections, the content of feldspar is between 41% and 74%, mainly 50%–60%, and the average is 61.7%. The albite component is slightly dominant.

Rock debris (R): The types of rock debris are relatively complex. It is mainly composed of epimetamorphic rock debris, including phyllite, metasiltstone, mica-quartz schist, and quartz-mica schist; followed by sedimentary rock debris, including micrite limestone, micrite dolomite, calcite debris, dolomite debris, flint debris; and the intermediate-basic magmatic rock debris is occasionally seen. The total content of various types of debris is between 3% and 34%, mainly 6%–16%, and the average is 10.2%.

Therefore, the mineral maturity of the Chang 6 Member sandstone in the study area is very low, indicating that the sedimentary environment has a low degree of transformation of the sediments. It is the product of the rapid promiscuous accumulation of sediments.

4.3 Sand body types in the chang 6 member

Three types of sediment gravity flow and traction bottom flow of sandy clastic flow, classical turbidite and slump rocks were identified in the Chang 6 Member of the Yanchang Formation. Among them, the sandy clastic flow is a kind of sand body genetic type developed in continental petroliferous basins and belongs to laminar flow; while the classical turbidite is formed by turbidite flow and belongs to turbulent flow; and the slump rock is a slump deformation body formed by sliding and slumping in deep water environment (Amaefule et al., 1988; Bennion et al., 2000; Jiang et al., 2006).

The above three lithologies are interdependent in space and transform in time. In terms of oil and gas-bearing properties, the sandy clastic flow is the best, followed by the classical turbidite, and the slump rock has the poorest gas-bearing properties (Liao et al., 2018; Liao et al., 2020). Further research shows that the sandy debris flow is the main contributor to the production of oil wells in the central areas of the lake basin, and its planar distribution controls the enrichment and high production of oil and gas.

Statistical analysis results of 200 samples from the Chang 6 Member of this area show that, compared with the channel sand bodies of the traction flows in the same period, the gravity flow sand bodies generally have higher content of matrix and poor overall storage performance, and the permeability of most samples is lower than 0.5 mD. On the whole, the physical properties of the sandy clastic flow reservoirs are better than those of turbidite, and the slump rocks have the worst physical properties due to the sand-mud mixture. The study of the microstructures of the sandstone reservoirs show that although massive sandstone (sand clastic flow) has a higher content of matrix (hydromica), its physical properties are generally better than the turbidite and slump rocks. Moreover, the sandy debris flow is dominated by the development of intergranular and dissolution pores.

4.4 Provenance of the chang 6 member

There are two provenance systems in the northeast and southwest of the study area, among them, the northeast one is the main source. The provenance demarcation line represents the connecting areas of the Wells Li 60-Bai 181-Hua 93-Bai 282-Cheng 97-Shan 105. The content of feldspar is higher than that of quartz in the northeast direction of the dividing line, while the content of quartz in the southwest direction is higher than that of feldspar.

Under cathode ray irradiation, there are three types of quartz luminescent colors with standard genetic significance: ① Quartz that emits blue-violet light is formed in plutonic or volcanic rocks, and will be rapidly cooled under high temperature above 573°C. ② Quartz with reddish brown and brown light is formed in regional metamorphic rocks with a temperature of 300–573°C, and its cooling rate is relatively "slow". Affected by pressure dissolution, temperature and pressure in diagenesis, authigenic quartz may also emit light brown light. ③ Non-luminous quartz is authigenic quartz formed during diagenesis, and the formation temperature is generally less than 300°C.

The quartz in the Well Bai 209 in the northern part of the Huaqing area emits blue-violet light (Figure 5A), reflecting the original characteristics of the parent rock of the upper-Mesoproterozoic granite gneiss high-grade metamorphic rock series in the Yinshan area. However, the Well Li37 in the south mainly emits brown-red light (Figure 5B), and it reflects the characteristics of the parent rock of the sedimentary rock in the southwestern Qinqi Fold Belt. From the above analysis, it can be seen that the quartz cathodoluminescence has two different regions, indicating that there are two kinds of parent rock sources in the Huaqing area.

The risk of production and construction in the provenance intersection area is relatively high, and the direction of

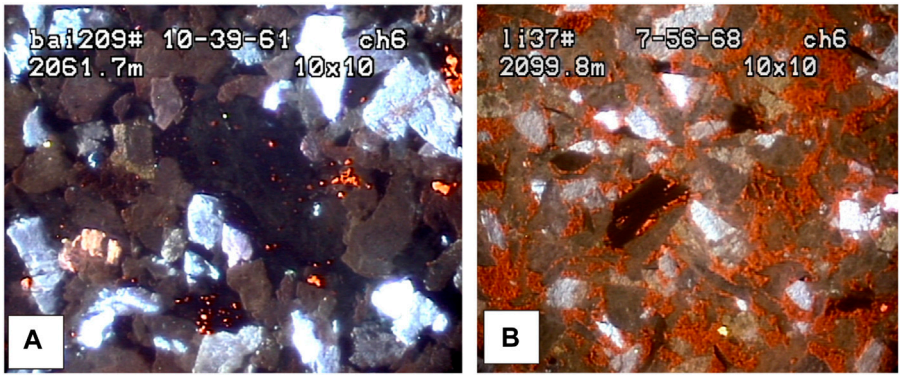

FIGURE 5
Microscope photos of the Chang 6 sandstone in the study area. **(A)** Well Bai 209, quartz has blue-brown-blue luminescence; **(B)** Well Li 37, quartz has brown-red luminescence.

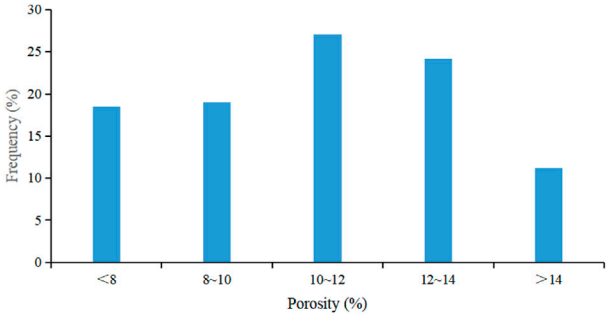

FIGURE 6
Distribution of porosity in the Chang 6 Member of the study area.

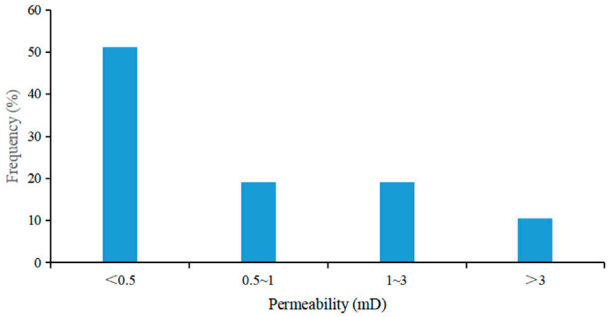

FIGURE 7
Distribution of permeability in the Chang 6 Member of the study area.

production and construction should be traced to the massive clastic flow sandstone on the main belt of the gravity flows in the northeast direction. The blocks that have formed commercial production capacity in the Huaqing area are basically in the main belt of gravity flows. Therefore, in the follow-up search for production and construction targets, the main sand belt of gravity flow that spreads from east to west is the main target.

5 Discussion

5.1 Evaluation of thick ultra-low permeability reservoirs

Permeability <1 mD is an ultra-low permeability reservoir. The Yanchang Formation in the Ordos Basin as a whole is a low permeability reservoir. Among them, the porosity of the Chang 6 oil layer group in the study area is generally less than 14%, and such reservoirs account for 88.8% of all samples (Figure 6); the permeability is generally less than 3 mD, and the reservoirs with permeability less than 1 mD account for 70.3% of the total samples (Figure 7).

For different oil layers in the Chang 6 Member, the sand bodies deposited in the late stage (Chang 6_1) have relatively good physical properties. Its average permeability is 1.2 mD. However, the older the horizons, the much pore poor the reservoir physical properties. The permeability of the Chang 6_2 and Chang 6_3 sandstones are 0.91 mD and 0.37 mD, respectively.

The thick sand layers of the Chang 6 Member in the study area are mainly formed by sandy debris flows with liquefied flow properties. The most important feature of the sandy debris flow is its liquefaction origin, and the main sources are the saturated water and fine sediments. After entering the hydrostatic deposition, the sandy debris flow did not carry out secondary

differentiation of sediments in the process of slump along the slope like turbidite, but declined as a whole. In addition, the liquefied property of sandy debris flow is also an important reason for its large single-stage slump thickness (Xu et al., 1999; Peng and Chen, 2013). Generally, the thickness of single-layer sandy debris flow sandstone can reach 10–15 m. In addition, it has the characteristics of multi-stage superposition, so a single well often encounters a sandstone reservoir with a thickness of nearly 40 m.

It is worth noting that the calcareous interlayers are often associated with large sets of thick sandstones in some areas. On the one hand, it is due to the large content of feldspar in the sandstone; on the other hand, it also shows that the later reformation of diagenesis has an important influence on the properties of the reservoir.

The background of near-source rapid deposition results in poor sorting and roundness of ultra-low permeability reservoirs (Bukar et al., 2021). It is mainly supported by matrix, which reflects its weak hydrodynamic environment. It can also be found from the observations under the microscope that a small number of particles have good roundness, while most of the particles have moderate to poor roundness, indicating the effect of secondary transportation. The sandstone is dominated by quartz and feldspar, and the content of feldspar is generally higher than that of quartz, which is very different from most conventional sedimentary reservoirs. On the one hand, it illustrates the alkaline environment of its parent source area; on the other hand, it also reflects the relatively short transport distance of sediment debris from a microscopic perspective (Xu et al., 2013; Zou et al., 2019). Feldspar is much less stable than quartz, and it will cause a lot of losses during long-distance transportation. Under normal circumstances, after entering the lake basin, the content of quartz is greater than that of feldspar, and the phenomenon that feldspar is greater than quartz in the center of the lake basin in Huaqing area is abnormal. From this, it can be judged that the formation of thick ultra-low permeability sandstone in this set of strata is closely related to the nature of its parent source.

A large number of core observations show that the continuous thickness of the sandy debris flows is large and the oil-bearing properties are good. Classical turbidite has a lithologic combination of frequently interbeded of sand and mud. Meanwhile, it has well-developed rhythmic bedding structures, and only some layers have good oil-bearing properties (oil-rich or oil-immersed). However, slump rocks are less oily (oil spots or traces). In order to further determine the oil and gas properties of sand bodies of different genetic types, 82 wells were selected in the Huaqing area, and the correlation between oil production and logging interpretation of the thickness of oil layers and the thickness of massive sandstones (sand clastic flow) was carried out respectively. Statistical results show that the level of oil testing production is highly correlated with the cumulative thickness of the massive sandstones

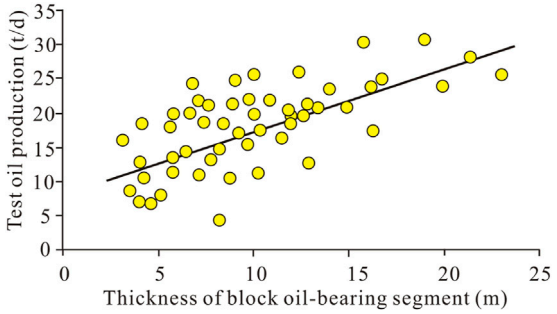

FIGURE 8
Relationship between massive sandstone thickness and oil test production.

(Figure 8). Therefore, the massive sandstone (sand debris flow) is the main contributor to oil well production, and its distribution directly controls the scale of hydrocarbon accumulation.

5.2 Analysis of pore types in ultra-low permeability reservoirs

According to the mercury injection test results of the Chang 6 Member of the Wells Bai 210–27 and Bai 209, the oil layer displacement pressure is 1.27 MPa, the median pressure is 7.52 MPa, the median radius is 0.11 μm, the maximum mercury injection saturation is 84.12%, and the mercury removal efficiency is 27.0%. The sorting of throats is good with the average sorting coefficient of 2.15, and small pores and fine throats are developed in the ultra-low permeability reservois.

The reservoir pore types of the Chang 6 Member in the study area include intergranular pores, dissolution pores (feldspar, detrital dissolution pores) and intercrystalline pores. Among them, intergranular and feldspar dissolution pores are the most important storage spaces in the Chang 6 Member sandstones (Figure 9).

1) Intergranular pores: This type of pores is the most important and common type of pores in the sandstone. The intergranular pores in the Chang 6 reservoir account for about 60% of the total surface porosity.
2) Feldspar dissolution pores: This kind of pores were formed by the dissolution of feldspar grains, and they belong to secondary pore type that developed in delta sedimentary bodies. The feldspar dissolved pores that developed in the Chang 6 reservoir account for 12–18% of the total surface porosity.
3) Laumontite dissolution pores: It is the secondary pores formed by the dissolution of the laumontite dissolution

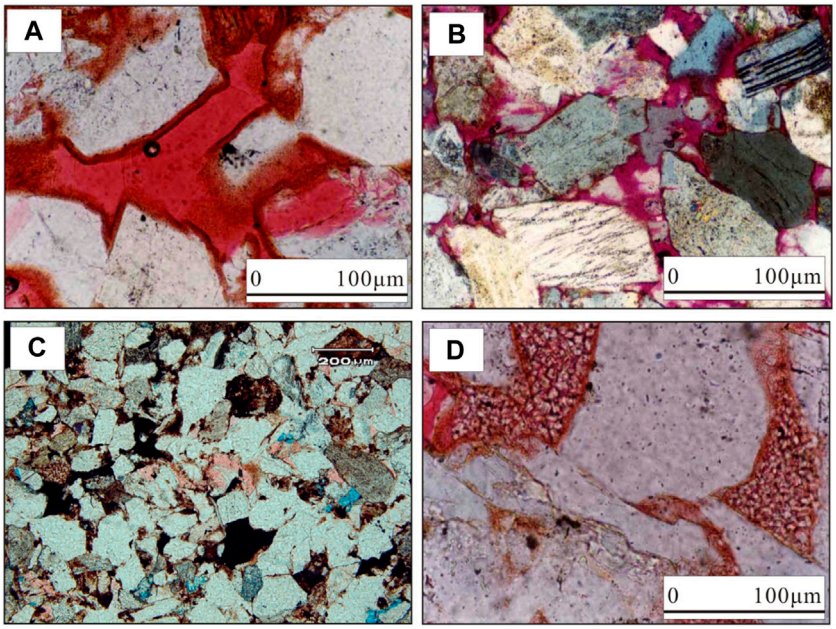

FIGURE 9
Main pore types that developed in the Chang 6 sandstones in the study area. **(A)** Well A8, 2190.42m, the pore combination of dissolution pores and intergranular pores; **(B)** Well Ping 40–20, 1167.84m, the laumontite was strongly dissolved; **(C)** Well Zhuang 33, 1678.38m, feldspar dissolution pores; **(D)** Well A14, 2133.50m, kaolinite intercrystalline pores.

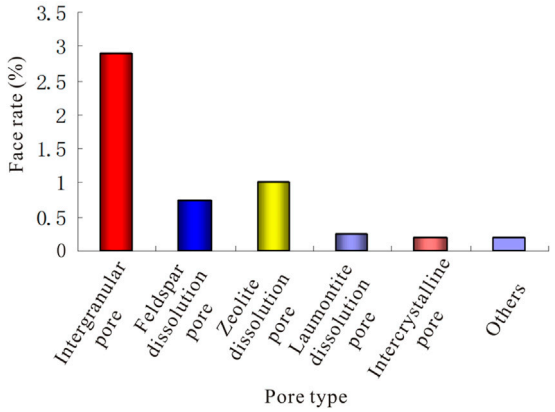

FIGURE 10
Pore types and proportions in the sandstone of the Chang 6 Member in the study area.

pores filled between the detrital particles or of the metasomatic detritus. Laumontite dissolution pores are commonly developed in the Chang 6 reservoirs, generally accounting for 10–20% of the total pore porosity, and their absolute content is 1.0% (Figure 10).

4) Intercrystalline pores and debris dissolution pores: The contribution of these two types of pores to the improvement of reservoir physical properties is relatively small, and their contribution to pore spaces generally located in intervals where turbidite is not developed.

5.3 Analysis of geological parameters affecting hydrocarbon enrichment

5.3.1 Permeability

In ultra-low permeability reservoirs, permeability is one of the important parameters that can reflect the essential properties of the reservoir. In the production process, the most easily obtained permeability results are calculated from the logging parameters. However, in practical applications, these results often deviate greatly from the actual situation. Different calculation standards and methods can also lead to different results for the same reservoir or similar results between different reservoirs. Clearly, none of these conditions can correctly reflect the changes of permeability of the reservoir.

The permeability obtained by the core analysis experiments is the actual reflection of the permeability of the core. However, due to the needs of economic benefits and production efficiency, core analysis is only performed on the exploratory wells, evaluation wells and a small number of skeleton wells in actual production. During the production process, the correlation between actual production and the permeability of core analysis is higher than

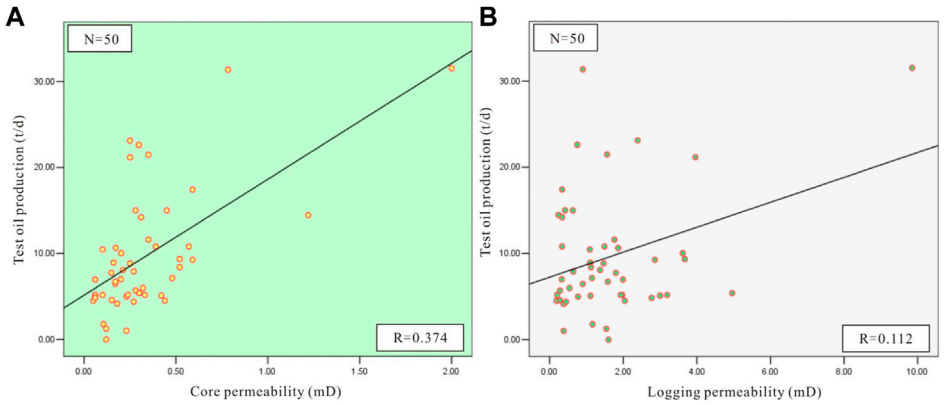

FIGURE 11
Correlation between permeability and test oil production. **(A)** Core analysis permeability; **(B)** Well log interpreted permeability.

that of logging interpretations (Figure 11). Therefore, how to accurately reflect the real permeability of the reservoir without increasing production input has become an urgent need in the process of the actural geological research.

Spontaneous potential is one of the important logging parameters to measure reservoir permeability. In the early days of resistivity logging, a non-artificial DC potential difference was observed in drilling, and it could be recorded with millivolt precision, which is called spontaneous potential. The measurement of spontaneous potential is very simple, that is, one measuring electrode is placed downhole and the other one is placed on the ground, and a spontaneous potential curve can be measured continuously. If the positive potential of the curve is used as the benchmark, the negative peak of the curve is generally sandstone with permeability. Therefore, the spontaneous potential curve can be used as a basic logging method to divide lithology and judge reservoir properties. But it is affected by mud filtrate, and the potential value between wells cannot be compared.

The obvious anomaly of spontaneous potential is a significant feature of the permeable layers, and the spontaneous potential curve is an effective tool to divide the permeable layers. Generally, the interface of the permeable layers can be determined by the half-amplitude point. In practical work, a permeable layer is often divided by the display of the spontaneous potential and the micro-electrode curve; and the apparent resistivity curve of the micro-electrode and the short electrode is used to determine the interface. It refers to the half-amplitude point of the natural potential.

Therefore, the potential value of the mudstone layer in the middle of the Chang 6 Member, which is stably developed in the whole area, is taken as the baseline. It represents the adsorption capacity to ions of similar mudstones in the whole area. Assuming that it is a constant value, the potential of the reservoir at the bottom of the Chang 6 Member is calculated by making a difference with it to obtain the potential amplitude. This result reflects the difference in ion adsorption capacity of reservoirs with the same mudstone layer. Furthermore, it objectively reflects the difference in permeability between reservoirs. It was found that the permeability has a high correlation with the potential amplitude (Figure 12). Therefore, the spontaneous potential is an important parameter to measure the permeability of the reservoir.

5.3.2 Thickness of oil layers

Reservoir thickness is an important parameter to measure reservoir scale and its potential. Usually, the thickness of the oil layer is closely related to the crude oil production. In most cases, we use the effective oil layer thickness after logging interpretation as the main standard of oil layer thickness. However, ultra-low permeability reservoirs have the characteristics of low porosity and ultra-low permeability, and their electrical parameters change little. Therefore, the limitation of the span of the parameter range makes it difficult to divide the effective oil layer thickness by conventional logging methods.

To minimize this disadvantage, the reservoirs interpreted by the logs were further sub-categorized. First, a classification template based on oil layers is established, and the Types I and II oil layers are used as the main body of the “main contribution layer” (test oil production >10 t/d). Then, the correlation analysis was carried out on the thicknesses of the main production layers and the oil layers explained by logging and the oil test results (Figure 13). The comparison shows that the correlation between the thickness of the main production layers and the oil test production is much higher than the thickness of the oil

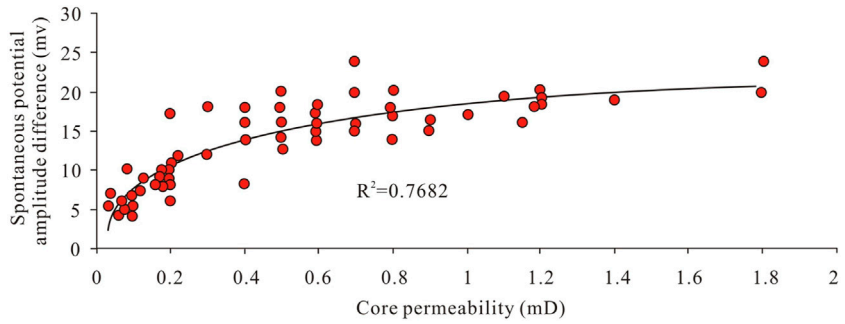

FIGURE 12
Correlation between spontaneous potential amplitude and measured core permeability of the Chang 6 Member in the study area.

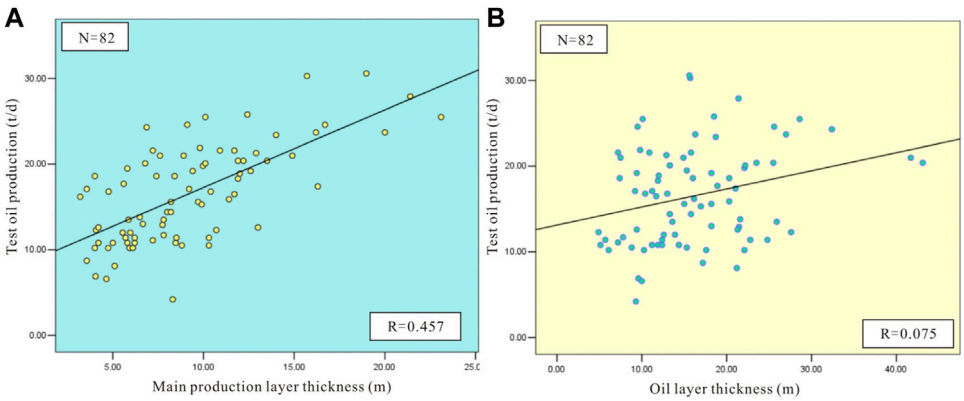

FIGURE 13
Correlation between the thickness of the main producing layers, oil layers and the test oil production in the Chang 6 Member. **(A)** Main producing layer thickness; **(B)** Oil layer thickness.

layers interpreted by logging. Therefore, the thickness of the main production layers is also an important factor affecting the oil content or productivity.

5.3.3 Resistivity

The resistivity of rock is closely related to lithology, reservoir physical properties and oil content. The resistivity of the oil layers in the ultra-low permeability reservoirs in the study area is basically between 18–70 Ω·m, except for the low-resistivity oil reservoirs (<25 Ω·m) in some areas of Bai 465 development zone, while the average value of resistivity in the rest of the areas is more than 30 Ω·m. The oil layer below 30 Ω·m tends to have relatively poor oil recovery effect. Generally, oil layers with resistances of 40–50 Ω·m have higher oil production. However, due to the high shale content and the influence of the surrounding rocks of the upper and lower calcareous sandstones, most of the reservoirs exceeding 70 Ω·m have poor oil content. Therefore, it is not simply considered that the higher the resistivity, the better the oil content, and the resistivity should be within a reasonable range.

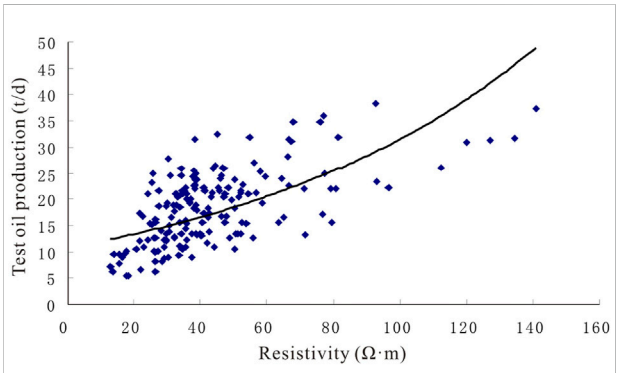

FIGURE 14
Correlation between resistivity and test oil production.

TABLE 1 Classification and evaluation criteria of the Chang 6 Member reservoirs in the study area.

Standard\Category	Type I	Type II	Type III
Dominant facies	Turbidite channel facies dominated by a large set of "box-shaped" SP and RT curves	Channel flanks dominated by "bell-shaped or funnel-shaped" SP and RT curves	Sheet sand facies at the outer edge of the channel that dominated by "low-amplitude hill type" SP and RT curves
Lithologic assemblage	Oil-bearing fine sandstone with small trough-like cross-bedding or massive bedding	Massive oil-bearing fine sandstone siltstone and a small amount of thin argillaceous and calcareous interlayers	Cross-bedded fine sandstone
Electrical characteristics	RT > 40 Ωm, SPAmplitude < -28 mv, H > 10 m	28 Ωm < RT < 40 Ωm, -28<SPAmplitude < -12 mv, 5<H < 10 m	RT < 28 Ωm, SPAmplitude < -12 mv, H < 5 m

RT-resistivity; $SP_{Amplitude}$-spontaneous potential amplitude difference; H oil layer thickness.

In this study, the resistivity values of nearly 200 oil-producing wells in the Bai 153 development area were used to analyze the correlation between the resistivity value and the test oil production, and the correlation degree was close to 60% (Figure 14). The conclusion is consistent with the actual logging interpretations in the development process. Therefore, resistivity is an important parameter affecting oil-bearing properties of ultra-low permeability reservoirs (Figure 14). For tight sandstones, high resistivity represents low water saturation and good hydrocarbon-bearing properties.

5.3 4 Drilling encounter rates of oil layers

Drilling encounter rates refer to the probabilities of encountering oil formations during drilling. A formation with a low oil layer drilling encounter rate cannot be called a main productive oil layer in terms of its scale and integrity, and even if its reservoir physical properties are good. According to the research, it has no obvious correlation with production. However, the drill encounter rate can reflect the thickness and connectivity of the sand bodies, so it is also an important indicator of the quality of the oil layers.

5.4 Evaluation criteria for hydrocarbon enrichment

On the basis of the above research, combined with the dominant facies, lithologic combinations and electrical properties, the evaluation criteria for hydrocarbon enrichment in the Chang 6 Member were formulated (Table 1). Using this standard, high-precision prediction of the sweet spot areas of the reservoirs can be achieved. This study can provide scientific guidance for the efficient development of continental ultra-low permeability tight sandstone oil reservoirs.

6 Conclusion

1) Three types of sand bodies, namely sandy debris flow, turbidite and slump rock, were identified in the Chang 6 Member of the Yanchang Formation in the study area. The pore types of the Chang 6 Member in the study area include intergranular pores, dissolution pores (feldspar, detrital dissolution pores), and intercrystalline pores. Among them, intergranular pores and feldspar dissolution pores are the most important storage spaces in the target layer.
2) The study found that the test oil production is highly correlated with the cumulative thickness of the massive sandstone segments. Therefore, massive sandstone (sand debris flow) is the main contributor to oil well production, and its distribution directly controls the accumulation of hydrocarbons and the high production of oil wells.
3) Geological parameters affecting reservoir enrichment include the permeability, oil layer thickness, resistivity, and reservoir penetration rate. The evaluation criteria for hydrocarbon enrichment in the Chang 6 Member were formulated combining the analysis of dominant facies, lithologic assemblages and electrical properties.

Data availability statement

The original contributions presented in the study are included in the article/supplementary material, further inquiries can be directed to the corresponding author.

Author contributions

JL is responsible for the idea and writing of this paper and LH, ZL, KT, LZ, JY and PY are responsible for the experiments and analysis.

Funding

This research was financially supported by the Forward Looking Basic Strategic Technology Research Projects of China National Petroleum Corporation (Title: Study on Reservoir Forming Law and the Key Technology of Lithologic Stratigraphic Oil and Gas Reservoirs) (No.2021DJ0406).

Conflict of interest

Authors JL, LH, ZL, KT and PY were employed by the Research Institute of Petroleum Exploration and Development Northwest Branch, and authors LZ and JY were employed by the PetroChina Yunmen Oil field Company.

Publisher's note

All claims expressed in this article are solely those of the authors and do not necessarily represent those of their affiliated organizations, or those of the publisher, the editors and the reviewers. Any product that may be evaluated in this article, or claim that may be made by its manufacturer, is not guaranteed or endorsed by the publisher.

References

Amaefule, J. O., Kersey, D. G., Norman, D. L., and Shannon, P. M. (1988). "Advances in formation damage assessment and control strategies," in Proceedings of the 39th Annual Technical Meeting of Petroleum Society of CIM and Canadian Gas Processors Association, Calgary, Alberta, June 11-15, 1988, 12–16. CIM Paper No. 88-39-65. doi:10.2118/88-39-65

Asante-Okyere, S., Ziggah, Y. Y., and Marfo, S. A. (2021). Improved total organic carbon convolutional neural network model based on mineralogy and geophysical well log data. *Unconv. Resour.* 1, 1–8. doi:10.1016/j.uncres.2021.04.001

Bennion, D. B., Thomas, F. B., and Ma, T. (2000). Formation damage processes reducing productivity of low permeability gas reservoirs. *SPE* 60325, 1–7. doi:10.2523/60325-MS

Bukar, M., Worden, R., Bukar, S., and Shell, P. (2021). Diagenesis and its controls on reservoir quality of the Tambar oil field, Norwegian North Sea. *Energy Geosci.* 2 (1), 10–31. doi:10.1016/j.engeos.2020.07.002

He, J., Feng, S. B., Huang, J., Yuan, X. Q., Han, P., and Li, T. Y. (2008). Effects of provenance on porosity development of Chang 6 sandstone of the Yanchang Formation in the center of Ordos Basin. *Acta Sedimentol. Sin.* 29 (1), 80–87. doi:10.1631/jzus.A1000105

Huang, Y. G., Chen, Z. Q., Wignall, P. B., Grasby, S. E., Zhao, L. S., Wang, X. D., et al. (2019). Biotic responses to volatile volcanism and environmental stresses over the Guadalupian-Lopingian (Permian) transition. *Geology* 47, 175–178. doi:10.1130/G45283.1

Jiang, H. Q., Yao, J., and Jiang, R. Z. (2006). *Reservoir engineering principles and methods*. The second edition. Dongying: China University of Petroleum Press, 101–108.

Jiang, W., Zhang, P., Li, D., Li, Z., Wang, J., Duan, Y., et al. (2022). Reservoir characteristics and gas production potential of deep coalbed methane: Insights from the no. 15 coal seam in shouyang block, Qinshui Basin, China. *Unconv. Resour.* 2, 12–20. doi:10.1016/j.uncres.2022.06.001

Katz, B., Gao, L., Little, J., and Zhao, Y. R. (2021). Geology still matters – unconventional petroleum system disappointments and failures. *Unconv. Resour.* 1, 18–38. doi:10.1016/j.uncres.2021.12.001

Li, A. R., Wang, W. X., Wu, F. L., Zhao, J. Z., and Zhang, H. (2013). Oil accumulation patterns of Chang 4+5 and Chang 6 in yan'an delta, Ordos Basin. *Oil Gas Geol.* 34 (5), 667–671. doi:10.11743/ogg20130513

Li, H. (2022). Research progress on evaluation methods and factors influencing shale brittleness: A review. *Energy Rep.* 8, 4344–4358. doi:10.1016/j.egyr.2022.03.120

Li, S. H., Fang, G. Q., Yang, J. L., Liao, J. B., and Fan, J. M. (2012). Origin of ultra-low permeability reservoirs in Ordos Basin and its significance. *Lithol. Reserv.* 24 (6), 32–37. doi:10.3969/j.issn.1673-8926.2012.06.008

Liao, J. B., Xi, A. H., Li, Z. Y., Liu, H. Q., Li, X. B., and Wan yan, R. (2018). Microscopic characterization and formation mechanisms of deep-water sandy-debris-flow and turbidity-current sandstones in a lacustrine basin: A case study in the Yanchang Formation of the Ordos Basin, China. *Pet. Sci.* 15, 28–40. doi:10.1007/s12182-017-0207-9

Liao, J. B., Xi, A. H., Liang, S. J., Zhou, X. P., Li, Z. Y., Di, J., et al. (2020). Genetic mechanisms of deep-water massive sandstones in continental lake basins and their significance in micro–nano reservoir storage systems: A case study of the Yanchang Formation in the Ordos Basin. *Nanotechnol. Rev.* 9, 489–503. doi:10.1515/ntrev-2020-0040

Liu, C., Zhao, H., and Sun, Y. (2009). Tectonic background of Ordos Basin and its controlling role for basin evolution and energy mineral deposits. *Energy Explor. Exploitation* 27 (1), 15–27. doi:10.1260/014459809788708219

Peng, S. M., and Chen, Y. Q. (2013). *Practical petroleum development geology and reservoir engineering method*. Beijing: Petroleum Industry Press, 1–494.

Tchistiakov, A. (2000). Colloid chemistry of *in-situ* clay-induced formation damage. *SPE* 58747, 1–5. doi:10.2118/58747-MS

Vafaie, A., Kivi, I. R., Moallemi, S. A., and Habibnia, B. (2021). Permeability prediction in tight gas reservoirs based on pore structure characteristics: A case study from south western Iran. *Unconv. Resour.* 1, 9–17. doi:10.1016/j.uncres.2021.08.001

Wang, H., Zhou, S., Li, S., Zhao, M., and Zhu, T. (2022). Comprehensive characterization and evaluation of deep shales from Wufeng-Longmaxi Formation by LF-NMR technology. *Unconv. Resour.* 2, 1–11. doi:10.1016/j.uncres.2022.05.001

Wang, Q. Z. (2005). *Research on depositional systems and pool-forming assemblages of Chang 1 and Chang 2 members of the Yanchang Formation from ansai-zichang area in the Ordos Basin*. Xi'an: Northwest University, 1–5. doi:10.1016/S1872-5791(08)60056-1

Wu, F. L., Wang, B. Y., Zhao, J. Z., Liu, H. B., Li, G. T., and Chen, M. Q. (2008). Origin and characteristics of oil pool sequence in Ordos Basin. *Acta Pet. Sin.* 29 (5), 639–643. doi:10.7623/syxb200805002

Xu, G. M., Xu, H. D., and Kong, X. Y. (1999). AppliIcation of high-resolution sequence stratigraphy in reservoir numerical simulation. *Oil Gas Geol.* 20 (2), 115–119. doi:10.11743/ogg19990204

Xu, L., Shi, Y. M., Xu, C. S., Yang, Y., Li, H., and Chai, Z. (2013). Influences of feldspars on the storage and permeability conditions in tight oil reservoirs: A case study of chang-6 group, Ordos Basin. *Petroleum Explor. Dev.* 40 (4), 481–487. doi:10.1016/S1876-3804(13)60061-0

Yang, H., Li, S. X., and Liu, X. Y. (2010). Characteristics and resource prospects of tight oil and shale oil in Ordos Basin. *Acta Pet. Sin.* 34 (1), 1–11. doi:10.7623/syxb201301001

Zeng, D. Q., Zhang, S. M., and Lu, L. Z. (2003). Types and characteristics of fractures in tight sandstone gas reservoirs with low permeability. *Acta Pet. Sin.* 24 (4), 36–39. doi:10.1007/BF02974893

Zhao, J. Y., Luo, J. L., Lei, X. L., Guo, D. Y., Wang, Y. D., Fan, W. H., et al. (2007). Provenance analysis of the sixth member of the Yanchang Formation in the yangjiayuanze oil prospect area, zichang oilfield, Ordos Basin. *Geol. China* 34 (3), 422–429. doi:10.1002/pon.1349

Zou, C. N., Zhu, R. K., Chen, Z. Q., Ogg, J. G., Wu, S. T., Dong, D. Z., et al. (2019). Organic-matter-rich shales of China. *Earth-Science Rev.* 189, 51–78. doi:10.1016/j.earscirev.2018.12.002

frontiers | Frontiers in Earth Science

TYPE Original Research
PUBLISHED 08 September 2022
DOI 10.3389/feart.2022.981037

OPEN ACCESS

EDITED BY
Hu Li,
Southwest Petroleum University, China

REVIEWED BY
Hexin Huang,
Chang'an University, China
Pei Li,
SINOPEC Petroleum Exploration and Production Research Institute, China

*CORRESPONDENCE
Hui Xiao,
xiaohui@xsyu.edu.cn

†Present address:
Hui Xiao,
School of Earth Science and Engineering, Xi'an Shiyou University, Xi'an, China

SPECIALTY SECTION
This article was submitted to Structural Geology and Tectonics, a section of the journal Frontiers in Earth Science

RECEIVED 29 June 2022
ACCEPTED 12 August 2022
PUBLISHED 08 September 2022

CITATION
Xiao H, Xie N, Lu Y, Cheng T and Dang W (2022), Experimental investigation of pore structure and its influencing factors of marine-continental transitional shales in southern Yan'an area, ordos basin, China. *Front. Earth Sci.* 10:981037. doi: 10.3389/feart.2022.981037

Experimental investigation of pore structure and its influencing factors of marine-continental transitional shales in southern Yan'an area, ordos basin, China

Hui Xiao[1,2,3*†], Nan Xie[2,3], Yuanyuan Lu[4], Tianyue Cheng[2,3] and Wei Dang[2,3]

[1]The Key Laboratory of Unconventional Petroleum Geology, Oil & Gas Survey, China Geological Survey, Beijing, China, [2]School of Earth Sciences and Engineering, Xi'an Shiyou University, Xi'an, China, [3]Shaanxi Key Laboratory of Petroleum Accumulation Geology, Xi'an Shiyou University, Xi'an, China, [4]CNOOC Research Institute Ltd., Beijing, China

The intensive study of the pore structure and its controlling factors of shale reservoir has important guiding significance for further exploration and exploitation of shale gas. This work investigated the effects of organic and inorganic compositions on the development of pore structures of the Upper Permian Shanxi shale in the southern Yan'an area, Ordos Basin. Based on the results of high-pressure mercury intrusion, low-pressure N_2 and CO_2 adsorption and organic geochemical experiments, X-ray diffraction and scanning electron microscope observations, the mineral composition, pore structure and its influencing factors of the transitional shale were studied systematically. The results indicate that the total organic carbon (TOC) content of the shale is between 0.12% and 5.43%, with an average of 1.40%. The type of the organic matter (OM) belongs to Type III and has over maturity degree with an average R_o of 2.54%. An important character of this kind of shale is the large proportion of clay mineral content, which ranges from 40.70% to 87.00%, and with an average of 60.05%. Among them, illite and kaolinite are the main components, and they account for 36.6% and 36.7% of the total clay minerals respectively, followed by chlorite and illite/smectite (I/S) mixed layer. The quartz content is between 10.6% and 54.5%, with an average of 35.49%. OM (organic matter) pores are mostly circular bubble-shaped pores, and most of them are micropores, while inorganic pores are well developed and mainly contributed by clay mineral pores and have slit-type, plate-like and irregular polygon forms. Mesopores are the major contributor to pore volume (PV), while micropores contribute the least to PV. The contribution of micropores to the specific surface area (SSA) is greater than 61%, followed by mesopores. Macropores have almost no contribution to the development of SSA. OM pores are the main contributor to the total specific surface area of the shale, with an average contribution rate of 61.05%, but clay mineral pores contribute more to the total pore volumes. In addition, both the content of chlorite and illite/smectite (I/S) mixed layer is positively correlated with the volume ratio of mesopores. It was found that high TOC, I/S mixed layer and chlorite content are all favorable conditions for the target shale.

KEYWORDS
clay-rich shale, transitional shale, pore structure, controlling factors, ordos basin

Introduction

As the demand for fossil fuels increases, unconventional resources have attracted an increasing attention from many countries (Dang et al., 2022). In 2017, China's shale gas production reached $9\times10^{10}m^3$, occupying 6.09% of the whole country's natural gas production. The commercial exploitation of shale gas in the Fuling area, Sichuan Basin, has made great breakthroughs, and industrial gas flow has also been achieved in the Guizhou and Yunnan Provinces. In addition, shale gas exploration has been carried out in the Ordos Basin, Qaidam Basin and Songliao Basin in China (Chen et al., 2016; Dang et al., 2016; Sun et al., 2021).

At present, there are a lot of detailed research on the reservoir evaluation of marine and continental shales, however, there is a lack of systematic research in transitional shales. The transitional shales are widely distributed in different sedimentary strata in China (Jiang et al., 2015; Li et al., 2020a; Li et al., 2020b; Zhang et al., 2020). Compared with the marine strata, shale reservoirs in transitional shales are rich in clay minerals and usually have a high value for the maturity of organic matters (Jiang et al., 2015; Yang et al., 2016; Santosh and Feng., 2020; Zheng et al., 2020; Li et al., 2021a). Distributions of pore structure parameters, which are important of shale gas storage and flow, have been widely concerned and evaluated by many scholars. According to the International Union of Pure and Applied Chemistry Classification (IUPAC), shale pores are divided into micropores (<2 nm), mesopores (2–50 nm), and macropores (>50 nm) according to their pore size. Generally, micropores provide the main accumulation sites for adsorbed gas, while mesopores and macropores provide the main accumulation sites for free gas (Curtis et al., 2012; Sun et al., 2015; Zhao et al., 2020). Therefore, the quantitative characterization of pore structures of different sizes in shale gas is critical.

Organic matter and mineral components are the two main factors controlling the development of shale pore structures. Organic matter in shale controls the development of nanopores and is an important contributor to specific surface area and pore space, therefore, it is important for shale gas adsorption and storage (Loucks et al., 2009; Wang et al., 2020; Lan et al., 2021; Zhao et al., 2021). The mineral components of quartz, clay, and carbonate rocks are all related to the development of pores and fractures in shale. The feature of high clay mineral content cannot be ignored when studying the pore structures of the transitional shale (Dang et al., 2017; Guozhang Li et al., 2019; Ma et al., 2019; Yong Li et al., 2019; He et al., 2020).

As to the transitional shale reservoirs, many scholars have focused on the evaluation of reservoir properties, influencing factors of gas content and its accumulation conditions, and prediction of favorable areas (Dang et al., 2017; Xiong et al., 2017; Xi et al., 2018; Yin et al., 2018; Guozhang Li et al., 2019; Kun Yu et al., 2019; Ma et al., 2019; Qi et al., 2019; Yin and Gao 2019). However, the development characteristics of shale pore structures of transitional shale are still not clear.

This study takes the Upper Paleozoic Shanxi Formations in the Ordos Basin as an example and various testing methods have been used to quantify the shale pore structures. The main objectives are: 1) to understand the basic geochemistry, mineral composition characteristics, pore development types and pore distribution characteristics of the transitional shale in the study area; 2) to analyze the main controlling factors of the pore structures of the transitional shale.

Samples and methods

Preparation of clay-rich shale samples

The Ordos Basin is the second largest sedimentary basin in the central China. It is a typical craton basin where multiple prototype basins overlap. It includes six sub-level tectonic units (Figure 1A). Since the Late Paleozoic, the Ordos Basin has experienced many transgressions and tectonic changes affected by regional structure movement, basement faulting, and sea-level rising and falling. A thick marine-continental transitional stratum was deposited in the Carboniferous-Permian of the Upper Paleozoic. The shale gas-bearing strata from bottom to top are the Benxi Formation, the Taiyuan Formation and the Shanxi Formation, respectively (Figure 1B) (Yan et al., 2015). The sedimentary environments are dominated by marsh-lagoon facies and marine-continental transition delta facies. Sandstone, coal, and black shale are widely developed in the Shanxi Formation. The shale of the Shanxi Formation is dominated by clay minerals, with an average mass fraction of over 50% (Sun et al., 2017; Yin et al., 2019; Zhu et al., 2019).

The study area belongs to the southern of the Yishan Slope (Figure 1A). A total of 10 groups of core samples in the Shanxi Formation were collected from the Wells C88 and C89 for this study. The depth of the samples ranges from 2 271.5 to 2 437.4 m. Total organic carbon (TOC), vitrinite reflectance (R_o), full-rock and clay X-ray diffraction (XRD), field emission—scanning electron microscopy (FE-SEM), low-temperature CO_2 and N_2 adsorption and high-pressure mercury injection (MICP) experiments were used to analyze the pore structures of shale reservoirs in the study area. Organic petrography analysis including R_o and TOC test,

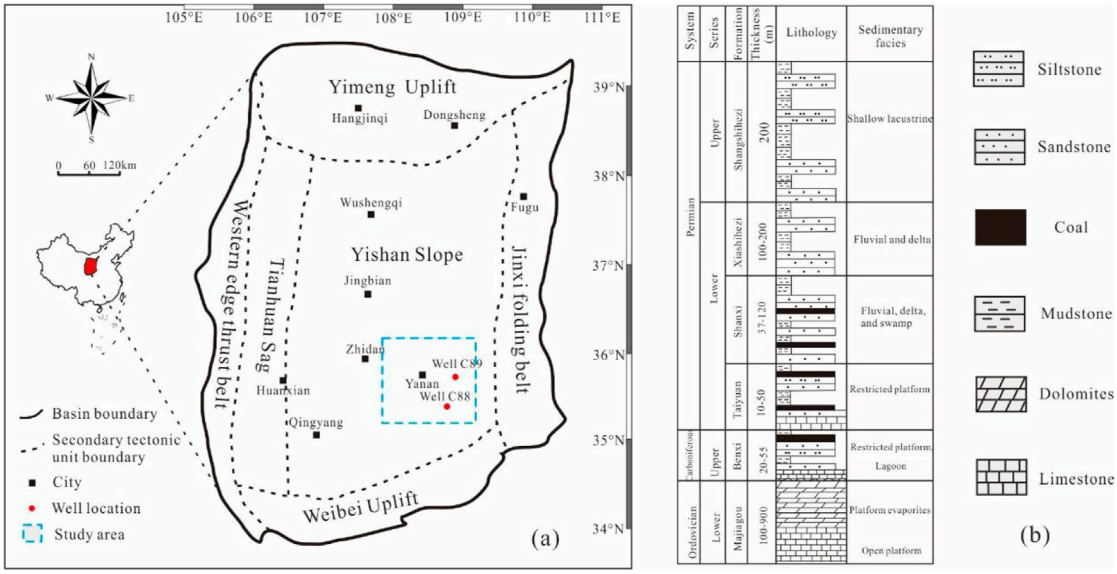

FIGURE 1
Location and well distribution of the study area **(A)** and generalized stratigraphic column of the Upper Paleozoic, Ordos Basin **(B)** (Modified after Yang et al., 2016).

and FE-SEM were all conducted at the Shaanxi Key Lab of Petroleum Accumulation Geology, Xi'an Shiyou University; the experiments of XRD, CO_2, and N_2 absorption analysis and MICP were performed by the Sichuan Province Key Laboratory of Shale Gas Evaluation and Exploration.

Experiment methods

The TOC content of the samples was determined using a carbon-sulfur analyzer (CS-230) from the American LECO Company based on the Chinese National Standards (GB/T19145-2003). Samples were milled and sieved to 100 mesh, and then 5 g powder sample were placed in HCl for 2 h to remove inorganic carbon and impurities and then washed with distilled water and dried. The R_o of the samples was examined using a Leitz MPV-SP photometer microscope according to the Chinses National standards (GB/T6948-1998). The test is performed at a temperature of 23°C ± 3°C, and the relative humidity is below 70%.

The whole rock and clay mineral compositions were analyzed by a D8 Discover X-ray diffractometer, following the Chinese Oil and Gas Industry Standards (SY/T 5163-2010). After crushing the sample particles to less than 200 mesh, 80 g sample were mixed with ethanol, ground into mortar, and placed on glass slides. The pretreated samples were scanned at rate of 4°/min, and the scanning range was 3–85°(2θ). The mineral content was semi-quantified using Jade ® software.

The FE-SEM of samples were determined using a TESCAN MALA3 LMH. Samples were observed under vacuum conditions with an acceleration voltage of 15 K_v and a resolution of 1 nm. In prior of SEM, the surfaces of the shale samples were etched *via* ion milling.

The low-temperature CO_2 adsorption and N_2 adsorption/desorption were performed on shale samples at 0°C and −195.8°C, respectively (2 g) using the Micromeritics ASAP 2460 specific surface analyzer. To characterize the overall size of the pores distributed in the shale samples, the SSA and PV distributions of micropores were obtained from the CO_2 adsorption data using the Density Function Theory (DFT) (Clarkson et al., 2013). The SSA distribution of mesopores and macropores were explained using the N_2 adsorption/desorption data by the Brunauer-Emmett-Teller (BET) model, and the PV distributions of pores ranging from 2–10 nm and 10–100 nm were obtained by the DFT and Barrett-Joyner-Halenda (BJH) models (Guozhang Li et al., 2019). In the past, the BJH, BET and DFT theory are the most used methods to extract the pore surface area and pore volume from the N_2 and CO_2 adsorption isotherms, and more importantly, these methods have been proved to be successful in characterizing the pore structures (Dang et al., 2020; Li et al., 2021b). MICP analysis were performed on the American Mike Auto Pore IV9520 type mercury pressure instrument. The maximum mercury inlet pressure is 227.4 MPa, the experimental interfacial tension σ is 480 dyn/cm, the wetting angle θ is 140°, and the mercury volume accuracy is 0.1 μl. The experiment is operated based on the Chinese Oil and Gas Industry Standards (SY/T 5346-2005).

TABLE 1 The mineral composition and geochemical parameters of transitional shale reservoirs in study area.

Samples	Depths (m)	TOC (%)	R_o (%)	Mineral composition (%)					
				Quartz	Clay	Illite	Kaolinite	I/S	Chlorite
A-1	2 271.45	1.56	2.43	29.4	69.2	23.46	20.01	16.56	8.97
A-2	2 284.62	0.82	2.23	24.8	76.3	27.36	30.40	6.84	11.40
A-3	2 293.00	1.24	2.46	36.1	59.1	18.29	31.27	4.72	4.72
A-4	2 301.77	0.62	2.39	39.3	58.8	22.04	23.78	4.06	8.12
A-5	2 304.31	0.72	2.72	31.2	69.2	24.84	28.98	4.83	10.35
A-6	2 306.69	0.80	2.53	21.2	79.5	21.33	41.87	8.69	7.11
A-7	2 431.09	0.11	—	10.6	87.0	36.54	18.27	13.05	19.14
A-8	2 433.52	5.42	2.44	27.4	58.9	20.30	19.72	4.64	13.34
A-9	2 435.84	1.23	—	24.7	68.4	29.24	21.08	4.08	13.60
A-10	2 437.41	0.86	—	28.4	67.1	29.48	15.41	16.75	5.36

Note: Clay content is absolute content.

Results

Mineral composition and organic geochemical characterization

The TOC content of the shale samples ranges from 0.11% to 5.42%, with an average of 1.34% (Table 1). Compared with previous research results, it is found that the organic matter content of the transitional shale varies greatly (Xiong et al., 2017; Xi et al., 2018; Gao, 2019; Guozhang Li et al., 2019; Ma et al., 2019). The range of R_o value ranges from 2.23% to 2.72%, with an average of 2.46% (Table 1), indicating that the shale samples in the study area are at over maturity stage, i.e., dry gas window (Nie et al., 2020). The shale in the study area and its vicinity mainly contains Type III kerogen and terrestrial microscopic components (vitrinite and inertinite) (Xi et al., 2017).

The XRD and clay analysis results show that the total clay content is distributed between 58.8% and 87.00%, with an average of 69.35%. Among clay minerals, illite and kaolinite have a relative high content, and their average value are 25.29% and 25.08% respectively. Followed by the chlorite and I/S contents, the average content are 10.21% and 8.42% respectively (Table 1). The quartz content ranges from 10.6% to 39.3%, with an average of 27.31%. It also contains a small amount of feldspar and pyrite. Compared with continental or marine shale, high clay mineral content has become another important feature of transitional shale (Xu et al., 2019a; Li et al., 2021a).

Studies on transitional shale found that clay minerals have a certain adsorption of organic matter. Organic matter can be attached to the surface of clay mineral particles, which is mainly manifested in a significant increase in the TOC content as the total clay mineral content in the shale increases (Dang et al., 2017; Hou et al., 2020). However, this study also found that with the increase of the TOC content, the clay mineral content decreases (Figure 2). After comparisons with previous studies of the transitional shale of the Shanxi Formation in the Ordos Basin and the marine shale of the Longmaxi Formation in Sichuan Basin, we found that the total clay minerals have a negative correlation with the TOC content (Xiong et al., 2017; Xu et al., 2019b; Xu and Gao., 2020). Further research is needed to confirm the correlation between the TOC and the total clay contents in different depositional environments.

Pore types

According to International Union of Pure and Applied Chemistry (IUPAC) classification, the N_2 adsorption curves of shale samples are mainly Type IV (Yong Li et al., 2019). When the relative pressure P/P_0 is in the range of 0.45–0.90, capillary condensation occurs in the curves and a hysteresis loop forms, indicating that there are many mesopores (2–50 nm) in the shale. When the relative pressure P/P_0 is small (<0.3), the adsorption curve changes gently with the increasing pressure. When P/P_0> 0.9, most samples show a steep upward trend with the increasing pressure.

The hysteresis loops in the N_2 adsorption curves are mainly H_3 and H_4 types, indicating that the pores in the shale are mostly slit-shaped and wedge-shaped pores. FE-SEM observations show that the shale pore types in the study area are mostly inorganic mineral pores such as clay mineral interlayer pores, intercrystalline pores, mineral intergranular pores, and intragranular dissolution pores (Figure 3). Figures 3A,B are pores related to clay minerals. This kind of pores are developed well and are mostly clay interlayer pores. The pore shape is mostly slit-shaped, the slit

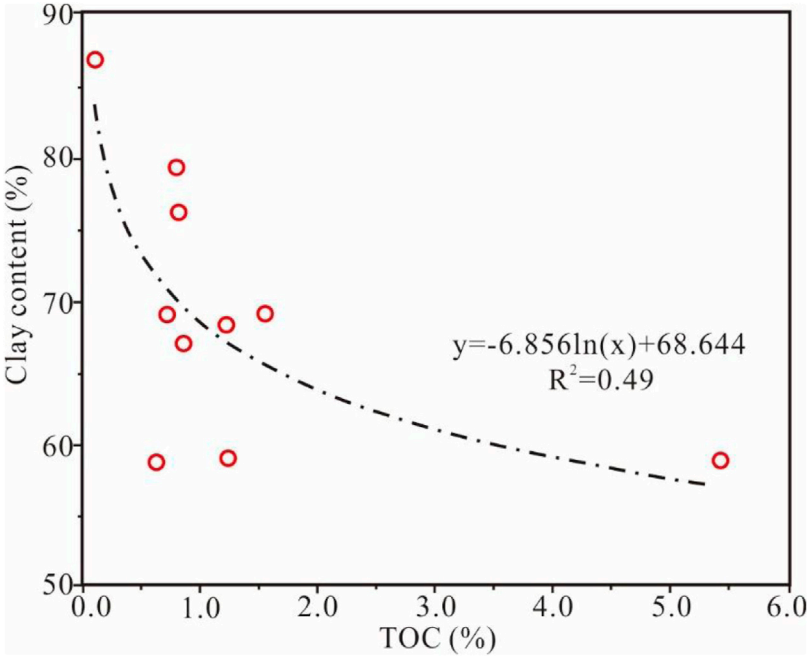

FIGURE 2
Relationship between shale TOC content and clay minerals.

width is mostly below 100 nm, and the slit length is mostly 2–3 μm. Figures 3C,D are pores related to brittle particles. This kind of pores are relatively less developed and are mainly intergranular and polygonal intergranular pores. The pore diameter of some intergranular pores reaches micron level, and a small number of particles develop intragranular dissolution pores. The contact slits between particles are mostly formed by the contact of brittle minerals and clay minerals, or by the density difference of different brittle minerals. From the FE-SEM observations, organic matter pores are less developed and are mostly shown as round bubbles. A few samples develop mesoporous organic pores, and the pore diameter can reach 10–20 nm (Figures 3E,F).

Pore structure characteristics

The distribution characteristics of the PV and the SSA of the 10 shale samples in the study area are listed in Table 2; Figure 4. The PV of micropores calculated by the DFT CO_2 and N_2 absorption data ranges from 0.000 63 cm^3/g to 0.007 13 cm^3/g, with an average of 0.002 47 cm^3/g and the SSA of micropores resulted from the BET CO_2 and N_2 absorption experiments varies between 2.054 m^2/g to 21.424 m^2/g, with an average of 7.564 m^2/g. The PV of mesopores calculated by the BJH N_2 absorption data is between 0.005 4 cm^3/g and 0.015 7 cm^3/g, with an average of 0.010 0 cm^3/g and the corresponding SSA is between 1.59 m^2/g and 5.88 m^2/g, with an average of 4.02 m^2/g. Macropores are characterized by the combination of N_2 adsorption and MICP data, while pores above 100 nm are based on MICP data (Yu et al., 2016). The PV of macropores range from 0.003 9 cm^3/g to 0.007 4 cm^3/g, with an average of 0.005 4 cm^3/g, and the corresponding SSA vary from 0.13 m^2/g to 0.28 m^2/g, with an average of 0.20 m^2/g. Combining with the pore characteristic distributions resulted from the CO_2, N_2 absorption, and MICP data, the average total PV is 0.017 cm^3/g, and the average total SSA is 11.79 m^2/g (Table. 2). The previous studies on the pore structures of transitional shale are consistent with the results of this paper (Cao et al., 2015; Wang et al., 2015).

Figure 4 shows that the total PV and SSA have no clear changing trend with the increase of TOC content. However, the PV and SSA proportion of micropores show a nonlinear increasing trend as the TOC content increases. The statistical results show that the main contributor of PV is mesopores, accounting for an average of 54.7% of the total PV, followed by the macropores, accounting for an average of 30.9% of the total PV. The micropores of PV, with an average of 14.4% of the total PV, takes the least proportion of PV, but SSA of the study shale is mainly dominated by the contribution of micropores, with an average 61.05% of the SSA. The SSA of the mesopores takes an average proportion of 36.9% of the total SSA.

According to statistics, the average volume of the mesopores accounts for 54.7% of the total pore volume, but the mesopore

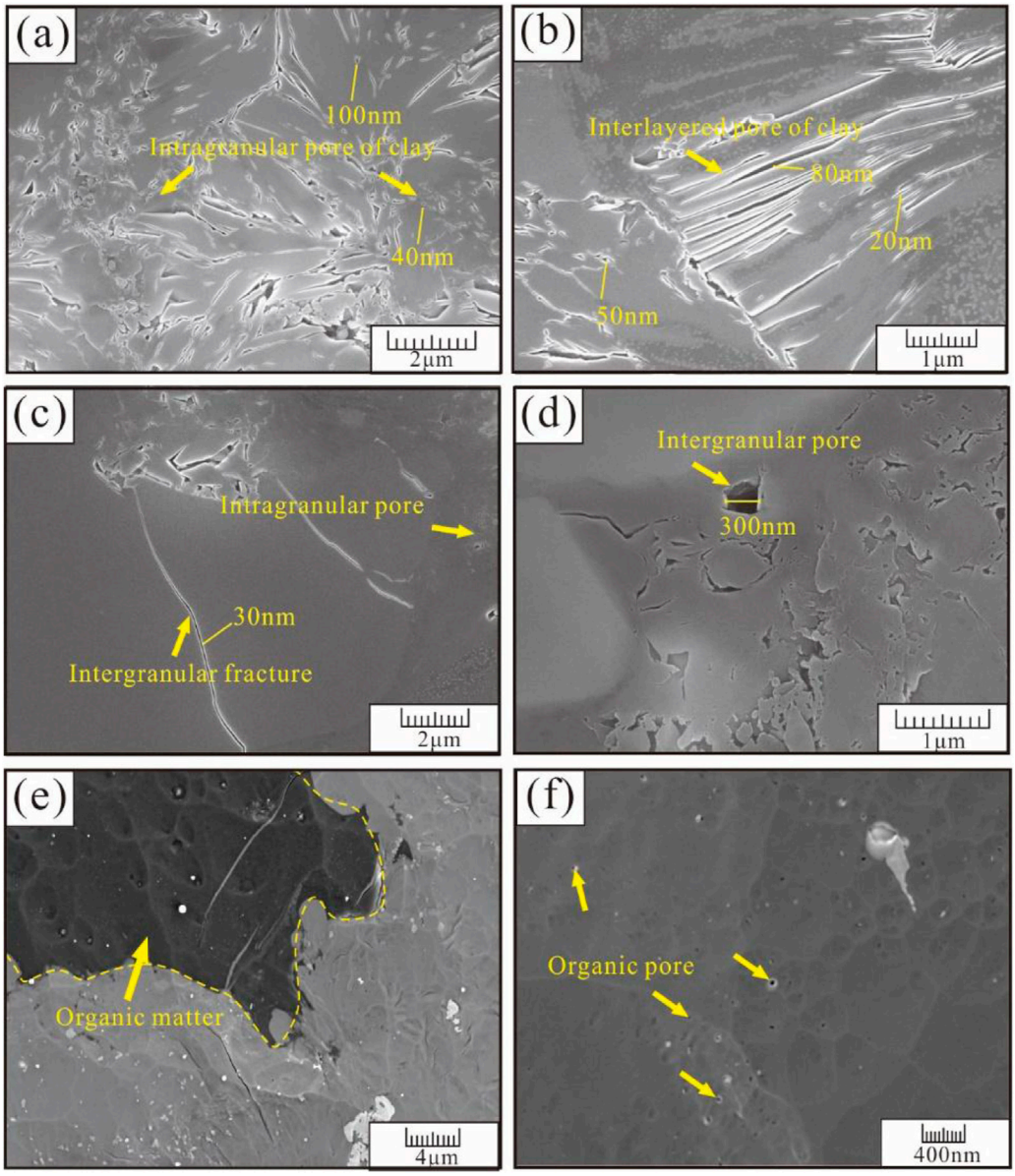

FIGURE 3
Development characteristics of different types of pores in shale reservoirs. **(A,B)** Clay mineral-related pores, the pores are relatively developed. Slit-shaped pores, strip-shaped interlayer pores, triangular and irregular polygonal intergranular pores and intragranular pores are developed; **(C,D)** Inorganic mineral-related pores. They are mainly composed of mineral intergranular pores and irregular residual intergranular pores, and there are a small number of intragranular dissolution pores with smaller pore size; **(E,F)** Organic matter-related pores (circled by yellow and white lines in the image). The pores are mostly round bubble pores. Organic matter pores are less developed and relatively small.

specific surface area only accounts for 36.97% of the total average surface area. The specific surface area is mainly dominated by the contribution of micropores, and the average specific surface area of micropores accounts for 61.05% of the total specific surface area. According to the average pore size calculation equation ($4V_p/A_s$) ×2 (V_p is the total pore volume and A_s is the total specific surface area) (Valenza et al., 2013), the average pore size of shale in the study area ranges from 5.73 to 18.89 nm. As the TOC content of the shale increases, the average pore size decreases rapidly and then becomes stable (Figure 5).

Pore-size distribution

It can be seen from Figure 6 that the interval of shale pore size distribution is wide. The micropores are mainly of the

TABLE 2 Pore structure parameters determined by CO_2, N_2 adsorption experiments and MICP experiments.

Sample	CO_2 and N_2 adsorption		MICP	CO_2 and N_2 adsorption		MICP	Total pore volume (cm^3 /g)	Total surface area (m^2 /g)	Average diameter (nm)
	DFT micropore volume (cm^3/g)	BJH mesopore volume (cm^3/g)	Macropore volume (cm^3/g)	BET micropore surface area (m^2/g)	BET mesopore surface area (m^2/g)	Macropore surface area (m^2/g)			
A-1	0.002 69	0.009 31	0.005 09	7.686	5.633	0.205	0.017 0	13.52	10.11
A-2	0.001 72	0.012 20	0.004 15	5.386	5.010	0.174	0.018 0	10.57	13.67
A-3	0.001 79	0.011 02	0.004 52	5.558	4.267	0.202	0.017 3	10.02	13.83
A-4	0.001 88	0.014 18	0.006 62	6.072	5.709	0.218	0.022 6	11.99	15.12
A-5	0.002 03	0.014 00	0.007 42	6.389	5.882	0.283	0.023 4	12.55	14.94
A-6	0.002 43	0.015 71	0.007 31	7.669	6.200	0.284	0.025 4	14.15	14.38
A-7	0.000 63	0.006 62	0.003 95	2.054	2.554	0.136	0.011 2	4.740	18.89
A-8	0.007 13	0.005 41	0.004 05	21.424	1.596	0.130	0.016 5	23.15	5.73
A-9	0.002 36	0.005 88	0.005 54	7.076	1.724	0.213	0.013 7	9.01	12.23
A-10	0.002 09	0.005 76	0.005 44	6.328	1.644	0.211	0.013 2	8.18	12.99

Note: Average diameter = (4 V_p/A_s) ×2 (V_p is total pore volume, A_s is total specific surface area).

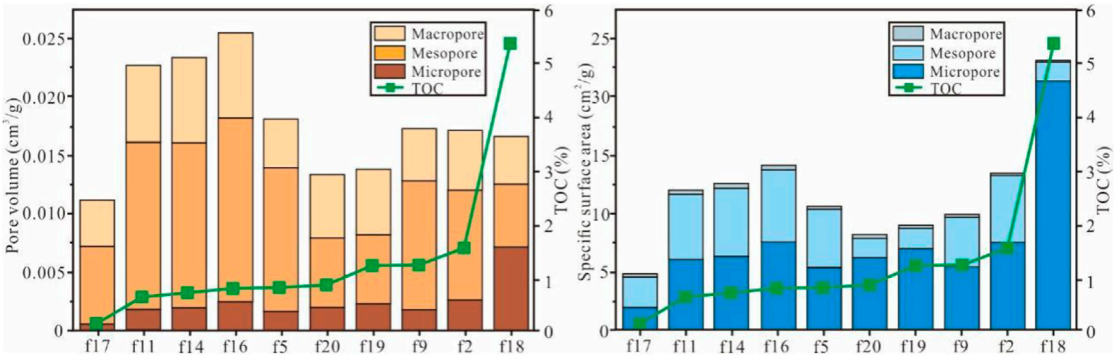

FIGURE 4
Distribution of pore volume and specific surface area of pores of different sizes in shale samples.

three-peak type, and the corresponding pore diameter ranges are 0.349 0 nm, 0.500 8 nm to 0.548 0 nm, and 0.785 5 nm to 0.859 4 nm. Because the lower limit of the CO_2 adsorption tests is 0.33 nm, then, during the pressure adsorption process, CO_2 will quickly occupy the pores, and will lead to the appearance of a peak of 0.33–0.4 nm (Kruk and Jaroniec 2001; Yuxi Yu et al., 2019), so the micropore distribution is mainly of a multi-modal type. The mesopores are of bimodal and unimodal types with peak pore sizes of 4 and 8 nm, respectively. The difference in pore size distribution of different samples indicates that the TOC content and mineral composition in shale are the main factors controlling the size and distribution of shale pores.

Discussions

Effect of organic matter content on pore structure

Organic matter not only affects the hydrocarbon generation potential in shale, but also generates many pores during the hydrocarbon generation process to provide storage space and migration channels for shale gas. Therefore, organic matter is one of the most important factors affecting the pore structures of shale reservoirs. Figure 7 shows the relationship between TOC and micropore pore volume. As the TOC content increases, the micropore volume increases, but it is negatively correlated with the

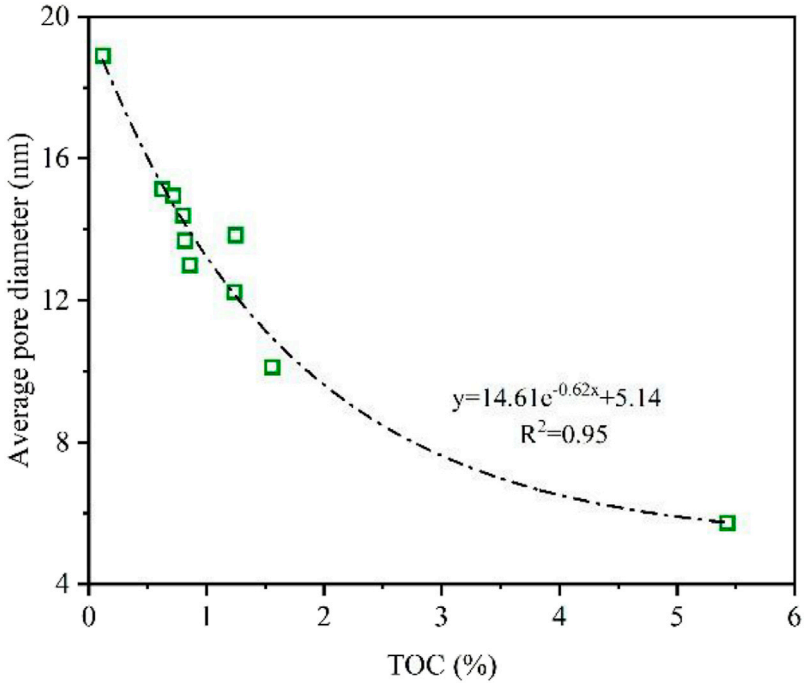

FIGURE 5
Relationship between TOC content and average pore diameter.

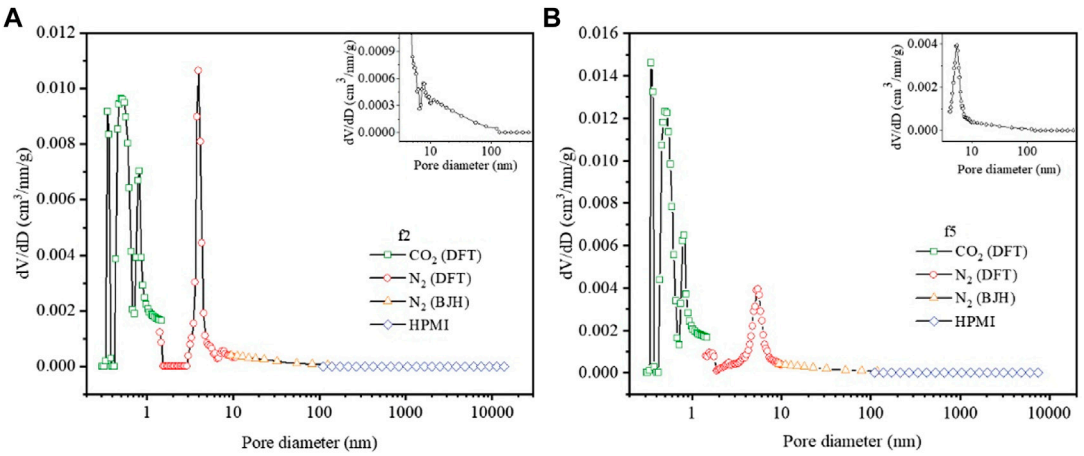

FIGURE 6
Shale pore size distribution combined with high pressure mercury intrusion, N_2 adsorption and CO_2 adsorption. Among them, the green dot pore size distribution curve is the interpretation results of CO_2 adsorption DFT model (<2 nm), the red dot pore size distribution curve is the interpretation results of N_2 adsorption DFT model (<10 nm), the yellow dot pore size distribution curve is the interpretation results of N_2 adsorption BJH model (<100 nm), and the blue point pore size distribution curve is the interpretation results of high pressure mercury intrusion Washburn equation (>100 nm). The inset in the upper right corner of the figure is an enlarged result of a curve with an aperture greater than 4 nm. **(A)** Sample f2; **(B)** Sample f5.

mesopores and macropores. In earlier studies conducted by Xiong et al. (2017) and Ma et al. (2019), they found that the TOC content in the marine-continental transitional shale mainly controls the development of mesopores, and the mesopore volume increases with the increasing TOC content. The rapid lithofacies changes, complex lithological combinations, and strong interlayer

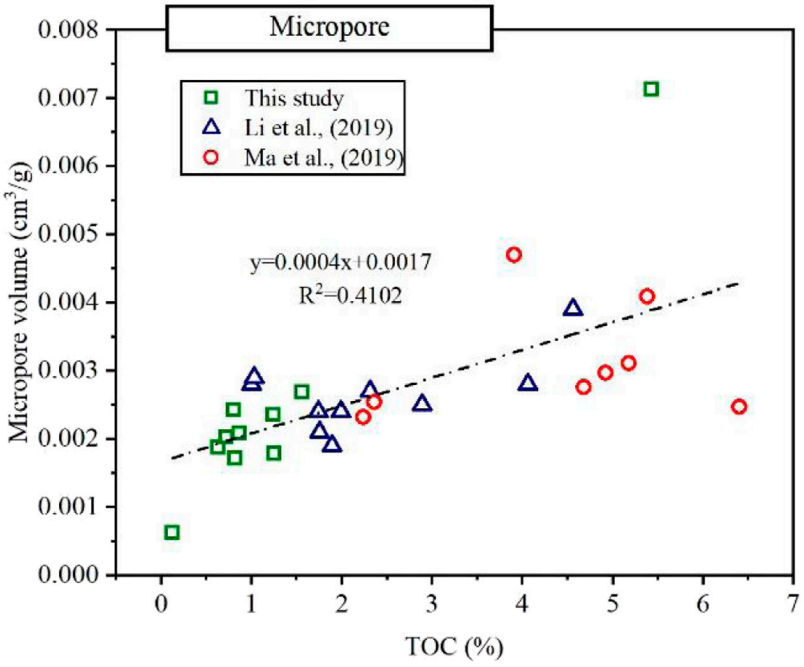

FIGURE 7
Relationship between TOC content and micropore pore volume in different marine-continental transitional shales. Notes: The blue dots are from the shale of the Shanxi Formation in the Linxing area of the Ordos Basin. Mature-high maturity shale. The clay minerals are mainly kaolinite (average 31%) (Yong Li et al., 2019). The red dots are from the Longtan Formation shale in Guizhou Province, which has a wide range of maturity (R_o is distributed between 0.86 and 2.04%). The clay minerals are mainly illite/smectite mixed layer (34% on average) (Ma et al., 2019).

heterogeneity of the marine-continental transitional shale can lead to inconsistent results. The analysis found that organic matter in the marine-continental transitional of different regions has a certain controlling effect on the degree of micropore development (Figure 7). According to Xi et al. (2018), maturity is the main factor controlling shale organic pore development, while the role of organic matter is relatively weak. The maturity controls the hydrocarbon generation potential of organic matter. When the organic matter enters the main hydrocarbon generation stage (the coal-bearing stratum Ro ranges from 0.75 to 0.9), the shale hydrocarbon generation potential is great, and the organic matter can generate a lot of pores. With the increase of TOC content, the decrease in total porosity is mainly due to two reasons. On the one hand, with the increase of organic matter, the compressibility of shale increases, and the filling of organic matter with pores leads to a decrease in pore volume (Xiong et al., 2017). On the other hand, the marine-continental transitional shale is mainly Type III kerogen. Compared with Types I and II, its macromolecular structures and chemical properties are relatively stable, which makes it difficult to change the structures of organic matter during pyrolysis and it is impossible to generate pores. Moreover, this type of kerogen is mainly gas-producing and has low hydrocarbon generation potential, which limits the development of organic matter pores. Organic matter pores are less developed and are mostly micropores. Mesopores and macropores are relatively undeveloped (Yang et al., 2016). FE-SEM observations showed that a small amount of mesoporous organic pores are developed in the shale in the study area (Figure 3F). The macropores are negatively correlated with the organic matter content or the correlation is not obvious, indicating that the marine-continental transitional shale is different from the marine shale. Organic matter in transitional shale is not related to the degree of macropore development. Previous studies have also shown that the macropores of the marine-continental transitional shales are mainly related to clay and brittle minerals (Ma et al., 2019).

The total specific surface area in the shale has a significant positive correlation with the TOC content, with R^2 of 0.64 (Figure 8A). It shows that with the increase of the TOC content, the specific surface area in shale increases. This is mainly because, compared with other pores, organic matter pores are mostly porous media with a large specific surface area during the generation and discharge of hydrocarbons (Dang et al., 2017). The TOC content has a significant positive correlation with the volume and specific surface area of the micropores, indicating that organic pores are mostly micropores (Figure 7 and Figure 8B), and the micropores have a larger specific surface area than the mesopores and macropores. Therefore, as the TOC content increases, the total pore specific surface area also tends to increase. However, the

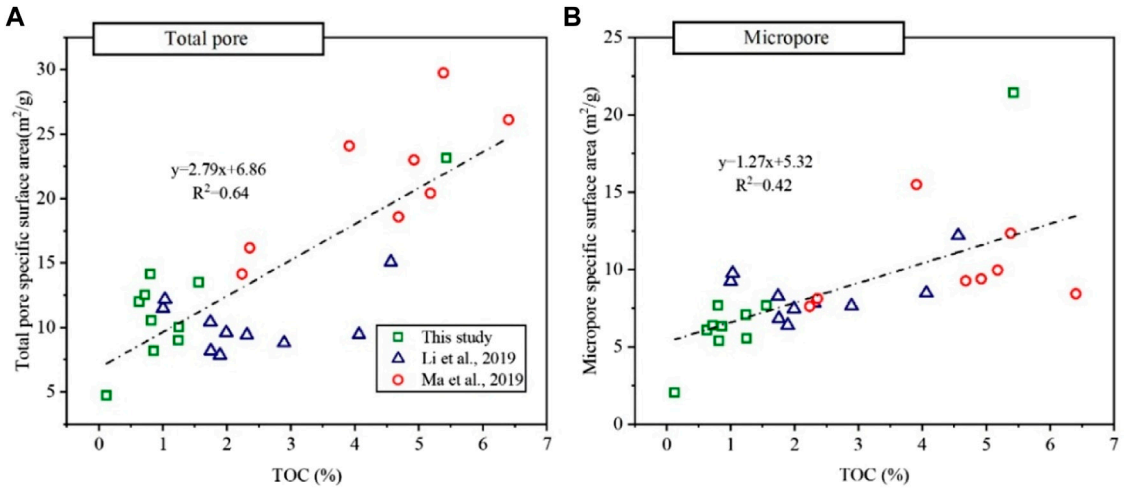

FIGURE 8
Relationship between TOC and pore specific surface area of marine-continental transitional shales in different regions. **(A)** Total pore; **(B)** Micropore.

relationship between the specific surface area of mesopores and macropores and the content of TOC is not obvious. The thermal evolution stage of organic matter has certain influence on the development of organic pores in transitional shale. Mature to highly mature samples have a higher degree of pore development (Guozhang Li et al., 2019). However, the Shanxi Formation shale in the Qinshui Basin has reached the over-mature stage. At this time, on the one hand, the organic hydrocarbon generation capacity is weak and there are no large pores, and some pores are destroyed due to reduced pore pressure (Zhang et al., 2019); on the other hand, over-mature shale leads to light hydrocarbon generation, organic carbonization and porosity reduction (Zhao et al., 2016).

Effect of minerals on pore structure

Due to the special structures and physical-chemical properties of clay minerals, pores of different shapes and sizes will be formed, and some cracks will develop. Diagenesis and sedimentary environment are two important factors controlling the type and combination of clay minerals. Different types of clay mineral crystals have different pore structures (Chalmers and Bustin, 2007; Chen et al., 2016). With the increase of the clay mineral content in the shale reservoir, the total PV shows an increasing trend (Figure 9), the mesopore and macropore volume also shows an increasing trend, while the micropores shows the opposite changing trend. This indicates that the clay minerals in the transitional shales affect the development of the total PV but have less influence on the development of micropores. According to Guozhang Li et al. (2019), the total clay content shows positive correlation with the PV of mesopores. Analyzed the characteristics of pure clay minerals and concluded that interlayer and intercrystalline pores were developed in the I/S mixed layers. These two types of pores are mainly medium to large pores with pore diameters of 1–6 nm and 20–100 nm, respectively, and the average pore diameters are 3.5 and 55 nm. Intercrystalline pores are mainly deceloped in chlorite. These pores are mesopores and macropores with a pore size distribution of 20–100 nm. The above analysis shows that different types of clay minerals develop pores of different sizes, and they are mostly mesopores and macropores. Therefore, clay content has a positive correlation with the PV except micropores.

With the increase of chlorite and I/S content in the shale reservoir, the mesopore volume increases significantly (Figure 10), but the content of kaolinite has a negative correlation with the mesopore volume. There was no significant correlation between the illite content and the mesopore pore volume. This indicates that chlorite and I/S contents are the main contributors to the mesopores. Research by Yang et al. (2016) suggested that I/S and illite in the transitional shale mainly affect the pore structures of the reservoir, while kaolinite and chlorite have a negative correlation with PV. Yong Li et al. (2019) believed that chlorite in clay minerals is the main factor affecting the pore structures of the transitional shales. It is obvious that different scholars have obtained inconsistent results when studying the effect of clay minerals on pore structures in transitional shales. Generally, compaction and different diagenetic evolution are the main factors that cause differences in shale clay mineral types and contents (Fu et al., 2015). Clay minerals are gradually transformed into relatively stable types, which changes the

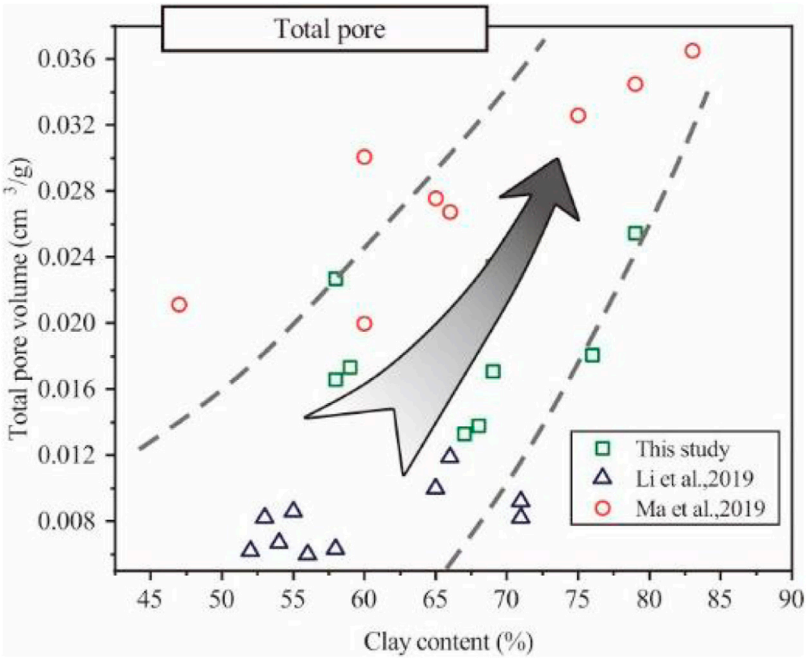

FIGURE 9
Correlation between total clay mineral content and pore volume in the marine-continental transitional shale in different regions.

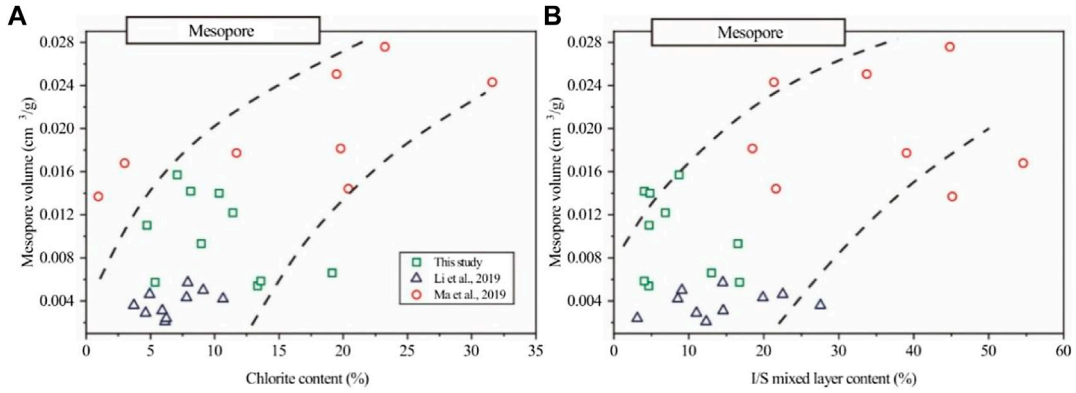

FIGURE 10
Correlation between clay minerals and mesopore volume in different marine-continental transitional shales. **(A)** Relationship between chlorite content and mesopore volume; **(B)** Relationship between I/S mixed layer content and mesopore volume.

molecular structures between layers, and the clay pores will change accordingly affected by the diagenetic evolutions. However, the research of different scholars does not deny the contribution of intercrystalline pores to the shale reservoir pores during different diagenetic stages (Chen et al., 2016). These studies suggested that the negative correlation between clay mineral types and PV was caused by the negative correlation between different clay minerals.

Brittle minerals in inorganic minerals such as quartz, feldspar, pyrite, and carbonate rocks are other factors that affect pore development in shale. The brittle mineral pores are greatly affected by the diagenesis during the sedimentation and burial. For example, compaction, pressure dissolution, cementation, and dissolution, all can cause the change of the development of theses pores. Figure 11 shows a weakly negative correlation between brittle minerals and the total pore volume. With the increase of brittle

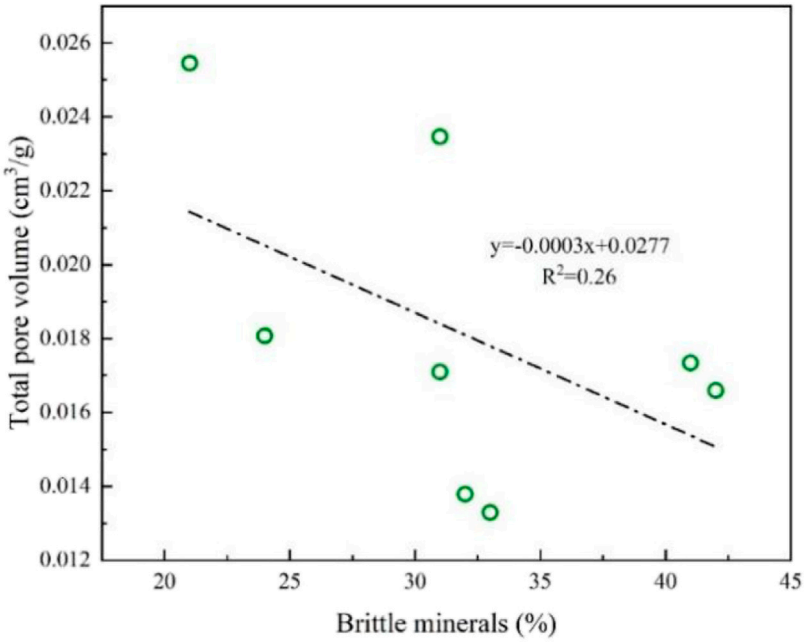

FIGURE 11
Correlation between brittle minerals and total pore volume in shale. Notes: Brittle minerals include quartz, feldspar, calcite, pyrite, and siderite.

mineral content, the total pore volume in the shale decreased slightly. This is mainly because the shale is very dense, and the acidic or alkaline fluids in the shale cannot dissolve quartz, feldspar and carbonate minerals, thus the dissolution pores are not developed. At the same time, secondary enlargement of quartz will also occupy pore spaces, thus leading to a decrease in the number of pores in shale (Kong et al., 2016).

Implications for favorable area prediction of transitional shale gas

Organic matter characteristics and mineral composition are two important parameters in the exploration and evaluation of shale gas reservoir sweet spots. The content of TOC in shale controls the degree of micropore development. Moreover, due to the hydrophilic nature of organic matter and strong intermolecular forces in micropores (Liang et al., 2016), TOC is also an important factor influencing methane adsorption capacity of shale reservoirs. The micropores contribute more to the specific surface area of shale. High TOC content increases the proportion of micropores and specific surface area in shale and can lead to the increase of the amount of shale gas adsorption. At the same time, TOC also provides a favorable location for shale gas storage. The composition of clay minerals is also an important factor that cannot be ignored. Different clay mineral contents and types have a greater impact on the pore structures of shale reservoir. High clay mineral contents provide more mesopores and macropores, and the total pore volume increases as well. When the organic matter content is low, mesopores in shales with high I/S and chlorite contents in clay minerals develop, which provides a favorable location for shale gas migration and accumulation. Therefore, the TOC content and the type and content of clay minerals are two important factors in the prediction and evaluation of sweet spots in the Upper Paleozoic clay-rich marine-continental transitional shale of the Ordos Basin.

Conclusion

- The pores in the marine-continental transitional shale in the Shanxi Formation, Ordos Basin are mostly slit-type and plate-type inorganic pores. Affected by the type of organic matter, organic matter has fewer pores and is mainly microporous, followed by a small number of mesopores. These pores are mostly bubble-like pores. Organic matter pores are the main contributors to specific surface area, with an average of 61.05%. With the increase of TOC content, the micropore volume and specific surface ratio in the reservoir increased significantly.
- For the marine-continental transitional clay-rich shale, clay mineral pores are the main pore types in inorganic pores, including clay interlayer pores, clay mineral intergranular pores, and inter-crystalline pores. With the increase of total clay content, the volume of total pores, mesopores and macropores in shale increased significantly. Chlorite and

I/S content have a greater impact on the pore development of clay minerals, followed by kaolinite and illite. Due to the special characteristics of shale and complex compaction and cementation, brittle mineral pores do not develop.

- Both TOC and clay minerals significantly affect the pore structure and methane adsorption capacity of marine-continental transitional clay-rich shale. Under the conditions of high TOC content, high I/S and chlorite content, micropores and mesopores in shale are relatively developed, and the reservoir pore space and adsorption capacity are large, which provide favorable conditions for shale gas accumulation (Li, 2021; Li, 2022).

Data availability statement

The original contributions presented in the study are included in the article/supplementary material, further inquiries can be directed to the corresponding author.

Author contributions

HX is responsible for the idea and writing of this paper, and TC and HW are responsible for the data interpretation.

Funding

This study was supported by Research on Clastic Sedimentology and Reservoir Evaluation (2019QNKYCXTD05).

Conflict of interest

YL is employed by the CNOOC Research Institute Ltd.

The remaining authors declare that the research was conducted in the absence of any commercial or financial relationships that could be construed as a potential conflict of interest.

Publisher's note

References

Cao, T., Song, Z., Wang, S., and Xia, J. (2015). A comparative study of the specific surface area and pore structure of different shales and their kerogens. *Sci. China Earth Sci.* 58, 510–522. doi:10.1007/s11430-014-5021-2

Chalmers, G. R. L., and Bustin, R. M. (2007). The organic matter distribution and methane capacity of the Lower Cretaceous strata of Northeastern British Columbia, Canada. *Int. J. Coal Geol.* 70 (1), 223–239. doi:10.1016/j.coal.2006.05.001

Chen, Q., Zhang, J., Tang, X., Dang, W., Li, Z., Liu, C., et al. (2016). Pore structure characterization of the lower permian marine-continental transitional black shale in the southern north China basin, Central China. *Energy fuels.* 30 (12), 10092–10105. doi:10.1021/acs.energyfuels.6b01475

Clarkson, C., Solano, N., Bustin, R., Bustin, A. M. M., Chalmers, G., He, L., et al. (2013). Pore structure characterization of North American shale gas reservoirs using USANS/SANS, gas adsorption, and mercury intrusion. *Fuel* 103, 606–616. doi:10.1016/j.fuel.2012.06.119

Curtis, M., Cardott, B., Sondergeld, C., and Rai, C. (2012). Development of organic porosity in the Woodford Shale with increasing thermal maturity. *Int. J. Coal Geol.* 103, 26–31. doi:10.1016/j.coal.2012.08.004

Dang, W., Zhang, J., Tang, X., Chen, Q., Han, S., Li, Z., et al. (2016). Shale gas potential of lower Permian marine–continental transitional black shales in the Southern North China Basin, central China: Characterization of organic geochemistry. *J. Nat. Gas Sci. Eng.* 28, 639–650. doi:10.1016/j.jngse.2015.12.035

Dang, W., Zhang, J., Wei, X., Tang, X., Chen, Q., Li, Z., et al. (2017). Geological controls on methane adsorption capacity of Lower Permian transitional black shales in the Southern North China Basin, Central China: Experimental results and geological implications. *J. Petroleum Sci. Eng.* 152, 456–470. doi:10.1016/j.petrol.2017.03.017

Dang, W., Zhang, J., Nie, H., Wang, F., Tang, X., Wu, N., et al. (2020). Isotherms, thermodynamics and kinetics of methane-shale adsorption pair under supercritical condition: Implications for understanding the nature of shale gas adsorption process. *Chem. Eng. J.* 383, 123191. doi:10.1016/j.cej.2019.123191

Dang, W., Nie, H., Zhang, J., Tang, X., Jiang, S., Wei, X., et al. (2022). Pore-scale mechanisms and characterization of light oil storage in shale nanopores: New method and insights. *Geosci. Front.* 13 (5), 101424. doi:10.1016/j.gsf.2022.101424

Fu, C. Q., Zhu, Y. M., and Chen, S. (2015). Diagenesis controlling mechanism of pore characteristics in the Qiongzhusi Formation Shale. *J. China Coal Geol.* 40, 439–448. doi:10.13225/j.cnki.jccs.2014.1588

Gao, F. (2019). Use of numerical modeling for analyzing rock mechanic problems in underground coal mine practices. *J. Min. Strata Control Eng.* 1 (1), 013004. doi:10.13532/j.jmsce.cn10-1638/td.2019.02.009

Guozhang Li, G., Qin, Y., Wu, M., Zhang, B., Wu, X., Tong, G., et al. (2019). The pore structure of the transitional shale in the Taiyuan formation, Linxing area, Ordos Basin. *J. Petroleum Sci. Eng.* 181, 106183–106186. doi:10.1016/j.petrol.2019.106183

He, X., Zhang, P., He, G., Gao, Y., Liu, M., Zhang, Y., et al. (2020). Evaluation of sweet spots and horizontal-well-design technology for shale gas in the basin-margin transition zone of southeastern Chongqing, SW China. *Energy Geosci.* 1 (3–4), 134–146. doi:10.1016/j.engeos.2020.06.004

Hou, E., Cong, T., and Xie, X. (2020). Ground surface fracture development characteristics of shallow double coal seam staggered mining based on particle flow. *J. Min. Strata Control Eng.* 2 (1), 013521. doi:10.13532/j.jmsce.cn10-1638/td.2020.01.002

Jiang, S., Xu, Z., Feng, Y., Zhang, J., Cai, D., Chen, L., et al. (2015). Geologic characteristics of hydrocarbon-bearing marine, transitional and lacustrine shales in China. *J. Asian Earth Sci.* 115, 404–418. doi:10.1016/j.jseaes.2015.10.016

Kong, L., Wan, M., Yan, Y., Zou, C., Liu, W., Tian, C., et al. (2016). Reservoir diagenesis research of silurian Longmaxi Formation in Sichuan Basin, China. *J. Nat. Gas Geoscience* 23, 203–211. doi:10.1016/j.jnggs.2016.08.001

Kruk, M., and Jaroniec, M. (2001). Gas adsorption characterization of ordered Organic–Inorganic nanocomposite materials. *Chem. Mat.* 13, 3169–3183. doi:10.1021/cm0101069

Kun Yu, K., Shao, C., Ju, Y., and Qu, Z. (2019). The genesis and controlling factors of micropore volume in transitional coal-bearing shale reservoirs under different sedimentary environments. *Mar. Petroleum Geol.* 102, 426–438. doi:10.1016/j.marpetgeo.2019.01.003

Lan, S. R., Song, D. Z., Li, Z. L., and Liu, Y. (2021). Experimental study on acoustic emission characteristics of fault slip process based on damage factor. *J. Min. Strata Control Eng.* 3 (3), 033024. doi:10.13532/j.jmsce.cn10-1638/td.20210510.002

Li, Y. (2021). Mechanics and fracturing techniques of deep shale from the Sichuan Basin, SW China. *Energy Geosci.* 2 (1), 1–9. doi:10.1016/j.engeos.2020.06.002

Li, H. (2022). Research progress on evaluation methods and factors influencing shale brittleness: A review. *Energy Rep.* 8, 4344–4358. doi:10.1016/j.egyr.2022.03.120

Li, Y., Zhou, D. H., Wang, W. H., Jiang, T. X., and Xue, Z. J. (2020a). Development of unconventional gas and technologies adopted in China. *Energy Geosci.* 1 (1–2), 55–68. doi:10.1016/j.engeos.2020.04.004

Li, L., Zhang, X., and Deng, H. (2020b). Mechanical properties and energy evolution of sandstone subjected to uniaxial compression with different loading rates. *J. Min. Strata Control Eng.* 2 (4), 043037. doi:10.13532/j.jmsce.cn10-1638/td.20200407.001

Li, P., Zhang, J., Rezaee, R., Dang, W., Tang, X., Nie, H., et al. (2021a). Effect of adsorbed moisture on the pore size distribution of transitional shales: Insights from clay swelling and lithofacies difference. *Appl. Clay Sci.* 34, 1–10. doi:10.1016/j.clay.2020.105926

Li, P., Zhang, J., Rezaee, R., Dang, W., Li, X., Fauziah, C., et al. (2021b). Effects of swelling-clay and surface roughness on the wettability of transitional shale. *J. Petroleum Sci. Eng.* 196, 108007. doi:10.1016/j.petrol.2020.108007

Liang, L., Xiong, J., Liu, X., and Luo, D. (2016). An investigation into the thermodynamic characteristics of methane adsorption on different clay minerals. *J. Nat. Gas Sci. Eng.* 33, 1046–1055. doi:10.1016/j.jngse.2016.06.024

Loucks, R., Reed, R., Ruppel, S., and Jarvie, D. (2009). Morphology, genesis, and distribution of nanometer-scale pores in siliceous mudstones of the mississippian barnett shale. *J. Sediment. Res.* 79, 848–861. doi:10.2110/jsr.2009.092

Ma, X., Guo, S., Shi, D., Zhou, Z., and Liu, G. (2019). Investigation of pore structure and fractal characteristics of marine-continental transitional shales from Longtan Formation using MICP, gas adsorption, and NMR (Guizhou, China). *Mar. Petroleum Geol.* 107, 555–571. doi:10.1016/j.marpetgeo.2019.05.018

Nie, H., Li, D., Liu, G., Lu, Z., Hu, W., Wang, R., et al. (2020). An overview of the geology and production of the Fuling shale gas field, Sichuan Basin, China. *Energy Geosci.* 1 (3–4), 147–164. doi:10.1016/j.engeos.2020.06.005

Qi, Y., Ju, Y., Huang, C., Zhu, H., Bao, Y., Wu, J., et al. (2019). Influences of organic matter and kaolinite on pore structures of transitional organic-rich mudstone with an emphasis on S2 controlling specific surface area. *Fuel* 237, 860–873. doi:10.1016/j.fuel.2018.10.048

Santosh, M., and Feng, Z. Q. (2020). New horizons in energy geoscience. *Energy Geosci.* 1 (1–2), 1. doi:10.1016/j.engeos.2020.05.005

Sun, M., Yu, B., Hu, Q.-H., Chen, S., Xia, W., and Ye, R. (2015). Nanoscale pore characteristics of the lower cambrian niutitang Formation shale: A case study from well yuke #1 in the southeast of chongqing, China. *Int. J. Coal Geol.* 154, 16–29. doi:10.1016/j.coal.2015.11.015

Sun, Z., Wang, Y., Wei, Z., Zhang, M., Wang, D., Wang, Z., et al. (2017). Shale gas content and geochemical characteristics of marine-continental transitional shale: A case from the Shanxi Formation of Ordos Basin. *J. China Univ. Min. Technol.* 46 (4), 859–868. doi:10.13247/j.cnki.jcumt.000663

Sun, C., Nie, H., Dang, W., Chen, Q., Zhang, G., Li, W., et al. (2021). Shale gas exploration and development in China: Current status, geological challenges, and future directions. *Energy fuels.* 35 (8), 6359–6379. doi:10.1021/acs.energyfuels.0c04131

Valenza, J. J., Drenzek, N., Marques, F., Pagels, M., and Mastalerz, M. (2013). Geochemical controls on shale microstructure. *Geology* 41 (5), 611–614. doi:10.1130/g33639.1

Wang, G., Ju, Y., Yan, Z., and Li, Q. (2015). Pore structure characteristics of coal–bearing shale using fluid invasion methods: A case study in the huainan–huaibei coalfield in China. *Mar. Petroleum Geol.* 62, 1–13. doi:10.1016/j.marpetgeo.2015.01.001

Wang, H., Shi, Z., Zhao, Q., Liu, D., Sun, S., Guo, W., et al. (2020). Stratigraphic framework of the Wufeng-Longmaxi shale in and around the Sichuan Basin, China: Implications for targeting shale gas. *Energy Geosci.* 1 (3–4), 124–133. doi:10.1016/j.engeos.2020.05.006

Xi, Z., Tang, S., Zhang, S., and Li, J. (2017). Nano-Scale pore structure of marine-continental transitional shale from liulin area, the eastern margin of Ordos Basin, China. *J. Nanosci. Nanotechnol.* 17, 6109–6123. doi:10.1166/jnn.2017.14501

Xi, Z., Tang, S., Wang, J., Yang, G., and Li, L. (2018). Formation and development of pore structure in marine-continental transitional shale from northern China across a maturation gradient: Insights from gas adsorption and mercury intrusion. *Int. J. Coal Geol.* 200, 87–102. doi:10.1016/j.coal.2018.10.005

Xiong, F., Jiang, Z., Li, P., Wang, X., Bi, H., Li, Y., et al. (2017). Pore structure of transitional shales in the Ordos Basin, NW China: Effects of composition on gas storage capacity. *Fuel* 206, 504–515. doi:10.1016/j.fuel.2017.05.083

Xu, H., Zhou, W., Hu, Q., Xia, X., Zhang, C., and Zhang, H. (2019a). Fluid distribution and gas adsorption behaviors in over-mature shales in southern China. *Mar. Petroleum Geol.* 109, 223–232. doi:10.1016/j.marpetgeo.2019.05.038

Xu, H., Zhou, W., Zhang, R., Liu, S., and Zhou, Q. (2019b). Characterizations of pore, mineral and petrographic properties of marine shale using multiple techniques and their implications on gas storage capability for Sichuan Longmaxi gas shale field in China. *Fuel* 241, 360–371. doi:10.1016/j.fuel.2018.12.035

Xu, N., and Gao, C. (2020). Study on the special rules of surface subsidence affected by normal faults. *J. Min. Strata Control Eng.* 2 (1), 011007. doi:10.13532/j.jmsce.cn10-1638/td.2020.01.011

Yan, D., Huang, W., and Zhang, J. (2015). Characteristics of marine continental transitional organic rich shale in the Ordos Basin and its shale gas significance. *Earth Sci. Froniters* 22 (6), 197–206. doi:10.13745/j.esf.2015.06.015

Yang, C., Zhang, J., Tang, X., Ding, J., Zhao, Q., Dang, W., et al. (2016). Comparative study on micro-pore structure of marine, terrestrial, and transitional shales in key areas, China. *Int. J. Coal Geol.* 171, 76–92. doi:10.1016/j.coal.2016.12.001

Yin, S., and Gao, Z. (2019). Numerical study on the prediction of "sweet spots" in a low efficiency-tight gas sandstone reservoir based on a 3D strain energy model. *IEEE Access* 7, 117391–117402. doi:10.1109/access.2019.2933450

Yin, S., Lv, D., and Ding, W. (2018). New method for assessing microfracture stress sensitivity in tight sandstone reservoirs based on acoustic experiments. *Int. J. Geomech.* 18 (4), 1–16. doi:10.1061/(asce)gm.1943-5622.0001100

Yin, S., Tian, T., and Wu, Z. (2019). Developmental characteristics and distribution law of fractures in a tight sandstone reservoir in a low-amplitude tectonic zone, eastern Ordos Basin, China. *Geol. J.* 54 (6), 1546–1562. doi:10.1002/gj.3521

Yong Li, Y., Wang, Z., Pan, Z., Niu, X., Yu, Y., and Meng, S. (2019). Pore structure and its fractal dimensions of transitional shale: A cross-section from east margin of the Ordos Basin, China. *Fuel* 241, 417–431. doi:10.1016/j.fuel.2018.12.066

Yu, Y., Luo, X., Lei, Y., Chen, M., Wang, X., and Zhang, L. (2016). Characterization of lacustrine shale pore structure: An example from the upper-triassic yanchang formation, Ordos Basin. *Nat. Gas. Geosci.* 27 (4), 716–726. doi:10.11764/j.issn.1672-1926.2016.04.0716

Yuxi Yu, Y., Luo, X., Wang, Z., Cheng, M., Lei, Y., Zhang, L., et al. (2019). A new correction method for mercury injection capillary pressure (MICP) to characterize the pore structure of shale. *J. Nat. Gas Sci. Eng.* 68, 102896–102896. doi:10.1016/j.jngse.2019.05.009

Zhang, M., Fu, X., Zhang, Q., and Cheng, W. (2019). Research on the organic geochemical and mineral composition properties and its influence on pore structure of coal-measure shales in Yushe-Wuxiang Block, South Central Qinshui Basin, China. *J. Petroleum Sci. Eng.* 34, 1–7. doi:10.1016/j.petrol.2018.10.079

Zhang, J., Tang, X., Huo, Z., Li, Z., Lee, E., Luo, K. Y., et al. (2020). Assessment of shale gas potential of the lower Permian transitional Shanxi-Taiyuan shales in the southern North China Basin. *Aust. J. Earth Sci.* 68, 262–284. doi:10.1080/08120099.2020.1762737

Zhao, W., Li, J., Yang, T., Wang, S., and Huang, J. (2016). Geological difference and its significance of marine shale gases in South China. *Petroleum Explor. Dev.* 43, 547–559. doi:10.1016/s1876-3804(16)30065-9

Zhao, Z., Wu, K., Fan, Y., Guo, J., Zeng, B., and Yue, W. (2020). An optimization model for conductivity of hydraulic fracture networks in the Longmaxi shale, Sichuan basin, Southwest China. *Energy Geosci.* 1 (1–2), 47–54. doi:10.1016/j.engeos.2020.05.001

Zhao, K. K., Jiang, P. F., Feng, Y. J., Sun, X. D., Cheng, L. X., and Zheng, J. W. (2021). Investigation of the characteristics of hydraulic fracture initiation by using maximum tangential stress criterion. *J. Min. Strata Control Eng.* 3 (2), 023520. doi:10.13532/j.jmsce.cn10-1638/td.20201217.001

Zheng, H., Zhang, J., and Qi, Y. (2020). Geology and geomechanics of hydraulic fracturing in the Marcellus shale gas play and their potential applications to the Fuling shale gas development. *Energy Geosci.* 1 (1–2), 36–46. doi:10.1016/j.engeos.2020.05.002

Zhu, W., Niu, L., and Li, S. (2019). Creep-impact test of rock: Status-of-the-art and prospect. *J. Min. Strata Control Eng.* 1 (1), 013003. doi:10.13532/j.jmsce.cn10-1638/td.2019.02.007

frontiers | Frontiers in Earth Science

TYPE Original Research
PUBLISHED 09 September 2022
DOI 10.3389/feart.2022.1012607

OPEN ACCESS

EDITED BY
Hu Li,
Southwest Petroleum University, China

REVIEWED BY
Qin Zhang,
China University of Petroleum, Beijing, China
Qrong Qin,
Southwest Petroleum University, China

*CORRESPONDENCE
Chao Gao,
ycgaochao@qq.com

SPECIALTY SECTION
This article was submitted to Structural Geology and Tectonics, a section of the journal Frontiers in Earth Science

RECEIVED 05 August 2022
ACCEPTED 18 August 2022
PUBLISHED 09 September 2022

CITATION
Wang X, Liang Q, Gao C, Xue P, Yin J and Hao S (2022), Hydrocarbon accumulation model influenced by "three elements (source-storage-preservation)" in lacustrine shale reservoir-A case study of Chang 7 shale in Yan'an area, Ordos Basin. *Front. Earth Sci.* 10:1012607. doi: 10.3389/feart.2022.1012607

Hydrocarbon accumulation model influenced by "three elements (source-storage-preservation)" in lacustrine shale reservoir-A case study of Chang 7 shale in Yan'an area, Ordos Basin

Xiangzeng Wang, Quansheng Liang, Chao Gao*, Pei Xue, Jintao Yin and Shiyan Hao

Shaanxi Yanchang Petroleum (Group) Corp., Ltd., Xi'an, China

The organic-rich shales of the Chang 7 Member in the Yan'an Formation of the Yan'an area, Ordos Basin is a hot spot for lacustrine shale gas exploration. In this paper, taking the Chang 7 Member shale in the Yan'an area as an example, the main controlling factors of lacustrine shale gas accumulation and the prediction of "sweet spots" are systematically carried out. The results show that the Yanchang Formation shale has the complete gas generating conditions. Shale gas accumulation requires three necessary accumulation elements, namely gas source, reservoir and good preservation conditions. The dynamic hydrocarbon generation process of the Chang 7 shale reservoirs is established according to the thermal simulation experiments of hydrocarbon generation, and the mechanism of catalytic degradation and gas generation in the Chang 7 Member under the background of low thermal evolution degree is revealed. The enriched authigenic pyrite can catalyze the hydrocarbon generation of organic matter with low activation energy, thereby increasing the hydrocarbon generation rates in the low-mature-mature stage. Different types of pores at different scales (2–100 nm) form a multi-scale complex pore network. Free gas and dissolved gas are enriched in laminar micro-scale pores, and adsorbed gas is enriched in nano-scale pores of thick shales, and silty laminates can improve the physical properties of the reservoir. This is because the laminar structure has better hydrocarbon generation conditions and is favorable for the migration of oil and gas molecules. The thickness of the lacustrine shale in the Chang 7 Member is between 40 and 120 m, which has exceeded the effective hydrocarbon expulsion thickness limit (8–12 m). At the end of the Early Cretaceous, the excess pressure of the Chang 7 shale was above 3 MPa. At present, horizontal wells with a daily gas production of more than 50,000 cubic meters are distributed in areas with high excess pressures during the maximum burial depth.

KEYWORDS

Ordos Basin, lacustrine shale gas, hydrocarbon generation, storage, accumulation model

1 Introduction

Organic-rich shale is widely developed in China, and the shale gas resource potential is huge (Ji et al., 2012; Zhao et al., 2016; Fan et al., 2020; Zheng et al., 2020). According to the sedimentary geological conditions, it is divided into marine shale, continental shale and marine-continental transitional shale (Lama and Vutukuri, 1978; Wu and Yu, 2007; Yang et al., 2016; Hong et al., 2020; Mahmud et al., 2020; Katz et al., 2021; Lan et al., 2021; Qie et al., 2021). Under the guidance of the theory of "binary control of hydrocarbon enrichment" of highly evolved marine shale gas in complex structural areas, the first large-scale shale gas field, i.e., Fuling Gas Field, was discovered in the southern China on 28 November 2012. Two-thirds of China's shale gas resources are distributed in lacustrine shale sedimentary strata. The current research practice has confirmed that the maturity of lacustrine shales in China is low (oil generation stage), and the gas generating range is small. How to find large-scale hydrocarbon accumulation areas is the main challenge of shale oil and gas exploration in China (Sun et al., 2017; Xu et al., 2019; Xue et al., 2021).

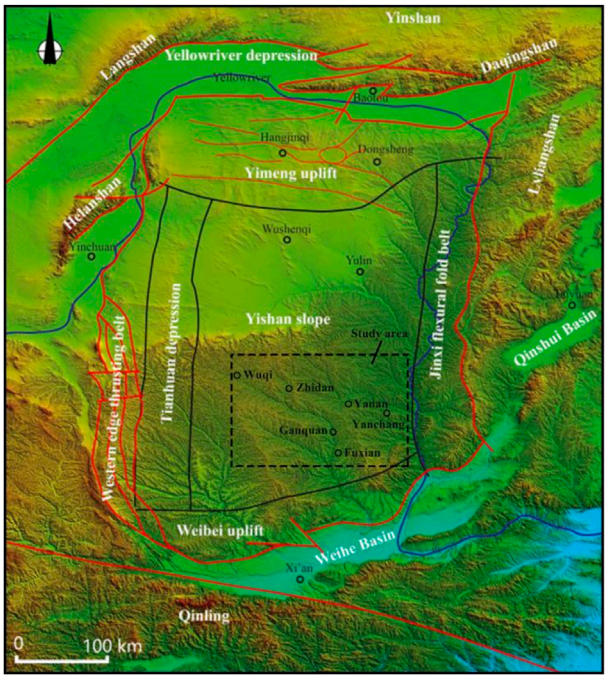

FIGURE 1
Location of the study area (modified by Xu et al., 2022).

The geological resources of lacustrine shale gas in the Ordos Basin are 2.42 × 10^{12} m^3. With the gradual breakthrough of lacustrine shale gas production and the continuous deepening of research work, the exploration of shale gas enrichment areas and high-yield areas has become the focus of current hydrocarbon exploration. Compared with marine shale, the reservoir heterogeneity of lacustrine shale is stronger (Ursula and Jorge., 2014; Liang et al., 2016; Li et al., 2019; Yu K. et al., 2019; Asante-Okyere et al., 2021). In addition, lacustrine shale also has the characteristics of high clay mineral content, high adsorbed gas ratio, low thermal evolution degree, low brittle mineral content, and low formation pressure. Therefore, the accumulation law of lacustrine shale gas is more complex, and its requirements for the oil and gas development technology are higher (Sun et al., 2017; Xu et al., 2019; Santosh and Feng., 2020; Vafaie et al., 2021). The mechanism of lacustrine shale gas accumulation has become a hot issue that has attracted much attention. In this paper, taking the Chang 7 Member shale in the Yan'an area as an example, the main controlling factors of lacustrine shale gas accumulation and the prediction of "sweet spots" are systematically carried out based on a large number of geochemical and reservoir characterization experiments. This study can provide a theoretical basis for supporting further exploration and development of lacustrine shale gas.

2 Databases and methods

2.1 Geological background

The study area is located in the southeastern part of the Ordos Basin, and the administrative area belongs to the Yan'an City, Shaanxi Province (Figure 1). Low-amplitude uplifts in the Ordos Basin are well developed. This area presents a regional slope that tilts from the east to the west. Several sets of organic-rich shale are deposited in the study area. The burial depth of the Chang 7 Member of the Mesozoic Yanchang Formation is between 500 and 2,000 m, which has good geological conditions and resource base for shale gas accumulation.

The sedimentary period of the Chang 7 Member was the heyday of the development of the lake basin, and it belonged to the sedimentary environment of shallow lacustrine to semi-deep lacustrine facies. 50–80 m shales ("Zhangjiatan" shale) are developed in the Chang 7 Member in the study area. The average clay mineral content of the Chang 7 shale is 46.71%, and the average content of the quartz and feldspar is 27.77% and 16.83%, respectively. In fact, the Chang 7 Member shale has lower brittle mineral content and stronger plasticity.

TABLE 1 Geochemical parameters of the Chang 7 Member samples of the hydrocarbon generation kinetic pyrolysis experiments.

Well	Depth (m)	Lithology	TOC (%)	S1 (mg/g)	S2 (mg/g)	S3 (mg/g)	TMAX (°C)	IH (mg/g·TOC)	IO (mg/g·TOC)
DT005	687.9	Shale	2.23	1.22	6.53	0.22	443	292	9

2.2 Materials and methods

2.2.1 Thermal simulation experiments of hydrocarbon generation

In this study, the Chang 7 shale samples from the Well DT005 in the study area were selected for the hydrocarbon generation kinetic experiments. The geochemical characteristics of the samples are listed in Table 1. It can be seen from Table 1 that the burial depth of the samples is 687.9 m. The TOC of the samples was 2.23%, the hydrogen index was 292 mg/g·TOC, and the T_{max} was 443°C. This shows that the thermal evolution degree of the samples is relatively low, which meets the requirements of the hydrocarbon generation kinetic pyrolysis experiments. In this experiment, an open system hydrocarbon generation kinetics pyrolysis experiment was used, and the open system hydrocarbon generation kinetics experiment could exclude secondary cracking during the experiments.

2.2.2 Experiments on pore structures and fluid occurrence

The instrument for analyzing the physical properties of tight rocks such as shale is the SPEC-PMR-20M nuclear magnetic resonance core analyzer. The main technical parameters and functions of the instrument are as follows: magnetic field frequency: 20 M; test area: Φ 25 mm × 40 mm cylinder. First, the pore structures and porosity of the organic matter in the sample before extraction are tested, which is the pore volume occupied by free gas (assuming that it is fully occupied by shale gas), that is, the gas-bearing porosity. The gas porosity minus the pore volume of adsorbed gas is the pore volume occupied by free gas. Then, an organic solvent was used to extract the chloroform pitch "A" content of the samples. The obtained porosity is the sum of the volume of liquid oil and gas-containing pores, namely the hydrocarbon-containing porosity; the difference between the porosity and the gas-containing porosity is the oil-containing porosity. Dissolved gas can be calculated according to the solubility of shale gas in liquid hydrocarbons and the saturations of oil.

3 Results

3.1 Development characteristics of high-quality source rocks

The TOC content of the Chang 7 shale in the study area is mainly distributed between 3% and 6%, with an average of 4.8%. However, it can be seen from the analysis of pyrolysis parameters and the triangular map of micro-composition (Figure 2A) that the sum of the exinite and inertic components of the Chang 7 shale basically exceeds 55%. It shows that the hydrogen-rich components favorable for hydrocarbon generation are abundant, which lays a material foundation for the generation of shale gas. The organic matter type of the Chang 7 Member is mainly Type II_1, followed by Type II_2, and there is no Type I organic matter. Its R_o is mainly distributed in 0.7%–1.2%. It belongs to high-quality source rock and is the main source rock of the Yanchang Formation.

From the chemical structures of microcomponents and their hydrocarbon-generating properties, it can be seen that the vitrinite is richer in short-chain alkyl groups than saprolite and chitinite, which is beneficial to the generation of natural gas. Therefore, the higher gas generation rate of the Yanchang Formation shale in the low-mature-mature evolution stage is closely related to the mixed organic matter composition of terrigenous higher plants and lower organisms (Figure 2B). The organic matter composition of the Barnett low-mature shales contain more than 80% asphaltene bodies (exinite), and the content of vitrinite is very low, which is obviously different from the Yanchang Formation shales. The gas generation activation energy of the Chang 7 shale is lower than that of the Barnett shale, which is favorable for a large amount of gas generation in the early stage of thermal evolution of the Chang 7 shale. The TOC of the Barnett shale sample used in the experiment is 5.51%, the R_o is 4.4%, and the organic matter type is Type II. Compared with the experimental samples in this study, the Barnett shale samples are less mature and the experimental heating rate is slightly lower. Comparative analysis shows that the average activation energy of kerogen gas generation in the Yanchang Formation shale is 56 kcal/mol, which is lower than that of the Barnett shale (average 62 kcal/mol). When $EasyR_o$ is 0.8%–1.3%, the gas generation potential of Chang 7 shale is 20–80 ml/gTOC, which is higher than that of Barnett shale (18–55 ml/gTOC) (Figure 3). It is an important manifestation of the difference in kerogen properties between lacustrine shale and marine shale in the Yanchang Formation. Taking the TOC of the Yanchang Formation shale as the benchmark of 5%, when it can reach the gas generation potential of 2 m^3/t rock, the organic matter maturity of the kerogen thermal simulation sample is about 1.0% $EasyR_o$ (Figure 4A). The increase of the total organic carbon content can reduce the maturity requirement (Figure 4B).

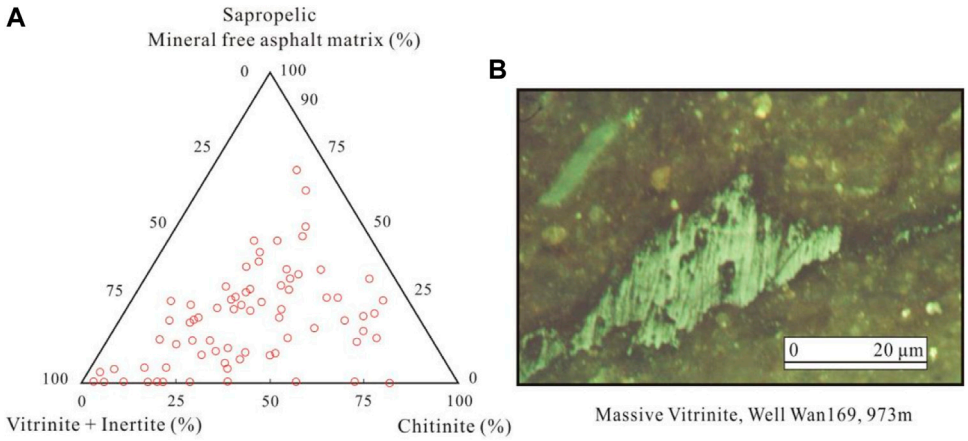

FIGURE 2
Composition of the Chang 7 Member shale in the study area. **(A)** Microscopic composition of kerogen in the Chang 7 member; **(B)** Massive vitrinite structure of the Chang 7 Member shale.

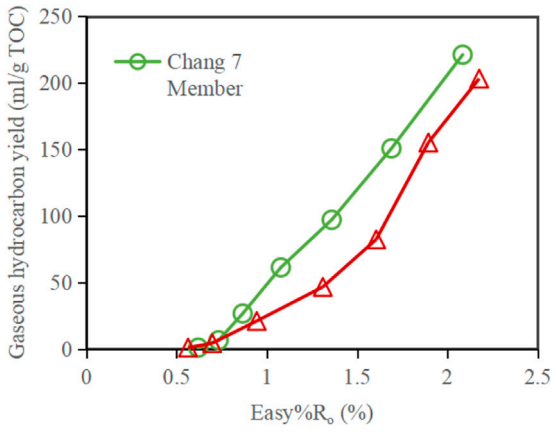

FIGURE 3
Comparison of kerogen gas generation potential between the Yanchang Formation shale and the Barnett Shale.

3.2 Catalysis of pyrite

From the perspective of hydrocarbon generation kinetics, pyrite and aromatic hydrocarbon compounds can also undergo addition reaction under certain conditions to generate organic sulfur-rich kerogen (Kong et al., 2016; Xiong et al., 2017; Mahmoodi et al., 2019; Jiang et al., 2022; Li., 2022). The kerogen rich in organic sulfur can be broken at a relatively low temperature due to the low bond energy of the C-S bond. Pyrite Fe^{2+} is a transition metal, it can significantly affect the electron cloud distribution of cracked organic matter, reduce the activation energy of cracking organic matter, and promote hydrocarbon generation (Loucks et al., 2012; Milliken et al., 2013; Sun et al., 2015; Zhang et al., 2020; Wang et al., 2022). As an inducer, pyrite can promote the formation of hydrocarbons by inducing the formation of free radicals in the process of organic hydrocarbon generation (Wyllie and Spangler, 1952; Tiab and Donaldson., 2004; Roy et al., 2014; Oluwadebi et al., 2019).

The morphological characteristics of pyrite in the Chang 7 Member shale are studied in detail. The analysis shows that a large number of pyrites are developed in the shale of the Chang 7 Member. Vertically, the abundance of pyrite and the content of organic carbon change synergistically, that is, their content has a strong positive correlation. The pyrite content of the Well Yaoye 1 is 0.2%–1% from the bottom of the Chang 7 Member (250–240 m). The pyrite content is very low, even below the detection limit of 5%. At the same depth, the organic carbon content of fine-grained sedimentary rocks does not exceed 5%, generally around 1%. In the 230–220 m interval, the pyrite content gradually increased to more than 10%, and some samples had more than 30% pyrite content. As the pyrite content increased, the organic carbon abundance also increased to above 10%, and some exceeded 25%. In the 220–190 m well section, the pyrite content showed a gradual downward trend, and the content was less than 1%. At the same time, the organic carbon content of the samples was mostly below 3%. Therefore, in the Chang 7 Member shale in the study area, high organic carbon content corresponds to high pyrite content, which is favorable for the formation of shale gas (Figure 5).

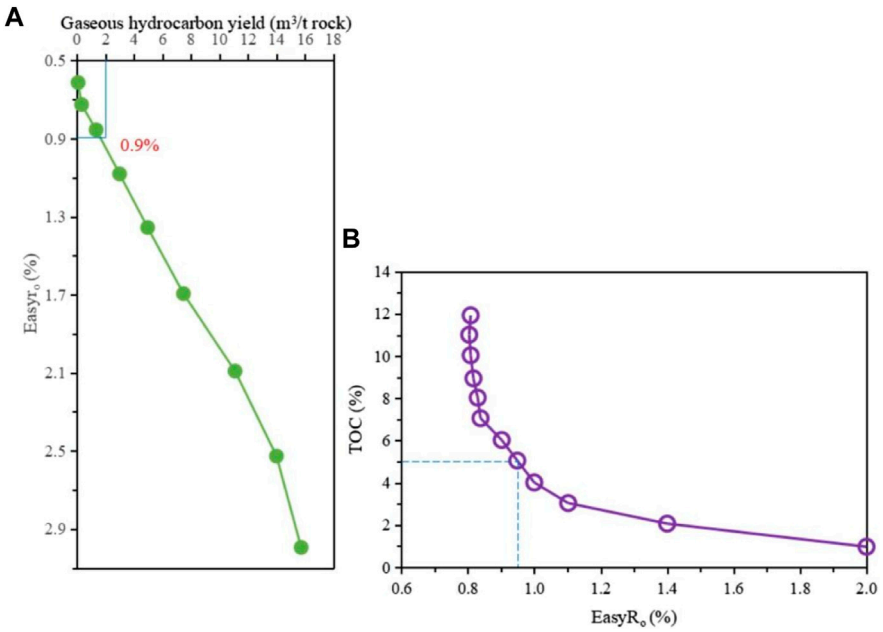

FIGURE 4
Relationship between hydrocarbon generation potential parameters of the Chang 7 Member shale. **(A)** Gas generation potential per unit mass of the Chang 7 shale (based on TOC of 5%); **(B)** Relationship between TOC and EasyRo.

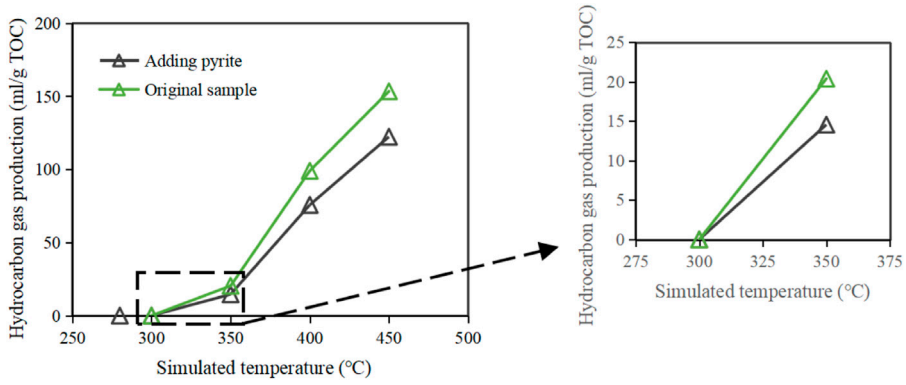

FIGURE 5
Comparison of gas generation potential before and after adding pyrite to the Chang 7 Member shale.

3.3 Characteristics of thermal evolution degree of shale reservoirs

The organic matter of the Chang 7 Member shale is mainly Type II_1, with R_o in the range of 0.5%–1.33%, and has low activation energy of gas generation. These characteristics are favorable for gas generation in mature stage.

During the thermal evolution of kerogen, gases such as methane continue to be generated. For the mixed kerogen of the Yanchang Formation, the generation rate is low in the period of low temperature, which is not conducive to the formation and enrichment of shale gas (Valenza et al., 2013; Wang et al., 2015; Yu Y. et al., 2019). However, stratigraphic uplift that began in the mid-Cretaceous limits the further production of natural gas in the shale. Therefore, in the process of natural gas formation, uplift or temperature decrease caused by tectonic evolution is an important external factor restricting the gas generation process of the Yanchang Formation shale. The analysis of paleo-tectonic

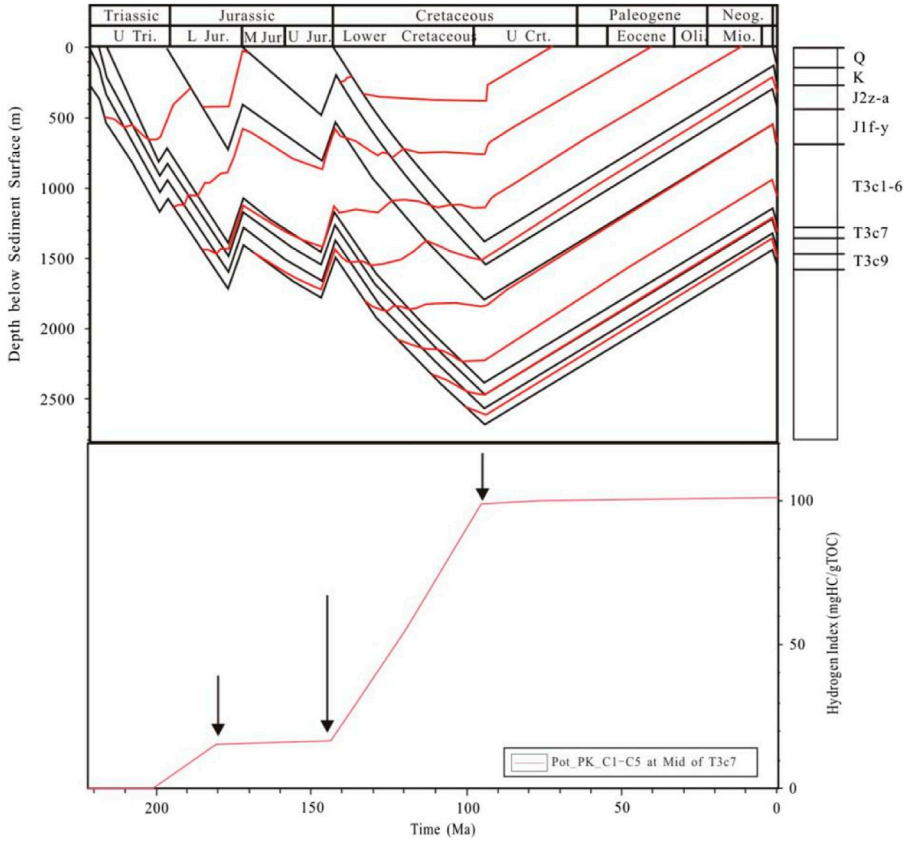

FIGURE 6
Hydrocarbon generation and evolution characteristics revealed by kerogen-enclosed high temperature and high pressure thermal simulation.

restoration and tectonic evolution history shows that the maximum burial depth corresponding to the bottom of the Yanchang Formation in different regions is different, and it is mainly distributed between 2,500 and 3,100 m.

According to the basin simulation results, the evolution process of shale gas generation in the Chang 7 Member in the study area can be divided into four stages (Figure 6): 1) At the end of the Late Triassic (before 200 Ma), there was basically no natural gas generation; 2) From the Early Jurassic to the end of the Late Jurassic (200–145 Ma), the generation rate of natural gas was low, and the generation of natural gas was stagnant due to structural uplift; 3) From the Late Jurassic to the end of the Early Cretaceous (145–95 Ma), the Yanchang Formation was rapidly buried and matured, and it was a period of massive natural gas generation; 4) From the end of the Early Cretaceous to the present (95 Ma-), the strata were uplifted and denuded, the gas generation rate of shale was greatly reduced, and the gas generation stopped. Under geological conditions, the cumulative gas conversion rate of the Yanchang Formation shale is about 30%.

The Trinity Basin Simulation System was used to evaluate the gas generation potential. According to the shale thickness and total organic carbon (TOC) content of the target layer, the gas generation intensity and potential of shale in different layers are calculated. The evaluation results show that the current cumulative maximum gas generation intensity of the Chang 7 Member shale in the study area is 9×10^8 m^3/km^2. The center of gas intensity is located in the areas of the Danba, Xiasiwan and Zhangjiawan cities. Field analysis shows that the total gas content of the Chang 7 Member shale ranges from 2.10 to 5.23 m^3/t, with an average of 3.8 m^3/t; the adsorbed gas content is 65%–85%, with an average of 70%; and the average free gas content is 20%. In addition to alkane gas, the gas components in the target layer also include non-hydrocarbon gases such as carbon dioxide and nitrogen. The content of heavy hydrocarbons in the hydrocarbon gas component is high, and the drying coefficient of the gas is generally low, and the drying coefficient (C_1/C_{1-5}) is generally lower than 0.95. This shows that the shale gas in this area is mainly wet gas (Figure 7).

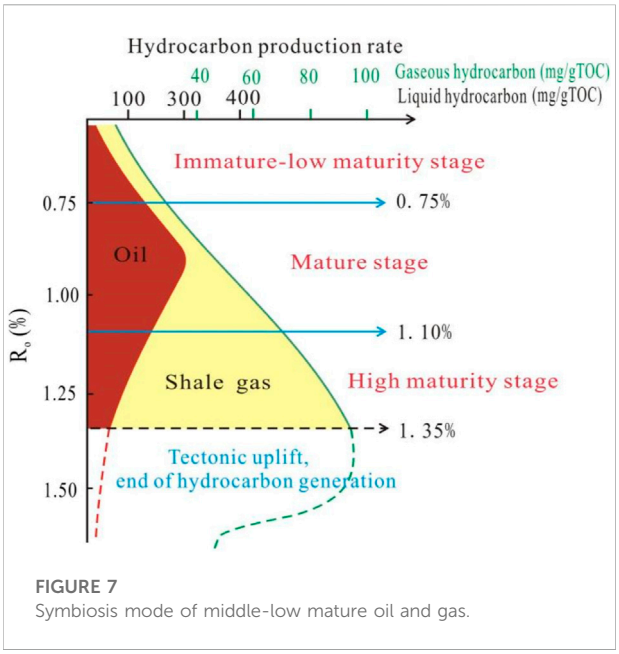

FIGURE 7
Symbiosis mode of middle-low mature oil and gas.

4 Discussion

4.1 Analysis of shale gas occurrence conditions based on multi-type and cross-scale complex pore network

Spaces of porous reservoir of various types and scales are the places where oil and gas occur in shale. The observation results under the microscope show that the residual intergranular pores between rigid clastic grains and intercrystalline pores of clay minerals are developed in the shale. Part of the edges of the intergranular pores were eroded to form erosion enlarged pores. The pore size of the intergranular pores in the Yanchang Formation shale is mainly ranges from 5 to 600 nm, with a maximum of 3.4 μm, and the pore size of most pores is less than 200 nm, with an average of 75 nm (Figure 8). Intragranular pores include intragranular dissolved pores such as feldspar and calcite, mold pores, intragranular pores in aggregates such as clay mineral aggregates and strawberry-like pyrite, and fossil cavity pores. The pore size of the intragranular pores in the Yanchang Formation shale is mostly less than 200 nm, and the maximum value can reach 4.7 μm. The intragranular pores with larger pore sizes are dissolved pores of feldspar particles, and the peak pore size is 20–30 nm.

The macropores of the Yanchang Formation shale are mainly occupied by free gas, followed by liquid hydrocarbons, and the volume of adsorbed gas is negligible.

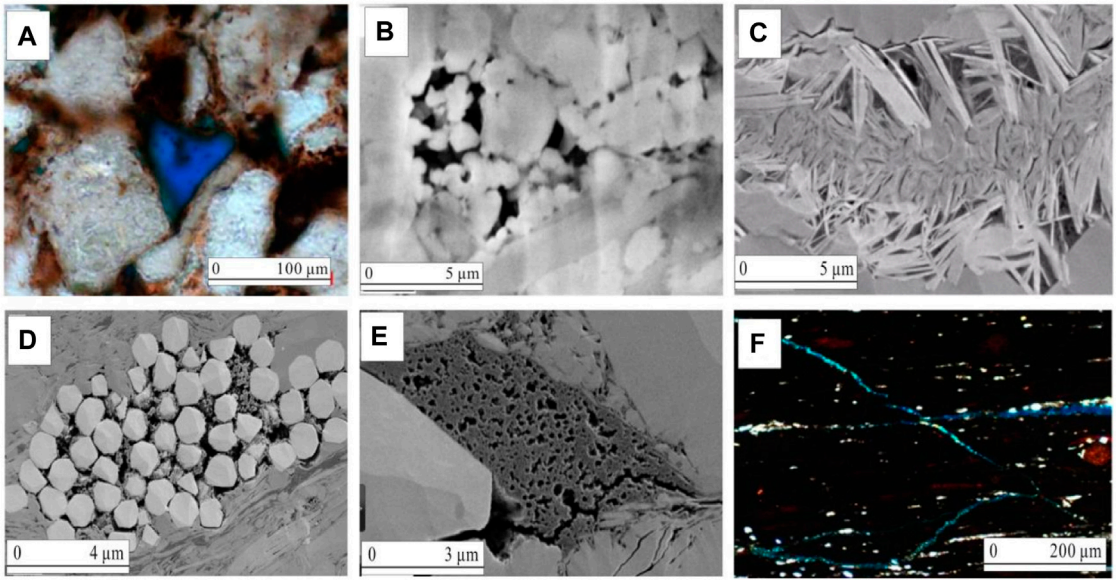

FIGURE 8
Micrographs of pore types in the Chang 7 shale. **(A)** Residual intergranular pores in siltstone interlayer, Well YY3, single polarized light, 1,325 m; **(B)** Intergranular dissolution pores, SEM, Well YY8, 1,522.8 m; **(C)** Intragranular pores of clay mineral aggregates, SEM, Well YY7, 1,140.1 m; **(D)** Intragranular pores of pyrite aggregates, SEM, Well YY22, 1,299.73 m; **(E)** Organic pores filled with organic matter in the inorganic intergranular pores between the debris particles, SEM, Well YY6, 1,307.32 m; **(F)** Laminates and bedding fractures, cross polarized light, Well YY11, 1,378.37 m).

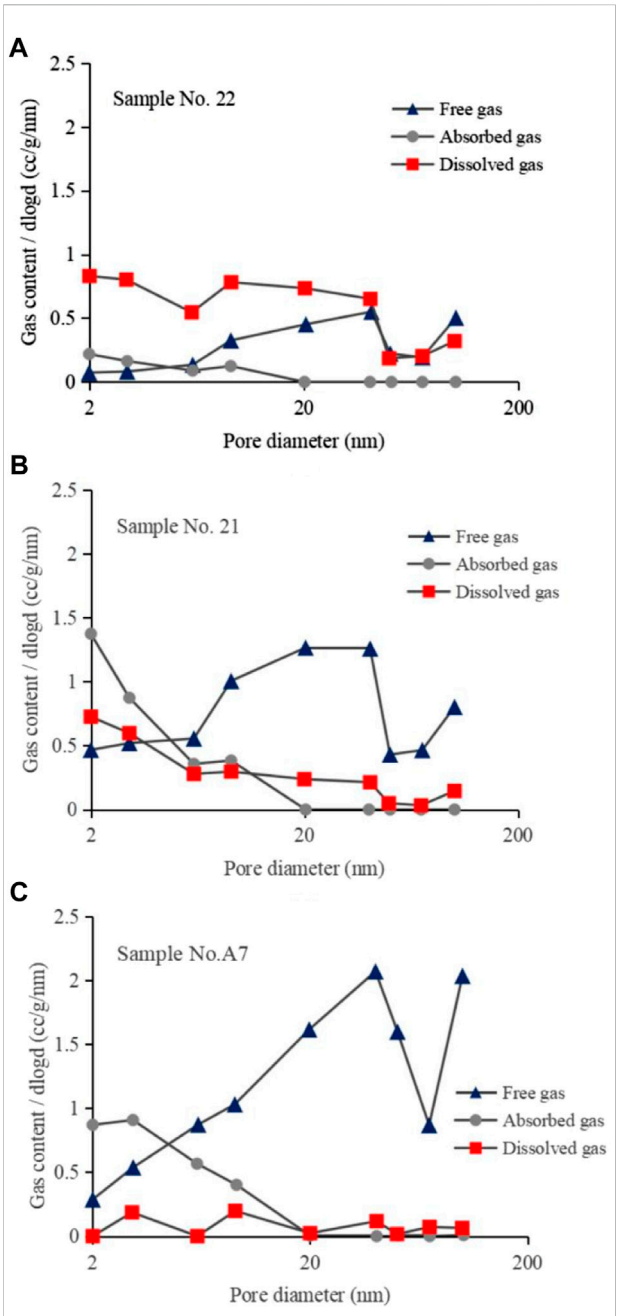

FIGURE 9
Occurrence volumes of various phase fluids in different pores in the 2–100 nm pore size range (25°C, 13 MPa). **(A)** Sample No. 22; **(B)** Sample No. 21; **(C)** Sample No. A7.

The ratio of adsorbed gas to free gas is 3:7. On the whole, the volume proportion of liquid hydrocarbons in the macropores of the three rock types is generally low (below 30%), with an average of 15%. Some siltstones (No. 34) and silt-bearing laminar shale (No. 21) have a relatively high volume of liquid hydrocarbons in large pores, accounting for 45% and 31%, respectively (Figure 9).

Figure 9 shows the volume changes of adsorbed gas, free gas and liquid hydrocarbons in the meso-macropores from 2 to 100 nm. The volume occupied by free gas in the pores generally increases with the increase of the pore size. In the silty laminar shale (A4, A7) and siltstone with low liquid hydrocarbon content, the pore volume occupied by free gas is always higher than that of liquid hydrocarbons (Wang et al., 2020; Yoshida and Santosh., 2020; Xu et al., 2022). Moreover, in the range of pore size >10 nm, the free gas storage volume in the pores increases rapidly. In argillaceous shale and silt-bearing laminar shale (No. 22 and 31) with high liquid hydrocarbon content, the pore volume occupied by liquid hydrocarbons is larger than that occupied by free gas in the pore size range of 2–10 nm. With the increase of pore size, the overall volume of free gas in the pores increases slowly, and the pore volume occupied by free gas and liquid hydrocarbons is basically the same.

On the whole, as the pore size increases, the free gas saturation in the pores increases rapidly, the adsorbed gas saturation decreases rapidly, and the overall variation of the dissolved gas saturation is relatively low (Yan et al., 2015; Zhang et al., 2019). Among them, some siltstones (No. 34) and silt-bearing laminar shale (No. A4) have high liquid hydrocarbon content in large pores with a diameter of more than 100 nm.

4.2 Control of diagenetic stage and thermal evolution on shale pore evolution

Combined with the results of this paper, a mode of shale pore evolution in the Yanchang Formation shale in the study area was proposed (Figure 10). The mode is divided into the following four stages: 1) Early diagenetic stage (R_o < 0.5%). At this stage, the hydrocarbon generation of organic matter is not obvious, and the diagenesis is dominated by mechanical compaction. Compaction affects the rapid reduction of pores; 2) Middle diagenetic stage A (0.5% < R_o< 1.2%). In this stage, the hydrocarbon generation of organic matter will produce organic acids to dissolve minerals such as feldspar, and on the other hand, there will be hydrocarbon generation pressurization. The diagenesis at this stage is dominated by the transformation of clay minerals. In addition, because the rock is in the oil-generating window as a whole, the compaction has a great influence, and the combination of these effects causes the pores to first decrease, then increase, and then decrease. 3) Middle diagenetic stage B (1.2% < R_o< 2%). At this stage, due to the organic matter entering the gas window, the hydrocarbon generation of organic matter leads to the development of a large number of organic pores. However, the dissolution effect of organic acid and hydrocarbon generation pressurization are not obvious at this stage. In addition, the transformation of clay minerals in diagenesis

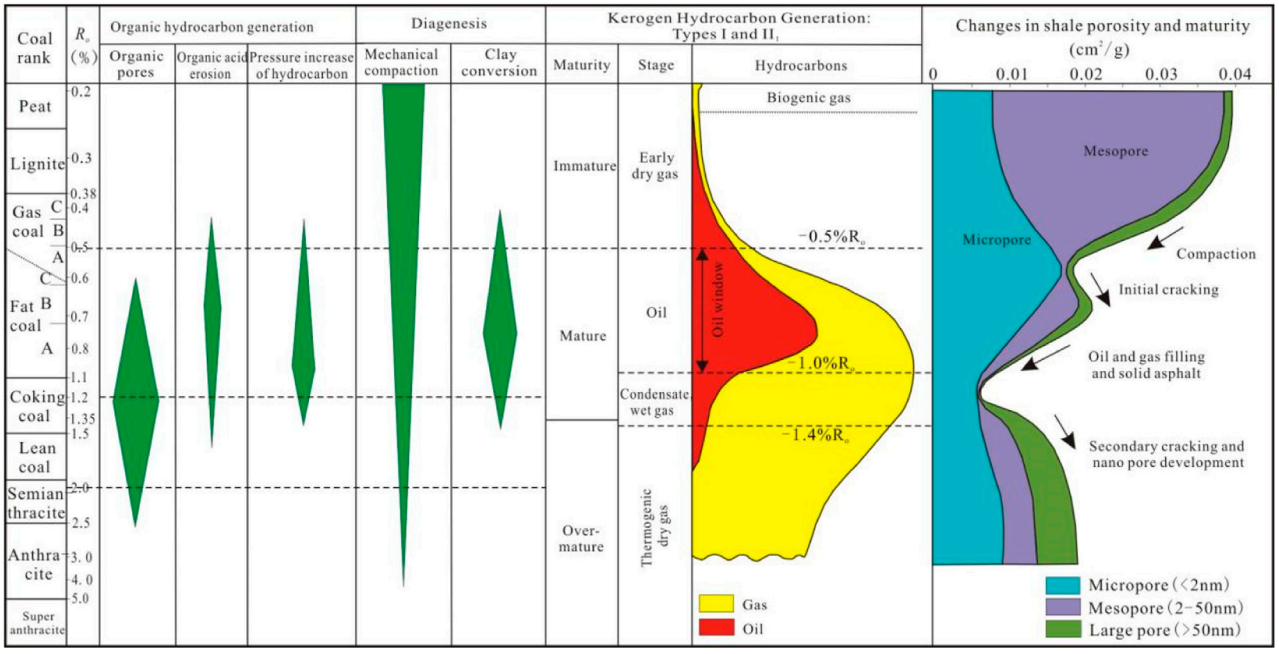

FIGURE 10
Evolution mode of pores in the Chang 7 Member shale in Yan'an area.

also basically stopped. As the compressive strength of rock increases, the effect of compaction on pores is further reduced. The combination of these effects leads to a continuous increase in porosity; 4) Late diagenetic stage (R_o > 2.0%). The effect of organic hydrocarbon generation is very weak, and the effect of compaction on pores is also very small. The pores are in a relatively stable state with small changes.

4.3 Self-sealing ability of thick shale and control of high pressure on shale gas preservation

4.3.1 Hydrocarbon expulsion limit

In the Ordos Basin, the tectonic activity in the Yanchang Formation is weak, the structure is relatively flat, and the open faults are not developed. The overlying thick mudstones, rather than structure, is the controlling factor for the preservation conditions of lacustrine shale gas. According to the distribution characteristics of parameters in laboratory experiments, gas logging and logging interpretation, there are differences in hydrocarbon expulsion in shale layers. The shale interval adjacent to the sandstone preferentially expels hydrocarbons and has a lower residual hydrocarbon content. Moreover, there is a thickness limit in the hydrocarbon expulsion section, and the effective hydrocarbon expulsion thickness is 8–12 m. The thickness of the lacustrine shale in the Chang 7 Member is relatively large (40–120 m), which exceeds the thickness limit of effective hydrocarbon expulsion in this area. Therefore, it has the characteristics of "self-sealing by thick mudstone cap".

4.3.2 Excess pressure

Excess pressure is the difference between actual pressure and hydrostatic pressure. The excess pressure at the maximum burial depth of shale is the main driving force for source rocks to expel hydrocarbons. The simulation calculation and actual measurement results show that the excess pressure of the Chang 7 Member at the end of the Early Cretaceous was between 5 and 30 MPa. And its overall distribution is a nearly north-south strip-like distribution, and the excess pressure value is between 10 and 20 MPa (Figure 11). The study found that the higher the abnormal high pressure value generated in the strata at the end of the Early Cretaceous, the richer the shale gas. This is because the larger the abnormal high pressure value generated in the formation, the better the sealing performance and the better the preservation conditions are. At the end of the Early Cretaceous, the excess pressure of the Chang 7 Member shale was basically above 3 MPa. The larger pressure difference has a good sealing ability for the shale gas in the laminae, so that the gas can be preserved for a long time.

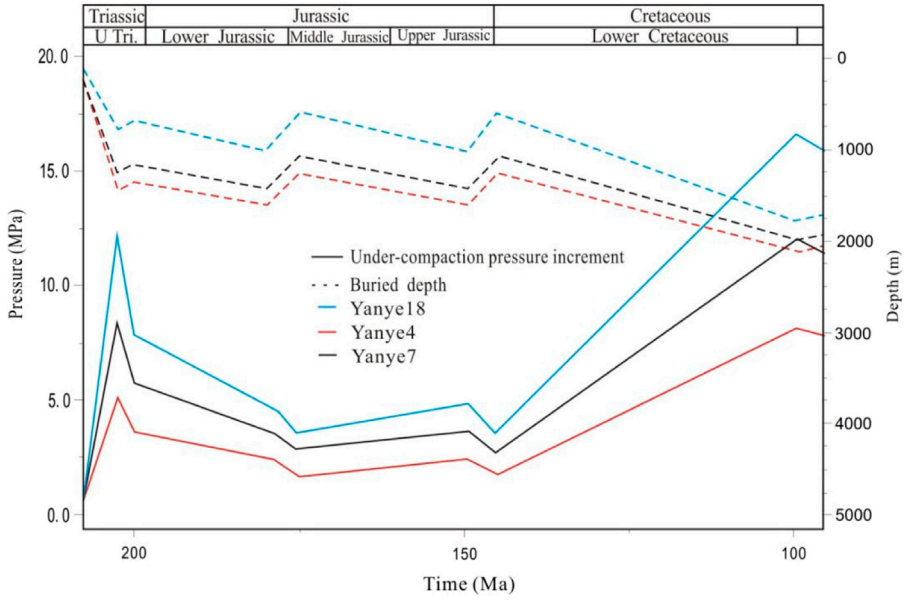

FIGURE 11
Evolution of excess pressure during disequilibrium compaction in the Chang 7 Member shale.

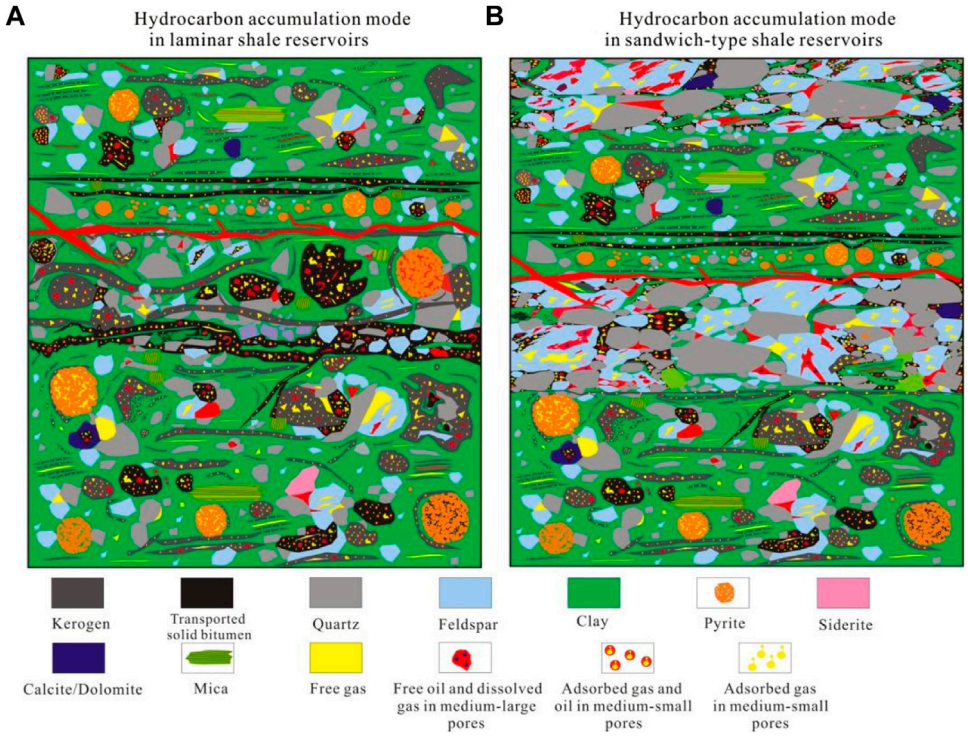

FIGURE 12
Accumulation patterns of hydrocarbons in lacustrine shale. **(A)** Hydrocarbon accumulation pattern of laminar shale gas reservoirs; **(B)** Hydrocarbon accumulation pattern in sandwich-type shale gas reservoirs.

4.4 Hydrocarbon accumulation modes and sweet spot types

As a "layered gas reservoir" with continuous distribution, the large-scale accumulation of shale gas requires basic geological conditions. Simply put, the gas source layer determines how much shale gas is produced, the reservoir determines where the shale gas exists, and the preservation conditions determine how much shale gas is left. The unity of "gas source layer, reservoir and cap layer" together constitutes the "ternary" controlling factors of shale gas enrichment. The accumulation modes of shale gas include the laminar type (with thick shale laminae) mode (Figure 12A) and the sandwich type (shale with thin sandstone) mode (Figure 12B).

4.4.1 Laminar type (with thick shale laminae) mode

This type of mode is mainly distributed in the lower part of the Chang 7 Member, that is, the gas accumulation mode of thick shale with sandy laminae. The organic carbon content of shale is more than 2%, R_o is 0.7%–1.1%, and a certain amount of crude oil associated gas is generated. The internal storage space of shale is mainly composed of intergranular pores, intercrystalline pores and a small amount of organic pores, and the porosity is 2%–6%. The driving force of hydrocarbon gas expulsion is mainly source-reservoir pressure difference (5–10 MPa), and hydrocarbons experience small-scale migration. The preservation condition is the formation pressure formed at the maximum burial depth at the end of the Early Cretaceous, and it is the residual pressure today. At the same time, the thick mudstone interlaced with the laminae also has a controlling effect on the preservation of shale gas.

4.4.2 Sandwich type (shale with thin sandstone) mode

The TOC of this type of shale is 1%–2%, the R_o is greater than 2.0%, and a large amount of hydrocarbon gas is generated, which is basically dry gas. The reservoir space is mainly intergranular pores, intercrystalline pores and intergranular dissolution pores, and the porosity is 2%–8%. Moreover, the driving force of hydrocarbon expulsion is mainly the pressure difference between source and reservoir, which is 3–5 MPa. At the same time, the thick mudstone intertwined with the sandstone has a controlling effect on the preservation of shale gas.

5 Conclusion

1) The Chang 7 Member in the Yanchang Formation has the basic gas generating conditions for shale gas. Shale gas accumulation in the Chang 7 Member requires three necessary accumulation elements, namely gas source, reservoir and good preservation conditions. The dynamic hydrocarbon generation process of shale reservoirs is established according to the thermal simulation experiment of hydrocarbon generation, and the mechanism of catalytic degradation and gas generation in the Chang 7 Member under the background of low thermal evolution is revealed.
2) The enriched authigenic pyrite can catalyze the hydrocarbon generation of organic matter with low activation energy, thereby increasing the hydrocarbon generation rate in the low-mature-mature stage. Different types of pores at different scales (2–100 nm) form a multi-scale complex pore network. Free gas and dissolved gas are enriched in laminar micro-scale pores, and adsorbed gas is enriched in nano-scale pores of thick shale, and silty laminates can improve the physical properties of the reservoir. This is because the laminar structure has better hydrocarbon generation conditions and is favorable for the migration of oil and gas molecules.
3) The thickness of lacustrine shale in the Chang 7 Member is between 40 and 120 m, which exceeds the effective hydrocarbon expulsion thickness limit (8–12 m) in the study area. At the end of the Early Cretaceous, the excess pressure of the Chang 7 shale was above 3 MPa. At present, horizontal wells with a daily gas production of more than 50,000 cubic meters are distributed in areas with high excess pressure during the maximum burial depth.

Data availability statement

The original contributions presented in the study are included in the article/supplementary material, further inquiries can be directed to the corresponding author.

Author contributions

XW and CG are responsible for the idea and writing of this paper and QL, PX, JY, and SH are responsible for the experiments and analysis.

Funding

This research was supported by the Major national science and technology project "Key technologies for exploration and development of lacustrine shale gas in Yan'an area (No. 2017zx05039)", the Key R&D Plan of Shaanxi Province, "Research on efficient CO_2 replacement mechanism and technology for Lacustrine high adsorption shale gas in Yanchang Exploration area (No. 2022GY-138)", and the Research Project of Yanchang Oil Field Co., Ltd., "Dynamics genesis mechanism and differential evolution of fine grain sedimentary in Lacustrine shale oil and gas reservoirs of Yanchang Formation in Yanchang Exploration area (ycsy2022jcts-B-49)".

Conflict of interest

Authors XW, QL, CG, PX, JY and SH were employed by the company Shaanxi Yanchang Petroleum (Group) Corp., Ltd.

Publisher's note

References

Asante-Okyere, S., Ziggah, Y. Y., and Marfo, S. A. (2021). Improved total organic carbon convolutional neural network model based on mineralogy and geophysical well log data. *Unconv. Resour.* 1, 1–8. doi:10.1016/j.uncres.2021.04.001

Fan, C. H., Li, H., Qin, Q. R., Shang, L., Yuan, Y. F., and Li, Z. (2020). Formation mechanisms and distribution of weathered volcanic reservoirs: A case study of the carboniferous volcanic rocks in Northwest Junggar Basin, China. *Energy Sci. Eng.* 8 (8), 2841–2858. doi:10.1002/ese3.702

Hong, D., Cao, J., Wu, T., Dang, S., Hu, W., and Yao, S. (2020). Authigenic clay minerals and calcite dissolution influence reservoir quality in tight sandstones: Insights from the central Junggar Basin, NW China. *Energy Geosci.* 1 (1–2), 8–19. doi:10.1016/j.engeos.2020.03.001

Ji, L., Zhang, T., Milliken, K. L., Qu, J., and Zhang, X. (2012). Experimental investigation of main controls to methane adsorption in clay-rich rocks. *Appl. Geochem.* 27, 2533–2545. doi:10.1016/j.apgeochem.2012.08.027

Jiang, W., Zhang, P., Li, D., Li, Z., Wang, J., Duan, Y., et al. (2022). Reservoir characteristics and gas production potential of deep coalbed methane: Insights from the no. 15 coal seam in Shouyang block, Qinshui Basin, China. *Unconv. Resour.* 2, 12–20. doi:10.1016/j.uncres.2022.06.001

Katz, B., Gao, L., Little, J., and Zhao, Y. R. (2021). Geology still matters – Unconventional petroleum system disappointments and failures. *Unconv. Resour.* 1, 18–38. doi:10.1016/j.uncres.2021.12.001

Kong, L., Wan, M., Yan, Y., Zou, C., Liu, W., Tian, C., et al. (2016). Reservoir diagenesis research of silurian longmaxi Formation in Sichuan Basin, China. *J. Nat. Gas Geoscience* 23, 203–211. doi:10.1016/j.jnggs.2016.08.001

Lama, R., and Vutukuri, V. (1978). *Handbook on mechanical properties of rocks, vol II.* Clausthal, Germany: Trans Tech Publications, 58–60. doi:10.1016/0013-7952(75)90018-6

Lan, S. R., Song, D. Z., Li, Z. L., and Liu, Y. (2021). Experimental study on acoustic emission characteristics of fault slip process based on damage factor. *J. Min. Strata Control Eng.* 3 (3), 033024. doi:10.13532/j.jmsce.cn10-1638/td.20210510.002

Li, G., Qin, Y., Wu, M., Zhang, B., Wu, X., Tong, G., et al. (2019). The pore structure of the transitional shale in the Taiyuan formation, Linxing area, Ordos Basin. *J. Petroleum Sci. Eng.* 181, 106183–106186. doi:10.1016/j.petrol.2019.106183

Li, H. (2022). Research progress on evaluation methods and factors influencing shale brittleness: A review. *Energy Rep.* 8, 4344–4358. doi:10.1016/j.egyr.2022.03.120

Liang, L., Xiong, J., Liu, X., and Luo, D. (2016). An investigation into the thermodynamic characteristics of methane adsorption on different clay minerals. *J. Nat. Gas Sci. Eng.* 33, 1046–1055. doi:10.1016/j.jngse.2016.06.024

Loucks, R. G., Reed, R. M., Ruppel, S. C., and Hammes, U. (2012). Spectrum of pore types and networks in mudrocks and a descriptive classification for matrix-related mudrock pores. *Am. Assoc. Pet. Geol. Bull.* 96, 1071–1098. doi:10.1306/08171111061

Mahmoodi, S., Abbasi, M., and Sharifi, M. (2019). New fluid flow model for hydraulic fractured wells with non-uniform fracture geometry and permeability. *J. Nat. Gas Sci. Eng.* 68, 102914–14. doi:10.1016/j.jngse.2019.102914

Mahmud, H., Hisham, M., Mahmud, M., Leong, V., and Shafiq, M. (2020). Petrophysical interpretations of subsurface stratigraphic correlations, Baram Delta, Sarawak, Malaysia. *Energy Geosci.* 1 (3–4), 100–114. doi:10.1016/j.engeos.2020.04.005

Milliken, K. L., Rudnicki, M., Awwiller, D. N., and Zhang, T. (2013). Organic matter-hosted pore system, Marcellus Formation (Devonian), Pennsylvania. *Am. Assoc. Pet. Geol. Bull.* 97, 177–200. doi:10.1306/07231212048

Oluwadebi, A., Taylor, K., and Ma, L. (2019). A case study on 3D characterisation of pore structure in a tight sandstone gas reservoir: The Collyhurst Sandstone, East Irish Sea Basin, Northern England. *J. Nat. Gas Sci. Eng.* 68, 102917–17. doi:10.1016/j.jngse.2019.102917

Qie, L., Shi, Y. N., and Liu, J. S. (2021). Experimental study on grouting diffusion of gangue solid filling bulk materials. *J. Min. Strata Control Eng.* 3 (2), 023011. doi:10.13532/j.jmsce.cn10-1638/td.20201111.001

Roy, B., Hart, B., Mironnova, A., Zhou, C. X., and Zimmer, U. (2014). Integrated characterization of hydraulic fracture treatments in the Barnett shale: The Stocker geophysical experiment. *Interpretation* 2 (2), T111–T127. doi:10.1190/INT-2013-0071.1

Santosh, M., and Feng, Z. Q. (2020). New horizons in energy geoscience. *Energy Geosci.* 1 (1–2), 1–3. doi:10.1016/j.engeos.2020.05.005

Sun, M., Yu, B., Hu, Q.-H., Chen, S., Xia, W., and Ye, R. (2015). Nanoscale pore characteristics of the Lower Cambrian Niutitang Formation Shale: A case study from Well Yuke #1 in the Southeast of Chongqing, China. *Int. J. Coal Geol.* 154, 16–29. doi:10.1016/j.coal.2015.11.015

Sun, Z., Wang, Y., Wei, Z., Zhang, M., Wang, D., Wang, Z., et al. (2017). Shale gas content and geochemical characteristics of marine-continental transitional shale: A case from the Shanxi formation of Ordos Basin. *J. China Univ. Min. Technol.* 46 (4), 859–868.

Tiab, D., and Donaldson, E. C. (2004). *Petrophysics: Theory and practice of measuring reservoir rock and fluid transport properties.* Elsevier, 56–59.

Ursula, I. V., and Jorge, O. P. (2014). Artificial neural networks applied to estimate permeability, porosity and intrinsic attenuation using seismic attributes and well- log data. *J. Appl. Geophys.* 107, 45–54. doi:10.1016/j.jappgeo.2014.05.010

Vafaie, A., Kivi, I. R., Moallemi, S. A., and Habibnia, B. (2021). Permeability prediction in tight gas reservoirs based on pore structure characteristics: A case study from South Western Iran. *Unconv. Resour.* 1, 9–17. doi:10.1016/j.uncres.2021.08.001

Valenza, J. J., Drenzek, N., Marques, F., Pagels, M., and Mastalerz, M. (2013). Geochemical controls on shale microstructure. *Geology* 41 (5), 611–614. doi:10.1130/G33639.1

Wang, G., Ju, Y., Yan, Z., and Li, Q. (2015). Pore structure characteristics of coal–bearing shale using fluid invasion methods: A case study in the huainan–huaibei coalfield in China. *Mar. Petroleum Geol.* 62, 1–13. doi:10.1016/j.marpetgeo.2015.01.001

Wang, H., Shi, Z., Zhao, Q., Liu, D., Sun, S., Guo, W., et al. (2020). Stratigraphic framework of the Wufeng-Longmaxi shale in and around the Sichuan Basin, China: Implications for targeting shale gas. *Energy Geosci.* 1 (3–4), 124–133. doi:10.1016/j.engeos.2020.05.006

Wang, H., Zhou, S., Li, S., Zhao, M., and Zhu, T. (2022). Comprehensive characterization and evaluation of deep shales from Wufeng-Longmaxi Formation by LF-NMR technology. *Unconv. Resour.* 2, 1–11. doi:10.1016/j.uncres.2022.05.001

Wu, J. S., and Yu, B. M. (2007). A fractal resistance model for flow through porous media. *Int. J. Heat Mass Transf.* 50 (19), 3925–3932. doi:10.1016/j.ijheatmasstransfer.2007.02.009

Wyllie, M. R. J., and Spangler, M. B. (1952). Application of electrical resistivity measurements to problem of fluid flow in porous media. *AAPG Bull.* 36, 359–403. doi:10.3406/geo.1951.13171

Xiong, F., Jiang, Z., Li, P., Wang, X., Bi, H., Li, Y., et al. (2017). Pore structure of transitional shales in the Ordos Basin, NW China: Effects of composition on gas storage capacity. *Fuel* 206, 291062–291515. doi:10.1130/abs/2017NE-291062

Xu, H., Zhou, W., Hu, Q., Xia, X., Zhang, C., and Zhang, H. (2019). Fluid distribution and gas adsorption behaviors in over-mature shales in southern China. *Mar. Petrol. Geol.* 109, 223–232. doi:10.1016/j.marpetgeo.2019.05.038

Xu, Z., Cheng, Y., Ao, C., Zhang, T., and Wang, S. (2022). Middle Jurassic palaeoclimate changes within the central Ordos Basin based on palynological records. *Paleobiodivers. Paleoenviron.* 13, 1–13. doi:10.1007/s12549-021-00518-8

Xue, F., Liu, X. X., and Wang, T. Z. (2021). Research on anchoring effect of jointed rock mass based on 3D printing and digital speckle technology. *J. Min. Strata Control Eng.* 3 (2), 023013. doi:10.13532/j.jmsce.cn10-1638/td.20201020.001

Yan, D., Huang, W., and Zhang, J. (2015). Characteristics of marine continental transitional organic rich shale in the Ordos Basin and its shale gas significance. *Earth Sci. Frontiers* 22 (6), 197–206. doi:10.13745/j.esf.2015.06.015

Yang, C., Zhang, J., Tang, X., Ding, J., Zhao, Q., Dang, W., et al. (2016). Comparative study on micro-pore structure of marine, terrestrial, and transitional shales in key areas, China. *Int. J. Coal Geol.* 171, 76–92. doi:10.1016/j.coal.2016.12.001

Yoshida, M., and Santosh, M. (2020). Energetics of the Solid Earth: An integrated perspective. *Energy Geosci.* 1 (1–2), 28–35. doi:10.1016/j.engeos.2020.04.001

Yu, K., Shao, C., Ju, Y., and Qu, Z. (2019a). The Genesis and controlling factors of micropore volume in transitional coal-bearing shale reservoirs under different sedimentary environments. *Mar. Petroleum Geol.* 102, 426–438. doi:10.1016/j.marpetgeo.2019.01.003

Yu, Y., Luo, X., Wang, Z., Cheng, M., Lei, Y., Zhang, L., et al. (2019b). A new correction method for mercury injection capillary pressure (MICP) to characterize the pore structure of shale. *J. Nat. Gas Sci. Eng.* 68, 102896–102905. doi:10.1016/j.jngse.2019.05.009

Zhang, D., Li, S., and Zhang, X. (2020). Experimental study on mining fault activation characteristics by a distributed optical fiber system. *J. Min. Strata Control Eng.* 2 (1), 013018. doi:10.13532/j.jmsce.cn10-1638/td.2020.01.010

Zhang, M., Fu, X., Zhang, Q., and Cheng, W. J. J. (2019). Research on the organic geochemical and mineral composition properties and its influence on pore structure of coal-measure shales in Yushe-Wuxiang Block, South Central Qinshui Basin, China. *J. Petrol. Sci. Eng.* 34, 1065–1079. doi:10.1016/j.petrol.2018.10.079

Zhao, W., Li, J., Yang, T., Wang, S., and Huang, J. (2016). Geological difference and its significance of marine shale gases in South China. *Petroleum Explor. Dev.* 43, 547–559. doi:10.1016/S1876-3804(16)30065-9

Zheng, H., Zhang, J., and Qi, Y. (2020). Geology and geomechanics of hydraulic fracturing in the Marcellus shale gas play and their potential applications to the Fuling shale gas development. *Energy Geosci.* 1 (1–2), 36–46. doi:10.1016/j.engeos.2020.05.002

frontiers | Frontiers in Earth Science

TYPE Original Research
PUBLISHED 13 September 2022
DOI 10.3389/feart.2022.1002745

OPEN ACCESS

EDITED BY
Shuai Yin,
Xi'an Shiyou University, China

REVIEWED BY
Zhenduo Zhao,
Jilin University, China
Zhicheng Zhou,
China University of Geosciences, China

*CORRESPONDENCE
Jishun Pan,
jspan123@126.com

SPECIALTY SECTION
This article was submitted to Structural Geology and Tectonics, a section of the journal Frontiers in Earth Science

RECEIVED 25 July 2022
ACCEPTED 15 August 2022
PUBLISHED 13 September 2022

CITATION
Pan J and Peng Y (2022), Experimental evaluation of microscopic pore structure and fluid migration characteristics of coal-measure sandstone reservoirs.
Front. Earth Sci. 10:1002745.
doi: 10.3389/feart.2022.1002745

Experimental evaluation of microscopic pore structure and fluid migration characteristics of coal-measure sandstone reservoirs

Jishun Pan* and Yicong Peng

College of Geosciences and Engineering, North China University of Water Resources and Electric Power, Zhengzhou, China

Research on the microscopic migration characteristics of fluids in coal measure sandstone has always been a hot spot in the evaluation of reservoir properties. In this study, taking the Yan'an Formation sandstone reservoirs in the Block A of the Ordos Basin as an example, the pore structures and fluid migration characteristics of coal-measure sandstones are systematically studied using a large number of thin sections, SEM (Scanning Electron Microscope), NMR (Nuclear Magnetic Resonance), relative permeability and water-flooding test results. The results show that the Jurassic sandstones in the target layer mainly develop lithic quartz sandstone, and the main pore types are intergranular and dissolution pores, followed by a small amount of intercrystalline pores. The surface porosity of the target sandstones mainly ranges from 7.90 to 10.79%, with an average value of 8.78%. The good correlation between porosity and permeability indicates that the target layer is a pore-type reservoir. The T_2 relaxation time of the target layer is mainly distributed within 100 ms. Moreover, the reservoir of the Yan'an Formation has a high saturation of movable fluids, which is mainly distributed in 43.17–71.24%, with an average value of 56.90%. Meanwhile, samples with fractures have higher movable fluid saturations. In addition, the average irreducible water saturation of the Yan'an Formation sandstone reservoir is 35.14%, and the final oil displacement efficiency is 51.14% on average. There is a good positive correlation between the oil displacement efficiency and the co-permeability zone. As the co-permeability zone range increased from 15 to 55%, the oil displacement efficiency increased from 30 to 65%. When the cores develop fractures, they have characteristics of high permeability, high oil recovery rate, high oil displacement efficiency in the anhydrous period, low irreducible water saturation and low residual oil saturation.

KEYWORDS

Yan'an formation, sandstone reservoir, relative permeability, nuclear magnetic resonance, pore structure

Introduction

The Jurassic Yan'an Formation reservoirs in the Ordos Basin have the characteristics of small oil-bearing area, therefore, the hydrocarbons are mainly distributed in small-scale traps. The physical properties of the reservoir and the development conditions of movable fluids are important parameters that determine the final cumulative production, reservoir evaluation and production cycle of oil and gas reservoirs (Ji et al., 2014; Liang et al., 2019; Lei et al., 2020; Bai et al., 2022). These properties are not only related to the pore throat diameter, but also comprehensively affected by factors such as rock porosity, pore connectivity, particle density, particle size, sorting and diagenesis (Lai et al., 2018; Guo et al., 2020; Asante-Okyere et al., 2021; Li et al., 2021). Affected by strong compaction and cementation, the matrix permeability of sandstone reservoirs is usually low. Tight sandstone reservoirs have strong heterogeneity and strong anisotropy, and the pore structures inside the rock is not only controlled by porosity but also by fluid composition. Therefore, a quantitative evaluation of the dual medium of rock and fluid components in tight reservoirs by experimental means can provide a new idea for the prediction of sweet spots in tight sandstone reservoirs (Shanley and Cluff., 2015; Liu et al., 2018; Yang et al., 2020; Mirzaei-Paiaman and Ghanbarian., 2021; Zhao et al., 2021; Li, 2022).

In the middle and late stages of waterflooding development, there is still a lot of crude oil that cannot be recovered from the formation and becomes the remaining oil. The study of the microscopic distribution of remaining oil is an important evaluation content for improving the oil recovery of tight oil reservoirs. However, in real reservoirs, the dynamic characteristics of the oil-water mutual displacement process and the distribution of remaining oil and water cannot be directly observed, so they can only be studied by experimental simulation methods (Qiao et al., 2019; Shi et al., 2019; Vafaie et al., 2021; Jiang et al., 2022). Laboratory simulation and experiments can not only provide technical support for the enhanced oil recovery, but also can provide theoretical support for the study of the reservoir development process, especially the distribution of oil and water in the pores in the high water cut stage (Wang et al., 2018; Chen et al., 2021; Katz et al., 2021; Lan et al., 2021; Wu et al., 2021). Due to the heterogeneity of the pore structures of the reservoir, the distribution of oil and water in the rock is much more complicated. The various forms of oil-water distribution require different measures to enhance the oil recovery from the reservoir.

The water flooding experiment can visually and quantitatively display the water flooding path, rate and scale, and then reveal the displacement mechanism of the microscopic remaining oil. The key to water flooding technology lies in the establishment of reservoir microscopic model and the design of technical process for experimental testing (Li et al., 2017; Li et al., 2018; He et al., 2020; Wang et al., 2022). Obviously, the rock sample model can more truly reflect the fluid migration law inside the reservoir. In this study, taking the Yan'an Formation sandstone reservoir in Block A of the Ordos Basin as an example, the pore structures and fluid migration characteristics of coal-measure sandstone are systematically studied using a large number of thin sections, SEM, NMR, relative permeability and water-flooding test results. This study can provide a reference for the formulation of efficient development plans for similar sandstone reservoirs.

Materials and methods

Geological background

The study area is located in Block A in the west of the Ordos Basin (Figure 1). From the structural background, the study area is located in the southern part of the Tianhuan Depression (Figure 1). Affected by the thrust and nappe of the western margin of the Ordos Basin, the tectonic activity in the study area was relatively strong, and a large number of small-scale faults are developed (Liang et al., 2019). The extension length of the fault is mostly distributed in 1–15 km, and the fault was mainly formed at the end of the Yanshanian Movement (Li et al., 2017). Low-amplitude uplift traps are developed in the local strata of the Yan'an Formation, and the traps are mainly distributed between 1–6 km^2.

The stratigraphic units of the Jurassic strata in this area include the Yan'an, Zhiluo and Anding Formations, among which, the Yan'an Formation has a thickness between 220–350 m. Thick river-lake delta deposits are developed in the Middle Jurassic Yan'an Formation period. In addition, coal seams are developed in the Yan'an Formation, and the Jurassic oil reservoirs in the study area are mainly distributed in the Lower system, which is also the main research target layer of this study.

The Middle Jurassic Yan'an Formation, as the main coal and oil-bearing strata in the basin, is relatively developed in the whole basin. The lithology is mainly gray and dark gray mudstone intercalated with coal seam, yellow-gray medium and fine-grained sandstone and siltstone. Because the sandstone at the bottom of the Zhiluo Formation has a strong scouring effect on the top strata of the underlying Yan'an Formation during the deposition process, the thickness of the Yan'an Formation in some areas becomes thinner. Figure 2 shows the stratigraphic unit division of the Yan'an Formation and the vertical lithologic features of the Yan'an Formation revealed by the Well Weisha 2 (Ji et al., 2014).

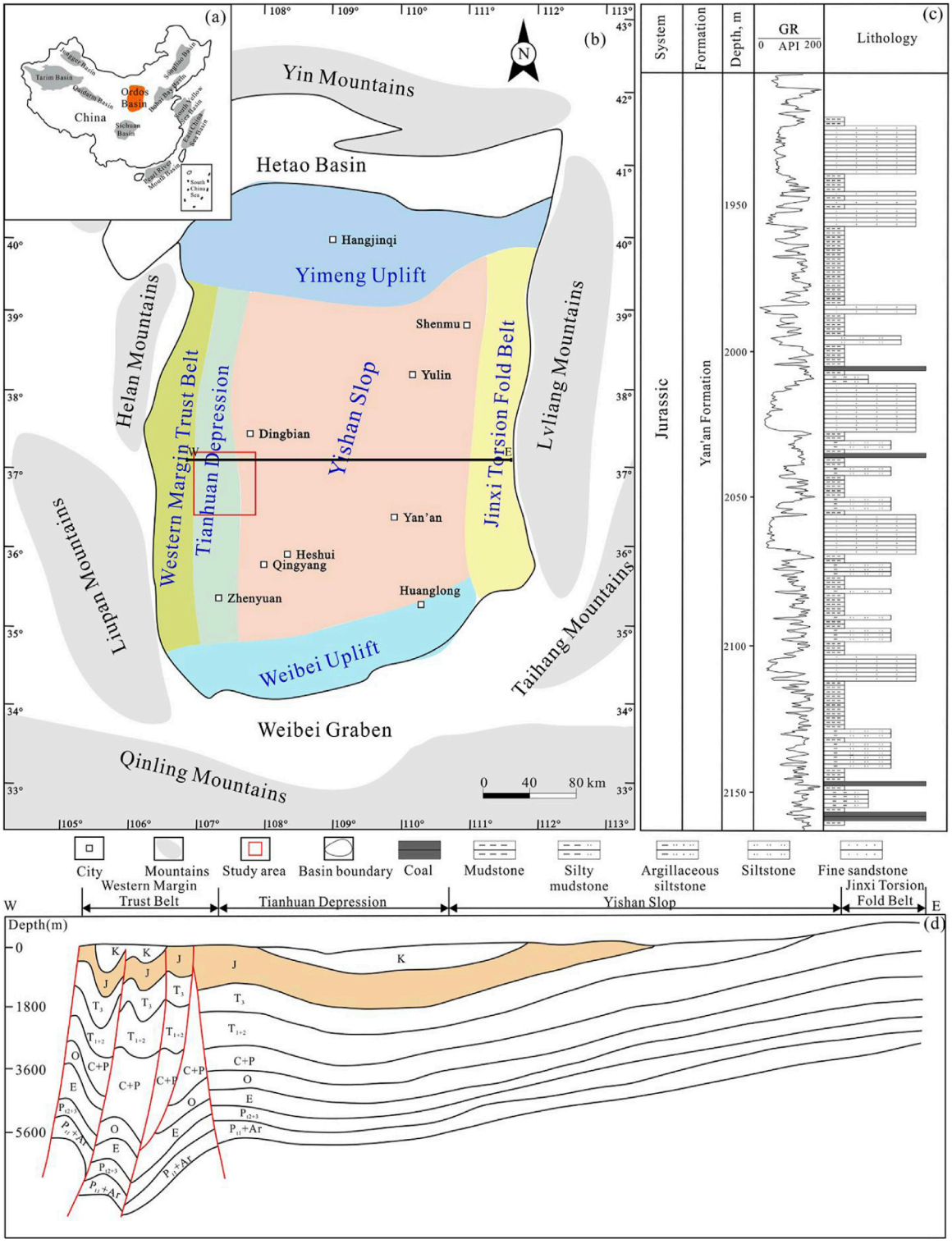

FIGURE 1
The study area is located in the western margin of the Ordos Basin in the western part of the North China Craton (NCC) (Zhong et al., 2021). Notes: **(A)** Location of the Ordos Basin; **(B)** Location of the study area; **(C)** Lithologic characteristics of the Yan'an Formation coal measures; **(D)** A stratigraphic profile in the central part of the Ordos Basin.

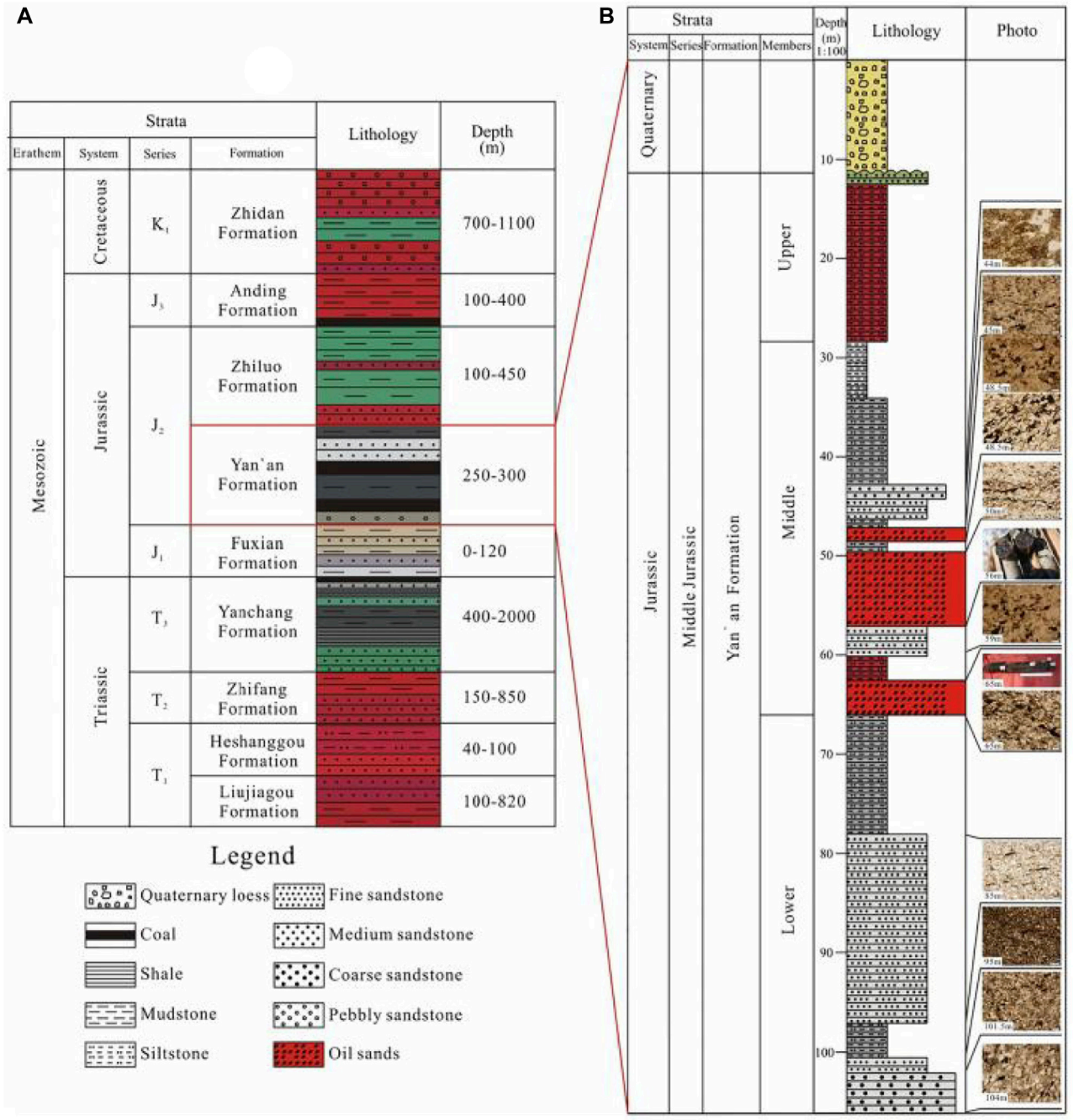

FIGURE 2
Division of stratigraphic units of the Jurassic strata in the Ordos Basin (Ji et al., 2014). Notes: **(A)** Stratigraphic units in Mesozoic strata; **(B)** Lithologic profile in Well Weisha 2.

Experiments

The experiments used in this study include thin section, scanning electron microscopy, nuclear magnetic resonance, and relative permeability tests. Thin sections and scanning electron microscopy were used to study the pore structures and the distribution of different mineral components in the sandstone. Furthermore, these experiments were used to better understand the lithology and physical properties of the Yan'an Formation sandstone.

The analysis and test of the movable fluid characteristics in this paper include nuclear magnetic resonance and relative permeability experiments. The NMR test instrument is a MagneT2000 tester. The

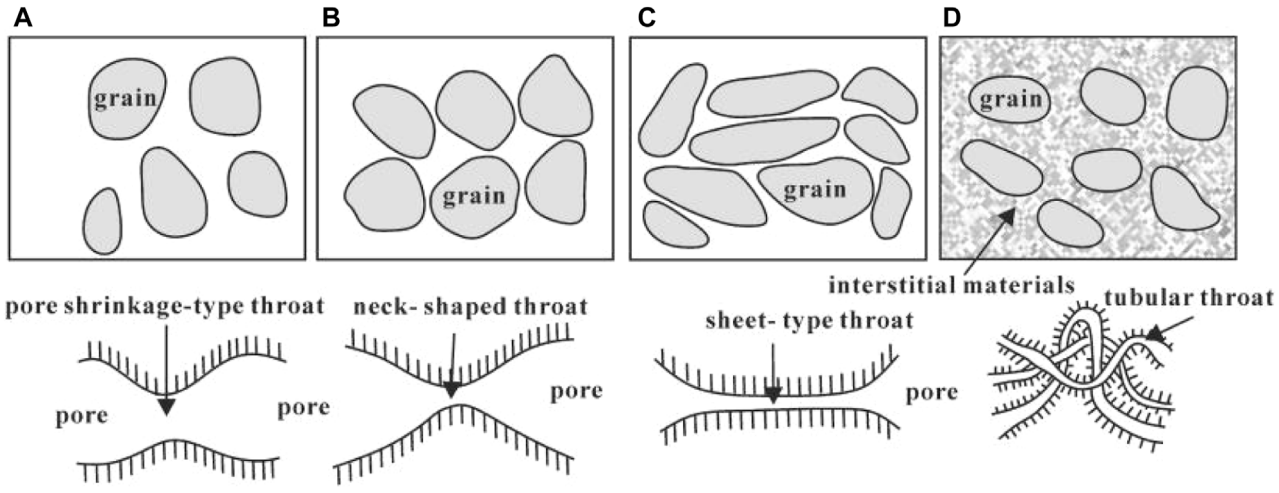

FIGURE 3
Major pore types in sandstone reservoirs (Zhong et al., 2021). **(A)** pore-shrinkage-type throat; **(B)** neck-shaped throat; **(C)** sheet-type throat; **(D)** tubular throat.

NMR test curve includes the T_2 time spectrum curve under the condition of 100% saturated formation water (before centrifugation) and the T_2 time spectrum curve after centrifugation at 450 psi. In the nuclear magnetic resonance test, the technical indicators are: the maximum working temperature is 155°C/0.5 h, the maximum working pressure is 137.9 MPa, the minimum resistivity of the drilling fluid is 0.02 Ω m, the electronic circuit AC voltage is 180 V, the frequency is 60 HZ, and the current is 250 mA. The probe DC voltage is 600 V and 800 mA/pulse. In addition, the "unsteady-state" experimental method was adopted to carry out the oil-water relative permeability test experiments on the cores. Through this test, the oil-water relative permeability curve and its characteristic parameters of the experimental samples can be obtained.

Results

Pore types

The lithologies of the Jurassic sandstones in the study area include lithic quartz sandstone, lithic feldspar sandstone and feldspar lithic sandstone. The sand bodies have poor lateral continuity, and most of the cross-sections are in the form of lenses with a flat top and a convex bottom. In addition, the sand bodies develop various types of cross-bedding, which are vertically bell-shaped and box-shaped. According to the difference of throats, the pore types of the Yan'an Formation sandstones mainly include four types (Figure 3) (Bhatti et al., 2020; Zhong et al., 2021). The first type has constricted throats with little difference in the size of pores and throats (Figure 3A); the second type has a thin-necked throat, and the size of the throats is significantly lower than the pores (Figure 3B); the third type has deformed sheet-like throats, which are associated with mineral compaction (Figure 3C); the fourth type has tubular throats, which are usually developed in the intercrystalline pores of interstitials, and the pores are mostly filled by kaolinite and illite (Figure 3D).

The observation results of casting thin section and electron microscope scanning show that there are various types of reservoir spaces in the target sandstone. The target layer mainly develops intergranular pores (Figure 4A), followed by dissolution pores and a small amount of intragranular pores. However, the dissolution pores are dominated by feldspar dissolution pores. The dissolution pores include intergranular dissolution pores, feldspar dissolution pores, detrital dissolution pores and a small amount of carbonate dissolution pores (Figure 4B).

The surface porosity of the target sandstone mainly ranges from 7.90 to 10.79%, with an average value of 8.78%. The content of residual intergranular pores in the Yan'an Formation is relatively high. Residual primary intergranular pores developed in strong hydrodynamic environments and were common in thin sections (Figure 4A). Intercrystalline pores are mainly developed in clay minerals such as kaolinite and illite. Intercrystalline pores refer to pores developed inside authigenic minerals. The larger the volume of kaolinite crystals, the better the development of intercrystalline pores (Schmitt et al., 2015; Ren et al., 2020; Zhao et al., 2020). This is due to the fact that kaolinite crystals are stacked together in a book-like form and are not sensitive to water. Therefore, a large

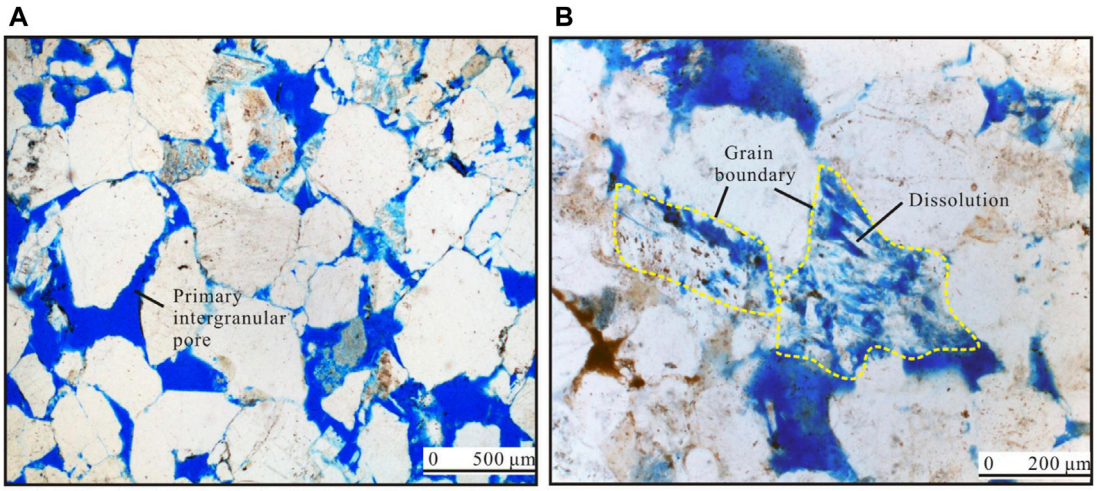

FIGURE 4
Development characteristics of pores in the target sandstone. Notes: **(A)** Well H1, 2251.4 m, detritus quartz sandstone; **(B)** Well H2, 2124.9 m, detritus quartz sandstone.

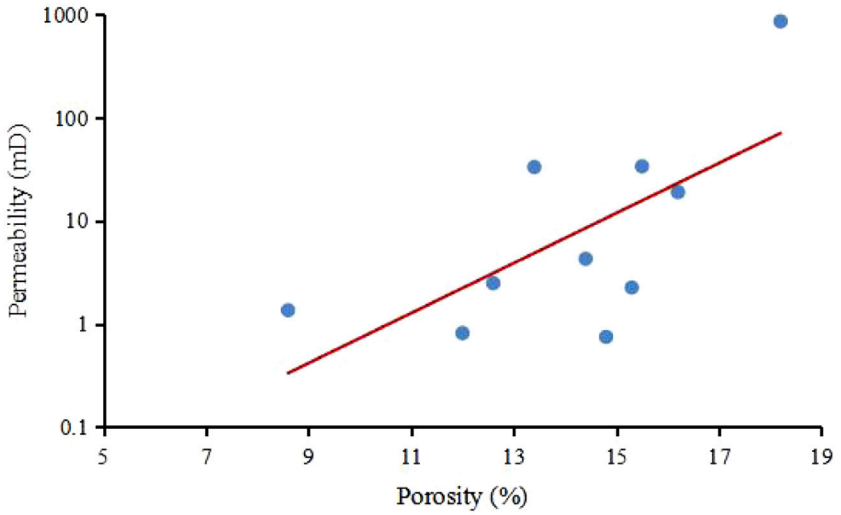

FIGURE 5
Relationship between porosity and permeability of the target layer.

number of intercrystalline pores between the crystal particles are retained.

Statistics show that feldspar has the highest degree of development of dissolved pores, and its content ranges from 0.77 to 1.55%, with an average of 1.17%. Followed by intergranular dissolved and debris dissolved pores, the content of which is distributed between 0.75 and 1.70%, with an average of 1.02%. Overall, the corrosion effect of the target layer is not strong. In addition, some micro-fractures are developed in the target layer, which can significantly improve the permeability of the reservoir.

The relationship between the porosity and gas permeability of the 10 groups of NMR samples tested is shown in Figure 5. It can be seen that there is a very good positive correlation between porosity and permeability. The porosity of the samples is mainly distributed in 9–17%, and the gas permeability is mainly

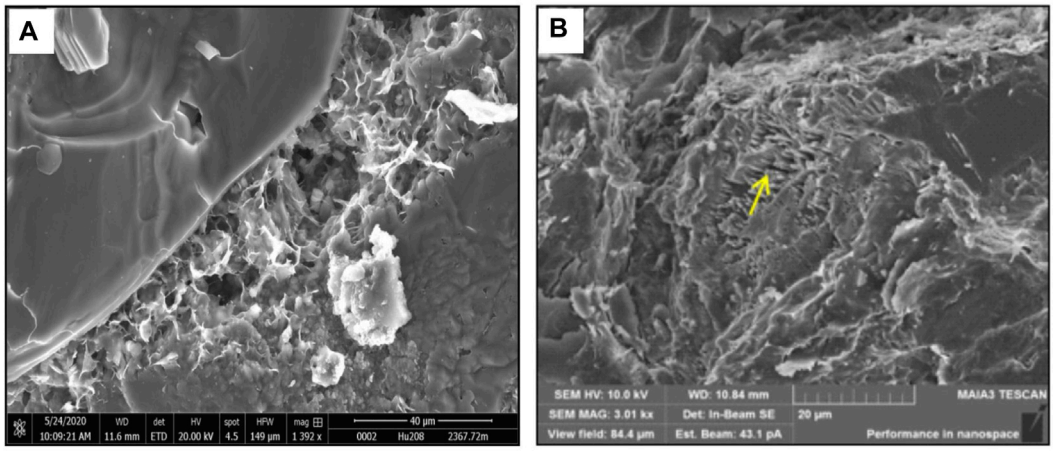

FIGURE 6
Development characteristics of clay mineral intercrystalline pores and detrital dissolution pores in the target layer. Notes: **(A)** Well X1, 2367.72 m, filamentous illite; **(B)** Well X5, 2248.13m, surface erosion of detrital particles.

distributed in 1 mD~35 mD. The target sandstone belongs to the medium-porosity and medium-permeability sandstone reservoir. The good correlation between porosity and permeability indicates that the target layer is a pore-type reservoir. Pores are mainly developed in the target layer, while fractures are less developed. The low degree of fracture development is related to the inactive tectonic activity in the Ordos Basin.

The target sandstone has experienced strong cementation. Cementation refers to the precipitation of supersaturated dissolved components in pore water under the conditions of elevated temperature and pressure, and then the clastic sediments are cemented into rocks (Wang et al., 2017; Zhong et al., 2021). The cementation experienced by the target layer mainly includes clay, siliceous, calcareous and feldspar cementations.

Statistics show that the clay cement content in the target layer ranges from 3.31 to 10.75%, with an average content of 5.65%. The authigenic clay minerals grow vertically from the pore surface to the pore center, and therefore, play a damaging role in reservoir porosity. The authigenic clay minerals in the study area are mainly kaolinite, illite, and a small amount of illite/smectite mixed layer and chlorite (Figure 6A).

Dissolution mainly occurs in the mature stage of organic diagenetic evolution, which is often consistent with the rapid transformation of smectite in the smectite/smectite clay minerals. It is also the peak period of organic acid production, so secondary pores are mostly formed in the middle diagenetic A stage. Intervals with strong dissolution are often secondary pore development segments, and are more likely to form favorable reservoirs. The dissolution of various components (clasts, matrix, cement, etc.) in the sandstone promotes the formation of a large number of secondary pores (Figure 6B). The development of dissolution pores has an extremely important influence on the physical properties of the reservoir.

T_2 spectrum classification

The movable fluid saturation of the sandstone samples of the target layer in the study area is distributed between 40 and 72%, with an average value of 54%. The different peak characteristics of the saturation component NMR curves before centrifugation can reflect the proportion of pores of different sizes in the rock. In addition, the T_2 relaxation time spectra of the NMR component curves before centrifugation can also reflect the pore size. When T_2 time is less than 1 ms, it indicates micropores (pore diameter <0.1 µm); when T_2 time is between 1 and 10 ms, it indicates small pores (pore diameter is between 0.1 and 0.5 µm); when T_2 time is between 10 and 100 ms, it indicates mesopores; when T_2 time is between 100 and 1000 ms, it indicates macropores (pore diameter is between 2.5 and 10 µm); when T_2 time is greater than 1000 ms, it indicates karst caves (pore diameter >10 µm). Generally, the types of NMR curves of sandstone reservoirs can be divided into three types: unimodal, bimodal and trimodal. Through analysis, it is considered that the NMR curve of the Yan'an Formation sandstone reservoir in the study area is relatively single in peak shape, with double peaks developed (Figure 7).

According to the different pore sizes reflected by the saturation component NMR curves before centrifugation, the pore types of the target sandstone reservoirs are divided into three categories: namely, micropore-small-pore-mesopore type (the left peak is significantly larger than the right peak), small pore-mesopore type (the left peak is significantly smaller than the

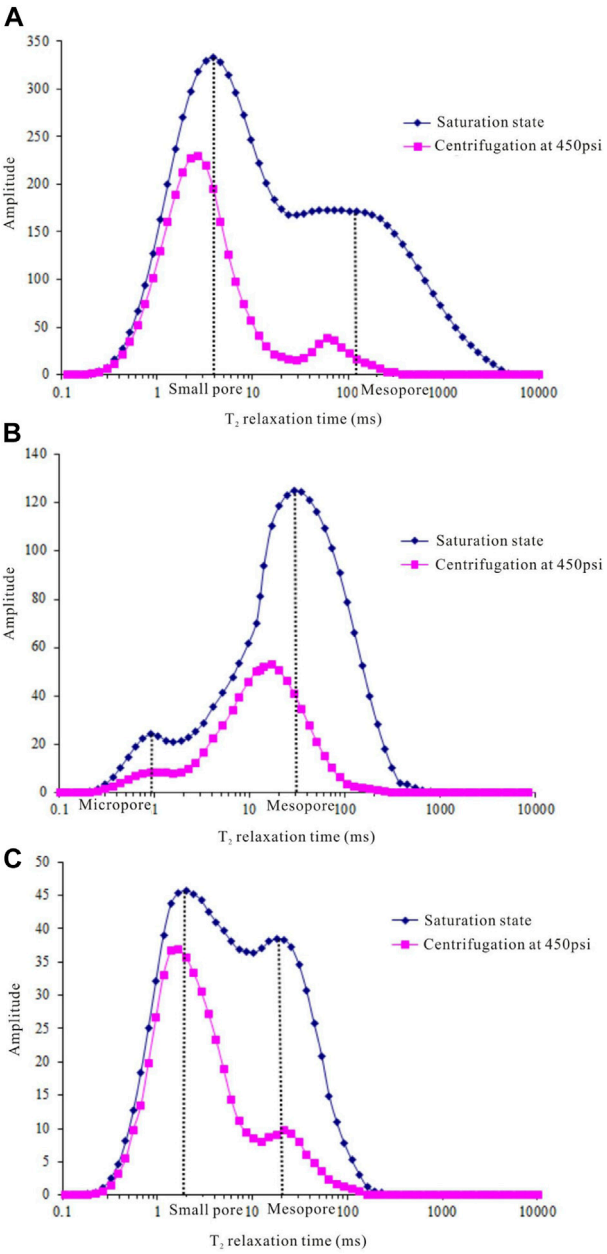

FIGURE 7
Three typical NMR curve types for Jurassic reservoirs. Notes: **(A)** Well L1, X-1 sample, 2131.7 m; **(B)** Well H4, X-2 sample, 2282.8m; **(C)** Well B8, X-3 sample, 2278.4 m.

right peak), micropore-small-pore-mesopore uniform distribution type (the left peak and the right peak have little difference).

The micropore-small-pore-mesoporous type is represented by the sample No. X-1 (Figure 7A). The saturation component curve before centrifugation shows that the T_2 relaxation time of the sample X-1 is mainly distributed in the range of 1–100 ms; the T_2 time distribution of the left peak is wider, which means that micropores and small pores dominate the rock sample. In addition, according to the coverage of the T_2 spectrum, the proportions of micropores and small pores are roughly the same. The small-mesopore type is represented by the sample No. X-2 (Figure 7B). The saturation component curve before centrifugation shows that the T_2 relaxation time of the X-2 sample is mainly distributed in the range of 10–100 ms; the T_2 time distribution of the right peak is wider, which means that the small pores and mesopores dominate the rock sample. The uniform distribution pattern of micropore-small-pore-mesopore is represented by the sample X-3 (Figure 7C). The saturation component curve before centrifugation shows that the T_2 relaxation time of the X-3 sample is mainly distributed in the range of 0.1–100 ms; and the T_2 time distribution range of the left and right peaks is wide, which means that the micropore, small pores and mesopores are well developed, and the proportion of small pores is higher on the whole.

For all samples, there is a T_2 relaxation time distribution in the interval of 100–1000 ms, but the proportion is small. It represents that a few large pores are also developed in the rock sample. In addition, there is an interval with T_2 relaxation time greater than 1000 ms in the micropore-small-pore-mesoporous samples. It shows that a few karst caves may be developed in this kind of rock samples, while no karst caves are developed in the other two types of samples.

Discussion

Analysis on the occurrence characteristics of movable fluid in coal-measure sandstone

The internal pores and throat spaces of sandstone reservoirs are narrow, and there is a certain distribution of irreducible water and movable water. Therefore, the T_2 time spectrum of NMR can be used to identify fluids with different occurrence states. The T_2 cut-off value can be determined according to the projected point value of the accumulated NMR signal intensity of the sample after centrifugation before the centrifugation (100% saturated water) on the T_2 accumulated signal intensity curve of the sample. The area covered by the post-centrifugation curve above the T_2 cut-off represents movable water, and correspondingly, the area covered by the post-centrifugation curve below the T_2 cut-off represents bound water.

The T_2 cut-off values of the sandstone samples were mainly distributed between 1 and 25 ms, with an average value of 8.24 ms. The correlation between T_2 cut-off value and porosity is not obvious. It is related to the complex pore structures of the studied sandstone and the narrow variation range of T_2 cut-off value distribution. In addition, there is a certain negative correlation between the T_2 cut-off value and the percentage of movable fluids in the rock samples. When the T_2

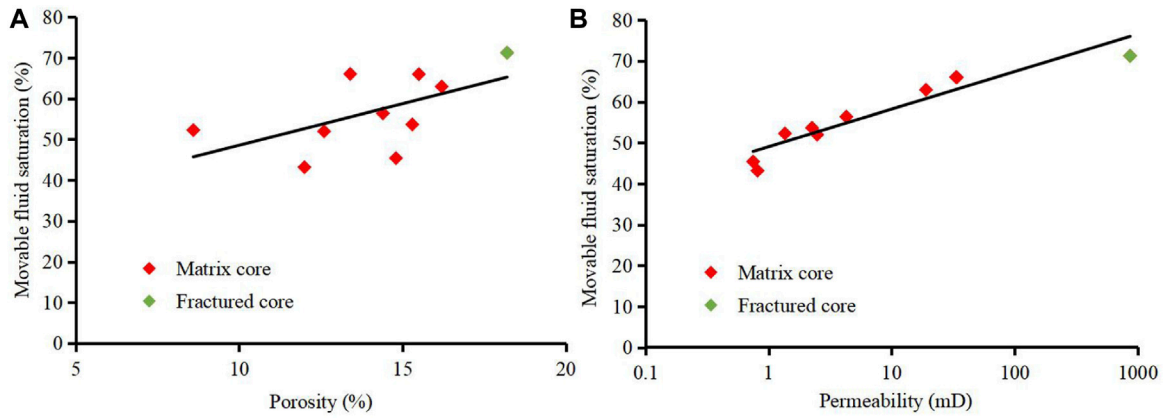

FIGURE 8
Relationship between physical parameters and movable fluid saturation of the target layer. Notes: **(A)** Relationship between porosity and movable fluid saturation; **(B)** Relationship between permeability and movable fluid saturation.

cut-off value is higher, the irreducible water saturation in the rock increases, and the corresponding percentage of movable fluid decreases. There is a very good negative correlation between mobile fluid percentage and irreducible water saturation.

Generally, the amount of movable fluid is mainly affected by the permeability of the reservoir, that is, it is mainly controlled by the throat in the reservoir space. Therefore, there is a certain positive correlation between the movable fluid content and the physical parameters. The experimental results show that the reservoir of the Yan'an Formation has high saturation of movable fluids. It was mainly distributed in 43.17–71.24%, with an average of 56.90% (Figure 8A). At the same time, the fractured samples have higher movable fluid saturations. This is because the existence of fractures greatly reduces the capillary pressure inside the tight rock, and some of the bound fluids are transformed into movable fluids. In addition, the movable fluid saturation has a significant correlation with permeability (Figure 8B). The results of well test productivity comparison show that when the movable fluid saturation is greater than 50%, the oil-producing well basically does not produce water. The tight sandstone of the Yan'an Formation has the characteristics of water wettability, and the pore surface is covered by irreducible water. The oil molecules mostly exist in a free state. Thus, high movable fluid saturation represents high oil saturation. Then, in the early stage of reservoir development, this type of reservoir only produces oil and basically does not produce water.

Analysis of relative permeability results of coal measures sandstone

For different samples, when the water saturation (S_w) changes in the same range, the oil and water relative permeability ratio K_o/K_w will change by different times, that is, the slope of the curve will be different. The smaller the slope, the smaller the change in the relative permeability ratio, and the more stable the oil and gas development effect is (Figure 9). Therefore, for the original low natural energy water-flooding reservoir, the water saturation of the tight reservoir will continue to increase with the increase of the injected water. Correspondingly, the oil-water ratio production index value will continue to decrease.

Generally, the relative permeability curve is divided into three stages: the oil phase seepage section in the state of irreducible water, the oil-water two-phase co-permeability area, and the water phase seepage in the residual oil state. Typical oil-water relative permeability curve types include Type I (concave K_w-K_o Line), Type II (descending K_o line - apex of the sloping K_w line), Type III (slowly rising K_w line - steeply falling K_o line). The target layer has the characteristics of Types I and II (Figure 10). In the oil-water two-phase seepage interval, the oil-level relative permeability of the Yan'an Formation reservoir is low. And its average residual oil saturation is 31%, and the oil-water two-phase co-seepage zone has a wide range (34% on average).

Analysis of water-flooding oil results of coal-measure sandstone

The results of water flooding experiments show that the average irreducible water saturation of the Yan'an Formation sandstone reservoir is 35.14%, and the average final oil displacement efficiency is 51.14% (Figure 11). There is a good positive correlation between the oil displacement efficiency and

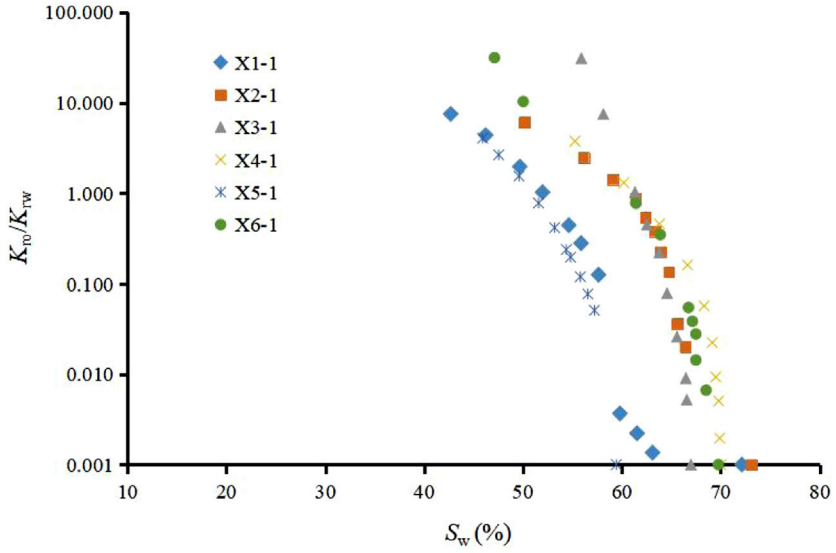

FIGURE 9
Relationship between oil-water relative permeability ratio and S_w.

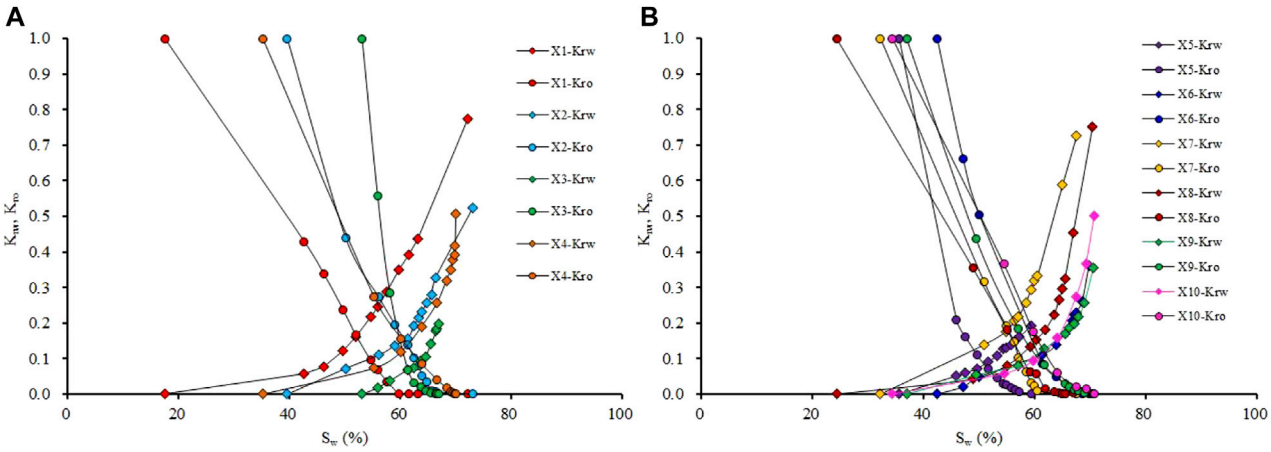

FIGURE 10
Oil-water relative permeability curves of Yan'an Formation sandstone samples. Notes: **(A)** Relative permeability curve characteristics of X1~X4 samples; **(B)** Relative permeability curve characteristics of X5~X10 samples.

the co-permeability zone (Figure 11A). As the co-permeability zone range increased from 15 to 55%, the oil displacement efficiency increased from 30 to 65%. There is a significant negative correlation between oil displacement efficiency and irreducible water saturation. That is, as the irreducible water saturation increases from 20 to 55%, the oil displacement efficiency decreases from 65 to 30%. This shows that high irreducible water content is unfavorable for oil displacement. In addition, there is a certain negative correlation between oil displacement efficiency and residual oil saturation (Figure 11C). The higher the residual oil content, the lower the oil displacement efficiency. There is a good power exponential positive correlation between oil displacement efficiency and average oil recovery rate (Figure 11D). However, if the oil production rate is too high, it will cause interlayer interference and pore pressure to drop too fast, which is not conducive to stable oil and gas production. Therefore, the oil recovery rate should be kept within a relatively reasonable range.

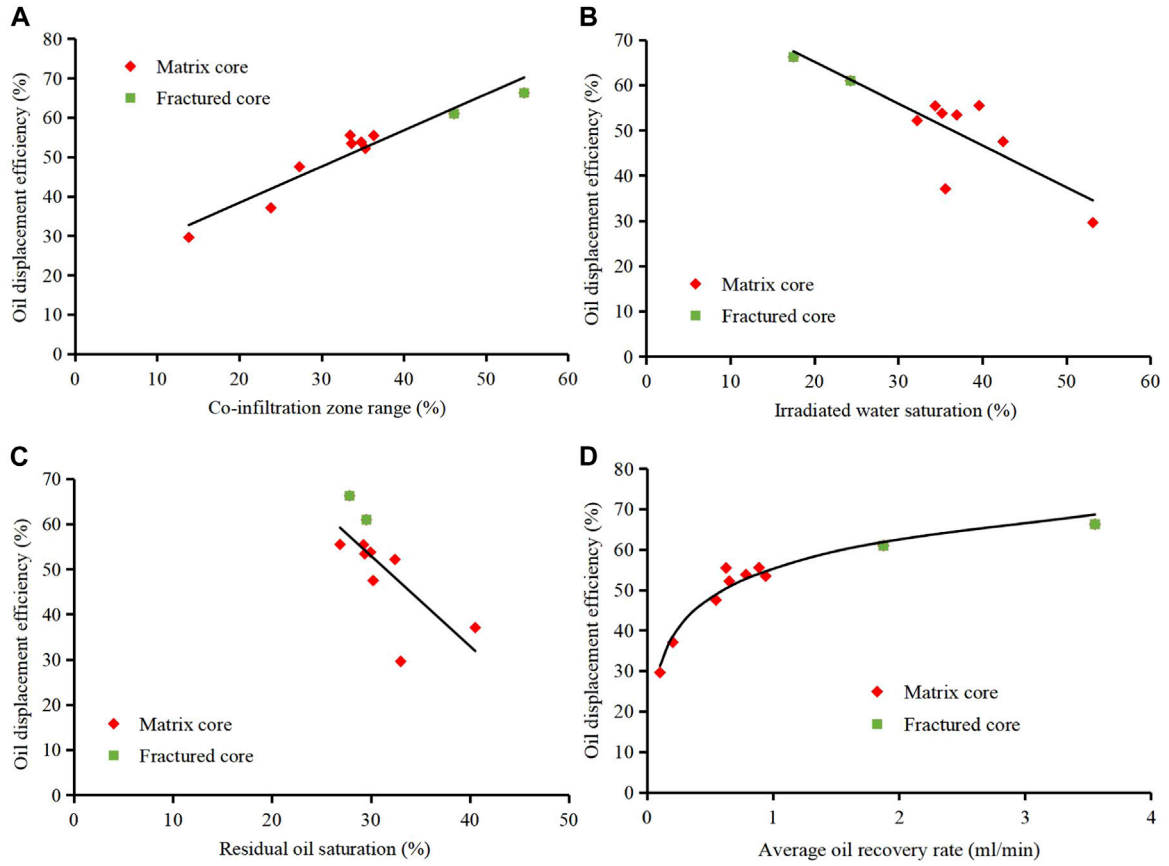

FIGURE 11
Water flooding characteristics of the target layer. Notes: **(A)** Relationship between oil displacement efficiency and co-permeability zone range; **(B)** Relationship between oil displacement efficiency and irreducible water saturation; **(C)** Relationship between oil displacement efficiency and residual oil saturation; **(D)** Relationship between oil displacement efficiency and average oil recovery rate.

This study found that when the cores have fractures, they have characteristics of high permeability, high oil recovery rate, high oil displacement efficiency in anhydrous period, low irreducible water saturation and low residual oil saturation (Figure 11). The initial productivity of the fractured samples is high, but the excessively high oil production rate can cause premature water breakthrough and reduce the productivity rapidly. At the same time, water channeling caused by fractures can form a high-speed seepage channel, which affects the displacement effect and recovery factor.

Conclusion

1) The Jurassic sandstones in the Yan'an Formation of the study area mainly develop lithic quartz sandstone, and the main pore types are intergranular and dissolution pores, followed by a small amount of intercrystalline pores. The surface porosity of the target sandstone mainly ranges from 7.90 to 10.79%, with an average value of 8.78%. The good correlation between porosity and permeability indicates that the target layer is a pore-type reservoir.
2) The T_2 relaxation time of the target layer is mainly distributed within 100 ms. The reservoir of the Yan'an Formation has high saturation of movable fluid, which is mainly distributed in 43.17–71.24%, with an average value of 56.90%. Moreover, samples with fractures have higher movable fluid saturation. In addition, the average irreducible water saturation of the Yan'an Formation sandstone reservoir is 35.14%, and the final oil displacement efficiency is 51.14% on average.
3) There is a good positive correlation between the oil displacement efficiency and the co-permeability zone. As the co-permeability zone range increased from 15 to 55%, the oil displacement efficiency increased from 30 to 65%. When the cores contain fractures, they will have characteristics of high permeability, high oil recovery rate, high oil displacement efficiency in anhydrous period, low irreducible water saturation and low residual oil saturation.

Data availability statement

The original contributions presented in the study are included in the article/Supplementary material, further inquiries can be directed to the corresponding author.

Author contributions

JP is responsible for the writing of this paper and YP is responsible for the idea of this paper.

Funding

This research was funded by the Natural Science Foundation of Xinjiang Uygur Autonomous Region—Surface Project (2019D01A34) "Accumulation Mechanism, Occurrence Characteristics and Basin Dynamics Environment of Shale (Stratification) Gas Source-Reservoir Complex".

Conflict of interest

The authors declare that the research was conducted in the absence of any commercial or financial relationships that could be construed as a potential conflict of interest.

Publisher's note

All claims expressed in this article are solely those of the authors and do not necessarily represent those of their affiliated organizations, or those of the publisher, the editors and the reviewers. Any product that may be evaluated in this article, or claim that may be made by its manufacturer, is not guaranteed or endorsed by the publisher.

References

Asante-Okyere, S., Ziggah, Y. Y., and Marfo, S. A. (2021). Improved total organic carbon convolutional neural network model based on mineralogy and geophysical well log data. *Unconv. Resour.* 1, 1–8. doi:10.1016/j.uncres.2021.04.001

Bai, J., Zhao, J., Ren, Z., Li, W., Wang, K., and Li, X. (2022). Paleogeographic and sedimentary evolution of meso–neoproterozoic strata in the Ordos Basin, Western North China Craton. *J. Petroleum Sci. Eng.* 215, 110600. doi:10.1016/j.petrol.2022.110600

Bhatti, A., Ismail, A., Raza, A., Gholami, R., Rezaee, R., Nagarajan, R., et al. (2020). Permeability prediction using hydraulic flow units and electrofacies analysis. *Energy Geosci.* 1 (1–2), 81–91. doi:10.1016/j.engeos.2020.04.003

Chen, G. B., Li, T., Yang, L., Zhang, G. H., Li, J. W., and Dong, H. J. (2021). Mechanical properties and failure mechanism of combined bodies with different coal-rock ratios and combinations. *J. Min. Strata Control Eng.* 3 (2), 023522. doi:10.13532/j.jmsce.cn10-1638/td.20210108.001

Guo, R., Xie, Q., Qu, X., Chu, M., Li, S., Ma, D., et al. (2020). Fractal characteristics of pore-throat structure and permeability estimation of tight sandstone reservoirs: A case study of chang 7 of the upper triassic yanchang Formation in longdong area, Ordos Basin, China. *J. Pet. Sci. Eng.* 184, 106555. doi:10.1016/j.petrol.2019.106555

He, X., Zhang, P., He, G., Gao, Y., Liu, M., Zhang, Y., et al. (2020). Evaluation of sweet spots and horizontal-well-design technology for shale gas in the basin-margin transition zone of southeastern Chongqing, SW China. *Energy Geosci.* 1 (3-4), 134–146. doi:10.1016/j.engeos.2020.06.004

Ji, W., Song, Y., Jiang, Z., Wang, X., Bai, Y., and Xing, J. (2014). Geological controls and estimation algorithms of lacustrine shale gas adsorption capacity: A case study of the triassic strata in the southeastern Ordos Basin, China. *Int. J. Coal Geol.* 134, 61–73. doi:10.1016/j.coal.2014.09.005

Jiang, W., Zhang, P., Li, D., Li, Z., Wang, J., Duan, Y., et al. (2022). Reservoir characteristics and gas production potential of deep coalbed methane: Insights from the no. 15 coal seam in shouyang block, Qinshui Basin, China. *Unconv. Resour.* 2, 12–20. doi:10.1016/j.uncres.2022.06.001

Katz, B., Gao, L., Little, J., and Zhao, Y. R. (2021). Geology still matters – unconventional petroleum system disappointments and failures. *Unconv. Resour.* 1, 18–38. doi:10.1016/j.uncres.2021.12.001

Lai, J., Wang, G., Wang, Z., Chen, J., Pang, X., Wang, S., et al. (2018). A review on pore structure characterization in tight sandstones. *Earth. Sci. Rev.* 177, 436–457. doi:10.1016/j.earscirev.2017.12.003

Lan, S. R., Song, D. Z., Li, Z. L., and Liu, Y. (2021). Experimental study on acoustic emission characteristics of fault slip process based on damage factor. *J. Min. Strata Control Eng.* 3 (3), 033024. doi:10.13532/j.jmsce.cn10-1638/td.20210510.002

Lei, Q., Zhang, L., Tang, H., Zhao, Y., Chen, M., and Xie, C. (2020). Describing the full pore size distribution of tight sandstone and analyzing the impact of clay type on pore size distribution. *Geofluids* 2020, 1–20. doi:10.1155/2020/5208129

Li, H. (2022). Research progress on evaluation methods and factors influencing shale brittleness: A review. *Energy Rep.* 8, 4344–4358. doi:10.1016/j.egyr.2022.03.120

Li, J., Zhang, X., Tian, J., Liang, Q., and Cao, T. (2021). Effects of deposition and diagenesis on sandstone reservoir quality: A case study of permian sandstones formed in a braided river sedimentary system, northern Ordos Basin, northern China. *J. Asian Earth Sci.* 213, 104745. doi:10.1016/j.jseaes.2021.104745

Li, P., Sun, W., Wang, Z., Huang, H., and Zhe, W. (2018). Features of microscopic pore structure and their influence on oil displacement efficiency in Chang 8^1 reservoir of Xifeng Oilfield, Ordos Basin. *Geoscience* 32 (6), 1194–1202.

Li, Z., Wu, S., Xia, D., Zhang, X., and Huang, M. (2017). Diagenetic alterations and reservoir heterogeneity within the depositional facies: A case study from distributary-channel belt sandstone of upper triassic yanchang Formation reservoirs (Ordos Basin, China). *Mar. Pet. Geol.* 86, 950–971. doi:10.1016/j.marpetgeo.2017.07.002

Liang, Y., Shan, X., Hao, G., Yousif, M., Wan, H., Habeeb, A., et al. (2019). Petrological and organic geochemical characteristics of oil sands from the middle jurassic yan'an Formation in the southern Ordos Basin, China. *Acta Geol. sinica-. Engl. Ed.* 12, 79–626. doi:10.1111/1755-6724.14203

Liu, Y., Hu, W., Cao, J., Wang, X., Tang, Q., Wu, H., et al. (2018). Diagenetic constraints on the heterogeneity of tight sandstone reservoirs: A case study on the upper triassic xujiahe Formation in the sichuan basin, southwest China. *Mar. Pet. Geol.* 92, 650–669. doi:10.1016/j.marpetgeo.2017.11.027

Mirzaei-Paiaman, A., and Ghanbarian, B. (2021). A new methodology for grouping and averaging capillary pressure curves for reservoir models. *Energy Geosci.* 2, 52–62. doi:10.1016/j.engeos.2020.09.001

Qiao, J., Zeng, J., Jiang, S., Feng, S., Feng, X., Guo, Z., et al. (2019). Heterogeneity of reservoir quality and gas accumulation in tight sandstone reservoirs revealed by pore structure characterization and physical simulation. *Fuel* 253, 1300–1316. doi:10.1016/j.fuel.2019.05.112

Ren, D., Yang, F., Li, R., Zhou, D., Liu, D., and Li, Y. (2020). Insight into the pore structures and its impacts on movable fluid in tight sandstones. *Geofluids* 2, 1–11. doi:10.1155/2020/8820023

Schmitt, M., Fernandes, C. P., Wolf, F. G., da Cunha, B., Neto, J. A., Rahner, C. P., et al. (2015). Characterization of Brazilian tight gas sandstones relating permeability and Angstrom-to micron-scale pore structures. *J. Nat. Gas. Sci. Eng.* 27, 785–807. doi:10.1016/j.jngse.2015.09.027

Shanley, K. W., and Cluff, R. M. (2015). The evolution of pore-scale fluid-saturation in low permeability sandstone reservoirs. *Am. Assoc. Pet. Geol. Bull.* 99, 1957–1990. doi:10.1306/03041411168

Shi, G., Shen, C., Zattin, M., Wang, H., Yang, C., and Liang, C. (2019). Late CretaceousCenozoic exhumation of the Helanshan Mt Range, Western Ordos fold-

thrust belt, China: Insights from structural and apatite fission track analyses. *J. Asian Earth Sci.* 176, 196–208. doi:10.1016/j.jseaes.2019.02.016

Vafaie, A., Kivi, I. R., Moallemi, S. A., and Habibnia, B. (2021). Permeability prediction in tight gas reservoirs based on pore structure characteristics: A case study from south western Iran. *Unconv. Resour.* 1, 9–17. doi:10.1016/j.uncres.2021.08.001

Wang, G., Chang, X., Yin, W., Li, Y., and Song, T. (2017). Impact of diagenesis on reservoir quality and heterogeneity of the Upper Triassic Chang 8 tight oil sandstones in the Zhenjing area, Ordos Basin, China. *Mar. Pet. Geol.* 83, 84–96. doi:10.1016/j.marpetgeo.2017.03.008

Wang, H., Alvarado, V., Mclaughlin, J. F., Bagdonas, D. A., Kaszuba, J. P., Campbell, E., et al. (2018). Low-field nuclear magnetic resonance characterization of carbonate and sandstone reservoirs from rock spring uplift of Wyoming. *J. Geophys. Res. Solid Earth* 123 (9), 7444–7460. doi:10.1029/2018JB015779

Wang, H., Zhou, S., Li, S., Zhao, M., and Zhu, T. (2022). Comprehensive characterization and evaluation of deep shales from Wufeng-Longmaxi Formation by LF-NMR technology. *Unconv. Resour.* 2, 1–11. doi:10.1016/j.uncres.2022.05.001

Wu, T., Li, L., Li, W., Gai, Y., Qiu, Y., Pan, G., et al. (2021). A quantitative study on source rocks in the Western Leidong depression, northern South China Sea. *Energy Geosci.* 2 (1), 73–82. doi:10.1016/j.engeos.2020.10.002

Yang, Y., Li, X., Zhang, Y., Mei, Y., and Ding, R. (2020). Insights into moisture content in coals of different ranks by low field nuclear resonance. *Energy Geosci.* 1 (3–4), 93–99. doi:10.1016/j.engeos.2020.05.004

Zhao, K. K., Jiang, P. F., Feng, Y. J., Sun, X. D., Cheng, L. X., and Zheng, J. W. (2021). Investigation of the characteristics of hydraulic fracture initiation by using maximum tangential stress criterion. *J. Min. Strata Control Eng.* 3 (2), 023520. doi:10.13532/j.jmsce.cn10-1638/td.20201217.001

Zhao, Z., Wu, K., Fan, Y., Guo, J., Zeng, B., and Yue, W. (2020). An optimization model for conductivity of hydraulic fracture networks in the Longmaxi shale, Sichuan basin, Southwest China. *Energy Geosci.* 1 (1–2), 47–54. doi:10.1016/j.engeos.2020.05.001

Zhong, X., Zhu, Y., Jiao, T., Qi, Z., Luo, J., Xie, Y., et al. (2021). Microscopic pore throat structures and water flooding in heterogeneous low-permeability sandstone reservoirs: A case study of the jurassic yan'an Formation in the huanjiang area, Ordos Basin, northern China. *J. Asian Earth Sci.* 219, 104903. doi:10.1016/j.jseaes.2021.104903

frontiers | Frontiers in Earth Science

TYPE Original Research
PUBLISHED 13 September 2022
DOI 10.3389/feart.2022.981127

OPEN ACCESS

EDITED BY
Shuai Yin,
Xi'an Shiyou University, China

REVIEWED BY
Qing Li,
China University of Petroleum, China
Chao Liang,
China University of Petroleum, China

*CORRESPONDENCE
Zhihui Zhang,
zhzhihui01@126.com

SPECIALTY SECTION
This article was submitted to Structural Geology and Tectonics, a section of the journal Frontiers in Earth Science

RECEIVED 29 June 2022
ACCEPTED 19 July 2022
PUBLISHED 13 September 2022

CITATION
Han C, Zhang Y, Wang G, Li H, Zhang Z and Li Q (2022), Qualitative–quantitative multiscale pore characteristics of black shale from the Upper Ordovician and Lower Silurian black shale in the Southern Sichuan Basin, China.
Front. Earth Sci. 10:981127.
doi: 10.3389/feart.2022.981127

Qualitative–quantitative multiscale pore characteristics of black shale from the Upper Ordovician and Lower Silurian black shale in the Southern Sichuan Basin, China

Chao Han[1], Yuetong Zhang[1], Guorui Wang[2], Hua Li[3], Zhihui Zhang[1]* and Qiang Li[1]

[1]College of Earth Science and Engineering, Shandong University of Science and Technology, Qingdao, China, [2]Shandong Geo-Surveying and Mapping Institute, Jinan, China, [3]Xishan Coal and Electricity (Group) Co., Ltd., Taiyuan, China

Accurate investigation of shale pores is critical to the assessment of shale-gas reservoir properties. Qualitative and quantitative methods have been commonly conducted in shale pore studies. In this study, we take the black shale from the Upper Ordovician and Lower Silurian black shale in the Southern Sichuan Basin as an example. Both qualitative and quantitative methods were used to study the pores at multiple scales, and we discuss the effectiveness of shale pore detection by multiple methods. The following results were obtained: 1) The black shale is composed of quartz, feldsaper, calcite, dolomite and clay minerals in the study area, and its average TOC and porosity are 2.19 and 2.12%, respectively. 2) The CT results show that the pore size of macropores (pore size >0.5 μm) mainly ranges from 2 to 16 μm. Nitrogen adsorption analysis shows that organic-rich shale has abundant organic matter pores with narrow necks and wide bodies. The pores of organic-poor shale are mainly composed of mineral-associated pores with narrow slit shapes. The NMR results show that with increasing TOC, the left peak T_2 relaxation times move leftwards, meaning that organic matter pores have a larger pore size than matrix pores at the mesopore scale. 3) CT data identify lamellation fractures and bed-cutting fractures, and their development is controlled by mineral type and content, TOC and laminae density. 4) The determination of segmentation thresholds in CT and transverse surface relaxivity in NMR seriously affects the accuracy of the results.

KEYWORDS

sichuan basin, black shale, pore characteristics, CT, NMR

Introduction

The remarkable success of the US shale gas revolution aroused wide concern among Chinese petroleum geologists (Jarvie et al., 2007; Wang et al., 2013; Lv et al., 2020). In recent years, China has achieved breakthroughs in shale gas exploration, and its known reserves have reached 2×10^{12} m^3, with an annual production of 200×10^8 m^3 in 2020 (Zhang et al., 2017; Li et al., 2021; Zhao et al., 2021). The black marine shale from the Upper Ordovician Wufeng Formation and Lower Silurian Longmaxi Formation in the Sichuan Basin has high organic matter content (TOC), high maturity, large thickness and wide distribution and is the main shale gas exploration target in China (Xu et al., 2020; Li et al., 2021). Shale gas reservoirs are typical "self-sources and self-reservoirs," and their pore types differ from those of conventional reservoirs. A previous study showed that the main pore sizes of black shales are nanopores.

A series of qualitative and quantitative approaches, such as low-pressure nitrogen and CO_2 gas adsorption, field emission-scanning electron microscopy (FE-SEM), nuclear magnetic resonance (NMR), high-pressure mercury intrusion (HPMI), and X-ray microcomputed tomography (CT), provide multiscale methods to determine pore properties, such as pore volume, pore size, specific surface area, and pore connectivity (Zhang et al., 2015; Ji et al., 2017; Huang et al., 2020; Li et al., 2020; Wang et al., 2020; Li, 2022). However, these methods cannot show pore distribution in three-dimensional space, limiting the further understanding of shale gas reservoir controlling factors. In this study, shale core samples from the Upper Ordovician Wufeng Formation and Lower Silurian Longmaxi Formation in the Sichuan Basin were collected. By combining organic geochemistry, petrology, CT scanning, helium porosity, NMR and low-pressure nitrogen adsorption, multiscale pore characteristics were investigated, and the effectiveness of shale pore detection by multiple methods was discussed.

Geological setting

The Sichuan Basin is located in southern China and covers a total area of 180×10^3 km^2 (Han et al., 2016, 2019; Wang et al., 2020). It was formed from multistage tectonic cycles, including the Caledonian, Hercynian, Indosinian, Yanshanian, and Himalayan movements. The basement of the Sichuan Basin is composed of pre-Sinian metamorphic rocks, including Archaean-early Proterozoic gneiss rock and meso-upper Proterozoic low metamorphic greenschist.

From the Sinian to the Middle Triassic, the Sichuan Basin mainly deposited marine carbonate, and its thickness ranged from 4 to 7 km. Since the Late Triassic, the Sichuan Basin has entered the inner land lake stage (Mou et al., 2011). The Longmaxi Formation, with thicknesses ranging from 160 to 600 m, is composed of black shale, while its lower member commonly contains black shales with high TOC and abundant graptolites. Its upper member is composed of argillaceous limestone, silty mudstone and siltstone, with low TOC content. From bottom to top, the TOC content of the Longmaxi Formation shows a decreasing trend (Han et al., 2016, 2018). Figure 1.

Samples and experiments

A total of 72 shale samples from the Lower Longmaxi Formation and Wufeng Formation were collected from four wells and one outcrop section in the southern Sichuan Basin. The mineral content of black shale samples was analysed using RINT-TTR3 X-ray Diffraction (XRD) at a current of 100 mA and a voltage of 45 kV. The TOC content was determined using a LECO CS-230 carbon analyser. CT scanning is completed by nano Voxel-3502 E at a current of 35 μA and a voltage of 50 kV, and its voxel size is 0.5 μm. NMR was performed by RecCore04. Low-temperature nitrogen adsorption was completed by QuadraSorb Station.

Experimental results

Mineralogy, porosity and organic geochemistry

XRD results show that the black shale of the Longmaxi Formation is composed of quartz (average: 30.78 wt%), calcite (average: 14.57 wt%), feldspar (average: 7.82 wt%), dolomite (average: 9.62 wt%), clay (36.04 wt%) and pyrite (2.54 wt%). Quartz, feldsaper, calcite, dolomite and clay occupy a large proportion, and their ternary diagram shows that their percentages vary greatly (Figure 2A). Clay mainly contains chlorite, illite and illite–smectite, and the ternary diagram shows that illite and illite–smectite account for the majority of the composition (Figure 2B). The distributions of TOC and porosity are shown in Figure 2A. The TOC of black shale ranges from 0.34 wt% to 7.7 wt%, with an average of 2.19 wt %, the highest TOC content in the bottom of the Longmaxi Formation (Figure 3A). The porosity of black shale ranges from 0.68 to 4%, with an average of 2.02% (Figure 3B).

CT results

The quantitative and qualitative data presented in this section, such as three-dimensional (3D) distribution pores and fractures, pore volume, and pore size, were calculated from CT data (Figures 4). The dataset comprised 3,950 2D images, each

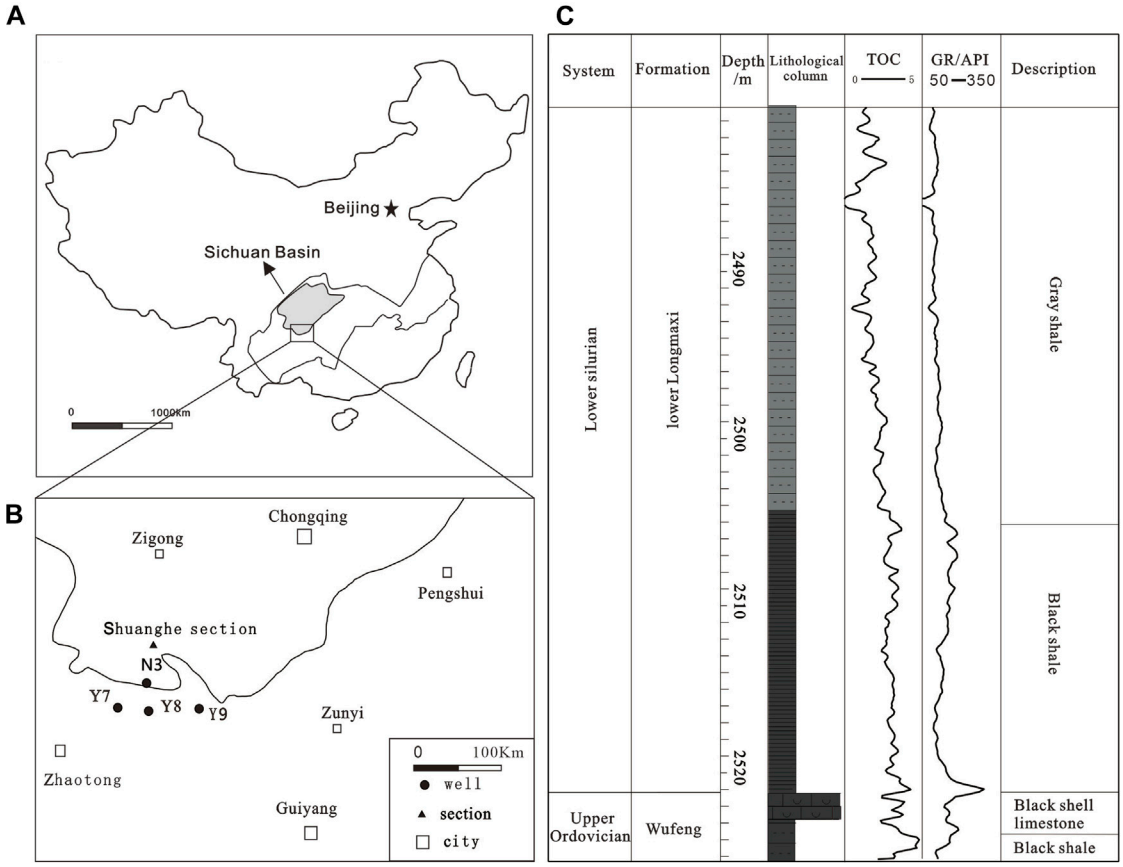

FIGURE 1
Geographic location and lithological column of the Longmaxi and Wufeng Formations. **(A)** Location of Sichuan Basin; **(B)** Location of the study area (modified according to Wang et al., 2013); **(C)** Lithological column Longmaxi and Wufeng formation, Well N3.

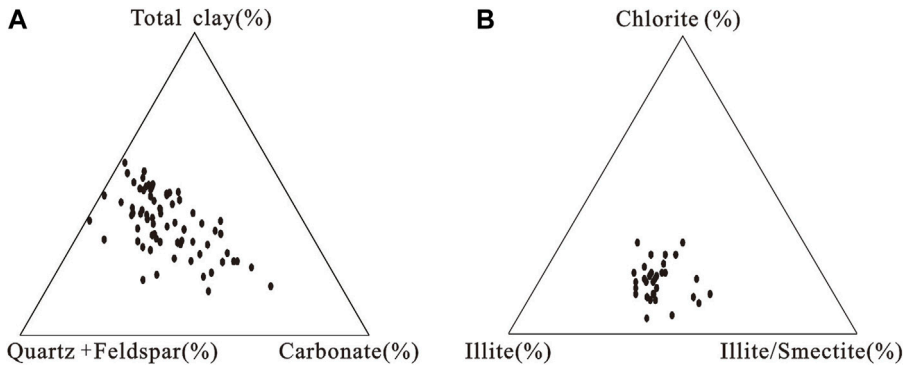

FIGURE 2
Ternary diagram of the XRD mineral composition **(A)** and clay type **(B)** for the study shale samples.

comprising square pixels with a side length of 0.5 μm. The distribution of fractures shows two distinct types. The first type is lamellation fractures parallel to bedding layers, showing good connectivity (Figures 5A,B), and its thickness mainly ranges from 40 to 70 μm (Figure 5C). The second type is bed-cutting fractures, which are composed of a series of

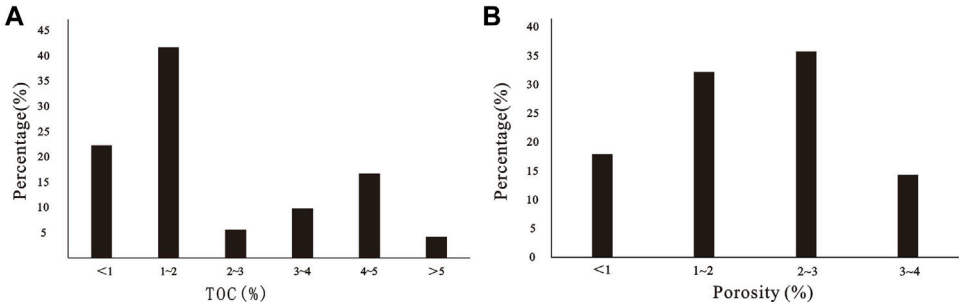

FIGURE 3
Distributions of TOC and porosity of black shale in the study area.

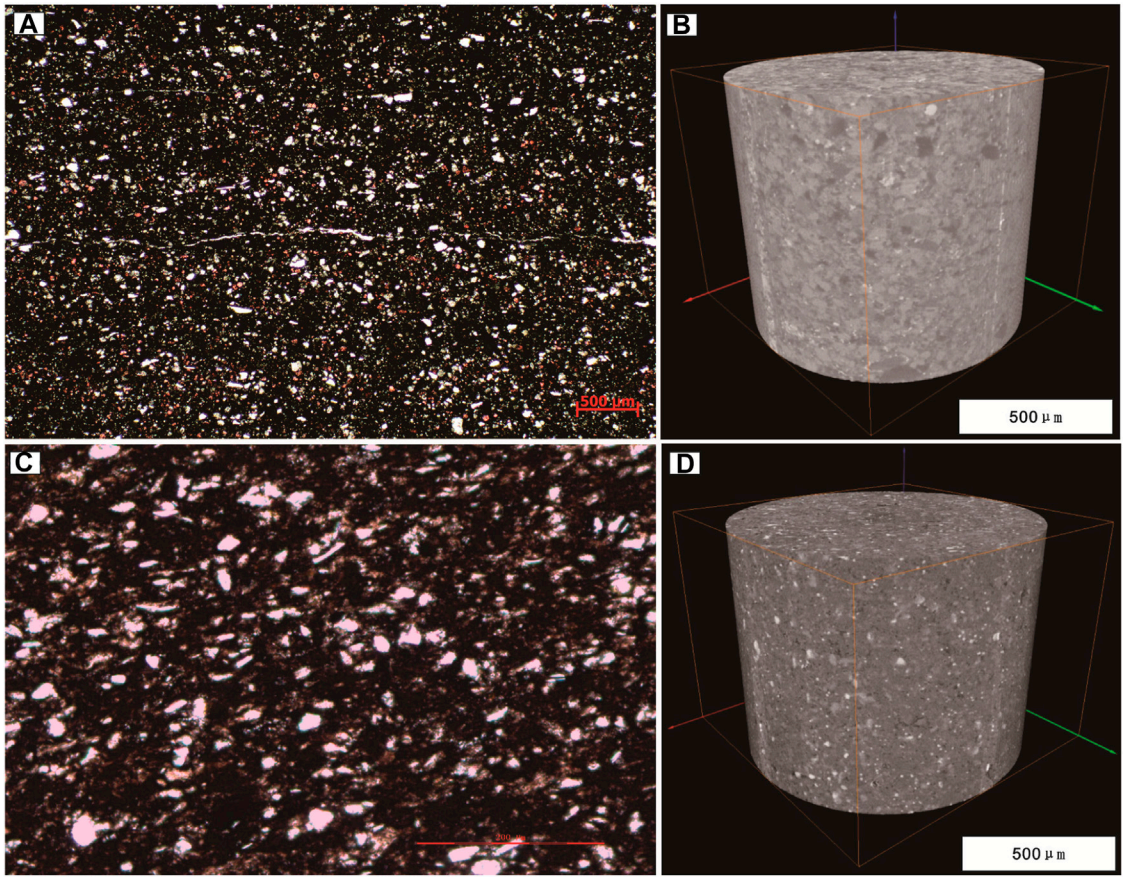

FIGURE 4
Thin section observations and three-dimensional image from CT of the black shale. **(A)** Thin section observations, Well Y7, 2275.26 m, sample 7–15, horizontal bedding. **(B)** Three-dimensional image of sample 7–15 from CT; **(C)** thin section observations, well Y7, 2286.71 m, sample 7–18; **(D)** three-dimensional image of sample 7–18 from CT.

isolated fractures and show irregular distribution and poor connectivity (Figures 5C,D). The widths of the fractures range from 20 to 110 μm, with lengths varying from 65 to 500 μm (Table 1), and their thicknesses are mainly 2–6 μm (Figure 5F). Figure 6 shows the pore three-dimensional (3D) distribution, the percentage number of pores and fractures, and the pore volume

10.3389/feart.2022.981127

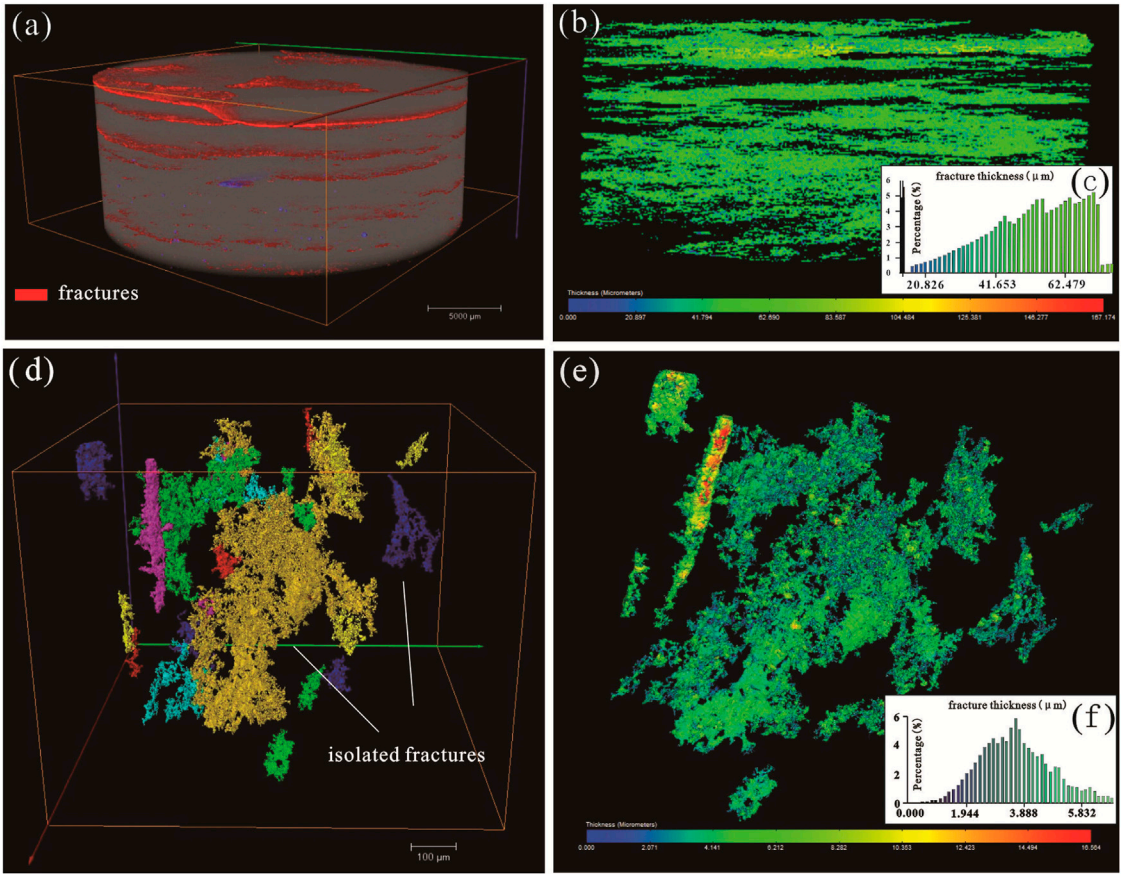

FIGURE 5
Three-dimensional distribution of the two types of fractures from the CT data. **(A)** Three-dimensional image of lamellation fractures from CT, sample tj-17, shuanghe section; **(B)** lamellation fractures were given different colours by their thickness, sample tj-17, shuanghe section; **(C)** thickness distribution of lamellation fractures, sample tj-17, shuanghe section; **(D)** three-dimensional image of bed-cutting fractures from CT, Well Y7, 2286.71 m, sample 7–18; **(E)** bed-cutting fractures were given different colours by their thickness, Well Y7, 2286.71 m, sample 7–18; **(F)** thickness distribution of bed-cutting fractures, Well Y7, 2286.71 m, sample 7–18.

TABLE 1 The size features of fractures.

Type code	1	2	3	4	5	6	7	8	9	10	11
width/um	52.03	101.86	79.98	34.65	105.35	29.98	55.36	98.78	27.56	41.03	33.16
length/um	485.89	419.88	376.42	171.97	208.08	180.89	110.64	176.12	403.77	65.08	97.53
Angle/°	37.27	62.37	26.17	38.88	28.18	35.45	64.61	76.48	76.64	62.069	66.73

distribution with different pore diameters. Limited by the low resolution of the CT technique (0.5 μm), pores larger than 0.5 μm were recognized. The pore volumes of the two selected samples account for 2.44 and 2.56%, and fractures account for 0.42 and 0.41%. The pore volume mainly comes from pores with diameters of 4–8 μm.

Low-temperature nitrogen adsorption

The nitrogen adsorption-desorption isotherms are shown in Figures 7, 8. According to the classification of the International Union of Pure and Applied Chemistry (IUPAC), these isotherms of black shale feature Type IV hysteresis loops. The hysteresis loop

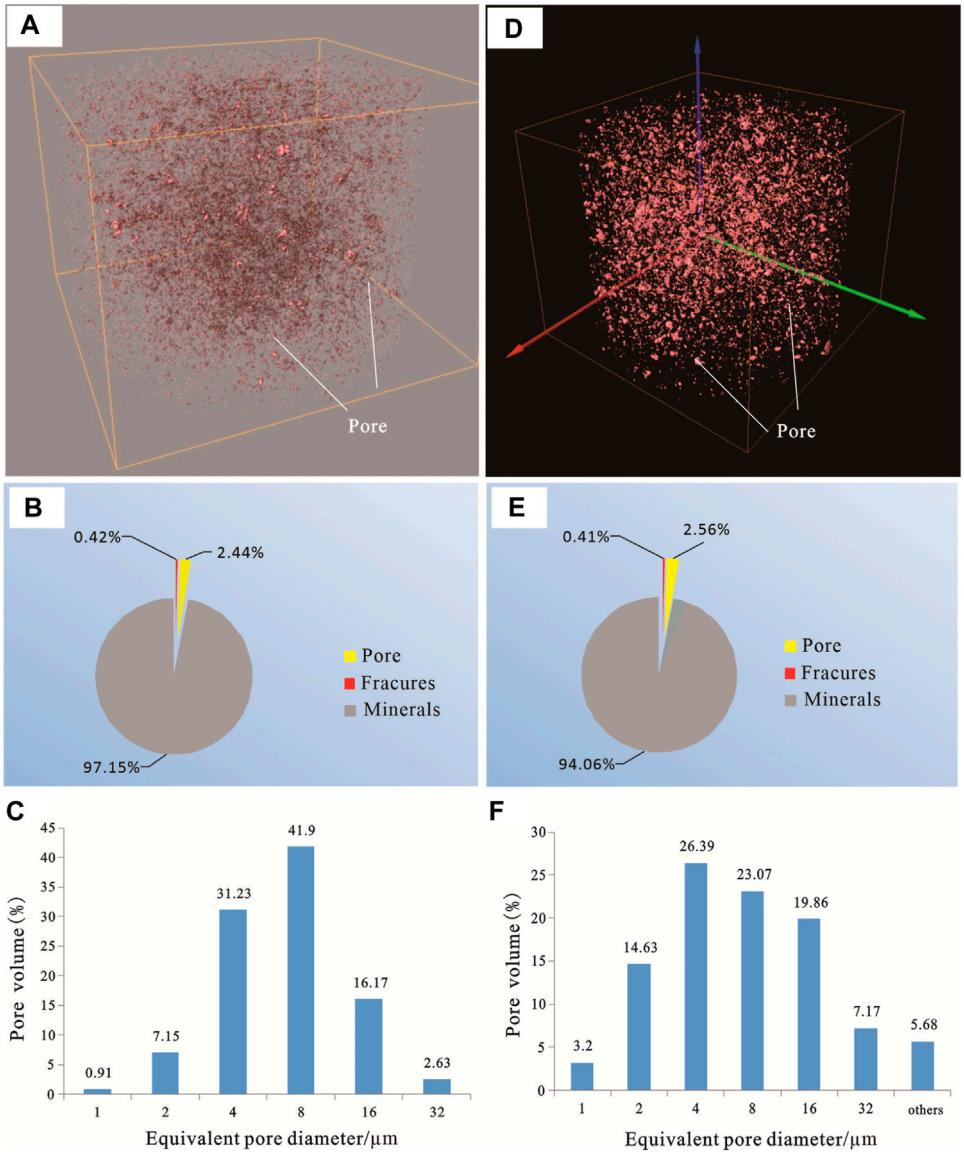

FIGURE 6
Pore features from CT data. **(A)** Three-dimensional distribution of pores, Well Y7, 2275.26 m, sample 7–15; **(B)** the percentage of pore volume, sample 7–15; **(C)** pore size distribution of sample 7–15; **(D)** three-dimensional distribution of pores, Well Y7, 2286.71 m, sample 7–18; **(E)** the percentage of pore volume, sample 7–18; **(F)** pore size distribution of sample 7–18.

shape shows that the organic-rich shale pore type is H_2 (inkbottle-shaped pore), which has narrow necks and wide bodies. These isotherms of organic-poor shale feature Type IV characterized H_4-type hysteresis loops, which means narrow slit-shaped pores developed (De Boer, 1958; Sing, 1985). Using nitrogen adsorption-desorption isotherms, BET surface areas and BJH pore volume were calculated. The pore size distribution (PSD) shows that pores with diameters of approximately 4 nm are the main source of pore volume (Figures 7B,C). The BET surface areas are in the range of 3.902–17.84 m^2/g (Figure 9A), and their average value is 11.93 m^2/g (Figure 9A). The BJH pore volumes range from 0.017 to 0.063 cc/g (Figure 9B), and their average value is 0.041 cc/g.

NMR analysis results

The current study suggest that the detected T_2 correlates with pore size in NMR measurements (Yao et al., 2010). Twelve black shale samples from two well cores were subjected to NMR

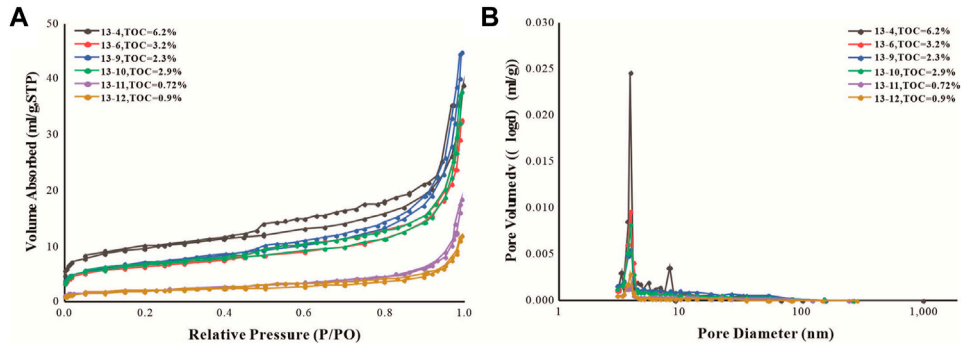

FIGURE 7
Nitrogen adsorption and desorption isotherms **(A)** and pore-volume distributions **(B)** for six representative core samples.

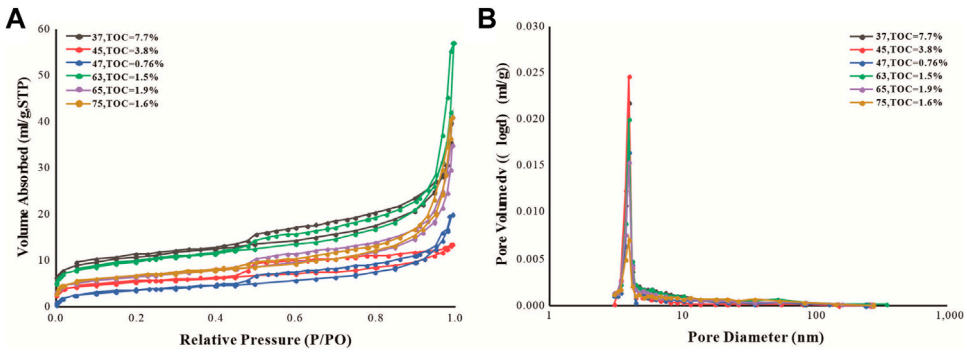

FIGURE 8
Nitrogen adsorption and desorption isotherms **(A)** and pore-volume distributions **(B)** for six outcrop samples.

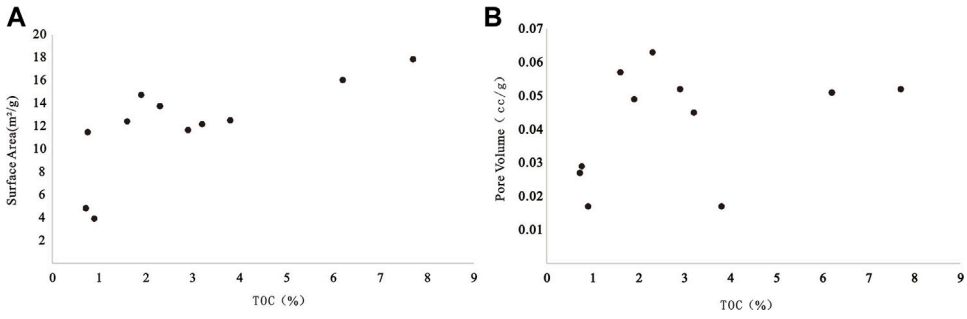

FIGURE 9
Relationship between TOC and surface area and pore volumes obtained from nitrogen adsorption isotherm analyses.

measurements. The NMR amplitudes of the black shale sample mainly show bimodal distributions, supplemented with few trimodal and unimodal distributions. The T_2 relaxation times of shale samples range from 0.01 to 110 ms (Figure 10). The first peak (P_1) normally was at 0–10 ms, the second peak was at 8–16 ms, and the third peak was at 13–110 ms. P_3 is interpreted as a fracture. Figure 9.

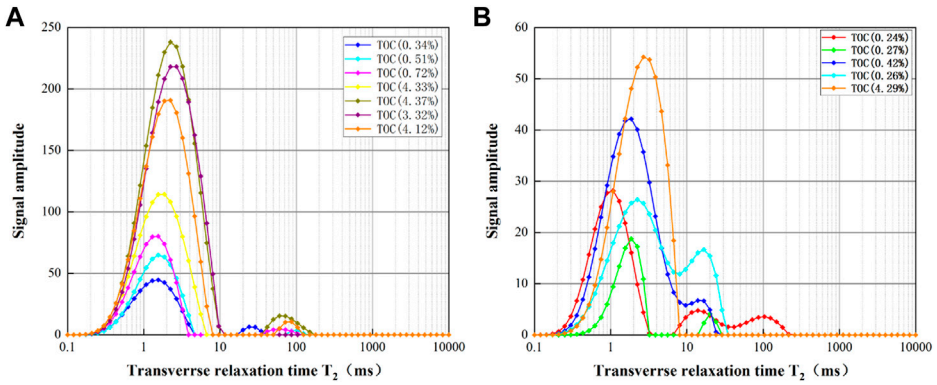

FIGURE 10
T_2 spectra for seven outcrop samples **(A)** and five core samples **(B)**.

The T_2 relaxation times are controlled by the pore size of the rock, and the relationship between the T_2 relaxation times and pore size can be expressed as follows (Liang et al., 2016; Zhang et al., 2017):

$$\frac{1}{T_2} = \frac{F_s * \rho_2}{r} \quad (1)$$

F_s is the geometric factor of pore shape, which is equal to two for a cylindrical pore and three for a spherical pore, r is the pore radius in nanometres, and ρ_2 is the proportionality constant between $1/T_2$ and the surface-to-volume ratio of the pore. For simplification purposes, the value of F_s is given as two because the pore morphology of shale is regarded as cylindrical.

$$r = 2_{\rho 2} * T_2 \quad (2)$$

Combined with the PSD from nitrogen adsorption, we define ρ_2 as 0.5 nm/ms. The pore radius can be derived from Eq. 2 and is expressed as Eq. 3:

$$r = 2T_2 \quad (3)$$

Therefore, the pore size of P_1 is 0–20 nm, and that of P_2 is 20–140 nm.

Discussion

Pore type and PSD in black shale

Based on the occurrence position, pore types are subdivided into interparticle pores found between particles and crystals, intraparticle pores located within particles and organic matter pores located within organic matter (Loucks, et al., 2012). On the basis of pore size, pores were divided into micropores (pore diameter<2 nm), mesopores (pore diameter 2–50 nm) and macropores (pore diameter>50 nm) (Sing, 1985).

In this study, limited by the low resolution of CT, pores with sizes larger than 0.5 μm were identified, and their pore sizes mainly ranged from 2 to 16 μm. The PSD from nitrogen adsorption shows that organic-rich shale commonly has a higher pore volume and surface area than organic-poor shale (Figure 9), and the peak of the PSD is approximately 4 nm. In Figure 10A, the peak of the T_2 relaxation times moves leftwards with increasing TOC, while this trend is not obvious in Figure 10B because their TOC gap is small. Since the T_2 relaxation times are positively related to pore size in NMR experiments (Liang et al., 2016; Zhang et al., 2017), the trend shows that organic pores have a larger pore size than matrix pores.

Our previous study showed that black shale has long-dimensional OM pores ranging from a few nanometres to one hundred nanometres, the pore size of interparticle pores ranges from 50 nm to 1 μm, and intraparticle pores have an obvious pore size distribution with pore sizes ranging from 25 nm to 3 μm in the southern Sichuan Basin (Han et al., 2016; Han et al., 2018). The relationship between shale composition and pore volumes shows that mesopore volumes had a moderate-strong positive correlation with TOC and carbonate content, while a moderate-weak negative correlation with quartz and clay content and macropore volumes had a moderate positive correlation with quartz content (Han et al., 2018). Both NMR and nitrogen adsorption show that organic pores are the main source of mesopores, which is consistent with previous studies proven by both qualitative and quantitative methods, such as N_2 gas adsorption and FE-SEM images (Yang et al., 2016; Han et al., 2018; He et al., 2021; Qian et al., 2022).

Fracture types and controlling factors

Fractures are a key factor controlling shale gas accumulation and productivity (Gale et al., 2017; Li et al., 2018; Chen et al., 2021; Zhao et al., 2021). CT imaging shows that the black shale has two distinct types of fractures, lamellation fractures and bed-cutting fractures, in the study area. The thickness of bed-parallel fractures is generally dozens of times that of bed-cutting fractures (Figure 5). The development of fractures is controlled by mineral type and content, TOC and laminae density (Zeng et al., 2013; Cai et al., 2020; Lan et al., 2021; Xu et al., 2021). Lamellation fractures are commonly related to the primary sedimentary structure of shale (Xiang et al., 2022). The minerals in shale are commonly arranged in layers, and the mineral type and content vary in different layers. As a result, adjacent layers have different compressive abilities when subjected to compressional stress, and lamellation fractures form at laminae interfaces (Zeng et al., 2013; Gu et al., 2020; Xu et al., 2021). Laminae density also affects the formation of lamellation fractures. When the laminae density is less than 4 cm^{-1}, the laminae density has an obvious correlation with the density of the lamellation fracture. However, when the laminae density is greater than 4 cm^{-1}, the density of the lamellation fracture remains at approximately 1 cm^{-1} with the increase in fracture (Xu et al., 2021). Shale composition is an important factor affecting fractures, including mineral composition and content and TOC content (Ding et al., 2012; Zeng et al., 2013; Yin and Wu, 2020; Li, 2022). The statistical results show that with increasing quartz content, the fracture density increases first when the quartz content is less than 50%, while the fracture density decreases when the quartz content is over 50% (Han et al., 2022). Because of the positive relationship between TOC and quartz content, the relationship between TOC and fracture density also shows a similar trend (Han et al., 2022).

Effectiveness evaluation of shale pore detection by multiple methods

Nitrogen adsorption, CT and NMR are popular methods to detect shale pore structure. Primitive CT data comprise 3,950 2D images, and the pore features calculated from CT data are severely affected by X-ray images. Meanwhile, OM and pores show similar and continuing thresholds in X-ray images, and it is difficult to accurately determine the boundaries (Wang et al., 2019). If the threshold value increased from 42 to 54, shale porosity could change from 14% to nearly 49% (Bai et al., 2013). Therefore, the determination of segmentation thresholds is a problem that cannot be ignored.

The NMR method has been used in reservoir characterization since 1956 (Brown and Fatt, 1956). With the development of NMR instruments, NMR has been widely used to determine petrophysical properties and fluid characteristics in coal and shale (Liu et al., 2020; Zheng et al., 2020; Zhao et al., 2022). From Ea. (2), ρ_2, called the transverse surface relaxivity, is a key parameter to calculate pore size. However, the value of ρ_2 varies from 2 nm/ms to 21 nm/ms in shale (Coates et al., 1999; Curtis et al., 2010; Sondergeld et al., 2010). Therefore, accurately obtaining the value of the transverse surface relaxivity is still a critical issue.

Conclusion

1. The black shale of the Longmaxi Formation is mainly composed of quartz, feldspar, calcite, dolomite and clay minerals in the study area; its TOC ranges from 0.34 to 7.7% (average: 2.19%) and has a porosity ranging from 0.68 to 4% (average of 2.02%).
2. Limited by low resolution, CT results could identify macropore features with pore sizes larger than 0.5 μm, and their pore size distribution is mainly from 2 to 16 μm. Nitrogen adsorption analysis shows that organic-rich shale contains abundant OM pores that have narrow necks and wide bodies, and its PSD peaks at approximately 4 nm. NMR analysis shows that PSD has two peaks: P_1 is 0–20 nm, and P_2 is 20–140 nm. The left peak of T_2 relaxation times moves leftwards with increasing TOC. This trend shows that organic matter pores have a larger pore size than matrix pores.
3. The black shale has two distinct types of fractures, lamellation fractures and bed-cutting fractures, in the study area. Their development is controlled by mineral type and content, TOC and laminae density.
4. Although NMR and CT have been widely used in shale pores, the determination of segmentation thresholds in CT and transverse surface relaxivity in NMR is still a problem to solve further.

Data availability statement

The original contributions presented in the study are included in the article/Supplementary Material, further inquiries can be directed to the corresponding author.

Author contributions

CH is responsible for the idea and writing of this paper and YZ, GW, ZZ, HL, and QL are responsible for the experiments.

Funding

This manuscript was supported by the National Natural Science Foundation of China (41702131 and 41972108).

Conflict of interest

The author GW was employed by Shandong Geo-surveying and Mapping Institute. The author HL was employed by Xishan Coal and Electricity (Group) Co. Ltd. Taiyuan, China.

The remaining authors declare that the research was conducted in the absence of any commercial or financial relationships that could be construed as a potential conflict of interest.

Publisher's note

All claims expressed in this article are solely those of the authors and do not necessarily represent those of their affiliated organizations, or those of the publisher, the editors and the reviewers. Any product that may be evaluated in this article, or claim that may be made by its manufacturer, is not guaranteed or endorsed by the publisher.

References

Bai, B., Elgmati, M., Zhang, H., and Wei, M. (2013). Rock characterization of Fayetteville shale gas plays. *Fuel* 105, 645–652. doi:10.1016/j.fuel.2012.09.043

Brown, R. J. S., and Fatt, I. (1956). Measurements of fractional wettability of oil fields' rocks by the nuclear magnetic relaxation method. *Trans. AIME* 207, 262–264. doi:10.2118/743-G

Cai, C., Kang, Y., Yang, Y., Wang, X., Li, Y., Huang, M., et al. (2020). The effect of shale bedding on supercritical CO2 jet fracturing: A experimental study. *J. Pet. Sci. Eng.* 195, 107798. doi:10.1016/j.petrol.2020.107798

Chen, G. B., Li, T., Yang, L., Zhang, G. H., Li, J. W., and Dong, H. J. (2021). Mechanical properties and failure mechanism of combined bodies with different coal-rock ratios and combinations. *J. Min. Strata Control Eng.* 3 (2), 023522. doi:10.13532/j.jmsce.cn10-1638/td.20210108.001

Coates, G. R., Xiao, L., and Prammer, M. G. (1999). *NMR logging principles and applications*. Houston: Haliburton Energy Services.

Curtis, M. E., Ambrose, R. J., and Sondergeld, C. H. (2010). "Structural characterization of gas shales on the micro-and nano-scales," in Paper presented at the Canadian Unconventional Resources and International Petroleum Conference, Calgary, Alberta, Canada, October 19–21, 2010. SPE137693. doi:10.2118/137693-MS

De Boer, J. H. (1958). *The structure and propertied of porous materials*. London: Butterwort-Heinemann.

Ding, W. L., Li, C., and Li, C. Y. (2012). Dominant factor of fracture development in shale and its relationship to gas accumulation. *Earth Sc Front.* 19 (2), 212–220.

Gale, J. F. W., Laubach, S. E., Olson, J. E., Eichhubl, P., and Fall, A. (2017). Natural fractures in shale: A review and new observations. *Bulletin* 101 (8), 2165–2216. doi:10.1306/08121413151

Gu, Y., Ding, W. L., Tian, Q. T., Xu, S., Zhang, W., Zhang, B., et al. (2020). Developmental characteristics and dominant factors of natural fractures in lower silurian marine organic-rich shale reservoirs: A case study of the Longmaxi Formation in the fenggang block, southern China. *J. Pet. Sci. Eng.* 192, 107277. doi:10.1016/j.petrol.2020.107277

Han, C., Han, M., Jiang, Z., Han, Z., Li, H., Song, Z., et al. (2019). Source analysis of quartz from the Upper Ordovician and Lower Silurian black shale and its effects on shale gas reservoir in the southern Sichuan Basin and its periphery, China. *Geol. J.* 54 (1), 438–449. doi:10.1002/gj.3192

Han, C., Jiang, Z., Han, M., Wu, M., and Lin, W. (2016). The lithofacies and reservoir characteristics of the upper ordovician and lower silurian black shale in the southern Sichuan Basin and its periphery, China. *Mar. Pet. Geol.* 75 (4), 181–191. doi:10.1016/j.marpetgeo.2016.04.014

Han, L., Li, X., Guo, W., Ju, W., Cui, Y., Liu, Z., et al. (2022). Characteristics and dominant factors for natural fractures in deep shale gas reservoirs: A case study of the wufeng-longmaxi formations in luzhou block, southern China1. *Lithosphere* 2022, 9662175. doi:10.2113/2022/9662175

Han, M., Han, C., Han, Z., Song, Z., Zhong, W., Li, H., et al. (2018). Mineral compositional controls on the porosity of black shales from the Wufeng and Longmaxi Formations (Southern Sichuan Basin and its surroundings) and insights into shale diagenesis. *Energy Explor. Exploitation* 36 (4), 665–685. doi:10.1177/0144598718763890

He, S., Li, H., Qin, Q., and Long, S. (2021). Influence of mineral compositions on shale pore development of longmaxi formation in the dingshan area, southeastern sichuan basin, china. *Energy fuels.* 35 (6), 10551–10561. doi:10.1021/acs.energyfuels.1c01026

Huang, Z. Q., Zhang, Y., Xie, L. Z., and ZhaoHeRen, P. B. L. (2020). Comparative study of porosity test methods for shale. *Arab. J. Geosci.* 13 (2), 94. doi:10.1007/s12517-020-5086-5

Jarvie, D. M., Hill, R. J., Ruble, T. E., and Pollastro, R. M. (2007). Unconventional shale-gas systems: The Mississippian Barnett Shale of north-central Texas as one model for thermogenic shale-gas assessment. *Am. Assoc. Pet. Geol. Bull.* 91, 475–499. doi:10.1306/12190606068

Ji, W., Song, Y., Rui, Z., Meng, M., and Huang, H. (2017). Pore characterization of isolated organic matter from high matured gas shale reservoir. *Int. J. Coal Geol.* 174, 31–40. doi:10.1016/j.coal.2017.03.005

Lan, S. R., Song, D. Z., Li, Z. L., and Liu, Y. (2021). Experimental study on acoustic emission characteristics of fault slip process based on damage factor. *J. Min. Strata Control Eng.* 3 (3), 033024. doi:10.13532/j.jmsce.cn10-1638/td.20210510.002

Li, H. (2022). Research progress on evaluation methods and factors influencing shale brittleness: A review. *Energy Rep.* 8, 4344–4358. doi:10.1016/j.egyr.2022.03.120

Li, X., Zhu, H., Zhang, K., Li, Z., Yu, Y., Feng, X., et al. (2021). Pore characteristics and pore structure deformation evolution of ductile deformed shales in the Wufeng-Longmaxi Formation, southern China. *Mar. Pet. Geol.* 127, 104992. doi:10.1016/j.marpetgeo.2021.104992

Li, Y. F., Sun, W., Liu, X. W., Zhang, D. W., Wang, Y. C., and Liu, Z. Y. (2018). Study of the relationship between fractures and highly productive shale gas zones, Longmaxi Formation, Jiaoshiba area in eastern Sichuan. *Pet. Sci.* 15 (3), 498–509. doi:10.1007/s12182-018-0249-7

Li, Y., Zhou, D., Wang, W., Jiang, T., and Xue, Z. (2020). Development of unconventional gas and technologies adopted in China. *Energy Geosci.* 1 (1–2), 55–68. doi:10.1016/j.engeos.2020.04.004

Liang, Xiao, Mao, Z. Q., Zou, C. C., Jin, Y., and Zhu, J. C. (2016). A new methodology of constructing pseudo capillary pressure (Pc) curves from nuclear magnetic resonance (NMR) logs. *J. Pet. Sci. Eng.* 147, 154–167. doi:10.1016/j.petrol.2016.05.015

Liu, Z. S., Liu, D. M., Zhou, Y. F., Cai, Y., Yao, Y., and Pan, Z. (2020). Application of nuclear magnetic resonance (NMR) in coalbed methane and shale reservoirs: A review. *Int. J. COAL Geol.* 2020, 103261. doi:10.1016/j.coal.2019.103261

Loucks, R. G., Reed, R. M., Ruppel, S. C., and Hammes, U. (2012). Spectrum of pore types and networks in mudrocks and a descriptive classification for matrix-related mudrock pores. *Am. Assoc. Pet. Geol. Bull.* 96, 1071–1098. doi:10.1306/08171111061

Lv, D., Song, Y., Wang, Z., Cong, P., and Van Loon, A. J. T. (2020). The complex transgression and regression history of the northern margin of the Palaeogene Tarim Sea (NW China), and implications for potential hydrocarbon occurrences. *Mar. Pet. Geol.* 112, 104041. doi:10.1016/j.marpetgeo.2019.104041

Mou, C. L., Zhou, K. K., and Liu, W. (2011). Early Paleozoic sedimentary environment of hydrocarbon source rocks in the Middle-Upper Yangtze region and petroleum and gas exploration. *Acta Geol. Sin.* 85 (4), 526–532. doi:10.1007/s12583-011-0163-z

Qian, C., Li, X., Shen, W., Zhang, Q., Guo, W., Hu, Y., et al. (2022). Study on the pore structure and fractal characteristics of different lithofacies of Wufeng–Longmaxi Formation shale in southern Sichuan Basin, China. *ACS Omega* 7 (10), 8724–8738. doi:10.1021/acsomega.1c06913

Sing, K. S. W. (1985). Reporting physisorption data for gas/solid systems with special reference to the determination of surface area and porosity (Recommendations 1984). *Pure Appl. Chem.* 57 (4), 603–619. doi:10.1351/pac198557040603

Sondergeld, C. H., Ambrose, C. S., and Rai, J. (2010). "Micro-structural studies of gas shales," in Paper presented at the SPE Unconventional Gas Conference, Pittsburgh, Pennsylvania, USA, February 23–25, 2010. SPE131771. doi:10.2118/131771-MS

Wang, Y., Dong, D., Yang, H., Wang, S., Huang, J., et al. (2013). Quantitative characterization of reservoir space in the lower silurian longmaxi shale, southern sichuan, China. *Sci. China Earth Sci.* 57 (2), 313–322. doi:10.1007/s11430-013-4645-y

Wang, Y., Wang, L., Wang, J., Jiang, Z., Wang, C. C., Fu, Y., et al. (2019). Multiscale characterization of three-dimensional pore structures in a shale gas reservoir: A case study of the longmaxi shale in Sichuan basin, China. *J. Nat. Gas. Sci. Eng.* 66, 207–216. doi:10.1016/j.jngse.2019.04.009

WangLiu, X. L., Wang, Y., Sheng, Y., Zheng, S., Wu, W., Luo, Z., et al. (2020). Comparison of the pore structures of lower silurian Longmaxi Formation shales with different lithofacies in the southern Sichuan Basin, China. *J. Nat. Gas. Sci. Eng.* 81, 103419. doi:10.1016/j.jngse.2020.103419

Xiang, J., Zhu, Y., Wang, Y., Chen, S., and Jiang, Z. (2022). Structural deformation and its pore-fracture system response of the Wufeng-Longmaxi shale in the Northeast Chongqing area, using FE-SEM, gas adsorption, and SAXS. *J. Pet. Sci. Eng.* 209, 109877. doi:10.1016/j.petrol.2021.109877

Xu, S., Hao, F., Shu, Z., Zhang, A., and Yang, F. (2020). Pore structures of different types of shales and shale gas exploration of the Ordovician Wufeng and Silurian Longmaxi successions in the eastern Sichuan Basin, South China. *J. Asian Earth Sci.* 193 (66), 104271. doi:10.1016/j.jseaes.2020.104271

Xu, X., Zeng, L., Tian, H., Ling, K., Che, S., Yu, X., et al. (2021). Controlling factors of lamellation fractures in marine shales: A case study of the fuling area in eastern Sichuan Basin, China. *J. Petroleum Sci. Eng.* 207, 109091. doi:10.1016/j.petrol.2021.109091

Yang, R., He, S., Yi, J., and Hu, Q. (2016). Nano-scale pore structure and fractal dimension of organic-rich Wufeng-Longmaxi shale from Jiaoshiba area, Sichuan Basin: Investigations using FE-SEM, gas adsorption and helium pycnometry. *Mar. Pet. Geol.* 70, 27–45. doi:10.1016/j.marpetgeo.2015.11.019

Yao, Y. B., Liu, D. M., Che, Y., Tang, D., Tang, S., and Huang, W. (2010). Petrophysical characterization of coals by low-field nuclear magnetic resonance (NMR). *Fuel* 89 (7), 1371–1380. doi:10.1016/j.fuel.2009.11.005

Yin, S., and Wu, Z. (2020). Geomechanical simulation of low-order fracture of tight sandstone. *Mar. Pet. Geol.* 100, 1–10. doi:10.1016/j.marpetgeo.2020.104359

Zeng, W., Zhang, J., Ding, W., Zhao, S., Zhang, Y., Liu, Z., et al. (2013). Fracture development in Paleozoic shale of Chongqing area (South China). Part one: Fracture characteristics and comparative analysis of main controlling factors. *J. ASIAN EARTH Sci.* 75, 251–266. doi:10.1016/j.jseaes.2013.07.014

Zhang, Q., Dong, Y., Liu, S., Elsworth, D., and Zhao, Y. (2017). Shale pore characterization using NMR Cryoporometry with octamethylcyclotetrasiloxane as the probe liquid. *Energy fuels.* 31 (7), 6951–6959. doi:10.1021/acs.energyfuels.7b00880

Zhang, X., Liu, C., Zhu, Y., Chen, S., Wang, Y., and Fu, C. (2015). The characterization of a marine shale gas reservoir in the lower Silurian Longmaxi Formation of the northeastern Yunnan Province, China. *J. Nat. Gas. Sci. Eng.* 27, 321–335. doi:10.1016/j.jngse.2015.08.070

Zhao, K. K., Jiang, P. F., Feng, Y. J., Sun, X. D., Cheng, L. X., and Zheng, J. W. (2021). Investigation of the characteristics of hydraulic fracture initiation by using maximum tangential stress criterion. *J. Min. Strata Control Eng.* 3 (2), 023520. doi:10.13532/j.jmsce.cn10-1638/td.20201217.001

Zhao, R., XueDong, H. Z., Lu, S., Li, J., Tian, S., wang, M., et al. (2022). Multi-scale pore structure characterization of lacustrine shale and its coupling relationship with material composition: An integrated study of multiple experiments. *Mar. Pet. Geol.* 140, 105648. doi:10.1016/j.marpetgeo.2022.105648

Zheng, H., Zhang, J., and Qi, Y. (2020). Geology and geomechanics of hydraulic fracturing in the Marcellus shale gas play and their potential applications to the Fuling shale gas development. *Energy Geosci.* 1 (1–2), 36–46. doi:10.1016/j.engeos.2020.05.002

frontiers | Frontiers in Earth Science

TYPE Original Research
PUBLISHED 20 September 2022
DOI 10.3389/feart.2022.1024748

OPEN ACCESS

EDITED BY
Shuai Yin,
Xi'an Shiyou University, China

REVIEWED BY
Zhonghu Wu,
Guizhou University, China
Jianhua He,
Chengdu University of Technology, China

*CORRESPONDENCE
Jiguang Tang,
tangjiguo115@126.com

SPECIALTY SECTION
This article was submitted to Structural Geology and Tectonics, a section of the journal Frontiers in Earth Science

RECEIVED 22 August 2022
ACCEPTED 05 September 2022
PUBLISHED 20 September 2022

CITATION
Zhang D, Tang J, Chen K, Wang K, Zhang P, He G and Tuo X (2022), Simulation of tectonic stress field and prediction of tectonic fracture distribution in Longmaxi Formation in Lintanchang area of eastern Sichuan Basin.
Front. Earth Sci. 10:1024748.
doi: 10.3389/feart.2022.1024748

Simulation of tectonic stress field and prediction of tectonic fracture distribution in Longmaxi Formation in Lintanchang area of eastern Sichuan Basin

Douzhong Zhang[1,2], Jiguang Tang[1]*, Kongquan Chen[2], Kaiming Wang[3], Peixian Zhang[3], Guisong He[3] and Xiusong Tuo[1,2]

[1]School of Geosciences, Yangtze University, Wuhan, China, [2]Cooperative Innovation Center of Unconventional Oil and Gas, Yangtze University, Wuhan, China, [3]Sinopec East China Oil & Gas Company, Nanjing, China

Shale is a low-porosity and low-permeability reservoir, and structural fractures are the main controlling factor for the migration and accumulation of shale gas. Moreover, tectonic fractures are controlled by the paleo-tectonic stress field. In this paper, taking the Longmaxi Formation of the Lintanchang area as an example, the finite element numerical simulation technology is used to analyze the distribution law of the paleo-tectonic stress field, and further, the fracture development areas under the superposition of two periods of tectonic stress are predicted using seismic, rock mechanics, and field data. The results show that the tectonic fractures developed in the Lintanchang area are mainly EW- and NNW-striking conjugate shear fractures formed in the Mid-Yanshanian period, followed by the NWW- and SWW-striking conjugate shear fractures formed in the late Yanshanian period. The distribution of tectonic fractures is affected by faults, folds, rock physical parameters and tectonic stresses. It is found that the comprehensive fracture coefficients of the anticline core and fault areas are both greater than 1.1, which are the areas with the most developed structural fractures, and these areas have poor shale gas preservation conditions. However, the comprehensive fracture coefficients of the western flanks of the anticline and the eastern and western dipping ends are between 1.0 and 1.1, which are areas with better shale gas preservation conditions. In addition, the development degree of tectonic fractures in the east and northwest areas of the Lintanchang anticline is lower than that in other areas. The comprehensive fracture coefficients of shale in these areas are between 0.9 and 1.0. The shale is in a state of "breaking without cracking", and shale gas can be well preserved.

KEYWORDS

Lintanchang area, finite element, numerical simulation, tectonic stress field, fracture prediction

1 Introduction

With the rapid development of global oil and gas exploration and development technologies, shale gas occupies an important position in the world and has attracted the attention of many countries (Jarvie et al., 2007; Pollastro, 2007; Ding et al., 2013; Melikoglu, 2014; Pireh et al., 2015). The Sichuan Basin is an important area for shale gas exploration and development in China. By 2021, the proven shale gas reserves exceeded 2×10^{12} m^3 (Zhang and Zhu, 2006; Guo and Zhang, 2014). The Lintanchang area is located in the eastern part of the Sichuan Basin and is a hot spot for shale gas exploration and development in the basin. The area is rich in shale gas reserves (Nie et al., 2021).

Low-porosity and low-permeability shale gas reservoirs have the characteristics of self-generation and self-storage of hydrocarbons, so structural fractures have become the main migration channels and important accumulation spaces of shale gas (Tingay et al., 2009; Lemonnier and Bourbiaux, 2010; Hennings et al., 2012; Yang et al., 2016). Predicting fracture-developed areas in shale reservoirs can significantly improve the exploration and development efficiency of shale gas (Montgomery et al., 2005; Bowker, 2007; Zeng et al., 2016). Structural fractures are an important fracture type in shale reservoirs, and the paleo-tectonic stress field controls the development of structural fractures. This is because fractures are mainly formed under the most intense period of tectonic stress activity. Intense tectonic activity causes the rock to undergo shear or conjugate shear ruptures along the direction of the maximum principal stress. The paleo-tectonic stress field controls the tectonic deformation, the development of faults and tectonic fractures. Numerical simulation based on the paleo-tectonic stress fields can effectively predict the development degree of tectonic fractures (Wei et al., 2019). Many scholars worldwide have carried out the prediction of structural fractures (Wclennan et al., 2009; Laubach et al., 2018; Milad et al., 2018; Liu C et al., 2019). These studies include logging analysis, imaging logging, seismic data inversion techniques, and numerical simulation of stress fields (Li, 2022; Li and Li., 2021; Qie et al., 2021; Ren et al., 2020; Wu et al., 2017; Xue et al., 2021; Zhao et al., 2021). Well logging analysis and imaging logging have high fracture prediction accuracy in a single well, but they cannot predict the planar distribution of fractures. Seismic data cannot effectively identify fractures affected by the resolution (Milad and Slatt, 2017). The numerical simulation of tectonic stress field is based on the theory of geomechanics and can be well applied to the evaluation of fracture development (Zeng et al., 2010; Liu D et al., 2019). The prediction of fractures via tectonic stress field simulation is based on geomechanical theory. The accumulation of tectonic stress causes rock deformation and ruptures. Based on the finite element method, the reservoir rock is divided into a series of finite elements, and the stress is transferred between the finite elements. When the stress exceeds the limit that the rock can bear, fractures will develop.

In this paper, taking the Longmaxi Formation shale in the Lintanchang area as an example, the finite element numerical simulation technology is used to analyze the distribution law of the paleo-tectonic stress fields, and further, the fracture development areas under the superposition of two periods of tectonic stress are predicted using seismic, rock mechanics, and field data. This study can provide a theoretical basis for the exploration and development of shale gas in the southern China.

2 Geological background

The Lintanchang area is located in the fold structural belt in the southeastern margin of the Sichuan Basin. It is located in the transition zone between the northern Guizhou Fold Belt and the southern margin of the Sichuan Basin. The east part of this area is the Mesozoic Jiangnan Xuefeng Thrust Belt, the south part is in contact with the Early Paleozoic mid-Guizhou Uplift, and the north part is connected with the “Sichuan Basin” of the third subsidence belt of the Neocathaysian Tectonic System (Li C et al., 2011) (Figure 1A). The main tectonic pattern in the Lintanchang area is controlled by the compressive tectonic stress field in the SE-NW direction caused by the intracontinental orogeny of the Xuefeng Uplift. Previous chronological studies on the Lintanchang and its surrounding areas show that (Li S et al., 2011; Deng et al., 2013), the Lintanchang area experienced the early Mid-Yanshanian (Jurassic) and late Mid-Yanshanian (Early Cretaceous), late Yanshanian (late Cretaceous), and Himalayan (Paleogene-Quaternary) tectonic movements. Among them, the tectonic stress in the Middle and Late Yanshanian is the strongest. This period is the formation period of the structures in the Lintanchang area (Wang et al., 2017; Fang et al., 2018). The spatial distribution of faults in the study area is mainly divided into NE and near-EW-trending fault systems (Figure 1B). In this study, the research object is the Silurian Longmaxi Formation shale. Clay siliceous shale is mainly developed in the Longmaxi Formation (Shi et al., 2019) (Figure 2). In addition, thrust structures are developed in the Longmaxi Formation (Figure 1C). Intense tectonic deformation resulted in the development of fractures in the Longmaxi Formation shale in the study area. The controlling factors of fracture development include environmental tectonic stress and a large number of brittle minerals inside the shale. The fracture density in the shale of the Longmaxi Formation is usually distributed in the range of 3–15/m.

3 Methods

3.1 Tectonic stress field simulation

There are many factors affecting the paleo-tectonic stress field, including the tectonic pattern, direction and magnitude of

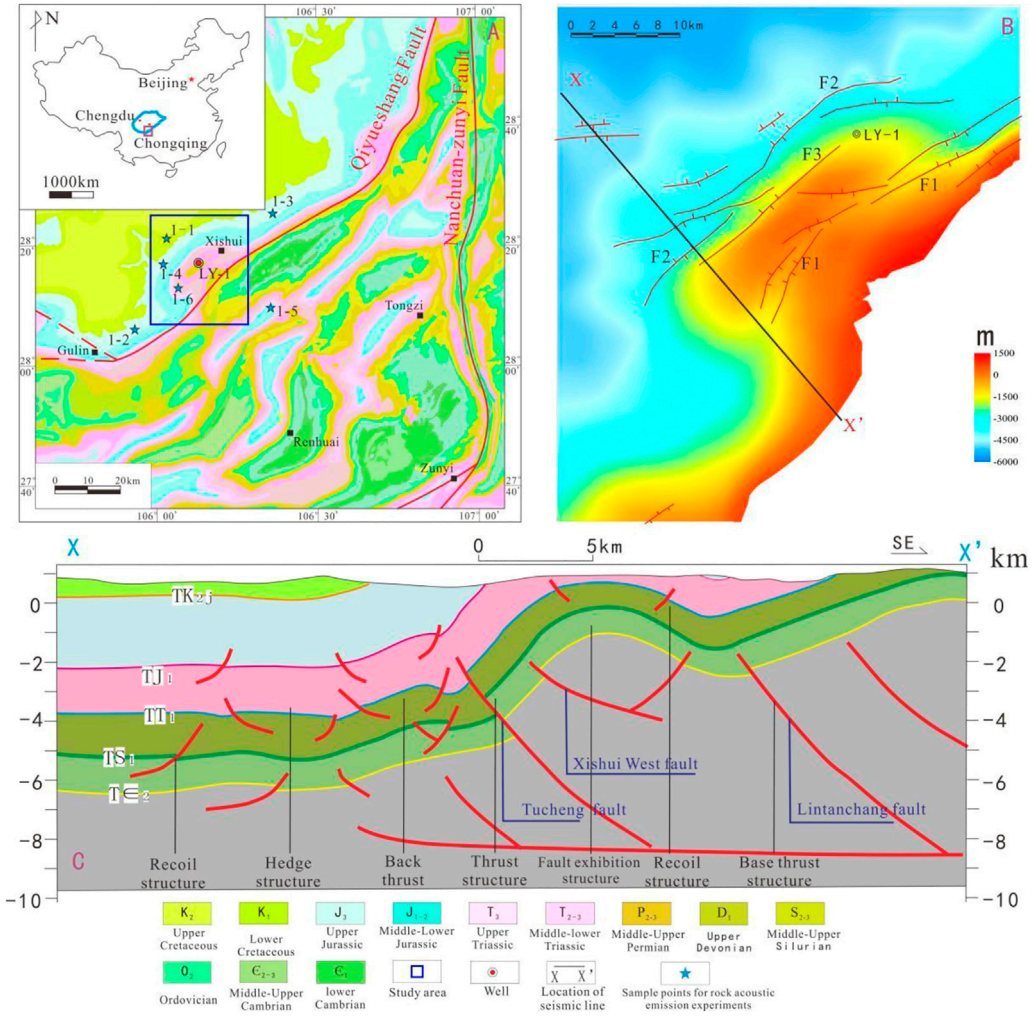

FIGURE 1
Regional structure of Lintanchang Area in eastern Sichuan Basin. Notes: **(A)** Geological map of Lintanchang area and adjacent areas in east Sichuan Basin (F1: Lintanchang Fault; F2: Tucheng Fault; F3: Xishuixi Fault); **(B)** Structure of the bottom surface of the Ordovician Wufeng Formation in the Lintanchang area; **(C)** Seismic interpretation profile of line X-X'.

tectonic stress, and rock mechanical properties (Timoshenko and Goodier, 1951; Laurent and Frantz, 2006; Wu et al., 2017). Generally, the stress in the core of an anticline structure is larger, and the stress in the rock with a high elastic modulus is larger. In this study, the ANSYS Software was used to carry out numerical simulation of tectonic stress fields in the target layer. The numerical simulation of tectonic stress field mainly includes: 1) geological model, 2) mechanical model, 3) mathematical model, and 4) fitting of numerical simulation results.

3.1.1 Geological model

Geological model is the basic model for numerical simulation of tectonic stress fields. From the analysis of paleo-tectonic stress, it can be concluded that the key tectonic deformation periods are the late Mid-Yanshanian and late Yanshanian periods (Deng et al., 2013; Ju et al., 2019; Li, 2022). The Himalayan tectonic activity had little effect on the tectonic pattern and the development of tectonic fractures in the study area (Figures 3A,B).

3.1.2 Mechanical model

On the basis of the geological model, the geological unit is assigned with rock mechanical parameters (elastic modulus, Poisson's ratio) and the mechanical model is obtained (Eissa and Kazi., 1988; Kuhlman, 1993). Based on the triaxial rock mechanics experiment, the dynamic and static parameter conversion formulas of the target layer are obtained (Formulas 1 and 2):

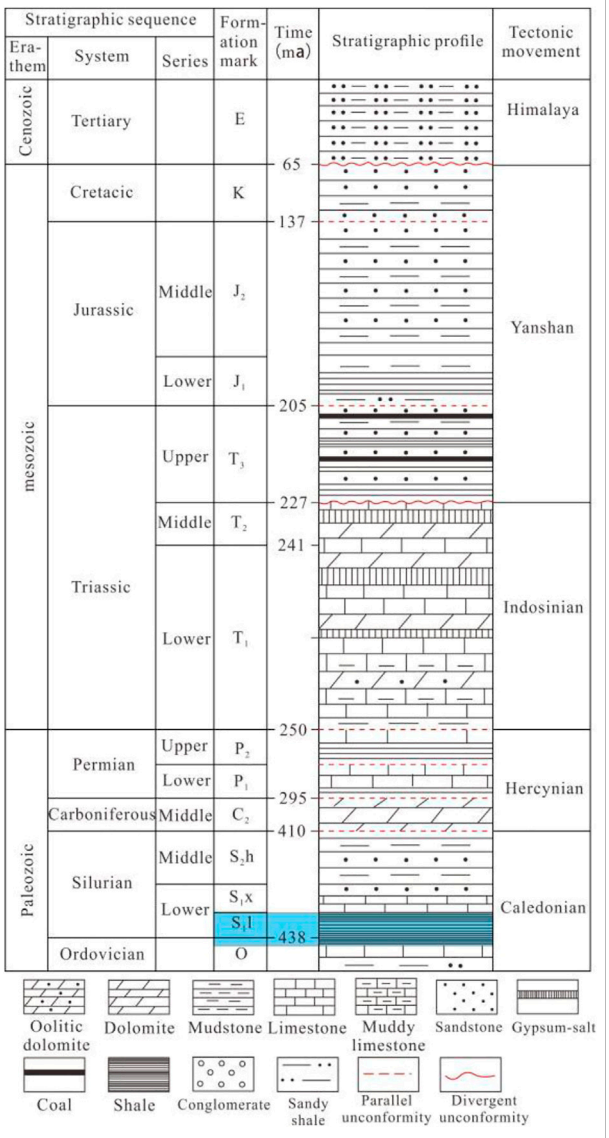

FIGURE 2
Stratigraphic systems and tectonic activities in the study area.

$$E_s = 0.2928E_d + 17.82 \quad (1)$$

$$\mu_s = 3.968\mu_d - 0.7551 \quad (2)$$

In the formula, E_S is the static Young's modulus (GPa); E_d is the dynamic Young's modulus (GPa); μ_S is the static Poisson's ratio; μ_d is the dynamic Poisson's ratio.

Due to the large differences in the distribution of static Young's modulus and Poisson's ratio in the region, different mechanical units are divided according to the distribution trend of rock mechanical parameters. Meanwhile, the average Young's modulus and equivalent Poisson's ratio of rocks in different regions are calculated (Table 1). The rock mechanical parameters of the fault are generally selected as 50–70% of the Young's modulus of the surrounding rock; while the Poisson's ratio of the fault zone is 0.02–0.1 larger than that of the normal depositional area (Fischer and Henk, 2013; Jiu et al., 2013).

3.1.3 Mathematical model

The established model is meshed by ANSYS Software, and the mesh type is mainly tetrahedral element type with 10 nodes. The Mid-Yanshanian model has a total of 31,288 nodes and 15,593 elements, and the Late Yanshanian model has a total of 45,195 nodes and 22,548 elements. After many simulations and inversions, in the mid-Yanshanian model, the maximum principal stress is applied from the 130° direction at 165 Ma, and the minimum principal stress is applied from the 220° direction at 120 MPa. In the late Yanshanian period, the maximum principal stress was applied from the 185° direction at 100 Ma, and the minimum principal stress was applied from the 95° direction at 70 MPa. The obtained simulation results are in good agreement with the actual results (Figures 3C,D).

When subjected to stress, any nodes in the model will be displaced, and its displacement in the three directions of x, y, and z can be expressed as u, v, w, and their matrix forms are as follows:

$$\begin{cases} u(x, y, z) = a_1x + b_1y + c_1z + d_1 \\ v(x, y, z) = a_2x + b_2y + c_2z + d_2 \\ u(x, y, 2) = a_3x + b_3y + c_3z + d_3 \end{cases} \quad (3)$$

In the formula, a_1, a_2, a_3, b_1, b_2, b_3, c_1, c_2, c_3, d_1, d_2, d_3 are matrix coefficients.

Based on the elastic equation, the relationship between the displacement and deformation of the elements is as follows:

$$\begin{cases} \varepsilon_x = \frac{\delta_u}{\delta_x}, \gamma_{xy} = \gamma_{yx} = \frac{\delta_v}{\delta_x} + \frac{\delta_u}{\delta_y} \\ \varepsilon_y = \frac{\delta_v}{\delta_y}, \gamma_{yz} = \gamma_{zy} = \frac{\delta_v}{\delta_z} + \frac{\delta_w}{\delta_y} \\ \varepsilon_z = \frac{\delta_w}{\delta_z}, \gamma_{zx} = \gamma_{xz} = \frac{\delta_w}{\delta_x} + \frac{\delta_u}{\delta_z} \end{cases} \quad (4)$$

In the formula, ε_x, ε_y, ε_z are the linear strain components; γ_{xy}, γ_{xz}, γ_{yz} are the shear strain components in the model deformation.

The relationship between strain and node displacement matrix can be simplified as follows:

$$\varepsilon = B\delta \quad (5)$$

In the formula, B is the geometric matrix; δ is the node displacement matrix.

Based on the elastic mechanics properties, the relationship between stress and strain is as follows:

$$\begin{cases} \varepsilon_x = \frac{1}{E}\left[\delta_x - \mu(\delta_y + \delta_z)\right], \gamma_{xy} = \gamma_{yx} = \frac{\tau_{xy}}{G} \\ \varepsilon_y = \frac{1}{E}\left[\delta_y - \mu(\delta_x + \delta_z)\right], \gamma_{yz} = \gamma_{zy} = \frac{\tau_{yz}}{G} \\ \varepsilon_z = \frac{1}{E}\left[\delta_z - \mu(\delta_x + \delta_y)\right], \gamma_{zx} = \gamma_{xz} = \frac{\tau_{zx}}{G} \end{cases} \quad (6)$$

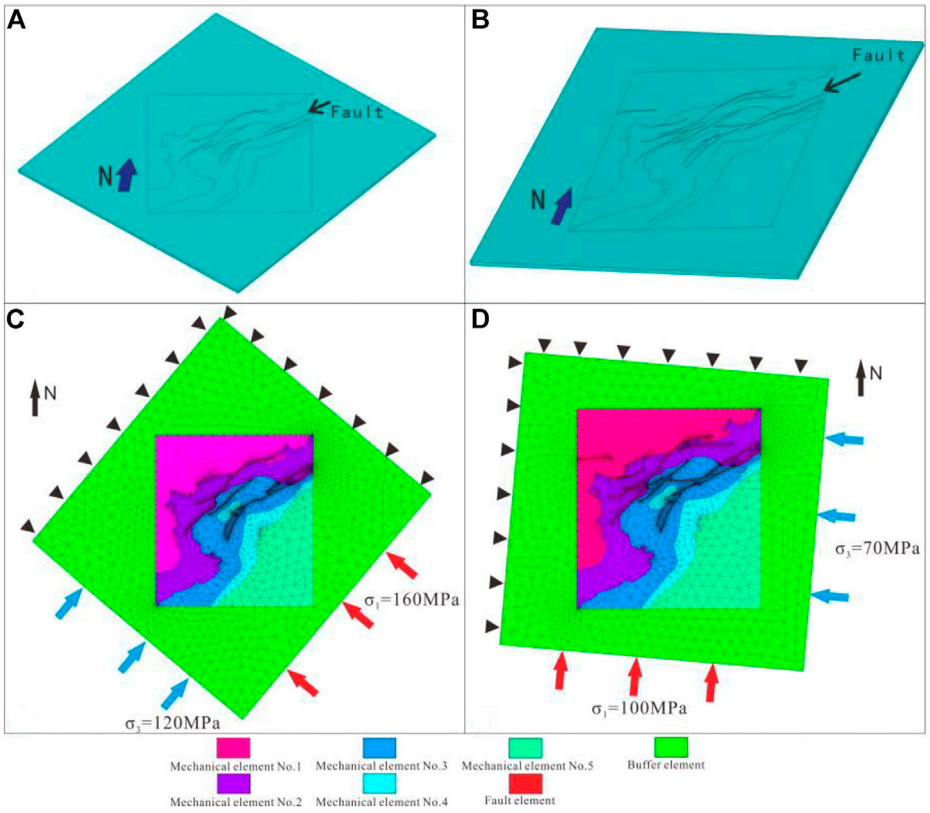

FIGURE 3
Finite element model of the target layer. **(A)** Middle Yanshanian geological model; **(B)** Late Yanshanian geological model; **(C)** Grid model and loading conditions in Middle Yanshanian; **(D)** Grid model and loading conditions in late Yanshanian.

In the formula, δ_x, δ_y, δ_z are normal stress components; τ_{xy}, τ_{yz}, τ_{xz} are shear stress components; E is elastic modulus; μ is Poisson's ratio; G is shear modulus.

The simplified formula is as follows:

$$[\delta] = [D][\varepsilon] \quad (7)$$

[D] is the elastic matrix.

3.2 Prediction of tectonic fractures

The shale of the Silurian Longmaxi Formation in the Lintanchang area has high content of brittle minerals such as quartz and feldspar, and is easy to form structural fractures (Shi et al., 2019). Structural fractures formed under tensile stresses can be predicted by the Griffith fracture criterion, and shear fractures formed by compressive stress can be predicted by the Mohr-Coulomb fracture criterion (Rybacki et al., 2016).

3.2.1 Fracture prediction method

3.2.1.1 Griffith rupture criterion

The Griffith fracture criterion is a tensile fracture criterion for brittle objects (Griffith, 1921). Griffith believes that there are many fine fractures inside the material. When subjected to external tensile stress, the damage of the material generally starts from the end of the seam and gradually extends until

TABLE 1 Rock mechanical properties of shale in Lintanchang area of eastern Sichuan Basin.

Rock mechanics parameters	Mechanics units					Fault zone	Buffer zone
	Unit 1	Unit 2	Unit 3	Unit 4	Unit 5		
Elastic modulus (GPa)	57.38	45.79	27.16	20.80	14.30	17	42
Poisson's ratio	0.329	0.27	0.19	0.15	0.12	0.34	0.22

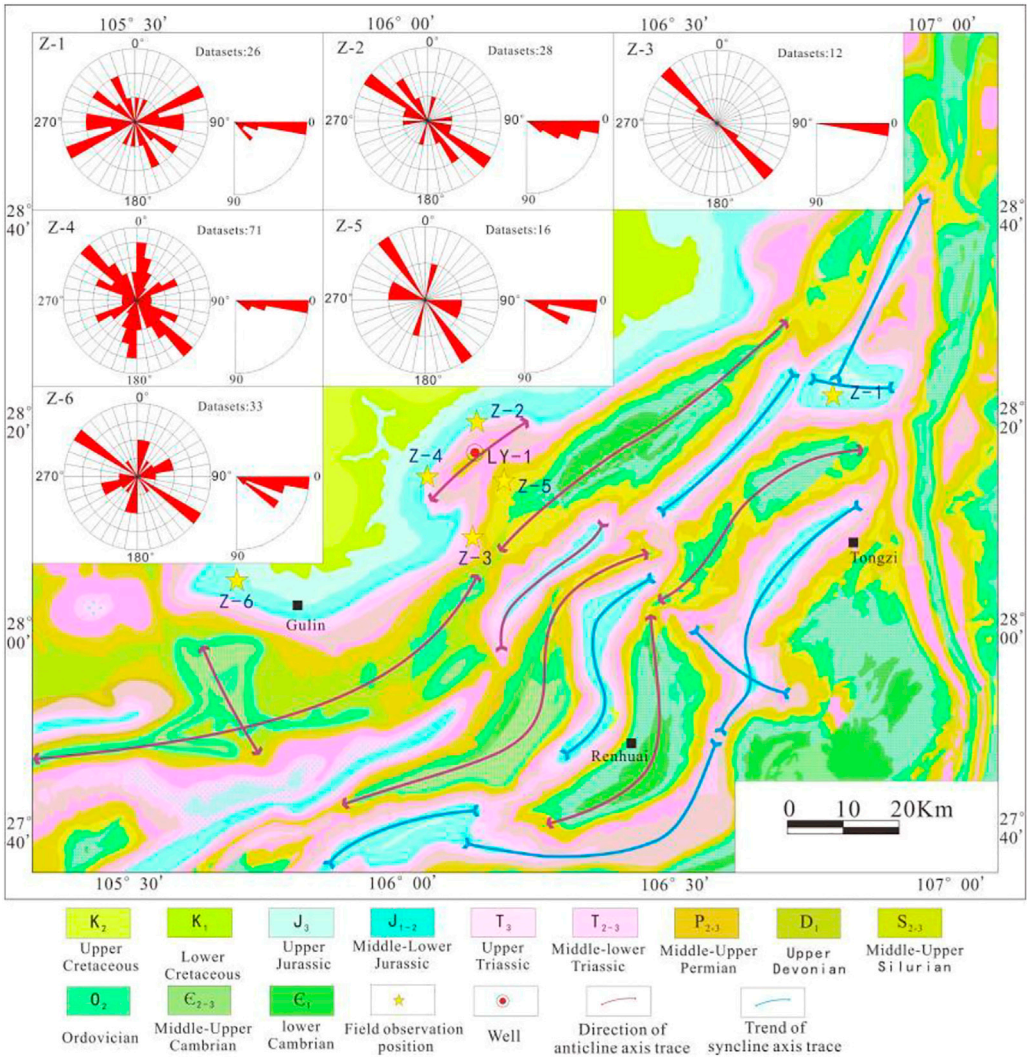

FIGURE 4
Direction of maximum principal stress (σ_1) restored by fault scratches and joints in Lintanchang area.

the material ruptures. The Griffith rupture criterion formula is as follows:

When $\sigma_1+3\sigma_3\geq 0$, the formula is:

$$(\sigma_1-\sigma_2)^2+(\sigma_2-\sigma_3)^2+(\sigma_1-\sigma_3)^2+24(\sigma_1+\sigma_2+\sigma_3)\sigma_T=0 \quad (8)$$

When $\sigma_1+3\sigma_3\leq 0$, the formula is:

$$\sigma_3+\sigma_T=0 \quad (9)$$

where σ_1, σ_2 and σ_3 are the maximum, intermediate and minimum principal stresses, respectively, and σ_T is the tensile stress.

3.2.1.2 Mohr-Coulomb rupture criterion

The basis of the Moore-Coulomb criterion theory is that the fracture of rock is mainly shear failure on a certain surface, and this shear failure is related to the relative state of the normal stress σ_n and shear stress τ_n on the surface (Dai and Meng, 1999). The formula is as follows:

$$|\tau|=C+\sigma_n \tan\varphi \quad (10)$$

$|\tau|$ is the shear strength on the shear plane, C is the cohesion force, φ is the rock internal friction angle, and σ_n is the normal stress on the shear plane.

3.2.2 Development mechanism of multi-stage tectonic fractures

In order to quantitatively predict the development degree of shear fractures in the reservoir, the shear fracture coefficient S is introduced, and the expression is:

$$S=\tau_n/\tau \quad (11)$$

S is the shear rupture coefficient of shear stress, MPa; τ_n is the shear strength of the rock, MPa.

In order to express the shear rupture coefficient S more clearly, the conversion formula is:

$$S = (\sigma 1 - \sigma 3)/[(\sigma 1 + \sigma 3)\sin\varphi + 2C\cos\varphi] \quad (12)$$

When $S>1$, the rock will form shear fracture.

The expression for tensile rupture rate is:

$$T = \sigma_T/\sigma_t \quad (13)$$

Where T is the tensile fracture rate, σ_T is the effective tensile stress, and σ_t is the rock tensile strength.

When $T>1$, the rock will form tensile fracture.

According to the field-measured structural fractures and the observation statistics of core fractures in Well LY-1, 90% are mainly shear fractures and 10% are extensional fractures in the Lintanchang area. The fracture coefficient I is used as the criterion for judging the degree of fracture development (Wu et al., 2017), and the formula is as follows:

$$K = aS + bT \quad (14)$$

In the formula, a is the proportion of shear fractures, and b is the proportion of tensile fractures.

According to the principle of rock mechanics, when $K<1$, no obvious fractures will be formed inside the rock; when $K=1$, fine fractures will gradually appear inside the rock; when $K>1$, the fine fractures inside the rock will expand accordingly, and connected to each other, forming large fractures.

From the tectonic deformation and tectonic evolution, it can be seen that the tectonic activity in the study area was the strongest in the Mid-Yanshanian period, followed by the late Yanshanian period. Therefore, the fracture development probability-shear rupture coefficient (S) in the Lintanchang area is mainly related to the tectonic activities of the Middle and the Late Yanshanian. The superposition method is used to obtain the comprehensive rupture coefficient, that is, the rupture coefficients of the two periods are superimposed, and the maximum value of them is taken as the evaluation parameter of the comprehensive rupture coefficient.

4 Results

4.1 Paleo-tectonic stress direction

According to the contact conditions of strata in the Lintanchang area, the characteristics of multi-phase joint structures and the results of analysis and testing experiments, the evolution process of the paleo-faults in the study area was restored. The paleo-tectonic stress field controls the structural shape of the strata, so the direction of paleo-tectonic stress can generally be restored by fault strike, fold strike, joint, and lamella (Ju et al., 2017). The north-south (nearly north-west) and east-west structures are in a composite relationship. Folds in both directions form distinct “ten”, “S" and “T" shapes across the superimposed folds, and north-south faults cut east-west folds. The NW-trending structure is restricted to the north by the E-W-trending anticline, indicating that the N-S-trending tectonic system in the area was formed a little later than the E-W-trending tectonic system (Figure 4). The phenomenon of joint cutting was observed in the field observation Z-4 point. The SW-trending conjugate shear joints cut the SEE-trending conjugate shear joints, proving that the formation of the north-south structure was later than that of the nearly east-west structure (Figure 5). The maximum principal stress (σ_1) direction of the recovery of conjugate shear joints is counted. It can be seen that the number of joints formed in the σ_1 direction is the largest in the direction of 120°–140°, followed by the joints in the direction of 350°–20°, and the ratio of thm is 13:7.

Through field geological survey of Lintanchang and surrounding areas, 186 groups of conjugate shear joint occurrence and fault scratch occurrence data were measured. After the formation was leveled layer by layer, the direction of maximum principal stress was plotted and a rosette diagram was drawn (Figure 4). According to statistics, since the Mesozoic in the study area, the two main tectonic stress directions are as follows:

(1) SEE-NW compressive stress field of the first stage: It is the NW compressive stress produced by intracontinental orogeny, and the maximum principal stress direction (σ_1) is about 120°–140°.
(2) The near-north-south compressive stress field of the second stage: The continuous NW-trending pushing of Xuefeng Mountain resulted in a strong left-lateral strike-slip movement of the Ziyun-Luodian Fault. The central area of Guizhou was strongly wedged into the Daloushan area, forming an arc-shaped outward extrusion. Furthermore, it forms a nearly north-south compressive stress in the study area, and the maximum principal stress direction (σ_1) is about 350°–20°.

4.2 Magnitude and period of paleo-tectonic stress

When the rock is under stress, a micro-fracture system that is adapted to the magnitude and direction of the force will be generated in its internal structure. In tectonic mechanics, such microscopic fractures are called Griffith fractures. When the rock mass is subjected to stress equal to or greater than the previous stress, the Kaiser points of rock acoustic emission counts will appear (Lshida, 2001; Zeng and Liu., 2010). Acoustic emission experiments can reflect the previous stress state, and then paleo-tectonic stress data are obtained (Guo et al., 2016; Ju and Sun, 2016). Seven samples were collected from strata in different

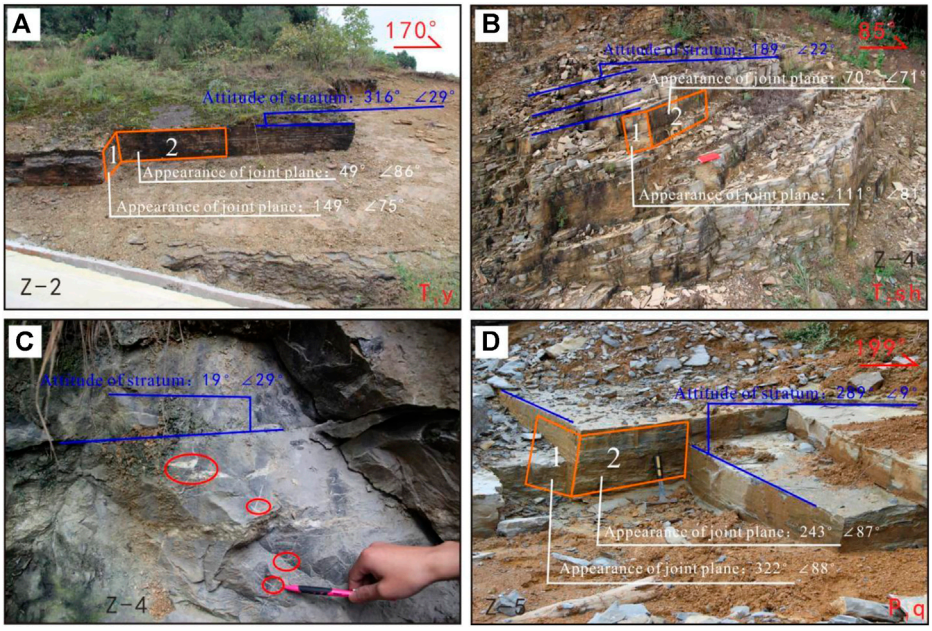

FIGURE 5
Photos of shale outcrops in Lintanchang area. **(A)** Observation point Z-2; **(B)** observation point Z-4; **(C)** observation point Z-4; **(D)** observation point Z-5.

periods in the study area. The test results show that the Triassic samples (T_1m, T_1y) have mainly experienced five periods of tectonic stresses since the Mesozoic (Triassic) (Figure 6). However, the Jurassic samples (J_2sn, J_3p) recorded three periods of tectonic movements in the late Mid-Yanshanian and later periods (Figure 6). The Cretaceous sample (K_2j^1) formed in the Late Yanshanianhave mainly experienced two periods of tectonic stresses (Late Yanshanian and Himalayas) (Figure 6). The test equipment is a TAW-1000 hydraulic servo experimental system and an AE acoustic emission detector. Three standard 25 mm × 50 mm cylindrical samples were taken in each of the X, Y and XY45° directions of the sample, and the experimental confining pressure was 30 MPa. The setting of confining pressure is determined according to the ancient burial depth and overpressure. The difference between the stress caused by the ancient burial depth and the overpressure is 30 MPa.

Combined with the apatite fission track experiments (Figure 7) (Deng et al., 2013) and the results of the acoustic emission experiments in this study, the tectonic activity stages were analyzed. It can be seen that the late Mid-Yanshanian and the late Yanshanian periods are the main tectonic transformation periods in the Lintanchang area. The maximum principal stress range at the end of the Mid-Yanshanian period is 156.15–170.65 MPa, and the minimum principal stress range is 119.68–158.93 MPa; the maximum principal stress range in the late Yanshanian period was 127.26–164.39 MPa, and the minimum principal stress range was 95.21–157.64 MPa (Table 2).

4.3 Paleo-fault evolution

From the analysis of the paleo-tectonic stress field in the area, it can be seen that in the early period of the Mid-Yanshanian, the study area was affected by the Xuefeng Orogenic Movement, and the SE-NW compressive stress field began to form in the area, and the stress was relatively small in this period. With the increase of the influence of Xuefeng Orogeny, the stress value of the study area also gradually increased. At the end of the Mid-Yanshanian period, the stress reached the maximum value, forming the main tectonic pattern along the northeast direction of the study area. In the late Yanshanian period, the stress environment in the study area changed to S-N extrusion, and nearly EW-trending folds and faults were formed in the area. During the Himalayan period, the strata in the area were uplifted as a whole, and the tectonic pattern did not change (Figure 8).

4.4 Paleostress prediction results

Compared with the experimental data of rock acoustic emission in the study, the deviation rates of the maximum principal stress and the minimum principal stress of the two-

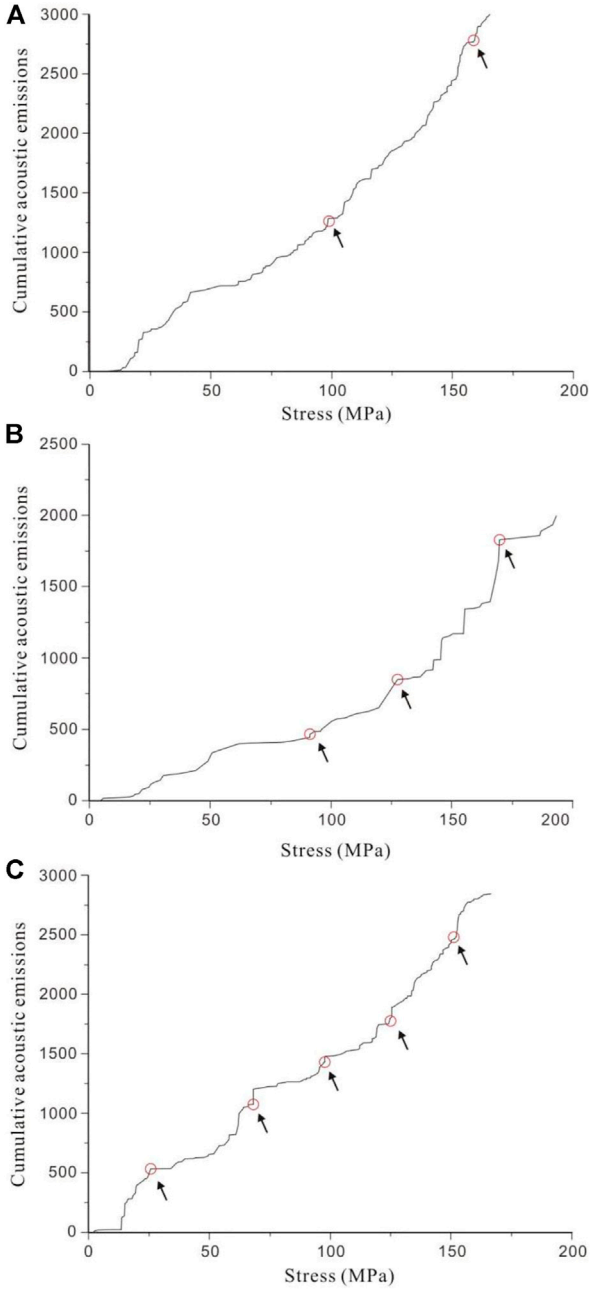

FIGURE 6
Acoustic emission experimental curves of shale samples (The sampling location is shown in Figure 1; **(A)**: Sample No. 1-1, Cretaceous sample; **(B)**: Sample No. 1-4, Jurassic sample; **(C)**: Sample No. 1-6, Triassic sample).

phase simulation results from the measured values are mostly below 10%. The maximum deviation value is 13.73 MPa. The deviation rate of differential stress is basically below 10%, and the maximum deviation value is 5.13 MPa, which is within a reasonable deviation range (Table 3). According to comprehensive analysis (An et al., 1998; Shan et al., 2004; Meng et al., 2009), the numerical simulation results conform to the actual geological laws.

5 Discussion

5.1 Stress field distribution law

5.1.1 Distribution of tectonic stress in Mid-Yanshanian period

The simulation results of the maximum horizontal principal stress (Figure 9A) show that the maximum principal stress of the Longmaxi Formation shale in the Lintanchang area of the Mid-Yanshanian period is concentrated at 94.09–236.23 MPa. A high value area of maximum principal compressive stress surrounding the anticline is formed in the north, south and west directions. The internal stress of the anticline core is relatively low, followed by the vicinity of the fault zone. The stress is distributed along the southwest-northeast trend of the fault zone with low values. The maximum horizontal principal stress is the lowest in the Lintanchang Anticline core, and its magnitude is 94.09–110 MPa. At the same time, the stress in the basin gradually increases along the dip of the wing, and the stress gradient has a significant correlation with the formation dip. Affected by the NE-trending fault, the maximum principal stress of the fault zone is lower than that of the surrounding strata. The distribution of this low-value zone is obviously banded along the fault strike, and the maximum principal stress of the foot wall is higher than that of the upper wall. In addition, the greater the fault strength, the greater the maximum principal stress gradient. At the end and turning point of the fault, the stress field is enriched to form a stress high value area.

During the Mid-Yanshanian period, the minimum principal stress of the Longmaxi Formation shale in the Lintanchang area was concentrated in the range of 45.91–126.44 MPa (Figure 9B). Similar to the influencing factors of the maximum horizontal principal stress distribution, the minimum horizontal principal stress distribution is also mainly controlled by the fault and depth. A high value area of minimum principal compressive stress surrounding the anticline is formed in the north, south and west directions. The core of the anticline and the vicinity of the fault zone are lower, and at the end of the fault and the turning point, the stress field is enriched to form a high stress area. Compared with the distribution of the maximum horizontal principal stress, the areas with high minimum horizontal principal stress in the Lintanchang area are in Longjunmiao-Yuanhou, Shabachang and Longjing areas, with the stress values ranging from 110 to 126.44 MPa.

5.1.2 Distribution of tectonic stress in Late Yanshanian period

In the Late Yanshanian period, the maximum principal stress of the target layer was concentrated at 82.37–167.93 MPa (Figure 10A). A high value area of maximum principal compressive stress is formed around the anticline in the south

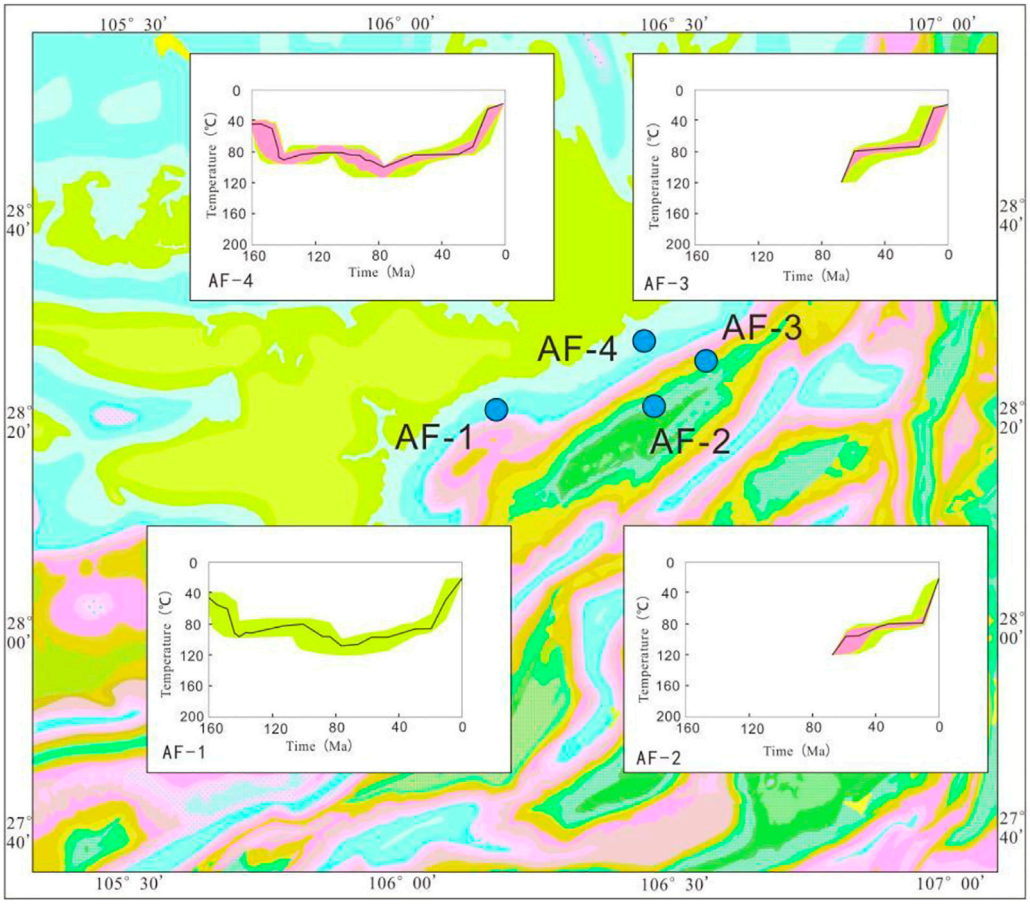

FIGURE 7
Thermal history simulation of apatite fission tracks in Lintanchang area (according to Deng et al., 2013).

TABLE 2 Test results of rock acoustic emission experiments in Lintanchang area of East Sichuan Basin.

Number	Formation	Effective stress	Early Yanshanian	Early middle Yanshanian	Late middle Yanshanian	Late Yanshanian	Himalayan
1–1	K_2j^1	σ_H (MPa)	—	—	—	164.39	94.8
		σ_h (MPa)	—	—	—	157.64	66.2
1–2	J_3p	σ_H (MPa)	—	—	164.06	136.96	102.41
		σ_h (MPa)	—	—	138.68	103.36	61.53
1–3	J_3p	σ_H (MPa)	—	—	159.17	127.26	102.55
		σ_h (MPa)	—	—	142.06	101.59	69.05
1–4	J_3p^1	σ_H (MPa)	—	—	170.48	145.07	82.67
		σ_h (MPa)	—	—	122.1	97.59	73.38
1–5	J_2sn	σ_H (MPa)	—	—	170.65	148.08	121.32
		σ_h (MPa)	—	—	158.93	133.39	103.56
1–6	T_1m	σ_H (MPa)	27.68	78.47	156.15	131.58	105.39
		σ_h (MPa)	17.10	54.36	131.62	105.21	86.18
1–7	T_1y	σ_H (MPa)	38.08	99.33	168.61	148.98	127.84
		σ_h (MPa)	13.96	39.08	119.68	103.88	57.85

Where σ_H is the maximum horizontal principal stress, σ_h is the minimum horizontal principal stress.

10.3389/feart.2022.1024748

TABLE 3 Comparison of tested and simulated results of paleo-tectonic stress field.

Peroid	Number	Maximum principal stress			Minimum principal stress			Differential stress		
		Measured (MPa)	Simulated (MPa)	Error (%)	Measured (MPa)	Simulated (MPa)	Error (%)	Measured (MPa)	Simulated (MPa)	Error (%)
Middle Yanshanian	1–4	170.48	172.72	1.31	122.1	119.21	−2.37	48.38	53.51	10.6
	1–6	156.15	143.73	−7.95	131.62	117.89	−10.43	24.53	25.84	5.34
Late Yanshanian	1–4	145.07	139.06	−4.14	97.59	89.9	−7.88	47.48	49.16	3.54
	1–6	131.58	129.1	−1.88	105.21	100.34	−4.63	26.37	28.76	9.06

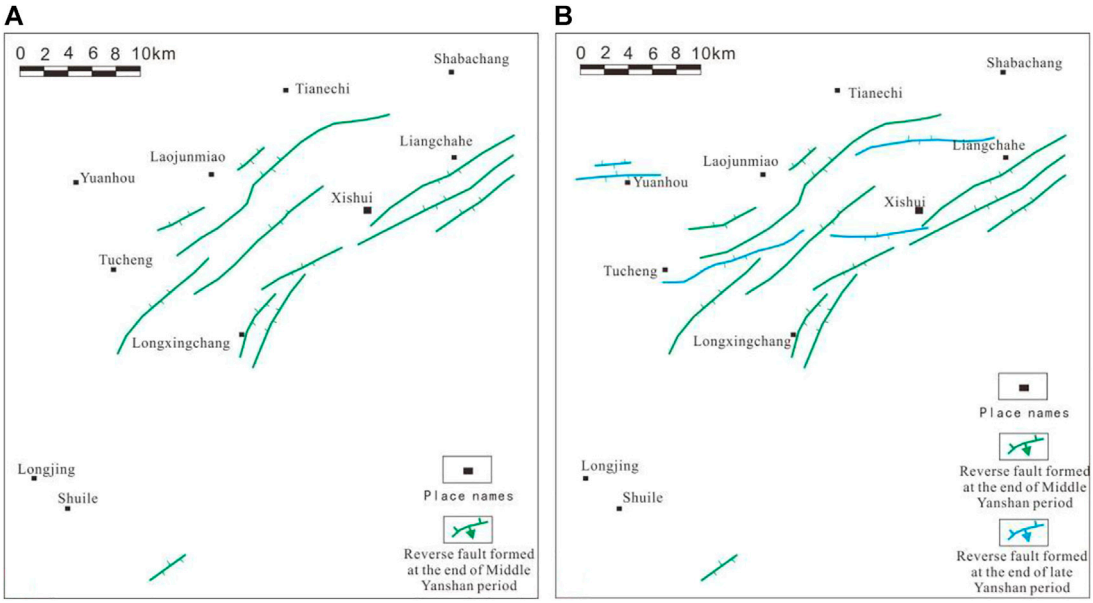

FIGURE 8
Evolution of paleo-faults in Lintanchang area ((**A**): end of Middle Yanshanian, **(B)** end of late Yanshanian).

and west directions. The maximum horizontal principal stress is the lowest at the core of the Lintanchang Anticline, and its magnitude is 82.37–95 MPa. The maximum horizontal principal stress is the highest in the footwall of Xiaoba-Longjing and Tucheng Faults, and its distribution ranges from 150 to 167.93 MPa. In addition, the stress value in the area south of Yongle area is also high, which is distributed in a near-east-west direction. Affected by the preexisting NE trending faults and the EW trending faults formed in this period, the fault zones with different strikes and their nearby areas with high and low stress values are also different. The distribution of the stress field is obviously affected by the fault structures, and the stress of the foot wall is higher than that of the upper wall.

The minimum principal stress of the Longmaxi Formation shale in the Lintanchang area of the late Yanshanian period is concentrated in the range of 54.34–128.63 MPa (Figure 10B). The distribution of stresses is also controlled by faults and depth. The areas with high minimum principal compressive stress are located in the north and southwest of the anticline, and are lower near the core of the anticline and the fault zone. Compared with the distribution of the maximum horizontal principal stress, the high value area of the minimum horizontal principal stress in the Lintanchang area is located in the Shabachang area, which is distributed in a cluster shape, and its stress value is 110–128.63 MPa.

5.2 Structural fracture distribution

5.2.1 Structural fracture direction

The paleo-tectonic stress field controls the development of tectonic fractures, and the direction of tectonic stress

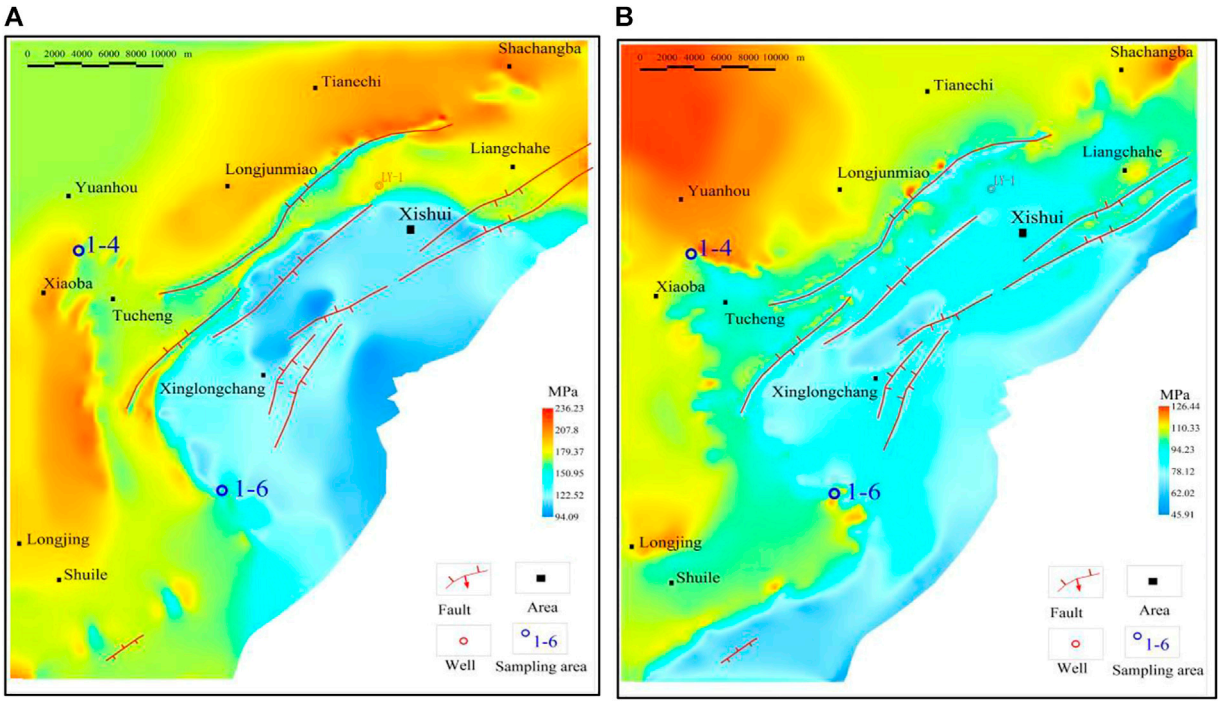

FIGURE 9
Numerical simulation results of paleo-tectonic stress field in Lintanchang area during the Middle Yanshanian period ((**A**): maximum principal stress; **(B)** minimum principal stress).

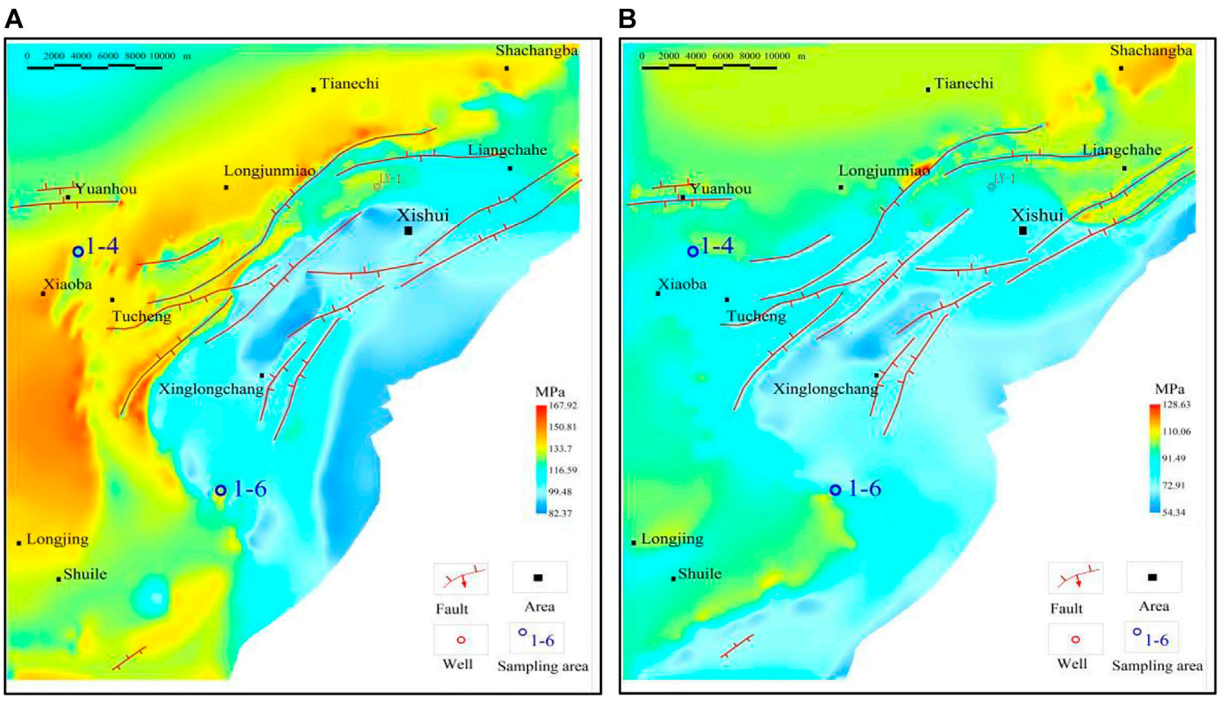

FIGURE 10
Numerical simulation results of the paleo-tectonic stress field in the Lintanchang area during the late Yanshanian period (**(A)**: maximum principal stress; **(B)** minimum principal stress).

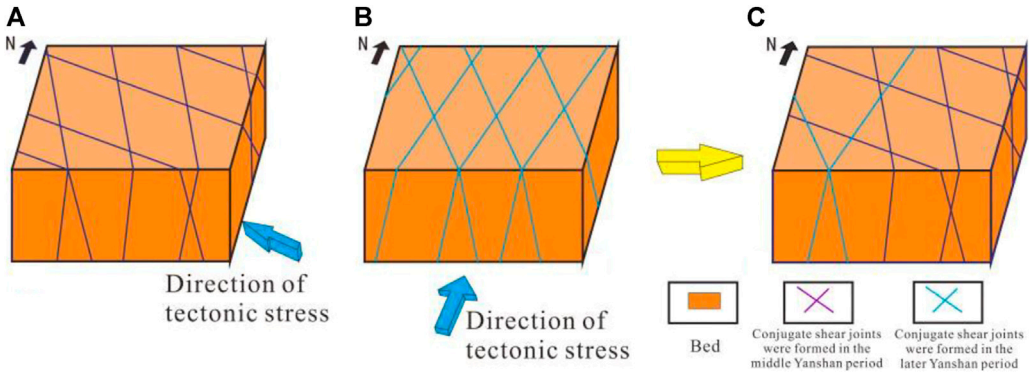

FIGURE 11
Developmental mode of conjugate shear fractures in Lintanchang Area. ((**A**): Striking of conjugate shear fractures formed in the Mid-Yanshanian period; **(B)** Striking of conjugate shear fractures formed in the Late Yanshanian period; **(C)** Distribution of conjugate shear fractures).

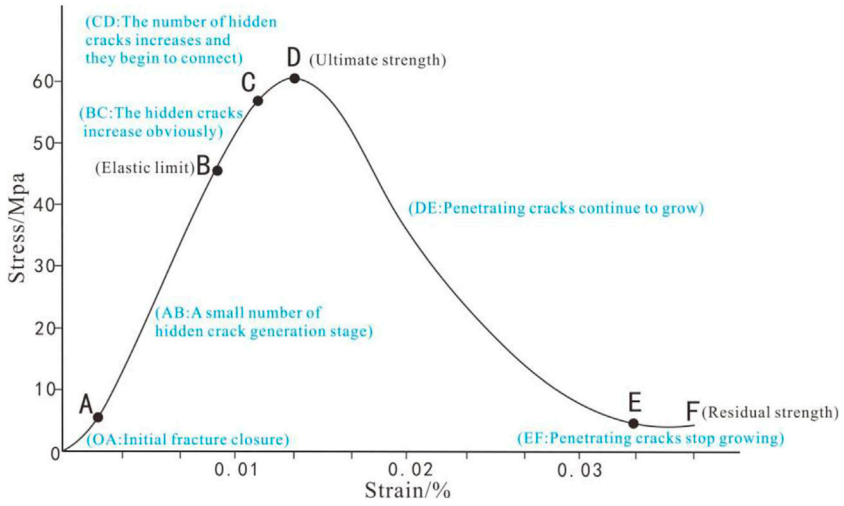

FIGURE 12
Relationship between stress and strain of shale sample.

determines the development direction of tectonic fractures (Zeng et al., 2007). The development of tectonic fractures in the Lintanchang area is mainly controlled by the tectonic stress in the middle and late Yanshanian period, among which the fractures formed in the Mid-Yanshanian period are the main ones, followed by the late Yanshanian period. The direction of tectonic stress in the Mid-Yanshanian period is SE130°, and the direction of tectonic stress in the Late Yanshanian period is NNE5°. Therefore, the direction of structural fractures in the area is dominated by two sets of conjugate shear fractures of SSE and SEE strikings, followed by two sets of conjugate shear fractures of SSW and SEE strikings (Figure 11).

5.2.2 Prediction of tectonic fracture distribution

In the process of rock fracture, it is transformed from elastic to plastic deformation, and then rock fracture occurs. However, according to rock mechanics experiments, when the stress value of the rock reaches a certain level, small-scale hidden fractures will first appear in the rock. With the gradual increase of stress, the density of hidden fractures in the rock gradually increases, and gradually connects to form larger-scale fractures. When the rock fracture limit is reached, fractures appear in the rock. Therefore, the degree of fracture development in the rock gradually increases with the increase of pressure (Figure 12).

TABLE 4 Evaluation results of structural fracture development areas in shale reservoirs in Lintanchang Area.

Shear rupture coefficient S	<0.9	0.9–1.0	1.0–1.1	>1.1
Fracture development	Not developed	Hidden fracture	Relatively developed	Highly developed
Grade	IV	I	II	III

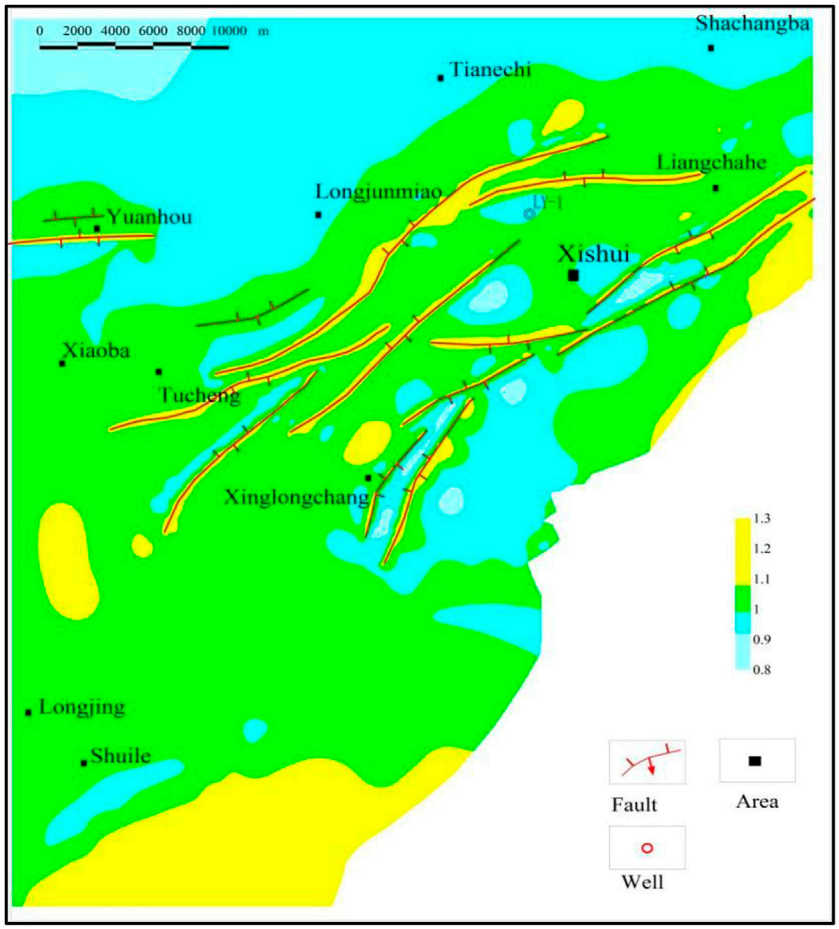

FIGURE 13
Prediction results of fracture development area in Lintanchang area.

For shale reservoirs, high fracture density is not conducive to the storage of shale gas. The high fracture density here refers to fractures near large-scale faults or open faults. Fractures are extremely developed in these areas, with a density of tens of fractures per meter. Extremely developed fractures and open faults caused the escape of natural gas. In this paper, based on petrophysical experiments and core observation data (Woodward, 1992; Wu et al., 2020), the development grades and fracture coefficient ranges of dominant fractures in shale reservoirs have been re-divided. The shear rupture coefficient *S* and the development of fractures are shown in Table 4.

The areas with the most developed structural fractures are located in the areas where the structural shear stress value is extremely large or small. The shear rupture coefficient *S* is larger in these regions. The greater the value of tectonic shear stress, the greater the degree of rock deformation. Moreover, the larger the shear rupture coefficient *S*, the more developed the structural fractures. In the fault distribution area, tectonic activity destroys the integrity of the rock formation. Then, the tectonic stress is partially released, and the tectonic shear stress value is very small. However, since there are many small (or associated) faults and joints in these areas, structural fractures are also relatively developed in these areas.

The prediction results of the fracture development degree in the east and west flanks of the Lintanchang Anticline are consistent with those observed in the field (Figure 13). The prediction results show that the comprehensive fracture rupture coefficient (*K*) in the area is between 0.8 and 1.3, and the distribution trend is greatly affected by the fault and structural position. The Grade I fracture development area is mainly distributed in the northwest of the area (the area of Shabachang-Swanchi-Longjunmiao) and the east flank of the Lintanchang Anticline. The grade II fracture development area is the most widely distributed, and it is mainly distributed in the west flank of the Lintanchang Anticline and the southern and northern dipping sections. The development areas of Grade III fractures are mainly the core area of the Lintanchang Anticline, the fault zone, and the east and south of the study area. However, the highest value of rupture coefficient is located in the fault zone, and the rupture coefficient in the fault zone is above 1.2. In addition, the rupture coefficients in the eastern and southern parts of the study area are between 1.1 and 1.2. The main fault has a larger influence on the fracture development area than other faults. The extent of the grade III fracture development zone at the endpoint and inflection point of the fault is larger than other areas of the fault. It is mainly caused by the stress concentration phenomenon in this area. The low value area of rupture coefficient is mainly distributed in the northwestern margin of the study area and the middle area of the fault. A fracture coefficient below 0.9 indicates a fracture-free zone. Since the tectonic stress is released in the fault region, the stress value in the middle region of adjacent faults decreases, and tectonic fractures do not develop.

6 Conclusion

(1) The tectonic fractures developed in the Lintanchang area of the Sichuan Basin are mainly EW- and NNW-striking conjugate shear fractures formed in the Mid-Yanshanian period, followed by the NWW- and SWW-striking conjugate shear fractures formed in the late Yanshanian period. The distribution of tectonic fractures is affected by faults, folds, rock physical parameters and tectonic stresses.

(2) The study area is affected by two periods of paleo-tectonic stress fields, their directions are 130° and 175°, and the maximum stress magnitudes are 165 and 100 MPa, respectively. The tectonic stress magnitude is mainly related to the burial depth, fault and tectonic position. According to the simulations, the maximum horizontal principal stress in the Mid-Yanshanian period is 94.09–236.23 MPa, and the minimum horizontal principal stress is 45.91–126.44 MPa. In the late Yanshanian period, the maximum horizontal principal stress is 82.37–167.93 MPa, and the minimum horizontal principal stress is 54.34–128.63 MPa.

(3) It is found that the comprehensive fracture coefficients of the anticline core and fault areas are both greater than 1.1, which are the areas with the most developed structural fractures, and these areas have poor shale gas preservation conditions. However, the comprehensive fracture coefficients of the western flank of the anticline and the eastern and western dipping ends are between 1.0 and 1.1, which are areas with better shale gas preservation conditions. In addition, the development degree of tectonic fractures in the east and northwest areas of the Lintanchang Anticline is lower than that in other areas. The comprehensive fracture coefficients of shale in these areas are between 0.9 and 1.0. The shale is in a state of "breaking without cracking", and shale gas can be well preserved.

Data availability statement

The original contributions presented in the study are included in the article/supplementary material, further inquiries can be directed to the corresponding author.

Author contributions

DZ and JT are responsible for the idea and writing of this paper and KC, KW, PZ, GH, and XT are responsible for the fracture data collection.

Funding

This research was funded by the project "Fine Structural Analysis and Shale Gas Preservation Evaluation in Nanchuan-Wulong Area" (No.P21087-6) of the Ministry of Science and Technology of Sinopec.

Conflict of interest

Authors KW, PZ, and GH were employed by the Sinopec East China Oil & Gas Company.

The remaining authors declare that the research was conducted in the absence of any commercial or financial relationships that could be construed as a potential conflict of interest.

Publisher's note

References

An, M. J., Shi, Y. L., and Li, F. Q. (1998). Genetic algorithm-finite element method inversion of the factors determining the recent tectonic stress field of part of East Asia area. *Acta seimol. Sin.* 11, 265–272. doi:10.1007/s11589-998-0034-6

Bowker, K. A. (2007). Barnett shale gas production, fort worth basin: Issues and discussion. *Am. Assoc. Pet. Geol. Bull.* 91 (4), 523–533. doi:10.1306/06190606018

Dai, J. S., and Meng, Z. P. (1999). Numerical simulation of Palaeozoic tectonic stress field in the Chengdao Area. *Sci. Geol. Sin.* 8 (2), 223–232. CNKI:SUN:DZKY.0.1999-02-011.

Deng, B., Liu, S., and Wang, G. (2013). Cenozoic uplift and exhumation in southern Sichuan Basin-Evidence from low-temperature.thcrmochronology. *Chin. J.Geophys.* 6, 1958–1973. (in Chinese with English abstract). doi:10.6038/cjg20130618

Ding, W., Zhu, D., Cai, J., Gong, M., and Chen, F. (2013). Analysis of the developmental characteristics and major regulating factors of fractures in marine–continental transitional shale-gas reservoirs: A case study of the carboniferous–permian strata in the southeastern ordos basin, central China. *Mar. Pet. Geol.* 45, 121–133. doi:10.1016/j.marpetgeo.2013.04.022

Eissa, E. A., and Kazi, A. (1988). Relation between static and dynamic Young's moduli of rocks. *Int. J. Rock Mech. Min. Sci. Geomechanics Abstr.* 25, 479–482. doi:10.1016/0148-9062(88)90987-4

Fang, H. H., Sang, S. X., Wang, J. L., and Ju, W. (2018). Pore characteristics and its significance on shale gas reservoir: A case study of the Longmaxi shale in the nanchuan region, chongqing, south China. *Int. J. Oil Gas. Coal Technol.* 18 (3-4), 512–536. doi:10.1504/IJOGCT.2018.093127

Fischer, K., and Henk, A. (2013). A workflow for building and calibrating 3-D geomechanical models &ndash a case study for a gas reservoir in the North German Basin. *Solid earth.* 4, 347–355. doi:10.5194/se-4-347-2013

Griffith, A. A. (1921). The phenomena of rupture and flow in solids. *Trans. Roy. Soc. Philosophical Trans.*221, 163–198. doi:10.1098/rsta.1921.0006

Guo, P., Yao, L., and Ren, D. (2016). Simulation of three-dimensional tectonic stress fields and quantitative prediction of tectonic fracture within the Damintun Depression, Liaohe Basin, northeast China. *J. Struct. Geol.* 86, 211–223. doi:10.1016/j.jsg.2016.03.007

Guo, T. L., and Zhang, H. R. (2014). Formation and enrichment mode of Jiaoshiba shale gas field, Sichuan Basin. *Petroleum Explor. Dev.* 41 (1), 31–40. doi:10.1016/S1876-3804(14)60003-3

Hennings, P., Allwardt, P., Paul, P., Zahm, C., Reid, R., Alley, H., et al. (2012). Relationship between fractures, fault zones, stress, and reservoir productivity in the Suban gas field, Sumatra, Indonesia. *Am. Assoc. Pet. Geol. Bull.* 96 (4), 753–772. doi:10.1306/08161109084

Jarvie, D. M., Hill, R. J., Ruble, T. E., and Pollastro, R. M. (2007). Unconventional shale-gas systems: The mississippian barnett shale of north-central Texas as one model for thermogenic shale-gas assessment. *Am. Assoc. Pet. Geol. Bull.* 91 (4), 475–499. doi:10.1306/12190606068

Jiu, K., Ding, W., Huang, W., You, S., Zhang, Y., and Zeng, W. (2013). Simulation of paleotectonic stress fields within Paleogene shale reservoirs and prediction of favorable zones for fracture development within the Zhanhua Depression, Bohai Bay Basin, east China. *J. Pet. Sci. Eng.* 110, 119–131. doi:10.1016/j.petrol.2013.09.002

Ju, W., and Sun, W. (2016). Tectonic fractures in the lower cretaceous xiagou formation of qingxi oilfield, jiuxi basin, NW China part one: Characteristics and controlling factors. *J. Pet. Sci. Eng.* 146, 617–625. doi:10.1016/j.petrol.2016.07.042

Ju, W., Wang, J., Fang, H., and Sun, W. (2019). Paleotectonic stress field modeling and prediction of natural fractures in the Lower Silurian Longmaxi shale reservoirs, Nanchuan region, South China. *Mar. Petroleum Geol.* 100, 20–30. doi:10.1016/j.marpetgeo.2018.10.052

Ju, W., Wang, J. L., Fang, H. H., Gong, Y. P., and Zhang, S. J. (2017). Paleostress reconstructions and stress regimes in the nanchuan region of Sichuan Basin, south China: Implications for hydrocarbon exploration. *Geosci. J.* 21 (4), 553–564. doi:10.1007/s12303-016-0066-1

Kuhlman, R., Heemstra, T., Ray, T., Lin, P., and Chariez, P. 1993. Field tests of downhole extensometer used to obtain Formation in- situ stress data. , *SPE25*, 905, 625–634. doi:10.2118/25905-MS

Laubach, S. E., Lamarche, J., Gauthier, B. D. M., Dunne, W. M., and Sanderson, D. J. (2018). Spatial arrangement of faults and opening-mode fractures. *J. Struct. Geol.* 108, 2–15. doi:10.1016/j.jsg.2017.08.008

Laurent, M., and Frantz, M. (2006). Chronologic modeling of faulted and fractured reservoirs using geomechanically based restoration: Technique and industry applications. *Am. Assoc. Pet. Geol. Bull.* 90, 1201–1226. doi:10.1306/02240605116

Lemonnier, P., and Bourbiaux, B. (2010). Simulation of naturally fractured reservoirs. State of the art. *Oil Gas. Sci. Technol. –. Rev. IFP.* 65, 239–262. doi:10.2516/ogst/2009066

Li, C., Chen, S., and Zhang, P. (2011). [Repair of acute avulsion-type achilles tendon rupture by locking-loop stereoscopic suture]. *Geol. China* 2, 47–49. (in Chinese with English abstract). doi:10.1007/s12583-011-0162-0

Li, H. (2022). Research progress on evaluation methods and factors influencing shale brittleness: A review. *Energy Rep.* 8, 4344–4358. doi:10.1016/j.egyr.2022.03.120

Li, L., and Li, S. J. (2021). Evolution rule of overlying strata structure in repeat mining of shallow close distance seams based on Schwarz alternating procedure. *J. Min. Strata Control Eng.* 3 (2), 023515. doi:10.13532/j.jmsce.cn10-1638/td.20210225.001

Li, S., Li, J., and Zhou, Y. (2011). Fission track evidence for Mesozoic-Cenozoic uplifting in the southeastern margin of Sichuan basin. *Acta Petrologica Mineralogica* 30 (2), 225–233. (in Chinese with English abstract). doi:10.1007/s11589-011-0776-4

Liu, C., Wang, X., and Zhao, C. (2019). Palcotectonic stress field simulation and fracture prediction of tight sandstone in the Shanxi Formation, southern Qinshui Basin, China. *Ucophysical Prospect. Petroleum* 58 (2), 292–302+312. (in Chinese with English abstract).

Liu, D., Yang, D., and Zhang, Z. (2019). Fracture identification for tight reservoirs by conventional and imaging logging: A case study of permian lucaogou Formation in jimsar sag, junggar basin. *Lithol. Reserv.* 31 (3), 76–85. (in Chinese with English abstract). doi:10.1190/int-2020-0048.1

Lshida, T. (2001). Acoustic emission monitoring of hydraulic fracturing in laboratory and field. *Constr. Build. Mat.* 15, 283–295. doi:10.1016/S0950-0618(00)00077-5

Melikoglu, M. (2014). Shale gas: Analysis of its role in the global energy market. *Renew. Sustain. Energy Rev.* 37, 460–468. doi:10.1016/j.rser.2014.05.002

Meng, W. G., Chen, Z. Y., Li, P., Guo, Y. M., Gao, X. Z., and Hui, X. F. (2009). Exploration theories and practices of buried-hill reservoirs: A case from liaohe depression. *Petroleum Explor. Dev.* 36, 136–143. doi:10.1016/S1876-3804(09)60116-6

Milad, B., Ghosh, S., Suliman, M., and Slatt, R. (2018). "Upscaled DFN models to understand the effects of natural fracture properties on fluid flow in the Hunton group tight limestone," in Proceedings of the SPE/AAPG/SEG Unconventional Resources Technology Conference, Houston, TX, July 23 2018, 25.

Milad, B., and Slatt, R. M. (2017). "Integrated 3-D seismic, outcrop, and core data for characterization of natural fractures of the hunton limestone and the woodford shale in central Oklahoma," in AAPG 2017 Annual Convention and Exhibition, Texas, Houston. United States, Search and Discovery Article #51382. doi:10.13140/RG.2.2.24808.37121

Montgomery, S. L., Jarvie, D. M., Bowker, K. A., and Pollastro, R. M. (2005). Mississippian barnett shale, fort worth basin, north-central Texas: Gas-shale play with multi-trillion cubic foot potential. *Am. Assoc. Pet. Geol. Bull.* 89 (2), 155–175. doi:10.1306/09170404042

Nie, H., Chen, Q., Zhang, G., Sun, C., Wang, P., and Lu, Z. (2021). An overview of the characteristic of typical Wufeng–Longmaxi shale gas fields in the Sichuan Basin, China. *Nat. Gas. Ind. B* 8 (3), 217–230. doi:10.1016/j.ngib.2021.04.001

Pireh, A., Alavi, S. A., Ghassemi, M. R., and Shaban, A. (2015). Analysis of natural fractures and effect of deformation intensity on fracture density in Garau formation for shale gas development within two anticlines of Zagros fold and thrust belt, Iran. *J. Pet. Sci. Eng.* 125, 162–180. doi:10.1016/j.petrol.2014.11.016

Pollastro, R. M. (2007). Total petroleum system assessment of undiscovered resources in the giant Barnett Shale continuous (unconventional) gas accumulation, Fort Worth Basin, Texas. *Am. Assoc. Pet. Geol. Bull.* 91, 551–578. doi:10.1306/06200606007

Qie, L., Shi, Y. N., and Liu, J. S. (2021). Experimental study on grouting diffusion of gangue solid filling bulk materials. *J. Min. Strata Control Eng.* 3 (2), 023011. doi:10.13532/j.jmsce.cn10-1638/td.20201111.001

Ren, H., Liu, C., and Liu, W. (2020). Stress field simulation and fracture development prediction of the Wufeng Formation-Longmaxi Formation in the fushun yongchuan block , Sichuan Basin. *J. Geomechanics* 26 (01), 74–83. (in Chinese with English abstract). doi:10.12108/yxyqc.20220105

Rybacki, E., Meier, T., and Dresen, G. (2016). What controls the mechanical properties of shale rocks? e Part II: Brittleness. *J. Pet. Sci. Eng.* 144, 39–58. doi:10.1016/j.petrol.2016.02.022

Shan, J. Z., Zhang, Z. W., Chen, S. S., and Xu, K. (2004). Photo-elastic experiments of paleotectonic stresses field and fracture development characters on Anfutun buried hill. *Damintun Sag. Pet. Explor. Dev.* 31, 1–18. doi:10.1007/BF02873097

Shi, H., Xiong, L., and Dong, X. (2019). Characteristics of shale lithofacies and Genesis of evolution sequence difference of Wufeng-Lower Longmaxi Formation in southern Sichuan. *Nat. Gas. Ind.* 39 (S1), 71–77. (in Chinese with English abstract). doi:10.11764/j.issn.1672-1926.2016.02.0377

Timoshenko, S. P., and Goodier, J. N. (1951). *Theory of elasticity*. 3rd ed. New York, 56–58.

Tingay, M. R. P., Hillis, R. R., Morley, C. K., King, R. C., Swarbrick, R. E., and Damit, A. R. (2009). Present-day stress and neotectonics of Brunei; Implications for petroleum exploration and production. *Am. Assoc. Pet. Geol. Bull.* 93 (1), 75–100. doi:10.1306/08080808031

Wang, J. L., Fang, H. H., Gong, Y. P., Zou, Y., and Liu, J. G. (2017). Control of medium to small-scale tectonic deformations on fracture development in Longmaxi Formation shale. *Arab. J. Geosci.* 10 (21-11), 23. doi:10.1007/s12517-016-2810-2

Wclennan, J. A., Allwardt, P., and Hennings, P. H. (2009). Multivariate fracture intensity prediction:Applicetion to Oil Mounain anticline, Wyoming. *AAPG Bull.* 93 (11), 1585–1595.

Woodward, W. J. (1992). Wave equation tomography. *Geophysics* 57 (1), 15–26. doi:10.1190/1.1443179

Wu, X., Wang, F., and Xi, X. (2020). Experimental investigation on the strength characteristic、and fracture mechanism of rock with orthogonally crossed cracks. *J. China Coal Soc.* 45 (07), 2681–2690. (in Chinese with English abstract). doi:10.13225/j.cnki.jccs.2020.0156

Wu, Z., Zuo, Y., Wang, S., Chen, J., Wang, A., Liu, L., et al. (2017). Numerical study of multi-period palaeotectonic stress fields in lower cambrian shale reservoirs and the prediction of fractures distribution: A case study of the niutitang Formation in feng'gang No. 3 block, south China. *Mar. Petroleum Geol.* 80, 369–381. doi:10.1016/j.marpetgeo.2016.12.008

Xue, F., Liu, X. X., and Wang, T. Z. (2021). Research on anchoring effect of jointed rock mass based on 3D printing and digital speckle technology. *J. Min. Strata Control Eng.* 3 (2), 023013. doi:10.13532/j.jmsce.cn10-1638/td.20201020.001

Yang, R., He, S., Yi, J., and Hu, Q. (2016). Nano-scale pore structure and fractal dimension of organic-rich wufeng-longmaxi shale from jiaoshiba area, Sichuan Basin: Investigations using FE-SEM, gas adsorption and helium pycnometry. *Mar. Pet. Geol.* 70, 27–45. doi:10.1016/j.marpetgeo.2015.11.019

Zeng, L. B., and Liu, H. T. (2010). Influence of fractures on the development of low permeability sandstone reservoirs: A case study from the taizhao district, daqing oilfield, China. *J. Pet. Sci. Eng.* 72, 120–127. doi:10.1016/j.petrol.2010.03.009

Zeng, L. B., Lyu, W. Y., Li, J., Zhu, L. F., Weng, J. Q., Yue, F., et al. (2016). Natural fractures and their influence on shale gas enrichment in Sichuan Basin, China. *J. Nat. Gas. Sci. Eng.* 30, 1–9. doi:10.1016/j.jngse.2015.11.048

Zeng, L. B., Qi, J. F., and Wang, Y. X. (2007). Origin type of tectonic fractures and geological conditions in low permeability reservoirs. *Acta Pet. Sin.* 28 4, 52. doi:10.1016/S1872-5813(07)60034-6

Zeng, L. B., Wang, H. J., Gong, L., and Liu, B. M. (2010). Impacts of the tectonic stress field on natural gas migration and accumulation: A case study of the kuqa depression in the tarim basin, China. *Mar. Pet. Geol.* 27, 1616–1627. doi:10.1016/j.marpetgeo.2010.04.010

Zhang, S. C., and Zhu, G. Y. (2006). Gas accumulation characteristics and exploration potential of marine sediments in Sichuan Basin. *Acta Pet. Sin.* 27 (5), 1–8. (in Chinese with English abstract). doi:10.7623/syxb201303004

Zhao, K. K., Jiang, P. F., Feng, Y. J., Sun, X. D., Cheng, L. X., and Zheng, J. W. (2021). Investigation of the characteristics of hydraulic fracture initiation by using maximum tangential stress criterion. *J. Min. Strata Control Eng.* 3 (2), 023520. doi:10.13532/j.jmsce.cn10-1638/td.20201217.001

frontiers | Frontiers in Earth Science

TYPE Original Research
PUBLISHED 23 September 2022
DOI 10.3389/feart.2022.1028439

OPEN ACCESS

EDITED BY
Wenlong Ding,
China University of Geosciences, China

REVIEWED BY
Chao Han,
Shandong University of Science and Technology, China
Ying Tang,
Xi'an Shiyou University, China

*CORRESPONDENCE
Kaijun Tan,
tankaijun20@126.com

SPECIALTY SECTION
This article was submitted to Structural Geology and Tectonics, a section of the journal Frontiers in Earth Science

RECEIVED 26 August 2022
ACCEPTED 07 September 2022
PUBLISHED 23 September 2022

CITATION
Tan K, Yao J, Chen J, Tang D, Qin Y and Wu Q (2022), Controlling effect of source-reservoir assemblage on natural gas accumulation: A case study of the upper triassic xujiahe formation in the sichuan basin.
Front. Earth Sci. 10:1028439.
doi: 10.3389/feart.2022.1028439

Controlling effect of source-reservoir assemblage on natural gas accumulation: A case study of the upper triassic xujiahe formation in the sichuan basin

Kaijun Tan[1]*, Jun Yao[1], Juan Chen[1], Dahai Tang[2], Yang Qin[1] and Qingpeng Wu[1]

[1]Research Institute of Petroleum Exploration and Development Northwest Branch, Lanzhou, China, [2]Northwest Sichuan Gas Mine of PetroChina Southwest Oil and Gas Field Company, Jiangyou, China

The enrichment law of tight sandstone gas in the Upper Triassic Xujiahe Formation in the Sichuan Basin has not been fully revealed. In this study, the controlling effect of source-reservoir assemblage on gas accumulation in the Xujiahe Formation was systematically investigated. The results show that pores and fractures are developed in the tight sandstone reservoirs of the Xujiahe Formation. The main pore types are intragranular dissolved and intergranular pores. The quality of sandstone reservoirs in the Xujiahe Formation is controlled by sedimentation, diagenesis and tectonic processes. Underwater distributary river channels and estuary bars are favorable microfacies for reservoir development, and chlorite cemented facies and dissolution-kaolinite cemented facies are the most favorable diagenetic facies. In addition, the natural gas composition and carbon isotope characteristics of the Xujiahe Formation are significantly different in different intervals of the same gas field and the same interval of adjacent gas fields. This shows that the natural gas has no obvious vertical mixing and lateral migration, and it has the distribution characteristics of "local enrichment". Then, the natural gas will be preferentially charged in the feldspar lithic sandstone and feldspar quartz sandstone with large thickness and good physical properties by means of short-range migration. According to the research, the hydrocarbon supply capacity of the single layer in each interval is weak, and it leads to the low filling degree of the gas reservoir and the insufficient separation of gas and water. On the whole, four sets of extra-source "lower generation and upper storage" assemblages and two sets of "self-generation and self-storage" source-reservoir assemblages are developed in the Xujiahe Formation. The development scale of natural gas is mainly controlled by the type of source-reservoir combination, and the areas with close source-reservoir contact and high hydrocarbon generation intensity are high-quality reservoir development areas.

KEYWORDS

sichuan basin, xujiahe formation, pore structure, natural gas composition, carbon

1 Introduction

The Upper Triassic Xujiahe Formation in the Sichuan Basin is rich in natural gas resources (Dai et al., 2005; Hu et al., 2014). So far, 32 gas fields and gas-bearing structures have been discovered in the Xujiahe Formation in the Zhongba, Bajiaochang, Chongxi, Guang'an and Hechuan areas. They are mainly distributed in the central and western Sichuan Basin. Therefore, the Xujiahe Formation has become one of the most important natural gas producing layers in the Sichuan Basin. The accumulation law of natural gas in the Xujiahe Formation in the Sichuan Basin has received extensive attention from many scholars (Dai et al., 2009; Dai et al., 2012; Dai, 2014; Wang et al., 2020; Li, 2021). The previous believed that the "sandwich" type reservoir-caprock assemblage of the Xujiahe Formation provided the basic geological conditions for the large-scale accumulation of natural gas. Moreover, it has been widely recognized that "continuous gas reservoirs" are widely developed in the Xujiahe Formation.

In recent years, with the deepening of exploration and development, discontinuous gas reservoirs have been discovered in the Xu 2, Xu 4, and Xu 6 Members, and the gas-water relationship is very complex. The source of the Xujiahe Formation is the Xu 1, Xu 3, and Xu 5 Members. Furthermore, the main controlling factors of hydrocarbon accumulation in continental tight reservoirs are not well understood (Du et al., 2007; Yu et al., 2014; Du et al., 2019). Therefore, the study of the enrichment law of natural gas in the Xujiahe Formation has become a hotspot. In this study, the characteristics of the source-reservoir assemblages of the Xujiahe Formation and their controlling effects on natural gas accumulation were systematically analyzed. This study can provide technical support for the efficient exploration and development of the Xujiahe Formation.

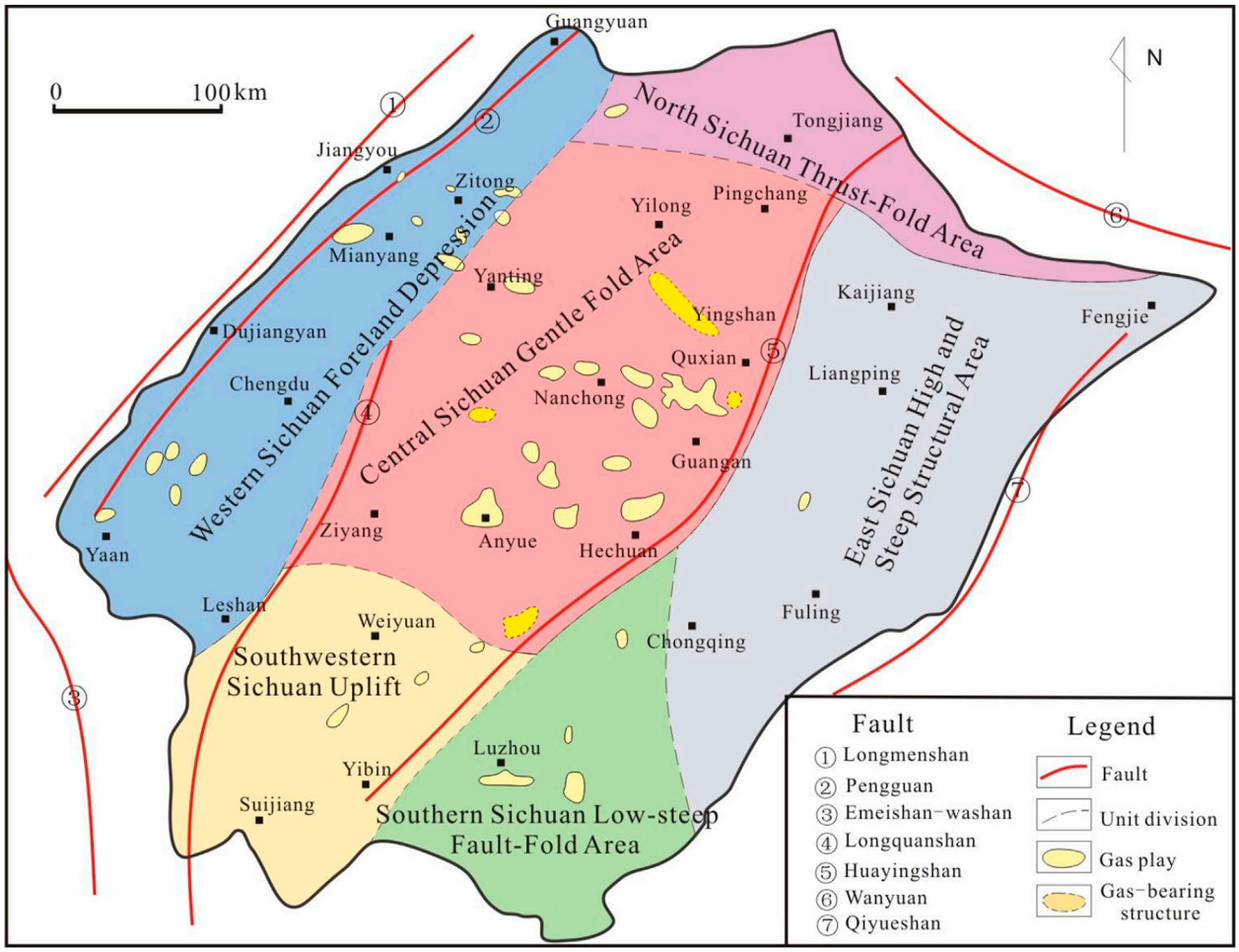

FIGURE 1
Structural location and gas reservoir distribution in the Sichuan Basin.

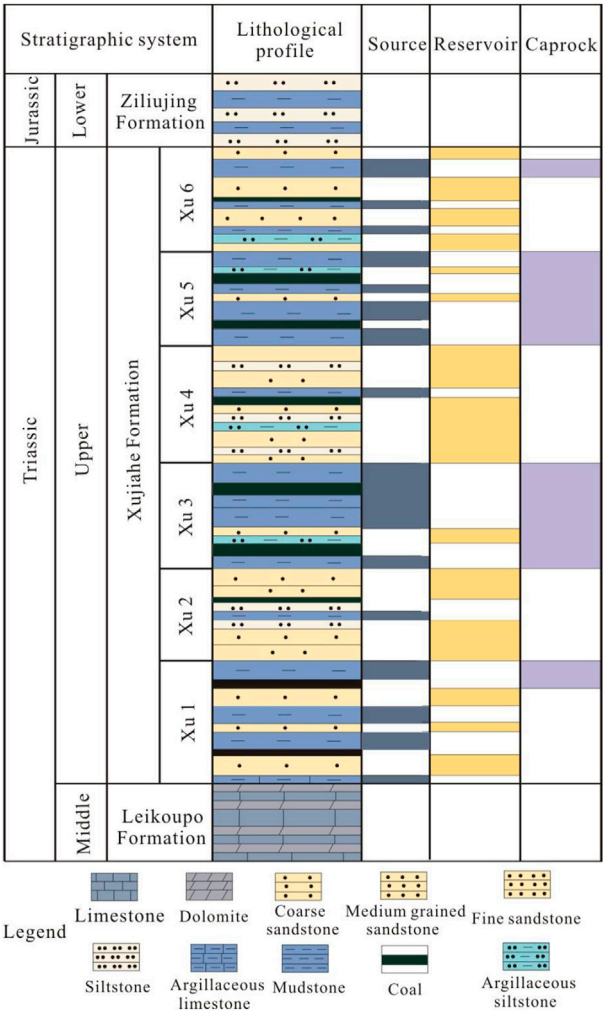

FIGURE 2
Source-reservoir assemblages of the Upper Triassic Xujiahe Formation in the Sichuan Basin.

2 Geological background

The Sichuan Basin is a large hydrocarbon-bearing superimposed basin in western China, with an area of about 18 km^2 × 10^4 km^2. The structural units in the Sichuan Basin are divided into the Western Sichuan Foreland Depression Area, the Central Sichuan Gentle Fold Area, the Northern Sichuan Thrust Fold Area, the Eastern Sichuan High-steep Tectonic Area, the Southern Sichuan Low-steep Fold Area, and the Southwestern Sichuan Uplift Area (Figure 1) (Dai et al., 2012).

During the Indosinian Movement in the late Triassic, the continuous uplift of the periphery of the Sichuan Basin transformed the basin into an inland lake basin (Dai., 2014). The strata of the Upper Triassic Xujiahe Formation were deposited with huge thick sand and mudstone. The deposition of the Xujiahe Formation is controlled by factors such as multiple provenances, multiple periods of tectonic movements, paleo-erosion surfaces and foreland basins (Du et al., 2019). The sedimentary thickness of the Xujiahe Formation in the western part of the basin is relatively large, up to more than 3,000 m, while that in the northern, eastern and western parts is relatively small, generally about 200 m–300 m. From bottom to top, the Xujiahe Formation is divided into Xu 1–Xu 6 Members (Figure 2). Among them, the Xu 1, Xu 3, and Xu 5 Members are mainly gray-black mudstone, carbonaceous mudstone interbeded with siltstone and thin coal seams; while the Xu 2, Xu 4, and Xu 6 Members are mainly gray-white, gray fine-medium-grained sandstone interbeded with a small amount of black mudstone and thin coal seams (Liao et al., 2014).

3 Experiments and methods

In this study, all natural gas samples were taken from the Xujiahe Formation of the Bajiaochang, Chongxi, Nanchong and Guang'an Gas Fields. Also, these samples were taken from the double valve cylinder at the outlet of the wellhead pressure gauge. In order to exclude the influence of external factors on natural gas samples, the samples were taken from normal production wells with a long production time and no chemical reagents have been added recently. A HP6890 gas chromatograph was used for chemical composition analysis, and individual hydrocarbon gas components were separated by capillary column (Plot Al2O3 50*0.53 mm). The gas chromatograph oven temperature was first set at 30°C and held for 10 min, then increased to 180°C at a rate of 10°C/min. In addition, the carbon isotope analysis was performed using a Delta S GC/C/IRMS isotope mass spectrometer. The gas components were separated by a gas chromatograph and then converted into CO_2 and injected into the mass spectrometer. The individual alkane gas components (C_1-C_5) and CO_2 were separated by column chromatography (Plot Q 30 m). The column ramp was ramped from 35°C to 80°C (8°C/min ramp rate) to 260°C (5°C/min ramp rate), and the oven temperature was maintained for 10 min at the final temperature. Each sample was analyzed 3 times, and its analytical precision was ± 0.5‰.

The rock thin sections were polished on both sides to a thickness of 0.03 mm. Further, thin sections were identified using a Zeiss Axio Scope A1 polarizing microscope. The cores were cut into cubes of about 1 cm^3 for scanning electron microscope observation. An FEI Quanta 450 FEG was used for environmental SEM observations. Its maximum magnification is 1 million times, the working voltage is 20 kV, and the electron beam incident beam current is 4 × 10^{-10} A.

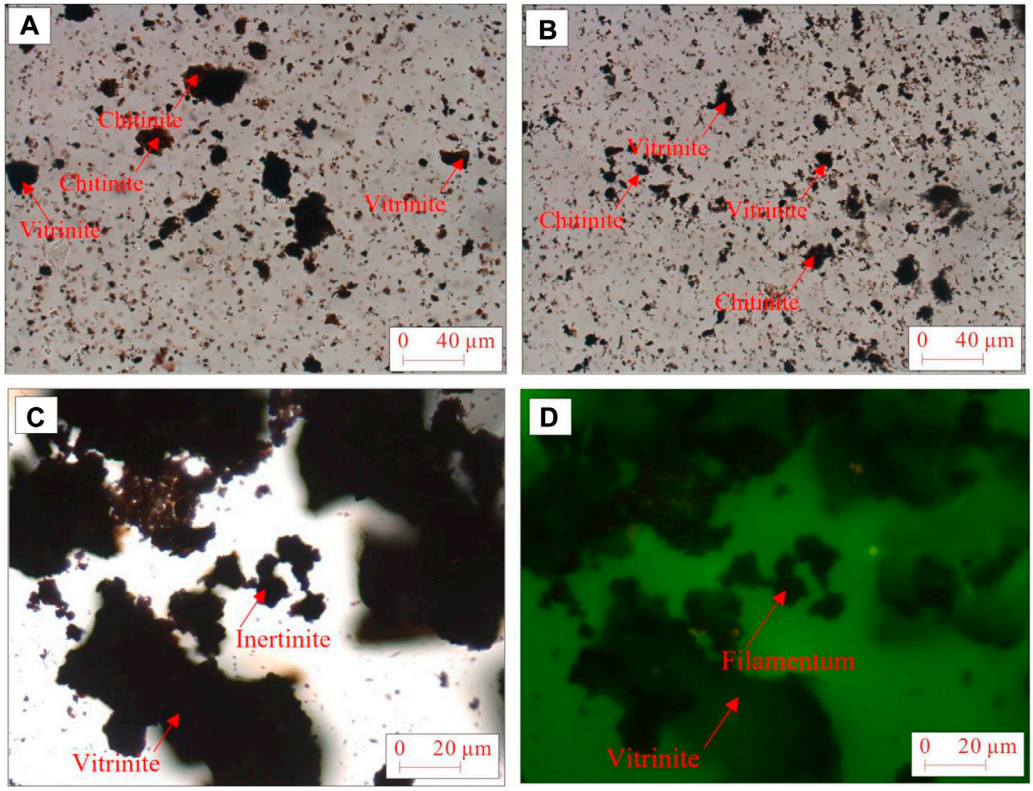

FIGURE 3
Microcomponents of kerogen in source rocks of Xujiahe Formation. **(A)** Jinhe Profile, Xu 1 Member; **(B)** Zhanggongling Profile, Xu 5 Member; **(C)** and **(D)** Well Jin 31, 3,017.92 m.

4 Results

4.1 Source-reservoir combination of extra-source "lower generation and upper storage"

The source rocks of the Upper Triassic Xujiahe Formation in the Sichuan Basin are the black shales and thin coal seams in the Xu 1, Xu 3, and Xu 5 Members. Thin mudstone and thin coal beds are also developed in the middle and lower parts of the Xu 2 and Xu 4 Members and the middle and upper parts of the Xu 6 Member. The Xujiahe Formation source rocks in the western Sichuan Basin are thicker, up to 1,000 m, while those in the northeastern and southern Sichuan Basin are thinner, generally less than 50 m–100 m. The organic carbon content of the Xujiahe Formation source rocks generally ranges from 0.5% to 9.7%, with an average of 1.95%. Moreover, the types of organic matter are mainly Type II_2 and Type III. The microscopic composition of kerogen is mainly vitrinite, while the content of inertite and chitinite is low, and saprolite is basically absent (Figure 3). The source rocks of the Xu 1, Xu 3, and Xu 5 Members are superimposed with the reservoirs of the Xu 1 (middle part), Xu 2, Xu 4, and Xu 6 Members, and four sets of good source-reservoir assemblages of extra-source "lower generation and upper storage" have been formed. The 4 sets of source-reservoir assemblages include: lower source rock (A1) and middle Xu 1 Member (A2) assemblage, upper Xu 1 Member source rock (A3) and Xu 2 Member reservoir (B1) assemblage, Xu 3 Member hydrocarbons source rock (B2) and Xu 4 Member reservoir (C1) assemblage, Xu 5 Member source rock (C2) and Xu 6 Member reservoir (C3) assemblage (Figure 2).

The reservoir rock types are mainly fine-medium-coarse-grained lithic feldspar sandstone, feldspar lithic sandstone, and lithic sandstone, followed by lithic quartz sandstone and feldspar quartz sandstone (Figure 4). Among them, the Xu 2 Member mainly develops feldspar quartz sandstone and lithic feldspar sandstone; the Xu 4 Member mainly develops lithic feldspar sandstone and feldspar lithic sandstone, followed by feldspar or lithic quartz sandstone; the Xu 6 Member mainly develops feldspar lithic sandstone, lithic sandstone, and lithic feldspar sandstone. The Xujiahe Formation reservoir rocks have the characteristics of low compositional maturity and high structural maturity, and the compositional maturity index (quartz/feldspar + debris) is generally between 1.5 and 4.0.

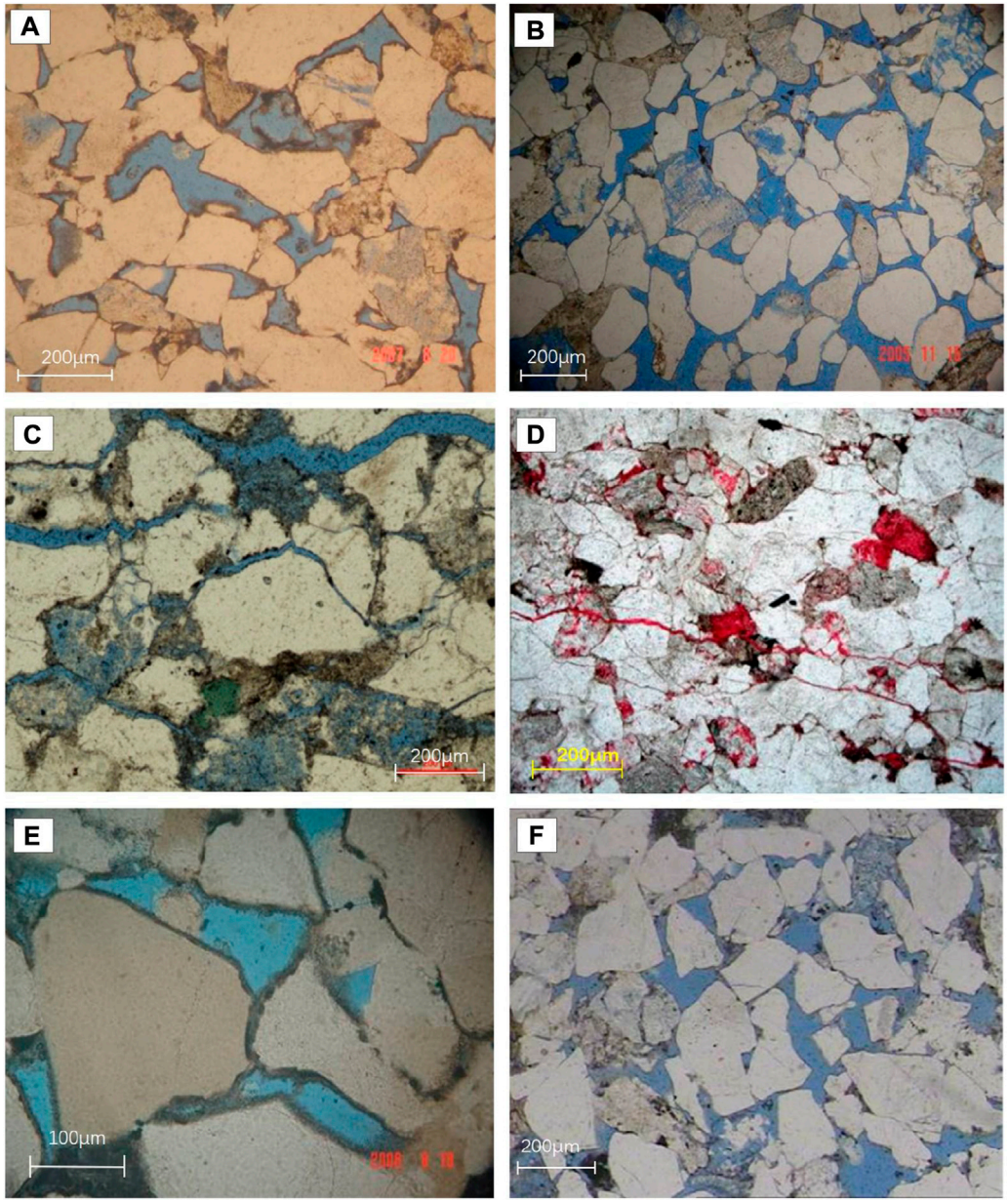

FIGURE 4
Microstructure characteristics of tight sandstones of Xujiahe Formation in the study area. **(A)** Well Hechuan 7, 2,191.18 m, detrital feldspar sandstone with developed intergranular pores; **(B)** Well Guang'an 101, 2080.15 m, detrital feldspar sandstone; **(C)** Well Penglai 11, 2,360.54 m, feldspar detrital sandstone; **(D)** Well Songhua 2, 3,595.19 m, detrital sandstone; **(E)** Well Guang'an 128, 2,337.45 m, detrital quartz sandstone; **(F)** Well Tong 6, 2,449.1 m, feldspar quartz sandstone.

The difference of maturity is mainly caused by the difference of surrounding provenance. In addition, the compositional maturity of the Xujiahe Formation reservoir rocks shows a downward trend from the Xu 2 to the Xu 6 Members. However, on the plane, the maturity of the reservoir rocks in the central Sichuan area is relatively high, while that in the peripheral areas is relatively low.

4.2 In-source "self-generation and self-storage" source-reservoir combination

For a long time, the natural gas exploration of the Upper Triassic Xujiahe Formation in the Sichuan Basin has always regarded the Xu 1, Xu 3, and Xu 5 Members as source rocks, and the Xu 2, Xu 4, and Xu 6 Members as reservoirs. However, there

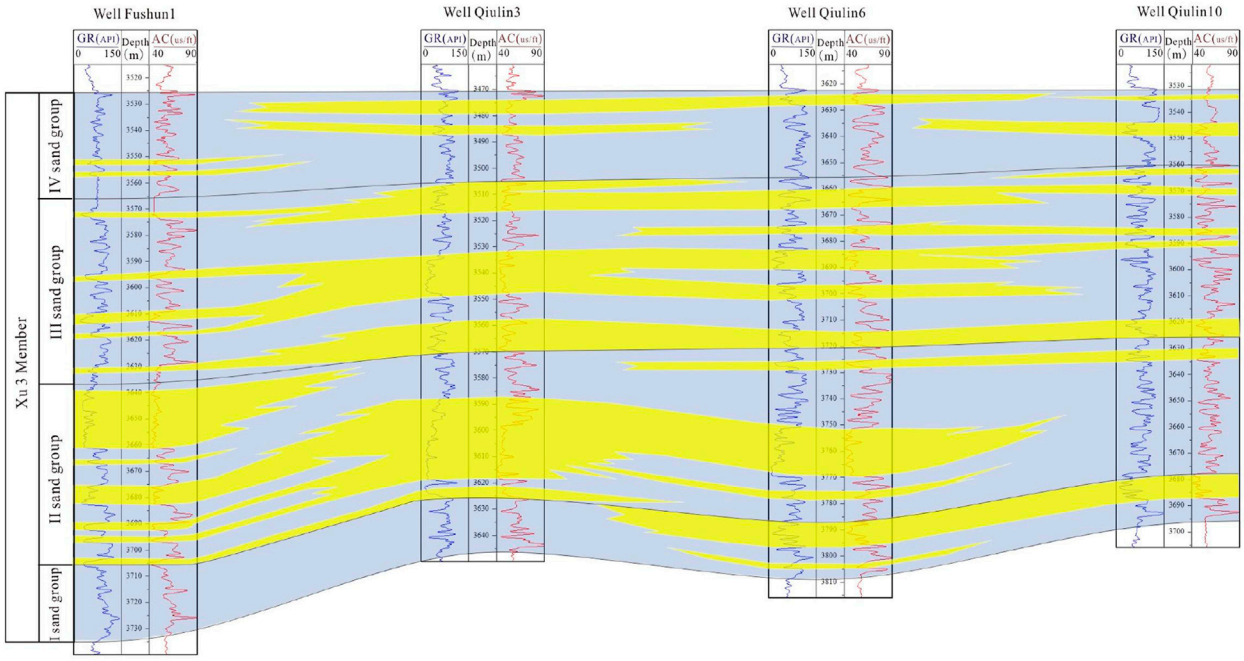

FIGURE 5
Well-connected profile of the source-reservoir assemblage within the source of the Xu 3 Member (the plane position is shown in Figure 8). Yellow represents sandstone and grey represents mudstone.

are few summaries on the distribution law of natural gas in the self-generation and self-storage combination within the source. Through the review of old wells, it is found that there are frequent oil and gas shows in the Xu 3 and Xu 5 members during the drilling process. At present, high-yield gas flows have been obtained in the Xu 3 and Xu 5 Members of many wells in the Jiulongshan, Zhongtaishan and Qiulin areas. In the source rocks of the Xu 3 and Xu 5 Members, not only mudstone and coal seams are developed, but sandstones are also extremely developed, and the sand bodies are widely distributed. Especially in the source rock areas in the western Sichuan Basin, the average sandstoned ratio is more than 30%. It was found that the in-source sandstones in these areas have large thickness, continuous lateral distribution and good physical properties. Therefore, the sandstones distributed in the source rock series are more likely to form large-scale accumulation of natural gas than the Xu 2, Xu 4, and Xu 6 Members.

4.2.1 Source-reservoir combination within the source of the Xu 3 Member

The Xu 3 Member is distributed in the whole basin and belongs to shallow lake deposits. Lacustrine sand bars are locally developed in the central Sichuan area. Alluvial fans and delta deposits are mainly developed in the northwest part of the basin, and delta deposits are mainly developed in the northeast and southeast parts of the basin. Distributary channels and sheet sands are the main microfacies types. Statistics show that the thickness of a single sand layer ranges from 5 m to 10 m, the maximum can reach 40 m, and its cumulative thickness can reach more than 150 m. The reservoir spaces of the tight sandstones are mainly intergranular dissolved pores, intragranular dissolved pores and microfractures. The average porosity is 4.28%, and the average permeability is 0.13 $\mu m^2 \times 10^{-3}$ μm^2. These reservoirs are distributed in a thin-layered or lenticular form, and they constitute a good source-reservoir assemblage with the mudstones developed in the Xu 3 Member (Figure 5).

4.2.2 Source-reservoir combination within the source of the Xu 5 Member

The sedimentary environment of the Xu 5 Member is similar to the Xu 3 Member. However, due to the uplift and denudation in the northwest part of the basin, the direction of the main water system has changed, and the main water system is mainly injected into the basin along the northeast and south directions. Delta deposits are mainly developed in the northern, northeastern and southern areas of the basin. Statistics show that the thickness of a single sand layer ranges from 10 m to 15 m, the maximum can reach 30 m, and the cumulative thickness can reach more than 100 m. Intergranular dissolved pores, intragranular dissolved pores and microfractures are the main types of pores. The average porosity is 4.48%, and

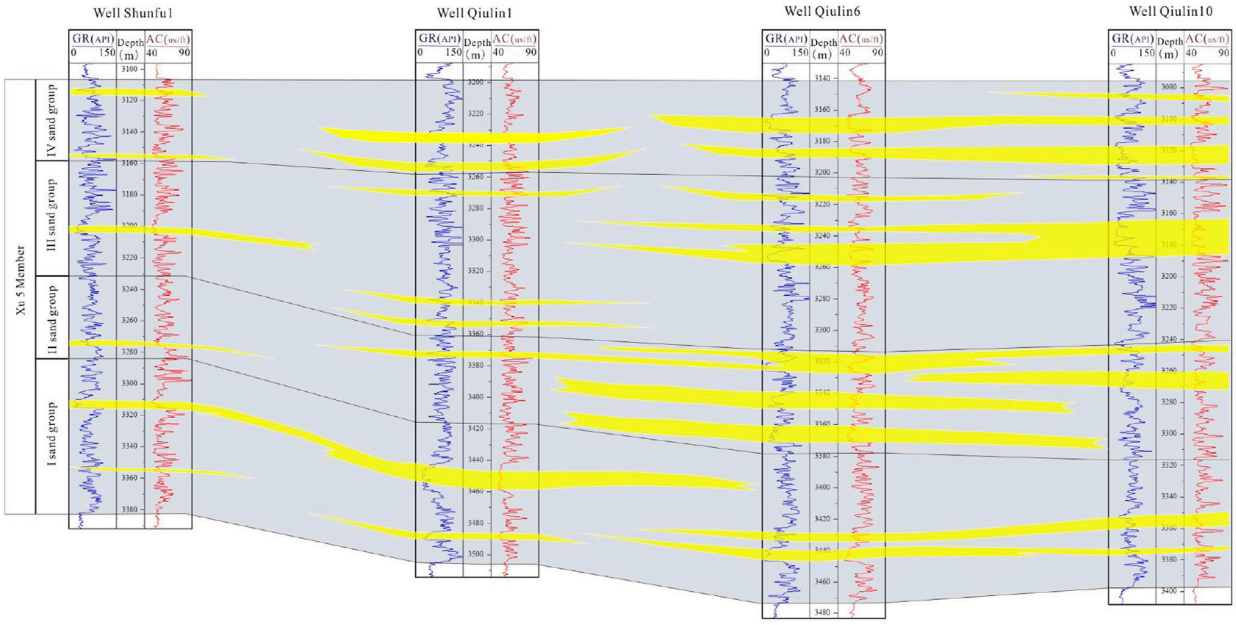

FIGURE 6
Well-connected profile of the source-reservoir assemblage within the source of the Xu 5 Member (the plane position is shown in Figure 8). Yellow represents sandstone and grey represents mudstone.

TABLE 1 Carbon isotopic characteristics of natural gas in typical gas fields of the Upper Triassic Xujiahe Formation in the Central Sichuan Basin.

Gas field	Interval	Natural gas composition (%)		Drying factor	Natural gas carbon isotope (δ13C‰)	
		CH4	C2H6		CH4	C2H6
Bajiaochang	T3x6	88.97~90.99/ 89.98 (2)	5.01~5.33/ 5.17 (2)	0.916~0.926/ 0.921 (2)	-40.86~-40.23/ -40.55 (2)	-26.17~-25.92/ -26.06 (2)
	T3x4	86.14~91.94/ 90.00 (16)	4.48~7.94/ 5.67 (16)	0.898~0.942/ 0.925 (16)	-39.32~-37.60/ -38.66 (3)	-26.26~-25.10/ -25.67 (3)
	T3x2	91.32~95.92/ 93.16 (4)	2.71~5.77/ 4.55 (4)	0.928~0.966/ 0.944 (4)	-41.00~-37.62/ -39.54 (3)	-26.73~-24.80/ -25.51 (3)
Xiongxi	T3x4	68.08~90.18/ 84.80 (16)	3.88~7.58/ 6.26 (16)	0.873~0.942/ 0.906 (16)	-43.80~-40.40/ -41.79 (7)	-28.30~-26.32/ -27.30 (7)
	T3x2	88.09~91.82/ 89.78 (6)	3.07~6.63/ 5.20 (6)	0.902~0.940/ 0.919 (6)	-42.80~-42.03/ -42.48 (3)	-28.20~-27.65/ -27.95 (3)
Nanchong	T3x4	84.64~88.50/ 86.43 (5)	6.47~8.14/ 7.63 (5)	0.893~0.920/ 0.902 (5)	-41.12~-39.70/ -40.44 (3)	-26.50~-26.00/ -26.30 (3)
	T3x2	89.95~91.49/ 90.65 (3)	3.89~4.83/ 4.49 (3)	0.917~0.932/ 0.923 (3)	-40.50~-40.44/ -40.47 (2)	-27.10~-26.51/ -26.81 (2)
Guangan	T3x6	85.98~95.86/ 89.58 (26)	2.03~7.59/ 6.17 (26)	0.895~0.942/ 0.919 (26)	-42.49~-37.09/ -39.50 (17)	-27.98~-25.52/ -26.90 (17)
	T3x4	70.93~94.71/ 91.51 (19)	3.18~5.43/ 4.43 (6)	0.934~0.961/ 0.946 (6)	-43.02~-36.91/ -39.04 (16)	-25.95~-23.63 /-24.75 (16)

Notes: Min~Max/Average (Number of Samples).

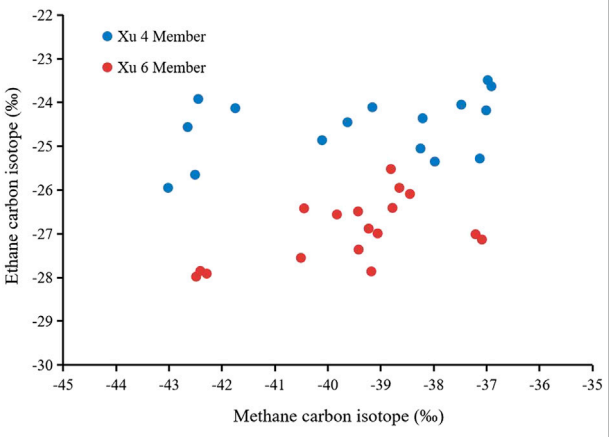

FIGURE 7
Relationship between methane and ethane carbon isotopes in the Xu 4 and Xu 6 Members of Guang'an Gas Field.

the average permeability is 0.35 $\mu m^2 \times 10^{-3}$ μm^2. Thin-layered or lenticular tight sandstones and widely developed mudstones in the Xu 5 Member constitute a good source-reservoir assemblage (Figure 6). The surface porosity of micro-fractures in the reservoir is usually only 0.5%–1%, but their existence plays an important role in improving the seepage capacity of the reservoir.

5 Discussion

5.1 Controlling effect of independent source-reservoir combination on natural gas distribution

5.1.1 Differences in natural gas characteristics in different layers of the same gas field

The natural gas in the Xujiahe Formation in the Sichuan Basin is dominated by hydrocarbon gas, and the total hydrocarbon volume coefficient is more than 95%. Among the hydrocarbon components, CH_4 dominates, while the non-hydrocarbon gases have lower contents of CO_2 and N_2, and most areas do not contain H_2S. It can be seen from Table 1 that the methane content and drying coefficient of the natural gas in some typical gas fields of the Xujiahe Formation in the central Sichuan area show a decreasing trend from the Xu 2 to Xu 4, and to Xu 6 Members. It shows that the natural gas sources of each interval are different.

Taking the Guang'an Gas Field as an example, the differences in the methane content and drying coefficient of the natural gas in the Xu 6 and Xu 4 Members of the Xujiahe Formation are obvious. The methane content of the natural gas in the Xu 6 Member of the Guang'an Gas Field is between 85.98% and 95.86%, with an average of 89.58%; and the drying coefficient is distributed between 0.895 and 0.942, with an average of 0.919. However, the content of methane in the natural gas of the Xu 4 Member ranges from 70.93% to 94.71%, with an average of 91.51; the drying coefficient is distributed between 0.934 and 0.961, with an average of 0.946. From bottom to top, the methane content and drying coefficient of the Xujiahe Formation gas gradually decreased, indicating that the natural gas in the Xu 4 and Xu 6 Members may have different sources.

The carbon isotope value of ethane in the natural gas of the Xu 6 Member of the Guang'an Gas Field ranges from −27.98‰ to −25.52‰, with an average of −26.90‰; while the ethane carbon isotope value of the natural gas in the Xu 4 Member ranges from −25.95‰ to −23.63‰, with an average of −24.75‰. The ethane carbon isotope value of natural gas in the Xu 4 Member is significantly higher than that in the Xu 6 Member (Figure 7). Therefore, the sources of natural gas in each interval of the Xujiahe Formation are obviously different. There is no mixing of source rock products in different intervals. In addition, the drying coefficient of the natural gas in the Xu 4 Member is significantly higher than that in the Xu 6 Member (Table 1). This shows that the maturity of the source rock supplying the natural gas of the Xu 4 Member is higher than that of the source rock supplying the natural gas of the Xu 6 Member. The natural gas in the Xu 4 Member did not migrate to the Xu 6 Member. Therefore, there is no obvious vertical mixing of the natural gas in the Xu 4 and Xu 6 gas reservoirs in the Guang'an Gas Field, and they are most likely to come from the Xu 3 and Xu 5 source rocks in the lower part of the gas reservoir, respectively.

5.1.2 Differences in natural gas properties in the same interval of adjacent gas fields

For a long time, it has been controversial whether the natural gas has obvious lateral migration in the same interval of adjacent gas fields. In this study, we compared the geochemical characteristics of natural gas in the Xu 4 Member in the Guang'an and Nanchong Gas Fields of the central Sichuan Basin (Table 1). For the Xu 4 Member of the Guang'an Gas Field, the average methane content of natural gas is 91.51%, the average drying coefficient is 0.946, the average carbon isotope of methane is −24.75‰, and the average carbon isotope of ethane is −24.75‰. However, for the Xu 4 Member of the Nanchong Gas Field, the average methane content of natural gas is 86.43%, the average drying coefficient is 0.902, the average methane carbon isotope is −40.44‰, and the average ethane carbon isotope is −26.30‰. The differences in natural gas composition and carbon isotope values indicate that the gas sources of the Xu 4 Member are different in the Guang'an and Nanqiang Gas Fields. In addition, the drying coefficient of natural gas in the Xu 4 Member of the Guang'an Gas Field is also significantly higher than that in the Nanchong Gas Field. This is because the maturity of the source rocks supplied by the natural gas in the Xu 4 Member of the Guang'an Gas Field is higher than that of

the Nanchong Gas Field, and this phenomenon is not caused by the component fractionation caused by the lateral migration of natural gas. If the high drying coefficient of natural gas in the Xu 4 Member of the Guang'an Gas Field is caused by migration and fractionation, then its methane carbon isotope should not be higher than that of the Xu 4 Member of the Nanchong Gas Field. Therefore, the difference in the geochemical characteristics of natural gas in the same interval of adjacent gas fields is caused by the different maturity of the source rocks supplying hydrocarbons in the gas reservoir, rather than by the lateral migration and fractionation of natural gas (Xiao et al., 2008; Luo et al., 2019; Wang et al., 2020).

5.2 Controlling effect of closely contacted source-reservoir assemblages on natural gas enrichment

5.2.1 Control of source rock on filling degree of hydrocarbons

Due to the dramatic changes in the plane depositional environment of the Xujiahe Formation, the distribution of source rocks is extremely uneven. The dark mudstone in the Xujiahe Formation has a large thickness. It gradually thins from the northwest to the southeast of the basin. In contrast, coal seams and carbonaceous mudstones are relatively thin in thickness and vary greatly on the plane. The thickness center of the Xujiahe Formation source rocks is distributed in the western Sichuan area, with an average thickness of 100 m–400 m, while that in the central Sichuan area is generally 20 m–60 m. Moreover, the source rocks in the Xujiahe Formation are basically in the early and middle stages of massive gas generation. The degree of thermal evolution decreased gradually from the Xu 1 Member (R_o is between 1.1% and 2.2%) to the Xu 3 Member (R_o is between 1.0% and 1.8%) and Xu 5 Member (R_o is between 0.8% and 1.4%). The thermal evolution degree of the Xujiahe Formation in the western Sichuan Basin is the highest (R_o is between 0.9% and 2.2%), followed by the northeastern Sichuan Basin (R_o is between 0.8% and 1.6%), and that in te central and southern Sichuan Basin are the lowest (R_o is less than 1.2%). The cumulative gas generation intensity of the Xujiahe Formation source rocks is between 10 m^3/km^2 and 100 $m^3/km^2 \times 10^8$ m^3/km^2. Among them, the gas generation intensity in the western Sichuan region is relatively high (generally greater than 20 $m^3/km^2 \times 10^8$ m^3/km^2), while that in the central and southern Sichuan regions is relatively small (10~20 $m^3/km^2 \times 10^8$ m^3/km^2).

It is difficult for the natural gas generated from the source rocks of the Xujiahe Formation to migrate laterally on a large scale after entering the highly heterogeneous reservoir. Short-range migration is the main migration mode of hydrocarbons (Jiu et al., 2013; Liao et al., 2014; Lan et al., 2021; Zhang et al., 2021). For the Xujiahe Formation in the central Sichuan area, the source rocks have a large cumulative thickness, a wide distribution range, and a high cumulative hydrocarbon generation intensity, but the gas generation intensity of each layer of source rocks is relatively small. For example, the average gas generation intensity of the Xu 1, Xu 3, and Xu 5 Members are 2.06 $m^3/km^2 \times 10^8$ m^3/km^2, 3.75 $m^3/km^2 \times 10^8$ m^3/km^2, and 6.29 $m^3/km^2 \times 10^8$ m^3/km^2, respectively. Due to the near-source accumulation of hydrocarbons, the natural gas generated by the source rocks of the Xu 1, Xu 3, and Xu 5 Members will be preferentially charged from the sandstones with good physical properties, and then supplied to the Xu 2, Xu 4, and Xu 6 Members, respectively. The single-layer hydrocarbon supply capacity of each interval is weak. The amount of natural gas generated is far less than the storage space of sandstone. Therefore, the charging of natural gas is insufficient, the gas reservoirs are independent of each other and the separation of gas and water is insufficient (Ni et al., 2011; Zhou et al., 2019; Morozov et al., 2021). It can be seen from Figure 8 that the high-yield wells are mainly distributed in the regions with gas saturation greater than 57.5%. In addition, the gas saturation has a good positive correlation with the hydrocarbon generation intensity of the source rocks. Areas with hydrocarbon generation intensity greater than 4 $m^3/km^2 \times 10^8$ m^3/km^2 have higher gas saturation and natural gas productivity.

5.2.2 Control of reservoir performance on production capacity of natural gas

The Xujiahe Formation is a set of coal-measure strata, and the developed tight sandstone reservoirs contain pores and fractures. Pores are the main reservoir space, and the types of pores include intragranular dissolved pores, intergranular pores, intragranular pores, intergranular dissolved pores, mold pores, matrix dissolved pores, and intercrystalline micropores of clay minerals (Figure 9). Among them, intragranular dissolved pores and intergranular pores are the main types of pores. The pore types have obvious regional distribution differences. Intergranular pores are mainly developed in the depression areas of the northwestern Sichuan Basin, while dissolution pores are not developed. Dissolution pores are mainly developed in the southwestern Sichuan Basin, especially the feldspar intragranular dissolved pores and intergranular dissolved pores, while the intergranular pores are rare. For the central, eastern and central-south transition zones of the Sichuan Basin, intergranular pores and intragranular dissolved pores are well developed. The pores in the southern Sichuan area are generally underdeveloped, and dissolved pores are the main pore type.

The regional differences in pore types are closely related to the reservoir rock types and diagenesis (Fan et al., 2005; Hao et al., 2016; Nicula1 et al., 2021; Saein and Riahi., 2017). When the feldspar and chlorite contents are high, the pores are relatively developed (Hu and Xie., 1997; Hu et al., 2012; Wan et al., 2012). The development scale of tight reservoirs in the Xujiahe

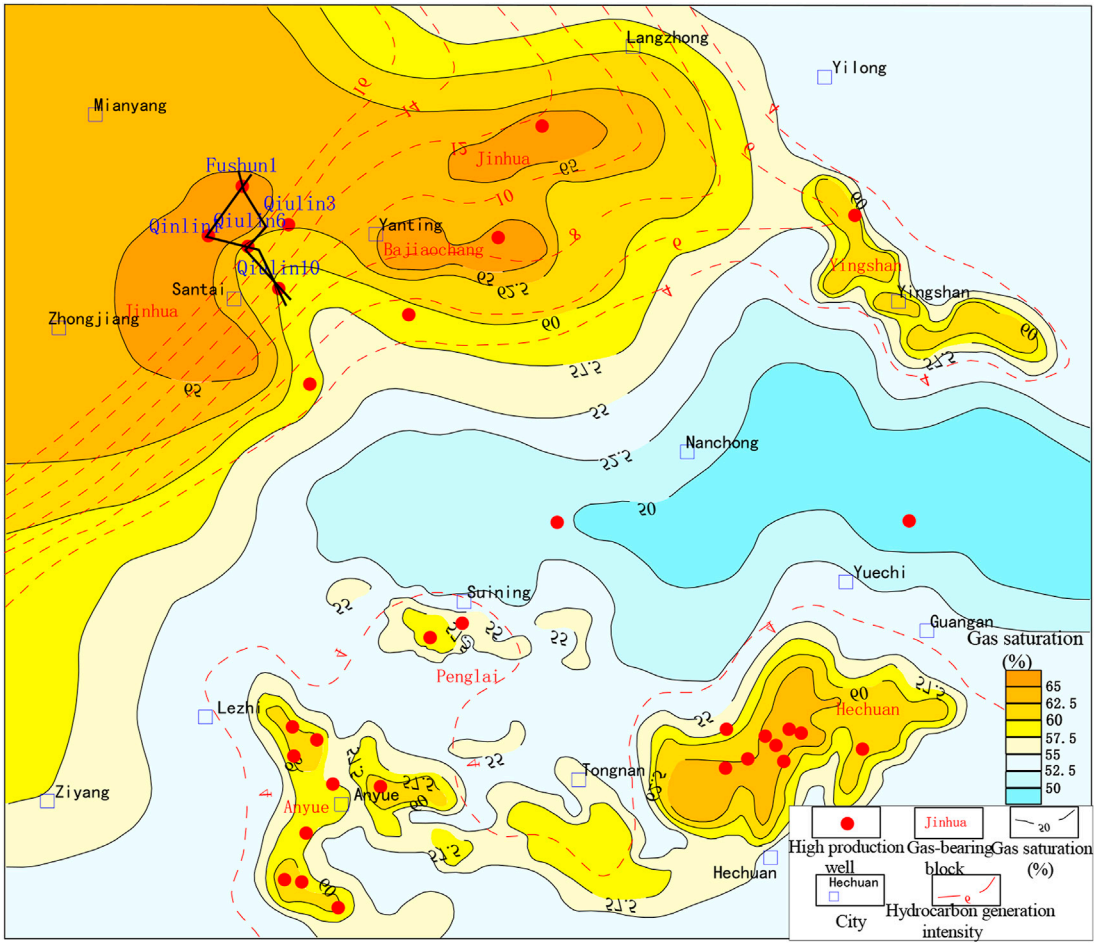

FIGURE 8
Coupling relationship between the gas saturation of the Xu 2 Member and the hydrocarbon generation intensity of the underlying Xu 1 Member in the central and western Sichuan areas.

Formation is mainly controlled by sedimentation, diagenesis and tectonic processes. Sedimentary facies, especially microfacies, are the basis for reservoir development (Yin et al., 2019; Mondal et al., 2021; Li., 2022). Distributary channels and estuary bars are favorable microfacies for reservoir development, while reservoirs in fluvial and lacustrine facies have poor physical properties. Compaction, dissolution and annular chlorite cementation are the main diagenetic processes that affect the development and evolution of reservoirs (Zhao et al., 2013; Yin et al., 2018; Zhao et al., 2020). Chlorite cemented facies and dissolution-kaolinite cemented facies are the most favorable diagenetic facies, while siliceous cemented facies and strong compaction facies are unfavorable diagenetic facies. The fractures formed by the Himalayan Movement can significantly improve the permeability of tight reservoirs.

Reservoir performance has obvious control effect on the filling degree of natural gas and the productivity of a single well (Montgomery et al., 2005; Lai et al., 2018; Hower and Groppo, 2021). Generally, the cumulative productivity of a single well exhibits a positive correlation with both reservoir thickness and porosity (Wu et al., 2015; Wu et al., 2016; Yang et al., 2021). The energy storage coefficient of high-yield wells is usually greater than 0.8, and the reservoir thickness is greater than 10 m. Under the background of low hydrocarbon generation intensity, natural gas will preferentially charge into sand bodies with good reservoir physical properties and relatively large pore diameters (0.1 μm–10 μm). Therefore, sand bodies with relatively high porosity and high permeability are the preferred targets for the preferential charging of natural gas.

According to the experimental analysis results of porosity, permeability and saturation of multiple sample points in the Xu 6 Member of Well GA108, the physical properties of the reservoir are positively correlated with gas saturations. In the 1931.00 m–1951.00 m interval, the average porosity of the

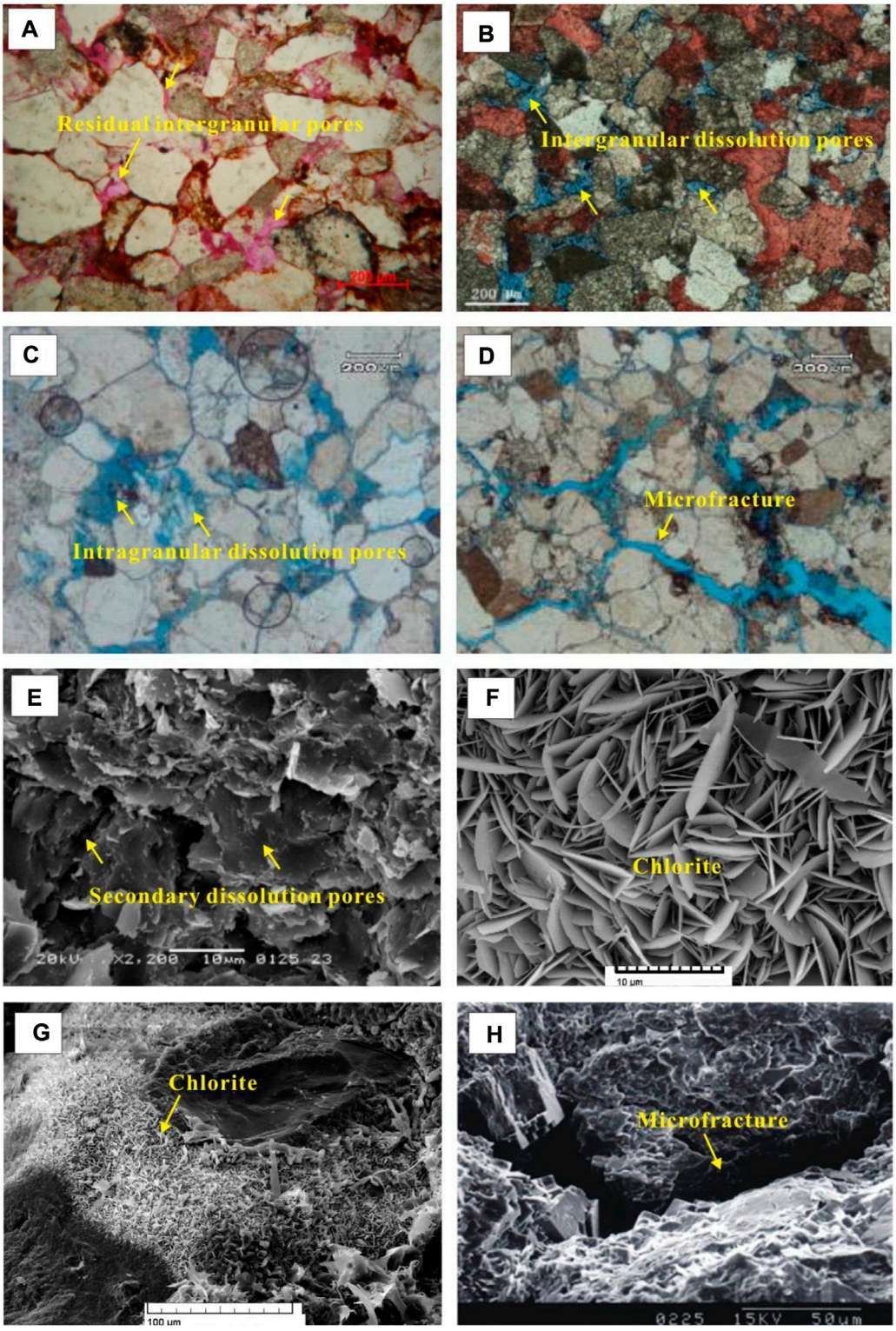

FIGURE 9
Microscopic characteristics of sandstone reservoirs in Xujiahe Formation. **(A)** Well Yu 1, 4,379.55 m, residual intergranular pores and intergranular dissolved pores; **(B)** Well Jinhua 3, 3,298.00 m, intergranular dissolved pores; **(C)** Well W6, 1,127.80 m, intergranular pores and intragranular dissolved pores; **(D)** Well Ma 14, 1,317.10 m, microfractures; **(E)** Well Qiulin 7, 3298 m, secondary dissolved pores; **(F)** Well Jiao 41, 3,076.0 m, needle-like and leaf-like chlorite; **(G)** Well Baoqian 001–16, 1,585.5 m, coniferous chlorite; **(H)** Well Guan 2, 3,665.85 m, open microfractures with dissolved surface.

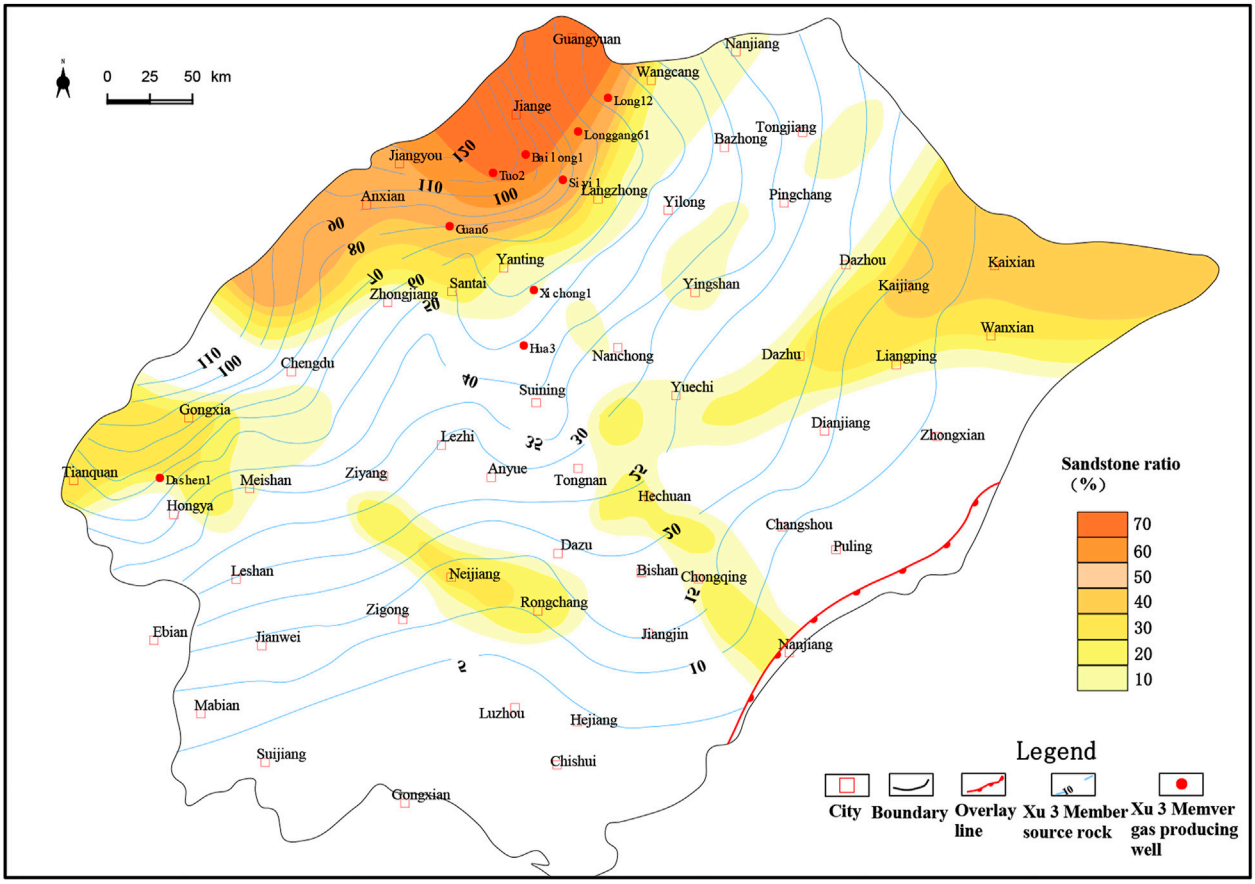

FIGURE 10
Superposition of source rock thickness and sandstone ratio of Xujiahe Formation in the Sichuan Basin.

reservoir is 8.73%, the average permeability is 0.236 $\mu m^2 \times 10^{-3}$ μm^2, and the average gas saturation is 60.73%. Obviously, good reservoir physical properties correspond to high gas saturations. However, in the 1926.22 m–1931.00 m well interval, the average porosity of the reservoir is 5.18%, the average permeability is 0.057 $\mu m^2 \times 10^{-3}$ μm^2, and the average gas saturation is only 39.68%. In addition, rock type and fractures also significantly affect the gas-bearing properties of the reservoir. The lithology of the Xujiahe Formation is mainly composed of detrital feldspar sandstone, feldspar detrital sandstone, detrital quartz sandstone and feldspar quartz sandstone. According to the observation results of 11 wells in the Guang'an Gas Field, the reservoir lithology in the wells with output greater than 2 $m^3/d \times 10^4$ m^3/d is mainly feldspar detrital sandstone and feldspar quartz sandstone. When the Xujiahe Formation reservoir is relatively tight, only the effective combination of pores and fractures can form a high-efficiency reservoir. For example, the productivity of gas layers drilling fractures of Well Y104 in the Anyue Gas Field is usually greater than 15 $m^3/d \times 10^4$ m^3/d.

5.2.3 Control of close-contact source-reservoir combination on large-scale enrichment of natural gas

The closely contacted source-reservoir assemblage has a significant controlling effect on the enrichment of natural gas in the Xujiahe Formation. Judging from the source-reservoir combination of the Xu 3 Member (Figure 10), the commercial gas wells that have been discovered so far are mainly distributed in areas with a sandstone ratio of more than 25%, while no commercial gas wells have been found in areas with a sandstone ratio of less than 25%. This is because areas with a sandstone ratio lower than 25% are usually pre-delta or lacustrine deposits, and the thickness of a single layer of sandstone is thin (1 m~3 m). Moreover, due to the large thickness of the mudstone around the sandstone, the compaction and cementation exerted on the sandstone are very strong, and the physical properties of the sandstone become very poor (Huang et al., 1996; Holt et al., 2015; Zhai et al., 2017). Therefore, the natural gas enrichment areas of the "self-generation and self-storage" source-reservoir

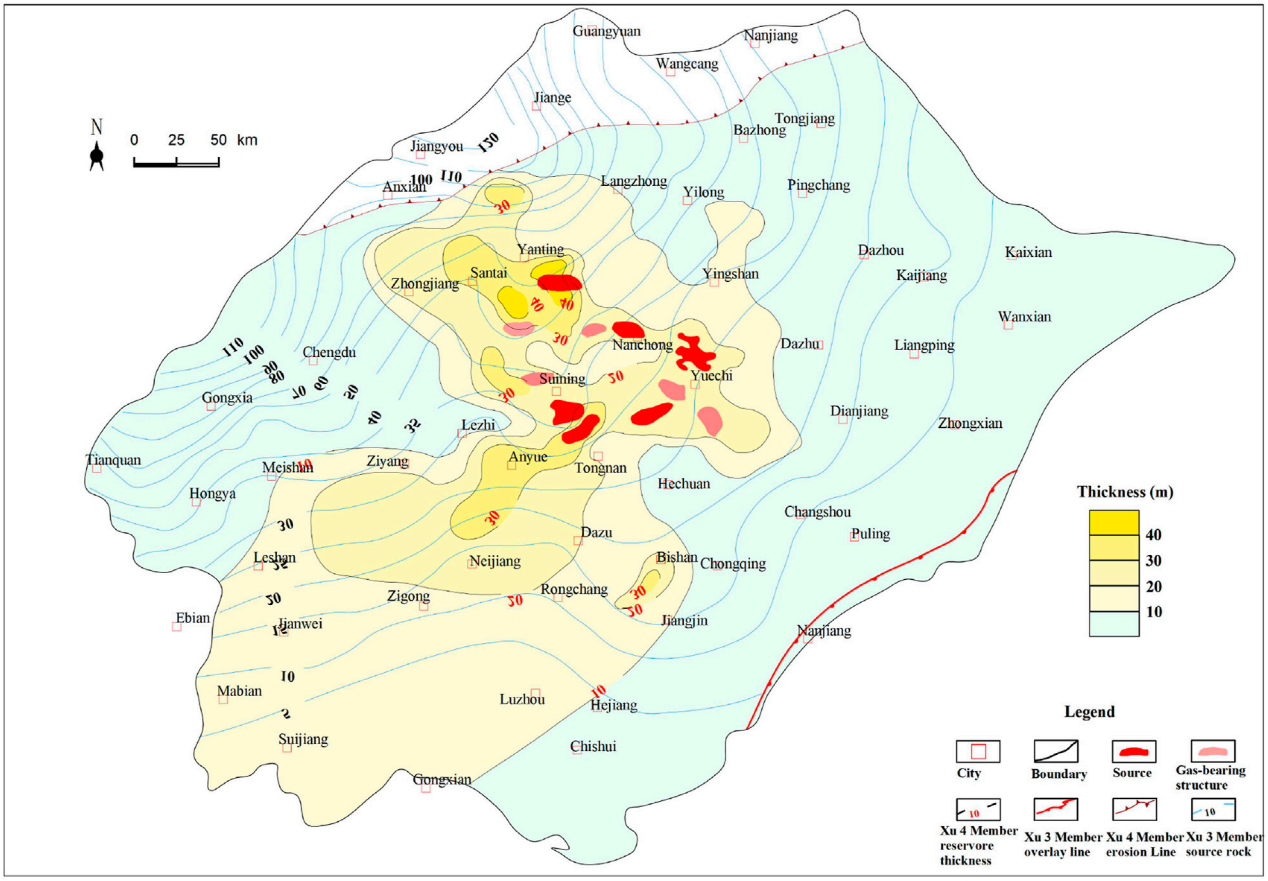

FIGURE 11
Relationship between the thickness of carbonaceous mudstone and coal seam in the Xu 3 Member and the reservoir thickness and natural gas distribution of the Xu 4 Member in the central and western Sichuan Basin.

combination in the Xu 3 Member are mainly distributed in the northwestern Sichuan area where the source and reservoir are in close contact and the sandstone ratio is greater than 25%.

The average organic carbon content of dark mudstone in the Xujiahe Formation is 1.95%, while that in the carbonaceous mudstone is generally more than 10%, and that in the coal seams is as high as 60%. The average hydrocarbon generation potentials of coal seams, carbonaceous mudstone, and dark mudstone in the Xujiahe Formation are: 97 mg/g, 15 mg/g, and 2.4 mg/g, respectively. Therefore, carbonaceous mudstone and coal seams with high organic carbon content and hydrocarbon generation potential are the main source rocks of the Xujiahe Formation. The reservoir thickness and physical properties of the Xu 4 Member gas reservoir in the Guang'an Gas Field are roughly the same as those of the Xu 6 Member. However, the movable water content of the Xu Member is generally high, and the gas production per well is very low. Then, the development of natural gas reserves in the Xu 4 Member is difficult. This is because the source rocks of the Xu 5 Member below the gas reservoir of the Xu 6 Member are a set of coal seams with an average thickness of more than 10 m. This set of coal seams is continuously distributed and the gas generation intensity is high (10 m^3/km^2 × 10^8 m^3/km^2). However, the source rocks of the Xu 3 Member below the Xu 4 Member are mainly mudstone, and the thickness of the coal seam is relatively thin, basically 3 m–5 m, and the gas generation intensity of the source rock is low. It can be seen from Figure 11 that the discovered gas reservoirs and gas-bearing structures in the Xu 4 Member in the central Sichuan Basin are mainly distributed in areas where carbonaceous mudstone and coal seams are relatively developed in the Xu 3 Member and the areas where the reservoir thickness of the Xu 4 Member is greater than 20 m. This fully shows that the natural gas enrichment areas of the source-reservoir combination of extra-source "lower generation and upper storage" are mainly distributed in the overlying reservoirs of the source rock development areas with close source-

reservoir contact and strong hydrocarbon generation intensity (Wang., 1994; Qin et al., 2019; Zhao et al., 2021).

6 Conclusion

1) The main pore types of tight sandstones in the Xujiahe Formation are intragranular dissolved pores and intergranular pores. The quality of sandstone reservoirs is controlled by sedimentation, diagenesis and tectonic processes. Underwater distributary channels and estuary bars are favorable microfacies for reservoir development. Moreover, chlorite cemented facies and dissolution-kaolinite cemented facies are the most favorable diagenetic facies.

2) The natural gas composition and carbon isotope characteristics of the Xujiahe Formation are significantly different in different intervals of the same gas field and the same interval of adjacent gas fields. This shows that the natural gas has no obvious vertical mixing and lateral migration, and it has the distribution characteristics of "local enrichment". Natural gas is preferentially charged in the feldspar lithic sandstones and feldspar quartz sandstones with large thickness and good physical properties by means of short-range migration.

3) On the whole, four sets of extra-source "lower generation and upper storage" assemblages and two sets of "self-generation and self-storage" source-reservoir assemblages are developed in the Xujiahe Formation. The areas with close source-reservoir contact and high hydrocarbon generation intensity are high-quality reservoir development areas.

Data availability statement

The original contributions presented in the study are included in the article/supplementary material, further inquiries can be directed to the corresponding authors.

Author contributions

KT is responsible for the idea and writing of this paper and JY, JC, DT, YQ, and QW areresponsible for the drawing and experimental testing.

Conflict of interest

Authors KT, JY, JC, YQ, and QW were employed by the Research Institute of Petroleum Exploration and Development Northwest Branch and author DT was employed by the Northwest Sichuan Gas Mine of PetroChina Southwest Oil and Gas Field Company.

Publisher's note

All claims expressed in this article are solely those of the authors and do not necessarily represent those of their affiliated organizations, or those of the publisher, the editors and the reviewers. Any product that may be evaluated in this article, or claim that may be made by its manufacturer, is not guaranteed or endorsed by the publisher.

References

Dai, J. (2014). *Giant coal-derived gas fields and the source in China*. Beijing: Science Press, 420–424. doi:10.1016/b978-0-12-805093-4.00001-x

Dai, J., Ni, Y., and Zou, C. (2012). Stable carbon and hydrogen isotopes of natural gases sourced from the Xujiahe Formation in the Sichuan Basin, China. *Org. Geochem.* 43 (2), 103–111. doi:10.1016/j.orggeochem.2011.10.006

Dai, J., Qin, S., and Tao, S. (2005). Developing trends of natural gas industry and the significant progress on natural gas geological theories in China. *Nat. Gas. Geosci.* 16 (2), 127–142. doi:10.3969/j.issn.1672-1926.2005.02.001

Dai, J. X., Ni, Y. Y., and Zong, N. (2009). Carbon isotope features of al-kane gases in the coal measures of the Xujiahe Formation inthe Sichuan Basin and their significance to gas-source correlation. *Oil Gas Geol.* 30 (5), 519–529. doi:10.11743/ogg20090501

Du, H., Wang, W., Shi, Z., Tan, J., Cao, H., and Yin, X. (2019). Geochemical characteristics and source of natural gas of the upper triassic Xujiahe Formation in malubei are a,northeastern Sichuan Basin. *Oil Gas Geol.* 40 (1), 34–38. doi:10.11743/ogg20190104

Du, M., Wang, S., Wan, M., Zhang, Q., and Wang, L. (2007). Geochemical characteristics and genetic types of natural gas in upper triassic Xujiahe Formation, Sichuan Basin. *Nat. Gas Explor. Dev.* 30 (2), 26–29.

Fan, R., Zhou, H., and Cai, K. (2005). Carbon isotopic geochemistry and origin of natural gases in the southern part of the Western Sichuan Depression. *Acta Geosci. Sin.* 26 (2), 157–162. doi:10.3321/j.issn:1006-3021.2005.02.009

Hao, B., Hu, S., and Huang, S. (2016). Geochemical characteristics and its significance of reservoir bitumen of longwangmiao Formation in moxi area, Sichuan Basin. *Geoscience* 30 (3), 614–626.

Holt, R. M., Fjær, E., Stenebråten, J. F., and Nes, O. M. (2015). Brittleness of shales: Relevance to borehole collapse and hydraulic fracturing. *J. Petroleum Sci. Eng.* 131, 200–209. doi:10.1016/j.petrol.2015.04.006

Hower, J. C., and Groppo, J. G. (2021). Rare Earth-bearing particles in fly ash carbons: Examples from the combustion of eastern Kentucky coals. *Energy Geosci.* 2 (2), 90–98. doi:10.1016/j.engeos.2020.09.003

Hu, G., Wang, W., and Liao, F. (2012). Geochemical characteristics and its influencing factors of light hydrocarbon in coal-derived gas: A case study of Sichuan Basin. *Acta Petrol. Sin.* 28 (3), 905–916. doi:10.3799/dqkx.2021.033

Hu, G., and Xie, Y. (1997). *Carboniferous gas fields in high steep structure of eastern Sichuan*. BeiJing: Petroleum industry press, 47–62.

Hu, W., Zhu, Y., and Li, Y. (2014). Geochemical charac-teristics and origin of natural gases from terrestrial strata inYuanba area of the northeastern Sichuan Basin. *J. Zhejiang Univ. Sci. Ed.* 41 (4), 468–476. doi:10.3785/j.issn.1008-9497.2014.04.020

Huang, J., Chen, S., Song, J., Wang, L., Gou, X., Wang, T., et al. (1997). Hydrocarbon source systems and formation of gas fields in Sichuan Basin. *Sci. China Ser. D-Earth Sci.* 40 (6), 32–42. doi:10.1007/BF02878579

Jiu, K., Ding, W. L., Huang, W. H., You, S. G., Zhang, Y. Q., and Zeng, W. T. (2013). Simulation of paleotectonic stress fields within Paleogene shale reservoirs and prediction of favorable zones for fracture development within the Zhanhua

Depression, Bohai Bay Basin, east China. *J. Petroleum Sci. Eng.* 110, 119–131. doi:10.1016/j.petrol.2013.09.002

Lai, J., Wang, G. W., Wang, S., Cao, J. T., Li, M., Pang, X. J., et al. (2018). Review of diagenetic facies in tight sandstones: Diagenesis, diagenetic minerals, and prediction via well logs. *Earth-Science Rev.* 185, 234–258. doi:10.1016/j.earscirev.2018.06.009

Lan, S. R., Song, D. Z., Li, Z. L., and Liu, Y. (2021). Experimental study on acoustic emission characteristics of fault slip process based on damage factor. *J. Min. Strata Control Eng.* 3 (3), 033024. doi:10.13532/j.jmsce.cn10-1638/td.20210510.002

Li, H. (2022). Research progress on evaluation methods and factors influencing shale brittleness: A review. *Energy Rep.* 8, 4344–4358. doi:10.1016/j.egyr.2022.03.120

Li, Y. (2021). Mechanics and fracturing techniques of deep shale from the Sichuan Basin, SW China. *Energy Geosci.* 2 (1), 1–9. doi:10.1016/j.engeos.2020.06.002

Liang, Y., Li, Y., Fu, X., Yuan, X., Yang, J., and Zheng, J. (2006). Origin and wholehydrocarbon geochemical characteristics of oil and gas from Xujiahe group of Chuanzhong-Chuannan Transitional Belt. *Nat. Gas. Geosci.* 17 (4), 593–596. doi:10.3969/j.issn.1672-1926.2006.04.034

Liao, F., Yu, C., and Wu, W. (2014). Stable carbon and hydrogen isotopes of natural gas from the Zhongba Gasfield inthe Sichuan Basin and implication for gas-source correlation. *Nat. Gas. Geosci.* 25 (1), 79–86. doi:10.11764/j.issn.1672-1926.2014.01.0079

Liu, Q., Dai, J., Li, J., and Zhou, Q. (2008). Hydrogen isotope composition of natural gases from the Tarim Basin and its indication of depositional environments of the source rocks. *Sci. China Ser. D-Earth Sci.* 51 (12), 300–311. doi:10.1007/s11430-008-0006-7

Luo, Y., Huang, H., Jakobsen, M., Yang, Y., Zhang, J., and Cai, Y. (2019). Prediction of porosity and gas saturation for deep-buried sandstone reservoirs from seismic data using an improved rock-physics model. *Acta Geophys.* 67, 557–575. doi:10.11743/ogg1995031510.1007/s11600-019-00274-6

Mondal, S., Chatterjee, R., and Chakraborty, S. (2021). An integrated approach for reservoir characterisation in deep-water krishna-godavari basin, India: A case study. *J. Geophys. Eng.* 18 (1), 134–144. doi:10.1093/jge/gxab002

Montgomery, S. L., Jarvie, D. M., Bowker, K. A., and Pollastro, R. M. (2005). Mississippian Barnett Shale, Fort Worth basin, north-central Texas: Gas-shale play with multi-trillion cubic foot potential. *Bulletin* 89 (2), 155–175. doi:10.1306/0209060513210.1306/09170404042

Morozov, V. P., Jin, Z., Liang, X., Korolev, E. A., Liu, Q., Kolchugin, A. N., et al. (2021). Comparison of source rocks from the lower silurian longmaxi Formation in the yangzi platform and the upper devonian semiluksk Formation in east European platform. *Energy Geosci.* 2 (1), 63–72. doi:10.1016/j.engeos.2020.10.001

Ni, Y., Liao, F., and Yao, L. (2019). Stable hydrogen isotopic characteristicsof natural gas from the Xujiahe Formation in the central Sichuan Basin and its implications for water salinization. *Nat. Gas. Geosci.* 30 (6), 880–896. doi:10.11764/j.issn.1672-1926.2019.05.015

Ni, Y., Ma, Q., Ellis, G., Dai, J., Katz, B., Zhang, S., et al. (2011). Fundamental studies on kinetic isotope effect (KIE) of hydrogen isotope fractionation in natural gas systems. *Geochimica Cosmochimica Acta* 75 (10), 2696–2707. doi:10.1016/j.gca.2011.02.016

Nicula, A., Ionescu, A., Pop, I., Roba, C., Forray, F. L., Orăşeanu, I., et al. (2021). Geochemical features of the thermal and mineral waters from the apuseni mountains (Romania). *Front. Earth Sci.* 9, 1–8. doi:10.3389/feart.2021.64817910.1016/j.jvolgeores.2019.02.014

Qin, S., Huang, C., and Zhang, B. (2019). Relationships of the iCa/nC4 and iCs/nCs ratios with maturity of coal-derived gases of Triassic Xujiahe Formation in central Sichuan Basin, SW China. *Petroleum Explor. Dev.* 46 (3), 474–481. doi:10.1016/S1876-3804(19)60030-3

Saein, A., and Riahi, Z. (2017)., 156. Iran, 1092–1104. doi:10.1017/S001675681700034610.1017/S0016756817000346Controls on fracture distribution in Cretaceous sedimentary rocks from the Isfahan region, Iran*Geol. Mag.*

Wan, M., Xie, B., Chen, S., Zou, C., Zhang, Q., and Ran, Y. (2012). Hydrocarbon source correlation of the upper Triassic reservoirs in the Sichuan Basin. *Nat. Gas. Ind.* 32 (3), 22–24.

Wang, H., Shi, Z., Zhao, Q., Liu, D., Sun, S., Guo, W., et al. (2020). Stratigraphic framework of the Wufeng-Longmaxi shale in and around the Sichuan Basin, China: Implications for targeting shale gas. *Energy Geosci.* 1 (3–4), 124–133. doi:10.1016/j.engeos.2020.05.006

Wang, S. (1994). Chemical characteristics of jurassic-sinian gasin Sichuan Basin. *Nat. Gas. Ind.* 14 (6), 1–5.

Wu, X., Liu, G., and Liu, Q. (2015). Geochemicalcharacteristics and origin of natural gas in the Xujiahe forma-tion in yuanba-tongnanba area of Sichuan Basin. *Oil Gas Geol.* 36 (6), 955–962. doi:10.11743/ogg20150610

Wu, X., Wang, P., and Liu, Q. (2016). The source of natural gas reservoir in the 5th member of the upper triassic Xujiahe Formation in xinchang gas field, the western sichuan depression and its implication. *Nat. Gas. Geosci.* 27 (8), 1409–1418.

Xiao, Z., Xie, Z., and Li, Z. (2008). Isotopic characteristics ofnatural gas of Xujiahe Formation in southern and middle of Si-chuan Basin. *Geochimica* 37 (3), 245–250. doi:10.3863/j.issn.1000-2634.2008.04.007

Yang, J. X., Luo, M. K., Zhang, X. W., Huang, N., and Hou, S. J. (2021). Mechanical properties and fatigue damage evolution of granite under cyclic loading and unloading conditions. *J. Min. Strata Control Eng.* 3 (3), 033016. doi:10.13532/j.jmsce.cn10-1638/td.20210510.001

Yin, S., Lv, D. W., and Ding, W. L. (2018). New method for assessing microfracture stress sensitivity in tight sandstone reservoirs based on acoustic experiments. *Int. J. Geomechanics* 18, 1–16. doi:10.1061/(ASCE)GM.1943-5622.0001100

Yin, S., Xie, R. C., Wu, Z. H., Liu, J., and Ding, W. L. (2019). *In situ* stress heterogeneity in a highly developed strike-slip fault zone and its effect on the distribution of tight gases: A 3D finite element simulation study. *Mar. Petroleum Geol.* 99 (1), 75–91. doi:10.1016/j.marpetgeo.2018.10.007

Yu, C., Gong, D., and Huang, S. (2014). Geochemical char-acteristics of carbon and hydrogen isotopes for the Xujiahe Formation natural gas in Sichuan Basin. *Nat. Gas. Geosci.* 25 (1), 87–97.

Zhai, L., Ni, Y., and Wu, C. (2017). Geochemical characteristics of the natural gas from the Xujiahe Formation in the central Sichuan Basin, China. *Nat. Gas. Geosci.* 28 (4), 539–549. doi:10.11764/j.issn.1672-1926.2017.02.016

Zhang, L., Liu, D., Gao, Y. J., and Zhang, M. (2021). Geochemical characteristics of gas and flowback water in lake facies shale: A case study from the junggar basin, China. *Front. Earth Sci.* 9, 1–14. doi:10.3389/feart.2021.63589310.3389/feart.2021.635893

Zhao, K. K., Jiang, P. F., Feng, Y. J., Sun, X. D., Cheng, L. X., and Zheng, J. W. (2021). Investigation of the characteristics of hydraulic fracture initiation by using maximum tangential stress criterion. *J. Min. Strata Control Eng.* 3 (2), 023520. doi:10.13532/j.jmsce.cn10-1638/td.20201217.001

Zhao, W., Bian, C., and Xu, Z. (2013). Similarities and differences between natural gas accumulations in Sulige gas field in Ordos Basin and Xujiahe gas field in central Sichuan Basin. *Petroleum Explor. Dev.* 40 (4), 400–406. doi:10.1016/S1876-3804(13)60054-3

Zhao, Z., Wu, K., Fan, Y., Guo, J., Zeng, B., and Yue, W. (2020). An optimization model for conductivity of hydraulic fracture networks in the Longmaxi shale, Sichuan Basin, Southwest China. *Energy Geosci.* 1 (1–2), 47–54. doi:10.1016/j.engeos.2020.05.001

Zhou, G., Wei, G., and Hu, G. (2019). Differences of continental hydrocarbon system between longgang and yuanba gasfields in Sichuan Basin. *Nat. Gas. Geosci.* 30 (6), 809–816. doi:10.3787/j.issn.1000-0976.2011.10.004

frontiers | Frontiers in Earth Science

TYPE Original Research
PUBLISHED 23 September 2022
DOI 10.3389/feart.2022.1011219

OPEN ACCESS

EDITED BY
Hu Li,
Southwest Petroleum University, China

REVIEWED BY
Haiyan Wu,
Chang'an University, China
Li Keyong,
Xi'an University of Science and Technology, China
Guo Yanqin,
Xi'an Shiyou University, China

*CORRESPONDENCE
Xinming Sun,
296027311@qq.com
Xuejiao Yuan,
yxjxx21@163.com

SPECIALTY SECTION
This article was submitted to Structural Geology and Tectonics, a section of the journal Frontiers in Earth Science

RECEIVED 03 August 2022
ACCEPTED 22 August 2022
PUBLISHED 23 September 2022

CITATION
Wei X, Sun X, Yuan X and Yang Y (2022), Characteristics and prediction of permian tight glutenite reservoirs in dinan 15 well block, junggar basin. *Front. Earth Sci.* 10:1011219. doi: 10.3389/feart.2022.1011219

Characteristics and prediction of permian tight glutenite reservoirs in dinan 15 well block, junggar basin

Xin Wei[1], Xinming Sun[1]*, Xuejiao Yuan[2,3]* and Yiming Yang[2,3]

[1]Karamay Vocational & Technical College, Karamay, China, [2]School of Geoscience and Technology, Southwest Petroleum University, Chengdu, China, [3]Natural Gas Geology Key Laboratory of Sichuan Province, Southwest Petroleum University, Chengdu, China

Glutenite reservoirs are characterized by rapid lateral change, strong heterogeneity, and complex main controlling factors. This research aims to identify macro and micro characteristics of glutenite reservoirs and establish criteria for identifying favorable reservoirs studies. To this end, the tight sandy conglomerate of the Upper Wuerhe Formation in the Permian Upper Wuerhe Formation in the Dinan 15 well area of the eastern slope of the Dongdaohaizi sag in the Junggar Basin is studied. The core observation, physical property analysis, sensitivity analysis, casting thin section, scanning electron microscope and logging data are adopted to comprehensively analyze the characteristics of glutenite reservoirs. By integrating various reservoir characteristic parameters, this work constructed a new set of reservoir evaluation criteria to predict favorable areas for the Upper Wuerhe Formation in Dongdaohaizi Sag. The results show that the lithology of the Upper Wuerhe Formation in the Dinan 15 well area is dominated by gray glutenite; the reservoir is an ultra-low porosity and ultra-low permeability reservoir with moderately weak water sensitivity and weak velocity sensitivity. The reservoir space types of the layers are mainly intergranular pores; the shape of the mercury intrusion curve and the pore throat radius distribution of the samples show that the reservoir is skewed, poorly sorted, and has the characteristics of small pores and thin throats. This work constructed evaluation criteria for reservoirs from I to III by utilizing lithology, physical properties, sensitivity, reservoir space type, and microstructural characteristics as key parameters. The favorable reservoir distribution area is mainly located in the west of the block, which is the focus of the next exploration of the Upper Wuerhe Formation area. The research results improved understanding of glutenite reservoir characteristics and will serve as significant guidance for the oil and gas exploration in the Dinan 15 well area.

KEYWORDS

reservoir characteristics, reservoir prediction, upper wuerhe formation, permian, dongdaohaizi sag, junggar basin, glutenite reservoirs

1 Introduction

Glutenite reservoirs are characterized by rapid lateral change, strong heterogeneity, and complex main controlling factors. Classifying their quality and predicting productivity are difficult, which have become a research hotspot in recent years (Jin et al., 2022). Glutenite reservoirs result from the deposition of near-source sediment and the mixed accumulation of coarse components such as sand and gravel (Qu et al., 2017; Lin et al., 2019; Pang et al., 2020). The complexity of the reservoir makes it difficult to select and evaluate high-quality glutenite reservoirs, and traditional qualitative and quantitative analyses are limited in this regard (Qu et al., 2017). At present, most studies on glutenite reservoirs focus on petrology, sedimentology, pore structure, etc., (Liu et al., 2018; Bian et al., 2020; Yang et al., 2020). Few studies have explored how reservoir capabilities affect fluids and the sensitivities of both acidity and alkalinity from the perspective of reservoir sensitivity. Besides, China has achieved breakthrough regarding oil and gas exploration in the glutenite reservoirs in Junggar Basin, Bohai Bay Basin, Songliao Basin, Erlian Basin, etc., (Wang et al., 2020a; Zhou et al., 2020; Hu et al., 2021a; Hu et al., 2021b; Lu et al., 2021). The oil and gas exploration in the representative Permian-Triassic glutenite reservoirs in Junggar Basin is so groundbreaking that it has become the current research focus of petroleum geology(Kuang et al., 2014; Zhi et al., 2018) Up to now, many large-scale oil and gas reservoirs containing glutenite as reservoirs have been identified in the Permian strata of the Junggar Basin, especially the identification of the billion-ton-grade glutenite reservoirs of oil and gas in the Baikouquan Formation, Mahu Sag, Junggar Basin, which has promoted the general research in the Permian and Triassic glutenite reservoirs in Junggar Basin (Zhi, 2016; Li et al., 2018; Xiao et al., 2019; Hu et al., 2020; Li, 2022). New progress in oil and gas exploration was realized in the glutenite reservoirs of the Permian Upper Wuerhe Formation of Shawan Sag, Dongdaohaizi Sag and Fukang Sag after the identification of the glutenite reservoirs in the Triassic Baikouquan Formation of Mahu Sag, further proving the magnificent exploration potential of glutenite reservoirs (Du et al., 2019; Zhao et al., 2019; Li et al., 2020; Gao, 2021; Guan et al., 2021). Additionally, Dongdaohaizi Sag is one of the important hydrocarbon-rich sags of the Junggar Basin, while the Permian Upper Wuerhe Formation has developed fan-delta glutenite reservoirs and is the important oil-bearing series of Dongdaohaizi Sag since it is close to the source rocks of the underlying Pingdiquan Formation and has developed faults connected with source rocks (Zhang, 2014; Jin et al., 2015).

The oil and gas exploration in Dongdaohaizi Sag with the Pingdiquan Formation as the source began from the 1990s until relatively significant breakthrough was realized in oil and gas exploration in 2013 when the glutenite reservoirs of the Upper Wuerhe Formation DN8 Well were deployed by following the idea of "separating blocks and controlling reservoirs", but a series of exploration of preliminary prospecting wells and appraisal wells that was deployed sequentially failed to achieve satisfactory results. According to the research of fine sedimentary paleogeomorphology (Zou et al., 2016; Xu et al., 2017; Cai et al., 2019; Wang et al., 2022), the Permian Upper Wuerhe Formation is regressive fan delta sedimentation, with wide distribution of favorable facies zones in the fan delta front. In 2019, DN14 and DN15 wells were deployed in the optimal favorable facies zones of the Upper Wuerhe Formation fan delta front, resulting in highly productive hydrocarbon flow, which is the evidence of the magnificent exploration potential of the Upper Wuerhe Formation, Dongdaohaizi Sag. Since the Upper Wuerhe Formation has been cumulatively influenced by multi-stage tectonic movement, featuring complex geological characteristics, the glutenite reservoirs and their prediction need to be further studied (Qu et al., 2017; Hu et al., 2021a).

According to previous studies, the porosity and permeability of a glutenite reservoir is generally less than 10.0% and 5.000 mD, respectively, featuring low porosity and permeability (Liu, 2015; Xu et al., 2017; Li et al., 2019; Wang et al., 2022), and is a near-source melange sedimentary system, with complex lithological compositions, diverse textures and structures of rocks, and frequent change in plane characteristics of lithofacies (Zou et al., 2016; Jin et al., 2017; Jin et al., 2022). Since diagenesis and pore evolution have critical influence over the physical characteristics of reservoirs (Fu et al., 2019; Lin et al., 2019), the characteristics of the glutenite reservoirs of the Permian Upper Wuerhe Formation on the eastern slope of Dongdaohaizi Sag, Junggar Basin have been researched to some extent, but studies like general analysis and classified evaluations on the characteristics of favorable reservoirs and through based on various characteristic parameters of reservoirs are quite rare. The study in this paper took the Permian Upper Wuerhe Formation on the eastern slope of Dongdaohaizi Sag, Junggar Basin as the example, and carried out a prediction of favorable areas of the Upper Wuerhe Formation in Dongdaohaizi Sag through a general analysis on the glutenite reservoir characteristics in combination with various parameters of reservoir characteristics using core observation, physical characteristic analysis, sensitivity analysis, casting thin section, scanning electronic microscopy (SEM), well logging, etc., in the hope of providing guidance for the exploration and development of the tight glutenite reservoirs in the area mentioned hereinabove.

2 General geological situation

Junggar Basin, located in the western China, is a typical large-scale hydrocarbon-bearing superimposed sedimentary basin in the western China (Yang et al., 2020; Zhang et al., 2021), with the geographic coordinates of E81°C–92°C, N43°C–48°C. It is

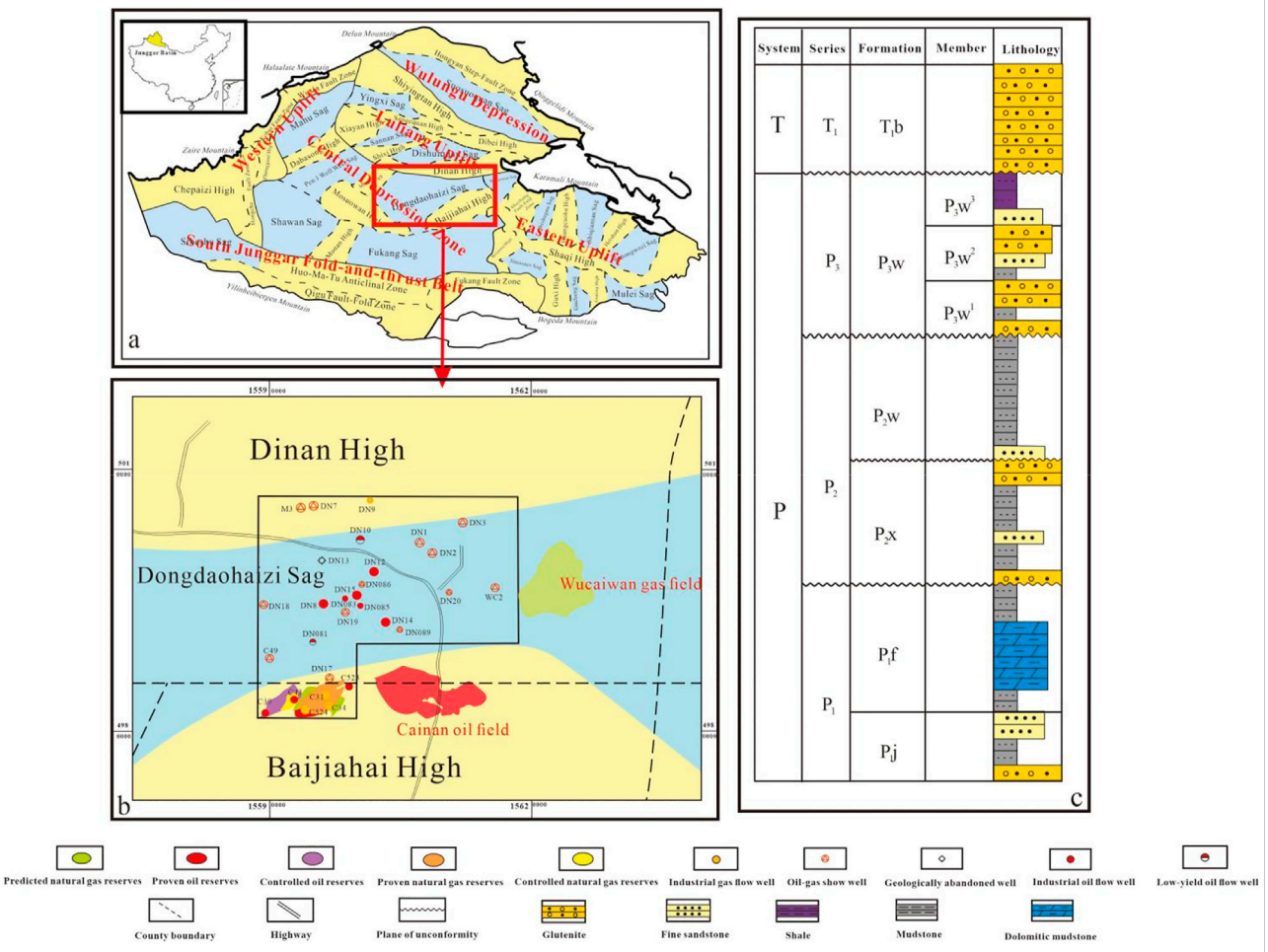

FIGURE 1
Basic regional pattern and comprehensive stratum column chart of study area. **(A)** Geographic location and Paleogene structure block plan of Dongdaohaizi Sag of the central depression, Junggar Basin; **(B)** Location of the Dinan 15 well in the study area; **(C)** Comprehensive column chart of the Upper Permian series, Junggar Basin.

surrounded by fold mountain systems, with the Hala'alat Mountain and the Zaire Mountain to the northwest, the Altai Mountain and the Kelameili Mountain to the northeast, and the northern Tianshan Mountains to the south. The plane shape of the basin is an approximate triangle, wide in the south and narrow in the north, about 700 km from west to east and about 370 km from north to south, with an area of 13.6×10^4 km^2. Junggar Basin consists of multiple tectonic units, including 6 primary tectonic units, i.e., Wulungu Sag, anteclise uplift, central depression, eastern uplift, western uplift, and northern Tianshan piedmont thrust, which can be further classified as 44 secondary tectonic units (Zhang, 2019; Zhang et al., 2020a; Zhang et al., 2022a; Zhang et al., 2022b).

Dongdaohaizi Sag, located in the northeast of the central depression of Junggar Basin, is between the Dishuiquan fault zone and the northern Dongdaohaizi fault zone, extending in a belt shape along the northeast-southwest direction and covering an area of 7,000 km^2 or so (Figure 1A). It is paleogeomorphologically an asymmetric double-fault graben-like sag and has a relatively simple internal structure, which is dominated by traction hook-shaped low-amplitude structures of downthrown blocks of faults. Dongdaohaizi Sag starts from the southern Dishuiquan fault and the Dinan uplift in the north, connected with the Baijiahai fault and the Baijiahai uplift in the south, bounded with No. 1 and 2 Faults of the northern Mosuowan, the Mosuowan uplift, and the northern Mosuowan uplift in the west, and connected with Wucaiwan Sag in the east (Ding, 2016; Zhang et al., 2022c; Zhang et al., 2022d). Additionally, the strata of Dongdaohaizi Sag are relatively completely developed, consisting of limestone stratum, Permian stratum, Triassic stratum, Jurassic stratum, Cretaceous stratum and Cenozoic stratum distributed from top

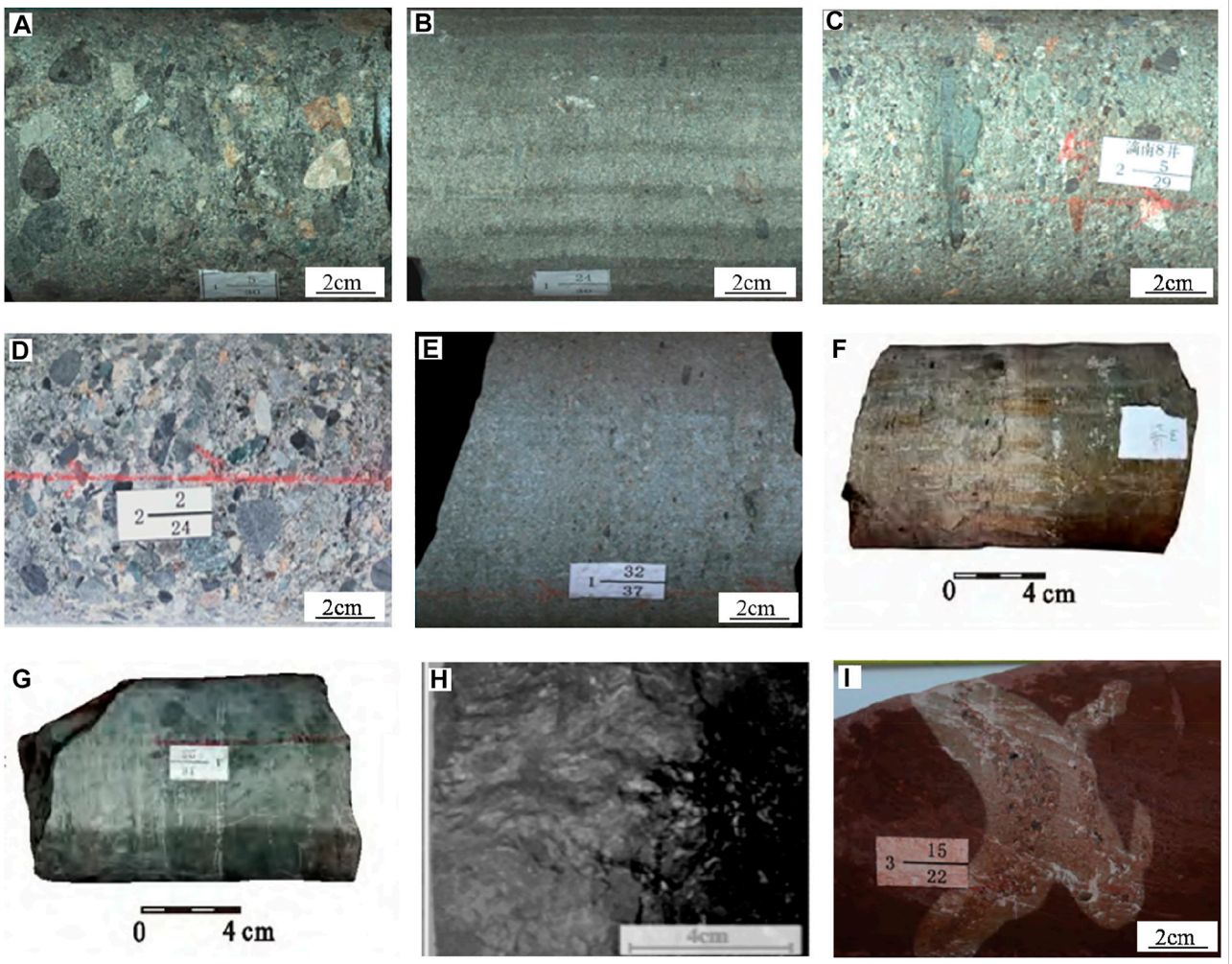

FIGURE 2
Basic lithological characteristics of the Upper Wuerhe Formation in the study area. **(A)** Glutenite, Dinan 19 well, P_3w_1, 3,922.37 m–3,922.52 m; **(B)** Pebbly sandstone, Dinan 19 well, P_3w_1, 3,922.37 m–3,922.52 m; **(C)** Glutenite, Dinan 15 well, P_3w_2, 3,732.99 m–3,733.17 m; **(D)** Glutenite, Dinan 15 well, P_3w_2, 3,792.18 m–3,792.36 m; **(E)**. Pebbly sandstone, Dinan 15 well, P_3w_2, 3,738.56 m–3,738.65 m; **(F)** Medium–fine sandstone, J202 well -13/27 (Zou et al., 2021); **(G)** Mudstone, siltstone, K82 well 4–16/26(Zou et al., 2021); **(H)** Brown mudstone, MH014 well, 3,736.98 m(Zhang et al., 2020b); **(I)** Mudstone, Dinan 11 well, P_3w_3, 4,603.63 m–4,603.81 m(Hu et al., 2021b).

to bottom. Among them, the Permian stratum has developed the Xiazijie Formation, the Lower Wuerhe Formation and the Upper Wuerhe Formation (Figure 1C). The early–middle Permian is the sag-filling sedimentation stage, and the Xiazijie Formation (P_2x) is a set of significantly thick greyish brown and brownish grey glutenite mixed with minor grey and brownish grey mudstone and sandstone. The Lower Wuerhe Formation (P_2w) is a set of grey and dark grey mudstone and sandy mudstone mixed with greyish green and brownish grey glutenite and lime mudstone. The dark mudstone rich in alga has formed the high-quality source rocks close to the source reservoirs of Dongdaohaizi Sag. Vertically, the contact between the Upper Wuerhe Formation and the overlying Baikouquan Formation is unconformable, so is the contact between the Upper Wuerhe Formation and the underlying Lower Wuerhe Formation (Feng, 2017; Wang J. et al., 2020; Li, 2022). The Upper Wuerhe Formation has developed large-scale regressive fan delta sedimentation, while the thick-bedded sandstone of the Wuerhe Formation Section I, the thin-bedded sandstone of the Wuerhe Formation Section II and the mudstone of the Wuerhe Formation Section III have formed a good reservoir cap combination and provide excellent geological conditions for the formation of large-area lithology-strata hydrocarbon reservoirs. In the study area of this paper, the regional structure of the Dinan 15 well block, located on the eastern slope of Dongdaohaizi Sag of the central depression, Junggar Basin, is administratively governed by Fuhai County, Altay Prefecture, Xinjiang Uygur Autonomous Region, about 6 km to the Cainan oilfield in the south, about 24 km to the

TABLE 1 Classification standard for physical characteristics of clastic rock reservoirs (by national reserves committee, 1997).

Reservoir classification	Porosity Φ(%)	Permeability K(× 10 μm$^{2-3}$ μm^2)
Super-high porosity and high permeability	$\Phi \geq 30$	$K \geq 2000$
High porosity and permeability	$25 \leq \Phi < 30$	$500 \leq K < 2000$
Medium porosity and permeability	$15 \leq \Phi < 25$	$50 \leq K < 500$
Low porosity and permeability	$10 \leq \Phi < 15$	$5 \leq K < 50$
Super-low porosity and low permeability	$\Phi < 10$	$K < 5$

Wucaiwan gas field in the east, and about 18 km to the Dishuiquan oilfield in the northeast (Figure 1B). The earth surface in this area is desert, with flat terrain, and has a ground elevation of 670 m–705 m and an average ground elevation of 691.7 m.

3 Fine-grained sedimentary rock reservoir characteristics

3.1 Lithological characteristics

The Upper Wuerhe Formation can be divided into three sections, i.e., P_3w_1, P_3w_2, and P_3w_3 from top to bottom. According to the photos of the cores from the Upper Wuerhe Formation, the lithology of P_3w_2 and P_3w_1 of the Upper Wuerhe Formation is respectively dominated by glutenite, followed by pebbly sandstone (Figure 2). Among the two sections, the Upper Wuerhe Formation P_3w_1 features fan delta plain facies and is lithologically dominated by grey glutenite, mixed with thin-bedded silty mudstone, poor in reservoir characteristics, and 50 m–110 m thick, while the Upper Wuerhe Formation P_3w_2 features fan delta front facies and is lithologically dominated by grey glutenite and interbedding of pebbly sandstone and brown mudstone, and thus is the main section of high quality reservoir development, with the thickness of 110 m–150 m.

3.2 Physical characteristics

In order to identify the physical characteristics of the Upper Wuerhe Formation glutenite reservoirs, analysis was conducted on 420 samples of Section II, the Upper Wuerhe Formation and 204 samples of Section I, the Upper Wuerhe Formation both collected from Dinan 15 well. The reservoir porosity and permeability of Section I, the Upper Wuerhe Formation are generally less than 8% and lower than 2.56 μm^2 × 10^{-3} μm^2, respectively, while those of Section II, the Upper Wuerhe Formation are generally less than 12% and lower than 5 × 10^{-3} μm^2, respectively. According to the classification standard for physical characteristics of clastic rock reservoirs (Table 1), generally speaking, the Upper Wuerhe Formation reservoirs in the study area are classified as super-low porosity and permeability reservoirs (Liu, 2015; Kang et al., 2019; Huang et al., 2020; Xiao et al., 2020).

According to the histograms of porosity and permeability of Section I, the Permian Upper Wuerhe Formation of Dinan 15 well (Figures 3A–D), the range, median and average of the porosity of 74 reservoir samples from Section I, the Upper Wuerhe Formation are 2.2%–11.6%, 4.61%, and 4.95%, while the range, median and average of the permeability of 65 reservoir samples from the same section are 0.01 μm^2–2.33 μm^2 × 10^{-3} μm^2, 0.028 μm^2 × 10^{-3} μm^2 and 0.058 μm^2 × 10^{-3} μm^2, respectively. Therefore, the reservoirs in this section feature super-low porosity and permeability. The range, median and average of the porosity of 35 oil reservoir samples are 5.0%–11.6%, 5.54% and 6.10%, respectively, while the range, median and average of the permeability of 30 oil reservoir samples are 0.016 μm^2~.33 μm^2 × 10^{-3} μm^2, 0.057 μm^2 × 10^{-3} μm^2, and 0.117 μm^2 × 10^{-3} μm^2, respectively. As shown in the histograms, the porosity of Section I, the Permian Upper Wuerhe Formation of Dinan 15 well is mostly less than 8% and its permeability is all below 2.56 μm^2 × 10^{-3}μm^2. Therefore, this section has poor physical characteristics and features typical super-low porosity and low permeability (Xiao et al., 2019).

The value distribution of porosity and permeability between every section is significantly different. According to the histograms of porosity and permeability of Section II, the Permian Upper Wuerhe Formation of Dinan 15 well (Figure 3E–H), the range, median and average of the porosity of 138 reservoir samples from Section II, the Upper Wuerhe Formation are 2.3%–17.2%, 6.89%, and 7.05%, respectively, while the range, median and average of the permeability of 124 reservoir samples from the same section are 0.01 μm^2–939 × 10^{-3} μm^2, 0.145 μm^2 × 10^{-3} μm^2, and 0.311 μm^2 × 10^{-3} μm^2, respectively. The range, median and average of the porosity of 85 samples are 5.2%–17.2%, 7.71%, and 8.25%, respectively, while the range, median and average of the permeability of 73 samples are 0.067 μm^2–939 μm^2 × 10^{-3} μm^2, 0.663 μm^2 × 10^{-3} μm^2, and 1.626 μm^2 × 10^{-3} μm^2, respectively. As shown in the histograms, the porosity of Section II, the Permian Upper Wuerhe Formation of Dinan 15 well is mostly less than 12% and its permeability is mostly

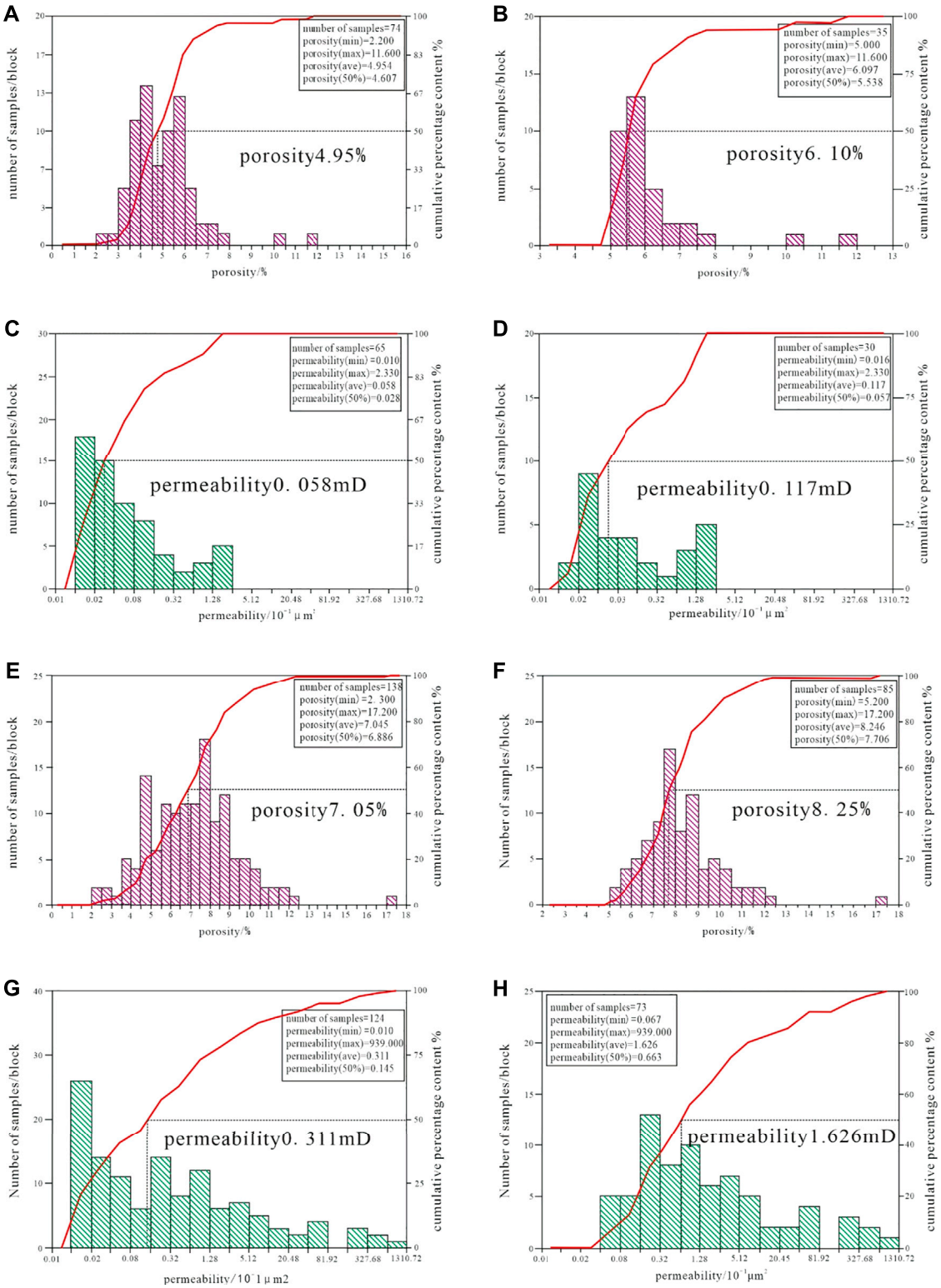

FIGURE 3
Porosity and permeability histograms of the Permian Upper Wuerhe Formation of Dinan 15 well block. **(A,B)** Porosity histogram of Section I, the Upper Wuerhe Formation; **(C,D)** Permeability histogram of Section I, the Upper Wuerhe Formation; **(E,F)** Porosity histogram of Section II, the Upper Wuerhe Formation; **(G,H)** Permeability histogram of Section II, the Upper Wuerhe Formation.

TABLE 2 Clay mineral content of the Upper Wuerhe Formation of Dinan 15 well block based on XDR.

Clay mineral content	Illite/smectite mixed layer	Illite	Kaolinite	Chloride	Sample qty
Range (%)	0–54.0	0–38.0	0–25.0	15.0–57.0	5
Average (%)	25.2	21.6	10.8	42.4	

TABLE 3 Statistical list of reservoir sensitivity analysis on the Upper Wuerhe Formation of Dinan 15 block.

No. of well	Depth of sample (m)	Experiment item	Porosity (%)	Kirschner permeability (mD)	Formation water permeability (mD)	Gas permeability (mD)	Damage rate (%)	Evaluation result
Dinan 081 well	4,022.77	Water sensitivity	4.88	0.517	0.0172	0.635	11.1	Weak
Dinan 10 well	3,398.52	Water sensitivity	4.27	0.282	0.0305	0.47	33.1	Below-middle
	3,398.52	Water and speed sensitivity	4.63	0.286	0.0314	0.474	10.5	Weak
	3,400	Water sensitivity	5.91	0.213	0.0269	0.403	33.8	Below-middle
	3,400	Water and speed sensitivity	6.31	0.285	0.0313	0.456	22.7	Weak
Dinan 12 well	3,447.57	Water and speed sensitivity	7.67	0.874	0.0634	1.58	19.4	Weak
	3,447.57	Water sensitivity	5.89	1.28	0.0268	2.47	45.2	Below-middle
Dinan 13 well	4,105.23	Water sensitivity	7.97	0.859	0.0428	1.54	47.2	Below-middle
	4,105.23	Water and speed sensitivity	8.85	2.75	0.138	3.34	47.9	Below-middle

below 5 $\mu m^2 \times 10^{-3}$ μm^2, and thus this section has poor physical characteristics and features typical super-low porosity and low permeability (Xiao et al., 2019; Zhang et al., 2020c; Zhang et al., 2022e; Yu et al., 2022). When compared with each other, Sections I and II of the Upper Wuerhe Formation are insignificantly different from each other in porosity, but the latter is better than the former regarding permeability.

3.3 Sensitivity characteristics

In order to identify the sensitivity characteristics of the Upper Wuerhe Formation glutenite reservoirs, this study conducted clay mineral X-ray diffraction (XRD) analysis on 5 core samples from the Upper Wuerhe Formation and experimental analysis on the reservoir characteristics of 9 samples in total from Dinan 081 well, 10 well, 12 well and 13 well of Dinan 15 well block. Since kaolinite, smectite, illite, chlorite, interstratified minerals, etc. have relatively large surface areas and extremely strong activities (like adsorbability, sensitivity to external fluid, etc.), they can significantly influence the injectability, adsorbability and modification of various injectants and are the main minerals that damage reservoirs. Therefore, the main factors that determine the degree of damage to the reservoir sensitivity are the content, constituent, distribution and attitude of clay minerals contained in clastic interstitial materials. The water sensitivity of a reservoir is the phenomenon where the reservoir permeability is decreased due to the expansion, dispersion, migration and blockage of clay minerals when incompatible external fluid enters the reservoir. The speed sensitivity of a reservoir means the possibility and degree of permeability decrease caused by migration and pore blockage of various particles in the reservoir due to the movement speed increase of fluid. According to the clay mineral XRD statistical results of the Upper Wuerhe Formation cores (Table 2), the primary clay mineral is chloride (15%–57%, average 42.4%), which actively reacts with acidic fluid, decreasing the physical characteristics of reservoirs, and thus is an acid sensitive mineral, and the secondary is illite-smectite mixed layers (0%–54%, average 25.2%), which are easily expanded with water and then block pores and thus are water sensitive minerals. Additionally, illite (0%–38%, average 21.6%) and kaolinite (0%–25%, average 10.8%) may migrate and block pores in the form of particles under the condition of high-speed fluid seepage, and thus are both speed sensitive minerals. Based on the

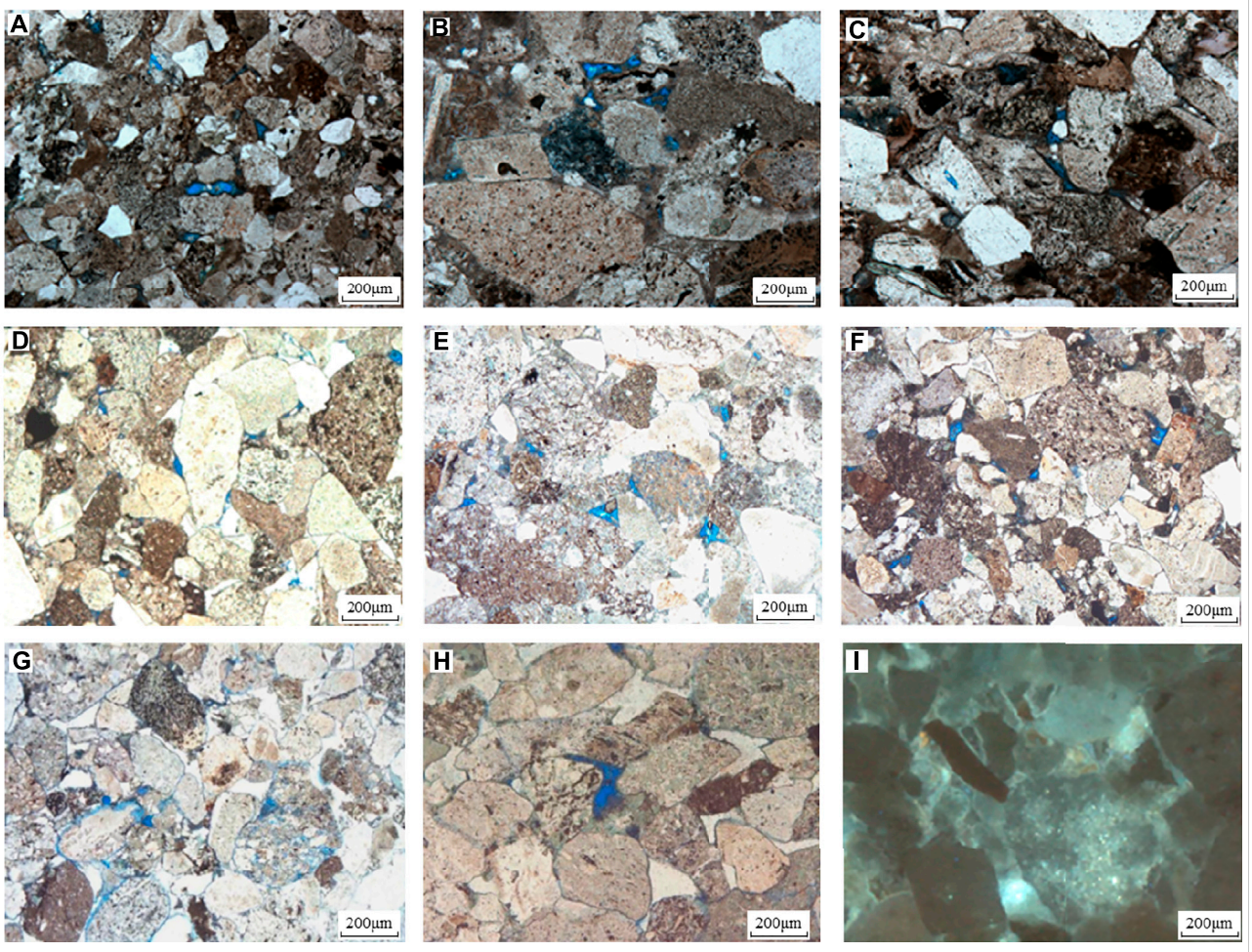

FIGURE 4
Microscopic thin section photos of pore types of the Permian Upper Wuerhe Formation reservoirs in the Dinan 15 well block. **(A)** Glutenite, intergranular pores 95%, intragranular dissolution pores 5%, Dinan 19 well, 3,926.8 m (P_3w_1); **(B)** Glutenite, intergranular pores 95%, intragranular dissolution pores 5%, Dinan 19 well, 3,922.57 m (P_3w_1); **(C)** Glutenite, intergranular pores 60%, intragranular dissolution pores 25%, tectonic fracture 15%, Dinan 19 well, 3,927.05 m (P_3w_1); **(D)** Medium sandstone, intergranular pores 95%, intragranular dissolution pores 4%, laumonite dissolution pores 1%, Dinan 14 well, 4,005.52 m (P_3w_1); **(E)** Sandy conglomerate, intergranular pores 60%, intragranular dissolution pores 30%, intergranular dissolution pores 10%, Dinan 15 well, 3,927.9 m(P_3w_2); **(F)** Sandy conglomerate, intergranular pores 70%, intergranular dissolution pores 20%, intragranular dissolution pores 10%, Dinan 15 well, 3,932.1 m (P_3w_2); **(G)** Sandy conglomerate, intergranular pores 50%, intergranular dissolution pores 20%, particle-edge fractures 20%, intragranular dissolution pores 10% Dinan 15 well, 3,728.87 m (P_3w_2); **(H)** pebbly unequal-particled sandstone, intergranular dissolution pores 90%, particle-edge fractures 5%, intragranular dissolution pores 5%, Dinan 8 well, 3,957.76m; **(I)** Pebbly unequal-particled lithic sandstone, part of the particles and interstitial materials luminous, Dinan 19 well, 3,924.99 m.

results of the experimental analysis on the reservoir sensitivity, it can be seen that the Upper Wuerhe Formation reservoirs feature below-middle water sensitivity and weak speed sensitivity (Table 3).

3.4 Reservoir space types and pore structures

Based on the cast thin section and SEM data combined with the pore characteristics, it is believed that the reservoir space types of the Upper Wuerhe Formation reservoirs of Dinan 15 well in the study area are diverse and dominated by intergranular pores, followed by intergranular dissolution pores, intragranular dissolution pores, and micro-fractures (Figure 4). Intergranular pores, which are mainly developed in glutenite and sandy conglomerate, are the preserved primary pores that have not been damaged by diagenesis; dissolution pores are divided into inter- and intra-granular ones and they are mainly developed in medium sandstone and gravel-bearing inequigranular sandstones. They are the secondary pores produced by the interaction between dissolution fluid and surrounding rock. Micro-fractures are also common in the

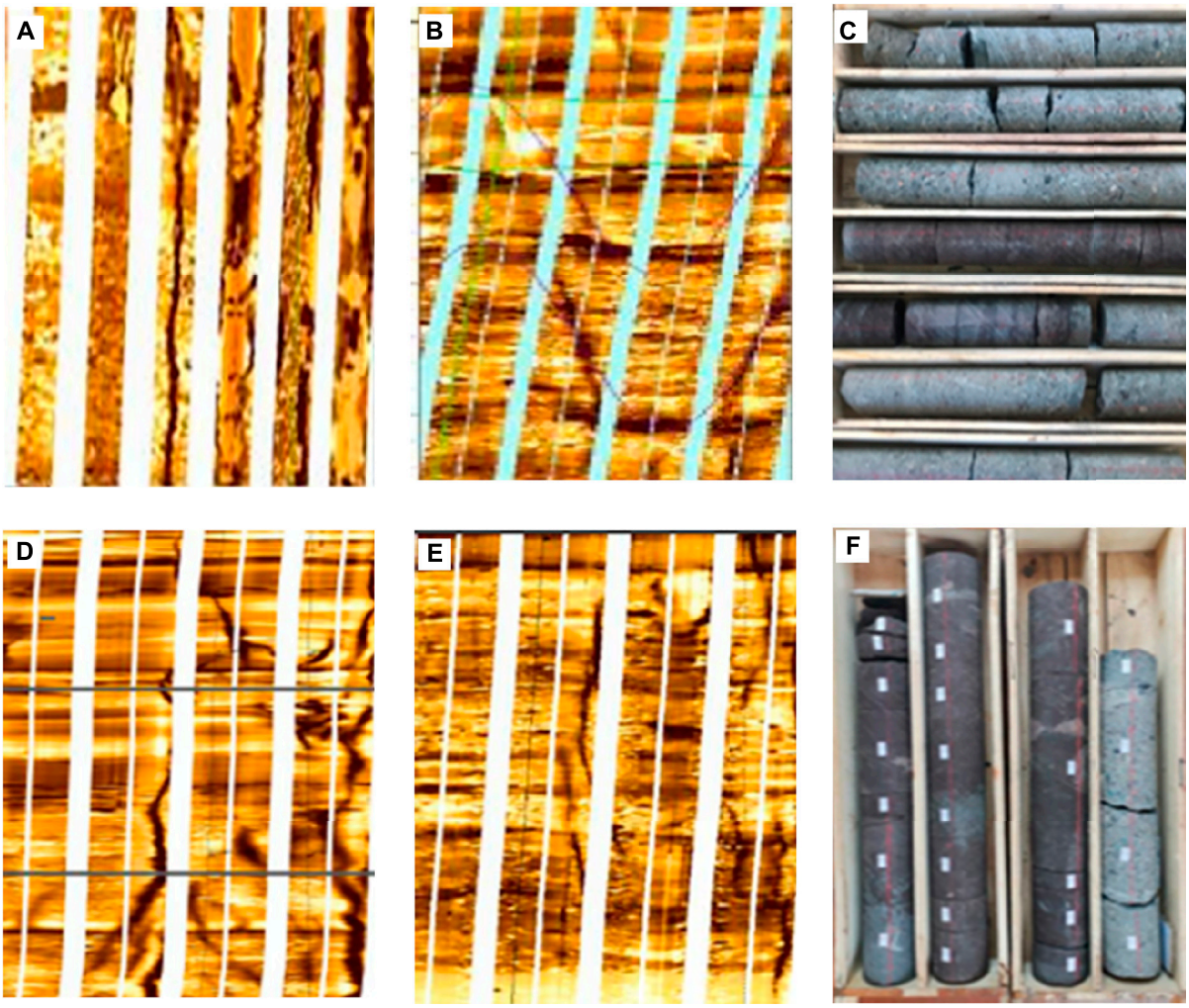

FIGURE 5
Development characteristics of fractures in imaging resistivity and cores. **(A)**. Glutenite, Dinan 14 well, 4000 m–4008 m; **(B)** Glutenite, Dinan 15 well, 3721 m–3735 m; **(C)** Core, Dinan 15 well, 3,731.8 m–3,739.1 m; **(D)** Glutenite, Dinan 14 well, 4,000 m–4,008 m; **(E)** Glutenite, Dinan 15 well, 3,795 m–3,797 m; **(F)** Core, Dinan 15 well, 3,796.5 m–3,799.8 m.

glutenite reservoirs in the study area. Due to the high content of brittle particles such as quartz and feldspar in the glutenite, a series of fractures are generated along the grain edges under the action of stress, providing space for oil and gas migration and storage.

According to the data of core collection and FMI micro-resistivity imaging, vertical fractures and high angle fractures exist in the Upper Wuerhe Formation reservoirs and are dominated by micro-factures (Figure 5). The internal edges of some fractures are straight, with a high degree of opening, and appear in groups. It is believed that the stress field changes brought about by regional tectonic activities form structural fractures that have a low filling degree and most of them can become effective seepage channels (Figures 5A,B); some fractures are not straight and have low degree of opening. Although the extension direction is consistent but the length is different, the interior is mostly filled with secondary minerals or organic matter, and the contribution to the reservoir and permeability is limited (Figures 5D, E)

10 samples, collected from Sections I and II of the Upper Wuerhe Formation of Dinan 15 well, were selected for high-pressure mercury injection experiment (Figure 6). Based on the experiment results, it can be seen that the mercury injection curves of the Upper Wuerhe Formation take on a shape of slope, indicating that the reservoirs feature slightly fine skewness, poor sorting, small pores and fine throat. The maximum capillary radius of the reservoirs is 0.817–32.978μm, with the average of 11.687μm, and their displacement pressure is 0.0223–0.9MPa, with the average of 0.501 MPa. This indicates that the glutenite reservoir in the studied section has a better pore-throat ratio and has a certain seepage capacity.

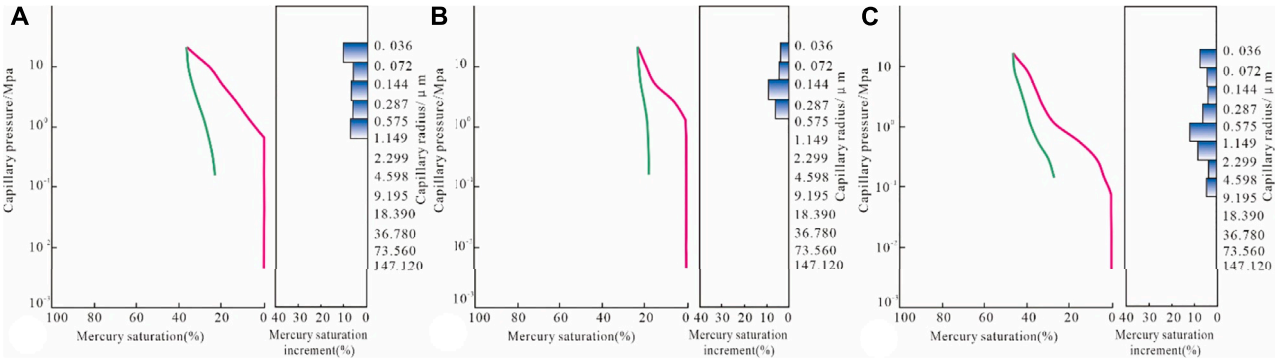

FIGURE 6
Capillary pressure curve of the Permian Upper Wuerhe reservoirs of Dinan 15 well block. **(A,B)** Capillary pressure curve of Section I reservoirs of the Upper Wuerhe Formation; **(C)** Capillary pressure curve of Section II reservoirs of the Upper Wuerhe Formation.

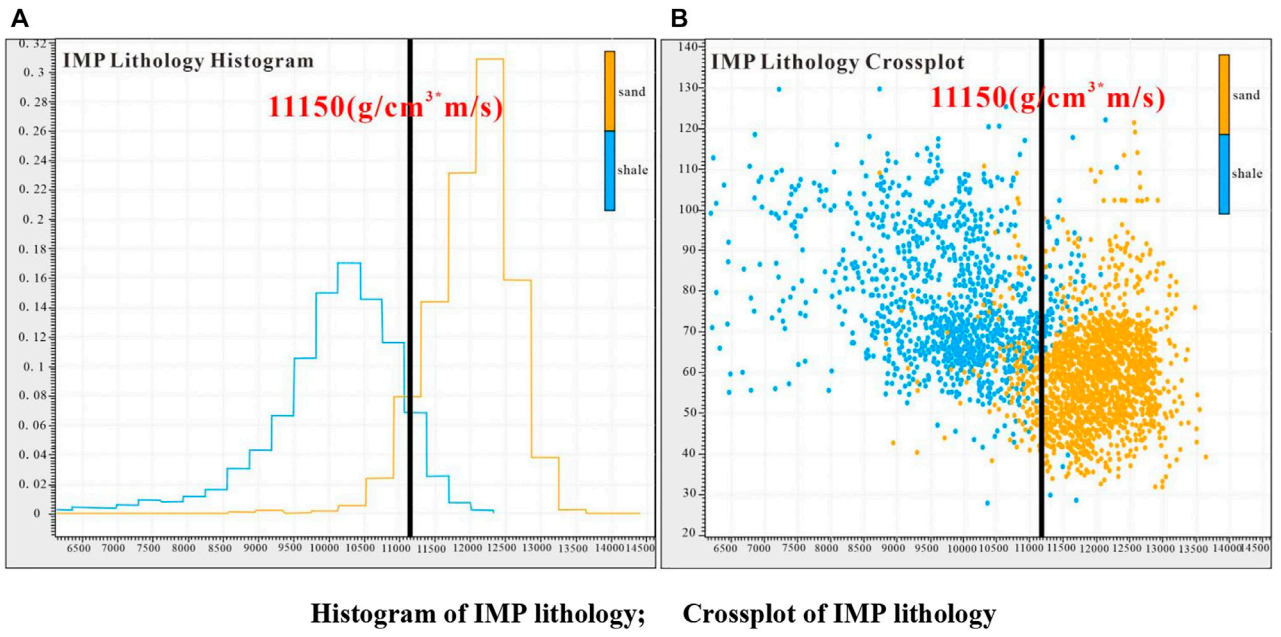

FIGURE 7
Gama-wave impedance crossplot of the Upper Wuerhe Formation of the Dinan 15 well block. **(A)** Histogram of IMP lithology; **(B)** Crossplot of IMP lithology.

3.5 Log response characteristics of reservoirs

The rock types of the Permian Upper Wuerhe Formation reservoirs of the Dinan 15 well block include glutenite, pebbly sandstone, medium–fine sandstone, siltstone, argillaceous siltstone and silty mudstone. The parameters, including sound waves, density, gamma, resistivity, wave impedance, etc. of the target sections of all prospecting wells and evaluation wells in the selected well block were adopted for analysis on the reservoir sensitivity parameters. According to the logging results and log interpretation combined with lithology and the analysis on the characteristics of the longitudinal wave impedance corresponding to the reservoirs, the lithology corresponding to the high-impedance-value part of the Permian Upper Wuerhe Formation of the Dinan 15 well block is glutenite and sandstone, with the average > 11,150 mg/scm, while that corresponding to the low-impedance-value part is mudstone, with a wave impedance value <10,000 mg/scm generally (Figures 7, 8).

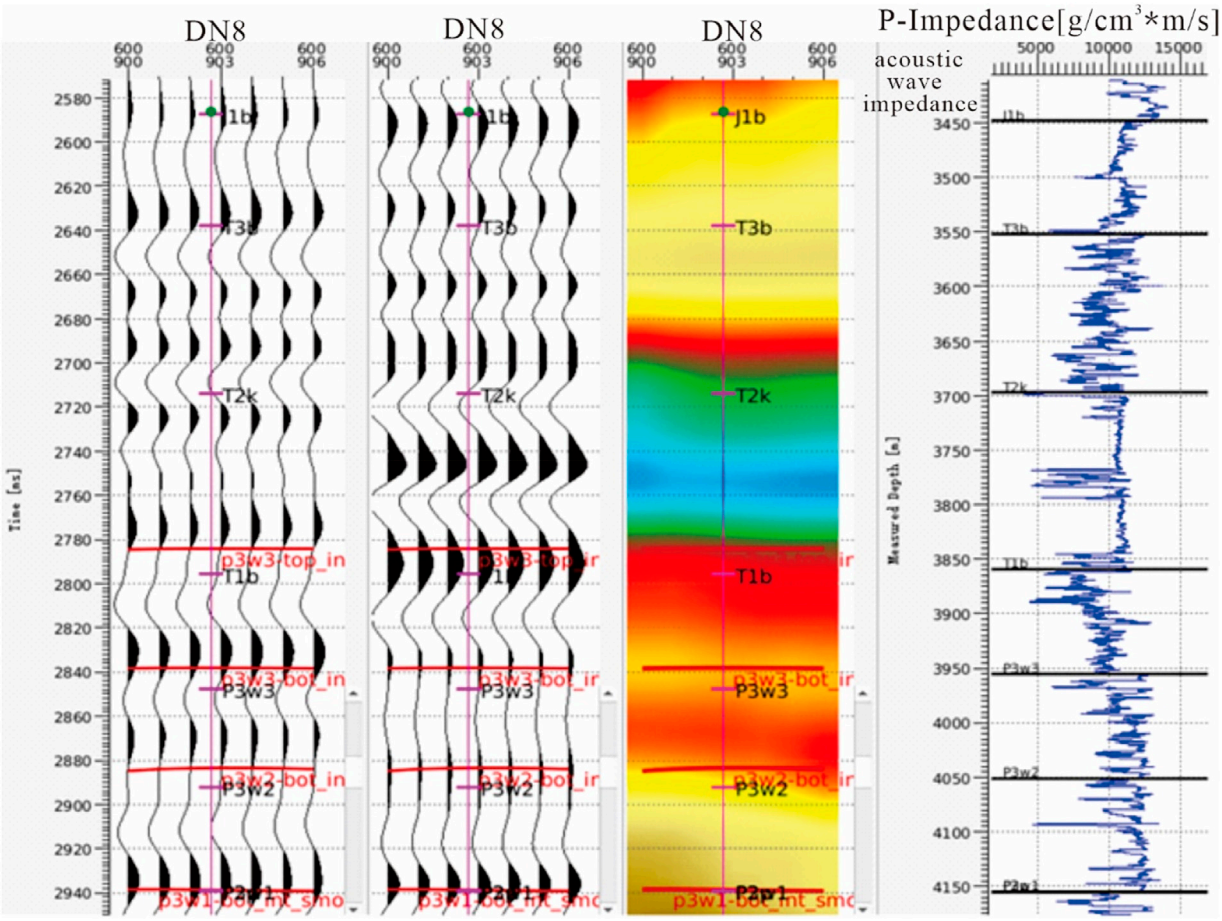

FIGURE 8
Identification results of reservoir rock types based on wave impedance parameters–a case of Dinan 8 well.

4 Reservoir prediction

4.1 Criteria for reservoir evaluation

Lithology reflects the material basis of a reservoir, physical characteristics embody the basic reserve capacity, sensitivity represents the anti-damage capability of a reservoir, and pore structures indicate the micro distribution regularities of reservoir space. Therefore, based on the above research and analysis, with lithology, physical characteristics, sensitivity, reservoir space types and microstructure characteristics adopted as the key parameters, the criteria for reservoir evaluation were established for the tight reservoirs in the study area, which are classified into three types of reservoirs, i.e., Type I, Type II, and Type III, with the reservoir quality decreasing from Type I to Type III (Table 4).

Type I reservoirs: the lithology is dominated by glutenite and pebbly sandstone. The average porosity and permeability are higher than 12% and 5 $\mu m^2 \times 10^{-3}$ μm^2, respectively. The reservoirs are weak water-sensitive and weak speed-sensitive. The primary reservoir space is intergranular pores and laumonite dissolution pores, and the secondary is intragranular dissolution pores. The pore throats are dominated by fine skewness, and are a combination of macro-mesopores and fine pore throats, with good pore throat connectivity. The maximum connecting pore throat radius is 9.195 μm–32.978 μm, and the log response is high impedance response.

Type II reservoirs: the lithology is dominated by medium–fine sandstone and siltstone. The average porosity and permeability are between 8% and 12% and 2.56 μm^2 $\times 10^{-3}$ μm^2~5 $\times$ $10^{-3}\mu m^2$, respectively. The reservoirs are below-middle water-sensitive and below-middle speed-sensitive. The primary reservoir space is intergranular pores and laumonite dissolution pores, and the secondary is intragranular dissolution pores. The pore throats are dominated by fine skewness, and are a combination of small-micropores and fine pore throats, with good pore throat connectivity. The maximum connecting pore throat radius is 1.267 μm–9.195 μm, and the log response is high impedance–medium impedance response.

TABLE 4 Criteria for reservoir classification established based on lithology, physical characteristics, sensitivity, reservoir space types, and microstructure characteristics.

Reservoir type	Lithology	Physical characteristics		Sensitivity	Reservoir space type	Pore structure characteristics		Log response
		Porosity/%	Permeability/$\times10^{-3}\mu m^2$			Pore throat distribution	Pore size distribution/μm	
I	Glutenite Pebbly sandstone	> 12	> 5	Weak water-sensitive Weak speed-sensitive	Primary: intergranular pores, laumonite dissolution pores Secondary: intragranular dissolution pores	Fine skewness Macro-mesopores Fine throat	9.195~32.978 17.719	High impedance
II	Middle–fine sandstone Siltstone	8–12	2.56–5	Below-middle water-sensitive Below-middle speed-sensitive	Primary: intergranular pores, laumonite dissolution pores Secondary: intragranular dissolution pores	Fine skewness Small-micropores Fine throat	1.267~9.195 5.442	Medium impedance–high impedance
III	Argillaceous siltstone Silty mudstone	< 8	< 2.56	Above-middle water-sensitive Above-middle speed-sensitive	Combination of a few residual intergranular pores and the internal micropores of interstitial materials	Fine skewness Small-micropores Micro throat	0.036~1.267 0.3195	Medium impedance–low impedance

Type III reservoirs: the lithology is dominated by argillaceous siltstone and silty mudstone. The average porosity and permeability are lower than 8% and 2.56 $\mu m^2 \times 10^{-3}\mu m^2$, respectively. The reservoirs are above-middle water-sensitive and above-middle speed-sensitive. The primary reservoir space is a combination of a few residual intergranular pores and the internal micropores of interstitial materials. The pore throat distribution is dominated by fine skewness and is a combination of small-micropores and micro pore throats, with poor pore throat connectivity. The maximum connecting pore throat radius is 0.036 μm–1.267 μm, and the log response is medium impedance–low impedance response.

4.2 Reservoir prediction

4.2.1 Lateral reservoir prediction

Based on the reservoir evaluation criteria established above combined with the indication of single well oil-bearing characteristics, Dinan 8 well, Dinan 083 well, Dinan 15 well, Dinan 12 well and Dinan 121 well in the west of the study area were selected to establish a well-tie profile in order to characterize the lateral reservoir distribution rules. As shown in Figure 9, Type I reservoirs pass through Dinan 083 and 15 wells along the direction from southwest to northeast, and are mainly distributed in the top and middle parts of Dinan 083 and 15 wells. Their single layers are thin and feature sand-mud interbedding, with continuously sedimentary sand bodies, good physical characteristics and oil-bearing characteristics. Oil and gas are in the same layer and the current production of oil and gas is 339.11t/d and 27980m^3/d, respectively. Besides, Type II reservoirs pass through Dinan 8, 083 and 15 wells along the direction from southwest to northeast, and are mainly distributed in the top and bottom parts of Dinan 8 well, and the bottom parts of Dinan 083 and 15 wells. Their single layers are relatively thick and feature local continuation, with good physical characteristics and oil-bearing characteristics. Oil-water and oil-gas are in the same layer and the current production of oil and gas of Dinan 8 and 083 wells is 26.37 t/d and 2,610 m^3/d, and 83.59 t/d and 13,190 m^3/d, respectively, and the oil production of Dinan 15 well is 42.02 t/d. Last but not least, Type III reservoirs pass through

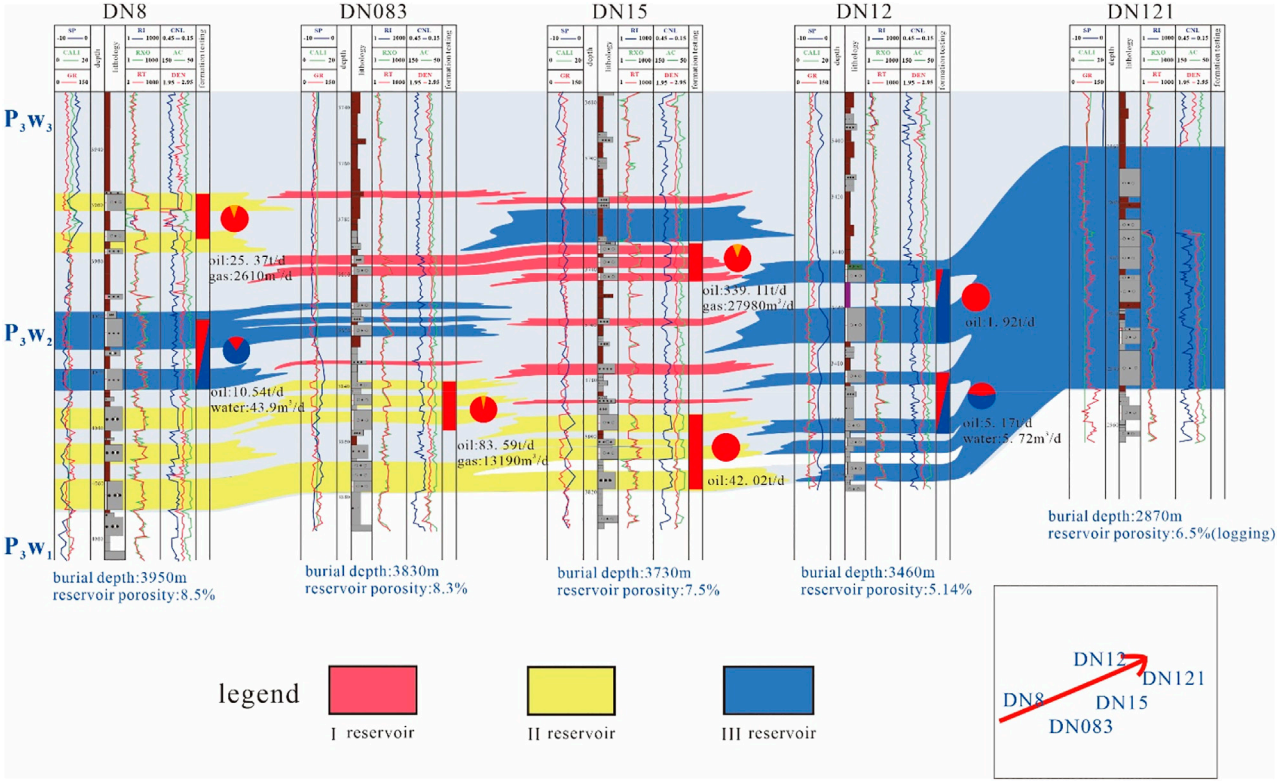

FIGURE 9
Prediction on reservoir distribution on the Dinan 8 well–Dinan 15 well–Dinan 121 well profile.

Dinan 8, 083, 15, 12 and 121 wells along the direction from southwest to northeast, and are mainly distributed in Dinan 121 well, the middle and bottom parts of Dinan 12 well, and the middle part of Dinan 8 well, and partially in the top part of Dinan 15 well and the middle part of Dinan 083 well along the direction from southwest to northeast. Their single layers are thick and feature block structures, with relatively poor physical characteristics and oil-bearing characteristics. The oil-bearing layers and oil-water are in the same layer and the current production of oil and gas of Dinan 8 and 12 wells is 10.54 t/d and 43.9 m^3/d, and 7.09 t/d and 5.72 m^3/d, respectively.

4.2.2 Reservoir plane prediction

Based on the criteria for reservoir evaluation and the prediction results of single-well and well-tie reservoirs, the diagrams of reservoir plane distribution were drawn. Wave impedance was utilized to distinguish reservoir areas and non-reservoir areas (Figures 10A,B). The grey-black areas are the low values of wave impedance, representing the non-reservoir areas, while the red-yellow areas are the high values of wave impedance, representing the reservoir areas. Plane prediction was conducted on the different reservoir types of P_3w_1 and P_3w_2 based on the plane distribution characteristics, including the parameters of lithology, physical characteristics, sensitivity, pore structures, etc., in accordance with the reservoir classification criteria (Figures 10C,D).

According to the plane distribution diagram of P_3w_1 reservoirs, Type I reservoirs are mainly distributed in the west of the study area, specifically in the areas of Dinan 20, 18, 21, 13, 10, 8, and 081 wells, with an area around 314 km^2. Besides, Type II reservoirs are mainly distributed in the center of the study area, specifically in the areas of Dinan 12, 086, 15, 083, 084, 19 085 and 089 wells, with an area around 529.87 km^2. Last but not the least, Type III reservoirs are mainly distributed in the east of the study area, specifically in the areas of Dinan 1, 2, 3, 201, 142 and 17 wells, with an area around 156.8 km^2.

According to the plane distribution diagram of P_3w_2 reservoirs, Type I reservoirs are mainly distributed in the west and east of the study area, specifically in the areas of Dinan 20, 201, 142, 13, 084, 083, 8, 081 and 141 wells, with an area around 530.66 km^2. Besides, Type II reservoirs are mainly distributed in the center and west of the study area, specifically in the areas of Dinan 21, 18, 3, 1, 2, 088, 12, 086, 15, 085, 14, 089 and 17 wells, with an area around 961.63 km^2. Last but not least, Type III reservoirs are mainly distributed in the southeast of the study

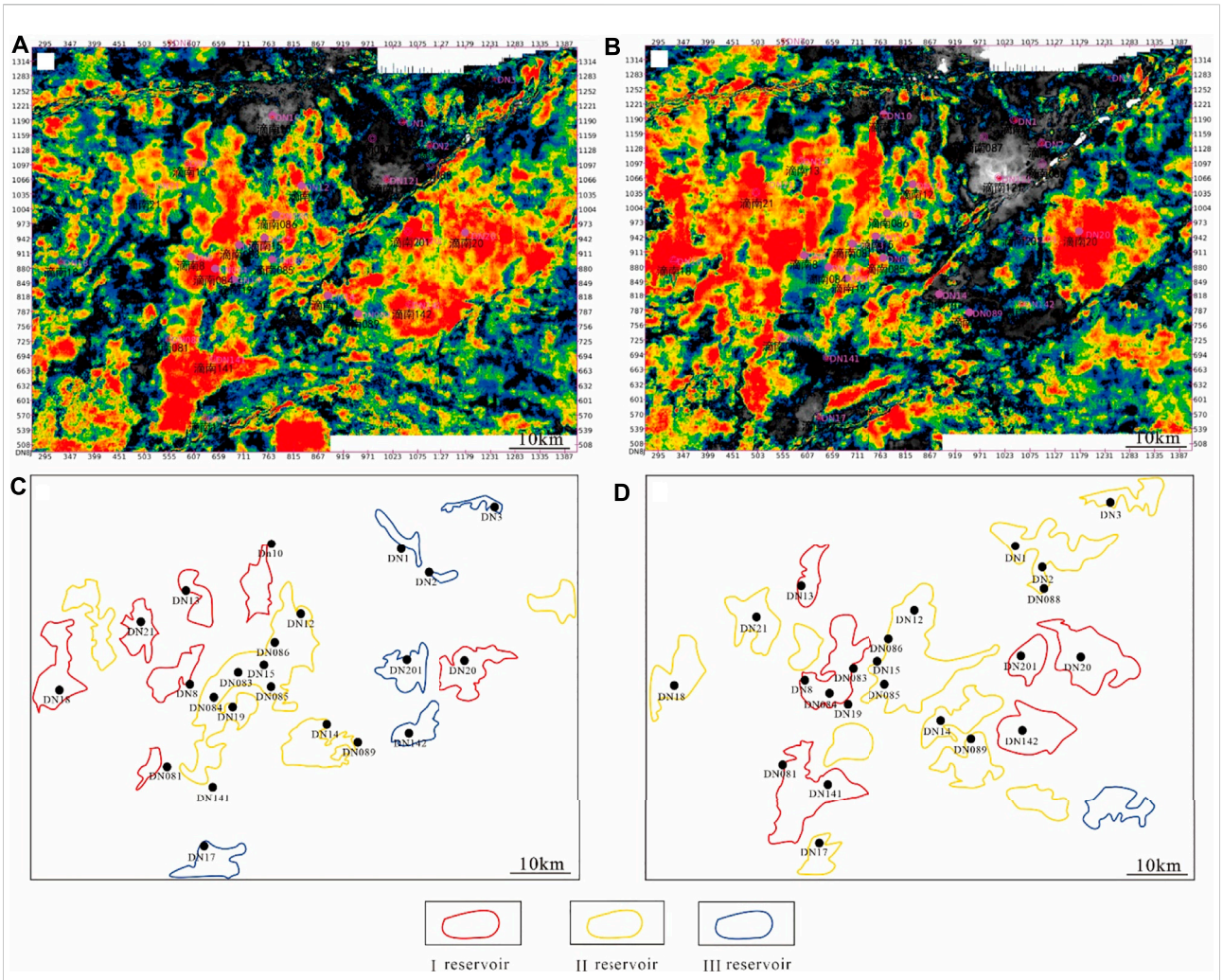

FIGURE 10
Inversion plans of the Permian Upper Wuerhe Formation of the Dinan 15 well block and plane prediction diagrams of Type I, II and III reservoirs. **(A)** Inversion plan of Section I, the Permian Upper Wuerhe Formation of the Dinan 15 well block; **(B)** Inversion plan of Section II, the Permian Upper Wuerhe Formation of the Dinan 15 well block; **(C)** Plane distribution diagram of Types I, II and III reservoirs of Section I, the Permian Upper Wuerhe Formation of the Dinan 15 well block; **(D)** Plane distribution diagram of Types I, II and III reservoirs of Section II, the Permian Upper Wuerhe Formation of the Dinan 15 well block.

area, specifically close to the areas of Dinan 142 and 20 wells, with an area of around 78.5 km^2.

5 Conclusion

(1) The lithology of the Upper Wuerhe Formation in the Dinan 15 well area is dominated by gray glutenite; at the same time, various rock types such as glutenite and medium sandstone are developed;

(2) The glutenite reservoirs of the Upper Wuerhe Formation in the Dinan 15 well block is an ultra-low porosity and ultra-low permeability reservoir, with moderately weak water sensitivity and weak velocity sensitivity. The shape of the mercury intrusion curve and the pore throat radius distribution of the samples show that the reservoir is skewed, poorly sorted, and has the characteristics of small pores and thin throats.

(3) This work constructed evaluation criteria for reservoirs from I to III by utilizing lithology, physical properties, sensitivity, reservoir space type, and microstructural characteristics as key parameters. The favorable reservoir distribution area is mainly located in the west of the block, which is the focus of the next exploration of the Upper Wuerhe Formation area.

Data availability statement

The raw data supporting the conclusions of this article will be made available by the authors, without undue reservation.

Author contributions

WX contributed to conception and design of the study. SX organized the database. YX performed the statistical analysis. WX wrote the first draft of the manuscript. SX, YX, and YY wrote sections of the manuscript. All authors contributed to manuscript revision, read, and approved the submitted version.

Funding

This study was supported by the open funds from the National Natural Science Foundation of China (No. 42102192), the open experiment fund of Southwest Petroleum University (2021KSP02029), and the Science and Technology Cooperation Project of the CNPC-SWPU Innovation Alliance. We sincerely appreciate all reviewers and the handling editor for their critical comments and constructive suggestions.

Conflict of interest

The authors declare that the research was conducted in the absence of any commercial or financial relationships that could be construed as a potential conflict of interest.

Publisher's note

All claims expressed in this article are solely those of the authors and do not necessarily represent those of their affiliated organizations, or those of the publisher, the editors and the reviewers. Any product that may be evaluated in this article, or claim that may be made by its manufacturer, is not guaranteed or endorsed by the publisher.

References

Bian, H., Han, B., Wang, F., Liu, G., Li, X., and Guo, Z. (2020). Characteristics and classification of glutenite reservoirs in Niudong area, north margin of Qaidam Basin. *J. Xi'an Univ. Sci. Technol.* 40 (5), 894–901. doi:10.13800/j.cnki.xakjdxxb.2020.0519

Cai, Y., Xia, Y., Huang, X., Wang, X., and Li, Y. (2019). Application of multi-attribute fusion technique in sedimentary facies research. *Collect. Works 2019 Geophys. Explor. Technol. Seminar China Petroleum Soc.* 2019, 723–726.

Ding, X. (2016). Analysis of hydrocarbon Genesis and accumulation stage of Dongdaohaizi Sag in Junggar Basin. *Sci. Technol. Eng.* 16 (10), 80–84+88.

Du, J., Zhi, D., Tang, Y., Jia, C., Yang, X., Abulimity, Y., et al. (2019). Prospects in upper permian and strategic discovery in shawan sag, Junggar Basin. *China Pet. Explor.* 24 (01), 24–35. doi:10.3969/j.issn.1672-7703.2019.01.004

Feng, T. (2017). *Permian tectonic-stratigraphic sequence and basin evolution in Junggar Basin*. Beijing: China University of Geosciences.

Fu, S., Lei, P., Xu, X., Cao, Y., Liu, Z., Zhang, S., et al. (2019). The characteristics and their controlling factors on reservoir in permian lower urho Formation in Mahu sag, Junggar Basin. *Nat. Gas. Geosci.* 30 (04), 468–477. doi:10.11764/j.issn.1672-1926.2019.01.015

Gao, F. (2021). Influence of hydraulic fracturing of strong roof on mining-induced stress insight from numerical simulation. *J. Min. Strata Control Eng.* 3 (2), 023032. doi:10.13532/j.jmsce.cn10-1638/td.20210329.001

Guan, X., Pan, S., Qu, Y., Xu, D., Zhang, H., Ma, Y., et al. (2021). Discovery and hydrocarbon exploration potential of beach-bar sand in Shawan Sag, Junggar Basin. *Lithol. Reserv.* 33 (01), 90–98. doi:10.10108/yxyqc.2021109

Hu, X., Qu, Y., Hu, S., Pan, J., Lu, Y., Xu, D., et al. (2020). Geological conditions and exploration potential of shallow oil and gas in slope area of Mahu Sag, Junggar Basin. *Lithol. Reserv.* 32 (02), 67–77. doi:10.12108/yxyqc.20200207

Hu, X., Ding, X., Zhang, X., Lei, L., Wang, X., et al. (2021a). Glutenite reservoir characteristics and main controlling factors of Es_3-Es_4 in northern zone of Bonan. *J. Northeast Petroleum Univ.* 45 (01), 55–61. doi:10.3969/j.issn.2095-4107.2021.01.006

Hu, X., Zou, H., Hu, Z., Li, Y., Huang, Y., Fu, X., et al. (2021b). Reservoir characteristics and main controlling factors of glutenite reservoir in fan dalta glutenite:a case study of the Upper Urho Formation of Permian in the east slope of Dongdaohaizi Sag, Junggar Basin. *J. Northeast Petroleum Univ.* 45 (06), 15–26. doi:10.3969/j.issn.2095-4107.2021.06.002

Huang, H. X., Li, R. X., Jiang, Z. X., Li, J., Chen, L., et al. (2020). Investigation of variation in shale gas adsorption capacity with burial depth: Insights from the adsorption potential theory. *J. Nat. Gas. Sci. Eng.* 73, 103043. doi:10.1016/j.jngse.2019.103043

Jin, G., Wang, T., Liu, Z., Xie, R., Shao, L., and Li, B. (2022). Classification and productivity prediction of glutenite reservoirs based on NMR logging. *ACTA PET. SIN.* 43 (5). doi:10.7623/syxb202205006

Jin, J., Luo, X., Liao, J., Yu, Q., Wang, D., Zhao, W., et al. (2015). Geochemical characteristics of permian Pingdiquan Formation hydrocarbon source rocks in Dongdaohaizi sag, Junggar Basin, China. *J. Chengdu Univ. Technol. Sci. Technol. Ed.* 42 (02), 196–202. doi:10.3969/j.issn.1671-9727.2015.02.07

Jin, J., Xun, K., Hu, W., Xiang, B., Wang, J., Cao, J., et al. (2017). Diagenesis of its influence on coarse clastic reservoirs in the Baikouquan Formation of Western slope of the Mahu depression, Junggar Basin. *Oil Gas Geol.* 38 (02), 323–333+406. doi:10.11743/ogg20170212

Kang, H., Xu, G., Wang, B., Wu, Y., Jiang, P., Pan, J., et al. (2019). Forty years development and prospects of underground coal mining and strata control technologies in China. *J. Min. Strata Control Eng.* 1 (1), 013501. doi:10.13532/j.jmsce.cn10-1638/td.2019.02.002

Kuang, L., Tang, Y., Lei, D., Wu, T., and Qu, J. (2014). Exploration of fan-controlled large-area lithologic oil reservoirs of triassic Baikouquan Formation in slope zone of Mahu depression in Junggar Basin. *China Pet. Explor.* 19 (06), 14–23. doi:10.13532/j.jmsce.cn10-1638/td.2019.02.002

Li, H. (2022). Research progress on evaluation methods and factors influencing shale brittleness: A review. *Energy Rep.* 8, 4344–4358. doi:10.1016/j.egyr.2022.03.120

Li, H., Qin, Q., Zhang, B., Ge, X., Hu, X., Fan, C., et al. (2020). Tectonic fracture Formation and distribution in ultradeep marine carbonate gas reservoirs: A case study of the maokou Formation in the jiulongshan gas field, sichuan basin, southwest China. *Energy fuels* 34 (11), 14132–14146. doi:10.1021/acs.energyfuels.0c03327

Li, H., Tang, H., Qin, Q., Zhou, J., Qin, Z., Fan, C., et al. (2019). Characteristics, formation periods and genetic mechanisms of tectonic fractures in the tight gas sandstones reservoir: A case study of xujiahe Formation in YB area, sichuan basin, China. *J. Petroleum Sci. Eng.* 178, 723–735. doi:10.1016/j.petrol.2019.04.007

Li, Y. Y., Qian, G., Gao, Y., Qin, J., Huang, W., Lu, S., et al. (2018). Identification criterion of the geological "sweet point" of conglomerate tight reservoir and its application of Baikouquan formation in Mahu sag, Junggar basin. *J. Northeast Petroleum Univ.* 42 (06), 85–94+10. doi:10.3969/j.issn.2095-4107.2018.06.009

Lin, H., Liu, P., Wang, T., Chen, S., Mu, X., Liu, Y., et al. (2019). Diagenetic evolution mechanism of deep glutenite reservoirs based on differences in parent rock types: A case study of lower submember of member 3 of shahejie Formation in chezhen sag, Bohai Bay Basin. *Acta Pet. Sin.* 40 (10), 1180–1191. doi:10.7623/syxb201910004

Liu, M. (2015). *Genesis analysis of low porosity and low permeability reservoirs in the Upper Wuerhe Formation of the Fifth Block*. Wuhan: Yangtze University.

Liu, M., Xie, R., Guo, J., and Jin, G. (2018). Characterization of pore structures of tight sandstone reservoirs by multifractal analysis of the NMR T2 distribution. *Energy fuels.* 32 (12), 12218–12230. doi:10.1021/acs.energyfuels.8b02869

Lu, H., Luo, H., Luo, F., Mao and Dengzhou (2021). Fan controlled large-area accumulation conditions and mode of upper Wuerhe Formation in MH1 well zone of Mahu sag. *Special Oil Gas Reservoirs* 28 (01), 42–50. doi:10.3969/j.issn.1006-6535.2021.01.006

Pang, X., Niu, C., Du, X., Wang, Q., and Dai, L. (2020). Quantitative characterization of differences in glutenite reservoir in the Member 1 and 2 of Shahejie Formation in the northeastern margin of Shijiutuo uplift, Bohai Sea. *Acta Pet. Sin.* 41 (9), 1073–1088. doi:10.7623/syxb202009004

Qu, J., Zhang, L., Wu, J., and You, X. (2017). Characteristics of sandy conglomerate reservoirs and controlling factors on physical properties of Baikouquan Formation in the Western slope of Mahu sag, Junggar Basin. *Xinjiang Pet. Geol.* 38 (1), 1–6. doi:10.7657/XJPG20170101

Wang, J., Zhang, C., Zheng, D., Song, W., and Ji, X. (2020b). Stability analysis of roof in goaf considering time effect. *J. Min. Strata Control Eng.* 2 (1), 013011. doi:10.13532/j.jmsce.cn10-1638/td.2020.01.005

Wang, R., Zheng, M., Yang, S., Zhao, X., Jiang, Y., Wan, M., et al. (2022). Characteristics and controlling factors of weakly cemented glutenite reservoir in permian upper urho formation, south slope of Mahu sag. *Special Oil Gas Reservoirs* 29 (01), 23–30. doi:10.3969/j.issn.1006-6535.2022.01.004

Wang, Y., Cui, M., Liu, L., and Dan, L. (2020a). Pore throat characteristics of glutenite reservoirs in Cretaceous of Fangzheng Depression. *J. Northeast Petroleum Univ.* 44 (02), 36–45. doi:10.3969/j.issn.2095-4107.2020.02.004

Xiao, J., Hao, Q., Zhang, S., and Fan, S. (2020). Influence of oil well casing on the law of strata pressure in working face. *J. Min. Strata Control Eng.* 2 (1), 013522. doi:10.13532/j.jmsce.cn10-1638/td.2020.01.003

Xiao, M., Yuan, X., Wu, S., Cao, Z., Tang, Y., Xie, Z., et al. (2019). Conglomerate reservoir characteristics of and main controlling factors for the Baikouquan Formation, Mahu sag, Junggar Basin. *Earth Sci. Front.* 26 (01), 212–224. doi:10.13745/j.esf.sf.2018.12.7

Xu, L., Chang, Q., Tao, Q., and Wang, W. (2017). Reservoir characteristics and control factors of Baikouquan Formation in triassic, mabei oilfield, Junggar Basin. *Geol. Rev.* 63 (S1), 277–278. doi:10.16509/j.georeview.2017.s1.132

Yang, B., Zhang, Z., and Zhang, C. (2020). Investigation of reservoir classification of glutenites in Bozhong 19-6 gas field. *Contemp. Chem. Ind.* 49 (12), 2786–2790. doi:10.13840/j.cnki.cn21-1457/tq.2020.12.033

Yu, X., Bian, J., and Liu, C. (2022). Determination of energy release parameters of hydraulic fracturing roof near goaf based on surrounding rock control of dynamic pressure roadway. *J. Min. Strata Control Eng.* 4 (1), 013016. doi:10.13532/j.jmsce.cn10-1638/td.20210908.001

Zhang, H. (2014). *Key sources of oil and gas reservoirs and accumulation in the northern belt of the haizi depression in the east of the Junggar Basin*. Chengdu: Southwest Petroleum University.

Zhang, K., Jia, C., Song, Y., Jiang, S., Jiang, Z., Wen, M., et al. (2020a). Analysis of lower cambrian shale gas composition, source and accumulation pattern in different tectonic backgrounds: A case study of weiyuan block in the upper yangtze region and xiuwu basin in the lower yangtze region. *Fuel* 263 (2020), 115978. doi:10.1016/j.fuel.2019.115978

Zhang, K., Jiang, S., Zhao, R., Wang, P., Jia, C., and Song, Y. (2022a). Connectivity of organic matter pores in the Lower Silurian Longmaxi Formation shale, Sichuan Basin, Southern China: Analyses from helium ion microscope and focused ion beam scanning electron microscope. *Geol. J.* 57, 1912–1924. doi:10.1002/gj.4387

Zhang, K., Jiang, Z., Song, Y., Jia, C., Yuan, X., Wang, X., et al. (2022b). Quantitative characterization for pore connectivity, pore wettability, and shale oil mobility of terrestrial shale with different lithofacies -- A case study of the Jurassic Lianggaoshan Formation in the Southeast Sichuan Basin of the Upper Yangtze Region in Southern China. *Front. Earth Sci. (Lausanne).* 2022, 864189. doi:10.3389/feart.2022.864189

Zhang, K., Peng, J., Liu, W., Li, B., Xia, Q., Cheng, S., et al. (2020b). The role of deep geofluids in the enrichment of sedimentary organic matter: A case study of the late ordovician-early silurian in the upper yangtze region and early cambrian in the lower yangtze region, south China. *Geofluids* 2020, 1–12. doi:10.1155/2020/8868638

Zhang, K., Peng, J., Wang, X., Jiang, Z., Song, Y., Jiang, L., et al. (2020c). Effect of organic maturity on shale gas Genesis and pores development: A case study on marine shale in the upper yangtze region, south China. *Open Geosci.* 12 (2020), 1617–1629. doi:10.1515/geo-2020-0216

Zhang, K., Song, Y., Jia, C., Jiang, Z., Han, F., Wang, P., et al. (2022c). Formation mechanism of the sealing capacity of the roof and floor strata of marine organic-rich shale and shale itself, and its influence on the characteristics of shale gas and organic matter pore development. *Mar. Petroleum Geol.* 140 (2022), 105647. doi:10.1016/j.marpetgeo.2022.105647

Zhang, K., Song, Y., Jiang, Z., Xu, D., Li, L., Yuan, X., et al. (2022d). Quantitative comparison of Genesis and pore structure characteristics of siliceous minerals in marine shale with different TOC contents - a case study on the shale of Lower Silurian Longmaxi Formation in Sichuan Basin, Southern China. *Front. Earth Sci. (Lausanne).* 2022, 887160. doi:10.3389/feart.2022.887160

Zhang, K., Song, Y., Jiang, Z., Yuan, X., Wang, X., Han, F., et al. (2022e). Research on the occurrence state of methane molecules in post-mature marine shales-A case analysis of the Lower Silurian Longmaxi Formation shales of the upper Yangtze region in Southern China. *Front. Earth Sci. (Lausanne).* 2022, 864279. doi:10.3389/feart.2022.864279

Zhang, X., Ma, Y., He, J., Gong, C., and Wang, Y. (2021). Formation mechanism of high quality reservoir in glutenite:as an example of group Wuerhe at permian in Mahu area of Junggar Basin. *Inn. Mong. Petrochem. Ind.* 47 (08), 103–110.

Zhang, Z. (2019). *Oil-gas source correlation and migration tracing in the deep western central depression of Junggar Basin*. East China: China University of Petroleum. doi:10.27644/d.cnki.gsydu.2019.000134

Zhao, W., Hu, S., Guo, X., Li, J., and Cao, Z. (2019). New concepts for deepening hydrocarbon exploration and their application effects in the Junggar Basin, NW China. *Petroleum Explor. Dev.* 46 (05), 856–865. doi:10.1016/s1876-3804(19)60245-4

Zhi, D. (2016). Discovery and hydrocarbon accumulation mechanism of quasi continuous high efficiency reservoirs of Baikouquan Formation in Mahu sag, Junggar Basin. *Xinjiang Pet. Geol.* 37 (04), 373–382. doi:10.7657/XJPG20160401

Zhi, D., Tang, Y., Zheng, M., Guo, W., Wu, T., Zou, Z., et al. (2018). Discovery, distribution and exploration practice of large oil provinces of Above?Source conglomerate in Mahu sag. *Xinjiang Pet. Geol.* 39 (01), 1–8. doi:10.7657/XJPG20180101

Zhou, X., Huang, X., Wang, Q., Ma, Z., and Chen, L. (2020). Identification and description of the multi- stage sandy conglomerate fan body in Shinan Steep Slope Zone, Bohai Sea. *J. Northeast Petroleum Univ.* 44 (02), 46–55+8. doi:10.3969/j.ssn.2095-4107.2020.02.005

Zou, N., Zhang, D., Qian, H., Wu, T., and Shi, J. (2016). Main controlling factors of glutenite reservoir of fan delta in Mabei slope, Junggar Basin. *Lithol. Reserv.* 28 (04), 24–33. doi:10.3969/j.issn.1673-8926.2016.04.004

Zou, Z., Guo, H., Niu, Z., Yang, X., Xiang, S., Li, Y., et al. (2021). Sedimentary characteristics and controlling factors of river-dominated fan delta:a case study from the Upper Urho Formation in Mahu sag of Junggar Basin. *J. Palaeogeogr.* 23 (4), 756–770. doi:10.7605/gdlxb.2021.04.049

frontiers | Frontiers in Earth Science

TYPE Original Research
PUBLISHED 27 September 2022
DOI 10.3389/feart.2022.996167

OPEN ACCESS

EDITED BY
Wenlong Ding,
China University of Geosciences, China

REVIEWED BY
Kuanhong Yu,
China University of Petroleum, Huadong, China
Xiaodong Zhao,
China University of Petroleum, Beijing, China

*CORRESPONDENCE
Peidong Su,
spdong@126.com

SPECIALTY SECTION
This article was submitted to Structural Geology and Tectonics, a section of the journal Frontiers in Earth Science

RECEIVED 17 July 2022
ACCEPTED 24 August 2022
PUBLISHED 27 September 2022

CITATION
Wang S, Yang X, Lu Y, Su P, Liu D, Meng L, Wang Q, Li L and Radwan AE (2022), Densification mechanism of deep low-permeability sandstone reservoir in deltaic depositional setting and its implications for resource development: A case study of the Paleogene reservoirs in Gaoshangpu area of Nanpu sag, China.
Front. Earth Sci. 10:996167.
doi: 10.3389/feart.2022.996167

Densification mechanism of deep low-permeability sandstone reservoir in deltaic depositional setting and its implications for resource development: A case study of the Paleogene reservoirs in Gaoshangpu area of Nanpu sag, China

Shilin Wang[1], Xiran Yang[2], Yuanyuan Lu[3], Peidong Su[1]*, Dong Liu[4], Lingjian Meng[4], Qi Wang[4], Liang Li[4] and Ahmed E. Radwan[5]

[1]School of Geoscience and Technology, Southwest Petroleum University, Chengdu, China, [2]Exploration and Development Research Institute, PetroChina Southwest Oil & Gas Field Company, Chengdu, China, [3]CNOOC Research Institute Ltd., Beijing, China, [4]Exploration and Development Research Institute, Jidong Oilfield Company, PetroChina, Tangshan, Hebei, China, [5]Faculty of Geography and Geology, Institute of Geological Sciences, Jagiellonian University, Kraków, Poland

A better understanding of reservoir densification mechanisms is very important for petroleum exploration and controlling the reservoir quality distribution in low-permeability reservoirs. Low porosity and low permeability, difficult reconstruction, and economic infeasibility are important factors restricting its efficient production. Systematic analysis was performed to study the evolution of different microfacies in the deltaic depositional setting of the Paleogene deep low-permeability Gaoshangpu reservoir, define their genetic mechanisms, delineate the dominant facies belts, and define the favorable diagenetic sequences that are important for exploration of high-quality reservoirs. To understand the tight genesis of the low-permeability reservoirs, we analyzed the sedimentological and diagenetic evolution characteristics of various microfacies (i.e., underwater distributary channel, distributary bay, mouth bar, and front sheet sand) using core data and physical property analysis of the reservoir sand body. The results show the underwater distributary channel and estuary bar sand body with medium-to fine-grained and poor–medium sorting. The diagenesis is dominated by strong compaction, calcareous, argillaceous cementation, and dissolution during stage B in early diagenesis and stage A in middle diagenesis. In the fan delta environment, the weak anti-compaction resistance of low-permeability reservoirs is mainly due to the large content of plastic particles, finer grain size, and medium–poor sorting, with an average porosity reduction rate of 65%. This is a key factor for densification of reservoirs above 3000 m. Comparison among different sandstone microfacies of the deltaic setting shows that the

sand body of the underwater distributary channel with low shale content has slightly stronger compaction resistance. The porosity reduction is not obvious at the depth of 3,000–4,000 m, but the loss of permeability at this depth section is significant, and the reservoir improvement from later dissolution is most obvious at this depth section. Calcareous cementation is the cause for densification of some mouth bars in the early stage and of underwater distributary channels in the middle and late stage. Under the influence of strong compaction and calcareous-filling pore throat, the sand body of the mouth bar has been basically densified at 3,000 m, resulting in limited reservoir transformation from later dissolution. The study shows that compaction is the main cause of reservoir densification, argillaceous and calcareous cementation is the secondary cause, and later dissolution is another main cause of reservoir enhancement. The research results can provide a reference and direction for reservoir development and search for the high-quality sweet spot in the deep and low-permeability reservoir.

KEYWORDS

reservoir characteristics, deep layer, low permeability, densification, Gaoshangpu oilfield, Nanpu sag

1 Introduction

Low-permeability sandstone reservoirs or tight reservoirs are one of the most important hydrocarbon resources worldwide (Law and Dicknson, 1985; Karim et al., 2010; Zou et al., 2012; Li et al., 2019a). Many researchers have investigated low-permeability reservoirs in terms of sedimentological, diagenesis, and petrophysical properties (i.e., porosity and permeability) for better control of these important reservoirs (Xi et al., 2015; Yang et al., 2016a; Lai et al., 2016; Li et al., 2021a). Typically, low-permeability sandstone reservoir productivity could be dependent on primary sedimentation conditions or secondary diagenetic and fractured types, as well as the development of enigmatic sweet spots or the basin petroleum system (Shanley et al., 2004; Zeng et al., 2010; Li et al., 2018a). Such low-permeability reservoirs have unique petrophysical and sedimentological characteristics that need to be fully understood to mitigate misunderstanding of these attributes and wrong subsurface interpretation. For example, identifying the densification mechanism in low-permeability reservoirs and the match between the pore evolution history and the hydrocarbon generation time is of interest to researchers in critical resource assessment (Bjørlykke, 2014). Diagenesis is the most effective reservoir control method for forming the current reservoir conditions (Xi et al., 2015). To predict the reservoir performance and define the formation mechanism of these low-permeability reservoirs, a comprehensive knowledge of the relationships between depositional fabric, routine vs. effective permeability, and pore geometry under the conditions of overburden stress is a fundamental request according to Shanley et al., 2004; Wang et al., 2013; Mingjie et al., 2014; Xi et al., 2015; Ren et al., 2019. The deep low-permeability reservoirs are expected to have more complex depositional and diagenetic features that impact the quality of these reservoirs. However, few studies have been directed toward the deep low-permeability reservoirs in different depositional settings and different microfacies, which remain scarce. Therefore, the example of the Paleogene deep low-permeability reservoir from the Gaoshangpu oilfield, Nanpu Sag, China was examined in this work.

The Gaoshangpu area is a main oil-producing area with high and stable production in Nanpu Sag and also an oil-rich depression in the Bohai Bay Basin. The Paleogene Submember 2 + 3 substratum in Section 3 of the Shahejie Formation (Es_3^{2+3}) is the main oil-bearing series in the Gaoshangpu oilfield (Liu et al., 2022), in which the low-permeability reserves account for more than 80% of the undeveloped reserves in the Jidong oilfield. With the deepening of exploration, the proportion of low-permeability reserves of undeveloped reserves in the Jidong oilfield is increasing, which has potential as an important strategic resource for stable production in the future. The buried depth of the low-permeability reservoir is 3,000–4100 m, with the oil-bearing interval having a depth of 600–700 m (Xu et al., 2020), and the production at different depths and blocks varies greatly. There are both conventional reservoirs and difficult-to-recover low-permeability reserves. The proven oil-bearing area of Es_3 is 17.4 km^2, and the proven geological reserves are 38.02 million tons, while daily oil production is about 251 tons, that is to say, the oil recovery rate is only 0.32%. Reservoir heterogeneity is strong, and physical property span is large with a porosity of 6%–24% and permeability of 0.5~100 $\mu m^2 \times 10^{-3}$ μm^2 (Liu et al., 2022; Yang et al., 2016b; Xie et al., 2017; Lai et al., 2018). The low-permeability reserves in deep Gaoshangpu reservoirs account for a large proportion of undeveloped reserves in the Jidong oilfield. The reasons for its inefficient exploitation include its tight and low-permeability features, as well as its hard-to-transform and

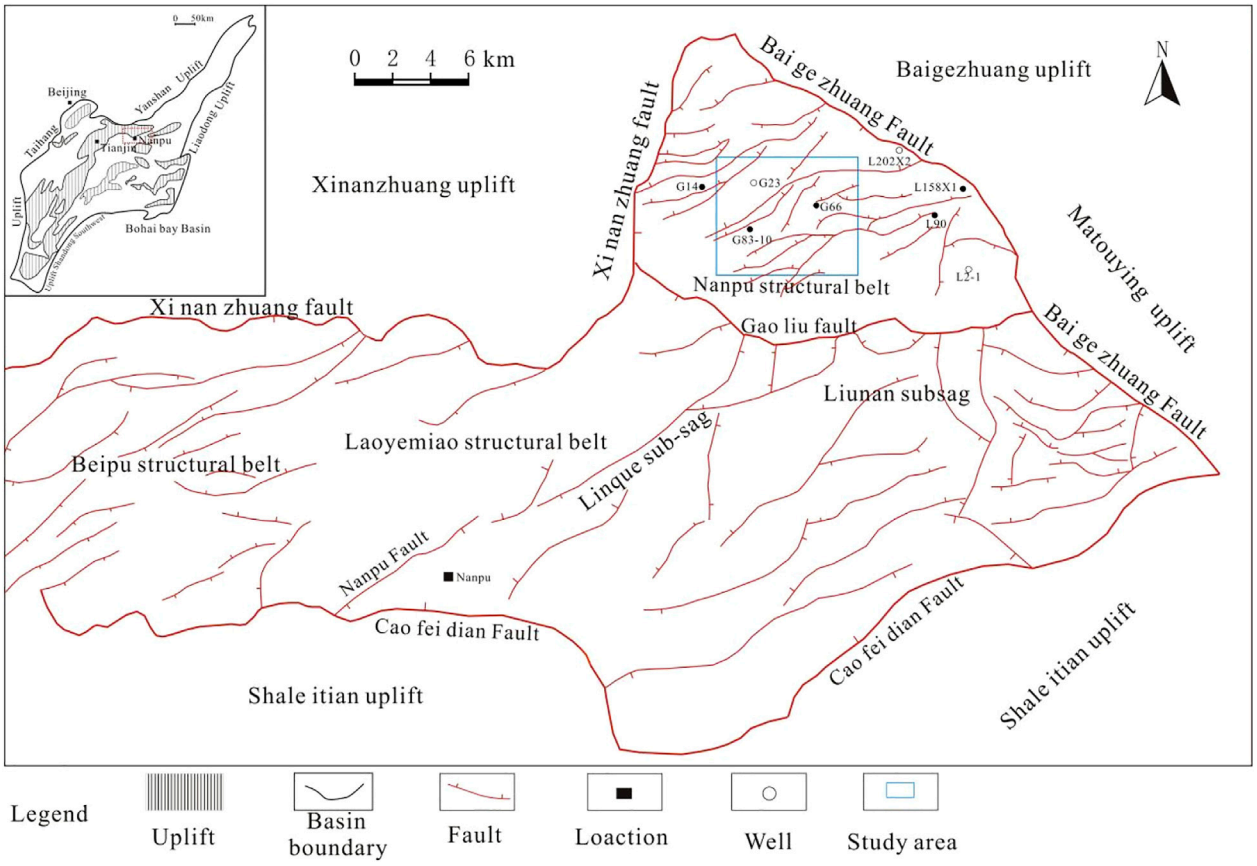

FIGURE 1
Structure location and well location map of the Gaoshangpu oilfield.

economically unfavorable nature. The evaluation and study of the deep low-permeability reservoir in Gaoshangpu is of great significance for the subsequent development policy and its efficient development. A great deal of study has been carried out on sedimentary characteristics, diagenetic evolution, heterogeneity, time-varying characteristics, sensitivity, etc. (Gao et al., 2016; Li et al., 2018b). The possibility and favorable controlling factors of the high-quality reservoirs in the middle and deep layers of Nanpu Sag are discussed in detail, which not only enhances the confidence in the exploration and development of deep oil and gas resources but also points out the direction for efficient exploration and development of high-quality reserves in the middle and deep layers. However, the difference in diagenetic evolution of different micro-facies reservoir sand bodies, the tight genetic mechanism of low-permeability reservoirs, and the diagenetic evolution of dominant reservoir facies sand bodies still need to be studied in depth. Also, it is the key factor in determining favorable sedimentary and diagenetic facies belts and predicting favorable desert areas. Based on the theories of sedimentology, reservoir geology, and development geology, the authors carried out the research through the data of core observation, thin section identification, scanning electron microscope, X-ray diffraction, and physical property analysis.

Through systematic analysis of the formation and evolution of different micro-facies reservoirs in the fan delta, the genetic mechanism of low-permeability reservoir and the dominant facies belts and favorable diagenetic sequences are defined, and meanwhile, the possibility of high-quality reservoirs formed in deep low-permeability reservoirs is further explored. It provides a geological basis for oilfield increase in reserves and production, as well as for efficient development of the Gaoshangpu reservoir, and meanwhile, it provides a reference for evaluation of other low-permeability reservoirs in Nanpu Sag and similar areas that have the same geological conditions.

2 Geological setting

Gaoshangpu oilfield is located in the northern part of Nanpu Sag and the eastern part of the structural belt next to

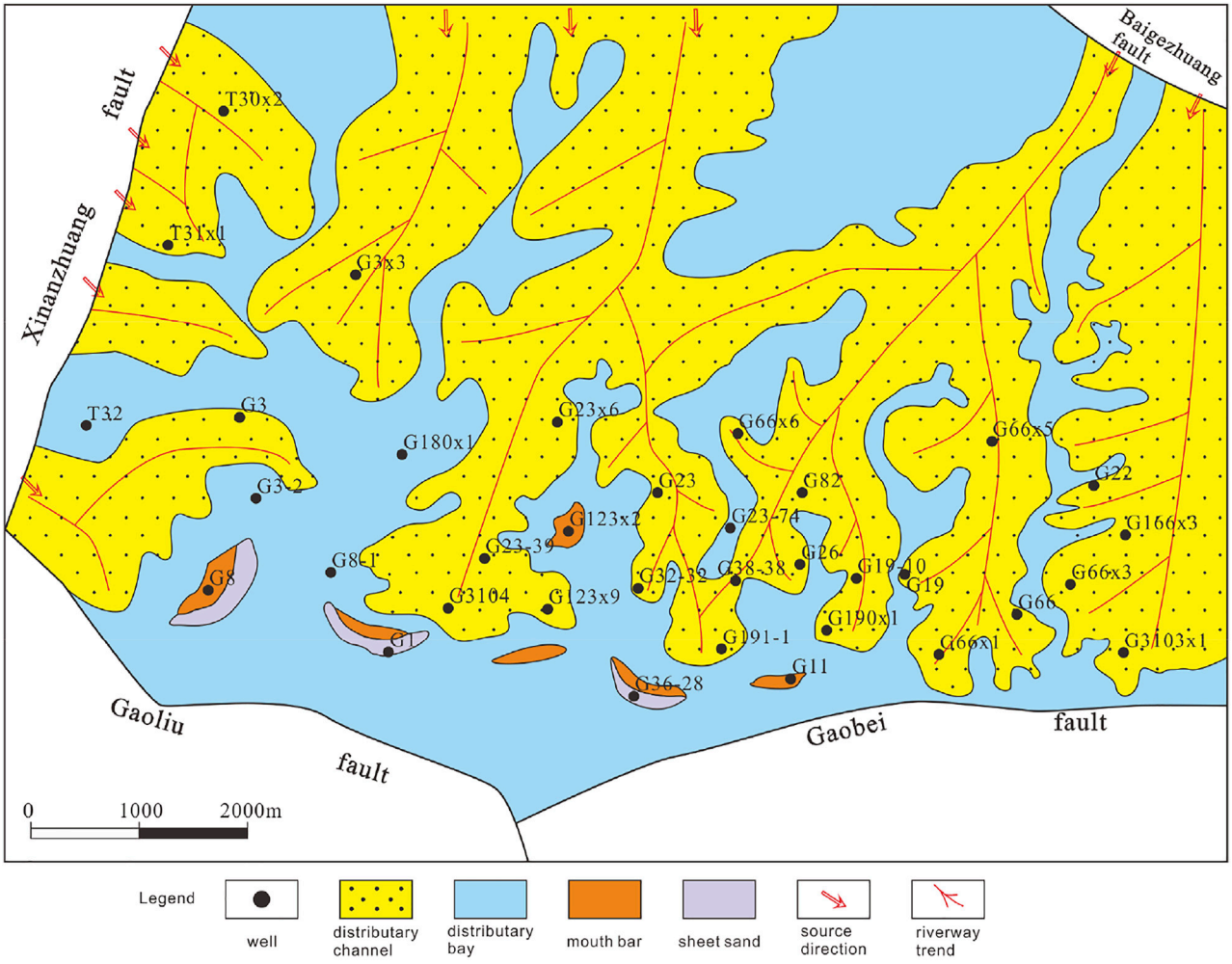

FIGURE 2
Sedimentary facies diagram of the Gaoshangpu Oilfield.

Liuzan oilfield. The northern part of the oilfield is sandwiched by the Xinanzhuang and Baigezhuang faults (Figure 1). It is an anticline structure complicated by faults. The main structure covers an area of about 20 km^2 with developed faults and broken fault blocks. The deep low-permeability Gaoshangpu reservoir, which is NW-trending, is located on the upthrown side of the Gaoliu fault in the steep slope zone of the Nanpu Sag. It is cut into several fault blocks by NW-trending, NE-trending, and nearly EW-trending faults. The Quaternary Pingyuan Formation (Q), Neogene Minghuazhen Formation (Nm), Guantao Formation (Ng), Paleogene Dongying Formation (Ed), and Shahejie Formation (Es) are developed from top to bottom in the Gaoshangpu oilfield. The Shahejie Formation can be further divided into Es_1, Es_2, and Es_3. There are five sets of marker beds in the whole formation. The largest marker bed in this area is the mudstone section of the oil group 0 in sub-member of Es_3.

Es_3 was in the developing stage in the fault basin. A set of fan delta sedimentary bodies deposited rapidly near the source and steep bank with strong alluvial capacity, and the provenance lies in the north and NE. Two subfacies developed, namely, fan delta front and pro-fan delta, of which the fan delta front can be divided into four microfacies as the underwater distributary channel, distributary bay, mouth bar, and front sheet sand, and the pro-fan delta mainly develops far sand bars (Figure 2). The sediments are dominated by lithic feldspar sandstone, with low component maturity and structural maturity. The sand body of an underwater distributary channel is characterized as fining upward, and the erosion surface can be seen in some locations. The natural gamma curve is box-shaped or bell-shaped. The sand body of the mouth bar is characterized as coarsening upward, with obvious cross bedding on the top and a funnel-shaped natural gamma curve.

3 Samples and methods

3.1 Samples

In this study, the experimental samples came from the sandstone of the third member of the Gaoshangpu Oilfield. In order to analyze the difference in the storage performance of the reservoir rock under different depositional environments and depth conditions, targeted sampling of reservoirs is carried out in different depositional environments, and the sampling depth is between 3,200 and 4300 m.

3.2 Experimental methods

3.2.1 Porosity and permeability test

The porosity and permeability tests of samples adopt the AP-608 overburden porosity-permeability tester. Before the experiment, the sandstone sample is made into a cylindrical shape of 1 cm × 3 cm (diameter × length), and the cylindrical sample is placed in the experiment process. In the Hassler core holder, the porosity and permeability tests are automatically measured by the instrument. The permeability is obtained by the non-steady state pulse attenuation, and the porosity test passes the Boyle's law test.

3.2.2 Storage space type

The observation of the storage space type adopts the casting thin section and scanning electron microscope. The casting thin section is made by the ZT-2 rock casting instrument. The samples will be evacuated during the production process. The casting body is made of colored epoxy resin. The observation of the type of thin pore space is carried out with an XP607 polarizing microscope.

The scanning electron microscope test uses a Quanta 450 environmental scanning electron microscope produced by FBI Company to observe the microscopic pore structure of shale. Before the experiment, the sample is cut into dimensions of 5 mm × 5 mm × 3 mm, and the surface of the experimental sample is polished with argon ions. At the same time, an ion mill is used to show and grind the sample to eliminate surface irregularities. The processed sample is placed on the sample table, and SEM is used to observe the type of pores on the polished surface.

3.2.3 Pore structure

The pore structure of the sample was obtained by a high-pressure mercury intrusion experiment PoreMaster60 automatic mercury intrusion instrument produced by the United States Conta Company. Before the experiment, the sample was made into a 2.5 cm × 3.5 cm (diameter × length) standard core. The test process was carried out in a well-ventilated, room-temperature environment. The experiment process adopted continuous pressure, and the pore median radius was automatically calculated by the instrument.

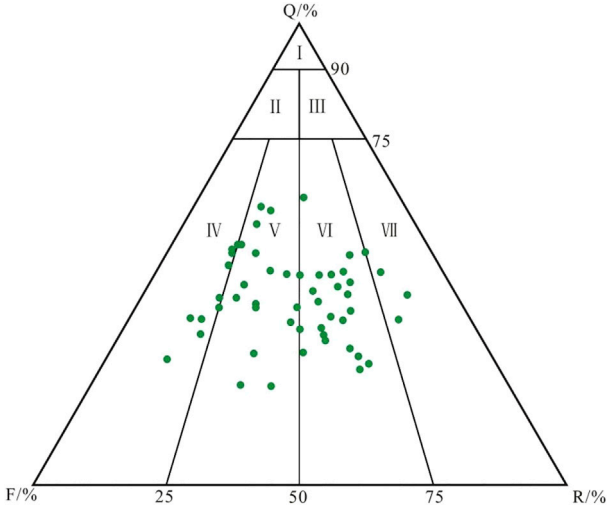

FIGURE 3
Triangular classification map of sandstone skeleton composition in deep low-permeability reservoirs in Gaoshangpu.

4 Results and discussion

4.1 Reservoir characteristics

4.1.1 Sedimentology characteristics

Es_3 is a set of fan delta sedimentary products, close to the provenance. Several types of sedimentary microfacies, such as underwater distributary channels, mouth bars, sheet sands, interdistributary bays, and distal bars, are developed. The sand bodies developed under different sedimentary microfacies have huge differences in scale and reservoir effectiveness. For the study area, the effective reservoir is mainly composed of an underwater distributary channel and mouth bar (Wang et al., 2010; Wang et al., 2013). The shale content in underwater distributary channels and mouth bars is low, with coarser grain sizes and larger-scale sand bodies. However, sheet sand, interdistributary bay, and distal bar mainly consist of argillaceous siltstone, siltstone, and mudstone with relatively small sand body scale. Therefore, the following mainly introduces the underwater distributary channel and mouth bar.

4.1.2 Lithological characteristics

Deep low-permeability Gaoshangpu reservoirs are dominated by medium and fine sandstones, with 67%–91% rigid grain composition and an average ratio of about 81.4%. The contents of cuttings, feldspar, and quartz are roughly the same, mostly feldspar sandstone and feldspar lithic sandstone

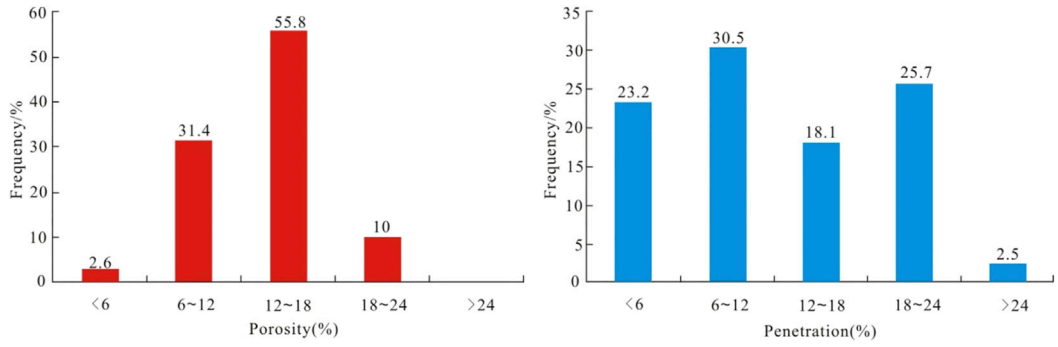

FIGURE 4
Histogram of physical property distribution of high-depth and low-permeability reservoirs.

(Figure 3). The cement is mainly argillaceous and calcareous, as well as quartz overgrowth. The argillaceous content is 2%–19%, with an average of about 8.4%. The average content of cement is 5.6%, and the main types of cement are porous cementation and line contact cement. The clay minerals are mainly composed of illite–montmorillonite mixed layer and chlorite. The detrital sediments are characterized by strong erosion, rapid transportation, and rapid accumulation (Fan et al., 2020b; Fan et al., 2020c).

The sand skeleton particles in the underwater distributary channel are poor–medium sorted with the sorting coefficient ranging between 1.41 and 2.17. The roundness is medium, the particle size lies between 0.18 and 0.59 mm, and the shale content is generally less than 7%. The mouth bar is characterized as inverse grading. The lithology is mainly fine sandstone and medium sandstone, with the sorting coefficient between 1.23 and 1.45. The roundness is good, with the particle size lying between 0.15 and 0.32 mm. Argillaceous content is slightly higher, ranging from 5% to 10%. The sediments in the distal bar are relatively fine, which are deposited in the process of the sand body being pushed to the lake, developing into a transitional relationship with the pre-delta mudstone, where very few thin coarse sand layers can be seen. The sorting coefficient is between 1.9 and 4.2. Sand body roundness is medium–good, with the particle size between 0.02 and 0.13 mm. The shale content is generally greater than 10%. The sediments of the sheet sand and the mouth bar are similar. The differences lie in the shape of the sand body and the amount of shale content. The shale content of sheet sand is slightly higher, which is mainly reflected in argillaceous lamina, silty mudstone, and mudstone interbedded development.

4.1.3 Physical characteristics

According to the analysis results of the rock porosity test, the porosity of the deep low-permeability Gaoshangpu reservoir is mainly distributed between 6%–20%, accounting for 80% porosity, with the average porosity being 14.3%. The reservoir permeability is mainly distributed in $1\ \mu m^2 \times 10^{-3}\ \mu m^2$–$10\ \mu m^2 \times 10^{-3}\ \mu m^2$ and $20\ \mu m^2 \times 10^{-3}\mu m^2$–$50\ \mu m^2 \times 10^{-3}\ \mu m^2$, and the average permeability is $9.98\ \mu m^2 \times 10^{-3}\ \mu m^2$. According to the classification standard of reservoir porosity in the petroleum industry (ST/T 6285-1997), the reservoir is a low-permeability to ultra-low-permeability reservoir (Figure 4). The physical properties of the underwater distributary channel and mouth bar are the best. The average porosity is 18.5% and 15.1%, respectively, and the average permeability is $17.8\ \mu m^2 \times 10^{-3}\ \mu m^2$ and $12.5\ \mu m^2 \times 10^{-3}\ \mu m^2$, respectively. The porosity and permeability of the interdistributary bay sand bodies have no obvious changes in different diagenetic stages, and the porosity is between 5% and 15%, and the permeability is between $0.01\ \mu m^2 \times 10^{-3}\ \mu m^2$ and $0.5\ \mu m^2 \times 10^{-3}\ \mu m^2$. The porosity and permeability of the far-bar sand bodies decrease with the deepening of the diagenetic stage. The porosity is between 5% and 20%, and the permeability is between $0.01\ \mu m^2 \times 10^{-3}\ \mu m^2$ and $0.5\ \mu m^2 \times 10^{-3}\ \mu m^2$. The porosity and permeability of the sheet sand reservoir have obvious differences at different depths. The porosity is between 5% and 15%, and the permeability is between $0.01\ \mu m^2 \times 10^{-3}\ \mu m^2$ and $5\ \mu m^2 \times 10^{-3}\ \mu m^2$.

4.1.4 Reservoir space types and characteristics

According to the observation results of the scanning electron microscope and microsection, the pore types of the reservoir include primary residual pore, intergranular solution pore, intragranular dissolved pore, mold pore, and other clay micropores (Figure 5). Intergranular and intergranular dissolution pores are well-developed (Figures 5A,E,F), accounting for 8%–90% and 5%–15%, respectively, and primary residual intergranular pores accounted for 3%–32.6%. The selective dissolution leads to uneven distribution of dissolved pores between and within grains, resulting in further enhancement of reservoir heterogeneity,

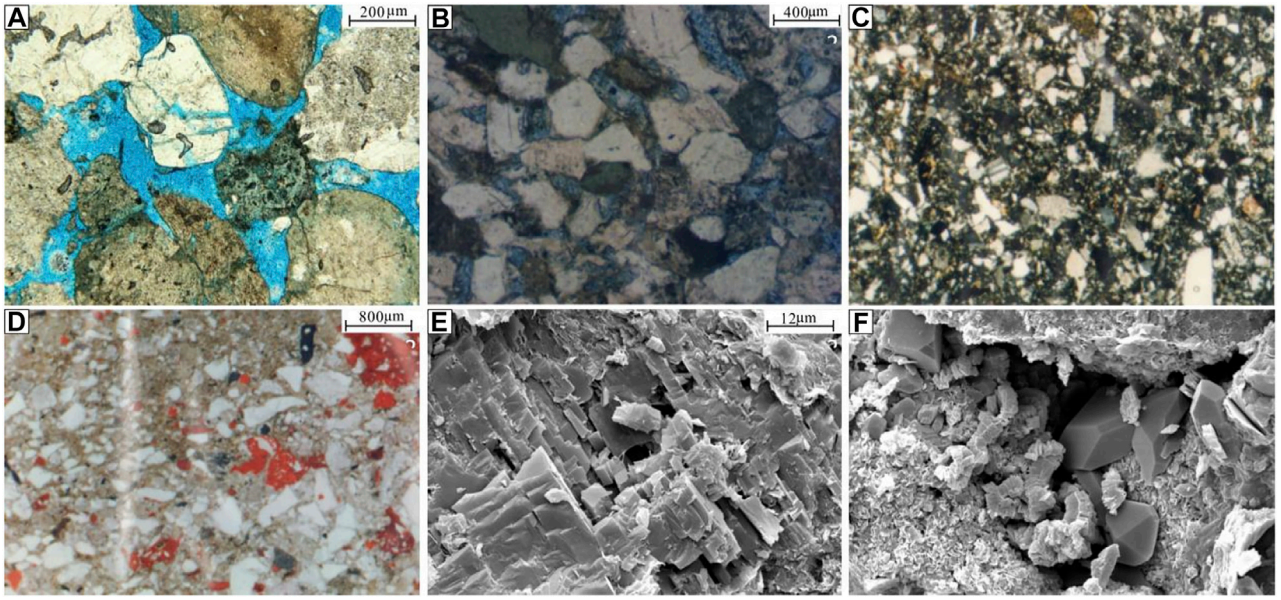

FIGURE 5
(A). Reservoir space types of the high-deep reservoir of the third member of Shahejie Formation in Gaoshangpu oilfield, Nanpu Sag. **(A)**. GJ3102-8, 3,131.24 m, gravel-bearing medium sandstone in the underwater distributary channel, with developed primary pores and a small amount of intergranular and intragranular dissolution pores, and the throats are flaky and bundled throats; **(B)**. G32-30, 3,476.1 m, distributary estuary bar fine sandstone, dissolution pores, mold holes, throats are mainly bundled, and fine throats; **(C)**. G58-33, 3629 m, sheet sand argillaceous fine siltstone, few remaining primary pores, mainly micropores, and intragranular dissolved pores in the clay, and fine throats as the main throat; **(D)**. G83-10,3663.8 m, far sand bar argillaceous fine siltstone, basic pores are basically not developed, a few secondary dissolved pores are developed, there are more clay micropores, poor pore permeability, and fine throat mainly; **(E)**. GJ5-44, 3169 m, intragranular dissolution pores of feldspar; **(F)**. GJ5-44, 3,164.8 m, remaining intergranular pores.

complicated pore throat structure, and poorer pore connectivity (Figure 5).

There are several types of pore throat structures, such as medium pore with medium–fine throat type, medium–fine pore with fine throat type, fine pore with fine throat type, and micropore with micro-throat type (Figure 5). Throat types are mainly necking, schistose, or micro-throats with poor connectivity (Figures 5B–D). The high-value range of the throat width is 15.38–62.32 μm and the low value range is 1.27–2.98 μm, with an average throat width between 5.73 and 19.97 μm. The coordination number indicates the number of throats connecting the pores. The maximum coordination number is 1–5, and the average coordination number is 0.02–0.42, which determines that it is a coarse throat with a low coordination number, and the pore connectivity is medium to poor.

4.2 Characteristics and evolution sequence of diagenesis

4.2.1 Features of diagenesis

The Es3 Formation in the Gaoshangbao oilfield is buried below 4000 m, and the diagenesis is complex (Figure 6). Based on the relationship between physical property and depth and the relationship between the initial porosity and the separation coefficient proposed by Lundegard, the primary porosity of the surface of the subaqueous distributary channel reservoir is estimated to be 37%–45%. The initial porosity of the mouth bar is 39%–55%. The overall compaction rate of the deep low-permeability Gaoshangpu reservoir is 66.3%, which shows medium–strong compaction. The cementation is dominated by carbonate minerals and argillaceous cementation, with a small amount of kaolinite and siliceous cementation filling and feldspar dissolution, which account for 7.5% of the secondary pores in the study area. The characteristics of reservoir diagenesis of different sedimentary microfacies are studied. The results show that the overall compaction of the underwater distributary channel is weak, and the particles are mainly in point or line contact. The content of shale is relatively small, and the cementation is mainly siliceous and calcareous cementation. The secondary growth of quartz can be enlarged to grades II–III. The authigenic microcrystalline quartz can also be seen (Figure 5E). The average content of quartz cement is 2.0%. Most corrosions are feldspar dissolution, and a small amount of corrosions are debris dissolution. The compaction is gradually enhanced in the middle and late stages of diagenesis with strong calcareous cementation (Li et al., 2019c; Li et al., 2020; Li et al.,

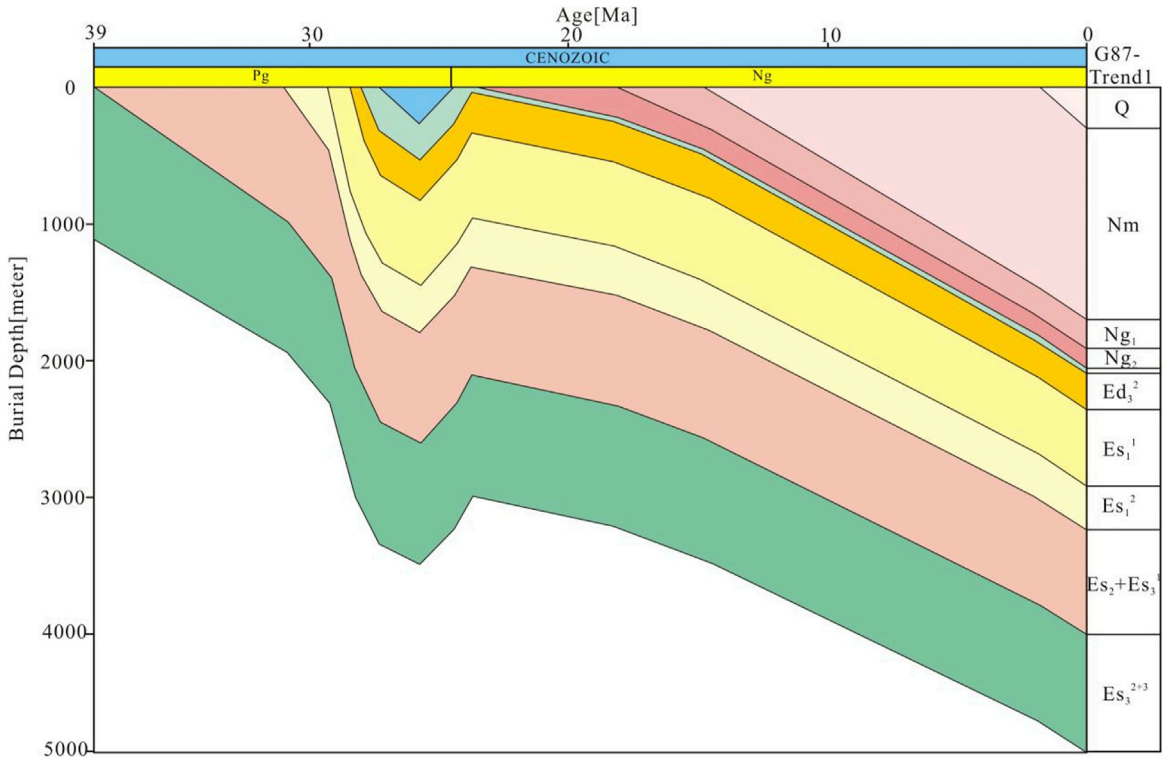

FIGURE 6
Burial history of Es_3^{2+3} in well G87 in the Gaoshangpu oilfield.

2021b; Li, 2022). The primary intergranular pores and solution pores are developed in the early stages, and the solution pores are dominant in the middle and late stages.

The reservoir sand body of the mouth bar was initially compacted above 3000 m, and then the reservoir was further densified by mechanical compaction. The diagenesis is mainly calcareous cementation and strong compaction. The average content of calcite is 5%, and the highest value can reach 14%. Calcite replacing feldspar could be seen, and the dissolution is weak. The silicon content increased, and calcareous cementation is obviously enhanced. Calcite–crystal cementation can be seen locally, showing a calcium tip on the curve. Intergranular pores are commonly found as residual intergranular micropores and dissolved pores, which come from feldspar and debris dissolution. The distal bar, sheet sand, and interdistributary bay have higher plastic mineral content. After strong mechanical compaction and calcareous cementation above 3000 m, a few intergranular pores with weak siliceous cementation and dissolution remain. Dissolution mostly occurs in feldspar and lithic minerals along fractures or bedding (Li et al., 2019b; Fan et al., 2020a; He et al., 2020; He et al., 2021; He et al., 2022a; Li et al., 2022a; Li et al., 2022b; Fan et al., 2022).

4.2.2 Diagenetic stages

Deep low-permeability Gaoshangpu reservoirs have been subjected to diagenesis, such as strong compaction, cementation, and dissolution (Guo et al., 2019). Sampling distraction in the study area showed that the reflectance of vitrinite ranged from 0.5% to 0.9% and the ratio of the illite/smectite interlayer from 25% to 70%, with an average of 55%. Primary pores and secondary pores are well-developed. Primary pores are mainly developed in the middle and lower parts of the layers, and secondary pores are concentrated in the lower part of the reservoir. According to the classification criteria for diagenetic stages of clastic rocks (ST/T5477—2003), the diagenetic stage in the studied reservoirs is between early diagenetic stage B and middle diagenetic stage A (Figure 7).

4.2.3 Diagenetic sequence

Diagenesis is an important factor affecting reservoir quality. Reservoir types with different pore structures and physical properties result from distinct diagenetic sequences, diagenetic stages, and diagenetic evolution (Zhu et al., 2009; He et al., 2022b; Wang et al., 2022). Based on the assemblage of diagenetic minerals of deep low-permeability Gaoshangpu reservoirs, it

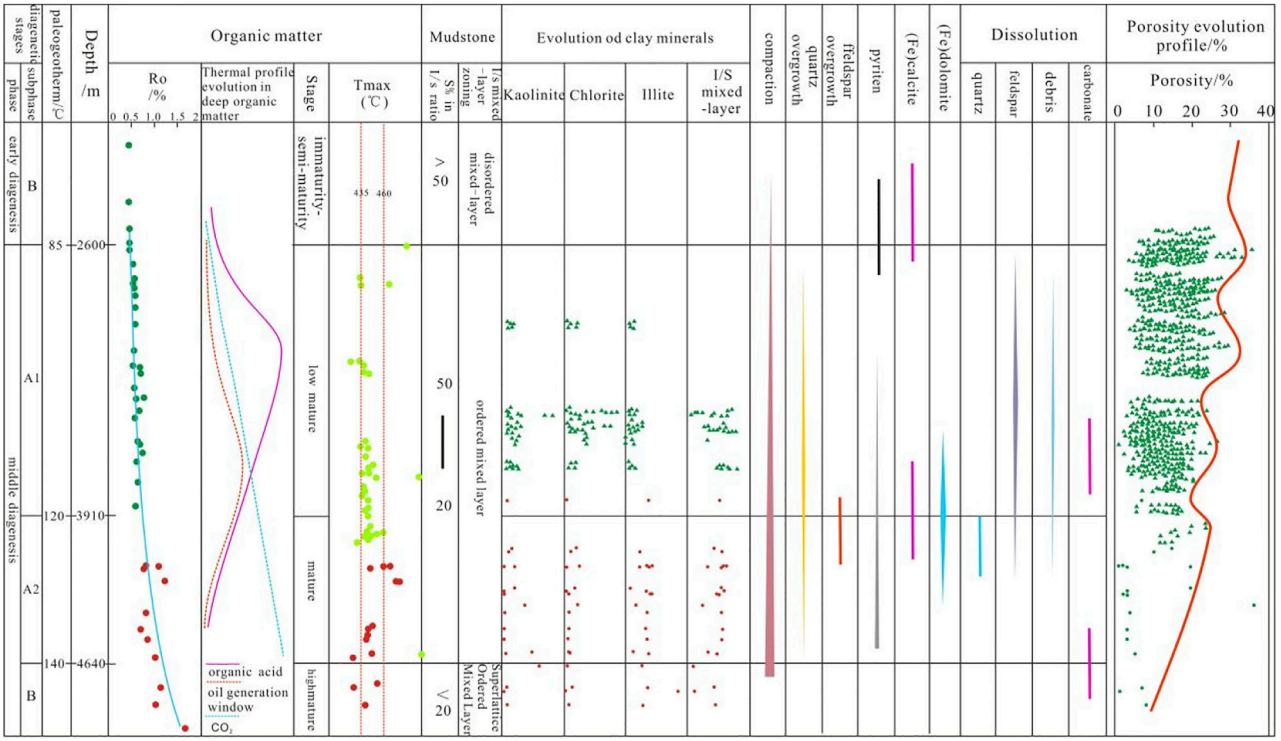

FIGURE 7
Division of diagenetic stages of the Gaoshangpu oilfield (modified by Jidong oilfield exploration and development research institute).

can be preliminarily determined that the sequence of diagenetic minerals or diagenesis is as follows:

Microcalcite-silica I stage overgrowth-weak dissolution of feldspar, debris-silica II stage overgrowth-kaolinite precipitation-large-scale feldspar, and lithic dissolution-silica III stage overgrowth-intergranular pores filled with quartz-(iron-bearing) calcite filling-dolosparite-weak dissolution.

4.3 Influencing factors of low-permeability reservoir

4.3.1 Influence of sedimentary environment and sediment composition on reservoir

Due to the difference in hydrodynamic conditions and transport distances in each sedimentary environment, skeleton composition, grain structure, and impurity content of different microfacies sand bodies have different characteristics, which also have a profound influence on the evolution sequence and degree of burial diagenesis (Jiang et al., 2004; Li et al., 2010). With the increase in shale content and the decrease of average grain size, the diagenetic compaction becomes more intense (Wu et al., 2020; ZinsaloJoël et al., 2021). The physical properties of the distributary channel, mouth bar, distal bar, and sheet sand reservoir at the same buried depth become worse successively. Due to the strong hydrodynamic conditions, the coarse sediment particles, slightly low content of miscellaneous base, and burial depth above 3500 m, the physical properties of the underwater distributary channel and distributary mouth sand bar are far better than those of the far sand bar and sheet sand. Among them, the underwater distributary channel is the best, and the permeability is nearly 10 times higher than that of the sand body of the mouth bar. Some far sand bars, sheet sand, beach bars, and thin sand layers in bay sand sheets buried more than 3000 m deep have already been densified.

When the buried depth exceeds 3000 m, the pore reduction of the underwater distributary channel is not obvious. However, the permeability decreases more significantly, while the situation of the sand body of the mouth bar is the opposite. Affected by water erosion, the energy of the water body of the underwater distributary channel is stronger when deposited; the mud content is lower than that of the mouth bar, and the pore is less affected by compaction. After the burial depth exceeds 3000 m, the overburden pressure of the skeleton particles increases and the porosity decreases only a little, but the contact between particles changes gradually from point contact to line contact, and thus the

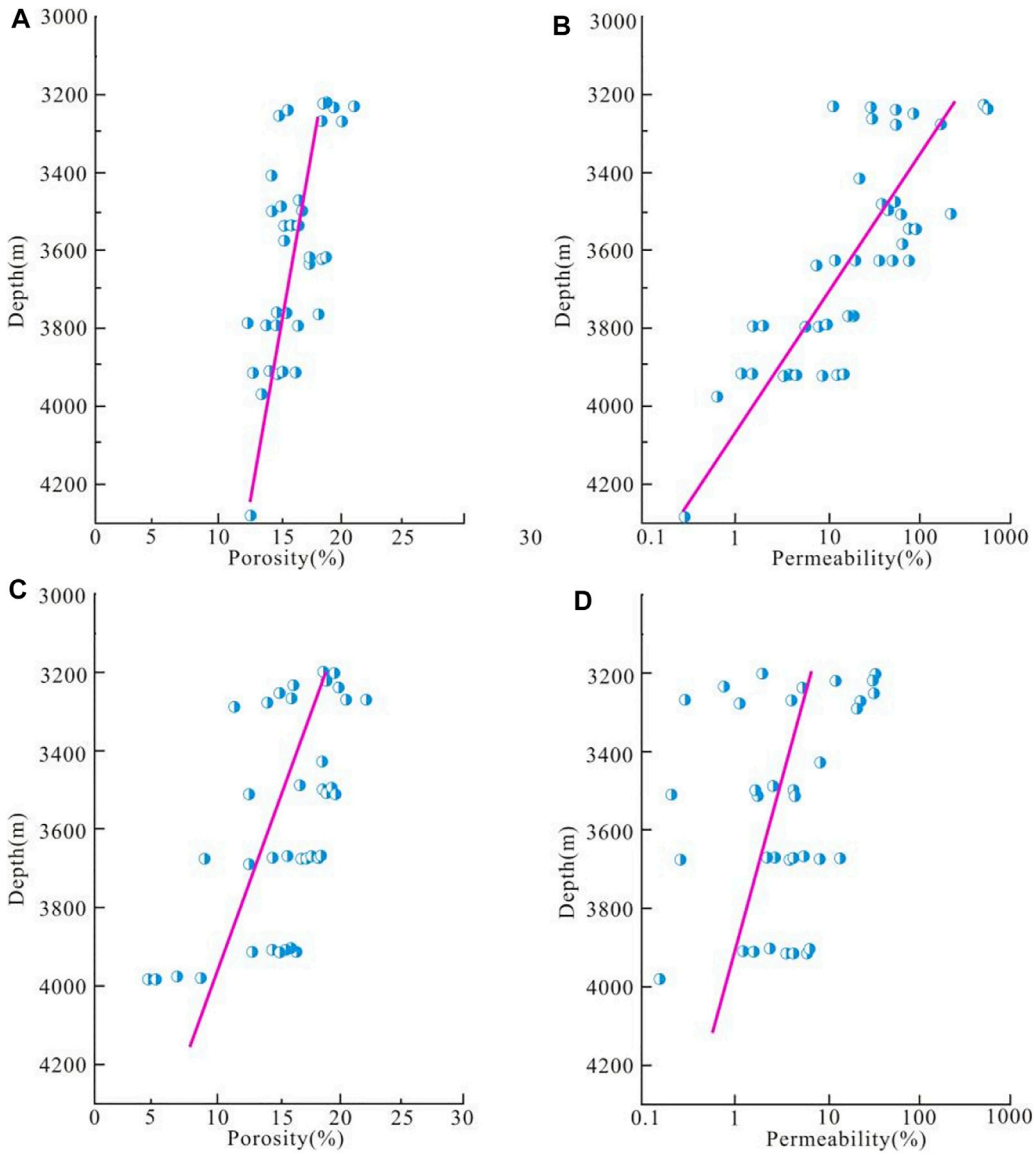

FIGURE 8
Physical properties of the underwater distributary channel and estuary dam reservoirs change with buried depth. **(A)**. Variation of porosity of the underwater distributary channel reservoir with buried depth. **(B)**. Variation of permeability of the underwater distributary channel reservoir with burial depth. **(C)**. Variation of porosity of the Hekouba reservoir with buried depth **(D)**. Variation of permeability of the Hekouba reservoir with buried depth.

throat radius is significantly reduced (Figure 8). Therefore, the permeability loss is more than that of the estuary bar, but the porosity loss of the estuary sand bar reservoir with finer grain size and more plastic content is more obvious. With the intensity of compaction, the pore throat size decreases significantly, leading to reservoir densification in the underwater distributary channel. The particle size and shale content not only determine the intensity of compaction in the early stage and fluid activity in the later stage of the reservoir but also the intensity of later corrosion and cementation.

4.3.2 Effect of compaction on reservoir densification

The mechanical compaction becomes stronger with the increase in the buried depth of the reservoir. Low-permeability Gaoshangpu reservoir is deeply buried, whose main diagenesis are compaction and pressure dissolution (Gao et al., 2016). Under the same material condition, the pore structures of reservoirs at different depths are compared. The result shows that with the increase of burial depth, the radius of the pore throat decreases in multiples, and the permeability

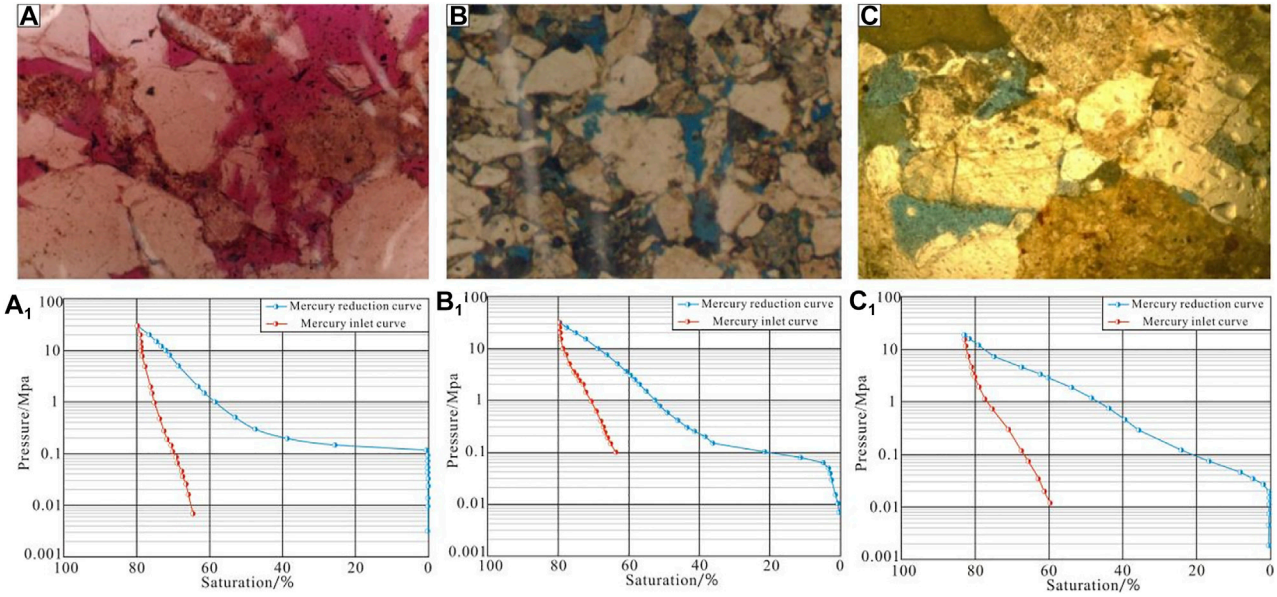

FIGURE 9
Microscopic characteristics of underwater distributary channel reservoirs at different depths and corresponding mercury intrusion characteristics. **(A)** a_1. G65-1, 3225 m, median particle size 0.32 mm, mud content 3%, sorting coefficient 1.76, pore throat radius: 3.73 μm; **(B)** b_1. G62-35, 3602 m, median particle size 0.3 mm, mud content 2%, sorting coefficient 1.85, pore throat radius: 1.48 μm; **(C)** c_1. G66X5, 4285 m, median particle size 0.34 mm, mud content 2%, sorting coefficient 1.68, pore throat radius: 0.4 μm.

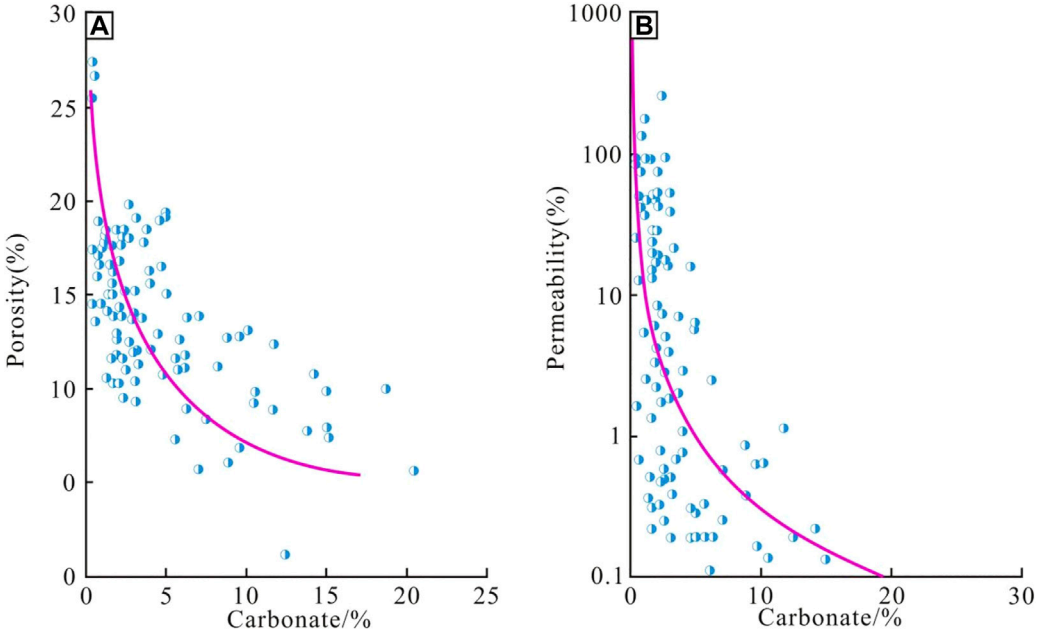

FIGURE 10
Relationship between carbonate content and physical properties of reservoir sand bodies in estuary bars and underwater distributary channels. **(A)**. Relationship between porosity and carbonate content; **(B)**. Relationship between permeability and carbonate content.

decreases exponentially. The original porosity of deep low-permeability Gaoshangpu reservoirs is 42%, and the porosity could be reduced to 17.26%–28.24% due to the compaction, with an average value of 20.8%. The compaction above 3800 m is generally less than 75% (Figures 9A,B), which is medium–strong compaction, while it could reach more than 75% below 3800 m, which is strong compaction. The average porosity below 3500 m in the study area is 15.5%, and the porosity reduction rate due to compaction is 65% (Figure 9C), which is medium–strong compaction. The proportion of reservoir porosity damaged by compaction increases gradually from the underwater distributary channel, mouth bar, far sand bar, and sheet sand. The underwater distributary channel sand bodies with coarse grain size, high maturity of grain structure, and low content of impurities have stronger compaction resistance, and the damage of porosity reduction by compaction is weak (Figure 9).

4.3.3 The differential effect of cementation on reservoir

Cementation is another main cause of reservoir densification. The degrees of cementation vary dramatically among low-permeability reservoirs of different microfacies. When the carbonate content exceeds 4%, the physical properties of the underwater distributary channel and mouth bar sand bodies show a significant decrease (Figure 10), with porosity basically less than 13% and the permeability less than 1 $\mu m^2 \times 10^{-3}$ μm^2. There are two explanations for it. On the one hand, the carbonate cementation of sand bodies at the edge of channel sand bodies or toward the lake, as well as the sand bodies developed in thin interbeds of sand and mud, is stronger. The porosity loss of the distal bar reservoir due to cementation is significantly higher than that of the estuary sand dam. On the other hand, during the cementation development, underwater distributary channels are deposited earlier than the mouth bar and distal bar sand bodies, with better preservation of intergranular pores and relatively undeveloped early calcium cementation. The components of early calcareous and argillaceous cement increased gradually in the mouth bar and distal sand bar reservoirs. While the primary intergranular pores and throat were poorly preserved, and the late calcareous cementation has an obvious influence on the underwater distributary channel reservoir with relatively well-preserved pores.

4.3.4 The effect of dissolution on reservoir

Dissolution is a commonly developed diagenesis in reservoirs in the study area, which plays an important role in improving the quality of reservoirs in the middle and late stages and is also the main reason for development of high-quality reservoirs (Wang et al., 2010; Lan et al., 2014; Wang and Chen, 2016; Li et al., 2018c; Li et al., 2022c). The organic acid released during the maturation of organic matter dissolves the feldspar particles in the reservoir. Affected by diageneses such as compaction and cementation of early diagenesis, the physical properties of the reservoir were damaged to some extent, and the effect of dissolution on the densified reservoir is limited. For underwater distributary channel reservoirs with good original properties, the cumulative porosity damage of compaction and cementation averages to about 50%. After compaction, the porosity of the mouth bar reservoir is damaged by more than 60% on average, and the fluid activity is restricted seriously in the later stage. The occurrence of reservoir dissolution is directly related to the activity of formation water. Among the underwater distributary channel sand bodies, feldspar has suffered strong dissolution, followed by mouth bar sand bodies. The physical properties of reservoirs in these genetic types of sand bodies may be improved obviously. Microscopic thin-section analysis shows that the content of feldspar-dissolved pores in low-permeability reservoirs is less than 5%, indicating that the lack of dissolution in low-permeability reservoirs is another important reason for reservoir compactness. After the dissolution of different microfacies reservoirs, the difference in reservoir quality is further increased.

4.4 Densification mechanism of deep low-permeability Gaoshangpu reservoir

By comparing different microfacies reservoirs with the same burial depth, it can be seen that after the early diagenetic evolution, reservoir sandbodies of different grain sizes, sorting, and shale contents have distinct characteristics at the depth of 3,000–3500 m (Figure 5). In the process of diagenetic evolution, the underwater distributary channel reservoirs with coarse grain size, less shale content, and better sorting preserved better primary intergranular pores (Figure 5A). Primary pores could be preserved at this depth, and dissolution pores and primary pores are developed in this section, which are favorable for dissolution of the reservoir as acid fluids carried by the expulsion process can enter the reservoir during the late formation water activity. The grain size of the reservoir sand body in the mouth bar is slightly finer, and the clay content is slightly larger (Figure 5B). Therefore, during the early stage of mechanical compaction, a large number of plastic particles in the reservoir have been adjusted by compaction, arranged in layers, accelerated by pressure solution, and so on, and therefore the porosity has been significantly reduced. The porosity of this depth interval is 5%–10% less than that of the subaqueous distributary channel reservoir sand body, and the permeability is about 10 mD–200 mD less. Most of the sandbodies in the interdistributary bay, distal bar, and sheet sand above 3000 m have been densified (Figures 5C,D). The reservoir is of low permeability and ultra-low-permeability with a porosity of only 5%–15%, permeability less than 10 mD, and a pore throat radius less than 0.2 μm. In the later stage, the fluid percolation capacity is poor and the dissolution

transformation is not obvious. The early densification of reservoirs results from strong compaction and pressure dissolution in the early stage with a high content of plastic particles and weak calcareous cementation in the early diagenetic stage. The reservoirs formed with different sedimentary microfacies above 3000 m are characterized by different grain sizes, shale content, and sorting, which are the main factors affecting the reservoir densification.

The mouth bar sand bodies penetrate into the lake, and the dissolved calcium in the river gradually precipitates out in the sediment. Calcareous cementation was developed in the early diagenetic stage, and hence a large amount of calcite with crystal cementation resulted in densification of the reservoir. In the later period, only a few particle components were dissolved by fluid activity, and some micropores and intergranular pores were formed. If the dissolution lasts for a long time, casting pores can be formed. Among some mouth bar sandbodies with a slightly higher clay content, calcareous cementation is generally not developed. In the process of diagenetic evolution, the compaction resistance of the reservoir is poor, so the reservoir section has been densified at this depth. High shale content, fine grain size, and calcareous cementation are the main reasons for low permeability and densification of the mouth bar reservoir. Its degree of corrosion is relatively less obvious than that of the underwater distributary channel sand body. The plastic particle content of distal bar and sheet sand is very high, and the compressive strength is weak. A large number of primary pores have been lost during the early diagenetic stage A. After the early diagenetic stage, argillaceous cementation and a small amount of calcareous cementation have filled up most of the primary pores. The porosity is only about 10%, and the permeability is as low as 0.5 mD–10 mD at a depth of 3,000–3500 m, which indicates that the early diagenetic stage has resulted in severe densification of these micro-facies reservoirs. Strong compaction is an important reason for reservoir compaction.

Volume fracturing is conducted to communicate some dead pores because of the underwater distributary channel with undeveloped calcareous cementation and parts of the reservoir sand body with decreased permeability of the mouth bar. The connectivity between pores and sand bodies ensures efficient production of such reservoirs. For low-permeability reservoirs with calcareous development, acidizing and fracturing could be used to improve connectivity and increase production.

In the sedimentary environment of fan delta, the fast accumulation of sediments, low degree of sorting and grinding, and relatively high content of mud and plastic particles, such as debris particles, lead to weak compaction resistance of reservoirs, which is the main reason for strong compaction of deep low-permeability Gaoshangpu reservoirs. When the reservoir is compacted and densified, there is limited space for later dissolution, and therefore, differential development of calcareous cementation leads to further densification of the reservoir. In summary, shale content, cuttings, and burial depth are the main factors that determine the density of deep low-permeability Gaoshangpu reservoirs. Calcareous cementation determines the middle and late diagenesis of the underwater distributary channel reservoir. The development of later dissolution has a significant effect on the improvement of underwater distributary channel reservoirs and is one of the important factors for favorable development of reservoirs. Calcareous cementation is more developed in mouth bar reservoirs in the early stages, resulting in the reservoir being densified at a depth of 3000 m, and the later-stage fluid erosion being weaker.

5 Conclusion

(1) In the sedimentary environment of the fan delta, factors such as rapid accumulation of sediments, high shale content, fine grain size, and medium sorting determine the weak compaction resistance of the deep low-permeability Gaoshangpu reservoir, which is the decisive factor for densification of the reservoir as the buried depth increases. Mechanical compaction and pressure solution lead to large porosity reduction and limited fluid dissolution in the later stage.

(2) The diagenetic evolution of the reservoir varies slightly under different sedimentary microfacies. Due to its relatively strong compaction resistance, the underwater distributary channel reservoir is significantly transformed by middle and late diagenesis. Dissolution is the main reason for reservoir improvement. During the middle stage of the diagenesis, the porosity was further reduced due to development of compaction, pre-solution, and cementation. At a depth of 3,000–4,000 m, compaction has a significant effect on reservoir permeability, which decreases by about 10 times, but the porosity does not reduce significantly.

(3) The sand body of the mouth bar is obviously influenced by sedimentation and diagenesis. Shale content, sorting, and particle size are decisive factors in the early diagenetic evolution. Strong compaction and calcareous cementation are the main reasons for densification of the reservoir at 3000 m, and delayed dissolution has a limited effect on reservoir reformation. The distal bar and sheet sand bar are most affected by sedimentation. In the early diagenesis stage, the reservoirs have been compacted and densified. However, the dissolution and transformation effect is very weak in the middle and late stages. The reservoir above 3000 m is of low permeability and ultra-low permeability.

(4) Feasible measures to efficiently exploit such reservoirs include volumetric fracturing at reservoirs with low

coordination numbers, communicating broadly developed dead pores, and improving connectivity.

(5) The study provides a geological basis for oilfield increase in reserves and production, as well as for efficient development of the Gaoshangpu reservoir, and meanwhile, provides a reference for evaluation of other low-permeability reservoirs in Nanpu Sag and similar areas that have the same geological conditions.

(6) The study provides a general reference for low-permeability reservoirs that are deposited in deltaic depositional settings.

Data availability statement

The original contributions presented in the study are included in the article/Supplementary Material; further inquiries can be directed to the corresponding author.

Author contributions

SW, XY, PS contributed in writing—review and editing, data curation, and writing—original draft preparation; YL, DL, LM, QW, LL and AR contributed in formal analysis, validation, and reviewing.

Conflicts of interest

YL is employed by CNOOC Research Institute Ltd., XY, DL, LM, QW, and LL are employed by Exploration and Development Research Institute, Jidong Oilfield Company, PetroChina.

The remaining authors declare that the research was conducted in the absence of any commercial or financial relationships that could be construed as a potential conflict of interest.

Publisher's note

All claims expressed in this article are solely those of the authors and do not necessarily represent those of their affiliated organizations, or those of the publisher, the editors, and the reviewers. Any product that may be evaluated in this article, or claim that may be made by its manufacturer, is not guaranteed or endorsed by the publisher.

References

Bjørlykke, K. (2014). Relationships between depositional environments, burial history and rock properties. Some principal aspects of diagenetic process in sedimentary basins. *Sediment. Geol.* 301, 1–14. doi:10.1016/j.sedgeo.2013.12.002

Fan, C. H., Li, H., Qin, Q. R., He, S., and Zhong, C. (2020a). Geological conditions and exploration potential of shale gas reservoir in Wufeng and Longmaxi Formation of southeastern Sichuan Basin, China. *J. Petroleum Sci. Eng.* 191, 107138. doi:10.1016/j.petrol.2020.107138

Fan, C. H., Li, H., Zhao, S. X., Qin, Q. R., Fan, Y., Wu, J. F., et al. (2020b). Formation stages and evolution patterns of structural fractures in marine shale: Case study of the lower silurian Longmaxi Formation in the changning area of the southern Sichuan basin, China. *Energy Fuel.* 34 (8), 9524–9539. doi:10.1021/acs.energyfuels.0c01748

Fan, C. H., Li, H., Qin, Q. R., Shang, L., Yuan, Y. F., and Li, Z. (2020c). Formation mechanisms and distribution of weathered volcanic reservoirs: A case study of the carboniferous volcanic rocks in northwest junggar basin, China. *Energy Sci. Eng.* 8, 2841–2858. doi:10.1002/ese3.702

Fan, C. H., Xie, H. B., Li, H., Zhao, S. X., Shi, X. C., Liu, J. F., et al. (2022). Complicated fault characterization and its influence on shale gas preservation in the southern margin of the Sichuan basin, China. *Lithosphere* 2022, 8035106. doi:10.2113/2022/8035106

Gao, Y., Zhang, J. L., Li, H. Y., and Yu, X. H. (2016). Diagenesis and porosity evolution of deep $Es_3$2+3 Formation in Gaoshangpu oilfield, Nanpu sag. *Fault-Block Oil Gas Field* 23 (06), 703–708. doi:10.6056/dkyqt201606005

Guo, X. S., Hu, D. F., Li, Y. P., Duan, J. B., Zhang, X. F., Fan, X. J., et al. (2019). Theoretical progress and key technologies of onshore ultra-deep oil/gas exploration. *Eng.* 5 (03), 458–470. doi:10.1016/j.eng.2019.01.012

He, P., Wang, Z. P., and Li, S. R. (2020). Diagenesis evolution of tight sandstone reservoirs in leping Formation of southern poyang depressio. *J. Hefei Univ. Technol. Sci.* 43 (08), 1122–1130. doi:10.3969/j.issn.1003-5060.2020.08.020

He, S., Li, H., Qin, Q. R., and Long, S. X. (2021). Influence of mineral compositions on shale pore development of Longmaxi Formation in the Dingshan area, southeastern Sichuan Basin, China. *Energy Fuel.* 35 (13), 10551–10561. doi:10.1021/acs.energyfuels.1c01026

He, S., Qin, Q. R., Li, H., and Zhao, S. X. (2022a). Geological characteristics of deep shale gas in the silurian Longmaxi Formation in the southern Sichuan basin, China. *Front. Earth Sci. (Lausanne)* 9, 818543. doi:10.3389/feart.2021.818155

He, S., Qin, Q. R., Li, H., and Wang, S. L. (2022b). Deformation differences in complex structural areas in the southern Sichuan basin and its influence on shale gas preservation: A case study of changning and luzhou areas. *Front. Earth Sci. (Lausanne)* 9, 818155. doi:10.3389/feart.2021.818534

Jiang, L. Z., Gu, J. Y., and Guo, B. C. (2004). Characteristics and mechanism of low permeability clastic reservoir in Chinese petroliferous basin. *Aata Pet. Sin.* 22 (01), 13–18. doi:10.14027/j.cnki.cjxb.2004.01.003

Karim, A., Pe-Piper, G., and Piper, D. J. (2010). Controls on diagenesis of lower cretaceous reservoir sandstones in the Western sable subbasin, offshore nova scotia. *Sediment. Geol.* 224 (1-4), 65–83. doi:10.1016/j.sedgeo.2009.12.010

Lai, J., Wang, G., Ran, Y., Zhou, Z., and Cui, Y. (2016). Impact of diagenesis on the reservoir quality of tight oil sandstones: The case of Upper Triassic Yanchang Formation Chang 7 oil layers in Ordos Basin, China. *J. Petrol Sci. Eng.* 145, 54–65. doi:10.1016/j.petrol.2016.03.009

Lai, J., Wang, G., Cai, C., Fan, Z., Wang, S., Chen, J., et al. (2018). Diagenesis and reservoir quality in tight gas sandstones: The fourth member of the upper triassic Xujiahe Formation, central Sichuan basin, southwest China. *Geol. J.* 53 (2), 629–646. doi:10.1002/gj.2917

Lan, C. L., Wang, J. G., Zhou, X. F., Dai, J. Y., Yang, M. H., and Cui, Z. Y. (2014). Impacts on sandstone reservoir quality of the third member of upper triassic yanchang formation, penyang oilfield of ordos basin, China. *Acta Petrol. Sin.* 30 (6), 1828–1840.

Law, B. E., and Dicknson, W. W. (1985). Conceptual model for origin of abnormally pressured gas accumulations in low-permeability reservoirs. *Am. Assoc. Pet. Geol. Bull.* 69 (8), 1295–1304. doi:10.1306/AD462BD7-16F7-11D7-8645000102C1865D

Li, H. (2022). Research progress on evaluation methods and factors influencing shale brittleness: A review. *Energy Rep.* 8, 4344–4358. doi:10.1016/j.egyr.2022.03.120

Li, C. L., Zhou, C. C., Li, X., Hu, F. L., Zhang, L., and Wang, W. J. (2010). A novel model for assessing the pore structure of tight sands and its application. *Appl. Geophys.* 7 (03), 283–291. doi:10.1007/s11770-010-0254-0

Li, H., Tang, H. M., Qin, Q. R., Fan, C. H., Han, S., Yang, C., et al. (2018a). Reservoir characteristics and hydrocarbon accumulation of Carboniferous volcanic weathered crust of Zhongguai high area in the Western Junggar Basin, China. *J. Cent. South Univ.* 25 (11), 2785–2801. doi:10.1007/s11771-018-3953-y

Li, J. J., Liu, Y., Gao, Y. J., Cheng, B. Y., Meng, F. L., and Xu, H. M. (2018b). Effects of microscopic pore structure heterogeneity on the distribution and morphology of remaining oil. *Petrol Explor. Dev.* 45 (06), 1112–1122. doi:10.1016/s1876-3804(18)30114-9

Li, Y., Shouli, X. U., Cai, L. I., Zhang, Y., Zhanjie, Z., and Peiyuan, Z. (2018c). Diagenesis-porosity evolution and "sweet spot" distribution of low permeability reservoirs: A case study from oligocene zhuhai Formation in wenchang A sag, pear river mouth basin, northern south China sea. *Petrol Explor. Dev.* 45 (2), 251–263. doi:10.1016/s1876-3804(18)30028-4

Li, H., Tang, H. M., and Zheng, M. J. (2019a). Micropore structural heterogeneity of siliceous shale reservoir of the Longmaxi Formation in the southern Sichuan Basin, China. *Minerals* 9, 548. doi:10.3390/min9090548

Li, H., Tang, H. M., Qin, Q. R., Wang, Q., and Zhong, C. (2019b). Effectiveness evaluation of natural fractures in Xujiahe Formation of Yuanba area, Sichuan basin, China. *Arab. J. Geosci.* 12 (6), 194. doi:10.1007/s12517-019-4292-5

Li, H., Tang, H. M., Qin, Q. R., Zhou, J. L., Qin, Z. J., Fan, C. H., et al. (2019c). Characteristics, formation periods and genetic mechanisms of tectonic fractures in the tight gas sandstones reservoir: A case study of Xujiahe Formation in YB area, Sichuan basin, China. *J. Petrol Sci. Eng.* 178, 723–735. doi:10.1016/j.petrol.2019.04.007

Li, H., Qin, Q. R., Zhang, B. J., Ge, X. Y., Hu, X., Fan, C. H., et al. (2020). Tectonic fracture formation and distribution in ultradeep marine carbonate gas reservoirs: A case study of the maokou Formation in the jiulongshan gas field, Sichuan basin, southwest China. *Energy Fuel.* 34 (11), 14132–14146. doi:10.1021/acs.energyfuels.0c03327

Li, H., Wang, Q., Qin, Q. R., and Ge, X. Y. (2021a). Characteristics of natural fractures in an ultradeep marine carbonate gas reservoir and their impact on the reservoir: A case study of the maokou Formation of the jls structure in the Sichuan basin, China. *Energy Fuel.* 35 (16), 13098–13108. doi:10.1021/acs.energyfuels.1c01581

Li, K., Xi, K. L., Cao, Y. C., Niu, X. B., Wu, S. T., Feng, S. B., et al. (2021b). Chlorite authigenesis and its impact on reservoir quality in tight sandstone reservoirs of the Triassic Yanchang formation, southwestern Ordos basin, China. *J. Petrol Sci. Eng.* 205, 108843. doi:10.1016/j.petrol.2021.108843

Li, J., Qin, Q. R., Li, H., and Wan, Y. F. (2022a). Numerical simulation of the stress field and fault sealing of complex fault combinations in Changning area, Southern Sichuan Basin, China. *Energy Sci. Eng.* 10, 278–291. doi:10.1002/ese3.1044

Li, J., Li, H., Yang, C., Wu, Y. J., Gao, Z., and Jiang, S. L. (2022b). Geological characteristics and controlling factors of deep shale gas enrichment of the Wufeng-Longmaxi Formation in the southern Sichuan Basin, China. *Lithosphere* 2022, 4737801. doi:10.2113/2022/4737801

Li, H., Zhou, J. L., Mou, X. Y., Guo, H. Z., Wang, X. X., An, H. Y., et al. (2022c). Pore structure and fractal characteristics of the marine shale of the Longmaxi Formation in the Changning Area, Southern Sichuan Basin, China. *Front. Earth Sci.* 10, 1018274. doi:10.3389/feart.2022.1018274

Liu, L., Sun, Y. H., Chen, C., Lou, R., and Wang, Q. (2022). Fault reactivation in No.4 structural zone and its control on oil and gas accumulation in Nanpu sag, Bohai Bay Basin, China. *Petrol Explor. Dev.* 49 (04), 824–836. doi:10.1016/s1876-3804(22)60313-6

Mingjie, L. I. U., Zhen, L. I. U., Jingjing, L. I. U., Wenqi, Z. H. U., Huang, Y., and Xing, Y. (2014). Coupling relationship between sandstone reservoir densification and hydrocarbon accumulation: A case from the yanchang Formation of the xifeng and ansai areas, ordos basin. *Petrol Explor. Dev.* 41 (2), 185–192. doi:10.1016/S1876-3804(14)60021-5

Ren, D., Zhou, D., Liu, D., Dong, F., Ma, S., and Huang, H. (2019). formation mechanism of the upper triassic yanchang formation tight sandstone reservoir in ordos basin—take chang 6 reservoir in jiyuan oil field as an example. *J. Petrol Sci. Eng.* 178, 497–505. doi:10.1016/j.petrol.2019.03.021

Shanley, K. W., Cluff, R. M., and Robinson, J. W. (2004). Factors controlling prolific gas production from low-permeability sandstone reservoirs: Implications for resource assessment, prospect development, and risk analysis. *Am. Assoc. Pet. Geol. Bull.* 88 (8), 1083–1121. doi:10.1306/03250403051

Wang, Y., and Chen, S. Y. (2016). Meandering river sand body architecture and heterogeneity: A case study of permian meandering river outcrop in palougou, baode, shanxi province:A case study of permian meandering river outcrop in palougou, baode, shanxi province. *Petrol Explor. Dev.* 43 (02), 230–240. doi:10.1016/S1876-3804(16)30026-X

Wang, Y. J., Song, X. M., and Gu, F. (2010). Sedimentary character and sand body structure in second and third sub-formation of Sha3 formation, north deep reservoir of Gaoshangpu oilfield. *Petroleum Geol. Recovery Effic.* 17 (2), 14–16. doi:10.13673/j.cnki.cn37-1359/te.2010.02.014

Wang, Y. L., Shao, G. C., Liu, J., and Fan, G. F. (2013). Reservoir characteristics research and evaluation classification of Maxi Sha-3 formation of Huabei oilfield. *Petroleum Reserv. Eval. Dev.* 3 (06), 1–4. doi:10.13809/j.cnki.cn32-1825/te.2013.06.001

Wang, S. L., Li, H., Lin, L. F., and Yin, S. (2022). Development characteristics and finite element simulation of fractures in tight oil sandstone reservoirs of Yanchang Formation in Western Ordos Basin. *Front. Earth Sci.* 9, 823855. doi:10.3389/feart.2021.823855

Wu, J., Liu, Z. G., Zhu, C., Gong, Q. S., Xia, Z. Y., Song, G. Y., et al. (2020). Characteristics of deep tight sandstone reservoirs and their controlling factors in the Middle-Lower Jurassic in the Yiqikelike area, Kuqa depression. *China Pet. Explor.* 25 (06), 58–67. doi:10.3969/j.issn.1672-7703.2020.06.006

Xi, K., Cao, Y., Jahren, J., Zhu, R., Bjørlykke, K., Haile, B. G., et al. (2015). Diagenesis and reservoir quality of the lower cretaceous quantou formation tight sandstones in the southern songliao basin, China. *Sediment. Geol.* 330, 90–107. doi:10.1016/j.sedgeo.2015.10.007

Xie, J., Hu, W. S., Chen, S. Y., Yu, S. B., and Chen, P. P. (2017). Reservoir architectural analysis of the braided fluvial delta of the lower oil layer in the 1st block of Tahe Oilfield[J]. *Petroleum Geol. Recovery Effic.* 24 (05), 46–52. doi:10.13673/j.cnki.cn37-1359/te.2017.05.007

Xu, K., Dai, J. S., Feng, J. W., Wang, B. F., ShangFang, L., Wang, S., et al. (2020). Predicting 3D heterogeneous *in situ* stress field of Gaoshangpu oilfield northern area, Nanpu sag, Bohai bay basin, China. *Arab. J. Geosci.* 13 (1), 43–15. doi:10.1007/s12517-019-5043-3

Yang, X. L., Dong, X. H., and Guo, A. H. (2016a). Sedimentary environment and reservoir characteristics during depositional stage of Es3 in Gaobei ramp region. *Lithol. Reserv.* 28 (01), 65–71. doi:10.3969/j.issn.1673-8926.2016.01.008

Yang, Z., He, S., Guo, X., Li, Q., Chen, Z., and Zhao, Y. (2016b). Formation of low permeability reservoirs and gas accumulation process in the daniudi gas field, northeast ordos basin, China. *Mar. Petrol Geol.* 70, 222–236. doi:10.1016/j.marpetgeo.2015.10.021

Zeng, L., Jiang, J., and Yang, Y. (2010). Fractures in the low porosity and ultra-low permeability glutenite reservoirs: A case study of the late eocene hetaoyuan Formation in the anpeng oilfield, nanxiang basin, China. *Mar. Petrol Geol.* 27 (7), 1642–1650. doi:10.1016/j.marpetgeo.2010.03.009

Zhu, R. K., Zhou, C. N., Zhang, X., He, W. B., and Wang, Z. F. (2009). Characteristics and formation mechanism of low porosity-low permeability reservoirs of the Triassic Xujiahe Formation in Jiannan area, eastern Sichuan Basin. *Sci. Sin.* 39 (03), 327–339. doi:10.7605/gdlxb.2014.01.009

ZinsaloJoël, M., Louis, L., and Raymond, J. (2021). Sustainable electricity generation from an Enhanced Geothermal System considering reservoir heterogeneity and water losses with a discrete fractures model. *Appl. Therm. Eng.* 192, 116886. doi:10.1016/j.applthermaleng.2021.116886

Zou, C., Zhu, R., Liu, K., Su, L., Bai, B., Zhang, X., et al. (2012). Tight gas sandstone reservoirs in China: Characteristics and recognition criteria. *J. Petrol Sci. Eng.* 88, 82–91. doi:10.1016/j.petrol.2012.02.001

frontiers | Frontiers in Earth Science

TYPE Original Research
PUBLISHED 29 September 2022
DOI 10.3389/feart.2022.1015460

OPEN ACCESS

EDITED BY
Shuai Yin,
Xi'an Shiyou University, China

REVIEWED BY
Yingquan Zhao,
Chengdu University of Technology, China
Chuanxin Li,
China University of Geosciences, China

*CORRESPONDENCE
Bin Li,
libinxnsy@outlook.com

SPECIALTY SECTION
This article was submitted to Structural Geology and Tectonics, a section of the journal Frontiers in Earth Science

RECEIVED 09 August 2022
ACCEPTED 08 September 2022
PUBLISHED 29 September 2022

CITATION
Zhang X, Li B, Peng J, Qu F, Zhang K, Yang S and Xu Q (2022), Experimental analysis of dissolution reconstruction of deep dolomite reservoirs: A case study of the Cambrian dolomite reservoirs in the Tarim Basin.
Front. Earth Sci. 10:1015460.
doi: 10.3389/feart.2022.1015460

Experimental analysis of dissolution reconstruction of deep dolomite reservoirs: A case study of the Cambrian dolomite reservoirs in the Tarim Basin

Xin Zhang[1], Bin Li[1,2]*, Jun Peng[1,2], Fang Qu[1], Kun Zhang[1,2], Suju Yang[3] and Qingqi Xu[3]

[1]School of Geoscience and Technology, Southwest Petroleum University, Chengdu, China, [2]Natural Gas Geology Key Laboratory of Sichuan Province, Southwest Petroleum University, Chengdu, China, [3]Design and Planning Institute of SINOPEC Northwest Company, Urumqi, China

The deeply buried carbonate reservoir of Cambrian is an important target of oil and gas exploration in the Tarim Basin. Understanding the dissolution mechanism of the deep-buried carbonate reservoir is an urgent problem to be solved. In this study, 11 carbonate samples from three types of deep reservoirs in Tarim Basin were selected as experimental objects, and the dissolution process of carbonate reservoir was simulated by using an advanced reaction system of continuous flow at high temperature and high pressure. The dissolution test of continuous flow shows that the burial depth has an effect on carbonate dissolution, with the increasing of the depths from shallow to deep, the dissolution ability of acidic fluids in carbonate rocks increases first and then decreases. A comparison of dissolution results from different lithologic samples shows that the incomplete dolomitization calcite in the diagenetic stage provides the material basis for dissolution in the later stage. The relationship between reservoir type and physical property is discussed, and it is found that the permeability of the fracture-type and pore-fracture samples increase significantly after dissolution, indicating the pre-existing pores of carbonate rocks may be critical to the formation of high-quality reservoirs in deeply buried conditions. An interesting phenomenon was found by comparing the dissolution rates of experimental samples shows that the dissolution rate of dolomite reservoir has a trend of first increasing and then decreasing under the deeply buried environment, which proves that there is an optimal dissolution range of dolomite in the deeply buried environment, which is conducive to the formation of dolomite reservoir. The genetic model of burial dissolution in deep carbonate reservoirs was established and indicated that the search for dolostone reservoirs near the Himalayan fault may be a new idea for Cambrian deep oil and gas exploration.

KEYWORDS

deep carbonate reservoir, simulation experiment, burial dissolution, Tarim Basin, Cambrian

1 Introduction

In recent years, global oil and gas exploration has made great breakthroughs in deep carbonate formation indicating deep dolostone is rich in oil and gas resources (Howarth and Alves, 2016; Zhu et al., 2019; Li and Goldberg, 2022; Ma et al., 2022). The abundant oil and gas displays have been found in the Cambrian super-deep dolomite reservoirs in the Tarim Basin of China (Huang et al., 2014; Valenciaa et al., 2020; Li and Goldberg, 2022). The high-porosity reservoirs of the TS1 well have been found at the depth of 8,848 m, which confirmed the good exploration prospects for ultra-deep reservoirs (Xiong et al., 2015; Zhu et al., 2018; Cheng et al., 2019; Jiao, 2019). Therefore, the cause of dissolution pores in deep carbonate reservoirs has become a hot study topic in petroleum geology. Many scholars believe that the dissolution of the quasi-synchronous period and supergene karst are of great significance to the carbonate reservoir (Yasuda et al., 2013; Luhmann et al., 2014; Li et al., 2019; Li et al., 2020; Tian et al., 2019). The main reason for the acceptance of this mechanism is that dissolution is easy to occur due to a large amount of fresh water on the surface (Cai et al., 2014). In contrast, some scholars believe that fluid activities in the deep burial stage have a great influence on the dissolution of carbonate reservoirs (Zhu et al., 2018; Jiao, 2019; Luo et al., 2022). But the source of acidic fluid dissolved in deep reservoirs is controversial. Some scholars believe that deep organic acids have a greater influence (Luhmann et al., 2014; Hao et al., 2015; Biehl et al., 2016; Valenciaa et al., 2020). Besides, the dissolution ability of dolomite is unclear (Hood et al., 2004; Tavakoli et al., 2019). Some scholars believe that the dolomite is not easy to dissolve and the reservoir space does not develop under the deep burial environment (Tutolo et al., 2015). Other scholars believe that dolomite is easily dissolved by deep fluids under the influence of faults at high temperatures and high pressure to form a high-quality reservoir (Howarth and Alves, 2016; Abarca et al., 2019; Lima et al., 2020; Valenciaa et al., 2020). From the perspective of petrology, thermodynamics, and dynamics, various simulated dissolution experiments show that the dissolution of dolomite is higher under burial conditions (Montes-Hernandez et al., 2016; Liu et al., 2018).

Given the above problems, this study designed the simulation experiment of high temperature and high-pressure dissolution dynamics. The theoretical mechanism for the deep-dissolved pore in the deep carbonate reservoirs was studied in this paper based on the dynamic properties of the reaction, the effect of deep dissolution method, and the microscopic observation and regional structural movement. It provides the reference for the formation mechanism research of deep dolomite reservoirs.

2 Experimental method

2.1 Experimental sample

To study the effect of dissolution transformation on different reservoir types and pore structures in a deep burial environment, the lithology of samples in the typical reservoirs of the Cambrian in the Tarim Basin is studied. Several wells, such as TS1, DG1, XH2, and YQ6 in the north, BT5 and MB1 in the northwest Tarim Basin (Figure 1). The mineral content and physical properties of each sample are shown in Table 1, and the microscopic characteristics are shown in Figure 2. The reservoir rock types are limestone and dolomite. The reservoir spaces are pore-type, pore-fracture type, and fracture type.

2.2 Experimental method

The pore structure characteristics of the experimental samples were observed by microscopic thin sections of the reservoir, and the identification results of reservoir space types were obtained by counting 300 points for each thin section. The dissolution experiments were carried out by the continuous flow diagenetic simulation system at the Key Laboratory of Carbonate Reservoirs of the Hangzhou Institute of Geology, as shown in Figure 3, PetroChina. The experimental equipment is a high-temperature and high-pressure dynamics simulation device independently designed by Hangzhou Institute. The laboratory is controlled at an initial temperature of 25°C and a humidity of 38%.

Since the deep carbonate rocks mainly experience the dissolution of fresh water in the supergenesis stage and the dissolution of organic acids and carbonic acid in the deep buried environment, the experiment was carried out in a continuous flow reaction system to simulate the flow dissolution process of acetic acid and CO_2 solution in carbonate pores during the two processes of shallow burial to deep burial and deep burial to shallow burial. The temperature range of the experiment was 30–180°C, the pressure range of the experiment was 5–60°MPa, and the experimental flow rate was 3 ml/min. Combined with industrial CT digital core analysis method and gas pore-permeability analyzer to quantitatively analyze the effect of an acidic fluid on sample pore and connectivity. The concentration of calcium and magnesium ions in the fluid was tested by Leeman Prodigy's full-spectrum direct reading spectrometer (4,015) and Thermo X Series II inductively coupled plasma mass spectrometry (SN01426C). The mineral composition was analyzed by X-ray diffractometer X'pert Pro, and the results were shown in Table 1. The porosity and permeability of the column sample were analyzed by FYKS-3under overburden pressure. The pore structure of samples was tested by Vltomelx S industrial CT. The

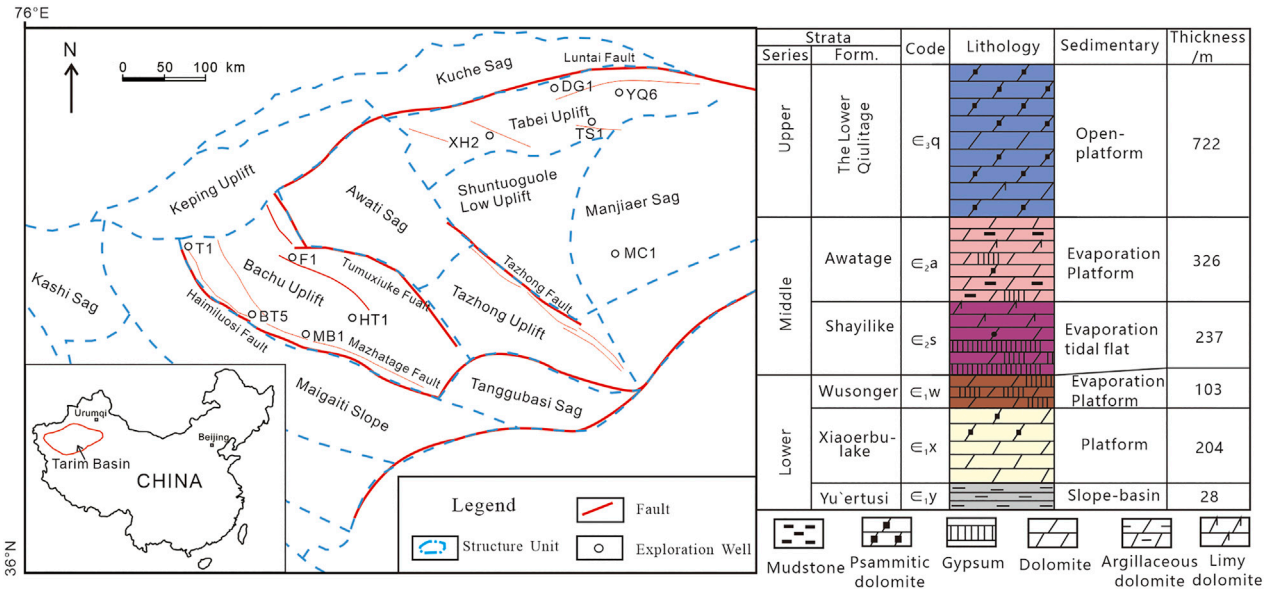

FIGURE 1
The distribution of Wells and Stratigraphic column of the Cambrian in the Tarim Basin (modified from Shen et al., 2016).

TABLE 1 Data of porosity, permeability, and mineral of experimental samples.

Well	Formation	Lithology	Storage space type	Porosity (%)	Permeability (10-3μm2)	Mineral composition (%)			
						Quartz	Calcite	Dolomite	lite
MB1	ϵ_2	Dolomitic limestone	Pore-fracture type	3.11	0.03	0.54	52.49	44.18	2.79
BT5	ϵ_1	Residual fine-crystalline dolarenite	Pore	8.75	65.70	0.53	—	99.47	—
DG1	ϵ	Fine-silty crystalline dolomite	Pore-fracture	2.03	0.02	5.55	—	94.45	—
XH2	ϵ_3	Dolarenite	Pore-fracture	7.53	1.67	15.60	—	84.40	—
YQ6	ϵ_3	Medium-crystalline dolomite	Fracture	2.86	3.74	0.39	6.27	93.34	—

test and analysis of the above items were carried out at a temperature of 25°C and a humidity of 40%.

2.3 Experimental process

Before the experiment, the prepared carbonate samples were loaded into the reaction kettle, and then the

Reactor was sealed. The prearranged 1 L reaction solution was poured into the high-pressure buffer vessel, and then the lid was tightened and closed to connect each valve interface. Firstly, carbonate samples were pretreated with reaction solution at room temperature, atmospheric pressure, and 3 ml/min flow rate for 0.5 h. Then the temperature and pressure are raised to the set value, respectively to carry on the experiment. Under the condition of setting the flow rate of the experiment, when the reaction system reaches a stable state, the samples of the solution after the reaction were collected. Generally, the two samples, each with a volume of about 6 ml were collected. The concentration of Ca^{2+} and Mg^{2+} was analyzed by ICP-OES.

3 Experimental result

3.1 Pre-existing constituents

To accurately understand the petrology and reservoir space characteristics of deep carbonate reservoirs. A total of 50 thin sections have been identified for rock structure in this study. The

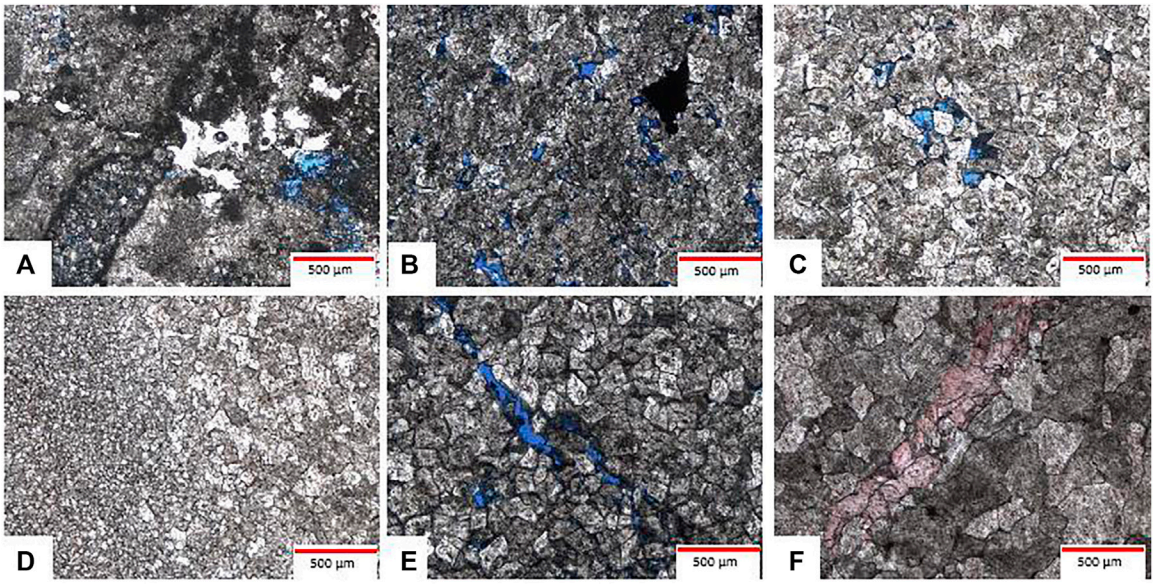

FIGURE 2
Microscopic petrological characteristics of experimental samples.Silty-crystalline dolomitic limestone, MB1,6007.32 m, ϵ2, thin sections, plane polarized light, ×50 **(B)** residual fine-crystalline dolarenite, BT5, 5,785.95 m, ϵ; **(C)** silty-crystalline dolomite, DG1, 6,260.1 m,ϵ, thin sections, plane polarized light,×50 **(D)** silty-crystalline dolomite, DG1,6260.1 m, ϵ, thin sections, plane polarized light, ×50; **(E)** fine-grain dolomite, XH2,5353.93 m,ϵ3, thin sections, plane polarized light, ×50; **(F)** medium-crystalline dolomite, YQ6, 7,116.9, ϵ3, dying cast thin sections, plane polarized light, ×50.

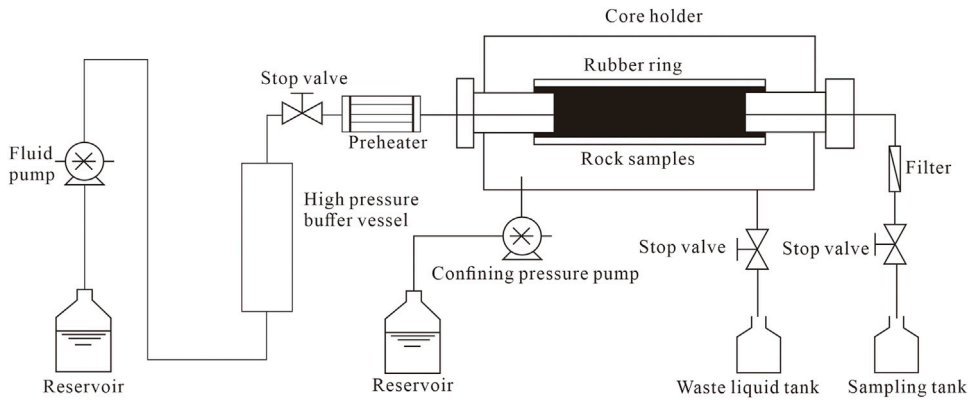

FIGURE 3
Sketch map of continuous flow diagenetic simulation system.

specific parameters are shown in Table 2. The carbonate constituents of the reservoir matrix are distributed between 0–72% with an average value of 11.49%. The main component of the rock is dolomite, with content ranging from 17.67 to.

97.33% and an average value of 76.32%. The quartz cement content was distributed at 0–23% with an average value of 3.08%. The pore types of reservoirs are mainly intercrystalline pores, intragranular pores, fracture pores, and vug pores, with average surface porosity of 5.44, 0.14, 1.40, and 1.83%, respectively. The total surface porosity is 0–39%, and the average value is 8.72%. The reservoir crystalline

Size is distributed between 0.015 and 0.6 mm with an average value of 0.11 mm. The reservoir is mainly dominated by silty-crystalline and fine-crystalline dolomite.

10.3389/feart.2022.1015460

TABLE 2 Statistical table of reservoir composition of Cambrian reservoir in Tarim Basin.

Well		BT5	DG1	MB1	XH2	YQ6
Samples		**23**	**7**	**5**	**8**	**7**
Carbonate constituents (%)	Range	0.33–72.0	6.33–47.01	2.67–47.00	1–67.00	1.33–25.00
	Ave	10.20	25.00	15.14	17.03	10.57
Total anhydrite (%)>	Range	0–4.3	0–2.33	0–2.33	0–20	0–3
	Ave	0.48	1.33	0.80	0.42	0.43
Total dolomite (%)	Range	25.33–97.33	43.67–74.67	48.01–88.67	17.67–83	72.33–95.33
	Ave	80.38	59.11	74.51	60.06	83.28
Total quartz (%)	Range	0–4.67	1.67–16.7	0–11.00	0–23	0.00
	Ave	0.52	8.46	3.27	11.39	0.00
Intragranular pore (%)	Range	0–2	0–0.33	0.00	0.00	0–2
	Ave	0.38	0.11	0.00	0.00	0.57
Intercrystallinepores (%)	Range	0.67–17.00	0–23.33	0–17.33	0–25.33	0–5.8
	Ave	5.43	7.78	6.69	10.34	2.00
Fracture pores (%)	Range	0–2.33	0–6.67	0–2.00	0.33–9.67	0–2.67
	Ave	0.45	2.22	0.40	2.42	0.81
Vug pores (%)	Range	0–9.67	0–3.67	0–4.33	0–4	0–9.33
	Ave	1.26	1.22	1.80	1.54	2.05
Total porosity (%)	Range	0.67–21.00	0–34	0–21.67	0.33–39	1.67–14
	Ave	7.30	11.33	8.89	14.17	5.43
Dolomite crystal size (mm)	Range	0.02–0.4	0.02	0.02–0.2	0.015–0.2	0.08–0.4
	Ave	0.16	0.02	0.08	0.12	0.23

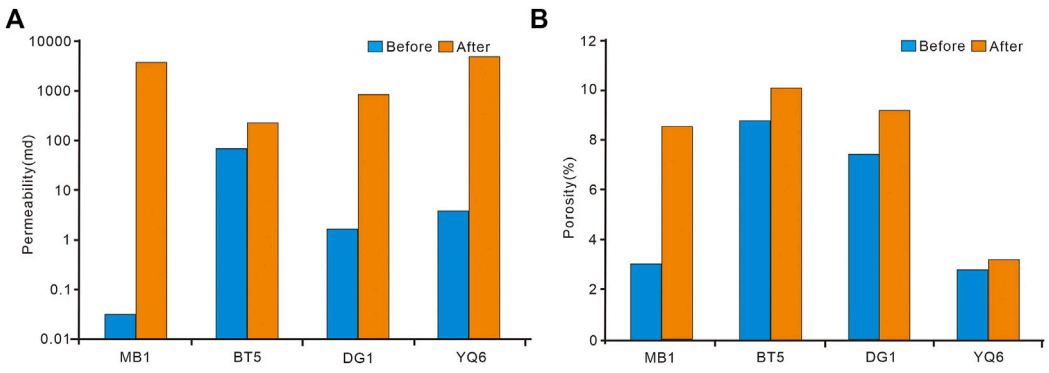

FIGURE 4
Histogram of carbonate porosity and permeability before and after dissolution **(A)** comparison of permeability before and after dissolution; **(B)** comparison of porosity before and after dissolution.

3.2 Dissolution results

3.2.1 Parameters analysis before and after the dissolution

The comparison of the data before and after the dissolution experiment can reflect the strength and effect of the dissolution. From Figure 4, it can be seen that the porosity and permeability of the carbonate reservoir increased after dissolution. The increase in permeability is larger than the increase of porosity, indicating that the dissolution is mainly connecting the internal pores of the rock with improved permeability accordingly (Figure 4A). As shown in Figure 4B, the growth of dolomitic limestone is significantly higher than that of the other three dolomite samples, indicating that the degree of

TABLE 3 Pore-throat parameters of residual fine-crystalline dolarenite before and after Dissolution (CT Scanning Results).

Before and after comparison	Pore				Throat			
	Quantity	Volume (μm^3)	Radius (μm)	Average radius (μm)	Quantity	Volume (μm^3)	Radius (μm)	Average radius (μm)
Before dissolution	12,132	2.654×10^9	2.865–55.13	21.84	21,860	1.41627×10^9	2.722–42.42	15.22
After dissolution	3,384	1.117×10^{10}	3.981–247.2	40.15	12,255	4.29356×10^9	2.845–170.1	40.22

dissolution of limestone is significantly higher than that of dolostone.

Based on the comparison of the parameters before and after the dissolution (Table 3), it can be seen that after the dissolution, the number of pores of the sample was reduced, but the volume was increased. Furthermore, the average radius of pores and throats was also increased from 21.84 to 40.15°μm, and from 15.22 to 40.2 μm.

Respectively. It also shows that the dissolution process could connect the pores of samples, which has a significant effect on the improvement of its permeability.

3.2.2 Comparison of CT scanning characteristics before and after the dissolution

CT scanning is an effective tool for the fine characterization of pore structure in rock. The dissolution is greatly affected by the heterogeneity of the original minerals, and the dissolution pores are developed in the areas with high calcite content. The dissolution fluid mainly corrodes along the microfracture of the original rock, which widens the fracture width and connects the interlayer pore system of the reservoir. Therefore, the dissolution effects of different reservoirs vary greatly.

From Figure 5A, the dissolution pores are unevenly distributed. The acidic fluid flows uniformly in the pores of the rock and then reacts with the minerals to transform the pores of the rock evenly. Therefore, the sample still pertains to the pore type after dissolution. As shown in Figure 5B, the dissolution occurs along with the pores, and fractures and dissolution pores increased. After dissolution, the pores and fractures expand to be connected, and the reservoir heterogeneity is significantly enhanced. Figure 5C showed that the dissolution pores increased along the fracture. The fracture is filled with calcite, and the acidic fluid mainly dissolves the calcite along the fracture. Besides, the dissolution greatly increases the permeability of the sample, but the porosity does not change much, and the fracture remains after the dissolution (Figure 5D).

3.2.3 The tendency of dissolution with temperature and pressure

The temperature and pressure are the important factors that affect the carbonate dissolution reaction under a deeply buried environment. Figure 6 reveals the variation of the concentrations of calcium and magnesium ions with temperature and pressure in the solution fluid. Under the same acidic fluid, temperature, and pressure conditions, the amount of dissolution of dolomitic limestone is larger than that of residual fine-crystalline dolarenite. With the increase in temperature and pressure, the amount of dissolution of dolomitic limestone first increased and then decreased. For higher temperature and pressure, the amount of dissolution of dolomitic limestone decreased sharply to the same amount as that of residual fine-crystalline dolarenite. It shows that the dissolution ability decreases with the increase in temperature and pressure.

To investigate the influence of buried history on the dissolution reaction of dolomite. In this paper, the reverse dissolution experiment of dolomite simulation was carried out at different temperatures and pressures from high to low. The amount of dissolution of the residual fine-crystalline dolarenite sample decreased with the decrease in temperature and pressure, and the dissolution rate peaked at 115°C and 45 MPa. According to the regional burial history (Xiong et al., 2015), with the uplift of the stratum, the dissolution of the dolomite reservoir increased at first and then decreased at about 4,000–6,000°m, which proves that there may be a dissolution range, which is referred to as the dissolution threshold in the deep dolomite reservoirs.

4 Discussion

4.1 Effect of original rock composition on dissolution

The dissolution ability of dolomite under a deeply buried environment is always the focus of carbonate reservoir research (Montes-Hernandez et al., 2016; Shen et al., 2016; Guo et al., 2020). Some scholars believed that the energy required for dolomite dissolution under burial conditions was less than that of calcite, and the automatic dissolution tendency was higher than that of calcite. Therefore, dolomite is more soluble than limestone under burial conditions (Zhu et al., 2015). Other scholars believed that in the shallow burial environment, limestone has a greater solubility in acetic acid solution than dolomite. But in a medium-deep burial

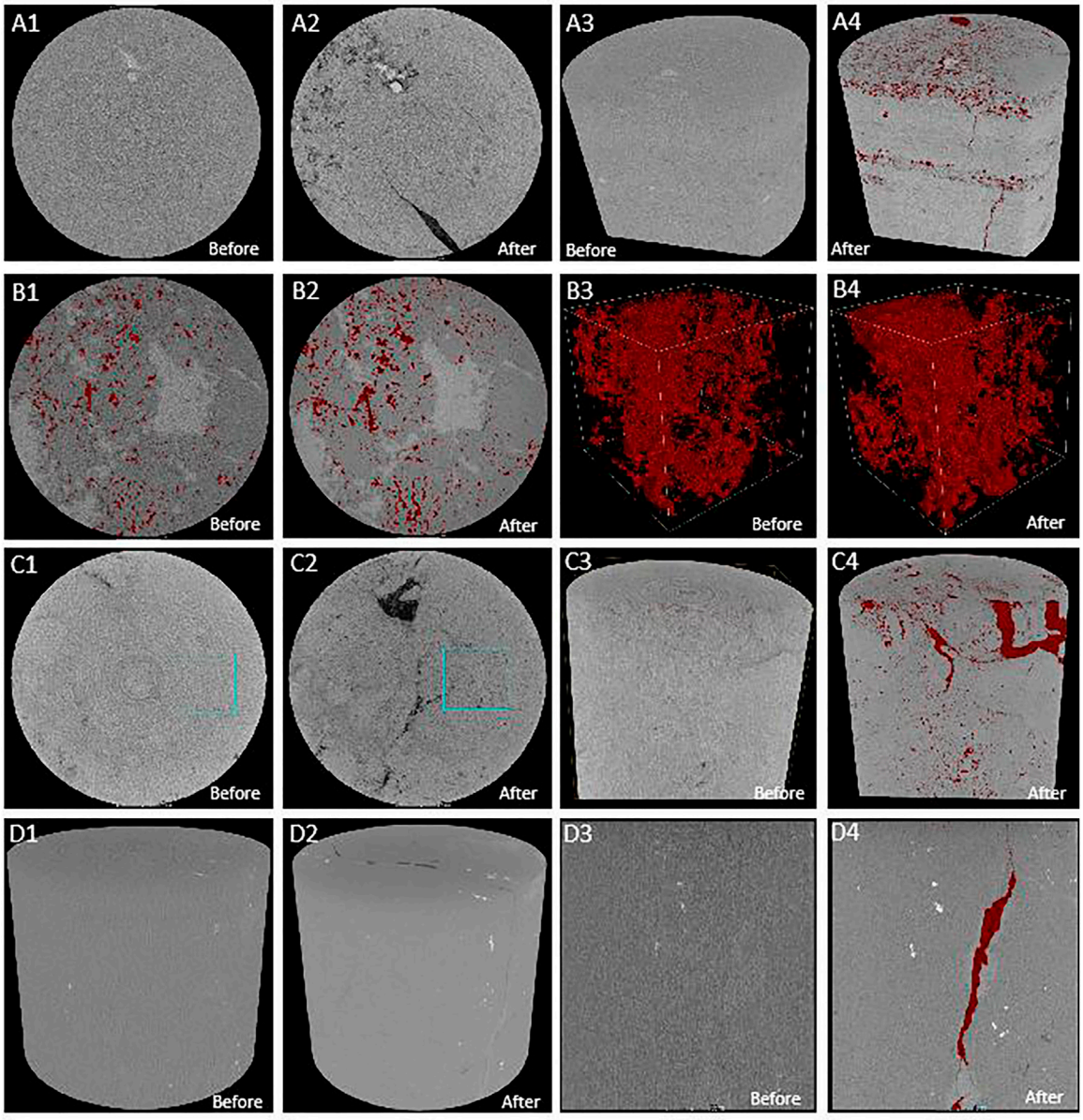

FIGURE 5
Comparison of CT images of the different reservoirs before and after dissolution **(A)** Comparison of pore structure of dolomitic limestone of MB1 well; **(B)** comparison of pore structure of residual fine-crystalline dolarenite of BT5 well **(C)** comparison of pore structure of fine-crystalline dolostone of XH2 well; **(D)** comparison of pore structure of medium-crystalline dolostone of YQ6 well.

environment (Dong et al., 2018), dolomite has a higher solubility in acetic acid solution than limestone (She et al., 2013; She et al., 2016), indicating temperature and pressure have a significant influence on the dissolution of the original rock. The results of this dissolution experiment (Figure 6) show that the dissolution in tensity of samples containing calcite is much higher. For example, the dolomitic limestone of the MB1 well has the largest amount of dissolution among the four samples. Under different temperature and pressure conditions, the dissolution of the dolomite sample is higher than that of BT5 well, indicating that calcite is more soluble than dolomite in a deep burial environment. Microscopic observation can be seen that the fine-medium crystal dolomite was subjected to dissolution and the intragranular pores developed (Figures 7A–C). The horizontal layer distribution is shown in the core of the MB1 well with the elongated dissolution pores (Figure 7D), the microfracture pores, and the interparticle pores of the BT5 well (Figures 7E,F), indicating that the pre-existing pores

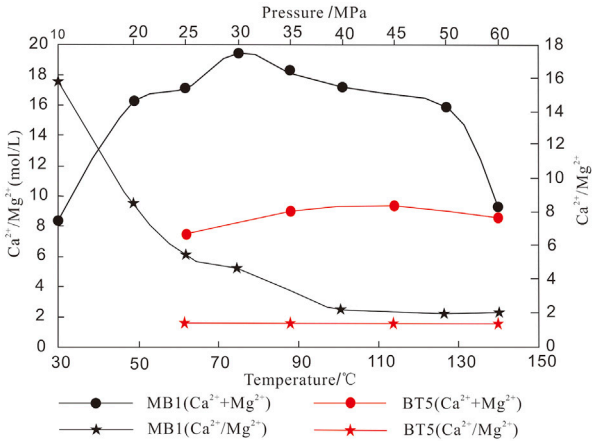

FIGURE 6
Variation trendy of dissolution results of residual fine-crystalline dolarenite and dolomitic limestone (Quoted from Peng et al., 2018).

formed in the early diagenesis are favorable for the formation of secondary pores. From reservoir pore structure statistics (Table 2), it can also be seen that the dissolved pores, intercrystalline pores (Figure 8A), and the surface porosity (Figure 8B), that the dissolution pores have a good correlation with the reservoir pores. Considering that the relatively large dissolution pores are related to the early limestone dissolution, it can be speculated that the dissolution may be attributed to calcite fossils in the early diagenetic period, which contributes to a deeper dissolution.

4.2 Influence of pore structure

The influence of preexisting pore structure on the burial dissolution of carbonate rocks is a problem worthy of attention (Luhmann et al., 2014). Due to the strong heterogeneity of the pore structure in deep reservoirs, it is difficult to draw effective conclusions and understandings. In this experiment two sets of comparative samples with a porosity of 2.027% and a permeability of 0.0148mD in the DG1 well were selected. The first set of early-developed pores and fractures were characterized by microscopic features as shown in Figure 2D. The second set had relatively denser lithology (Figure 2D), and early connected pores have not been fully developed. Under the temperature and pressure conditions of 40°C and 70 MPa, the acidic fluid never passed the second set of samples. After 4 hours of reaction, there was no obvious dissolution phenomenon observed on the surface of the sample. The experimental results show that the pre-existing pores and fractures stimulate the dissolution

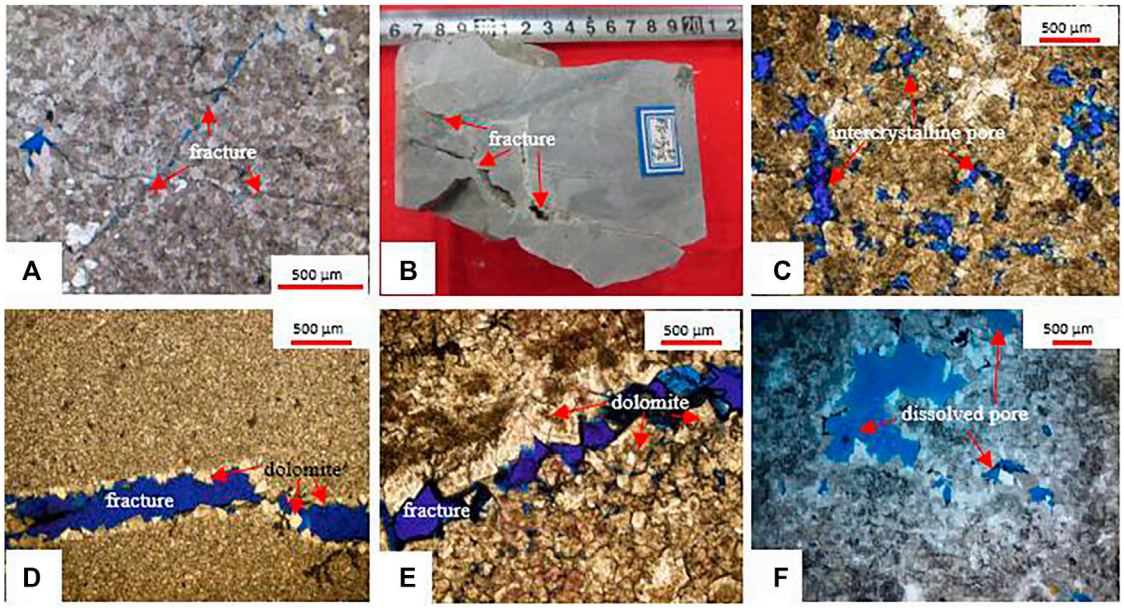

FIGURE 7
Characteristics of dissolution pores in Cambrian reservoirs. **(A)** medium-crystalline dolomite, BT5, ϵ_3, 4,812.9 m, cross-polarized light, ×50 **(B)** fine-crystalline dolomite, BT5, ϵ_3, 4,811.01–4,811.10 m; **(C)** residual fine-crystalline dolarenite, BT5, ϵ_1, 5,784.8 m, plane polarized light, ×50 **(D)** fracture filled with allochthonous dolomite, XH2, $\epsilon_3$5,595.761 m, blue thin sections, plane polarized light, ×50; **(E)** fine-crystalline dolostone, YQ6, $\epsilon_3$7,119.93 m, blue thin sections, plane polarized light, ×50; **(F)** fine-crystalline dolomite, TS1, $\epsilon_3$7,875.66–74 m, blue thin sections, plane polarized light, ×50.

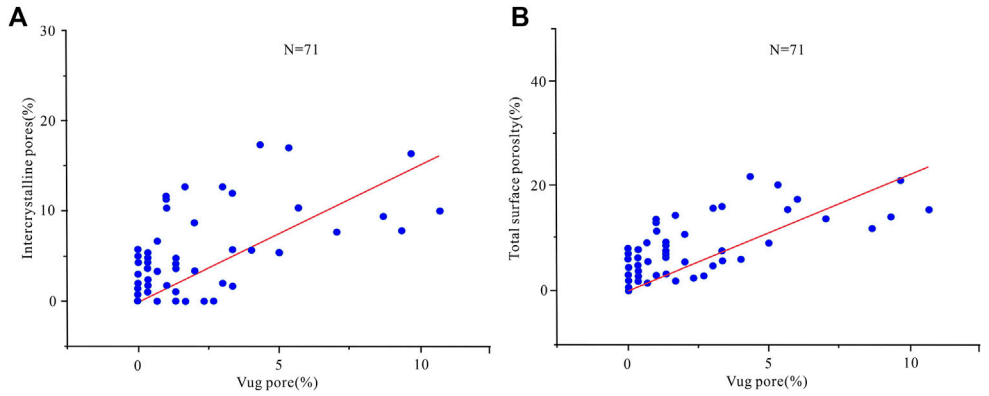

FIGURE 8
Relationship between dissolution pores and surface porosity of Cambrian reservoirs in Tarim Basin **(A)** Intercrystalline pore vs. dissolution pore; **(B)** total surface porosity vs. dissolution pore.

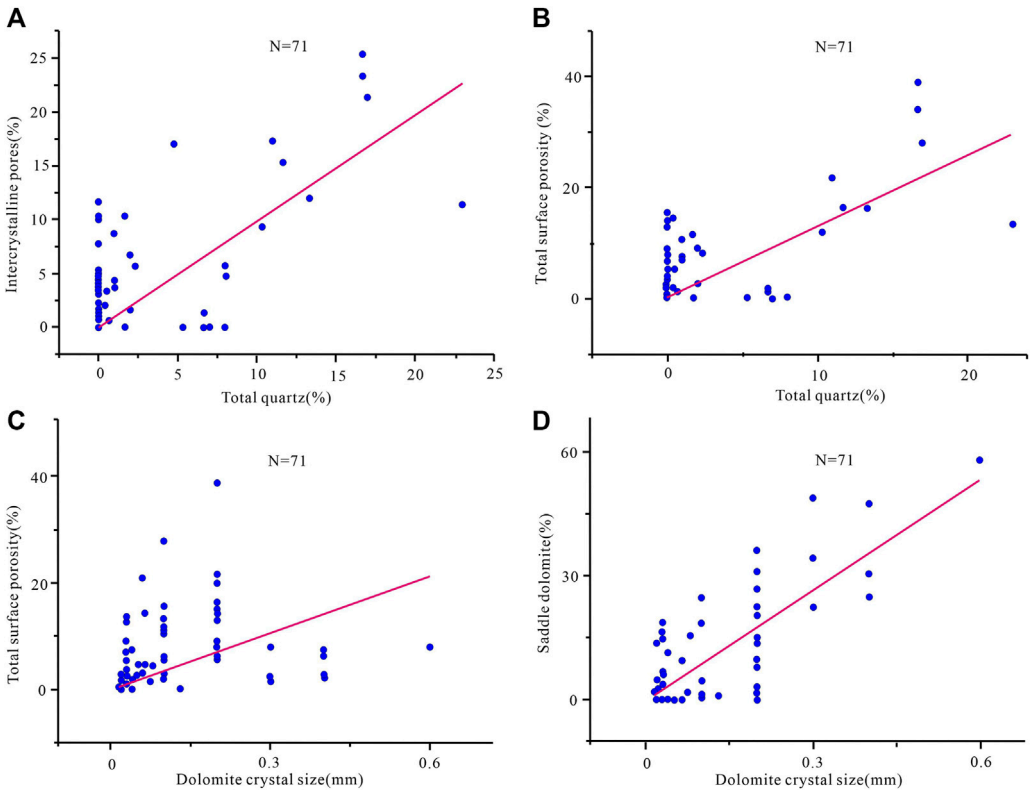

FIGURE 9
Relationship between reservoir composition and surface porosity of Cambrian in Tarim Basin **(A)** Quartz cement vs. intercrystalline pore; **(B)** quartz cement vs. total surface porosity **(C)** dolomite crystalline size vs. total surface porosity; **(D)** dolomite crystalline size vs. saddle dolomite content.

process, and the dissolution under buried conditions is caused by the dissolution and the adjustment of pre-existing pores.

According to the characteristics of the variations in porosity and permeability, the porosity of the sample increased after dissolution to some extent, while the permeability generally

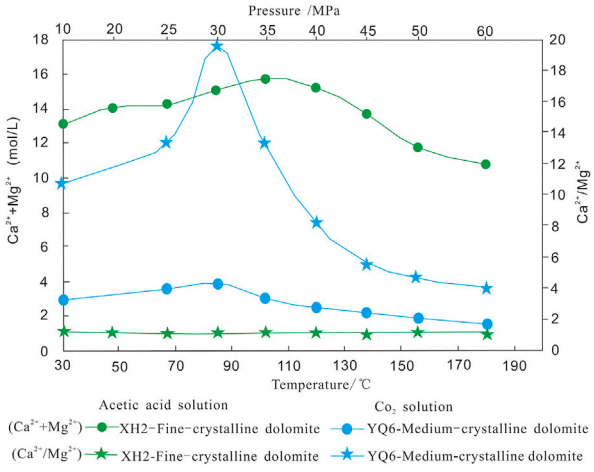

FIGURE 10
Variation trend of dissolution results of fine-grained dolomite and medium-dolomite with temperature and pressure.

increased dramatically. It indicates that dissolution can connect pores and improve the seepage capacity. Especially for the samples with fractures, dissolution forms the dominant channels, which greatly increases the permeability. It is found that the increase in the permeability measured by the experiment can reach up to 1,257.26%.

The pore structure of the original rock controls the characteristics of the fluid flow and determines the result of the dissolution (Lambert et al., 2006; Beckert et al., 2016; Kirstein et al., 2016; Shen et al., 2016; Abarca et al., 2019). The Cambrian strata in the Tarim Basin have experienced multi-stage tectonic activities, and tectonic fractures developed, which provides a good seepage channel for the intrusion of diagenetic fluids (Figures 7A–F). It can be seen that the quartz content in the reservoir has a certain correlation with the intercrystalline pore (Figure 9A) and the total surface porosity (Figure 9B). It can be considered that the acidic fluid mostly percolates and dissolves along with the early pre-existing pore system, and precipitated.

Based on the relationship obtained between the dolomite crystal size and the total surface porosity (Figure 9C) and the saddle dolomite content (Figure 9D), it can be seen that the pores formed in the early diagenetic period provide a seepage channel for the later dolomitization. It is of great significance and may be the main reason for the formation of high-quality deep carbonate reservoirs.

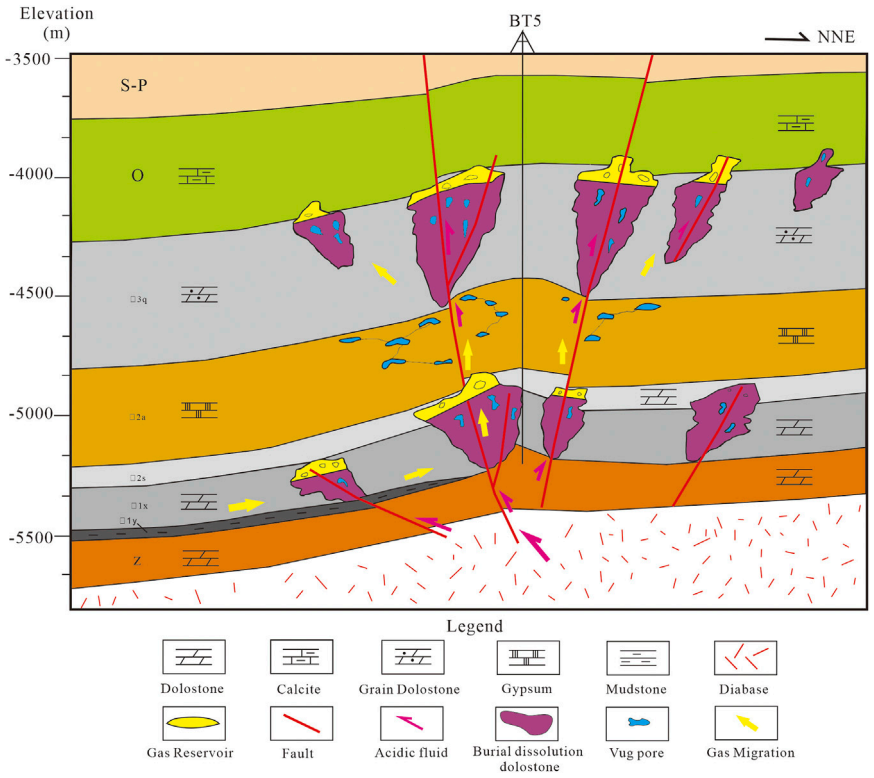

FIGURE 11
The schematic model showing that faults and host facies control the fluid flow in the formation of dissolution pores in the Cambrian reservoir in the Tarim Basin.

4.3 Burial dissolution

Burial dissolution is an important geologic process for the formation of deep carbonate reservoirs. The typical characteristics are that the dissolved pores in the Cambrian reservoir are distributed obviously along the stratum (Figure 7C). The part of the dissolved pores was filled by bitumen, which reflects that the reservoir was reformed by deep fluids (Figures 7D–F). The important condition for deep burial dissolution is the presence of a large number of acidic fluids. There is still no consensus on the source of acid fluid in a deeply buried environment. Some scholars believe that the acidic dissolution of large-scale reservoirs requires a large number of organic acid sources, but the existing source rocks cannot meet this condition under a closed environment (Ehrenberg et al., 2012; Shen et al., 2016). Therefore, the source of carbon dioxide buried deep in the environment is the key to explaining this phenomenon (Guo et al., 2020; Lima et al., 2020; Valenciaa et al., 2020). From the CO_2 solution experiment, it can see that the amount of mineral dissolution increased at first and then decreased with the increase in temperature and pressure (Figure 10), and the amount of dissolution of the acetic acid solution was larger than that of the CO_2 solution. However, the simulation experiment results show that there is a high-efficiency range of carbonic acid dissolution in a deep-buried environment, and the temperature is about 70–120°C.

The combined analysis of the experimental results and the burial history indicates that in the shallow to middle burial depth (3000–5000 m) if sufficient acidic fluid exists, the carbonate reservoir may develope.

Large-scale dissolution pore (Feng et al., 2013; Shen et al., 2016). Fracture is an important factor affecting burial dissolution. Considering the importance of shallow burial on the dissolution of dolomite reservoirs, some scholars have suggested that the dissolution and precipitation of carbonates have a reverse dissolution mode (Valenciaa et al., 2020), and the variation of fluid saturation caused by tectonic uplift or basin subsidence is an important mechanism for controlling the formation of secondary pores (Shen et al., 2016). The CO_2 dissolved in the hydrothermal solution at high temperature and high pressure, and the carbonic acid that formed corroded and altered the residual pores along the seepage channels, such as fractures and intergranular solution pores (Figure 7). Due to the influence of tectonics, acidic fluid connected some pre-existing residual pores and expanded primary pores and fractures along with fractures and intercrystalline pores (Figure 11), which forms a secondary pore system with good local connectivity. This indicates that late-stage tectonics is important for the formation of high-quality deep reservoirs. Therefore, according to the distribution of extensional faults and the characteristics of hydrocarbon migration, it is of great concern to search for the Cambrian dolostone reservoirs near the Himalayan faults.

5 Conclusion

1) The high temperature and high-pressure carbonate simulation experiment show that the organic acid (acetic acid solution) has a higher ability to dissolve the carbonate rock than the carbon dioxide solution. In the shallow-middle depth stage, the dissolution ability of acidic fluids on carbonate rocks tends to increase first and then decrease, indicating that there is a favorable range of dissolution pores in carbonate reservoirs.
2) The pore structure of the original rock has a great influence on the dissolution of deep reservoirs. The porosity and permeability of the porous reservoir increased correspondingly after dissolution, and the permeability of the fracture-type and pore-fracture samples was improved after dissolution, indicating that the pre-existing pores formed in shallow-middle depth may be the key to the formation of high-quality reservoirs in a deeply buried environment.
3) In this study, a dolomite regression dissolution simulation experiment was designed to confirm that the dissolution of dolomite reservoirs tended to increase first and then decrease, corresponding to the shallow-middle buried stage and ranging from 3,000 to 5,000 m.
4) The genetic model of burial dissolution in deep carbonate reservoir is established and shows that the dissolution of CO_2 to form carbonic acid in the hydrothermal fluid can promote an increase of porosity in carbonate reservoirs. Therefore, according to the distribution of the extensional fault and the characteristics of hydrocarbon migration, it is important to search for the Cambrian dolostone reservoir near the Himalayan faults.

Data availability statement

The original contributions presented in the study are included in the article/Supplementary Material, further inquiries can be directed to the corresponding author.

Author contributions

XZ: data curation. BL: conceptualization, methodology. JP: visualization. FQ: conception, design and consult. KZ: supervision. SY: validation. QX: data.

Funding

This research was supported by the Regional innovation Cooperation Project from the Science and Technology Department of Sichuan Province (grant number No.21QYCX0048).

Acknowledgments

We would like to acknowledge Design and Planning Institute of SINOPEC Northwest Company for their assistance. We are grateful to Shuai Yin and two reviewers for the constructive reviews of the manuscript.

Conflict of interest

Authors SY and QX were employed by the company Design and Planning Institute of SINOPEC Northwest Company.

The remaining authors declare that the research was conducted in the absence of any commercial or financial relationships that could be construed as a potential conflict of interest.

Publisher's note

All claims expressed in this article are solely those of the authors and do not necessarily represent those of their affiliated organizations, or those of the publisher, the editors and the reviewers. Any product that may be evaluated in this article, or claim that may be made by its manufacturer, is not guaranteed or endorsed by the publisher.

References

Abarca, E., Idiart, A., Grandia, F., Rodríguez-Morillas, N., Pellan, C., Zen, M., et al. (2019). 3D reactive transport modeling of porosity evolution in a carbonate reservoir through dolomitization. *Chem. Geol.* 513, 184–199. doi:10.1016/j.chemgeo.2019.03.017

Beckert, B., Vandeginste, V., and John, C. M. (2016). Relationship between karstification and burial dolomitization in Permian platform carbonates (Lower Khuff-Oman. *Sediment. Geololgy* 342, 165–179. doi:10.1016/j.sedgeo.2016.07.001

Biehl, B. C., Reuning, L., Schoenherr, J., Lewin, A., Leupold, M., and Kukla, P. A. (2016). Do CO2-charged fluids contribute to secondary porosity creation in deeply buried carbonates? *Mar. Petroleum Geol.* 76, 176–186. doi:10.1016/j.marpetgeo.2016.05.005

Cai, C. F., He, W. X., Jiang, L., Li, K. K., Xiang, L., and Jia, L. (2014). Petrological and geochemical constraints on porosity difference between Lower Triassic sour- and sweet-gas carbonate reservoirs in the Sichuan Basin. *Mar. Petroleum Geol.* 56, 34–50. doi:10.1016/j.marpetgeo.2014.04.003

Cheng, B. H., Liu, Z., Cao, X., Wu, Z., and Chen, Z. (2020). Origin of deep oil accumulations in carbonate reservoirs within the north Tarim Basin: Insights from molecular and isotopic compositions. *Org. Geochem.* 139, 103931. doi:10.1016/j.orggeochem.2019.103931

Dong, K. D., Zhu, A. D., and Hill, A. D. (2018). The role of temperature on optimal conditions in dolomite acidizing: An experimental study and its applications. *J. Petroleum Sci. Eng.* 165, 736–742. doi:10.1016/j.petrol.2018.03.018

Ehrenberg, S. N., Walderhaug, O., and Bjørlykke, K. (2012). Carbonate porosity creation by mesogenetic dissolution: Reality or illusion? *Bulletin* 96, 217–233. doi:10.1306/05031110187

Feng, J. J., Cao, K., Hu, X., Peng, Y., Chen, Y., Wang, M., et al. (2013). Dissolution and its impacts on reservoir formation in moderately to deeply buried strata of mixed siliciclastic-carbonate sediments, northwestern Qaidam Basin, northwest China. *Mar. Petroleum Geol.* 39, 124–137. doi:10.1016/j.marpetgeo.2012.09.002

Guo, R. S., Zhang, X., Bai, K., Wang, X., Sun, X., and Liu, X. (2020). Hydrothermal dolomite reservoirs in a fault system and the factors controlling reservoir formation-A case study of Lower Paleozoic carbonate reservoirs in the Gucheng area, Tarim Basin. *Mar. Petroleum Geol.* 120, 104506. doi:10.1016/j.marpetgeo.2020.104506

Hao, F., Zhang, X. F., Wang, C. W., Li, P. P., Guo, T. L., Zou, H. Y., et al. (2015). The fate of CO2 derived from thermochemical sulfate reduction (TSR) and effect of TSR on carbonate porosity and permeability, Sichuan Basin, China. *Earth-Science Rev.* 141, 154–177. doi:10.1016/j.earscirev.2014.12.001

Hood, S. D., Campell, S., Kamp, P. J. J., and Nelson, S. (2004). Burial dolomitisation in a non-tropical carbonate petroleum reservoir: The oligocene tikorangi formation, taranaki basin, New Zealand. *Sediment. Geol.* 172, 117–138. doi:10.1016/j.sedgeo.2004.08.005

Howarth, V., and Alves, T. M. (2016). Fluid flow through carbonate platforms as evidence for deep-seated reservoirs in Northwest Australia. *Mar. Geol.* 380, 17–43. doi:10.1016/j.margeo.2016.06.011

Huang, T. Z., Jiang, H. S., and Ma, Q. Y. (2014). Hydrocarbon accumulation characteristics in lower paleozoic carbonate reservoirs of Tarim Basin. *Petroleum Nat. Gas Geol.* 35, 780–787. doi:10.1007/BF02875312

Jiao, F. Z. (2019). Practice and knowledge of volumetric development of deep fractured-vuggy carbonate reservoirs in Tarim Basin, NW China. *Petroleum Explor. Dev.* 46, 576–582. doi:10.1016/s1876-3804(19)60037-6

Kirstein, J. H., Hellevang, B. G., Haile, G., and Gaupp, G, R. (2016). Experimental determination of natural carbonate rock dissolution rates with a focus on temperature dependency. *Geomorphology* 261, 30–40. doi:10.1016/j.geomorph.2016.02.019

Lambert, L., C., Durlet, J., Loreau, G., and Marnier, R. (2006). Burial dissolution of micrite in Middle East carbonate reservoirs (Jurassic-Cretaceous) keys for recognition and timing. *Mar. Petroleum Geol.* 23, 79–92. doi:10.1016/j.marpetgeo.2005.04.003

Li, B., and Goldberg, K. (2022). Diagenesis and reservoir quality of Cambrian carbonates in the Tarim Basin, northwestern China. *J. Asian Earth Sci.* 223, 104972. doi:10.1016/j.jseaes.2021.104972

Li, B., Xia, Q. S., Peng, J., Yang, S. J., Xu, Q. Q., and Zeng, L. (2019). Characteristics and dolomitization of the lower qiulitage group reservoir in bachu uplift, Tarim Basin, China. *Earth Sci. Res. J.* 23, 199–208. doi:10.15446/esrj.v23n3.81914

Li, H., Qin, Q. R., Zhang, B. J., Ge, X. Y., Hu, X., Fan, C. H., et al. (2020). Tectonic fracture formation and distribution in ultradeep marine carbonate gas reservoirs: A case study of the maokou formation in the jiulongshan gas field, sichuan basin, southwest China. *Energy & Fuels* 34 (11), 14132–14146. doi:10.1021/acs.energyfuels.0c03327

Lima, B. E. M., Tedeschi, A. L. S., Pestilho, R. V., Santos, J. C., Vazquez, J. V. P., Guzzo, L. F., et al. (2020). Deep-burial hydrothermal alteration of the Pre-Salt carbonate reservoirs from northern Campos Basin, offshore Brazil: Evidence from petrography, fluid inclusions, Sr, C and O isotopes. *Mar. Petroleum Geol.* 113, 104143. doi:10.1016/j.marpetgeo.2019.104143

Liu, W., Liu, N. S., Qiu, Q. C., and Xu, Q. (2018). The evolution of pore-fluid pressure and its causes in the Sinian-Cambrian deep carbonate gas reservoirs in central Sichuan Basin, southwestern China. *J. Petroleum Sci. Eng.* 169, 96–108. doi:10.1016/j.petrol.2018.05.057

Luhmann, A. J., Kong, B. M., Tutolo, N., Garapati, B. C., Bagley, M. O., Saar, W. E., et al. (2014). Experimental dissolution of dolomite by CO2-charged brine at 100°C and 150bar: Evolution of porosity, permeability, and reactive surface area. *Chem. Geol.* 380, 145–160. doi:10.1016/j.chemgeo.2014.05.001

Luo, C., Chen, X., Shi, Z., Chen, J., Wu, T., Shi, C., et al. (2022). Effects of precipitation and dissolution of carbonate cements on the quality of deeply buried high-temperature and overpressured clastic reservoirs: XD 10 block, yinggehai basin, south China sea. *Mar. Petroleum Geol.* 139, 105591. doi:10.1016/j.marpetgeo.2022.105591

Ma, Y., Cai, X., Yun, L., Li, Z., Li, H., Deng, S., et al. (2022). Practice and theoretical and technical progress in exploration and development of Shunbei ultra-deep carbonate oil and gas field, Tarim Basin, NW China. *Petroleum Explor. Dev.* 49 (1), 1–20. doi:10.1016/s1876-3804(22)60001-6

Montes-Hernandez, G., N., Findling, F., and Renard, F. (2016). Dissolution-precipitation reactions controlling fast formation of dolomite under hydrothermal conditions. *Appl. Geochem.* 73, 169–177. doi:10.1016/j.apgeochem.2016.08.011

Peng, J., Wang, X., and Han, H. (2018). Simulation experiment for the dissolution mechanism of carbonate rock of Cambrian in the Tarim Basin. *Petroleum Exploration and Development* 45, 1–11. doi:10.11698/PED.2018.03.00

She, M., Shou, J. F., He, X. Y., Wang, Y., and Zhu, Y. (2013). Experiment of dissolution mechanism of carbonate rocks:surface dissolution and internal dissolution. *Mar. oil gas Geol.* 18, 55–61. doi:10.1155/2017/8439259

She, M., Shou, J. F., Sheng, A. J., and Pan, L. Y. (2016). Experimental simulation of dissolution law and porosity evolution of carbonate rock. *Petroleum Explor. Dev.* 43 (4), 564–573. doi:10.1016/s1876-3804(16)30072-6

Shen, A. J., Zheng, J. F., Chen, Y. Q., Ni, X. F., and Huang, L. L. (2016). Characteristics, origin and distribution of dolomite reservoirs in LowerMiddle cambrian, Tarim Basin, NW China. *Pet. Explor Dev.* 43 (3), 375–385. doi:10.1016/s1876-3804(16)30044-1

Tavakoli, V., and Jamalian, A. (2019). Porosity evolution in dolomitized Permian–Triassic strata of the Persian Gulf, insights into the porosity origin of dolomite reservoirs. *J. Petroleum Sci. Eng.* 181, 1–12. doi:10.1016/j.petrol.2019.106191

Tian, F., X., Luo, W., and Zhang, S. (2019). Integrated geological-geophysical characterizations of deeply buried fractured-vuggy carbonate reservoirs in Ordovician strata, Tarim Basin. *Mar. Petroleum Geol.* 99, 292–309. doi:10.1016/j.marpetgeo.2018.10.028

Tutolo, B. M., Kong, X. Z., Seyfried, W. E., and Saar, M. O. (2015). High performance reactive transport simulations examining the effects of thermal, hydraulic, and chemical (THC) gradients on fluid injectivity at carbonate CCUS reservoir scales. *Int. J. Greenh. Gas Contro* 39, 285–301. doi:10.1016/j.ijggc.2015.05.026

Valenciaa, F. L., and Layab, J. C. (2020). Deep-burial dissolution in an oligocene-miocene giant carbonate reservoir (perla limestone), gulf of Venezuela basin: Implications on microporosity development. *Mar. Petroleum Geol.* 113, 1–21. doi:10.1016/j.marpetgeo.2019.104144

Xiong, Y. X., Chen, Y. Q., Guan, B. Z., Deng, L. P., Ni, X. F., and Xiong, R. (2015). Distribution of northern platform margin and implications to favorable exploration regions on lower cambrian xiaoerbulake formation, Tarim Basin. *J. Sedimentology* 33, 408–415. doi:10.14027/j.cnki.cjxb.2015.02.020

Yasuda, E., Ronaldo Gonçalves, S., and Santos, O. (2013). Kinetics of carbonate dissolution and its effects on the porosity and permeability of consolidated porous media. *J. Petroleum Sci. Eng.* 112, 284–289. doi:10.1016/j.petrol.2013.11.015

Zhu, D., Q., Meng, Z., Jin, Q., Liu, W., and Hu, J. (2015). Formation mechanism of deep Cambrian dolomite reservoirs in the Tarim basin, northwestern China. *Mar. Petroleum Geol.* 59, 232–244. doi:10.1016/j.marpetgeo.2014.08.022

Zhu, G., Zhang, Y., Zhou, X., Zhang, Z., Du, D., Shi, S., et al. (2019). TSR, deep oil cracking and exploration potential in the Hetianhe gas field, Tarim Basin, China. *Fuel* 236, 1078–1092. doi:10.1016/j.fuel.2018.08.119

Zhu, G., Y., Cao, L., Yan, H., Yang, C., Sun, Z., Zhang, T., et al. (2018). Potential and favorable areas of petroleum exploration of ultra-deep marine strata more than 8000 m deep in the Tarim Basin, Northwest China. *J. Nat. Gas Geoscience* 3, 321–337. doi:10.1016/j.jnggs.2018.12.002

frontiers | Frontiers in Earth Science

TYPE Original Research
PUBLISHED 30 September 2022
DOI 10.3389/feart.2022.1029309

OPEN ACCESS

EDITED BY
Wenlong Ding,
China University of Geosciences, China

REVIEWED BY
Jishun Pan,
North China University of Water Conservancy and Electric Power, China
Meng Meng,
Los Alamos National Laboratory (DOE), United States

*CORRESPONDENCE
Sen Yang,
ysedu27@163.com

SPECIALTY SECTION
This article was submitted to Structural Geology and Tectonics, a section of the journal Frontiers in Earth Science

RECEIVED 27 August 2022
ACCEPTED 13 September 2022
PUBLISHED 30 September 2022

CITATION
Yang S, Shu Z, Zhang Q, Zhao Y, Chen Z and Zhang L (2022), Experimental study on compatibility of reservoir and polymer gel profile control agent. *Front. Earth Sci.* 10:1029309. doi: 10.3389/feart.2022.1029309

Experimental study on compatibility of reservoir and polymer gel profile control agent

Sen Yang[1,2]*, Zheng Shu[1], Qunshuang Zhang[3], Yuanshou Zhao[4], Zongli Chen[5] and Lei Zhang[5]

[1]Petroleum Engineering School, Southwest Petroleum University, Chengdu, China, [2]International Business Center, Sinopec Huadong Oilfield Service Corporation, Nanjing, China, [3]Gepetto Oil Technology Group Co., Ltd, Chengdu, China, [4]Oil Production Plant 4 of PetroChina Changqing Oilfield Company, CNPC, Yulin, China, [5]Fracturing Company, Great Wall Drilling Corporation, CNPC, Panjin, China

The coupling relationship between polymer gel system and reservoir pores is an important basis for scientific formulation of tertiary oil recovery programs. The polymer gel profile control agent can significantly modify the fluid migration path inside the reservoir. In this study, artificial cores were used to carry out indoor water flooding experiments after polymer gel injection that considering formation permeability, polymer concentration and polymer injection rates. Based on the accurate records of the breakthrough pressure and injection volume during water flooding, as well as a large number of observations of the microscopic morphology of the cores after the polymer gel profile control and displacement, a set of criteria for determining reservoir-matched polymer gel profile control agents is proposed. The experimental results show that a complex spatial network structure is formed after the gelation of the polymer gel system. As the polymer concentration increases, the network structure of the gel system becomes denser. At the same time, the unit network structure is becoming smaller, and the order of the grid chain structure becomes clearer. Under the condition of low polymer concentrations, the backbone structures of the gel are obvious, but there are a lot of fine pores. When the polymer concentration is greater than 1,500 mg/L and the injection rate is less than 0.15 ml/min, the water flooding breakthrough pressure is greater than 0.2 MPa, the plugging rate is greater than 95%, and a good plugging effect is obtained.

KEYWORDS

polymer gel profile control agent, microscopic morphology, artificial core, pores, plugging rate, compatibility

1 Introduction

In the middle and late stages of the development of strong heterogeneity reservoirs, the oil saturation in the large pores will be greatly reduced (Liu, 2000; Liu, 2019; Zhao, 2012). Furthermore, the pore structures of the reservoir has undergone significant changes due to the continuous scouring of fluids for a long time. Then, a large

amount of injected fluids preferentially enter the large pores and continue to perform inefficient circulation, thereby reducing the displacement effect (Fan, 2013; Niu et al., 2003).

Low permeability, low productivity, fractured heterogeneous sandstone reservoirs are widely developed in China (Liu et al., 2014a; Wang et al., 2016a). In the process of water injection development, a large number of secondary large pores are formed due to the long-term scouring of the formation by the injected water (Li et al., 2006; You et al., 2009). The large pores exacerbate the injection-production contradiction and cause the injected water to continuously intrude into the oil wells along the large pores and fractures. Therefore, the water flooding sweep coefficient is reduced (Liang, 2008; Liu et al., 2018; Xu et al., 2002). At this time, the water cut of the oil well rises rapidly when the recovery degree is not high, and the oil field enters the high water cut period. The use of composite slug profile control technology for plugging large pores in the deep formation has been proved to be effective in terms of the oil enhancement effect by many field tests. Particle profile control agent is a new type of liquid flow diverting agent (Qing et al., 2017; Yang et al., 2017). It migrates in the strata in four modes: blockage, smooth passage, deformation passage, and broken passage. Therefore, it can effectively improve the reservoir heterogeneity and enhance the displacement effect. In recent years, particle profile control agents have been widely used in different oil fields (Jia et al., 2016; Nie, 2017). In addition, the depth profile control agent is a deep liquid flow diverting agent with unique physicochemical properties and can significantly improve the heterogeneity and water injection development effect of deep reservoirs in the high water cut or ultra-high water cut stage (Sun et al., 2016; Tian, 2013; Zhao et al., 2015). In recent years, it has been successfully applied in some oil fields, and has attracted more and more attention of oilfield chemical engineers.

Old oil fields usually undergo several adjustments during their development, such as water drive, carbon dioxide drive, acidizing, fracturing and reservoir reconstruction, the general well spacing of a well group is 150 m. At present, most of the old oil fields in China have entered the later development stage of ultra-high water cut, the maximum water content can reach to 95%. Serious inefficiency and ineffective circulation further increase the difficulty of oil recovery (Liang, 2008; Liu et al., 2018). The previous have made some achievements in the application of gel profile control technology to improve the ineffective water circulation. It can be said that whether the gel profile control agent dynamically gels in the deep formation determines the feasibility of the deep profile control technology (Liu et al., 2014; Liu et al., 2014a). The gel-forming effect of the gel profile control agent is related to whether the technology is really effective and can be applied on a large scale (Qing et al., 2017; Yang et al., 2017). At present, short cores are usually used to evaluate the short-distance plugging pressure of gel profile control agents. Therefore, the long-distance plugging performance of the gel cannot be well understood. Quantitative evaluation of the dynamic gel-forming properties of gel profile control agents in deep formations will help people better understand their plugging mechanisms.

After the oilfields entered the late stage of ultra-high water cut, the inefficient and ineffective circulation intensified, and the development of remaining oil became more and more difficult. Deep profile control measures are effective means to improve the inefficient and ineffective circulation in the well (Guo et al., 2007; Wang et al., 2006; Yuan et al., 2006). The compatibility of profile control agent system and reservoir closely affects the effect of deep control measures. Different types of reservoirs have different requirements on the performance of profile control and plugging systems. Therefore, it is necessary to carry out flooding experiments under different control conditions of polymer concentration, core permeability and polymer injection rate. Through this study, the relationship between the breakthrough pressure under different reservoir conditions and the microstructures of the polymer profile control agent can be elucidated, and the matching relationship between the polymer gel profile control agent and the pores can be determined.

2 Materials and methods

2.1 Preparation of polymer gel profile control agent

2.1.1 Experimental materials

Cr^{3+} cross-linking agent: its effective content is 90%; stabilizer: its effective content is 90%; experimental water: The polymer gel profile control agent solution is prepared with water. The composition and content of the water used in this experiment are shown in Table 1.

2.1.2 Preparation

First, a graduated cylinder is used to measure an amount of the formulated polymer, to which a certain amount of crosslinking agent is added while stirring. Then, the stabilizer and additives are added, and stirring is continued until the crosslinker, stabilizer, and additives are uniformly dispersed in the solution. The prepared gel profile control agent was put into jars of different labels in turn, and put into a 45 °C incubator for constant temperature treatment. The basic parameters of the configured polymer gel profile control agents are shown in Table 2.

2.2 Artificial core preparation

In this paper, the rock samples from the Jian 255 coring well in China's A Oilfield are selected as the research object (Figure 1), and the instruments of the displacement experiment are shown in Figure 2. The permeability distribution of the samples is between 1,130 mD and

TABLE 1 ionic composition of experimental water.

Water Type	Parameters							
	Cation (mg/L)				Anion (mg/L)			Total Salinity (mg/L)
	Na^+	Ca^{2+}	Mg^{2+}	HCO_3^{2-}	Cl^-	SO_4^{2-}	CO_3^{2-}	
Clean water	231.2	34.1	24.3	225.1	88.7	36.0	90.0	729.3
Sewage	1,265.0	32.1	7.3	1708.6	780.1	9.6	210.1	4,012.7

TABLE 2 Composition of polymer gel profile control agent.

Formula	Polymer Concentration (mg/L)	Chromium Crosslinker (%)	Stabilizer Concentration (mg/L)	Polychrome Ratio
1	700	0.15	0.03	1:2
2	1,000	0.20	0.03	1:2
3	1,500	0.30	0.03	1:2
4	2500	0.30	0.03	1:2

FIGURE 1
Cylindrical cores for displacement experiments.

FIGURE 2
Instruments for core flooding experiments.

3542 mD. It can effectively represent the distribution range of rock permeability in strong water wash, low-efficiency-ineffective circulation area. Core flooding experiments were performed in a high-speed, high-pressure environment. Its essence is to study the process of the formation or plugging of large pores during the flushing treatment of natural cores. In this study, the parameters of natural cores after water flooding were used to determine the preparation method of artificial cores. The coincidence rate between artificially prepared cores and natural cores is greater than 80%.

2.2.1 Preparation steps

(1) Preparation of fine quartz sand and cement for making artificial cores.
(2) Mixing sand: The quartz sand required for making the model is mixed in proportion and placed in a square plate and stirred evenly. The medicines required to configure the cement are weighed separately as required, and after mixing, they are poured into the quartz sand and stirred thoroughly. The agitated sand sample is sieved to make the sand and cement mix more uniform.
(3) Molding: acetone is used to clean the mold before the sand is loaded into the mold. The scraper is used to move back and

TABLE 3 Comparison of physical parameters between artificial and natural cores.

Core no	Type	K (10^{-3}μm^2)	Permeability Coincidence (%)	ϕ (%)	Porosity coincidence (%)	r_{ave} (μm)	Average Pore Radius Coincidence (%)
2–74	N	1378.0	—	27.9	—	24.43	—
180523A-1	A	1296.0	94.0	28.6	97.5	23.425	95.9
180523A-2		1212.0	88.0	28.6	97.5	22.863	93.6
2–118-2	N	2336.0	—	28.6	—	28.764	—
180620A-1	A	2212.0	94.7	27.1	94.8	27.632	96.1
180620A-2		2198.0	94.1	28.9	99.0	28.136	97.8
2–109-1	N	3789.5	—	30.9	—	30.49	—
180702A-1	A	3809.0	99.5	29.6	95.8	29.632	97.2
180702A-2		3669.0	96.8	28.6	92.6	28.622	93.9

Notes: K-permeability; ϕ-porosity; r_{ave}-average pore radius; N-natural core; A-Artificial Core.

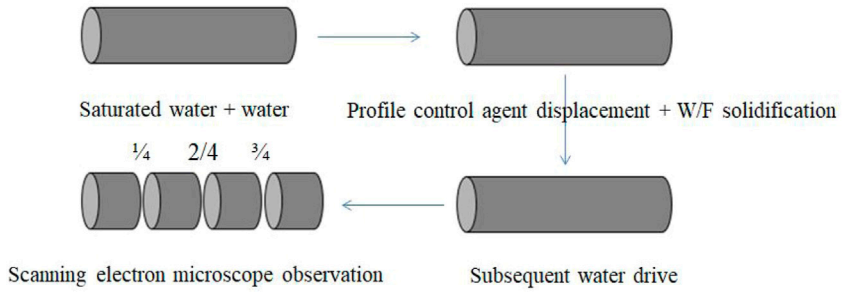

FIGURE 3
Schematic diagram of experimental process.

forth in the horizontal direction, and the depth of the scraper needs to be adjusted continuously until the sand is uniform. This step ensures that the sand is filled evenly. The press plate is then used to compact the sand.

(4) Applying pressure: The sand-loaded mold is placed on the pressure testing machine and the mold is kept horizontal. It is placed on the center line of the press platen and the platen is to be actuated vertically. Moreover, the press is slowly boosted to the design value (usually 3 MPa) and the pressure is released for 15 min. Then, the side and end plates of the mold are carefully removed.

(5) Heating and curing: The pressed core is put into the oven, the oven temperature is adjusted to 85 °C, and the baking time is set to 6–8 h. Then, the core is taken out and left to cool naturally.

(6) Cutting: The solidified cores are cut to the required specifications with a cutting machine.

2.2.2 Physical parameters of artificial and natural cores

The conformity of the parameters of the artificial and natural cores after strong water washing was compared. The lowest coincidence values of permeability, porosity and average pore radius are 88, 92.6 and 93.6%, respectively. It is obvious that the conformity of all parameters has reached more than 80% (Table 3).

2.3 Experimental equipments and methods

2.3.1 Experimental equipments

High temperature and high pressure incubator, RS6000 rheometer (Germany HAAKE company), ISCO pump, FEI Tecnai G2 F20 scanning electron microscope

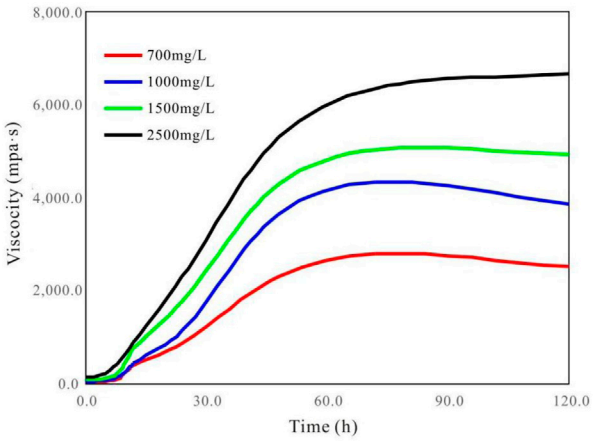

FIGURE 4
Variation of viscosity of polymer gel profile control agent system with time.

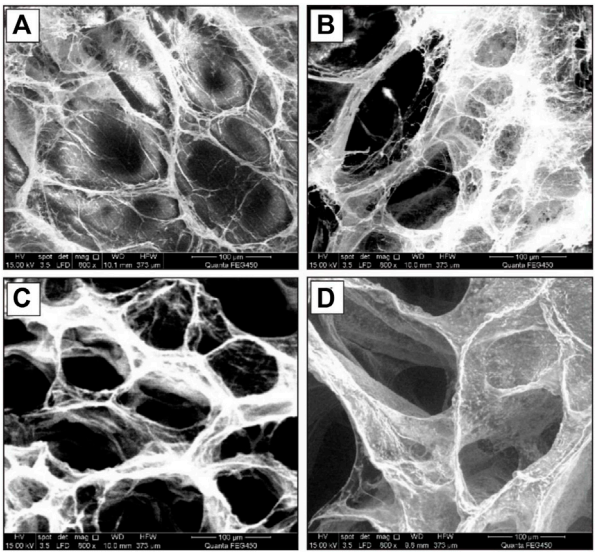

FIGURE 5
Micromorphology of profilers with different polymer viscosities before and after gelling. **(A)** 700 mg/L, before, Sample 1; **(B)** 2500 mg/L, after, Sample 1; **(C)** 700 mg/L, before, Sample 2; **(D)** 2500 mg/L, after, Sample 2.

(American Gatan company), core holder, vacuum pump, intermediate container, pipelines.

2.3.2 Experimental materials

Experimental water: shown in Table 1; polymer: effective content of 90%; Cr^{3+} crosslinking agent: effective content of 90%; stabilizer: effective content of 90%; experimental core: artificial core.

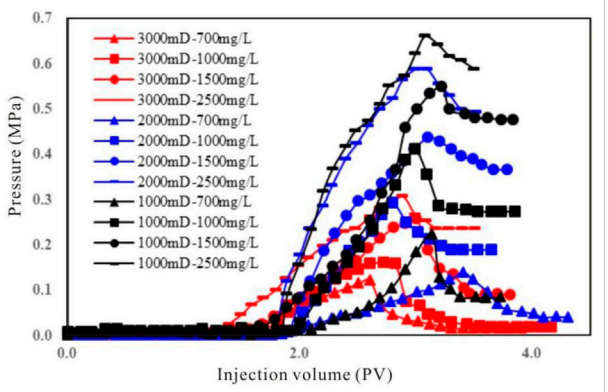

FIGURE 6
Water displacement pressure curves of core samples.

2.3.3 Experimental program

2.3.3.1 Determination of properties of polymer gel profile control agents

(1) First, polymer gel profile control agents with polymer concentrations of 700 mg/L, 1,000 mg/L, 1,500 mg/L, and 2500 mg/L were prepared, respectively. Then, their peak viscosity and gelling time were recorded. The microscopic morphology of the polymer gel profile modifiers under different polymer concentrations after gelation was observed;

(2) Polymer gel profile control agents with polymer concentrations of 700 mg/L, 1,000 mg/L, 1,500 mg/L and 2500 mg/L were prepared respectively. Their viscosity peaks and gelling times after shearing were recorded. After gelation, the microscopic morphology of the polymer gel profile control agent at different polymer concentrations was observed. In addition, the properties of polymer gel profile modifiers subjected to and not subjected to shearing were compared.

2.3.3.2 Core flooding experiments

(1) Before the experiment, the cores were put into the experimental water to be emptied and saturated until no bubbles overflowed. After the cores were saturated with experimental water, they were transferred to a 45 °C incubator for constant-speed water flooding experiments. The pressure of the water flooding experiment was recorded every 20 min until the displacement pressure no longer changed;

(2) A certain volume of polymer gel profile control agent was injected into the experimental core. At the same time, the pressure change data during the injection of the gel system was recorded. When the injection was completed, the experimental core was placed in a 45 °C incubator for 4 days;

(3) Further, the core is subjected to subsequent water flooding experiments at the same injection rate as in step (1), and the

TABLE 4 In-core breakthrough pressure and plugging coefficient under different polymer concentrations and core permeability.

Core Permeability (mD)	1000 mD				2000 mD				3000 mD			
Polymer concentration (mg/L)	700	1,000	1,500	2500	700	1,000	1,500	2500	700	1,000	1,500	2500
Breakthrough pressure (MPa)	0.22	0.41	0.55	0.67	0.14	0.29	0.44	0.59	0.12	0.16	0.26	0.31
Plugging rate (%)	97.9	99.1	99.5	99.6	94.8	98.8	99.5	99.6	93.3	94.4	99.3	99.6

TABLE 5 Gel display of various parts of the core under electron microscope.

Gel Concentration (mg/L)	Permeability (mD)	Core Part		
		Front	Central	Back
700	1,000	++	+	+
	2000	+	+	—
	3000	+	—	—
1,000	1,000	+++	++	+
	2000	+	+	+
	3000	+	+	+
1,500	1,000	+++	+++	++
	2000	+++	+++	+
	3000	+	+++	+
2500	1,000	+++	+++	+++
	2000	+++	+++	++
	3000	+++	+++	+

In the table, "+" represents the amount of gel at the observation site, "+++" means complete plugged with a large amount of gel, "++" indicates that most areas are plugged, with a moderate amount of gel, "+" means not plugged, with little amount of gel, and "/" means no gel is displayed.

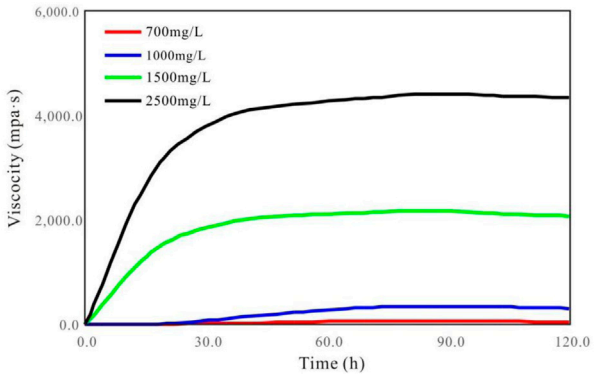

FIGURE 7
Variation of viscosity with time of polymer gel profile control agent system under shearing action.

data of displacement pressure changes are recorded until they no longer change;

(4) Calculation of core plugging rate and evaluation of gel plugging performance;

(5) After the completion of the subsequent water flooding experiments, the experimental cores were cut into four equal parts according to 1/4, 2/4, and 3/4. A scanning electron microscope was used to observe the fresh end face after cutting and the retention of the gel. The results are shown in Figure 3.

3 Results

3.1 Effects of polymer concentration on gelling viscosity and microscopic morphology

Under the conditions of 700 mg/L, 1,000 mg/L, 1,500 mg/L and 2500 mg/L polymer concentration, the results of the variation law of the viscosity of the polymer gel system with time are shown in Figure 4. It can be seen that with the increase of the polymer concentration, the gel viscosity of the polymer gel profile control agent will increase firstly, and the viscosity will tend to be stable after gelation. When the polymer concentration is lower than 1,500 mg/L, the viscosity of the polymer gel profile modifier will decrease after reaching the peak value.

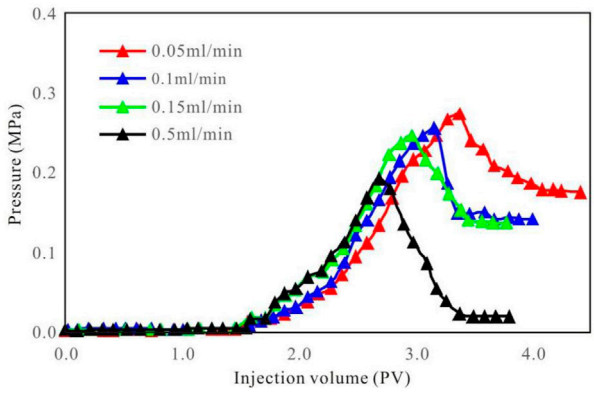

FIGURE 8
Variation of core pressure under different injection rates.

TABLE 6 Breakthrough pressure and plugging coefficient in cores under different injection rates.

Progress (ml/min)	0.05	0.10	0.15	0.50
Breakthrough pressure (MPa)	0.27	0.26	0.25	0.19
Plugging rate (%)	99.4	99.3	99.3	94.4

The microscopic morphology observations show that the network structures of the gel profile control agent became denser with the increase of polymer concentration before gelation (Figure 5). In addition, the wall thickness is increased, the voids are reduced, and the overall surface is rough. After gelation, the surface of the colloid was smoother, and its grid structure was clearer (Figure 5).

3.2 Plugging effect in cores with different permeability under different polymer concentrations

First, the polymer gel systems with concentrations of 700 mg/L, 1,000 mg/L, 1,500 mg/L and 2500 mg/L were injected into cores with gas permeabilities of 3000 mD, 2000 mD and 1,000 mD respectively according to the injection volume of 0.3 PV. They were held at 45°C for 4 d, and then brine was used to carry out flooding experiments. The pressure changes of the cores are recorded, and then the breakthrough pressure and plugging rate are obtained.

According to the experimental results in Figure 6; Table 4, it can be seen that the core permeability has the greatest influence on the plugging effect. When the permeability is 1,000 mD, the decrease of polymer concentration has little effect on the plugging rate and effective plugging is formed. The second is the effect of polymer concentration on the plugging effect, that is, with the increase of core permeability, only higher polymer concentration can achieve effective plugging of cores.

The microscopic observations in Table 5 are consistent with the macroscopic experimental results. For example, in a core with a permeability of 3000 mD, when the polymer concentration is 700 mg/L, the breakthrough pressure is low, and the pressure difference before and after the breakthrough is small. Observed under the electron microscope, there is a very small amount of gel at the front of the core, so the breakthrough pressure is low. There is no gel at the middle and back ends of the core, so the pressure drops quickly after the breakthrough and the difference is small compared to before the breakthrough.

Combined with the observation results of the microscopic morphology of the polymer gel profile control agents, it can be found that the final determination of the plugging effect is the network structures after the final gelation of the polymer gel profile control agents. The large pores inside the core can be effectively plugged only if the conditions of a tight and smooth network structure, few voids, thick trunks and branches are met.

4 Discussion

4.1 Influence of shear action on gel viscosity of profile control agent

We performed physical shear simulations of laboratory-formulated polygel profile modifiers. The variation law of solution viscosity before and after shearing is shown in Figure 7. It can be seen that the gel-forming viscosity of the polymer gel profile modifier increases with the increase of the polymer concentration. When the polymer concentration is lower than 1,500 mg/L, the viscosity of the polymer gel profile control agent after gelation first reaches a peak value, and then decreases significantly.

It was found by scanning electron microscopy that the network structure of the polymer gel profile control agent was destroyed after being subjected to shear stress. When the polymer concentration is lower, the network structure is destroyed at a higher rate (Lu, 2016; Wang et al., 2005; Wang et al., 2016). Furthermore, the structure after gelation is not strong and the polymer gel system cannot effectively seal the formation.

4.2 Evaluation of plugging effect at different injection rates

When the polymer gel profile control agent is injected into the reservoir, and if the injection speed is too slow, the volume of the profile control agent injected within a certain period of time will be too small and the reservoir cannot be effectively plugged (Xie et al., 2016). However, if the injection speed is too fast, the shearing effect of the profile control agent during the migration

TABLE 7 Judgment criterion for matching between polymer gel profile control agent and reservoir.

Criterion	Unplugged	Plugged, Migration, plugged	Plugged
Distribution law and retention morphology	A small amount of colloid is retained at the pores and on the rock surface, and the gel will flow out of the core with water	After the colloid migrated to the middle of the core with the injected water, a large amount of it was retained in the middle and front of the core	A large amount of colloid is retained on the injection end face and front end of the core, and it hardly migrates effectively with the subsequent injection of water
Plugging rate (%)	≦95	95–99%	≧99
Breakthrough pressure (MPa)	≦0.2	0.2–0.4	≧0.4

TABLE 8 Matching relationship between polymer gel system and reservoir under different schemes.

Conditions	700 mg/L	1,000 mg/L	1,500 mg/L	2500 mg/L
3000 mD	Unplugged	Unplugged	Plugged, migration, Plugged	Effectively plugged
2000 mD	Unplugged	Plugged, migration, Plugged	Effectively plugged	Effectively plugged
1,000 mD	Plugged, migration, Plugged	Effectively plugged	Effectively plugged	Effectively plugged

process is relatively large, so that the spatial structures of the profile control agent are destroyed and the plugging performance is reduced.

The effect of different injection rates on the plugging performance of the polymer gel system was systematically analyzed. First, the polymer gel profile control agent was formulated with a concentration of 1,500 mg/L polymer, 0.30% crosslinking agent and 0.03% stabilizer. It was injected into the cores at constant rates of 0.05 ml/min, 0.10 ml/min, 0.150 ml/min, and 0.5 ml/min, respectively. Brine was used for core flooding after 4 days of holding at 45°C. Finally, the pressure change data in the core is used to calculate the breakthrough pressure and the plugging rate.

It can be seen from Figure 8; Table 6 that when the injection rate of the profile control agent is increased to 0.5 ml/min, the injection rate has a great influence on the plugging ability of the profile control agent in the cores. The faster the injection rate, the lower the plugging performance of the profile control agent in the cores.

Combined with the observation results of the microscopic morphology of the polymer gel profile control agent, it can be found that when the injection speed is increased, the shear effect of the polymer gel profile control agent is enhanced. It causes the network structure of the polymer gel profile control agent to be destroyed after gelation, and the plugging strength is significantly affected.

4.3 Compatibility and judgment criteria of polymer gel profile control agent and reservoir

In this study, three plugging state models "absolute plugging", "plugging-migration" and "absolute migration" were established. These models comprehensively consider the breakthrough pressures of polymer gel profile control agent in the cores, the plugging rates, the microscopic morphology of the gel profile control agents, and the gel display in the cores after displacement.

Based on the experimental results, we propose three criteria for evaluating the compatibility of polymer gel profile control agent and reservoir. A detailed description of the pressure conduction law, the plugging rate range, and the distribution state and morphological characteristics of the gel system under different matching relationships is shown in Table 7.

Finally, the effects of polymer viscosity and core permeability on the plugging effect under different experimental conditions are summarized, and the results are shown in Table 8. This study can provide a guiding reference for similar studies.

5 Conclusion

(1) In this study, artificial cores were used to carry out indoor water flooding experiments after polymer gel injection, considering formation permeability, polymer concentration and polymer injection rate. Based on the accurate records of the breakthrough pressure and injection volume during water flooding, as well as a large number of observations of the microscopic morphology of the cores after the polymer gel profile control and displacement, a set of criteria for determining reservoir-matched polymer gel profile control agents is proposed.

(2) A complex spatial network structure is formed after the gelation of the polymer gel system. As the polymer

concentration increases, the network structure of the gel system becomes denser. At the same time, the unit network structure is becoming smaller, and the order of the grid chain structure becomes clearer. Under the condition of low polymer concentration, the backbone structure of the gel is obvious, but there are a lot of fine pores.

(3) There are three situations for the distribution of polymer gel system in the cores: a. When a small amount of polymer gel system stays in the front surface and pores of the core, the plugging is ineffective; b. When a large amount of polymer gel system stays in the pores and the front and middle parts of the core, some pores can be effectively blocked; c. When a large amount of polymer gel system blocks the front surface of the core, it can effectively block the pores inside the core.

(4) When the polymer concentration is greater than 1,500 mg/L and the injection rate is less than 0.15 ml/min, the water flooding breakthrough pressure is greater than 0.2 MPa, the plugging rate is greater than 95%, and a good plugging effect is obtained.

Data availability statement

The original contributions presented in the study are included in the article/supplementary material further inquiries can be directed to the corresponding author.

Author contributions

SY is responsible for the idea and writing of this paper and ZS, QZ, YZ, ZC, and LZ are responsible for the experiments.

Conflict of interest

Author SY was employed by the Sinopec Huadong Oilfield Service Corporation; Author QZ was employed by the Gepetto Oil Technology Group Co., Ltd; Author YZ was employed by the Oil Production Plant four of PetroChina Changqing Oilfield Company; Authors ZC and LZ were employed by the Great Wall Drilling Corporation, CNPC.

The remaining authors declare that the research was conducted in the absence of any commercial or financial relationships that could be construed as a potential conflict of interest.

Publisher's note

All claims expressed in this article are solely those of the authors and do not necessarily represent those of their affiliated organizations, or those of the publisher, the editors and the reviewers. Any product that may be evaluated in this article, or claim that may be made by its manufacturer, is not guaranteed or endorsed by the publisher.

References

Fan, Y. (2013). Performance evaluation of deep profile control agent, 88–92 [Northeast Petroleum University]. doi:10.3863/j.issn.1674-5086.2013.02.018

Guo, Y., Li, S., Lv, S., Yang, L., and Wang, K. (2007). Synthesis and properties evaluation of pre-crosslinking particles as profile modification agent. *Prog. fine Petrochem. industry* 21 (10), 78–82. doi:10.3969/j.issn.1009-8348.2007.10.002

Jia, X., Xiong, C., and Zhang, S. (2016). *A method for evaluating reservoir adaptability of polymer gel profile control agent*. cn103995083b, 8–11.

Li, H., Zhao, H., and Zhao, P. (2006). Study on hydrophobically associating polymer gel profile control agent for high temperature and high salt reservoirs in Zhongyuan. *Oilfield Chem.* 23 (1), 50–53. doi:10.1016/j.asw.2014.12.001

Liang, W. (2008). Study on preparing artificial cores. *Petroleum pipes Instrum.* 22 (2), 72–74. doi:10.3969/j.issn.1004-9134.2008.02.023

Liu, C., Wang, Q., Sun, Y., Gao, M., Liu, W., and Wang, Z. (2014a). Research and application of new technology limits for polymer flooding field application. *Petroleum Geol. recovery factor* 14 (2), 36–40. doi:10.1684/bdc.2014.1970

Liu, J., Chang, C., Yu, J., and Zhao, H. (2014). Comprehensive potential tapping test before tertiary oil recovery for class II and III reservoirs in the east of Block 1 (2), 41–45 [Daqing Petroleum Geology and development]. doi:10.3969/J.ISSN.1000-3754.2014.02.014

Liu, J., Lu, X., and Zhang, Y. (2018). Effect of surfactant and alkali on the gelling effect of cr3+ polyacrylamide gel and its mechanism. *J. Petroleum (petroleum Process.* 34 (3), 614–622. doi:10.3969/j.issn.1001-8719.2018.03.023

Liu, X. (2019). Evaluating method of the strength and elasticity of the particle profile-controlling agent for strong-alkali ASP flooding. *Daqing Petroleum Geol. Dev.* 38 (2), 99–104. doi:10.19597/j.issn.1000-3754.201809028

Liu, X., and Shang, H. (2020). Evaluation of dynamic gelling performance of gel profile control agent in deep formation. *Daqing Petroleum Geol. Dev.* 39 (1), 86–90. doi:10.13840/j.cnki.cn21-1457/tq.2022.07.009

Liu, Z. (2000). Research and application of deep profile control technology in Laojunmiao Oilfield, 22–25 [Southwest Petroleum Institute]. doi:10.1016/S0022-0248(99)00406-6

Lu, Y., and Ho, R. C. M. (2016). An association between neuropeptide Y levels and leukocyte subsets in stress-exacerbated asthmatic mice. *Neuropeptides* 15 (4), 53–58. doi:10.1016/j.npep.2015.11.091

Nie, C. (2017). Injection pressure variation and prediction of ASP flooding in Daqing Oilfield. *Special oil gas reservoirs* 12 (1), 77–80. doi:10.3969/j.issn.1006-6535.2017.01.023

Niu, Q., Cai, S., and Hu, X. (2003). Deep profile control and plugging technology for large channel. *Drill. Prod. Technol.* 26 (1), 30–31. doi:10.1088/1755-1315/252/5/052076

Qing, H., Song, R., Yang, H., Li, S., Jin, Y., and Liu, J. (2017). Influencing factors of EOR after strong alkali ASP flooding. *Daqing Petroleum Geol. Dev.* 23 (4), 88–92. doi:10.19597/J.ISSN.1000-3754.201609026

Sun, Y., Long, Y., Song, F., and Yu, J. (2016). Evaluation of plugging performance of nano micron polymer particle dispersion system in low permeability reservoir. *Petroleum Geol. recovery factor* 13 (4), 22–27. doi:10.13673/j.cnki.cn37-1359/te.2016.04.014

Tian, X. (2013). Research and application of ASP flooding depth profile control technology. *Drill. Prod. Technol.* 12 (1), 33–36. doi:10.3969/J.ISSN.1006-768X.2013.01.18

Wang, J., Zhang, X., Yuan, Y., Liu, J., and Peng, X. (2006). Application performance evaluation of particle profile control agent under high salinity. *Prog. fine Petrochem. industry* 11 (12), 23–28. doi:10.1016/S1003-9953(10)60145-4

Wang, P., lin, Y., and Luo, J. (2016). Application of flexible steering agent technology in oil field water shutoff and profile control, 101–105 [China Petroleum Society China Petroleum Institute]. doi:10.3969/j.issn.1004-275X.2019.07.069

Wang, Z., Li, Y., Lv, C., and Meng, J. (2005). Performance evaluation of pre-gelled swellable particle profile control agent. *Daqing Petroleum Geol. Dev.* 12 (6), 77–79. doi:10.3969/j.issn.1000-3754.2005.06.028

Wang, Z., Lu, X., Zhang, J., and Zhang, B. (2016a). Comparison of oil displacement effects of various profile control and displacement agents after strong alkali ASP flooding. *J. Xi'an Petroleum Univ.* 22 (4), 88–92. doi:10.1016/S1876-3804(19)30011-4

Xie, B., Wang, L., and Lu, Q. (2016). Experiment on influence of oil displacement agent on cementing quality. *Daqing Petroleum Geol. Dev.* 21 (1), 101–105. doi:10.3969/J.ISSN.1000-3754.2016.01.018

Xu, W., Wei, Z., and Bai, B. (2002). Study on the performance of low temperature weak gel profile control and displacement agent//national rheological academic conference Chinese Chemical Society, 123–127 [Chinese society of mechanics]. doi:10.4028/www.scientific.net/AMM.587-589.1332

Yang, Z., Wang, L., Gao, T., and Song, K. (2017). A new method for optimizing injection slug combination parameters of ASP flooding. *Daqing Petroleum Geol. Dev.* 13 (3), 44–49. doi:10.3969/J.ISSN.1000-3754.2017.03.021

You, Q., Yu, H., and Wang, Y. (2009). Research progress of deep profile control technology in domestic oilfields. *Fault block oil gas field* 13 (4), 74–77. doi:10.1088/1755-1315/384/1/012134

Yuan, Y., Wang, J., Huang, Y., and Liu, J. (2006). Development and performance evaluation of composite crosslinked polymer weak gel profile control and flooding agent. *Inn. Mong. Petrochem. Ind. Co. Ltd.* 23 (2), 43–47. doi:10.13534/j.cnki.32-1601/te.2014.01.007

Zhao, G. (2012). Preparation and performance evaluation of gel dispersion, 44–47 [China University of Petroleum (East China)]. doi:10.19346/j.cnki.1000-4092.2017.02.014

Zhao, X., Chen, Z., Chen, W., Ma, H., Zhai, D., and Ren, Z. (2015). Research status and development trend of granular profile control and water shutoff agents. *Petroleum Drill. Prod. Technol.* 15 (4), 90–94. doi:10.3969/j.issn.1009-0622.2018.04.007

frontiers | Frontiers in Earth Science

TYPE Original Research
PUBLISHED 04 January 2023
DOI 10.3389/feart.2022.1022911

OPEN ACCESS

EDITED BY
Hu Li,
Southwest Petroleum University, China

REVIEWED BY
Youli Wan,
Ministry of Land and Resources, China
Qingyu Zhang,
Institute of Karst Geology, Chinese Academy of Geological Sciences, China

*CORRESPONDENCE
Wei Luo,
weelo515@163.com

SPECIALTY SECTION
This article was submitted to Structural Geology and Tectonics, a section of the journal Frontiers in Earth Science

RECEIVED 19 August 2022
ACCEPTED 27 October 2022
PUBLISHED 04 January 2023

CITATION
Hu X, Luo W, Zang D, Wang W, Yi C and Li J (2023), Key factors affecting hydrocarbon accumulation in ancient dolomite gas reservoirs of Xixiangchi formation (Southern Sichuan Basin, China).
Front. Earth Sci. 10:1022911.
doi: 10.3389/feart.2022.1022911

Key factors affecting hydrocarbon accumulation in ancient dolomite gas reservoirs of Xixiangchi formation (Southern Sichuan Basin, China)

Xiuquan Hu[1], Wei Luo[1,2]*, Dianguang Zang[2], Wenzhi Wang[3], Chi Yi[1] and Jianghan Li[1]

[1]College of Energy, Chengdu University of Technology, Chengdu, China, [2]BGP Southwest Geophysical Research Institute, CNPC, Chengdu, China, [3]Exploration and Development Research Institute, PetroChina Southwest Oil and Gas Field Company, Chengdu, China

The Upper Cambrian Xixiangchi Formation in the Southern Sichuan Basin, China, has favorable hydrocarbon accumulation conditions. The accumulation factors and enrichment conditions of this formation were key considerations in this study. By analyzing core, thin section, seismic, and geochemical data, the research shows that there are many sets of granular and crystalline dolomite reservoirs in the Xixiangchi Formation vertically, with thin thickness of single-reservoir. During the transformation of karst and tectonism, dissolution pores and fractures developed to form an ideal reservoir space. The reservoir of the Xixiangchi Formation is connected to the Lower Cambrian source rock through a fault system. The high-energy shoal facies of the Xixiangchi Formation are located on the oil and gas migration path, providing an appropriate reservoir space for forming the source reservoir configuration relationship between the lower generation and upper reservoir. The key factors affecting hydrocarbon accumulation in the Xixiangchi Formation are sufficient oil and gas supply, development of inherited paleo-uplift, effective transportation system, and favorable reservoir-forming combination. The inherited paleo-uplift controls the distribution of gas reservoirs. Owing to the short migration distance of oil and gas, hydrocarbon is found near source hydrocarbon accumulation, and the paleo-uplift slope area should be targeted for exploration in future studies.

KEYWORDS

xixiangchi formation, sichuan basin, hydrocarbon accumulation, dolomite gas reservoir, paleo-uplift

Introduction

Many dolomite oil and gas reservoirs have been found worldwide, mainly in North America, Asia, and Europe, and a few in Africa and South America (Saller and Henderson, 1998; Dutton et al., 2005; Ma et al., 2011; Manche and Kaczmarek, 2019). Oil production stems chiefly from the Late Cretaceous and Late Permian, gas production from the Late

Jurassic and Early Permian, and condensate gas production from the Late Triassic to Late Jurassic and Late Devonian (Ma et al., 2011). Recently, dolomite gas fields have also been found in the ancient strata of the Early Cambrian (Du et al., 2014; Lin et al., 2020) and Neoproterozoic sediments (Wei et al., 2015; Xu, 2017), which demonstrates the exploration potential of deep, ancient dolomite gas fields. The geological conditions present in the Sichuan basin from the Ediacaran to the Cambrian allowed for the formation of large-scale natural gas fields. The space-time effective configuration of large ancient source rocks, ancient carbonate reservoirs, long-term inherited large-scale paleo-uplift, and crude oil cracking in ancient reservoirs led to the accumulation of natural gas (Wei et al., 2008; Du et al., 2014; Xu et al., 2014; Yang et al., 2021). In the past decades of exploration, the Xixiangchi formation gas field was found only in Weiyuan area, with 21 industrial gas wells and proven reserve of 85 × 10^8 m^3 (Lin et al., 2017; Li et al., 2020). In recent years, commercial gas flow was obtained from well MX 23 and well GS 16 in the Xixiangchi Formation of the Moxi area, indicating that the prospect of finding natural gas in the Xixiangchi Formation is broad, providing a backup exploration field in the Sichuan Basin, China (Li et al., 2020; Lin et al., 2020).

Current research on the Xixiangchi Formation has focused on the central area of the Sichuan Basin, and the research content mainly involves sequence stratigraphy (Zhao, 2015; Li et al., 2017; Liu et al., 2018; Li et al., 2020; Lin et al., 2020; Jia et al., 2021), lithofacies paleogeography (Liu et al., 2011; Jiang et al., 2016; Shi et al., 2020). and reservoir characteristics (Feng et al., 2001; Shen et al., 2007; He et al., 2011; Zhang et al., 2011; Li et al., 2019; Yang et al., 2019a; Su et al., 2020). Although the success of Well MX 23 and Well GS 16 has improved our confidence in the exploration of Xixiangchi Formation, the complexity of hydrocarbon accumulation in Xixiangchi Formation is the main difficulty we face. Based on this, this paper, according to outcrop data, core observations, thin section identifications, and experimental analysis, on the analysis of hydrocarbon accumulation conditions of Xixiangchi Formation in the southern Sichuan Basin, combined with drilling exploration results, discusses the key factors affecting hydrocarbon accumulation in ancient dolomite gas reservoirs, defines the favorable exploration direction, and hopes to improve the drilling success rate in the exploration process.

Geological setting

The Sichuan Basin is a superimposed basin formed on the Yangtze Craton (Figure 1A). The sedimentary cover consists of Ediacaran to Middle Triassic marine strata and Late Triassic to Cenozoic terrestrial strata (Shen et al., 2007; He et al., 2011; Liu et al., 2011; Zhang et al., 2011; Li et al., 2019; Su et al., 2020; Li et al., 2022). In the late Ediacaran, The Tongwan movement raised the Ediacaran strata to the surface, and the Dengying Formation experienced large-scale supergene karstification (Du et al., 2014; Xu et al., 2014; Yang et al., 2021). In Cambrian, Sichuan Basin was a period of stable cratonic basin development, showing a sedimentary pattern of high in the west and low in the east (He et al., 2011). In the late Cambrian Xixiangchi period, evaporative salt basin was developed in the central part of Sichuan Basin, and a rapid large-scale transgression occurred in its early sedimentary period, making Sichuan basin covered by a large range of restricted platform facies. The closed environment of evaporation and concentration in the platform evolved into an open - semi-open environment, and the Chongqing - Yibin area changed from evaporative salt basin to intra-platform depression sedimentation (Figure 1) (Yang et al., 2019a; Gu et al., 2020). The water energy on both sides of the platform depression was relatively high, and high energy granular beach belts were developed. The Xixiangchi period was dominated by salty seawater sedimentary environment and warm or hot subtropical climate, and the ancient seawater temperature was mainly 19°C–25°C (Li et al., 2019). The Ordovician began to water-transgress, and the Sichuan Basin was dominated by shelf-to-basin facies. At the end of the Silurian, the Late Caledonian movement came the uplift and denudation of the Leshan-Longnusi paleo-uplift, resulting in an angular unconformity between the Cambrian and Permian strata in the southwestern Sichuan Basin (Su et al., 2020; Luo et al., 2022). The Xixiangchi Formation in the Southwestern Sichuan Basin is denuded (Gu et al., 2020; Li et al., 2020) (Figure 1B).

Granular rocks in the Xixiangchi Formation are mostly in the inverse grain sequence, with a finer bottom and coarser top, representing carbonate platform shoal deposits of an upward shallowing epeiric sea. Under the control of paleomorphology and sea level fluctuation (Gu et al., 2020; Jia et al., 2021), the shoals at the platform margin were large in scale and thickness, but the shoals at the inner platform were small in scale, thin in thickness, and frequently migrate laterally (Zhao, 2015). After the dolomitization and dissolution transformation of the granular shoal reservoir of the Xixiangchi Formation (Shi et al., 2020), the reservoir spaces developed intergranular, intercrystalline, and dissolved pores (Jiang et al., 2016; Li et al., 2020). There is a strip of denudation zones in the West, wherein a weathering crust reservoir developed (Gu et al., 2020; Li et al., 2020). Supergene karstification (Xu et al., 2014) and penecontemporaneous karstification (Du et al., 2014) are key factors contributing to the formation of high-quality dolomite reservoirs. Multistage tectonic movement caused the Xixiangchi Formation to develop structural fractures, which connected the pore spaces and helped improve reservoir connectivity (Lin et al., 2017).

From West to East, the Xixiangchi Formation in the Sichuan Basin successively developed an evaporation platform, restricted platform, open platform, platform margin, slope, and basin. Owing to the influence of ancient land on the west side of the Sichuan Basin (Feng et al., 2001), the western part of the basin is characterized by mixed deposition of clastic and carbonate rocks, and the lithology is dominated by fine sandstone, sandy dolomite, and dolomite. From West to East, the terrigenous clastic content decreases gradually, and

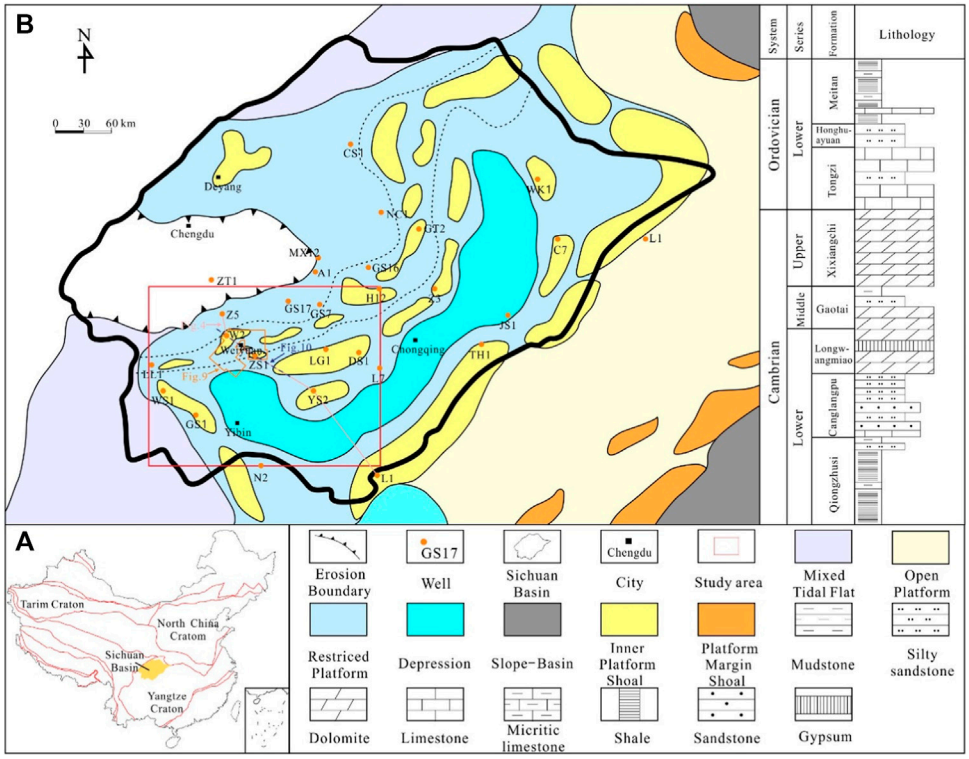

FIGURE 1
Comprehensive geological map of the study area. **(A)** Sketch map of tectonic units in China and the location of study area [modified form Luo et al.(2016)]; and **(B)** Lithofacies and paleogeography map of the Cambrian Xixiangchi period in Sichuan Basin [modified form Gu et al.(2020)].

dolomitic flats dominated by argillaceous dolomite begin to appear. There is a NE-trending platform depression along Yibin to Chongqing, and the sediments there are composed mainly of fine crystalline dolomite. On both sides of the platform depression is the NE trending intra-platform granular shoal belt, and the lithology is sandy clastic dolomite, oolitic dolomite, and coarse crystalline dolomite. The hydrodynamic force at the platform margin was strong, and the scale of the granular shoal was larger than that of the intra platform. The Eastern side of the Sichuan Basin is a slope-to-basin environment, and its lithology is dominated by limestone and argillaceous limestone (Li et al., 2019; Gu et al., 2020; Jia et al., 2021) (Figure 1B).

Methods and methods

The samples used in the lithological identification and geochemical analysis were obtained from wells in the Southwestern Sichuan Basin (Figure 1). Approximately 219 samples were polished on both sides, and thin sections were impregnated with blue epoxy resin for pore observation. The thin section samples were polished to 0.03 mm. Before identification, thin sections were stained with a mixed solution of alizarin red and potassium ferricyanide and observed using a LEICA DMLP-217400 microscope in the State Key Laboratory of Petroleum Exploration and Development.

The samples were washed with toluene and methanol to remove hydrocarbon and salt precipitations, and then dried at 80°C for 48 h before measurement. Clean and dry samples were weighed first, then placed in a sealed container and evacuated up to a vacuum pressure of 0.001 psi. Therefore, the container was filled with an equal amount of NaCl brine and gradually pressurized for several hours until a fixed pressure of 2000 psi. Finally, the initial porosity was estimated based on the weight difference between dry and saturated samples, which was taken as the volume of brine injected into each core sample. At each selected stress step when the equilibrium based on defined criteria was reached, the expelled fluid volume at each stress loading was measured and then brine injected to the sample in order to calculate the brine permeability using Darcy model (steady-state method) (Rashid et al., 2017). The estimated porosity can be made to within ± 0.1 porosity unit using the apparatus and protocols at the State Key Laboratory of Petroleum Exploration and Development.

Use gas analyzer (MAT-271) and isotope mass spectrometer (Delta-V-Advantage) to analyze gas components and carbon isotopes respectively, the gas collected in the bottle is sealed with saturated salt water and injected into the gas injection port of the gas chromatograph with a syringe. The gas is brought into

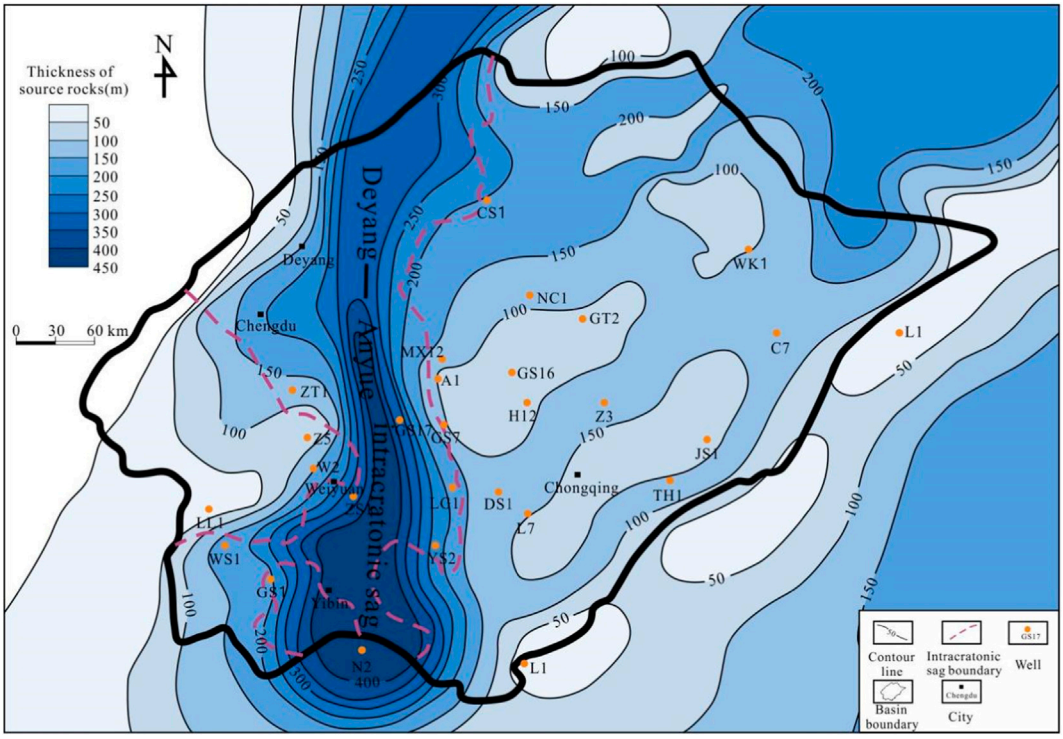

FIGURE 2
Thickness distribution of Lower Cambrian source rock in Sichuan Basin [modified from Yang et al. (2019a)].

the chromatographic column by helium and divided into methane, ethane, propane, butane monomer components. Each monomer component is oxidized into carbon dioxide gas at high temperature after entering the oxidation furnace, and finally brought into the mass spectrometer for isotope testing (Li et al., 2022; Li, 2022; Zhang et al., 2022). The measurement accuracy is ±0.1‰, which is completed in the State Key Laboratory of Oil and Gas Reservoir Geology and Exploitation.

Geological conditions of hydrocarbon accumulation

The geological conditions necessary for the formation of carbonate gas reservoirs are manifested mainly in terms of hydrocarbon source conditions, reservoir characteristics, cap rock sealing efficiency, and reservoir forming time-space allocation.

High-quality source rocks developed underneath

The source rock of the Lower Cambrian Qiongzhusi Formation is the most important source rock in the Sichuan Basin, providing hydrocarbon for the overlying Xixiangchi Formation (Shi et al., 2018). The type of organic matter in the source rocks of the Qiongzhusi Formation is type I kerogen (Xiong et al., 2021), and the total organic carbon (TOC) content is between 0.5% and 4.0%, with an average of 2.0%. The degree of thermal maturity of source rocks was high, and the pyrobitumen reflectance values were greater than 2.5%. The Qiongzhusi source rocks have thermal maturities that range from postmature to overmature, and the generation capability of the source rock has been high in the past, resulting in a high amount of oil. Gas is produced primarily *via* oil and kerogen cracking (Shi et al., 2018).

The high-quality Lower Cambrian source rocks were mainly deposited in the intracratonic sag (Figure 2). The thickness of the black shale in the Qiongzhusi Formation is 200–300 m in the Weiyuan area. The thickness of the carbonaceous shale of the Qiongzhusi Formation in well GS 17 was more than 350 m. The Qiongzhusi Formation in well GS seven on the east side of the intracratonic sag was incomplete, missing the lower members of the Qiongzhusi Formation, and the thickness of the mudstone was only 100 m. The source rocks of the Qiongzhusi Formation are distributed in a NNE direction on the plane, approximately 500 km long from North to South and 35–110 km wide from East to West. The source rocks in the Southern Sichuan Basin are characterized by extreme thickness, wide distribution, high TOC content, high degree of thermal maturity, and high hydrocarbon generation capacity. Therefore, the southern Sichuan Basin is regarded as a favorable target for future gas exploration.

Reservoir characteristics of Xixiangchi formation

The analysis of drilling cores and field outcrop data shows that the Xixiangchi Formation reservoir lithology is dominated by granular and crystalline dolomite (Figures 3A–I), which belong to the intraplatform shoal environment. Many dissolution holes and fractures developed in the reservoir (Figures 3E–J), which were evidently modified by karstification and tectonism (Lin et al., 2017; Tian et al., 2019; Li et al., 2020; Lin et al., 2020). According to drilling and outcrop data, the thickness of dolomite in the Xixiangchi Formation is 70–340 m, which can be divided into three stages of fourth-order sequences (Gu et al., 2020; Ning et al., 2020; Shi et al., 2020). The reservoir developed in the middle and upper parts of the highstand systems tract (HST). The thickness of a single set of reservoirs is approximately 2–5 m; the cumulative thickness of the reservoir is typically less than 20 m, and the horizontal distribution distance of the reservoir is short (Figure 4). Sedimentary facies controled the distribution of granular beach, which was developed in shallow water area of high landform. The granular beach was exposed due to the sea level decline in highstand systems tract stage, and the granular beach in the high part of the ancient landform was exposed in a large area for a long time. The penecontemporaneous meteoric freshwater dissolution caused by the sea level decline form a large number of dissolution holes, which was conducive to improving the physical properties of the reservoir (Figures 3E,H,I). In the late Caledonian movement, the southwestern part of Sichuan Basin was aggressively uplifted, resulting in the formation of the Leshan-Longnusi paleo-uplift (Su et al., 2020). After approximately 120 Ma denudation from Caledonian to Hercynian (Pang et al., 2007), the Xixiangchi Formation in the southwestern Sichuan Basin was denuded (He et al., 2011; Liu et al., 2011). Epigenic karstification occurred at the top of the Xixiangchi Formation in the area near the denudation line (Gu et al., 2020; Li et al., 2020). Owing to strong dissolution, intercrystalline solution pores developed in the rocks at the top of the Xixiangchi Formation near the denudation line (Figure 3I). The epigenic karst zone rises around the Leshan-Longnusi paleo-uplift and is distributed in a "strip-like" belt 20–50 km wide (Li et al., 2020). Owing to tectonic movement after deposition, multiple vertical fractures can be identified from the image logging data obtained by drilling in the Weiyuan area (Figure 3J). The development of fractures can improve the permeability and connectivity of reservoirs.

The thickness of a single set of reservoirs is approximately 2–5 m, and the lateral extension distance of the reservoir is short. The reservoir developed in the middle and upper parts of the highstand systems tract and paleogeomorphic highlands.

Regional stable cap rock

The direct cap rock above the Xixiangchi Formation in the Southern Sichuan Basin is an Ordovician mudstone. The Lower Ordovician Tongzi Formation and the Upper Cambrian Xixiangchi Formation are in parallel unconformity-conformity contact (Li et al., 2020). The Tongzi Formation in the southern Sichuan Basin is dominated by siltstones, limestones, and thin mudstones. The sedimentary paleogeography of the Lower Ordovician Honghuayuan Formation was similar to that of the Tongzi Formation. Its lithology is dominated by siltstone, and the limestone and mudstone contents are reduced. The Lower Ordovician Meitan Formation and the Upper Ordovician Wufeng Formation are characterized by deep-water sedimentary formations dominated by black shale deposits (Li et al., 2015). The Lower Ordovician Meitan Formation in southern Sichuan was a shelf deposit. The lithology is mainly black mudstone with a thickness of between 30 and 120 m (Figure 5); The Upper Ordovician Wufeng Formation is a deep-water shelf deposit, and the lithology is mainly black carbonaceous shale, siliceous shale, and graptolite shale intercalated with thin-layer radiolarians Siliceous rock; its deposition thickness is less than 20 m. The Meitan Formation has a large stratum thickness, fine lithological grain size, undeveloped pores, and good sealing ability.

The analysis results of the formation water in the Xixiangchi Formation of seven gas wells in the Weiyuan Gas Field show that the mass concentration of Cl^- was between 42,795 and 64,261 ppm, the mass concentration of SO_4^{2-} was 114–775 ppm, and the total water formation was between 42,795 and 64,261 ppm. The degree of chemical conversion is between 69.30 and 100.89 g/L, and the water type is calcium chloride, reflecting the better preservation conditions of Xixiangchi gas reservoirs and demonstrating that the Xixiangchi gas reservoirs have strong cap rock sealing ability.

The cap rock lithology of Xixiangchi formation is mainly mudstone, and the mudstone is stably distributed, which can be used as the regional cap rock of Xixiangchi formation.

Gas reservoir characteristics of Weiyuan gas field

The structure of the Xixiangchi Formation in the Weiyuan Gas Field is a dome-shaped anticline that was shaped during the Himalayan period (Mei, 2015). According to the porosity analysis statistics of 219 samples from the Xixiangchi Formation reservoirs in the Southern Sichuan Basin (Figure 6A), the reservoir porosity was between 0.16% and 5.64%, with an average value of 2.21%, and the number of samples with porosity greater than 2% accounted for 60.0% of the total number of samples. According to the permeability analysis statistics of 198 samples (Figure 6B), the reservoir permeability is between 4.96×10^{-6} and 419 mD, with an average value of 0.098 mD, and the number of samples with permeability greater than 0.01 mD accounted for 24.7% of the total number of samples. Reservoirs are typically characterized by

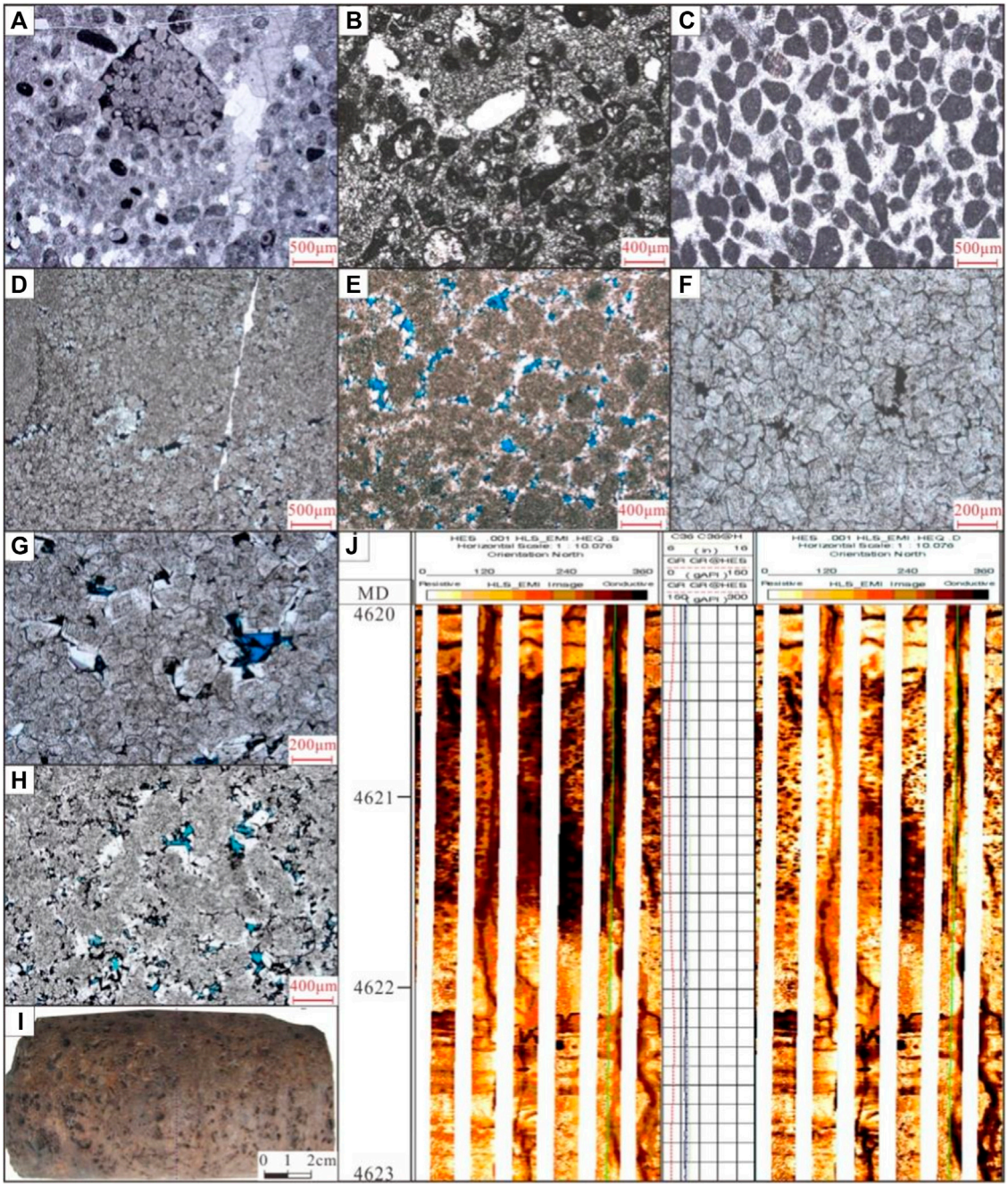

FIGURE 3
Reservoir space types of Xixiangchi Formation in the Southern Sichuan Basin. **(A)** Well WH1, Xixiangchi Formation, 2,209 m, medium granular dolomite; **(B)** Well N2, Xixiangchi Formation, 2,100 m, medium to coarse granular dolomite; **(C)** Well WH1, Xixiangchi Formation, 2,232 m, medium granular dolomite; **(D)** Well DS1, Xixiangchi Formation, 5,332.3 m, fine crystalline dolomite, developed intermediate dissolved pores; **(E)** Well H12, Xixiangchi Formation, 4,848.6 m, fine crystalline dolomite with residual grain texture, intercrystalline dissolved pores developed; **(F)** Well L1, Xixiangchi Formation, 2,105 m, coarse crystalline dolomite, intercrystalline dissolved pores developed and filled with bitumen; **(G)** Well LL1, Xixiangchi Formation, 2,246.50 m, coarse crystalline dolomite, intercrystalline dissolved pores developed and filled with bitumen; **(H)** Well LG1, Xixiangchi Formation, 4,624.38 m, fine crystalline dolomite with residual grain texture, intercrystalline dissolved pores developed and filled with bitumen; **(I)** Well WS1, Xixiangchi Formation, 2,254 m, granular dolomite, with intergranular dissolved pores and vugs; **(J)** Well H12, Xixiangchi Formation, 4,620–4,623 m image logging feature map, developed pinhole dissolution holes and vertical seams.

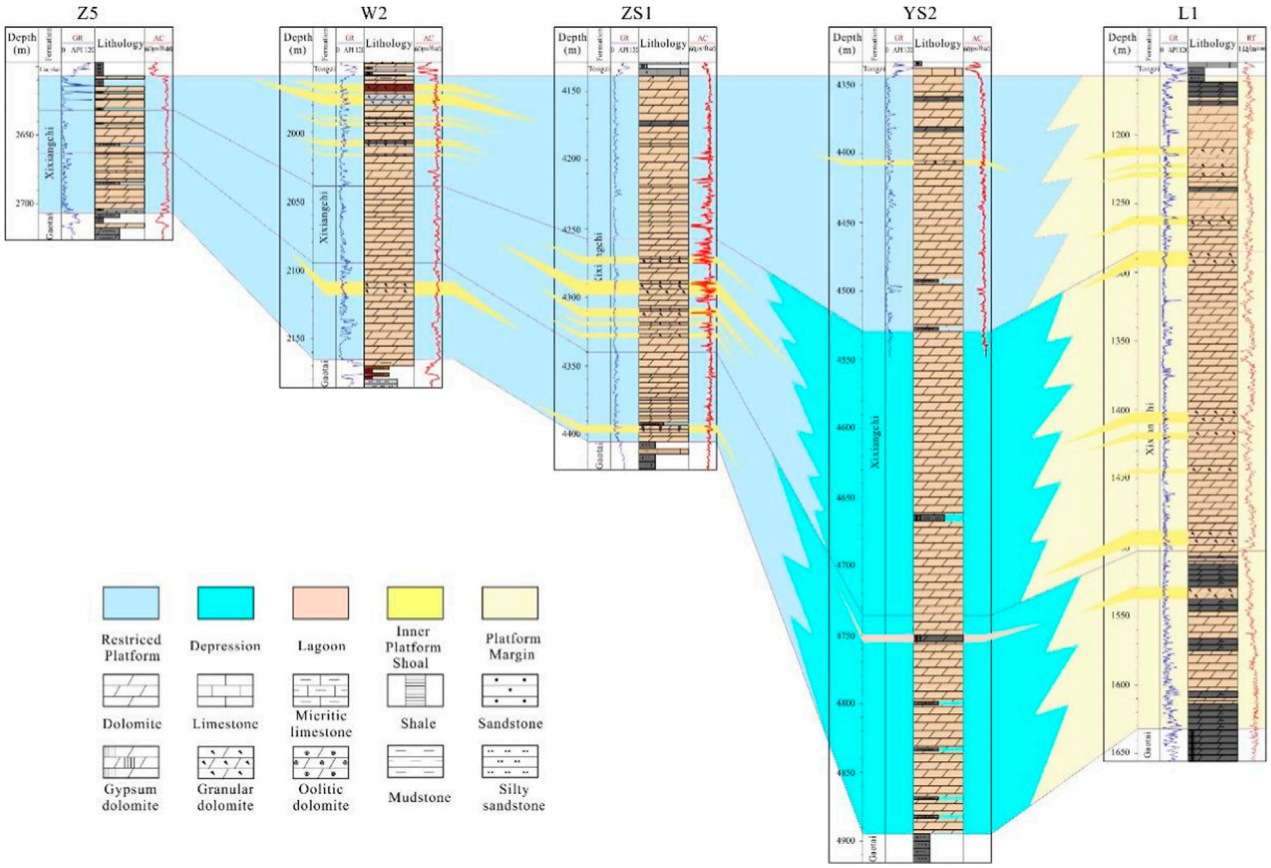

FIGURE 4
The stratigraphic correlation diagram and reservoir distribution of Xixiangchi Formation from well Z5 to well L1.

low porosity and ultralow permeability. The fractures in the core can be divided into two types: high-angle fractures with inclinations of 70°–85° and horizontal fractures with inclinations of less than 5° (Figure 3J). Owing to strong heterogeneity of the dolomite reservoirs, there are multiple gas reservoirs in the Xixiangchi Formation of the Weiyuan Gas Field and their spatial distribution is limited by tight dolomite. Affected by later tectonic movement, the distribution of oil and gas was controlled by both structure and lithology. Structural traps form in the high part of the anticline, and structural-lithological composite traps develop mostly in the structural slope area.

Discussion

Sufficient oil and gas supply is the basis for hydrocarbon accumulation

The distribution of Lower Cambrian high-quality source rocks in the Sichuan Basin is controlled by the distribution of the Deyang–Anyue intracratonic sag. Presently, the Anyue super large gas field has been discovered in the eastern margin of the intracratonic sag (the reservoirs are mainly Dengying and Longwangmiao Formations), and the Weiyuan Gas Field developed on the west side of the intracratonic sag (the reservoirs are mainly Dengying and Xixiangchi Formations). The source rock in the intracratonic sag is a product of an anoxic environment and has high paleo productivity (Yang et al., 2021). The CH_4 content of the Xixiangchi Formation in Weiyuan Gas Field was between 85.4% and 89.4% (Figure 7A), the C_2H_6 content was less than 0.1%, and the dryness coefficient of gas was greater than 99% (Figure 7B).

The hydrocarbon component characteristics of gas (Figures 7C,D) in the Dengying and Xixiangchi Formations of the Weiyuan Gas Field are similar. The gas in the Dengying and Xixiangchi Formation reservoirs mainly originates from the cracked gas of ancient oil reservoirs and the gas generated from the source rocks of the Qiongzhusi Formation (Dai, 2003; Wei et al., 2015; Xu, 2017). Therefore, the gas of Xixiangchi Formation comes from the pyrolysis of crude oil

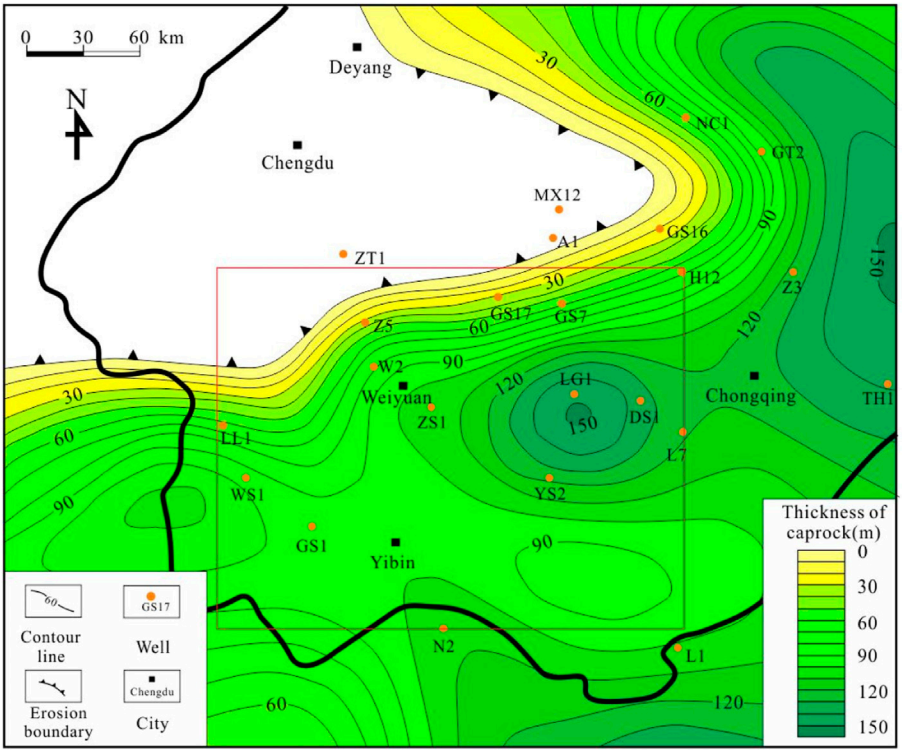

FIGURE 5
The thickness map of the direct caprock of Xixiangchi Formation.

and the cracking of source rock of Qiongzhusi Formation. There is a thick-bedded high-quality source rock of the Qiongzhusi Formation in the southern Sichuan Basin with a small oil and gas migration distance and sufficient oil and gas supply, which is the material basis for hydrocarbon accumulation in the Xixiangchi Formation reservoir.

Taking GS17 Well as an example to conduct a one-dimensional simulation of the Sichuan Basin, Figure 8 shows that the source rocks of the Qiongzhusi Formation entered the oil-generation threshold in the Late Ordovician and began to discharge hydrocarbons. In the Late Silurian, the Caledonian movement led to the overall uplift of the Sichuan Basin, stagnation of sedimentation, strong denudation of the surface, temperature decrease of the source rocks, and sharp weakening of hydrocarbon generation. From the beginning of the Early Permian, the Sichuan Basin began a large-scale transgression, and the entire basin was submerged in water.

With increasing burial depth, the source rocks of the Qiongzhusi Formation entered the hydrocarbon generation peak again from the Late Permian to Late Triassic. Subsequently, from Late Triassic to Middle Jurassic, the value of vitrinite reflectivity (Ro max %) reached 1.3% and began to enter the stage of generating wet gas. Since the Middle Jurassic, the Ro value has reached 2.0%, and since then, it has entered the stage of generating dry gas.

The source rocks of the Qiongzhusi Formation began to discharge hydrocarbons in the Late Ordovician, then reached the oil generation peak from the Late Permian to Late Triassic. Subsequently, began to generate wet gas from Late Triassic to Middle Jurassic. From the Middle Jurassic to present, it is the stage of generating dry gas.

Inherited paleo-uplift controls hydrocarbon accumulation

The study of sedimentary-tectonic evolution history of the Early Paleozoic Sichuan Basin indicates that the Leshan-Longnusi paleo-uplift had taken shape by the end of the Early Cambrian (Su et al., 2015). The deposition of the Xixiangchi Formation in the southern Sichuan area is controlled by Leshan-Longnusi paleo-uplift and its paleogeomorphology, which is dominated by relatively high mixed tidal flat deposition in the Northern part. The water body gradually deepened to the South and transitioned to a clear water carbonate platform deposition (Figure 1B). The greater the thickness of the Xixiangchi Formation, the lower the paleogeomorphology at that time. Water depth controlled the change in the sedimentary facies. The Leshan-Longnusi

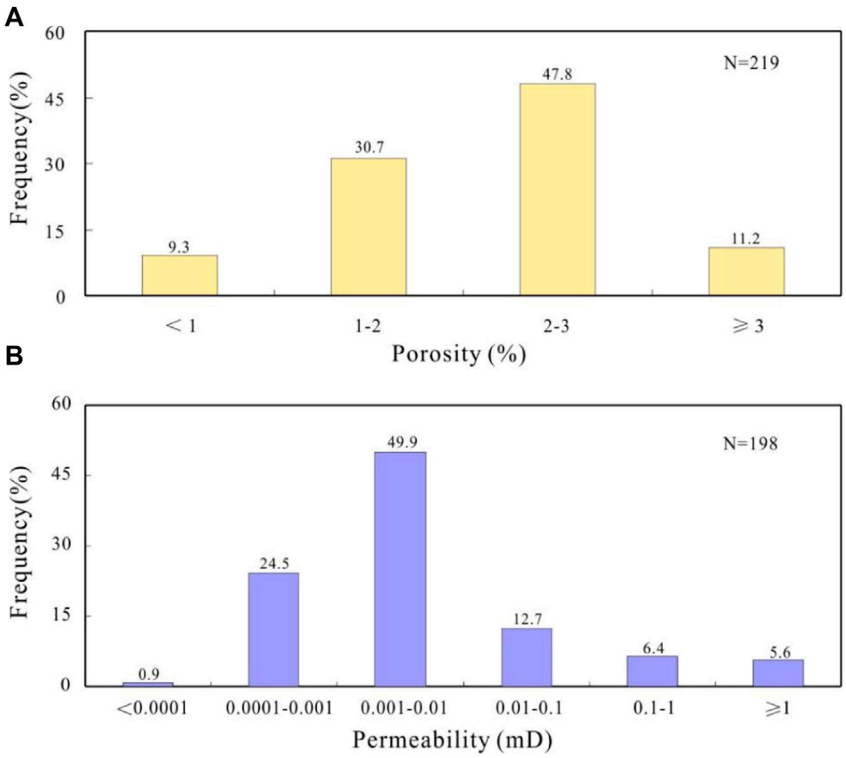

FIGURE 6
Reservoir physical property distribution map of Xixiangchi Formation in southern Sichuan basin. **(A)** Reservoir porosity distribution map of Xixiangchi Formation; **(B)** Reservoir permeability distribution map of Xixiangchi Formation.

paleo-uplift continued to rise during the Cambrian-Silurian (Mei, 2015). At the end of the Silurian, the Caledonian Movement caused the Leshan-Longnusi paleo-uplift to undergo significant indigenous structural deformation. The southwestern part of Sichuan Basin was the core of the Leshan-Longnusi paleo-uplift, and its structural axis was the Ya'an-Ziyang-Suining area, resulting in the denudation and leveling of the Silurian-Cambrian strata in the structural axis. During the Hercynian and Indosinian periods, the paleotectonic pattern maintained the shape of the late Caledonian period, and the Southern Sichuan Basin continued to be located between the high part of the paleo-uplift and the Southern slope of the paleo-uplift. During the Indosinian period, Sichuan Basin entered the development stage of foreland basin, the Eastern part was uplifted, the Western part was subsiding, and the Triassic strata became significantly thinner from West to East, which made the Leshan-Longnusi paleo-uplift tectonic axis move to Southeast. The Himalayan Movement greatly uplifted the Weiyuan structure and became a new tectonic highpoint in the Southern Sichuan Basin.

With the history of tectonic evolution in Southern Sichuan Basin, and through the analysis of the thermal evolution history of source rock of the Qiongzhusi Formation (Figure 8), it is evident that the source rock of the Qiongzhusi Formation entered the hydrocarbon generation window before the formation of the Leshan-Longnusi paleo-uplift in the late Caledonian. Ancient oil reservoirs may be formed on the slope and high part of the paleo-uplift. During the Hercynian-Indosinian period, the tectonic framework of the Leshan-Longnusi paleo-uplift was stable, and the source rock of Qiongzhusi Formation began to generate hydrocarbon, on a large scale, for the second time. Large-scale ancient oil reservoirs were formed in different types of traps in the Ziyang, Anyue, Weiyuan, and Moxi-Gaoshiti areas (both sides of the Deyang-Anyue rift trough), which was specifically manifested as a large amount of residual asphalt in the reservoir pores of the Xianxixiangchi Formation, which is the product of the thermal cracking of ancient oil reservoirs (Lin et al., 2017; Li et al., 2020) (Figure 3H).

Since the Yanshanian period, the source rock of Qiongzhusi Formation had entered the high-temperature gas generation stage with a Ro value greater than 2.0%, and the ancient oil reservoirs of the Dengying, Longwangmiao, and Xixiangchi Formations began to crack into gas (Xu et al., 2014). During

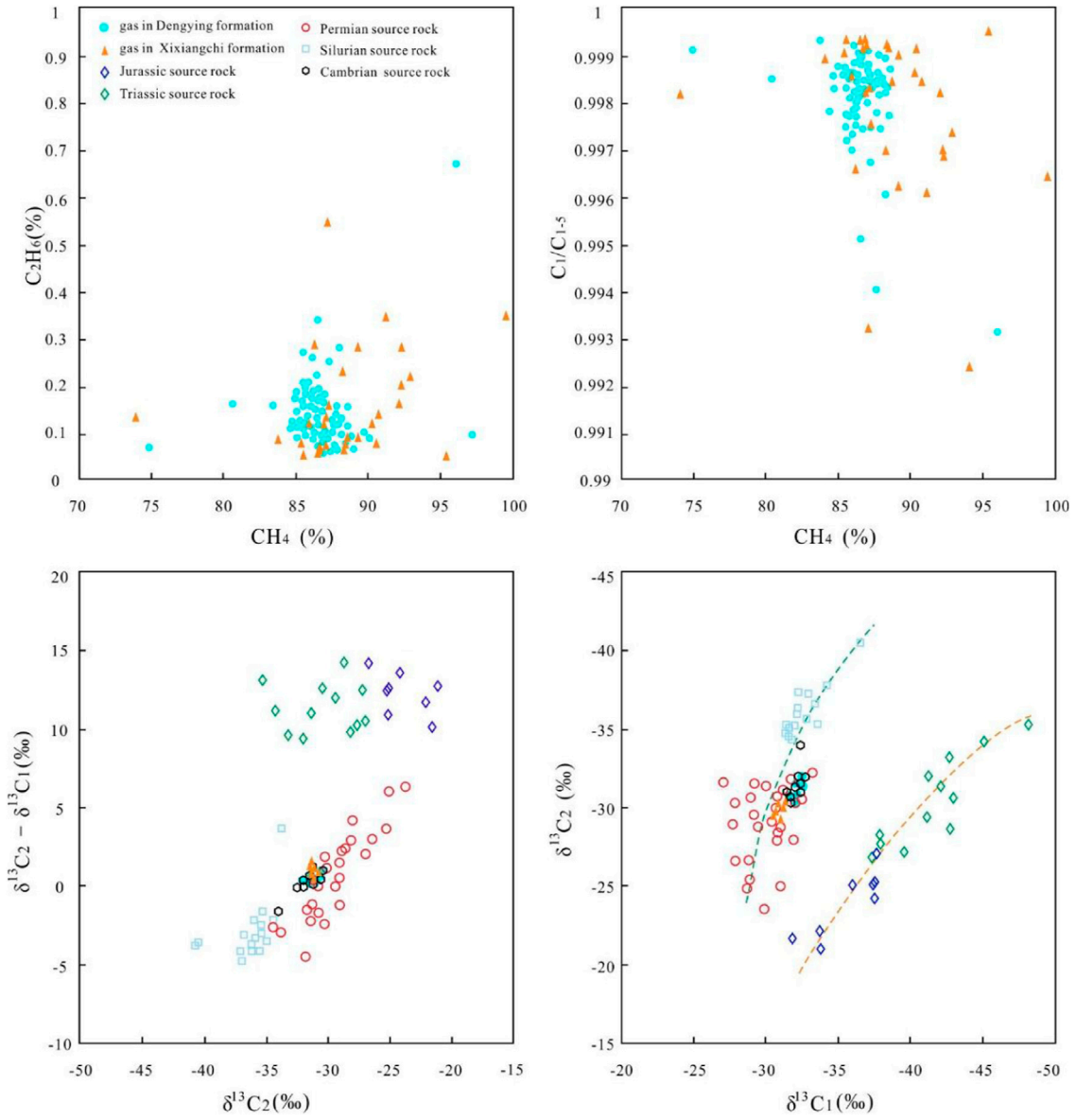

FIGURE 7
Characteristic diagram of natural gas component. **(A)** The relationship between methane content and ethane content; **(B)** The relationship between methane content and drying coefficient; **(C)** Carbon isotopic relationship between ethane and ($\delta^{13}C_2$-$\delta^{13}C_1$); **(D)** Carbon isotopic relationship between methane and ethane.

the Himalayan period, owing to the continuous compression of the Qinghai-Tibet Plateau to the Sichuan Basin, the eastern margin of the Qinghai-Tibet Plateau collided with the western margin of the Sichuan Basin, forming the Longmenshan orogenic belt (He et al., 2011; Yang et al., 2019b). The tectonic stress continued to transfer to the interior of the basin, resulting in the Weiyuan anticline becoming the highest structural point of the Leshan-Longnusi paleo-uplift today. Concurrently, the pyrolysis gas of the ancient oil reservoirs and the high-temperature pyrolysis gas of the Qiongzhusi Formation source rock accumulated near the structural high point and slope of Weiyuan, indicating the complexity of the methane carbon isotope (Xu et al., 2014).

The hydrocarbon fluid migrates from the high potential energy area to the low potential energy area (Allan, 1989). The elevated position around the hydrocarbon depression was the dominant migration direction of the hydrocarbon fluid. The high-energy particle beach facies located in the oil and gas migration path provides a suitable reservoir space for oil and gas accumulation. The oil and gas accumulation of the

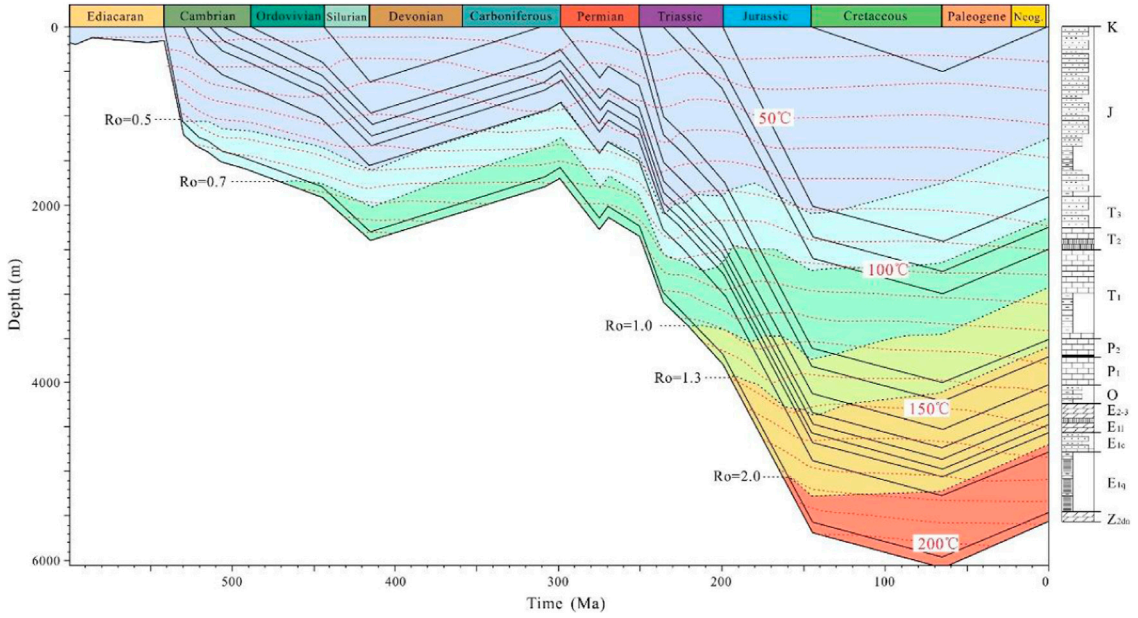

FIGURE 8
Hydrocarbon generation-evolution history of source rocks in Well GS17.

Xixiangchi Formation in the Southern Sichuan area is controlled by sedimentation and structure. Granular dolomite and crystalline dolomite developed in the high-energy facies belt of Xixiangchi Formation located in the high part and slope area of the paleo structure, becoming the most favorable areas for oil and gas accumulation after the transformation of quasi-syngenetic-epigenetic karstification (Lin et al., 2015; Li et al., 2020; Shi et al., 2020). The inherited paleo-uplift provides favorable conditions for oil and gas accumulation and controls the distribution range of oil and gas reservoirs. The accumulation of oil and gas is closely related to the sediment-tectonic evolution of the Sichuan Basin. Many oil and gas reservoirs formed around the Leshan-Longnusi paleo-uplift.

Effective transportation system is a crucial factor in hydrocarbon accumulation

The oil and gas resources in the reservoir pores are movable fluids. The migration and accumulation of oil and gas are controlled by changes in the fluid potential of spaces. The gradient zone and low potential energy area of the fluid potential are the pointing zones for oil and gas migration. Oil and gas migrate from the high-potential-energy area to the low-potential-energy area and accumulate in the low-potential-energy area with suitable preservation conditions (Allan, 1989). However, the existence of a fault system may affect the spatial distribution characteristics of fluid potential. Owing to the fractures formed by tectonic movement, several fractures developed in the rock stratum. In the fault system, owing to a decrease in fluid potential energy, the fluid migrates from the high-potential-energy area to the fault system area, and oil and gas fill the trap along the fracture (Guo et al., 1996; Chen, 2011). Because the fault activity is periodic, the fault system can not only be a favorable channel for vertical large-scale oil and gas migration and accumulation, but also be a crucial factor for the destruction of oil and gas reserve. A fault system is a principal factor in controlling the migration, accumulation, and loss of oil and gas.

Based on the analysis of contiguous 3D seismic data and the distribution position of drilling reservoirs in the Weiyuan area, the seismic coaxial energy was weakened, and the low-frequency signal was enhanced when the reservoirs of the Xixiangchi Formation were developed. Therefore, the amplitude and frequency attribute data can be fused to obtain a new attribute distribution map of the Xixiangchi Formation, which can be used to qualitatively describe the distribution characteristics of the reservoir in the plane of the Xixiangchi Formation (Figure 9). The yellow to red areas represent the reservoir development areas, and the green to blue areas represent the undeveloped areas. Simultaneously, the ant property can clearly and effectively depict the spatial distribution of the formation fault system. Through the analysis of ant properties at the bottom boundary of the Xixiangchi Formation in the Weiyuan area, is evident that several fractures developed in the Xixiangchi Formation in the

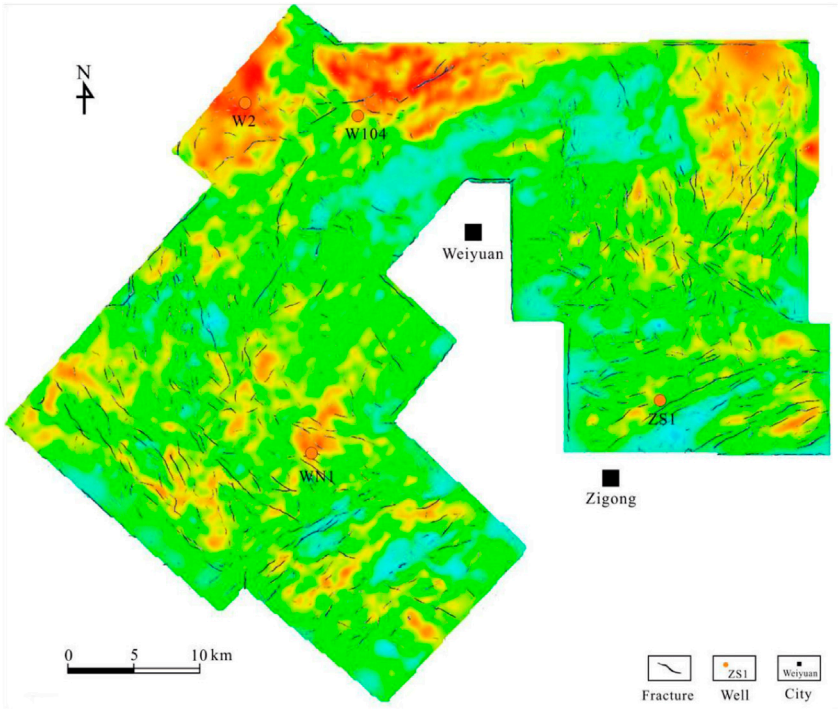

FIGURE 9
Distribution map of superimposed fractures in Xixiangchi Formation in Weiyuan area.

Weiyuan area, and the directions of the fractures are controlled by ground stress, mainly in the NE–SW, near S–N, and NW–SE directions. Many developed fractures are effective transportation systems and are also necessary conditions for oil and gas to migrate from source areas to traps.

The yellow to red areas represent the reservoir development areas, the green to blue areas represent the undeveloped areas, and the dark areas represent fractures.

Favorable reservoir forming combination is the key factor for hydrocarbon accumulation

Under the transformation of karstification and tectonization, dissolution pores and cracks developed in the granular and grain dolomite of the Xixiangchi Formation in the southern Sichuan Basin. The reservoirs were superimposed vertically, but the thickness of a single reservoir was low. The gas source of the Xixiangchi Formation originates from the source rocks of the underlying Qiongzhusi and Maidiping Formations and the cracked gas formed by the cracking of ancient oil reservoirs. During the deposition of the overlying Tongzi, Honghuayuan, and Meitan Formations, the water energy was low, and the sediment grain size was fine. In particular, the pores of the mudstone caprock in the Meitan Formation were not developed, and the sealing ability was strong. This thick mudstone is a regional caprock (Li et al., 2015).

The high-quality reservoirs developed in the restricted platform granular beach of the Xixiangchi Formation in the southern Sichuan Basin are distributed mainly in the Southern part of the Deyang-Anyue rift trough, which is a thick layer area of high-quality source rocks of the Lower Cambrian. According to the analysis results of hydrocarbon generation and evolutionary history of the Qiongzhusi Formation source rock (Figure 8), the Late Caledonian, Indosinian, and Yanshanian periods were the peak periods of hydrocarbon generation and expulsion. The high-quality reservoirs in the Xixiangchi Formation are connected to the Lower Cambrian source rock in the rift trough through the fault system, forming the source-reservoir configuration relationship of the lower generation and upper storage. Short-distance migration of oil and gas is beneficial for the formation of oil and gas reservoirs. The high-quality reservoir had the characteristics of near-source accumulation (Figure 10).

The dolomite reservoir of the grain beach in the Xixiangchi Formation is in the paleo-uplift slope area at an elevated position

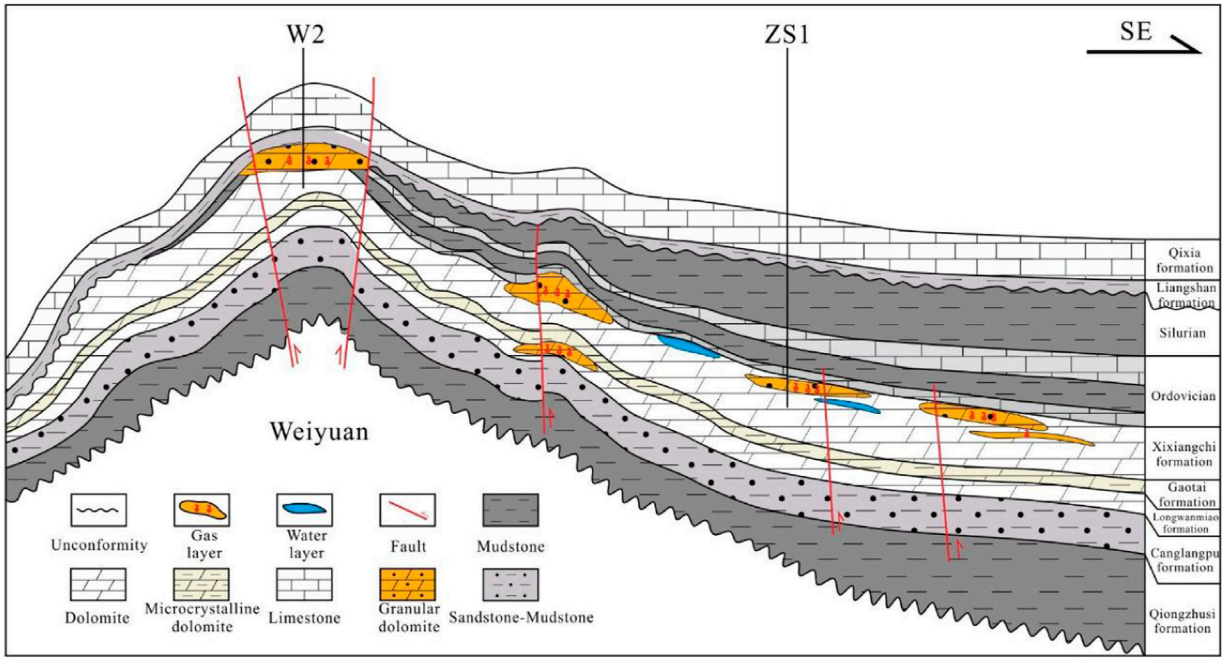

FIGURE 10
Hydrocarbon accumulation pattern in Xixiangchi Formation (Southern Sichuan Basin).

around the hydrocarbon generation depression. The high-quality reservoirs in the Xixiangchi Formation are connected to the Lower Cambrian source rock in the rift trough through the fault system, forming a source-reservoir configuration relationship between the lower generation and upper storage.

Because of the small single-layer thickness and small lateral extension distance of the reservoirs, the reservoir is quite heterogeneous. Oil and gas accumulation is controlled by lithological changes under the structural background. In addition to the structural traps in the Weiyuan area, the trap types in the Southern Sichuan area are mainly structural-lithologic traps. Late Yanshanian-Himalayan tectonic activity was strong, resulting in strong uplift of the basin margin and the formation of Weiyuan and Luzhou-Kaijiang paleo-uplifts and high-steep structural belt in Eastern Sichuan. According to the analysis results of the formation water of the Xixiangchi Formation in southern Sichuan Basin, the formation water type is calcium chloride, which indicates that the gas reservoirs of the Xixiangchi Formation have suitable preservation conditions.

From the analysis of the main controlling factors of hydrocarbon accumulation, the regional distribution of high-quality source rocks, near-source high-quality reservoirs, and inherited structural uplift are the most favorable areas for the distribution of oil and gas fields. Combined with the source rock, reservoirs, caprock, structures, faults, preservation conditions, and other factors, it is evident that the oil and gas sources of the Xixiangchi Formation in the Southern Sichuan area are sufficient. High-quality fractured vuggy reservoirs developed, and the sealing ability of the upper cover layer was strong. Tectonism plays a positive role in the formation of traps, and the fault system communicates with the source and storage space. The fractures improved the physical properties of the reservoirs, and the preservation conditions were good in the later period. Therefore, the area where shoal reservoirs and fractures developed in the ancient uplift slope is the next key exploration area in the Xixiangchi Formation.

Conclusion

1) The thick-bedded source rock of the Qiongzhusi Formation entered the oil-generation threshold during the Late Ordovician, when it began to discharge hydrocarbons. In the Late Silurian, the hydrocarbon generation effect weakened significantly. From the Early Permian to the Late Triassic, the source rock entered the peak of hydrocarbon generation again. Since the Middle Jurassic, the source rock has entered the stage of large-scale dry gas generation, resulting in the overlying Xixiangchi Formation dolomite reservoir having a sufficient gas supply.
2) The dolomite reservoir of the Xixiangchi Formation developed many dissolved pores and fractures, which were affected by karst

and structural transformation. The underlying source rock of the Qiongzhusi Formation provides sufficient gas. Under the high sealing performance of the Upper Ordovician strata, the Xixiangchi Formation had ideal reservoir-forming conditions.

3) Hydrocarbon accumulation in the Xixiangchi Formation is closely related to the sedimentary-tectonic evolution of the Sichuan Basin. The inherited paleo-uplift provides favorable conditions for hydrocarbon accumulation and controls the distribution range of gas reservoirs. The dolomite reservoir of the grain beach in the Xixiangchi Formation is in the paleo-uplift slope area at an elevated position around the hydrocarbon generation depression. The fault system connects the reservoirs and source rock, forming a source–reservoir configuration relationship between the lower generation and upper storage. Short-distance migration of oil and gas is beneficial for the formation of oil and gas reservoirs. Therefore, further exploration should focus on the paleo-uplift slope.

Data availability statement

The data analyzed in this study is subject to the following licenses/restrictions: The original contributions presented in the study are included in the article/Supplementary Material, further inquiries can be directed to the corresponding author. Requests to access these datasets should be directed to huxiuquan15@cdut.edu.cn.

Author contributions

XH: conceptualization, funding acquisition, methodology, Writing-original draft. WL: Conceptualization, methodology. DZ: Formal analysis, methodology, Writing-original draft. WW: Formal analysis, methodology, Writing-review and editing. CY: Formal analysis, investigation. JL: Investigation, writing—review, and editing.

Funding

This study was financially supported by the National Natural Science Foundation of China (Grant No. 42172175).

Acknowledgments

We would like to thank PetroChina Southwest Oil and Gas Field Company for providing the data and allowing the publication of this article.

Conflict of interest

The author WW was employed by PetroChina Southwest Oil and Gas Field Company.

The remaining authors declare that the research was conducted in the absence of any commercial or financial relationships that could be construed as a potential conflict of interest.

Publisher's note

References

Allan, U. S. (1989). Model for hydrocarbon migration and entrapment within faulted structures. *Am. Assoc. Pet. Geol. Bull.* 73 (7), 803–811. doi:10.1306/44b4a271-170a-11d7-8645000102c1865d

Chen, M. M. (2011). *The relationship between wubao fault zone in gaoyou depression and hydrocarbon A ccumulation*. Beijing, China: China University of Petroleum. [in Chinese].

Dai, J. X. (2003). Pool-forming periods and gas Sources of Weiyuan gasfield. *Petroleum Geol. Exp.* 25 (5), 473–480. [in Chinese]. doi:10.3969/j.issn.1001-6112.2003.05.010

Du, J. H., Zhou, C. N., Xu, C. C., He, H. Q., Shen, P., Yang, Y. M., et al. (2014). Theoretical and technical innovations in strategic discovery of a giant gas field in Cambrian Longwangmiao Formation of central Sichuan paleouplift, Sichuan Basin. *Petroleum Explor. Dev.* 41 (3), 294–305. doi:10.1016/s1876-3804(14)60035-5

Dutton, S. P., Kim, E. M., Broadhead, R. F., Raatz, W. D., Breton, C. L., Ruppel, S. C., et al. (2005). Play analysis and leading-edge oil-reservoir development methods in the Permian basin: Increased recovery through advanced technologies. *Am. Assoc. Pet. Geol. Bull.* 89 (5), 553–576. doi:10.1306/12070404093

Feng, Z. Z., Peng, Y. M., Jin, Z. K., Jiang, P. L., Bao, Z. D., Luo, Z., et al. (2001). Lithofacies palaeogeography of the cambrian in south China. *J. Palaeogeogr.* 3 (1), 1–14+98. 101[in Chinese]. doi:10.7605/gdlxb.2001.01.001

Gu, M. F., Li, W. Z., Zhou, Q., Zhou, G., Zhang, J. Y., Lv, X. J., et al. (2020). Lithofacies palaeogeography and reservoir characteristics of the cambrian xixiangchi formation in Sichuan basin. *Mar. Orig. Pet. Geol.* 25 (02), 162–170. [in Chinese].

Guo, Z. Q., Xiao, D. M., and Tang, J. S. (1996). Function of discordogenic faults during forming of hydrocarbon pools. *Acta Pet. Sin.* (3), 27–32. [in Chinese]. doi:10.3321/j.issn:0253-2697.1996.03.004

He, D. F., Li, D. S., Zhang, G. W., Zhao, L. Z., Fan, C., Lu, R. Q., et al. (2011). Formation and evolution of multi-cycle superposed Sichuan Basin, China. *Chin. J. Geol.* 46 (03), 589–606. [in Chinese]. doi:10.3969/j.issn.0563-5020.2011.03.001

Jia, P., Huang, F. X., Lin, S. G., Song, T., Gao, Y., Lv, W. N., et al. (2021). Sedimentary facies and sedimentary model of middle upper Cambrian Xixiangchi group in Sichuan Basin and its adjacent areas. *Geoscience* 35 (03), 807–818. [in Chinese]. doi:10.19657/j.geoscience.1000-8527.2021.026

Jiang, W. J., Hou, M. C., Xing, F. C., Li, Y., Shi, X., and Wang, C. (2016). Characteristics and main controlling factors of dolomite reservoirs of CambrianLoushanguan Group in the southeastern Sichuan Basin. *Lithol. Reserv.* 28 (05), 44–51. [in Chinese]. doi:10.3969/j.issn.1673-8926.2016.05.005

Li, H. (2022). Research progress on evaluation methods and factors influencing shale brittleness: A review. *Energy Rep.* 8, 4344–4358. doi:10.1016/j.egyr.2022.03.120

Li, H., Tang, H. M., Qin, Q. R., Zhou, J. L., Qin, Z. J., Fan, C. H., et al. (2019b). Characteristics, formation periods and genetic mechanisms of tectonic fractures in the tight gas sandstones reservoir: A case study of xujiahe Formation in YB area, Sichuan basin, China. *J. Pet. Sci. Eng.* 178, 723–735. doi:10.1016/j.petrol.2019.04.007

Li, H., Zhou, J. L., Mou, X. Y., Guo, H. X., Wang, X. X., An, H. Y., et al. (2022b). Pore structure and fractal characteristics of the marine shale of the longmaxi Formation in the changning area, southern Sichuan basin, China. *Front. Earth Sci. (Lausanne).* 10, 1018274. doi:10.3389/feart.2022.1018274

Li, J., He, D. F., and Mei, Q. H. (2015). Tectonic-depositional environment and proto-type basins evolution of the Ordovician in Sichuan Basin and adjacent areas. *Acta Pet. Sin.* 36 (04), 427–445. [in Chinese]. doi:10.7623/syxb201504004

Li, J., Li, H., Yang, C., Wu, Y. J., Gao, Z., and Jiang, S. L. (2022a). *Geological characteristics and controlling factors of deep shale gas enrichment of the Wufeng-Longmaxi Formation in the southern Sichuan Basin*. China: Lithosphere, 4737801. doi:10.2113/1970/4737801

Li, W., Fan, R., Jia, P., Lu, Y. Z., Zhang, Z. J., Li, X., et al. (2019a). Sequence stratigraphy and lithofacies paleogeography of the middle–upper cambrian Xixiangchi group in the Sichuan basin and its adjacent area, SW China. *Petroleum Explor. Dev.* 46 (02), 238–252. doi:10.1016/S1876-3804(19)60005-4

Li, W., Jia, P., Fan, R., Lu, Y. Z., Li, X., and Deng, S. H. (2017). Carbon isotope characteristics of the Middle-Upper Cambrian Xixiangchi Group and bottom boundary marks of Furong series in Sichuan Basin and its adjacent areas. *Nat. Gas. Ind.* 37 (10), 1–10. [in Chinese]. doi:10.3787/j.issn.1000-0976.2017.10.001

Li, W. Z., Wen, L., Gu, M. F., Xia, M. L., Xie, W. R., Fu, X. D., et al. (2020). Development models of Xixiangchi Formation karst reservoirs in the Late Caledonian in the central Sichuan Basin and its oil-gas exploration implication. *Nat. Gas. Ind.* 40 (9), 30–38. [in Chinese]. doi:10.3787/j.issn.1000-0976.2020.09.004

Li, W. Z., Zhang, J. Y., Hao, Y., Ni, C., Tian, H., Zeng, Y. Y., et al. (2019c). Characteristics of carbon and oxygen isotopic, paleoceanographic environment and their relationship with reservoirs of the Xixiangchi Formation, southeastern Sichuan Basin. *Acta Geol. sin.* 93 (2), 487–500. [in Chinese]. doi:10.3969/j.issn.0001-5717.2019.02.015

Lin, Y., Chen, C., Shan, S. J., Zeng, Y. Y., Liu, X., and Chen, Y. L. (2017). Reservoir characteristics and main controlling factors of the cambrian xixiangchi formation in Sichuan basin. *Petroleum Geol. Exp.* 39 (5), 610–617. [in Chinese]. doi:10.11781/sysydz201705610

Lin, Y., Zhong, B., Chen, C., Zeng, Y. Y., Chen, Y. L., and Bao, Z. F. (2020). Geological characteristics and controlling factors of gas accumulation of Xixiangchi Formation in central Sichuan Basin, China. *J. Chengdu Univ. Technol. Technol. Ed.* 47 (02), 150–158. [in Chinese]. doi:10.3969/j.issn.1671-9727.2020.02.03

Liu, S. G., Deng, B., Li, Z. W., and Sun, W. (2011). The texture of Sedimentary Basin-orogenic belt system and its influence on oil/gas distribution: A case study from Sichuan Basin. *Acta Petrol. Sin.* 27 (03), 621–635. [in Chinese].

Liu, X., Zeng, Y. Y., Wen, L., Lin, Y., Chen, Y., Chen, W., et al. (2018). Distribution prediction on favorable sedimentary-facies belts of Xixiangchi Formation, central Sichuan Basin. *Nat. Gas Explor. Dev.* 41 (02), 15–21. [in Chinese].

Luo, W., Liu, C. Y., Zhang, D. D., Wang, J. Q., Niu, H. Q., and Guo, P. (2016). Geochemistry characteristics of the middle jurassic zhiluo Formation in helan mountain-liupan mountain area and their geological significances. *J. Palaeogeogr.* 18 (6), 1030–1043. [in Chinese].

Luo, W., Shi, Z. J., Tian, Y., and Hu, X. (2022). Characteristics and forming processes of reef-shoal reservoir in changhsing formation of the eastern Sichuan basin in dianjiang, China. *Arab. J. Sci. Eng.* 47, 725–737. doi:10.1007/s13369-021-05863-6

Ma, F., Yang, L. M., Gu, J. Y., Chen, X., Zhao, Z., Jin, Y. N., et al. (2011). The summary on exploration of the dolomite oilfields in the world. *Acta Sedimentol. Sin.* 29 (05), 1010–1021. Available at: https://doi.10.14027/j.cnki.cjxb.2011.05.014.

Manche, C. J., and Kaczmarek, S. E. (2019). Evaluating reflux dolomitization using a novel high-resolution record of dolomite stoichiometry: A case study from the cretaceous of central Texas, USA. *Geology* 47 (6), 586–590. doi:10.1130/G46218.1

Mei, Q. H. (2015). *Tectonic evolution and formation mechanism of leshan-longnusi paleo-uplift, Sichuan basin*. Beijing, China: China University of Geosciences. (Beijing) [in Chinese].

Ning, M., Lang, X. G., Huang, K. J., Li, C., Huang, T. Z., Yuan, H. L., et al. (2020). Towards understanding the origin of massive dolostones. *Earth Planet. Sci. Lett.* 545, 116403. doi:10.1016/j.epsl.2020.116403

Pang, Y. J., Dai, Z. Y., Liu, S. H., Peng, C. Y., and Feng, R. W. (2007). Restoration method of Ordovician weathering crust paleo-geomorphology of Leshan-Longnv temple paleohigh and its features in central Sichuan. *Petroleum Geol. Eng.* (05), 8–10+15+11. [in Chinese]. doi:10.3969/j.issn.1673-8217.2007.05.003

Rashid, F., Glover, P., Lorincz, P. I., Hussein, D., and Lawrence, J. (2017). Microstructural controls on reservoir quality in tight oil carbonate reservoir rocks. *J. Petroleum Sci. Eng.* 156, 814–826. doi:10.1016/j.petrol.2017.06.056

Saller, A. H., and Henderson, N. (1998). Distribution of porosity and permeability in platform dolomites: Insight from the Permian of west Texas. *AAPG Bull.* 82 (8), 1528–1550. doi:10.1306/1D9BCB01-172D-11D7-8645000102C1865D

Shen, C. B., Mei, L. F., Xu, Z. P., and Tang, J. G. (2007). Architecture and tectonic evolution of composite basin-mountain system in sichuan basin and its adjacent areas. *Geotect. Metallogenia* (03), 288–299. [in Chinese]. doi:10.16539/j.ddgzyckx.2007.03.002

Shi, C. H., Cao, J., Tan, X. C., Luo, B., Zeng, W., Hong, H. T., et al. (2018). Hydrocarbon generation capability of Sinian-Lower Cambrian shale, mudstone, and carbonate rocks in the Sichuan Basin, southwestern China: Implications for contributions to the giant Sinian Dengying natural gas accumulation. *Am. Assoc. Pet. Geol. Bull.* 102 (5), 817–853. doi:10.1306/0711171417417019

Shi, S. Y., Wang, T. S., Liu, W., Jiang, H., Li, Q. F., Liu, X., et al. (2020). Reservoir characteristic and gas exploration potential in cambrian xixiangchi formation of Sichuan basin. *Nat. Gas. Geosci.* 31 (06), 773–785. [in Chinese].

Su, G. P., Li, Z. Q., Ying, D. L., Li, G., Ying, W. F., Yang, Y. Y., et al. (2020). Formation and evolution of the Caledonian paleo-uplift and its genetic mechanism in Sichuan Basin. *Acta Geol. Sin.* 94 (06), 1793–1812. [in Chinese]. doi:10.19762/j.cnki.dizhixuebao.2020080

Tian, X. W., Zhang, X. H., Peng, H. L., Ma, K., Yang, D. L., and Sun, Y. T. (2019). Productivity differences of gas reservoirs in the fourth member of EdiacaranDengying Formation in GaoshitiMoxi area, central Sichuan basin. *XinJiang Pet. Geol.* 40 (6), 673–679. [in Chinese].

Wei, G. Q., Chen, G. S., Du, S. M., Zhang, L., and Yang, W. (2008). Petroleum systems of the oldest gas field in China: Neoproterozoic gas pools in the Weiyuan gas field, Sichuan Basin. *Mar. Petroleum Geol.* 25 (4-5), 371–386. [in Chinese]. doi:10.1016/j.marpetgeo.2008.01.009

Wei, G. Q., Du, J. H., Xu, C. C., Zhou, C. N., Yang, W., Shen, P., et al. (2015). Characteristics and accumulation modes of large gas reservoirs in Sinian-Cambrian of Gaoshiti-Moxi region, Sichuan Basin. *Acta Pet. Sin.* 36 (01), 1–12. [in Chinese]. doi:10.7623/syxb201501001

Xiong, L., Ge, Z. W., Wang, T., Wen, Z. T., Zhong, W. J., Zhou, Y., et al. (2021). Exploration potential of cambrian Qiongzhusi Formation in southern Sichuan basin. *Reserv. Eval. Dev.* 11 (01), 14–21+55. [in Chinese]. doi:10.13809/j.cnki.cn32-1825/te.2021.01.003

Xu, C. C., Shen, P., Yang, Y. M., Luo, B., Huang, J. Z., Jiang, X. F., et al. (2014). Accumulation conditions and enrichment patterns of natural gas in the lower cambrian Longwangmiao Fm reservoirs of the leshan-longnüsi paleohigh, Sichuan basin. *Nat. Gas. Ind.* 34 (3), 1–7. [in Chinese]. doi:10.3787/j.issn.1000-0976.2014.03.001

Xu, F. H. (2017). *Fluid system and hydrocarbon accumulation of EdiacaranDengying Formation and cambrian Longw angmiao Formation in central sichuan*. Chengdu, China: Chengdu University of Technology. [in Chinese].

Yang, X. F., Huang, Z. S., Wang, X. Z., Wang, Y. P., Li, K., and Zeng, D. M. (2019a). Origin of crystal dolomite and its reservoir formation mechanism in the xixiangchi formation, upper cambrian in southeastern Sichuan Basin. *Carbonates Evaporites* 34, 1537–1549. doi:10.1007/s13146-019-00499-y

Yang, Y., Luo, B., Zhang, B. J., Xiao, D., Xiao, W. Y., and Cao, J. (2021a). Differential mechanisms of organic matter accumulation of source rocks in the Lower Cambrian Qiongzhusi Formation and implications for gas exploration fields in Sichuan Basin. *Petroleum Geol. Exp.* 43 (4), 611–619. [in Chinese]. doi:10.11781/sysydz202104611

Yang, Y. M., Wang, W. Z., Wen, L., Luo, B., Zhang, X., Chen, X., et al. (2021b). Sedimentary evolution characteristics and large-scale natural gas accumulation pattern of microbial carbonate in the slope area of major paleouplift, Sichuan Basin. *Nat. Gas. Ind.* 41 (03), 38–47. [in Chinese]. doi:10.3787/j.issn.1000-0976.2021.03.005

Yang, Y. M., Yang, Y., Yang, G., Song, J. R., Wen, L., Deng, C. G., et al. (2019b). Gas accumulation conditions and key exploration & development technologies of Ediacaranand Cambrian gas reservoirs in Anyue gas field. *Acta Pet. Sin.* 40 (04), 493–508. [in Chinese]. doi:10.7623/syxb201904011

Zhang, K., Song, Y., Jiang, Z. X., Xu, D. S., Li, L. T., Yuan, X. J., et al. (2022). Quantitative comparison of Genesis and pore structure characteristics of siliceous minerals in marine shale with different TOC contents - a case study on the shale of Lower Silurian Longmaxi Formation in Sichuan Basin, Southern China. *Front. Earth Sci. (Lausanne).* 10, 887160. doi:10.3389/feart.2022.887160

Zhang, Y. Q., Dong, S. W., Li, J. H., and Shi, W. (2011). Mesozoic multi-directional compressional tectonics and formation-reformation of Sichuan basin. *Geol. China* 38 (02), 233–250. [in Chinese]. doi:10.3969/j.issn.1000-3657.2011.02.001

Zhao, A. W. (2015). *Study on lithofacies and palaeogeography in the cambrian Xixiangchi group of Sichuan basin and its adjacent areas*. Chengdu: Southwest Petroleum University. [in Chinese].

frontiers | Frontiers in Earth Science

TYPE Original Research
PUBLISHED 05 January 2023
DOI 10.3389/feart.2022.1016973

OPEN ACCESS

EDITED BY
Shuai Yin,
Xi'an Shiyou University, China

REVIEWED BY
Bingshan Ma,
Southwest Petroleum University, China
Ronghu Zhang,
PetroChina Hangzhou Research Institute of Geology, China

*CORRESPONDENCE
Shangfeng Zhang,
jpuzhangsf@163.com

SPECIALTY SECTION
This article was submitted to Structural Geology and Tectonics, a section of the journal Frontiers in Earth Science

RECEIVED 11 August 2022
ACCEPTED 15 September 2022
PUBLISHED 05 January 2023

CITATION
Yang H, Zhang S, Su A, Guan D, Wang Y and Su W (2023), Alternating acid and alkaline diagenesis in the Shahejie Formation of E12 structure in the Laizhou Bay Sag, Bohai Bay Basin. *Front. Earth Sci.* 10:1016973. doi: 10.3389/feart.2022.1016973

Alternating acid and alkaline diagenesis in the Shahejie Formation of E12 structure in the Laizhou Bay Sag, Bohai Bay Basin

Haifeng Yang[1], Shangfeng Zhang[2]*, Ao Su[2], Dayong Guan[1], Yaning Wang[2] and Wen Su[1]

[1]Tianjin Branch of CNOOC (China), Tianjin, China, [2]School of Geosciences, Yangtze University, Wuhan, China

The high-quality reservoirs in the Shahejie Formation of the Laizhou Bay Sag, Bohai Bay Basin, Eastern China formed in the Paleogene saline lacustrine environment and show complex diagenetic evolutionary processes caused by alternating acid and alkaline fluids. Through observations under an optical microscope and a scanning electron microscope, casting thin sections, and plane porosity measurements, this study investigated the diagenesis differences in the third member of the Shahejie Formation (Es_3 Member) in the root and central portions of a fan delta in the E12 structure in the eastern Laizhou Bay Sag, respectively. The Es_3 reservoirs in the well A-1 which have no any hydrocarbon shows, are relatively tight, and have high argillaceous content, poor particle sorting, strong mechanical compaction, and intense carbonate cementation due to long-term activities of alkaline fluids. Moreover, they were not altered by organic acid due to the far lateral distance from source rocks. By contrast, the Es_3 reservoirs in the well A-2 with hydrocarbon accumulations, contain an anomalously high porosity zone due to the superimposition of five episodes of alternate acid-alkaline fluids. The diagenetic fluids controlling the formation of the high-quality Es_3 reservoirs are sourced from connate saline pore waters, gypsum dehydration, salt diapir, and organic acid. Moreover, chlorite coats in the reservoirs in the well A-2 inhibit secondary overgrowth of quartz and, thus, protect primary pores. The chlorite coats and alkaline-acid dissolution alterations are critical to the formation of the high-quality reservoirs in well A-2.

KEYWORDS

acid-alkaline alternation, diagenetic fluids, chlorite coat, Laizhou Bay Sag, high quality reservoir

Introduction

Secondary pores by diagenesis are crucial to the formation of moderate to deep high-quality reservoirs in sedimentary basins (Bloch et al., 2002). As revealed by many cases, anomalously high porosity zones that deviate from normal compaction trend are frequently visible at one or more depth intervals from the profiles of depth vs porosity of many oilfields (Volkmar and Mc Donald, 1979; Su et al., 2018a; Vafaie et al., 2021). In addition to disequilibrium compaction, secondary dissolution can create a large amount of extra reservoir space, and the resultant high-quality reservoirs are of great practical significance for predicting favorable hydrocarbon accumulation areas (Katz et al., 2021; Jiang et al., 2022; Wang et al., 2022). Numerous previous studies indicated that a number of fluids in sedimentary basins, including organic carboxylic acid and CO_2 released from the thermal evolution of organic matter (Surdam et al., 1984), basinal hot fluids (Anna et al., 2009; Su et al., 2021a), meteoric freshwaters infiltrating downward (Ehrenberg, 1993), and deep mantle-derived CO_2 (Su et al., 2018b), can cause reservoir dissolution.

In recent years, sec1osited in saline lacustrine settings (Su et al., 2021b), such as the Shahejie Formation in the Dongying Depression of the Bohai Bay Basin—a rifted lacustrine basin in eastern China (Wang et al., 2013; Li, 2017; Meng et al., 2017). Alkaline lakes were formed by the gradual salinization of lake water due to a semi-arid to arid climate, whose salt sources may originate from transgressions, an input of weathered ancient evaporites around lacustrine basins, or deep geothermal brine activities during basin rifting (Yuan et al., 2005). At present, the formation and controlling factors of favorable reservoirs in initially alkaline lacustrine sediments are not yet fully understood. In particular, the diagenetic fluids continuously change during fluid evolution, which creates a main challenge and area of focus to understand the control of high-quality reservoirs by an alternating acid and alkaline diagenetic environments.

Two wells have recently been drilled in the E12 structure in the Laizhou Bay Sag, which has a similar geological setting to the Dongying Depression. The two wells lie in the root and central portions of a fan delta in the Shahejie Formation. However, well testing has shown that they have significantly varying volumes of hydrocarbon accumulations. The previous study revealed that the differential hydrocarbon accumulation may be caused by the quality of reservoirs. Therefore, we collected cores from the Shahejie reservoirs in the two wells in the E12 structure, and systematically compared and analyzed reservoir diagenesis through microscopic observations. The main purpose is to explore the formation of high-quality reservoirs under the control of the diagenetic fluid evolution in a saline lacustrine basin and, thus, to provide a reference for the prediction of excellent reservoirs in other analogous petroliferous basins.

Geological setting

The Laizhou Bay Sag is located in the southern portion of the Meso-Cenozoic Bohai Bay Basin (in eastern China) with abundant petroleum resources. This area borders the Laibei uplift in the north and the Weibei uplift in the south and is bounded by the large-scale Tanlu strike-slip fault zones in the east, covering an area of approximately 1,780 km^2 and appearing as a rhomboid. As a Cenozoic half-graben developing above the Mesozoic basement, the Laizhou Bay Sag is a dustpan-shaped sag that is faulted in the south and is overlapped in the north and contains a central uplift zone and three sub-sags in the northeast, north, and south (Xue et al., 2022; Figure 1A).

Tectonically, the Laizhou Bay Sag was formed by the comprehensive action of the individual and locally superimposed extensional and strike-slip stresses. Normal faults primarily developed in the sag during the early-middle rifting stages (Yang et al., 2021), while strike-slip faults dominated in the sag during the late rifting. The Cenozoic strata deposited in the sag include the Paleocene Kongdian Formation, the Shahejie Formation, the Oligocene Dongying Formation, the Neogene Guantao and Minghuazhen formations, and the Quaternary Pingyuan Formation (Niu et al., 2022). Among them, the Eocene Shahejie Formation contains the most important reservoir and source rock intervals of the Laizhou Bay Sag (Yang et al., 2021). The fourth member of the Shahejie Formation (the Es_4 Member) was deposited in an arid to semi-arid climate. Meanwhile, medium-low water level saline lakes developed in this member, wherein large amounts of anhydrite and gypsum-bearing mudstones were deposited (Chen et al., 2019). The Es_3 Member was mainly deposited in a transitioning climate from relatively arid to humid. During the deposition of Es_3 Member, the water level of the Bohai Bay Basin increased, and the lake water gradually became less saline with an increase in the injected fresh water. As a result, dark mudstones were deposited in the deep lacustrine environment, and large-scale fan deltas and turbidite fan sedimentary systems developed at the margin of the Laizhou Bay Sag. During the deposition of the Neogene Guantao and Minghuazhen formations, salt arches formed in the Laizhou Bay Sag under the influence of the Tanlu strike-slip fault activity (Figure 1B). Furthermore, the salt diapirs penetrated into the north portion of the sag and their penetration depth decreased as the strike-slip weakened.

This study investigated the E12 structure, which lies in the southeast of Laizhou Bay Sag (Figure 1A). The drilling target in the study area mainly includes the fan delta sedimentary system that developed during the deposition of the Es_3 Member (Figure 1B). Two exploration wells, A-1 and A-2, were drilled in the study area. Previous sedimentary facies analysis has shown that well A-1 mainly lies in the root of a fan

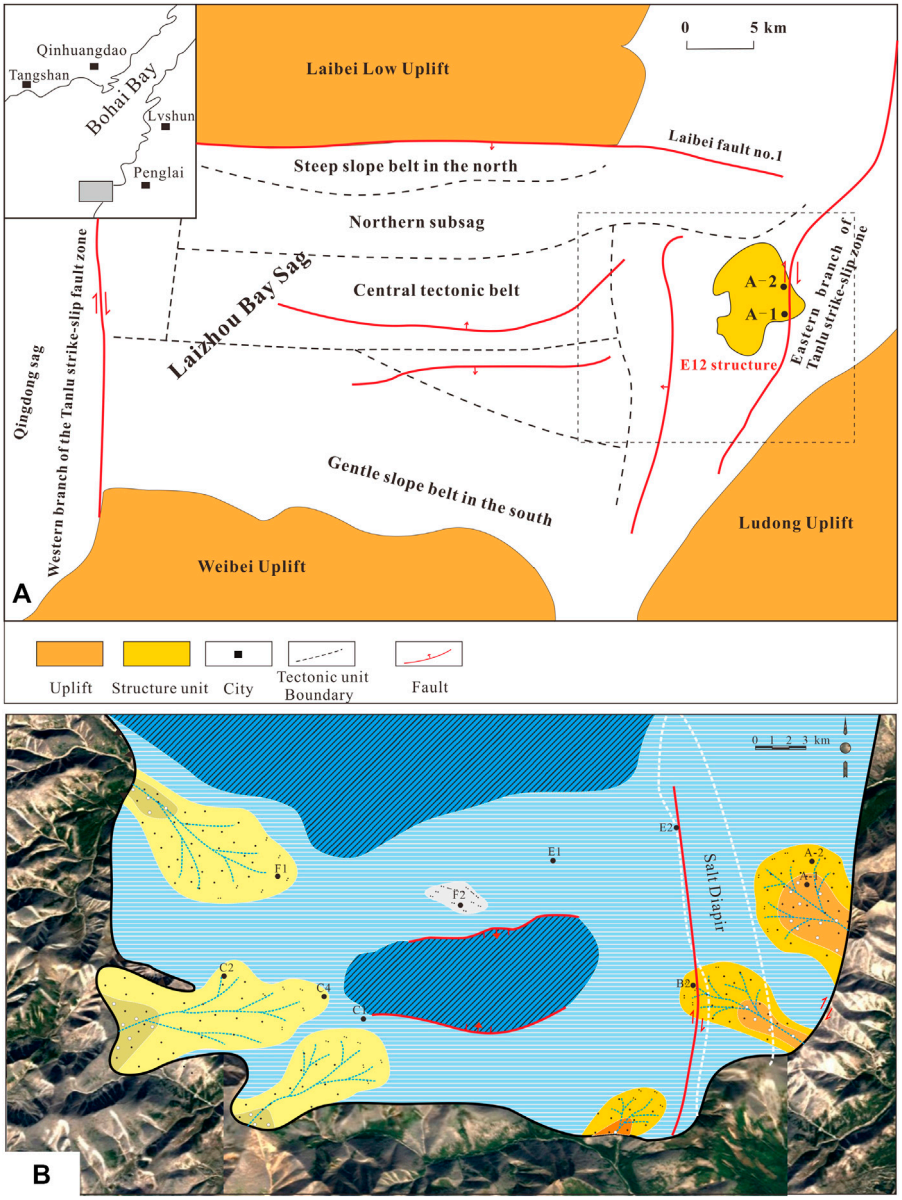

FIGURE 1
Regional geological location maps of the Laizhou Bay Sag and sub-structural units **(A)** and sedimentary facies during deposition of the Es_3 Formation **(B)**.

delta while well A-2 is located in the central portion of a fan delta. High-quality reservoirs of the Es_3 Member were only encountered in well A-2, indicate the differences in the development of high-quality reservoirs in the E12 structure.

Experiments and testing

A total of 75 sandstone core samples were collected from the Shahejie Formation reservoirs at exploration wells A-1 and A-2 in the E12 structure. Polished optical thin sections were prepared for microscopic petrological observations. Polarization microscopes Leica DMRP 551007 and Zeiss Imager A1 equipped with 4×, 10×, and 20× lenses were employed to identify the compositions of sandstone particles as well as the petrological and diagenetic characteristics, aiming to determine diagenetic minerals affecting porosity and permeability, and estimate the cement content and plane porosity. The methods proposed by Longiaru (1987) and Powers (1953) were used to determine

the sorting and particle roundness of the sandstone samples. In addition, blue epoxy resin was added to several representative casting thin sections to prepare casting thin sections for the quantitative identification of pore types (e.g., primary intergranular pores and secondary dissolution pores) and plane porosity estimation. Some thin sections were stained with alizarin red and potassium ferricyanide solution to identify different types of carbonate cements in sandstones.

Some polished thin sections with sputtered carbon films were prepared. The detrital sandstone particles, pores, and authigenic minerals were observed and photographed using a ZEISS EVO/MA15 scanning electron microscope (SEM) combined with an X-ray quantitative energy spectrum system in backscattered electrons (BSE) and secondary electron (SE) modes. The instruments operated at a humidity of 50%, a temperature of 25°C, an acceleration voltage of 0.2–30 kV, and a probe current of 0.5 PA to 5 μA.

The sandstone samples collected from well A-2 was measured to determine their plane porosity. Meanwhile, the content and types of clay minerals in multiple mudstones collected from well A-2 were analyzed using X-ray diffraction (XRD). First, large mudstones were crushed and ground into 300 mesh powders, from which organic matter and carbonate components were then removed. Afterward, the mudstones were air dried, mixed with ethylene glycol, and heated to 300°C and then to 550°C. Finally, the composition of clay minerals with particles <2 μm was analyzed qualitatively and semi-quantitatively. A more detailed testing procedure is described in Peltonen et al., 2009. The XRD test was conducted using a D/Max 2500 Powder X-Ray Diffractometer supplied by Rigaku, which operated at a temperature of 20 ± 5°C, voltage of 40 kV, and current of 200 mA.

Types and characteristics of diagenesis

Tight reservoirs in the Es_3 member in well A-1

The observations under a microscope show that the Es_3 reservoirs in well A-1 have poor physical properties overall, which were identified by three main characteristics. *1*) The reservoirs have a high argillaceous content, with abundant intergranular argillaceous fillers frequently visible (Figure 2A). *2*) The grains are poorly sorted, with a wide grain size range of 500–50 μm (Figures 2B–E). *3*) Carbonate cements have developed, and ferrodolomite cements are widely present in intergranular pores, intragranular pores, and fractures (Figure 2D). In addition, the Es_3 reservoirs in well A-1 have experienced strong mechanical compaction, leading to widely distributed micro-cracks (Figures 2C,D) and the flexure of plastic mica fragments (Figure 2F). Therefore, the diagenetic facies of Es_3 reservoirs generally feature strong compaction combined with alkaline cementation. Since well A-1 is located in the root of a proximal fan delta, the reservoir grains contain too many argillaceous matrixes and block pores, are poorly sorted, and have a low granule structure maturity, resulting in poor inherent reservoir conditions of the Es_3 Member. At present, this member has a burial depth of approximately 2000–2300 m and is still in the mechanical compaction stage. Moreover, the lack of rigid quartz grains causes weak resistance on compaction. Accordingly, many argillaceous fillers are compacted under the strong force of the overlying load, resulting in a rapid reduction in primary pores. These account for the tightness of the Es_3 reservoirs. In addition, dolomite precipitation is widely distributed in the reservoirs, resulting in further tightness of the reservoirs. The possible reasons are as follows. Well A-1 is located in the fan root near faults (Figure 1B), and strong carbonate cementation might have occurred under the influence of long-term alkaline fluids. However, this member still has poor physical properties overall due to the lack of acid dissolution.

Diagenetic characteristics of the Es_3 reservoirs in well A-2

Distribution of anomalously high porosity zone

Core samples were systematically collected from the reservoirs at a burial depth of 1100–2400 m in well A-2. Casting thin sections were prepared using the core samples, the pore types and plane porosity were tested, and accordingly, the porosity-depth evolution profile of the well was established (Figure 3). As indicated by this profile, a zone with anomalously high porosity exists at a burial depth of approximately 2000–2400 m in the Shahejie Formation reservoirs in well A-2, with a maximum porosity of 28%. The relationships of intergranular pores and secondary dissolution pores with the depth (Figure 3) show that the anomalously high porosity zone mainly results from both intergranular pores and secondary dissolution pores, with the former making more contributions. According to the XRD results, the illite/smectite mixed layers in mudstones corresponding to the anomalously high porosity zone have smectite content lower than 20% and thus are at the stage of superlattice ordered mixed layers. According to the Chinese petroleum industry standard SY/T5477-2003 *The division of diagenetic stages in clastic rocks*, the reservoirs at a burial depth of 1100–2400 m are at the middle diagenetic stage (A_2).

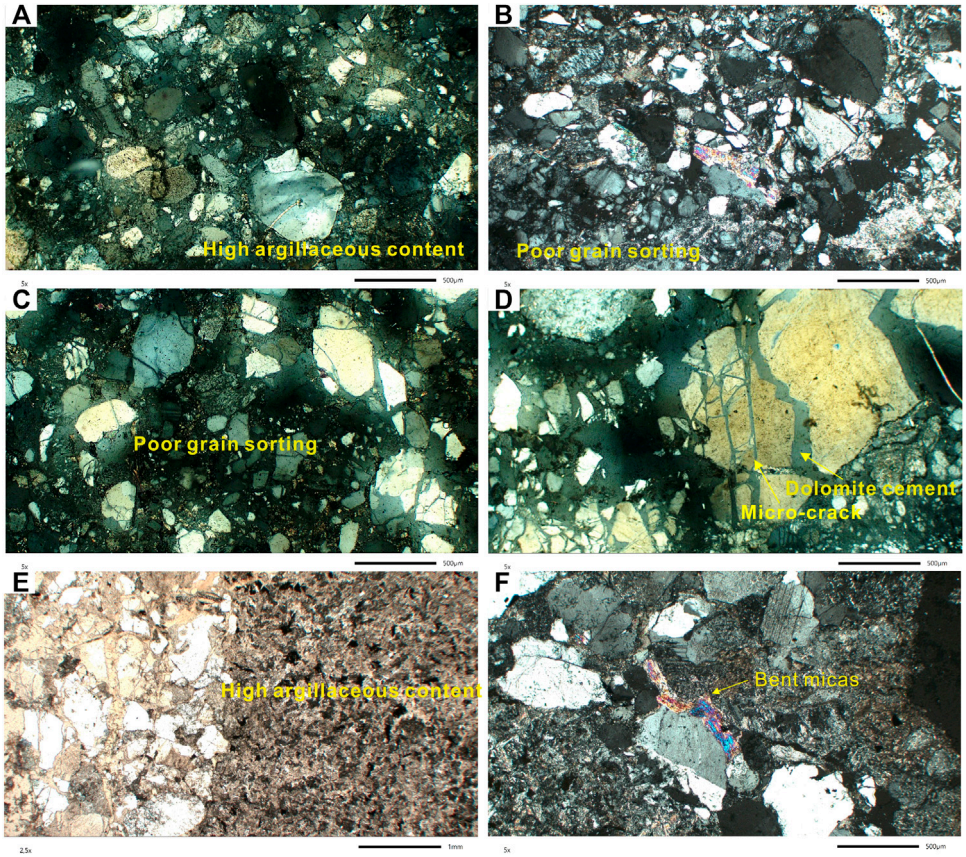

FIGURE 2
Diagenetic facies of strong compaction combined with alkaline cementation in the Es_3 reservoir sandstones in well A-1. Note: **(A)** Orthogonal light, 2199 m, high argillaceous content; **(B)** orthogonal light, 2367 m, poor grain sorting; **(C)** orthogonal light, 2281 m, poor grain sorting, compaction-induced micro-cracks developing; **(D)** orthogonal light, 2253 m, compaction-induced micro-cracks developing and filled with dolomites; **(E)** transmission light, 2360 m, high argillaceous content; **(F)** orthogonal light, 2360 m, bent micas.

Acid dissolution diagenetic facies

Specific typomorphic minerals and their genetic assemblages form by the changes in the acidity and alkalinity of aqueous media in the diagenetic environment. Therefore, they become important factors in determining the diagenetic environment (Wang et al., 2020). The casting thin sections show that the with anomalously high porosity zone at a burial depth of 2000–2400 m in well A-2 exhibit significant acid dissolution, which is typical of constructive diagenesis. The commonly visible dissolution includes the secondary pores by the dissolution of the feldspar grains or volcanic lithoclasts in the reservoir sandstones, as well as the dissolution of intergranular calcite cements. Among them, the intragranular dissolution pores of feldspars predominate (Figure 4A). Some feldspar grains have been dissolved completely, leaving behind moldic pores (Figure 4B), while some have only been partially dissolved along cleavage planes (Figure 4C). The lithic grains are mainly dissolved inward from the edges, generally forming a “bay” (Figure 4D). Secondary dissolution micropores of feldspar grains (Figure 4E) were also observed under a scanning electron microscope, with euhedral quartz and book-shaped kaolinite crystals frequently visible near the corroded feldspars (Figure 4F). The assemblage consisting of secondary dissolution pores, authigenic quartz, and kaolinite is typical acid dissolution diagenetic facies. With the inflow of acidic fluids and the feldspar dissolution, potassium ions flow away with the fluids, leaving the precipitation of authigenic quartz and authigenic kaolinite crystals (Zhang et al., 2017). These acidic fluids are likely the organic acids released from the evolution of organic matter in adjacent source rocks.

At present, the content of the illite/smectite mixed layers shows that the anomalously high porosity zone is at the middle diagenetic stage (A_2) and has entered the phase of

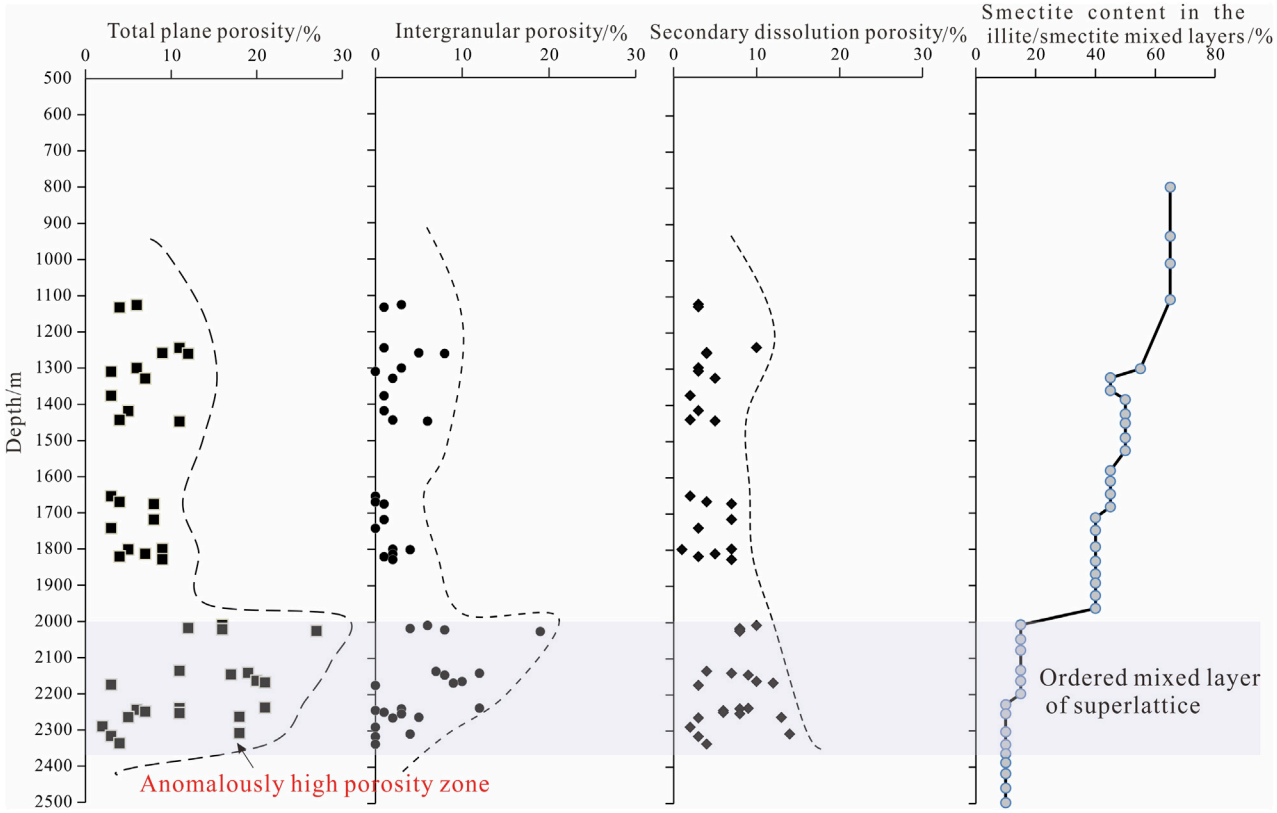

FIGURE 3
Plots of depth vs total plane porosity, intergranular porosity, secondary dissolution porosity, and smectite content in the illite/smectite mixed layers in well A-2.

organic acid release. The well A-1, located at the root of a fan delta, occur in the vicinity of fault zones. It is noteworthy that, the fault has long acted as a channel for the upward flow of deep alkaline fluids. However, the reservoirs of this well have not been altered by the acid fluids laterally expelled from multiple sets of source rocks due to the far distance.

Alkaline dissolution diagenetic facies

Quartz dissolution

Quartz grains in the anomalously high porosity zone were frequently dissolved by extensive alkaline fluids, many of which were dissolved into the shape of irregular sawteeth and bays (Figure 5A), significantly increasing the intergranular pores. Quartz grains are dissolved when the pH of pore water is greater than 9. In fact, quartz dissolution is common in many geological processes (Su et al., 2020), such as sponge activities, tectonic shear stress zones, and alkaline hydrothermal activities (Hippertt, 1994; Bavestrello et al., 1995). A significant feature of the study area is that clastic quartz grains are mainly dissolved by alkaline fluids, with no overgrowth boundary observed.

Chlorite coats

Another major feature of the anomalously high porosity zone is the well-developed authigenic chlorite coats, covering the outer edges of dissolved quartz grains (Figure 5B). The SEM observations show that acicular chlorites adhere to the grain surfaces (Figure 5C), suggesting that the quartz dissolution occurred earlier than or simultaneously with the growth of chlorite coats. As a special type of clay minerals, chlorites are rich in iron and magnesium and are typically deposited in alkaline environments. In the Es_3 reservoirs of the study area, the detrital quartz grains are encapsulated in chlorite coats, without quartz overgrowth boundary. The secondary overgrowth of quartz grains in sandstones is considered controlled by thermal dynamics, and the quartz sedimentation rate generally starts to increase significantly at temperatures greater than 80–100°C (Lander et al., 2008). Accordingly, deep reservoirs are often cemented by siliceous materials, significantly increasing the likelihood of low porosity and permeability conditions. Based on the present geothermal gradient of the Laizhou Bay Sag, the geotemperature

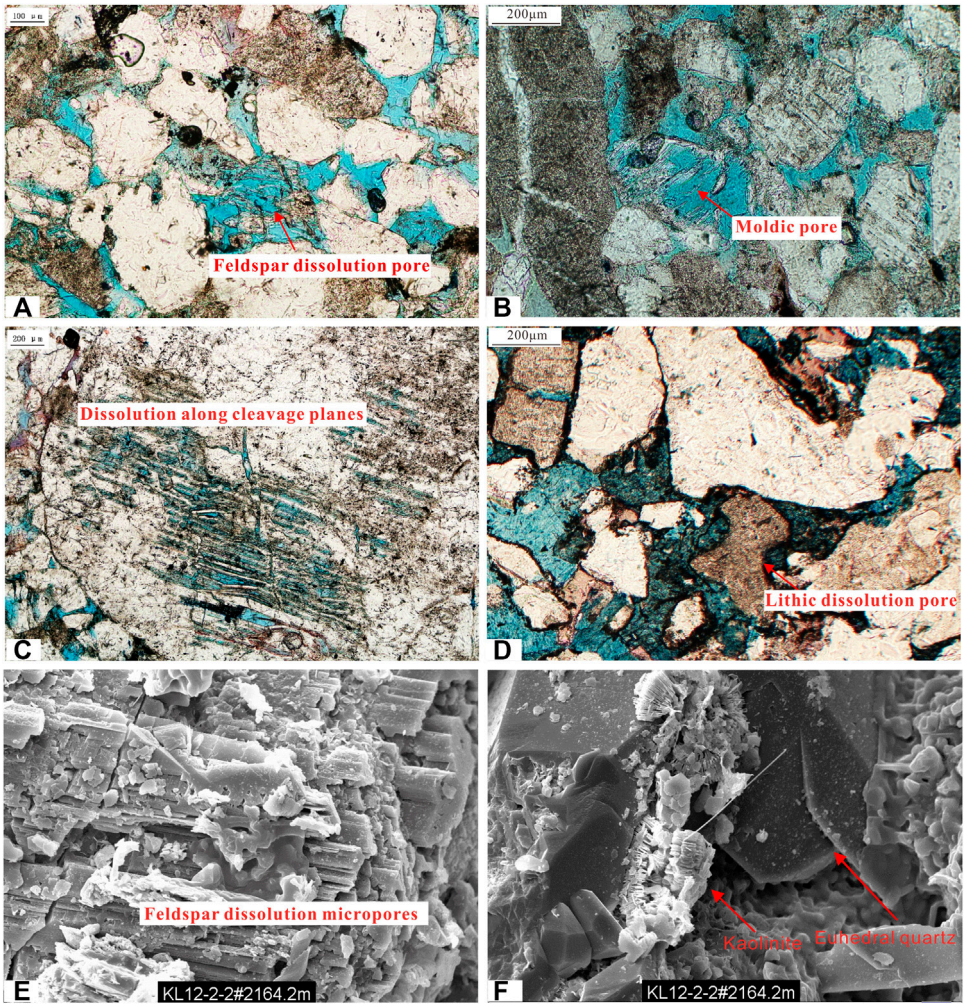

FIGURE 4
Acid dissolution diagenetic facies of the anomalously high porosity zone of the Es_3 reservoirs in well A-2. Note: **(A)** Casting thin section, 2164.2 m, feldspar dissolution pores; **(B)** Casting thin section, 2168.4 m, moldic pores; **(C)** Casting thin section, 2147.5 m, feldspar dissolution along cleavage planes; **(D)** Casting thin section, 2168.4 m, lithic dissolution; **(E)** SEM, 2162.2 m, feldspar dissolution micropores; **(F)** SEM, 2162.2 m, book-shaped kaolinite and euhedral quartz.

corresponding to the anomalously high porosity zone is above 80°C, which is within the onset temperature for the secondary overgrowth of quartz grains. Therefore, the absence of quartz overgrowth boundary in the study area is likely because the growth of chlorite coats inhibited the formation of quartz cements during the burial process. Consequently, the frequent contact between quartz grains and pore water has been restricted. This effect has been reported in many studies worldwide (Qu et al., 2015; Cao et al., 2022). In addition, the high-quality Es_3 reservoirs in well A-2 have a burial depth of 2000–2400 m and are already in the stage of strong mechanical compaction. However, unbent micas were frequently observed on the casting thin sections (Figure 5D), indicating that chlorite coats may have resisted compaction to some extent. Authigenic chlorite content was detected in the mudstones near the high-quality Es_3 reservoirs (Figure 6), indicating that the chlorite coats in the reservoirs may be a major contributor to the preservation of primary intergranular pores in the sandstones. The chlorites in the study area may be derived from the reactions of alkaline pore water rich in iron and magnesium with other minerals.

Carbonate cementation

As shown by the casting thin sections stained with alizarin red, strong carbonate cementation has occurred at some depths in the

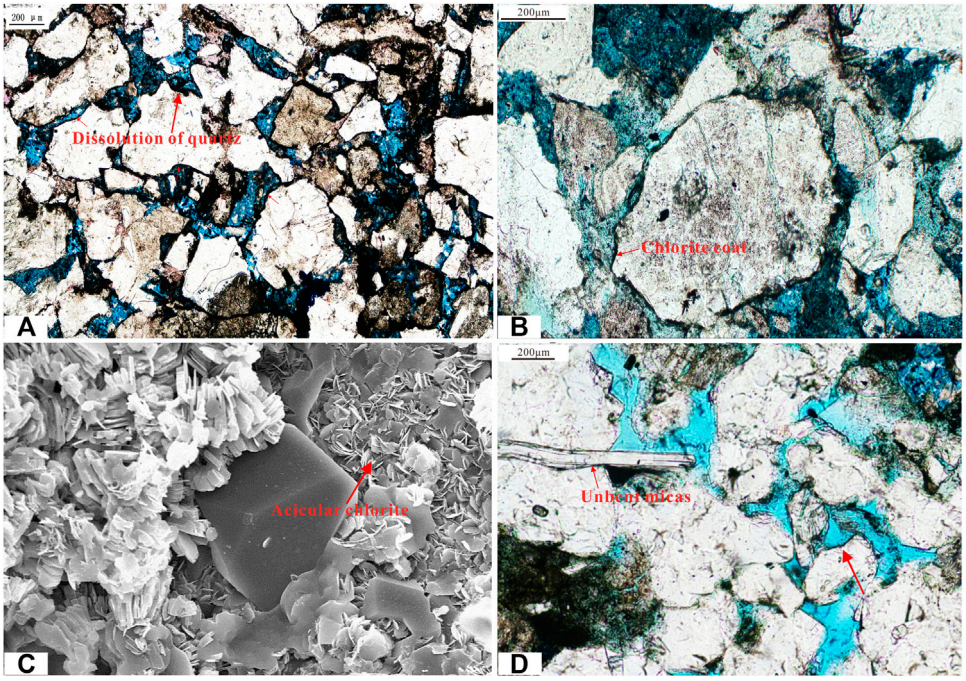

FIGURE 5
Alkaline dissolution of quartz grains, chlorite coats, and weak compaction in the anomalously high porosity zone of the Es_3 reservoirs in well A-2. Note: **(A)** Casting thin section, 2174.5 m, dissolution of quartz grains; **(B)** casting thin section, 2174.5 m, a chlorite coat attached on the surface of dissolved quartz grains; **(C)** SEM, 2175 m, acicular chlorite; **(D)** casting thin section, 2273.5 m, unbent micas.

high-quality reservoirs in well A-2. In addition, early calcite cements closely adhere to the grain surfaces of the grains coated with a chlorite film (Figure 7A), indicating that two episodes of alkaline fluid activities occurred and that the quartz dissolution and chlorite coats occurred after the sedimentation of early calcite. However, late acidic dissolution has created marks on the calcite cements. Moreover, a large number of intergranular and intragranular pores (e.g., the moldic pores of feldspars formed by acid dissolution) are filled by late dolomite cements (Figure 7B). These observations indicate that at least one episode of acidic fluid activity occurred in the reservoirs after the precipitation of early calcite, followed by another episode of alkaline fluid activity. We argue that the Fe and Mg ions needed for the sedimentation of ferrodolomites may be released during the conversion of clay minerals.

Alternating acid and alkaline diagenesis

As revealed by diagenetic observations of the high-quality reservoirs in the anomalously high porosity zone in the Es_3 Member in well A-2, the reservoirs have undergone multiple episodes of alternating activities of acid and alkali fluids. Different types of diagenesis created both alkaline diagenetic facies (e.g., the dissolution of quartz grains, chlorite precipitation, and the cementation of calcite and ferrodolomite) and acidic diagenetic facies (e.g., the dissolution of feldspars and lithics, the precipitation of authigenic kaolinite and quartz, and the dissolution of calcite cements). The Es_3 reservoirs underwent the superposition of these multiple episodes of diagenesis, forming the high porosity zone. Based on the contact relationships between various mineral assemblages in the reservoirs, the diagenetic sequence of the Es_3 reservoirs in well A-2 can be qualitatively established. The alternating acid and alkaline dissolution processes of the high-quality reservoirs are as follows (Figure 8).

First, the earliest episode of alkaline fluids (likely weak alkaline pore waters) in the Es_3 reservoirs in well A-2 caused the dissolution of quartz grains, which was possibly accompanied by the growth of chlorite coats. Previous studies have shown that salt lakes mainly developed during the deposition of the Es_4 Member in the Bohai Bay Basin and that the lake water gradually became less saline during the deposition of the Es_3 Member. Therefore, it is likely that the connate saline sedimentary water was discharged from the underlying Es_4 Member under compaction and entered the Es_3 reservoirs along faults.

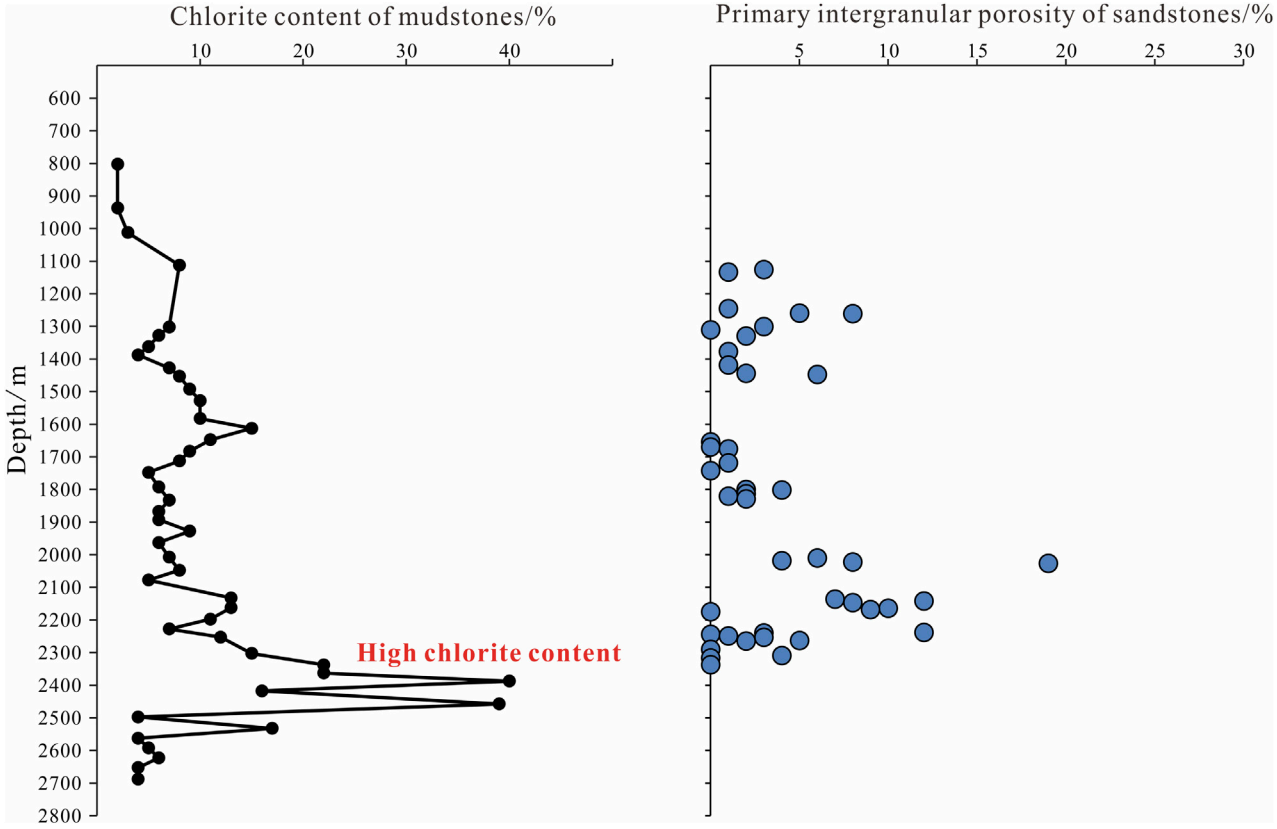

FIGURE 6
Profiles of depth vs chlorite content of mudstones and depth vs primary intergranular porosity of sandstones in well A-2.

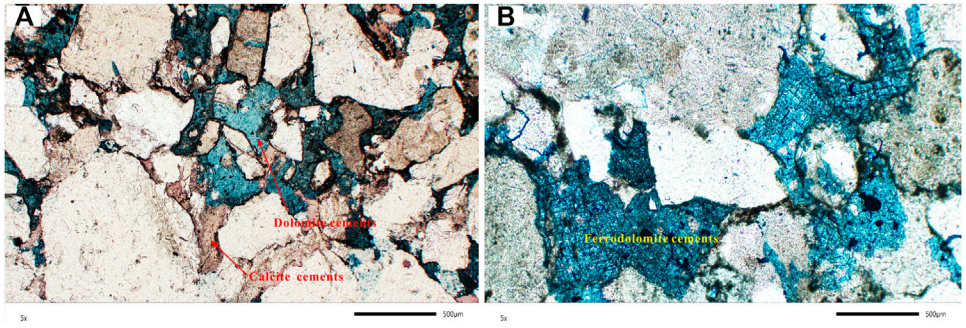

FIGURE 7
Carbonate cements in the anomalously high porosity zone of the Es_3 reservoir sandstones in well A-2. Note: **(A)** Casting thin section, 2175 m, the secondary pores formed due to the dissolution of early filled calcite were filled with ferrodolomites; **(B)** casting thin section, 2175 m, the moldic pores of feldspars formed by acid dissolution were filled with ferrodolomites.

Subsequently, the pH of pore water gradually decreased as alkaline dissolution proceeded. Meanwhile, as the second episode of slightly acidic fluids, CO_2 formed by the biodegradation of organic matter in nearby source rocks under increased burial temperature entered the Es_3 reservoirs. As a result, the alkaline dissolution of quartz ceased, and the pore

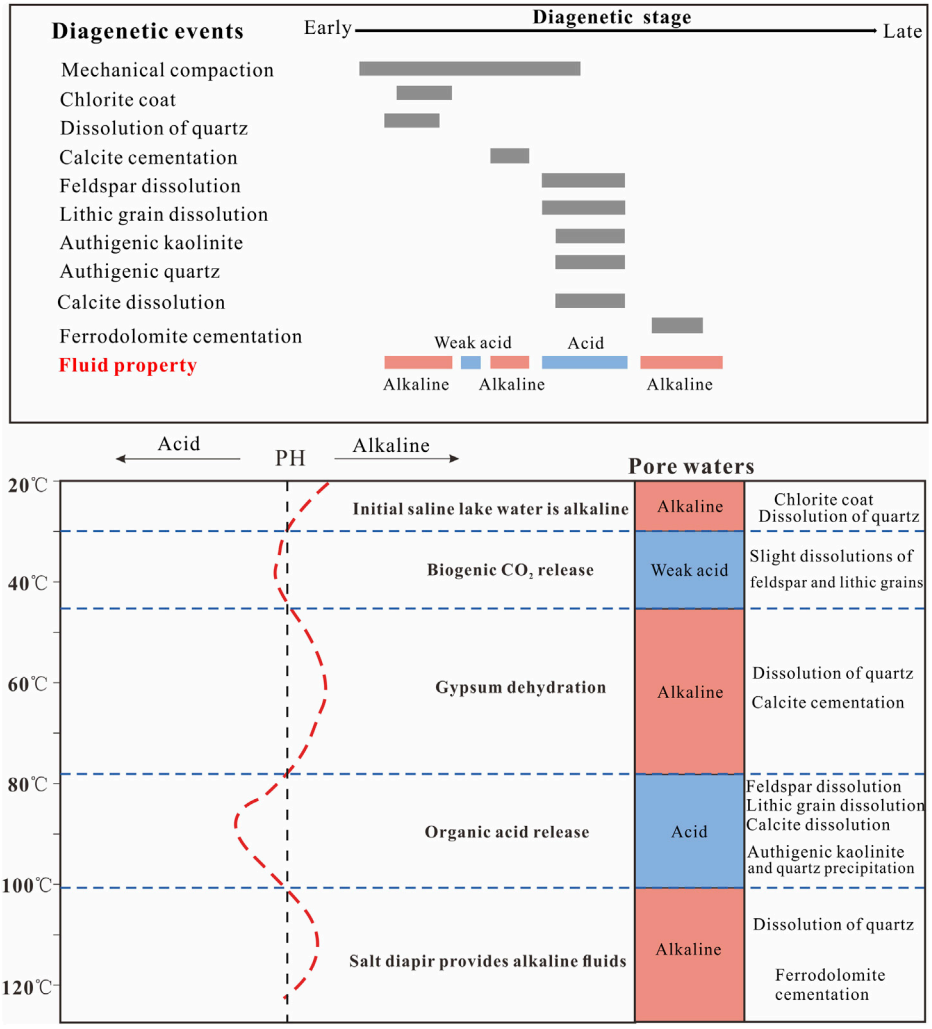

FIGURE 8
Diagenetic sequence and diagenetic fluid evolution in the anomalously high porosity zone of the Es_3 reservoirs in well A-2.

waters gradually became slightly acidic. Afterward, the third episode of alkaline fluids flowed into the Es_3 reservoirs, resulting in extensive calcite intercrystalline cementation. These alkaline fluids are probably related to the large-scale dehydration (starting at approximately 45°C) of the gypsum deposited in the Es_4 Member at the early diagenetic stage, i.e., $CaSO_4{\cdot}2H_2O \rightarrow CaSO_4{\cdot}1/2H_2O{+}3/2H_2O$. With an increase in the burial, organic matter gradually matured and released large quantities of organic acid fluids. The fourth episode of acid fluids caused the massive dissolution of the early calcite cements originally precipitated in the reservoirs, creating a large number of secondary dissolution pores. Meanwhile, authigenic kaolinite and quartz precipitated. During the deposition of the Neogene Guantao and Minghuazhen formations, the salt diapir activities were triggered by the activity of the Tanlu strike-slip fault zones. The upwelling alkaline waters, representing the last episode of alkaline fluids, entered the reservoirs and caused the precipitation of ferrodolomite cements, leading to the reduction of reservoir physical properties to a certain extent.

For the Es_3 reservoirs in well A-2, the multiple episodes of alternating dissolution of acid and alkali fluids have different effects on the formation of the high-quality reservoirs. The first episode of alkaline fluids, represented by the connate saline sedimentary waters, is the most critical to the formation of the high-quality reservoirs. This is because the early alkaline fluids dissolved numerous detrital quartz grains. More importantly, chlorite coats were formed during the early diagenetic stage, effectively impeding the subsequent secondary overgrowth of quartz and resisting the compaction to some extent. Therefore, the chlorite coats protected the primary intergranular pores, which is evident from the relationship between

porosity and depth. The second episode of slightly acidic fluids containing biodegradable CO_2 has limited effects on the anomalously high porosity zone due to the limited amount of CO_2 produced from the organic matter biodegradation. The third episode of alkaline fluids formed by the large-scale dehydration of gypsum led to massive calcite cementation, which severely blocked pores. Nevertheless, the calcite cementation actively maintained the pores for the formation of the high-quality reservoirs because the early calcite cements not only inhibited the reservoir compaction but also provided a material basis for the late dissolution of organic acids. The fourth episode of organic acid fluids, leading to the dissolution of minerals such as calcites and feldspars, caused a significant and favorable alteration. The last episode of large-scale alkaline fluids, which originated from the salt diapirism induced by late strike-slip faulting, caused massive ferrodolomite cementation in the reservoir and thus reduced the physical properties of the reservoirs.

With high mud content and poor sorting property, the Es_3 reservoirs in well A-1 drilled at the root of a fan delta have poor congenital physical properties. Moreover, carbonate cementation occurred in the reservoirs in well A-1 under the long-term action of alkaline fluids, causing the reservoirs to be tighter. Compared with the reservoirs in well A-2 drilled at the central portion of a fan delta, the reservoirs at well A-1 are far away from source rocks and lack access to the acidic fluids. This is likely an important reason for the present-day low porosity.

Conclusions

(1) The Es_3 reservoirs in well A-1 drilled in the root of a fan delta in the Laizhou Bay Sag have poor physical properties and no hydrocarbon shows. The Es_3 reservoir sandstones in well A-1 have high argillaceous content, are poorly sorted, and underwent strong compaction. Moreover, massive ferrodolomite cementation occurred under the long-term activities of alkaline fluids. In addition, owing to the far lateral distance from source rocks, the Es_3 reservoirs could not effectively communicate with the organic acid fluids and, thus, lacked access to the acid dissolution.

(2) An anomalously high porosity zone has developed at a burial depth of 2000–2400 m in the Es_3 member of well A-2. The high-quality reservoirs underwent the diagenesis of five episodes of alternating acid and alkali fluids. The first episode of alkaline fluids originated from the connate saline pore waters from the underlying Es_4 member due to compaction. These fluids are critical to the formation of high-quality reservoirs and caused the dissolution of quartz grains and precipitation of chlorite coats on the outer edges of the quartz which impeded the overgrowth. The second episode of slightly acid fluids were derived from CO_2 formed by the biodegradation of organic matter and had limited effects on the reservoirs. The third episode of alkaline fluids from the dehydration of Es_4 gypsum, leading to massive calcite cementation and thus resisting compaction. The fourth episode of organic acid fluids released from the lateral source rock caused the acid dissolution, greatly favoring the physical properties. The last episode of alkaline fluids from the salt diapirs associated with strike-slip fault activity led to the blockage of partial pores by ferrodolomites, lowering the reservoir physical properties.

Data availability statement

The original contributions presented in the study are included in the article/Supplementary Material, further inquiries can be directed to the corresponding author.

Author contributions

HY is responsible for the idea and writing of this paper and SZ, AS, DG, YW, and WS are responsible for the data interpretation.

Funding

This research was funded by the National Natural Science Foundation of China (NO. 41472098).

Conflict of interest

Authors HY, DG, and WS were employed by the Tianjin Branch of CNOOC (China).

The remaining authors declare that the research was conducted in the absence of any commercial or financial relationships that could be construed as a potential conflict of interest.

Publisher's note

References

Anna, B., Susanne, G., and Peter, K. (2009). Porosity-preserving chlorite cements in shallow-marine volcaniclastic sandstones: Evidence from Cretaceous sandstones of the Sawan gas field, Pakistan. *Am. Assoc. Pet. Geol. Bull.* 93 (5), 595–615. doi:10.1306/01300908096

Bavestrello, G., Arillo, A., Benatti, U., Cerrano, C., Cattaneo-Vietti, R., Cortesognoi, L., et al. (1995). Quartz dissolution by the sponge Chondrosia reniformis (Porifera, Demospongiae). *Nature* 378 (6555), 374–376. doi:10.1038/378374a0

Bloch, S., Lander, R. H., and Bonnell, L. (2002). Anomalously high porosity and permeability in deeply buried sandstone reservoirs: Origin and predictability. *AAPG Bull.* 86 (2), 301. doi:10.1306/61EEDABC-173E-11D7-8645000102C1865D

Cao, Y. C., Yuan, G. H., Yang, H. J., et al. (2022). Current situation of oil and gas exploration and research progress of the origin of high-quality reservoirs in deep-ultra-deep clastic reservoirs of petroliferous basins. *Acta Pet. Sin.* 43 (01), 112. doi:10.11867/j.issn.1001-8166.2016.07.0718

Chen, Y., Zhang, Y., Zhu, Z. J., et al. (2019). Early sedimentary sequence and petroleum geological significance of faulted basins: A case study on the lower Es4 in bonan sag, jiyang depression. *China Pet. Explor.* 4 (3), 313–322. doi:10.3969/j.issn.1672-7703.2019.03.004

Ehrenberg, S. N. (1993). Preservation of anomalous high porosity in deeply buried sandstones by grain-coating chlorite: Examples from the Norwegian continental shelf. *AAPG Bull.* 77 (7), 1260.

Hippertt, J. F. (1994). Microstructures and c-axis fabrics indicative of quartz dissolution in sheared quartzites and phyllonites. *Tectonophysics* 229 (3-4), 141–163. doi:10.1016/0040-1951(94)90026-4

Jiang, W., Zhang, P., Li, D., Li, Z., Wang, J., Duan, Y., et al. (2022). Reservoir characteristics and gas production potential of deep coalbed methane: Insights from the no. 15 coal seam in shouyang block, Qinshui Basin, China. *Unconv. Resour.* 2, 12–20. doi:10.1016/j.uncres.2022.06.001

Katz, B., Gao, L., Little, J., and Zhao, Y. R. (2021). Geology still matters–Unconventional petroleum system disappointments and failures. *Unconv. Resour.* 1, 18–38. doi:10.1016/j.uncres.2021.12.001

Lander, R. H., Larese, R. E., and Bonnell, L. M. (2008). Toward more accurate quartz cement models: The importance of euhedral versus noneuhedral growth rates. *Am. Assoc. Pet. Geol. Bull.* 92 (11), 1537–1563. doi:10.1306/07160808037

Li, J. Y. (2017). Temporal-spatial evolution of diagenetic environment and diagenesis pore evolutionary process of red beds in the eastern Dongying Sag, Bohai Bay Basin. *Oil Gas Geol.* 38 (01), 90. doi:10.11743/ogg20170110

Longiaru, S. (1987). Visual comparators for estimating the degree of sorting from plane and thin section. *J. Sediment. Res.* 57 (4), 791–794. doi:10.1306/212f8c60-2b24-11d7-8648000102c1865d

Meng, T., Liu, P., Qiu, L. W., Wang, Y., Liu, Y., Lin, H., et al. (2017). formation and distribution of the high quality reservoirs in a deep saline lacustrine basin: A case study from the upper part of the 4th member of Paleogene Shahejie Formation in bonan sag, jiyang depression, Bohai Bay Basin, east China. *Petroleum Explor. Dev.* 44 (06), 948–959. doi:10.1016/s1876-3804(17)30107-6

Niu, C. M., Yang, H. F., Zhao, D. J., et al. (2022). Study on the ultra-late hydrocarbon accumulation and migration lagging effect in laizhouwan sag, Bohai sea. *Editor. Comm. Earth Science-Journal China Univ. Geosciences* 47 (02), 464. doi:10.3799/dqkx.2021.099

Peltonen, C., Marcussen, Ø., Bjørlykke, K., and Jahren, J. (2009). Clay mineral diagenesis and quartz cementation in mudstones: The effects of smectite to illite reaction on rock properties. *Mar. Petroleum Geol.* 26 (6), 887–898. doi:10.1016/j.marpetgeo.2008.01.021

Powers, M. C. (1953). A new roundness scale for sedimentary particles. *J. Sediment. Res.* 23 (2), 117.

Qu, X. Y., Liu, Z., Gao, Y., et al. (2015). The influence and formation environment of chlorite coatings in the clastic rock. *Acta Sedimentol. Sin.* 33 (04), 786. doi:10.14027/j.cnki.cjxb.2015.04.017

Su, A., Chen, H., Chen, X., He, C., Liu, H., Li, Q., et al. (2018a). The characteristics of low permeability reservoirs, gas origin, generation and charge in the central and Western Xihu depression, East China Sea Basin. *J. Nat. Gas Sci. Eng.* 53, 94–109. doi:10.1016/j.jngse.2018.01.034

Su, A., Chen, H., Chen, X., Liu, H., Liu, Y., and Lei, M. (2018b). New insight into origin, accumulation and escape of natural gas in the Songdong and Baodao regions in the eastern Qiongdongnan basin, South China Sea. *J. Nat. Gas Sci. Eng.* 52, 467–483. doi:10.1016/j.jngse.2018.01.026

Su, A., Chen, H., Yang, W., Feng, Y. X., Zhao, J. X., and Lei, M. (2021a). Hydrocarbon gas leakage from high-pressure system in the yanan sag, qiongdongnan basin, south China sea. *Geol. J.* 56 (10), 5094–5108. doi:10.1002/gj.4225

Su, A., Chen, H., Zhao, J. X., and Feng, Y. X. (2020). Integrated fluid inclusion analysis and petrography constraints on the petroleum system evolution of the central and southern Biyang Sag, Nanxiang Basin, Eastern China. *Mar. Petroleum Geol.* 118, 104437. doi:10.1016/j.marpetgeo.2020.104437

Su, A., Chen, H., Zhao, J. X., Feng, Y. X., and Nguyen, A. D. (2021b). Exhumation filling and paleo-pasteurization of the shallow petroleum system in the north slope of the biyang sag, nanxiang basin, China. *Mar. Petroleum Geol.* 133, 105267. doi:10.1016/j.marpetgeo.2021.105267

Surdam, R. C., Boese, S. W., and Crossey, L. J. (1984). The chemistry of secondary porosity. *AAPG Mem.* 37 (2), 127.

Vafaie, A., Kivi, I. R., Moallemi, S. A., and Habibnia, B. (2021). Permeability prediction in tight gas reservoirs based on pore structure characteristics: A case study from south western Iran. *Unconv. Resour.* 1, 9–17. doi:10.1016/j.uncres.2021.08.001

Volkmar, S., and Mc Donald, A. D. (1979). *The role of secondary porosity in the course of sandstone diagenesis*. Tulsa, Oklahoma: SEPM Society for Sedimentary Geology.

Wang, H., Zhou, S., Li, S., Zhao, M., and Zhu, T. (2022). Comprehensive characterization and evaluation of deep shales from Wufeng-Longmaxi Formation by LF-NMR technology. *Unconv. Resour.* 2, 1–11. doi:10.1016/j.uncres.2022.05.001

Wang, J., Cao, Y. C., and Gao, Y. J. (2013). Diagenetic characteristics and formation mechanism of Paleogene red-bed reservoirs in Dongying Sag. *Acta Pet. Sin.* 34 (02), 283. doi:10.7623/syxb201302010

Wang, J., Zhou, L., Liu, J., Zhang, X., Zhang, F., and Zhang, B. (2020). Acid-base alternation diagenesis and its influence on shale reservoirs in the permian lucaogou formation, jimusar sag, junggar basin, NW China. *Petroleum Explor. Dev.* 47 (05), 962–976. (In Chinese with English abstract). doi:10.1016/s1876-3804(20)60109-4

Xue, Y. G., Yang, H. F., Wang, H., et al. (2022). Discovery and significance of KL10-2 Neogene large oilfield in deep subsag zone of Laizhouwan sag, Bohai sea. *China Offshore Oil Gas* 34 (01), 17. doi:10.11935/j.issn.1673-1506.2022.01.003

Yang, H. F., Tu, X., Zhao, D. J., et al. (2021). Organic facies characteristics of source rocks on the 3rd and 4th member of Shahejie Formation in the southern laizhouwan depression, Bohai Bay Basin, China. *J. Chengdu Univ. Technol. Sci. Technol. Ed.* 48 (01), 72. doi:10.3969/j.issn.1671-9727.2021.01.08

Yuan, W. F., Chen, S. Y., and Zeng, C. M. (2005). Research development and prospects on Paleogene sea transgression in Bohai Bay Basin. *Acta Sedimentol. Sinca* (04), 604.

Zhang, H., Liao, M. G., Yao, J. L., et al. (2017). Authigenic minerals and their influences on the physical properties of tight sandstone reservoirs: An example from the Chang-3 oil reservoirs in the Longdong region, Ordos basin. *Sediment. Geol. Tethyan Geol.* 37 (03), 22.

frontiers | Frontiers in Earth Science

TYPE Original Research
PUBLISHED 05 January 2023
DOI 10.3389/feart.2022.1034069

OPEN ACCESS

EDITED BY
HU LI,
Southwest Petroleum University, China

REVIEWED BY
Jianguo Zhang,
China University of Geosciences, China
Junhui Wang,
China University of Petroleum, China
Kun Zhang,
Southwest Petroleum University, China

*CORRESPONDENCE
Yunbo Zhang,
zhangyb2014@foxmail.com

SPECIALTY SECTION
This article was submitted to Structural Geology and Tectonics, a section of the journal Frontiers in Earth Science

RECEIVED 01 September 2022
ACCEPTED 13 September 2022
PUBLISHED 05 January 2023

CITATION
Zhang Y, Wang R, Xu J, Wu X, Li Y, Lin Y and Wang B (2023), Hydrocarbon accumulation conditions and favorable exploration zones in the Lunpola Basin, Tibet.
Front. Earth Sci. 10:1034069.
doi: 10.3389/feart.2022.1034069

Hydrocarbon accumulation conditions and favorable exploration zones in the Lunpola Basin, Tibet

Yunbo Zhang[1]*, Rui Wang[1], Jie Xu[2], Xinhe Wu[1], Yinglie Li[1], Yanhua Lin[1] and Buqing Wang[3]

[1]Oil and Gas Survey, China Geological Survey, Beijing, China, [2]China University of Geosciences (Beijing), Beijing, China, [3]Changsha Natural Resources Comprehensive Survey Center CGS, Changsha, China

By systematically reviewing and summarizing the previous studies on the petroleum geology of the Lunpola Basin, combined with the latest oil and gas exploration results, the oil and gas accumulation conditions of this basin are summarized, and the favorable zones with the most exploration potential are pointed out. The results show that: ① The Paleogene mainly develops three sets of source rocks, including Niu-1 section, Niu-2 section and lower Niu-3 subsection. The lithology is mainly semi-deep and deep lacustrine gray-dark shale. Among them, the source rock of Niu-2 section is the best. However, the source rock of Niu-1 section is only developed in the Jiangjiacuo depression. The effective source rocks have the largest thickness in the central and western parts of the basin and have the best hydrocarbon-generating capacity. The thickness and abundance of the source rocks have decreased eastward. The organic matter are mainly Type I and Type II_1, with a maturity of 0.58%–1.08%. ② The study area is dominated by clastic rock reservoirs, which can be divided into three types according to the strata distribution, and the overall reservoir conditions are not good. The reservoir porosity is between 0.1% and 32.6%, mainly between 2.0% and 10.0%, with an average of 6.5%; the permeability is between 0.0005 mD and 116.0 mD, mainly between 0.01 mD and 0.5 mD, which means ultra-low porosity and ultra-low permeable fracture-porous reservoirs. ③ Three sets of seals are mainly developed in the Lunpola Basin, including two regional seals of the middle Niu-2 subsection and Dingqinghu section, and a direct seal of upper Niu-2 subsection. These three sets of seals are well developed and have good preservation conditions in the relatively stable central depression and the footwall of thrust nappe structural belt . ④ The oil and gas reservoirs in the Lunpola Basin have the distribution law of "structural traps in the north and south, and lithologic traps in the center". Structural traps are mainly distributed in the thrust nappe belt in the north and the Changshan uplift in the south, forming "self-generation and self-storage" or "lower-generation and upper-storage" reservoirs. While lithologic traps are mainly distributed in the central sag, forming "self-generation and self-storage" reservoirs. ⑤ The source-reservoir-caprock combination conditions are good in the structural traps in the footwall of the northern thrust nappe belt and the lithologic traps in the southern slope belt of Jianjiacuo depression,, and they are the most favorable oil and gas exploration zones in the Lunpola Basin.

KEYWORDS

lunpola basin, hydrocarbon accumulation conditions, hydrocarbon accumulation pattern, controlling factor, favorable oil and gas exploration zones

1 Introduction

In 2020 and 2021, China's crude oil production is 195 million tons and 199 million tons, respectively. Meanwhile the crude oil import is 542 million tons and 513 million tons, respectively. The foreign dependence of crude oil is as high as 73.5% and 72%, respectively. Therefore, oil imports have remained high (Snowball column for incoming calls and power outages, 2021). With the continuous advancement of China's industrialization process, energy consumption is increasing year by year. It is expected that China's dependence on foreign oil and gas resources will continue to rise for a long period of time in the future, which will inevitably affect China's national energy security and social and economic development to a certain extent. Finding large-scale strategic replacement areas for oil and gas resources and building reserve bases for oil and gas resources are of great significance to improving China's energy security. At present, in addition to the Tarim mega-basin, only the Tibet basin has potential to be another large-scale oil and gas resource strategic replacement area (Qiu, 1997). The Lunpola Basin is located on the southern side of the middle section of the Bangong Lake-Nujiang Great Fault Zone in the northern Tibet Plate. It is a Paleogene continental basin on the junction zone of the Qiangtang block and the Gangdise block (Bangong-Nujiang suture) (Figure 1). The basin is narrowly distributed in the east-west direction, with north-south zones and east-west blocks (Zhang and Zou, 1995; Lei et al., 1996; Lu et al., 1997). The range of the basin is 88°30′–90°30′ in longitude and 31°20′–32°20′ in latitude, with a length of about 200 km from east to west, a width of 10–30 km from north to south, and an area of about 3600 km^2. The Lunpola Basin is one of the numerous Paleogene continental basins in the Tibet. So far, it has the best petroleum geological conditions and has the highest exploration degree in the Tibet. Moreover, the industrial oil and gas flow has been initially obtained (Zhang and Zou, 1995; Lei et al., 1996; Ma et al., 1996; Lu et al., 1997), which further highlights the great significance of the oil and gas resource survey in the Lumpola Basin.

Previous studies on the Lunpola Basin mainly focused on the structural geological characteristics of the basin (Luo, 1993; Pan, 1994; Pan, 1995; Xiao and Huang, 1996; Ai et al., 1998; Kapp et al., 2005; DeCelles et al., 2007; DeCelles et al., 2007; Ma et al., 2013; Wu et al., 2016; Liu and Li, 2017), sedimentary evolution characteristics (Li and Fan, 2015a; Liu Y. et al., 2017; Lou and Liu, 2017; Wei et al., 2017; Zhao et al., 2019), source rock characteristics (Xu et al., 1996; Gu et al., 1999; Yuan and Xu, 2000; Sun et al., 2012; Pan et al., 2016; Liu Z. et al., 2017; Li, 2018a; Geng et al., 2019; Wang et al., 2019), reservoir conditions (Huang, 1994; Huang and Xiao, 1997; Li H. et al., 2022), geochemical characteristics of crude oil (Li and Tang, 1998; Fu et al., 2003; Li and Fan, 2015b; Li et al., 2016), comprehensive study of petroleum geology (Luo et al., 2016;

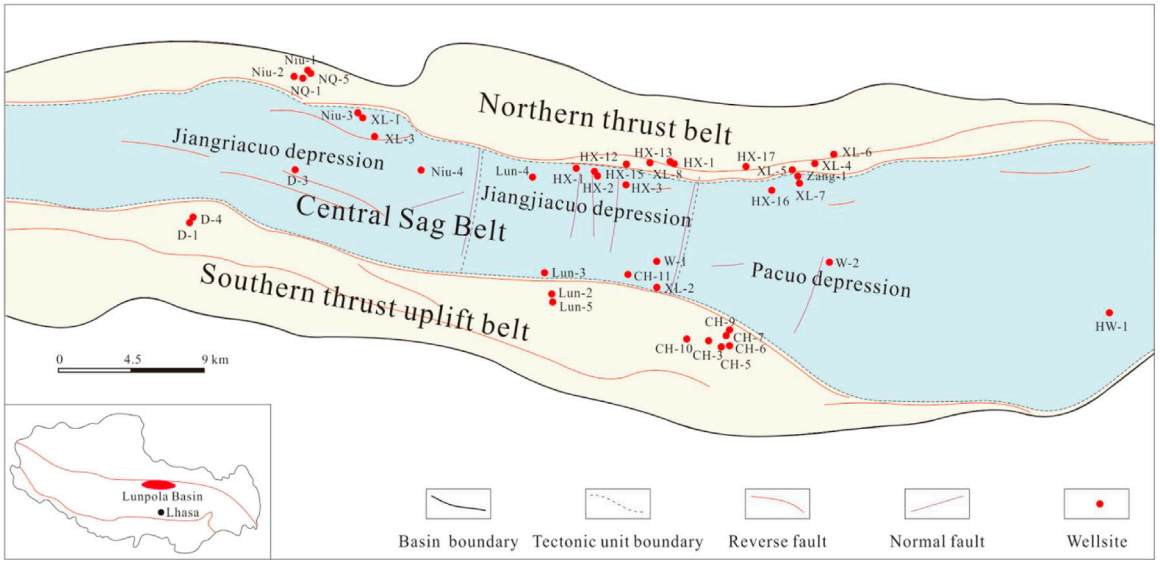

FIGURE 1
The tectonic division map of the Lunpola basin.

Lei and Fu, 1995; Zou et al., 1997; Fu and Xiao, 1998; Zhang et al., 2000; Sun et al., 2015; Fan et al., 2015; Pan et al., 2019), and oil and gas resource evaluation (Qiu, 1997; Gu et al., 1999; Chen et al., 2017; Wang et al., 2020),. Previous studies proposed the northern thrust nappe belt (Luo et al., 1994; Pan, 1994; Lei and Fu, 1995; Zou et al., 1997; Ai et al., 1998; Wu et al., 2016; Geng et al., 2019), southern slope belt (Luo, 1993; Fan et al., 2015; Liu Y. et al., 2017), and the central depression (Luo, 1993; Luo et al., 1994; Ma et al., 1996; Zou et al., 1997; Du et al., 2004; Pan et al., 2016; Wang et al., 2019), especially the Jiangriacuo depression (Pan, 1994; Liu Z. et al., 2017; Geng et al., 2019; Wang et al., 2019), the Jiangjiacuo depression or the tectonic-transformed area in the central depression (Lei et al., 1996; Xiao and Huang, 1996; Geng et al., 2019; Pan et al., 2019) is a favorable zone for oil and gas exploration in the Lunpola Basin. However, with the continuous advancement of oil and gas exploration, the exploration focus has changed from structural traps to lithologic traps. Two exploratory wells, Wang one and Wang 2, were designed for the lithologic trap targets, but the drilling results were not good (Li F. et al., 2018; Li H. et al., 2019). Therefore, it is urgent to reinvestigate the characteristics of oil and gas accumulation in the Lunpola Basin to clarify the main controlling factors of oil and gas accumulation, and point out the next exploration direction for oil and gas exploration in the Lunpola Basin.

2 Geologic overview

The Lunpola Basin is a basin developed on the basis of Yanshan Orogeny, which is deposited through subsidence, pull-apart and faulting process (Du et al., 2004). At the end of the Late Oligocene, the strong Himalayan movement caused the basin to be compressive and deformed, and the Oligocene Dingqinghu Formation was subjected to strong denudation, resulting in the current faults and the "dumbbell-shaped" structural features of the north-south zone and east-west block of the basin (Lei et al., 1996; Yuan and Xu, 2000; Li and Fan, 2015a). The basin gradually deepens from east to west. The eastern Pacuo area is generally a pattern of northward deepening and southward thrusting. The central Jiangjiacuo area is a south-north converging area and the west is a southward deepening and northward thrust pattern. From north to south, the basin can be divided into three first-order tectonic belts: the northern thrust nappe belt, the central depression belt and the southern thrust-uplift belt (Lei and Fu, 1995; Fu and Xiao, 1998; Liu Z. et al., 2017; Li J. et al., 2022). The central depression belt is further divided into three secondary tectonic units, including Jiangriacuo, Jiangjiacuo and Pacuo depressions (Figure 1).

Based on a comprehensive study of drilling data and seismic data, it is found that from bottom to top, the Eocene Niubao Formation (E_2n), the Oligocene Dingqinghu Formation (E_3d) and the Quaternary (Q) were successively deposited in the Cenozoic (Figure 2). The Niubao Formation (E_2n) is a set of brown-red clastic rocks intercalated with dark gray shale and gray-white marl, with a depositional thickness of 3000 m. From bottom to top, Niubao Formation can be divided into Niu-1, Niu-2 and Niu-3 section. The sedimentary characteristics of the Niu-1, Niu-2 and Niu-3 section has changed dramatically from the base to top, with grain size changing from coarse to fine tocoarse, the lithological color from red to black tored, which reflects the sedimentary cycles of proluvial fluvial facies - shallow lacustrine - semi-deep lacustrine facies - shallow lacustrine facies through time. This means that the sedimentary water body changes from shallow to deep and then to shallow. The sedimentary types mainly include alluvial fan (Niu-1section - lower Niu-2 subsection), fan delta (upper Niu-2 subsection - Ding-2 section), shallow lake (upper Niu-2 subsection - Dingqinghu Formation), semi-deep lacustrine - deep lacustrine (Niu-2 section, Ding-1 and Ding-2 sections). In the northeastern and southwestern steep slopes of the basin, sandy conglomerate bodies of nearshore subaqueous fans are mainly developed, while in the southeastern and northwestern parts, fan delta are mainly developed. The Changshan area in the southeast is the most important provenance area of the basin. Dingqinghu Formation (E_3d) is a set of semi-deep lacustrine-shallow lacustrine sedimentary assemblages mainly composed of gray-dark shale with oil shale, marl and fine sandstone, with a maximum deposition thickness of 1400 m. Dingqinghu Formation is also a good regional seal for the basin.

3 Hydrocarbon accumulation conditions

At present, a number of heavy oil and conventional oil and gas reservoirs have been discovered in the Lunpola Basin, including the Hongxingliang heavy-oil field and the Luomadiku conventional oil field in the central and eastern part of basin (Zou et al., 1997). In general, oil fields (reservoirs) are usually distributed in traps related to faults, and oil and gas are mainly distributed in Niu-2 and Niu-3 sections. On the plane, oil and gas reservoirs are mainly distributed on the northern and southern sides of the basin. In the northern basin, the heavy oil is mainly distributed in the northern thrust nappe belt from Ejiazu to Diezong area, which was formed at the end of the Oligocene. The buried depth of oil layer is only 200–500 m. In the southern basin, the petroleum is found in the thrust uplift belt in the south, from Lunpori to Changshan area, and adjacent to Jiangjiacuo and Pacuo oil-generating depressions in the north. Fan delta is developed in the Niubao Formation-Dingqinghu Formation in this area, especially near the Changshan structure, which is an inherited uplift anticline. The northern slope of the central depression zone, including the northern slopes of Jiangriacuo and Jiangjiacuo depressions, are another oil and gas accumulation

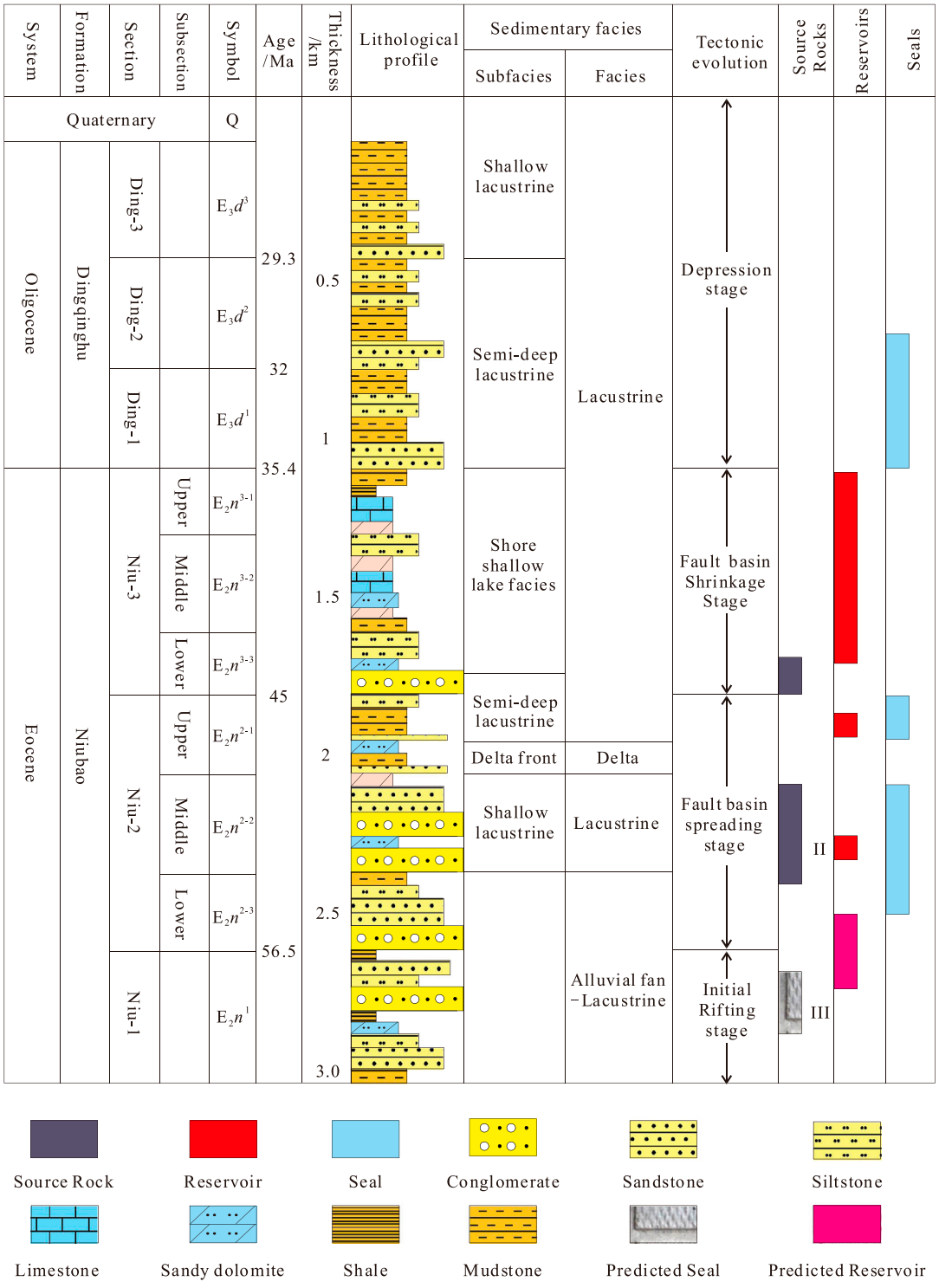

FIGURE2
The comprehensive histogram of the Lunpola basin.

TABLE 1 Organic matter microscopic components in downhole samples in Lunpola Basin.

Well name	Depth/m	Layer	Component and content (%)								Types of organic matter
			Bacterioalgae	Lipid group	Mirror group	Inert group	Humus matrix	Mixed matrix	Semi-filament and semi-lens	Fluorescence vitrinite	Shell debris	
Zang-1	1780	E2n2	9.30	2.10	3.68	0.88	80.00		1.05	2.11	0.88	I
	1994	E2n2	3.59	3.00	3.39	1.40	44.71	37.72	3	2.00	0.2	II1
XL-1	297.25	E2n3-2	6.53	9.42	2.69	0.96	73.32	3.46	1.34	1.34	0.96	I
	815	E2n3-1	4.67	2.91	3.11	0.78	85.22		0.78	2.34	0.19	I
	900	E2n3-1	0.18	2.57	3.67	2.57	44.04	42.57	1.84	1.47	1.10	II1
XL-2	940.32	E3day1	3.17	1.87	1.68	2.24	87.31		2.43	1.12	0.19	I
	1305	E2n3-2	0.18	2.17	2.66	0.71	90.94		1.07	1.78	0.53	I

area. In addition, HX-3 and HX-4 wells in the northern Jiangjiacuo depression also show good oil and gas performance. The abundant oil and gas shows indicate that the basin has good hydrocarbon-bearing properties and hydrocarbon accumulation conditions, but it also indicates that the oil and gas distribution in the study area is extremely complex after the later reworking (Fu and Xiao, 1998). Therefore, based on the previous research results, the author uses the research data of Wang-1 and Wang-2 wells to investigate the hydrocarbon accumulation conditions in the Lunpola Basin, and establish the hydrocarbon accumulation pattern in the study area.

3.1 Hydrocarbon source rock features

The source rocks are the primary geological element in the petroleum system. The study of source rocks is an important geological basis for reducing the risk of oil and gas exploration. The existence of source rocks determines the existence of petroleum systems and the direction of oil and gas exploration. Previous studies (Gu et al., 1999; Pan et al., 2016; Li Y. et al., 2018; Geng et al., 2019; Wang et al., 2019) believe that the main source rocks in the Lunpola Basin are mainly developed in Niu-2 section (E_2n^2) and lower Niu-3 subsection ($E_2n^{3\text{-}1}$). (Liu Y. et al., 2017). concluded that the southwestern depositional center had well-developed source rocks during the depositional period of Niu-1 section, through detailed field geological survey, seismic data reprocessing, and sedimentary fillings (thickness change), *etc.* This understanding breaks the point of view that Niu-1 section is a set of red beds without source rocks (Liu Z. et al., 2017).

3.1.1 Basic characteristics

Using the geochemical data of various samples, the source rocks of Niubao Formation were evaluated in terms of development scale, organic matter abundance, type and maturity. The results show that the Paleogene in Lunpola Basin mainly developed three sets of main source rocks, Niu-1 section, Niu-2 section and lower Niu-3 subsection. The source rock of Niu-1 section only develops in the Jiangriacuo depression in the southwest of the basin, and is exposed to the surface near the Bangor-382 Bridge in the southwest of the basin (Liu Y. et al., 2017). The lithology is semi-deep lacustrine-deep lacustrine black mud shale and few fine sandstone, with a thickness of 100–200 m. The organic parent material mainly comes from lower aquatic organisms, and the type of organic matter is mainly type I, with a small amount of type II_1~III mixed (Liu Z. et al., 2017). The lithology of the source rocks in Niu-2 section is mainly semi-deep lacustrine-deep lacustrine gray-dark gray mudstone and shale, with an average thickness of 300 m. The types of organic matter are mainly type I and II_1 (Table 1), and the organic matter abundance is 0.50%–3.52%. The type of organic matter is mainly

TABLE 2 Characteristics of main source rocks in the lumpura basin.

Layer	Average thickness/m	Maximum thickness/m	Organic matter abundance/%	Organic matter type	Maturity of organic matter (ro)/%	Remarks
E2n3-1	150	200	0.56–2.69% /1.00	Type I is predominant Small amount of type III	0.58–0.80	Changshan, Palongyaoma, Luomadiku, Hongxingliang and Jiangriacuo all developed
E2n2	300	600	0.50–3.52% /1.03	Type I is predominant Small amount of type III	0.66–1.14	Changshan, Palongyaoma, Luomadiku, Hongxingliang and Jiangriacuo all developed
E2n1	100–200			Type I is predominant Small amount of type II1 and III mixed		Only developed in Jiangriacuo depression

type I, and the maturity is 0.66%–1.14%. This set of source rocks is widely distributed in the basin and has the most favorable conditions for hydrocarbon generation. The organic matter abundance and type of lower Niu-3 subsection are superior, but the maturity is low. Considering the current oil and gas exploration situation, the thickness and abundance of the source rock in Niu-2 section show a decreased trend from west to east, and the source rock conditions in the central and western parts of the basin are generally better than those in the east (Gu et al., 1999; Li Y. et al., 2018; Geng et al. et al., 2019). For example, the Well XL-3 has good oil shows with oil bubble found on the core, reflecting the favorable oil source conditions in the Jiangriacuo depression and its periphery in the western part of the basin.

3.1.2 Oil-source correlation

Two indicator of light hydrocarbon components, cyclohexane and methylcyclohexane, can reflect the type of Kerogen. It is generally considered that light component cyclohexane <27% and methylcyclohexane <35% is sapropelic parent material, light component cyclohexane> 27% and methylcyclohexane>50% is humic parent material, and Methylcyclohexane between 35% and 50% is a mixed parent material. The distribution of methylcyclohexane in the source rock of Niu-2 section (E_2n^2) is 25%–50%, and the parent material type is characterized by sapropelic to mixed type. Methylcyclohexane in the source rock of Niu-3 lower subsection (E_2n^{3-1}) is between 40% and 60%, reflecting the mixed parent material type. The methylcyclohexane in crude oil is basically bounded by 20%–50%, which indicates that the parent material type is sapropel type to mixed type. The distribution of light hydrocarbon composition is between Niu-2 section and Niu-3 subsection. Accordingly, it is believed that the crude oil mainly comes from the source rocks of Niu-2 section and lower Niu-3 subsection.

In addition, the comparison of the carbon number distribution characteristics between the source rock extracts and crude oil reveals: ① the carbon number distribution of the crude oil from Niu-2 upper subsection (E_2n^{2-3}, 1730–1740 m) and Niu-2 middle subsection (E_2n^{2-2}, 1934–1942 m) in Well Zang-1, and Niu-2 section in Well XL-1 (E_2n^2,1457–1470 m), are similar with the source rock extracts from Niu-2 section, reflecting the feature of "Self-generation and self-storage". ② The carbon number distribution characteristics of the crude oil from middle Niu-3 subsection in Well XL-5 (E_2n^{3-2}, 1354.6–1350.6 m) and lower Niu-3 subsection in Well XL-4 (E_2n^{3-1}, 1446 m), are the same as the source rock extracts from Niu-3 subsection in Well XL-5 (E_2n^{3-1}), indicating that the crude oil comes from the source rock of lower Niu-3 subsection. The crude oil in middle Niu-3 subsection in Well XL-5 is characterized by "lower-generation and upper-storage", while Well XL-4 shows the feature of "self-generation and self-storage". ③ The carbon number composition distribution of saturated hydrocarbons in the crude oil of lower Niu-3 subsection in Well Wang-1 is similar to that in the crude oil of lower Niu-3 subsection in Well XL-4, middle Niu-3 subsection in Well XL-5 and Well Zang-1. Therefore, it is considered to have a certain relationship among them. To sum up, it has been found that the crude oil in the Lunpola Basin mainly comes from the source rocks of Niu-2 section and Niu-3 subsection, which is consistent with previous studies (Lu et al., 1997; Li and Tang, 1998).

3.2 Reservoir characteristics

The reservoir rocks in Lunpola Basin are dominated by clastic rock reservoirs (Ai et al., 1998), including Niu-1, Niu-2 and Niu-3 sections. The overall physical properties of the reservoirs are not good, and they are mainly located in the southern uplift belt and the northern thrust nappe belt in the basin. The sedimentary facies of the reservoir are mainly delta plain subfacies and subaqueous distributary channels, such as the sandy conglomerates of the distributary channel in Niu-3 section in Well Wang-1, and the scour surface at the bottom of the core is obvious (Figure 3). Based on previous researches (Lei and Fu, 1995; Zhang and Zou, 1995) and the latest research results, the reservoirs of Niubao Formation can be divided into three types

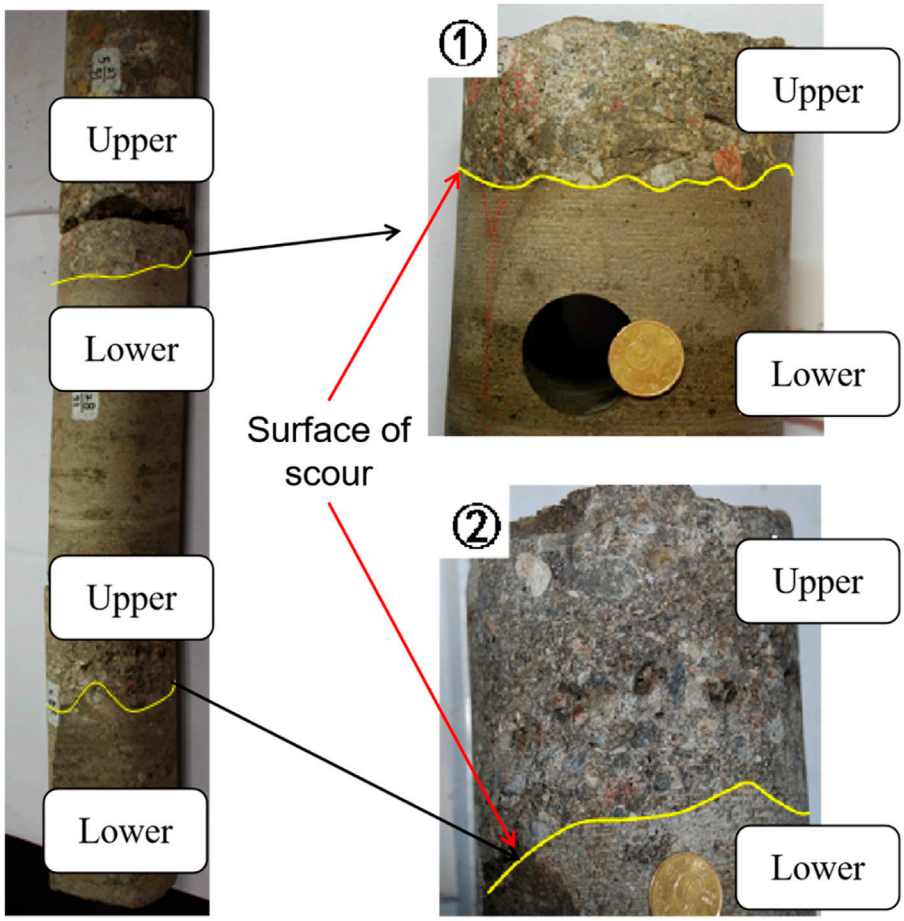

FIGURE 3
The core of underwater distributary channel in Well Wang-1.

according to their strata distribution: ①The first type is the coastal delta sandstone in lower Niu-3 subsection with a burial depth of 900–1600 m generally. It is characterized by large reservoir thickness (>5 m) and good physical properties, but shallow burial depth and poor sealing conditions. ② The second type is the coastal beach sandstone interbedded with dark-grey mudstone and shale in Niu-2 section, with a buried depth of 1200–2300 m. The reservoir sealing conditions are good, but the thickness of this type of reservoir is relatively thin, mostly less than 1 m. Therefore, its oil and gas production capacity is not optimistic. ③ The third type is the channel sandstone and nearshore subaqueous fan sandstone developed at the bottom of Niu-2 section and the top of Niu-1 section. The depth is generally greater than 2300 m. This type of reservoir has a large thickness and relatively coarse lithology. Its lower part is directly connected to the source rock of Niu-1 section. While its upper part is covered by the dark-gray mudstone and shale of Niu-2 section. It should be noticed that this set of reservoirs is deeply buried and less affected by the later tectonic movement. Therefore, its potential oil-gas bearing capacity and productivity cannot be underestimated. Therefore, the Niu-1 section may be an exploration target for obtaining major breakthroughs in oil and gas.

There are various types of pores in the reservoir, mainly including intergranular dissolved pores, intragranular dissolved pores, fractures and a very small amount of primary intergranular pores (Figure 4). The overall performance is fractured-porous reservoir. The reservoirs are mainly developed in the Niu-2 and Niu-3 sections. The measured porosity is mostly less than 15%, with an average of 7.12%. The permeability is usually less than 40.4mD, and the geometric mean is 0.1031mD. Statistics show that the reservoir porosity of Niu-2 section is –14%, with an average of 5.2%. The permeability is 0.0062–19.27mD, and the geometric average is 0.08mD. The reservoir porosity of Niu-3 section is 0.1%–32.6%, with an average of 7.73%. The permeability ranges from 0.0005 to 116 mD, and the geometric mean is 0.12 mD (Table 3). According to "Oil and gas reservoir evaluation

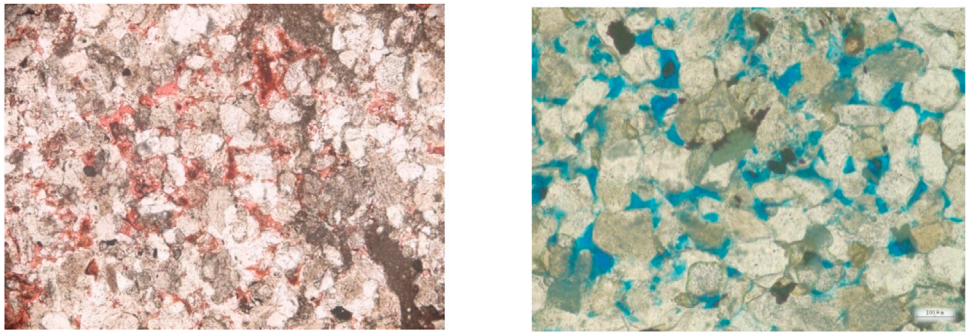

FIGURE 4
Reservoir space types of clastic rocks in Niubao Formation.

TABLE 3 Statistical of the physical properties of drilling reservoirs in the lumpura basin.

Layer	Sample number	Porosity/%	Permeability/10−3μm2
Niu-3 section	194	0.1–32.6	0.0005–116
		7.73	0.12
Niu-2	62	0.5–14.0	0.04–3.61
section		5.2	0.08
Average		7.12	0.1031

method of SY6285-2011-T″, the reservoir porosity in this area is between 0.1% and 32.6%, mainly between 2.0% and 10.0%, with an average of 6.5%, which belongs to ultra-low porosity reservoir. A few wells has porosity of –30.0%, which is a medium-high porosity reservoir. The permeability is between 0.0005 mD and 116.0 mD, mainly between 0.01 mD and 0.5 mD, which is an ultra-low permeability reservoir. Occasionally, the permeability of some samples is between 1.0 mD and 500 mD, which is a medium-low permeability reservoir. According to comprehensive evaluation, the reservoirs in this area are generally ultra-low porosity-ultra-low permeability fracture-pore reservoirs, and medium-low porosity and medium-low permeability fracture-pore reservoirs are locally developed. In addition, the physical properties of the reservoirs developed at the bottom of Niu-2 section and the upper part of Niu-1 section have not been verified by drilling, but it is inferred from the results of regional data analysis that these reservoirs have good physical properties.

3.3 Sealing characteristics

The Lunpola Basin has undergone late uplift and denudation, and Niubao Formation or Mesozoic and older strata are widely exposed in the northern thrust nappe tectonic belt and the southern thrust uplift belt. Therefore, the sealing condition is one of the controlling factors for the hydrocarbon accumulation in the study area. During the stage of prototype basin and basin reformation, several sets of thick semi-deep lacustrine-deep lacustrine shale were deposited, which played a good role in sealing oil and gas. Except for the poor sealing capacity of Niu-1 section, the other layers have a certain degree of sealing ability. There are two types of seals developed in the Lunpola Basin, namely the direct seal of upper Niu-2 subsection and the regional seals of middle Niu-2 subsection and Dingqinghu Formation. According to the drilling results of Well Wang-1, there is a set of high-quality seal about 100 m thick developed in upper Niu-2 subsection, which can play a good role in sealing the hydrocarbon in the lower Niu-2 section or its own. Most of the fluorescent thin sections of Niu-2 section in Well Wang-1 show normal blue light, and the logging shows that the total hydrocarbons are higher than the above strata, which confirms the good capping ability of upper Niu-2 subsection. Similarly, the dark shale in middle Niu-2 subsection is both a good source rock and a regional seal with good sealing ability (Du et al., 2004), which is widely distributed in the basin (Table 4). It can be seen that in the relatively stable central depression belt, several sets of seals are

TABLE 4 Macroscopic development characteristics of Paleogene seals in Lunpola basin.

Single-layer feature	Niu-2 section	Dingqinghu formation
Lithology	Mudstone, shale	Mudstone, shale
Sedimentary facies	Shallow-semi-deep-deep lacustrine	Shallow-semi-deep-deep lacustrine
Maximum cumulative thickness/m	1258	975
Maximum single-layer thickness/m	78	52.9
Depth/m	1600–3000	0–1400
Formation time	Before oil generation	Before main oil generation
Plasticity	Better	Good
Distribution	Stability	More stable
Evaluation	Good	Better

relatively developed, which is conducive to the preservation and accumulation of generated oil and gas in the basin. In the areas with relatively strong tectonic movements on the northern and southern sides of the basin, due to the deep burial depth, the damage degree of the seals of Niubao Formation is relatively low, and thus it still has a good sealing ability.

3.4 Hydrocarbon accumulation pattern

On the basis of the tectonic evolution of the basin, the hydrocarbon accumulation conditions of source rocks, reservoirs and seals in the Lunpola Basin were comprehensively analyzed, and the hydrocarbon accumulation pattern of Lunpola Basin was constructed (Figure 5). As shown in Figure 5, the structural traps are located in the thrust nappe belt in the north and the Changshan uplift area in the south, and lithologic traps in the central basin. The oil and gas generated from the source rocks of Niu-2 and Niu-3 sections migrated to the traps along the faults or sandstones, forming "self-generation and self-storage" or "lower-generation and upper-storage" reservoirs. While lithologic traps are mainly developed in the central depression belt. The oil and gas generated by the source rocks are transported to nearby sand bodies to form "self-generation and self-storage" reservoirs. It can be seen that the hydrocarbon accumulation in the Lunpola Basin is mainly controlled by source rocks, reservoirs and preservation conditions.

Since the end of the Eocene, the source rocks of Niu-2 began to mature and generate hydrocarbons, and oil and gas migrated along micro-fractures, faults and sandstones, forming oil and gas reservoirs in the paleo-uplift developed in the Changshan area in the south and the Hongxingliang area in the north. At the end of the Oligocene, under the influence of the north-south oriented compression, the two belts in the north and south of the basin were thrust and overthrow successively. The paleo-reservoirs formed in the northern part of the basin were adjusted to shallow depth to form bituminous plugs. At the same time, for the oil reservoirs of Niubao Formation in the southern Changshan area, due to thrust and folds (the anticline shape is still complete), the oil from Niubao Formation migrated to the overlying Dingqinghu Formation along the micro-fractures, unconformity surface and permeable rock strata. Since the Late Miocene, affected by the strong uplift of the Qinghai-Tibet Plateau, the paleo-reservoirs in the north and south of the basin have been further adjusted and destroyed, resulting in the loss of oil and gas and the formation of heavy oil reservoirs by water washing, oxidation and biodegradation of the ancient reservoirs at the edge of the basin. However, the mid-deep buried subtle traps in the northern thrust belt and the lithologic traps in the central depression belt have good preservation conditions and can still form normal oil reservoirs (Li F. et al., 2018; Li Y. et al., 2019). The industrial oil flow tested in Well Zang-1 has well confirmed the oil and gas enrichment law of the subtle structures in the lower part of the northern thrust nappe belt (Lu et al., 1997; Gu et al., 1999). The source rock of Niu-1 section in the Jiangriacuo depression has a larger burial depth and is less affected by tectonic movements in the later period. Therefore, it has better preservation conditions and other oil and gas geological elements for lithologic oil and gas reservoirs formation.

4 Favorable area prediction

The lithology and lithofacies of continental deposits change frequently and the reservoir distribution is relatively limited. Therefore, it is difficult for large-scale and long-distance hydrocarbon migration after oil and gas generation, resulting in the oil and gas reservoirs often developed in the center of oil-generating depressions and its periphery (Ju et al., 2016;; Li, 2022a). As mentioned above, the good source rocks are widely developed in the Lunpola Basin. The reservoir is mainly low porosity - ultra-low permeability fracture - porosity reservoir with poor physical property. In addition, the strong tectonic

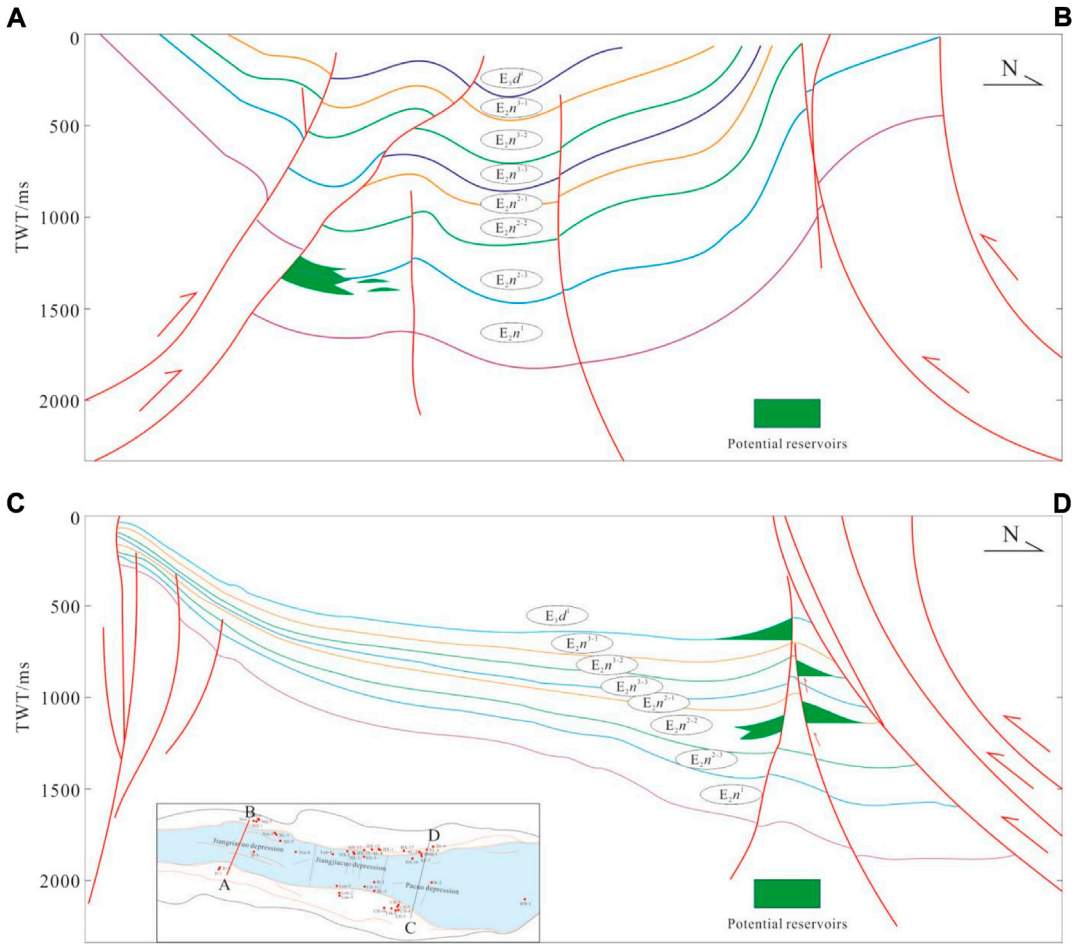

FIGURE 5
Prediction diagram of hydrocarbon accumulation pattern in Lunpola Basin.

movements have a great destructive effect on the oil and gas reservoirs that have been formed in the early stage. Therefore, reservoir conditions and post-preservation conditions are the main controlling factors for hydrocarbon accumulation in the study area. Based on this, two favorable exploration zones are proposed, the footwall of the northern thrust nappe belt and the southern slope of the Jiangriacuo depression (Figure 6).

4.1 Footwall of the northern thrust nappe belt

The northern thrust nappe belt is located between the Hongxingliang fault zone and the Dayushan North fault zone, and is represented by a set of thrust nappe rock bodies (such as Dayushan, Hongxingliang, Niubao, *etc.*) formed by thrusting from north to south. The stratum is mainly composed of Niubao Formation, with coarse lithology, steep slope, and basin marginal sedimentary facies. Because the upper wall of the main thrust fault shields or absorbs most of the tectonic stress, the two flanks of the anticline and the overlying Niu-3 section formed in this area have been completely eroded, resulting in the accumulated oil and gas in it to leak out completely. On the other hand, the deformation of the footwall of the thrust fault is relatively slight, and most of the strata remain horizontal or form some wide and gentle folds. Some extensional structures formed during the basin construction period, such as normal faults and their associated structures, are preserved, which is conducive to the preservation of oil and gas (Figure 7) (Pan, 1994; Zhang and Zou, 1995; Ai et al., 1998). This is also confirmed by the exploration practice of Well Zang-1 and Well HX-16.

It can be seen from Figure 7 that the northern thrust nappe belt is adjacent to the hydrocarbon-generating center of the Jiangjiacuo-Pacuo depressions, and there is a set of Tertiary sediments in the footwall of the thrust fault, indicating that the

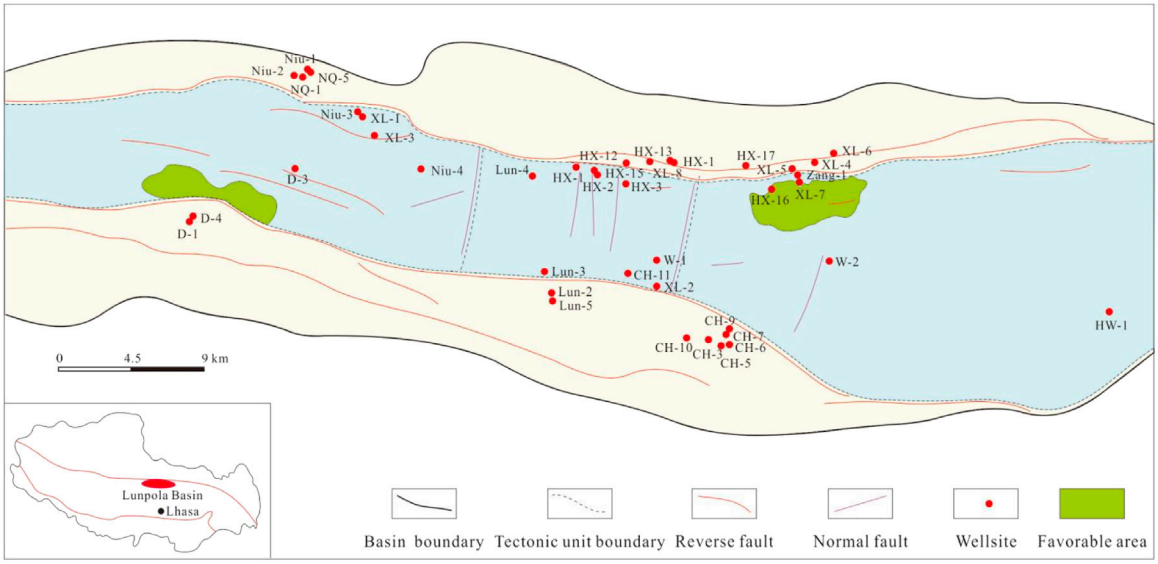

FIGURE 6
Prediction of the favorable areas for oil and gas exploration in the Lunpola Basin.

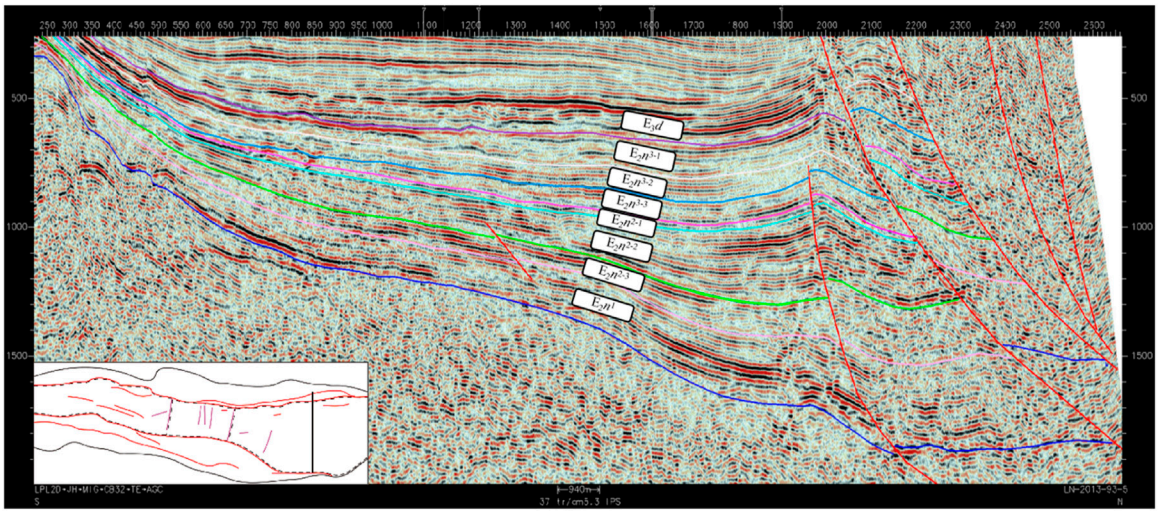

FIGURE 7
Seismic interpretation along line LN 2013–93.5 in NS direction in the eastern Lunpola Basin.

oil source conditions in this area are good. Along the main fault footwall in the northern boundary of Lunpola Basin, sedimentary systems such as nearshore subaqueous fans, fan deltas and alluvial fans are developed connecting or overlapping with normal faults, improving the reservoir physical conditions (Li H. et al., 2019; Li H. et al., 2022). After the Oligocene, the local structures developed were sealed by thrust faults or the regional seals in the area, forming a good hydrocarbon preservation condition. In addition, the northern uplift zone was the oil and gas migration and accumulation zone at the end of the Eocene (Lei et al., 1996). It can be seen that regardless of oil source

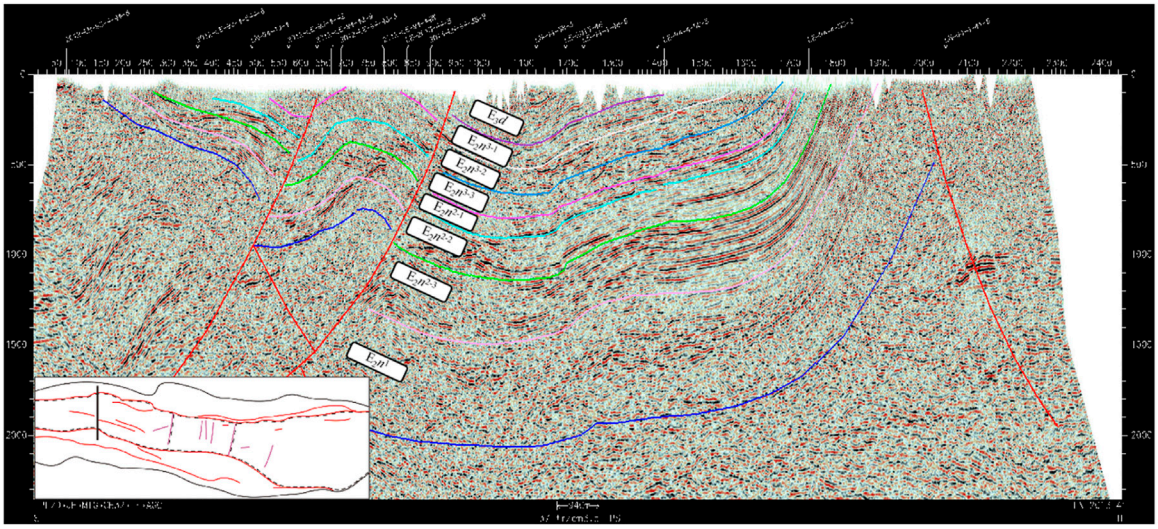

FIGURE 8
Seismic interpretation along line LN 2013–41 in NS direction in the western Lunpola Basin.

conditions, storage conditions, structural conditions, and later preservation conditions in this area, the footwall of the northern thrust nappe belt has best configuration and superposition of hydrocarbon accumulation elements, especially in the eastern Luomadiku area. We suggest the future exploration will focus on structural traps in the footwall of the northern thrust nappe belt, by using 3D seismic data to identify traps and design wells, to achieve new breakthroughs in oil and gas exploration.

4.2 Deep exploration zone in the south slope of jiangjiacuo depression

Sedimentological studies reveal that in the early depositional stage of Niubao Formation, there were obvious syn-depositional faults developed on the southern side of Jiangriacuo (Figure 8). A set of semi-deep lacustrine-deep lacustrine dark shale were deposited in the southwestern depositional center, with an effective thickness of 100–200 m, which is a set of potentially effective source rocks (Liu Z. et al., 2017). As the water depth gradually became shallower, a set of nearshore subaqueous fan sandbodies were deposited in the upper part of Niu-1 section (Liu Y. et al., 2017). This set of sand bodies, together with the coarse-grained sediments deposited in the lower part of Niu-2 section, constituted the third type of reservoir in the study area. This set of reservoirs has a large thickness, relatively coarse lithology, and relatively good reservoir conditions. The regional seals of Niu-2 section are widely developed. In addition, because this set of reservoirs is deeply buried, and negative influence from the later tectonic movement, e.g., the uplift of the Qinghai-Tibet Plateau, is relatively weak. This reservoir has the best oil and gas preservation condition at present. Therefore, its potential oil and gas bearing capacity and productivity should not be underestimated.

5 Conclusion

1) The Paleogene in the Lunpola Basin mainly has three sets of main source rocks, lower Niu-3 subsection, Niu-1 and Niu two sections. The lithology is mainly semi-deep lacustrine-deep lacustrine gray-dark gray mudstone and shale. Among them, the source rock of Niu-1 section is only developed in the Jiangriacuo depression in the western part of the basin, while the source rock of Niu-2 section are the most favorable in the region. The effective source rocks have the largest thickness in the central and western parts of the basin, and have the best hydrocarbon-generating capacity. To the east, the thickness and abundance of the source rocks show a decreased trend. The types of organic matter are mainly Type I and Type II_1, with a maturity of 0.58–1.08%.
2) The study area mainly develops clastic rock reservoirs, which can be divided into three types according to the characteristics of strata distribution. The reservoir conditions are generally poor. The reservoir porosity is between 0.1% and 32.6%, mainly between 2.0% and 10.0%, with an average of 6.5%. The permeability is between 0.0005mD and 116.0mD, mainly between 0.01mD and 0.5mD. It can be defined as a fracture-

porous reservoir with ultra-low porosity and ultra-low permeability

3) There are mainly two types and three sets of seals developed in the Lunpola Basin, including two sets of regional seals in middle Niu-2 subsection and Dingqinghu Formation, and one set of direct caprock in upper Niu-2 subsection. In the relatively stable central depression belt and the footwall of the thrust nappe belt in the northern part of the basin, the seals are relatively developed and have good preservation conditions.
4) The oil and gas reservoirs in the Lunpola Basin have the distribution law of "structural traps in the north and south, and lithologic traps in the center". Structural traps are mainly developed in the thrust nappe belt in the north and the Changshan uplift area in the south, forming "self-generation and self-storage" or "lower-generation and upper-storage" reservoirs. While lithologic traps are mainly developed in the central depression belt, forming "self-generation and self-storage" reservoirs.
5) The footwall of the northern thrust nappe belt and the deep strata of the southern slope of Jiangriacuo depression are the most favorable oil and gas exploration areas in future exploration in the Lunpola Basin.

Data availability statement

The original contributions presented in the study are included in the article/supplementary material, further inquiries can be directed to the corresponding author.

Author contributions

ZY completed the writing and revision of the manuscript, XJ completed the polishing of English, and others completed the drawing and other related content.

Funding

This work was supported by National Shale Oil and Gas Resources Potential and Comprehensive Evaluation of Oil and Gas Blocks (Fund number: DD20221852).

Conflict of interest

The reviewer JZ declared a shared affiliation with the author JX to the handling editor at the time of review

The authors declare that the research was conducted in the absence of any commercial or financial relationships that could be construed as a potential conflict of interest.

Publisher's note

All claims expressed in this article are solely those of the authors and do not necessarily represent those of their affiliated organizations, or those of the publisher, the editors and the reviewers. Any product that may be evaluated in this article, or claim that may be made by its manufacturer, is not guaranteed or endorsed by the publisher.

References

Ai, H., Lan, L., Zhu, H., Zhang, K., and Zou, T. (1998). Formation mechanism and petroleum geological characteristics of Lunpola tertiary basin. *Acta Pet. Sin.* 19 (2), 21–27.

Chen, P., Fei, Q., and Lu, Y. (1998). The relationship between the evolution of clay minerals and the maturity of source rocks in the Lunpola basin. *Exp. Pet. Geol.* 20 (3), 282~286.

Chen, S., Liu, B., Liu, X., and Liu, Z. (2017). A preliminary study of the Paleogene shale oil potential in Lunpola basin, Tibet. *Acta Geosci. Sin.* 38 (5), 839–846.

DeCelles, P. G., Quade, J., Kapp, P., Fan, M., Dettman, D. L., and Ding, L. (2007). High and dry in central Tibet during the late Oligocene. *Earth Planet. Sci. Lett.* 253 (3-4), 389–401. doi:10.1016/j.epsl.2006.11.001

Deng, T., Wu, F., Wang, S., Su, T., and Zhou, Z. (2019). Significant shift in the terrestrial ecosystem at the Paleogene/Neogene boundary in the Tibetan Plateau. *Chin. Sci. Bull.* 64 (27), 2894–2906. doi:10.1360/tb-2019-0053

Ding, L. (2007). Late Cretaceous to middle Tertiary basin evolution in the central Tibetan Plateau: Changing environments in response to tectonic partitioning, aridication, and regional elevation gain. *Geol. Soc. Am. Bull.* 119 (5-6), 654–680.

Du, B., Tan, F., and Chen, M. (2004). Sedimentary features and petroleum geology of the Lunpola basin, xizang. *Sediment. Geol. Tethyan Geol.* 24 (4), 46–54.

Fan, X., Pan, L., Li, F., Li, J., Hou, D., and Hao, J. (2015). Hydrocarbon accumulation mechanism and play fairways of the paleocene in Lunpola basin, Tibet. *Oil Gas Geol.* 36 (3), 362–377.

Fu, X., Lu, Y., and Xiao, Q. (2003). Discussion on the Vertical characteristics of oil-gas oxygenation level and its preservation condition in Petroleum Basin-A case study on the continental Tertiary Basin in Lunpola, Tibet. *Exp. Pet. Geol.* 25 (6), 773–776.

Fu, X., and Xiao, Q. (1998). Occurrence characteristics and formation regularity of oil and gas in Lupola Basin, Tibet. *Zhongyang Oil Gas Explor.* (1), 1–7.

Geng, T., Mao, X., Wang, H., Fan, X., and Wu, C. (2019). Thermal evolution history and prediction of favorable zones in Lunpola Basin. *Litho Log. Reserv.* 31 (6), 67–78.

Gu, Y., Shao, Z., Ye, D., Zhang, X., and Lu, Y. (1999). Characteristics of source rocks and resource prospect in the Lunpola Basin, Tibet. *Exp. Pet. Geol.* 21 (4), 340–345.

Huang, Z. (1994). [The study of insertion sequence on IS2. I. Polarity and inserted direction of IS2]. *Tibet. Geol.* 21 (2), 161–168.

Huang, Z., and Xiao, Q. (1997). A study of reservoir characteristic of sandstone of the Niubao formation in Lunpola Basin, North Xizang. *Tibet. Geol.* (2), 31–40.

Ju, Y., Qi, Y., Fang, L., Zhu, H., Wang, G., and Wang, G. (2016). China shale gas reservoir types and its controlling factors. *Adv. Earth Sci.* 31 (8), 782–799.

Kapp, P., Yin, A., Harrison, T. M., and Ding, L. (2005). Cretaceous-Tertiary shortening, basin development, and volcanism in central Tibet. *Geol. Soc. Am. Bull.* 117 (7-8), 865–878. doi:10.1130/b25595.1

Lei, Q., and Fu, X. (1995). Analysis of petroleum geological characteristics of tertiary continental basin in Lunpola, Tibet. *Zhongyang Oil&Gas Explor.* (1), 1–8.

Lei, Q., Fu, X., and Lu, Y. (1996). Petroleum geological features of tertiary terrestrial Lunpola basin, xizang(tibet). *Earth Science-Journal China Univ. Geosciences* 21 (2), 168–173.

Li, D., Xing, F., Chen, X., Liu, Z., Chen, T., and Zhou, S. (2020). Reservoir characteristics and main controlling factors of lacustrine dolostones in the Eocene Niubao Formation, Lunpola Basin. *J. Northeast Petroleum Univ.* 44 (2), 24–35.

Li, F., Xiang, W., and Xu, H. (2018b). Self-assembly regulated anticancer activity of platinum coordinated selenomethionine. *Biomaterials* 12 (5), 17–25. doi:10.1016/j.biomaterials.2017.12.001

Li, H. (2022). Research progress on evaluation methods and factors influencing shale brittleness: A review. *Energy Rep.* 8, 4344–4358. doi:10.1016/j.egyr.2022.03.120

Li, H., Tang, H. M., Qin, Q. R., Zhou, J. L., Qin, Z. J., Fan, C. H., et al. (2019b). Characteristics, formation periods and genetic mechanisms of tectonic fractures in the tight gas sandstones reservoir: A case study of xujiahe Formation in YB area, sichuan basin, China. *J. Petroleum Sci. Eng.* 178, 723–735. doi:10.1016/j.petrol.2019.04.007

Li, H., Zhou, J. L., Mou, X. Y., Guo, H. X., Wang, X. X., An, H. Y., et al. (2022a). Pore structure and fractal characteristics of the marine shale of the longmaxi Formation in the changning area, southern sichuan basin, China. *Front. Earth Sci.* 10, 1018274. doi:10.3389/feart.2022.1018274

Li, J., Li, H., Yang, C., Wu, Y. J., Gao, Z., and Jiang, S. L. (2022b). Geological characteristics and controlling factors of deep shale gas enrichment of the Wufeng-Longmaxi Formation in the southern Sichuan Basin, China. *Lithosphere* 2022, 4737801. doi:10.2113/2022/4737801

Li, Q., and Tang, P. (1998). Distribution and genesis of heavy oil in Hongxingliang clamping zone of Lunpola basin. *Zhongyang Oil Gas Explor.* (2), 15–20.

Li, Y., and Fan, X. (2015a). Geological origin of crude oil thickening in the reservoir of Niubao Formation in Lunpola basin, Tibet. *Petroleum Geol. Recovery Effic.* 22 (6), 32–46.

Li, Y., and Fan, X. (2015b). Structure-sedimentary model and subtle reservoirs in fault-depression basins--An example of the Paleogene System in the Lunpola Basin, Tibet. *Geol. Explor.* 51 (4), 0789–0796.

Li, Y., Wu, X., Wang, R., and Xia, X. (2019a). New findings of oil and gas from Wang 2 well in rumpela basin, Tibet. *China Geol.* 46 (3), 662–663.

Li, Y., Wu, X., Wang, R., and Xia, X. (2018a). New findings of oil and gas in central depression of Lunpola Basin. *Tibet. China Geol.* 45 (4), 853–854.

Li, Y., Ye, J., Cao, Q., Liu, Y., and Liu, Z. (2016). Geochemical characteristics of crude oil in Lunpola Basin. *Tibet. Special Oil Gas Reservoirs* 23 (3), 71–74.

Liu, Y., Ye, J., Cao, Q., Liu, Z., and Yang, B. (2017a). Preliminary prediction and evaluation of source rocks in the Lunpola basin, Tibet, China. *Earth Sci.* 42 (4), 601–612.

Liu, Z., Cao, Q., and He, Z. (2017b). Sedimentary characteristics and gas-oil exploration significance of the first member of Niubao Formation in the Lunpola Basin, Tibet. *Geol. Sci. Technol. Inf.* 36 (6), 174–180.

Liu, Z., and Li, X. (2017). Late tectonic deformation characteristics and stress mechanism in Lunpola Basin, Tibet Plateau. *Petroleum Geol. Exp.* 39 (6), 819–824.

Lou, G., and Liu, S. (2017). Sedimentary response characteristics of lake salinization in Lunpola Basin. *Complex Hydrocarb. Reserv.* 10 (4), 1–6.

Lu, Y., Shao, Z., and Bai, S. (1997). Geochemical properties of crude oil in zang-1 well, Lunpola basin, northern Tibet. *Exp. Pet. Geol.* 19 (4), 377–381.

Luo, B., Lu, Y., Luo, X., Qi, K., Fu, X., and Liu, X. (1994). Preliminary understanding of petroleum geological characteristics of Lunpola basin in Tibet. *Zhongyang Oil&Gas Explor.* (1), 16–21.

Luo, X. (1993). Discussion on structural characteristics and oil exploration direction of Lunpola Basin, Tibet. *Zhongyang Oil&Gas Explor.* (1), 8–12.

Ma, L., Zhang, E., Ju, J., Lei, Q., and Zou, J. (1996). Basic characteristics of Paleogene deposition systems tract in Lunpola basin, xizang(tibet). *Earth Science-Journal China Univ. Geosciences* 21 (2), 174–178.

Ma, P., Wang, L., and Ran, B. (2013). Subsidence analysis of the cenozoic Lunpola Basin, central Qinghai-Tibetan plateau. *Acta Petrol. Sin.* 29 (3), 990–1002.

Pan, L., Cao, Q., Liu, Y., Li, Y., Wang, Y., and Li, Z. (2016). Maturity history of source rocks in the Eocene Niubao Formation, Lunpola basin. *Petroleum Geol. Exp.* 38 (3), 382–388.

Pan, L., Wang, J., Li, X., and Ma, C. (2019). Strike-slip faults and their effects on the hydrocarbon accumulation in the central depression of the Lunpola Basin in Xizang. *Sediment. Geol. Tethyan Geol.* 39 (2), 27–34.

Pan, Z. (1995). Analysis of tectonic lithofacies model in Lunpola basin, Tibet. *Zhongyang Oil Gas Explor.* (2), 8–13.

Pan, Z. (1994). Structural analysis and favorable zone evaluation of Lunpola basin, Tibet. *Zhongyang Oil&Gas Explor.* (2), 1–12.

Qiu, D. (1997). Some aspects of the assessment of the oil and gas resources in Xizang(Tibet). *Tethyan Geol.* 21, 1–6.

Snowball column for incoming calls and power outages (2021). *Data of crude oil and oil products of China in 2021*. [EB/OL]. 2022 [23 May 2022] Https://xueqiu.com/4774493504/216058575.

Sun, T., Wang, C., Li, Y., and Wei, Y. (2012). Characteristics and significance of sedimentary organic matter in the Paleocene of Lunpola Basin, central Tibet. *Geochimica* 41 (6), 530–537.

Sun, W., Li, Z., Xiao, Q., Wang, X., and Wang, C. (2015). Analysis of petroleum accumulation of Paleogene Niubao Formation in middle-deep underground on north margin of Lunpola basin, Tibet, China. *J. Chengdu Univ. Technol. Technol. Edtion)* 42 (4), 419–426.

Wang, H., Mao, X., Geng, T., Fan, X., and Li, W. (2019). Characteristics and distribution prediction of source-rocks in the Niubao Formation of continental Lunpola basin. *Special Oil Gas Reservoirs* 26 (6), 35–40.

Wang, R., Wu, X., Xia, X., Li, Y., Cao, J., Xiang, Z., et al. (2020). Suppression of p66Shc prevents hyperandrogenism-induced ovarian oxidative stress and fibrosis. *J. Transl. Med.* 26 (1), 84–95. doi:10.1186/s12967-020-02249-4

Wei, W., Lu, Y., Liu, Z., Pan, L., Lin, W., and Jian, H. (2017). Sequence stratigraphic framework and sedimentary model of Niubao Formation in Lunpola basin, central Tibet. *Petroleum Geol. Exp.* 39 (1), 32–40.

Wu, Z., Zhao, Z., Ye, P., and Ji, C. (2016). The siling Co-Lunpola thrust systems in the central Tibetan plateau. *Acta Geosci. Sin.* 37 (4), 441–448.

Xiao, Q., and Huang, Z. (1996). Characteristics of geological structure and oil and gas in Lunpola Basin. *Zhongyang Oil Gas Explor.* (2), 8–14.

Xu, S., Mei, L., and Deng, S. (1996). Simulation of hydrocarbon generation and expulsion history in Lunpola basin of xizang(tibet). *Earth Science-Journal China Univ. Geosciences* 21 (2), 179–183.

Yuan, C., and Xu, S. (2000). Characteristics of geotemperature field and maturity history of source rocks in Lunpola Basin, Xizang (Tibet). *Exp. Pet. Geol.* 22 (2), 156–160.

Zhang, D., and Zou, J. (1995). Analysis on the situation of oil and gas exploration and development in the central and eastern part of Lunpola Basin, Tibet. *Zhongyang Oil Gas Explor.* (2), 1–7.

Zhang, K., Mou, Z., Zhu, H., Ai, H., Feng, F., and Luo, Y. (2000). Systematic analysis of reservoir-forming dynamics in Lunpola basin, Tibet. *Xinjiang Pet. Geol.* 21 (2), 93–96.

Zhao, S., Xie, X., Liu, Z., Lu, Y., Xiao, S., and Deng, Y. (2019). Control of tectonic-paleogeomorphology on deposition system of faulting-subsiding basin:A case from the Eocene Niubao Formation in Lunpola basin, central Tibet. *Geol. Sci. Technol. Inf.* 38 (2), 53–64.

Zou, J., Wu, Y., Wei, J., and Zhang, X. (1997). Seismic geological analysis and evaluation of Lunpola Basin. *Tibet. Tibet. Geol.* (1), 19–28.

frontiers | Frontiers in Earth Science

TYPE Original Research
PUBLISHED 06 January 2023
DOI 10.3389/feart.2022.1042927

OPEN ACCESS

EDITED BY
Wenlong Ding,
China University of Geosciences, China

REVIEWED BY
Nan Wu,
Yangtze University, China
Wei Yang,
Southwest Petroleum University, China
Ke Xu,
PetroChina Tarim Oilfield Company, China
Li Dong,
SINOPEC Petroleum Exploration and Production Research Institute, China

*CORRESPONDENCE
Junhao He,
913844322@qq.com

SPECIALTY SECTION
This article was submitted to Structural Geology and Tectonics, a section of the journal Frontiers in Earth Science

RECEIVED 13 September 2022
ACCEPTED 22 December 2022
PUBLISHED 06 January 2023

CITATION
Si S, Zhao Y, Er C, Bai Y, Wu W and He J (2023), Reservoir properties and genesis of tight sandstones—A case study from the Gaotaizi oil layer in the Qijia area, Songliao basin.
Front. Earth Sci. 10:1042927.
doi: 10.3389/feart.2022.1042927

Reservoir properties and genesis of tight sandstones—A case study from the Gaotaizi oil layer in the Qijia area, Songliao basin

Shanghua Si[1,2], Yutao Zhao[3], Chuang Er[1], Yubin Bai[1], Weitao Wu[1] and Junhao He[1]*

[1]School of Earth Sciences and Engineering, Xian Shiyou University, Xian, China, [2]Shaanxi Key Laboratory of Petroleum Accumulation Geology, Xian, China, [3]Exploration and Development Research Institute of Jilin Oilfield Company Ltd. Songyuan, Jilin, China

The primary focus of oil and gas exploration for tight sandstone reservoirs is on a quantitative characterization of reservoir properties. This paper uses the tight sandstone reservoir developed in the Gaotaizi oil layer in the Qijia area of the Songliao Basin as an example. The petrology, physical properties, pore–throat characteristics, and the genesis of the densification of the oil-bearing sandstones are elucidated using casting thin-sections, scanning electron microscopy, 3D computerized tomography (CT), and petrophysical experimental techniques. The results show that the Gaotaizi oil layer is mainly composed of clastic rocks and contains small amounts of shell limestone. The clastic rocks are mainly lithic feldspar sandstone and feldspar lithic sandstone, while residual intergranular pores, intergranular dissolved pores, intragranular dissolved pores, intragranular pores and intercrystalline pores constitute the different pore types. Mercury intrusion and 3D computerized tomography analysis showed that micro-nano pores account for 53% of the total pores present. The pore–throat coordination number is distributed between 1 and 4, with an average of 1.8. The pores and throats in the Gaotaizi reservoir have poor connectivity. The porosity distribution of the Gaotaizi oil layer is 1.4%–22.5%, with an average of 9.5%, while the permeability distribution ranges from 0.01 to 27.10 mD, with an average of 0.41 mD. It is an ultra-low porosity and ultra-low permeability tight reservoir. The Gaotaizi oil layer is divided into three types of reservoirs through a systematic study of its pore developmental characteristics. Diagenetic processes like compaction and cementation result in a reduction in porosity and permeability. Compaction, calcite and siliceous cementation, and illite packing are primarily responsible for reservoir densification.

KEYWORDS

tight reservoir, diagenesis, pore structure, Gaotaizi oil layer, Qijia area

1 Introduction

The increasing proportion of unconventional oil and gas resources in the global total makes the study of tight oil and gas reservoirs more pertinent (Fu, 2014; Shi et al., 2019; Zhang, 2016; Katz et al., 2021; Wang et al., 2022). The key to these reservoirs lies in the fine characterization of their properties. Tight reservoirs have a complex pore network space composed of pores and pore throats (Feng et al., 2019; Meng et al., 2020; Wu et al., 2021; Yang et al., 2022a). Pores, in a broad sense, are generally defined as free spaces between multiple framework particles, in which

various fluids exist. Pore throats are essentially the narrow, elongated paths between rock grains that facilitate communication between and play a decisive role in the flow of fluids between pores (Shi et al., 2014; 2015; Li et al., 2016; Jiang et al., 2022). For the evaluation of conventional reservoirs, porosity and permeability are key parameters that reflect the basic physical properties of the reservoir. However, in the evaluation of unconventional oil and gas reservoirs, factors such as reservoir sedimentary cycle, structure and reservoir heterogeneity are considered, in addition to porosity and permeability (Wang et al., 1994; Asante-Okyere et al., 2021; Yang et al., 2022b; Niu et al., 2022; Owusu et al., 2022). Developing a combination of various experimental and simulation techniques that quantitatively characterize the internal pore structures of tight reservoirs is the future of reservoir geology.

The Gaotaizi oil layer occurs within Cretaceous strata in the Qijia area of the Songliao Basin, China. It is a typical tight sandstone reservoir that has, in the past, been studied to assess its depositional environment, hydrocarbon accumulation conditions and diagenesis. The sand bodies developed in Gaotaizi oil layer in the Qijia area are sheet sand microfacies deposits from an underwater distributary channel. These large-area sand bodies create good reservoir conditions for the formation of fault–lithologic reservoirs such as sandstone lens bodies, sand body pinch-outs, and fault blocking. Diagenesis obviously controls the formation and distribution of oil and gas in the Gaotaizi oil layer in the Qijia area, and industrial oil and gas layers are usually formed in the middle diagenetic stage. From the edge to the center of the Qijia area, the diagenetic intensity gradually increases. The Gaotaizi oil layer in the Qijia area of the Songliao Basin has good source, reservoir and hydrocarbon accumulation conditions. The systematic study of the genesis of reservoir densification is crucial for the evolution of reservoir pore structures and the prediction of sweet spots. In this paper, the tight sandstone developed in the Gaotaizi oil layer in the Qijia area of the Songliao Basin is assessed; its petrology, physical properties, pore–throat characteristics, and the genesis of the densification of the oil-bearing sandstones are elucidated using casting thin-sections, scanning electron microscopy, 3D computerized tomography (CT), and petrophysical experimental techniques. The results of this study could potentially improve our understanding of the origins of reservoir densification in the Gaotaizi oil layer.

2 Geological setting

The Songliao Basin is a large Mesozoic and Cenozoic sedimentary basin superimposed on the Paleozoic basement in eastern China. The central part of the Songliao Basin is called the Central Depression Area, and includes the Qijia area—which is where this study is based. The Central Depression Area is the primary structural unit of the basin, and it is a large negative structural unit that experienced predominantly (relative) subsidence during basin development. The Central Depression Area has been the subsidence and deposition center of the Songliao Basin for a long time, and its present structural form is that of a slightly undulating large duplex syncline. The Qijia area is adjacent to the Daqing Placanticline in the east, western slope in the west, and Gulong Sag in the south. The study area encompasses about 3000 km^2 (Figure 1). The Mesozoic and Cenozoic strata in this area are composed of Cretaceous, Paleogene, Neogene, and Quaternary sediments from bottom to top. The strata are divided into five oil-bearing zones, namely the Saltu, Putaohua, Gaotaizi, Fuyu, and Yangdachengzi layers. The Qijia area has well-developed strata, and the total thickness of the Jurassic to Tertiary sedimentary rocks varies between 7 and 10 km. There are several sets of source-reservoir-caprock assemblages developed here, including the target layer of this study—the Cretaceous Gaotaizi oil layer.

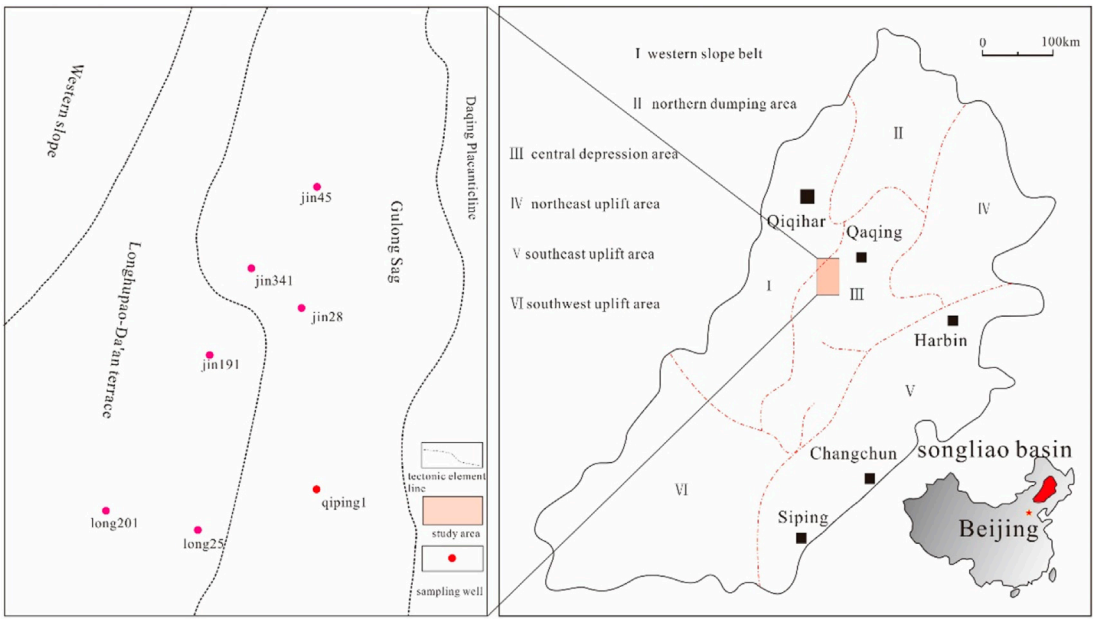

FIGURE 1
Location of the study area and distribution of the sampling well.

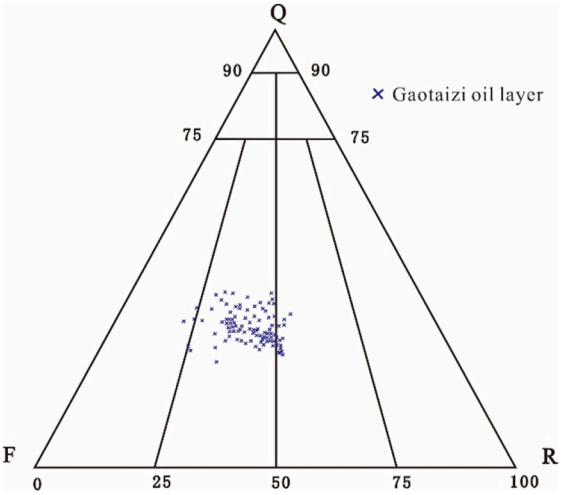

FIGURE 2
Classification of sandstones of Gaotaizi oil layer in Qijia area.

3 Materials and methods

Cast thin-sections, mercury intrusion, physical property testing, field emission scanning electron microscopy, and micro-nano CT high-resolution imaging techniques were used to study the intrinsic properties of the Gaotaizi tight sandstone reservoir; a total of 100 samples and six wells were selected for this study (Figure 1). Cores from wells Jin 341, Jin 191, and Long 25 were chosen for the scanning electron microscope experiment. Cores of wells Qiping one and Long 25 were selected for the casting thin-section observation experiment. Cores of wells Jin 341, Jin 191, and Jin 45 were selected for the micro nano CT experiment.

Scanning electron microscopy is used for high-resolution topography observation of conductive and non-conductive samples. A field emission scanning electron microscope was used to study the internal structures of the samples. During sample preparation, samples were taken from fresh sections of bulk samples. A JCF-1600 ion sputterer was used to spray the conductive layer directly on the samples, and a JSM-7500F field emission scanning electron microscope was used to acquire secondary electron images. The resolution of the secondary electron images is 1 nm, and its magnification is 25–300,000 times.

The basic principle of high-pressure mercury intrusion is the process whereby the non-wetting phase of mercury overcomes capillary resistance and enters pores. At this time, the injection pressure is the capillary resistance under the corresponding pore throat size. The volume of mercury entering the pores represents the size of the connected pore volume at this pore throat size. An AutoPore IV9520 automatic mercury porosimeter from Micromerics was used for this experiment, and a computer controls the process of mercury intrusion and extrusion. The pressure can reach 414 MPa, and the pore diameter ranges from 10^{-3}–1000 μm. The sample volume used in the experiment was in the range of 9.85–14.08 cm^3.

In 3D CT, X-rays penetrate an object and ray intensity is attenuated due to density differences in the sample; the degree of attenuation follows the Beer-Lambert law. When X-rays penetrate the core, the density differences inside the sample result in different degrees of attenuation, forming a series of gray value images on the detector probe. In this study, a MicroX-CT400 CT machine was used for the 3D CT scanning experiments. The X-ray light source voltage of the CT machine is 60–140 KV, the exposure time is 30s, and the spatial resolution is 0.8 μm.

4 Results

4.1 Reservoir petrological characteristics

The Cretaceous Gaotaizi oil layer in the Qijia area is mainly composed of clastic rocks that contain a small amount of shell limestone. The clastic rocks are predominantly lithic feldspar sandstone, followed by feldspar lithic sandstone (Figure 2). The content of detrital components is 51%–97%, with an average value of 84.1%. Among detrital components, the content of quartz is 15%–37%, with an average of 28.6% and the content of feldspar is 19%–45%, with an average of 32.8%. The debris content is 14%–37%, with an average of 18.6%, of which igneous rock debris is the main component. Mesoclastic components range from 0% to 29%, with an average value of 3.8%. The average content of interstitials was 15.9%. Among the interstitials, the content of calcite is 0%–29%, with an average of 8.9%; the content of illite is 0%–11%, with an average of 3.5%; and the total amount of authigenic quartz and feldspar is about 3%.

4.2 Physical characteristics

The physical property test results of 2854 samples from 70 wells in the Gaotaizi reservoir in the Qijia area were used as basic data for physical property analysis. The porosity has a normal distribution; the distribution interval is 1.4%–22.5%, the main frequency is 2%–16%, and the average value is 9.5%. The permeability of the Gaotaizi reservoir has a wide distribution range; statistical results show that the distribution interval is 0.01–27.1 mD, the main frequency is 0.01–3 mD, the average value is 0.41 mD, and the median value is 0.09 mD. The samples with permeability less than 1 mD accounted for 91.6% of the total samples, and the samples with permeability less than 2 mD accounted for 96.0% of the total samples (Figure 3). Following the physical property classification standard of clastic rock reservoirs issued by the National Reserves Commission (Table 1), the Gaotaizi oil layer in the Qijia area is characterized as an ultra-low porosity and ultra-low permeability reservoir.

The porosity and permeability of the Gaotaizi oil layer in the Qijia area have an obvious positive correlation. As the porosity increases, the permeability of the rock samples increases exponentially, but the data points are discretely distributed. Samples with the same porosity can differ by a factor of up to 1000 in the maximum permeability; however, samples with the same permeability can differ in porosity by a factor of up to 10 (Figure 4).

4.3 Developmental features of pore throats

4.3.1 Pore types

Quantitative analysis of cast thin-sections, ordinary scanning electron microscopy and field emission scanning electron microscopy suggest that multiple pore types are developed in the Gaotaizi oil layer in the Qijia area. These include residual intergranular, intergranular dissolved, intragranular dissolved, intragranular and intercrystalline pore types; a significant number

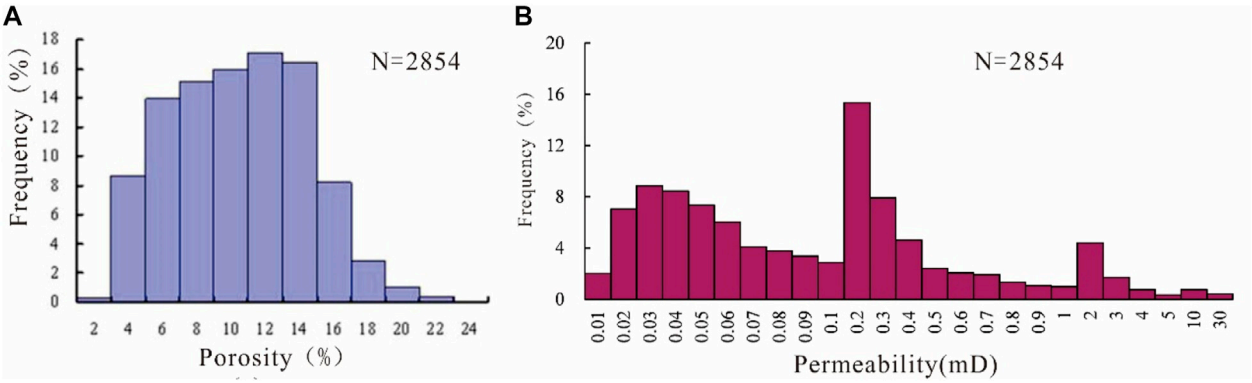

FIGURE 3
Frequency distribution characteristics of the **(A)** porosity and **(B)** permeability of the Gaotaizi reservoir in the Qijia area.

TABLE 1 Classification standards for physical properties of clastic rock reservoirs.

Reservoir classification	Porosity φ (%)	Permeability k (mD)
ultra-high porosity and ultra-high permeability	φ≥30	k≥2000
high porosity and high permeability	25≤φ<30	500≤ k<2000
medium porosity and medium permeability	15≤φ<25	50≤ k <500
low porosity and low permeability	10≤φ<15	5 ≤k <50
ultra-low porosity and ultra-low permeability	φ<10	k <5

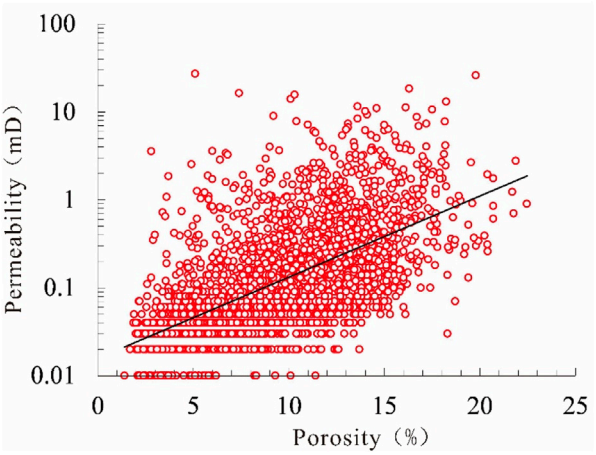

FIGURE 4
Relationship between the porosity and permeability of the Gaotaizi oil layer in the Qijia area.

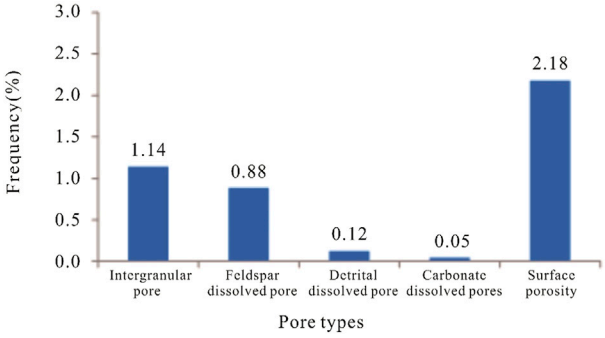

FIGURE 5
Bar chart of the pore types developed in the sandstones of the Gaotaizi oil layer in the Qijia area.

are of the residual intergranular and dissolution pore types (Figure 5; Figure 6).

4.3.2 Pore throat size

4.3.2.1 Pore size

A large number of fine pores are developed in the Gaotaizi oil layer in the Qijia area. In this study, field emission scanning electron microscopy and 3D CT high-resolution imaging technology, combined with conventional analysis and testing methods are used to compile a multi-scale, quantitative characterization of the pore characteristics of the oil layer. Pores with diameters greater than 1 μm are defined as micro-scale pores, pore diameters between 1000 and 500 nm are defined as sub-micron pores, and pores with diameters less than 500 nm are defined as nano-scale pores.

The identification of micron-scale pores was carried out using the traditional casting thin-section method. The reservoir space of the Gaotaizi oil layer is mainly composed of residual intergranular pores and dissolution pores. The pore radius in the oil layer is mainly between 10 and 20 μm, and the maximum value is as high as 50 μm. The average surface porosity and average porosity of the Gaotaizi

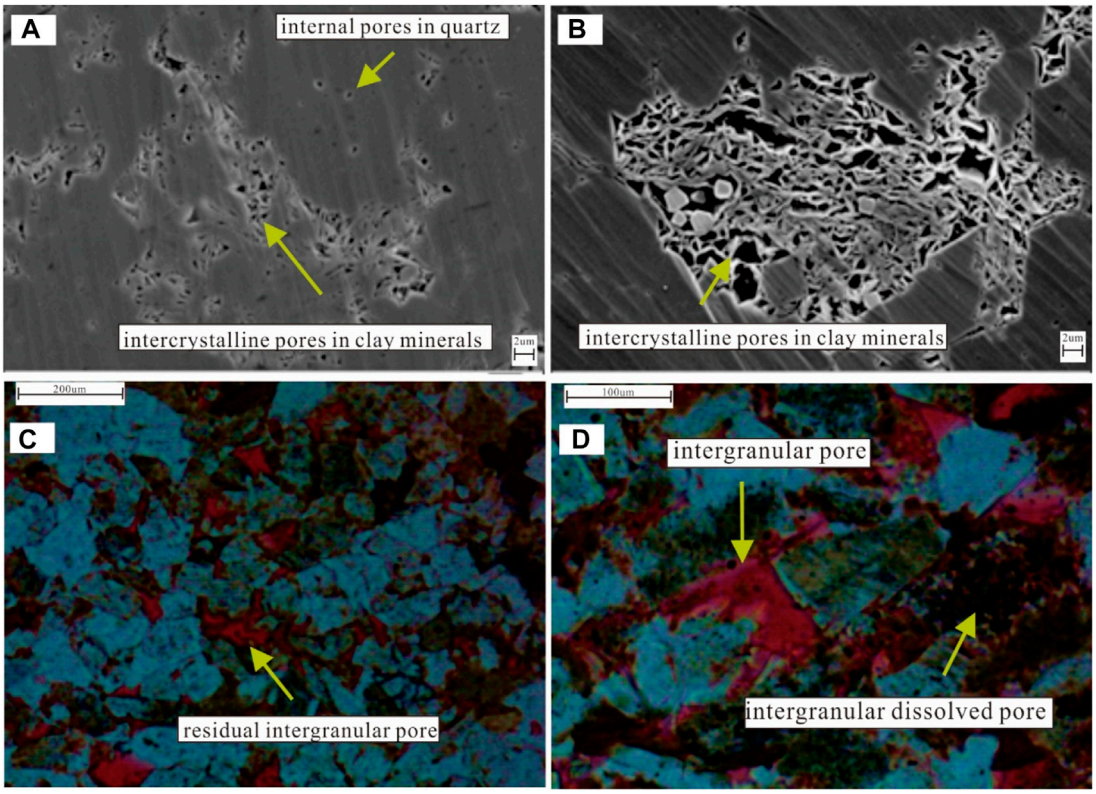

FIGURE 6
Photomicrographs of the main pore types developed in the Gaotaizi oil layer in the Qijia area; **(A)** Well Jin 341, 2076.49m, residual intergranular pores; **(B)** Well Jin 191, 1863.8m, intergranular and intergranular dissolved pores; **(C)** Well Qiping 1, 1956.12m, intercrystalline pores and quartz intragranular pores; **(D)** Well Long 25, 2043.43m, intracrystalline pores.

reservoir in the Qijia area are 2.2% and 9.5%, respectively, and the micron-sized pores account for about 23% of the total porosity.

Precise quantitative characterization of micron-scale pores is achieved using CT. According to the CT analysis results of the six groups of samples, the average pore radius of the samples was 2 μm, the average throat radius was 0.58 μm, the average throat length was 9.66 μm, and the coordination number ranged from 2.5 to 22.0, with an average of 10.5. A high coordination number indicates good pore–throat connectivity. The CT analysis results showed that the porosity of the samples was 3.0%–8.1%, with an average value of 6.2%. This value is lower than the average porosity of 12% found in conventional physical property tests. Conventional physical property analysis measures the sum of pore volumes at different scales. The comparison between CT porosity and conventional porosity shows that micro-nano pores account for 53% of reservoir pores.

Sub-micron pores can be qualitatively identified by ordinary scanning electron microscopy and field emission scanning electron microscopy (Figures 6C,D). Observational data suggests that the sub-micron pores are mainly composed of clay mineral intracrystalline pores, quartz intragranular pores, and intragranular dissolved pores; their content accounts for about 10% of the total number of pores.

4.3.2.2 Average pore throat size

According to the mercury intrusion data of 94 samples from ten wells, the Gaotaizi oil layer in the Qijia area is dominated by nano-scale pore throats. The space with pore throat radius of less than 1 μm accounts for 97%, and the space with pore throat diameter of less than 1 μm accounts for 90% (Figure 7). According to the relationship between the pore throat radius distribution and the cumulative mercury injection percentage (Figure 8), reservoirs are divided into three types. The pore throat radius of Type I reservoirs is 0.05–2 μm, the average porosity is 10.7%, and the average permeability is 0.62 mD. The pore throat radius of Type II reservoirs is 0.005–0.1 μm, the average porosity is 7.7%, and the average permeability is 0.1 mD. The pore throat radius of Type III

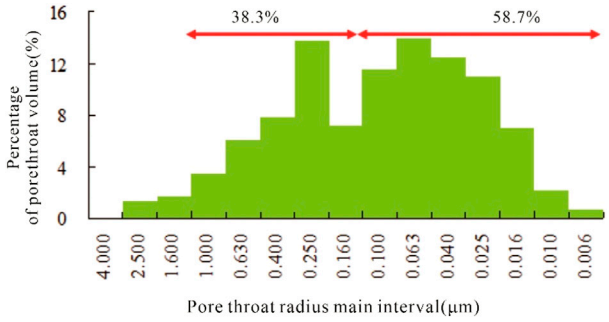

FIGURE 7
Distribution of the pore throat radius in the Gaotaizi reservoir in the Qijia area.

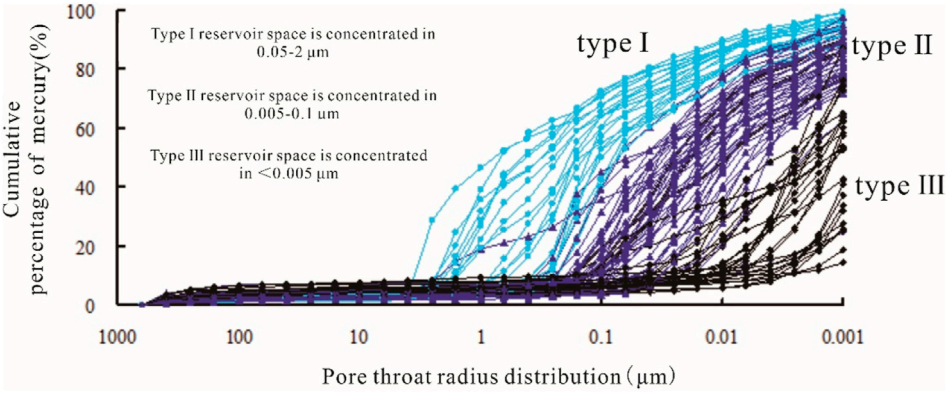

FIGURE 8
Characteristics of the pore throat radius of the Gaotaizi reservoir in the Qijia Area.

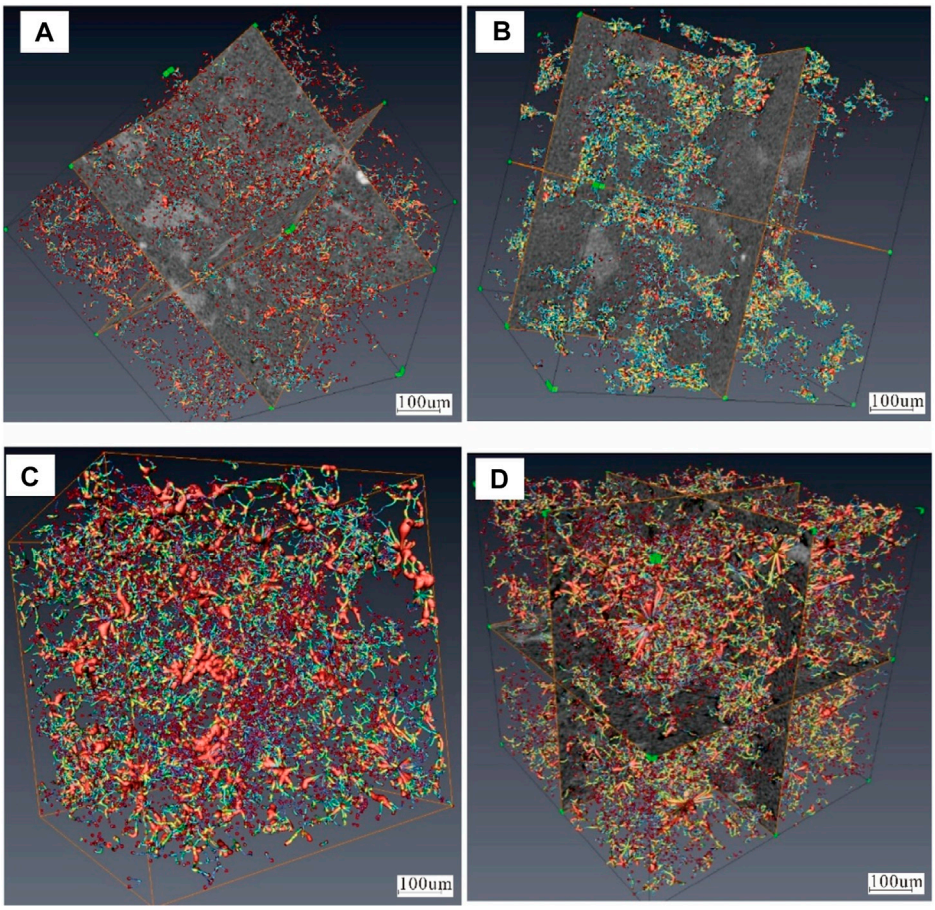

FIGURE 9
Three-dimensional pore–throat structures of the Gaotaizi oil layer based on three-dimensional CT scanning; **(A)** Jin 341 well, dry layer, carbonate cementation, porosity of 2.6%; **(B)** Jin 341 well, oil immersion, porosity of 5.8%, good pore connectivity; **(C)** Jin 191 well, oil immersion, porosity of 7.9%, well developed pores and good connectivity; **(D)** Jin 45 well, dry layer, porosity of 8.1%, extremely well-developed pores and good connectivity, coordination number of 13.4.

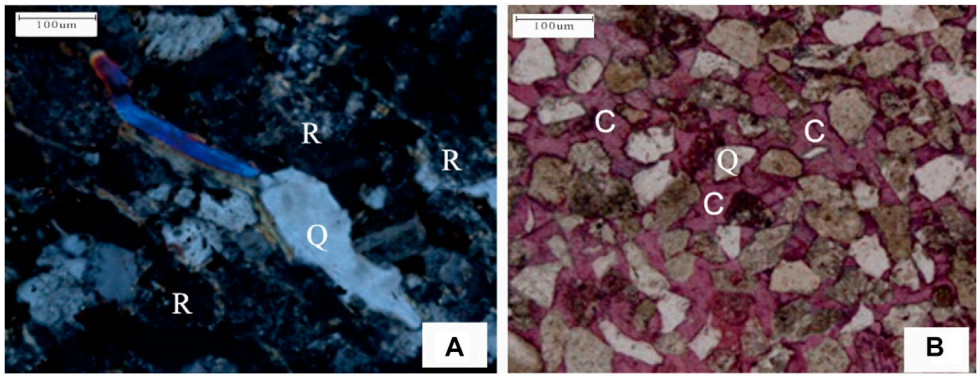

FIGURE 10
Photomicrographs of the compaction and cementation in the Gaotaizi oil layer in the Qijia area; **(A)** Well Jin 341, 2076.49 m, compaction; **(B)** Well Qiping 1, 1956.12 m, cementation.

reservoirs is less than 0.005 μm, the average porosity is 4.9%, and the average permeability is 0.1 mD.

4.3.3 Pore structure characteristics

The Gaotaizi oil layer in the Qijia area has poor pore structures. The pore–throat coordination number is mainly distributed between 1 and 4, with an average of 1.8. It can go as high as 13.4 for some pore–throat coordination number. The pores and pore throats are poorly connected (Figure 9). There is strong heterogeneity in the distribution of pore throats in the Gaotaizi oil layer; the distribution of pores and pore throats as reflected in a sample with a diameter of 2 mm is extremely uneven. This suggests that the sandstone was strongly affected by sedimentation and diagenesis, which enhances the complexity of fluid seepage.

5 Discussion

5.1 Analysis of controlling factors of reservoir densification

5.1.1 Compaction

A delta front facies depositional environment characterizes the Gaotaizi oil layer in the Qijia area. Large amounts of siltstone formed in this environment. After the sediments passed the syngeneic stage and entered the burial diagenetic stage, the effects of compaction that pervaded the burial had great influence on the physical properties of the reservoir (Liu et al., 2019; Vafaie et al., 2021). The Gaotaizi oil layer suffered intense compaction as a consequence of fine grain size and high shale content, resulting in low reservoir porosity and permeability (Figure 10). Calculations suggest that the original porosity of the reservoir reduced by 60% due to compaction. Compaction is an important mechanism that results in porosity reduction. Increasing overlying stress ensures that the fluids in the rock pores are continuously discharged, changing the physical properties of the reservoir drastically (Tian et al., 2019; Jiang et al., 2020). The magnitude of the overburden stress is mainly related to the burial depth of the strata. Therefore, depth is an important parameter reflecting the strength of compaction.

The formation and evolution of strata in the Qijia area show are linked to the changing reservoir properties. From the younger Nenjiang Formation to the older Quantou Formation, reservoir porosity and permeability generally decrease linearly with increasing burial depth. The decreasing trend of porosity is the most obvious. From 1 to 2 km, the porosity decreases by about 10%. Increasing the depth of burial increases the vertical ground stresses. Under normal compaction conditions, rock porosity should gradually decrease; however, a sharp decrease in porosity in the initial stage is followed by a more gradual decrease with increasing burial depth. Therefore, vertical ground stresses are usually most sensitive to the porosity of tight reservoirs, while the sensitivity to permeability is relatively low (Figures 11A,B).

The density of the rock increases linearly with increasing burial depth, reflecting the tighter arrangement of the grains (Figure 11C). Some zones that develop have abnormal porosity and permeability, but normal rock density. These abnormal physical properties are mainly dissolved pore development belts. In the Qijia area, the abnormal physical properties are mainly developed in the Qingshankou and Quentou formations.

5.1.2 Cementation

Many kinds of cements are produced during the diagenesis of tight sandstones (Nabawy et al., 2009; Zhang et al., 2009; Jiang et al., 2020; Liu et al., 2023). The precipitation of cements further aggravates the process of densification of the reservoir. It is difficult for a single diagenetic mechanism or diagenetic product to make reservoirs tight; current tight reservoirs are usually the result of the coupling of various diagenetic changes.

There is an obvious negative correlation between the physical properties and the carbonate content of the Gaotaizi oil layer in the Qijia area (Figure 12). When the carbonate content is less than 4%, the distribution interval of porosity and permeability is large; they have no clear relationship with carbonate content. When the carbonate content is greater than 4%, the porosity and permeability decrease rapidly with increasing carbonate content. Here, the relationship between porosity and carbonate rock content is more obvious; thus, carbonate rock content has a greater impact on porosity, than on permeability.

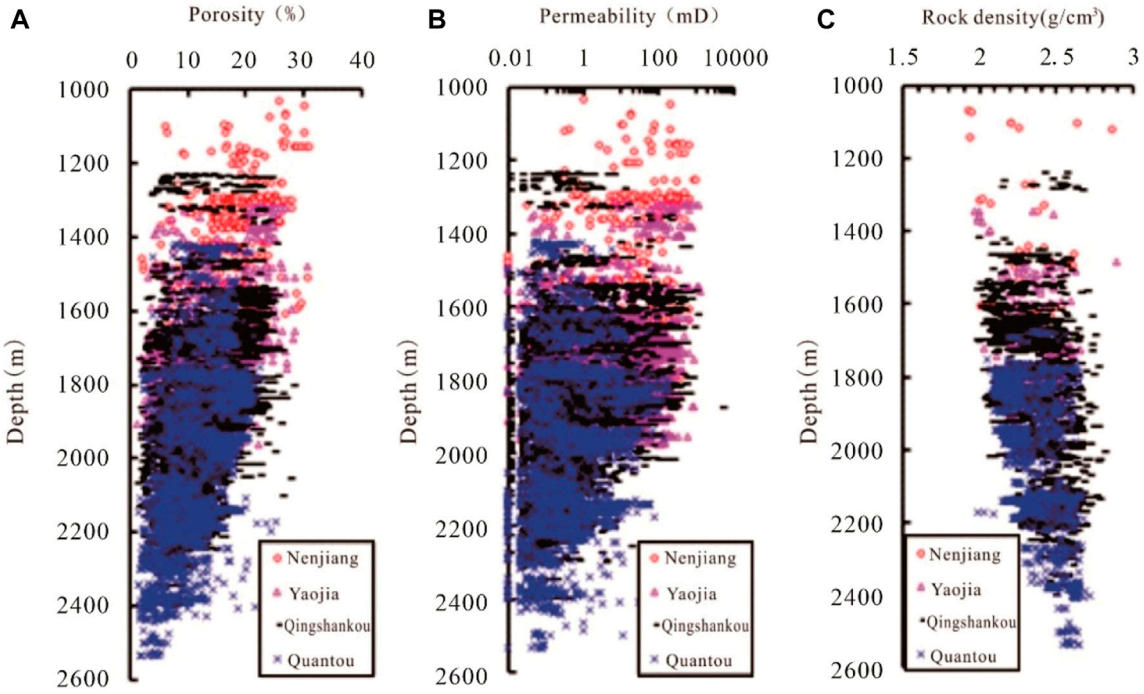

FIGURE 11
Variation of **(A)** porosity, **(B)** permeability, and **(C)** rock density of tight sandstone reservoirs with depth in the Qijia area.

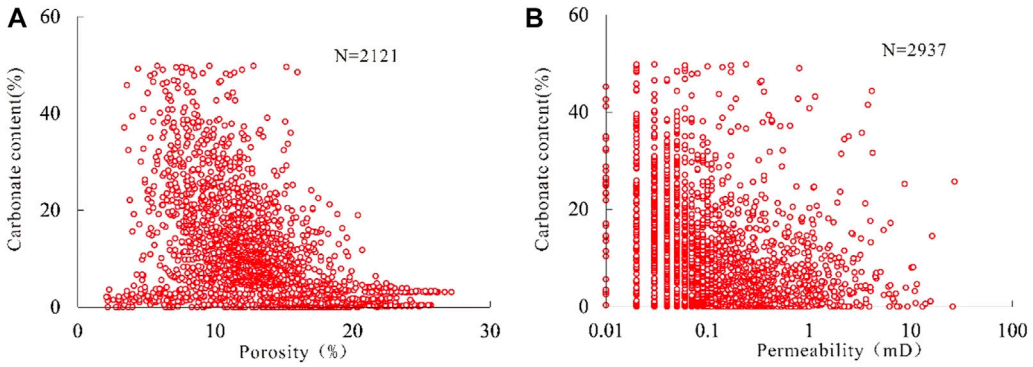

FIGURE 12
Relationship of **(A)** porosity and **(B)** permeability with carbonate content of the Gaotaizi oil layer.

There are two stages of carbonate cementation in the Gaotaizi oil layer in the Qijia area. Generally, early calcite cementation in the cores aids the development of dry layers. The boundary between the lower oil layer and the dry layer is clear, reflecting the early formation of this type of calcite. Late calcite cementation occurs mainly in the form of plaques that persist primarily in residual intergranular pores or metasomatic feldspar dissolution pores after compaction (Figures 5C,D). In addition to carbonate cements, a small amount of authigenic quartz also developed in the Gaotaizi oil layer. Under the influence of strong cementation and compaction, the Gaotaizi oil layer was transformed into a tight reservoir.

5.1.3 Secondary illite clay minerals

Illite clay minerals are particularly developed in the Gaotaizi oil layer in the Qijia area (Figure 13). Under the microscope, these minerals are mostly infected by crude oil, and appear black or brown. Illite typically occurs in three forms; as flakes, needles, and bridges. The coniferous and bridging illites of secondary origin are dominant, while the flaky illites were likely formed during original deposition. Illite clay minerals are packed into various pore spaces. Their existence drastically reduces the porosity of the reservoir, while simultaneously increasing the difficulty of fluid percolation through the pores. Therefore, their presence severely affects the physical properties of the reservoir. A large number of intercrystalline pores

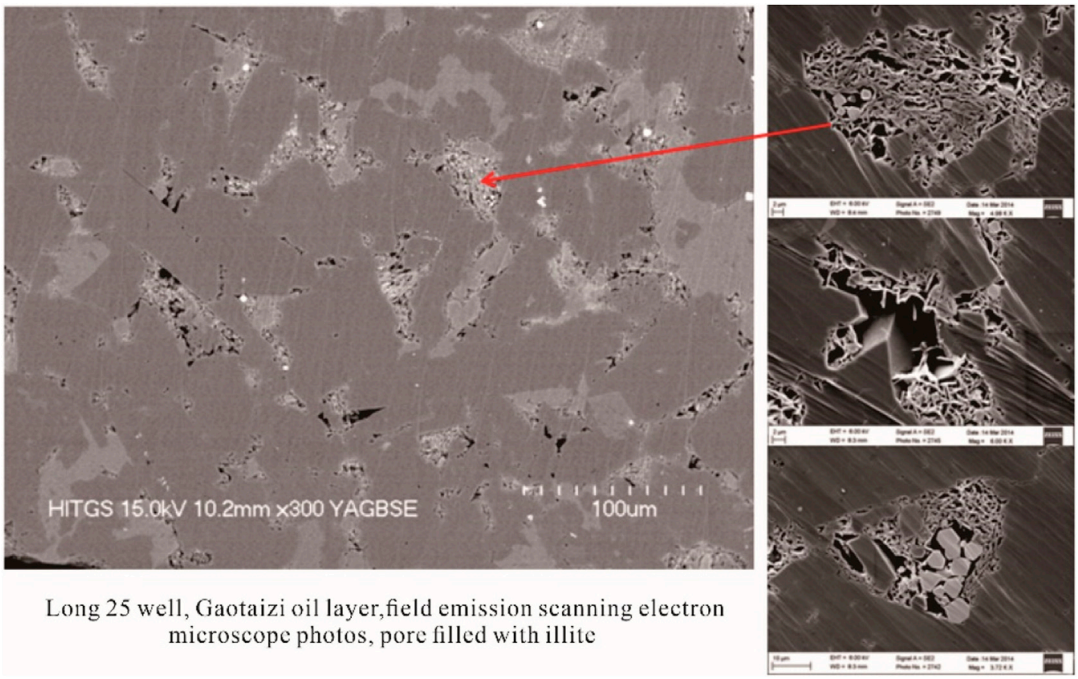

FIGURE 13
Developmental characteristics of the illite clay minerals in the Gaotaizi reservoir under field emission scanning electron microscopy.

Diagenetic stage / Diagenetic events	Early diagenetic stage		Middle diagenetic stage	
	Stage A	Stage B	Stage A	Stage B
Paleogeotemperature/°C	25 °C ~65 °C	65 °C ~85 °C	85 °C ~140 °C	140 °C ~175 °C
Ro/%	<0.35	0.35~0.5	0.5~1.3	1.3~2.0
Compaction				
Pyrite				
kaolinite				
Felsic enlargement				
Authigenic quartz				
Early calcite cementation				
Late calcite cementation				
Ankerite cementation				
Feldspar dissolution				
Debris dissolution				
Illite-montmorillonite mixed layer				
Illite				

FIGURE 14
Diagenetic evolution sequence of tight sandstone of Gaotaizi oil layer in Qijia area.

are developed in illite clay minerals, although they are not effective spaces for the storage of oil.

5.2 Diagenetic evolution of Gaotaizi oil layer

The Gaotaizi oil layer in the Qijia area has undergone a complex process of diagenesis (Figure 14). Compaction persisted throughout the entire diagenetic process, and was strongest in the early stage of diagenesis. At this stage, a small amount of kaolinite formed on the surface of detrital particles such as quartz and feldspar. Feldspars experienced hydration in the shallow burial stage, and provided a material source for the early secondary increase of quartz. In the middle diagenetic stage, as the degree of the thermal evolution of organic matter increased, organic matter entered a low maturity stage. A large number of organic acids were generated, soluble minerals such as feldspar were dissolved, and secondary pores were formed. It provided space and a material source for late calcite cementation. When the organic matter entered the oil generation threshold, a large volume of hydrocarbons were expelled from the source layer. These hydrocarbons entered the pores of the reservoir, changed the original fluid environment, and inhibited cementation. In areas where hydrocarbon charging was not affected, the process of cementation continued. Thus, compaction, calcite cementation, siliceous cementation, and illite filling are the main reasons for reservoir densification. Analyzing the diagenetic evolution of the Gaotaizi reservoir in the Qijia area suggests that the reservoir has entered the middle diagenetic stage, which is conducive to the formation of tight reservoirs.

6 Conclusion

1) The petrology, physical properties, pore–throat characteristics, and the genesis of the densification of the oil-bearing tight sandstones in the Gaotaizi oil layer in the Qijia area of the Songliao Basin are explained using casting thin-sections, scanning electron microscopy, 3D CT, and petrophysical experimental techniques.
2) The Gaotaizi oil layer is mainly composed of clastic rocks and contains a small amount of shell limestone. The clastic rock types are mainly lithic feldspar sandstone, followed by feldspar lithic sandstone. The pores are primarily of the residual intergranular, intergranular dissolved, intragranular dissolved, intragranular and intercrystalline pore types.
3) Mercury intrusion and 3D CT analysis show that micro-nano pores account for 53% of the total pores present. The pore–throat coordination number is distributed between 1 and 4, with an average of 1.8. The pores and pore throats in the Gaotaizi reservoir have good connectivity. The porosity distribution of the Gaotaizi oil layer ranges from 1.4% to 22.5%, with an average of 9.5%. The permeability distribution ranges from 0.01 to 27.10 mD, with an average of 0.41 mD. Thus, the Gaotaizi oil layer is an ultra-low porosity and ultra-low permeability tight reservoir.
4) The systematic study of the developmental characteristics of pores allows the Gaotaizi oil layer to be divided into three types of reservoirs. Diagenetic processes including compaction and cementation result in a reduction in porosity and permeability. Thus, compaction, calcite cementation, siliceous cementation, and illite packing are the primary reasons for the densification of the Gaotaizi reservoir.

Data availability statement

The original contributions presented in the study are included in the article/supplementary material, further inquiries can be directed to the corresponding author.

Author contributions

SS developed the idea for this paper and wrote the manuscript; YZ, CE, YB, WW, and JH were involved in data interpretation.

Acknowledgments

This paper is financially supported by the Science and Technology Department of Shaanxi Province project “Multi-periods mixed source shale oil accumulation contribution and its controlling factors of Qingshankou Formation in Gulong Sag, Songliao Basin”, Grant No.:2023-YBGY-077. The authors wish to acknowledge to the project.

Conflict of interest

Author YZ was employed by Exploration and Development Research Institute of Jilin Oilfield Company Ltd.

The remaining authors declare that the research was conducted in the absence of any commercial or financial relationships that could be construed as a potential conflict of interest.

Publisher’s note

References

Asante-Okyere, S., Ziggah, Y. Y., and Marfo, S. A. (2021). Improved total organic carbon convolutional neural network model based on mineralogy and geophysical well log data. *Unconv. Resour* 1, 1–8. doi:10.1016/j.uncres.2021.04.001

Feng, J., Zhang, B. W., Feng, Z. H., Wang, Y. C., Zhang, J. H., and Fu, X. F., (2019). Crude oil movement in tight sandstone reservoirs in the northern Songliao Basin Sexual Influencing Factors. *Petroleum Explor. Dev* 46 (2), 312–321. doi:10.11698/PED.2019.02.11

Fu, X. L. (2014). Distribution of Gaotaizi oil layers and accumulation analysis in Qijia area of northern Songliao Basin, China. *J. Chengdu Univ. Technol. Nat. Sci. Ed* 41 (4), 422–427. doi:10.3969/j.issn.1671-9727.2014.04.03

Jiang, W., Zhang, P., Li, D., Li, Z., Wang, J., and Duan, Y., (2022). Reservoir characteristics and gas production potential of deep coalbed methane: Insights from the no. 15 coal seam in shouyang block, Qinshui Basin, China. *Unconv. Resour* 2, 12–20. doi:10.1016/j.uncres.2022.06.001

Jiang, Y. L., Liu, X. J., Zhao, X. Z., Jin, F. M., Liu, J. D., and Lv, X. Y. (2020). Comprehensive identification of oil and gas accumulation period by fluid inclusion technique and reservoir bitumen characteristics: A case study of the paleozoic buried hill in beidagang, huanghua depression. *Earth Sci* 45 (3), 980–988. doi:10.3799/dqkx.2019.016

Katz, B., Gao, L., Little, J., and Zhao, Y. R. (2021). Geology still matters – unconventional petroleum system disappointments and failures. *Unconv. Resour* 1, 18–38. doi:10.1016/j.uncres.2021.12.001

Li, Y. L., Zhang, Y. F., Yin, S. L., Cong, L., Yan, M., and Tian, X. X. (2016). Multi-scale characterization of tight sandstone reservoir space: A case study of Gaotaizi oil layer in Qijia area, Songliao Basin. *Petroleum Nat. Gas Geol* 37 (6), 915–922. doi:10.11743/ogg20160613

Liu, C., Jiang, T., Yang, Y., and Ma, J. (2023). Temporal and spatial variations of high-resolution strontium, carbon, and oxygen isotopic chemostratigraphy at the end-Permian crisis boundary in South China. *Gondwana Res* 113, 89–101. doi:10.1016/j.gr.2022.10.015

Liu, R. C., Ren, Z. L., Ma, K., Zhang, Y. Y., Qi, K., and Yu, C. Y., (2019). Classification of hydrocarbon accumulation phases of yanchang formation in southern ordos basin. *Geoscience* 33 (6), 1263–1274. doi:10.19657/j.geoscience.1000-8527.2019.06.12

Meng, Y. L., Zhang, L., Tao, S. Z., Li, G. H., Li, X. N., and Dai, T. J., (2020). Subdivision and application of diagenetic stages of clastic rocks: Taking Qijia-Gulong area in Songliao Basin as an example. *China Univ. Min. Technol. Chin. J* 49 (5), 920–930. doi:10.13247/j.cnki.jcumt.001158

Nabawy, B. S., Géraud, Y., Rochette, P., and Bur, N. (2009). Pore-throat characterization in highly porous and permeable sandstones. *AAPG Bull* 93 (6), 719–739. doi:10.1306/03160908131

Niu, X., Feng, S., You, Y., Xin, H., Liang, X., and Hao, B., (2022). Analyzing major controlling factors of shale oil 'sweet spots' in the Chang-7 member of the Triassic Yanchang Formation, Ordos Basin. *Unconv. Resour* 2, 51–59. doi:10.1016/j.uncres.2022.07.001

Owusu, E. B., Tetteh, G. M., Asante-Okyere, S., and Tsegab, H. (2022). Error correction of vitrinite reflectance in matured black shales: A machine learning approach. *Unconv. Resour* 2, 41–50. doi:10.1016/j.uncres.2022.07.002

Shi, L. Z., Qi, Y., Zhang, Y. S., Wang, Z. Z., and Wang, B. (2019). Simulation of "four history" and its geological significance in Qijia area, Songliao Basin. *Geol. Explor* 55 (2), 661–672. doi:10.12134/j.dzykt.2019.02.021

Shi, L. Z., Wang, Z. Z., Zhang, G., Zhang, Y. S., and Xing, H. Y. (2015). Formation conditions and distribution law of tight oil in Qijia area, Songliao Basin. *Petroleum Explor. Dev* 42 (1), 44–50. doi:10.11698/PED.2015.01.05

Shi, L. Z., Wang, Z. Z., and Zhang, Y. S. (2014). Distribution and geological characteristics of tight oil in Gaotaizi oil layer in Qijia area, Songliao Basin. *Nat. Gas. Geosci* 25 (12), 1943–1950. doi:10.11764/j.issn.1672-1926.2014.12.1943

Tian, X. R., Zhang, Y. Y., Zhou, Q. G., Yu, Z. C., and Guo, Z. J. (2019). Tight oil charging characteristics of the Lower Permian Fengcheng formation in Mahu sag, Junggar Basin: Evidence from fluid inclusions in alkaline minerals. *Aata Petrloei Sin* 40 (6), 646–659. doi:10.7623/syxb201906002

Vafaie, A., Kivi, I. R., Moallemi, S. A., and Habibnia, B. (2021). Permeability prediction in tight gas reservoirs based on pore structure characteristics: A case study from south western Iran. *Unconv. Resour* 1, 9–17. doi:10.1016/j.uncres.2021.08.001

Wang, C., Song, G. X., and Liu, Z. W. (1994). Enclosure of authigenic mineral from northern part of songliao basin and its application. *Petroleum Geol. Oilfield Dev. Daqing* 13 (4), 19–22. doi:10.19597/j.issn.1000-3754.1994.04.006

Wang, H., Zhou, S., Li, S., Zhao, M., and Zhu, T. (2022). Comprehensive characterization and evaluation of deep shales from Wufeng-Longmaxi Formation by LF-NMR technology. *Unconv. Resour* 2, 1–11. doi:10.1016/j.uncres.2022.05.001

Wu, W. T., Zhao, J. Z., Meng, Q. A., Lin, T. F., Zhang, G., and Zhang, J. Y., (2021). Accumulation mechanism of tight sandstone oil in Gaotaizi oil layer in Qijia area, Songliao Basin. *Petroleum Nat. Gas Geol* 42 (6), 1376–1388. doi:10.11743/ogg20210612

Yang, X., Fan, J., Zhang, Y., Li, W., Du, Y., and Yang, R. (2022). Microscopic pore structure characteristics of tight limestone reservoirs: New insights from section 1 of the permian maokou formation, southeastern sichuan basin, China. *Unconv. Resour* 2, 31–40. doi:10.1016/j.uncres.2022.08.001

Yang, Y., Chen, S., Dai, C., Wang, X., Li, X., and Zeng, Q., (2022). Prediction of glutenite reservoirs using an adaptive Bayesian seismic inversion in the slope zone of Mahu Depression in Junggar Basin, NW China. *Unconv. Resour* 2, 21–30. doi:10.1016/j.uncres.2022.06.002

Zhang, J. C., James, L., and William, S. (2009). Stress, porosity, and failure-dependent compressional and shear velocity ratio and its application to wellbore stability. *J. Petroleum Sci. Eng* 69, 193–202. doi:10.1016/j.petrol.2009.08.012

Zhang, J. Y. (2016). The main controlling factors for oil-bearing properties of tight sandstone reservoirs in source rocks in continental depression basins: A case study of Gaotaizi oil layer in Qijia sag, central depression, northern Songliao Basin. *J. Sedimentology* 34 (5), 991–1002. doi:10.14027/j.cnki.cjxb.2016.05.018

frontiers | Frontiers in Earth Science

TYPE Original Research
PUBLISHED 06 January 2023
DOI 10.3389/feart.2022.1047535

OPEN ACCESS

EDITED BY
Hu Li,
Southwest Petroleum University, China

REVIEWED BY
Guodong Yang,
Wuhan University of Science and Technology, China
Xinghua Yang,
Shanxi Normal University, China

*CORRESPONDENCE
Shaocong Ji,
jishaocong@mail.cgs.gov.cn

SPECIALTY SECTION
This article was submitted to Structural Geology and Tectonics, a section of the journal Frontiers in Earth Science

RECEIVED 18 September 2022
ACCEPTED 24 October 2022
PUBLISHED 06 January 2023

CITATION
Zhang Q, Liang B, Ji S and Li J (2023), Isotopic characteristics of carbon and oxygen within ordovician carbonate paleokarst in the tazhong region and their paleoenvironmental significance. *Front. Earth Sci.* 10:1047535. doi: 10.3389/feart.2022.1047535

Isotopic characteristics of carbon and oxygen within ordovician carbonate paleokarst in the tazhong region and their paleoenvironmental significance

Qingyu Zhang[1,2], Bin Liang[1,2], Shaocong Ji[1,2]* and Jingrui Li[1,2]

[1]Institute of Karst Geology, Chinese Academy of Geological Sciences Karst Dynamics Laboratory, Ministry of Natural Resources, Guilin, China, [2]International Research Center on Karst Under the Auspices of UNESCO, National Center for International Research on Karst Dynamic System and Global Change, Guilin, China

The Tazhong region is a key area for oil and gas exploration and development within the Tarim basin. In this region, development of Ordovician carbonate paleokarsts has been found to be extremely heterogeneous. To investigate the developmental stages of these Ordovician carbonate karsts and their corresponding paleoenvironmental conditions, oxygen and carbon isotopic characteristics of calcite paleokarst fissure fillings were examined in conjunction with rock-structure analyses. Results show that $\delta^{18}O$ (PDB) values tend towards negative values in general, ranging from −3.97% to −12.7% (average value −7.64%), which is indicative of the presence of paleokarstification *via* dissolution by atmospheric freshwater. Values of $\delta^{13}C$ (PDB) span a relatively large range, from 2.48% to −2.13% (average value of 0.23%). This shows that the paleokarst in this area has gone through two stages of supergene and burial diagenesis, and the process of paleokarst is complex. The paleotemperature at which the karst fissure-filling deposits were formed ranged from 6.5 to 47.1°C (average value of 21.8°C), and the salinity of the medium has Z values from 117.48 to 130.24 (average value of 123.94). Four different paleokarsification settings were thus revealed: a marine depositional environment, an atmospheric freshwater karst-filling environment, a shallow-burial paleokarsification environment and a deep-burial high-temperature environment. It has thus been shown that the karst pores, fissures and caves formed by paleokarstification over multiple stages are the main reservoir spaces in this region. This study will serves as a basis for karst reservoir predictions, and exploration and development in this region.

KEYWORDS

carbon-oxygen isotopes, paleokarsts, paleoenvironments, carbonates, ordovician, tarim basin

Introduction

Tarim Basin is the largest oil and gas sedimentary basin in China (Wu et al., 2012), and karst reservoirs, such as the pores, fissures and caves that are formed due to paleokarstification, are important reservoir spaces in carbonate rocks (Wang and Al-Aasm 2002; Chen et al., 2007; Zhang et al., 2011). Deep-burial karst reservoirs are an important type of reservoir in marine carbonate oil and gas fields. These have generally undergone long periods of geological and environmentally driven changes, including repeated dissolution and filling caused by various factors and fluids. These reservoirs are characteristically very deeply buried, tectonically complex and highly heterogeneous (Li et al., 1996; Zhu et al., 2005), thus causing immense difficulties in predicting the location and character of deeply buried carbonate paleokarst reservoirs (Li, 2022a; Li et al., 2019; Li et al., 2022; Li et al., 2022b; Zhang et al., 2022a; Zhang et al., 2022b; Zhang et al., 2022c; Zhang et al., 2022d).

The carbon and oxygen isotopic compositions of marine carbonates from different geological periods are directly affected by the diagenetic fluids that were generated in each developmental period, and they can serve as an important background value for studies on diagenesis (Arthur et al., 1988; Huang et al., 2014). Under different climatic conditions, carbon and oxygen isotopes will have correspondingly different enrichment characteristics, which are stable over time and have excellent regional comparability (Taylor 1968; Li and Wan 1999; Valley and Cole 2001). Therefore, the carbon and oxygen isotope compositions of carbonate karst fissure fillings are some of the most important tracers in paleoclimatic studies and paleogeological environment reconstructions, and are also highly significant for studies on the development of paleokarsts and karst reservoirs (Tian and Zheng 1995).

In 1948, Nobel Prize winner H.C. Urey suggested that $\delta^{18}O$ values may be used to examine paleoocean temperature (Urey, 1948; Kuypers et al., 1999). In Epstein and Mayeda, 1953 further realized Urey's theory; they established the basic principles for using $\delta^{18}O$ values to calculate paleosalinity levels and determined that the $\delta^{18}O$ value increased with increases in salinity. For a long time, experts and scholars have made great progress in studying the sedimentary environment and diagenesis of carbonate rocks in the Tarim Basin by using the stable carbon and oxygen isotopic composition of carbonate rocks (Zhang et al., 2015; Zhang et al., 2016a; Zhang et al., 2016b; Zhong et al., 2012; Gao et al., 2011; Zhao et al., 2012). Furthermore, much research has been performed using the carbon and oxygen isotope compositions of karst cave-filling stalagmites and stalactites to reconstruct paleoclimates and paleoenvironments since the Permian period (Liu et al., 1997; Liu et al., 2004; Zhang et al., 2015; Huang et al., 2016).

The Ordovician carbonate karst cave systems of the Tazhong region in the Tarim basin are buried in the range of 5550–6480 m beneath the surface, and the development of karst pores, fissures, caves and large-scale underground river systems in this region is highly heterogeneous. With continuous improvements in oil and gas exploration and development technologies in the Tazhong region, ancient karst reservoirs have become the most important type of reservoir in carbonate formations. However, distinguishing the various developmental stages of karst remains a major issue, which restricts the geological modeling of karst reservoirs formed under different phases of karst development, and presents problems for the prediction of favorable regions in effective karst reservoirs.

The distribution patterns and controlling factors of karst reservoirs have previously been studied in the Tazhong region (Han et al., 2012; Liu et al., 2013). Luo et al. (2011) have performed a thorough study of how reservoirs are altered by the developmental characteristics of fissures; additional studies have addressed reservoir traps, geological structure and diagenesis (Yang et al., 2012). However, studies of the carbon and oxygen isotope characteristics of Ordovician carbonate karst fillings in this region are relatively superficial, and the results of existing studies are rather controversial (Shen 2006). Thus, contemporary understanding of the region's patterns of change is relatively weak. In this work, drilled cores of karst fillings from various depths were systematically obtained, and multivariate statistical methods were applied to investigate the geochemical carbon and oxygen isotope characteristics of karst fissure fillings, to evaluate the developmental stages of the paleokarsts in this region, and to assess the environment of its fillings. This work will provide new geochemical information that will improve scientific understanding of the developmental patterns of karst reservoirs.

Study area and methodology

Geographical setting

The Tazhong region is located in a low rise in the middle of the central uplift of the Tarim basin, and it is a large, mostly intact anticline composed of multiple secondary structural belts (Han et al., 2012; Sun et al., 2012). The region can be further divided into 3 tectonic elements: the Tazhong No. 1 Fault, the Tazhong North Slope, and the Central Fault Belt (Figure 1). The Tazhong No. 1 Fault controls the basic structure of the Tazhong Uplift. During the Early-Middle Ordovician, the Tazhong No. 1 Fault caused severe erosion within the Tazhong Uplift, which formed the weathering crust at the top of the Yingshan Formation of the Lower Ordovician. During this period, the Yijianfang Formation of the Middle Ordovician and Tumuxiuke Formation of the Upper Ordovician suffered erosion or loss, with remnants remaining only in certain locations.

The Ordovician layers of the Tazhong region are mainly composed of the Lower Ordovician Penglaiba (O_1p) and Yingshan (O_1y) Formations, and the Upper Ordovician

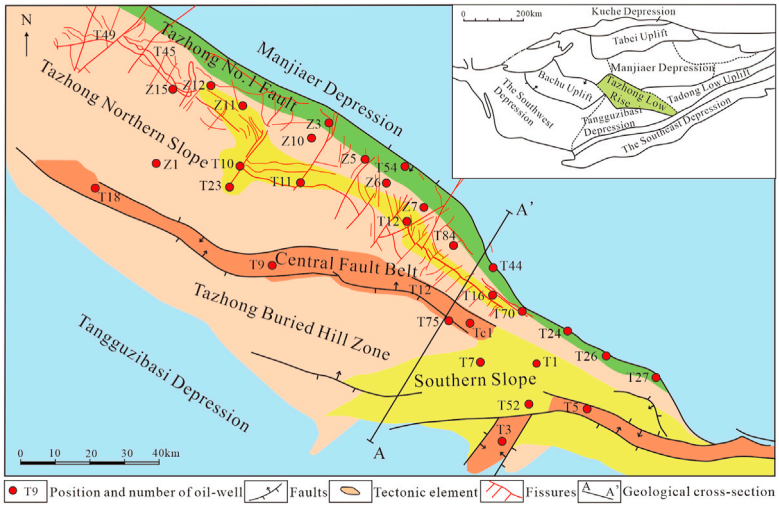

FIGURE 1
Geological map of tectonics and distribution of sampled wells within the Tazhong region of the Tarim basin.

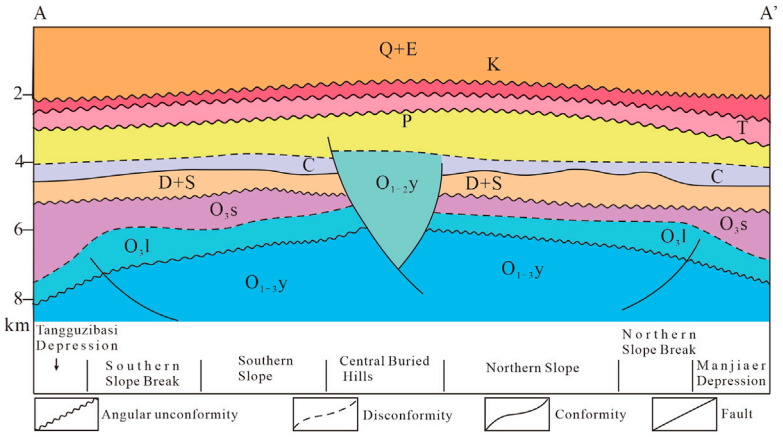

FIGURE 2
Schematic diagram of geological cross-section of the Tazhong Uplift in the southwest-to-northeast direction.

Lianglitag (O_2l) and Sangtamu (O_3s) Formations. The Upper Ordovician layer is not fully in contact with the overlying Silurian layer and the underlying Lower Ordovician layer. As compared to the stratigraphy of the Tabei region (Liu et al., 2013; Lu 2015), the Tazhong region is missing the layers corresponding to the Middle Ordovician Yijiangfang and Upper Ordovician Tumuxiuke Formations (Figure 2). The Yingshan Formation in the Tazhong region is dominated by high-energy sandy deposits with multiperiodic developments in the vertical direction that overlap with each other. The formation is relatively large in scale, and stretches from the northeast to the southeast, with a linear shape and belt-like distribution. The large, thick sets of shoal bodies that have developed over time are the basis for karst developments in the Yingshan Formation. The depositional discontinuity in this region provides favorable conditions for the development of karst in the carbonates of the Lower Ordovician Yingshan Formation. Exploration works have shown that the Lower Ordovician Yingshan Formation has large fractured karst reservoirs, and is thus a very important oil and gas producing stratum within carbonates in this region.

The Yingshan Formation in Tazhong can be divided into four segments from the bottom to the top. The lithology of the fourth segment ($O_{1\text{-}2}y^4$) mainly comprises sandy dolarenite,

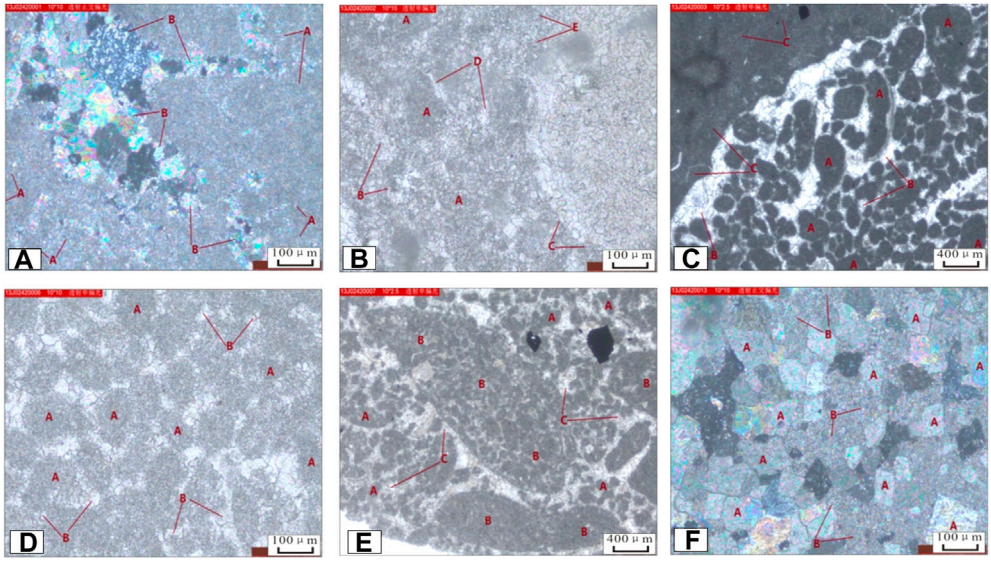

FIGURE 3
Petrological characteristics of carbonates from the Ordovician Yingshan Formation. **(A)**: T43-1 depth of 5280 m, O1-2y, microcrystalline limestone, orthogonally-polarized transmission 10*10. A: microcrystalline calcite, B: recrystallized calcite; **(B)**: T43-1, depth of 5285 m, O1-2y, fine-grained calcarenite, single-polarized transmission, 10**10. A: sand chip, B: powdered calcite, C: microcrystalline calcite, D: sparry calcite, E: powdery crumbs; **(C)**: 542, depth of 5289 m, O1-2y, micritic sparry calcarenite, single-polarized transmission, 10*2.5. A: sand chip, B: sparry calcite, C: argillaceous calcite ; **(D)**: T42-1, depth of 5273 m, O1-2y, sparry calcarenite, single-polarized transmission, 10*10. A: sand chip, B: sparry calcite; **(E)**: T44, depth of 5269 m, O1-2y, sparry calcirudite, single-polarized transmission, 10*2.5. A: sand chip, B: gravelly debris, C: sparry calcite; **(F)**: T8-5, depth of 6175 m, O1-2y, fine-grained dolomite with intense dolomitization, orthogonally-polarized transmission, 10*10. A: dolomite, B: calcite.

dolomitic micritic limestone and finely-crystalline dolomite; the lithology of the third segment (O_1-$2y^3$) mainly comprises dolomitic micritic limestone; the lithology of the second segment ($O_{1\text{-}2}y^2$) is mainly interbedded calcarenite and dolomitic micritic limestone; the first segment can be divided into an upper sub-segment ($O_{1-2}y^{1\text{upper}}$) and lower sub-segment ($O_{1-2}y^{1\text{lower}}$), with the lower sub-segment being composed of a thick layer of sparry calcarenite, while the upper sub-segment is mainly composed of micritic calcarenite sandwiching a thin layer of micritic limestone (Figure 3). As a result, the Yingshan Formation is being eroded layer by layer from the north towards the south, and the exposed strata are gradually declining. This erosion occurs in parallel with the direction of the Tazhong No. 1 Fault in a strip-like distribution. Around the Tazhong No. 1 Fault, the upper and lower sub-segments of the first Yingshan segment are being exposed sequentially. In the south, the second ($O_{1-2}y^2$) and third ($O_{1-2}y^3$) Yingshan segments are being exposed around the Tazhong No. 1 Fault.

A: T43-1 depth of 5280 m, $O_{1\text{-}2}y$, microcrystalline limestone, orthogonally-polarized transmission 10*10. A: microcrystalline calcite, B: recrystallized calcite; b: T43-1, depth of 5285 m, $O_{1\text{-}2}y$, fine-grained calcarenite, single-polarized transmission, 10*10. A: sand chip, B: powdered calcite, C: microcrystalline calcite, D: sparry calcite, E: powdery crumbs; c: 542, depth of 5289 m, $O_{1\text{-}2}y$, micritic sparry calcarenite, single-polarized transmission, 10*2.5. A: sand chip, B: sparry calcite, C: argillaceous calcite; d: T42-1, depth of 5273 m, $O_{1\text{-}2}y$, sparry calcarenite, single-polarized transmission, 10*10. A: sand chip, B: sparry calcite; e: T44, depth of 5269 m, $O_{1\text{-}2}y$, sparry calcirudite, single-polarized transmission, 10*2.5. A: sand chip, B: gravelly debris, C: sparry calcite; f: T8-5, depth of 6,175 m, $O_{1\text{-}2}y$, fine-grained dolomite with intense dolomitization, orthogonally-polarized transmission, 10*10. A: dolomite, B: calcite.

Samples and experiment

The experimental samples were mainly obtained from 25 Ordovician cores of paleokarst fissure fillings drilled from various depths within the Tazhong region of the Tarim basin (Figure 1), with a total of 49 samples. All samples were obtained in a range of 1.25–480 m below the top of the Ordovician strata, and the depths at which the samples were obtained, from the surface, ranged from 5553.5 m to 6,472.5 m. Three of the obtained samples were limestone samples of the Yingshan Formation, while the remaining 46 samples were karst fissure fillings (4 of which were grey-green calcite mudstone fillings, while 42 were samples of calcite fillings) (Table 1). These obtained samples are representative of the overall characteristics of karstification in the Ordovician carbonates of the Tazhong region.

TABLE 1 Carbon and oxygen isotopic characteristics of Ordovician carbonate karst fissure fillings from the Tazhong region.

Sampled well	Well depth of sample (m)	Stratum	Type of paleokarst fracture/ cavity	Lithological characteristics of filling	Isotopic characteristics		$\delta^{18}O_{Correction}$	Paleotemperature	Paleosalinity
					$\delta^{13}C$(PDB)	$\delta^{18}O$(PDB)			
					‰	‰		(°C)	Z value
T49	5553.5	$O_{1\text{-}2}y$	Dissolved cavity	Calcite	−0.4	−10.76	−4.32	36.3	121.12
T201-1H	5876.4	$O_{1\text{-}2}y$	Dissolved cavity	Calcite	−0.13	−6.29	0.15	15.4	123.90
T201-1H	5898.5	$O_{1\text{-}2}y$	Dissolved cavity	Calcite	0.25	−7.89	−1.45	22.3	123.88
T452	5897.3	$O_{1\text{-}2}y$	Dissolved cavity	Calcite	0.6	−5.76	0.68	13.2	125.66
T452	5913.7	$O_{1\text{-}2}y$	Dissolved cavity	Calcite	−0.53	−8.28	−1.84	24.0	122.09
T452	6243.2	$O_{1\text{-}2}y$	Dissolved fracture	Calcite	0.58	−8.6	−2.16	25.5	124.21
Z3	5699.3	$O_{1\text{-}2}y$	Dissolved fracture	Calcite	0.76	−11.83	−5.39	42.1	122.97
Z9	6162.6	$O_{1\text{-}2}y$	Dissolved fracture	Calcite	0.15	−12.41	−5.97	45.3	121.43
Z171	5973.5	$O_{1\text{-}2}y$	Dissolved fracture	Calcite	0.09	−9.11	−2.67	28.0	122.95
Z171	5999.5	$O_{1\text{-}2}y$	Dissolved fracture	Calcite	−0.23	−8.79	−2.35	26.4	122.45
Z442H	6276.1	$O_{1\text{-}2}y$	Dissolved fracture	Calcite	−1.76	−11.11	−4.67	38.2	118.16
Z442H	6302.5	$O_{1\text{-}2}y$	Dissolved fracture	Calcite	−1.68	−9.21	−2.77	28.5	119.27
Z105H	6352.3	$O_{1\text{-}2}y$	Bedrock	Limestone	0.33	−5.21	1.23	11.1	125.38
Z43-1	5825.6	$O_{1\text{-}2}y$	Bedrock	Limestone	0.02	−5.94	0.5	13.9	124.38
Z43-1	5859.6	$O_{1\text{-}2}y$	Bedrock	Limestone	−0.38	−7.16	−0.72	19.0	122.96
Z43-1	5967.3	$O_{1\text{-}2}y$	Dissolved Cavity	Calcium mudstone	0.8	−5.76	0.68	13.2	126.07
Z43-1	6055.8	$O_{1\text{-}2}y$	Dissolved Cavity	Calcium mudstone	0.99	−5.76	0.68	13.2	126.46
Z43-1	6132.8	$O_{1\text{-}2}y$	Dissolved Cavity	Calcium mudstone	1.04	−6.7	−0.26	17.1	126.09
Z43-1	6276.9	$O_{1\text{-}2}y$	Dissolved Cavity	Calcium mudstone	0.66	−6.48	−0.04	16.1	125.42
T12	6324.3	$O_{1\text{-}2}y$	Dissolved Fracture	Calcite	−1.79	−8.39	−1.95	24.6	119.46
T12	6358.7	$O_{1\text{-}2}y$	Dissolved Fracture	Calcite	−1.43	−8.33	−1.89	24.3	120.22
T12	6472.5	$O_{1\text{-}2}y$	Dissolved Fracture	Calcite	0.87	−9.08	−2.64	27.8	124.56
T35	6123.7	$O_{1\text{-}2}y$	Dissolved Fracture	Calcite	2.4	−3.97	2.47	6.5	130.24
T35	6153.4	$O_{1\text{-}2}y$	Dissolved Fracture	Calcite	2.38	−5.12	1.32	10.7	129.62
T35	6198.6	$O_{1\text{-}2}y$	Dissolved Fracture	Calcite	2.11	−4.45	1.99	8.3	129.41
T63	5783.2	$O_{1\text{-}2}y$		Calcite	1.83	−5.52	0.92	12.3	128.30

(Continued on following page)

10.3389/feart.2022.1047535

TABLE 1 (*Continued*) Carbon and oxygen isotopic characteristics of Ordovician carbonate karst fissure fillings from the Tazhong region.

Sampled well	Well depth of sample (m)	Stratum	Type of paleokarst fracture/ cavity	Lithological characteristics of filling	Isotopic characteristics		$\delta^{18}O_{Correction}$	Paleotemperature	Paleosalinity
					$\delta^{13}C$(PDB)	$\delta^{18}O$(PDB)			
					‰	‰		(°C)	Z value
			Dissolved Fracture						
T63	5976.3	$O_{1\text{-}2}y$	Dissolved Fracture	Calcite	0.77	−8.15	−1.71	23.4	124.82
T83	6218.5	$O_{1\text{-}2}y$	Dissolved Fracture	Calcite	1.01	−5.09	1.35	10.6	126.83
T83	6242.5	$O_{1\text{-}2}y$	Dissolved Fracture	Calcite	1.16	−5.52	0.92	12.3	126.93
T84	6012.7	$O_{1\text{-}2}y$	Dissolved Fracture	Calcite	0.57	−10.71	−4.27	36.0	123.13
T84	6033.2	$O_{1\text{-}2}y$	Dissolved Fracture	Calcite	0.34	−5.86	0.58	13.6	125.08
T84	6051.1	$O_{1\text{-}2}y$	Dissolved Fracture	Calcite	−0.51	−8.87	−2.43	26.8	121.84
T162	5568.4	$O_{1\text{-}2}y$	Dissolved Fracture	Calcite	−2.13	−10.95	−4.51	37.3	117.48
T201-1H	5595.5	$O_{1\text{-}2}y$	Dissolved Fracture	Calcite	0.24	−6.8	−0.36	17.5	124.41
T201-1H	5742.6	$O_{1\text{-}2}y$	Dissolved Fracture	Calcite	−1	−12.7	-6.26	47.0	118.93
Z29	5553.5	$O_{1\text{-}2}y$	Dissolved Fracture	Calcite	2.48	−5.42	1.02	11.9	129.68
Z32	6311.2	$O_{1\text{-}2}y$	Dissolved Fracture	Calcite	−1.3	−9.51	−3.07	29.9	119.90
Z41	5818.9	$O_{1\text{-}2}y$	Dissolved Fracture	Calcite	−1.21	−4.26	2.18	7.6	122.70
Z41	5845.3	$O_{1\text{-}2}y$	Dissolved Fracture	Calcite	−1.57	−7.61	−1.17	21.0	120.29
Z41	5866.9	$O_{1\text{-}2}y$	Dissolved Fracture	Calcite	−2.63	−8.44	−2	24.8	117.71
Z43-1	6012.7	$O_{1\text{-}2}y$	Dissolved Fracture	Calcite	−0.17	−9.77	−3.33	31.2	122.09
Z49	5990.5	$O_{1\text{-}2}y$	Dissolved Cavity	Calcite	1.67	−8.26	−1.82	24.0	126.61
Z49	6018.4	$O_{1\text{-}2}y$	Dissolved Cavity	Calcite	2.31	−7.08	-0.64	18.7	128.51

(Continued on following page)

10.3389/feart.2022.1047535

TABLE 1 (*Continued*) Carbon and oxygen isotopic characteristics of Ordovician carbonate karst fissure fillings from the Tazhong region.

Sampled well	Well depth of sample (m)	Stratum	Type of paleokarst fracture/ cavity	Lithological characteristics of filling	Isotopic characteristics		$\delta^{18}O_{Correction}$	Paleotemperature	Paleosalinity
					$\delta^{13}C$(PDB)	$\delta^{18}O$(PDB)			
					‰	‰		(°C)	Z value
Z49	6037.8	$O_{1-2}y$	Dissolved Cavity	Calcite	2.03	−4.74	1.7	9.3	129.10
Z49	6051.2	$O_{1-2}y$	Dissolved Fracture	Calcite	2.22	−6.08	0.36	14.5	128.82
Z51	5734.6	$O_{1-2}y$	Dissolved Fracture	Calcite	−0.23	−11.05	−4.61	37.8	121.33
Z106	5835.8	$O_{1-2}y$	Dissolved Fracture	Calcite	−0.57	−5.08	1.36	10.6	123.60
Z166H	5973.3	$O_{1-2}y$	Dissolved Fracture	Calcite	0.47	−4.64	1.8	8.9	125.95
Z171	6217.4	$O_{1-2}y$	Dissolved Fracture	Calcite	−1.08	−9.9	−3.46	31.9	120.16

After the samples were observed as slices, fresh sections were then ground to 200-mesh, and an on-line analysis of the carbon and oxygen isotope values was performed using a combination of the Gasbench II and MAT253 system. The accuracy of the analysis was calibrated using the GBW04405, GBW04406, GBW04416 and GBW04417 Chinese national standards, with the NBS18 standard being used for monitoring measurements. The standard deviations of the $\delta^{13}C$ and $\delta^{18}O$ values were found to be 0.005% and 0.07%, respectively. The test results were reported in the PDB standard, and the temperature and humidity at which the tests were performed at were 25°C and 60%, respectively. The serial number of the test is QC-2-030-2013. The testing of the samples was performed at the Karst Geology Resources and Environment Test Center of the Ministry of Land and Resources.

Results and analysis

Geochemical characteristics of carbon and oxygen isotope values

The ^{13}C and ^{18}O enrichment levels of marine carbonates are mainly affected by factors such as sea level rises and falls, organic carbon sources, burial rates, and the redox conditions within the diagenetic environment of the sediment (Zheng and Chen, 2000). Hence, changes of diagenetic environment and properties of diagenetic fluid in sediments will change the resulting carbon and oxygen isotopic compositions of the carbonates. The results of the analysis of carbon and oxygen isotopes in the 49 limestone and calcite Ordovician carbonate filling samples from the Tazhong region (42 calcite samples, 4 calcite mudstone samples and 3 limestone samples) are shown in Table 1.

Many test results based on the PDB standard have shown that most modern inorganic marine carbonates have $\delta^{13}C$ and $\delta^{18}O$ values that approach 0% (Gu 2000; Liu et al., 2004). Based on the test results of the samples (Table 1), the Ordovician carbonate karst fissure fillings from the Tazhong region have $\delta^{13}C$ and $\delta^{18}O$ values that are clearly distinct from modern values, and they also have a high level of variability. The $\delta^{13}C$ (PDB) values ranged from 2.48% to −2.13%, and had an average value of 0.23%; the $\delta^{18}O$ values ranged from −3.97% to −12.7%, with an average value of −7.64%.

Compared to previous examinations of older carbonates, this study's results are distinctly different from those of Gu (2000), Liu et al. (2008) and Gao et al. (2011). Gu (2000) found an average $\delta^{18}O$ isotope value of −4% to −5% for Devonian to Cambrian marine carbonates. Liu et al. (2008) found that the $\delta^{13}C$ values of microcrystalline limestone from the Tahe oilfields were distributed between −1.697% and 0.921%, with an average value of −0.45%; the corresponding $\delta^{18}O$ values were distributed between −8.64% and −4.153%. Gao et al. (2011) found that the marine carbonates in the outcrop zone of Tabei to have $\delta^{13}C$ and $\delta^{18}O$ values ranging between −5.0% and 5.0% and −6.0%

to −4.0%, respectively. These results uniformly display a characteristically high level of ^{18}O depletion.

Liu et al. (2004) found that the calcite fillings of Ordovician carbonate karst fissures from Lunguxi had $\delta^{13}C$ values of −0.70% to −6.50%, with an average value of −1.76%, and $\delta^{18}O$ values of −3.75%–17.10%, with an average value of −9.42%. This is similar to the carbon and oxygen isotopic characteristics of calcite Ordovician karst fissure fillings from the Tahe oilfields (average $\delta^{13}C$ and $\delta^{18}O$ values of −0.807% and −9.14% from 21 data points; Liu et al., 2008).

The Lungudong (average $\delta^{13}C$: −1.40%, average $\delta^{18}O$: −10.74%, 25 data points; Zhang et al., 2015) and Lunguxi [$\delta^{13}C$ (PDB): 6.03% to −8.69%, average $\delta^{13}C$: −1.40%; $\delta^{18}O$: −5.78%–17.28%, average $\delta^{18}O$: −10.74%; Zhang et al., 2016a] regions, as well as the Halahatang region ($\delta^{13}C$ (PDB): 2.12% to −4.09%, average $\delta^{13}C$: −0.65%; $\delta^{18}O$: −4.14% to −15.71%, average $\delta^{18}O$: −9.95%) are not very different from each other, with only a few data points drifting towards extreme values (Zhang et al., 2016b).

The $\delta^{13}C$ and $\delta^{18}O$ distributions in calcite and calcite mudstone samples obtained from reservoir spaces such as dissolved cavities and fractures within the Tazhong region have significant variability. Nonetheless, the $\delta^{18}O$ values are distinctly negative-biased, with an average value of -7.64%; the $\delta^{13}C$ values tend towards both negative and positive extremes, which reflects on a paleogeological environment in which paleokarstification occurred *via* shallow to deep burial karstification, followed by alterations and filling through dissolution in later periods. The distribution of $\delta^{13}C$ values from 2.48% to −2.13% with nearly equal positive and negative distributions provides further proof of the complexity of paleokarstification processes in this region.

Relationship between paleosalinity levels and carbon/oxygen isotopic ratios

The analysis of stable carbon and oxygen isotopic ratios is a frequently used procedure in paleoenvironmental studies, as these ratios reflect the sedimentary environment and typically change across stratigraphic boundaries (Guo et al., 2010). In seawater, the $\delta^{18}O$ value increases as salinity increases (Wang et al., 2014), since ^{16}O is preferentially evaporated and transformed into atmospheric precipitation; the remaining seawater, which is now higher in salinity, becomes enriched in ^{18}O. However, as $\delta^{18}O$ levels are more strongly affected by karstification, they are less accurate as a measure of primitive sedimentary environments (Wang et al., 2014). Zhang (1985) analyzed the isotopic compositions of Cambrian and Ordovician carbonate samples obtained from various regions of China, and found that during karstification, the isotopic exchange reaction between ^{13}C and ^{12}C is significantly weaker than that between ^{18}O and ^{16}O. Hence, the isotopic composition of carbon can reflect changes in primitive sedimentary environments.

Keith and Weber (1964) derived the following empirical equation using $\delta^{13}C$ and $\delta^{18}O$ values in limestone to produce a criterion for discriminating between marine and non-marine carbonates:

$$Z = 2.048 \times (\delta^{13}C + 50) + 0.498 \times (\delta^{18}O + 50) \quad (1)$$

The $\delta^{13}C$ and $\delta^{18}O$ values in the formula are both in the PDB standard. Marine carbonates have $Z > 120$, while freshwater carbonates have $Z < 120$. When $Z = 120$, the environment of the carbonate is then of the uncertain type. This conclusion has been confirmed by many subsequent research results (Zhong et al., 2012). Table 1 shows that the $\delta^{13}C$ values of the 49 tested samples are distributed within the range of −2.63%–2.48%, while the distribution range of their Z values is 117.48–130.24. Except for 7 samples that had a distribution between 117.48–119.9, the remaining 42 samples had Z values larger than 120, within a distribution range of 120.16–130.24. This signifies that development and filling processes of the karst fracture/cavity systems in the Tazhong region have been modified by a multitude of superimposed karstification processes, including freshwater karstification of the paleoweathering crust, karstification by a mix of seawater and freshwater, as well as burial karstification.

Analysis of the correlations between $\delta^{13}C$ and $\delta^{18}O$ with Z (Figures 4A,B) show that the $\delta^{13}C$ values in this region correlate very well with Z, with a correlation coefficient of 0.9560, but $\delta^{18}O$ correlates poorly with Z, and has a correlation coefficient of only 0.7414. This indicates that isotopic fractionation in carbonates is mainly controlled by the redox conditions of the environment, and $\delta^{13}C$ and $\delta^{18}O$ are both affected by medium salinity, with $\delta^{13}C$ particularly showing a significant level of correlation with the salinity of the medium (Keith and Weber 1964; Zhang 1985; Wang et al., 2014).

The relationship between oxygen isotopic ratios and paleotemperatures

The primary factor that determines oxygen-isotope ratios in carbonate depositional environments is temperature, so changes in the oxygen-isotope content reflect changes in paleotemperature in the diagenetic environment (Scholle and Arthur 1980; Huang et al., 2014). Lower $\delta^{18}O_{PDB}$ values reflect higher paleotemperatures, and higher $\delta^{18}O_{PDB}$ values conversely reflect a lower paleotemperature.

A calibration for the “periodic effect” was performed based on the correlation between $\delta^{18}O$ values and geological period given by Keith and Weber (1964), with the average $\delta^{18}O$ value of karst fillings in the Tazhong region being −7.64%. The average $\delta^{18}O$ value of marine limestones from the Paleozoic era is approximately −1.2%, which differs by −6.44% from the average found in this study. An average

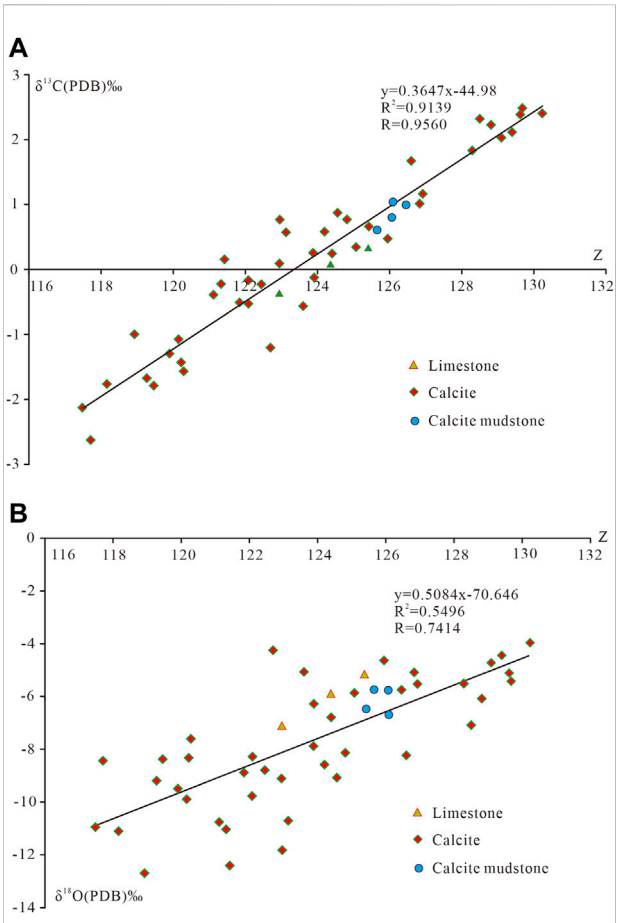

FIGURE 4
(A) The δ13C-Z correlation of Ordovician paleokarst fissure fillings from the Tazhong region. **(B)** The δ18O-Z correlation of Ordovician paleokarst fissure fillings from the Tazhong region.

$\triangle\delta^{18}O$=6.44‰ was then used as the calibration value for the "periodic effect" (Shao 1994).

The paleotemperature was calculated using the formula derived by Craig (1961) based on the relationship between the oxygen isotopic ratio and paleotemperature.

$$T(℃) = 16.9 - 4.2 \times (\delta O_c - \delta O_w) + 0.13 \times (\delta O_c - \delta O_w)^2 \quad (2)$$

In this formula, the equivalence $\delta O_c - \delta O_w = (\delta^{18}OCaCO3 - \delta^{18}OH2O) + 0.22$ was used, since the $\delta^{18}O$ value of $CaCO_3$ obtained in the lab is in the PDB standard, while the $\delta^{18}O$ of water is in the SMOW (Standard Mean Ocean Water) standard; the calculated $\delta^{18}OCaCO3$ thus needed to be calibrated in temperature calculations using Eq. 2. As the $\delta^{18}O$ value of the Ordovician ocean remains unknown for now, it was temporarily assumed to be the same as that of modern oceans; i.e., $\delta^{18}OH2O = 0$ (SMOW standard) (Shao 1994).

Hence, in this study's calculations on the paleotemperatures of karst fillings and the carbonate matrix from the Tazhong region, the overall equation for calculating the paleotemperature of karst filling samples is:

$$T(℃) = 16.9 - 4.2 \times \left(\delta^{18}O_{CaCO_{3correction}} + 0.22\right) + 0.13 \times \left(\delta^{18}O_{CaCO_{3correction}} + 0.22\right)^2 \quad (3)$$

These calculations have shown that the Formation paleotemperatures of Ordovician carbonate karst fillings from the Tazhong region ranged from 6.5°C to 47.1°C, with an average paleotemperature of 21.8°C. This result shows that the carbonate karst fillings have undergone the following dissolution and filling processes: surface exposure, followed by shallow burial, and finally deep burial.

Discussion

Analysis of filling environments and paleokarst developmental periods

The $\delta^{18}O$ values of limestones and calcite paleokarst fillings from the Tazhong region show a bias towards negative values, and a large range of $\delta^{13}C$ values. This is related to the uplifting of the surface during the Ordovician period, which placed the entire surface in an open environment, thus causing widespread dissolution by atmospheric precipitation, whose CO_3^{2-} anions are characteristically highly enriched in ^{12}C and ^{16}O (Gasparrini et al., 2006; Azmy et al., 2009).

Based on the $\delta^{13}C$-$\delta^{18}O$ relational diagram shown in Figure 5, the calcite Ordovician carbonate paleokarst fillings can be divided based on their paleokarst depositional environments into 4 different types, as shown in Table 2.

Type I is a marine depositional environment that reflects the isotopic characteristics of the syndiagenetic marine depositional environment as well as early paleokarstification and sedimentation. The calcite fillings within the karst fractures and cavities of Ordovician Yingshan Formation carbonates have $\delta^{13}C$ values of 1.77–2.48% and $\delta^{18}O$ values of −7.26 to -3.97%. The burial depth, temperature, and leaching dissolution of the sediments have an effect on $\delta^{13}C$ and $\delta^{18}O$ value. As the salinity increases, the $\delta^{13}C$ and $\delta^{18}O$ values both increase. The $\delta^{18}O$ value decreases as temperature increases; as the temperature and burial depth increase, the $\delta^{18}O$ value will become biased towards negative values (McCaig et al., 2000). As the $\delta^{13}C$ value is intimately related to paleosalinity, and is only weakly affected by temperature, its value closely reflects the depositional environment of these syndiagenetic marine paleokarsts.

Type II is an atmospheric freshwater karstification environment, which reflects on the isotopic characteristics of the atmospheric freshwater karstification and depositional environment that occurred during the period in which bare

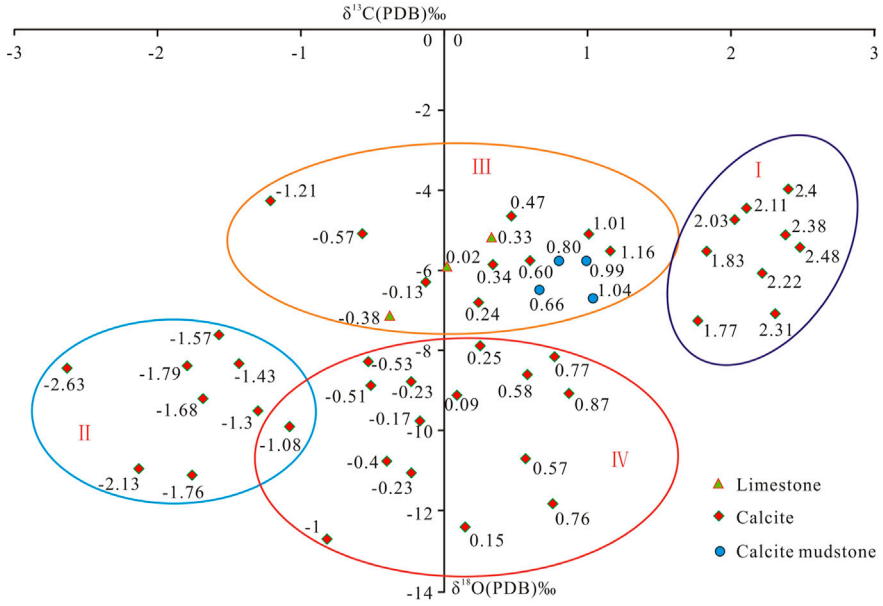

FIGURE 5
Bivariate δ13C-δ18O plot of Ordovician paleokarst fissure filings from the Tazhong region. Roman numerals refer to developmental periods shown in Table 2.

TABLE 2 Paleokarst developmental periods and characteristics of corresponding filling environment.

Developmental period	Formative environment	Isotopic characteristics	
		$\delta^{13}C$(PDB)‰	$\delta^{18}O$(PDB)‰
I	Marine deposition and filling	1.77~2.48	−7.26~-3.97
II	Atmospheric freshwater karstification	−2.63~−1.08	−11.11~−7.61
III	Shallow burial karstification	−1.21~1.16	−9.11~−4.62
IV	Deep burial karstification	−1.01~0.76	−12.70~−9.77

paleokarsts were exposed *via* the weathering crust. The calcite paleokarst fissure fillings had $\delta^{13}C$ values in the range of −2.63 to −1.08%, and $\delta^{18}O$ values in the range of −11.11 to -7.61%. Due to the influence of atmospheric freshwater (Gasparrini et al., 2006), the $\delta^{13}C$ value of the fillings is significantly lower than that of the bedrock, as these were formed in an open to semi-open environment. Atmospheric precipitation infiltrates along fractures and joints, dissolving and filling the carbonate bedrock to form fractures and cavities. As the diagenetic $\delta^{18}O$ value is determined by the temperature and isotopic composition of the medium, and atmospheric freshwater is depleted in ^{18}O but enriched in ^{12}C, $\delta^{13}C$ drifts towards negative values, while $\delta^{18}O$ tends towards highly negative values (Shields et al., 2003).

Type III is a shallow-burial karstification environment, in which calcite karst fissure fillings have $\delta^{13}C$ values of −1.21 to 1.16% and $\delta^{18}O$ values of −9.11 to −4.62%. The $\delta^{18}O$ value is significantly biased towards negative values, while the $\delta^{13}C$ value spans both negative and positive values, which indicates that the paleokarsts have undergone freshwater karstification before entering the shallow-burial kastification period: i.e., a successive mode of paleokarst development. Furthermore, the decomposition and methanation (CH_4) of organic material by methanogenic bacteria creates ^{12}C-enriched CH_4 and ^{13}C-enriched CO_2. Since the CO_2 released from methane fermentation participates in paleokarstification and deposition processes, the calcite fillings in the karst fractures and cavities become enriched in ^{13}C. The 3 micritic limestone (bedrock) samples and 4 calcite mudstone cavity-filling

samples all have carbon-isotope ratios that fall within this range.

Type IV is a deep-burial karstification environment, whose calcites have $\delta^{13}C$ values of −1.01 to 0.76% and $\delta^{18}O$ values of −12.70 to −9.77%, thus showing more negative $\delta^{18}O$ values. This study's calculations show that the paleotemperatures reached a maximum of 47.1°C, indicating that hot fluids played a significant role in the Formation and burial conditions of these calcite karst fissure fillings. As the fillings were affected and altered by ^{18}O-deficient hot fluids from deep regions during the deep burial stage, its $\delta^{18}O$ values characteristically show a significant negative bias (Lavoie and Chi 2006; Liu et al., 2012).

Geological significance

Changes in the carbon and oxygen isotopic compositions of carbonates are an embodiment of changes in the paleoclimate and paleooceanic environment, and thus serve as useful aids for studies of geological processes and depositional characteristics (Loucks 1999). The karst developments of carbonate rocks of Ordovician Yingshan Formation in Tazhong area are filled to different degrees by calcite and calcite mudstones. Early calcite fillings show bead-like dissolution pores that are caused by dissolution in a later period, and thus reflect the multi-periodic characteristics of the paleokarst.

Under equilibrium isotope fractionation, $\delta^{18}O$ is mainly controlled by environmental temperature changes, and the temperature-controlled water-rock reactions and isotopic fractionation coefficient gives the $\delta^{18}O$ value a −0.24%/°C temperature gradient (Hendy and Wilson 1986). The $\delta^{18}O$ values of calcite and calcite mudstones in Tazhong paleokarst fillings tend towards negative values, far below that of seawater, thus showing that the karst was developed through the influence of atmospheric precipitation in paleoweathering crusts.

As the burial depth increases, temperature and pressure also increase. The $\delta^{13}C$ values do not change as prominently as $\delta^{18}O$ values and tend to be more stable, as they are primarily determined by the organic carbon content and hydrocarbon (CH_4) conversion within the rocks. However, as compared to $\delta^{18}O$, $\delta^{13}C$ is more easily affected by evaporation, kinetic fractionation and early deposition of carbonates, causing its value to become biased towards positive values (Gent et al., 2001; Guo et al., 2010).

The calcite and calcite mudstone fillings in this research area have $\delta^{13}C$ (PDB) values between 2.48% and −2.13%, with an average value of 0.23%. The $\delta^{13}C$ values span a larger range and tend towards both extremes, signifying the presence of mixed seawater-freshwater karstification. This also reveals that the karsts have undergone multiple periods of transformation, including syndiagenesis, freshwater karstification, and burial karstification.

Based on statistical analysis of the conventional physical properties of 252 rock cores drilled from 25 wells, the experimentally measured porosity was 0.16%–11.25%, with an average of 0.82%; the measured permeability was 0.005–161 mD, with an average of 3.667 mD; the permeability as interpreted from well logs ranged from 0.007 to 225.532 mD, with an average value of 2.895 mD. This indicates that the porosity of the Yingshan Formation matrix primarily consists of low-porosity and low-permeability reservoirs, and that the effective reservoirs are mainly fracture-cavity systems composed of dissolved fractures, pores and cavities formed by paleokarstification. This finding thus provides a direction for the exploration and development of oil and gas fields and the prediction of favorable reservoir zones in the Tazhong region within the Tarim basin. Urey, 1948, Kuypers et al., 1999, Liu et al., 2004, Li, 2022a, Li et al., 2019, Li et al., 2022, Li et al., 2022b, Zhang et al., 2022a, Zhang et al., 2022b, Zhang et al., 2022c, Zhang et al., 2022d, Fan et al., 2022.

Conclusion

Using typical calcite and calcite mudstone paleokarst fissure-filling samples that are representative of the region, the stable carbon and oxygen isotopic characteristics of these samples were analyzed, and the developmental periods and depositional environment of the paleokarsts were reconstructed. The analysis of calcite carbon and oxygen isotopic ratios indicated that their $\delta^{13}C$ (PDB) values spanned a relatively large range, from 2.48% to −2.13%, with an average value of 0.23%; its $\delta^{18}O$ values ranged from −3.97% to −12.7%, with an average value of −7.64%.

The paleotemperatures at which the fillings were deposited within the paleokarst fissures was found to range from 6.5°C to 47.1°C, with an average value of 21.8°C. The Z values of the medium salinity ranged between 117.48 and 130.24, with an average value of 123.94; $\delta^{13}C$ values were found to correlate closely with the Z value, with a correlation coefficient of 0.958. Four types of carbonate paleokarstification and depositional environments have thus been revealed: a marine syndiagenetic depositional environment, an atmospheric freshwater karst-filling environment, a shallow-burial karstification paleoenvironment, and a deep-burial, high-temperature paleoenvironment. These results show that the dissolved pores, cavities and fractures formed by paleokarstification during later periods are the main effective reservoir spaces within the Tazhong region, thus providing a scientific basis for well placements in exploration and development work, and karst reservoir predictions.

Data availability statement

The original contributions presented in the study are included in the article/supplementary material, further inquiries can be directed to the corresponding author.

Author contributions

All authors listed have made a substantial, direct, and intellectual contribution to the work and approved it for publication.

Acknowledgments

We would like to thank the National Key Research and Development Program (No. 2018YFC0604301), the National Natural Science Foundation of China (No. 41302122), the Geological Survey Program of the China Geological Survey (No. DD20190562 and DD20221658), and the basic research program of Institute of Karst Geology, Chinese Academy of Geological Sciences (No. 2021008) for supporting this article. We would also like to express our sincere gratitude to the reviewers and editors for their valuable comments on this article.

Conflict of interest

The authors declare that the research was conducted in the absence of any commercial or financial relationships that could be construed as a potential conflict of interest.

Publisher's note

All claims expressed in this article are solely those of the authors and do not necessarily represent those of their affiliated organizations, or those of the publisher, the editors and the reviewers. Any product that may be evaluated in this article, or claim that may be made by its manufacturer, is not guaranteed or endorsed by the publisher.

References

Arthur, M. A., Dean, W. E., and Pratt, L. M. (1988). Geochemical and climatic effects of increased marine organic carbon burial at the Cenomanian/Turonian boundary. *Nature* 335, 714–717. doi:10.1038/335714a0

Azmy, K., Knight, I., Lavoie, D., and Chi, G. (2009). Origin of dolomites in the boat harbour formation, st. George group, in Western newfoundland, Canada: Implications for porosity development. *Bull. Can. Petroleum Geol.* 57 (1), 81–104. doi:10.2113/gscpgbull.57.1.81

Chen, J. S., Li, Z., Wang, Z. Y., Tan, X. C., Li, L., and Ma, Q. (2007). Paleokarstification and reservoir distribution of ordovician carbonates in Tarim basin. *Acta Sedimentol. Sin.* 25 (6), 858–868. (in Chinese).

Craig, H. (1961). Isotopic variations in meteoric waters. *Science* 133, 1702–1703. doi:10.1126/science.133.3465.1702

Epstein, S., and Mayeda, T. K. (1953). Variation of O18 content of waters from natural sources. *Geochim. Cosmochim. Acta* 4, 213–224. doi:10.1016/0016-7037(53)90051-9

Fan, C. H., Xie, H. B., Li, H., Zhao, S. X., Shi, X. C., Liu, J. F., et al. (2022). Complicated fault characterization and its influence on shale gas preservation in the southern margin of the Sichuan Basin, China. *Lithosphere*, 8035106. doi:10.2113/2022/8035106

Gao, Q. D., Zhao, K. Z., Hu, X. F., and Pan, W. Q. (2011). C-O, Sr isotope composition of the carbonate in Ordovician in Tarim Basin and implication for fluid origin. *J. Zhejiang Univ. Sci. Ed.* 38 (5), 579–583. (in Chinese).

Gasparrini, M., Bechstaedt, T., and Boni, M. (2006). Massive hydrothermal dolomites in the southwestern Cantabrian Zone (Spain) and their relation to the Late Variscan evolution. *Mar. Pet. Geol.* 23 (5), 543–568. doi:10.1016/j.marpetgeo.2006.05.003

Gent, D. D., Baker, A., Massault, M., Proctor, C., Gilmour, M., Pons-Branchu, E., et al. (2001). Dead carbon in stalagmites: Carbonate bedrock paleodissolution vs. ageing of soil organic matter: Implications for ^{13}C variations in speleothems. *Geochim. Cosmochim. Acta* 20, 3443–3457. doi:10.1016/s0016-7037(01)00697-4

Gu, J. Y. (2000). Characteristics and origin analysis of dolomite in lower Ordovician of Tarim Basin. *XJ Pet. Geol.* 21 (2), 120–122. (in Chinese).

Guo, H., Du, Y. S., and Huang, J. H. (2010). Habitat types and palaeoenvironments of the mesoproterozoic gaoyuzhuang Formation in pingquan, hebei province. *J. Palaeogeogr.* 12 (3), 269–280.

Han, J. F., Zhang, H, Z., Yu, H. F., Ji, Y. G., Sun, C. H., Han, J., et al. (2012). Hydrocarbon accumulation characteristics and exploration on large marine carbonate condensate field in Tazhong Uplift. *Acta Petrol. Sin.* 28 (3), 769–782. (in Chinese).

Hendy, C. H., and Wilson, A. T. (1986). Palaeoclimatic data from speleothems. *Nature* 216, 48–51. doi:10.1038/219048a0

Huang, S. J., Lan, Y. F., Huang, K. K., and Lu, J. (2014). Vug fillings and records of hydrothermal activity in the middle permian qixia formation,Western sichuan basin. *Acta Petrol. Sin.* 30 (3), 687–698. (in Chinese).

Huang, S. J., Li, X. N., Hu, Z. W., Liu, S. B., Huang, K. K., and Zhong, Y. J. (2016). Comparison of carbon and oxygen isotopic composition of Feixianguan carbonates, Early Triassic, between east and west sides of Kaijiang-Liangping trough, Sichuan Basin, and the significance for paleoceanography. *Geochimica* 45 (1), 24–40. (in Chinese).

Keith, M. H., and Weber, J. N. (1964). Carbon and oxygen isotopic composition of selected limestones and fossils. *Geochim. Cosmochim. Acta* 28 (11), 1787–1816. doi:10.1016/0016-7037(64)90022-5

Kuypers, M. M., Pancost, R. D., and Sinninghe Damsté, J. S. (1999). A large and abrupt fall in atmospheric CO_2 concentration during Cretaceous times. *Nature* 399, 342–345. doi:10.1038/20659

Lavoie, D., and Chi, G. X. (2006). Hydrothermal dolomitization in the lower silurian La vieille Formation in northern new brunswick: Geological context and significance for hydrocarbon exploration. *Bull. Can. Petroleum Geol.* 54 (4), 380–395. doi:10.2113/gscpgbull.54.4.380

Li, D., Liang, D., and Jia, C. (1996). Hydrocarbons accumulations in the Tarim basin, China. *AAPG Bull.* 80, 1587–1603.

Li, H. (2022a). Research progress on evaluation methods and factors influencing shale brittleness: A review. *Energy Rep.* 8, 4344–4358. doi:10.1016/j.egyr.2022.03.120

Li, H., Tang, H. M., Qin, Q. R., Zhou, J. L., Qin, Z. J., Fan, C. H., et al. (2019). Characteristics, formation periods and genetic mechanisms of tectonic fractures in the tight gas sandstones reservoir: A case study of xujiahe Formation in YB area, sichuan basin, China. *J. Pet. Sci. Eng.* 178, 723–735. doi:10.1016/j.petrol.2019.04.007

Li, H., Zhou, J. L., Mou, X. Y., Guo, H. X., Wang, X. X., An, H. Y., et al. (2022b). Pore structure and fractal characteristics of the marine shale of the longmaxi Formation in the changning area, southern sichuan basin, China. *Front. Earth Sci.* 10, 1018274. doi:10.3389/feart.2022.1018274

Li, J., Li, H., Yang, C., Wu, Y. J., Gao, Z., and Jiang, S. L. (2022). Geological characteristics and controlling factors of deep shale gas enrichment of the Wufeng-Longmaxi Formation in the southern Sichuan Basin, China. *Lithosphere*, 4737801. doi:10.2113/1970/4737801

Li, X. Q., and Wan, G. J. (1999). Problems in studies on carbon and oxygen stable isotopes in carbonates. *Adv. Earth Sci.* 14 (3), 262–268.

Liu, C. G., Li, G. R., Zhu, C. L., and Liu, G. Y. (2008). Geochemistry characteristics of carbon, oxygen and strontium isotopes of calcites filled in karstic fissure-cave in lower-middle Ordovician of Tahe Oilfield, Tarim Basin. *Earth Science-Journal China Univ. Geosciences* 33 (3), 377–386. (in Chinese).

Liu, J. Q., Li, Z., Huang, J. C., and Yang, L. (2012). Distinct sedimentary environments and their influences on carbonate reservoir evolution of the Lianglitag Formation in the Tarim basin, Northwest China. *Sci. China Earth Sci.* 42 (12), 1641–1655. doi:10.1007/s11430-012-4457-5

Liu, K. Y., Bourdet, J., Zhang, B. S., Zhang, N., Lu, X., Liu, S., et al. (2013). Hydrocarbon charge history of the Tazhong Ordovician reservoirs, Tarim

Basin as revealed from an integrated fluid inclusion study. *Petroleum Explor. Dev.* 40 (2), 183–193. (In Chinese). doi:10.1016/s1876-3804(13)60021-x

Liu, X. P., Wu, X. S., and Zhang, X. Z. (2004). Geochemistry characteristics of carbon and oxygen isotopes of Ordovician carbonate paleokarst reservoir in the Western region of Lungu, Tarim Basin. *J. Xi'an Shiyou Univ. Nat. Sci. Ed.* 19 (4), 69–72. (in Chinese).

Liu, Z. H., Dai, Y. N., and Lin, Y. S. (2004). Paleoenvironmental reconstruction based on hydrochemistry and tufa stable isotopes: Case study of Xiangshui River, LiBo, Guizhou. *Quatern Sci.* 24 (4), 447–454. (in Chinese).

Liu, Z. H., Yuan, D. X., and He, S. Y. (1997). Stable carbon isotope geochemical and hydrochemical features in the system of carbonate-H_2O-CO_2 and their implications: Evidence from several typical karst areas of China. *Acta Geol. Sin.* 71 (3), 281–288. (in Chinese).

Loucks, R. G. (1999). Paleocave carbonate reservoirs: Origins, burial-depth modification, spatial complexity, and reservoir implications. *AAPG Bull.* 83 (11), 1795–1834.

Lu, H. Z., and Shan, Q. (2015). Composition of ore forming fluids in metal deposits and fluid inclusion. *Acta Petrol. Sin.* 31 (4), 1108–1116. (in Chinese).

Luo, C. S., Yang, H. J., Li, J. H., Xie, H. W., and Huang, G. J. (2011). Characteristics of high quality Ordovician reservoirs and controlling effects of faults in the Tazhong area, Tarim Basin. *Petroleum Explor. Dev.* 38 (6), 716–724. (in Chinese).

McCaig, A. M., Tritlla, J., and Banks, D. A. (2000). Fluid mixing and recycling during Pyrenean thrusting: Evidence from fluid inclusion halogen ratios. *Geochim. Cosmochim. Acta* 64, 3395–3412. doi:10.1016/s0016-7037(00)00437-3

Scholle, P. A., and Arthur, M. A. (1980). Carbon isotope fluctuations in Cretaceous pelagic limestones: Potential stratigraphic and petroleum exploration tool. *AAPG Bull.* 64, 67–87.

Shao, Y. L. (1994). The relation of the oxygen and carbon isotope in the carbonate rocks to the paleotemperature etc. *J. China Univ. Min. Technol.* 23 (1), 39–45. (in Chinese).

Shen, A. J., Wang, Z. M., Yang, H. J., and Ni, X. F. (2006). Genesis classification and characteristics of Ordovician carbonate reservoirs and petroleum exploration potential in Tazhong region, Tarim basin. *Mar. Orig. Pet. Geol.* 11 (4), 1–12. (in Chinese).

Shields, G. A., Carden, G. A., Veizer, J., Meidla, T., Rong, J. Y., and Li, R. Y. (2003). Sr, C and O isotope geochemistry of ordovician brachiopods: A major isotopic event around the middle-late ordovician transition. *Geochim. Cosmochim. Acta* 67 (11), 2005–2025. doi:10.1016/s0016-7037(02)01116-x

Sun, C. H., Yu, H. F., Wang, H. S., Liu, H., Zhang, Z. H., Han, J., et al. (2012). Vugular formation of carbonates in Ordovician Yingshan reservoir in Tazhong northern slope of Tarim basin. *Nat. Gas. Geosci.* 23 (2), 230–236. (in Chinese).

Taylor, H. P. (1968). The oxygen isotope geochemistry of igneous rocks. *Contr. Mineral. Petrol.* 19, 1–71. doi:10.1007/bf00371729

Tian, J. C., and Zheng, Y. F. (1995). The evolution pattern of the carbon and oxygen isotopes in the Permian marine carbonate rocks from Guizhou. *J. Chengdu Inst. Technol.* 22 (1), 78–82. (in Chinese).

Urey, H. C. (1948). Oxygen isotopes in nature and in the laboratory. *Science* 108, 489–496. doi:10.1126/science.108.2810.489

Valley, J. W., and Cole, D. R. (2001). Stable isotope geochemistry. *Rev. Mineral. Geochem* 43, 1–662.

Wang, B. Q., and Al-Aasm, I. S. (2002). Karst-controlled diagenesis and reservoir development: Example from the Ordovician main-reservoir carbonate rocks. *AAPG Bull.* 86 (9), 1639–1658.

Wang, Q., Wang, X. Z., Xu, J. L., and Liu, Z. K. (2014). Carbon and oxygen isotope stratigraphy research in Chashgui area. *J. Southwest Petroleum Univ. Sci. Technol. Ed.* 36 (3), 27–34. (in Chinese).

Wu, G. H., Li, H. H., Zhang, L. P., Wang, C. L., and Zhou, B. (2012). Reservoir forming conditions of the Ordovician weathering crust in the Maigaitislope, Tarim basin, NW China. *Petroleum Explor. Dev.* 39 (2), 144–153. (in Chinese).

Yang, H. J., Li, K. K., Pan, W. Q., Xiao, Z. Y., and Cai, C. F. (2012). Burial hydrothermal dissolution fluid activity and its transforming effect on the reservoirs in Ordovician in Central Tarim. *Acta Petrol. Sin.* 28 (3), 783–792. (in Chinese).

Zhang, B., Zheng, R. C., Wang, X. B., Luo, Y., Li, W., Wen, H. G., et al. (2011). Paleokarst features and reservoir distribution in the Huanglong Formation of eastern Sichuan. *Petroleum Explor. Dev.* 38 (3), 257–267. (in Chinese). doi:10.1016/s1876-3804(11)60032-3

Zhang, K., Jiang, Z., Song, Y., Jia, C., Yuan, X., Wang, X., et al. (2022a). Quantitative characterization for pore connectivity, pore wettability, and shale oil mobility of terrestrial shale with different lithofacies -- A case study of the Jurassic Lianggaoshan Formation in the Southeast Sichuan Basin of the Upper Yangtze Region in Southern China. *Front. Earth Sci. (Lausanne).* 10, 864189. doi:10.3389/feart.2022.864189

Zhang, K., Song, Y., Jia, C., Jiang, Z., Han, F., Wang, P., et al. (2022b). Formation mechanism of the sealing capacity of the roof and floor strata of marine organic-rich shale and shale itself, and its influence on the characteristics of shale gas and organic matter pore development. *Mar. Petroleum Geol.* 140, 105647. doi:10.1016/j.marpetgeo.2022.105647

Zhang, K., Song, Y., Jiang, Z., Xu, D., Li, L., Yuan, X., et al. (2022d). Quantitative comparison of Genesis and pore structure characteristics of siliceous minerals in marine shale with different TOC contents - a case study on the shale of Lower Silurian Longmaxi Formation in Sichuan Basin, Southern China. *Front. Earth Sci. (Lausanne).* 10, 887160. doi:10.3389/feart.2022.864279

Zhang, K., Song, Y., Jiang, Z., Yuan, X., Wang, X., Han, F., et al. (2022c). Research on the occurrence state of methane molecules in post-mature marine shales-A case analysis of the Lower Silurian Longmaxi Formation shales of the upper Yangtze region in Southern China. *Front. Earth Sci. (Lausanne).* 10, 864279. doi:10.3389/feart.2022.887160

Zhang, Q. Y., Chen, L. X., Liang, B., Cao, J. W., Dan, Y., and Li, J. R. (2015). Research of geochemistry characteristics of carbon and oxygen isotopes of ordovician palaeokarst reservoir in the east of lungu-7, north Tarim basin. *Geol. Sci. Technol. Inf.* 34 (2), 52–56. (in Chinese).

Zhang, Q. Y., Liang, B., Qin, F. R., Cao, J. W., Dan, Y., and Li, J. R. (2016a). Environmental and geochemical significance of carbon and oxygen isotopes of Ordovician carbonate paleokarst in Lunnan, Tarim Basin. *Environ. Earth Sci.* 75 (14), 1074–1083. doi:10.1007/s12665-016-5882-0

Zhang, Q. Y., Qin, F. R., Liang, B., Cao, J. W., Dan, Y., Li, J. R., et al. (2016b). Characteristics of Ordovician paleokarst inclusions and their implications for paleoenvironmental and geological history in Halahatang area of northern Tarim Basin. *Carbonates Evaporites* 33, 43–54. doi:10.1007/s13146-016-0325-2

Zhang, X. L. (1985). Relationship between carbon and oxygen stable isotope in carbonate rocks and paleosalinity and paleotemperature of sea water. *Acta Sedimentol. Sin.* 3 (4), 17–30. (in Chinese).

Zhao, W. F., Liu, H. G., and Wang, G. L. (2012). C and O isotope geochemical characteristics of reservoir crevice fillings in Ordovician, Yuqi West Area. *J. Guizhou Univ. Nat. Sci.* 29 (3), 34–39. (in Chinese).

Zheng, Y. F., and Chen, J. F. (2000). *Stable isotope geochemistry*, 10. Beijing: Science Press, 12.

Zhong, J. H., Mao, C., Li, Y., Yuan, X., Niu, Y., et al. (2012). Discovery of the ancient ordovician oil-bearing karst cave in liuhuanggou, north Tarim basin and its significance. *Sci. China Earth Sci.* 55, 1406–1426. (in Chinese). doi:10.1007/s11430-012-4467-3

Zhu, G. Y., Zhang, S. C., Liang, Y. B., Dai, J., and Li, J. (2005). Isotopic evidence of TSR origin for natural gas bearing high H_2S contents within the Feixianguan Formation of the northeastern Sichuan Basin, southwestern China. *Sci. China Ser. D-Earth. Sci.* 48 (11), 1960–1971. (in Chinese). doi:10.1360/082004-147

frontiers | Frontiers in Earth Science

TYPE Original Research
PUBLISHED 06 January 2023
DOI 10.3389/feart.2022.1037532

OPEN ACCESS

EDITED BY
Hu Li,
Southwest Petroleum University, China

REVIEWED BY
Senlin Yin,
Yangtze University, China
Hao Lu,
Southwest Petroleum University, China

*CORRESPONDENCE
Dong Mengling,
2472872603@qq.com

SPECIALTY SECTION
This article was submitted to Structural Geology and Tectonics, a section of the journal Frontiers in Earth Science

RECEIVED 06 September 2022
ACCEPTED 21 September 2022
PUBLISHED 06 January 2023

CITATION
Yanqian L, Mengling D, Kunchi C and Feixu D (2023), Study on particle plugging in propagating fractures based on CFD-DEM.
Front. Earth Sci. 10:1037532.
doi: 10.3389/feart.2022.1037532

Study on particle plugging in propagating fractures based on CFD-DEM

Liu Yanqian[1], Dong Mengling[2]*, Cai Kunchi[3] and Dai Feixu[4]

[1]Oilfield Service Jianghan Corporation, SINOPEC, Qianjiang, China, [2]Jianghan Oilfield, SINOPEC, Qianjiang, China, [3]Chuanqing Drilling Engineering Company Limited CNPC, Chengdu, China, [4]Tarim Oilfield CNPC, Korla, China

In the drilling and completion process of fractured formations, wellbore stability is a key factor affecting the safety of drilling and completing engineering. Previous studies have demonstrated that propping moderately and plugging fractures with soluble particles can improve formation fracture pressure. When it comes to particle transport in 3D rough propagation fractures, the interactions between particle-fracture-fluid need to be considered. Meanwhile, size-exclusion, particle bridging/strain effects all influence particle transport behavior and ultimately particle plugging effectiveness. However, adequate literature review shows that fracture plugging, and fracture propagation have not been considered together. In this study, a coupled CFD-DEM method was put forward to simulate the particle plugging process of propagating fracture, and the effects of positive pressure difference, fracture roughness, particle concentration, and particle shape on the plugging mechanism were examined. It is concluded through the study that: 1) Positive pressure difference too large will lead to excessive fracture aperture, making the particles unable to form effective plugging in the middle of the fracture; positive pressure difference too small will lead to fracture aperture too small, making particles unable to enter into and plug the fracture. 2) No matter how the concentration, particle size and friction coefficient change, they mainly affect the thickness of the plugging layer, while the front end of the particle is still dominated by single-particle bridging, and double-particles bridging and multiple-particles bridging are hardly ever seen. For the wellbore strengthening approaches, such as stress cages, fracture tip sealing, *etc.*, specific analysis should be carried out according to the occurrence of extended fractures. For example, for fractures with low roughness, the particles rarely form effective tight plugging in the middle of the fracture, so it is more suitable for fracture tip sealing; For the fracture with high roughness, if the positive pressure difference is controlled properly to ensure reasonable fracture extension, the particle plugging effect will be good, and the stress cage method is recommended for borehole strengthening.

KEYWORDS

propagating fractures, CFD-DEM, particle, stress cage, plugging, carbonate reservoir

Introduction

According to statistics, about 57% of the world's oil and gas reserves and 60% of the world's oil and gas production come from carbonate reservoirs, and almost all high-production wells are in carbonate reservoirs (Moore and Wade, 2013; Fan et al., 2022; Li 2022). In the drilling and completion process of natural fractured formations in extensive and complex distribution, the safe density range of drilling fluid is narrow; if the drilling fluid density is too high, the naturally closed fractures may be opened to expand, bringing about loss of drilling fluid at various degrees in the drilling and completion process (Li et al., 2014; Li et al., 2018). Once happening, the drilling fluid leakage may cause not only drilling fluid loss, consumption of loss control materials, but also reservoir damage, in serious cases, even well collapse and blowout, which threatens safe and efficient drilling and makes non-productive time and operating costs increase significantly (Civan, 2015; Li J. et al., 2022). But the opening of fracture is not entirely a bad thing, as previous studies have demonstrated that propping moderately and plugging fractures with soluble particles can help stop fracture extension and improve wellbore stability (Feng and Gray, 2015; Feng et al., 2016; Li et al., 2019; Figure 1).

Figuring out the particle plugging mechanisms of propagation fracture is the basis of effective plugging. In terms of plugging mechanisms of fractured strata, a lot of research has been carried out mainly by means of core experiment, physical simulation experiment and numerical simulation. Some researchers have evaluated the coupling relationship between fracture width, fracture roughness, particle properties and pressure-bearing capacity of plugging layer through core and steel plate seam experiments, and obtained laws such as 1/3 bridging, ideal filling bridging, and 1/2 bridging (Kuzmina et al., 2018; Feng et al., 2020; Li H. et al., 2022). However, the vast majority of experiments have high occasionality, long experimental cycle, and high time and economic costs, and cannot explain the bridging and plugging mechanism of plugging particles visually from a microscopic perspective. Numerical simulation method can simulate restricted experiments and facilitate the analysis of microscopic mechanisms. In recent years, CFD-DEM numerical simulation methods (including LBM-DEM) have been widely used in studying solid-phase particle invasion and plugging in fractures. Boutt (2006) observed particle trapping behavior of fracture roughness by LBM-DEM method. Koyama (2008) analyzed the effects of fracture shear and fracture surface coupling on colloidal transport with particle tracking method. Zhang (2019a) investigated the wall effect and hydrodynamic behavior in coupled rough fracture with CFD-DEM method. In addition, particle bridging and size exclusion effects in regular fractures (Pu and Wang, 2014; Dai and Grace, 2016; Zeng et al., 2016; Huang et al., 2018; Jia et al., 2020; Zhu et al., 2020) and uncoupled actual fractures (Feng et al., 2018) have also been investigated extensively, and a large number of quantitative relationships between the particle bridging probability and particle concentration, particle size and fracture width have been proposed. Zhu et al. (2020) also analyzed the particle plugging behavior during the dynamic variation of fracture width under positive pressure difference with a combined CFD-DEM finite element method.

Fracture extension, which is essentially a problem of the weakening of fracture closure under different normal effective stresses, belongs to the domain of fracture stress sensitivity study. To date, a large number of experimental and numerical simulation studies have been carried out and a large number of theoretical equations have been obtained in this aspect. Lab experiments on rough rock fractures focused more on the study of the effect of normal stress on fluid flow in rock fracture, that is known as stress sensitivity test (Cao and Lei, 2018; Zhang J. et al., 2019; Yang et al., 2020). When it comes to particle transport in three-dimensional rough propagation fractures, it is necessary to consider not only the effect of fracture extension on fluid flow, but also the interaction between particle-fracture-fluid. Size exclusion, particle bridging/strain effect of particles all

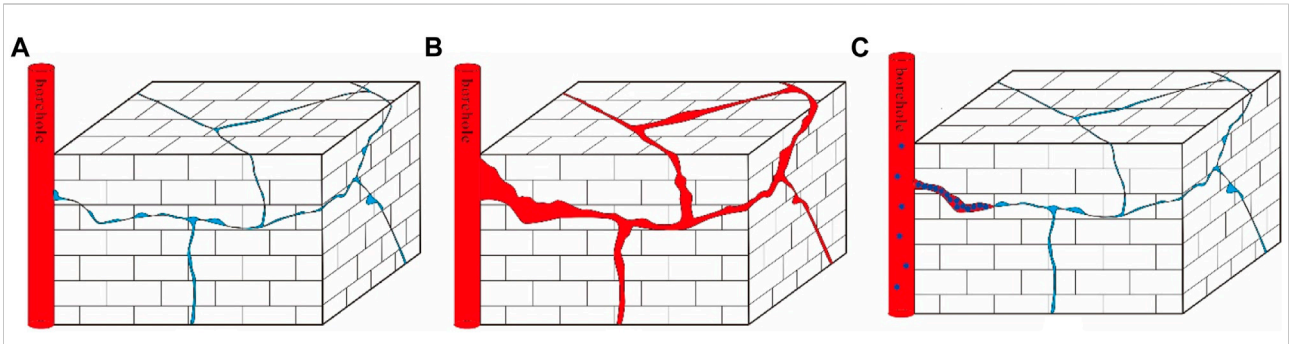

FIGURE 1
Plugging process of propagation fracture. **(A)** Before fracture extension; **(B)** Fracture extension due to positive pressure difference; **(C)** Re-closed fracture after plugging.

influence transport behavior and ultimately plugging effect of the particles (Ahfir et al., 2017; Khan et al., 2017; Wu et al., 2018; Xu et al., 2018). Although a lot of research on the static fracture plugging and stress sensitivity has been done and a large number of research results have been obtained, fracture plugging and fracture extension have not been considered together. The purpose of this study is to find out the transport and plugging mechanism of plugging particles under the action of macroscopic pressure gradient and fracture expansion. To this end, firstly, synthetic fractures with different roughnesses were generated using a self-profiling fractal model based on geological features. Then, the behavior and mechanisms of transport, plugging and permeability variation of plugging particles in propagation fractures with different roughnesses and positive pressure differences were examined by CFD-DEM method.

Methodology and theoretical background

Plugging particles in drilling fluid will enter into the reservoir with drilling fluid under positive pressure difference, and the dynamic behavior between plugging particles, drilling fluid and fracture in this process belongs to the domain of coupling of liquid and solid phases. The CFD-DEM coupling algorithm considers the couplings between plugging particles, plugging particles and drilling fluid, plugging particles and fracture medium, and drilling fluid and fracture medium, and is able to capture the micro-mechanisms of particle transport, precipitation, capture, and plugging.

Generation of propagation fractures

Current methods obtaining fracture morphology include contact or non-contact quantitative scanning methods, and numerical synthesis method. But due to the uncertainty of fracture formation, the cost of obtaining a large number of fractures with different geometric information is huge. Therefore, in this study, the software Synfrac designed by the University of Leeds was used to generate synthetic fractures (Ogilvie et al., 2006). Synthetic fractures not only have almost the same geometric characteristics as natural fractures, but also can have specific parameter values and be generated independently to test the effect of specific parameter variables of fracture propagation and particle flow. The mathematical model proposed by Brown (1995) was used to generate synthetic fractures. In this method, a two-dimensional complex amplitude spectrum with random phase component obeying a decaying power law was constructed, and Fourier inverse transformation was done to the amplitude spectrum to obtain a self-affine curved surface. To ensure that all samples had the same dimensions and the same vertical scale, the initial sample of 50 mm × 50 mm was corrected to a resolution of 512 × 512, which was configured with a standard deviation of 1 mm for the height of the irregular rough surface to obtain a geometrically isotropic fracture surface (Figure 2). According to previous studies, fracture samples of similar roughness generated by different random numbers have similarity in hydraulic laws, so the simulation results of one random number are given in this paper.

The fracture roughness coefficient (JRC) proposed by Barton and Choubey (1977) can be calculated using the following equation (Tse and Cruden, 1979):

$$\mathrm{JRC} = 32.2 + 32.47 \log Z_2, \tag{1}$$

Where: Z_2 is the root mean square of the first order derivative of the fracture surface, which can be expressed in discrete form as:

$$Z_2 = \left[\frac{1}{N_t}\sum\left(\frac{h_{i-1} - h_i}{x_{i-1} - x_i}\right)^2\right]^{1/2}, \tag{2}$$

Where x_i and h_i denote coordinates of the fracture surface profile and N_t is the number of sampling points along the fracture length. In this study, fractures of the following three roughnesses as shown in Figure 2 were generated, and their JRC coefficients are shown in Table 1.

Generation of propagation fracture

For rough fractures, the fracture deformation is governed by the following equation:

$$\Delta b = b_0\left(1 - e^{-\sigma_n/K_n}\right), \tag{3}$$

Where,$b_0$is the mechanical aperture of compression fracture;$K_n$is the equivalent closure stiffness of structural surface;$\Delta b$is the fracture closure deformation;$\sigma_n$is the normal stress. When fluid fills the fracture, according to the effective stress equation, the following equation is obtained:

$$b = b_0 \exp\left(-\frac{\sigma_1 - \alpha p}{K_n}\right), \tag{4}$$

Where:$\alpha$is the Biot coefficient;$p$is the formation fluid pressure. The expression derived by Walsh (1981) for the permeability of the plate-like fracture model based on the Poiseuille flow equation is:

$$\left(\frac{k}{k_0}\right)^{1/3} = 1 - \frac{\sqrt{2}RMS}{b_0}\ln\left(\frac{\sigma_1 - \alpha p}{\sigma_1}\right), \tag{5}$$

Where:$RMS$is the root mean square of the fracture surface height distribution, which characterizes the roughness of the fracture surface. According to Darcy's law and the Poiseuille equation, the relationship between permeability and fracture hydraulic aperture is as follows:

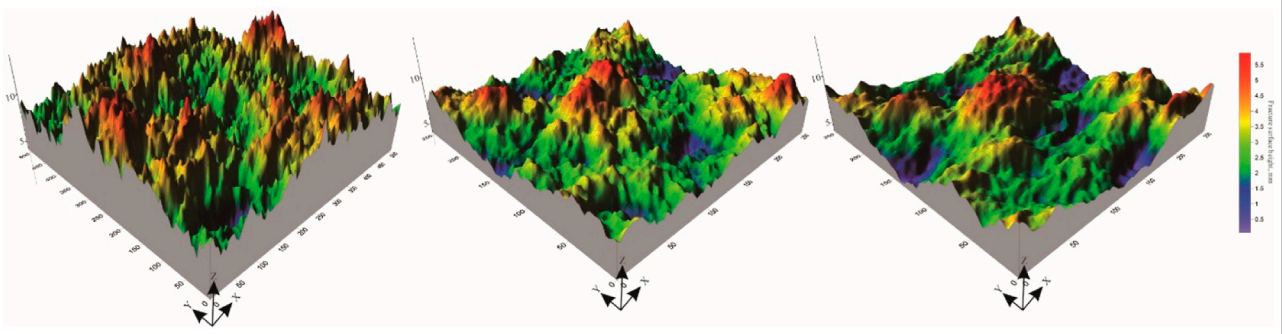

FIGURE 2
Features of generated fracture surfaces.

TABLE 1 Geometric characteristics of propagating fractures.

Fracture roughness	Positive pressure difference, MPa	Fracture aperture, mm	Root mean square, mm	Standard deviation	Pore volume, mm^3
JRC=5	2	2.01	2.16	0.78	3,155
	5	2.30	2.44	0.80	3,276
	10	2.92	3.01	0.82	3,563
JRC=10	2	1.56	1.65	0.54	2,130
	5	1.76	1.84	0.57	2,281
	10	2.08	2.16	0.62	2,432
JRC=15	2	3.87	4.04	1.01	19,811
	5	4.09	4.23	1.04	22,183
	10	4.49	4.61	1.06	23,401

$$k = \frac{b_h^2}{12}. \tag{6}$$

It can be obtained that

$$\left(\frac{b_h}{b_{h0}}\right)^{2/3} = 1 - \frac{\sqrt{2}RMS}{b_0}\ln\left(\frac{\sigma_1 - \alpha p}{\sigma_1}\right). \tag{7}$$

For natural rough fractures, the fracture roughness influences the degree of fracture closure, and the variation of the fracture mechanical aperture is obtained by correcting the following relationship.

$$b = \sqrt{b_h JRC^{2.5}}. \tag{8}$$

An initial fracture often has a high degree of closure and a large contact area. When its two opposing surfaces just touch or penetrate each other, the contact distance is negative, representing a contact area with zero pore size. The numerical generation of the propagation fracture was simulated by assigning rising expansion increments to the upper surface of the fracture under different positive pressure differences, and after gradual lifting of the upper surface of the fracture, part of the contact was released and some new voids were created at the same time. In this study, the evolution of geometric characteristics of initial fractures with JRC of 5, 10 and 15 at the positive pressure differences of 0–10 MPa were simulated (Figure 3; Table 1).

Governing equations for particle-laden flow in fractures

Governing equation of particle transport

In the computational study, the plugging particle transport was solved by the discrete element method in the Lagrangian framework, and the plugging particles followed the second law. When the plugging particles transport in the fracture with drilling fluid, each plugging particle is subjected to the actions of surrounding drilling fluid, adjacent particles and adjacent fracture surface, so the external forces on the

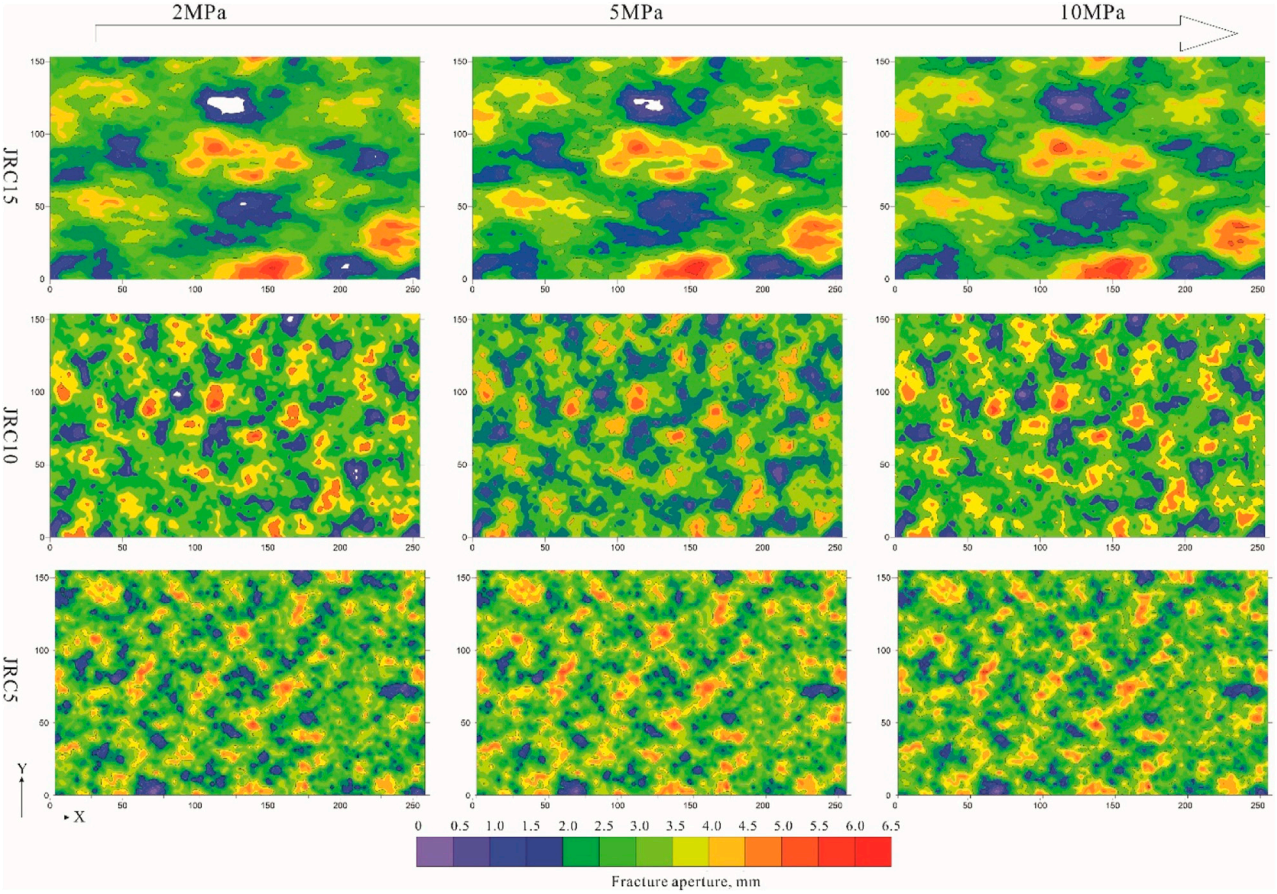

FIGURE 3
Characteristics of propagating fractures.

plugging particle during transport include its own gravity, traction, buoyancy and contact force *etc.* Its motion mainly includes translation and rotation, and the governing equations are as follows:

$$\begin{cases} m_p \dfrac{\mathrm{d}u_p}{dt} = \mathbf{F}_{p,n} + \mathbf{F}_{p,t} + \mathbf{F}_{p,e} + \mathbf{F}_{p,\mathrm{g}}, \\ \mathbf{I}_p \dfrac{d\boldsymbol{\omega}_p}{dt} = \mathbf{r}_{p,c} \times \mathbf{F}_{p,t} + T_{p,r}, \end{cases} \tag{9}$$

Where $\mathbf{F}_{p,n}$ and $\mathbf{F}_{p,t}$ are normal and tangential contact forces, respectively,$\mathbf{F}_{p,\mathrm{g}}$is the gravitational force,$\mathbf{F}_{p,e}$is the force exerted on the particle by the fluid surrounding the particle, such as traction, pressure gradient force and buoyancy,$\mathbf{r}_{p,c}$and$T_{p,r}$are the particle vector radius and the additional torque of the particle, respectively,$\mathbf{u}_p$and$\boldsymbol{\omega}_p$are the translational and rotational velocities, respectively, and m_p and $\mathbf{I}_p$ are the mass and inertia moment of the particle, respectively.

CFD-DEM coupling method

Besides the interactions between particles and between particle and fracture surface, the interaction between drilling fluid and plugging particle also need to be considered. The drilling fluid flow is often solved by the finite volume method, but the coupling interaction between plugging particle and drilling fluid are often solved in two ways, particle unresolved (Unresolved) and particle-resolved (Resolved) CFD-DEM methods, their main difference is the ratio of particle diameter to fluid grid size. The choice of the specific method depends on the scale of the engineering issue: size of particles, and flow field resolution *etc.* The particle non-resolved CFD-DEM is suitable for large-scale calculations, which require particle diameter smaller than the CFD grid size. It uses an empirical model to calculate the force of the fluid on the particle and will calculate the reaction force of the particle on the fluid based on Newton's third law, which is expressed as a source term in the N-S

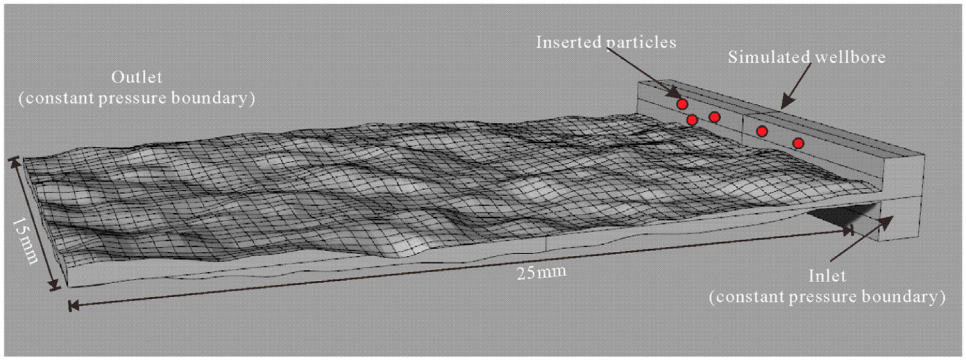

FIGURE 4
Schematic illustration and CFD mesh of the fracture.

equation, while the occupation of the flow field space by the particle is reflected in the volume fraction calculation. The method uses an empirical model and a relatively coarse flow field, so it is able to calculate industrial-level particle flow issues.

In this study, the fluid had a Reynolds number of less than 200, the flow regime of drilling fluid was laminar flow, and the requirement of flow field resolution in a single fracture was not high, so the CFD-DEM method with non-resolved particles was used for the evaluation of plugging particle intrusion damage and temporary plugging in fracture-type reservoirs; while fracture-pore type reservoir has complex pore structure and flow field, and small vortices which would have serious influence on plugging particle retention, so the flow field must be resolved in detail, therefore, solid-phase intrusion damage in fracture-pore reservoirs was simulated by the particle-resolved CFD-DEM method.

In the particle unresolved CFD-DEM method, the fluid was assumed to be continuous and incompressible and can be described by the locally averaged N-S equation.

$$\frac{\partial \alpha_f \rho_f}{\partial t} + \nabla \cdot \left(\alpha_f \rho_f \mathbf{u}_f\right) = 0, \tag{10}$$

$$\frac{\partial \left(\alpha_f \mathbf{u}_f\right)}{\partial t} + \nabla \cdot \left(\alpha_f \mathbf{u}_f \mathbf{u}_f\right) = -\alpha_f \frac{\nabla p}{\rho_f} - \mathbf{S} + \nabla \cdot \boldsymbol{\tau}, \tag{11}$$

Where: α_f is the volume fraction of drilling fluid, ρ_f is the drilling fluid density, $\mathbf{u}_f$ is the drilling fluid velocity, ∇p is the pressure gradient during drilling, $\boldsymbol{\tau}$ is the drilling fluid stress tensor, t is the time step, $\mathbf{S}$ is the momentum exchange source term, F_d is the drag force. There are many classical models for drag calculation, and the Di Felice drag model was used in this study, which can be expressed as:

$$\begin{aligned} \mathbf{F_d} &= \frac{1}{2}\rho_f\left(\mathbf{u}_f - \mathbf{u}_p\right)\left|\mathbf{u}_f - \mathbf{u}_p\right| C_d \frac{\pi D_p^2}{4} \alpha_f^{(2-\chi)} \\ C_d &= \left(0.63 + \frac{4.8}{\mathrm{Re}}\right)^2 \\ \chi &= 3.7 - 0.65 \exp\left[-\frac{(1.5 - \log_{10}\mathrm{Rep})^2}{2}\right] \end{aligned}, \tag{12}$$

Where: C_d is the coefficient of drag force, which is a function of the particle Reynolds numberRep.

As a simplification, the DEM calculation at the coupling step time was required to ensure that the fluid forces on the particle remained constant, while the coupling was performed after about 50–100 DEM steps.

Boundary conditions

Continuous particles of the desired concentration were created in the simulated borehole to simulate steady particle inflow. Constant pressure boundary conditions were applied at the inlet (top of the borehole) and outlet (end of the fracture), and anti-slip wall conditions were applied at the fracture surface (Figure 4). In this study, the fluid was assumed to be a Newtonian fluid in laminar flow regime, and the specific fluid parameters are shown in Table 1. The plugging particles were assumed to be calcium carbonate particles most commonly used in drilling operations (Table 2). The selection of CFD grid size depends on the balance between the fracture surface details, fluid details and the computational stability of the fluid volume fraction.

TABLE 2 Parameters used in the simulation.

Fluid parameter	Value	Particle parameter	Value
Fluid density, ρ_f	2.16 g/cm^3	Density, ρ_p	2.3 g/cm^3
Fluid plastic viscosity, μ_f	17 ma.s	Young's modulus	40 GPa
Positive pressure difference	2–10 MPa	Poisson's ratio	0.25
		Diameter, Dp	A (0.2 mm), B (0.15 mm), C (0.1 mm)
		Sliding friction coefficient	0.4–1.2
		Rolling friction coefficient	0.4–1.2

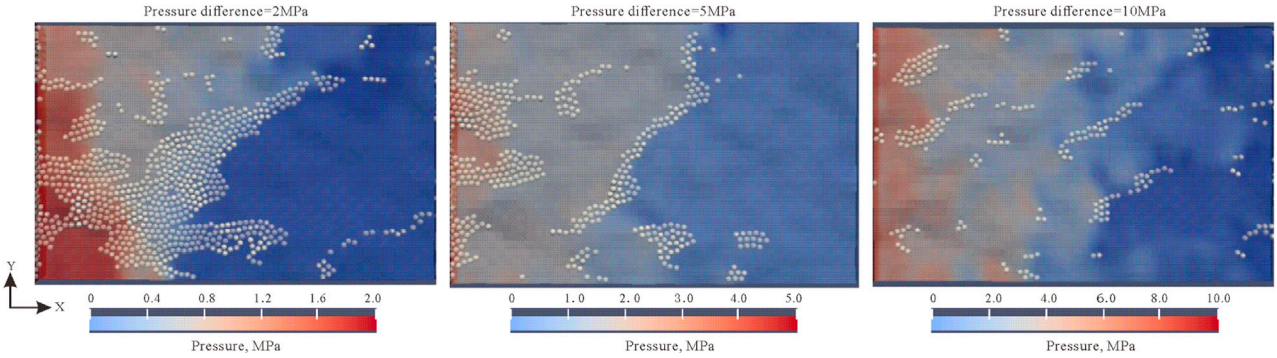

FIGURE 5
Variation of fracture plugging law under different positive pressure differences in JRC15 (at the particle concentration of 10%, friction coefficient of 0.9, particle size of 100% A).

Resluts and discussion

Evolution of fracture plugging law under different positive pressure differences

With the increase of positive pressure difference, the fracture gradually opened, extended, and increased in average width, at which time it becomes difficult for the particles to bridge and plug. The white particles in all plugging results figures represent the particles in a static state (velocity less than 0.01 m/s) after plugging (Figure 5), and the white particles in the following figures have the same meaning. It can be seen from Figure 5 that when the positive pressure difference was less than 5 MPa, the particles formed a large area of stable bridging and plugging, but when the positive pressure difference was greater than 5 MPa, the particle bridging was difficult, and only slight bridging was formed in a small part of the area, and the fracture was not plugged on the whole. In terms of the shape of plugging layer, when the positive pressure difference was 2 MPa, the plugging layer was thicker, and effective plugging was formed in a large part of the fracture, and only a few grooves were left for drilling fluid and plugging particles to move; when the positive pressure difference was 5 MPa, although particle bridging plugging was also formed, the plugging layer was thinner, and the number of grooves for fluid movement after plugging increased; when the

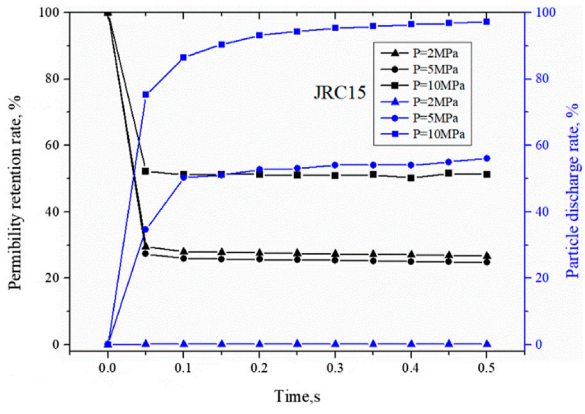

FIGURE 6
Variations of fracture permeability retention rate and particle discharge rate of JRC15 with time at different positive pressure differences.

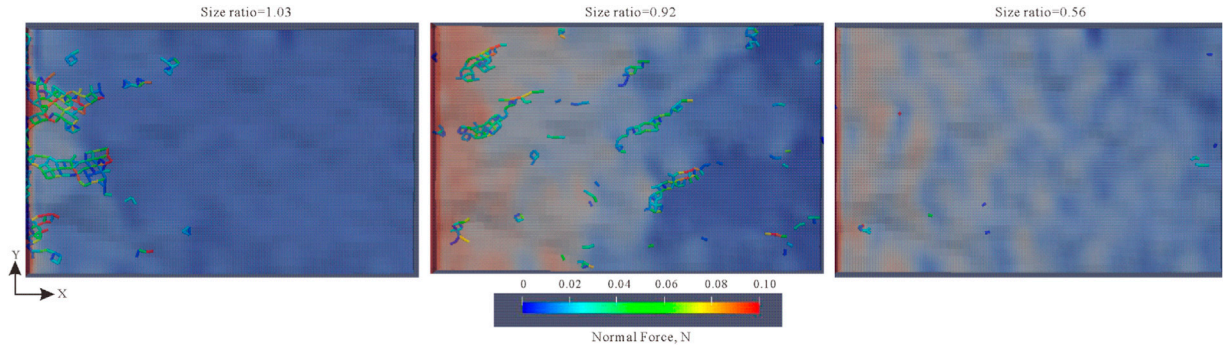

FIGURE 7
Force chain structure of plugging formed by different sizes of particles in JRC15.

positive pressure difference was 10 MPa, the plugging layer was sporadically distributed, each plugging position had less plugging particles, most of the grooves still provided a large amount of flow space. From the perspective of fluid pressure gradient distribution, we can see that when the positive pressure difference was less than 5 MPa, a stable pressure plugging zone was formed at the front of the plugging layer, but the pressure plugging was more serious when the positive pressure difference was 2 MPa; but when the positive pressure difference was 10 MPa, the pressure gradient was basically linearly distributed, which means that the plugging completely failed at this point. In actual drilling operation, this situation will not only lead to the failure of borehole reinforcement, but also lead to man-made well leakage, and must be avoided.

Figure 6 shows the variations of permeability retention rate and particle discharge rate in the plugging process, where permeability retention rate is defined as the ratio of fracture permeability after particle injection k to fracture permeability before particle injection k_0.

$$\text{Permibility retention rate} = \frac{k}{k_0} \times 100\%. \tag{13}$$

Particle discharge efficiency is defined as the ratio of the total number of particles discharged from the end of the fracture N to the total cumulative number of particles injected N_{sum}.

$$\text{Particle discharge rate} = \frac{N}{N_{sum}} \times 100\%. \tag{14}$$

It can be seen from Figure 6 that when the positive pressure difference was less than 5 MPa, a stable plugging layer was formed gradually within 0.1 s, and the permeability retention rate was less than 30% at this point; when the positive pressure difference was 10 MPa, the permeability of the fracture after particle injection decreased to some extent, but finally stabilized at about 50%. From the particle discharge rate, we can see that when the positive pressure difference was 2 MPa, basically no particles were discharged and all particles were involved in bridging; when the positive pressure difference was 5 MPa, the particle discharge rate increased to 60%, which means that although effective plugging was formed at this point, there were still a large number of particles continuously invading into the deep part of the fracture, and the pressure and fluid were not completely isolated in this case, which is not conducive to well wall stability and reservoir protection; when the positive pressure difference was 10 MPa, the particle discharge rate gradually approached 100% over time, that is, all injected particles invaded to the deep part of the reservoir and no stable bridging was formed, which was a complete failure.

Figure 7 shows force chain structures of the plugging layers formed by different sizes of particles under the positive pressure difference of 10 MPa. It can be seen from the figure that when the particle size/average fracture width ratio was 1.03, the particles formed a stable plugging layer near the entrance, and the force chain strength of the plugging layer was high overall; when the particle size/average fracture width ratio was 0.92, the particles formed a plugging layer at local parts of the fracture, and the force chain strength of plugging layer was weaker; when the particle size/average fracture width ratio was 0.56, no strong force chain formed inside the whole fracture.

Evolution of fracture plugging law under different fracture roughnesses

The different roughness of the fracture surface affects the geometric structure of flow space in the fracture, which in turn affects the transport pattern of fluid and particles in it. In this study, the transport and plugging of particles in fractures with different roughnesses at different positive pressure differences were simulated, as shown in Figure 8. The particle size/initial average fracture width ratio in the figure was 0.9. It can be seen that when the positive pressure difference was 2MPa,

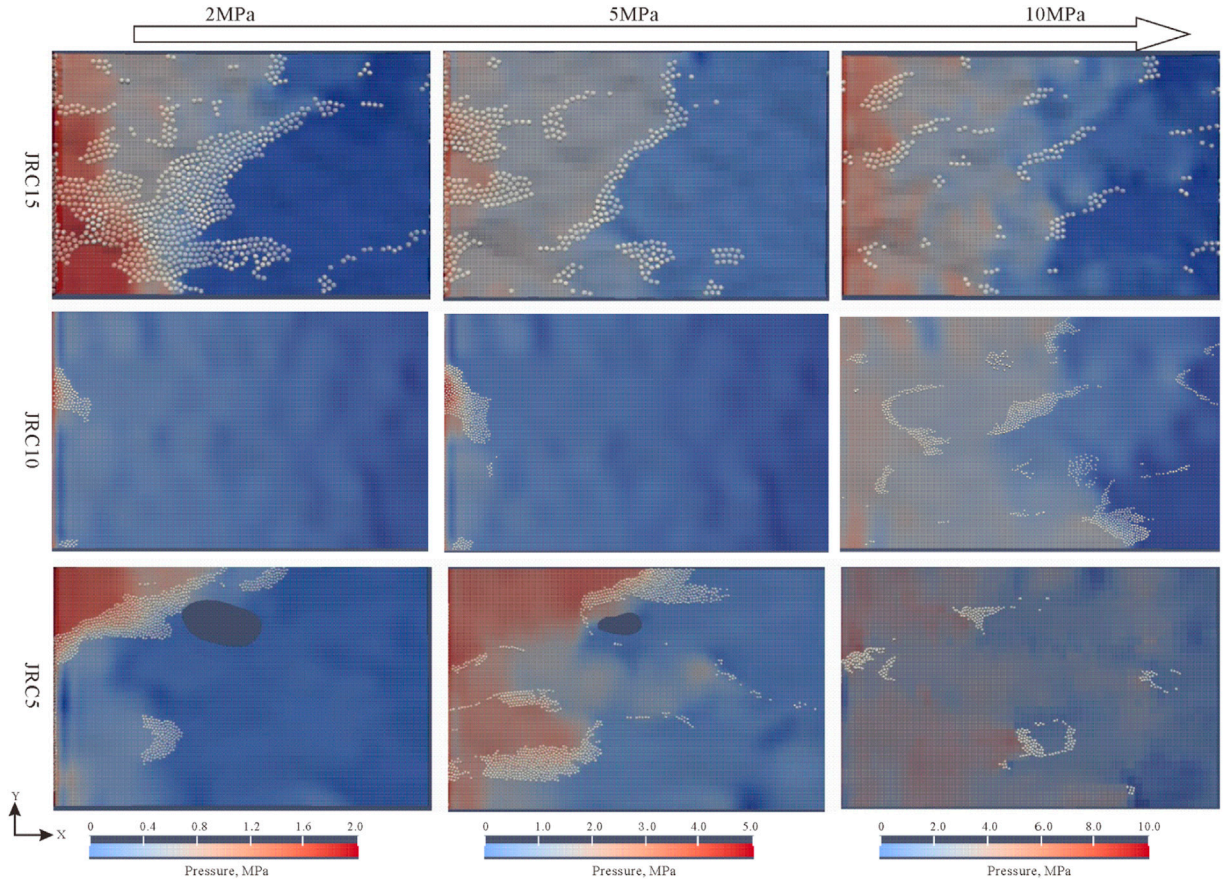

FIGURE 8
Particle plugging results of fractures with different roughnesses at different positive pressure differences (particle concentration of 10%, friction coefficient of 0.9, particle size/fracture width of 0.9).

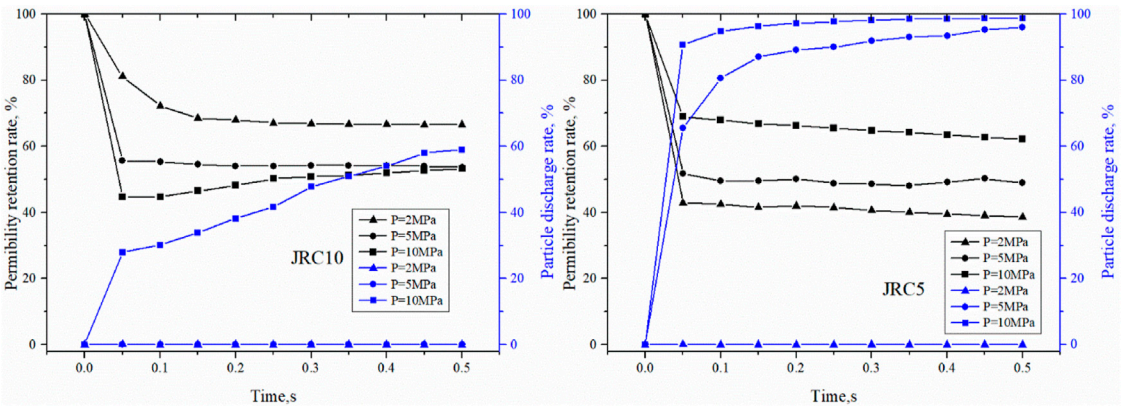

FIGURE 9
Variations of permeability retention rate and particle discharge rate of fractures with different roughnesses at different positive pressure differences.

JRC5 and JRC10 only had a plugging layer near the fracture entrance, while the particles could not make into the lower half of the fracture; and in the fracture JRC15, the particles filled the whole fracture to form tight plugging, resulting in obvious pressure seal. When the positive pressure difference was 5 MPa, both fractures JRC5 and JRC10 had plugging only in the local parts but several grooves remained for fluid flow, and the pressure and fluid isolation were poor; in contrast, in fracture JRC15, although the plugging layer was thin, a long continuous plugging zone formed in the middle of the fracture, and a tight plugging layer was likely to form with subsequent injection of fine particles. When the positive pressure difference was 10MPa, all the fractures were not effectively plugged.

Figure 9 shows the variations of permeability retention rate and particle discharge rate with time in fractures JRC5 and JRC10. In combination with Figure 6, it can be seen that with the increase of fracture roughness, permeability retention rate shows a trend of gradual decrease. When the positive pressure difference was 2–5 MPa, the permeability retention rates of JRC5, JRC10 and JRC 15 were 40–50%; 40–60%, and 20–30% respectively. When the positive pressure difference was 10 MPa, all the three fractures had higher permeability retained after particle injection regardless of the roughness, indicating the plugging effect was poor. In terms of the particle discharge rate, it can be found that when the positive pressure difference was 2MPa, all the three fractures had a particle discharge rate close to 0%. But combined with the graph of plugging effect, it can be seen that JRC5 and JRC10 had plugging layer at their entrances and a large amount of grooves retained for fluid flow, so the plugging layers in them were poor in stability and tightness. When the positive pressure difference was 5 MPa, the particle discharge rates in JRC5 gradually approached 100%, while that in JRC15 was stable at about 60%. In other words, the grooves in JRC5 were not plugged finally, while in JRC15, a better plugging layer formed with the injection of particles. When the positive pressure difference was 10 MPa, all the fractures had a particle discharge rate close to 100%, indicating no effective plugging was formed.

From the above discussion, it can be seen that for the fracture with low fracture roughness, the particles injected either form a plugging layer at the entrance or plug local parts of the fracture, and are hard to form effective tight plugging in the middle of the fracture. Therefore, for this kind of fracture, strengthening well wall by the stress cage way may not be effective, and the fracture tip plugging is recommended to prevent further expansion of the fracture. Whereas for fractures with high roughness, as long as the positive pressure difference is controlled properly to ensure a reasonable fracture expansion, the particle plugging effect is good, and the stress cage way is recommended for well wall strengthening.

Effect of particle concentration on the plugging of propagating fractures

Traditionally, particle concentration is one of the key factors affecting particle bridging. Zhu (2022) showed that particle concentration and particle size were in exponential relation with bridging probability, and when the fracture width/grain size ratio was less than 1.5, particle concentration had little influence on bridging probability; when the fracture width/grain size ratio was larger than 1.5, the particle bridging requires higher particle concentration. In this study, the particle bridging modes at particle concentrations of 5%, 10%, 20%, and 30% were simulated (Figure 10). The results show on the whole, the particle bridging was basically not affected by particle concentration, and in all these cases, the particles formed scattered plugging in local parts of the fracture. This may be because most of the particle bridging was dominated by single particle bridging, and two-particle bridging and multiple-particle bridging were hard to form, so the particle concentration had little influence on particle bridging.

But it can be seen from the permeability retention rate and particle discharge rate curves (Figure 11) that the particle concentration has certain effect on the bridging process. From the particle discharge rate, it can be seen that the particle discharge rate rapidly reaches a stable peak with the increase of particle concentration, indicating that the increase of particle concentration accelerates the formation of particle bridging and plugging to some extent. It can be seen from the permeability retention rate curve, the smaller the particle concentration, the higher the permeability retention rate is, which also proves that the increase of concentration is conducive to bridging. But from the perspective of reservoir damage control, in the case that the fracture is not plugged at either high or low particle concentrations, the larger the particle concentration, the greater the number of particles invading the reservoir is, and the greater the damage to the reservoir is, which is not conducive to oil and gas discovery and production.

Plugging law of propagating fracture with compound particles

In the actual drilling and completion process, particles are not homogeneous particles, but are combined by particles of several different sizes. In this study, the plugging effects of particles of three different sizes, A (0.2 mm), B (0.15 mm) and C (0.10 mm), in different formulations were simulated. The red (A), blue (C) and green (B) particles in Figure 12 represent static particles of different particle sizes. It can be seen from Figure 12 that the plugging layers formed by formulations 1# and 3# were thicker; but the plugging layers of all the

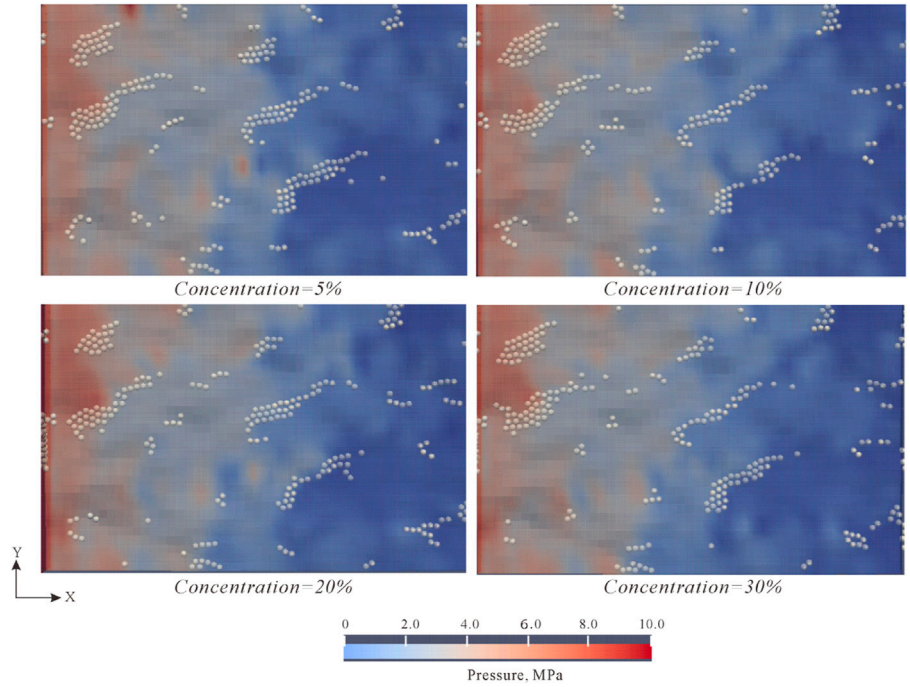

FIGURE 10
Plugging results at different particle concentrations in JRC15 (at the positive pressure difference of 10 MPa, friction coefficient of 0.9, and particle size/slit width of 0.9).

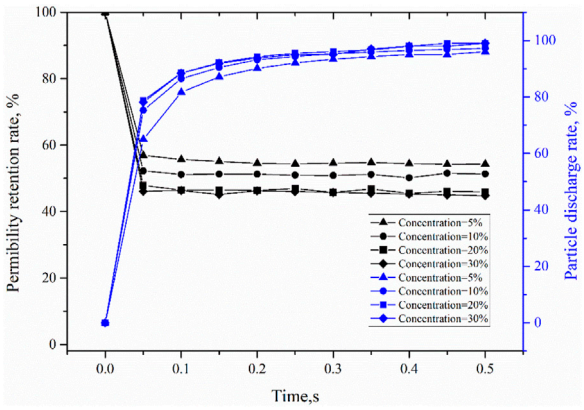

FIGURE 11
Variations of permeability retention rate and particle discharge rate of JRC15 with time at different particle concentrations.

formulations were similar in the front, where large particles were at the very fore-end, and the particles injected later unable to pass through the bridging layer formed by large particles accumulated to make the plugging layer thicker. The reason of the thicker plugging layer of formulation 1# is that it is easier for a large number of small particles to enter the fracture and accumulate; the reason of the thicker plugging layer of formulation 3# may be that in the case with higher content of large particles, if the overall concentration is maintained at a constant level, the particles are smaller in total number and thus likely to enter the middle-rear end of the fracture to accumulate.

The plugging layer is a porous medium formed by the accumulation of particles, and the relationship between the size distribution of the plugging particles and the absolute permeability (K) can be expressed by the Kozeny-Carman equation (Akgiray and Saatçı, 2001):

$$K = a\frac{\phi^3 D_p^2}{(1-\phi)^2}, \tag{15}$$

Where,ϕ is the porosity of plugging layer,$D_p$is the particle size of plugging particles, and$a$is the proportionality and unity factor. The smaller the particle size, the lower the permeability of the plugging layer will be. Meanwhile, the larger the proportion of small particles in the compound formulation, the lower the porosity of the plugging layer will be too, and so does the permeability of the plugging layer. The variations of

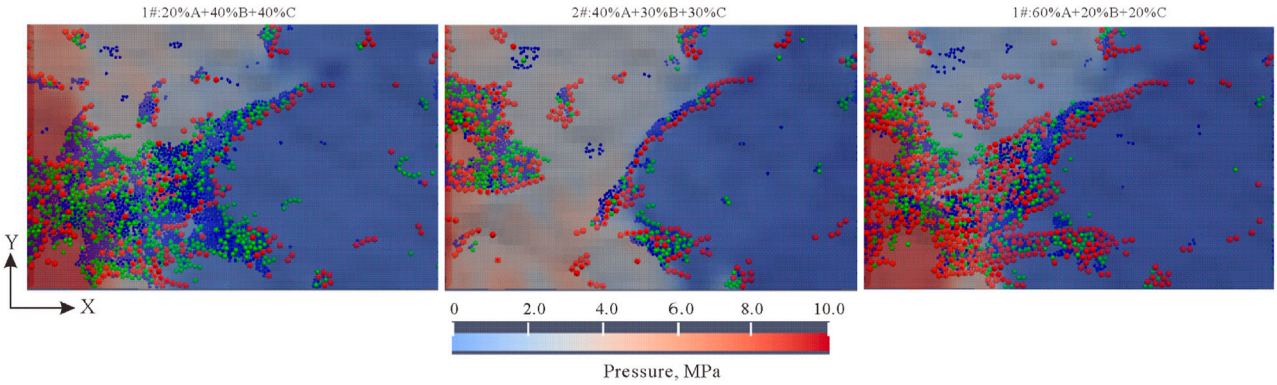

FIGURE 12
Plugging results of compound particles in JRC15 (at the positive pressure difference of 10 MPa and friction coefficient of 0.9).

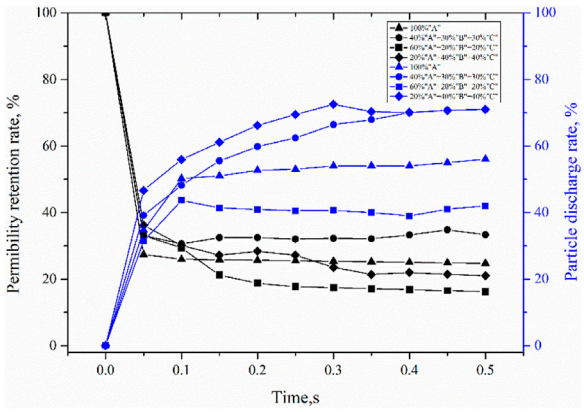

FIGURE 13
Variations of permeability retention rate and particle discharge rate of compound particles in JRC15.

permeability retention rate and particle discharge rate of different formulations were examined in this study (Figure 13). It can be seen from the permeability retention rate curves that the higher the content of large particles, the tighter the plugging layer formed by the compound formulation with high content of large particles. It can be seen from the particle discharge rate curve that the higher the content of large particles in the compound formulation, the lower the particle discharge rate is. Although according to Eq. 15, the higher the content of small particles, the tighter the plugging layer is, meanwhile, more small particles may also intrude into and cause damage to the reservoir.

Effect of particle shape on the plugging of propagating fracture

The particle shape affects the particle bridging mode. In this study, the plugging results of different shaped particles were simulated by changing the friction coefficient. It can be seen from Figure 14 that the plugging layer became thicker with the increase of friction coefficient. At the same time, with the increase of friction coefficient, the particle bridging was still dominated by single particle bridging, and the plugging layers remained similar in the front-end morphology, but moved forward slightly in the front-end position. In other words, the more irregular the particle shape is, the thicker the plugging layer is, and the more easier it is for the particles to bridge.

Figure 15 shows the variations of permeability retention rate and particle discharge rate when plugging with particles of different friction coefficients. When the friction coefficient of the particles was 0.3, the final particle discharge rate stabilized at about 90% and the permeability retention rate at about 40% ultimately; while when the friction coefficient of the particles was 1.2, the particle discharge rate and permeability retention rate stabilized at only 30% and 30% at last. It can be seen that the larger the friction coefficient, the more easier it is for the particles to bridge and plug, and the tighter the plugging layer is. But the permeability retention rate of the fracture plugged with particles of 1.2 in friction coefficient was higher than that plugged with particles of 0.9 in friction coefficient. The possible reason for this is that the larger the friction coefficient, the more likely the particles form plugging at the fracture entrance, preventing the particles from entering deep into the fracture.

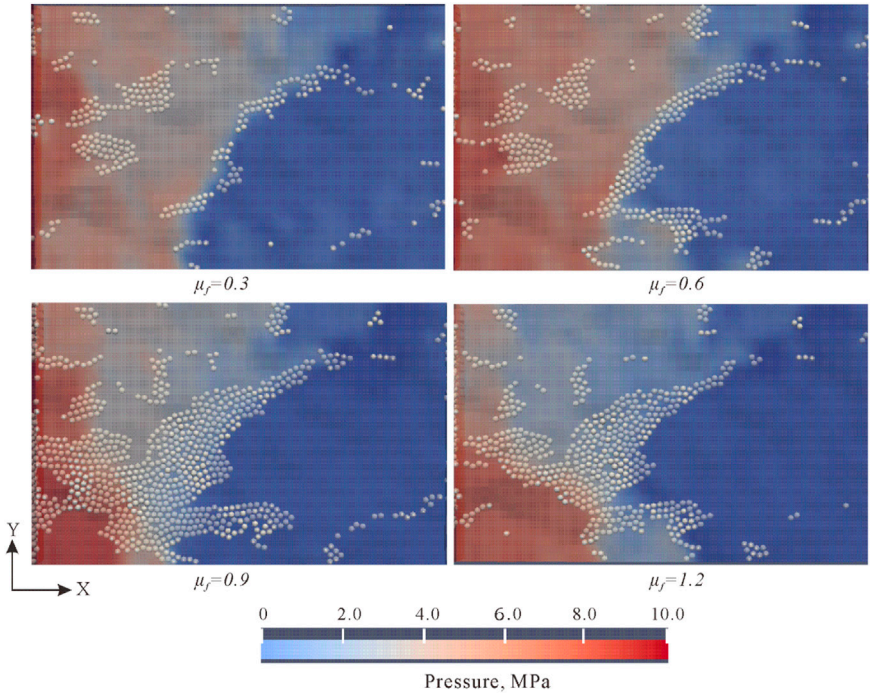

FIGURE 14
Plugging results of particles with different friction coefficients in JRC15.

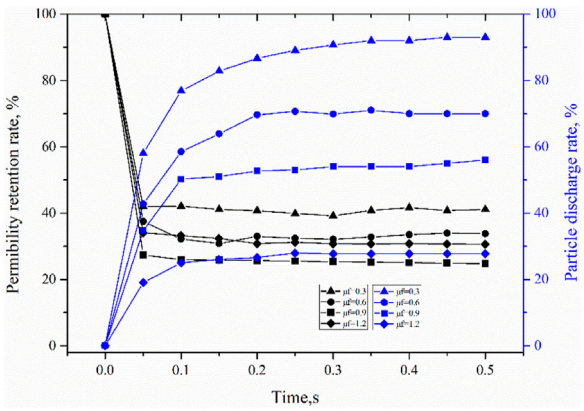

FIGURE 15
Variations of permeability retention rate and particle discharge rate of JRC 15 plugged with particles of different friction coefficients.

Conclusion

In this study, a coupled CFD-DEM method was used to simulate the plugging processes of propagating leaky fractures with particles, and the effects of positive pressure difference, fracture roughness, particle concentration, compound particle formulation, and particle shape on plugging mechanism of propagating fracture were analyzed based on distribution images of plugging particles, permeability retention rate and particle discharge rate. The following conclusions have been reached:

(1) When the positive pressure difference is less than 5 MPa, the particles can form stable bridging and plugging over a large area, but when the positive pressure difference is greater than 5 MPa, the particle bridging becomes difficult, and only slight bridging is formed in small parts of the fractures, unable to isolate the fluid and pressure completely. In the process of strengthening the wellbore by particle plugging, attention should be paid to the change of positive pressure difference. Positive pressure difference too large will lead to too large fracture aperture, so the particles cannot form effective plugging in the fracture; while positive pressure difference too small will lead to too small fracture aperture, so the particles cannot enter into the fracture to form plugging.
(2) In general, the particle bridging is basically not affected by particle concentration, which may be because that particle bridging is mostly dominated by single particle bridging and double particle bridging and multiple particle bridging are hard to come about.

(3) When the compound formula of large particles and small-medium particles is used to plug a fracture, the tighter the plugging layer, the lower the particle discharge rate is, which is conducive to fracture plugging and reservoir damage control.
(4) With the increase of friction coefficient of particles, the plugging layer becomes thicker, but the particle bridging is still dominated by single particle bridging, and the plugging layer remains basically the same in front-end morphology.
(5) For the wellbore strengthening approaches, such as stress cages, fracture tip sealing, *etc.*, specific analysis should be carried out according to the occurrence of extended fractures. For example, for fractures with low roughness, the particles rarely form effective tight plugging in the middle of the fracture, so it is more suitable for fracture tip sealing; For the fracture with high roughness, if the positive pressure difference is controlled properly to ensure reasonable fracture extension, the particle plugging effect will be good, and the stress cage method is recommended for borehole strengthening.

Data availability statement

The datasets presented in this study can be found in online repositories. The names of the repository/repositories and accession number(s) can be found in the article/Supplementary Material.

Author contributions

DM: Methodology, Software, Writing-Original draft preparation. LY: Conceptualization, Investigation. CK: Writing-Reviewing. DF: Data curation.

Conflict of interest

LY was employed by Oilfield Service Jianghan Corporation, SINOPEC. DM was employed by Jianghan Oilfield, SINOPEC. CK was employed by Chuanqing Drilling Engineering Company Limited CNPC. DF was employed by Tarim Oilfield CNPC

Publisher's note

References

Ahfir, N. D., Hammadi, A., Alem, A., Wang, H., Le Bras, G., and Ouahbi, T. (2017). Porous media grain size distribution and hydrodynamic forces effects on transport and deposition of suspended particles. *J. Environ. Sci.* 53, 161–172. doi:10.1016/j.jes.2016.01.032

Akgiray, Ö., and Saatçı, A. M. (2001). A new look at filter backwash hydraulics. *Water Sci. Technol. Water Supply* 1 (2), 65–72. doi:10.2166/ws.2001.0022

Barton, N., and Choubey, V. (1977). The shear strength of rock joints in theory and practice. *Rock Mech.* 10 (1), 1–54. doi:10.1007/BF01261801

Boutt, D. F., Grasselli, G., Fredrich, J. T., Cook, B. K., and Williams, J. R. (2006). Trapping zones: The effect of fracture roughness on the directional anisotropy of fluid flow and colloid transport in a single fracture. *Geophys. Res. Lett.* 33 (21), 1522–1534. doi:10.1029/2006GL027275

Brown, S. R. (1995). Simple mathematical model of a rough fracture. *J. Geophys. Res.* 100 (B4), 5941–5952. doi:10.1029/94JB03262

Cao, N., and Lei, G. (2019). Stress sensitivity of tight reservoirs during pressure loading and unloading process. *Petroleum Explor. Dev.* 46 (1), 138–144. doi:10.1016/S1876-3804(19)30013-8

Civan, F. (2015). *Reservoir formation damage*. Gulf Professional Publishing. Houston, Texas.

Dai, J., and Grace, J. R. (2010). Blockage of constrictions by particles in fluid-solid transport. *Int. J. Multiph. flow* 36 (1), 78–87. doi:10.1016/j.ijmultiphaseflow.2009.08.001

Fan, C. H., Xie, H. B., Li, H., Zhao, S., Shi, X., Liu, J., et al. (2022). Complicated fault characterization and its influence on shale gas preservation in the southern margin of the sichuan basin, China, *China. Lithosphere* 2022, 8035106. doi:10.2113/2022/8035106

Feng, Q., Cha, L., Dai, C., Zhao, G., and Wang, S. (2020). Effect of particle size and concentration on the migration behavior in porous media by coupling computational fluid dynamics and discrete element method. *Powder Technol.* 360, 704–714. doi:10.1016/j.powtec.2019.10.011

Feng, Y., and Gray, K. E. (2016). A fracture-mechanics-based model for wellbore strengthening applications. *J. Nat. Gas Sci. Eng.* 29, 392–400. doi:10.1016/j.jngse.2016.01.028

Feng, Y., Jones, J. F., and Gray, K. E. (2016). A review on fracture-initiation and-propagation pressures for lost circulation and wellbore strengthening. *SPE Drill. Complet.* 31 (2), 134–144. doi:10.2118/181747-PA

Feng, Y., Li, G., Meng, Y., and Guo, B. (2018). A novel approach to investigating transport of lost circulation materials in rough fracture. *Energies* 11 (10), 2572. doi:10.3390/en11102572

Huang, H., Babadagli, T., Li, H., Develi, K., and Zhou, D. (2020). A visual experimental study on proppants transport in rough vertical fractures. *Int. J. Rock Mech. Min. Sci.* 134, 104446. doi:10.1016/j.ijrmms.2020.104446

Khan, H. J., Mirabolghasemi, M. S., Yang, H., Prodanovic, M., DiCarlo, D. A., and Balhoff, M. T. (2017). Study of formation damage caused by retention of bi-dispersed particles using combined pore-scale simulations and particle flooding experiments. *J. Petroleum Sci. Eng.* 158, 293–308. doi:10.1016/j.petrol.2017.08.061

Koyama, T., Li, B., Jiang, Y., and Jing, L. (2008). Numerical simulations for the effects of normal loading on particle transport in rock fractures during shear. *Int. J. Rock Mech. Min. Sci.* 45 (8), 1403–1419. doi:10.1016/j.ijrmms.2008.01.018

Kuzmina, L. I., Osipov, Y. V., and Zheglova, Y. G. (2018). Analytical model for deep bed filtration with multiple mechanisms of particle capture. *Int. J. Non-linear Mech.* 105, 242–248. doi:10.1016/j.ijnonlinmec.2018.05.015

Li, H. (2022). Research progress on evaluation methods and factors influencing shale brittleness: A review. *Energy Rep.* 8, 4344–4358. doi:10.1016/j.egyr.2022.03.120

Li, S., Kang, Y., You, L., Li, D., and Lian, Z. (2014). Experimental and numerical investigation of multiscale fracture deformation in fractured-vuggy carbonate reservoirs. *Arab. J. Sci. Eng.* 39 (5), 4241–4249. doi:10.1007/s13369-014-1018-6

Li, Y., Kang, Z. J., Xue, Z. J., and Zheng, S. (2018). Theories and practices of carbonate reservoirs development in China. *Petroleum Explor. Dev.* 45 (4), 712–722. doi:10.1016/S1876-3804(18)30074-0

Li, H., Tang, H. M., Qin, Q. R., Zhou, J., Qin, Z., Fan, C., et al. (2019). Characteristics, formation periods and genetic mechanisms of tectonic fractures in the tight gas sandstones reservoir: A case study of xujiahe formation in YB area, sichuan basin, China. *J. Petroleum Sci. Eng.* 178, 723–735. doi:10.1016/j.petrol.2019.04.007

Li, J., Qiu, Z., Zhong, H., Zhao, X., and Huang, W. (2020). Coupled CFD-DEM analysis of parameters on bridging in the fracture during lost circulation. *J. Petroleum Sci. Eng.* 184, 106501. doi:10.1016/j.petrol.2019.106501

Li, J., Li, H., Yang, C., Wu, Y., Gao, Z., and Jiang, S. (2022a). Geological characteristics and controlling factors of deep shale gas enrichment of the Wufeng-Longmaxi Formation in the southern Sichuan Basin, China. *Lithosphere* 2022, 4737801. doi:10.2113/2022/4737801

Li, H., Zhou, J. L., Mou, X. Y., Guo, H., Wang, X., An, H., et al. (2022b). Pore structure and fractal characteristics of the marine shale of the longmaxi formation in the changning area, southern sichuan basin, China. *Front. Earth Sci.* 10, 1018274. doi:10.3389/feart.2022.1018274

Moore, C. H., and Wade, W. J. (2013). *Carbonate reservoirs: Porosity and diagenesis in a sequence stratigraphic framework*. Newnes. London, UK.

Ogilvie, S. R., Isakov, E., and Glover, P. (2006). Fluid flow through rough fractures in rocks. II: A new matching model for rough rock fractures. *Earth Planet. Sci. Lett.* 241 (4), 454–465. doi:10.1016/j.epsl.2005.11.041

Tse, R., and Cruden, D. M. (1979). Estimating joint roughness coefficients. *Int. J. Rock Mech. Min. Sci. Geomechanics Abstr.* 16 (5), 303–307. doi:10.1016/0148-9062(79)90241-9

Walsh, J. B. (1981). Effect of pore pressure and confining pressure on fracture permeability. *Int. J. Rock Mech. Min. Sci. Geomechanics Abstr.* 18 (5), 429–435. doi:10.1016/0148-9062(81)90006-1

Wang, G., and Pu, X. (2014). Discrete element simulation of granular lost circulation material plugging a fracture. *Part. Sci. Technol.* 32 (2), 112–117. doi:10.1080/02726351.2013.829546

WuFan, J. Y. R. F., Wu, F., and Li, C. (2019). Combining large-sized model flow experiment and NMR measurement to investigate drilling induced formation damage in sandstone reservoir. *J. Petroleum Sci. Eng.* 176, 85–96. doi:10.1016/j.petrol.2019.01.005

Xu, C., You, Z., Kang, Y., and You, L. (2018). Stochastic modelling of particulate suspension transport for formation damage prediction in fractured tight reservoir. *Fuel* 221, 476–490. doi:10.1016/j.fuel.2018.02.056

Yang, Y., Tao, L., Yang, H., Iglauer, S., Wang, X., Askari, R., et al. (2020). Stress sensitivity of fractured and vuggy carbonate: An X-ray computed tomography analysis. *J. Geophys. Res. Solid Earth* 125 (3), e2019JB018759. doi:10.1029/2019JB018759

Zeng, J., Li, H., and Zhang, D. (2016). Numerical simulation of proppant transport in hydraulic fracture with the upscaling CFD-DEM method. *J. Nat. Gas Sci. Eng.* 33, 264–277. doi:10.1016/j.jngse.2016.05.030

Zhang, G., Gutierrez, M., and Chao, K. (2019a). Hydrodynamic and mechanical behavior of multi-particle confined between two parallel plates. *Adv. Powder Technol.* 30 (2), 439–450. doi:10.1016/j.apt.2018.11.023

Zhang, J., Wei, C., Ju, W., Yan, G., Lu, G., Hou, X., et al. (2019b). Stress sensitivity characterization and heterogeneous variation of the pore-fracture system in middle-high rank coals reservoir based on NMR experiments. *Fuel* 238, 331–344. doi:10.1016/j.fuel.2018.10.127

Zhu, B., Tang, H., Zhao, F., and Tang, H. (2020). Numerical simulation of particulate suspension transport and permeability impairment in an actual rough fracture under normal stresses. *Energy Sci. Eng.* 8 (4), 1165–1180. doi:10.1002/ese3.576

Zhu, B., Tang, H., Yin, S., Gongyang, C., Feng, Z., and Ling, L. (2022). Experimental and numerical investigations of particle plugging in fracture-vuggy reservoir: A case study. *J. Petroleum Sci. Eng.* 208, 109610. doi:10.1016/j.petrol.2021.109610

frontiers | Frontiers in Earth Science

TYPE Original Research
PUBLISHED 06 January 2023
DOI 10.3389/feart.2022.1015832

OPEN ACCESS

EDITED BY
Hu Li,
Southwest Petroleum University, China

REVIEWED BY
Jianguo Zhang,
China University of Geosciences, China
Liuqin Chen,
East China University of Technology, China
Li Hongbo,
Yangtze University, China

*CORRESPONDENCE
Xingchao Jiang,
22195067@qq.com
Long Huang,
116643724@qq.com

SPECIALTY SECTION
This article was submitted to Structural Geology and Tectonics, a section of the journal Frontiers in Earth Science

RECEIVED 10 August 2022
ACCEPTED 20 September 2022
PUBLISHED 06 January 2023

CITATION
Wang M, Jiang X, Lei B, Huang L and Pan J (2023), Tectonic evolution and its control on oil–gas accumulation in southern East China Sea since the Jurassic.
Front. Earth Sci. 10:1015832.
doi: 10.3389/feart.2022.1015832

Tectonic evolution and its control on oil–gas accumulation in southern East China Sea since the Jurassic

Mingjian Wang[1,2], Xingchao Jiang[3,4]*, Baohua Lei[1], Long Huang[1]* and Jun Pan[1]

[1]Qingdao Institute of Marine Geology, China Geological Survey, Ministry of Natural Resources, Qingdao, China, [2]Laboratory for Marine Mineral Resources, Pilot National Laboratory for Marine Science and Technology, Qingdao, China, [3]Hubei Key Laboratory of Petroleum Geochemistry and Environment, Yangtze University, Wuhan, China, [4]Key Laboratory of Exploration Technologies for Oil and Gas Resources, Ministry of Education, Yangtze University, Wuhan, China

Based on the results from the previous research on Mesozoic igneous rocks, as well as tectonic environments in the northern South China Sea and southern East China Sea (NSCS-SECS), geophysical parameters, strata, and characteristics of seismic facies in NSCS-SECS were investigated. These findings were combined with results from the analysis of the balanced profile evolution to re-evaluate the tectonic evolution of SECS since the Jurassic. Furthermore, burial history and simulation of wells in the SECS were analyzed using well, seismic and source rock data. Furthermore, favorable models of oil–gas accumulation in the Lower–Middle Jurassic were proposed in combination with studies on elements and conditions of the petroleum system. The results demonstrated that the NSCS-SECS had consistent tectonic settings and comparable strata from the Jurassic to the Cretaceous time. There was a large unified basin in this period. The basin experienced two evolutionary stages, respectively, the fore-arc depression basin in the Early–Middle Jurassic ($J_{1\text{-}2}$) and the back-arc faulted basin in the Late Jurassic–Cretaceous (J_3-K). There was considerable deposition of dark mudstones in the SECS during the Lower–Middle Jurassic. The Keelung Sag was the depositional center accumulating the thickest section of the Lower–Middle Jurassic source rocks which entered a high-maturity stage. Hence, it was the hydrocarbon generation center in the SECS. The process of generating hydrocarbons from Lower–Middle Jurassic source rocks was of high complexity from northwest to southeast. The Lower–Middle Jurassic source rock at the northwest edges of the basin experienced two hydrocarbon generation stages, while the Keelung Sag toward the southeast experienced three hydrocarbon generation stages. The models and types of oil–gas accumulation in various evolutionary phases were different due to the control by tectonic evolution. Oil and gas that were generated by Lower–Middle Jurassic source rocks in the Keelung Sag migrated and accumulated in the western high-tectonic units. Research findings provide insights into Mesozoic oil and gas exploration in the NSCS-SECS.

KEYWORDS

Early–Middle Jurassic, tectonic evolution, source rocks, burial history, accumulation models, southern East China Sea

1 Introduction

The East China Sea Basin is a large overlapping Mesozoic–Cenozoic petroliferous basin in offshore China. It has experienced multiple stages of tectonic deformation since the Mesozoic and has complex geological conditions (Zheng et al., 2005; Yang et al., 2012, 2019; Zhong et al., 2018; Wang et al., 2020). Oil and gas exploration in the East China Sea Basin is divided into two stages, before and after 2005: 1) exploration was primarily focused on Cenozoic reservoirs prior to 2005; 2) Mesozoic reservoirs were better understood due to improvement in seismic acquisition and processing technology after 2005. Thus, oil and gas exploration gradually moved to deep strata. However, some challenges were experienced: 1) the study area was located in the junctional zone between the Eurasian Plate, Pacific Plate, and India–Australia Plate from the Mesozoic to Cenozoic time and experienced high-complexity evolution of the Yanshan Movement, as well as a strong reconstruction of the Himalayan Movement, resulting in complex tectonic characteristics; 2) there were relatively limited drilling core and geophysical data in the study area.

Previous studies have mainly discussed the offshore geological conditions from adjacent onshore areas. Tectonics, geochemistry, and ancient geography remain controversial in the Mesozoic tectonic structures of SECS (Zheng et al., 2005; Yang et al., 2012, 2019; Suo et al., 2015; Chen et al., 2016; Xu et al., 2016, 2017; Li et al., 2017; Zhong et al., 2018; Zhang et al., 2019; Si et al., 2021).

Li et al. (2012) indicated for the first time that the NSCS-SECS may be a large unified sedimentary basin during the Mesozoic, and this was based on seismic and well data combined with gravity and magnetic inversion results in the SECS. He postulated that the western boundary of the Jurassic Basin was the Yandang old uplift. There were continuous extensive distributions of Mesozoic strata in the NSCS-SECS and the sedimentary depth gradually decreased from southwest to northwest (Qiu and Wen, 2004; Li et al., 2014). Xu et al. (2017) discovered an early Cretaceous igneous belt with a NE trend in the NSCS-SECS. Zhou (2002) identified a NE trend Mesozoic subduction accretion zone in NSCS, which was likely to be extended toward the SECS. Both the igneous belt and the subduction accretion zone were related to the movements of the old Pacific Plate (Zhou et al., 2005; Xu et al., 2017), suggesting that the NSCS-SECS was under the influence of the same setting tectonic during the Mesozoic. The analysis of gravity and magnetic inversion and well data suggests that the Mesozoic basement underlying the sedimentary rocks in the NSCS-SECS was the extension of the Caledonian Fold Belt in Southern China toward offshore areas (Lu et al., 2011; Sun et al., 2014), showing consistent basement properties. Overall, the NSCS-SECS showed similar and comparable features in terms of Mesozoic igneous lithology, geochemical signatures, tectonic environment, formation age, geophysical properties, and sedimentary strata.

In the SECS, previous studies have mainly focused on the Cenozoic basin structure, evolution, as well as Cenozoic oil and gas resource potential, which have achieved considerable results (Zheng et al., 2005; Sun et al., 2017; Zhong et al., 2018). However, there were relatively fewer studies on the Mesozoic geological structures. Currently, the evolutionary process of the Mesozoic Basin, including the basin type, the dynamic mechanism, as well as the generation and accumulation of hydrocarbons based on Mesozoic source rocks are still under debate (Yang et al., 2012; Yang et al., 2017; Yang et al., 2019; Wang et al., 2019; Wang et al., 2020; Wang et al., 2022a; Xiao et al., 2019; Liu et al., 2020). These limited understandings of Mesozoic tectonic evolution and oil and gas resource potentials.

From the comparative analysis of the Mesozoic basin basement, sedimentary strata, and dating of magmatic rocks combined with the analysis of regional tectonic dynamics in the NSCS-SECS, it is believed that the NSCS-SECS was a large unified basin in the Mesozoic period. These findings guided our discussion throughout these periods. Based on this, Jurassic oil and gas accumulation elements and conditions in the SECS were systematically analyzed, and favorable accumulation models were proposed to provide a geological basis for oil and gas exploration.

2 Geological setting

Mesozoic is the most important tectonic revolutionary period in eastern China. During this period, the evolution from the Indosinian tectonic domain to the Coastal Pacific tectonic domain was completed, and the complex tectonic settings and evolutionary process in offshore eastern China were formed. The NSCS-SECS area covered the present-day East China Sea Basin, the West Taiwan Basin, the southwest Taiwan Basin, and the east-central region of the Pearl River Mouth Basin (eastern side of the Yangjiang–Yitong'ansha Fault). It extended to the northern Yandang Swell in the East China Sea Shelf Basin as the northern boundary, the Yangjiang–Yitong'ansha Fault as the southwest boundary, and the Bijia Uplift–Diaoyu Island Fold Belt as the southeast boundary. It was separated from the mainland in the northwest by the Changle–Nan'ao Fault (Figure 1). The NSCS-SECS was generally NE-NNE trended. It was mainly controlled by NEE-NE-NNE trend faults from south to north, followed by the NW trend fault. The study area was chosen as the southern region of the East China Sea, located in the northern

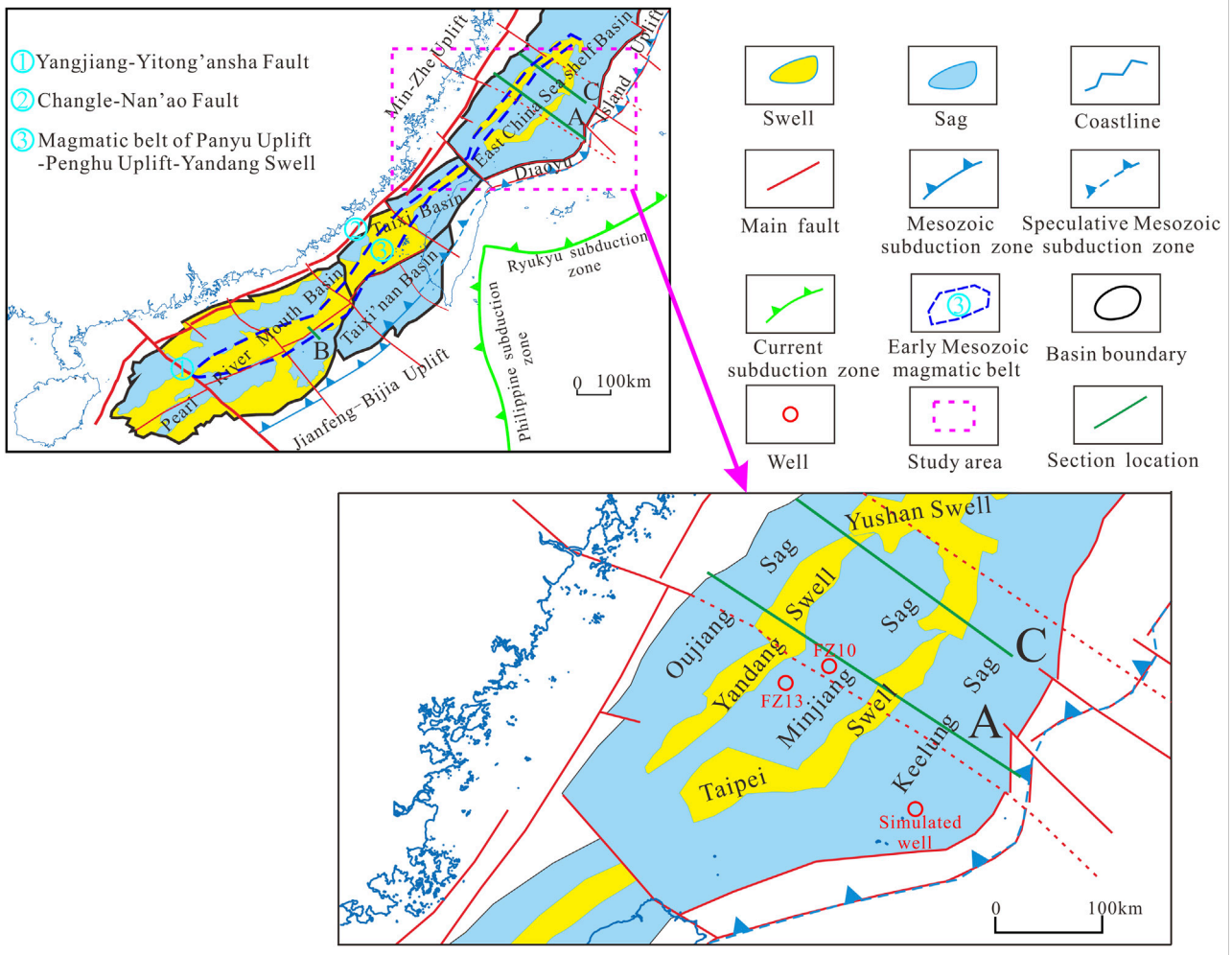

FIGURE 1
Overview of tectonic configurations along the NSCS-SECS. The current tectonic map of the SECS Basin is shown at the bottom right (modified from Zhou et al., 2005; Lu et al., 2011; Sun et al., 2014; Li S. et al., 2018).

region of the NSCS-SECS area. The study area was bounded by the Diaoyu Island Fold Belt to the east, West Taiwan Basin to the south, Zhemin Uplift Zone to the west, and separated from the northern region of the basin by the Yushan Swell to the north (Figure 1).

Rocks underlying the basin are similar to the Caledonian–Early Indosinian metamorphic rocks in South China, showing lithological consistency with onshore areas in Zhejiang and Fujian provinces (Yang et al., 2019). Sedimentary processes forming strata were dominant since the Mesozoic, among which the Jurassic–Cretaceous systems were mainly marine and paralic facies (Yang et al., 2015). The Cenozoic Basin covered a large area and the sedimentary environment was generally characterized by marine facies in the south and continental facies in the north (Zhong et al., 2018). Although controlled by NE-NNE trend faults, the East China Sea Basin has a characteristic tectonic distribution of NE trend belts intersected by NW faults. There were five tectonic units in the basin from west to east, namely, Oujiang Sag, Yandang Swell, Minjiang Sag, Taibei Swell, and Keelung Sag. Jurassic strata were developed in the tectonic units east of the Oujiang Sag.

3 Data and methods

The main data used in this article, including strata thickness data, lithological data, vitrinite reflectance (R_o) from dark mudstone and coal seams, and sandstone reservoir properties, were collected by oil and gas resource strategic research projects and published articles over the past 10 years. Additional

information from gravity and magnetic results published by Zhang et al. (2010) was also included in the data package. The study benefited from seismic reflection data provided by the Qingdao Institute of Marine Geology, Geological Survey of China.

The region from NSCS to SECS was considered in this study as one entity and was placed in the unified Mesozoic geotectonic settings. The basin evolution and the dynamic mechanism focusing on regional dynamic analysis since the Jurassic were discussed combining analysis of the typical balanced seismic profile from the SECS. The kerogen type and vitrinite reflectance (R_o) were measured by the fluorescence microscope and optical microscope. Reservoir porosities were obtained from the core test, observation of thin section in the core sample, and interpretation of logging data. Lower–Middle Jurassic source rock quality, reservoir properties, and seal rock development were systematically analyzed based on seismic and well data (FZ13 and FZ10) in the SECS. Burial and thermal histories of Well FZ10 and the maturity simulation were analyzed in combination with findings of tectonic evolution using seismic interpretation results, paleogeotemperature gradient data, and R_o test data. In addition, the process of generating hydrocarbons from Lower–Middle Jurassic source rocks was determined. Based on this, the favorable accumulation models of oil–gas generated by Lower–Middle Jurassic source rock were proposed by combining analysis of elements and conditions of oil–gas accumulation.

4 Results

4.1 Comparison of Mesozoic tectonic environments and sedimentary strata between the NSCS and SECS

4.1.1 Geochemistry and age of Mesozoic igneous rocks

Xu et al. (2016) , Xu et al. (2017) studied the Mesozoic igneous rock samples that were found in more than 20 wells from the NSCS and more than 10 wells from the SECS. He observed a NE-SW trend belt of Early Jurassic (198–187 Ma) island arc igneous rocks from Shenhu Uplift–Panyu Uplift–Penghu Uplift in NSCS to Yandang Swell in the SECS, with low-potassium tholeiitic granite–diorite lithologies. This indicated that NSCS-SECS underwent the same tectonic environment at the beginning of the Jurassic. Moreover, Jurassic–Cretaceous I-type magmatic arc granites were recognized in the NSCS. The zircon U–Pb age had two peaks at 162–148 Ma and 137–102 Ma.

Zhang et al. (2019) and Si et al. (2021) tested granitoids in the SECS and Paleocene clastic rocks of the Lishui Depression. The results demonstrated that the zircon U–Pb age of the granitoids was 193–172 Ma and 115–111 Ma. Zircon has typical magmatic arc characteristics of fluid activity uranium (U) enrichment and high field intensity element (Nb) depletion. The zircon age of clastic rocks was Jurassic–Early Cretaceous, including three peaks of 194–184 Ma, 148–133 Ma, and 119–98 Ma. The age of the early clastic zircon peak (194–184 Ma) corresponded to the Early Jurassic igneous formation time proposed by Xu et al. (2016), Xu et al. (2017), while the late age peak (119–98 Ma) corresponded to the zircon age (137–102 Ma) of granitoids in the NSCS.

Overall, the wells in the NSCS-SECS revealed that the geochemical signature and age of Jurassic–Cretaceous igneous rocks were consistent, and both formed in the subduction-controlled magmatic arc environment of the East Asian Paleoplate.

4.1.2 Interpretation of geophysical data from the Early Jurassic magmatic belt

Zhou et al. (2005) recognized a NE trend (about 45°) subduction accretion zone in NSCS from the interpretation of gravity, magnetic, and wide-angle seismic data. This subduction accretion zone had an oblique intersection with current submarine topography and Cenozoic tectonic, indicating that it formed before the Cenozoic. In addition, this subduction accretion zone was shifted to the left by the NW trend fault forming an echelon, which agreed with the Mesozoic stress field. However, the time of formation of this subduction accretion zone was not discussed in this study. The Mesozoic subduction accretion zone would certainly cause strong tectonic movement and volcanism. The magmatic belt of Shenhu Uplift–Panyu Uplift–Penghu Uplift–Yandang Swell was presented by Xu et al. (2017), as a NE trend moniliform belt with low positive magnetic anomaly value on the map (Zhang et al., 2010). It extended from the NSCS to the SECS along a northeasterly direction, which corresponded to the northwest boundary of the Early–Middle Jurassic Basin. This magmatic belt was generally parallel to the Mesozoic subduction accretion zone proposed by Zhou et al. (2005). Therefore, it was proposed that this magmatic belt was also formed by plate subduction in this period. The interpretation of the igneous belt and the geochemical data can prove each other, which further confirmed that NSCS-SECS was in the same tectonic environment at the beginning of the Jurassic.

4.1.3 Basement properties and Mesozoic fracture

The basement of the Mesozoic Basin in the northern East China Sea was the extension of the Lower Yangtze Fold Belt toward the sea, while similar structures from the SECS to the NSCS (east side of the Yangjiang–Yitong'ansha fault) were the extension of the Caledonian Fold Belt in southern China toward the offshore (Lu et al., 2011; Sun et al., 2014). The basin basement in the NSCS-SECS was developed over the continental crust in a stable rigid basement. The basement of the Mesozoic Basin is regularly distributed.

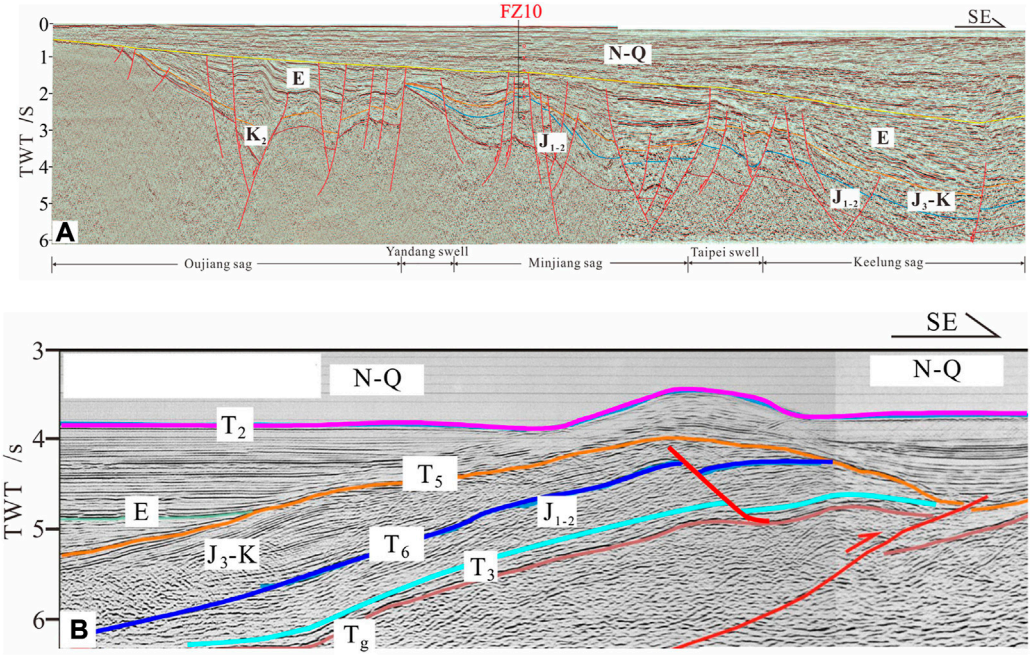

FIGURE 2
Seismic interpretation of SE oriented profiles showing the distribution of sedimentary strata along the SECS **(A)** and NSCS **(B)**. T_3 label represents the Late Triassic; J_{1-2} represents the Early–Middle Jurassic; J_3-K represents the Late Jurassic–Cretaceous; E represents the Paleocene; N-Q represents the Neocene–Quaternary; T_2 represents the boundary between the Neogene and Paleogene; T_5 represents the boundary between the Paleogene and Cretaceous; T_6 represents the boundary between the Late Jurassic and Middle Jurassic; and T_g represents the bottom boundary of the Mesozoic.

The bottom part is essentially formed by Presinian crystalline rocks (Li, 2001; Li et al., 2014; Sun et al., 2014; Li S. et al., 2018), and the lithological features discussed earlier were diverse in different basins. Specifically, the basement underlying Mesozoic sedimentary rocks in SECS was formed by Proterozoic metamorphic rocks, Mesozoic intrusive rocks, and acidic volcanic rocks (Li, 2001). The rocks of this basement along the West and southwest Taiwan basins are Late Paleozoic schist, marbles, and igneous (Liu et al., 2006; Li et al., 2014). The basement of the Pearl River Mouth Basin east of the Yangjiang–Yitong'ansha Fault was mainly formed by Early Jurassic granites and granodiorites (Liu et al., 2006; Li et al., 2014). The basement lithology can be compared with rocks in Zhejiang, Fujian, and Guangdong provinces sharing the same age (Wang et al., 2022b). Seismic, gravity, and magnetic data reveal that Mesozoic fractures with a NE and NW trend were developed from NSCS to SECS (Yi et al., 2012; Lu et al., 2015; Liu et al., 2019). Precisely, the NE trend was the main tectonic direction and was developed early, while the NW trend fault was developed slightly late and intersected by the NE trend fault (Figure 1), which was the left-lateral strike-slip fault (Sun et al., 2014; Xia et al., 2018). Faulting played an important role in adjusting the tectonic deformation in the area. The Mesozoic tectonic structure appears to be separated by those large basement faults in the NSCS-SECS with the characteristics of NE trend belts intersected by NW faults (Yi et al., 2012).

4.1.4 Jurassic–Cretaceous strata

There were extensive distributions of the Mesozoic formation from NSCS to SECS, with continuous and comparable lateral strata. In the Early–Middle Jurassic, there was stable marine sedimentation from NSCS to SECS, accompanied by a gradual reduction in the water depth and transition of sedimentary facies from bathyal–abyssal plain facies to littoral–neritic facies (Qiu and Wen, 2004). The Lower–Middle Jurassic (J_{1-2}) was a group of low to moderate amplitude, less continuous to continuous reflectors, external sheet-wedge, and parallel–sub-parallel internal structures in seismic profiles (Figure 2). The Lower–Middle Jurassic (J_{1-2}) in the basin was in conformable contact with the underlying Upper Triassic Series and in unconformable contact at the basin edges. The NSCS was mainly developed with Late Jurassic to Cretaceous bathyal and littoral–neritic facies, which were gradually transitioned to neritic, paralic, and continental facies in SECS. In seismic, the Upper Jurassic–Cretaceous (J_3-K) is interpreted as a set of mid–high amplitude, continuous lamellar reflectance, with external wedge, and

internal divergent structures (Figure 2). The top of Upper Jurassic–Cretaceous strata was often bare, which was an unconformable angular contact with the overlying Cenozoic strata.

4.2 Characteristics of the Jurassic source rock

The thickness of the Lower–Middle Jurassic succession from regional geological analysis and seismic data interpretation is approximately 1,500–4,000 m and the sedimentation center is at the Keelung Sag, with a thickness of 4,000 m. A comprehensive analysis of well and seismic data indicates that the water depth in the SECS gradually decreased from northwest to southeast, along which it developed with sedimentation of fluvial, paralic, neritic, and bathyal–abyssal facies. Jurassic dark mudstones are generally distributed to the northeast and the total thickness ranges from 100 to 700 m. The depocenter is in the mid-south of the Keelung Sag, which is about 600–800 m thick (Wang et al., 2019).

In the study area, wells FZ13 and FZ10 intersected Jurassic strata located eastward near the coast of the Panyu Uplift–Penghu Uplift–Yandang Swell (Figure 1). Coastal neritic dark mudstones and paralic facies coal seams are dominant in these two wells. The statistics of geochemical core data from these wells indicate that the organic carbon content of the dark mudstone is 0.69%–0.98%, reaching a maximum of 1.24%. Rock-Eval pyrolysis S1+S2 was between 0.63 and 1.97 mg/g. These dark mudstones were determined to be source rocks of moderate abundance. The organic content in carboniferous source rocks can reach 67%–75% and pyrolysis S1+S2 was between 155 and 169.6 mg/g, belonging to rich source rocks. Most of the organic matter in the Jurassic source rocks was type III and some reached type II. Type III source rocks are generally humic-type source rocks capable of generating gas.

Currently, no wells have been drilled at the Keelung Sag. Many wells in the west Taiwan Basin adjacent to the south of the study area revealed that abyssal plain shale was developed in the Lower and Middle Jurassic, with organic content ranging from 0.6% to 1.8%, compared to the surrounding strata in the same period. They can be good source rocks due to their high organic content (Qiu and Wen, 2004; Zhou et al., 2006). At the beginning of the Middle Jurassic, the water depth in the SECS gradually increased along the southeast and was mainly of medium–high amplitude, sub-parallel to parallel reflection in the seismic data, which has been identified as the stable sedimentation of the bathyal–abyssal facies (Yang et al., 2015; Yang et al., 2017; Wang et al., 2019). This was conducive to aggregation and accumulation of organic matter. Thus, we postulate that the Keelung Sag, which is the depocenter of Early–Middle Jurassic sedimentation, had good conditions for the generation of hydrocarbons.

4.3 Characteristics of the reservoir and seal rock

4.3.1 Mesozoic reservoir

Mesozoic reservoir data statistics from wells FZ13 and FZ10 suggest that the reservoir was composed mainly of sandstones and siltstones of coastal–neritic facies (Figure 3), and the reservoir pore spaces were mainly composed of primary porosity and secondary fractures. The porosity gradually decreased with an increasing depth, influenced by the compaction, cementation, and subsidence of clay minerals. Generally, the buried depth of 3,100 m can be used as a limit. The porosity above 3,100 m was higher than 10%, showing good accumulation properties. The porosity below 3,100 m decreased markedly and was mostly less than 10%, showing relatively low permeability. Overall, the porosity of Lower Jurassic sandstones was generally less than 10% due to compaction and diagenesis influences (Table 1). Current studies show that tectonism-controlled fracture development in tight reservoirs can significantly improve reservoir properties (Li et al., 2019; Fan et al., 2022; Li H. et al., 2022; Li J. et al., 2022). This evolved secondary pores and cracks in the sedimentary layers, leading to porosity enhancement. The porosity of the Upper Jurassic–Lower Cretaceous sandstone was generally between 15%–20% (Table 1). Porosity in the layers developed with secondary pores and cracks can exceed 20%. The porosity of the Upper Cretaceous sandstone is generally greater than 20%, showing good reservoir accumulation properties.

4.3.2 Cenozoic reservoir

Sandstone is the main reservoir rock type, from silt to gravel in terms of grain size. Moreover, fine-medium grain sandstone is dominant. The Eocene Pinghu and Oligocene Huaguang formations are the most important strata (Figure 3). The reservoir pore spaces are mainly primary pores, secondary pores, micropores, and microcracks. Among them, the primary pores have the greatest contribution and the microcracks connected different types of pores effectively, thus improving the pore permeability of the reservoir. The porosity of Cenozoic Paleogene reservoir is generally 10%–25% and permeability is mostly less than 1,000 mD. Both porosity and permeability are not related to the buried depth.

4.3.3 Seal rock

Analysis of the core data shows that the overlying Cenozoic strata in the SECS were mainly composed of mudstones (Figure 3). The abyssal plain, bathyal, and paralic facies were developed during the Lower–Middle Jurassic, accompanied by extensive development of thick mudstone layers. In particular, thick layers of mudstone and shale were well developed at the Keelung Sag, being the depocenter of sedimentation, which was not only the good source rock but also the excellent regional seal rock. Upper Cretaceous coastal and paralic facies mudstones

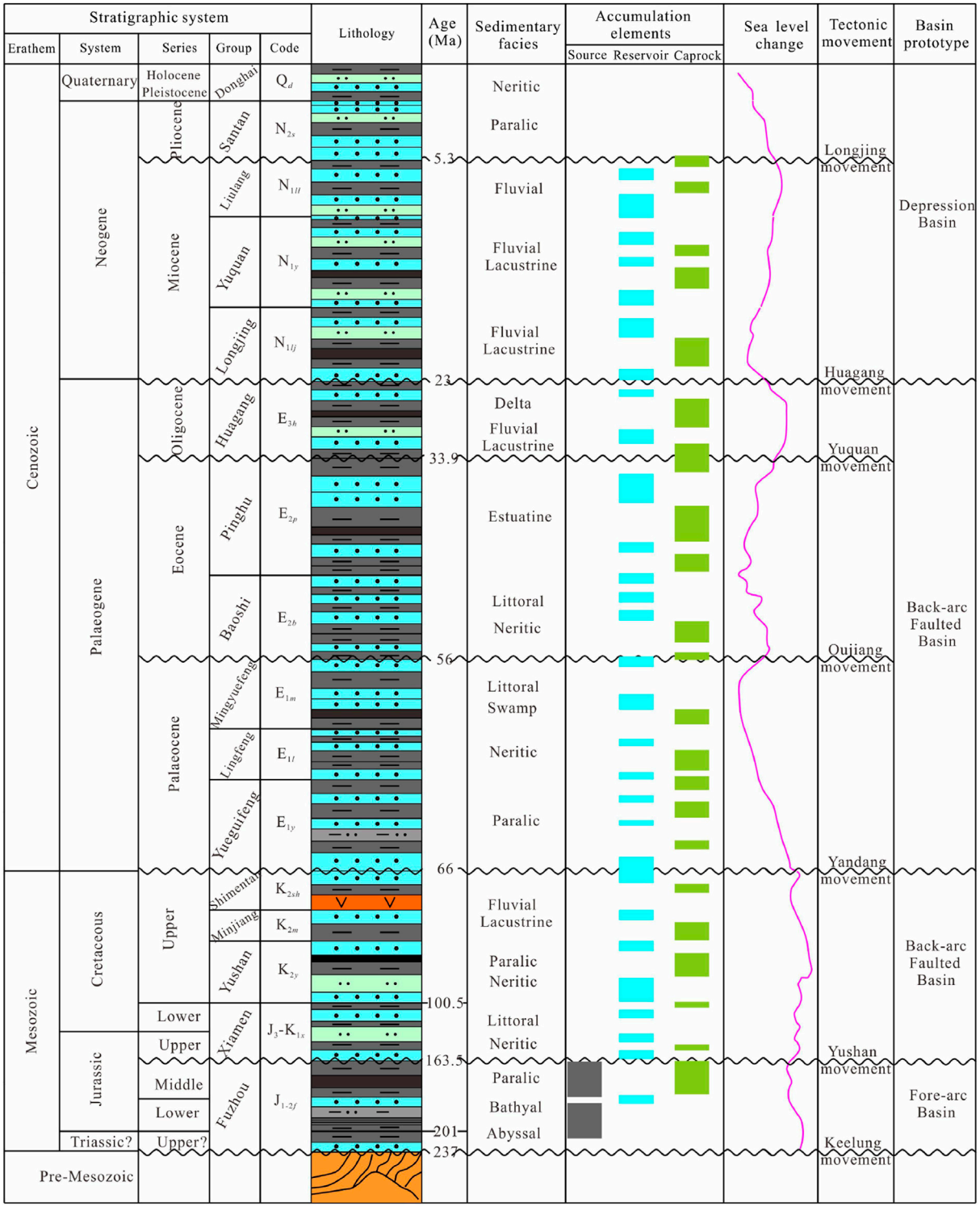

FIGURE 3
Stratigraphic chart of the SECS showing a combination of sedimentary facies, sea level changes, tectonic, and petroleum system since the Triassic (modified from Chen et al., 2016; Yang et al., 2012, 2017; Xiao et al., 2019; Wang et al., 2022a; as well as using drilling data of wells FZ10 and FZ13).

TABLE 1 Porosity distribution of the Mesozoic reservoir across wells FZ10 and FZ13 estimated from three strata (J, K_1, and K_2).

Strata	Porosity range (%)		Proportion of porosity<10% (%)		Proportion of porosity ranging 10%–15% (%)		Proportion of porosity ranging 15%–25% (%)		Proportion of porosity>25% (%)	
	FZ10	FZ13	FZ10	FZ13	FZ10	FZ13	FZ10	FZ13	FZ10	FZ13
K2	10.03–24.61	10.72–29.04	0	0	11.6	36.4	88.4	54.5	0	9.1
K1	7.76–19.99	4.09–22.64	21.9	55.6	58.9	31.7	19.2	12.7	0	0
J	5.78–12.67	5.8–8.97	75	100	25	0	0	0	0	0

have great thickness and extensive distribution and are good regional seal rocks. The Cenozoic regional seal rock mainly includes thick mudstones of neritic facies from the Paleocene Lingfeng Formation and the Eocene Baoshi Formation.

5 Discussion

5.1 Basin evolution since the Jurassic

Based on previous analysis, the NSCS-SECS was integrated and was a large unified basin during the Mesozoic. This basin extended to the northern Yandang Swell region of the East China Sea Basin as the northern boundary, the Yangjiang–Yitong'ansha Fault as the southwest boundary, and the Bijia Uplift–Diaoyu Island Fold Belt as the southeast boundary. It was separated from the mainland in the northwest by the Changle–Nan'ao Fault. This large basin has experienced consistent tectonic evolution since the Jurassic.

5.1.1 Fore-arc depression basin in the Early–Middle Jurassic

The study area has been controlled by the subduction of the Neo-Tethyls and Paleo-Pacific Plate into the Eurasian Plate since the Early Jurassic and the latter dominated. The Paleo-Pacific Plate melted and underwent metamorphic dehydration, accompanied by the NWW trend of low-angle progressive subduction from the Paleo-Pacific Plate to the Eurasian Plate (Li and Li, 2007; Li S et al., 2018), which induced the melting of the overlying continental crust of the obduction plate or the mantle wedge part (Li et al., 2017). Strong volcanism occurred along the Shenhu Uplift–Panyu Uplift–Penghu Uplift–Yandang Swell at the continental edges. Xu et al. (2017) demonstrated that these rocks had the geochemical characteristics of island arc igneous rocks. They were formed in the Early Jurassic based on the Zircon U–Pb age test. Hence, it can be postulated that the NSCS-SECS was in the Andes-type active continental margin stage for the development of the continental igneous arc. There was a fore-arc depression basin in front (southeast side) of the Panyu Uplift–Penghu Uplift–Yandang Swell igneous arc (Wang et al., 2022b) (Figure 4).

Figure 5 shows the balanced profile analysis in the SECS. The center of the strata's thickness was at the Keelung Sag and the eastern region of the Taibei Swell during the Early–Middle Jurassic. The strata were gradually thinned from the center of the basin to the northwest and southeast regions. The basin center was dominated by bathyal–abyssal facies, and the water depth decreased to the northwest and southeast. Meanwhile, the sedimentary facies transitioned into neritic and paralic facies.

5.1.2 Back-arc faulted basin in the Late Jurassic–Cretaceous

5.1.2.1 Late Jurassic–Early Cretaceous

The subduction direction from the Paleo-Pacific Plate to the Eurasian Plate changed to the NNW trend, in the Late Jurassic–Early Cretaceous, accompanied by an increase in the subduction angle (Suo et al., 2015; Li S. et al., 2018). The NSCS-SECS was in the left-lateral strike-slip extensional stress field environment (Sun et al., 2014; Xia et al., 2018). This was the peak stage of lithospheric thinning in eastern China, accompanied by strong fractures and volcanic activity. The lithology described from the well-core data was characterized by neutral-acid intrusive and eruptive rocks, belonging to I-type igneous arc granitoids. Most of the rocks contained common hornblendes and have enrichment of active fluid components and strong depletion of Ta-Nb-Ti. These were significantly different from I-type or A-type granites in South China at the same age. The Zircon U–Pb age had two peaks, which corresponded to twice strong Paleo-Pacific Plate subduction activities (Maruyama et al., 1997; Li et al., 1998; Xu et al., 2016; Xu et al., 2017; Yuan et al., 2018; Zhang et al., 2019). These rocks are mainly distributed in Dongsha Uplift, Shenhu Uplift, and Panyu Uplift in the NSCS and extended to the SECS. Furthermore, the rifting activity from the mainland to the offshore at the end of the Yanshan period and the cooling trend disclosed by the zircon/apatite fission track revealed that the Paleo-Pacific Plate had subduction retreat during 125–100 Ma (Suo et al., 2015; Li S et al., 2018). Balanced profile analysis showed that this stage was mainly

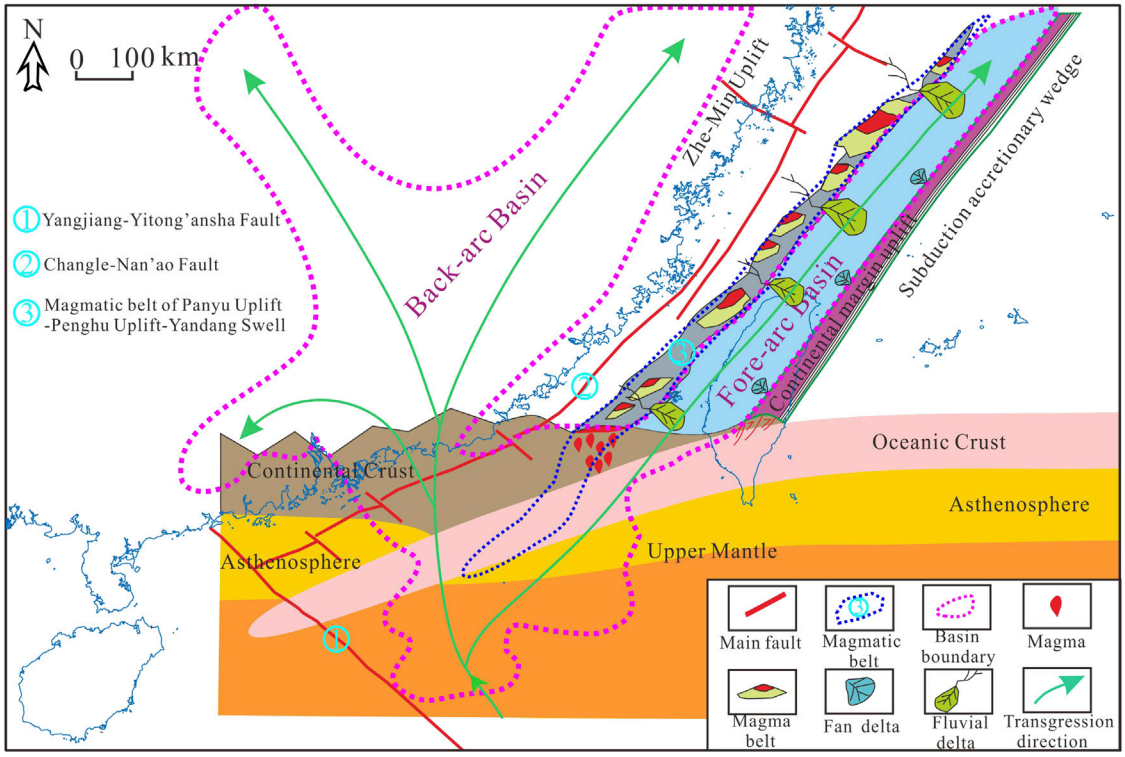

FIGURE 4
Plane view of the Early–Middle Jurassic Basin (pink dotted lines) and transgression direction (green arrow lines) in the NSCS-SECS, as well as the sedimentary system in the SECS. In the vertical section, we show the deep structural features, the magma activity, and the basin formation mechanism (modified from Zhou et al., 2005; Yi et al., 2012; Wu, 2014; Wang et al., 2022a; 2022b).

characterized by the development of NE trend boundary faults (e.g., western fault of Diaoyu Island which is shown in Figures 1, 5). Moreover, basin distribution and sedimentary strata were controlled by these boundary faults (Figure 5). In the Late Jurassic–Early Cretaceous, the NSCS-SECS was in the development stage of the back-arc faulted basin (Wang et al., 2022a; 2022b) (Figure 6). Water depth gradually increased from northwest to southeast and gradually evolved from continental to marine facies. The Keelung Sag was the depositional center at this stage, where it was primarily developed with bathyal–abyssal facies.

5.1.2.2 Late Cretaceous

Since the Late Cretaceous, the Pacific Plate replaced the Izanagi Plate (part of the Paleo-Pacific Plate) and was subducted into the NWW direction. Meanwhile, the Indian Plate began to move rapidly northward and collide with the Eurasian Plate (Xu et al., 2017). The ophiolite that was developed in eastern Taiwan, China, and the Philippines should be the remnant of the Late Mesozoic subducted oceanic crust (Dimalanta and Yumul, 2006; Dimalanta and Yumul, 2006; Asis and Jasin, 2012). The findings from studying lithology, chronology, and tectonic environment of igneous rocks over the same span period in coastal areas of southeast China (Chen et al., 2008; Hong, 2012), revealed that the lithology was mainly two-peak volcanic rocks (rhyolite/basalt) and A-type granite, which was formed in the regional extensional tectonic environment around 100–72 Ma (Ye, 2019). In the Late Cretaceous, the NSCS was in the weak tectonic belt under the interaction of the Pacific Plate, Eurasian Plate, and Indian Plate. A mantle plume was formed which extruded to the southeast and an NW-SE trending extensional stress field was generated. The NSCS area split to the southeast and a back-arc extensional faulted basin was formed. However, only a small-scaled retreat of the Pacific subduction zone occurred in SECS north of the weak tectonic belt. The SECS developed a faulted depression gradually eastward of the former Yandang old uplift. Compared with the earlier tectonic period, sedimentation of the basin was extended, but it was still a back-arc extensional faulted basin (Figure 7). This tectonic event corresponded to the Yandang Movement.

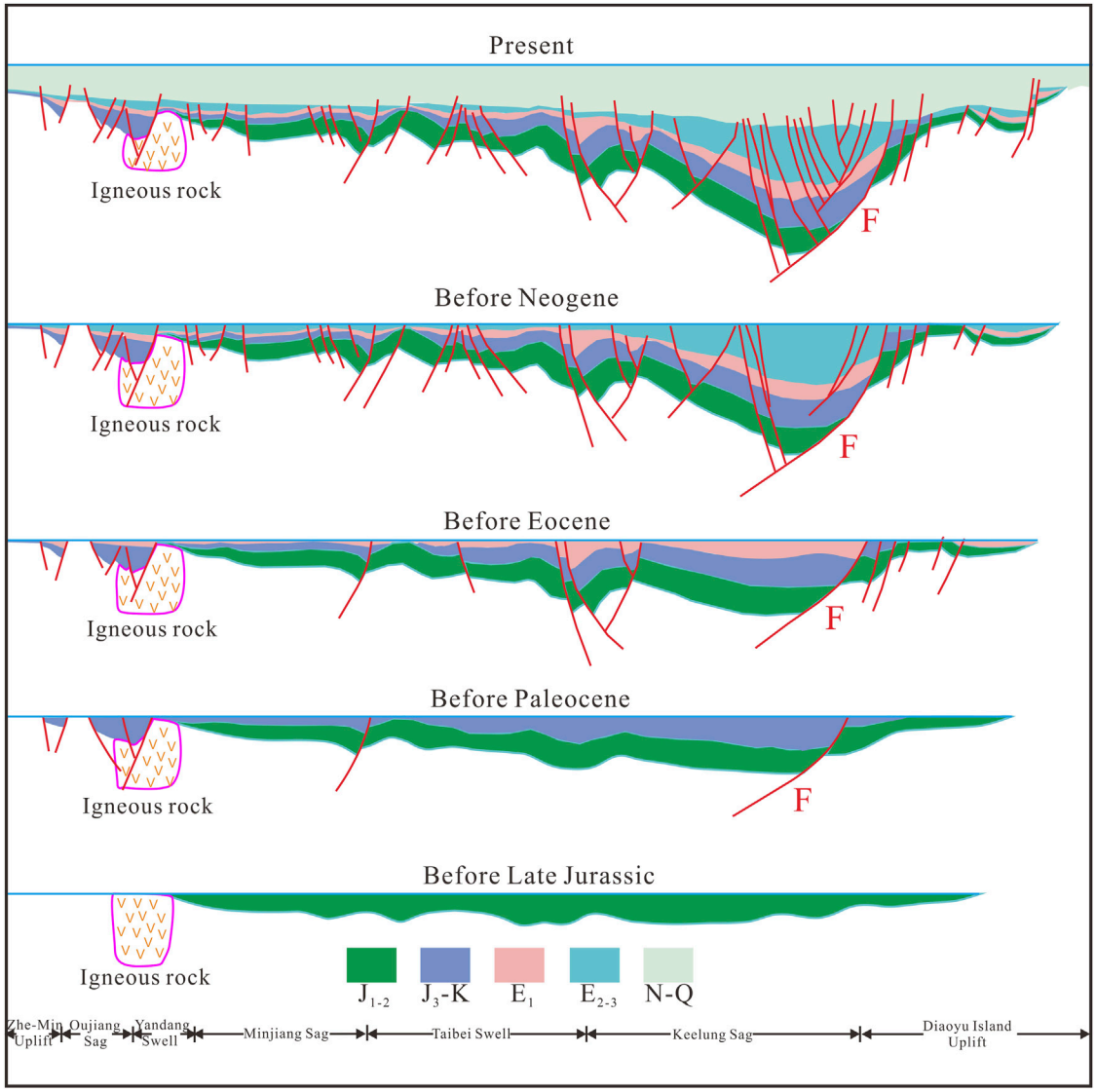

FIGURE 5
Tectonic evolution of SECS constructed from balanced section analysis in the southeast direction (F represents the western fault of Diaoyu Island in Figure 5). The J_{1-2} label represents the Early–Middle Jurassic; J_3-K represents the Late Jurassic–Cretaceous; E_1 represents the Paleocene; E_{2-3} represents the Eocene–Oligocene; and N-Q represents the Neocene–Quaternary.

5.2 Basin evolution since the Paleogene

Tectonic differential evolutionary characteristics in the NSCS-SECS have become increasingly prominent since the Paleogene, compared to before. Many scholars have studied the Cenozoic tectonic evolutionary process in the SECS and research results were consistent (Yang et al., 2012; Yang et al., 2017; Li et al., 2017; Zhong et al., 2018; Liu et al., 2020). The subduction influence of the Pacific Plate and the Philippine Sea Plate on SECS is more evident.

5.2.1 Paleogene back-arc faulted basin

In the Late Paleocene, the direction of motion of the Pacific Plate changed from NWW to NNW and SECS was in the simple shear stress field, thus resulting in a series of half-graben depression. This tectonic event corresponded to the Oujiang Movement. The direction of the Pacific Plate movement turned to the NWW at the end of the Eocene. Meanwhile, the Philippine Plate has begun to make NWW sloping subduction below the Eurasian Plate. The SECS underwent the tectonic event (Yuquan Movement) that was dominated by shear compression at the end of Eocene. In the Paleogene, the SECS was in a back-arc faulted

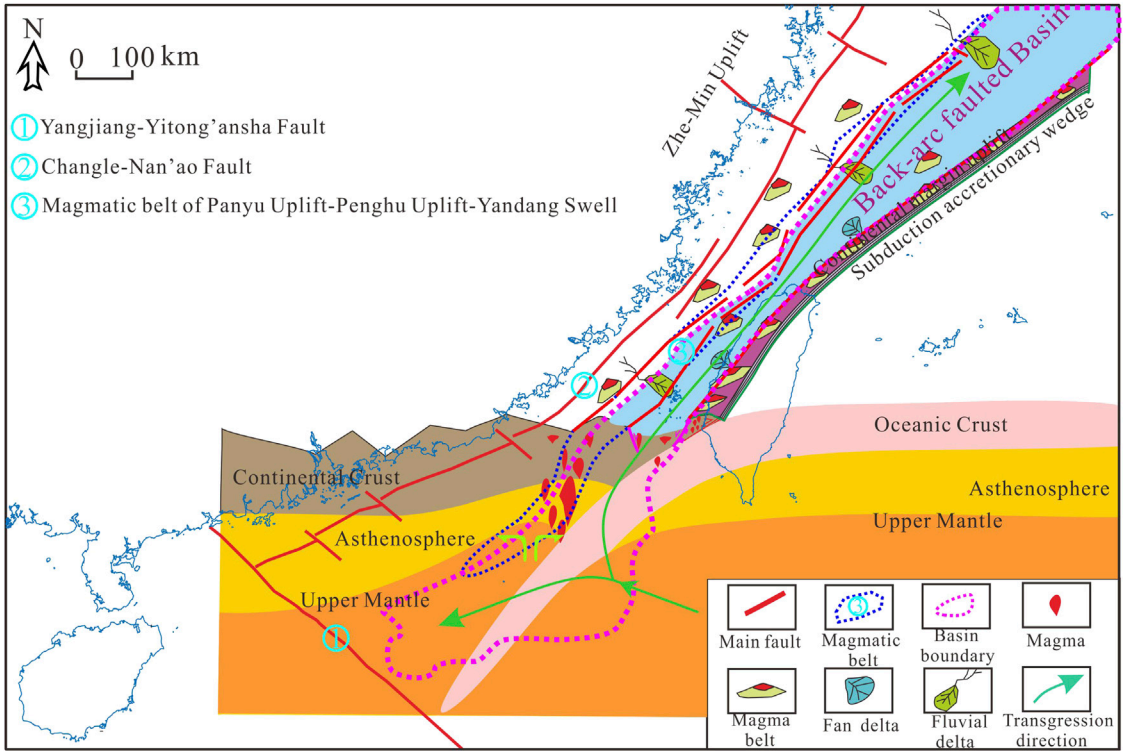

FIGURE 6
Plane view of the Late Jurassic–Early Cretaceous Basin (pink dotted line) and transgression direction (green arrow lines) in the NSCS-SECS, as well as the sedimentary system in the SECS. In the vertical section, we show the deep structural features, the magma activity, and the basin formation mechanism (modified from Zhou et al., 2005; Yi et al., 2012; Wu, 2014; Wang et al., 2022a; 2022b).

basin evolution stage, characterized by faults to the east and overlaps to the west. The center of early sedimentation was in the faulted Oujiang depression and the center of late sedimentation migrated eastward to the Keelung Sag, with characteristics of thick in the east and thin in the west. There were clastic rocks developed in paralic, neritic, and abyssal facies.

5.2.2 Neogene–Quaternary depression basin

There was little rifting development in the SECS from Neogene to the Quaternary, which was the evolutionary stage of thermal subsidence, followed by sedimentary deposition of fluvial, alluvial plain, and marine facies, with high strata thickness to the east and low to the west. Although this stage was relatively stable, there were still under tectonic events. In the Middle and Late Miocene, the Philippine Plate accelerated to assembly toward the Eurasian Plate and the regional stress field changed from the dextral slip transtension to sinistral slip transpression (Suo et al., 2015). The SECS underwent uplifting extrusion. The Oligocene–Lower Miocene strata are missing in the western depression of the basin due to denudation, marginal sea closure, and structural inversion (Zhou, 2002). This event corresponded to the Longjing Movement.

5.3 Hydrocarbon generation of the Jurassic source rocks

The SECS has experienced multiple stages of tectonic deformation since the Jurassic. The Lower–Middle Jurassic source rocks experienced multiple stages of uplift and burial, which corresponded to various stages of hydrocarbon generation. Well FZ10 was on the western edge of the NSCS-SECS Mesozoic Basin, and the buried depth of Lower–Middle Jurassic source rocks was relatively shallow. The R_o of the Lower–Middle Jurassic dark mudstones, in most samples, ranged between 0.65% and 0.78% and the source rocks were mature. From the single-well burial history and thermal evolution of FZ10 (Figure 8), the Lower–Middle Jurassic source rocks started generating hydrocarbons since the Late Paleocene and ceased in the Oligocene due to the tectonic uplift. The SECS subsided again

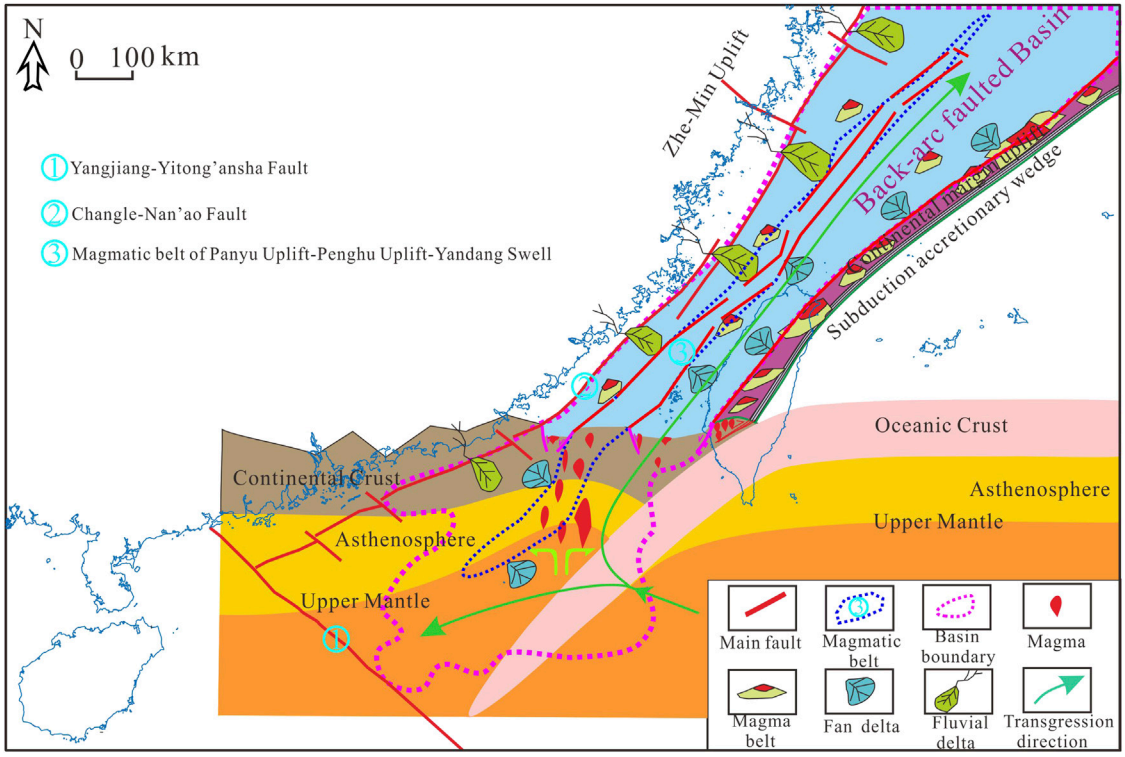

FIGURE 7
Plane view of the Late Cretaceous Basin (pink dotted line) and transgression direction (green arrow lines) in the NSCS-SECS, as well as the sedimentary system in the SECS. In the vertical section, we show the deep structural features, the magma activity, and the basin formation mechanism (modified from Zhou et al., 2005; Yi et al., 2012; Wu, 2014; Wang et al., 2022b).

in Neogene, reactivating the Lower–Middle Jurassic source rocks to another stage of hydrocarbon generation.

Thermal maturity analysis indicates that the Keelung Sag became the depocenter of the Lower–Middle Jurassic source rocks. Our results of seismic data interpretation were used for well simulation chosen to analyze the burial history of the Keelung Sag (Figure 9). The Lower–Middle Jurassic source rocks at the Keelung Sag reached maturity stage in the Late Jurassic and hydrocarbon generation was interrupted in the early Late Cretaceous due to the tectonic uplift. Hydrocarbon generation was reactivated after the heat flow reached the maximum temperature again and lasted until the Late Oligocene when another uplift stage occurred. The Keelung Sag is believed to have entered another thermal subsidence stage after Neogene. As the buried depth increased, the source rocks returned to generate hydrocarbons since then. The Lower–Middle Jurassic dark mudstones were deposited at the Keelung Sag and generated oil and gas that could migrate and accumulate in reservoirs along the western Taibei Turning zone and high topographic zones in other regions.

5.4 Jurassic oil–gas migration and accumulation model

Paralic and littoral facies sedimentation with good porosity sand bodies occurred in the SECS from the Upper Jurassic-Cretaceous and Paleogene systems. Oil and gas generated by Lower–Middle Jurassic source rocks can migrate through these sand bodies. Yushan Movement occurred in the end of the Middle Jurassic. The SECS entered the back-arc faulted basin development stage and formed some faults. The Yandang Movement in the Late Cretaceous was an extensional regime, during which abundant normal faults were developed, accompanied by extensive volcanism. The Huagang Movement occurred in the Late Paleogene and was a compressive shear tectonic movement, with weak tectonic deformation and no-fault development. This mainly induced regional uplift and denudation in the SECS, and the local tectonic was further shaped. The regional unconformities formed by the Yushan, Yandang, and Huagang movements were important pathways for oil–gas lateral migration. In addition, there were several

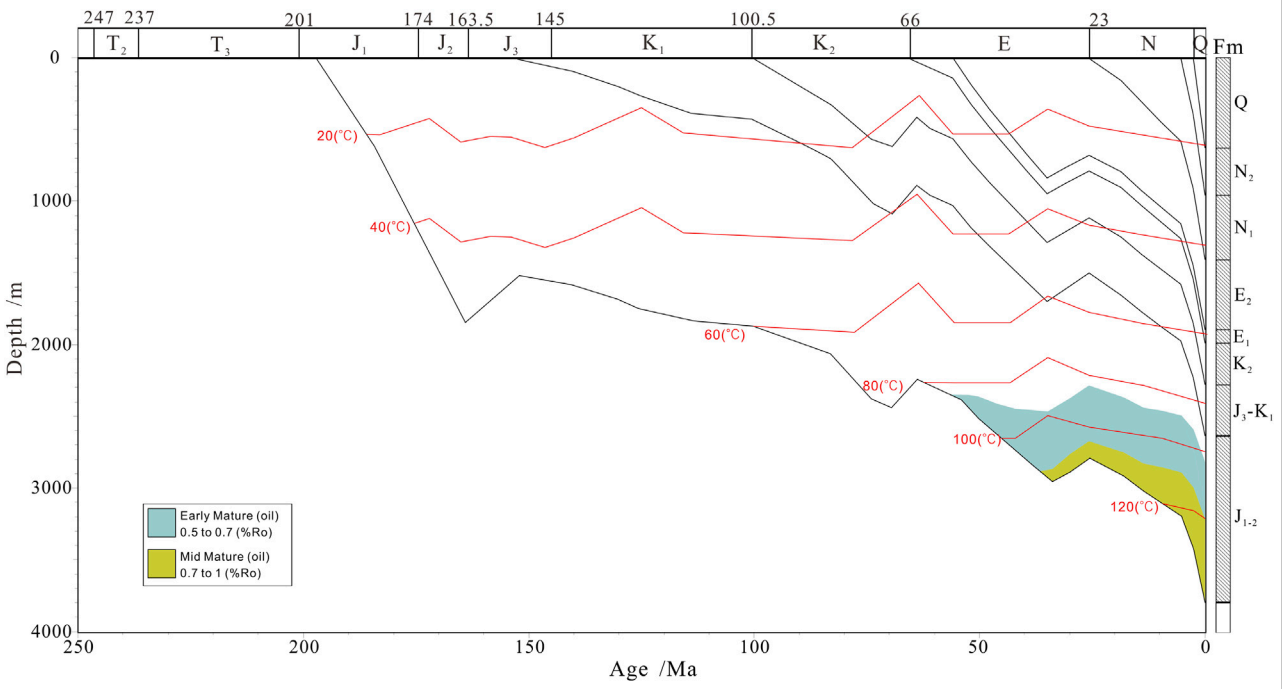

FIGURE 8
Burial history and thermal evolution of the Well FZ10 (location is shown in Figure 1). The fill colors represent different stages of maturity evolution. The J_{1-2} label represents the Early–Middle Jurassic; J_3-K_1 represents the Late Jurassic–Early Cretaceous; K_2 represents the Late Cretaceous; E_1 represents the Paleocene; E_2 represents the Eocene; N_1 represents the Miocene; N_2 represents the Pliocene; and Q represents the Quaternary.

local conformities in the region, which were also conducive to lateral oil and gas migration.

Figure 10 illustrates the combination of hydrocarbon generation, accumulation and seal rock, as well as oil–gas migration characteristics in the SECS. The oil–gas accumulation model of the Lower–Middle Jurassic source rocks is shown in Figure 11.

The process of generating hydrocarbons in different tectonic units differs significantly in the study area. This process becomes more complicated from the basin edges to the Keelung Sag, which was the depocenter of sedimentation. Well FZ10 was drilled on the edge of the large Mesozoic East China Sea Basin. The thermal evolution level of the Lower–Middle Jurassic source rocks was relatively low and only experienced two stages of hydrocarbon generation at the Middle Paleogene and Neogene–Present. The burial history diagram at the Keelung Sag suggests that the thermal evolution level of the Lower–Middle Jurassic source rocks was high and experienced three stages of hydrocarbon generation in the Early Cretaceous–mid Late Cretaceous, Middle Paleogene, and Neogene–Present. In addition, the Lower–Middle Jurassic source rocks at the Keelung Sag were the hydrocarbon generation center in the SECS associated with the high organic content, good kerogen types, and great thickness. The SECS entered the hydrocarbon generation stage during the first development stage of the back-arc faulted basin in the Early Cretaceous–mid Late Cretaceous vertical and lateral oil–gas migration generated by Lower–Middle Jurassic source rocks were relatively active, which formed mainly Mesozoic fault block, and lithologies forming oil–gas reservoirs (Figure 11). Faults with positive structures evolved during the second development stage of the back-arc faulted basin in the Middle Paleogene. Faults intersected the Lower–Middle Jurassic source rocks and affected the oil–gas reservoir formed in the early stage. Oil and gas generated from the Lower–Middle Jurassic source rocks can migrate into shallow traps and accumulate in reservoirs along faults, unconformities, and sand bodies, which formed mainly Mesozoic–Cenozoic reservoirs created by fault blocks and, combination of structural and stratigraphical compounds (traps) (Figure 11). The depression-forming basin stage occurred during the Neogene, which was characterized by integral uplift or subsidence. Tectonic activities were weak. The oil and gas generated by the Lower–Middle Jurassic source rocks lacked good migration pathways, which accumulated in the reservoirs of the surrounding traps (Figure 11).

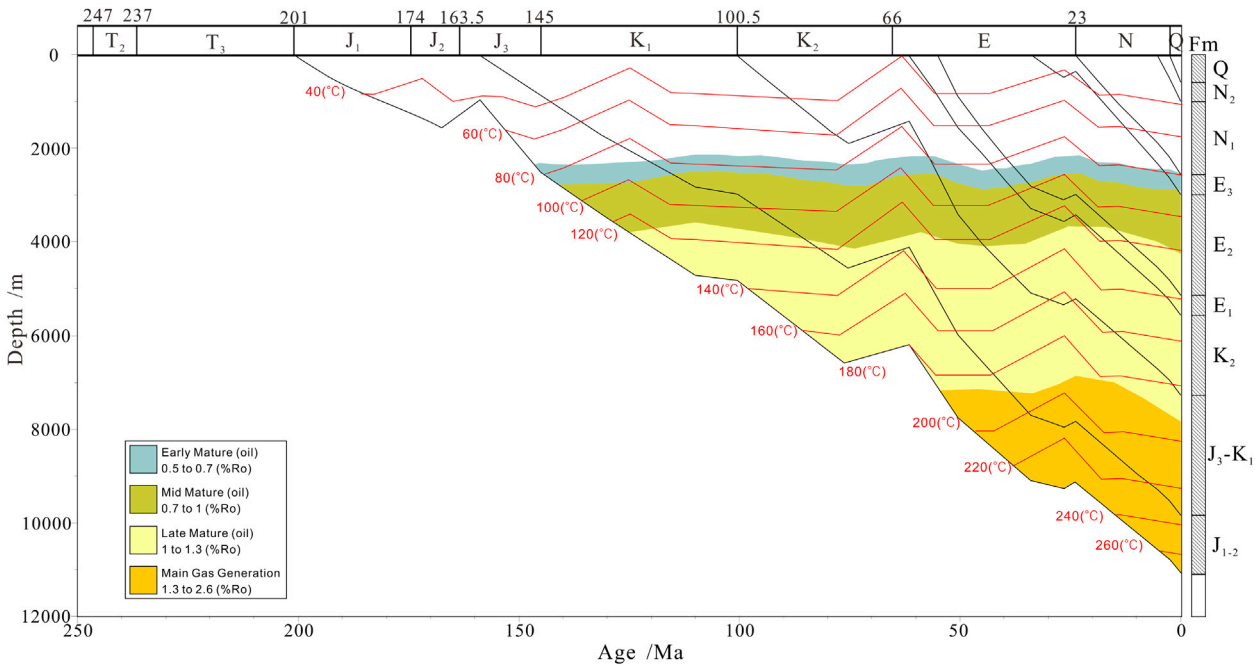

FIGURE 9
Burial history and thermal evolution at the Keelung sag (well location is shown in Figure 1). The fill colors represent different stages of maturity evolution. The $J_{1\text{-}2}$ label represents the Early–Middle Jurassic; J_3-K_1 represents the Late Jurassic–Early Cretaceous; K_2 represents the Late Cretaceous; E_1 represents the Paleocene; E_2 represents the Eocene; E_3 represents the Oligocene; N_1 represents the Miocene; N_2 represents the Pliocene; and Q represents the Quaternary.

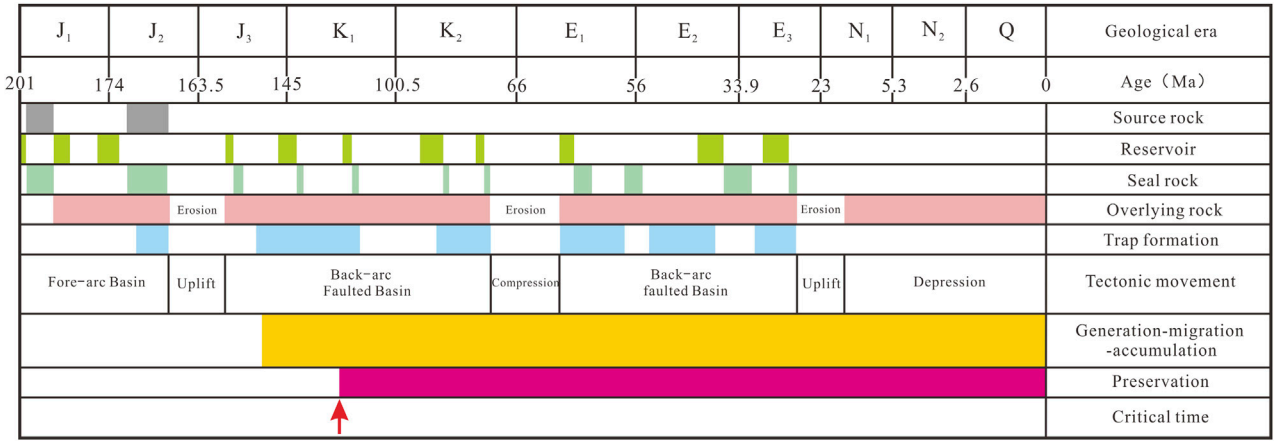

FIGURE 10
Petroleum system event chart summarizes the Jurassic oil-gas accumulation elements and processes at the Keelung Sag. The J_1 label represents the Early Jurassic; J_2 represents the Middle Jurassic; J_3 represents the Late Jurassic K_1 represents the Early Cretaceous; K_2 represents the Late Cretaceous; E_1 represents the Paleocene; E_2 represents the Eocene; E_3 represents the Oligocene; N_1 represents the Miocene; N_2 represents the Pliocene; and Q represents the Quaternary.

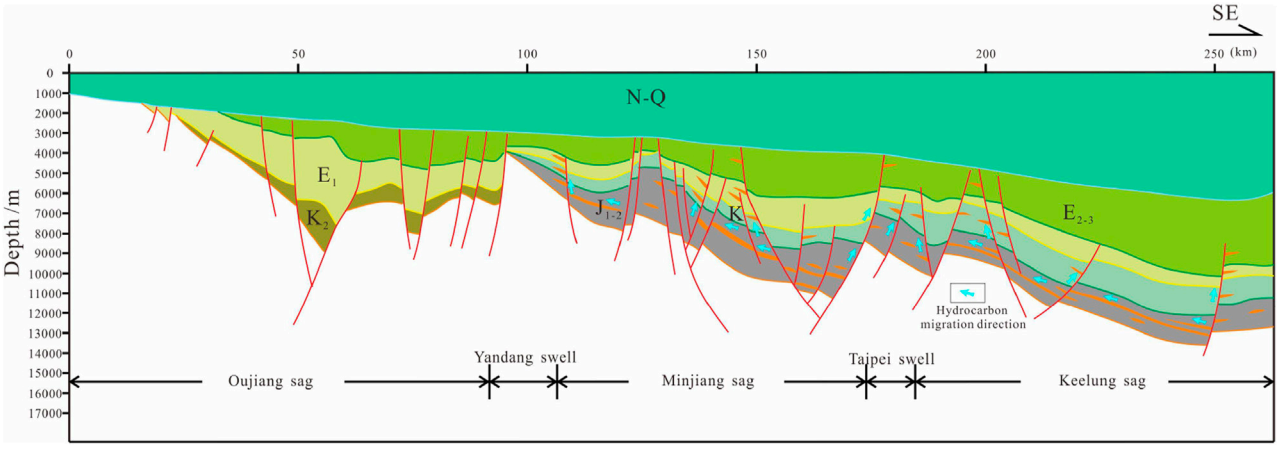

FIGURE 11
Favorable Jurassic oil-gas accumulation models in the SECS (location of the Section C is shown in Figure 1). The fill colors represent different strata. The J_{1-2} label represents the Early–Middle Jurassic; J_3-K represents the Late Jurassic–Cretaceous; K_2 represents the Late Cretaceous; E_1 represents the Paleocene; E_{2-3} represents the Eocene–Oligocene; and N-Q represents the Neogene–Quaternary.

6 Conclusion

(1) The NSCS-SECS was generally a large sedimentary basin during the Jurassic–Cretaceous period, which experienced two evolutionary stages from the Early–Middle Jurassic (J_{1-2}) fore-arc depression basin, to the Late Jurassic–Cretaceous (J_3-K) back-arc faulted basin. The NSCS-SECS entered the differential evolution process since the Cenozoic.

(2) The Keelung Sag in the SECS experienced three stages of hydrocarbon generation controlled by tectonic evolution in the Early Cretaceous–mid Late Cretaceous, Middle Paleogene, and Neogene–Present. However, other regions experienced only two stages of hydrocarbon generation. The Lower–Middle Jurassic source rocks at the Keelung Sag have a great thickness, high organic content, good kerogen type, and high thermal evolution level. It was the hydrocarbon generation center in the SECS.

(3) Oil and gas generated by the Lower–Middle Jurassic source rocks at the Keelung Sag migrated and accumulated in the western high tectonic traps along favorable sand bodies, unconformities, fractures, and pathways. It was the faulted basin including two rifting stages, in the Early Cretaceous–middle Late Cretaceous and Middle Paleogene. Active fault migration occurred, mainly forming Mesozoic–Cenozoic fault blocks and tectonic–lithological oil–gas reservoir. The study area remains in the depression basin development stage since the Neogene. The tectonic activities were weak and the oil and gas generated by the source rocks accumulated mainly in the surrounding traps.

Data availability statement

The original contributions presented in the study are included in the article/Supplementary Material; further inquiries can be directed to the corresponding authors.

Author contributions

MW: substantial contributions to the conception and design of the work and writing of the original draft. XJ: evaluation of source rocks; establishment of the burial model; and review and editing. BL: interpretation of the seismic section; writing—review and editing; and supervision. LH: substantial contributions to the conception and design of the work and writing—review and editing. JP: tectonic evolution analysis. All persons who have made substantial contributions to the work reported in the manuscript, including those who provided editing and writing assistance but who are not authors, are named in the Acknowledgments section of the manuscript.

Funding

This study was financially supported by the geological survey program of China Geological Survey (DD20221710, DD20160137, and DD20190208), earthquake science and technology spark program of the China Earthquake Administration (XH22014A), and the National Natural Science Foundation of China (41606079).

Acknowledgments

The authors would like to thank the reviewers who gave many constructive suggestions on the manuscript. They would like to express their gratitude to EditSprings (https://www.editsprings.cn) for the expert linguistic services provided.

Conflict of interest

The authors declare that the research was conducted in the absence of any commercial or financial relationships that could be construed as a potential conflict of interest.

The reviewer LH declared a shared affiliation with the author MW to the handling editor at the time of review.

Publisher's note

All claims expressed in this article are solely those of the authors and do not necessarily represent those of their affiliated organizations, or those of the publisher, the editors, and the reviewers. Any product that may be evaluated in this article, or claim that may be made by its manufacturer, is not guaranteed or endorsed by the publisher.

References

Asis, J., and Jasin, B. (2012). Aptian to turonian radiolaria from the darvel bay ophiolite complex, kunak, sabah, kunak, sabah. *Bull. Geol. Soc. Malays.* 58, 89–96. doi:10.7186/bgsm58201213

Chen, C. H., Lee, C. Y., Lu, H. Y., and Hsieh, P. S. (2008). Generation of late cretaceous silicic rocks in SE China: Age, major element and numerical simulation constraints. *J. Asian Earth Sci.* 31 (4-6), 479–498. doi:10.1016/j.jseaes.2007.08.002

Chen, L., Guo, F., Steel, R. J., and Li, Y. (2016). Petrography and geochemistry of the late cretaceous redbeds in the Gan-hang belt, southeast China: Implications for provenance, source weathering, and tectonic setting. *Int. Geol. Rev.* 58 (10), 1196–1214. doi:10.1080/00206814.2016.1141378

Dimalanta, C. B., and Yumul, G. P. (2006). Magmatic and amagmatic contributions to crustal growth in the Philippine island arc system: Comparison of the Cretaceous and post-Cretaceous periods. *Geosci. J.* 10 (3), 321–329. doi:10.1007/BF02910373

Fan, C., Xie, H., Li, H., Zhao, S., Shi, X., Liu, J., et al. (2022). Complicated fault characterization and its influence on shale gas preservation in the southern margin of the sichuan basin, China, *Lithosphere*, 2022. 8035106. doi:10.2113/2022/8035106

Hong, W. T. (2012). *Research on the cretaceous bimodal volcanic rocks at yunshan Caldera,Yongtai county, fujian province*. Nanjing: Nanjing University.

Li, S., Wang, Y., and Wu, S. (2018). Meso-cenozoic tectonothermal pattern of the Pearl River Mouth basin: Constraints from zircon and apatite fission track data. *Earth Sci. Front. Univ. Geosciences(Beijing); Peking Univ.* 25 (1), 95–107. doi:10.13745/j.esf.yx.2017-5-20

Li, G., Gong, J., Yang, C., Yang, C., Wang, W., Wang, H., et al. (2012). Stratigraphic features of the Mesozoic "Great east China sea"-A new exploration field. *Mar. Geol. Quat. Geol.* 32 (3), 97–104. doi:10.3724/SP.J.1140.2012.03097

Li, H., Zhou, J., Mou, X., Guo, H., Wang, X., An, H., et al. (2022). Pore structure and fractal characteristics of the marine shale of the longmaxi formation in the changning area, southern sichuan basin, China. *Front. Earth Sci.* 10, 1018274. doi:10.3389/feart.2022.1018274

Li, H., Tang, H., Qin, Q., Zhou, J., Qin, Z., Fan, C., et al. (2019). Characteristics, formation periods and genetic mechanisms of tectonic fractures in the tight gas sandstones reservoir: A case study of xujiahe formation in YB area, sichuan basin, China. *J. Pet. Sci. Eng.* 178, 723–735. doi:10.1016/j.petrol.2019.04.007

Li, J., Li, H., Yang, C., Wu, Y., Gao, Z., and Jiang, S. (2022). Geological characteristics and controlling factors of deep shale gas enrichment of the Wufeng-Longmaxi Formation in the southern Sichuan Basin, China. *Lithosphere* 2022, 4737801. doi:10.2113/2022/4737801

Li, J., Qi, B., Xu, H., Liu, X., and Yang, T. (2014). Cenozoic tectonic evolution of Wuqiuyu depression, Taixi basin. *Mar. Geol. Front.* 30 (9), 36–42. doi:10.16028/j.1009-2722.2014.09.016

Li, P., Liang, H., and Dai, Y. (1998). Exploration perspective of basement hydrocarbon accumulations in the Pearl River Mouth basin. *China Offshore Oil Gas* 12 (6), 361–369.

Li, S., Zang, Y., Wang, P., Suo, Y., Li, X., Liu, X., et al. (2017). Mesozoic tectonic transition in South China and initiation of Palaeo-Pacific subdcution. *Earth Sci. Front. Univ. Geosciences(Beijing); Peking Univ.* 24 (4), 213–225. doi:10.13745/j.esf.yx.2017-4-13

Li, W. (2001). Oil and gas prospects for the multicycle composite basin in the east China sea shelf. *Petroleum Geol. Exp.* 23 (2), 141–145. doi:10.11781/sysydz200102141

Li, S., Suo, Y., Li, X., Wang, Y., Cao, X., Wang, P., et al. (2018). Mesozoic plate subduction in West Pacific and tectono-magmatic response in the East Asian ocean-continent connection zone. *Chin. Sci. Bull.* 63 (16), 1550–1593. doi:10.1360/n972017-01113

Li, Z. X., and Li, X. H. (2007). formation of the 1300-km-wide intracontinental orogen and post orogenic magmatic province in mesozoic south China: A flat-slab subduction model. *Geol.* 35 (2), 179–182. doi:10.1130/G23193A.1

Liu, J., Xu, H., Jiang, Y., Wang, J., and He, X. (2020). Mesozoic and Cenozoic basin structure and tectonic evolution in the East China Sea basin. *ACTA Geol. SIN.* 94 (3), 675–691. doi:10.19762/j.cnki.dizhixuebao.2020115

Liu, Y., Wu, Z., Chen, Y., Wu, K., He, M., Zhang, J., et al. (2019). Spatial and temporal difference of Paleogene rift structure and its controlling factors in the northern South China sea: A case study of Pearl River Mouth basin. *J. China Univ. Min. Technol.* 48 (2), 367–376. doi:10.13247/j.cnki.jcumt.000933

Liu, Z., Wang, Y., Deng, A., and Gao, H. (2006). Petroleum geological characteristics and petroleum system of Taiwan strait basin. *Petroleum Geol. Exp.* 28 (6), 523–528. doi:10.3969/j.issn.1001-6112.2006.06.004

Lu, B., Sun, X., Zhang, G., Zhang, B., Lang, Y., and Wang, P. (2011). Seismic-potential field response characteristics and identification of basement lithology of the northern South China Sea basin. *Chin. J. Geophys.* 54 (2), 563–572. doi:10.3969/j.issn.0001-5733.2011.02.036

Lu, B. L., Wang, P. J., Zhang, G. C., and Wang, W. Y. (2015). Characteristic of regional fractures in South China Sea and its basement tectonic framework. *Prog. Geophys.* 30 (4), 1544–1553. doi:10.6038/pg20150408

Maruyama, S., Isozaki, Y., Kimura, G., and Terabayashi, M. (1997). Paleogeographic maps of the Japanese Islands: Plate tectonic synthesis from 750 Ma to the presentPaleogeographic maps of the Japanese Islands: Plate tectonic synthesis from 750 Ma to the present. *Isl. Arc* 6 (1), 121–142. doi:10.1111/j.1440-1738.1997.tb00043.x

Qiu, Y., and Wen, N. (2004). Mesozoic of the South in the area of the China eastern sea Sea and its significance northern margin for oil/gas exploration. *Geol. Bull. China* 23 (2), 142–146. doi:10.3969/j.issn.1671-2552.2004.02.007

Si, Q., Xu, C., and Gao, S. (2021). Late Mesozoic magmatic arc of East China Sea developed with plate subduction:constraints from detrital zircons in well FZ211. *Acta Geol. Sin.* 95 (6), 1743–1753. doi:10.19762/j.cnki.dizhixuebao.2020093

Sun, J., Yang, C., Wang, J., and Han, B. (2017). Tectonic evolution of the Jilong Sag and its petroleum potential. *Mar. Geol. Front.* 33 (4), 38–42. doi:10.16028/j.1009-2722.2017.04006

Sun, X., Zhang, X., Zhang, G., Lu, B., Yue, J., and Zhang, B. (2014). Texture and tectonic attribute of Cenozoic basin basement in the northern South China Sea. *Sci. China Earth Sci.* 57, 1199–1211. doi:10.1007/s11430-014-4835-2

Suo, Y. H., Li, S. Z., Zhao, S. J., Somerville, I. D., Yu, S., Dai, L. M., et al. (2015). Continental margin basins in east asia: Tectonic implications of the meso-cenozoic east China sea pull-apart basins. *Geol. J.* 50 (2), 139–156. doi:10.1002/gj.2535

Wang, M., Pan, J., Gao, H., Huang, L., and Li, X. (2022a). Mesozoic basin evolution and hydrocarbon potential in north South China Sea and south East

China Sea. *Earth Sci. Front. Univ. Geosciences(Beijing); Peking Univ.* 29 (2), 1–9. doi:10.13745/j.esf.sf.2021.7.8

Wang, M. J., Xiao, G. L., Yang, C. Q., Yang, C. Q., Chen, X., and Huang, L. (2019). Characteristics and evaluation of Mesozoic source rocks in the southeastern East China Sea continental shelf. *China Geol.* 1 (2), 133–141. doi:10.31035/cg2018079

Wang, M., Xu, Y., Huang, L., Pan, J., and Li, X. (2022b). *Strata in east China sea and adjacent areas*. Beijing, China: Geological Publishing House.

Wang, M., Zhang, Y., Pan, J., Huang, L., Chen, X., Luo, D., et al. (2020). Geological structure of the large section in eastern China's sea areas and its constraint on comprehensive stratigraphic division. *Geol. China* 47 (5), 1474–1485. doi:10.12029/gc20200513

Wu, S. (2014). *Depositional process for the mesozoic epicontinental marine basin in northern South China sea*. Chengdu: Chengdu University of Technology.

Xia, L., Lin, C., Li, X., and Hu, Y. (2018). Characteristics of fault structures in Pearl River Mouth basin and control effect of them on sedimentary basin. *J. Xi'an Shiyou Univ. Nat. Sci. Ed.* 33 (5), 1–18. doi:10.3969/j.issn.1673-064X.2018.05.001

Xiao, G., Wang, M., Yang, C., and Pang, Y. (2019). Numerical simulation of Mesozoic hydrocarbon generation, migration and accumulation in the southern East China Sea. *Mar. Geol. Quat. Geol.* 39 (6), 138–149. doi:10.16562/j.cnki.0256-1492.2019070304

Xu, C., Shi, H., Barnes, C. G., and Zhou, Z. (2016). Tracing a late Mesozoic magmatic arc along the Southeast Asian margin from the granitoids drilled from the northern South China Sea. *Int. Geol. Rev.* 58 (1), 71–94. doi:10.1080/00206814.2015.1056256

Xu, C., Zhang, L., Shi, H., Brix, M. R., Huhma, H., Chen, L., et al. (2017). Tracing an early jurassic magmatic arc from south to east China seas. *Tectonics* 36, 466–492. doi:10.1002/2016TC004446

Yang, C., Han, B., Yang, Y., Yang, C., Sun, J., Yan, Z., et al. (2017). Oil and gas exploration in the mesozoic of east China Sea shelf basin: Progress and challenges. *Mar. Geol. Front.* 33 (4), 1–8. doi:10.16028/j.1009-2722.2017.04001

Yang, C., Li, G., Gong, J., and Yang, C. (2015). Petroleum geological conditions and exploration prospect of the mesozoic in southeast China sea area. *J. Jilin Univ. Earth Sci. Ed.* 15 (1), 1–12. doi:10.13278/j.cnki.jjuese.201501101

Yang, C., Yang, C., Li, G., Liao, J., and Gong, J. (2012). Mesozoic tectonic evolution and prototype basin characteristics in the southern East China Sea Shelf Basin. *Mar. Geol. Quarternary Geol.* 32 (3), 105–111. doi:10.3724/SP.J.1140.2012.03105

Yang, C., Yang, Y., Yang, C., Sun, J., Wang, J., Xiao, G., et al. (2019). Tectono-sedimentary evolution of the mesozoic in the southern East China Sea shelf basin and its bearing on petroleum exploration. *Mar. Geol. Quat. Geol.* 39 (6), 30–40. doi:10.16562/j.cnki.0256-1492.2019070305

Ye, Q. (2019). *The late mesozoic structure systems in the northern South China sea margin: Geodynamics and their influence on the cenozoic structures in the Pearl River Mouth basin*. Wuhan: China uviversity of Geosciences.

Yi, H., Zhang, L., and Lin, Z. (2012). Mesozoic tectonic framework and basin distribution characteristics of northern margin of South China Sea. *Petroleum Geol. Exp.* 34 (4), 388–394. doi:10.3969/j.issn.1001-6112.2012.04.008

Yuan, W., Yang, Z., Zhao, X., Santosh, M., and Zhou, X. (2018). Early jurassic granitoids from deep drill holes in the east China Sea basin: Implications for the initiation of palaeo-pacific tectono-magmatic cycle. *Int. Geol. Rev.* 60 (7), 813–824. doi:10.1080/00206814.2017.1351312

Zhang, C., Xu, C., He, M., and Gao, S. (2019). Late mesozoic convergent continental margin with magmatic arc from east to south China seas: A review. *Adv. Earth Sci.* 34 (9), 950–961. doi:10.11867/j.issn.1001-8166.2019.09.0950

Zhang, H., Zhang, X., and Wen, Z. (2010). *Magnetic anomaly map of geological and geophysical map series of Eastern China and adjacent regions(1:100 0000)*. Beijing: China ocean press.

Zheng, Q., Zhou, Z., Cai, L., Lu, Y., and Cao, Q. (2005). Meso-cenozoic tectonic setting and evolution of east China Sea shelf basin. *Oil &Gas Geol.* 26 (2), 197–201. doi:10.11743/ogg20050210

Zhong, K., Zhu, W., Gao, S., and Fu, X. (2018). Key geological questions of the formation and evolution and hydrocarbon accumulation of the east China Sea shelf basin. *Earth Sci.* 43 (10), 3485–3497. doi:10.3799/dqkx.2018.282

Zhou, D., Chen, H., Sun, Z., and Xu, H. (2005). Three mesozoic sea basins in eastern and southern south China Sea and their relation to tethys and paleo-pacific domains. *J. Trop. Oceanogr.* 24 (2), 16–25. doi:10.3969/j.issn.1009-5470.2005.02.003

Zhou, D. (2002). Mesozoic strata and sedimentary environment in SW Taiwan basin of NE South China Sea and peikang high of Western Taiwan. *J. Trop. Oceanogr.* 21 (2), 50–57. doi:10.3969/j.issn.1009-5470.2002.02.006

Zhou, D., Wang, W., Wang, J., Pang, X., Cai, D., and Sun, Z. (2006). Mesozoic subduction-accretion zone in northeastern south China sea inferred from geophysical interpretations. *Sci. China (Series D)* 36 (3), 471–482. doi:10.1007/s11430-006-0471-9

frontiers | Frontiers in Earth Science

TYPE Original Research
PUBLISHED 09 January 2023
DOI 10.3389/feart.2022.1033344

OPEN ACCESS

EDITED BY
Wenlong Ding,
China University of Geosciences, China

REVIEWED BY
Zhonggui Hu,
Sedimentology, Sequence stratigraphy, Geochemical, China
Fengcun Xing,
Chengdu University of Technology, China

*CORRESPONDENCE
Hao Kuang,
kwanghow@foxmail.com

SPECIALTY SECTION
This article was submitted to Structural Geology and Tectonics, a section of the journal Frontiers in Earth Science

RECEIVED 31 August 2022
ACCEPTED 26 September 2022
PUBLISHED 09 January 2023

CITATION
Kuang H, Liu H, Tan X, Yu J, Song H, Zhou R, Wang J and Liu F (2023), Study on factors affecting the petro physical properties of sandstone and conglomerate reservoirs of Baikouquan Formation, Junggar Basin. *Front. Earth Sci.* 10:1033344. doi: 10.3389/feart.2022.1033344

Study on factors affecting the petro physical properties of sandstone and conglomerate reservoirs of Baikouquan Formation, Junggar Basin

Hao Kuang[1,2]*, Hao Liu[1,2], Xianfeng Tan[1,2], Jingwei Yu[3], Haiqiang Song[4], Runchi Zhou[1,2], Junmin Wang[1,2] and Fei Liu[5]

[1]School of Petroleum and Natural Gas Engineering, Chongqing University of Science and Technology, Chongqing, China, [2]Chongqing Key Laboratory of Complex Oil and Gas Exploration and Development, Chongqing, China, [3]Petroleum Institute, China University of Petroleum (Beijing) at Karamay, Xinjiang, China, [4]Shaanxi Yanchang Petroleum International Exploration and Development Engineering Co., Ltd., Shaanxi, China, [5]Chongqing Gas Field, PetroChina Southwest Oil and Gas Field Company, Chongqing, China

In recent years, oil and gas exploration of the Baikouquan Formation in the northwestern margin of the Junggar Basin has seen major breakthroughs have been made in oil and gas exploration. Sandstone and conglomerate reservoirs are developed in the Baikouquan Formation in this area, but the factors affecting the differences in petro physical properties of these two types of reservoirs are still unclear. In this paper, taking the Baikouquan Formation in the Hongcheguai area on the northwestern margin of the Junggar Basin as an example, a large number of core observations, thin sections, scanning electron microscopy, and petro physical property test data were used to evaluate the petro logical characteristics, reservoir space types, digenesis and pore evolution of the sandstone and conglomerate reservoirs. The results show that the sandstone and conglomerate rocks of the Baikouquan Formation in the study area have a large content of tuffaceous components. The sandstone reservoirs are dominated by primary intergranular pores, and the conglomerate reservoirs are dominated by secondary dissolved pores. In addition, the porosity is negatively correlated with rock permeability for the conglomerate rocks of the Baikouquan Formation. However, the porosity is positively correlated with rock permeability of the sandstone reservoirs. According to the analysis of the digenetic process, the compaction and cementation can lead to a significant decrease in the petro physical properties of the reservoir. While dissolution can improve the petro physical properties of the sandstone reservoirs to a small extent, and can improve that of the conglomerate reservoirs to a greater extent. Moreover, local fractures are important factors affecting the petro physical properties of the conglomerate reservoirs. The existence of abnormal high pressure has a certain effect on the preservation of primary pores. On the whole, the controlling factors of the petro physical properties of the conglomerate reservoirs in the Baikouquan Formation include sedimentation, diagenesis, and tectonic actives, while that of the sandstone reservoirs mainly include sedimentation and diagenesis.

KEYWORDS

conglomerate, sandstone, reservoir, petro physical properties, controlling factors, Baikouquan formation

1 Introduction

At present, the complex lithologic reservoir is the key object of oil and gas exploration for the continental sedimentary systems in China. Conventional single genetic control methods are difficult to accurately elucidate the oil and gas enrichment laws in complex lithologic reservoirs. The petro physical properties of tight reservoirs are the comprehensive products of sedimentation, diagenesis and tectonic activities. Therefore, only by determining the influencing factors of physical properties can the accuracy of oil and gas exploration be improved (Gao et al., 2021; Liu et al., 2021). The Junggar Basin is a large-scale oil and gas-producing superimposed basin in China. The geological conditions of the northwestern margin of the Junggar Basin are complex, and the oil reservoirs with multiple lithologies are widely distributed in the Triassic (Yu et al., 2018; Meng et al., 2019). At present, the research on the Triassic reservoirs in this area is mainly concentrated in the Karamay and Baiqiantan Formations, but there is limited research on the Lower Triassic Baikouquan Formation. A systematic research on the reservoir petrology, petro physical properties, pore types and diagenesis can provide scientific guidance for efficient oil exploration and development (Lei et al., 2015; Zhang et al., 2018; Qu et al., 2019).

In recent years, with the fine oil and gas exploration of the Baikouquan Formation in the northwestern margin of the Junggar Basin, major breakthroughs have been made in oil and gas exploration. It also confirmed the possibility of large-scale lithologic reservoirs in the Baikouquan Formation. Well S1 revealed that the lithologies of oil layers include conglomerate rocks and sandstones. These two types of reservoirs are widely concerned by researchers due to their strong heterogeneity caused by diverse sedimentary environments and multiple diagenesis. The previous research mainly focused on sandstone, and the research on the reservoir properties of conglomerate rocks is still very limited (Yu et al., 2015; Qu et al., 2019). Due to the complex lithology and less analysis of controlling factors for high-quality reservoirs, the success rate of exploration wells hinders further exploration of oil and gas in this area.

In this paper, taking the Baikouquan Formation in the Hongcheguai area on the northwestern margin of the Junggar Basin as an example, core observations, thin sections, scanning electron microscopy, and petro physical property test data were used to evaluate the petro logical characteristics, reservoir space types, diagenesis and pore evolution of sandstone and conglomerate reservoirs. This research can provide new ideas for the exploration of complex lithological reservoirs in similar areas.

2 Materials and methods

2.1 Geological background

The Hongcheguai area is located on the northwestern edge of the Junggar Basin (Figure 1A) and is an important oil-producing area in the Xinjiang Oilfield. The target layer is the Triassic Baikouquan Formation. The Triassic stratum in the basin is a west-dipping monocline (Figure 1B). During the deposition of the Baikouquan Formation, the depositional environment of the northwestern margin of the Junggar Basin was affected by syngenetic faults and humid climate. The provenance of the Baikouquan Formation are from the northwest areas. With a small amount of volcanic activity, a large set of sandstone and conglomerate deposits of the Baikouquan Formation were formed. The Baikouquan Formation is in unconformity contact with the underlying Permian, and its thickness ranges from 200 m to 400 m.

2.2 Experiments

The experiments used in this study include mercury intrusion, thin section, scanning electron microscopy, X-ray diffraction and petro physical property tests. The core diameter of the mercury injection experiment is 2.5 cm and the length is 2.0 cm. Meanwhile, the mercury porosimeter PM33GT-17 produced by Quantachrome in the United States was used. The high-pressure power system is composed of high-pressure metering pumps, the working pressure range is 0.002–50 MPa, the pressure balance time is ≥60 s, and the number of measurable pressure points reaches 100. The experiment was completed in the Xinjiang Oilfield Experimental Inspection Institute.

The sample size of the ordinary and cast thin sections is 25 mm × 5 mm. The sample was washed with oil, and the pressure of the cast rubber was 6 MPa. The experiment was completed in the Xinjiang Oilfield Experimental Inspection and Research Institute, and a total of 60 thin sections were produced.

The sample size of the scanning electron microscope is 10–15 mm in diameter and 5 mm in length. The intensity of the electron beam is 10.9 mA and the high voltage is 5 kV. According to the "Analysis Method of Rock Samples by Scanning Electron Microscope" SY/T5162-1997, 20 samples were scanned with a scanning electron microscope JSM-5500LV. The experiment was conducted at the Xinjiang Oilfield Experimental Inspection Institute.

X-ray diffraction requires grinding sandstone samples to powder. The X-ray spectrometer QUANTAX400 was used to carry out the X-ray experiments. The instrument voltage is 40 kV and the current is 250 mA. According to "Quantitative Analysis

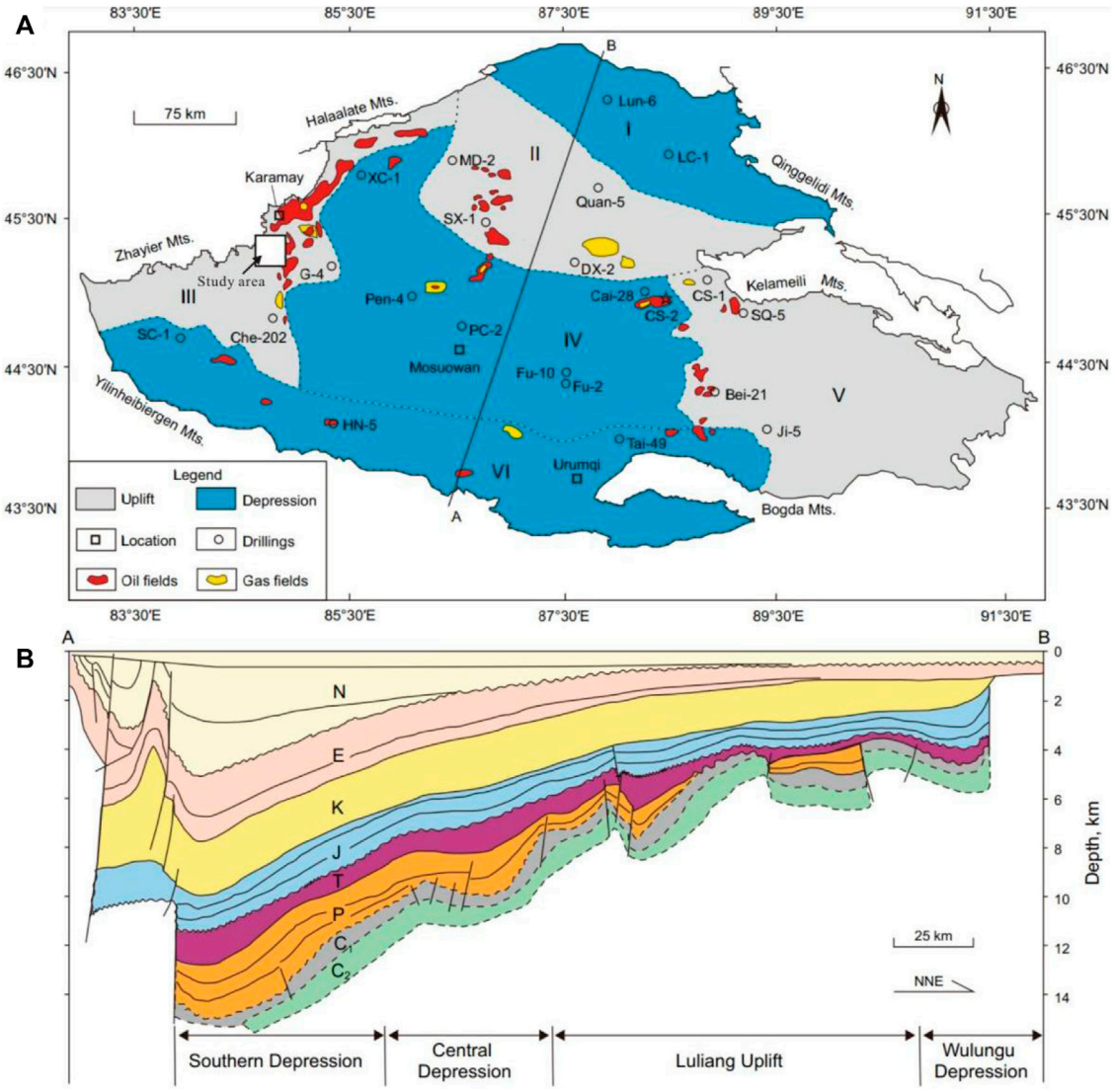

FIGURE 1
Location and strata distribution in the study area (Hu et al., 2020, modified) I. Wulungu Depression; II. Luliang Uplift; III. Western Uplift; IV. Central Depression; V. Eastern Uplift; VI. Southern Depression; Mts. Mountains. **(A)** The Location of Junggar Basin and study area **(B)** The stratigraphic section of **(A,B)**, Which had been shown in **(A)**.

Method for Energy Spectrum of Rocks and Minerals" SY/T6189-1996, the test temperature is 20°C and the humidity is 50%. The X-diffraction experiment was completed in the Xinjiang Oilfield Experimental Inspection Institute.

3 Results

3.1 Lithology and sedimentary structure

Through a large number of core observations, the sandstone, conglomerate rocks, mudstone, argillaceous siltstone and silty mudstone are developed in the Triassic Baikouquan Formation in the study area. In addition, the horizontal beddings, bottom channel scouring, and massive beddings can be seen frequently in the Baikouquan Formation.

The washed channel surface (Figure 2A) is extremely developed in the target layer of the study area. At its bottom, there are directional arrangement of mud gravel components. The particle size of the mud gravel components can be up to 10 cm. They are generally formed by the scouring of the unconsolidated mudstones at the bottom of the river channels.

Parallel bedding (Figure 2B) is mainly developed in sandstones or granular limestones. Under strong hydrodynamic conditions, the

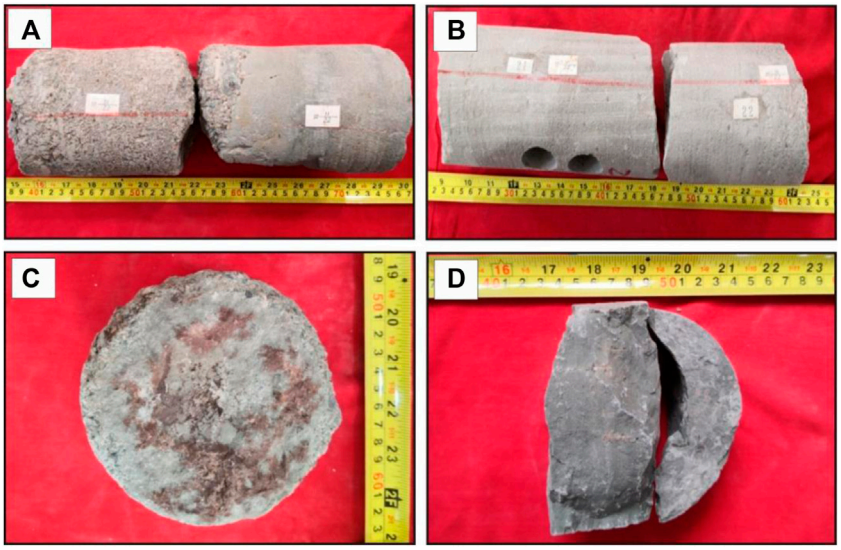

FIGURE 2
Development characteristics of different types of sandstones in Baikouquan Formation.**(A)** Well G6, 3024.4 m, flushed river channel surface; **(B)** Well G6, 3024.6 m, parallel bedding; **(C)** Well G103, 3307.82 m, maroon mudstone; **(D)** Well G6, 3025.2 m, horizontal bedding.

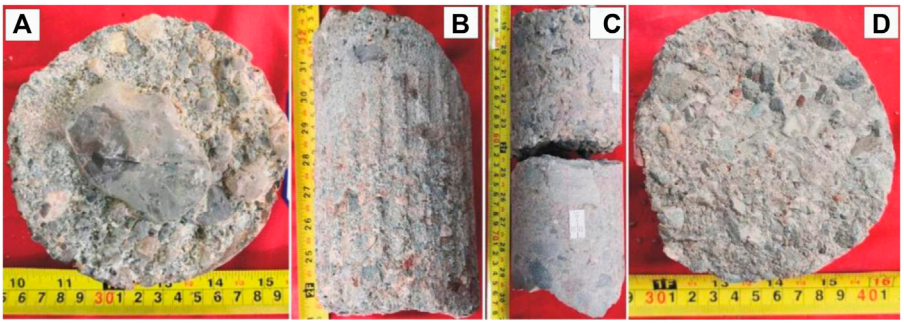

FIGURE 3
Types of conglomerate rocks in the Baikouquan Formation in the study area. **(A)** Well G10, Quan 2 Member, 3595.75 m, medium-grained conglomerate; **(B)** Well G103, Quan 2 Member, 3303.3 m, unequal-grained sandy conglomerate; **(C)** Well S1, Quan 2 Member, 4635.8 m, sand -containing medium grained conglomerate; **(D)** Well G6, Quan 3 Member, 3026.2 m, small-grained conglomerate.

sand migrates from a flat bed in a high flow state, and the continuous rolling sand on the bed produces a horizontal fine layer separated by thickness and fineness. Parallel-beddings are generally formed in rapids and high-energy environments, such as river channels and lakeshore environments (Feng., 1993; Li., 2001; Wang., 2016).

Maroon-red mudstones (Figure 2C) are less developed in the target layer in the study area, reflecting that the target layer was in a semi-oxidative-semi-reduced depositional environment during this period.

Horizontal beddings (Figure 2D) are mainly developed in fine clastic rocks. It is formed by suspended sedimentation under relatively weak hydrodynamic conditions.

Massive beddings can be seen in the coring segments of the Baikouquan Formation, and are mainly existed in siltstones, argillaceous siltstones and silty mudstones. Its internal materials are relatively uniform.

The conglomerate rocks in the Baikouquan Formation in the study area are mainly exhibit small and medium grain size, and different types of conglomerates develop in different members of the Baikouquan Formation. Among them, medium-grained conglomerate rocks are more common in the Quan 2 Member, and small-grained conglomerate is relatively developed in the Quan 3 Member (Figure 3). The main features of the conglomerate rocks in the Baikouquan

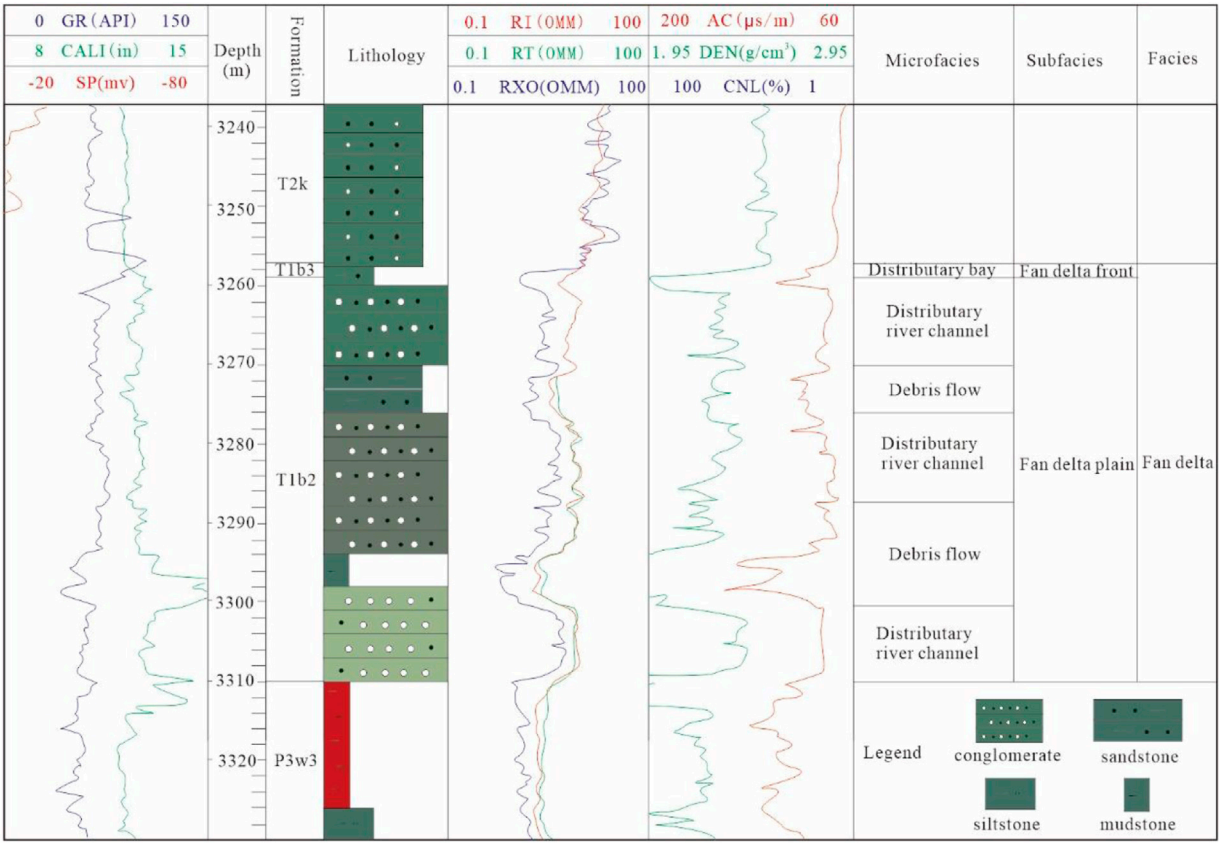

FIGURE 4
Logging response of fan delta plain micro facies in the Baikouquan Formation (T1b3 and T1b2) in Well G103.

Formation are: ① Most of the conglomerate is gray, with good roundness, sub-circular and sub-angular shape, and poor sorting. The comparison shows that the conglomerate rocks in the Quan 2 Member have poor sorting, and the small-grained conglomerate rocks in the Quan 3 Member have good sorting; ② Gravels have different particle sizes, some of which are more than 8 cm. The composition of the gravels is mainly magmatic rocks, followed by metamorphic and sedimentary rocks (Qiu and Xue., 1997; Ma et al., 2000).

3.2 Single well sedimentary micro facies

The Quan 1, 2, and 3 Members of the Baikouquan Formation in the study area belong to fan delta facies. The tectonic subsidence of the Triassic in the study area is relatively large, and the terrain is in an active period and is conducive to the formation of fan deltas (Scherer., 1987; Jin et al., 2017; Hu et al., 2020). Fan delta plain deposits are widely developed in the Baikouquan Formation in the study area.

The fan delta plain deposits are mainly composed of clastic flow, distributary channel and interchannel bay deposits (Beard and Weyl., 1973; Luo., 1991; Chen et al., 2015). The lithology of the distributary channel is relatively coarse, and it is composed of gravel-bearing sandstones and pure sandstones. Gravel-bearing sandstones and pure sandstones are light gray or gray-white, and are loose and granular. Its composition is mainly quartz, followed by feldspar and a little mica, and it has several positive cyclic features that taper upwards vertically (Figure 4).

3.2.3 Debris flow sedimentary micro facies

It is mainly composed of variegated conglomerate with high content of miscellaneous matrix, poor sorting and poor roundness. In addition, they are mostly supported by matrix, arranged in a disorderly manner, and thick and massive; they are mostly distributed in the root and middle part of the fan body and in areas with large terrain slopes; and argillaceous-supported conglomerate rocks are developed (Figure 4).

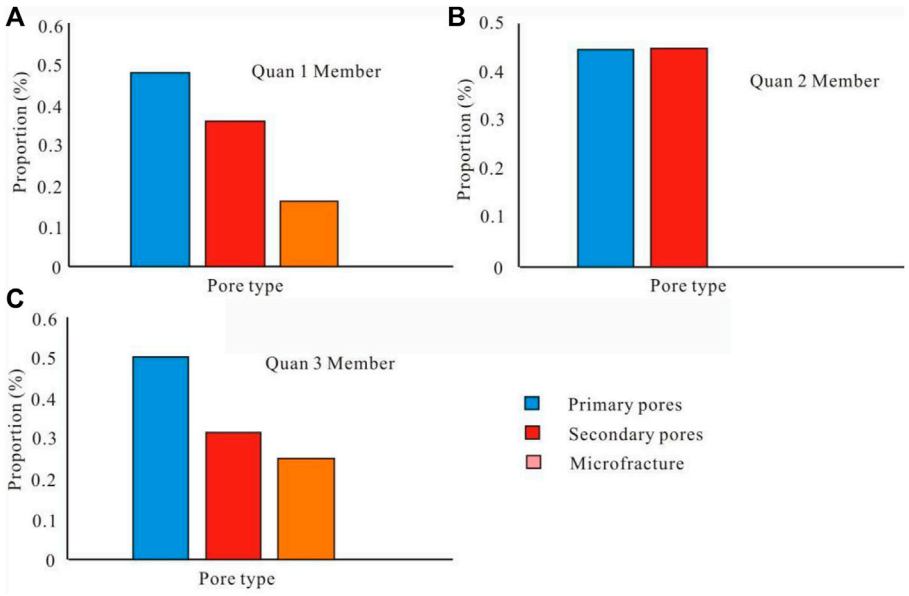

FIGURE 5
Distribution histogram of pore types in the Baikouquan Formation in the study area. **(A)** Quan 1 Member; **(B)** Quan 2 Member; **(C)** Quan 3 Member.

3.2.2 Distributary channel sedimentary micro facies

It is an important micro facies type in the fan delta plain sub facies, and its deposition thickness can account for more than 70% of the plain sub facies. It is formed by frequent lateral migration and accumulation of river channel sand bars during deposition (Li et al., 2004; Yu et al., 2015; Liu et al., 2019). The grain size of the distributary channel sediments is relatively coarse, and fine-grained sediments can be seen locally. They consist of several upwardly tapering layers. The thickness of a single sequence generally ranges from 0.5 m to 4 m. Its bottom is in scouring contact, and there are sediments of gravel retained by the river bed on it (Wang et al., 2007; Wang et al., 2008; Yu et al., 2018).

3.2.1 Interchannel bay sedimentary micro facies

It is uncommon in fan delta plains.

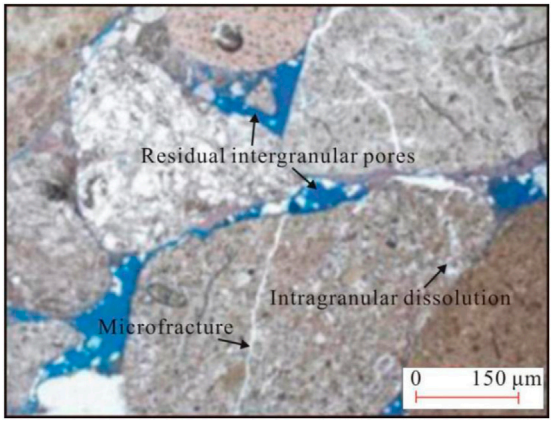

FIGURE 6
Microscopic characteristics of pore types in the Baikouquan Formation in the study area. Well S1, 4631.89m, Quan 1 Member, residual intergranular pores.

3.3 Developmental characteristics of pores

The reservoir properties and reservoir space types of clastic rocks vary with burial depth and diagenesis. Generally, the pore types change from shallow to deep as follows: development of primary pores → development of mixed pores → development of secondary pores → reduction of secondary pores and development of fractures. During this process, the internal structures of the rocks change from loose to dense.

Microscopic observations show that the reservoir spaces of the Baikouquan Formation sandstone and conglomerate reservoirs in the study area are mainly primary intergranular pores (Figure 5), followed by intragranular dissolved pores, microfractures, and intergranular dissolved pores. For the Quan 2 Member, the

contents of primary pores and secondary pores are similar. For the Quan 3 Member, not only primary pores are mainly developed, but also micro-fractures and secondary pores are relatively developed as well.

3.3.1 Primary intergranular pores

The primary pores refer to the pores preserved after the original pores have undergone a series of diagenesis such as compaction and cementation. This type of pores is common in both sandstone and conglomerate reservoirs in the Baikouquan Formation (Figure 6). Most of the remaining primary pores are polygonal pores between particles, and the pores are filled with calcite or kaolinite components.

3.3.2 Secondary pores

Secondary pores refer to pores formed by dissolution or compaction in sandstones. Common types of secondary pores include intragranular dissolved pores, microfractures, and intergranular dissolved pores. The main types of secondary pores in the Baikouquan Formation sandstone and conglomerate reservoirs in the study area are intragranular and intergranular dissolved pores.

3.3.2.1 Intragranular and intergranular dissolution pores

Intragranular dissolved pores are mainly feldspar and detrital dissolved pores. This type of pores is common, but the connectivity is poor. The proportion of the feldspar and detrital dissolved pores accounts for 5%–10%, respectively. In addition, the intergranular dissolved pores are mainly dissolved pores formed by the dissolution of feldspar particles and intergranular calcite, zeolite and other cements, and their edges are serrated or have harbor-like form. The proportion of intergranular dissolved pores ranges from 25% to 40%.

3.3.2.2 Micro fractures

Micro fractures are mainly formed due to the complex external stresses in the rock. Micro-fractures can be seen in the cores of the Baikouquan Formation, some of which are unfilled effective fractures, and some are completely filled with quartz. The filled quartz is mainly formed by the accumulation of silica released from the dissolution of volcanic rock debris. Quartz fillings account for 20%–30% of all fillings. The fine fractures are mainly distributed along the grain edges, which are usually effective fractures formed by the dissolution of acidic fluids. The proportion of this type of fractures is 10%.

4 Discussion

4.1 Comparison of petro logical characteristics

Through statistical classification of the reservoir rocks, it is found that the reservoir rocks of the Baikouquan Formation in the Hongcheguai area are mainly conglomerate rocks, followed by sandstones (Figure 7).

4.1.1 Sandstone reservoir

According to the statistics of the clastic content of the sandstone samples in the Baikouquan Formation, the rock types of the Baikouquan Formation in the study area are mainly lithic sandstones. The relative mass fraction of the lithic components is 75%–80%, with an average of 77.5%. The debris components are mainly magmatic rock debris; the metamorphic rock debris components are mainly altered rocks; and the sedimentary rock debris components are mainly mudstone. In addition, the relative mass fraction of the quartz debris in the sandstones is 3%–15%, with an average of 5.25%. The quartz component is mainly composed of single crystal quartz (Figures 7A,B). Most of the single crystal quartz comes from magmatic rocks, and the secondary enlarged-edge quartz is rare in the reservoir sandstones.

4.1.2 Conglomerate reservoir

The conglomerate reservoir rock types of the Baikouquan Formation mainly include small-grained and medium-grained conglomerate rocks (Figures 7C,D). The conglomerate rocks are mostly gray, and the roundness of the gravel is good. The particles are often sub-circular, sub-angular, and the overall sorting is poor. In addition, the gravels vary in size, some are more than 8 cm. The gravel compositions are mainly magmatic rocks (mainly tuff), followed by metamorphic rocks and sedimentary rocks.

The mass fraction of miscellaneous bases in conglomerate reservoirs ranges from 1% to 7%, with an average of 4.3%; the mass fraction of miscellaneous bases in sandstone reservoirs ranges from 1% to 8%, with an average content of 4.25%. The hetero-bases contained are mainly composed of mud-grade minerals. The widely distributed cement mineral components in the sandstones are mainly authigenic clay minerals (kaolinite), (iron) calcite, *etc.*, with a small amount of laumontite and siliceous minerals. Among them, clay minerals and calcite are the main materials that act as cements for the clastic particles. The roundness of sandstone is mainly sub-edge-sub-circular, and a small amount is sub-circular and round. The structural maturity of the sandstones is better than that of the conglomerate rocks. Detritus components are generally supported by particles. The sandstone particles are mostly in point and point-line contacts. The main cementation type is contact cementation, followed by press-embedded type and press-embedded- porous type.

4.2 Analysis of differences in petro physical properties

Reservoir petro physical properties are the main factors that determine reservoir quality and productivity (Meng et al., 2019; Tang et al., 2019). According to 66 groups of petro physical property data, the reservoir porosity of the

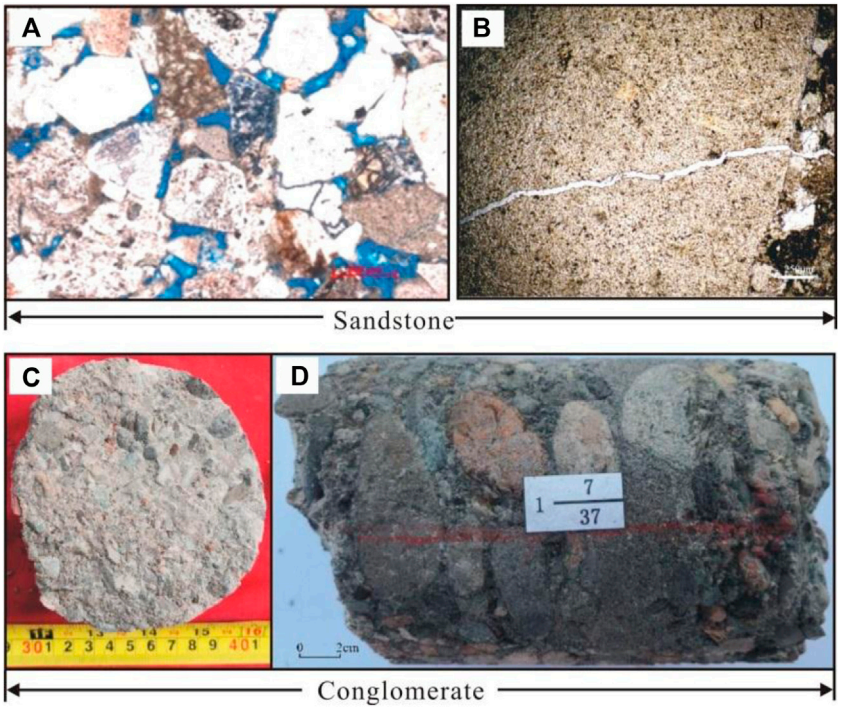

FIGURE 7
Cores and microscopic images of sandstones and conglomerate rocks of the target layer in the study area. Notes: **(A)** Well C5, 4,068.93 m, sandstone, residual intergranular pores; **(B)** Well S1, 4,636.5 m, sandstone, micro-cracks; **(C)** Well G6, 3,026.2 m, gray conglomerate; **(D)** Well S1, 4,963.68 m, gray-green conglomerate.

Baikouquan Formation ranges from 4.4% to 16.69%, with an average value of 10.37%; the permeability ranges from 0.15×10^{-3} μm^2 to 142×10^{-3} μm^2, with an average value of 6.85×10^{-3} μm^2. The porosity distribution range of the conglomerate reservoirs is 4.4%–16.69%, with an average value of 9.23%; the permeability distribution range is 0.15×10^{-3} μm^2~142×10^{-3} μm^2, with an average value of 9.11×10^{-3} μm^2. The conglomerate rocks appear as low-porosity and low-permeability reservoirs as a whole, but low-porosity, medium- and high-permeability reservoirs are locally developed. The comparison results show that the Petriphysical properties of conglomerate reservoirs are better than those of the sandstone reservoirs.

The correlation between the porosity and permeability of the reservoir rocks can reflect the physical characteristics of the reservoir to a certain extent. For clastic reservoirs, generally, the greater the effective porosity, the higher the rock permeability. That is, the permeability increases regularly with the increase of the effective porosity, and it reflects that the petro physical properties of clastic rock reservoirs are mainly affected by sedimentation (Xue et al., 2002; Yu et al., 2014). The porosity and permeability of the Baikouquan conglomerate show a negative correlation (Figure 8A), that is, as the porosity increases, the permeability gradually decreases. It reflects that with the increase of burial depth, the diagenetic environment of the conglomerate rocks of the Baikouquan Formation has changed greatly, and the petro physical properties of the conglomerate rocks has been greatly transformed by diagenesis, resulting in a complex relationship between rock porosity and permeability. On the whole, the porosity and permeability of the conglomerate reservoirs show a negative correlation, and the porosity and permeability of the sandstone reservoirs show a positive correlation (Figure 8B).

From the typical curves of high pressure mercury injection in the Baikouquan Formation, it can be found that the displacement pressures of the conglomerate reservoirs are not consistent. Among them, one type is a high discharge pressure curve, which shows that the mercury saturation is low, and the mercury intake curve shows a trend of rapid growth. It reflects that there is little difference in pore structures, at the same time, the mercury removal efficiency is not high, and the small throat is not conducive to the movement of fluids inside the pores. This type of mercury injection curve is most common in sandstone reservoirs (Figure 8A, samples C1 and C2). The other type has a lower discharge pressure, which shows that the mercury saturation is relatively high, and the mercury saturation increases with the increase of the discharge pressure. It reflects that the pore structures are quite different,

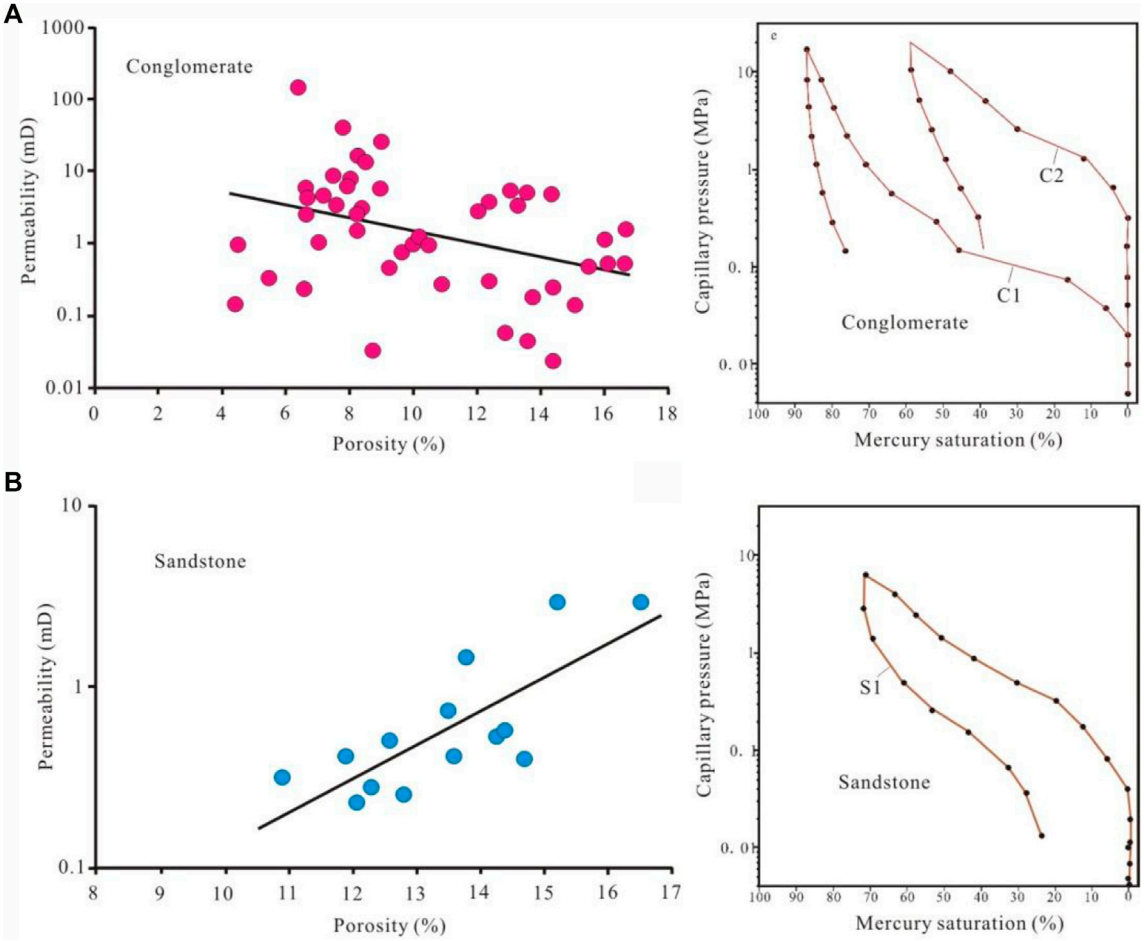

FIGURE 8
Relationship between porosity and permeability and mercury intrusion characteristics of conglomerate and sandstone reservoirs. **(A)** Porosity-permeability relationship(left) and mercury intrusion curve(right) of conglomerate, **(B)** Porosity-permeability relationship(left) and mercury intrusion curve(right) of sandstone.

and the mercury removal efficiency is extremely low. Fine throats severely block the movement of fluids inside the pores (Figure 8B, sample S1). The pore structures of the sandstone reservoirs is more uniform than that of the conglomerate reservoirs in the Baikouquan Formation.

With the increase of the burial depth and the influence of sedimentation and diagenesis, the reservoir rocks have changed from loose to dense, and the petro physical properties of the reservoirs have changed significantly. At the same time, the types of storage spaces have also changed continuously. Observations and statistics of 60 thin sections of the Baikouquan Formation in the study area revealed that the reservoir space mainly includes primary intergranular pores, secondary dissolved pores and microfractures, and the primary intergranular pores are dominated (Figure 9A). Primary intergranular pores are developed in both conglomerate and sandstone reservoirs, most of which are polygonal pores among grains. In the range of burial depth of 3,000–5,000 m, the preservation of a large number of primary pores is speculated to be related to the abnormal pressures and cementation of clay minerals (Figure 9B). Secondary dissolved pores are widely developed in the conglomerate reservoirs, and they are less developed in the sandstone pores, including intragranular and intergranular dissolved pores (Figures 9C,D). Dissolved pores in grains are common in feldspar pores, and feldspar pores are usually distributed along a certain direction (along the cleavage direction). The intergranular dissolution pores are mainly formed by the dissolution of feldspar particles and intergranular calcite, zeolite and other cements. The edges of the dissolution pores are sawtooth or bay-shaped (Figures 9E,F). Microfractures are common in both conglomerate and sandstone reservoirs. The filling of quartz in structural fractures is mainly

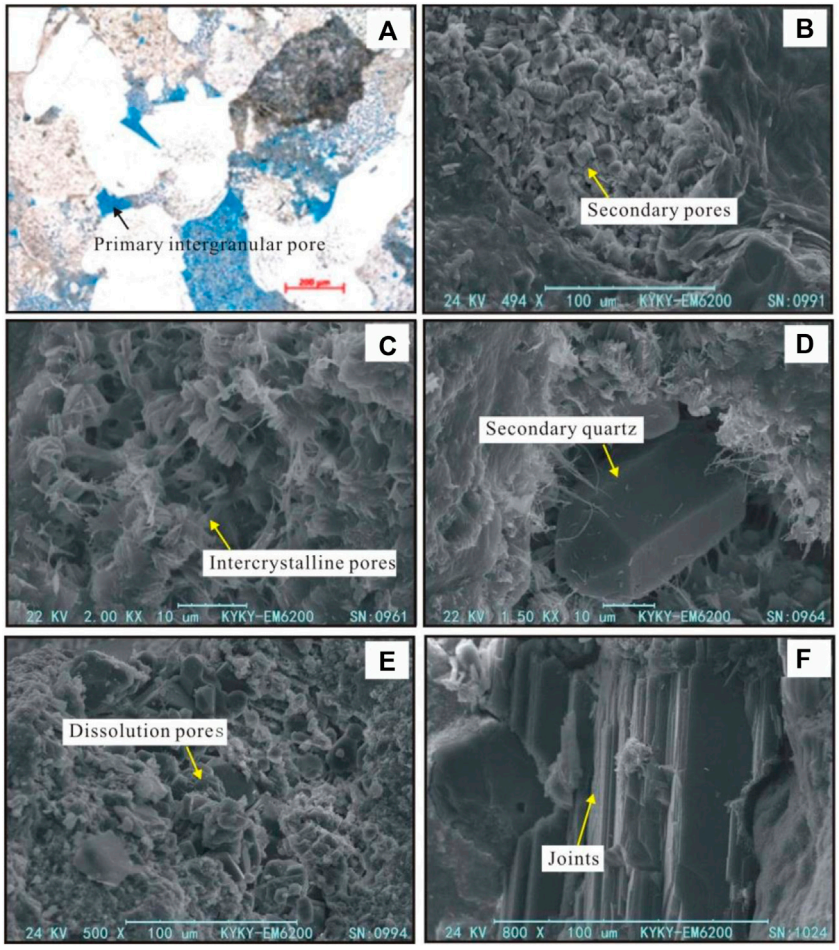

FIGURE 9
Pore types and development characteristics of different minerals of the target layer. Notes: **(A)** Well S1, 4,631.42 m, primary intergranular pores; **(B)** Well J1, 4,216.68 m, secondary pores in conglomerate; **(C)** Well S1, 4,636.5 m, intercrystalline pores in illite in conglomerate; **(D)** Well S1, 4,636.5 m, secondary quartz; **(E)** Well S1, 4,636.5 m, dissolution pores in conglomerate; **(F)** Well G10, 3,596 m, joints of calcium zeolite components.

due to the accumulation of silica released by the dissolution of volcanic rock cuttings, and this type accounts for 20%–30%; the proportion of diagenetic fractures formed by acid fluid dissolution is about 10%.

4.3 Controlling factors for differences in petro physical properties of sandstone and conglomerate reservoirs

The petro physical properties of the reservoir are controlled by factors such as sedimentation, diagenesis, and tectonic processes.

4.3.1 Sedimentary micro facies

The sedimentary environment of the Baikouquan Formation reservoir sandbodies in the study area is mainly fan delta system. It has diverse sedimentary micro facies, including clastic flow (distributed in fan-delta plain), underwater clastic flow (distributed in fan-delta front), distributary river channel (distributed in fan-delta plain), and underwater distributary channel (distributed in fan-delta front) (Figure 10). The oil layers are mostly distributed near the distributary river channels and underwater distributary river channel, where the sand ratio is distributed between 0.3 and 0.9. According to coring and petro physical property data, it is found that the reservoir petro physical properties in the underwater distributary river channel environment are the best, followed by the distributary river channel sand bodies, and the clastic flow and underwater clastic flow reservoirs have poor petro physical properties (Figure 11A).

Affected by ancient geomorphology, provenance, and hydrodynamic conditions, the sedimentary fabric characteristics of the Baikouquan Formation (referring to

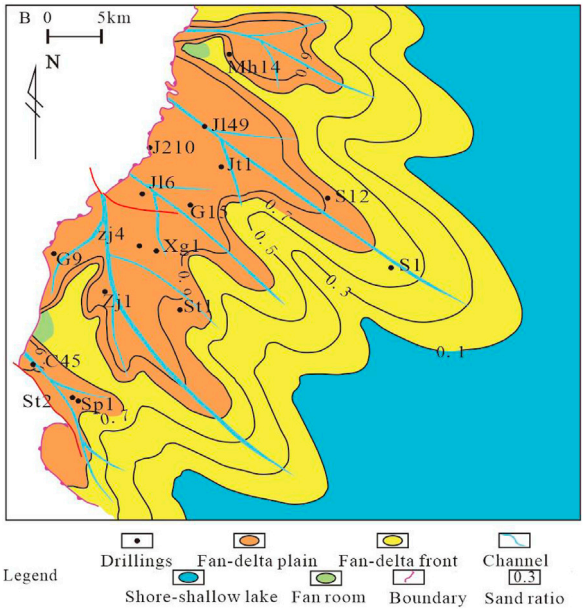

FIGURE 10
Planar distribution of sedimentary micro facies of the target layer in the study area.

particle size, clastic composition, interstitial volume fraction) are quite different. The consistency of porosity and permeability of the conglomerate reservoirs is poor. As the depth increases, the porosity and permeability tend to improve to varying degrees (Figure 11B). However, the porosity and permeability of the sandstone reservoirs decrease significantly as the depth increases (Figure 11C). The reason is that the composition of gravel is mainly tuffaceous components, and its compression resistance is weak. At the same time, the gravel particles are relatively large, and the volume fraction of the interstitials between the particles is large. Under the action of strong compaction, the primary pores are severely damaged. At a burial depth of 4,000 m, the feldspar and volcanic debris in the reservoir rocks are susceptible to dissolution, resulting in secondary pores. At the same time, the dissolution between particles improves the connectivity between pores, and the permeability of the reservoir is improved as well. Therefore, the proportion of secondary dissolved pores in the pore types of the conglomerate rocks is relatively large. The sandy particles are relatively small, and the rounding and sorting of the particles are better. Especially under strong hydrodynamic conditions, the mass fraction of mud is low. The rigid component (mainly quartz) has a large volume fraction, which offsets the impact of compaction to a certain extent. Parts of the original pores are preserved. Since the volume fraction of the shaped soluble particles is small, the later dissolution does not contribute much to the improvement of petro physical properties. Therefore, the pore types of the sandstones in the Baikouquan Formation are mainly primary pores.

4.3.2 Diagenesis

The compaction of the target layer causes a loss of 50%–90% of the porosity between the primary grains. According to previous empirical formulas (Yu et al., 2022), it is calculated that the average compaction intensity of the conglomerate reservoirs is 62.6%; and the average compaction intensity of the sandstone reservoirs is 50.2%. Therefore, the degree of

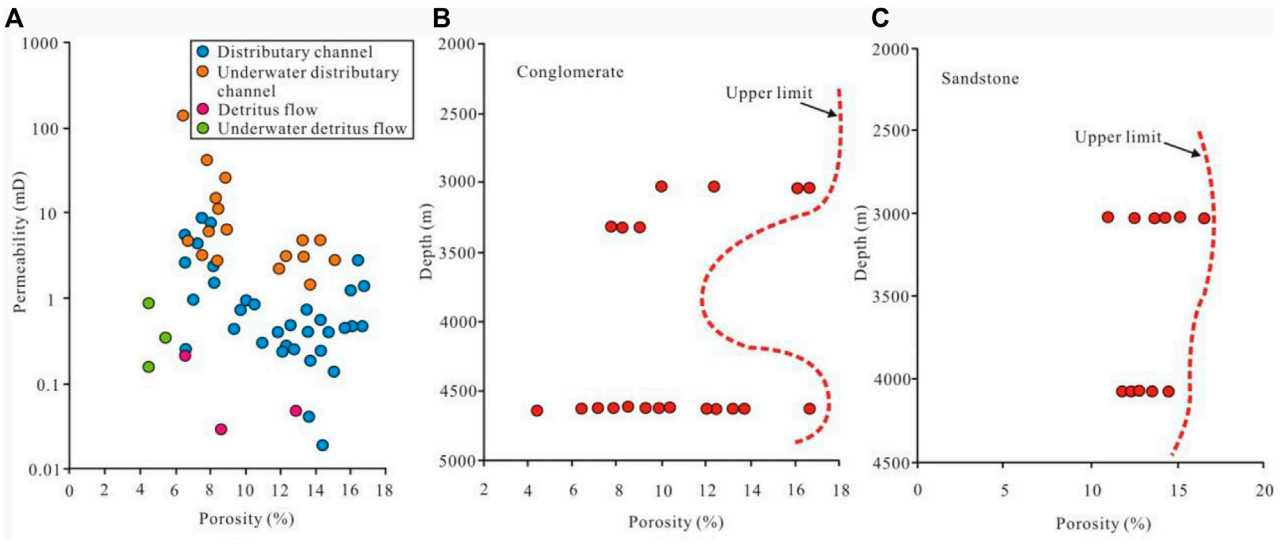

FIGURE 11
Distribution of petro physical parameters of sandstone and conglomerate in the target layer. **(A)** Distribution of porosity and permeability in different sedimentary microfacies, **(B)** Distribution of porosity with depth of conglomerate, **(C)** Distribution of porosity with depth of sandstone.

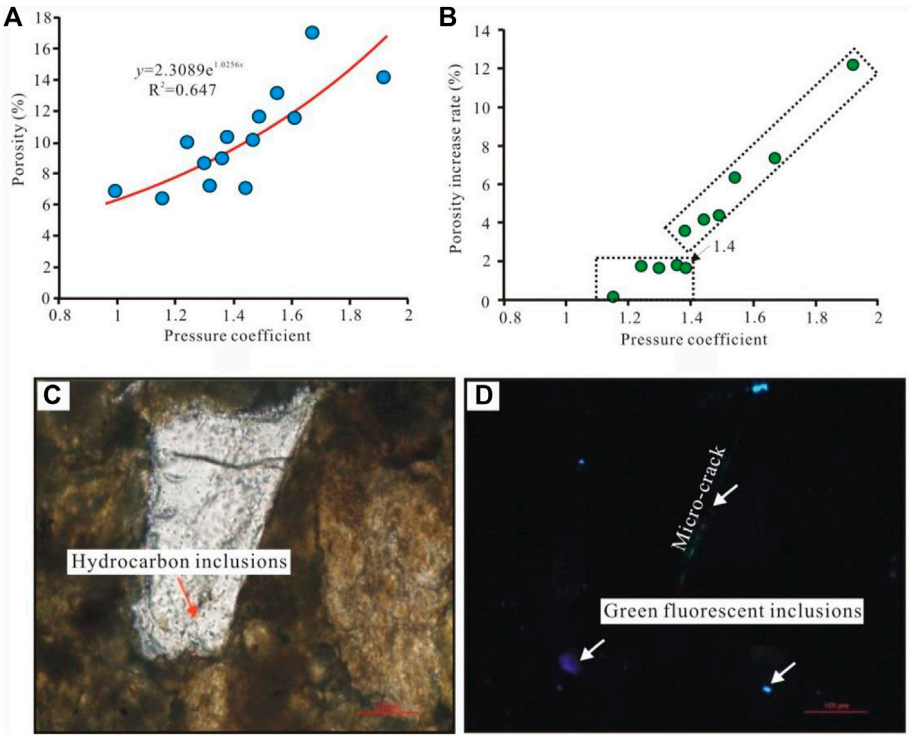

FIGURE 12
Effect of overpressure caused by tectonic action on the petro physical properties of reservoirs in the Baikouquan Formation. Notes: **(A)** Relationship between pore pressure and porosity; **(B)** Relationship between pore pressure and porosity increase rate; **(C)** and **(D)** Well S1, 4,630.56 m, hydrocarbons are distributed in bands along the micro-cracks cut through the quartz particles.

compaction of the conglomerate reservoirs is much higher than that of the sandstone reservoirs. According to the compaction strength classification scheme, the Baikouquan Formation in the study area belongs to the strong compaction area, which is the main factor for the deterioration of the pore structures. The mass fraction of cements was used to calculate the porosity loss caused by cementation, and it was found that the cementation caused an average loss of primary porosity of 10%. The average mass fraction of cements in the conglomerate reservoirs is 10.2%, and the average mass fraction of cements in the sandstone reservoirs is 13%. Therefore, the loss of pores caused by the cementation of sandstone reservoirs is greater than that of the conglomerate reservoirs.

After strong compaction and cementation, the primary pores in the pore type are almost destroyed. The secondary pores originate from the dissolution of particles, and the development of dissolution is of great significance to the improvement of storage properties. It can be seen from Figure 11B that with the increase of buried depth, the porosity of the conglomerate reservoirs decreases first and increases afterwards; with the increase of buried depth, the porosity of the sandstone reservoirs gradually decreases (Figure 11C). It reflects that the dissolution is of great significance to the improvement of the petro physical properties of the conglomerate reservoirs.

The development of dissolution has multi-stage characteristics. Early feldspar and plastic debris were dissolve to promote the formation of clay minerals and clay films. The development of the clay films is beneficial to slow down the compaction effect on the destruction of the primary pores, but it destroys the normal shape of the throats, resulting in a decrease in permeability and an increase in the heterogeneity of the throats. In the later period, the dissolution of calcite and pyroclastic (tuffin) is of great significance to the improvement of porosity and permeability. According to statistical results, the dissolved pore porosity of the conglomerate reservoirs increased by an average of 10%, and the dissolved pore porosity of the sandstone reservoirs increased by an average of 3%. Therefore, secondary pores are more developed in conglomerate reservoirs.

4.3.3 Tectonic effect

Multi-phase tectonic movements have a controlling effect on the formation of paleomorphology in the study area. The western area is a convex area, which gradually expands towards the eastern slope. The formation of the ancient landforms has an important influence on the distribution of sediments. The lower slope area of the slope break zone controls the front facies

sediments and has strong hydrodynamic conditions, which is a favorable conglomerate reservoir development area.

The abnormal pressure caused by tectonic action has a certain protective effect on the development of primary pores (Figures 12A,B). The strong squeezing action causes fractures in the particles. The development of micro-fractures can be observed in the thin sectiones of the conglomerate reservoirs. Combined with fluorescent thin sections, it is found that on the one hand, fractures lead to an increase in the micro-heterogeneity of the reservoir and improve the seepage ability of fluids in low-porosity and low-permeability reservoirs. On the other hand, they provide channels for oil and gas migration and accumulation (Figures 12C,D). This is also the reason of the differences of the petro physical properties of the conglomerate and sandstone reservoirs. The controlling factors of the petro physical properties of the conglomerate and sandstone reservoirs are different. The controlling factors of the sandstone reservoirs include sedimentation (sedimentary micro facies and fabric), diagenesis, and abnormal pressure. However, the petro physical properties of the conglomerate reservoirs are also controlled by the development of fractures.

5 Conclusion

(1) The sandstone and conglomerate rocks of the Baikouquan Formation in the study area have a large content of tuffaceous components. The sandstone reservoirs are dominated by primary intergranular pores, and the conglomerate reservoirs are dominated by secondary dissolved pores.
(2) The porosity is negatively correlated with rock permeability for the conglomerate rocks of the Baikouquan Formation. However, the porosity is positively correlated with rock permeability of the sandstone reservoirs.
(3) According to the analysis of the diagenetic process, the compaction and cementation can lead to a significant decrease in the petro physical properties of the reservoir. While dissolution can improve the petro physical properties of the sandstone reservoirs to a small extent, and can improve that of the conglomerate reservoirs to a greater extent. Moreover, local fractures are important factors affecting the petro physical properties of the conglomerate reservoirs. The existence of abnormal high pressure has a certain effect on the preservation of primary pores.
(4) On the whole, the controlling factors of the petro physical properties of the conglomerate reservoirs include sedimentation, diagenesis, and tectonics, while the petro physical properties of the sandstone reservoirs are mainly controlled by sedimentation and diagenesis.

Data availability statement

The original contributions presented in the study are included in the article/Supplementary Material, further inquiries can be directed to the corresponding author.

Author contributions

HK is responsible for the idea and writing of this paper and XT, JY, RZ, JW, HS, FL and HL are responsible for the data analysis.

Funding

This research was supported by the General Project of Chongqing Natural Science Foundation of China (cstc2019jcyj-msxmX0008), the Natural Science Fund of Xinjiang Uygur Autonomous Region, China (2021D01A201), and the Talent Introduction Project of Karamay campus of China University of Petroleum (Beijing) (RCYJ2016B-01-010).

Conflict of interest

Author HS was employed by the Shaanxi Yanchang Petroleum International Exploration and Development Engineering Co., Ltd. and author FL was employed by the Chongqing Gas Field, PetroChina Southwest Oil and Gas Field Company.

The remaining authors declare that the research was conducted in the absence of any commercial or financial relationships that could be construed as a potential conflict of interest.

Publisher's note

References

Beard, D. C., and Weyl, P. K. (1973). Influence of texture on porosity and permeability of unsolidated sand. *AAPG Bull.* 57 (2), 349–369.

Chen, B., Li, Z., and Su, B. (2015). Controlling factors of low permeability reservoirs of the triassic Formation in cheguai region, Junggar Basin. *Nat. Gas. Geosci.* 26 (S2), 73–82.

Feng, Z. (1993). *Sedimentary petrology*. Beijing: Petroleum Industry Press, 1–4.

Gao, Y., Lu, Z., and Jiang, Q. (2021). Application of petro physical faciesfor sandy-conglomerate reservoir evaluation: A case upper wuerhe reservoir in the M1 well block Junggar Basin. *Sci. Technol. Eng.* 21 (8), 3068–3075. doi:10.3969/j.issn.1671-1815.2021.08.013

Hu, D., Rao, S., Wang, Z., and Hu, S. (2020). Thermal and maturation history for carboniferous source rocks in the Junggar Basin, northwest China: Implications for hydrocarbon exploration. *Pet. Sci.* 17, 36–50. doi:10.1007/s12182-019-00392-2

Jin, J., Kang, X., and Hu, W. (2017). Diagenesis and its influence on coarse clastic reservoirs in the Baikouquan Formation of Western slope of the mahu depression,Junggar Basin. *Oil Gas Geol.* 38 (2), 323–333+405. doi:10.11743/ogg20170212

Lei, D., Qu, J., and An, Z. (2015). Hydrocarbon accumulation conditions and enrichment regularity of low-permeability glutenite reservoirs of Baikouquan Formation in Mahu Sag, Junggar Basin. *Xinjiang Pet. Geol.* 36 (6), 642–647.

Li, H., Wu, T., and Wu, B. (2004). Distribution and controlling factors of high quality clastic deeply buried reservoirs in China. *Geol. Sci. Technol. Inf.* 23 (4), 76–82. doi:10.3969/j.issn.1000-7849.2004.04.016

Li, L. (2001). The diagenesis model of tertiary sandstone reservior in bozhong area. *China Offshore Oil Gas(Geology)* 15 (2), 111–119.

Liu, J., Wang, Q., and Feng, J. (2021). Complex sandstone reservoirs evaluation based on petro physical facies classification:a case study of Huizhou Sag in the Pearl River Mouth Basin. *China Pet. Explor.* 26 (2), 92–102. doi:10.3969/j.issn.1672-7703.2021.02.010

Liu, N., Tang, Q., and Liu, J. (2019). Microscopic heterogeneity of Toutunhe Formation and its relationship with crucial short-term base lelve cycle in Fudong slope area, Junggar Basin. *Petroleum Geol. Exp.* 41 (2), 234–242. doi:10.11781/sysydz201902234

Luo, Z. (1991). The theoretical approach and the case application of the control of reservoir evaluation for the clastic reservoir by means of clay minerals. *J. Chengdu Coll. Geol.* 18 (3), 1–11.

Ma, Q., Chen, S., Zhang, Q., and GuoWang, S. S. (2000). *Overpressure basin and hydrocarbon accumulation*. Beijing: Geological Publ. House, 1–29.

Meng, X., Wang, X., and Chen, Y. (2019). KE89-MAh9 paleo-salient discovery in the slope of Mahu Sag and its hydrocarbon exploration significance. *Oil Geophys. Prospect.* 54 (1), 217–228. doi:10.13810/j.cnki.issn.1000-7210.2019.01.025

Qiu, Y., and Xue, S. (1997). *Assessment technique of hydrocarbon reservoir beijing*. Beijing: Petroleum Industry Press, 59–64.

Qu, J., Yang, R., and Tang, Y. (2019). Large-area petroleum accumulation model of the triassic glutenite reservoirs in the mahu sag, Junggar Basin: Triple control of fan, fault and overpressure. *Acta Geol. Sin.* 93 (4), 915–927. doi:10.3969/j.issn.0001-5717.2019.04.011

Scherer, M. (1987). Parameters influencing porosity in sandstones: A model for sandstone porosity predication. *AAPG Bull.* 71 (5), 485–491.

Tang, Y., Guo, W., and Wang, X. (2019). A new breakthrough in exploration of large conglomerate oil province in mahu sag and its implications. *Xinjiang Pet. Geol.* 40 (2), 127–137. doi:10.7657/XJPG20190201

Wang, Q. (2016). Quantitative assessment of the fult-sandbody trasportability forshawan-Formation in chepaizi area of Junggar Basin. *Petroleum Geol. Oilfield Dev. Daqing* 35 (6), 15–20. doi:10.3969/J.ISSN.1000-3754.2016.06.003

Wang, Y., Zhong, J., and Ma, F. (2008). The mechanism of secondary porosity in the deep-seated gravel reservoirs on the steep slope belt, jiyang depression. *Acta Geol. Sin.* 82 (2), 1152–1160. doi:10.3321/j.issn:0001-5717.2008.08.017

Wang, Z., Li, Y., and Zhang, J. (2007). Analysis on main formation mechanisms of abnormal fluid pressure in the Upper Triassic, West Sichuan area. *Oil Gas Geol.* 28 (1), 43–50. doi:10.3321/j.issn:0253-9985.2007.01.006

Xue, S., Liu, W., and Xue, L. (2002). *Sedimentary geology of lake basin and oil-gas exploration*. Beijing: petroleum industry press, 40–41.

Yu, J., Fu, H., and Zhang, Z. (2018). Petro physical facies of toutunhe Formation in fudong slope area, Junggar Basin. *Oil Gas Geol.* 39 (1), 129–139. doi:10.11743/ogg20180113

Yu, J., Luo, G., and Li, B. (2022). Diagenesis and diagenetic facies of upper wuerhe Formation in the shawan sag. *Geoscience* 36 (4), 1095–1104. doi:10.19657/j.geoscience.1000-8527.2022.206

Yu, J., Ren, W., and Wang, W. (2015). Formation mechanism of toutunhe abnormal pressure of middle jurassic in fudong slope area, Junggar Basin. *Xinjiang Pet. Geol.* 36 (5), 521–525. doi:10.7657/XJPG20150504

Yu, J., Zheng, R., and Yin, X. (2014). A comprehensive research on reservoir heterogeneity of Toutunhe Formation in slope area, east of Fukang sag, Junggar Basin. *J. Chengdu Univ. Technol. Sci. Technol. Ed.* 41 (5), 567–576. doi:10.3969/j.issn.1671-9727.2014.05.05

Zhang, Z., Yuan, X., and Wang, S. (2018). Alkaline-lacustrine deposition and paleoenvironmental evolution in permian fengcheng formation at the mahu sag, Junggar Basin, NW China. *Petroleum Explor. Dev.* 45 (6), 972–984. doi:10.1016/s1876-3804(18)30107-1

frontiers | Frontiers in Earth Science

TYPE Original Research
PUBLISHED 09 January 2023
DOI 10.3389/feart.2022.1032597

OPEN ACCESS

EDITED BY
Shuai Yin,
Xi'an Shiyou University, China

REVIEWED BY
Jie Chi,
China University of Petroleum (Huadong), China
Sijian Zheng,
China University of Mining and Technology, China

*CORRESPONDENCE
Chuan Yu,
yuchuan03041512@aliyun.com

SPECIALTY SECTION
This article was submitted to Structural Geology and Tectonics, a section of the journal Frontiers in Earth Science

RECEIVED 31 August 2022
ACCEPTED 21 September 2022
PUBLISHED 09 January 2023

CITATION
Li W, Luo T, Yu C, Tian X, Sun C, Wang W, Wang S, Zhong Z, Zhang Y and Liu J (2023), Structural deformation characteristics and its influence on shale gas preservation of the Wufeng–Longmaxi Formation in the Wuxi area, Chongqing, China. *Front. Earth Sci.* 10:1032597. doi: 10.3389/feart.2022.1032597

Structural deformation characteristics and its influence on shale gas preservation of the Wufeng–Longmaxi Formation in the Wuxi area, Chongqing, China

Wei Li[1,2], Tongtong Luo[2,3], Chuan Yu[1,4]*, Xuesong Tian[1,4], Chaoya Sun[1,2], Wei Wang[1,4], Shengxiu Wang[1,4], Zheng Zhong[1,2], Ye Zhang[1,4] and Jun Liu[1,4,5]

[1]National Joint Engineering Research Center for Shale Gas Exploration and Development, Chongqing Institute of Geology and Mineral Resources, Chongqing, China, [2]ChongQing Shale Gas Exploration and Development Company Limited, Chongqing, China, [3]CCDC Geological Exploration and Development Research Institute, Chengdu, China, [4]Key Laboratory of Shale Gas Exploration, Ministry of Natural Resources, Chongqing Institute of Geology and Mineral Resources, Chongqing, China, [5]Key Laboratory of Deep Underground Science and Engineering (Ministry of Education), Institute of New Energy and Low-Carbon Technology, Sichuan University, Chengdu, China

The Upper Ordovician Wufeng to Lower Silurian Longmaxi Formation has a good material basis for marine shale gas development, and the structural preservation condition is the key factor to control the rich and integrated shale gas reservoirs in the Wuxi area of Chongqing City, China. Based on the seismic-structural interpretation data, combined with the regional structural background and drilling effect, the structural deformation characteristics and shale gas structural preservation conditions are comprehensively analyzed in the study area. The Wuxi area is located at the structural junction of the Sichuan Basin and southern Dabashan along with strong structural deformations. Seven rows of NW to near EW structural belts are mainly developed. The fold styles and fault development degrees of different structural belts are different, and the difference in the structural preservation conditions of shale gas is also obvious. The study results reveal that the shale gas structure preservation conditions of the Wufeng–Longmaxi Formation in the Wuxi area are overall poor and only locally better. The structure preservation conditions for shale gas enrichment and accumulation are divided into four grades, such as the good Class I area, the general Class II area, the poor Class III area, and the very poor Class IV area. Among them, the Heiloumen structural zone and Huangcaoping buried structural zone nearby the Sichuan Basin have good preservation conditions and are classified as the good Class I preservation area. The macroscopic preservation type of shale gas in the Wufeng–Longmaxi Formation of the Wuxi area belongs to the complex structural preservation of the basin margin. Three structural preservation modes of shale gas in the study area have also been confirmed, including the lost destruction type, lost residual type, and trap preservation type. The trap preservation type is more conducive to the preservation of shale gas, which is the most favorable structural mode for shale gas exploration.

KEYWORDS

structural deformation characteristics, preservation mode, shale gas, Wufeng–Longmaxi Formation, Wuxi county of Chongqing city

Introduction

With the recently substantive breakthroughs and commercial development of marine shale gas in the Changning, Weiyuan, Fuling, Zhaotong, Fushun–Yongchuan, Pengshui, Nanchuan, and Dingshan areas from the Sichuan Basin and its surroundings, China's shale gas exploration and development has entered a very rapid pace, especially the exploration and development progress of shale gas in the complex structural regions at the margin of the Sichuan Basin (Jin et al., 2018; Potter, 2018; Ma et al., 2020; Liu et al., 2021a; Nie et al., 2021; Li et al., 2022; Wang et al., 2022). The Wuxi area of Chongqing city is situated in the transition zone between the northeastern margin of the Sichuan Basin and the Dabashan thrust belt, which belongs to the typical complex structural region of the basin margin. In this area, the black shale of the Upper Ordovician Wufeng to Lower Silurian Longmaxi Formation, which has the characteristics of large thickness, high organic matter abundance, and thermal evolution degrees, was widely developed in a similar sedimentary environment to shale gas fields today (Liu et al., 2016; Liu et al., 2018; Wang et al., 2018; Nie et al., 2019; Wang et al., 2019; Wu et al., 2019; Tang et al., 2020; Zhang et al., 2020). This also implies that the shale, as an important target stratum, has a good material basis for shale gas accumulation, and the Wuxi area is considered a favorable shale gas exploration area. Meanwhile, a number of shale gas geological survey wells have also been arranged in this area since 2012 and the WX2 well in the Wenfeng anticline deployed by PetroChina has obtained a good shale gas performance, with 2.32 and 8.39 m^3/t of mean and maximum gas-bearing contents, showing that the Wufeng–Longmaxi Formation in the area is of favorable shale gas exploration and developmental potential (Liang et al., 2015; Liu et al., 2017; Wu et al., 2017; Shi et al., 2018; Liu et al., 2021b; Zhao et al., 2021; Zhao et al., 2022). Although some shale gas exploration wells have achieved effective exploration results in this area, such as X202, X203, and X205 wells, none of them is up to the commercial production scale. Furthermore, the complex geological structural conditions have an important impact on the accumulation and preservation of shale gas in the Wufeng–Longmaxi Formation and deserve more attention. Due to the certain constraint of self-contained, self-sourced, and self-accumulating reservoirs, a detailed evaluation of structural deformation characteristics may be conducted through the comprehensive analysis of shale gas enrichment, accumulation, and preservation. This study will systematically analyze the structural deformation characteristics and shale gas structural preservation conditions of the Wuxi area in Chongqing city based on the seismic-structural interpretation in the study area, combined with the regional tectonic background and actual drilling results. This may provide the geological basis for favorable shale gas exploration and development of the Upper Ordovician Wufeng to Lower Silurian Longmaxi Formation in the area, which is of great significance for us to understand shale gas accumulation and preservation in the complex structural belts at the margin of the Sichuan Basin.

Geological setting

Multi-phase structural transformation went through the Wuxi area in geological history, and the structural deformation was much stronger than that within the Sichuan Basin (Chen et al., 2016; Yang et al., 2019). Due to the superimposed deformation of the southern Dabashan thrust-fold belt and the high-angle tectonic belt of the eastern Sichuan Basin, the overall structural style presented the complex fold of northwest (NW) to near east-west (EW) (Figure 1). Bounded by major deep-large faults, the area could be divided into three secondary structural units, such as the southern Dabashan ramp fault belt in the northeast, the southern Dabashan frontal fold belt in the middle, and the high-angle fold belt of the eastern Sichuan Basin in the southwest (Yu et al., 2018). In other words, from the inside to the outside of the Sichuan Basin, the magnitude of strata uplift and denudation, the intensity of fold deformation, and the degree of fault development all gradually increased. Towards the northern side of the Wanyuan–Wuxi fault, the structural mode mainly presented as a linear complex fold extending in an NW arc shape and anticlinoria and synclinore were arranged alternately (Figure 1). The fold often showed the branching and merging phenomenons, and the surfaced and underground faults were relatively developed, which have associated with back thrust and ramp fault combinations, respectively, and finally disappeared to the deep or merged with the main detachment fault belt. The Upper Cambrian to Middle Silurian strata occurred in the anticlinoria and the Permian and Triassic strata were exposed to the synclinore (Figures 2A–D). Towards the southern side of the Wanyuan–Wuxi fault and the northern side of the Shashi hidden fault, the intensity of structural deformation weakened and the structural mode transitioned into NNW complex closed-open folds with a relatively complete shape (Figure 2E). Surfaced faults in this location were not developed and there were many underground hidden faults according to the seismic and remote sensing image data. Towards the southern side of the Shashi hidden fault nearby the internal Sichuan Basin, the structural mode was relatively stable and wide with fewer faults, and the Triassic to Jurassic strata were exposed on the surface (Figure 2F). Under the structural superposed deformation, the fold style in this location changed complexly and focused on the wide-gentle fold and box-shaped anticline (Figure 3).

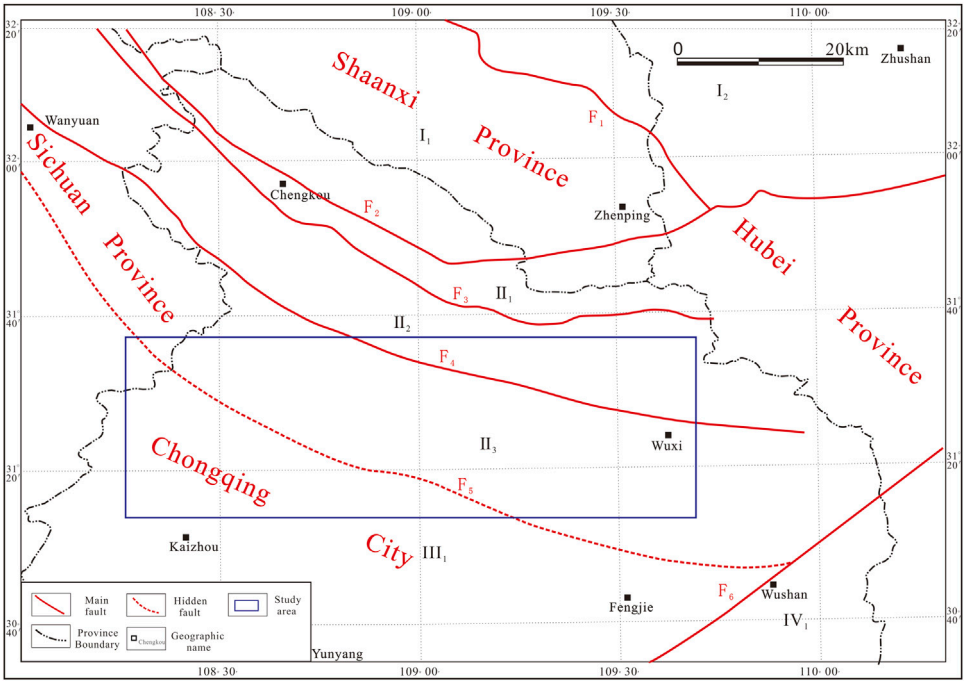

FIGURE 1
Geological structure of the study area. F_1, Hongchunba–Zengjiaba fault; F_2, Chengkou fault; F_3, Wuping fault; F_4, Wanyuan–Wuxi fault; F_5, Shashi hidden fault; F_6, Qiyaoshan basement fault; I_1, southern Dabashan linear synclinore–epimetamorphic belt; I_2, northern Dabashan dome-shaped anticlinoria–hypometamorphic belt; II_1, southern Dabashan imbricate fault belt; II_2, southern Dabashan ramp fold belt; II_3, southern Dabashan frontal fold belt; III_1, high-angle fold belt of eastern Sichuan Basin; IV_1, Qiyaoshan depression and fold belt.

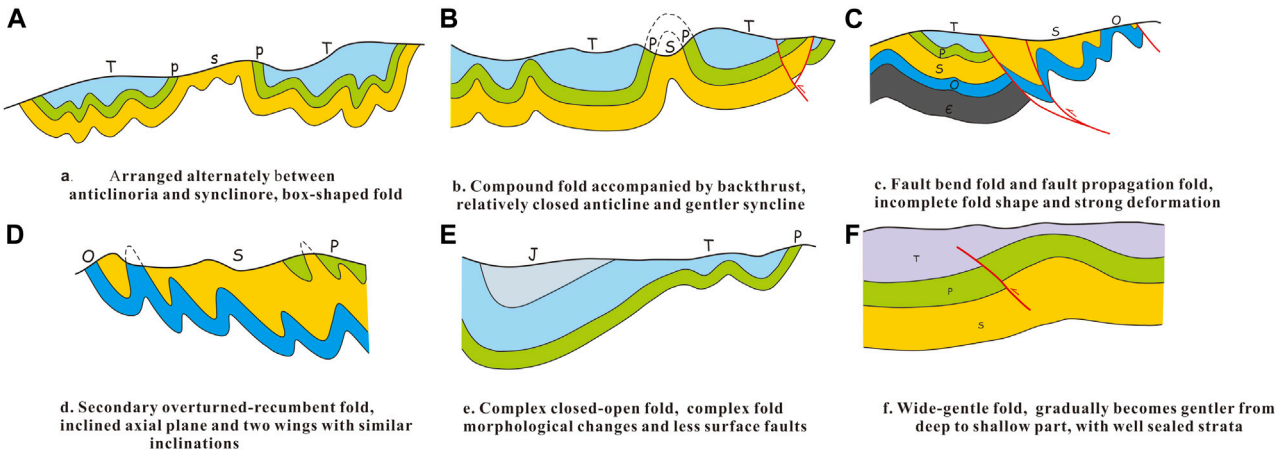

FIGURE 2
Main structural styles in the study area.

Structural partitioning and deformation characteristics

According to the interpretation results of seismic-structural data and regional structural distribution characteristics, taking the top boundary structures of Middle Ordovician as an example, the demonstration area can be divided into seven main NW to near EW structural belts from the north to south direction (Figures 3, 4). The detailed deformation characteristics of each structural belt are described as follows.

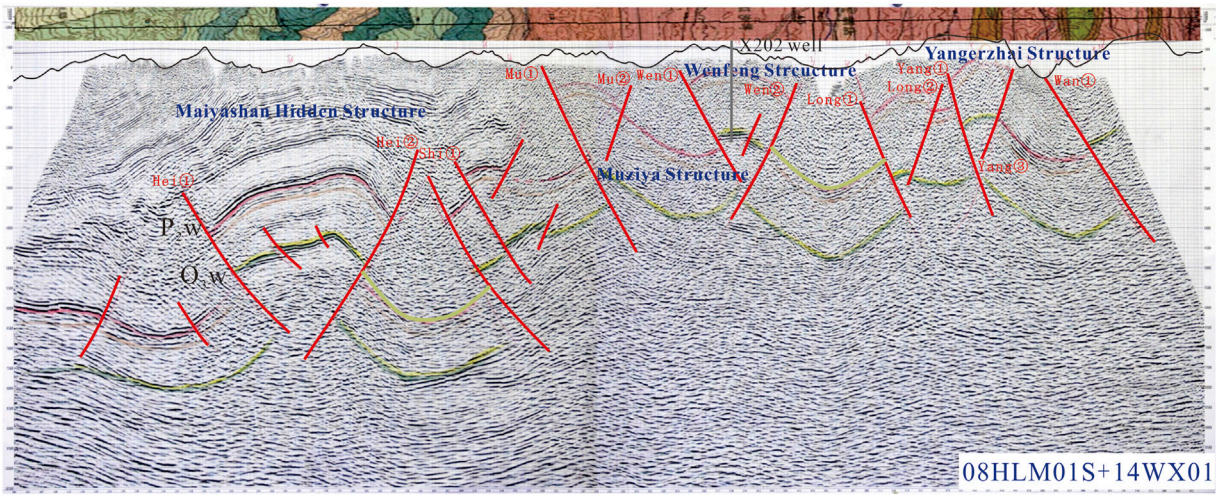

FIGURE 3
A–A′ seismic-structural profile in the study area.

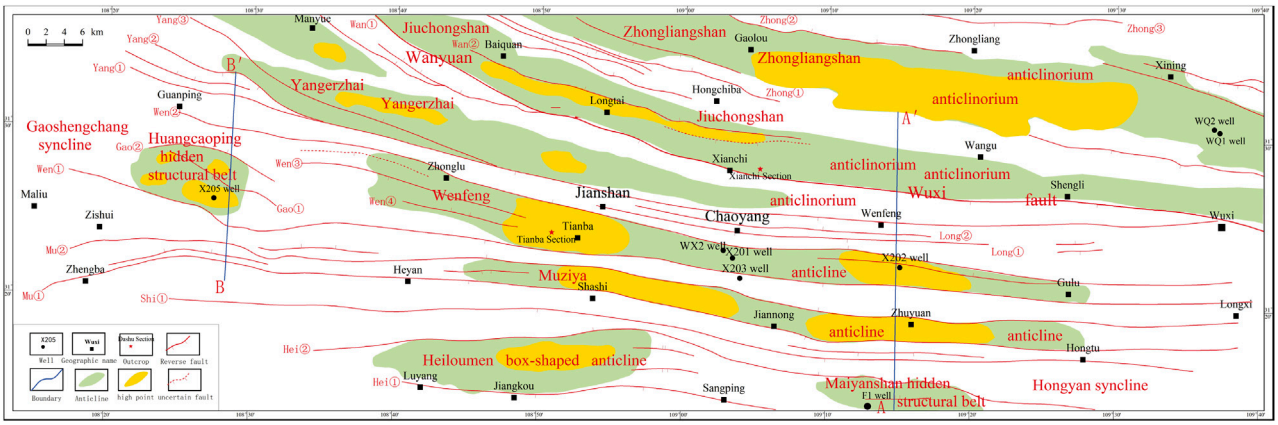

FIGURE 4
Top boundary of Middle Ordovician in the study area.

Heiloumen structural belt

The Heiloumen structural belt locates at the southern margin of the study area with the NWW to near the EW strike and mainly develops a box-shaped anticline. Its southern and northern flanks are controlled by the Hei① and Hei② faults, respectively. There are two structural high points, which are distributed on the eastern and western sides of the structural belt. The western high point belongs to the box-shaped anticline with a relatively gentle form and the Lower Triassic Jialingjiang Formation is exposed in the core of the anticline. The eastern high point is connected with the saddle of the Maiyanshan hidden structure, which is located in the southern part of the Hongyan syncline. The structural form of this point is relatively wide and gentle, and the Middle Triassic Leikoupo Formation is exposed along the axis of the anticline, and the secondary faults are well developed.

Muziya structural belt

The Muziya structural belt lies between the Mu① and Mu② faults, which is a strip-like anticline with an NWW direction. Its whole structural form is steep in the south and gentle in the north

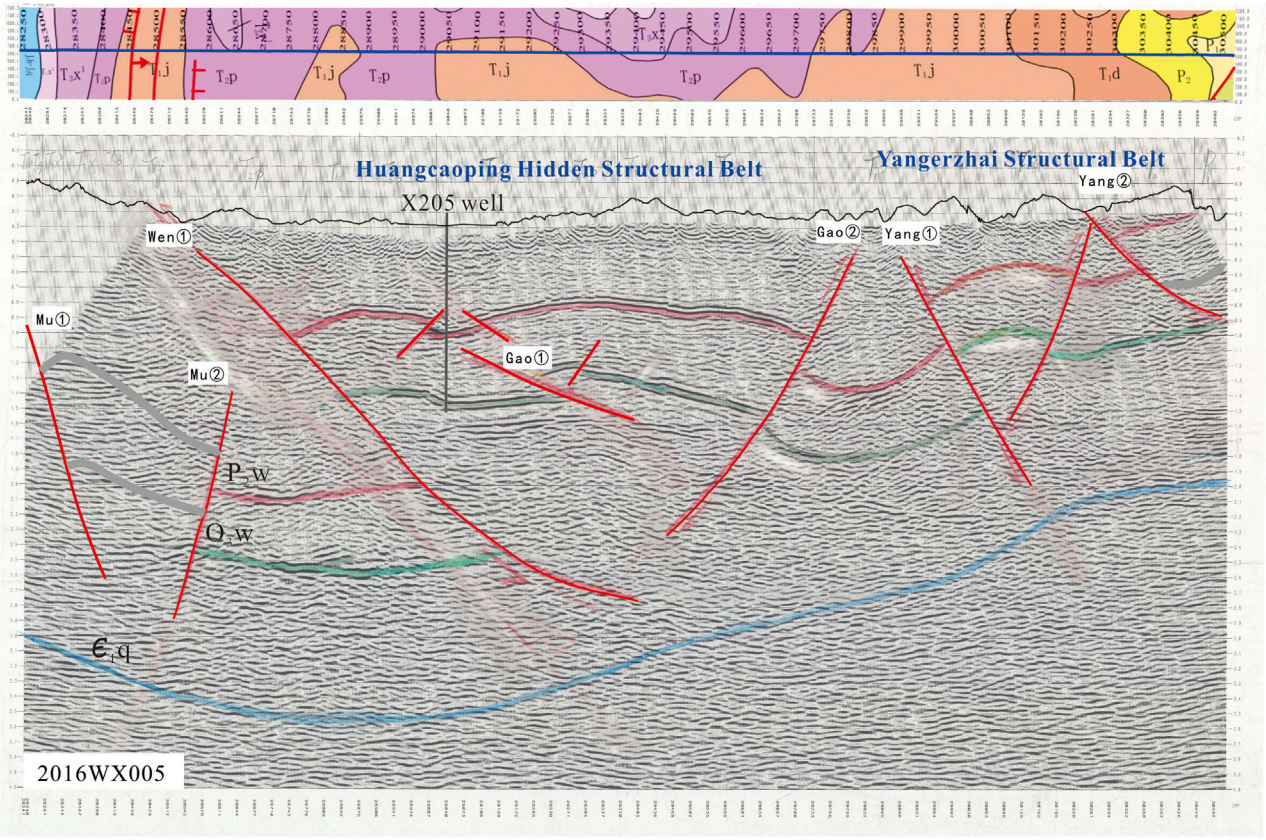

FIGURE 5
B–B′ seismic-structural profile in the study area.

and some secondary faults are developed along the axis of the anticline. The belt includes eastern and western structural high points, and the Lower to Middle Permian strata and Lower Triassic Jialingjiang Formations are exposed at the anticline core at the western and eastern high points, respectively.

Wenfeng structural belt

The Wenfeng structural belt distributes the hanging walls of Wen① and Wen② faults, which is classified as an NWW-trending strip-like anticline. The structural form is relatively stable as a whole steep in the south and gentle in the north. There are also some secondary faults in the axis zone of the anticline. The belt is divided into eastern and western high points, and its main high point is the Tianba anticline. The fluctuations of strata uplift and denudation in this belt are relatively large, so the exposed Lower Silurian Longmaxi shale formation is denuded and the oldest stratum on the surface is the Upper Cambrian. The Lower Triassic Feixianguan Formation is exposed at the core of the anticline in the eastern high point.

Huangcaoping hidden structural belt

The Huangcaoping hidden structural belt lies at the west-dipping end of the Wenfeng anticline, which is controlled by Wen① and Gao② faults, consisting of two rows of hidden high structural belts, namely, the southern and northern high structure zones (Figure 5). The general distribution of the two hidden zones is an NWW direction and its structural form has the characteristics of being relatively wide and gentle. In the southern hidden structural zone, there are two high structural high points, namely, Huangcaoping① and Huangcaoping② high points. The distribution of the northern hidden structural zone is very similar to that of the southern zone and there are also two high structural points, namely, Huangcaoping③ and Huangcaoping④. The belt is located at the structural transition zone and the extended distance and scale of the four high structural points are short and small. Furthermore, the buried depth of the two high structural points is superficial and the Lower to Middle Triassic strata are mainly exposed on the surface.

Yangerzhai structural belt

The Yangerzhai structural belt, occurring on the hanging wall of the Yang① fault and the footwall of the Wanyuan–Wuxi fault, is a typical NWW-trending anticlinorium. The two flanks of the anticline are very steep, with strong structural deformation, and develop secondary overturned recumbent folds and faults. The entire structural belt is wide in the west and narrow in the east, with two structural high points, and the Silurian is the oldest exposed strata in the core of the anticline.

Jiuchongshan structural belt

The Jiuchongshan structural belt locates the hanging wall of the Wanyuan–Wuxi fault, which is also an NWW-trending anticlinorium along with strong compression and deformation. The styles of secondary folds are complex, including fault bend fold and fault propagation fold, and most of their fold forms are closed and the formation occurrence changes repeatedly, mostly at high angles and locally reversed. The strata uplift and denudation in this belt are generally large and the local compression and fragmentation are also serious. The Upper Cambrian to Lower Triassic strata are exposed at the surface and the Wufeng–Longmaxi Formation is broadly denuded in the middle part of the structural belt.

Zhongliangshan structural belt

The Zhongliangshan structural belt lies at the northeastern margin of the Wuxi area and is arranged parallel to the Jiuchongshan anticlinorium. The strata are often strongly deformed with generally developed secondary folds and faults. Furthermore, the surfaced and underground structures are obviously inconsistent and the fold form changes significantly in the deep underground, with mostly high dip angles. On the surface of this structure belt, the Middle–Lower Silurian to Lower Triassic strata are exposed along with severe compression and fragmentation and multiple high-angle fractures.

Structural preservation conditions for shale gas enrichment

The influence of structure on the accumulation of shale gas

Generally, structural preservation conditions are the key factors controlling the enrichment and accumulation of conventional oil and gas. For the self-contained, self-sourced, and self-accumulating shale gas reservoir, due to the particular tight degree and adsorption mechanism of black shale itself, its anti-destructive ability is very strong so that whether or not the suitable structural preservation conditions remain uncertain, they are worthy of a deeper discussion (Hao et al., 2013; Nie et al., 2021).

According to the shale gas drilling data, the organic-rich black shale of the Wufeng–Longmaxi Formation is well developed in the Wuxi area and has a good material basis for shale gas enrichment, and the dark shale of the Wufeng–Longmaxi Formation is well developed in this area, with a thickness of more than 40 m and an organic carbon content of more than 2%, indicating the high over-mature evolution stage and well-developed organic micro-pores in the shale (Figure 6). Quartz contents generally reach more than 2%, with strong brittleness and good storage performance, representing a good material basis for shale gas development. But the gas-bearing differences are very obvious in the same shale layers from different structural locations in this area (Figure 7). For example, there are good shale gas-bearing properties of the Wufeng–Longmaxi Formation in the X205, X202, and WX2 wells, while that in X203, WQ2, and WQ1 wells are relatively poor. Thus, there is no absolute correlation between the organic matter abundance of black shale and the gas-bearing content. The X203 well is located on the southern flank of the middle section of the Wenfeng anticline. By drilling the core data from the upper part of the first bed of the Longmaxi Formation, strong compression and deformation occur in the well area and the formation dip angle changes greatly, locally with small crumpling, high-angle fractures, and a relatively broken core. This could imply that some secondary faults were encountered and no good gas-bearing properties were found during the drilling process of the Lower Longmaxi Formation, with less than 0.5 m^3/t and less than 0.8 m^3/t of natural desorption and total gas-bearing contents, indicating a large loss of gas in the shale layer that has already occurred, and further enrichment and accumulation of shale gas in the Longmaxi Formation were destroyed because of the poor structural preservation conditions (Figures 8A, B). The WQ1 and WQ2 wells are located in the eastern section of Zhongliangshan anticlinorium of the southern Dabashan ramp fold belt. The structural conditions are more complex than those of the southern Dabashan frontal fold belt. The drilling cores show that the favorable shale of the Longmaxi Formation is generally broken, with high-angle trending, strong structural deformation, and numerous fractures (Figures 8C–F). In addition, there are poor gas-bearing shale target layers from the two cores, which are less than 0.5 m^3/t and 0.8 m^3/t of gas-bearing contents in the WQ2 and WQ1 wells, respectively. In other words, good external structural preservation conditions can play a critical role in the gas-bearing properties of black shale layers in addition to the shale itself having a good material basis for shale gas enrichment and accumulation. Therefore, the quality of structural preservation conditions is the key factor controlling the enrichment and accumulation of shale gas in the Wuxi area.

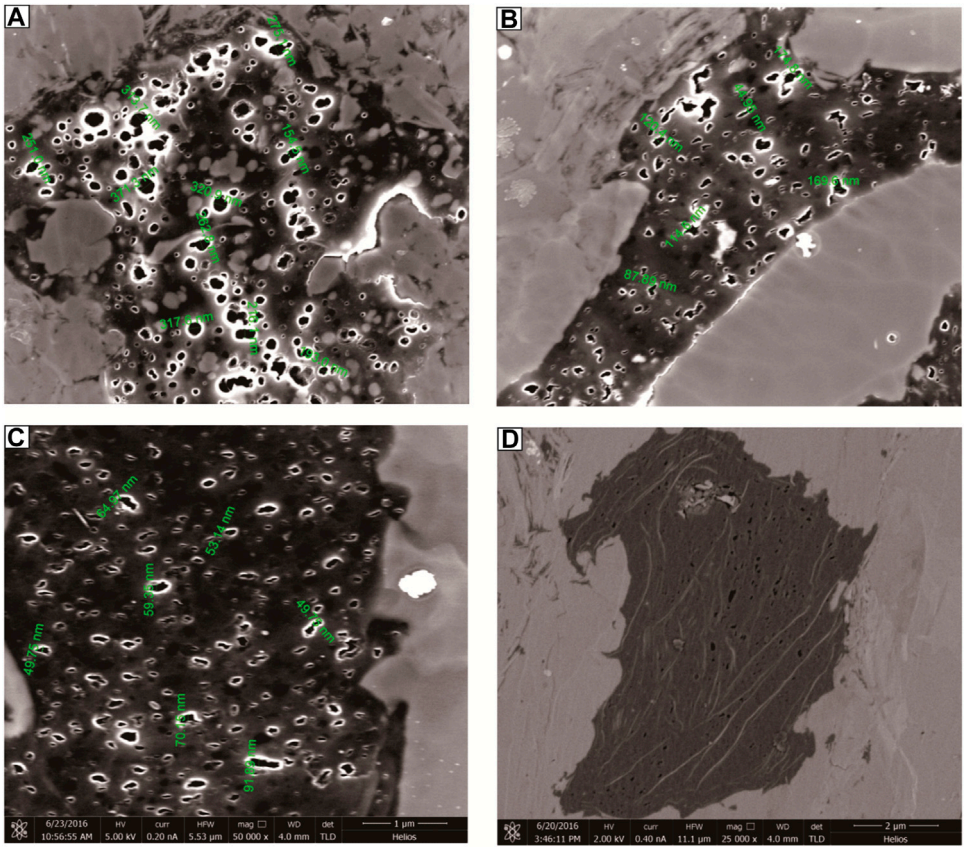

FIGURE 6
Development characteristics of organic micro-pores in the dark shale of the Wufeng–Longmaxi Formation in the Wuxi area. **(A)** Gray black shale, X202 (1888.99 m); **(B)** black carbonaceous shale, X202 (1955.85 m); **(C)** gray black silty shale, X203 (3,616.64 m); **(D)** black carbonaceous shale, X203 (3,634.83 m).

The partitioning evaluation of structural preservation conditions

The preservation conditions are one of the major controlling factors for shale gas enrichment, accumulation, and high gas production and an important aspect of shale gas geological evaluation (Liu et al., 2016; Feng et al., 2018; Wu et al., 2019). By the analytic results of a lot of previous research on the preservation conditions of shale gas (Tang et al., 2015; Xie, 2018; Sun et al., 2021), the structural condition is a major controlling factor for shale gas preservation, such as formation uplift and denudation, structural deformation intensity, faults and fractures, and capping conditions. At present, the evaluation of shale gas preservation depends on the combination methods of qualitative and quantitative analysis. Due to different regional tectonic backgrounds and differentiated degrees of research data, there is still no unified standard for the evaluation of shale gas preservation conditions. The Wuxi area is located in the basin-mountain coupling region and the macroscopic preservation type of shale gas is complex structural preservation of the basin margin. Through the detailed analysis of the structural conditions, the structural deformation is much stronger, so the structural preservation conditions are generally poor but are locally good and there are differentiated preservation conditions of shale gas in different regions.

By the deformation characteristics of each structural belt, combined with the actual drilling effect of shale gas, the structural preservation conditions of shale gas in the Wufeng–Longmaxi Formation can be evaluated in the area. Structure preservation conditions are divided into four grades, namely, the good Class I area, the general Class II area, the poor Class III area, and the very poor Class IV area (Figure 9; Table 1). In the compound fold belt at the northern side of the Wanyuan–Wuxi fault, the Jiuchongshan and Zhongliangshan structural belts have structural deformation, which is generally strong, and both the surfaced and underground faults are well developed. The shale target layer of the Lower Silurian has extensive exposure and denudation, with high-angle fractures and very poor structural preservation condition of shale gas, belonging to the Class IV area. In the Yangerzhai structural belt, Tianba anticline,

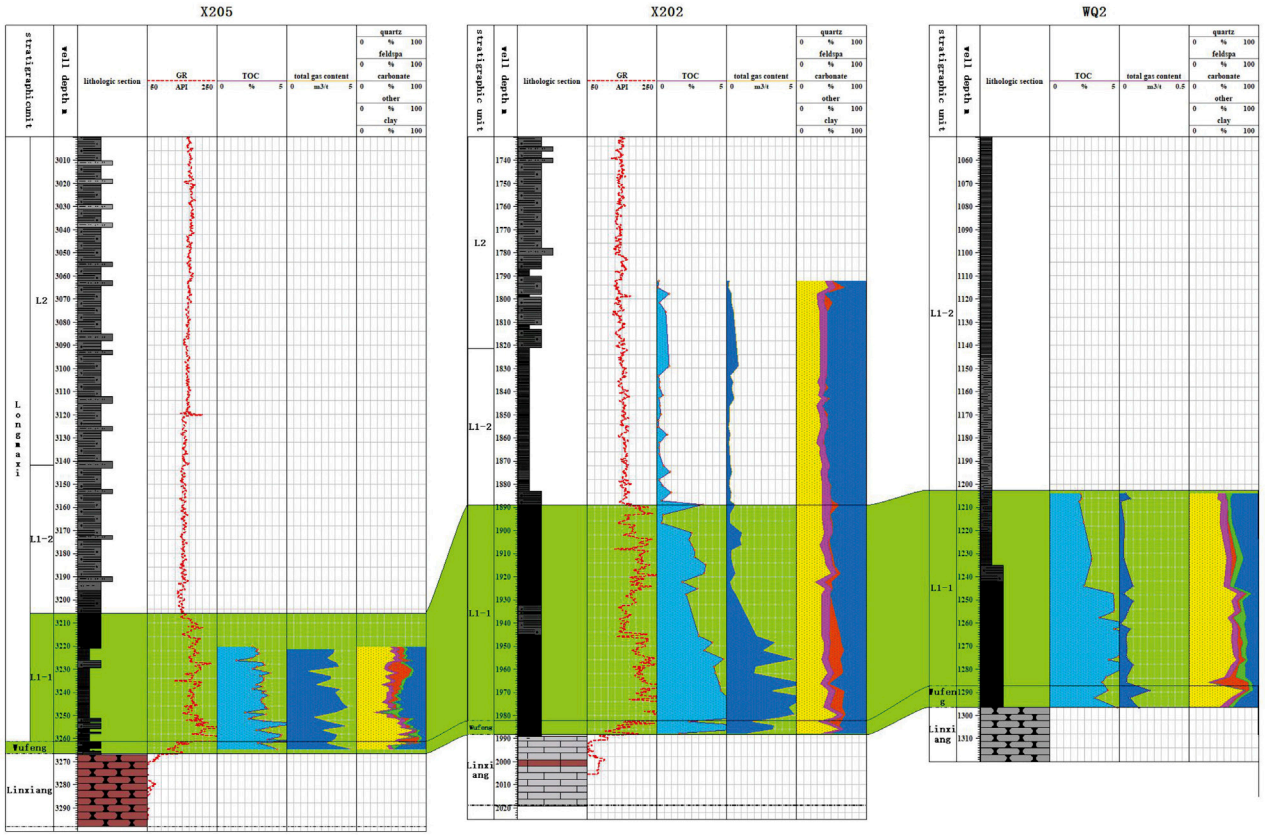

FIGURE 7
Connecting the well profile of shale target layers in the Wufeng–Longmaxi Formation.

and the western pinching end of the Muziya structural belt, the whole structural deformation is strong with relatively fragmented strata, mainly constructing anticlinoria and closed secondary folds. Faults are relatively well-developed with locally large faults, and the degree of formation uplift and denudation is rather large. The Permian to Lower Triassic strata are mainly exposed at the surface and the Lower Silurian is presented and denuded locally, such as the Tianba anticline. The capping condition of the region is generally poor, belonging to the Class III area. In the Muziya structural belt and fold region at the southern side of the Wenfeng structural belt, the structure form is rather stable, which is mainly composed of asymmetric folds and open folds. There is a low development degree of faults in this region, with relatively well-developed high-angle fractures larger than 3 km from the surfaced large fault. Moreover, the degree of formation uplift and denudation is rather small and the distance from the denudation zone of the shale target layer is more than 5 km. The Triassic strata are mainly exposed at the surface and partially exposed to the Lower Jurassic. The capping condition of the region in general belongs to the Class II area. In the Heiloumen structural region at the southern side of the Muziya structural belt and on the Huangcaoping hidden structure at the western pinching end of the Wenfeng structural belt, the structure form is stable, wide, and gentle, dominated by wide and gentle anticline. There is a relatively low development degree of faults in this region, larger than 5 km from the surfaced large fault. Moreover, the degree of formation uplift and denudation is rather small and the distance from the denudation zone of the shale target layer is more than 10 km. The Upper Triassic to Middle–Lower Jurassic strata are mainly exposed at the surface, and the capping condition of the region is good, belonging to the Class I area.

Structural preservation modes for shale gas enrichment

Through the comprehensive analysis of the structural preservation conditions of shale gas enrichment and accumulation in the Wufeng–Longmaxi Formation in the Wuxi area, the different structural preservation characteristics in different structural belts and their differences are very obvious.

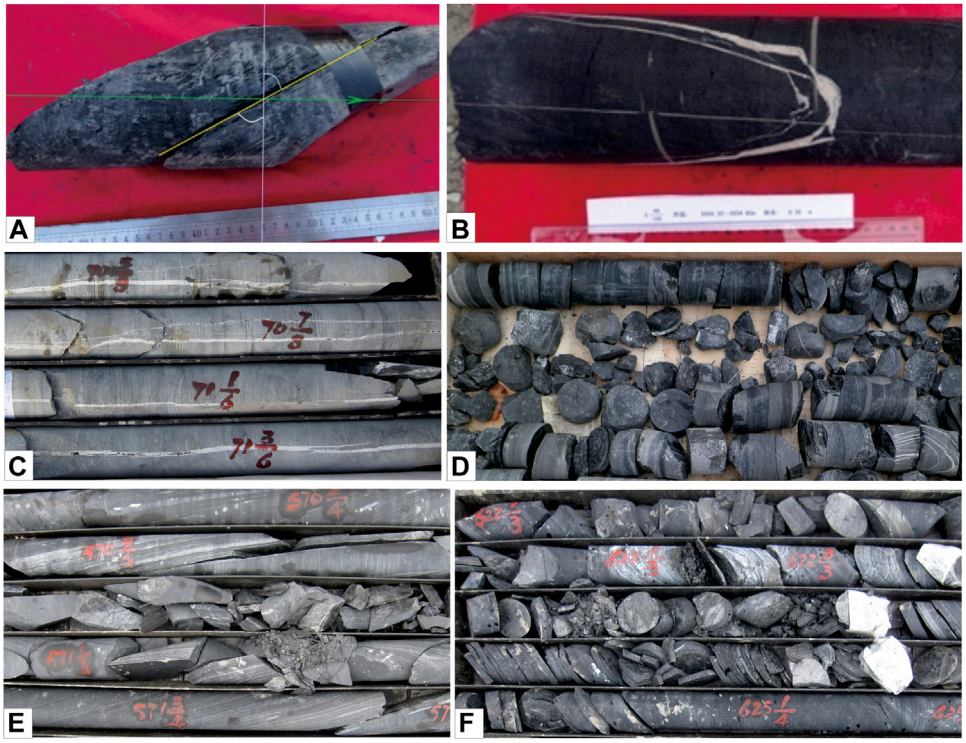

FIGURE 8
Typical drilling core photographs of the Longmaxi Formation. **(A)** X203 well, 3,553.50 m, with high-angle strata, and the red line direction is the stratum layer; **(B)** X203 well, 3,586.75 m, with high-angle fractures, and the fracture surface is filled with calcite veins; **(C)** WQ1 well, 258.35–261.20 m, with vertical fractures, and the fracture surface is filled with calcite veins; **(D)** WQ1 well, 343.75–348.62 m, with seriously broken strata and the core is broken into pieces; **(E)** WQ2 well, 1,174.50–1,177.64 m, with high-angle strata and light sandy lamina; **(F)** WQ2 well, 1,192.71–1,296.85 m, with a seriously crumpled and deformed strata, and the rock core is broken into pieces along the bedding plane.

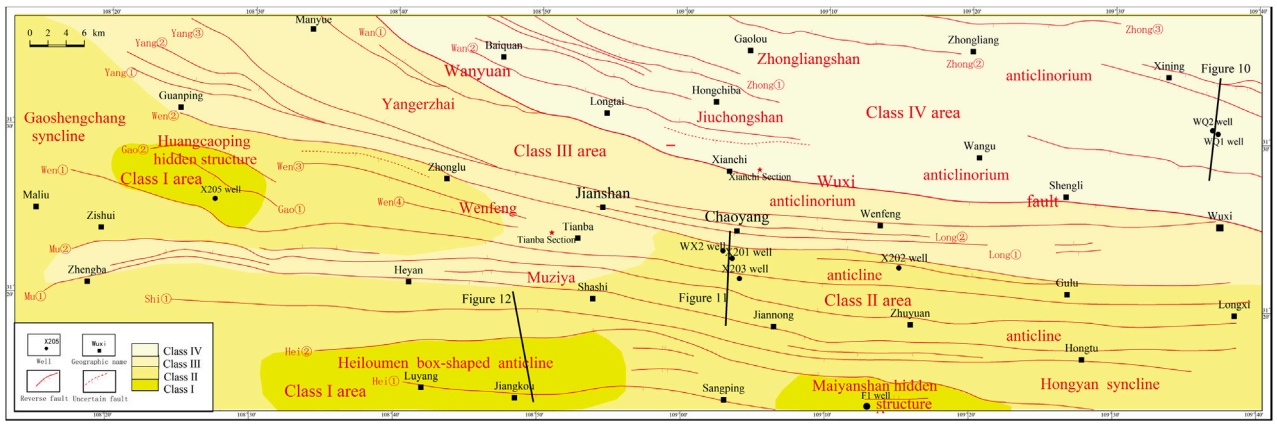

FIGURE 9
Partitioning evaluation of structural preservation conditions of shale gas enrichment and accumulation in the Wufeng–Longmaxi Formation.

TABLE 1 Grading evaluation of structural preservation conditions of shale gas enrichment and accumulation in the Wufeng–Longmaxi Formation.

Preservation type	Preservation condition grade	Structural location	Structural style	Development degree of faulted fractures	Uplift and denudation	Capping condition of the surfaced strata	Structural deformation	Evaluation of the preservation condition
	Class I area	Huangcaoping hidden structural belt and Heiloumen structural belt	Wide and gentle anticline	Relatively low development degree of faulted fractures larger than 5 km from the surfaced large fault	Weak formation uplift and denudation and the distance from the denudation zone of shale target layer more than 10 km	Middle–Upper Triassic to Lower–Middle Jurassic	Weak and stable	Good
Complex structural preservation of the basin margin	Class II area	Southern side of the Wenfeng structural belt and Muziya structural belt	Asymmetric fold and open fold	Relatively well-developed high-angle fractures larger than 3 km from the surfaced large fault	Relatively weak formation uplift and denudation and the distance from the denudation zone of shale target layer more than 5 km	Triassic	General	General
	Class III area	Yangerzhai structural belt, Tianba anticline, and the western pinching end of the Muziya structural belt	Anticlinoria and closed secondary folds	Relatively well-developed faulted fractures, with locally large faults	Rather strong formation uplift and denudation and the Lower Silurian denuded locally	Permian to Lower Triassic	Strong	Poor
	Class IV area	Jiuchongshan structural belt and Zhongliangshan structural belt	Compound fold	Cell developed surfaced and underground faulted fractures	Strong formation uplift and denudation and extensively exposed shale target layer of the Lower Silurian, with high-angle fractures	Upper Cambrian to Lower Triassic	Strong	Very poor

10.3389/feart.2022.1032597

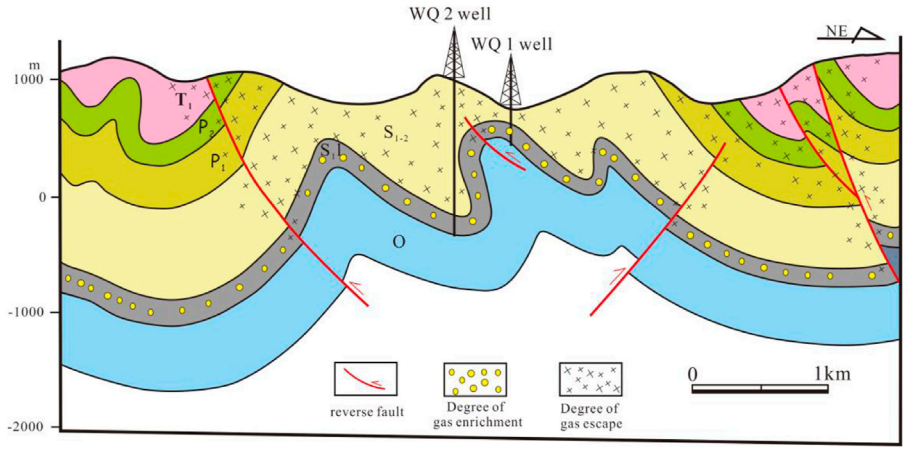

FIGURE 10
Structural preservation mode of shale gas enrichment and accumulation in the Wufeng–Longmaxi Formation-lost destruction type.

According to the differences in the structural styles and deformation intensity in the area, there are three structural preservation modes of shale gas enrichment and accumulation in the Wufeng–Longmaxi Formation. Its specific characteristics are as follows.

Lost destruction type

The lost destruction type focuses on the southern Dabashan ramp fault-fold belt with strong structural transformation. Intense structural compression deformation and formation uplift and denudation lead to complex fold changes in the Wuxi area, such as the development of faults and fractures, so that the formation capping condition becomes worse (Figure 10). The shale gas in the target layer of the Lower Silurian Longmaxi Formation has a large amount of it escape towards the superficial layers along the faulted fracture zones; especially the development of the enormous fault is directly connected with the surface. In most of the belts, the surface is dominated by the Lower Silurian and even the target shale layer is denuded. The direct release of overlying pressure leads to the vertical loss of shale gas, resulting in a low enrichment degree of shale gas in the target layer and the destruction of effective shale gas accumulation.

Lost residual type

The lost residual type mainly develops on the southern Dabashan frontal fold belt with weak structural transformation. The surfaced faults and fractures are of the non-development type, and the Permian to Triassic strata are exposed, which have certain capping conditions, but the deformation of underground folds is very complex and thrust faults are well-developed in this belt (Figure 11). The shale gas escapes to the superficial layers along the structurally weak regions such as faulted fracture channels. Even so, the most of shale adsorbed gas is effectively preserved due to the unique compactness and adsorption of the black shale interval itself. Although good gas-bearing properties have been found in some drilling wells because of the massive loss of free gas, which gives rise to lower formation pressure and insufficient energy; it is difficult to achieve commercial production with the scale of adsorbed gas. For example, the average gas content of the shale target layer in the X202 well is 2.07 m^3/t, but the formation pressure coefficient is only 0.67 and no industrial gas flow is obtained.

Trap preservation type

The trap preservation type mainly manifests in the Heiloumen structural belt and Huangcaoping hidden structural belt near the interior of the Sichuan Basin with stable, wide, and gentle structural forms and the weak development of faulted fractures. The structural style in this region is dominated by wide-gentle fold and suspected box-shaped fold, and the Triassic to Jurassic strata are exposed at the surface with good capping conditions (Figure 12). The overlying capping layers in the two structural belts are rather thick, especially the Middle Triassic gypsum-salt rock layer has played a very good capping effect on the shale gas reservoir. Although there are also some faults developed in the deep underground, they are only developed in the Lower Triassic strata, so the loss of shale gas is very limited and the mode is more

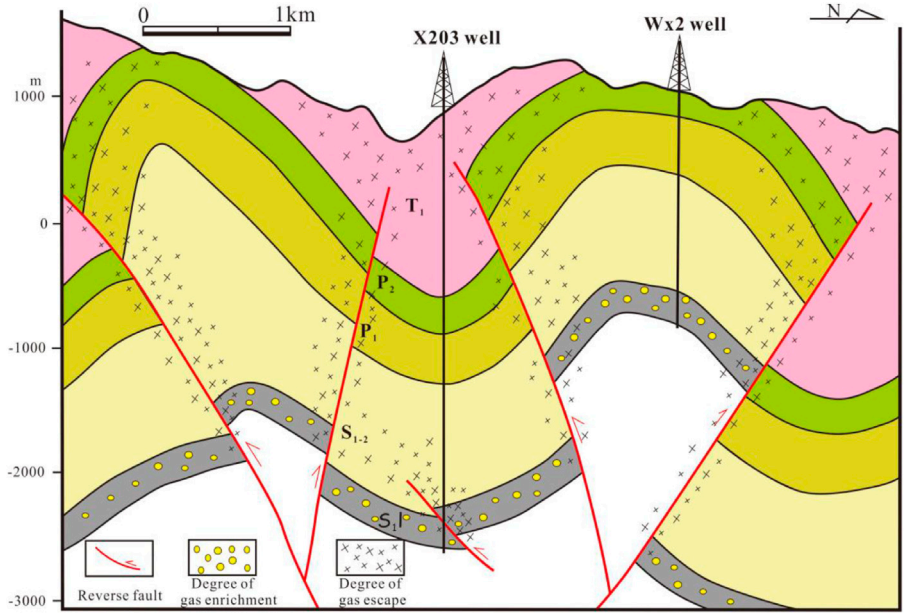

FIGURE 11
Structural preservation mode of shale gas enrichment and accumulation in the Wufeng–Longmaxi Formation-lost residual type.

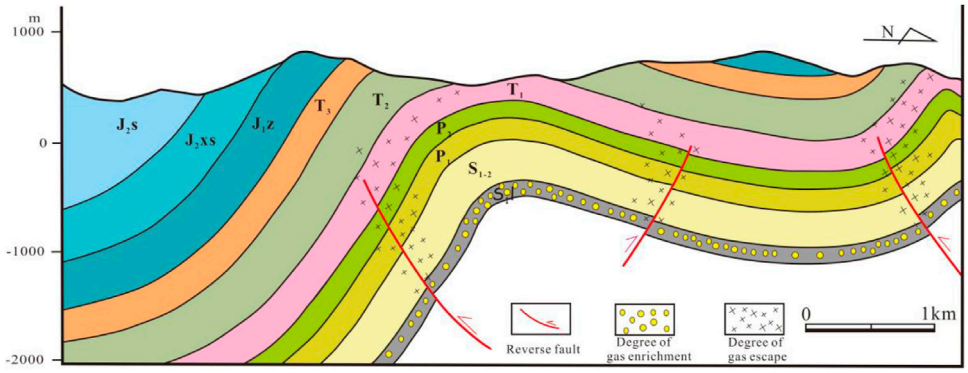

FIGURE 12
Structural preservation mode of shale gas enrichment and accumulation in the Wufeng–Longmaxi Formation-trap preservation type.

conducive to the enrichment, accumulation, and preservation of shale gas in the high structural points.

Conclusion

(1) The Wuxi area lies in the transition zone between the Dabashan thrust-fold belt and the Sichuan Basin, belonging to a superimposed transformation area with strong structural deformation. The area can be divided into seven structural belts, including the Heiloumen structural belt, Muziya structural belt, Wenfeng structural belt, Huangcaoping hidden structural belt, Yangerzhai structural belt, Jiuchongshan structural belt, and Zhongliangshan structural belt.

(2) The macroscopic preservation type of shale gas in the Wufeng–Longmaxi Formation of the Wuxi area belongs to the complex structural preservation of the basin

margin. The structural preservation conditions of shale gas enrichment and accumulation in the Wuxi area are divided into four grades, such as the good Class I area, the general Class II area, the poor Class III area, and the very poor Class IV area. Among them, the Heiloumen structural zone and Huangcaoping buried structural zone near the Sichuan Basin have good preservation conditions and are classified as good Class I preservation areas.

(3) Three structural preservation modes of shale gas in the Wuxi area have been identified, including lost destruction type, lost residual type, and trap preservation type. The trap preservation type is more conducive to the preservation of shale gas, which is the most favorable structural mode for shale gas exploration (Wang et al., 2006; Liu and Wang, 2016).

Data availability statement

The original contributions presented in the study are included in the article/Supplementary Material; further inquiries can be directed to the corresponding author.

Author contributions

WL and TL: validation, writing—original draft, and investigation. CY, SW, ZZ, and JL: visualization. CY, XT, CY, WW, YZ, and JL: conceptualization, methodology, supervision, writing—review and editing, project administration, and funding acquisition.

Funding

The research was financially supported by the projects of the Chongqing Municipal Bureau of Planning and Natural Resources (KJ-2021026), the Natural Science Foundation of Chongqing (cstc2021jcyj-msxmX0624 and CSTB2022NSCQ-MSX1221), the Science and Technology Department of Sichuan Province (2021YFH0048), and the project funded by the China Postdoctoral Science Foundation (2020M683253 and 2022T150774).

Conflict of interest

Authors WL, TL, CS, and ZZ were employed by Chongqing Shale Gas Exploration And Development Company Limited.

The remaining authors declare that the research was conducted in the absence of any commercial or financial relationships that could be construed as a potential conflict of interest.

Publisher's note

References

Chen, Q., Zhang, J. C., Tang, X., Li, W., and Li, Z. (2016). Relationship between pore type and pore size of marine shale: An example from the Sinian–Cambrian formation, upper Yangtze region, South China. *Int. J. Coal Geol.* 158, 13–28. doi:10.1016/j.coal.2016.03.001

Feng, Z. Q., Dong, D. Z., Tian, J. Q., Qiu, Z., Wu, W., and Zhang, C. (2018). Geochemical characteristics of Longmaxi formation shale gas in the weiyuan area, Sichuan Basin, China. *J. Pet. Sci. Eng.* 167, 538–548. doi:10.1016/j.petrol.2018.04.030

Hao, F., Zou, H. Y., and Lu, Y. C. (2013). Mechanisms of shale gas storage: Implications for shale gas exploration in China. *Am. Assoc. Pet. Geol. Bull.* 97 (8), 1325–1346. doi:10.1306/02141312091

Jin, Z. J., Nie, H. K., Liu, Q. Y., Zhao, J., and Jiang, T. (2018). Source and seal coupling mechanism for shale gas enrichment in upper ordovician wufeng formation-lower silurian Longmaxi formation in Sichuan Basin and its periphery. *Mar. Petroleum Geol.* 97, 78–93. doi:10.1016/j.marpetgeo.2018.06.009

Li, S. Z., Zhou, Z., Nie, H. K., Zhang, L. F., Song, T., Tao, S., et al. (2022). Distribution characteristics, exploration & development, geological theories research progress and exploration directions of shale gas in China. *China Geol.* 5 (1), 110–135. doi:10.1016/S2096-5192(22)00090-8

Liang, F., Bai, W. H., Zou, C. N., Wang, H., Wu, J., Ma, C., et al. (2015). Shale gas enrichment pattern and exploration significance of well wuxi-2 in northeast chongqing, NE Sichuan Basin. *Petroleum Explor. Dev.* 43 (3), 386–394. doi:10.1016/s1876-3804(16)30045-3

Liu, Y. F., Qiu, N. S., Xie, Z. Y., Yao, Q., and Zhu, C. (2016). Overpressure compartments in the central paleo-uplift, Sichuan Basin, southwest China. *Am. Assoc. Pet. Geol. Bull.* 100 (5), 867–888. doi:10.1306/02101614037

Liu, J., Yao, Y. B., Liu, D. M., and Elsworth, D. (2017). Experimental evaluation of CO_2 enhanced recovery of adsorbed-gas from shale. *Int. J. Coal Geol.* 179, 211–218. doi:10.1016/j.coal.2017.06.006

Liu, Q. Y., Jin, Z. J., Wang, X. F., Yi, J., Meng, Q., Wu, X., et al. (2018). Distinguishing kerogen and oil cracked shale gas using H, C-isotopic fractionation of alkane gases. *Mar. Petroleum Geol.* 91, 350–362. doi:10.1016/j.marpetgeo.2018.01.006

Liu, J., Xie, L. Z., He, B., Zhao, P., and Ding, H. Y. (2021a). Performance of free gases during the recovery enhancement of shale gas by CO_2 injection: A case study on the depleted wufeng–longmaxi shale in northeastern Sichuan Basin, China. *Pet. Sci.* 18 (2), 530–545. doi:10.1007/s12182-020-00533-y

Liu, J., Xie, L. Z., He, B., Gan, Q., and Zhao, P. (2021b). Influence of anisotropic and heterogeneous permeability coupled with *in-situ* stress on CO_2 sequestration with simultaneous enhanced gas recovery in shale: Quantitative modeling and case study. *Int. J. Greenh. Gas Control* 104, 103208. doi:10.1016/j.ijggc.2020.103208

Liu, N. Z., and Wang, G. Y. (2016). Shale gas sweet spot identification and precise geosteering drilling in Weiyuan Block of Sichuan Basin, SW China. *Petroleum Explor. Dev.* 43 (6), 1067–1075. doi:10.1016/s1876-3804(16)30124-0

Ma, X. H., Xie, J., Yong, R., and Zhu, Y. (2020). Geological characteristics and high production control factors of shale gas reservoirs in Silurian Longmaxi Formation, southern Sichuan Basin, SW China. *Petroleum Explor. Dev.* 47 (5), 901–915. doi:10.1016/s1876-3804(20)60105-7

Nie, H. K., Jin, Z. J., Sun, C. X., He, Z., Liu, G., and Liu, Q. (2019). Organic matter types of the wufeng and Longmaxi formations in the Sichuan Basin, south China: Implications for the formation of organic matter pores. *Energy fuels.* 33 (9), 8076–8100. doi:10.1021/acs.energyfuels.9b01453

Nie, H. K., Chen, Q., Zhang, G. R., Sun, C., Wang, P., and Lu, Z. (2021a). An overview of the characteristic of typical Wufeng-Longmaxi shale gas fields in the Sichuan Basin, China. *Nat. Gas. Ind. B* 8 (3), 217–230. doi:10.1016/j.ngib.2021.04.001

Nie, H. K., He, Z. L., Liu, G. X., Du, W., Wang, R., and Zhang, G. (2021b). Genetic mechanism of high-quality shale gas reservoirs in the Wufeng-Longmaxi Fms in the sichuan basin. *Nat. Gas. Ind. B* 8 (1), 24–34. doi:10.1016/j.ngib.2020.06.002

Potter, C. J. (2018). Paleozoic shale gas resources in the Sichuan Basin, China. *Am. Assoc. Pet. Geol. Bull.* 102 (6), 987–1009. doi:10.1306/0828171607817072

Shi, Z. S., Qiu, Z., Dong, D. Z., Lu, B., Liang, P., and Zhang, M. (2018). Laminae characteristics of gas-bearing shale fine-grained sediment of the silurian Longmaxi formation of well Wuxi 2 in Sichuan Basin, SW China. *Petroleum Explor. Dev.* 45 (2), 339–348. (in Chinese with the English abstract). doi:10.1016/S1876-3804(18)30040-5

Sun, C. X., Nie, H. K., Dang, W., Chen, Q., Zhang, G., Li, W., et al. (2021). Shale gas exploration and development in China: Current status, geological challenges, and future directions. *Energy fuels.* 35 (8), 6359–6379. doi:10.1021/acs.energyfuels.0c04131

Tang, J. G., Li, Y., Wang, K. M., and Qi, Z. Y. (2015). Comprehensive evaluation of effective preservation zone of Longmaxi Formation shale gas in the Southeast Sichuan Basin. *Nat. Gas. Ind.* 35 (5), 15–23. (in Chinese with the English abstract).

Tang, L., Song, Y., Jiang, S., Li, L., Li, Z., Li, Q., et al. (2020). Sealing mechanism of the roof and floor for the wufeng-longmaxi shale gas in the southern Sichuan Basin. *Energy fuels.* 34 (6), 6999–7018. doi:10.1021/acs.energyfuels.0c00983

Wang, Z. C., Zhao, W. Z., Xu, A. N., Li, D. H., Cui, Y., et al. (2006). Structure styles and their defoimationmechanigns of Dabashan foreland thrust belt in the North or Sichuan basin. *Geoscience* 20 (3), 429–435. (in Chinese with the English abstract).

Wang, P. W., Zou, C., Li, X. J., Jiang, L., Li, J., Mei, J., et al. (2018). Main geological controlling factors of shale gas enrichment and high yield in Zhaotong demonstration area. *Acta Pet. Sin.* 39 (7), 744–753. doi:10.7623/syxb201807002

Wang, C., Zhang, B. Q., Hu, Q. H., Shu, Z., Sun, M., and Bao, H. (2019). Laminae characteristics and influence on shale gas reservoir quality of lower silurian Longmaxi formation in the jiaoshiba area of the Sichuan Basin, China. *Mar. Petroleum Geol.* 109, 839–851. doi:10.1016/j.marpetgeo.2019.06.022

Wang, W., Li, D. H., Cheng, L. J., Zhang, Y., Wang, J., Zhang, Z., et al. (2022). Petrophysical characterization and gas accumulation of wufeng-longmaxi shale reservoir in eastern margin of Sichuan Basin, SW China. *Geofluids* 2022, 1–14. doi:10.1155/2022/6877500

Wu, J., Liang, F., Lin, W., Bai, W., Ma, C., Yu, R., et al. (2017). Reservoirs characteristics and gas bearing capacity of Wufeng-Longmaxi Formation shale in Well WX-2, northeast Chongqing area. *Acta Pet. Sin.* 38 (5), 512–524. doi:10.7623/syxb201705004

Wu, J., Zhou, W., Sun, S. S., Zhou, S., and Shi, Z. (2019). Graptolite-derived organic matter and pore characteristics in the Wufeng-Longmaxi black shale of the Sichuan Basin and its periphery. *Acta Geol. sinica-. Engl. Ed.* 93 (4), 982–995. doi:10.1111/1755-6724.13860

Xie, J. (2018). Rapid shale gas development accelerated by the progress in key technologies: A case study of the changning-weiyuan national shale gas demonstration zone. *Nat. Gas. Ind. B* 5 (4), 283–292. doi:10.1016/j.ngib.2017.12.007

Yang, S. C., Hu, W. X., Wang, X. L., Jiang, B., Yao, S., Sun, F., et al. (2019). Duration, evolution, and implications of volcanic activity across the Ordovician–Silurian transition in the Lower Yangtze region, South China. *Earth Planet. Sci. Lett.* 518, 13–25. doi:10.1016/j.epsl.2019.04.020

Yu, C., Zeng, C. L., Zhou, X., Nie, H., and Yu, Z. (2018). Tectonic preservation unit division and zoning evaluation of shale gas in the Lower Cambrian of Dabashan thrust belt. *Nat. Gas. Geosci.* 29 (6), 853–865. (in Chinese with the English abstract). doi:10.11764/j.issn.1672-1926.2018.05.016

Zhang, Y. Y., He, Z. L., Lu, S. F., Jiang, S., Xiao, D., Long, S., et al. (2020). Characteristics of microorganisms and origin of organic matter in wufeng formation and Longmaxi formation in Sichuan Basin, south China. *Mar. Petroleum Geol.* 111, 363–374. doi:10.1016/j.marpetgeo.2019.06.054

Zhao, P., Xie, L. Z., Fan, Z. C., Deng, L., and Liu, J. (2021). Mutual interference of layer plane and natural fracture in the failure behavior of shale and the mechanism investigation. *Pet. Sci.* 18 (2), 618–640. doi:10.1007/s12182-020-00510-5

Zhao, P., He, B., Zhang, B., and Liu, J. (2022). Porosity of gas shale: Is the NMR-based measurement reliable? *Petroleum Sci.* 19 (2), 509–517. doi:10.1016/j.petsci.2021.12.013

frontiers | Frontiers in Earth Science

TYPE Original Research
PUBLISHED 10 January 2023
DOI 10.3389/feart.2022.1043148

OPEN ACCESS

EDITED BY
Shuai Yin,
Xi'an Shiyou University, China

REVIEWED BY
Da Gao,
Yangtze University, China
Haitao Sun,
China University of Petroleum, China

*CORRESPONDENCE
Haizhou Qu,
quhaizhou@swpu.edu.cn

SPECIALTY SECTION
This article was submitted to Structural Geology and Tectonics, a section of the journal Frontiers in Earth Science

RECEIVED 13 September 2022
ACCEPTED 30 September 2022
PUBLISHED 10 January 2023

CITATION
Qu H, Yan Z, Zheng C, Xu W, He F, Sun Q, Zhang X and Li M (2023), Quantitative characterization and origin of differences in pore parameter distribution: A case study of the lower cambrian longwangmiao formation in the gaoshiti area of central Sichuan Basin.
Front. Earth Sci. 10:1043148.
doi: 10.3389/feart.2022.1043148

Quantitative characterization and origin of differences in pore parameter distribution: A case study of the lower cambrian longwangmiao formation in the gaoshiti area of central Sichuan Basin

Haizhou Qu[1,2]*, Zanxu Yan[1,2], Chao Zheng[3], Wei Xu[3], Fuwei He[3], Qimeng Sun[3], Xinyu Zhang[1,2] and Minxing Li[1,2]

[1]State Key Lab of Oil and Gas Reservoir Geology and Exploitation, Southwest Petroleum University, Chengdu, Sichuan, China, [2]School of Geoscience and Technology, Southwest Petroleum University, Chengdu, Sichuan, China, [3]Research Institute of Exploration and Development of PetroChina Southwest Oil and Gasfield Company, Chengdu, Sichuan, China

The research on the developmental characteristics and evolution process of pores in dolomite reservoirs is a hot spot in petroleum geology. In this paper, taking the dolomite reservoirs of the Longwangmiao Formation in the Gaoshiti area as an example, the differential distribution and evolution of pore parameters have been systematically studied combined with downhole cores, logging, cast thin sections, and scanning electron microscope data. We used statistical methods and image analysis techniques to quantitatively characterize the pore distribution of the Longwangmiao Formation in the study area. Moreover, the factors controlling the distribution of pores in the dolomite of the Longwangmiao Formation were identified, namely, lithology, sedimentary facies and diagenesis. Finally, the evolution mode of pores of the Longwangmiao Formation was constructed. The results show that the main types of pores developed in the Longwangmiao Formation in the study area include intergranular and intragranular dissolved pores, intercrystalline dissolved pores and mold pores. Among them, the intergranular dissolved pores are the main pore type. The pores with surface porosity higher than 0.5% in the Long 2 Member in the study area account for 46% of the total pores, while those in the Long 1 Member account for 25.5%. Therefore, the degree of development of pores in the Long 2 Member is better than the Long 1 Member. In addition, the granular dolomite in the grain shoal facies is favorable for the formation of large-scale pores, and the oolitic dolomite is the most favorable reservoir type. The most favorable factors for the development of pores are the atmospheric freshwater dissolution and dolomitization in the quasi-contemporaneous period; the former caused the formation of a large number of intergranular dissolved pores, while the dolomitized particles and their ring-edge cements in the latter promoted the retention of residual intergranular dissolved pores. The dissolution, dolomite cementation and hydrothermal action in the burial stage promoted the reformation of pores.

KEYWORDS

gaoshiti area, Longwangmiao formation, quantitative characterization of pore parameters, pore distribution, diagenesis, pore evolution model

1 Introduction

In recent years, breakthroughs have been made in marine carbonate oil and gas exploration in the Sichuan Basin of China. For example, the largest marine carbonate monolithic gas reservoir in China, the Anyue Gas Field, has been discovered in the Gaomo area (Katz et al., 2021; Niu et al., 2022). Fine and quantitative characterization of pore structures is the key to study reservoir performance in gas reservoirs. This research mainly focuses on the type, shape and distribution of pores, pore structures and pore connectivities, as well as the qualitative and quantitative studies on the genesis and evolution mode of pores (Kun et al., 2014). Techniques for qualitative characterization of pores generally include cast thin sections, scanning electron microscopy, cathodoluminescence, and X-ray diffraction analysis (Franziska et al., 2021; Xiangchun et al., 2021; Jiang et al., 2022). They can be used to directly observe and describe the types and morphological characteristics of pores. However, for the quantitative characterization of pores, it generally needs to combine high-pressure mercury intrusion, gas adsorption, nuclear magnetic resonance, CT, image analysis software, etc. (Qiang et al., 2021; Cheng et al., 2022) to finely describe the distribution characteristics of pores with full pore size (Fenshu et al., 1995; Nan, 2020; Qiang et al., 2021; Vafaie et al., 2021).

At present, the research on the Lower Cambrian carbonate oil and gas reservoirs in the Sichuan Basin mainly focuses on the Longwangmiao Formation (Jinhu et al., 2014; Xi et al., 2017). According to previous studies, the shoal facies reservoirs developed in the Longwangmiao Formation are mainly hosted in sandy dolomite and oolitic dolomite, and the reservoir space is dominated by pores, caves and fractures of secondary origin, and its physical properties are characterized by medium-low porosity and low permeability (Da et al., 2022). However, there are still some problems that need to be improved: 1) Existing studies have ignored lithology and sedimentary facies as the main controlling factors of reservoirs (Zitong, 2007); 2) The effects of diagenesis, such as dissolution, dolomitization and dolomite cementation, on the development and evolution of reservoir pores at different diagenetic stages have not been elucidated (Da et al., 2021; Xing et al., 2021). In this paper, taking the dolomite reservoirs of the Longwangmiao Formation in the Gaoshiti area as an example, the differential distribution and evolution of pore parameters have been systematically studied combined with downhole cores, logging, cast thin sections, scanning electron microscope data, statistical methods and image analysis techniques. This study can provide new ideas for hydrocarbon exploration in the dolomite reservoirs of the Longwangmiao Formation.

2 Geological background

The study area is located in the Gaoshiti area in the central part of the Sichuan Basin. Its geographical location is located in the Ziyang City and the Tongnan County (Guoqi et al., 2015). This area belongs to the Leshan-Longnüsi paleo-uplift area in the central part of the Sichuan Basin (Caineng et al., 2014; Roberts, 2018; Yang et al., 2022) (Figure 1).

The Lower Cambrian Longwangmiao Formation in the study area are in integrated contact with the overlying Gaotai Formation and the underlying Canglangpu Formation. From bottom to top, the Longwangmiao Formation is divided into the Long 1 and Long 2 Members. Sandy dolomite, mud (powder) crystalline dolomite, clot dolomite and oolitic dolomite are mainly developed in the Long 1 Member; while the sand dolomite and oolitic dolomite are mainly developed in the Long 2 Member (Xuefei et al., 2015; Benjian et al., 2018). The strata of the Longwangmiao Formation in the study area show a gradually thickening trend from northwest to southeast. The Longwangmiao Formation in this area belongs to the limited platform sediments. The lower part of the Long 1 Member is the thick intra-platform shoal and the inter-shoal sea sediment, and the upper part is shallower and has a tidal flat environment. The lower part of the Long 2 Member is dominated by sandy shoal-oolitic shoal, inter-shoal sea-tidal flat-intra-platform shoal, and tidal flat deposits are mainly developed in the upper part (Genshun et al., 2013; Weiqiang et al., 2022). Pores are mostly developed in the granular dolomite in the upper part of Long 1 Member and the middle and upper part of Long 2 Member, and the pore types are mainly secondary pores (Choquette and Pray, 1974; Lucia, 1995). At present, it is believed that the distribution of Longwangmiao Formation reservoirs is relatively scattered, and most of them are concentrated in the Gaoshi 6~Gaoshi 102 well area in the middle of the work area (Anjiang et al., 2017; Hongliu et al., 2018).

3 Methods

In this paper, taking the Cambrian Longwangmiao Formation dolomite in the Gaoshiti area as an example, we carried out core observations, casting thin sections and scanning electron microscope experiments. Cores from the Longwangmiao Formation with a total of 345 m from eight wells in the study area were used for core observations. Cast thin sections were used for observations under polarized light microscopy. Its purpose is to obtain the lithology, pore types, pore size, and surface porosity parameters of pores or cavities. A total of 367 cast thin sections were used for the extraction of pore

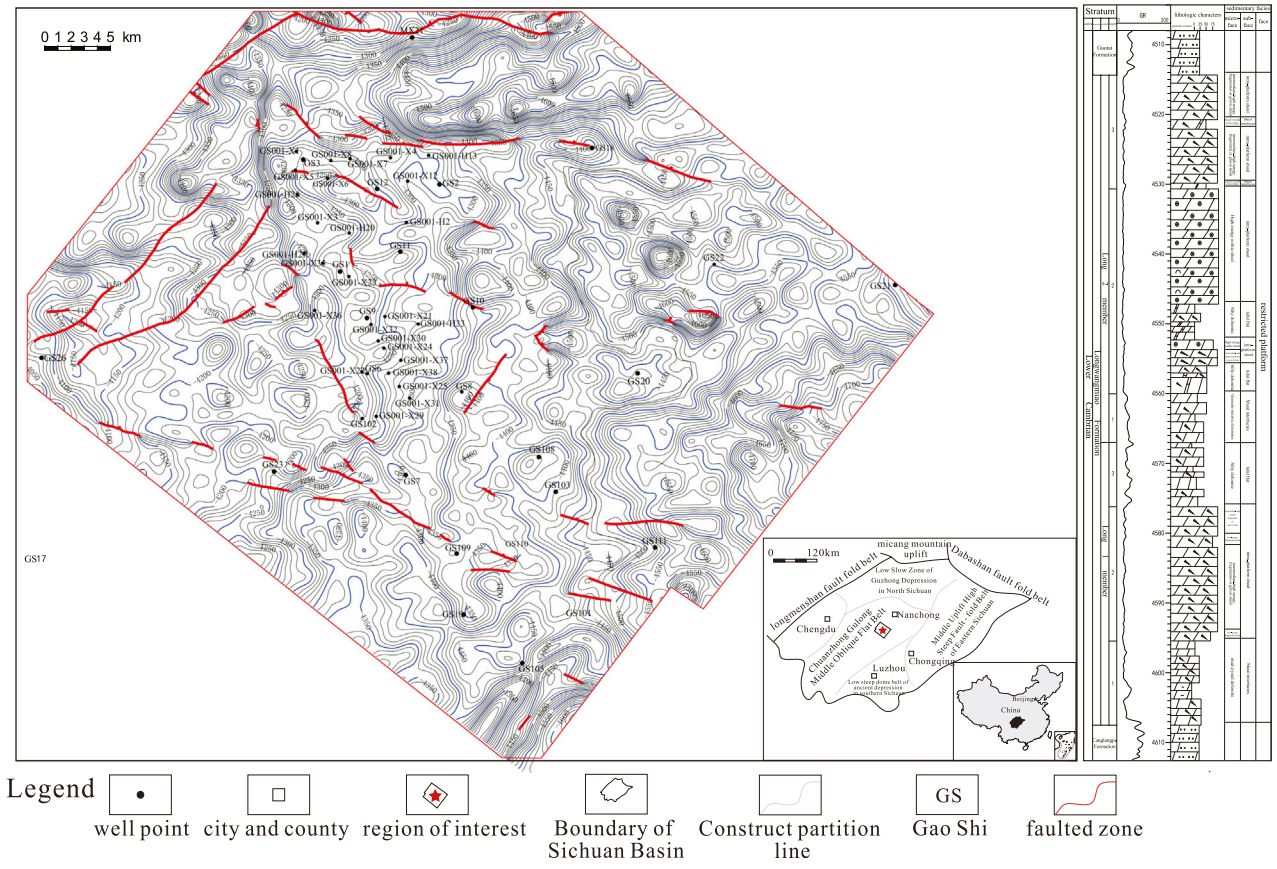

FIGURE 1
Location, structure, well distribution and division of stratigraphic units in the study area.

parameters. The differences in the development and distribution of pores in the Longwangmiao Formation of different wells are compared by combining the constraints of stratigraphy, lithology, natural gamma, resistivity and sedimentary facies type.

The statistical methods and image analysis techniques were used to quantitatively characterize the pore distribution of the Longwangmiao Formation in the study area. Moreover, the factors controlling the distribution of pores in the dolomite of the Longwangmiao Formation were identified, namely, lithology, sedimentary facies and diagenesis. Finally, the evolution mode of pores of the Longwangmiao Formation was constructed.

4 Results

4.1 Pore types

The main types of pores developed in the Longwangmiao Formation in the study area include intergranular dissolved pores, intragranular dissolved pores, intercrystalline dissolved pores, intercrystalline pores, mold pores, and dissolved pores/cavities.

4.1.1 Intergranular dissolved pores

Intergranular dissolved pores are mainly developed in granular dolomite such as sandy dolomite and oolitic dolomite. This type of pores are usually irregular and curved pores with scattered distribution and good pore connectivity, and the pore diameters are distributed between 0.01 mm and 1 mm (Figures 2A,B). Under the microscope, the intergranular dissolved pores formed in the later stage are mostly half or fully filled with asphalt and dolomite.

4.1.2 Intragranular dissolved pores

Intragranular dissolved pores are irregular in shape (curved edges) and mostly exist in the isolated form. Moreover, the isolated intragranular dissolved pores and intergranular dissolved pores with poor connectivity are associated with each other. Together, they constitute the storage space of granular dolomite (Figure 2B). The pore diameter of intragranular dissolved pores is mainly between 0.01 and 0.5 mm, and some of the pores are semi-filled with bright crystal dolomite or asphalt.

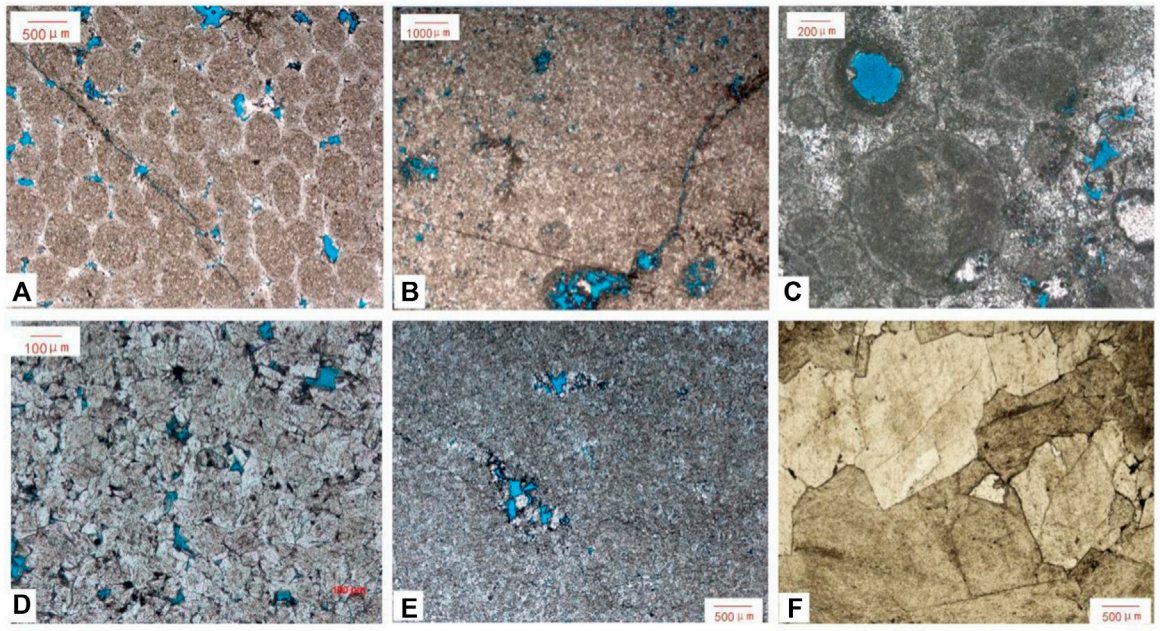

FIGURE 2
Development characteristics of different pore types in the Longwangmiao Formation in the study area. **(A)** Intergranular dissolved pores, oolitic dolomite, Well GS6, 4546.25, single polarized light; **(B)** Intergranular and intragranular dissolved pores, sandy dolomite, 4662.5 m, Well GS23, single polarized light; **(C)** Mold pore, sand dolomite, well GS7, 4635.55 m, single polarized light; **(D)** Intercrystalline pores and intercrystalline dissolved pores, sugar-like fine-crystalline dolomite, Well GS11, 4571.57 m, single polarized light; **(E)** Intercrystalline dissolved pores, powder crystal dolomite, Well GS11, 4584.22 m, single polarized light; **(F)** Intracrystalline dissolved pores, giant crystal dolomite, well MX12, 4637.41–4637.84 m, single polarized light.

4.1.3 Mold pores

Mold pores are usually developed in granular dolomite, and their shape and size depend on the shape of the particles and the degree of dissolution. The mold pores are generally regular oval or circular, and the maximum diameter of the pores does not exceed 0.2 mm. This type of pores are mostly distributed in isolated form, with extremely poor connectivity, and semi-filled asphalt is occasionally seen (Figure 2C).

4.1.4 Intercrystalline pores

Intercrystalline pores mainly appear in sugar-like dolomite whose original rock structures have been destroyed. They have straight boundaries and are mostly developed between dolomite crystals. The pore diameter is mostly less than 0.5 mm. It was observed under the microscope that the larger the dolomite crystal, the higher the degree of eumorphism, and the more developed the intercrystalline pores (Figure 2D).

4.1.5 Intergranular dissolved pores

Intercrystalline dissolved pores coexist with intercrystalline pores. The straight boundaries are partially eroded into irregular curved or microdentate morphologies. In addition, the pore diameter is mostly less than 0.5 mm, and the surface porosity is usually between 0.1% and 0.5% (Figure 2E). Microscopic observation showed that the intergranular dissolved pores were mostly half or fully filled with asphalt.

4.1.6 Intracrystalline dissolved pores

Intragranular dissolved pores are generally isolated on the surface of dolomite crystals. Its morphology is relatively regular and the pores are not connected (Figure 2F). Most of the intragranular dissolved pores have a pore size ranging from 1.5 μm to 4 μm. However, some of this type of pores can also be observed with naked eyes. Under the scanning electron microscope, it was observed that some dissolved pores in the crystals were half filled with nanocrystals, so that the porosity was reduced to a certain extent.

4.2 Longitudinal pore distribution characteristics

The pores of the Longwangmiao Formation in the study area are well developed in the Long 2 Member. They are mainly developed in the oolitic dolomite and sandy dolomite of granular shoal facies, and the pore types are mainly intergranular dissolved pores. From bottom to top, the content of intragranular dissolved pores decreases, the content of intergranular dissolved pores increases,

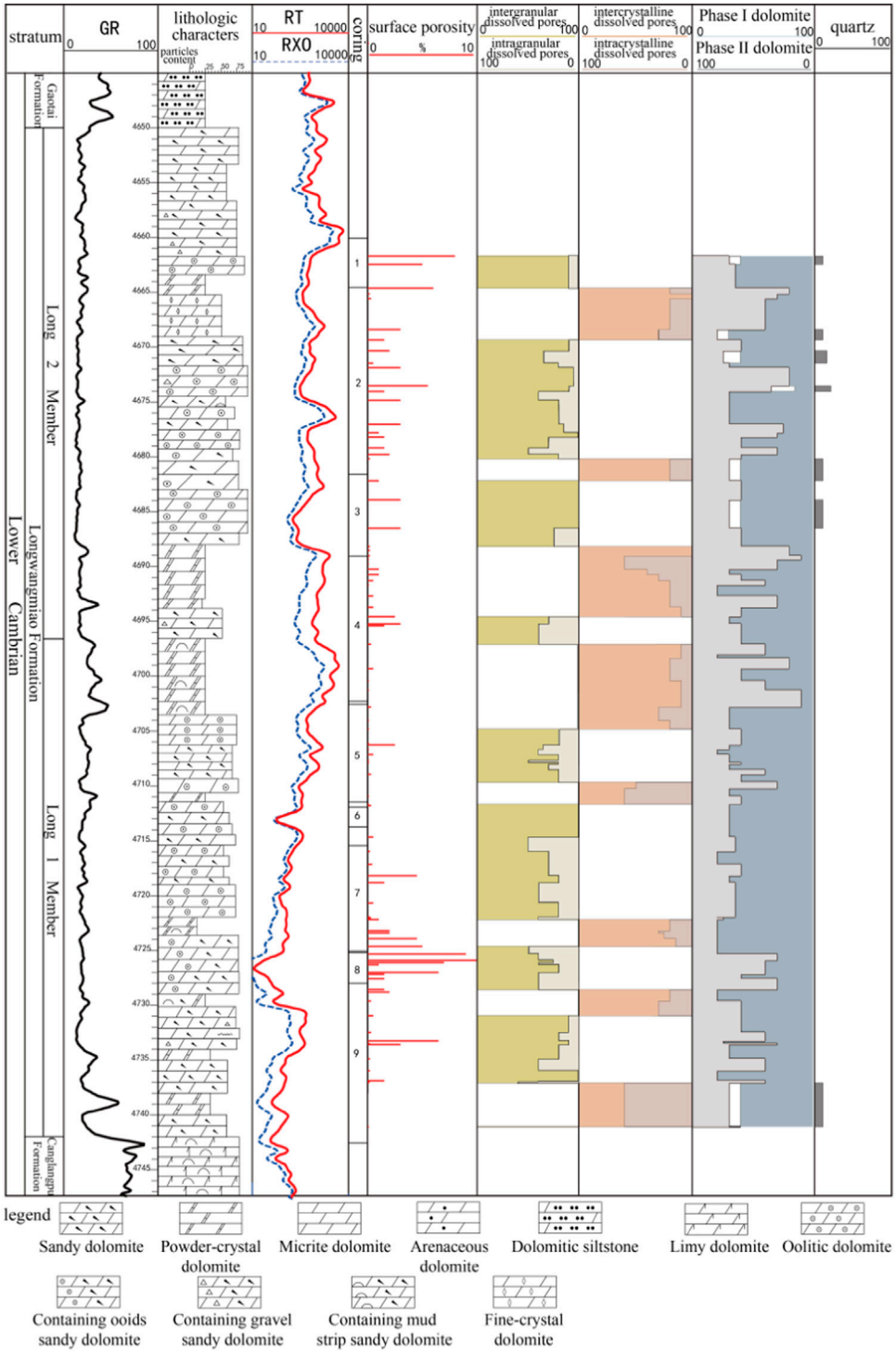

FIGURE 3
Development characteristics of pores of the Longwangmiao Formation in Well Gaoshi 23 in the study area.

the content of dolomite in the first stage decreases, while that in the second stage increases, and the total surface porosity decreases. For horizons, pores with surface porosity higher than 0.5% in the Long 2 Member account for 46% of total pores, while pores with surface porosity higher than 0.5% in the Long 1 Member account for 25.5% of total pores.

In terms of lithology, the average surface porosity of pores in oolitic dolomite and sandy dolomite is higher, which are 2.8% and 1.5%, respectively. In terms of lithofacies, the average surface porosity of pores in oolitic shoal and sandy shoal is higher, which are 2.8% and 2.7%, respectively. In terms of pore types, intergranular dissolved pores accounted for 74.8% of the pores developed in granular dolomite, and intergranular dissolved pores accounted for 72.6% of the pores developed in granular dolomite.

In the entire Longwangmiao Formation, intergranular dissolved pores account for a relatively high proportion, accounting for about 60% of the total pores in the Long 1 Member, and about 65% of the Long 2 Member. For the fillings inside the pores, the average content of the cement formed in the second stage is 55.6%, and that formed in the first stage is 43.4%. In the case of high quartz content, even if the intergranular dissolved pores and the first-stage cement content are high, the rock face porosity is low (Figure 3).

4.3 Lateral distribution of pores

The surface porosity of the Longwangmiao Formation in the study area is proportional to the thickness of the granular shoal, intergranular dissolved pores and the content of the first-phase cements; however, it is inversely proportional to the second-phase cements and the quartz.

From west to east, the stratigraphic thickness of the granular shoal in the Longwangmiao Formation tends to decrease, while the proportion of the intergranular dissolved pores tends to decrease. At the same time, in the pore-developed section, the content of cements in the first stage decreased, while the cements in the second stage increased, and the surface porosity gradually decreased from 1.6% to 0.6%. From south to north, the granular shoal shows a thickening trend, and the proportion of dissolved pores between grains shows an upward trend. At the same time, in the pore-developed section, the content of cements in the first stage increased, while the cements in the second stage decreased, and the surface porosity gradually increased from 1.2% to 1.9% (Figure 4). It is revealed that the surface porosity of the pores of the Longwangmiao Formation in the study area is closely related to the content of grains, intergranular dissolved pores, two-phase cements, and quartz.

5 Discussion

5.1 Influence of lithology on differential distribution of pores

The pore distribution is related to the content, size and shape of the particles. Granular dolomite is the main reservoir rock type of the Longwangmiao Formation in the study area. Among them, the development degree of pores in the oolitic dolomite is higher than that in sandy dolomite (Figure 5), and the thickness of the granular dolomite in the Long 2 Member is thicker than that of the Long 1 Member. The pore distribution of the Longwangmiao Formation dolomite has significant vertical differences.

At the same time, in the granular dolomite, the oolitic dolomite samples with a surface porosity greater than 0.5 accounted for 69%, the sandy dolomite samples with a surface porosity greater than 0.5 accounted for 52%, and the oolitic dolomite had a higher surface porosity than the sandy dolomite (Figures 6A,B). In the grain dolomite, the samples with a surface porosity greater than 0.5 accounted for 36% of the total samples; in the crystalline dolomite, the samples with a surface porosity greater than 0.5 accounted for 4% of the total samples; the grain dolomite had a higher face porosity than the crystalline dolomite (Figure 6). The proportion of oolitic dolomite in the Long 2 Member with a surface porosity greater than 0.5% is 62%; while the samples with a surface porosity greater than 0.5% in the Long 1 Member is 7%. The proportion of sandy dolomite samples with surface porosity greater than 0.5% in the Long 2 Member is 44%; while the samples with surface porosity greater than 0.5% in the Long 1 Member is 8%.

The average total surface porosity of various lithologies is arranged in descending order: oolitic dolomite1.9%, sandy dolomite 1.51%, fine crystal dolomite 0.93%, powder crystal dolomite 0.38% and micrite dolomite 0.2% (Figures 6A–F). According to the above analysis, most of the high-porosity reservoirs of various lithologies are distributed in the Long 2 Member, so the development of pores in the Long 2 Member is good. In the same horizon, the proportion of surface porosity of different lithologies is significantly different. Granular dolomite is the main reservoir rock in the Longwangmiao Formation in the study area, and oolitic dolomite has the best development of pores.

5.2 Influence of sedimentary facies on differential distribution of pores

The distribution of pores is controlled by sedimentary facies. The granular shoal is the main reservoir lithofacies of the Longwangmiao Formation in the study area. Among them, the oolitic shoal is the most developed, and its development thickness in the Long 2 Member is higher than that of the Long 1 Member. Therefore, the development of pores has an obvious horizon differences.

Statistics show that the samples with a surface porosity greater than 0.5% in the granular shoal accounted for 36% of the total samples; the samples with a surface porosity greater than 0.5 in the dolomitic flat and the intershoal sea accounted for 4% of the total samples (Figure 7E). At the same time, the proportion of samples with oolitic shoal facies greater than 0.5 was 69%;

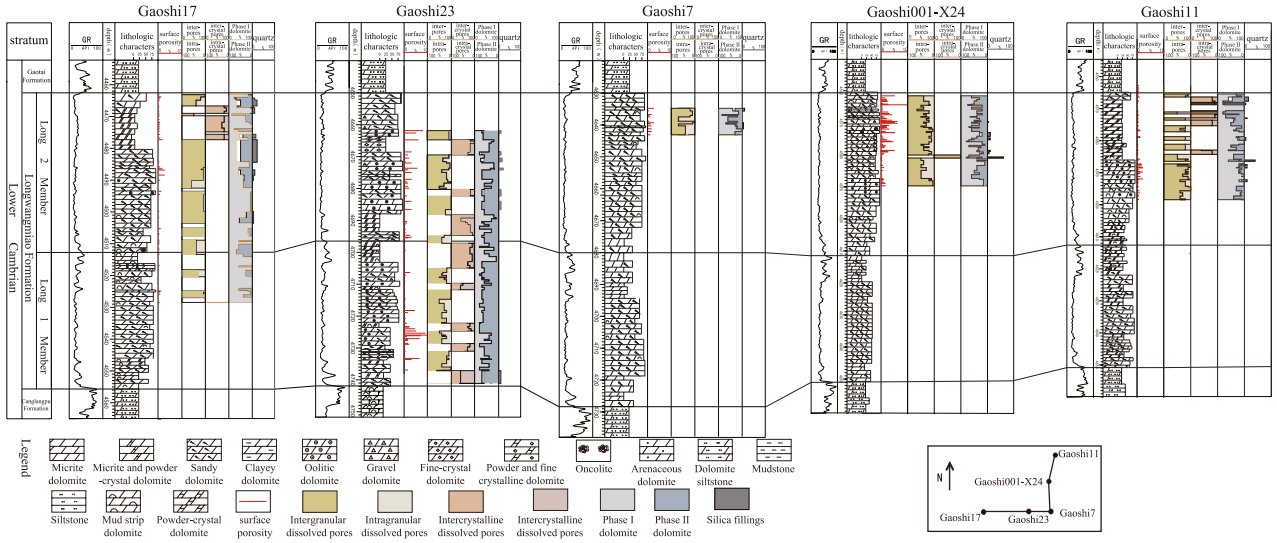

FIGURE 4
Comparison of pore development characteristics of the Longwangmiao Formation in the study area through Wells Gaoshi 17-Gaoshi 23-Gaoshi 7-Gaoshi 001-X24 -Gaoshi 11.

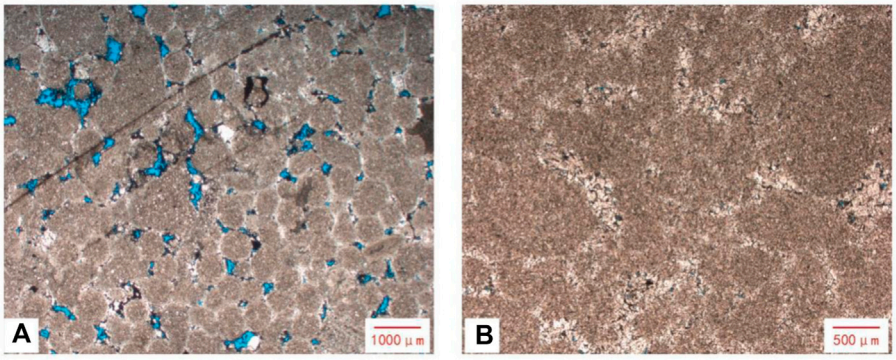

FIGURE 5
Microscopic characteristics of different types of granular pores in the Longwangmiao Formation in the study area. **(A)** Oolitic dolomite pores, GS6, 4546.78–4546.88 m, single polarized light; **(B)** Sandy dolomite pores, GS17, 4505.2 m, single polarized light.

while the proportion of samples with sandy shoal facies greater than 0.5% was 52% (Figures 7A,B).

The average total surface porosity of each lithofacies is arranged in descending order: oolitic shoal 1.9%, sandy shoal 1.22%, dolomitic flat 0.38% and shoal interfacies 0.2% (Figures 7A–E). According to the analysis, most of the high-porosity reservoirs of various lithofacies are distributed in the Long 2 Member, so the Long 1 Member reservoir has a good degree of pore development. In the same horizon, the proportion of face porosity of different lithofacies is obviously different. The granular shoal is the main reservoir lithofacies in the Longwangmiao Formation in the study area, and the oolitic shoal, as the main reservoir lithofacies in the Longwangmiao Formation, has the best degree of pore development.

5.3 Influence of diagenesis on differential distribution of pores

The dolomite of the Longwangmiao Formation in the study area has experienced a complex diagenetic system during the long burial process (Mindong et al., 2014; Haas

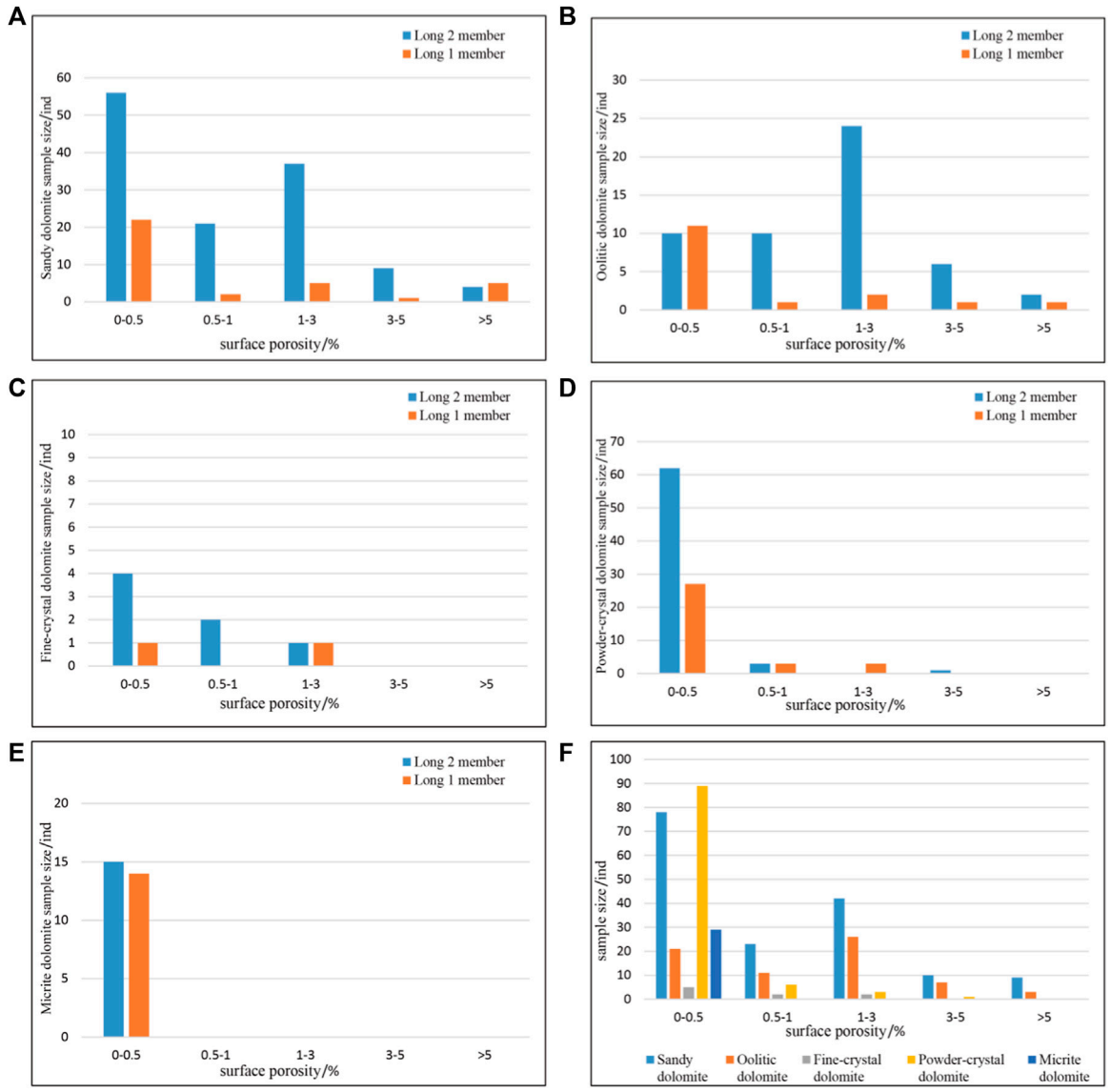

FIGURE 6
Histogram of surface porosity distribution of various lithologies of the Longwangmiao Formation in the study area. **(A)** Sandy dolomite; **(B)** Oolitic dolomite; **(C)** Fine-crystal dolomite; **(D)** Powder-crystal dolomite; **(E)** Micrite dolomite; **(F)** Histogram of surface porosity distribution in the Longwangmiao Formation.

et al., 2017; Mengyan et al., 2017; Pajdak et al., 2017; Qiang et al., 2021).

Among them, the main diagenesis controlling the development of pores is the dissolution of atmospheric fresh water between dolomite particles, dolomitization, dolomite cementation and hydrothermal action (Feifei, 2018). Tectonic activities promote the formation of tectonic fractures. These fractures aremostly filled with siliceous minerals such as dolomite and quartz and asphalt in the late diagenetic stage (Jingjie et al., 2020; Lingfang et al., 2020; Ying et al., 2019; Ke et al., 2022).

5.3.1 Dissolution

The dissolution of the dolomite in the Longwangmiao Formation in the study area includes the atmospheric freshwater dissolution in the paracontemporaneous period and the burial dissolution in the mesodiagenetic stage. Atmospheric freshwater dissolution is the main factor controlling the development of intergranular and intragranular dissolved pores in granular dolomite. They are positively correlated with the surface porosity (Figures 8C,D), and the positive correlation between the intergranular dissolved pores and the surface porosity is better.

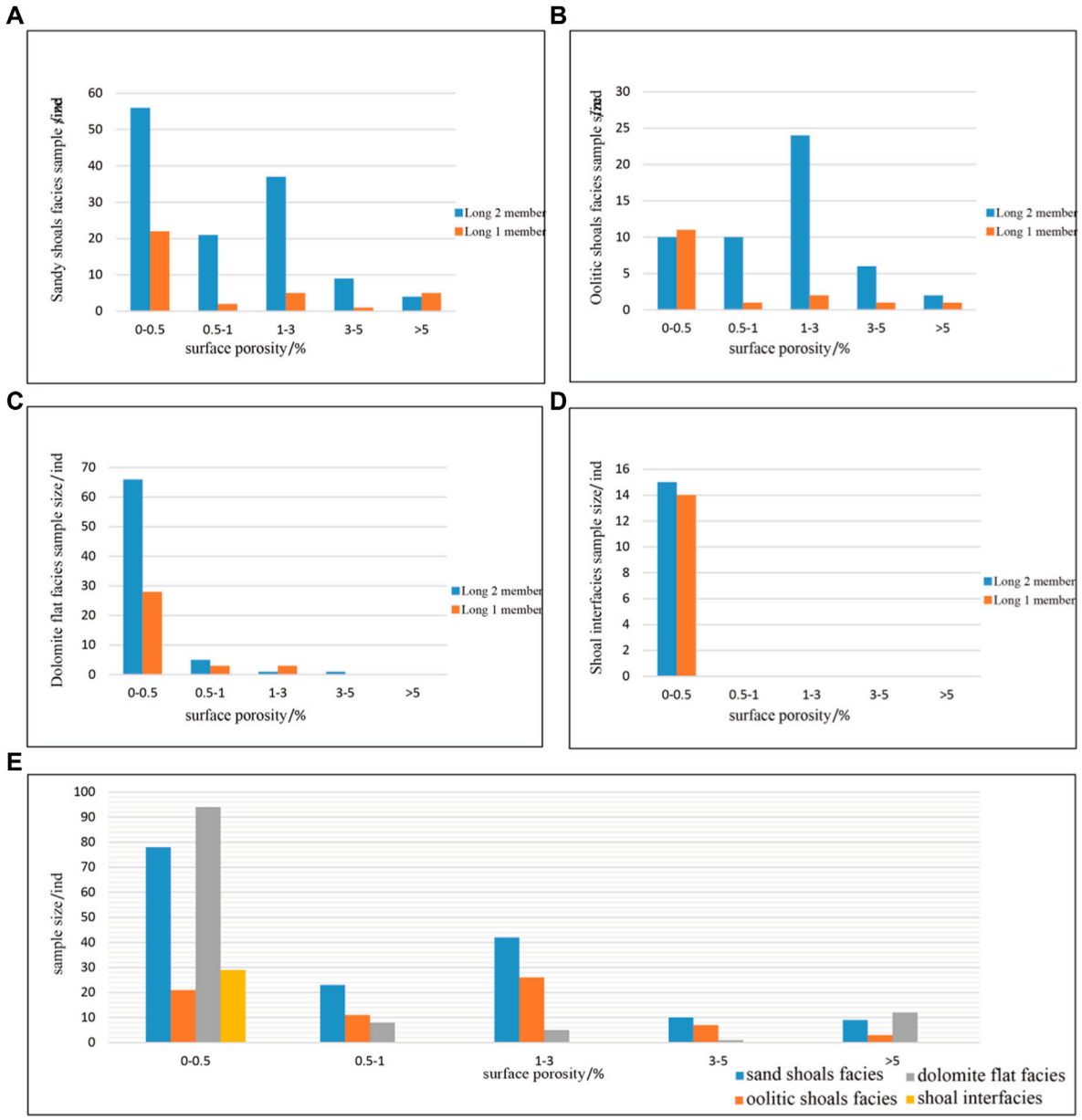

FIGURE 7
Histogram of surface porosity distribution of various lithofacies of the Longwangmiao Formation in the study area. **(A)** Histogram of surface porosity distribution of sandy shoals facies; **(B)** Histogram of surface porosity distribution of oolitic shoals facies; **(C)** Histogram of surface porosity distribution of dolomite flat facies; **(D)** Histogram of surface porosity distribution of shoal interfacies; **(E)** Histogram of surface porosity distribution in the Longwangmiao Formation.

Intercrystalline and intracrystalline dissolved pores are developed in crystalline dolomite, and the correlation between these two types of dissolved pores and surface porosity is not obvious (Figures 8A,B). Therefore, dissolution in crystalline dolomite is not the main factor controlling pore distribution. Burial dissolution usually results in enlarged dissolution of structural fractures, but they are usually partially or fully filled with bitumen (Figure 9C). Therefore, the correlation between tectonic fractures and surface porosity is poor (Figure 8E).

5.3.2 Dolomitization and dolomite cementation

The dolomite developed in the target layer in the study area is generally the product of dolomitization and

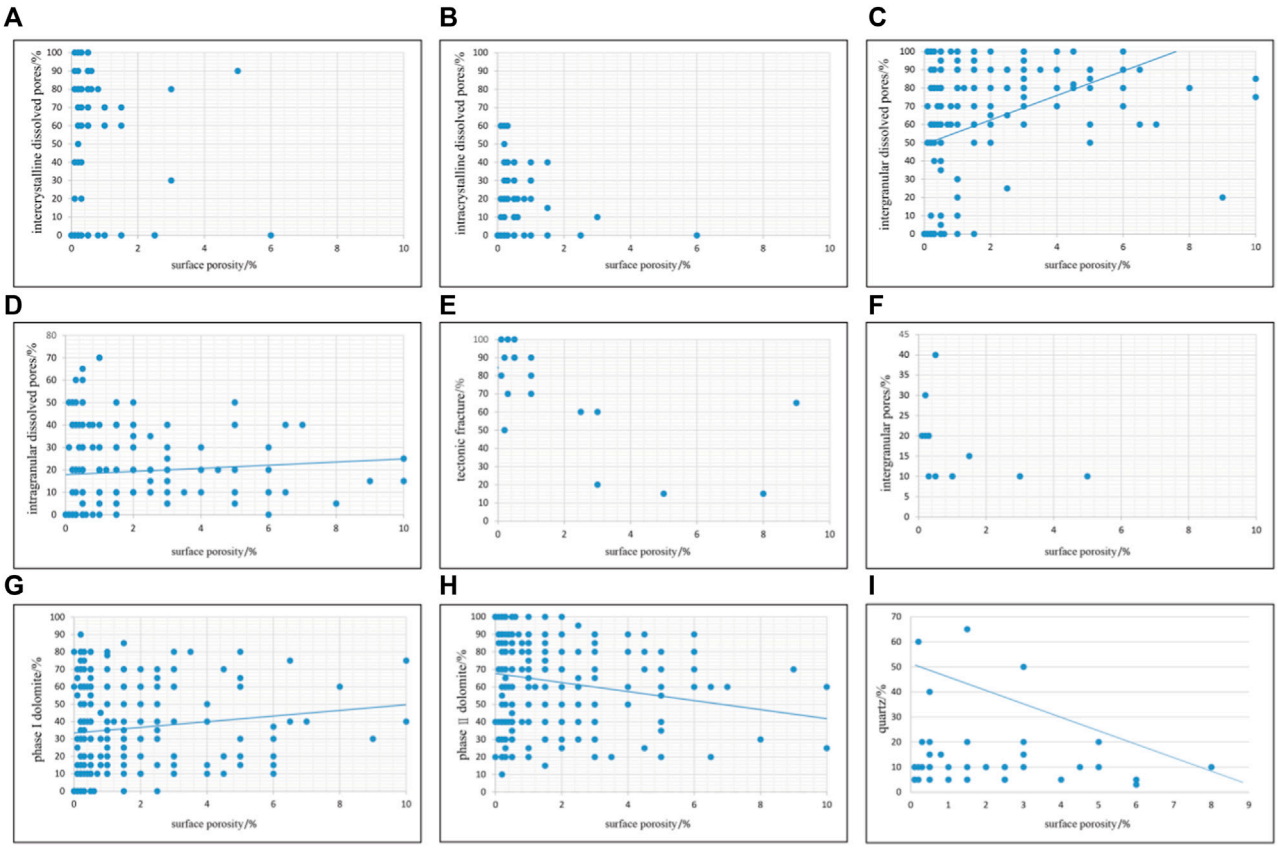

FIGURE 8
Surface porosity distribution under various diagenesis of the Longwangmiao Formation in the study area. **(A)** Relationship between intercrystalline dissolved pores and surface porosity; **(B)** Relationship between intracrystalline dissolved pores and surface porosity; **(C)** Relationship between intergranular dissolved pores and surface porosity; **(D)** Relationship between intragranular dissolved pores and surface porosity; **(E)** Relationship between tectonic fracture and surface porosity; **(F)** Relationship between intergranular pores and surface porosity; **(G)** Relationship between phase I dolomite and surface porosity; **(H)** Relationship between phase II dolomite and surface porosity; **(I)** Relationship between hydrothermal quartz and surface porosity.

dolomite cementation. This study shows that dolomitization and dolomite cementation have different effects on pore development at different diagenetic stages (Dawei et al., 2021): ① Quasi-contemporaneous evaporative seawater stage: This stage represents the main stage of dolomitization. Affected by strong evaporation and reflux infiltration, dolomitization occurs in high-porosity, high-permeability limestone. A large number of intercrystalline pores are developed in crystalline dolomite (Lianqiang et al., 2019), but according to statistics, there is no correlation between intercrystalline pores and surface porosity (Figure 8F). At the same time, in granular dolomite, dolomitization led to the replacement of calcite cements around intergranular dissolved pores with dolomite. Therefore, the first-phase powder-fine-grained dolomite metasomatism has a good positive correlation with surface porosity (Figure 8G). They support and protect the residual pores (Figure 9A); ② In the early diagenetic stage, the cementation of dolomite resulted in the formation of the second-stage fine-medium crystalline dolomite cements in the intergranular dissolved pores, and some of the pores were filled (Figure 9B). The content of fine-medium crystalline dolomite cements in the second stage is negatively correlated with the surface porosity (Figure 8H); ③ In the middle diagenetic stage, dolomite cementation continued, and coarse-megacrystalline dolomite was occasionally seen.

5.3.3 Hydrothermal action

In the late diagenetic stage, the dissolution of the deep burial environment promotes the expansion dissolution of the fractures and dissolved pores. Afterwards, siliceous minerals such as quartz are formed through hydrothermal action and fill the

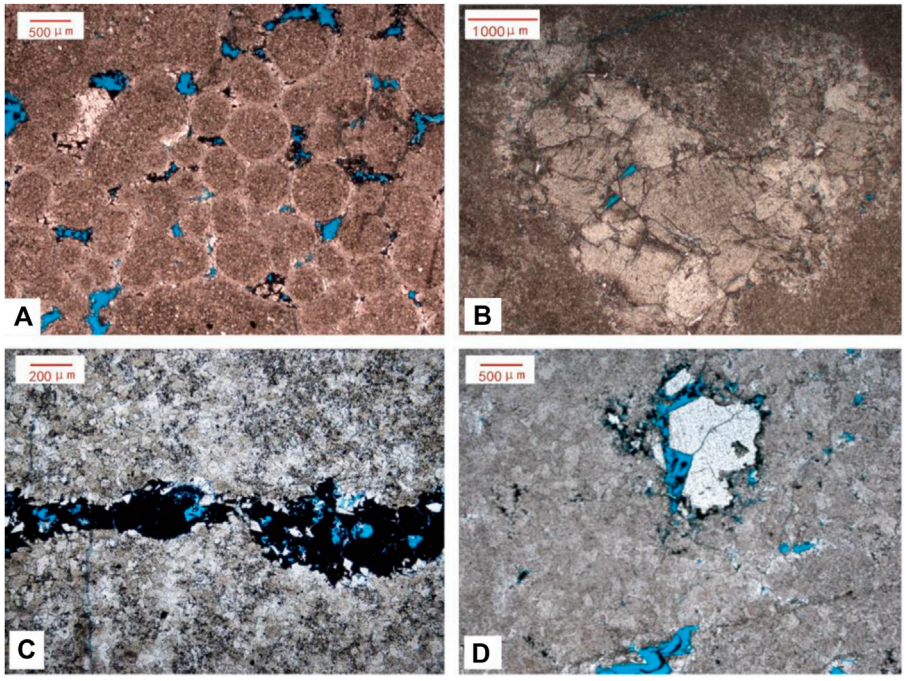

FIGURE 9
Diagenesis types and characteristics of the Longwangmiao Formation in the study area. **(A)** The first-stage annular dolomite cement developed around the grains, Well GS6, 4545.49 m, single polarized light; **(B)** Pores filled with medium and coarse-grained cements from the second stage, Well GS23, 4691.65 m, single polarized light; **(C)** Structural dissolving fracture nearly completely filled with dolomite and asphalt, Well MX16, 4755.47 m, single polarized light; **(D)** Pore filled with hydrothermal quartz, well GS001-X24, 4580.27 m, single polarized light.

pores. According to statistics, quartz composition is negatively correlated with surface porosity (Figure 8I). Therefore, siliceous minerals such as quartz formed by hydrothermal action severely block the pores, thereby reducing the porosity of the rock (Figure 9D).

5.4 Diagenetic sequence and pore evolution

According to the analysis of the pore development characteristics and controlling factors of the Longwangmiao Formation, the diagenetic evolution of the reservoir and the development law of pores are obtained (Chilingar and Bissell, 1966; Davies and Smith, 2006; Mindong et al., 2014).

(1) Normal seawater stage of quasi-contemporaneous period: The Longwangmiao Formation carbonate rocks in the study area were formed in a seawater diagenetic environment. The earliest bright-crystalline fibrous calcite cements were formed under the action of cementation. They grow ring-like around the grain edges and destroy the primary intergranular pores, leading to a dramatic drop in porosity (Figure 10A).
(2) Quasi-contemporaneous atmospheric freshwater stage: It represents a sedimentary environment in which the sea level is gradually decreasing. At this time, the sediments of the granular shoal such as sandy shoal and oolitic shoal on the sedimentary high landform were briefly exposed to the atmospheric sedimentary rock environment. The reservoir is subjected to selective dissolution by freshwater leaching, and a large number of intergranular dissolved pores and a small amount of intragranular dissolved pores are formed. The development of dissolved pores improves the overall porosity of the study area (Figure 10B).
(3) Quasi-contemporaneous evaporating seawater stage: Evaporation causes the magnesium-rich fluids to permeate and flow downward, and all the interstitials and particles are dolomized. At this stage, the early calcite cement was replaced by dolomite, and the first-stage dolomite began to form in the intergranular dissolved pores. The edges of the intergranular pores began to precipitate clean straight euhedral powder-crystalline dolomite, and fine-grained rhombic dolomite cements were partially visible (Figure 10C). The dolomite developed at the edge of the

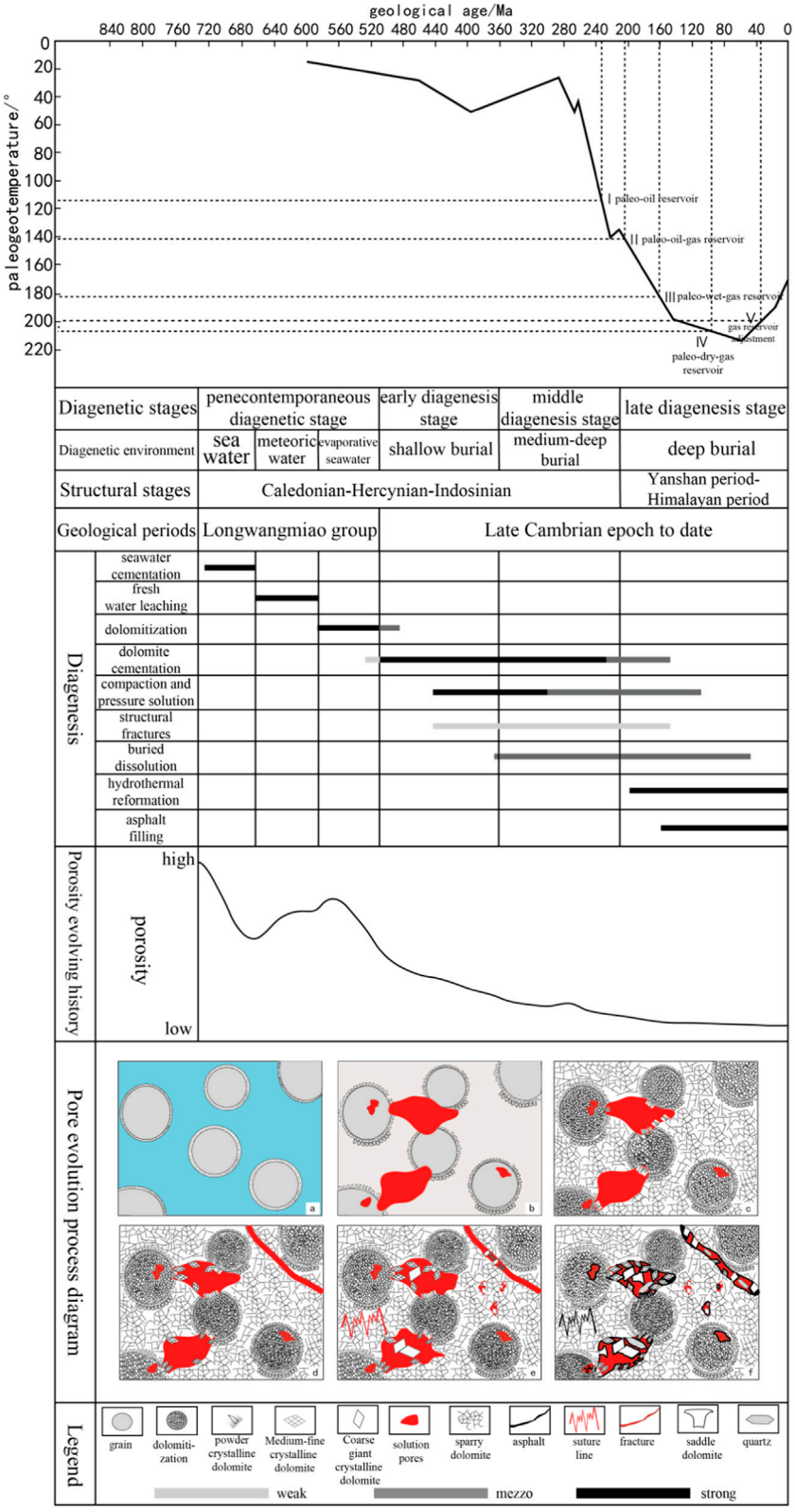

FIGURE 10
Schematic diagram of the burial history, diagenesis sequence and pore evolution of the Longwangmiao Formation in the study area. **(A)** is the Normal seawater stage of quasi-contemporaneous period, **(B)** is the Quasi-contemporaneous atmospheric freshwater stage, **(C)** is the Quasi-contemporaneous seawater stage, and **(D)** is the Early seawater stage. **(E)** is Middle stage, **(F)** is Late stage.

first-stage ring grains can support and protect the residual pores to a certain extent.

(4) Early diagenetic stage: At this stage, the reservoir begins to enter a shallow burial environment. However, due to the support and protection of the first-stage dolomite, the pore structures were not destroyed. But at this time, dolomite cementation occurs again, so that fine-medium-crystalline euhedral rhombic dolomite cements are generally formed in the pores. They continue to fill intra-particle, inter-particle pores and cause a dramatic reduction in porosity. In addition, weak structural rupture also occurred, and a small number of structural fractures were formed (Figure 10D).

(5) Middle diagenetic stage: As the depth increases, the reservoir enters a medium-deep burial environment. Further dolomite cementation occurs at this stage, and coarse-crystalline and giant-crystalline dolomite cements are formed. At this stage, pressure-dissolution begins to occur, and a large number of sutures begin to develop. A small number of fractures were formed by tectonic action, but the fractures were mostly filled with dolomite or asphaltene at a later stage (Figure 10E). Therefore, fractures have little effect on the reservoir performance of the reservoir. Overall, the porosity at this stage continued to decrease.

(6) Late diagenetic stage: In deep burial environments, intergranular dissolved pores, structural fractures and their internal fillings will further develop under the action of hydrothermal fluids and acidic fluids (Qilong et al.,2020). However, cements such as euhedral saddle-shaped dolomite and euhedral quartz formed by hydrothermal action and asphalt formed by oil and gas cracking are partially or fully filled (Figure 10F). At this stage, the porosity reaches a minimum value.

6 Conclusion

(1) The factors controlling the distribution of pores in the dolomite of the Longwangmiao Formation in the Gaoshiti area were identified, namely, lithology, sedimentary facies and diagenesis, and in turn, the pore evolution model of the Longwangmiao Formation was constructed.

(2) The main types of pores developed in the Longwangmiao Formation in the study area include intergranular dissolved pores, intragranular dissolved pores, intracrystalline dissolved pores and mold pores\. Among them, intergranular dissolved pores are the main pore type.

(3) The proportion of pores with surface porosity greater than 0.5% in the Long 2 Member in the study area is 46%, while that in the Long 1 Member is 25.5%. Therefore, the degree of development of pores in the Long 2 Member is better than that of the Long 1 Member. In addition, the grain dolomite in the grain shoal facies is favorable for the formation of large-scale pores, and the oolitic dolomite is the most favorable reservoir type.

(4) The development of pores in the Longwangmiao Formation in the study area is controlled by lithology and sedimentary facies. The average porosity of various lithologies is: oolitic dolomite 1.9%, sandy dolomite 1.51%, fine crystal dolomite 0.93%, powder crystal dolomite 0.38%, and micrite dolomite 0.2%. Moreover, the average porosity of different sedimentary facies is: 1.9% for oolitic shoals, 1.22% for sandy shoals, 0.38% for dolomitic flats, and 0.2% for shoal interfacies.

(5) The development of pores in the Longwangmiao Formation in the study area is controlled by different diagenesis in different stages: ① In the normal seawater stage of the quasi-contemporaneous period, seawater cementation caused the formation of calcite cements at the edge of the earliest ring grains, and the destruction of primary pores led to a sharp decrease in porosity; ② In the atmospheric freshwater stage of the quasi-contemporaneous period, the granular shoal sediments were leached by freshwater in the atmospheric sedimentary environment, and a large number of intergranular dissolved pores were formed; ③ During the evaporative seawater stage of the quasi-contemporaneous period, the dolomitization caused by strong evaporation and reflux infiltration resulted in the formation of dolomite cements at the edge of the ring grains. Under the support of cements, a large number of residual pores are retained; ④ In the early diagenetic stage, the dolomite cementation promoted the formation of the second-stage fine-medium crystalline dolomite cements in the shallow burial environment, and then, a large number of pores were filled and the porosity decreased sharply; ⑤ In the middle diagenetic stage, further dolomite cementation in the middle-deep burial stage resulted in the formation of coarse-megacrystalline dolomite. At this time, almost all the pores are filled, and the porosity continues to decrease; ⑥ In the late diagenetic stage, the saddle-shaped dolomite, quartz and other minerals are formed under the action of deep burial environment and hydrothermal fluids, and the pores and fractures are partially or fully filled with bitumen formed along with oil and gas migration, and the final reservoir porosity reaches the lowest level.

Data availability statement

The original contributions presented in the study are included in the article/supplementary material, further inquiries can be directed to the corresponding author.

Author contributions

HQ and ZY are responsible for the idea and writing of this paper, XZ and ML are responsible for the data interpretation and CZ, WX, FH, and QS are responsible for sample collection and data testing.

Funding

This research was financially supported by the National Natural Science Foundation of China (41702163 and 41702122) and the Science and Technology Cooperation Project of the CNPC-SWPU Innovation Alliance (No. 2020CX010301).

Conflict of interest

The authors declare that the research was conducted in the absence of any commercial or financial relationships that could be construed as a potential conflict of interest.

Publisher's note

All claims expressed in this article are solely those of the authors and do not necessarily represent those of their affiliated organizations, or those of the publisher, the editors and the reviewers. Any product that may be evaluated in this article, or claim that may be made by its manufacturer, is not guaranteed or endorsed by the publisher.

References

Anjiang, S., Anping, H., Liyin, P., and Min, P. (2017). Origin and distribution of grain dolostone reservoirs in the cambrian Longwangmiao Formation, Sichuan Basin, China. *Acta Geol. Sin.* 91 (1), 13072. doi:10.1111/1755-6724.13072

Benjian, Z., Di, X., Xingzhi, W., Like, Z., Sicong, L., and Xun, Y. (2018). Sedimentary characteristics and distribution patterns of grain shoals in the lower cambrian Longwangmiao Formation, southern Sichuan Basin, SW China. *Arab. Geosci.* 11, 135. doi:10.1007/s12517-018-3486-6

Caineng, Z., Jinhu, D., Chunchun, X., Zecheng, W., Baomin, Z., Guoqi, W., et al. (2014). Formation, distribution, resource potential, and discovery of Sinian–Cambrian giant gas field, Sichuan Basin, SW China. *Petroleum Explor. Dev.* 41 (03), 306–325. doi:10.1016/S1876-3804(14)60036-7

Cheng, Z., Yong, S., Yiren, F., Peiqiang, Y., Xinmin, G., Fei, W., et al. (2022). Application and prospect of low-field nuclear magnetic resonance technology in accurate characterization of coal pore structure. *J. China Coal Soc.* 47 (02), 828–848. doi:10.13225/j.cnki.jccs.xr21.1766

Chilingar, G. V., and Bissell, H. J. (1966). Dolomitization and limestone diagenesis. A symposium. *Chem. Geol.* 1, 272–275. doi:10.1016/0009-2541(66)90022-2

Choquette, P. W., and Pray, L. C. (1974). Geological nomenclature and classification of porosity in sedimentary carbonates. *AAPG Bull.* 54, 207–250.

Da, G., Mingmin, W., Ye, T., Lili, H., Chunyan, S., Xinmiao, H., et al. (2022). Control of sea level changes on high-frequency sequence and sedimentary evolution of Lianglitage Formation in the Tazhong Area. *Geol. China*, 1, 19

Da, G., Mingyi, H., Anpeng, L., Wei, Y., Wuren, X., and Chunyan, S. (2021). High-Frequency sequence and microfacies and their impacts on favorable reservoir of Longwangmiao Formation in central Sichuan Basin. *Earth Sci.* 46 (10), 3520–3534. doi:10.3799/dqkx.2020.382

Davies, G. R., and Smith, L. B. (2006). Structurally controlled hydrothermal dolomite reservoir facies: An overview. *Am. Assoc. Pet. Geol. Bull.* 90 (11), 1641–1690. doi:10.1306/05220605164

Dawei, L., Chunfang, C., Yongjie, H., Yanyan, P., and Lei, J. (2021). Multistage dolomitization and Formation of ultra-deep lower cambrian Longwangmiao Formation reservoir in central Sichuan Basin, China. *Mar. Petroleum Geol.* 123, 104752. doi:10.1016/j.marpetgeo.2020.104752

Feifei, Z. (2018). *Reservoir properties and controlling factors of dolomite in Longwangmiao Formation, northeastern Sichuan Basin*. Beijing: D. China University of Petroleum.

Fenshu, J., Pingping, S., and Kewen, L. (1995). Fractal characteristics of sandstone pore structure and its application. *Fault-Block Oil Gas Field* 1, 16–21.

Franziska, S., Liwen, H., Pierre, D., Xianghui, X., Donald, L., and Smith, O. M. (2021). Synchrotron X-ray microtomography and multifractal analysis for the characterization of pore structure and distribution in softwood pellet biochar. *Biochar* 3 (4), 671–686. doi:10.1007/S42773-021-00104-3

Genshun, Y., Jingao, Z., Weihong, Z., Jianyong, Z., Liyin, P., Yi, H., et al. (2013). Characteristics and distribution rule of lower cambrian Longwangmiao grain beach in Sichuan Basin. *Mar. Orig. Pet. Geol.* 18 (04), 1–8. doi:10.3969/j.issn.1672-9854.2013.04.001

Guoqi, W., Jinhu, D., Chunchun, X., Can, Z., Wei, Y., Ping, S., et al. (2015). Characteristics and accumulation modes of large gas reservoirs in Sinian-Cambrian of Gaoshiti-Moxi region, Sichuan Basin. *Acta Pet. Sin.* 36 (01), 1–12. doi:10.7623/syxb201501001

Haas, J., Hips, K., Budai, T., Gyori, O., Lukoczki, G., Kele, S., et al. (2017). Processes and controlling factors of polygenetic dolomite Formation in the transdanubian range, Hungary: A synopsis. *Int. Earth Sci.* 106 (3), 991–1021. doi:10.1007/s00531-016-1347-7

Hongliu, Z., Wenzhi, Z., Zhaohui, X., Qilong, F., Suyun, H., Zecheng, W., et al. (2018). Carbonate seimic sedimentology: Acase study of cambrian Longwangmiao Formation gaoshiti-moxi area, Sichuan Basin, China. *Petroleum Explor. Dev.* 45 (05), 775–784. doi:10.11698/PED.2018.05.03

Jiang, W., Zhang, P., Li, D., Li, Z., Wang, J., Duan, Y., et al. (2022). Reservoir characteristics and gas production potential of deep coalbed methane: Insights from the no. 15 coal seam in shouyang block, Qinshui Basin, China. *Unconv. Resour.* 2, 12–20. doi:10.1016/j.uncres.2022.06.001

Jingjie, Y., Jinmin, S., and Shugen, L. (2020). etcGenetic analysis of dolomite in the lower cambrian Longwangmiao Formation in northeastern sichuan. *Acta Sedimentol. Sin.* 38 (06), 1284–1295. doi:10.14027/j.issn.1000-0550.2019.108

Jinhu, D., Cai, Z., Chunchun, X., Haiqing, H., Ping, S., Yueming, Y., et al. (2014). Theoretical and technical innovations in strategic discovery of a giant gas field in Cambrian Longwangmiao Formation of central Sichuan paleo-uplift, Sichuan Basin. *Petroleum Explor. Dev.* 41 (03), 294–305. doi:10.1016/S1876-3804(14)60035-5

Katz, B., Gao, L., Little, J., and Zhao, Y. R. (2021). Geology still matters – unconventional petroleum system disappointments and failures. *Unconv. Resour.* 1, 18–38. doi:10.1016/j.uncres.2021.12.001

Ke, Z., Feng, B., Liu, Y., Cui, Z., and Liu, X. (2022). Dissolution and sedimentation patterns of typical minerals in artificial reservoirs under different environments. *Unconv. Resour.* 2, 60–71. doi:10.1016/j.uncres.2022.08.004

Kun, J., Suping, Y., Hao, W., Miaochun, L., and Zhongyi, T. (2014). Advances in characterization of pore system of gas shales. J. *Geol. China Univ.* 20 (01), 151–161. doi:10.16108/j.issn1006-7493.2014.01.009

Lianqiang, Z., Haifeng, Y., and Xuemei, L. (2019). Mineral filling period and hydrocarbon accumulation of cambrian Longwangmiao Formation in Anyue structure, Sichuan Basin. *Petroleum Geol. Experimen* 41 (06), 812–820.

Lingfang, Z., Yixiong, Q., Xiaobo, S., Bo, C., Donghua, Y., and Yong, L. (2020). Characterization, distribution and origin of dolomite reservior in the upper Lei 4 member of the Middle Triassic, Pengzhou gas field, Western Sichuan Basin. *Oil Gas Geol.* 41 (01), 177–188. doi:10.11743/ogg20200116

Lucia, J. F. (1995). Rock-fabric/petrophysical classification of carbonate pore space for reservoir characterization. *AAPG Bull.* 79, 1275–1300.

Mengyan, X., Mingyi, H., Da, G., Di, W., Jingyi, W., and Lingshan, L. (2017). Characteristivs and main controlling factors of lower cambrian Longwangmiao

Formation beach-facies reservoirs in gaoshiti-moxi area, central Sichuan Basin. *J. Guilin Univ. Technol.* 37 (01), 37–46.

Mindong, J., Wei, Z., Xiucheng, T., Ling, L., Zongyin, L., Bing, L., et al. (2014). Characteristics and controlling factors of beach-controlled karst reservoirs in cambrian Longwangmiao Formation, moxi-gaoshiti area, Sichuan Basin, NW China. *Petroleum Explor. Dev.* 41 (06), 712–723. doi:10.1016/S1876-3804(14)60085-9

Mindong, J., Xiucheng, T., Wei, Z., Ling, L., and Zongyin, L. (2014). Beach-controlled karst reservoir characteristics and controlling factors of Longwangmiao Formation in Moxi-Gaoshiti area, Sichuan Basin, China. *Petroleum Explor. Dev.* 41 (6), 650–660.

Nan, Q. (2020). Research progress of microscopic pore structure characterization of reservoir. *Petrochem. Ind. Appl.* 39 (11), 17–22. doi:10.3969/j.issn.1673-5285.2020.11.004

Niu, X., Feng, S., You, Y., Xin, H., Liang, X., Hao, B., et al. (2022). Analyzing major controlling factors of shale oil 'sweet spots' in the Chang-7 member of the Triassic Yanchang Formation, Ordos Basin. *Unconv. Resour.* 2, 51–59. doi:10.1016/j.uncres.2022.07.001

Pajdak, A., Godyn, K., Kudasik, M., and Murzyn, T. (2017). The use of selected research methods to describe the pore space of dolomite from copper ore mine, Poland. *Environ. Earth Sci.* 76 (11), 1–16. doi:10.1007/s12665-017-6724-4

Qiang, D., Jian, C., Bo, Y., Zixin, J., Fei, L., Ziwen, Z., et al. (2021). Quantitative characterization and classification of pore structure in chang 4+5 member in block hu-154, ordos basin. *Xinjiang Pet. Geol.* 42 (04), 410–417. doi:10.7657/XJPG20210403

Qilong, F., Suyun, H., Zhaohui, X., Wenzhi, Z., Shuyuan, S., and Hongliu, Z. (2020). Depositional and diagenetic controls on deeply buried Cambrian carbonate reservoirs: Longwangmiao Formation in the Moxi–Gaoshiti area, Sichuan Basin, southwestern China. *Mar. Petroleum Geol.* 117, 104318. doi:10.1016/j.marpetgeo.2020.104318

Roberts, J. A. (2018). Dolomite and dolomitization," in *M. Encyclopedia of geochemistry* (Berlin: Springer-Verlag).

Vafaie, A., Kivi, I. R., Moallemi, S. A., and Habibnia, B. (2021). Permeability prediction in tight gas reservoirs based on pore structure characteristics: A case study From south western Iran. *Unconv. Resour.* 1, 1–8. doi:10.1016/j.uncres.2021.04.001

Weiqiang, Y., Pingping, L., Haoru, C., Zheng, L., Caijun, L., Zhehang, X., et al. (2022). Origin and significance of carbonate shoal depositional cycles: A case study of the cambrian Longwangmiao Formation, Sichuan Basin, SW China. *Asian Earth Sci.* 226, 105083. doi:10.1016/J.JSEAES.2022.105083

Xi, L., Zhenhua, G., Yujin, W., Xiaohua, L., Manlang, Z., Wuren, X., et al. (2017). Geological characteristics and development strategies for Cambrian Longwangmiao Formation gas reservoir in Anyue gas field, Sichuan Basin, SW China. *Petroleum Explor. Dev.* 44 (3), 428–436. doi:10.1016/S1876-3804(17)30049-6

Xiangchun, L., Jiaxing, G., Shuang, Z., Yi, L., Mengya, W., and Weidong, L. (2021). Combined characterization of scanning electron microscopy, pore and crack analysis system, and gas adsorption on pore structure of coal with different volatilization. *Earth Sci.* 47 (5), 1876–1889. doi:10.3799/dqkx.2021.195

Xing, T., Dailin, Y., Jiayi, Z., Yiting, S., Yunlong, W., Yu, Y., et al. (2021). Microscopic characterization of dolomite reservoir based on CT imaging technique-a case study of the fourth member of Sinian Dengying Formation in Moxi-Longnvsitai area, central Sichuan. *Acta Sedimentol. Sin.* 39 (05), 1264–1274. doi:10.14027/j.issn.1000-0550.2020.055

Xuefei, Y., Xingzhi, W., and Hao, T. (2015). Study on sedimentary microfacies of Longwangmiao Formation in moxi area, central Sichuan Basin, China. *Acta Sedimentol. Sin.* 33 (05), 972–982. doi:10.14027/j.cnki.cjxb.2015.05.013

Yang, X., Fan, J., Zhang, Y., Li, W., Du, Y., and Yang, R. (2022). Microscopic pore structure characteristics of tight limestone reservoirs: New insights from section 1 of the permian maokou formation, southeastern Sichuan Basin, China. *Unconv. Resour.* 2, 31–40. doi:10.1016/j.uncres.2022.08.001

Ying, R., Dakang, Z., honglong, G., Haitao, S., Hao, P., Xiaowei, Z., et al. (2019). Origin of dolomite of the lower cambrian Longwangmiao Formation, eastern Sichuan Basin, China. *Carbonates Evaporites* 34 (3), 471–490. doi:10.1007/s13146-017-0409-7

Zitong, Q. (2007). *Carbonate reservoir Geology*. Beijing: China University of Petroleum Press.

frontiers | Frontiers in Earth Science

TYPE Original Research
PUBLISHED 10 January 2023
DOI 10.3389/feart.2022.1041164

OPEN ACCESS

EDITED BY
Shuai Yin,
Xi'an Shiyou University, China

REVIEWED BY
Yi Ding,
Chengdu University of Technology, China
Meng Wang,
Chongqing University of Science and Technology, China

*CORRESPONDENCE
Zhanlei Wang,
28142547@qq.com

SPECIALTY SECTION
This article was submitted to Structural Geology and Tectonics, a section of the journal Frontiers in Earth Science

RECEIVED 10 September 2022
ACCEPTED 29 September 2022
PUBLISHED 10 January 2023

CITATION
Gu Y, Wang Z, Yang C, Luo M, Jiang Y, Luo X, Zhou L and Wang H (2023), Effects of diagenesis on quality of dengying formation deep dolomite reservoir, Central Sichuan Basin, China: Insights from petrology, geochemistry and in situ U-Pb dating.
Front. Earth Sci. 10:1041164.
doi: 10.3389/feart.2022.1041164

Effects of diagenesis on quality of dengying formation deep dolomite reservoir, Central Sichuan Basin, China: Insights from petrology, geochemistry and *in situ* U-Pb dating

Yifan Gu[1,2], Zhanlei Wang[1,2]*, Changcheng Yang[3], Mingsheng Luo[3], Yuqiang Jiang[1,2], Xiaorong Luo[1,2], Lu Zhou[1,2] and Haijun Wang[1,2]

[1]School of Geoscience and Technology, Southwest Petroleum University, Chengdu, China, [2]The Unconventional Reservoir Evaluation Department, PetroChina Key Laboratory of Unconventional Oil and Gas Resources, Chengdu, China, [3]PetroChina Southwest Oil and Gas Field Company, Chengdu, China

The Ediacaran Dengying Formation in Central Sichuan Basin is the deep dolomite gas reservoir with the largest natural gas reserves in China, providing an excellent example for understanding the effect of diagenesis evolution on deep dolomite reservoir quality. By integrating petrology, geochemistry and *in situ* U-Pb dating, this study aims to reveal the genesis of different rock fabrics and their corresponding diagenetic events, and to discuss the temporal relationship of diagenetic events and their effects on the reservoir quality of Dengying Formation. Two phases of dolomite and three phases of dolomite cement are identified in Ediacaran Dengying Formation deep dolomite reservoirs of Central Sichuan Basin as follows: 1) matrix dolomites (MD), 2) fine-medium crystalline dolomites (FMD), 3) fibrous dolomites (FD), 4) medium-coarse crystalline dolomites (MCD), and 5) saddle dolomite (SD). By analyzing petrographic and temporal relationships between these fabrics, it is suggested that the deep dolomite reservoir of Dengying Formation in Central Sichuan Basin has experienced six diagenetic stages, including 1) syndiagenetic stage, 2) the first-time early diagenetic stage, 3) epidiagenetic stage, 4) the second-time early diagenetic stage, 5) middle diagenetic stage and 6) late diagenetic stage. Microbial dolomitization during syndiagenetic stage produced limited increase in reservoir porosity, but it is of great significance for preservation of reservoir spaces. Silicification is most unfavorable for reservoir formation, but its duration and influence range are very limited. At epidiagenetic stage, the physical properties of Dengying Formation dolomite reservoir have been greatly improved. Two-time early diagenetic stages are both destructive for preservation of reservoir spaces. During middle diagenetic stage, two-stage of hydrothermal alterations occurred, corresponding to Late Silurian to Devonian and Late Permian, respectively. Hydrothermal alteration of the MD is both constructive and

destructive, but overall it is constructive, and the improvement of physical properties is limited. For the karstified MD, both two-stage hydrothermal alterations were destructive, resulting in damage of reservoir physical properties caused by cementation by two-stage SD and one-stage MVT minerals.

KEYWORDS

deep dolomite reservoir, ediacaran dengying formation, diagenetic stage, geochemistry, U-Pb dating, central sichuan basin

1 Introduction

The worldwide exploration practice shows that there are abundant oil and gas resources in dolomite strata (Zhao et al., 2014; Zhao et al., 2018), and remarkable exploration success has been achieved in shallow-middle buried dolomite reservoir (Zou et al., 2011; Jiang et al., 2017; Wang et al., 2018; Gu et al., 2020; Gu et al., 2021). Previous studies have proposed that, affected by destructive diagenesis such as compaction and cementation, with the increase of burial depth and the aging of strata, the porosity in dolomite reservoir gradually decreases, and it is difficult for effective reservoirs to exist in deep buried dolomite strata (Schmoker and Hally, 1982; Ehrenberg et al., 2009). However, in recent years, with the increasing progress of exploration technology, the oil and gas exploration of dolomite reservoirs has gradually advanced to deep strata (buried depth>4500 m) and ultra-deep strata (buried depth >6000 m), and more and more successful examples have been found in Sichuan Basin and Tarim Basin (Guo et al., 2016; Zhao et al., 2021; Li et al., 2022a). Although there have been some successful cases, the exploration and development of deep or ultra-deep dolomite reservoirs still face huge technical and commercial risks. In particular, these dolomite reservoirs are characterized by large burial depth and generally experienced complex diagenetic alteration processes (Du et al., 2018; Peng B. et al., 2018; Gu et al., 2019). Correspondingly, the reservoir rock exhibits extremely complicated characteristics due to the superimposition of multiple diagenetic events (Wang et al., 2014; Xu et al., 2016; Zhu et al., 2019). Therefore, understanding the relationship between different diagenetic stages and corresponding effect on reservoir characteristics is of great significance for the future exploration of deep dolomite reservoir.

At present, the Ediacaran Dengying Formation in the Central Sichuan Basin is the deep dolomite gas reservoir with the largest natural gas reserves in China, and its proven reserves are close to $6 \times 10^{11} m^3$ (Zhao et al., 2021). The abundant drilling cores of the Dengying Formation provide an excellent study target for the effect of diagenesis evolution on the quality of deep dolomite reservoirs. In terms of the reservoir-forming mechanism of deep dolomite reservoirs in the Dengying Formation, most of the viewpoints believe that the supergene karstification during Tongwan Movement plays a key role (Wang et al., 2014; Zhou et al., 2016; Zhou et al., 2020; Su et al., 2022). Zhu et al. (2015) agreed with this view, but also emphasized the constructive role of recrystallization during supergene karstification. After 2013 (Shi et al., 2013; Liu et al., 2014; Peng J. et al., 2018; Gu et al., 2019), scholars have noticed the existence of multi-stage hydrothermal alteration in deep dolomite reservoir of the Dengying Formation and proposed that hydrothermal alteration increases the porosity of the Dengying Formation matrix dolomite by 3%–5% (Liu et al., 2014). However, Jiang et al. (2016) proposed that porosity could only increase by 2% after hydrothermal alteration. In addition to the above viewpoints, some scholars believe that the Dengying large-scale high-quality reservoir is mostly formed in the early sedimentary-diagenetic stage. Although previous studies have obtained these valuable understandings, the temporal relationship between the diagenetic events of the Dengying Formation, the corresponding fluid genesis and its influence on the quality of deep dolomite reservoirs are still unclear.

The purpose of this study is to reveal the genesis of different rock fabrics and corresponding diagenetic events, and to discuss the temporal relationship of diagenetic events and their effects on the reservoir quality. The results of this study not only provide an in-depth understanding of the genetic mechanism of deep ancient dolomite reservoirs, but also provide a scientific basis for future exploration of the Ediacaran Dengying Formation in Sichuan Basin.

2 Geological background

The Sichuan Basin, situated in the northwest region of the Upper Yangtze platform (Ding et al., 2021) (Figure 1A), is the most petroliferous basin for oil and gas exploration of unconventional reservoir in China (He et al., 2021; Zhou et al., 2021; Li H. et al., 2022; Li et al., 2022b; Li, 2022). The study area is located in the Central Sichuan Basin. In this area, the Ediacaran Dengying Formation and the underlying Doushantuo Formation are in conformable contact, but is in unconformable contact with the overlying mudstone (or shale) of the Lower Cambrian Qiongzhusi Formation. According to rock type, microbial content and sedimentary structure, the Dengying Formation can be divided into four members from bottom to top. The first, second and fourth members are all composed of

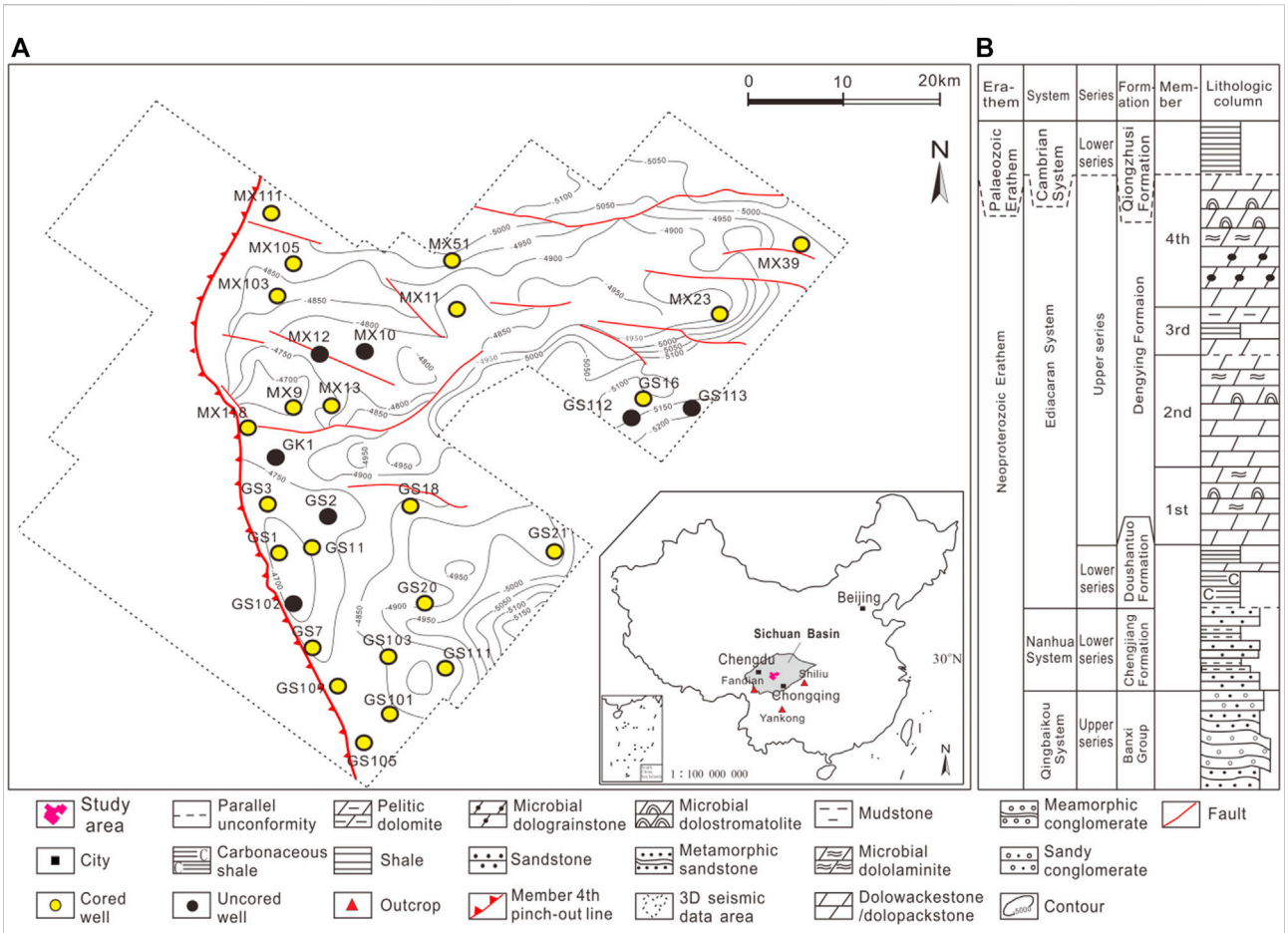

FIGURE 1
(A) The spatial distribution map showing the study area and drilling wells in the Central Sichuan Basin. **(B)** Generalized stratigraphy of the Ediacaran Dengying Formation in the study area (modified from Gu et al., 2019).

dolomite, except for the third member composed of mudstone and argillaceous dolomite (Jiang et al., 2016). The matrix dolomite (MD) consists of microbial dololaminite, microbial dolostromatolite, dolowackestone and dolopackstone (Figure 1B).

3 Samples and methods

At first, 157 samples from drilling cores of the Dengying Formation were doubly polished, followed by blue epoxy-impregnation and staining with Alizarin red for identification of different rock fabrics. And then petrographic relationships of different fabrics were delineated using a CL8200MK5 cathodoluminescence (CL) microscope. Eighteen samples were selected for Sr isotope measurement through a Finnigan Triton thermal ionization mass spectrometer (TIMS). Eighty-four samples were selected for stable isotopic ($\delta^{18}O$, $\delta^{13}C$) measurement using MAT253 isotope mass spectrometer. The $\delta^{18}O$ and $\delta^{13}C$ data are normalized to Vienna Pee Dee Belemnite (V-PDB) standard and corrected by fractionation factors proposed by Fairchild and Spiro (1987). Twenty-seven samples were selected for rare earth element (REE) contents measurement through inductively coupled plasma-mass spectrometry (ICP-MS) at Sichuan Origin & Microspectrum Corporation. Firstly, the 27 samples were dissolved by hydrofluoric acid and nitric acid in a closed container. The hydrofluoric acid were wiped out by evaporation on the electric heating plate, and then dissolved by nitric acid. After dilution, the samples are directly measured by ICP-MS. The analytical uncertainties are estimated to be 5%. Standard rock reference material (GSD-9) were used to monitor the analytical accuracy and precision.

Laser *in situ* U-Pb isotopic dating was carried out through LA-ICP-MS (Element XR) at Sichuan Origin & Microspectrum Corporation in Chengdu. For the dolomite samples selected for dating, spots with higher ^{238}U intensities, higher $^{238}U/^{206}Pb$ ratios and lower $^{207}Pb/^{206}Pb$ ratios were selected for further U-Pb isotope analysis. Additional spots may be selected from the

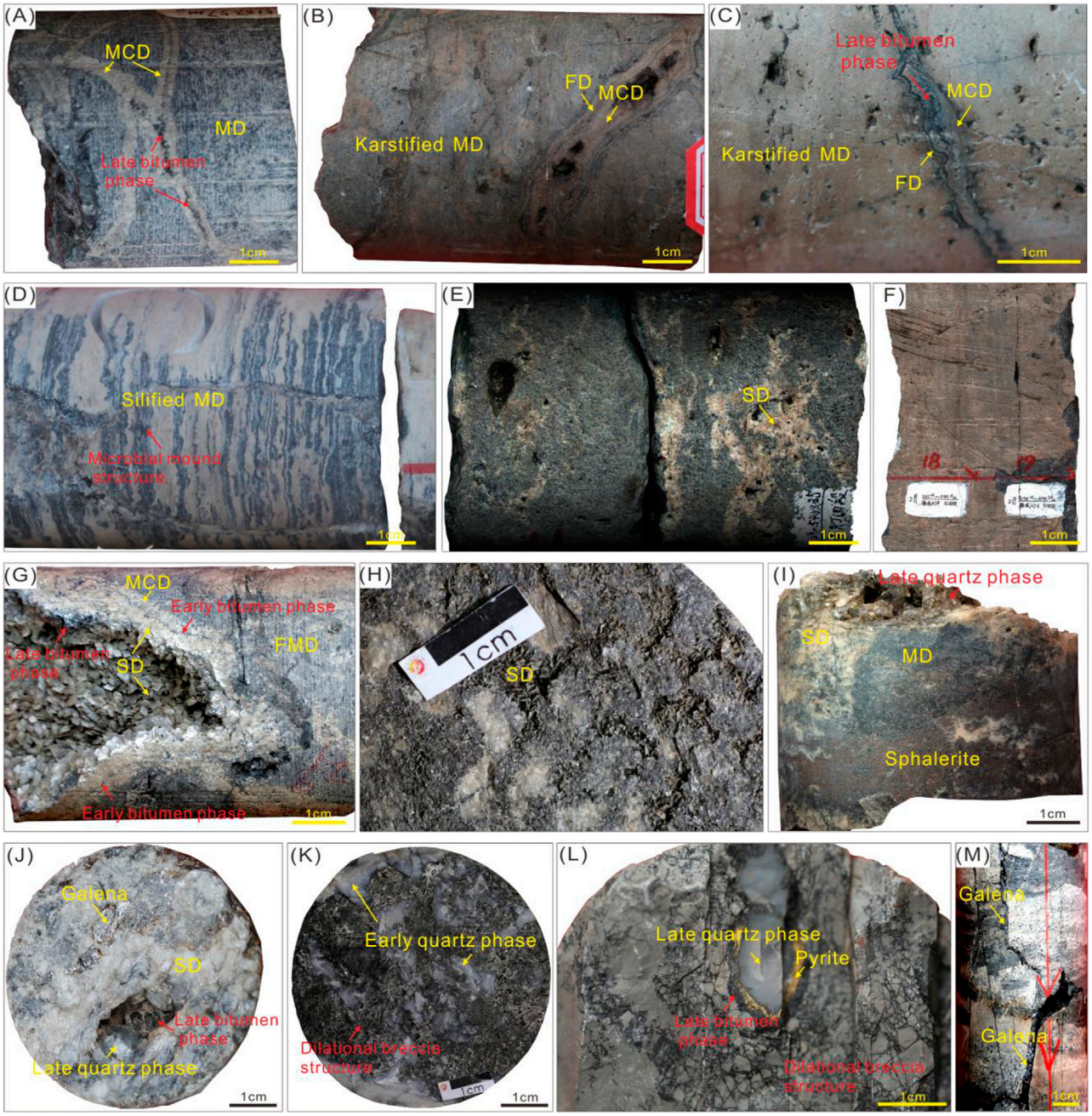

FIGURE 2
Macroscopic characteristics for the Dengying Formation from drilling cores in Central Sichuan Basin. **(A)** MCD and late bitumen phase filled in fractures within the MD, Well GS20, 4th Member, 5187.57 m. **(B)** FD and MCD filled in vugs within karstified MD, Well GS102, 4th Member, 5085.11 m–5085.36 m. **(C)** The original sedimentary structures in the MD have almost disappeared, Well GS7, 4th Member, 5266.49 m–5266.59 m. **(D)** The original microbial mound structures are well preserved in silified MD, Well GS18, 4th Member, 5184.13 m. **(E)** Scattered intercrystalline pores within FMD, Well GS16, 4th Member, 5453.35 m. **(F)** Scattered intercrystalline pores within FMD, Well MX103, 4th Member, 5195.24 m. **(G)** MCD, early bitumen phase and saddle dolomite (SD) coats inner wall of hydrothermal dissolved vug within FMD, Well GS20, 4th Member, 5195.7 m **(H)** SD with curved or lobate crystal faces filled between dilational breccias, Well MX51, 4th Member, 5335.7 m **(I)** SD, sphalerite and late quartz phase filled in vugs within karstified MD, Well GS102, 4th Member, 5043.93 m. **(J)** Mississippi Valley-Type minerals including galena and late quartz phase, Well GS109, 4th Member, 5316.08 m. **(K)** Early quartz phase filled between dilational breccias, Well MX51, 4th Member, 5401.77 m. **(L)** Pyrite and late quartz phase filled in vugs within dilational breccia structure, Well MX39, 4th Member, 5309.3 m. **(M)** Galena filled in fractures within MD, Well GS101, 4th Member, 5517.2 m.

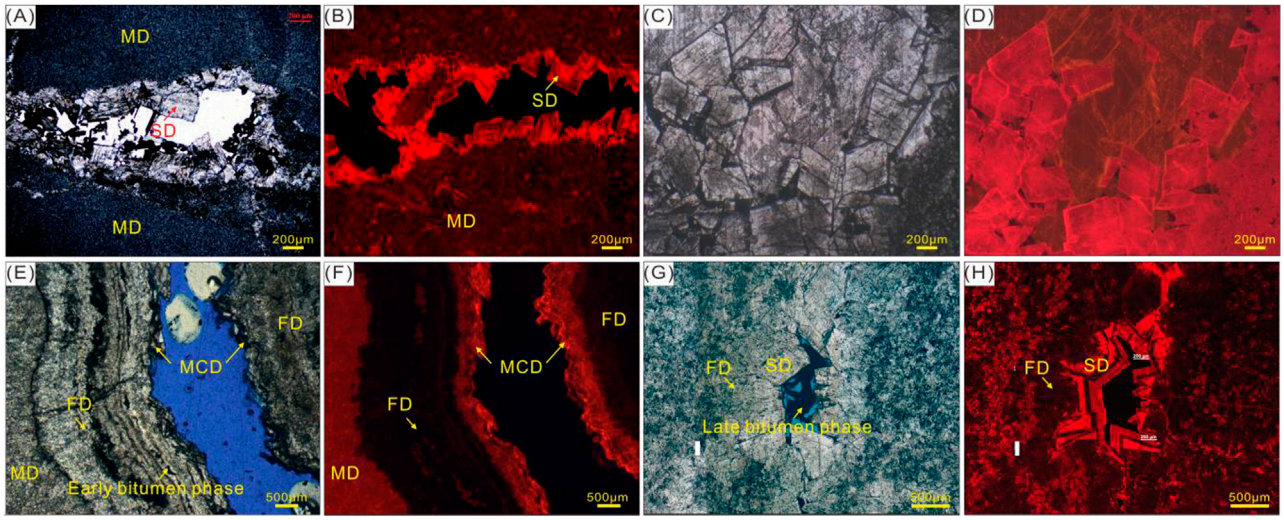

FIGURE 3
Microscopic characteristics for the Dengying Formation from drilling cores in Central Sichuan Basin. **(A)** SD along vug interwall within MD under PPL, Well GS1, 4th Member, 4970 m (Gu et al., 2019). **(B)** SD exhibits bright red and banded structure whereas MD exhibit dull red under CL, Well GS1, 4th Member, 4972 m. **(C)** FMD with cloudy core and clear rim, Well GS16, 4th Member, 5450.15 m. **(D)** FMD exhibits bright red under CL, Well GS16, 4th Member, 5450.15 m. **(E,F)** FD shows nonluminescent and MCD exhibit bright red under CL, Well GS102, 4th Member, 5079.65 m. **(G,H)** FD shows non-luminescent, and SD exhibit bright red and banded structure under CL, Well GS16, 4th Member, 5462 m.

vicinity of those pre-screened spots with the highest $^{238}U/^{206}Pb$ ratios, so that sufficient U-Pb isotope spot analyses can be obtained for each sample. We use laser spot size of 160 um in diameter, laser energy of 3 J/cm^2 and repetition rate of 10 Hz. The measurement cycle comprised a cleaning sequence of 20 shots, a preablation background of 15 s, an ablation period of 25 s and a washout time of 8 s. The duty cycle included only ^{206}Pb, ^{208}Pb, ^{232}Th, and ^{238}U. The samples were measured together with NIST-614 glass standard and several matrix-matched laboratory working calcite standards, such as WC-1. Repeated measurements of the NIST-614 glass standard bracketing the unknown samples and calcite standards were used to correct for $^{207}Pb/^{206}Pb$ fractionation and for instrument-related drift in the $^{206}Pb/^{238}U$ ratios. WC-1 calcite standard independently dated to 254.4 ± 6.4 Ma (Roberts et al., 2017) was also dated together with the dolomite samples as the control standard to ensure reproducibility, which gave results within 2% of the reference value among different sessions.

4 Results

4.1 Petrological characteristics

4.1.1 Dolomite phases

4.1.1.1 *Matrix dolomites (MD)*

Microscopically, the crystal size of the MD is usually less than 50 μm (Gu et al., 2019). Without constructive diagenesis, the reservoir space of MD is hardly developed due to tiny crystal size (Figure 3A). After alteration by dissolution, large numbers of pores or vugs are formed within MD (Figures 2A,B), and the original sedimentary structures of MD have almost disappeared (Figure 2C). But after early-stage silicification, the silicified MD becomes extremely dense and less susceptible to other diagenesis (Figure 2D). Under CL, the MD is nonluminescent (Figure 3B).

4.1.1.2 *Fine-medium crystalline dolomites (FMD)*

The FMD has a crystal size of 200–450 μm (Gu et al., 2019), most of which is characterized by a nonplanar anhedral or planar subhedral texture with cloudy cores and clean rims (Figure 3C). A large number of scattered intercrystalline pores have developed between crystals filled with bitumen (Figures 2E,F). Under cross-polarized light, the FMD shows typical patterns of wavy extinction (Gu et al., 2019). Under CL, the FMD is bright red with a zonal texture (Figure 3D).

4.1.2 Dolomite cement phases

4.1.2.1 *Fibrous dolomites (FD)*

The FD is present as an isopachous fibrous dolomite coating vug internal walls (Figures 3E,F), which is commonly distributed between larger saddle dolomite (or medium-coarse crystalline dolomite) crystals and host-rock (Figure 3G). In terms of CL color, crystal habit, and size, the FD exhibit obvious difference from saddle dolomite (Figure 3H). The FD under CL is nonluminescent (Figure 3F) and mainly consists of fibrous dolomite with 500 μm in size (Figure 3H) which is clearly

darker than saddle dolomite in transmitted light (Figure 3G). Locally, a fine, dark bitumen line is observed separating FD and saddle dolomite cements (Figure 3E).

4.1.2.2 *Medium-coarse crystalline dolomites (MCD)*

The MCD cements predominantly coat vugs or fractures, showing a sharp contact with the host MD (Figure 3E). The MCD primarily comprises of clear, coarse dolomite crystals growing along internal walls of reservoir spaces, with a bright red luminescence under CL (Figure 3F). A dark bitumen line is ubiquitously present between MCD and saddle dolomite cements (Figure 2G), suggesting an oil emplacement episode predating saddle dolomite cements.

4.1.2.3 *Saddle dolomites (SD)*

Saddle dolomite is the most common dolomite cement in cores and thin sections of the Dengying Formation (Figures 2G,H). Macroscopically, the SD is characterized by curved crystal faces and grayish white in color (Figures 2H,I). In some core samples, the SD coexist with MVT minerals such as sphalerite, galena, and quartz (Figures 2I,J). Under CL, the SD is characterized by alternating luminescence between bright red and dark red (Figures 3G,H).

4.2 Mississippi valley-type (MVT) minerals

MVT Pb-Zn mineral assemblages were occasionally found in pores, vugs, and fractures of the host-rock MD (Figure 2J), but they are relatively low in abundance on the whole. Brownish red sphalerite (Figure 2I), glassy (or gray-white) quartz (Figures 2J,K), golden yellow pyrite (Figure 2L) and silver-white galena mainly occur as fracture- and/or vug-filling minerals (Figure 2M).

4.3 Geochemistry and fluid inclusion

4.3.1 Oxygen, carbon, and strontium isotopes

According to data from previous studies and this study (Zhou et al., 2016; Feng et al., 2017; Peng B. et al., 2018; Gu et al., 2019; Zhou et al., 2020; Su et al., 2022), the MD yields $\delta^{18}O$ values varying from −7.80‰ to + 0.89‰V-PDB (average −4.17‰V-PDB, n=51) and $\delta^{13}C$ values of −0.46‰ to + 7.14‰V-PDB (average + 2.66‰V-PDB, n=51). The FD yields $\delta^{18}O$ values varying from −4.34 to −1.25‰V-PDB (average −3.02‰V-PDB, n=14) and $\delta^{13}C$ values of + 1.12‰ to + 5.36‰V-PDB (average + 2.80‰V-PDB, n=14). The FMD yields $\delta^{18}O$ values varying from −13.84‰ to −4.94‰V-PDB (average −8.37‰V-PDB, n=33) and $\delta^{13}C$ values of −1.93‰ to + 5.29‰V-PDB (average + 1.69‰V-PDB, n=33). The MCD yields $\delta^{18}O$ values varying from −13.32‰ to −8.70‰V-PDB (average −11.32‰V-PDB, n=22) and $\delta^{13}C$ values of −0.32‰ to + 4.96‰V-PDB (average + 2.09‰V-PDB, n=22). The SD yields $\delta^{18}O$ values varying from −14.76‰ to −6.80‰V-PDB (average −12.11‰V-PDB, n=21) and $\delta^{13}C$ values of −5.43‰ to + 2.94‰V-PDB (average −1.20 ‰VPDB, n=21) (Figure 4A).

The MD has $^{87}Sr/^{86}Sr$ ratios ranging from 0.707789 to 0.709800 (average 0.708804, n=10) (Zhou et al., 2016; Feng et al., 2017; Gu et al., 2019; Su et al., 2022). The $^{87}Sr/^{86}Sr$

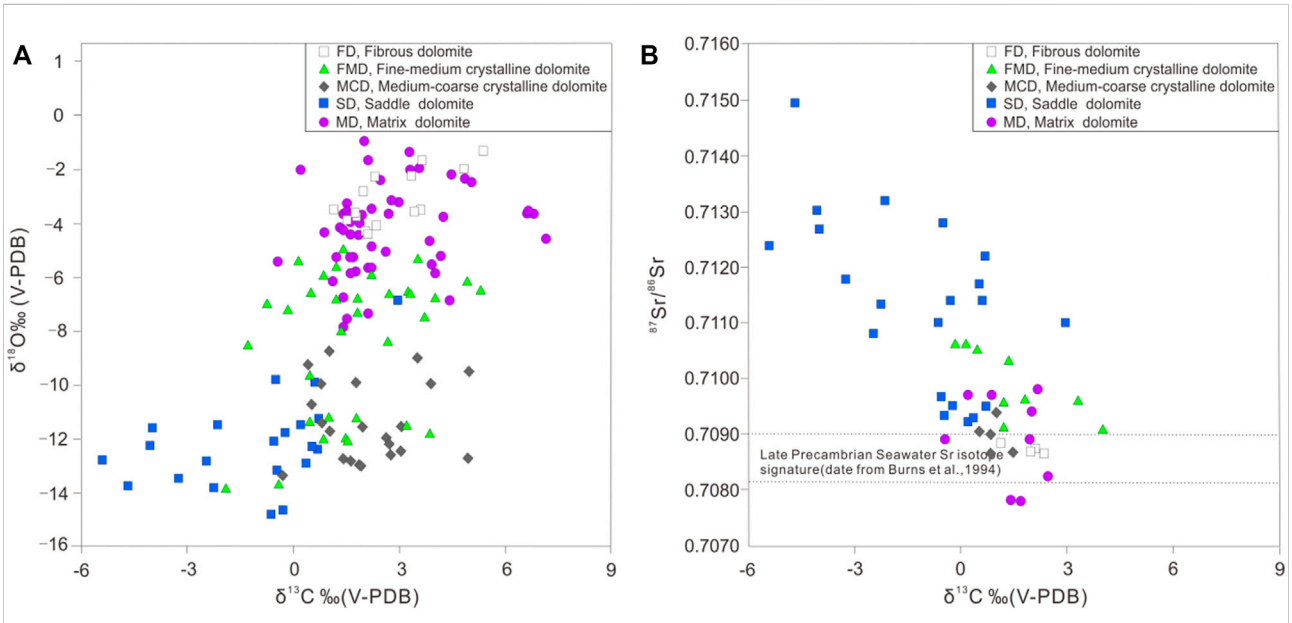

FIGURE 4
(A) Crossplot of $\delta^{13}C$ and $\delta^{18}O$ for different rock fabrics in the Dengying Formation of Central Sichuan Basin (FD, MCD, and SD data are from Feng et al., 2017; Su et al., 2022). **(B)** Crossplot of $\delta^{13}C$ and $^{87}Sr/^{86}Sr$ for different rock fabrics in the Dengying Formation of Central Sichuan Basin ($^{87}Sr/^{86}Sr$ data for FD, MCD, and SD are from Feng et al., 2017; Su et al., 2022; $^{87}Sr/^{86}Sr$ data for late Precambrian seawater are from Burns et al., 1994).

ratios of the FD and MCD have a narrow distribution (Figure 4B), ranging from 0.708645 to 0.708832 and 0.708703 to 0.709359, respectively (Su et al., 2022). The FMD has $^{87}Sr/^{86}Sr$ ratios ranging from 0.709060 to 0.710600 (average 0.709877, n=9) (Zhou et al., 2016; Feng et al., 2017). The $^{87}Sr/^{86}Sr$ ratios of the SD has a wide distribution (Figure 4B), ranging from 0.709218 to 0.714959 (average 0.711343, n=21) (Feng et al., 2017; Gu et al., 2019; Su et al., 2022).

4.4 Rare earth elements (REEs)

The distribution patterns of REEs are widely applied as indicators reflecting origin of diagenetic fluid such as dolomitization fluids (Du et al., 2018; Gu et al., 2019). For example, positive Eu anomalies are often used to indicate the occurrence of hydrothermal activities (Gu et al., 2019; Qi et al., 2021; Su et al., 2022). REE+Y data shown as Post-Archaean Australian Shale (PAAS)-normalized diagrams (Shahida et al., 2013) for different dolomite fabrics are shown in Figure 5. The REE+Y patterns for the MD are characterized by slightly Ce negative anomalies, and slightly Eu positive anomalies (Figure 5A). The REE+Y patterns for the silicified MD are characterized by strongly Ce negative anomalies (Figure 5B). The REE+Y patterns for the FD are characterized by slightly Ce negative anomalies (Figure 5C). The MCD shares similar REE+Y patterns with the MD (Figure 5D). The REE+Y patterns for the FMD are characterized by Ce negative anomalies and strongly Eu

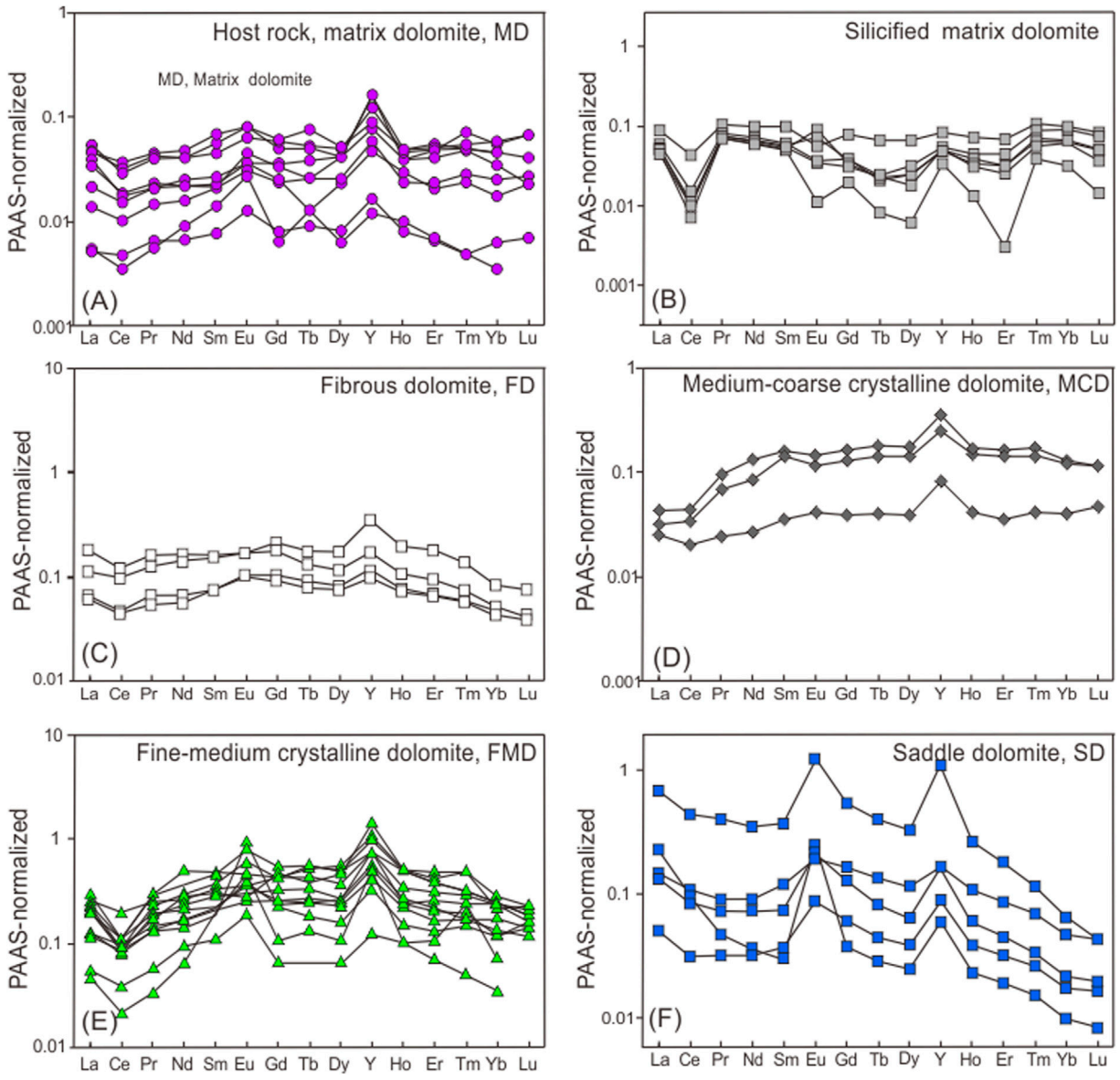

FIGURE 5
REE + Y distribution patterns for different rock fabrics in the Dengying Formation of Central Sichuan Basin (FD and SD data are from Su et al., 2022).

positive anomalies (Figure 5E). The REE+Y patterns for the SD are characterized by strongly Eu positive anomalies (Figure 5F).

4.5 Fluid inclusions

The results of fluid-inclusion petrography and microthermometry for different rock fabrics are displayed in Figure 6. The measurement focuses on primary and pseudo-secondary aqueous inclusions within the dolomite fabrics and quartz cement. Notably, the FD and MD crystals are not suitable for homogenization temperature (Th) measurement owing to its tiny crystal size.

The isopachous FD was formed in a subaerial or submarine environment, suggesting a relatively low precipitation temperature (Ding et al., 2019). Although associated fluid inclusion Th could not be determined, both Th of primary fluid inclusions within Ediacaran halites in the study area and silicon-oxygen isotopes of cherts consistently record Ediacaran seawater temperatures ranging between 13°C and 40°C (Meng et al., 2011). The Th distribution for the MCD range from 77.2°C to 92.8°C, suggesting relatively low-temperature of corresponding diagenetic fluids (Figure 6A). The FMD has Th value in the range between 101.4°C and 152.0°C. The SD has two temperature ranges of 116.5°C–183.0°C and 191.2°C–250.3°C, suggesting two episodes of hydrothermal fluids (Figure 6B). The Th distribution of quartz is similar to that of SD, and it also has two temperature ranges, 115.5°C–162.3°C and 198.6°C–227.2°C, respectively. It is suggested that the two stages of quartz phases were precipitated from two different episodes of hydrothermal fluids.

5 Discussion

5.1 Origin and formation timing of dolomite phases

5.1.1 Matrix dolomite (MD)

Although the dolomitization mechanism of the Ediacaran Dengying Formation is still controversial, we agree with the views that dolomitization of the Dengying Formation occurs in the syndiagenetic stage in terms of well-preserved microbial structure (Peng J. et al., 2018; Zhou et al., 2020). To better understand this unique dolomitization mechanism, a few studies illustrate that microorganisms survived and reproduced in shallow water platforms. After death, they deposited together with carbonate sediments. When the microbial-rich carbonate sediments are below the sediment-water interface, the water body changes from an oxidizing condition to a reducing condition. The organic matter in the microorganism began to decompose under the action of sulfate-reducing bacteria, which decreased sulfate in the seawater to overcome the kinetic barriers of dolomite precipitation and accelerated this process (Zhou et al., 2020).

5.1.2 Fine-medium crystalline dolomites (FMD)

Petrological relationships indicate that the FMD is the part of the MD in which the dolomite crystals become larger after recrystallization (Figure 2E). Compared to MD, the FMD has a more negative $\delta^{18}O$ and a higher $^{87}Sr/^{86}Sr$ ratios, and the FMD isotope data points are concentrated between MD range and SD range (Figure 4). The REE+Y distribution patterns of the FMD also has the characteristics of MD and SD. The above geochemical characteristics confirm the close affinity between FMD and MD, SD (Figure 5). Based on Th measurement results, the Th distribution of the FMD is more close to early SD phase (Figure 6). The U-Pb ages of the two first-stage SD samples measured in this study are 408 ± 40 Ma and 403 ± 30 Ma, respectively (Figure 7). Combined with the burial history curve (Liu et al., 2018a; Su et al., 2022), it is suggested that the Dengying Formation is in the middle diagenetic stage at this time (Figure 8), so the FMD is the product of the recrystallization of MD caused by the first hydrothermal fluid during middle diagenetic stage.

5.2 Origin and formation timing of dolomite cement phases

5.2.1 Fibrous dolomites (FD)

Petrological relationships indicate that the FD is the earliest cement coating the inner walls of vugs formed in the epidiagenetic stage. The U-Pb age of the FD is 553.6 ± 6.4 Ma, suggesting the FD precipitate during the Tongwan Movement in the epidiagenetic stage (Su et al., 2022). There has long been controversy regarding the parent fluids (freshwater or seawater) that led to the precipitation of FD (Tang et al., 1980; Wang et al., 2014; Lin et al., 2018). The FD is nonluminescent under CL (Figure 3), suggesting oxidizing parent fluids (Dorobek, 1987). The REE+Y distribution patterns of FD and MD have the same characteristics, and the $^{87}Sr/^{86}Sr$ ratios of FD are in the range of coeval seawater (Figure 4). Integrated with latest studies (Peng B. et al., 2018; Peng J. et al., 2018; Ding et al., 2019), it is suggested that the formation of the FD is derived from marine flooding of the karst system during epidiagenetic stage.

5.2.2 Medium-coarse crystalline dolomites (MCD)

Petrological relationship shows that the MCD precipitated later than the FD, but earlier than the early bitumen phase. The U-Pb ages of three MCD samples in this study are very close, which are 513 ± 11 Ma, 510 ± 31 Ma and 520 ± 11 Ma, respectively (Figure 7). Combined with the burial history curve (Liu et al., 2018a; Su et al., 2022), it is illustrated that MCD was formed in the second-time early diagenetic stage of the Dengying Formation.

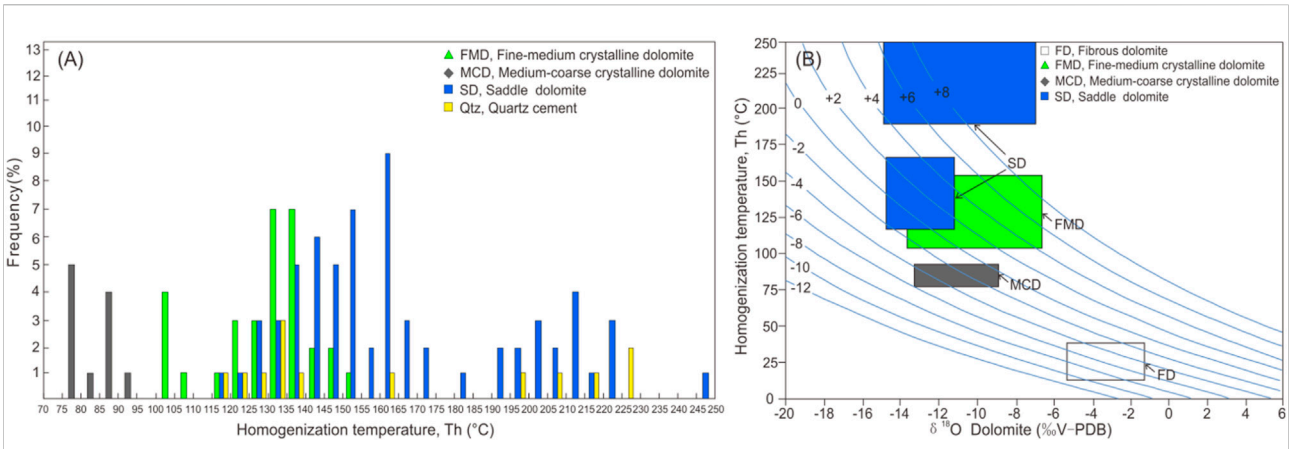

FIGURE 6
(A) Homogenization temperature (Th) distribution of fluid inclusions for different rock fabrics in the Dengying Formation of Central Sichuan Basin and surrounding area (all the Th data are from Feng et al., 2017; Peng J. et al., 2018; Gu et al., 2019; Zhou et al., 2020; Su et al., 2022). **(B)** Crossplot of $\delta^{18}O$ and precipitation temperature for different dolomite fabrics in the Dengying Formation of Central Sichuan Basin and surrounding area (all the Th data are from Feng et al., 2017; Peng B. et al., 2018; Gu et al., 2019; Zhou et al., 2020; Su et al., 2022). The $\delta^{18}O$ (V-SMOW) of dolomite parent fluids was calculated using the equation proposed by Land (1983).

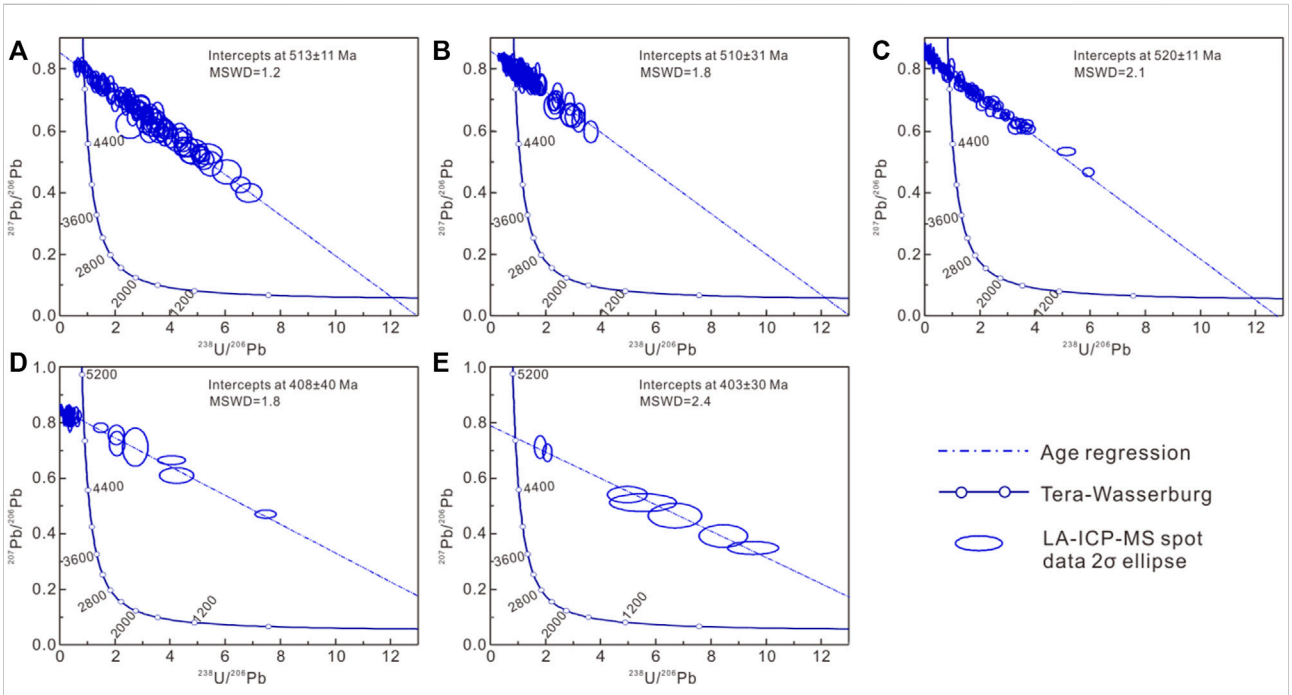

FIGURE 7
(A–C) Tera-Wasserburg Concordia plots showing $^{238}U/^{206}Pb$ vs. $^{207}Pb/^{206}Pb$ of medium-coarse crystalline dolomite (MCD) cement phase in the Dengying Formation of Central Sichuan Basin. **(D,E)** Tera-Wasserburg Concordia plots showing $^{238}U/^{206}Pb$ vs. $^{207}Pb/^{206}Pb$ of early saddle dolomite (SD) cement phase in the Dengying Formation of Central Sichuan Basin.

The REE+Y distribution patterns of MCD does not have Eu positive anomaly, suggesting non-hydrothermal origin (Figure 5). At the same time, its Th is also within the normal range of the early diagenetic stage and is not significantly higher than ambient temperature. Moreover, the $^{87}Sr/^{86}Sr$ ratios of MCD is very closed to coeval seawater and generally similar to host MD record, suggesting that the parent fluids of MCD probably modified coeval seawater.

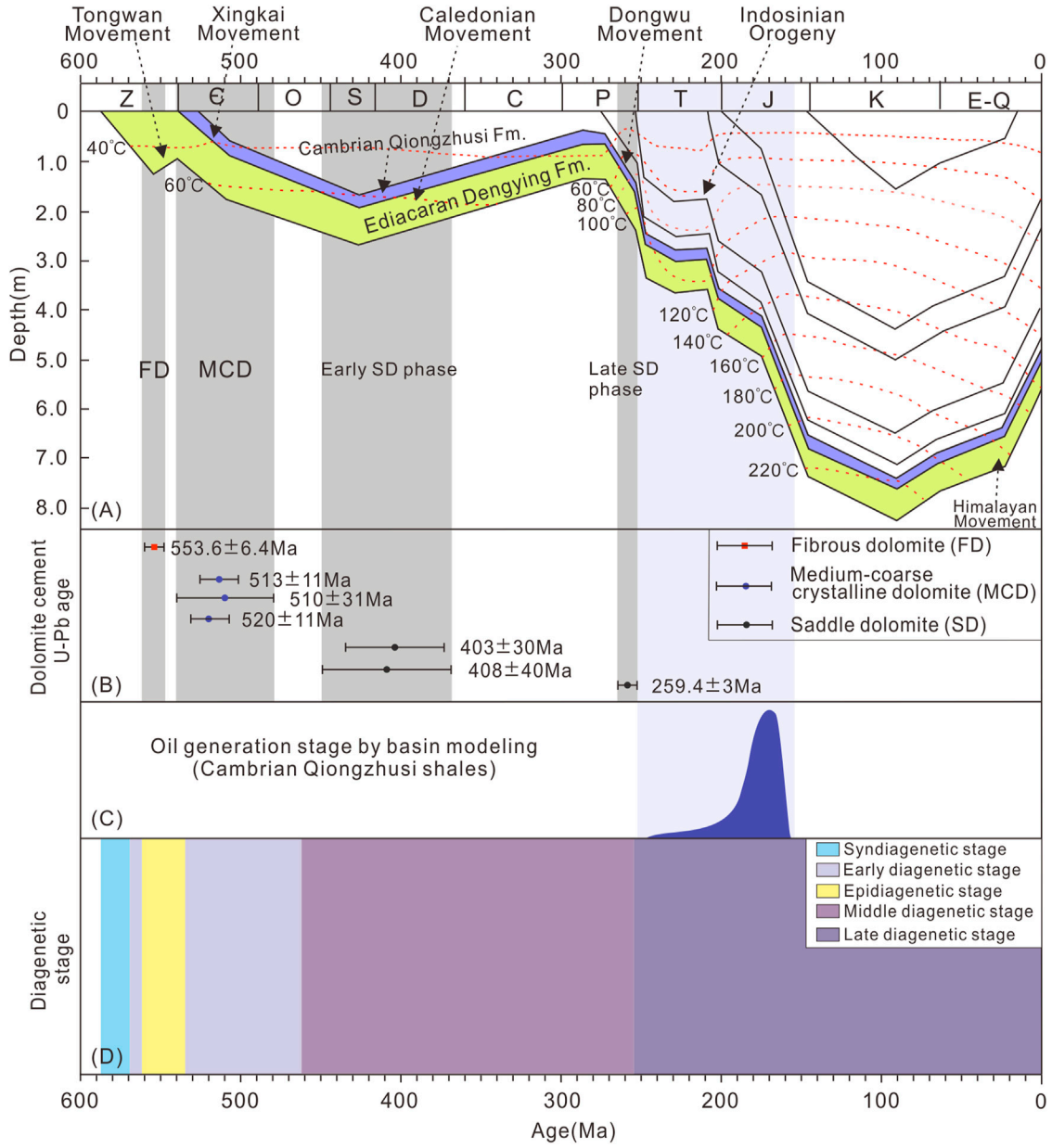

FIGURE 8
(A) Burial-thermal-tectonic evolution history in the Central Sichuan Basin (modified from Liu et al., 2018a; Su et al., 2022). **(B)** *In situ* U-Pb ages for different dolomite cements of the Dengying Formation in the Central Sichuan Basin (data of FD and late SD phase are from Su et al., 2022). **(C)** Oil generation stage of the Cambrian Qiongzhusi shales by basin modeling (Liu et al., 2018b). **(D)** Diagenetic stage of the Dengying Formation in the Central Sichuan Basin.

5.2.3 Saddle dolomites (SD)

The Th measurement results show that the formation of SD can be clearly divided into two episodes (Figure 6), suggesting two episodes of hydrothermal activities. Previous studies have also suggested that there were two-stage hydrothermal activities in the Dengying Formation in the Sichuan Basin, namely, the Late Ediacaran-Early Cambrian and the Late Devonian-Middle Triassic (Liu et al., 2014). Some studies suggest that the second-stage should be limited to the Late Devonian-Late Permian (Jiang et al., 2016; Peng B. et al., 2018). U-Pb dating shows that the early SD phase was precipitated during the Late Silurian to Devonian (Figure 7), when the Dengying Formation was in the middle diagenetic stage. This study did not obtain the U-Pb age of the late SD phase, but Su et al. (2022) determined the U-Pb age of 259.4 ± 3 Ma, this time interval

matches the Late Permian hydrothermal activity triggered by eruption of Emeishan flood basalts (from 257.22 ± 0.37 Ma to 260.55 ± 0.07 Ma) (Huang et al., 2022). Because the Caledonian movement caused the Dengying Formation to be uplifted in the Devonian-Carboniferous and then subsided gradually, the Dengying Formation was still in the middle diagenetic stage in the Late Permian (Figure 8).

5.2.4 Origin of mississippi valley-type (MVT) minerals

Previous studies have noticed the MVT minerals in the Dengying Formation. In view of its coexistence with SD, its hydrothermal origin can be determined (Figure 2). The petrological relationship shows that MVT minerals such as galena, sphalerite, and pyrite coexist with the late quartz phase (Figures 2J–L), indicating that MVT minerals are precipitated from the second-episode hydrothermal fluid. Thus MVT minerals were formed in the Late Permian, when the Dengying Formation was undergoing the middle diagenetic stage.

5.3 Controlling factors and porosity evolution of reservoir

When the Dengying Formation was in syndiagenetic stage for the first time, there were a large number of primary reservoir spaces within microbial sedimentary structures. During

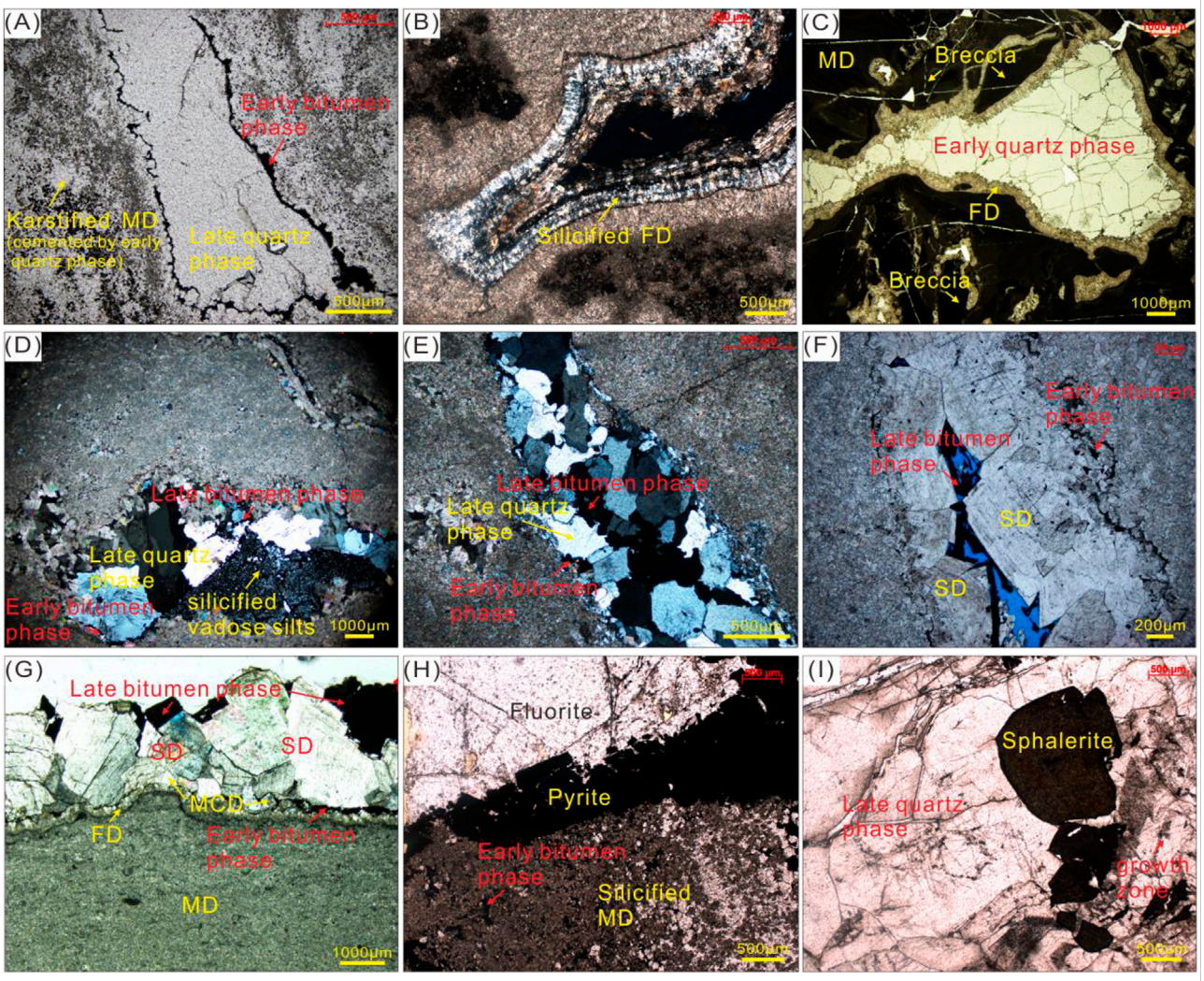

FIGURE 9
Microscopic characteristics of petrographic relationships between different rock fabrics in the Dengying Formation of Central Sichuan Basin. **(A)** Karstified MD cemented by early quartz phase under PPL, Well GS18, 5184.13 m–5184.72 m. **(B)** Silified fibrous dolomites (FD) along inner wall of vugs exhibit grayish white under XPL, Well GS102, 5094.66 m. **(C)** Fibrous dolomites (FD) predating early quartz phase filled along inner wall of vugs formed in epidiagenetic stage, Well MX108, 5304.5 m. **(D)** Vadose silts formed during epidiagenetic stage are silicified by hydrothermal fliuds, Well GS102, 5045.53 m. **(E)** Late quartz phase between two-stage bitumen phase, Well GS102, 5102.89 m. **(F)** Saddle dolomite (SD) between two-stage bitumen phase, Well GS1, 4985 m (Jiang et al., 2016). **(G)** Saddle dolomite (SD) predating fibrous dolomites (FD) and early bitumen phase, Well GS18, 5177.82 m. **(H)** Silicified matrix dolomite (MD) predate early bitumen phase and MVT minerals (pyrite and fluorite), Well MX51, 5383.48 m. **(I)** Coexisting relationship between sphalerite and late quartz phase characterized by growth zone, Well GS109, 5317.4 m.

syndiagenetic stage, the carbonate sediments have not completed the mineral stabilization process, and the mineral components with unstable chemical properties are selectively dissolved by meteoric freshwater, resulting in the formation of secondary reservoir spaces. Meanwhile, microbial dolomitization has limited increase in reservoir porosity, but it can increase the anti-compaction ability, which is of great significance to the preservation of reservoir spaces. Silicification is the most unfavorable for reservoir formation in the syndiagenetic stage. The average porosity of the silified MD is 0.22% lower than the MD (the median decreased by 0.20%), and the average permeability is decreased by 0.220 mD (the median decreased by 0.002 mD) (Figure 10). After silicification in the syndiagenetic stage, the mineral composition of the MD changed from magnesium calcium carbonate to silica, and the later constructive diagenetic alterations were almost ineffective (Figure 2D). Fortunately, the duration and influence range of silicification in the syndiagenetic stage are very limited and will not cause large-scale destructive effects. The Ediacaran is a period of major plate tectonic recombination and extensive non-orogenic volcanic activity (Chen et al., 2009). It is presumed that submarine volcanic activity provides silicon-rich hydrothermal fluids for silicification at the syndiagenetic stage (Ma et al., 2014).

With the increase of buried depth, the Dengying Formation gradually entered the early diagenetic stage. Zhou et al. (2020) proposed that diagenesis in the early diagenetic stage is not conducive to the preservation of reservoir spaces in the Dengying Formation. After this stage, the porosity of dolomite reservoir in the Dengying Formation decreases to below 5%.

The tectonic uplift caused by Tongwan Movement led the Dengying Formation to enter the epidiagenetic stage (Figure 8A). At this stage, the interior and top of the Dengying Formation are generally eroded to varying degrees, forming a large number of non-fabric selective karst pores (Figure 9A), fissures (Figure 9B), and vugs (Figure 9C). Within these secondary reservoir spaces, typical marks of epidiagenetc stage, such as vadose silts, are observed (Figure 9D). After this stage, the average porosity increased by 1.51% (median increased by 1.36%), and the average permeability increased by 0.611 mD (median increased by 0.033mD) (Figure 10). However, because the fractures and vugs of the drilling cores are very developed (Figure 2), the plunger samples for measurement cannot reflect the real reservoir physical properties, and the actual increment of porosity and permeability far exceeds the measured data. Therefore, some scholars have proposed that the total porosity of the Dengying Formation reservoir increased by 10%–20% during epidiagenetic stage (Zhou et al., 2020).

With the end of Tongwan movement, the sea level rose again, and the reservoir space of the Dengying Formation experienced the marine flooding (Ding et al., 2019). The FD precipitated directly from the seawater filling the reservoir spaces along the inner walls (Figures 9B,C). In the second-time early diagenetic stage, the MCD cement directly precipitated from the altered seawater continues to fill the remaining reservoir spaces.

With the increase of burial depth, the Dengying Formation enters middle diagenetic stage. During this period, two stages of hydrothermal alterations occurred, corresponding to Late Silurian to Devonian and Late Permian, respectively. Significant differences in the alteration effects of hydrothermal fluids on MD and karstified MD are revealed. Under the first-stage hydrothermal alteration, the MD recrystallized to form FMD rich in intercrystalline pores. This process increases the average porosity by 1.64% (median increased by 1.28%) and the average permeability by 0.226 mD (median increased by 0.002 mD) (Figure 10). On the other hand, under the action of the first-stage hydrothermal activity, the MD underwent dilational

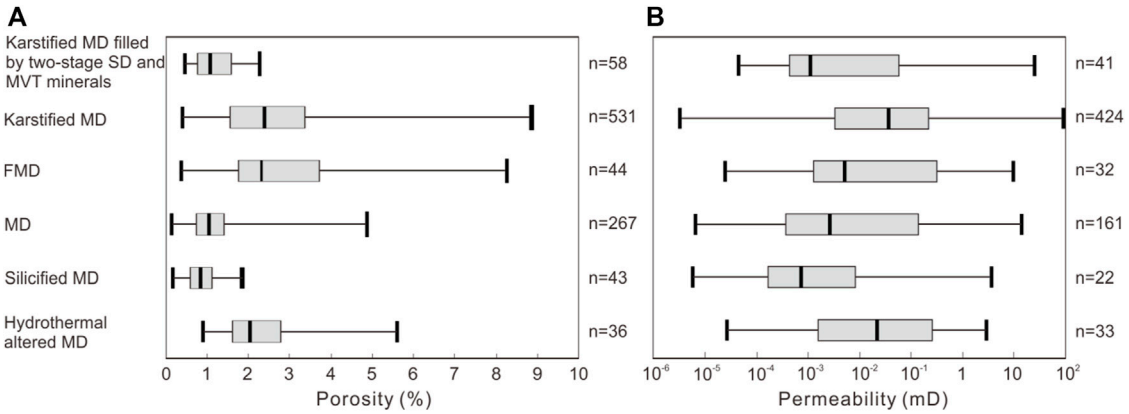

FIGURE 10
(A) Boxplot of porosity distribution in different rock fabrics of the Dengying Formation, Central Sichuan Basin. **(B)** Boxplot of permeablity distribution in different rock fabrics of the Dengying Formation, Central Sichuan Basin.

fracturing and dissolution, accompanied by subsequent precipitation of the first-stage SD cement. The second-stage hydrothermal activity did not lead to the recrystallization of the MD, but only showed dissolution and filling. The filling minerals not only had the second-stage SD cement, but also had MVT minerals such as pyrite, galena, quartz and sphalerite. After two-episode hydrothermal alterations, the average porosity of the MD increased by 1.15% (median increased by 1.01%) and the average permeability decreased by 0.135 mD (median increased by 0.019 mD) (Figure 10). In terms of the karstified MD, both hydrothermal alterations were destructive (Figure 9), resulting in an average porosity decrease of 1.44% (median decreased by 1.32%) and an average permeability decrease of 0.139 mD (median decreased by 0.036 mD) (Figure 10). As mentioned above, since karstified MD samples are all core plunger samples, the actual damage of reservoir physical properties caused by hydrothermal alteration is much worse.

6 Conclusions

1) Two phases of dolomite and three phases of dolomite cement are distinguished in the Ediacaran Dengying Formation deep dolomite reservoirs of Central Sichuan Basin as follows: (1) matrix dolomites (MD), (2) fine-medium crystalline dolomites (FMD), (3) fibrous dolomites (FD), (4) medium-coarse crystalline dolomites (MCD), and (5) saddle dolomite (SD). The FMD is the product of the recrystallization of MD caused by the first hydrothermal fluid during middle diagenetic stage. The FD is derived from marine flooding of the karst system during epidiagenetic stage. The MCD is derived from modified coeval seawater during the second-time early diagenetic stage. The early SD phase is precipitated during the Late Silurian to Devonian, when the Dengying Formation was in the middle diagenetic stage. The late SD phase is precipitated during the Late Permian, while the Dengying Formation is still in the middle diagenetic stage.
2) Syndiagenetic microbial dolomitization has limited increase in reservoir porosity, but it is of great significance to the reservoir space preservation. Syndiagenetic silicification is the most unfavorable for reservoir formation, but it will not cause large-scale destructive effects. Epidiagenetic stage trigger great increase of physical properties of the Dengying Formation dolomite reservoir. Two-stage early diagenetic stages are both destructive to reservoir space maintenance. During middle diagenetic stage, two-stage of hydrothermal alterations occurred, corresponding to Late Silurian to Devonian and Late Permian, respectively. Hydrothermal alteration of the MD is both constructive and destructive, but overall it is constructive, but the improvement of physical properties is limited. Two-stage hydrothermal alterations lead to damage of reservoir physical properties for the karstified MD.

Data availability statement

The raw data supporting the conclusions of this article will be made available by the authors, without undue reservation.

Author contributions

YG contributed as the major author of the article. CY and ML conceived the project. HW, LZ, and YJ collected the samples. ZW and XL analyzed the samples. All authors contributed to the article and approved the submitted version.

Funding

This study was funded by the National Natural Science Foundation of China (Grant No. 41972165) and National Natural Science Foundation of China (Grant No. 42202166).

Conflict of interest

Authors CY and ML were employed by the company PetroChina Southwest Oil and Gas Field Company.

The remaining authors declare that the research was conducted in the absence of any commercial or financial relationships that could be construed as a potential conflict of interest.

Publisher's note

References

Burns, S. J., Haudenschild, U., and Matter, A. (1994). The strontium isotopic composition of carbonates from the late Precambrian (560–540 Ma) Huqf Group of Oman. *Chem. Geol.* 111 (1-4), 269–282. doi:10.1016/0009-2541(94)90094-9

Chen, D., Wang, J., Qing, H., Yan, D., and Li, R. (2009). Hydrothermal venting activities in the early cambrian, south China: Petrological, geochronological and stable isotopic constraints. *Chem. Geol.* 258 (3-4), 168–181. doi:10.1016/j.chemgeo.2008.10.016

Ding, Y., Chen, D., Zhou, X., Guo, C., Huang, T., and Zhang, G. (2019). Cavity-filling dolomite speleothems and submarine cements in the Ediacaran Dengying microbialites, South China: Responses to high-frequency sea-level fluctuations in an "aragonite-dolomite sea". *Sedimentology* 66 (6), 2511–2537. doi:10.1111/sed.12605

Ding, Y., Li, Z., Liu, S., Song, J., Chen, D., Sun, W., et al. (2021). Sequence stratigraphy and tectono-depositional evolution of a late Ediacaran epeiric platform in the upper Yangtze area, South China. *Precambrian Res.* 354, 106077. doi:10.1016/j.precamres.2020.106077

Dorobek, S. L. (1987). Petrography, geochemistry, and origin of burial diagenetic facies, Siluro-Devonian Helderberg group (Carbonate rocks), central Appalachians. *Am. Assoc. Pet. Geol. Bull.* 71 (5), 492–514. doi:10.1306/94886EDE-1704-11D7-8645000102C1865D

Du, Y., Fan, T., Machel, H. G., and Gao, Z. (2018). Genesis of upper cambrian-lower ordovician dolomites in the tahe oilfield, Tarim Basin, NW China: Several limitations from petrology, geochemistry, and fluid inclusions. *Mar. Petroleum Geol.* 91, 43–70. doi:10.1016/j.marpetgeo.2017.12.023

Ehrenberg, S. N., Nadeau, P. H., and Steen, O. (2009). Petroleum reservoir porosity versus depth: Influence of geological age. *Am. Assoc. Pet. Geol. Bull.* 93 (10), 1281–1296. doi:10.1306/06120908163

Fairchild, J., and Spiro, B. (1987). Petrological and isotopic implications of some contrasting Late Precambrian carbonates, NE Spitsbergen. *Sedimentology* 34 (6), 973–989. doi:10.1111/j.1365-3091.1987.tb00587.x

Feng, M. Y., Wu, P. C., Qiang, Z. T., Liu, X. H., Duan, Y., and Xia, M. L. (2017). Hydrothermal dolomite reservoir in the Precambrian dengying formation of central Sichuan basin, Southwestern China. *Mar. Petroleum Geol.* 82, 206–219. doi:10.1016/j.marpetgeo.2017.02.008

Gu, Y., Jiang, Y., Lei, X., Chen, Z., Zhou, L., Fu, Y., et al. (2021). The major controlling factors and different oolitic shoal reservoir characteristics of the Triassic Feixianguan Formation, Eastern LonggangArea, NE Sichuan Basin, SW China. *Acta Geol. sinica-. Engl. Ed.* 95 (3), 895–908. doi:10.1111/1755-6724.14672

Gu, Y., Jiang, Y., Qing, H., Feng, L., Feng, L., Fu, Y., et al. (2020). Reservoir characteristics, pore structure, and main controlling factors of oolitic shoal reservoir in feixianguan formation: A case study from eastern kaijiang-liangping trough. *Arab. J. Geosci.* 13, 309. doi:10.1007/s12517-020-05286-x

Gu, Y., Zhou, L., Jiang, Y., Jiang, C., Luo, M., and Zhu, X. (2019). A model of hydrothermal dolomite reservoir facies in Precambrian dolomite, Central Sichuan Basin, SW China and its geochemical characteristics. *Acta Geol. sinica-. Engl. Ed.* 93 (1), 130–145. doi:10.1111/1755-6724.13770

Guo, C., Chen, D., Qing, H., Dong, S., Li, G., Wang, D., et al. (2016). Multiple dolomitization and later hydrothermal alteration on the Upper Cambrian-Lower Ordovician carbonates in the northern Tarim Basin, China. *Mar. Petroleum Geol.* 72, 295–316. doi:10.1016/j.marpetgeo.2016.01.023

He, Z., Ma, Y., Zhu, D., Duan, T., Geng, J., Zhang, J., et al. (2021). Theoretical and technological progress and research direction of deep and ultra-deep carbonate reservoirs. *Oil Gas Geol.* 42 (3), 533–546. doi:10.11743/ogg20210301

Huang, H., Huyskens, M. H., Yin, Q., Cawood, P. A., Hou, M., Yang, J., et al. (2022). Eruptive tempo of Emeishan large igneous province, southwestern China and northern Vietnam: Relations to biotic crises and paleoclimate changes around the Guadalupian-Lopingian boundary. *Geology* 50 (9), 1083–1087. doi:10.1130/G50183.1

Jiang, Y., Gu, Y., Li, K., Li, S., Luo, M., and He, B. (2018). Space types and origins of hydrothermal dolomite reservoirs in the Middle Permian strata, Central Sichuan Basin. *Nat. Gas. Ind.* 38 (2), 16–24. doi:10.3787/j.issn.1000-0976.2018.02.003

Jiang, Y., Gu, Y., Liu, F., Liu, D., Chen, W., Liao, Y., et al. (2017). Discovery and exploration significance of Permian-Triassic trough and platforrrn margin facies in Zhongxian-Yuchi area, eastern Sichuan Basin. *Acta Pet. Sin.* 38 (12), 1343–1355. doi:10.7623/syxb201712

Jiang, Y., Tao, Y., Gu, Y., Wang, J., Qiang, Z., Jiang, N., et al. (2016). Hydrothermal dolomitization in Dengying Formation, gaoshiti-moxi area, Sichuan Basin, SW China. *Petroleum Explor. Dev.* 43 (1), 54–64. doi:10.1016/S1876-3804(16)30006-4

Land, L. S. (1983). "The application of stable isotopes to studies of the origin of dolomite and to problems of diagenesis of clastic sediments," in *Stable isotopes in sedimentary Geology, SEPM short course*. Editors M. A. Arthur, T. F. Anderson, I. R. Kaplan, J. Veizer, and L. S. Land (Tulsa, Oklahoma, 4.1–4.22.

Li, H. (2022). Research progress on evaluation methods and factors influencing shale brittleness: A review. *Energy Rep.* 8, 4344–4358. doi:10.1016/j.egyr.2022.03.120

Li H., H., Zhou, J., Mou, X., Guo, H., Wang, X., An, H., et al. (2022). Pore structure and fractal characteristics of the marine shale of the longmaxi formation in the changning area, southern Sichuan Basin, China. *Front. Earth Sci.* 10, 1018274. doi:10.3389/feart.2022.1018274

Li, J., Bai, B., Bai, Y., Lu, X., Zhang, B., Qin, S., et al. (2022a). Fluid evolution and hydrocarbon accumulation model of ultra-deep gas reservoirs in Permian Qixia Formation of northwest Sichuan Basin, SW China. *Petroleum Explor. Dev.* 49 (4), 719–730. doi:10.1016/s1876-3804(22)60305-7

Li, J., Li, H., Yang, C., Wu, Y. J., Gao, Z., and Jiang, S. L. (2022b). Geological characteristics and controlling factors of deep shale gas enrichment of the Wufeng-Longmaxi Formation in the southern Sichuan Basin, China. *Lithosphere* 2022 (12), 4737801. doi:10.2113/2022/4737801

Lin, X., Peng, J., Hou, Z., Han, H., Li, X., and Ma, C. (2018). Study on characteristics and geneses of algal dolostone of the upper sinian Dengying Formation in the hanyuan-ebian area of sichuan province, China. *Acta Sedimentol. Sin.* 36 (1), 57–71. doi:10.3969/j.issn.1000-0550.2018.008

Liu, S., Huang, W., Jansa, L. F., Wang, G., Song, G., Zhang, C., et al. (2014). Hydrothermal dolomite in the upper sinian (upper proterozoic Dengying Formation, east Sichuan Basin, China. *Acta Geol. Sin. - Engl. Ed.* 88 (5), 1466–1487. doi:10.1111/1755-6724.12312

Liu, W., Qiu, N. S., Xu, Q. C., and Chang, J. (2018b). The quantitative evaluation of the pressurization caused by hydrocarbon generation in the Cambrian Qiongzhusi Formation of the Gaoshiti-Moxi area, Sichuan Basin. *Petroleum Sci. Bull.* 3 (3), 262–271. doi:10.3969/j.issn.2096-1693.2018.03.024

Liu, W., Qiu, N., Xu, Q., and Liu, Y. (2018a). Precambrian temperature and pressure system of Gaoshiti-Moxi block in the central paleo-uplift of Sichuan Basin, southwest China. *Precambrian Res.* 313, 91–108. doi:10.1016/j.precamres.2018.05.028

Ma, W., Liu, S., Huang, W., Chen, C., and Zhang, C. (2014). Fabric characteristics and formation mechanism of chert in sinian Dengying Formation, eastern chongqing. *Acta Geol. Sin.* 88 (2), 239–253. doi:10.3969/j.issn.0001-5717.2014.02.007

Meng, F., Ni, P., Schiffbauer, J. D., Yuan, X., Zhou, C., Wang, Y., et al. (2011). Ediacaranseawater temperature: Evidence from inclusions of sinian halite. *Precambrian Res.* 184 (1-4), 63–69. doi:10.1016/j.precamres.2010.10.004

Peng, B., Li, Z., Li, G., Liu, C., Zhu, S., Zhang, W., et al. (2018). Multiple dolomitization and fluid flow events in the precambrian Dengying Formation of Sichuan Basin, southwestern China. *Acta Geol. Sin. - Engl. Ed.* 92 (1), 311–332. doi:10.1111/1755-6724.13507

Peng, J., Zhang, H., and Lin, X. (2018). Study on characteristics and Genesis of botryoidal dolostone of the upper sinian Dengying Formation: A case study from hanyuan region, sichuan. China. *Carbonates Evaporites* 33, 285–299. doi:10.1007/s13146-017-0343-8

Qi, L., Gu, Y., He, P., Wang, Z., Jiang, Y., Li, S., et al. (2021). Hydrothermal dolomitization in the middle permian in the central Sichuan Basin, SW China: Evidence from petrology, geochemistry, and fluid inclusions. *Arab. J. Geosci.* 14, 55. doi:10.1007/s12517-020-06386-4

Roberts, N. M. W., Rasbury, E. T., Parrish, R. R., Smith, C. J., Horstwood, M. S. A., and Condon, D. J. (2017). A calcite reference material for LA-ICP-MS U-Pb geochronology. *Geochem. Geophys. Geosyst.* 18 (7), 2807–2814. doi:10.1002/2016GC006784

Schmoker, J. W., and Hally, R. B. (1982). Carbonate porosity versus depth:A predictable relation for South Florida. *AAPG Bull.* 66 (12), 2561–2570.

Shahida, W., Naila, S., and Yasir, F. (2013). Rare Earth and high field-strength elements in the multani mitti clay: A study using inaa. *Geostand. Geoanal. Res.* 37 (2), 197–205. doi:10.1111/j.1751-908X.2012.00186.x

Shi, Z., Wang, Y., Tian, Y., and Wang, C. (2013). Cementation and diagenetic fluid of algal dolomites in the sinian Dengying Formation in southeastern Sichuan Basin. *Sci. China Earth Sci.* 56 (2), 192–202. doi:10.1007/s11430-012-4541-x

Su, A., Chen, H., Feng, Y., Zhao, J., Wang, Z., Hu, M., et al. (2022). *In situ* U-Pb dating and geochemical characterization of multi-stage dolomite cementation in the Ediacaran Dengying Formation, Central Sichuan Basin, China: Constraints on diagenetic, hydrothermal and paleo-oil filling events. *Precambrian Res.* 368, 106481. doi:10.1016/j.precamres.2021.106481

Tang, T., Xue, Y., and Yu, C. (1980). The characters and environment significance of the Sinian algae-carbonates in the southern part of China. *Chin. Sci. Bull.* 32 (18), 853–855. CNKI:SUN:KXTB.0.1980-18-010.

Wang, G., Liu, S., Li, N., Wang, D., and Gao, Y. (2014). Formation and preservation mechanism of high quality reservoir in deep burial dolomite in the Dengying Formation on the northern margin of the Sichuan Basin. *Acta Petrol. Sin.* 30 (3), 667–678. doi:10.1134/S1075701514020044

Wang, Z., Jiang, C., Jiang, Y., Zhang, J., and Gu, Y. (2018). Distribution patterns and controlling factors for reservoir characteristic difference of oolitic shoals, Feixian'guan Formation, eastern Longgang area, SW China. *Arab. J. Geosci.* 11, 751. doi:10.1007/s12517-018-4082-5

Xu, F., Xu, G., Liang, J., Yuan, H., Liu, Y., and Xu, F. (2016). Multi-stage fluid charging and critical period of hydrocarbon accumulation of the Sinian Dengying Formation in central Sichuan Basin. *Acta Geol. Sin. Engl. Ed.* 90 (4), 1549–1550. CNKI:SUN:DZXW.0.2016-04-034.

Zhao, W., Shen, A., Zheng, J., Qiao, Z., Pan, L., Hu, A., et al. (2018). Genetic types and distinguished characteristics of dolomite and the origin of dolomite reservoirs. *Petroleum Explor. Dev.* 45 (6), 983–997. doi:10.1016/s1876-3804(18)30103-4

Zhao, W., Shen, A., Zheng, J., Qiao, Z., Wang, X., and Lu, J. (2014). The porosity origin of dolostone reservoirs in the Tarim, Sichuan and Ordos basins and its implication to reservoir prediction. *Sci. China Earth Sci.* 44 (9), 2498–2511. doi:10.1007/s11430-014-4920-6

Zhao, W., Xie, Z., Wang, X., Shen, A., Wei, G., Wang, Z., et al. (2021). Sinian gas sources and effectiveness of primary gas-bearing system in Sichuan Basin, SW China. *Petroleum Explor. Dev.* 48 (6), 1260–1270. doi:10.1016/s1876-3804(21)60285-9

Zhou, Y., Jiang, Y., Liang, J., Gu, Y., Fu, Y., and Xiao, Y. (2020). Characteristics and controlling factors of dolomite karst reservoirs of the Sinian Dengying Formation, central Sichuan Basin, southwestern China. *Precambrian Res.* 343, 105708. doi:10.1016/j.precamres.2020.105708

Zhou, Y., Yang, F., Ji, Y., Zhou, X., Zhang, C., and Xiao, Y. (2021). Reservoir characteristics and major controlling factors of the cambrian xixiangchi formation, central Sichuan Basin, southwest China. *J. Energy Eng.* 147 (6), 04021051. doi:10.1061/(ASCE)EY.1943-7897.0000803

Zhou, Z., Wang, X., Yin, G., Yuan, S., and Zeng, S. (2016). Characteristics and Genesis of the (sinian) Dengying Formation reservoir in central sichuan, China. *J. Nat. Gas Sci. Eng.* 29, 311–321. doi:10.1016/j.jngse.2015.12.005

Zhu, D., Zhang, D., Zhang, R., Feng, J., and He, Z. (2015). Fluid alteration mechanism of dolomite reservoirs in Dengying Formation, South China. *Acta Pet. Sin.* 36 (10), 1188–1198. doi:10.7623/syxb201510002100

Zhu, X., Gu, Y., Jiang, Y., Tang, T., Xu, W., Li, K., et al. (2019). Characteristic and reservoir body classification & evaluation of Sinian Dengying karst reservoirs in the Gaoshiti Block of central Sichuan Basin. *Nat. Gas. Ind.* 39 (3), 38–46. doi:10.3787/j.issn.1000-0976.2019.03.005

Zou, C., Xu, C., Wang, Z., Hu, S., Yang, G., Li, J., et al. (2011). Geological characteristics and forming conditions of the large platform margin reef-shoal gas province in the Sichuan Basin. *Petroleum Explor. Dev.* 38 (6), 641–651. CNKI:SUN:SKYK.0.2011-06-002.

frontiers | Frontiers in Earth Science

TYPE Original Research
PUBLISHED 12 January 2023
DOI 10.3389/feart.2022.1052734

OPEN ACCESS

EDITED BY
Shuai Yin,
Xi'an Shiyou University, China

REVIEWED BY
Teng Zhao,
China University of Geosciences, China
Xiaowei Lv,
Chengdu University of Technology, China

*CORRESPONDENCE
Haihua Zhu,
zhhswpu@163.com

SPECIALTY SECTION
This article was submitted to Structural Geology and Tectonics, a section of the journal Frontiers in Earth Science

RECEIVED 24 September 2022
ACCEPTED 28 December 2022
PUBLISHED 12 January 2023

CITATION
Zhang R, Zhang B, Wang M, Zhu H, Zhang S, Tang W, Zhou H, Li Y, Bai R, Jia M, Zhu Y and Han L (2023), Paleo-sedimentary environment and lithofacies of Jurassic Da'anzhai Member in the Central Sichuan Basin-A case study of Well Ren'an 1.
Front. Earth Sci. 10:1052734.
doi: 10.3389/feart.2022.1052734

Paleo-sedimentary environment and lithofacies of Jurassic Da'anzhai Member in the Central Sichuan Basin-A case study of Well Ren'an 1

Rui Zhang[1,2], Benjian Zhang[2], Minglei Wang[3], Haihua Zhu[4,5]*, Shaomin Zhang[2], Wenqiang Tang[2], Hongfei Zhou[2], Yucong Li[2], Rong Bai[2], Min Jia[2], Yiqing Zhu[2] and Luyuan Han[2]

[1]Key Laboratory of Exploration Technologies for Oil and Gas Resources, Ministry of Education, Yangtze University, Wuhan, China, [2]PetroChina Southwest Oil & Gas Field Company, Chengdu, China, [3]PetroChina Research Institute of Petroleum Exploration & Development, Beijing, China, [4]School of Geoscience and Technology, Southwest Petroleum University, Chengdu, China, [5]The Unconventional Reservoir Evaluation Department, PetroChina Key Laboratory of Unconventional Oil and Gas Resources, Chengdu, China

The Jurassic Da'anzhai Member in Sichuan Basin is an important target for shale oil exploration. Whole rock X-ray diffraction analysis, thin section, SEM and TOC testing, as well as major and trace element analysis are used to analyze the relationship of lithofacies and pore types with the sedimentary environment of the Da'anzhai Member in the Central Sichuan Basin. The results show the Da'anzhai Member in the Well Ren'an 1 (RA1) is divided into six types of lithofacies, based on a three-level division method of mineral composition-TOC-mineral structure— namely, massive mud-bearing shell limestone lithofacies (F), thick argillaceous shell limestone lithofacies (E), laminated clay silt shale lithofacies (D), thin shell calcareous shale lithofacies (C), laminated shell-bearing shale lithofacies (B), and thick clay shale lithofacies (A). The pore spaces include intergranular pores, intergranular dissolution pores, authigenic calcite intergranular pores, authigenic quartz intercrystalline pores, intergranular pores of clay minerals or pyrite nodules, as well as organic pores. The Da'anzhai Member was deposited in a semi-deep to shallow lake sedimentary environment, with relatively low salinity. This strata experienced moderate-to-strong chemical weathering as a result of the semi-arid, warm and humid paleoclimate environmental conditions that persisted during its deposition; low weathering and dry paleoclimate conditions occurred periodically. Paleoenvironment is an important influence on the lithofacies and pore types of the Da'anzhai Member. The persistence of arid climate conditions contributed to a decline in water depth, relatively high salinity, low organic productivity, and the deposition of carbonate rocks that characterize lithofacies E and F; mostly intercrystalline pores formed in these lithofacies in response to the prevailing arid climate conditions. Conversely, warm, and humid climate conditions increased the inflow of fresh water, terrigenous debris, and nutrients into the lacustrine basin that led to the deposition of fine-grained sedimentary rocks of lithofacies A, B, and C. These lithofacies are characterized by abundant nano pores, such as clay intercrystalline pores and organic pores.

KEYWORDS

lithofacies, shale, sedimentary environment, Da'anzhai Member, Central Sichuan Basin

1 Introduction

The Sichuan Basin, located in the northwest Yangtze Platform, covers an area of about 19 $km^2 \times 10^4$ km^2. It is a typical multi-stage tectonic superposition basin, and the oil and gas source rocks in the Sichuan Basin are thick and widely distributed (Liu et al., 2012). Previous studies on the shale formations of the Da'anzhai Member are few, and mainly focus on their stratigraphy, lacustrine shale sedimentary facies, organic matter abundance, formation of source rocks, and hydrocarbon generation potential (Yang et al., 2005; Zheng, 2014; Chen et al., 2015). Paleo-environmental studies focus on basin evolution during the Silurian and Triassic (Wang et al., 2016; Zhou et al., 2021). A previous study on the sedimentary paleo-environment of the Da'anzhai section in Central Sichuan suggests the presence of a brackish—fresh water environment, characterized by moist and anoxic reduction (Lei et al., 2021).

Various types of lithofacies are recognized in the Da'anzhai Member. Wang C. Y et al. (2022) classified 17 lithofacies and five fine-grained sedimentary facies assemblages in the Yuanba area of the Sichuan Basin. However, the relationship between paleoenvironment and lithofacies and pore types of the Da'anzhai Member is rarely discussed.

Shale is a typical fine-grained sedimentary rock and an important carrier of hydrocarbon molecules (Curtis, 2002; Li et al., 2019; Li et al., 2022; Meakin et al., 2013; Su et al., 2018; Zhu et al., 2018; Zou et al., 2010). Its mineral composition, major and trace elements, as well as type and abundance of organic matter are closely related to the sedimentary environment and climate conditions at the time of deposition (Fu et al., 2018; Huo et al., 2022; Milliken, 2014). Studying these factors typically employs laboratory-based measurements of major and trace element geochemistry, organic geochemistry biomarkers, rare Earth element geochemistry, and isotope geochemistry (Gao et al., 2020).

In this paper, the lithofacies types, paleoclimate, paleo-water depth, paleo-productivity, paleo-redox environment, paleo-productivity, and the control of sedimentary environment on lithofacies in the Da'anzhai Member are studied from samples of Well RA1, in the Longgang area of the Central Sichuan Basin, using thin sections, X-ray diffraction (XRD), and elemental geochemical experiments.

2 Geological background

The study area is located in the Renhe Gentle Tectonic Belt which is a part of the Central Sichuan Gentle Fold Area (Figure 1) (Huang et al., 2018). Its tectonic evolution was controlled mainly by the rigid basement of the Qinling Mountains and the Sichuan Basin; some gentle, low hill-like anticlines were developed in this area. Drilling data suggests that the Da'anzhai Member, which is the focus of this study, is 70–100 m thick; gray-brown limestone, gray-black shale, and gray-brown limestone are developed within this member. It is divided into the Da 3, Da 2, and Da 1 sub-members, from bottom to top. Medium and thick, massive shell limestone intercalated with shale are developed in the Da 1 sub-member; gray-black and black shale interbedded with gray-black shale and gray-brown limestone are developed in the Da 2 sub-member; and massive shell limestone are developed in the Da 3 sub-member (Xiao et al., 2021).

The Da'anzhai Member of the Ziliujing Formation is an integrated contact with both, the overlying transition layer and the underlying Ma'anshan Formation. Its depositional period marks a period of time when the regional extension regime was at its weakest; orogen activity was the most stable during this period. The depression rate of the whole Sichuan Basin was higher as compared to the accumulation rate of terrigenous debris. Furthermore, the largest lake basin in the Early Jurassic was formed here A significant part of the Da'anzhai Member in the study area formed as part of a semi-deep lake—deep lake sedimentary facies deposition. A lacustrine transgression occurred during the depositional period of the Da 3 sub-member, and the largest lake basin was formed during the Da 2 sub-member stage.

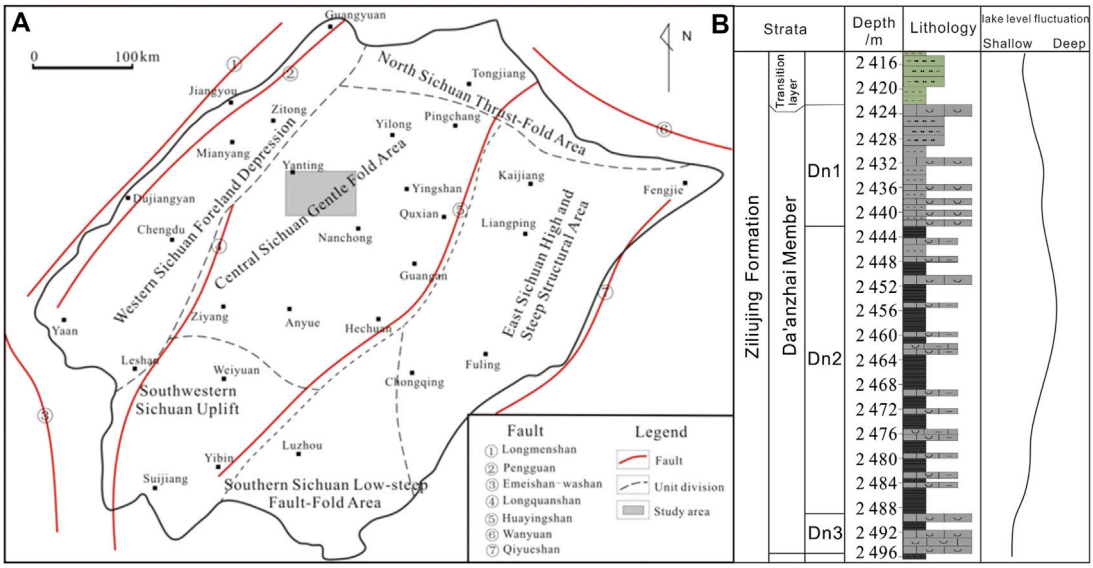

FIGURE 1
(A) Regional geology map of the Sichuan Basin marking the study area and **(B)** the stratigraphic column of the Da'anzhai Member of the Ziliujing Formation.

Lacustrine regression occurred during the late stage of deposition of the Da 2 sub-member. By the late stage of sedimentation of the Da 1 sub-member, the lake had dropped to a lower level and shell limestones are well developed here (Li and He, 2014).

3 Samples and methods

Fifty-six samples, collected from the Da'anzhai Member of Well RA1 at depths ranging from 2,432.26 to 2,485.13 m, are used in this study. All samples, pulverized to 200 mesh size powder, were split into several parts for analysis, including whole-rock X-ray diffraction (XRD), organic carbon and major and trace elements testing.

TOC content was determined by the combustion method of Krom and Berner (1983); measurements were done with a LECO-230 carbon and sulfur analyzer. Samples were treated with hydrochloric acid to remove carbonates prior to measurement. The reproducibility of TOC measurements is better than .1%.

Mineral compositions were analyzed by the X-ray diffraction (XRD) method using a D/Max 2500 PC type powder X-ray diffractometer. Standard powder diffraction data provided by the Consortium International Data Center for Powder Diffraction (JCPDS-ICDD) was used as a standard. The whole-rock mineral content in the shale samples was calculated by the K-value method.

An AxiosMAX XRF was used for X-ray fluorescence spectrometry to measure the oxides of major elements, including SiO_2, Al_2O_3, CaO, K_2O, Na_2O, Fe_2O_3, MnO, MgO, TiO_2, and P_2O_5. Analytical procedures were in accordance with Chinese National Standard GB/T 14506.28-2010, and the FeO was analyzed according to GB/T 14506.14-2010. The precision of the major element data is ≤3%.

An inductively coupled plasma mass spectrometer (ICP-MS PE300D) was used to determine the trace element contents in accordance with GB/T 14506.30-2010. For all samples, a fixed volume (40 mg) was first toasted in an oven at 105°C for 1–2 h and cooled to room temperature, then digested with 2.5 mL HF and .5 mL HNO_3 in a tightly sealed Teflon screw–cap beaker at 190°C for 24 h, and then dried. The dried sample was dissolved again in 5 mL 30% (v/v) HNO_3 for 3 h at 130°C and diluted to 25 mL before testing. The lower detection limit for elements was $0.n \times 10^{-12}$–$n \times 10^{-12}$(n = 1–9).

4 Results

4.1 Lithofacies type

The three-level lithofacies division method of mineral composition-TOC-mineral structure (Michaelis et al., 2002) are used to divide the lithofacies of the Da'anzhai Member in Well RA1. Main components of the fine-grained sedimentary rocks in the target layer include calcite, clay, and quartz, followed by dolomite and feldspar. The content of calcite ranges from 5.0% to 56.1%, with an average of 18.5%; the clay minerals are mainly illite, with a content of 35%–49%, with an average of 42%; the content of quartz varies between 6.12% and 51.57%, with an average of 33.7%. Of these minerals, most of the clays and quartz come from the weathering of rocks at the edge of the basin; they are physically transported into the lake basin. The calcite is mostly formed by bio-chemical precipitation in the basin. Due to the difference in their origins, both clay minerals and quartz showed a significant negative correlation with carbonate components (Figure 2).

The internal composition of the rock can reflect its environment of development. Felsic, clay and carbonate minerals are the end members in a triangle diagram, where their content is capped at 50% (Figure 3). Four rock categories are defined here: siltstone, clay rock, carbonate rock, and mixed fine-grained rocks. Organic matter plays an important role in oil and gas generation, in diagenesis, as well as in organic pore evolution (Fu et al., 2018; Zhou et al., 2020). Therefore, organic matter abundance should be considered when classifying shale facies types. Statistics show that the organic matter abundance (TOC) of the Da'anzhai section is low, with TOC ranging from .6% to 3.16%, with an average of 1.27%. The lower limit of TOC for the Da'anzhai shale oil reservoirs is 1.5%. The lower content of TOC (0%–1.5%) means that the Da'anzhai section is largely poor in organic matter, except for where a locally higher content of TOC (>1.5%) signals an enriched organic zone.

Based on a comprehensive consideration of mineral content, organic matter abundance, and sedimentary structures, the Da'anzhai Member of Well RA1 is divided into six lithofacies: massive mud-bearing shell limestone, Lithofacies F; thick argillaceous shell limestone, Lithofacies E; laminated clay silt shale, Lithofacies D; thin shell calcareous shale, Lithofacies C; laminated shell-bearing shale, Lithofacies B; and massive siliceous shale, Lithofacies A (Figure 3).

4.1.1 Massive siliceous shale (Lithofacies A)

The mineral debris is mainly mud grade with silt debris scatter distributed in massive mud-bearing shell limestone lithofacies (Figure 4). Clay minerals are cryptocrystalline and have microscopic scale-like structures. Organic matter is scattered in the form of spots, and in short thin strips. The average content of felsic minerals, clay minerals, carbonate components, and TOC were 40.15%, 50.61%, 9.24%, and 1.578%, respectively.

4.1.2 Laminated shell-bearing shale (Lithofacies B)

Mainly argillaceous structures are mainly developed in the laminated shell-bearing shale lithofacies (Figure 4B). Small amounts of silt and shell debris are distributed in short, thin strips. Clay minerals are cryptocrystalline and have microscopic scale-like structures. Organic matter is scattered in spots and short, thin strips. The average content of felsic minerals, clay minerals, carbonate components, and TOC were 43.29%, 43.23%, 13.48%, and 1.41%, respectively.

4.1.3 Thin shell calcareous shale (Lithofacies C)

Clay minerals are well developed in this thin shell calcareous shale lithofacies (Figure 4C). They have a cryptocrystalline structure, and lamellar oriented shells are visible. Organic matter is distributed as spots and in short, thin strips. The average content of felsic minerals, clay minerals, carbonate components, and TOC were 37.68%, 39.45%, 22.87%, and 1.33%, respectively.

4.1.4 Laminated clay silt shale (Lithofacies D)

Muddy laminae and granular laminae are developed within the laminated clay silt shale lithofacies (Figure 4D). These structures are mainly composed of cryptocrystalline clay minerals and terrigenous silt, and the silt components in some samples have directional distribution characteristics. The average content of felsic minerals, clay minerals, carbonate components, and TOC were 34.75%, 40.33%, 18.49%, and 1.29%, respectively.

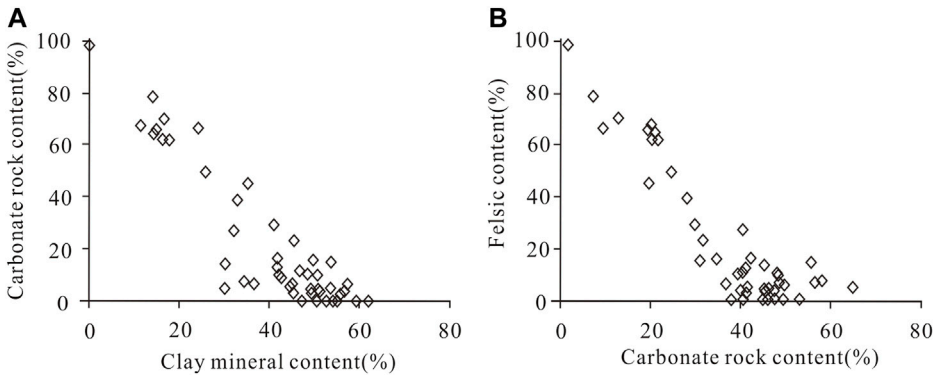

FIGURE 2
(A) Relationship between carbonate and clay minerals and **(B)** carbonate minerals and felsic components in the target layer of Well RA1.

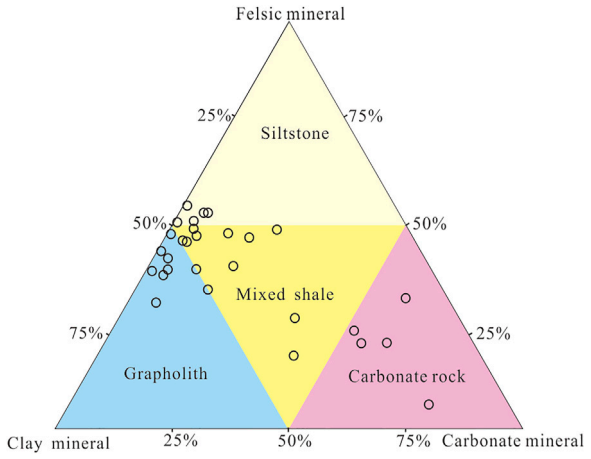

FIGURE 3
Triangular mineral composition diagram of Well RA1.

4.1.5 Medium-thick argillaceous shell limestone (Lithofacies E)

The sedimentary structure of the medium-thick argillaceous shell limestone lithofacies is massive (Figure 4E). Its main lithology is shell limestone with argillaceous components. The average content of felsic minerals, clay minerals, carbonate components, and TOC were 31.22%, 26.73%, 42.03%, and 1.15%, respectively.

4.1.6 Massive mud-bearing shell limestone (Lithofacies F)

Shell limestones are developed in massive mud-bearing shell limestone facies (Figure 4A). The average content of felsic minerals, clay minerals, carbonate components, and TOC were 41.36%, 35.78%, 22.85%, and 1.04%, respectively.

4.2 Pore structure features

Many pore types are identified in the Da'anzhai Member; karst caves, fractures, dissolution pores, and intercrystalline pores were reported from the shell limestones (Pang et al., 2018); fractures, organic pores, and inorganic pores were reported from the shales (Zhu et al., 2022). In this paper, the pores of the Da'anzhai Member are divided into two types, inorganic and organic pores. Inorganic pores are further divided into six subtypes, according to their mode of origin and distribution. Of these, the intercrystalline pores in shell calcite are distributed within the large shell (Figure 5A). The pores that formed during the recrystallization process of the shell are polygonal, with straight and regular edges; they have large pore diameters. The process of shell recrystallization may be accompanied by dissolution, resulting in the formation of intercrystalline dissolution pores in shell calcite. These pore edges are typically smooth (Figure 5B).

Intercrystalline pores of authigenic calcite refer to the intercrystalline pores within the calcite cement (Figure 5C). They are mostly distributed between the shells or in the early shielding space formed by them. In the diagenetic process, shell calcite is easily replaced by quartz, and a large number of quartz intercrystalline pores can form within the authigenic quartz (Figure 5D). Clay intercrystalline pores are the most common, which are distributed among platelet clay minerals (Figure 5E). They usually occur as flakes, in large numbers, and with small pore sizes. Microscopic observations show that their pore sizes range from 5 to 550 nm, with peak distribution between 50 and 99 nm. Intergranular pores of pyrite refer to the pores between authigenic pyrite crystals (Figure 5F), which are filled either completely or partly with organic matter; they are unevenly distributed and have weak local connectivity. Organic pores are distributed in amorphous asphaltene bodies (Figures 5G, H), and the degree of development is low. Pores in kerogen are rare. Pores in organic matter are small and round, with pore size mainly distributed from 0 to 149 nm, with peak distribution at 55–99 nm.

5 Discussion

The content of major and trace elements in sedimentary rocks can be used to characterize the water media and paleoclimate changes during the formation of the strata (Wang et al., 2019). This is because the physical and chemical properties of the elements, and the paleoclimate have a tremendous influence on the distribution of elements (McLennan et al., 1993; Nesbitt and Young, 1989). The geochemical properties of elements are complex. The adsorption of specific mineral particles to specific elements, the exchange of

FIGURE 4
Photographs of cores showing the developmental characteristics of different lithofacies in Well RA1; **(A)** massive mud-bearing shell limestone, Lithofacies F, 2,435.28–2,435.45 m; **(B)** laminated shell-bearing shale, Lithofacies B, 2,466.94–2,466.97 m; **(C)** thin shell calcareous shale, Lithofacies C, 3,496.51–3,496.68 m; **(D)** laminated clay silt shale, Lithofacies D, 2,466.84–2,466.97 m; **(E)** medium-thick argillaceous shell limestone, Lithofacies E, 2,459.19–2,459.27 m; **(F)** massive mud-bearing shell limestone, Lithofacies F, 2,466.31–2,466.84 m.

elements between sediments and aqueous media, the chemical properties of the elements themselves, and the paleoenvironment all affect the distribution of elements. Elemental geochemical indicators can, under different sets of conditions, offer limited interpretations of the sedimentary environment. For example, redox-sensitive trace elements can be used to characterize redox conditions only when they are concentrated from the water body, rather than from terrigenous detritus. In this study, the poor correlation of these redox-sensitive trace elements with Th indicate that U, V, Ni, and Cr in the sediments concentrated through authigenic enrichment rather than from detrital input (Figure 6).

5.1 Paleoclimate evaluation

In sedimentary environments, with stable tectonic activity, climate has significant influence on the depositional environment; it controls the temperature, Eh, pH, and paleosalinity. Common indicators used to describe paleoclimate conditions include the paleoclimate index (*C*), Sr, Cu and Sr/Cu, Fe/Cu, Mg/Ca, Fe/Mn, and SiO_2/AlO_3. In this study, the chemical index of alteration (*CIA*) and climate index (*C*) were used to analyze the paleoclimate conditions prevalent at the time of formation of the Da'anzhai Member. Paleoclimate and parent rock composition can affect the weathering intensity, and *CIA* is an effective indicator parameter of paleoclimate. Following Fu et al. (2017), CIA is calculated as

$$CIA = 100 \times Al_2O_3 / (Al_2O_3 + CaO + Na_2O + K_2O) \quad (1)$$

A larger chemical index of alteration (*CIA*) indicates stronger chemical weathering influenced by a relatively warm and humid climate. Generally, elements such as Fe, Mn, V, Cr, Ni, Co are easily enriched in sedimentary rocks under wet conditions. However, in a dry environment, the evaporation of water enhances the alkalinity in the water body; as a result, basic metal ions such as Na, K, Ca, Mg, Sr, Ba are accumulated in the sediments. The ratio of the above-mentioned types of elements can be used to evaluate the paleoclimate. In this study, the climate index (*C*) and the chemical index of alteration (*CIA*) were used to study the paleoclimate of the

10.3389/feart.2022.1052734

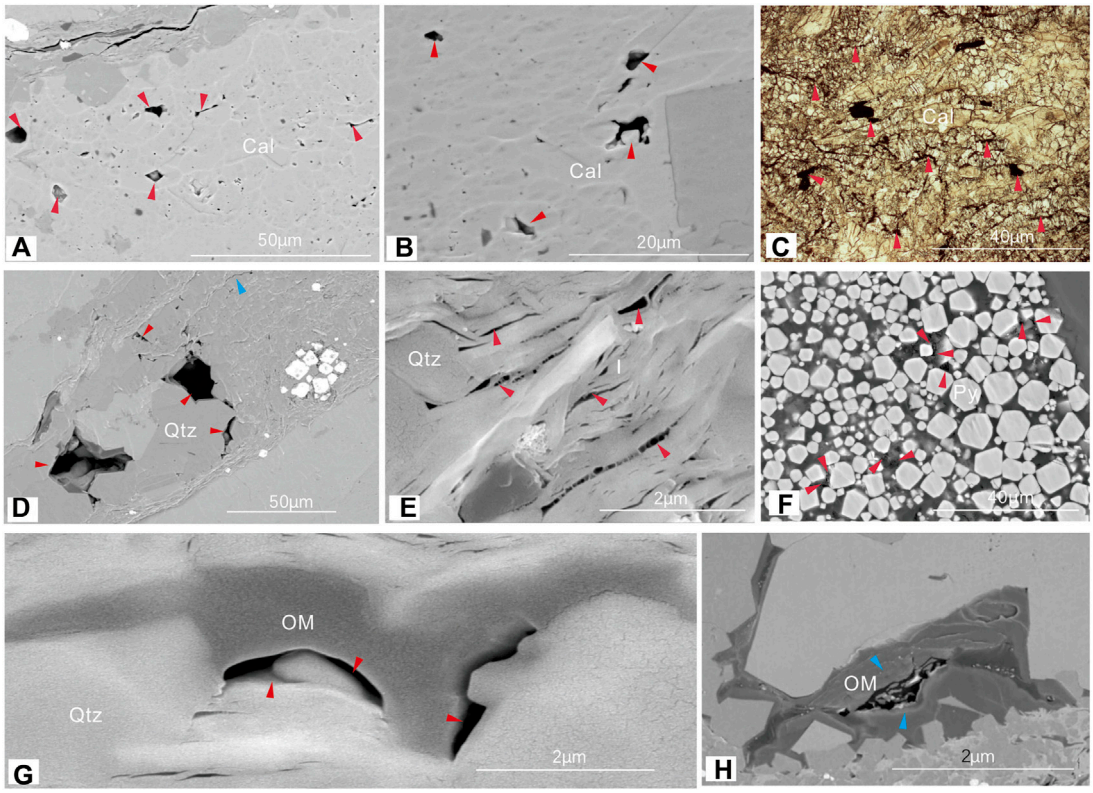

FIGURE 5
Photomicrographs of shale reservoirs in the Da'anzhai Member in Well RA1; **(A)** intergranular pores in shell calcite, 2,453.13 m; **(B)** intergranular dissolution pores in shell calcite, 2,453.13 m; **(C)** authigenic calcite intergranular pores (red arrow), 2,449.94 m; **(D)** authigenic quartz intercrystalline pores and shell edge fractures, 2,461.05 m; **(E)** intergranular pores of clay minerals, 2,464.4 m; **(F)** intergranular pores of pyrite nodules, filled with organic matter, 2,464.4 m; **(G)** organic pores in asphaltenes, 2,449.94 m; **(H)** organic pores in asphaltenes, 2,451.23 m.

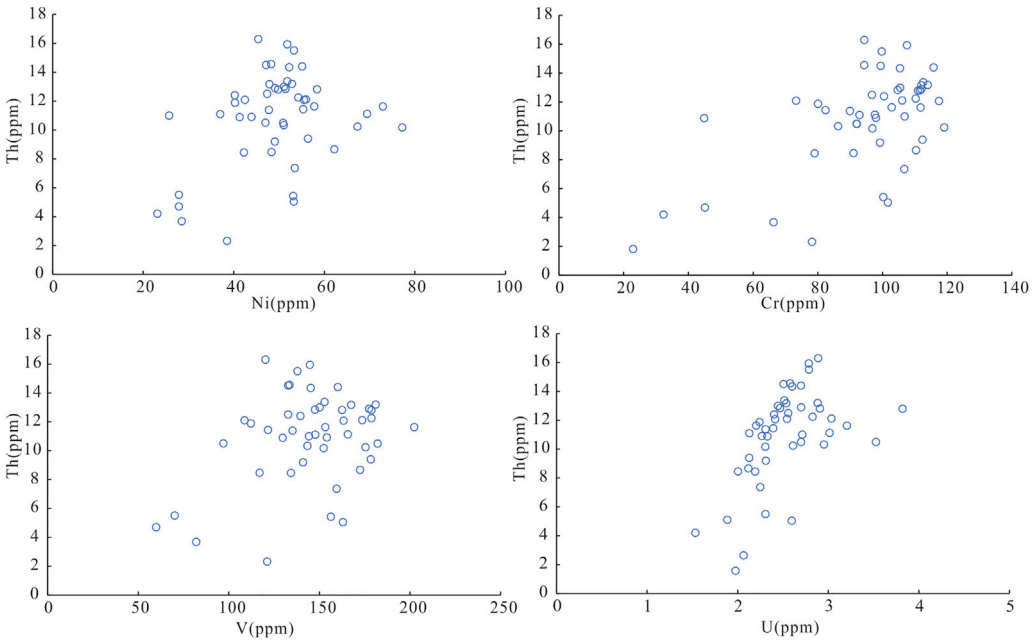

FIGURE 6
Binary cross-correlation plots of Th–Ni, Cr, V, and Th–U.

TABLE 1 Paleoclimate discrimination criteria based on the climate index (C) and chemical index of alteration (CIA) degree.

Climate index (*C*)	Chemical index of alteration (*CIA*)	Degree of chemical weathering	Paleoclimatic conditions
<.2	50–65	Low	Arid climate
.2–.6	65–85	Moderate	Semi-arid climate
>.6	85–100	Strong	Humid climate

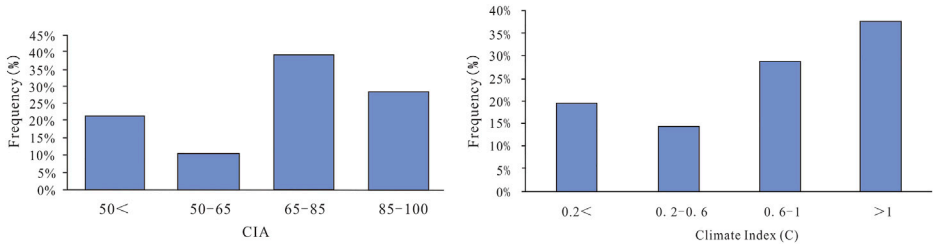

FIGURE 7
Frequency distribution of the chemical index of alteration (*CIA*) and climate index (*C*) for Well RA1.

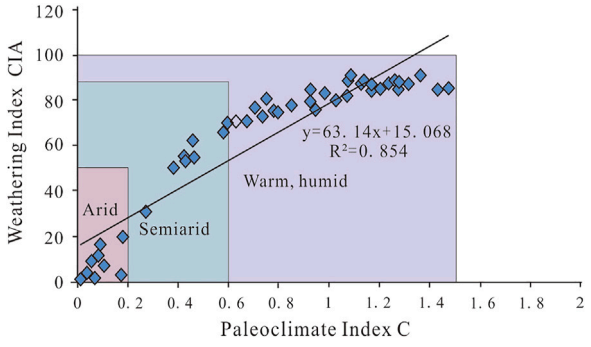

FIGURE 8
Distribution of climate Index (*C*) and chemical index of alteration (*CIA*) in the Da'anzhai Member of the Central Sichuan Basin.

Da'anzhai Member. The criteria for determining paleoclimate conditions are shown in Table 1. The defined paleoclimate indicator from Shi et al. (2022) is:

$$C - \text{value} = \sum(\text{Fe} + \text{Mn} + \text{V} + \text{Cr} + \text{Ni} + \text{Co}) \Big/ \times \sum(\text{Ca} + \text{Mg} + \text{Na} + \text{K} + \text{Sr} + \text{Ba}) \quad (2)$$

The analysis shows that the chemical index of alteration (*CIA*) of the shale samples from Well RA1 is distributed in the range of .96–90.87, with an average value of 63.02; most of the samples had *CIA* values above 65. The *CIA* of Well RA1 is also slightly lower than that of Well G10 which is located closer to the land source. The average *CIA* value of the Da'anzhai section of Well Gong 10 is 83 (Xiao et al., 2021). In addition, the paleoclimate index (*C*) for the shale samples from Well RA1 is distributed between .016 and .147, with an average value of .76 (Figure 7). A comprehensive analysis of the paleoclimate—based on both, the climate index (*C*) and chemical index of alteration (*CIA*), show that during the deposition of the Da'anzhai Member, most of the strata experienced moderate-to-strong chemical weathering in a semi-arid, warm and humid paleoclimate environment, and accompanied by a few episodes of dry paleoclimate conditions characterized by a lower weathering intensity (Figures 7, 8).

5.2 Evaluation of paleosalinity

Salinity is a good indicator of the environmental characteristics of a water body at any given time, and paleosalinity is the salinity of a water body at various times in geological history. Paleosalinity can be reproduced using paleontology, petrology, and isotope fractionation. The sedimentary environment of the Da'anzhai Member in the study area is very complex, and this study uses trace element content and ratio analysis to replicate its paleosalinity.

Recent studies report that the Da'anzhai Member in the Central Sichuan Basin was deposited in a typical continental freshwater lake basin environment, and that it experienced a complete sedimentary cycle of lacustrine transgression and regression (Xiao et al., 2021; Xu et al., 2022). The chemical properties of strontium (Sr) and barium (Ba) are similar, i.e. they can enter a solution in the form of soluble salts, and are very sensitive to changes in paleosalinity (Lin et al., 1999; Tribovillard et al., 2006; He et al., 2016). Strontium is more soluble than barium. With the increasing salinity of the formation water, Ba^{2+} will reach saturation first and precipitate as sulfates earlier than Sr^{2+}. Afterwards, as the salinity increases further, Sr^{2+} will precipitate. Therefore, a high Sr/Ba value reflects high paleo-salinity, and *vice versa*. A high Sr content also indicates an arid environment (Lin et al., 1999), consistent with high salinity aqueous media indicated by high Sr/Ba values. However, this indicator still has certain errors in the characterization of water salinity in continental lake basins. These errors are primarily because carbonate minerals tend to capture Sr and thus affect the

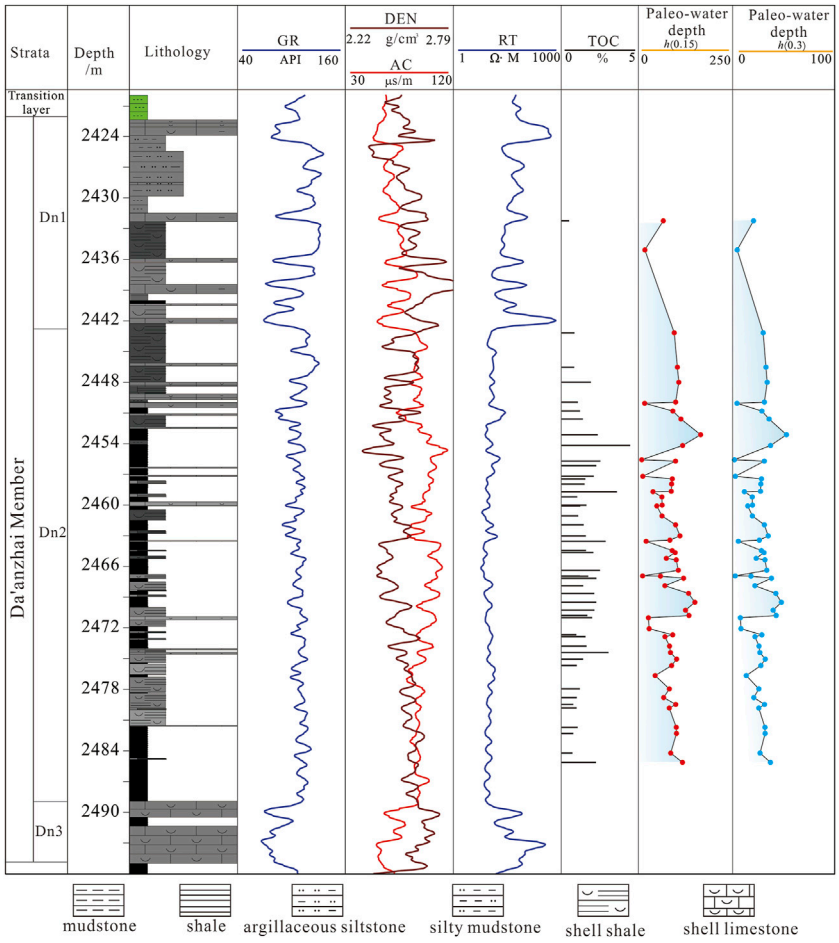

FIGURE 9
Vertical distribution of paleo-water depths in Well RA 1 in the Central Sichuan Basin; GR, gamma logging; DEN, Density Logging; AC, Acoustic logging; TOC, total organic carbon; Rt, True formation resistivity, Dn1, Dn2, Dn3: sub-members of the Da'anzhai member.

accuracy; Sr/Ba>1 is the salinization condition of lake water in marine or arid environments; 1>Sr/Ba>.5 is a brackish water phase; and Sr/Ba<.5 is the fresh water phase (Wu and Zhou, 2000).

The test results show that the Sr/Ba of the Da'anzhai Member of Well RA1 is .098–1.40, with an average value of .266. This indicates that the Da'anzhai Member of Well RA1 was deposited in a freshwater depositional environment, while a brackish water environment persisted periodically.

5.3 Evaluation of paleo-water depth

Shales developed in the Da'anzhai Member are generally considered to represent the semi-deep—deep lacustrine facies, but quantitative research on their genesis is lacking. In particular, there is no report on the paleo-water depth of the Da'anzhai Member based on geochemical methods. The calculation of paleo-water depths is based on the analysis of the mass fraction of cobalt (Co) in sedimentary rocks. This is a new method, which has achieved good results in practical applications (Wang X. J et al., 2022). In this paper, this method is used to estimate the water depth of the paleo-lake basin during the depositional period of the Da'anzhai Member of Well RA1. The formula from Wang X. J et al. (2022) is as follows:

$$V_s = V_o \times Nco/(Sco - t \times Tco) \quad (3)$$

$$h = 3.05 \times 10^5/(Vs1.5) \quad (4)$$

where h is the paleo-water depth, m; V_s is the deposition rate of the sample; V_o is the deposition rate of the normal lake at that time, 150–300 m/Ma; *Sco* is the cobalt abundance in the sample; *Nco* is the cobalt abundance in normal lake sediments, 20 (ppm); *Tco* is the cobalt abundance in the provenance, 4.68 (ppm); t is the cobalt contribution of the provenance to the sample (Fu et al., 2018). The distribution of rare Earth elements (REEs) in the upper crustal rocks is stable, so t can be replaced by ratio of lanthanum content of the samples to that of terrigenous clastic rocks (McLennan et al., 1993).

h(150) and h(300) are the paleo-water depth with deposition rates of 150 m/Ma and 300 m/Ma calculated from Eq. 4 respectively. The paleo-water-depth h(150) of Well RA1 ranges from 9.6 to 201.6 m, with an average value of 99.45 m; the paleo-water-depth h(300) is distributed between 3.4 and 71.3 m, with an average value of 35.16 m. This indicates that the Da'anzhai Member of Well RA1 was deposited

TABLE 2 Relationship between lithofacies and sedimentary environment in Well RA1.

Lithofacies	Ancient water depth *h* (150)	Ancient water depth h (300)	Paleosalinity Sr/Ba	Climate *CIA*	Climate *SR/CU*	Redox (v/(v+Ni))	Ancient productivity	TOC (%)
Massive argillaceous shell limestone facies F	9.6–31.5	3.4–11.1	2.1–8.9	17.3–72.5	1.0–4.0	.21–.75	111.9–474.8	.5–1.2
Thick argillaceous shell limestone lithofacies E	30.5–34.0	10.8–12.0	.5–1.4	23.5–73.0	5.0–20.8	.75–.78	126.28–695.78	.72–1.2
Thin shell calcareous shale lithofacies C	24.0–109.0	8.5–38.5	.3–2.2	45.1–81.5	6.8–30.7	.67–.74	179.1–695.8	1.1–3.6
Laminar shell-bearing shale lithofacies B	58.8–201.7	20.8–71.3	.3–.8	50.1–80.2	5.0–98.8	.70–.79	542.3–1042.9	1.0–3.1
Thick siliceous shale A	75.8–182.9	26.8–64.7	.1–.4	49.5–79.7	5.4–44.9	.66–.78	457.2–1198.8	.7–4.5

in a semi-deep lake—shallow lake sedimentary environment (Figure 9).

5.4 Evaluation of paleoproductivity and paleo-oxidation reduction

Excess barium refers to barium derived from biological action, which is obtained by subtracting the Ba element in terrigenous debris from the total content of Ba element (Lin et al., 1999). It is calculated using the formula:

$$w(Baxs) = w(Ba)sample - w(Al)sample \times w(Ba)w(Al)PAAS \quad (5)$$

In the formula, (Ba)sample and (Al)sample are the mass fractions of Ba and Al in the tested sample, respectively; PAAS is a post-Archaean Australian shale (He et al., 2016). [w(Ba)/w(Al)]PAAS is the ratio of the mass fraction of Ba and Al elements in the shale samples, which is .0077.

When the calculated w(Baxs) value is greater than 1000 μg/g, the sedimentary system has a high paleoproductivity (He et al., 2016). The w(Baxs) values in Well RA1 range from 111.89 to 1,359.84 μg/g, with an average value of 630.71 μg/g. These results indicate that the Da'anzhai Member had poor paleoproductivity.

The redox-sensitive element ratios of fine-grained sediments have been widely used in the recovery of paleo-sedimentary environment identification (for example, V/Cr, V/(V+Ni), U/Th and δU). Compared with a single element, ratios of different elements have a strong anti-interference ability when judging ancient redox conditions. Thus, the stability of the calculation results is higher. Generally, in continental sedimentary basins, V/(V+Ni)>.5 represents anaerobic conditions, .5>V/(V+Ni)>.45 represents oxygen-poor conditions, and V/(V+Ni)<.45 represents oxygen-rich conditions. The result shows that the V/(V+Ni) difference in the Da'anzhai Member of Well RA1 is relatively obvious; its distribution ranges from .21 to .799, with an average value of .70. This feature indicates that the Da'anzhai Member of Well RA1 formed in an anaerobic depositional environment.

5.5 Evaluation of deposition rates

The deposition rate is a key factor that affects the production, degradation, and dilution of organic matter. Initially, the organic matter content increases with the deposition rate. When the deposition rate reaches a critical value, the organic matter starts to decrease despite the continuous increase of the deposition rate. A settling rate that is too low will cause the organics to degrade during the oxidation process, while a settling rate that is too high will dilute the organics. Analytically determining deposition rates are based on the analysis of element geochemistry, and the commonly used geochemical parameters are $(La/Yb)_N$, $(La/Yb)_N$ (Fu,2018). It represents the ratio of the La and Yb contents in the samples to the normalized values of the chondrites. La and Yb were used for the calculations because they represent LREE and HREE, respectively, and their content can be easily and accurately determined.

A lower deposition rate promotes the fractionation of fine-grained rare Earth elements when the suspended particles remain in the lake for a longer time. The rare Earth elements in the lake water

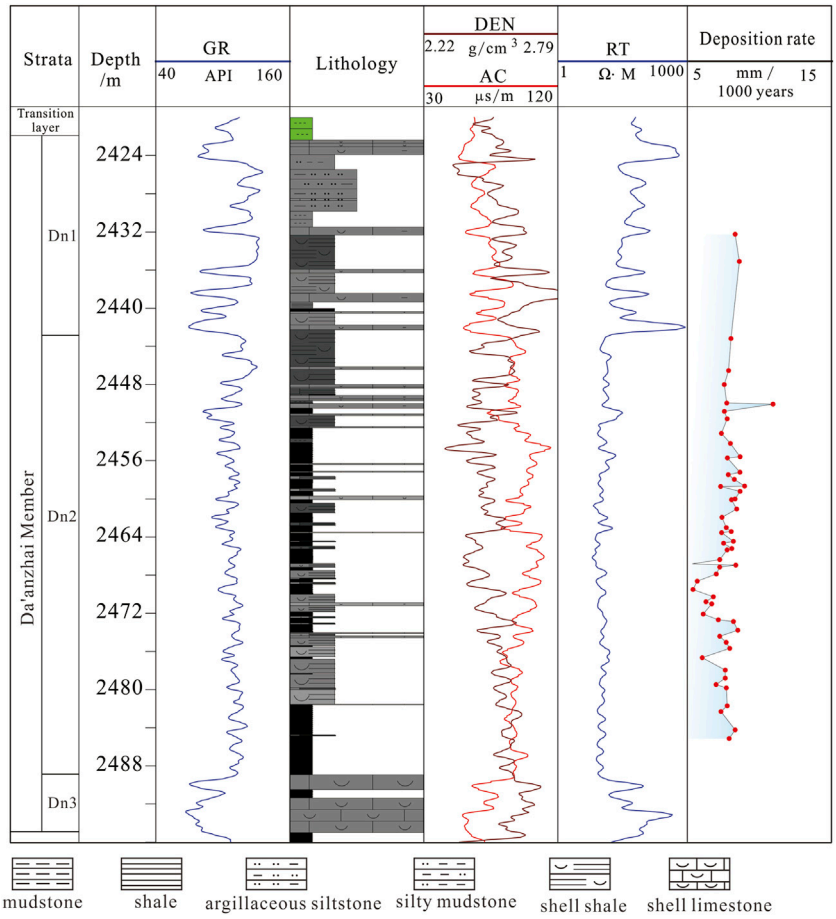

FIGURE 10
Vertical variation of sedimentation rates in Da'anzhai Member of Well RA1. GR, Natural gamma ray logging; AC, Acoustic logging; Rt, True formation resistivity logging, Dn1–Dn3: sub-member of Da'anzhai member.

have sufficient time to be adsorbed by the clay and react with the organic matter, which in turn leads to a significant differentiation of the rare Earth elements. In general, light rare earths are preferentially adsorbed by organic matter and clay fragments. They are converted into stable rare Earth complexes in lake water. A $(La/Yb)_N$ value of less than eight reflects a high deposition rate, and a $(La/Yb)_N$ value greater than ten reflects a low deposition rate.

The $(La/Yb)_N$ values of the samples in the study area range from 4 to 14 (Figure 10). This reflects a frequent change in the deposition rates. The $(La/Yb)_N$ value has a weak negative correlation with the TOC content, and the data points are scattered. It reflects three situations: 1) A lower deposition rate with the $(La/Yb)_N$ value greater than 10, and insufficient sediment supply and organic matter input. At this time, organic matter is easily degraded and oxidized, resulting in a lower TOC content; 2) A moderate deposition rate with the $(La/Yb)_N$ value between 8 and 10, and the organic matter input increases with increasing deposition rate; 3) A high deposition rate with the $(La/Yb)_N$ value less than 8, and an excessive deposition rate causes organic matter dilution. Therefore, the deposition rate when the $(La/Yb)_N$ value is between 8 and 10 is most favorable for the enrichment of organic matter. The $(La/Yb)_N$ value of the Da'anzhai Member ranges from 8 to 10, with an average value of 8.50. Here, the organic matter input increases with the deposition rate.

5.6 Influence of paleoenvironment on lithofacies

By comparing the evolution of the paleoenvironment and the distribution of lithofacies types (Table 2), it is found that different sedimentary paleoenvironmental conditions result in differences in rock characteristics (Zhang et al., 2015). Furthermore, it has a certain control on the distribution of lithofacies types.

In the sedimentary environment of continental lake basins, a change in the climate affects other paleoenvironmental elements to a large extent, which in turn affects the distribution characteristics of different types of lithofacies.

The arid climate lead to the reduction of water flow into the lake. This resulted in strong evaporation of the water body and its shallowing, and high salinity, low organic productivity, and the deposition of carbonate rocks with low TOC (Figure 11), such as lithofacies E and F (Table 2). Therefore, the major pore spaces of the lithofacies in arid climate are mostly intercrystalline pores (Figure 12).

Conversely, a warm and humid climate increased the volume of fresh water entering the lake. This inflow carried a large amount of terrigenous debris into the lake basin, increasing the content of quartz and feldspar in the sediment. A large amount of nutrients also entered the lake basin, which made organisms flourish, and the TOC in the

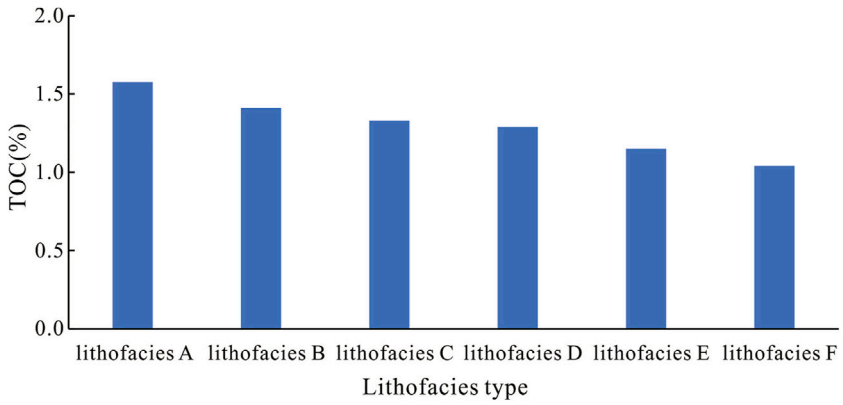

FIGURE 11
Average TOC content of each lithofacies type from Well RA1.

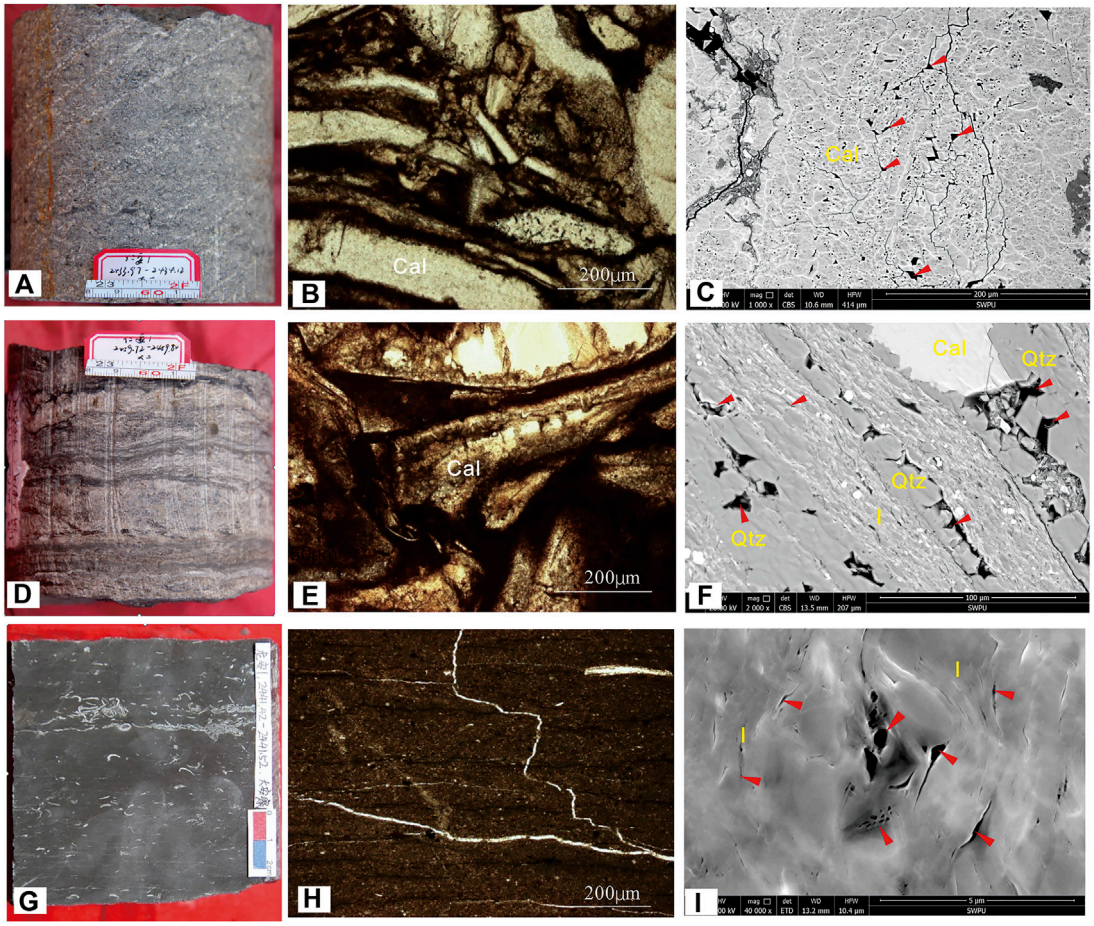

FIGURE 12
Core photographs of typical lithofacies and corresponding thin section microscopic image as well as pore characteristics under SEM of Well RA1. **(A)** massive mud-bearing shell limestone, 2,433.97–2,433.12 m; **(B)** microscopic photos of massive mud-bearing shell limestone, 2,433.97–2,433.12 m; **(C)** intercrystalline pores of shell calcite (Cal), 2,433.97–2,433.12 m; **(D)** medium-thick argillaceous shell limestone, 2,459.72–2,458.80 m; **(E)** microscopic photos of medium-thick argillaceous shell limestone, 2,459.72–2,458.80 m; **(F)** intercrystalline pores of quartz (Qtz) and clay minerals**(I)**, 2,459.72–2,458.80 m; **(G)** laminated shell-bearing shale, 2,441.42–2,441.52 m; **(H)** microscopic photos of laminated shell-bearing shale, 2,441.42–2,441.52 m; **(I)** intercrystalline pores of clay mineral **(I)**, 2,441.42–2,441.52 m.

sediments increase accordingly (Figure 11). Furthermore, the deepening of the water body reduced its salinity. This weakened the stratification of the water body and reduced the carbonate rock content. Multi-sedimentary mixed fine-grained sedimentary rocks were formed, such as facies A, B, C (Table 2) and the proportion of smaller pores, such as clay intercrystalline pores and organic pores increased (Figure 12).

When the overall climatic conditions remain unchanged, carbonate rocks are mostly developed in relatively shallow water environments. The deepening of the water body gradually decreases the volume of carbonate rocks being formed; mixed fine-grained sedimentary rocks gradually develop as well. Changes in the paleoenvironment and paleo-water medium conditions are direct reasons for the periodic prosperity and death of organisms; this provides sufficient organic matter. If the original productivity of the lake is certain, the reduced water medium environment is conducive to the preservation of organic matter. Organic matter is mostly decomposed under oxidative conditions.

The TOC content of fine-grained sedimentary rocks that form in relatively high salinity environments is usually high. This is because the water body is highly stratified under the conditions of a highly saline medium. The circulation between the surface water and the bottom water is blocked, forming a reducing environment at the bottom of the lake basin. A strong reducing environment is conducive to the preservation of organic matter. Regardless of gravity flow events, the content of the silt components in rocks will be affected to some extent by the depth of the water body and the supply of terrigenous debris. In a relatively shallow water environment, high terrigenous input resulted in the development of siltstone and silty fine-grained sedimentary rocks. With increasing distance from the shore and decreasing terrigenous input, the content of quartz and feldspar in the sediments also decrease accordingly.

6 Conclusion

1) The lithofacies of the Da'anzhai Member are divided into six types based on mineral composition, TOC and mineral structure—namely, massive mud-bearing shell limestone lithofacies (F), thick argillaceous shell limestone lithofacies (E), laminated clay silt shale lithofacies (D), thin shell calcareous shale lithofacies (C), laminated shell-bearing shale lithofacies (B), and thick clay shale lithofacies (A).
2) The pore types of the Da'anzhai Member include inorganic pores and organic pores. Inorganic pores are further classified into six sub-types including intergranular pores or intergranular dissolution pores in shell calcite, authigenic calcite intergranular pores, authigenic quartz intercrystalline pores, intergranular pores of clay minerals, and intergranular pores of pyrite nodules.
3) The Da'anzhai Member of Well RA1 was deposited in semi-deep to shallow lake sedimentary environment with relative low salinity and low organic productivity. During the deposition of the Da'anzhai Member, the strata were subjected to moderate-strong chemical weathering in semi-arid to warm and humid paleoclimate conditions. Weaker weathering and dry paleoclimate conditions occurred periodically.
4) The paleoenvironment was an important influence on the lithofacies and pore types of the Da'anzhai Member. The arid climate lead to a decline in water depth (Da1 and Da 3), which in turn resulted in relatively high salinity, low organic productivity, and the deposition of carbonate rocks that characterize lithofacies E and F. The major pore spaces of these carbonate rocks are mostly intercrystalline with comparatively larger radii. The warm and humid climate increased inflow of fresh water (Da2), terrigenous debris as well as nutrients into the lacustrine basin and led to the deposition of fine-grained sedimentary rocks (lithofacies A, B, C) which are characterized with abundant nano pores, such as clay intercrystalline pores and organic pores.

Data availability statement

The original contributions presented in the study are included in the article/supplementary material, further inquiries can be directed to the corresponding author.

Author contributions

RZ developed the idea for this paper and wrote the manuscript. BZ, MW, HAZ, SZ, WT, HOZ, YL, RB, MJ, and LH were involved in the logging interpretations.

Funding

This study was supported by a Science and Technology Cooperation project of the CNPC–SWPU Innovation Alliance (2020CX050103) and a National Natural Science Foundation of China grant (42202176).

Conflict of interest

Authors RZ, BZ, SZ, WT, HZ, YL, RB, MJ, YZ, and LH were employed by the PetroChina Southwest Oil & Gas Field Company.

The remaining authors declare that the research was conducted in the absence of any commercial or financial relationships that could be construed as a potential conflict of interest.

Publisher's note

References

Chen, S. J., Zhang, H. X., Lu, J. G., Yang, Y. M., Liu, C. W., Wang, L., et al. (2015). Controlling factors of Jurassic Da'anzhai Member tight oil accumulation and high production in central Sichuan Basin, SW China. *Petrol. explor. dev+.* 42 (2), 206–214. doi:10.1016/S1876-3804(15)30007-0

Curtis, J. B. (2002). Fractured shale-gas systems. *AAPG Bull.* 86 (11), 1921–1938. doi:10.1306/61EEDDBE-173E-11D7-8645000102C1865D

Fu, J. H., Li, S. X., Xu, L. M., and Niu, X. B. (2018). Paleo-sedimentary environmental restoration and its significance of chang 7 member of triassic yanchang formation in ordos basin, NW China. *Petrol. explor. Dev.* 45 (6), 998–1008. doi:10.1016/s1876-3804(18)30104-6

Fu, X. G., Wang, J., Zeng, S. Q., Feng, X. L., Wang, D., and Song, C. Y. (2017). Continental weathering and palaeoclimatic changes through the onset of the Early Toarcian oceanic anoxic event in the Qiangtang Basin, eastern Tethys. *Palaeogeogr. Palaeocl.* 487 (1), 241–250. doi:10.1016/j.palaeo.2017.09.005

Gao, Y., Huang, H., Tao, H., Carroll, A. R., Qin, J., Chen, J., et al. (2020). Paleoenvironmental setting, mechanism and consequence of massive organic carbon burial in the Permian Junggar Basin, NW China. *J. Asian Earth Sci.* 194 (1), 104222. doi:10.1016/j.jseaes.2019.104222

He, C., Ji, L., Wu, Y., Su, A., and Zhang, M. (2016). Characteristics of hydrothermal sedimentation process in the Yanchang Formation, south Ordos Basin, China: Evidence from element geochemistry. *Sediment. Geol.* 345, 33–41. doi:10.1016/j.sedgeo.2016.09.001

Huang, D., Duan, Y., Li, Y. C., Chen, H. B., Yan, W. P., and Dai, H. M. (2018). Study on the lower limit of organic carbon content in freshwater lacustrine shale oil and gas: A case study of daanzhai section of jurassic in Sichuan Basin. *China Petrol. explor.* 23 (6), 38–45. doi:10.3969/j.issn.1672-7703.2018.06.005

Huo, F., Wen, H. G., Li, L., Luo, B., Zhou, G., Xu, W. L., et al. (2022). Influence of the depositional environment on the formation of organic-rich marine shale: A case study of the first discovery of anisian shale in the Sichuan Basin. *J. Pet. Sci. Eng.* 214, 110577. doi:10.1016/j.petrol.2022.110577

Krom, M. D., and Berner, R. A. (1983). A rapid method for the determination of organic and carbonate carbon in geological samples. *J. Sedi. Res.* 53 (2), 660–663. doi:10.1306/212F8260-2B24-11D7-8648000102C1865D

Lei, W., Chen, D., Zhang, R., Liu, Z. Y., and Zhang, S. M. (2021). Lithological combination types and characteristics of continental shale strata in the second submember of Da'anzhai in central sichuan. *Earth Sci.* 46 (10), 3657–3672. doi:10.3799/dqkx.2021.023

Li, H., Tang, H. M., Qin, Q. R., Zhou, J. L., Qin, Z. J., Fan, C. H., et al. (2019). Characteristics, formation periods and genetic mechanisms of tectonic fractures in the tight gas sandstones reservoir: A case study of xujiahe formation in YB area, Sichuan Basin, China. *China. J. Petrol. Sci. Eng.* 178, 723–735. doi:10.1016/j.petrol.2019.04.007

Li, H., Zhou, J. L., Mou, X. Y., Guo, H. X., Wang, X. X., An, H. Y., et al. (2022). Pore structure and fractal characteristics of the marine shale of the longmaxi formation in the changning area, southern Sichuan Basin, China. *Front. Earth Sci.* 10, 1018274. doi:10.3389/feart.2022.1018274

Li, Y. Q., and He, D. F. (2014). Early Jurassic tectonic sedimentary environment and prototype basin evolution in Sichuan Basin and its adjacent areas. *Acta. Petrol. Sin.* 35 (2), 219–232. doi:10.7623/syxb201402002

Lin, H. L., Lai, C. T., Ting, H. C., Wang, L. J., Michael, S., and Huang, J. J. (1999). Late pleistocene nutrients and sea surface productivity in the south China sea: A record of teleconnections with northern hemisphere events. *Mar. Geol.* 156 (1), 197–210. doi:10.1016/S0025-3227(98)00179-0

Liu, S. G., Deng, B., Li, Z. W., and Sun, W. (2012). Architecture of basin-mountain systems and their influences on gas distribution: A case study from the Sichuan Basin, south China. *J. Asian Earth Sci.* 47, 204–215. doi:10.1016/j.jseaes.2011.10.012

McLennan, S. M., Hemming, S., McDaniel, D. K., and Hanson, G. N. (1993). Geochemical approaches to sedimentation, provenance, and tectonics. *Geol. Soc. Am. Special Pap.* 284, 21–40. doi:10.1130/SPE284-p21

Meakin, P., Huang, H., Malthe-Sorenssen, A., and Thogersen, K. (2013). Shale gas: Opportunities and challenges. *Environ. Geosci.* 20 (4), 151–164. doi:10.1306/eg.05311313005

Michaelis, W., Seifert, R., Nauhaus, K., Treude, T., Thiel, V., Blumenberg, M., et al. (2002). Microbial reefs in the black sea fueled by anaerobic oxidation of methane. *Science* 297 (5583), 1013–1015. doi:10.1126/science.1072502

Milliken, K. (2014). A compositional classification for grain assemblages in fine-grained sediments and sedimentary rocks. *J. Sediment. Res.* 84 (12), 1185–1199. doi:10.2110/jsr.2014.92

Nesbitt, H. W., and Young, G. M. (1989). Formation and diagenesis of weathering profiles. *J. Geol.* 97 (2), 129–147. doi:10.1086/629290

Pang, Z. L., Tao, S. Z., Zhang, Q., Yang, J. J., Zhang, T. S., Yang, X. P., et al. (2018). Reservoir micro structure of Da'anzhai member of jurassic and its petroleum significance in central Sichuan Basin, SW China. *Petrol. explor. dev+.* 45 (1), 68–78. doi:10.1016/s1876-3804(18)30006-5

Shi, J. Z., Cui, H. F., Xu, W., Song, B., and Wang, B. W. (2022). Sedimentary environment and organic matter enrichment model of black shale from cretaceous bayingebi formation in balongwula, yingen-ejin banner basin. *Geol. Bull. China* 41 (8), 1430–1444. doi:10.12097/j.issn.1671-2552.2022.08.010

Su, K. M., Lu, J. G., Zhang, G. W., Chen, S. J., Li, Y., Xiao, Z. L., et al. (2018). Origin of natural gas in jurassic Da'anzhai member in the Western part of central Sichuan Basin, China. *J. Petrol. Sci. Eng.* 167, 890–899. doi:10.1016/j.petrol.2018.04.014

Tribovillard, N., Algeo, T. J., Lyons, T., and Riboulleau, A. (2006). Trace metals as paleoredox and paleoproductivity proxies: An update. *Chem. Geol.* 232 (1–2), 12–32. doi:10.1016/j.chemgeo.2006.02.012

Wang, C. Y., Chang, J., Li, N., Hong, H. T., Li, Y. N., Wang, X. J., et al. (2022). Paleo-water-depth reconstruction of early jurassic lakes in the eastern Sichuan Basin. *Acta. Petrol. Sin.*, 1–16. doi:10.14027/j.issn.1000-0550.2022.036

Wang, S. F., Dong, D. Z., Wang, Y. M., Li, X. J., Huang, J. L., and Guan, Q. Z. (2016). Sedimentary geochemical proxies for paleoenvironment interpretation of organic-rich shale: A case study of the lower silurian longmaxi formation, southern Sichuan Basin, China. *J. Nat. Gas. Eng.* 28, 691–699. doi:10.1016/j.jngse.2015.11.045

Wang, W., Huang, D., Yi, H. Y., Zhao, R. R., Cen, Y. J., and Li, Y. C. (2019). Fine division and geochemical characteristics of freshwater lacustrine shale sublayers: A case study of daanzhai member of jurassic in Sichuan Basin. *Petrol. Geol. Expt.* 41 (5), 724–730. doi:10.11781/sysydz201905724

Wang, X. J., Zhou, Y. S., Peng, J., Li, J., Li, H. L., Wang, Y. M., et al. (2022). Major breakthrough of shale gas in the jurassic qianfoya formation in puguang area in the northeastern Sichuan Basin. *China Petrol. explor.* 27 (5), 52–61. doi:10.3969/j.issn.1672-7703.2022.05.005

Wu, Z. P., and Zhou, Y. Q. (2000). A new method to calculate the deposition rate -- the characteristic element method of cosmic dust. *J. Depos.* 18 (3), 395–399. doi:10.14027/j.cnki.cjxb.2000.03.012

Xiao, Z. L., Chen, S. J., Zhang, S. M., Zhang, R., Zhu, Z. Y., Lu, J. G., et al. (2021). Sedimentary environment and model for lacustrine organic matter enrichment: Lacustrine shale of the early jurassic Da'anzhai formation, central Sichuan Basin, China. *J. Palaeogeog.* 10 (4), 584–601. doi:10.1016/j.jop.2021.09.002

Xu, Q., Liu, B., Song, X. M., Wang, Q. P., Chen, X. D., Li, Y., et al. (2022). Hydrocarbon generation and organic matter enrichment of limestone in a lacustrine mixed sedimentary environment: A case study of the jurassic Da'anzhai member in the central Sichuan Basin, SW China. *Petrol. Sci.* doi:10.1016/j.petsci.2022.10.002

Yang, X. P., Zou, C. N., Tao, S. Z., Wang, Z. C., Li, J., and Wang, S. Q. (2005). Characteristics of upper triassic-jurassic oil and gas system in Sichuan Basin and oil and gas abundance law. *China Pet. Explor* 10 (2), 15–22. doi:10.3969/j.issn.1672-7703.2005.02.003

Zhang, S., Chen, S. Y., Yan, J. H., Tan, M. Y., Zhang, Y. Y., Gong, W. L., et al. (2015). Characteristics of shale lithofacies and reservoir space in the 3rd and 4th members of Shahejie Formation, the west of Dongying Sag. *Nat. Gas. Geosci.* 26 (2), 320–332. doi:10.1176/j.issn.1672-1926.2015.02.0320

Zheng, R. (2014). High resolution sequence stratigraphy of Da'anzhai formation, lower jurassic in Sichuan Basin. *Acta. Petrol. Sin.* 16 (2), 42–49. doi:10.14027/j.cnki.cjxb.1998.02.009

Zhou, G. Z., Hu, Z. M., Liu, X. G., Wu, J. F., Chang, J., and Chen, X. K. (2021). Palaeoenvironmental analysis of the lower silurian longmaxi formation in the zhaotong area of the Sichuan Basin, south China: Implications for organic matter accumulation mechanisms. *Geol. J.* 56 (3), 1358–1381. doi:10.1002/gj.3934

Zhou, Y., Yang, F. L., Ji, Y. L., Zhou, X. F., and Zhang, C. H. (2020). Characteristics and controlling factors of dolomite karst reservoirs of the Sinian Dengying Formation, central Sichuan Basin, southwestern China. *Precambrian Res.* 343, 105708. doi:10.1016/j.precamres.2020.105708

Zhu, H. H., Chen, L., Cao, Z. L., Wang, M. L., Hong, H. T., Li, Y. C., et al. (2022). Microscopic pore characteristics and controlling factors of black shale in the Da'anzhai Member of Jurassic Ziliujing Formation, central Sichuan Basin. *Oil Gas Geol.* 43 (5), 1115–1126. doi:10.11743/ogg20220509

Zhu, H. H., Zhang, T. S., Liang, X., Zhang, Z., and Zhang, L. (2018). Insight into the pore structure of Wufeng-Longmaxi black shales in the south Sichuan Basin, China. *J. Petrol. Sci. Eng.* 171, 1279–1291. doi:10.1016/j.petrol.2018.08.061

Zou, C. N., Dong, D. Z., Wang, S. J., Li, J., Li, X., Wang, Y., et al. (2010). Geological characteristics and resource potential of shale gas in China. *Petrol. explor. dev+.* 37 (6), 641–653. doi:10.1016/S1876-3804(11)60001-3

frontiers | Frontiers in Earth Science

TYPE Original Research
PUBLISHED 12 January 2023
DOI 10.3389/feart.2022.1059909

OPEN ACCESS

EDITED BY
Hu Li,
Southwest Petroleum University, China

REVIEWED BY
Zhe Wang,
China University of Geosciences
Wuhan, China
Wei Ni,
China University of Geosciences
Wuhan, China

*CORRESPONDENCE
Yahao Huang,
hyhtr08916@163.com

SPECIALTY SECTION
This article was submitted to Structural Geology and Tectonics,
a section of the journal
Frontiers in Earth Science

RECEIVED 02 October 2022
ACCEPTED 08 November 2022
PUBLISHED 12 January 2023

CITATION
Tang Y, Wu Y, Wang R, Huang Y, Xue Y, Chen Z, Xu T, Wang T and Li H (2023), Fluid evolution and paleo-pressure recovery by Raman quantitative analysis in the Shahejie Formation of the western slope belt in Dongpu Sag, Bohai Bay Basin, China.
Front. Earth Sci. 10:1059909.
doi: 10.3389/feart.2022.1059909

Fluid evolution and paleo-pressure recovery by Raman quantitative analysis in the Shahejie Formation of the western slope belt in Dongpu Sag, Bohai Bay Basin, China

Youjun Tang[1,2], Yijun Wu[1], Ruyue Wang[3], Yahao Huang[1,2]*, Yifan Xue[1], Zhonghong Chen[1], Tianwu Xu[4], Ting Wang[1] and Hongbo Li[1]

[1]Key Laboratory of Exploration Technologies for Oil and Gas Resources (Yangtze University), Ministry of Education, Wuhan, China, [2]State Key Laboratory of Oil and Gas Reservoir Geology and Exploitation, Chengdu University of Technology, Chengdu, China, [3]SINOPEC Petroleum Exploration and Production Research Institute, Beijing, China, [4]Exploration and Development Research Institute, Zhongyuan Oilfield Company, SINOPEC, Puyang, China

Inorganic and organic fluids are widely found in sedimentary basins during oil and gas migration and accumulation. This research investigates two types of sandstone reservoirs with different pressure states and fluid evolution of the Shahejie Formation in the western slope belt of Dongpu Sag. Based on petrographic observations, micro-Raman spectroscopy, and fluorescent spectrometry, petroleum inclusions, CH_4-bearing inclusions, and CO_2-bearing inclusions were discovered in quartz-hosted minerals. The pressure–temperature–time–composition (P–T–t–X) properties of the CH_4 and CO_2 inclusions were obtained by quantitative Raman analysis and thermodynamic models. Minimum trapped pressure was predicted by the thermodynamic modeling of petroleum inclusions. Saffron yellow petroleum inclusions represent an early Oligocene oil-charging event (~32–30 Ma), and the two kinds of reservoirs were all kept in moderate-overpressure conditions (average pressure coefficient: 1.26). Due to rapid uplift and denudation (Dongying movement) in the middle Oligocene in step II, crude oil degrades into CH_4 and CO_2 (density of CH_4 gas inclusions: 0.1010–0.1339 g/cm^3; density of CO_2 gas inclusions: 0.450–0.612 g/cm^3) and retains low-maturity (0.67–1.04%) bitumen *in situ*. Tectonic destruction causes the reservoir to be released to normal pressure. With the reburial of the Es_3 Formation, step II entered the middle stage of oil generation again (average pressure coefficient: 0.90). However, in step I, with secondary hydrocarbons occurring, second-stage oil (performance for pale blue fluorescence in petroleum inclusions) accumulated at ~12–0 Ma (late Miocene–Pliocene). The second oil charging event in step I remains a reservoir under high-overpressure conditions (average pressure coefficient: 1.67).

KEYWORDS

quantitative Raman spectroscopy, CH_4 and CO_2, fluid inclusion, Shahejie Formation, Dongpu Sag

Introduction

Reservoir pore fluid plays an important role in petroliferous basins and can reflect the dynamic process of hydrocarbon generation, migration, and accumulation (Dickinson, 1953; Tingay et al., 2009; Guo et al., 2011). Fluid activity (e.g., petroleum, CH_4, and CO_2) in natural strata can be trapped by lattice defects and fracture healing in minerals to form primary or secondary fluid inclusions (Mclimans, 1987; Goldstein, 2001). As independent geochemical systems, geo-fluid parameters such as temperature, pressure, components, and sources contained in fluid inclusions are codes of geological interpretation in relevant geological processes (Haszeldine et al., 1984; Roedder, 1984; Goldstein, 2003). Paleo-fluid pressure recovery and fluid source traces can be used as an index of oil and gas reservoir transformation and adjustment or for research on fault sealing (Gay et al., 2007; Weibull et al., 2010; Li et al., 2010; Wang et al., 2016; Guo et al., 2022). The maintenance of the overpressure state and fluid source are signs of good oil and gas enrichment and preservation conditions (Li et al., 2019; Li et al., 2022; Wang et al., 2016). The most direct and accurate method is to obtain the thermodynamic and physical–chemical data through the entrapment condition of the fluid inclusions (Burruss, 1987; Huang et al., 2018).

Laser Raman microprobe (LRM) spectroscopy, as a new micro-area analysis technique, has the characteristics of high precision and *in situ*, non-destructive and rapid analysis (Zozulya et al., 1998; Osborne and Haszeldine, 1993; Van den Kerkhof and Hein, 2001; Munz et al., 2004). Owing to the Raman quantitative function model, in the wide variation of pressure–temperature, Raman spectroscopy directly determining the total composition and total density of inclusions at abnormal temperatures can be carried out (Seitz et al., 1996; Pironon et al., 2003). Microthermometric measurement and LRM spectroscopy performed for fluid inclusions, combined with thermodynamic modeling, enable fluid inclusion quantitative analysis (e.g., composition, entrapped pressure, and bulk density), representing a key approach to reconstruct *P–T* entrapment conditions (Fabre and Couty, 1986; Gao et al., 2020; Dubessy et al., 1989, 2001; Burke, 2001). Raman spectroscopy can measure CH_4 and CO_2 solubility, salinity, pressure, or density in individual gaseous and aqueous inclusions (peak shift, peak separation, peak area ratio, peak height ratio, etc.) (Dubessy et al., 2001; Azbej et al., 2007; Baumgartner and Bakker, 2009; Caumon et al., 2014; Ou et al., 2015; Zhang et al., 2016; Gao et al., 2017); however, Raman quantitative microanalyses in geological applications are still weak.

The transition of diagenetic fluids in different environments leads to changes in the concentrations of key trace elements and isotopic compositions. The knowledge of alterations of rare earth elements (REEs) (e.g., seawater origin, meteoric water leaching-percolation, redox reactions, and hydrothermal origin) can be used to identify the extent and characteristics of diagenetic alterations of vein-filling minerals (Munz et al., 2004). These data can then provide information on the migration of geological fluids, stages of vein filling, and variations in diagenetic environments (Saimd and Ali, 2006).

Dongpu Sag is located in the southern Bohai Bay Basin in east China, and the western slope belt of Dongpu Sag is one of the main areas for oil and gas exploration and development in the SINOPEC Zhongyuan Oilfield. Fracture controls the structure-deposition evolution and formation of oil accumulation. Under the microscope work, in addition to oil inclusions, large numbers of primary and secondary gas-bearing fluid inclusions and pore-filled bitumen were found. Raman probe *in situ* analysis revealed that the fluid inclusions contain CH_4 and CO_2 gas. The purpose of this paper is to determine the paleo-fluid composition, paleo-pressure, and fluid charging period in the Shahejie Formation.

Geological setting

Dongpu Sag is located in the southern Bohai Bay Basin, which is part of Linqing Sag (Figure 1). According to the basement morphology and fault features, Dongpu Sag can be divided into five secondary-structural units: western slope belt; western sag belt; central uplift belt; eastern depression belt; and Dong Mingji fault step belt. The sedimentary cover of Dongpu Sag experienced two major stages: Paleogene rift and Neogene depression (Zuo et al., 2017). From old formation to new formation, this was filled with the Paleogene fourth member of the Shahejie Formation (Es_4), the third member of the Shahejie Formation (Es_3), the second member of the Shahejie Formation (Es_2), the first member of the Shahejie Formation (Es_1) and the Dongying Formation (E_d), the Neogene Guantao Formation (N_g), the Minghuazhen Formation (N_m), and the Quaternary. Among them, Es_3 is the basin period of greatest prosperity. It represents the main formation stage of the source rock, salt rock, and favorable reservoir. It can be further divided into the lower (Es_3^3), middle (Es_3^2), and upper (Es_3^1) sections (Figure 2).

The study area is located in the central part of the western slope belt (Figure 1A). Large faults in the area, such as Changyuan, Shijiaji, Xingzhuang, Wuxingji, and Mazhai, are distributed in the style of goose spread. The slope belt is cut into two east–west fault belts (step I and step II in Figure 1C). Regionally, the Shahejie Formation in the western slope belt of Dongpu Sag mainly develops the source rocks of the first, third, and fourth members of the Paleogene strata, and the lithology is mainly dark mudstone, oil shale, calcareous, dolomitic shale, and calcareous rock. The kerogen type of source rocks is mainly

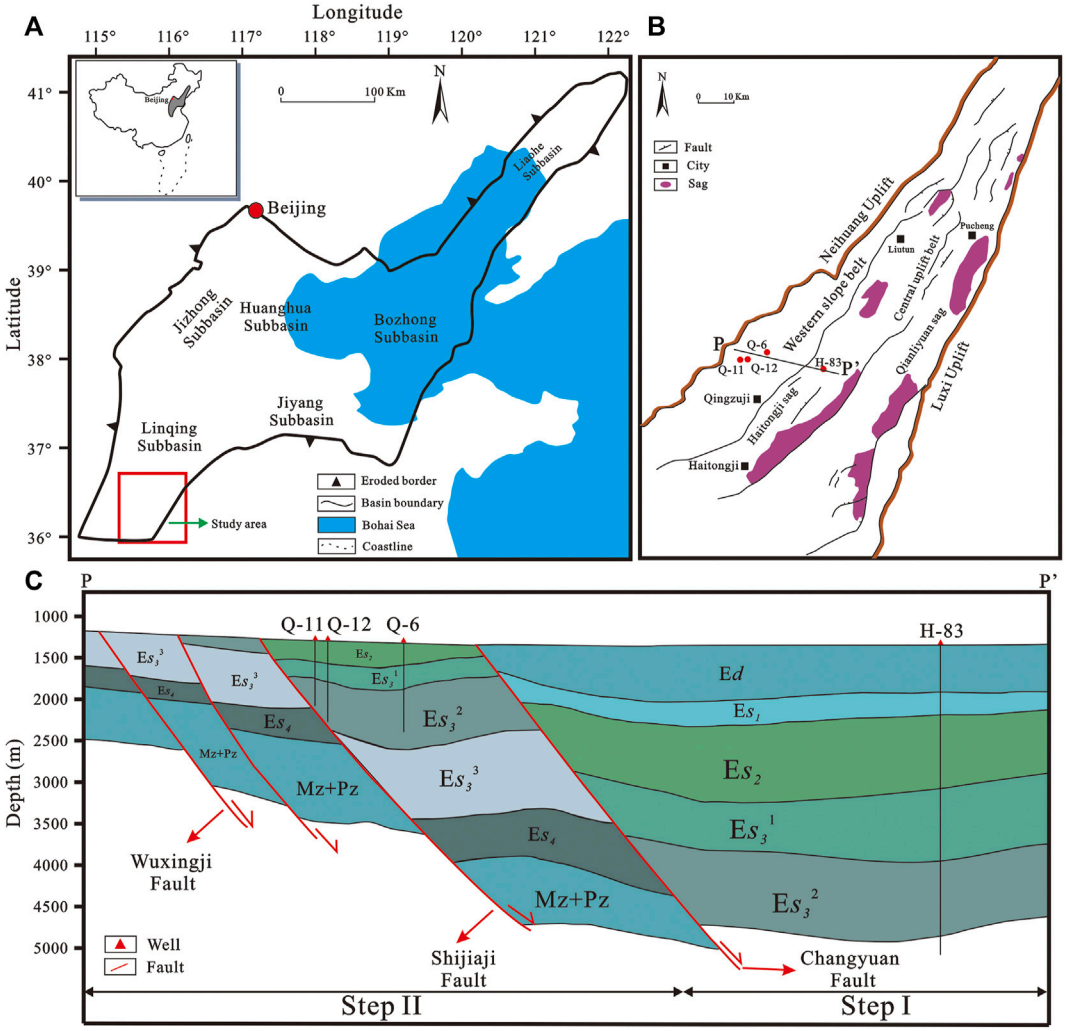

FIGURE 1
(A) Location map of Dongpu Sag in the Bohai Bay Basin. **(B)** Structural unit division map of Dongpu Sag. **(C)** Profile p-p′ of the present western slope belt. The location of line p-p′ is indicated in Figure 1 (adopted from Luo et al., 2016).

mixed, and its parent material mainly comes from lower organisms and some higher plants (Song et al., 2010). The source rocks enter the maturity stage (R_o=0.5%) at a burial depth of approximately 2,500 m, enter the high maturity stage (R_o=1.3%) at a burial depth of approximately 4,000 m, and enter the dry gas stage (R_o=2.0%) at a burial depth of approximately 5,000 m. Source rocks of middle and lower sub-members of Es_3 have also reached the mature hydrocarbon generation stage, which leads to step II having various oil sources, resulting in the wide distribution of oil and gas and enrichment. In the western slope belt, Es_3^3 and Es_3^2 are dominated by the underwater fan, the sedimentary center of the Es_3^3 period is located in the Huzhuangji area, and the filling deposition of the fan middle channel is widely developed, which is mainly composed of gravel medium fine sandstone (Wu and Ye, 2009; Luo et al., 2016). The sedimentary center of the Es_3^2 period moved east to Liutun–Haitongji Sag. At this time, due to the intense activity of the Changyuan and Xingzhuang faults, miniature slump fans often developed in the fault block. The upper member of Es_3 is mainly deltaic deposit, and the development degree of sandstone is relatively poor, mainly distributed channel sand and sheet sand. Structural, lithologic, stratigraphical, and structural–stratigraphical types of traps developed in the study area (Liu et al., 2019).

Sampling and methods

Approximately 30 sandstone core samples were collected from well H-83 in step I and well Q-6, well Q-11, and well Q-12

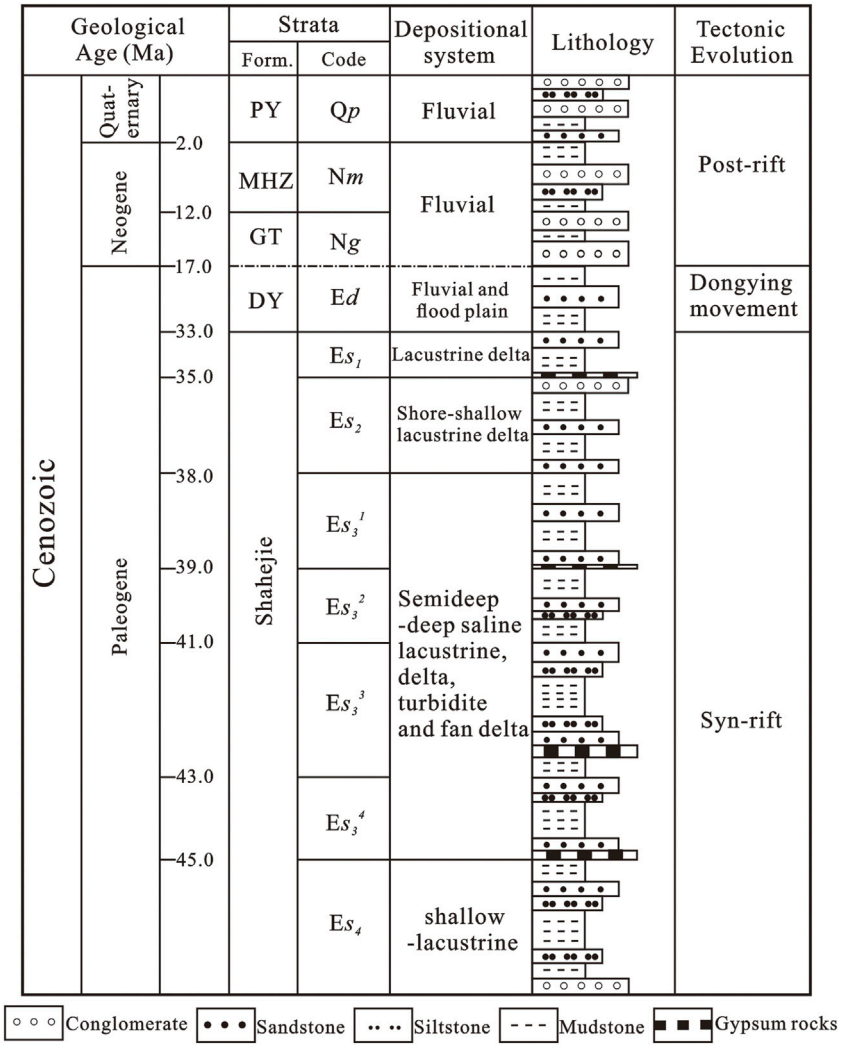

FIGURE 2
Cenozoic stratigraphic column of Dongpu Sag. PY: Ping Yuan Formation; MHZ: Ming Hua Zhen Formation; GT: Guan Tao Formation; DY: Dong Ying Formation.

in step II of the Es_3^2 Formation. The study by Huang et al. (2018) offers further details on sheet disposal in the context of avoiding fluorescence interference.

Optical microscopy and microthermometry

A petrographic examination was conducted using an Olympus BX60 microscope (10×, 20×, 50×, and 100×). The homogenization temperature (T_h) and ice melting temperature (T_m) for aqueous fluid inclusions were measured using a Linkam (TH–600) heating–cooling stage. The precision (reproducibility) of the T_h and T_m values was ±1°C and ±0.1°C, respectively.

Fluorescence

Oil inclusions can be illuminated with ultraviolet (UV) light to identify the degree of maturity (Burruss, 1991; Chang and Huang, 2008). A fluorescence spectrum device (Nikon 80I microscope connected to a high-pressure mercury lamp with a lamp excitation wavelength of 300–380 nm) was used for the spectral acquisition of oil-bearing inclusions. Fluorescence spectrum parameters usually include the selected λ_{max} value (wavelength relevant to maximum intensity) and QF_{535} values (ratio of the 535–750 nm integral area to the 430–535 nm integral area) for characterizing the emission spectra of oils and maturity (Munz, 2001; Ping et al., 2019). Typical petroleum inclusions were selected to reconstruct the composition and pressure–

temperature (P–T) entrapment conditions by microthermometry and volumetric analysis using confocal laser scanning microscopy (for details, see Ping et al., 2013; Pironon and Bourdet, 2008). This reliable method requires T_h and the degree of bubble filling (F_v) as known parameters to determine the C_{7+} molar proportion of petroleum inclusions. The quantitative correlation among the C_{7+} mole fraction and T_{hoil} and F_v can be used to predict the minimum trapped pressure.

Raman spectroscopy

The Raman instrument used was a JY/Horiba LABRAM HR800 (532-nm green laser; 400–500 mW output power) at China University of Geosciences (Wuhan) equipped with 10×/20×/50× long-focus objectives. Peak calibration was used with ~520.7 cm^{-1} polished silicon during the experiments. Components of gaseous fluid inclusions were investigated by setting a 200-μm confocal hole and 300-gr·mm^{-1} grating with a 2,650 cm^{-1} grating center. The accumulative time varied from 0 to 500 s to acquire the optimal signal-to-noise ratio. Options of precise resolution (1,800 gr·mm^{-1} grating and 50-μm aperture) are also necessary for acquiring accurate Raman shifts in terms of single gas phase inclusions. At the same time, neon lamp-corrected measurement should also be applied to acquire strict Raman wavenumbers (Kawakami et al., 2003; Wang et al., 2011; Dubessy et al., 2012; Huang et al., 2018). The density of pure CH_4 inclusions can be calculated by measuring the Raman shift of the C–H symmetric stretching band (v_1) of CH_4 (Seitz et al., 1993, 1996; Lu et al., 2007) at room temperature (25°C, ensured homogenization). After Raman spectrographic collection, the density of pure CH_4 fluid inclusions can be determined by applying different equations (for more details, see Zhang et al., 2016). The density of pure CO_2 inclusions can be measured as the separation between Fermi diad peaks of CO_2 (Rosso and Bodnar, 1995). After the acquisition of the Raman spectrum in the homogenized state, the density of CO_2 inclusions is calculated by applying multiple regression formulas (see Huang et al., 2018; Wang et al., 2019).

NaCl aqueous inclusions bearing dissolved CH_4 are usually coeval with CH_4-rich fluid inclusions in microfractures or isolated within quartz overgrowths. The quantitative factor (PAR/$m$$CH_4$) of CH_4–H_2O–NaCl ternary fluids depends on salinity and temperature. To exactly calculate the CH_4 solubility in a NaCl aqueous inclusion at a known temperature, the salinity must be determined first. The salinity of the aqueous fluid inclusions can be determined using the Raman spectra of the v(OH) stretching vibration of water (e.g., Dubessy et al., 1989; Caumon et al., 2015).

I_{3425}/I_{3260} was calculated using the integral Raman intensity ratio of wavenumber intensity at 3,425 cm^{-1} to wavenumber intensity at 3,260 cm^{-1} at 25°C (Guillaume et al., 2003; Becker et al., 2008; Caumon et al., 2014). The measured I_{3425}/I_{3260} and temperature were substituted into Eq. 1 ($R^2 > 0.997$; Ou et al., 2015):

$$S = -0.116\,IR^2 + 5.805\,IR - 6.933 \quad (1)$$

The integration of the Raman peak area ratio (PAR) of the CH_4 v_1 band (~2,917 cm^{-1}) to the OH stretching band of water in homogenized aqueous inclusions can determine the CH_4 concentration of water-rich fluid inclusions (mol/kg; Ou et al., 2015):

$$PAR/m\mathrm{CH_4} = \mathrm{a}T + \mathrm{b} \quad (2)$$

where T is the experimental temperature (K) in a homogeneous state. The slope (a) and intercept (b) are determined by the square root of mNaCl (see Ou et al., 2015). Based on these parameters and the model of Duan et al. (2003) and Duan and Mao (2006), the density and homogenization pressure (P_h) of water-rich fluid inclusions can be obtained.

The integration of the Raman peak intensity ratio (HR) of the upper band (at ~1,380 cm^{-1}) of the CO_2 Fermi dyad to the OH stretching band of water placed into the formula mentioned previously permits calculation of the concentration of CO_2 in water (mol/kg; Guo et al., 2014):

$$\frac{HR}{mCO_2} = a \times T + b,\ atT > 404.45.$$
$$a = -2.39 \times 10^{-4},\ b = 0.202. \quad (3)$$

With these parameters, the density of water-rich fluid inclusions can be obtained based on Duan and Sun (2003).

Raman spectroscopy calculation of organic maturity

Thermal maturity can be estimated through multilinear regression analysis of Raman spectroscopic parameters of carbonaceous material (Wilkins et al., 2014, 2015, 2018). The peak separation distance, peak height ratio, and full width at half maximum (FWHM) of the G (1250–1450 cm^{-1}) and D (1500–1605 cm^{-1}) bands can be used to calculate the equivalent vitrinite reflectance (EqVR%). The application details of the equations are described by Liu et al. (2013).

Basin modeling

BasinMod–1D (Version 7.06) software was adopted for the simulation of burial and thermal histories, which integrates the lithology, stratigraphic thickness, erosion

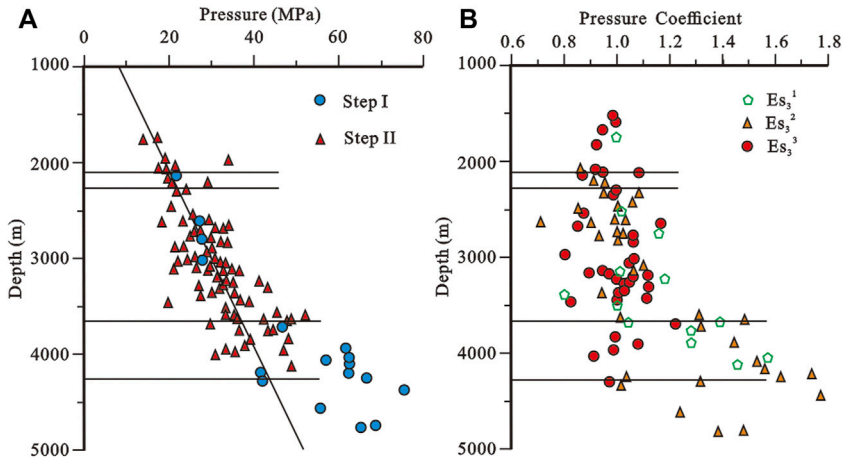

FIGURE 3
(A) Statistics of measured formation pressure and depth at different structural steps in the western slope belt of Dongpu Sag. **(B)** Statistics of the current pressure coefficient and depth at different horizons in the western slope belt of Dongpu Sag.

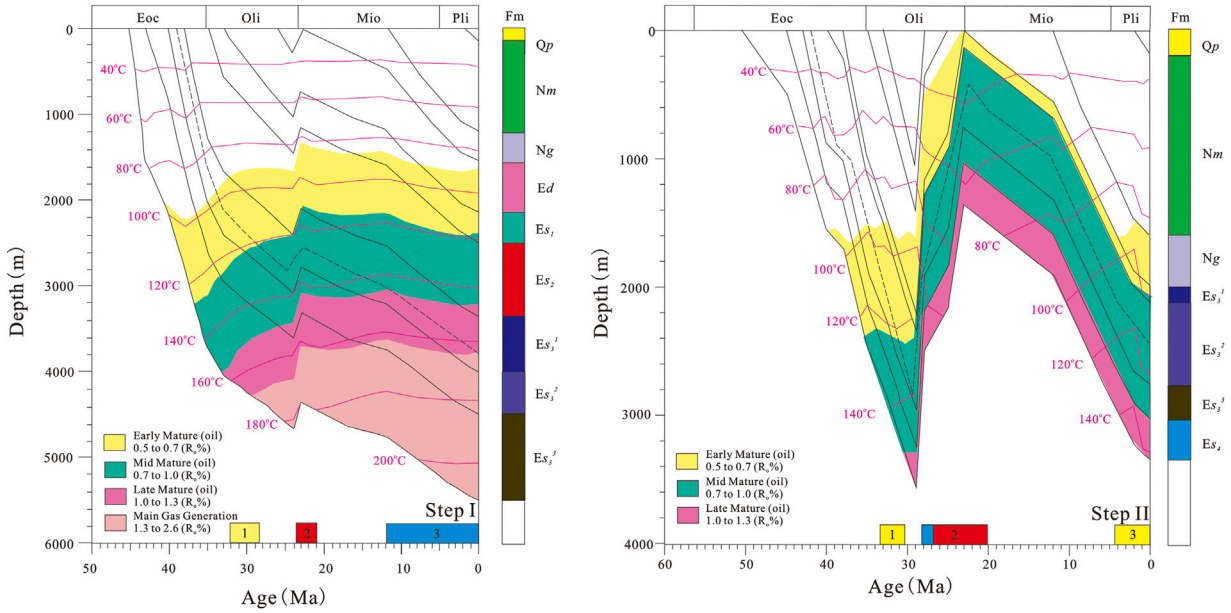

FIGURE 4
Paleocene Formation burial histories of steps I and II, illustrating the CH_4 and CO_2 charging times and multiple-staged oil charging times. The yellow frame represents the trapped period of yellow petroleum inclusions, the red frame represents the trapped period of CH_4 and CO_2, and the blue frame represents the trapped period of blue petroleum inclusions.

thickness, absolute age, vitrinite reflectance, and measured borehole temperature data. Well completion reports (e.g., DST data) from the SINOPEC Zhongyuan Oilfield provide the measured R_o and borehole temperature values (Figure 3). Thermal history simulation was mainly corrected using the vitrinite reflectance and temperature. The simulation results of the burial history of well Q-12 in step II and well H-83 in step I are shown in Figure 4.

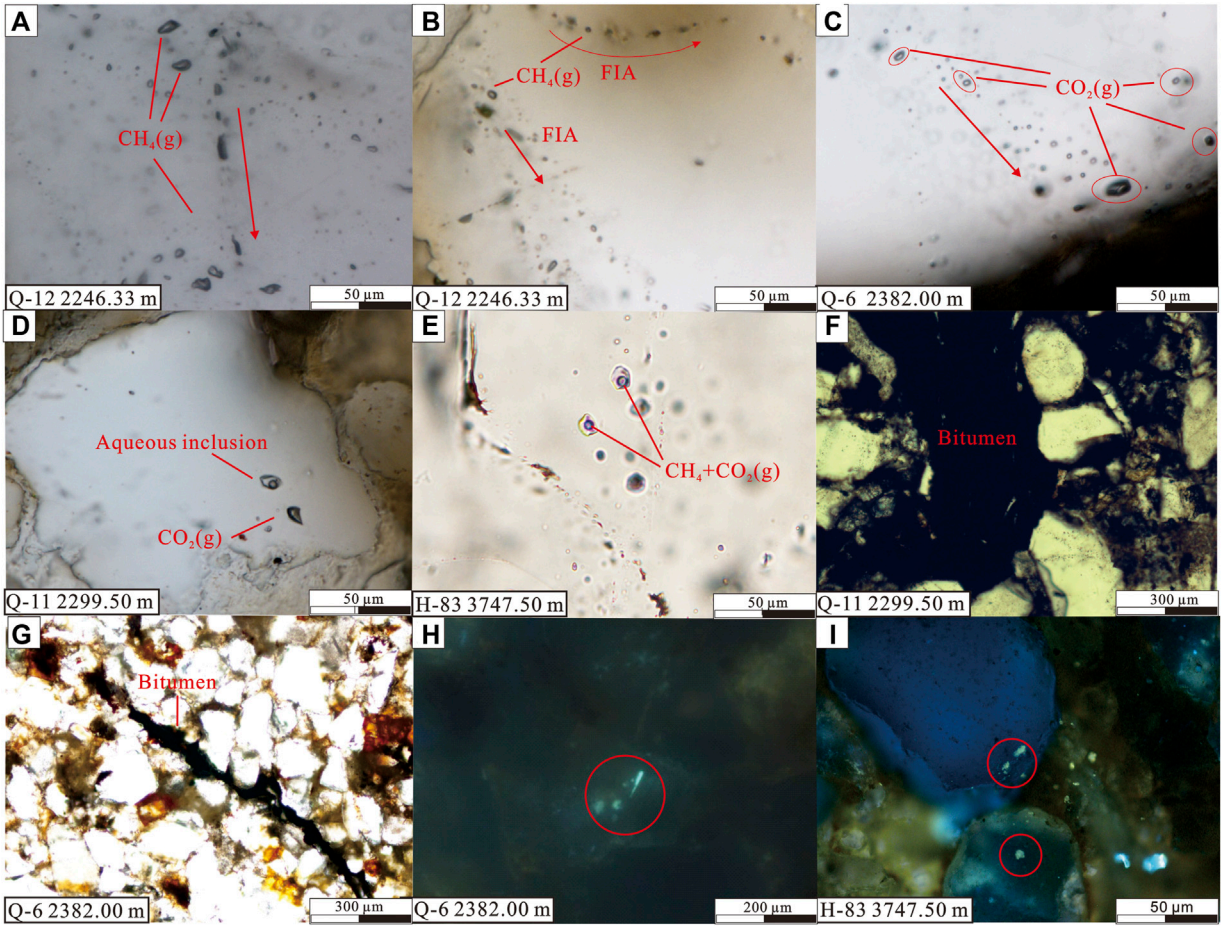

FIGURE 5
Typical microphotographs of fluid inclusions in the western slope belt of Dongpu Sag: **(A,B)** single-gas phase inclusions distributed along microfractures or in quartz grains; **(C,D)** CO_2 gaseous inclusions arranged in the same direction in microfractures or coexisting with dissolved CO_2 aqueous inclusions in quartz; **(E)** CH_4 and CO_2 dissolved aqueous inclusions exist in quartz; **(F,G)** bitumen as band shapes exist in pores of mineral grains; **(H)** blue-green fluorescent liquid hydrocarbon inclusions are located inside quartz particles; **(I)** yellow fluorescent liquid hydrocarbon inclusions are located in the interior of quartz overgrowths. Component identification of gas inclusions based on Raman spectroscopy qualitative analysis.

Results

Reservoir pressure characteristics

Analysis of oil testing pressure data shows that the reservoir pressure of different structural units in the study area has different development characteristics (Figure 3). The measured burial depth of the formation pressure point between 1,100 and 4,900 m ranges from 14.0 to 76.0 MPa, the pressure coefficient is 0.77–1.80, and the formation pressure increases with the burial depth. Es_1, Es_2, Es_3, and Es_4 were dominated by normal pressure. The shallow strata (<3,400 m) of Es_3^1 and Es_3^2 are mainly normal pressure, but the deep part is mostly in overpressure conditions. Overpressures are widespread in step I, but step II mainly occurs under normal pressure conditions, and faults in the distribution of the reservoir pressure have a significant control effect.

Fluid inclusion classification

CH_4, H_2O, CO_2, and petroleum fluids can be trapped by quartz grains or overgrowths during diagenetic processes. Petrographic observations at room temperature and the identification of UV fluorescence and Raman characteristic peaks can be comprehensively used to precisely classify the fluid inclusion assemblages (FIAs) into five types (Figures 5, 6):

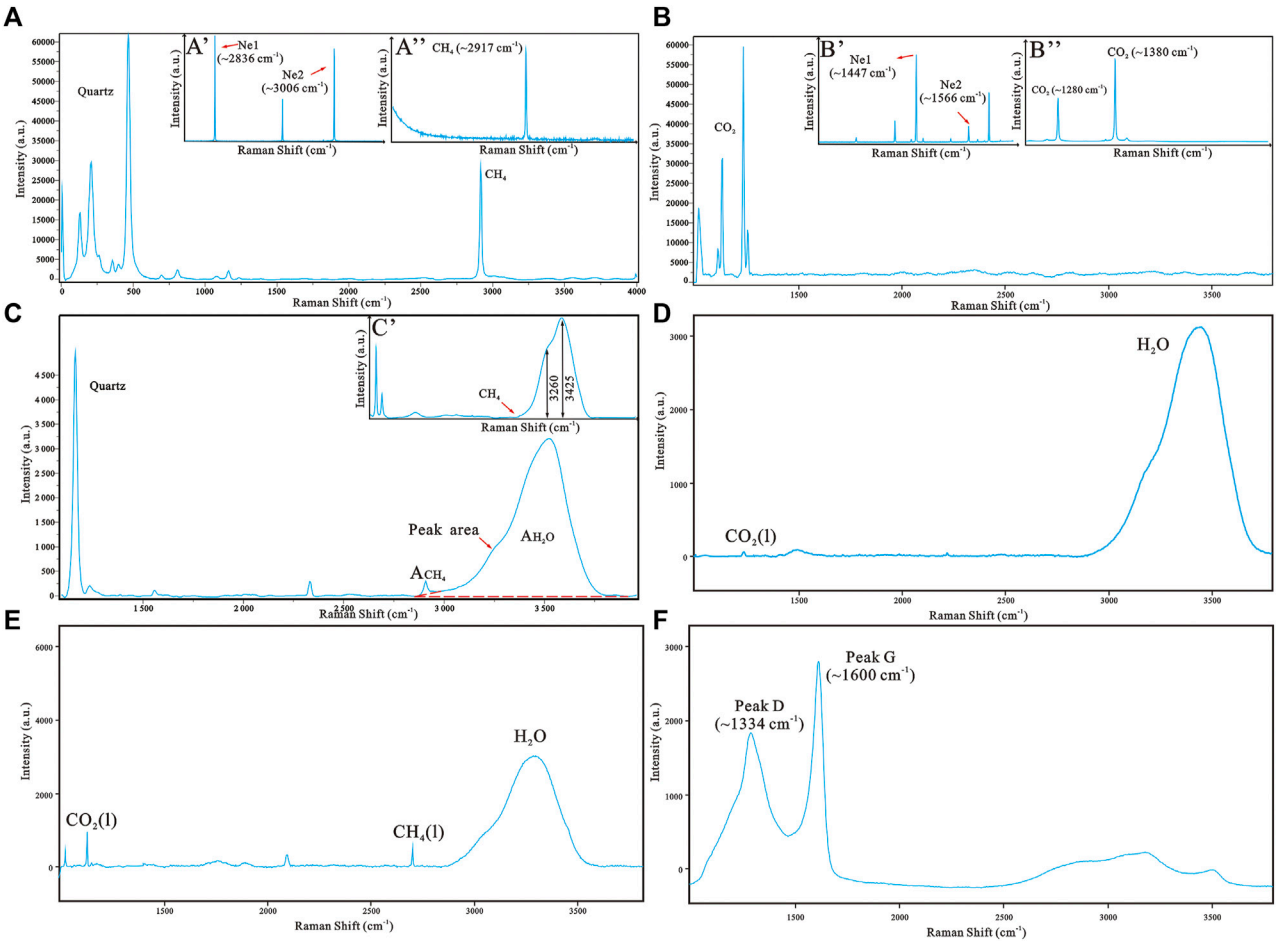

FIGURE 6
Classical Raman spectra of CH_4- and CO_2-bearing fluid inclusions: **(A)** spectra of the pure CH_4 component collected using the 300 gr.mm^{-1} grating in quartz [the CH_4 symmetric stretching band (v_1) peak was collected using the 1,800 gr.mm^{-1} grating with a Ne lamp]; **(B)** spectra of the pure CO_2 component collected using the 300 gr.mm^{-1} grating in quartz [the CO_2 Fermi double peak was collected using the 1,800 gr.mm^{-1} grating with a Ne lamp]; **(C)** spectra of CH_4–H_2O–NaCl components collected using the 300 gr.mm^{-1} grating obtained in the homogeneous state [(C′) is the spectra of the liquid part at room temperature]; **(D)** spectra of CO_2–H_2O–NaCl components collected using the 300 gr.mm^{-1} grating obtained in the homogeneous state; **(E)** spectra of CH_4–CO_2–H_2O–NaCl components collected using the 300 gr.mm^{-1} grating obtained in the homogeneous state; **(F)** G (~1334 cm^{-1}) and D (~1600 cm^{-1}) peaks of bitumen were collected at room temperature.

Inclusion type I

These single-vapor (VCH_4) inclusions are most abundant in microfractures or occur in the overgrowths and are usually coeval with dissolved CH_4 aqueous inclusions (Figures 5A,B), representing secondary generation. The diameters vary from 8 to 15 μm with rectangular or irregular shapes.

Inclusion type II

This type of inclusion is one-phase CO_2 gas inclusions coexisting with CO_2-dissolved aqueous inclusions found along healed microfractures and quartz overgrowths (Figures 5C,D), implying a secondary origin. The diameters range from 10 to 17 μm. The sizes and shapes of primary and secondary inclusions do not significantly differ.

Inclusion type III

With the spectral collection of homogeneous inclusions, dissolved CO_2 and CH_4 aqueous inclusions are found in quartz grains. They generally have elliptical to circular shapes (Figure 5E). The diameters range from 10 to 17 μm.

Inclusion type IV

These inclusions are two-phase (L and V) petroleum inclusions. The characteristics of QF_{535} and λ_{max} show saffron yellow and pale blue fluorescence. They are distributed along microfractures or occur in clusters (Figures 5H,I), implying primary and secondary origins. The diameters range from 7 to 15 μm. These HC inclusions are irregular, elliptical, and rod-shaped.

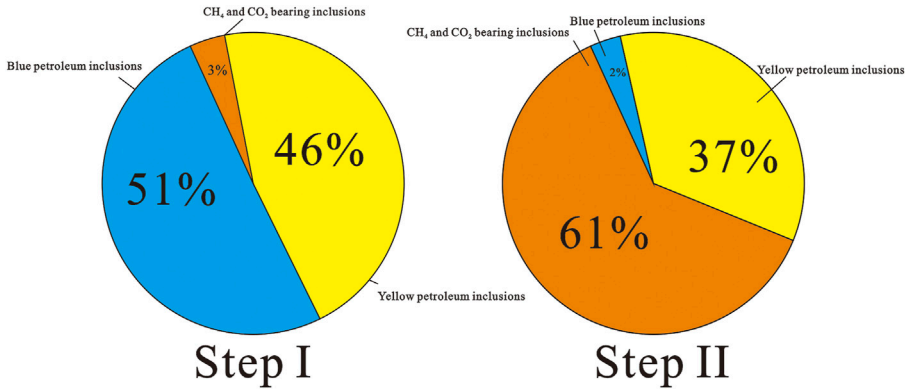

FIGURE 7
Statistics of the abundance of different types of inclusions in different structural steps.

The abundance statistics of different component types of fluid inclusions have indicative significance for the fluid activity characteristics of reservoirs (Figure 7). The low abundance of CH_4 and CO_2 gas inclusions accounts for only 3% in well H-83 of step I. Blue and yellow fluorescent inclusions accounted for 51% and 46%, respectively. The abundance of blue fluorescent inclusions in each well in step II was low (2%), while that of CH_4 and CO_2 gas was high (61%), and that of yellow fluorescent oil accounted for 37%.

Microthermometry

Aqueous fluid inclusions coeval with CH_4 and CO_2 inclusions in quartz were selected for salinity measurements by the method of height ratio (I_{3425}/I_{3260}) calculation of the water band. Secondary aqueous fluid inclusions coeval with petroleum inclusions were heated to a homogeneous state by the disappearance of the vapor bubble. The salinities (wt% NaCl equivalent) of these fluid inclusions were calculated based on their final ice-melting temperatures ($T_{m,\ ice}$; Bodnar, 1993). Figures 8A–D show the statistical distribution of salinity and homogenization temperature of different types of inclusions in each well located in step I and Step II, respectively. The homogenization temperature and salinity of reservoir inclusions in step I have the following characteristics. The homogenization temperatures of aqueous inclusions, which are coeval with CO_2 and CH_4 gas inclusions, range from 110 to 130°C (Figure 8A). The salinity interval of these water-rich inclusions varies between 2.7 and 4.9 wt% NaCleq (Figure 8B). The bimodal T_h distribution of aqueous inclusions coeval with yellow petroleum inclusions is 110–130°C, and that coeval with blue petroleum inclusions is 150–160°C. The $T_{m,\ ice}$ of these water-rich inclusions varies between −2.6 and −5.2°C, with a salinity interval of 4.7–8.1 wt% NaCleq. In wells Q-6, Q-11, and Q-12, the homogenization temperatures of aqueous inclusions, which are coeval with CH_4 gas inclusions, range from 95 to 110°C (Figure 8C). The salinity interval of these water-rich inclusions varies between 3.5 and 5.3 wt% NaCleq. The homogenization temperatures of aqueous inclusions, which are coeval with CO_2 gas inclusions, range from 90 to 100°C and 105 to 110°C. The salinity interval is 3.4–7.3 wt% NaCleq. The bimodal T_h distribution of aqueous inclusions coeval with yellow petroleum inclusions is 115–130°C, and that coeval with blue petroleum inclusions is 100–110°C. The $T_{m,\ ice}$ of these water-rich inclusions varies between −2.3 and −9.8°C, with salinity intervals of 3.9–13.7 wt% (Figure 8D).

Quantitative Raman analysis of fluid inclusions

The pressure and density of secondary CH_4 gas fluid inclusions in quartz can be measured using quantitative Raman analysis. Figures 6A,C exhibit the typical Raman spectrum of CH_4-system fluid inclusions, which were classified based on the petrographic characteristics and compositions in a homogeneous state. Table 1 lists the data for 15 pure CH_4 inclusions (in type I), including their densities, obtained from the C–H symmetric stretching band (v_1) of methane (Figure 6A, A′ and A″). The density varies from 0.1772 to 0.1785 g/cm^3 in the wells of step I (average value: 0.1779 g/cm^3). The density varies from 0.1010 to 0.1339 g/cm^3 in the wells of step II (average value: 0.1126 g/cm^3). The homogenization pressure (P_h) is calculated using the thermodynamic model (Peng and Robinson, 1960) with consideration of the densities and T_h of coeval aqueous inclusions. P_h varies from 38.00 to 38.06 MPa (average value: 38.03 MPa) in step I and from 18.29 to 25.50 MPa (average value:

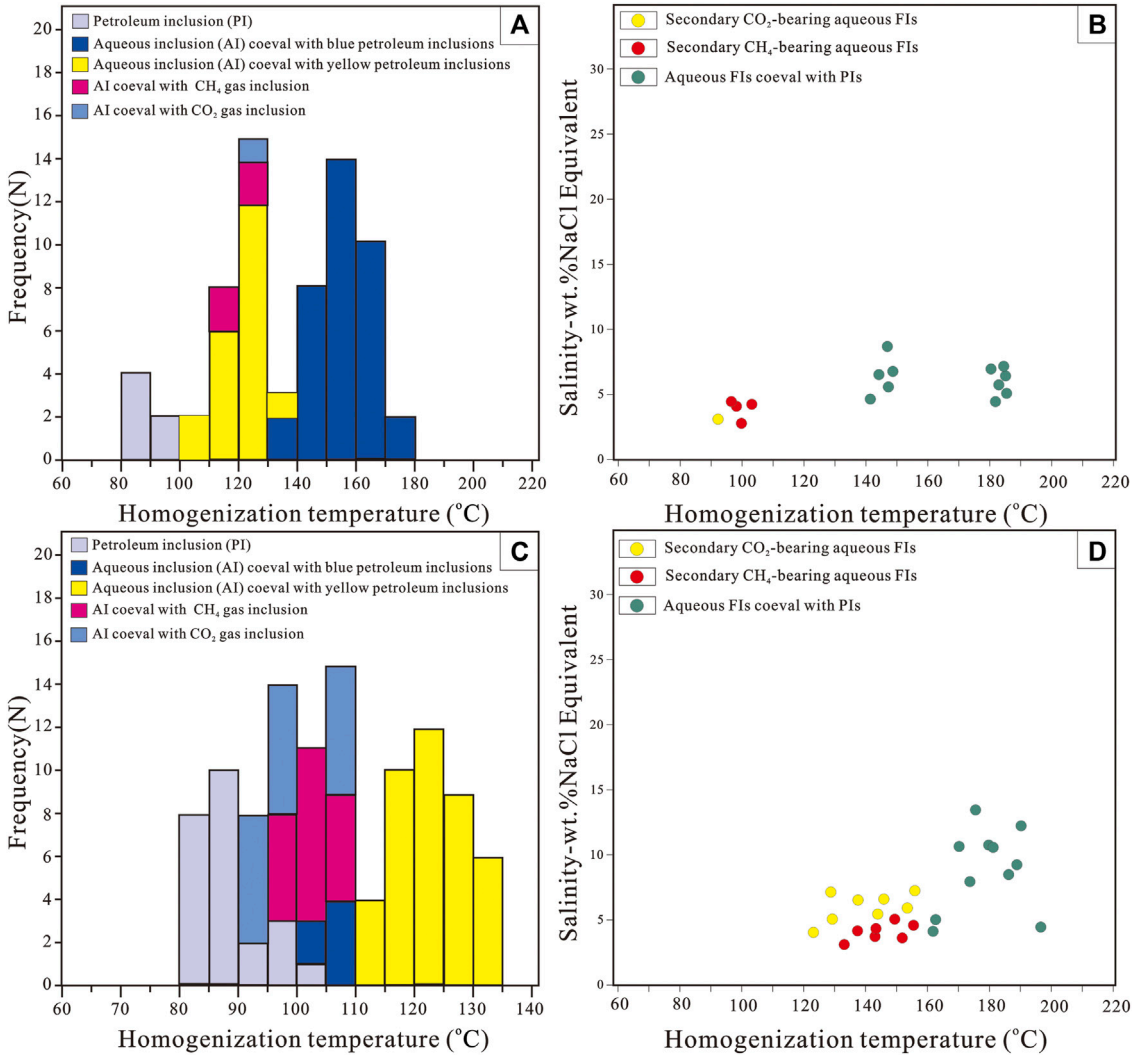

FIGURE 8
Homogenization temperature and salinity statistics of aqueous inclusions coeval with CO_2, CH_4, and petroleum inclusions in detrital grains in the Es_3^2 Formation of step I **(A,B)** and step II **(C,D)**.

20.90 MPa) in step II. Meanwhile, with the discovery of CO_2-bearing inclusions (Figure 6B), 13 pure CO_2 inclusions (in type II) were quantified and are shown in Table 2. The density varies from 0.608 to 0.662 g/cm^3 (average value: 0.555 g/cm^3) in step I and from 0.450 to 0.612 g/cm^3 (average value: 0.555 g/cm^3) in step II. P_h varies from 32.82 to 39.56 MPa (average value: 36.19 MPa) in step I and from 19.34 to 28.68 MPa (average value: 24.94 MPa) in step II.

Tables 3, 4 show the data compilation of four dissolved CH_4 inclusions in NaCl aqueous inclusions (in type I) and three dissolved CO_2 inclusions in NaCl aqueous inclusions (in type I), which were analyzed by Raman spectroscopy in a homogeneous state (Figures 6C,D). The methane content (mCH_4) of the dissolved methane inclusions can be determined and ranges from 0.387 to 0.690 mol/kg. The CO_2 content (mCO_2) of the dissolved CO_2 inclusions can be mainly determined and ranges from 0.223 to 0.335 mol/kg.

Raman spectral calculation of bitumen maturity

The Raman maturity method can achieve targeted and convenient determination (e.g., organic matter in reservoir sandstone). A large amount of residual bitumen was found in the Paleocene reservoirs of the western slope belt in Dongpu Sag (Figures 5F,G). Residual bitumen is usually observed in the grain pores of quartz. The Raman peak parameters of bitumen were

TABLE 1 Summary of Raman quantitative analysis of pure CH_4 inclusions.

No.	Well	Depth (m)	ν_{true} (cm^{-1})	Density (g/cm^3)[a]	Coeval aqueous inclusions homogenization temperature (°C)	Reconstructed trapped pressure (MPa)[b]	Pressure coefficient
1	Q-12	2299.5	2914.75	0.1046	101.5	18.98	0.90
2	Q-12	2299.5	2914.72	0.1058	103.1	19.31	0.92
3	Q-12	2299.5	2914.68	0.1073	103.1	19.59	0.93
4	Q-12	2246.3	2914.49	0.1149	107.8	21.47	1.01
5	Q-12	2246.3	2914.36	0.1201	106.0	22.36	1.05
6	Q-11	2398.4	2913.55	0.1331	108.8	25.21	1.18
7	Q-11	2398.4	2913.58	0.1339	108.8	25.50	1.20
8	Q-11	2398.4	2913.55	0.1314	108.8	25.00	1.17
9	Q-11	2591.7	2914.84	0.1010	107.5	18.72	0.88
10	Q-6	2595.5	2914.72	0.1058	111.7	19.97	0.91
11	Q-6	2588.0	2914.81	0.1022	98.6	18.29	0.91
12	Q-6	2588.0	2914.82	0.1018	104.8	18.67	0.89
13	Q-6	2588.0	2914.84	0.1019	104.8	18.69	0.90
14	H-83	3747.50	2912.35	0.1785	120.8	38.00	1.45
15	H-83	3747.50	2912.38	0.1772	123.5	38.06	1.42

[a]: Density calculated following Zhang et al. (2016).
[b]: Homogenization pressure calculated following Peng and Robinson (1960).

TABLE 2 Summary of Raman quantitative analysis of pure CO_2 inclusions.

No.	Well	Depth (m)	Distance of fermi doublet (cm^{-1})	Density (g/cm^3)[a]	Coeval saline inclusion homogenization temperature (°C)	Reconstructed trapped pressure (MPa)[b]	Pressure coefficient
1	Q-12	2246.3	103.31	0.450	98.5	19.34	0.88
2	Q-12	2246.3	103.54	0.540	98.5	23.36	1.06
3	Q-12	2246.3	103.43	0.496	98.5	21.28	0.97
4	Q-12	2299.5	103.65	0.586	100.8	26.44	1.20
5	Q-12	2299.5	103.56	0.548	100.8	24.32	1.11
6	Q-11	2398.4	103.58	0.557	100.8	24.76	1.13
7	Q-11	2398.4	103.65	0.586	100.8	26.44	1.20
8	Q-6	2588.0	103.63	0.578	101.0	25.99	1.18
9	Q-6	2588.0	103.62	0.573	105.7	26.92	1.22
10	Q-6	2595.5	103.63	0.578	104.3	26.82	1.22
11	Q-6	2595.5	103.71	0.612	103.1	28.68	1.30
12	H-83	3747.50	103.70	0.608	119.4	32.82	1.23
13	H-83	3747.50	103.83	0.665	125.3	39.56	1.50

[a]: Density calculated following Huang et al. (2018).
[b]: Homogenization pressure calculated following Peng and Robinson (1960).

obtained by *in situ* Raman observation and software calculation, and equivalent vitrinite reflectance (EqVR%) was calculated (Table 5). In the Es_3^2 Formation of wells Q-12, Q-11, and Q-6, the separation of the G and D peaks can be used to calculate the maturity of bitumen (Figure 6F). The EqVR% of these residual bitumen ranges between 0.67% and 1.04%. They are characterized by low maturity.

TABLE 3 Dissolved CH_4 in NaCl aqueous inclusions obtained by Raman quantitative analysis.

No.	Well	Depth (m)	PAR (CH_4/H_2O)	IR (I3425 cm^{-1}/I3260 cm^{-1})[a]	Salinity ($mol.kg^{-1}$)[b]	Homogenization temperature (°C)	mCH_4 ($mol.kg^{-1}$)[c]
1	Q-12	2299.5	0.015335	1.44435	1.21	108.8	0.690
2	Q-12	2299.5	0.013145	1.47508	1.38	107.5	0.595
3	Q-12	2246.3	0.008459	1.52394	1.64	99.3	0.387
4	Q-11	2398.4	0.009840	1.48286	1.42	95.6	0.446

[a]: IR: peak intensity ratio, calculated by collecting spectra at 25 °C.
[b]: Salinity calculated following Ou et al. (2015).
[c]: *m*CH4 calculated following Ou et al. (2015).

TABLE 4 Dissolved CO_2 in NaCl aqueous inclusions obtained by Raman quantitative analysis.

No.	Well	Depth (m)	HR (CO_2/H_2O)	IR (I3425 cm^{-1}/I3260 cm^{-1})[a]	Salinity ($mol.kg^{-1}$)[b]	Homogenization temperature (°C)	mCO_2 ($mol.kg^{-1}$)[c]
1	Q-12	2299.5	0.022	1.66	2.38	98.1	0.223
2	Q-12	2299.5	0.025	1.47	1.35	100.8	0.254
3	Q-6	2595.5	0.033	1.53	1.68	103.1	0.335

[a]: IR: peak intensity ratio, calculated by collecting spectra at 25 °C.
[b]: Salinity calculated following Ou et al. (2015).
[c]: *m*CH4 calculated following Guo et al. (2014).

TABLE 5 Raman spectral parameters of vitrinite from Dongpu Sag samples.

No.	Well	Depth (m)	*v*G–*v*D cm^{-1}	HG/HD cm^{-1}	RaMM EqVR%[a]
1	Q-12	2246.3	221.17	0.924	0.67
2	Q-12	2246.3	221.91	0.916	0.71
3	Q-12	2246.3	227.48	0.922	1.01
4	Q-12	2299.5	227.78	0.932	1.02
5	Q-12	2299.5	226.82	0.934	0.97
6	Q-11	2398.4	225.22	0.939	0.88
7	Q-11	2398.4	226.91	0.963	0.98
8	Q-11	2591.7	228.17	0.757	1.04
9	Q-11	2591.7	225.33	0.949	0.89
10	Q-11	2591.7	227.90	0.990	1.03
11	Q-6	2588.0	227.16	0.947	0.99
12	Q-6	2588.0	223.60	1.056	0.80
13	Q-6	2595.5	225.91	0.970	0.92
14	Q-6	2595.5	225.43	0.913	0.90

*v*G–*v*D: separation of the positions of the G and D bands. H: height of peak. RaMM: Raman maturity.
Method. EqVR%: equivalent vitrinite reflectance.
[a]: Equations following Liu et al. (2013).

Minimum trapped pressure of petroleum inclusions

According to parameters, such as homogenization temperature, petroleum inclusion composition, and bubble filling degree of oil inclusions and coexisting aqueous inclusions, the minimum trapped pressure (P_t) of inclusions can be obtained by PVTsim software simulation and fluorescence spectra (Figure 9).

The content of CH_4 (C_1) in petroleum inclusions of the Es_3^2 Formation in wells Q-6, Q-11, and Q-12 ranges from 14.92% to 30.82%, and the content of C_{7+} (hydrocarbons

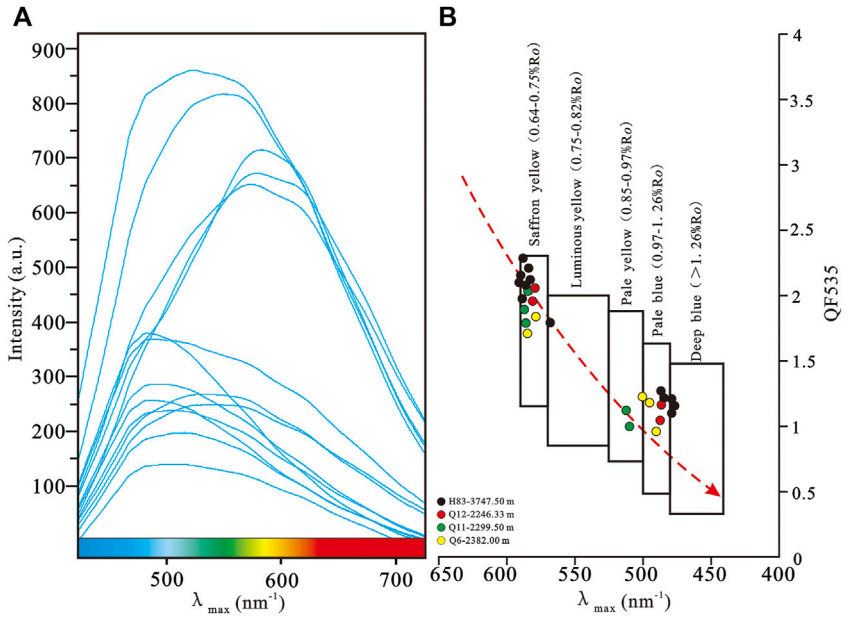

FIGURE 9
Microfluorescence spectra of liquid hydrocarbon inclusions **(A)** and λ_{max} (wavelength of the maximum intensity) *versus* QF_{535} (ratio of the 535–750 nm flux to the 430–535 flux) diagram **(B)**.

with carbon numbers over 7) varies from 43.33% to 61.08%. The oil content of petroleum inclusions varies from 80.5 to 95.7°C. The minimum trapped pressures of yellow and blue petroleum inclusions range from 19.08 to 27.87 MPa. The content of C_1 in the petroleum inclusions of the Es_3^2 Formation in the H-83 well ranges from 25.88% to 52.01%, and the content of C_{7+} varies from 19.98% to 48.60%. The oil content of petroleum inclusions varies from 80.5 to 88.7°C. The minimum trapped pressure of blue petroleum inclusions ranges from 42.91 to 54.46 MPa, and the minimum trapped pressure of yellow petroleum inclusions ranges from 32.76 to 34.45 MPa (Table 6).

Discussion

Fluid evolution sequence in the western slope belt

From the microscopic observation of the Es_3^2 Formation in the sandstone reservoir sample, three kinds of fluid activities (petroleum, CH_4, and CO_2) are identified. Microthermometry was used to measure the homogenization temperature of aqueous inclusions, which was related to different types of fluid inclusions (petroleum, CH_4, and CO_2). The T_h throwing-dot method can be used to estimate the CH_4, CO_2 and oil accumulation times (Figure 4) (Haszeldine et al., 1984; Horsfield and McLimans, 1984). Burial histories show the reservoir in two different steps undergoing different fluid evolution processes. In well H-83 of step I, saffron yellow petroleum inclusions with maturation ranges of 0.64–0.75% R_o accumulated at ~32–29 Ma (T_h interval: 110.0–130.0°C; yellow frame in Figure 4). CH_4 and CO_2 fluid accumulated at ~24–21 Ma (T_h interval: 120–130.0°C; red frame in Figure 4). Late generated oil (pale blue petroleum inclusions) with high maturation in 0.97–1.26% R_o accumulated at ~12–0 Ma (T_h interval: 150.0–160.0°C; blue frame in Figure 4). In wells Q-6, Q-11, and Q-12 of step II, saffron yellow petroleum inclusions accumulated at ~33–30 Ma, and after the uplift and denudation of the Dongying movement, the source rocks were buried deep again. Secondary oil generation accumulated at 4–0 Ma (T_h interval: 115.0–125.0°C; yellow frame in Figure 4). Low-abundance pale blue petroleum inclusions and high-abundance CH_4 and CO_2 gas inclusions are observed, which accumulated at ~28–20 Ma (T_h interval: 95.0–110.0°C; red and blue frame in Figure 4).

Degradation and oxidation of crude oil

Currently, all development wells in step I and step II produce oil and no natural gas. In each well of step II, except for the discovery of multistage petroleum fluids, the greatest significance is that a large abundance of CH_4- and CO_2-gas-bearing inclusions is detected *in situ* by LRM spectroscopy. At the same time, a large amount of bitumen fills the grain pores of the sandstone

TABLE 6 Petroleum inclusion trapped pressure analysis summary.

No.	Well	Depth (m)	T_{hoil}	T_{haq} (°C)	Fv (%)	C_1 (mol%)	C_{7+} (mol%)	Fluorescence color	Reconstructed trapped pressure (MPa)[a]	Pressure coefficient
1	Q-12	2299.5	89.5	120.8	5	24.36	50.19	Yellow	27.86	1.26
2	Q-12	2299.5	90.1	125.4	4	15.48	59.78	Yellow	26.84	1.22
3	Q-12	2299.5	91.6	115.4	6	29.43	44.83	Blue	26.11	1.19
4	Q-12	2299.5	83.1	101.3	4	20.05	54.73	Yellow	19.08	0.87
5	Q-12	2299.5	80.5	103.1	4	21.73	52.96	Yellow	22.28	1.01
6	Q-11	2398.4	88.6	114.5	6	30.82	43.33	Yellow	27.87	1.23
7	Q-11	2398.4	91.5	115.6	6	29.48	44.78	Blue	26.29	1.20
8	Q-11	2591.7	95.7	120.9	6	27.43	46.96·	Yellow	25.84	1.04
9	Q-6	2595.5	91.5	123.4	5	23.21	51.40	Yellow	27.64	1.24
10	Q-6	2588.0	90.5	118.6	4	15.22	60.09	Yellow	22.69	1.03
11	Q-6	2588.0	91.8	120.6	4	14.38	61.08	Yellow	22.74	1.01
12	H-83	3747.50	83.6	120.2	16	52.01	19.98	Blue	44.66	1.78
13	H-83	3747.50	88.7	124.3	15	49.84	21.87	Blue	42.91	1.71
14	H-83	3747.50	87.7	146.7	16	51.19	20.67	Blue	54.46	1.60
15	H-83	3747.50	86.6	136.6	14	49.06	22.61	Blue	49.16	1.82
16	H-83	3747.50	86.3	153.8	7	35.85	37.66	Blue	51.48	1.42
17	H-83	3747.50	80.5	113.6	6	34.23	39.52	Yellow	33.38	1.29
18	H-83	3747.50	81.0	120.4	5	28.95	45.35	Yellow	34.45	1.31
19	H-83	3747.50	86.8	125.1	5	25.88	48.60	Yellow	32.76	1.26

[a]: Reconstructed trapped pressure calculated following Ping et al. (2013).

reservoir. The EqVR% of bitumen ranges from 0.67% to 1.04%. According to the vitrinite reflectivity and occurrence, it belongs to the degraded and oxidized bitumen formed *in situ*. The coexistence of CH_4 and CO_2 gas in fluid inclusions indicates that the early oil in the reservoir underwent degradation and oxidation. Crude oil with a high carbon number will produce many light components (mainly methane) and CO_2 after degradation and leave low-maturity bitumen *in situ* (Revesz et al., 1995; Head et al., 2010). The CH_4 and CO_2 fluid trapping period occurred after the first stage of the oil charging event. At this time, step II of the western slope belt experienced a strong uplifting structure and erosion because of the Dongying movement. Strong tectonic movement over a short period of time causes the opening of the fault and the exposure of crude oil. The Dongying movement has different tectonic control functions for different fault blocks. Compared with step II, step I has a very weak tectonic uplift and denudation, and the differences in the abundance of CH_4 and CO_2 gas inclusions in the two regions are also indicative (Figure 7).

Palaeo-pressure characteristics

Aqueous inclusions are simultaneously observed alongside gas/petroleum inclusions, indicating that immiscible FIAs were trapped during mineral crystallization (Roedder, 1984; Goldstein, 1986; Diamond, 2001; Hurai, 2010). Isochore calculations of fluid trapped pressure follow the approach of a two-phase immiscible field (Pironon, 1990; Thiery et al., 2000; Gao et al., 2017). Based on the combination of the Raman spectra with the relevant thermodynamic model (Peng and Robinson, 1960; Duan and Mao, 2006), the component concentration and density of the water-rich and gas-rich phases can be obtained (Dubessy et al., 2001; Becker et al., 2008; Lecumberri-Sanchez et al., 2012; Mao et al., 2013).

In petroliferous sedimentary basins, reservoir pore fluids usually consist of oil, gas, and formation water. Pore fluid pressure is one of the key parameters for reservoir fluid evaluation. The parameters of the formation fluid pressure and pressure coefficient are usually used in pore pressure characterization. The formation fluid pressure coefficient (P_c) here refers to the ratio of the actual formation fluid pressure (P_f) to the hydrostatic pressure (P_{hyd}) at the same depth. It is a main parameter used to identify abnormal formation pressure (Law and Spencer, 1998). In this study, measured formation pressure and temperature data sets from drill stem tests (DSTs) were supplied by the SINOPEC Zhongyuan Oilfield (Figure 3). The current measured pressure coefficient of the Es_3^2 Formation ranges from 1.50 to 1.66 (high overpressure) in step I and from 0.95 to 1.02 (normal pressure) in step II (Table 6). The trapped pressure of fluid inclusions represents the pore fluid pressure in the

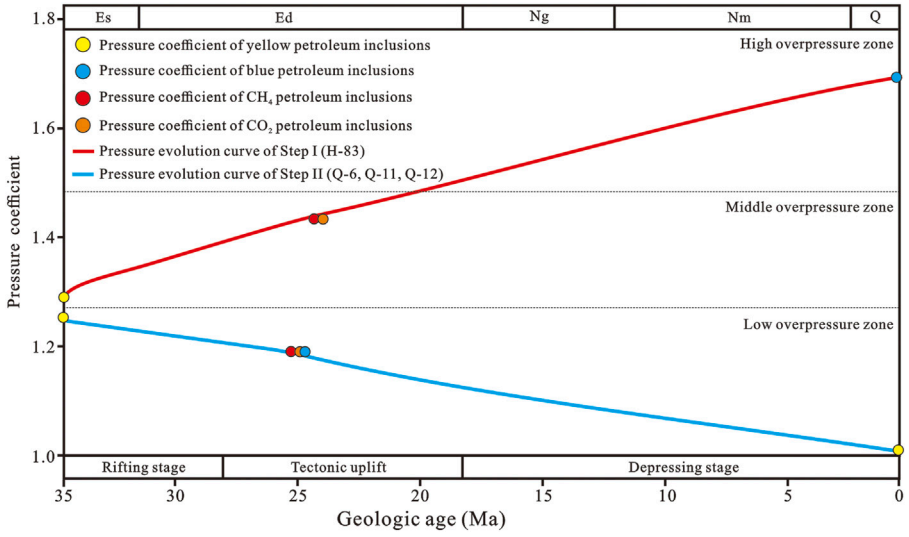

FIGURE 10
Pressure coefficient evolutionary process of fluid inclusions in the Es_3^2 Formation in different tectonic steps of the western slope belt of Dongpu Sag.

initial conditions (Parry and Bruhn, 1990; Evans, 1995). Recovering the paleo-pressure of pure CH_4 and CO_2 gas inclusions by Raman spectroscopy quantitative analysis and the minimum trapped pressure of petroleum inclusions calculated by the predictive model, we obtained the pressure evolution of the two stages of the oil charging event and one gas charging event in different tectonic units (Figure 10). In the early Oligocene, step I and step II entered the basin rifting stage, and the source rock was in the middle stage of oil generation. Saffron yellow petroleum inclusions are largely trapped in reservoir sandstone. The reservoir maintains moderate overpressure with a pressure coefficient between 1.25 and 1.28. In the middle Oligocene, and the Dongying movement resulted in severe uplift and denudation of step II. The late Oligocene–Miocene oil reservoir degraded into CH_4 and CO_2 gas reservoirs, and the reservoir pore pressure decreased (average P_c: 1.20). The wells of step I have only minor uplift denudation. With the reburial of the Es_3 Formation, step I entered late oil generation in the late Miocene, and the maturity simulation was basically the same as the maturity of the pale blue petroleum inclusions. The pore pressure of the reservoir is approximately 1.67, which is at high overpressure conditions, and step II enters the middle stage of oil generation again (R_o %: 0.5–0.7). The maturity of late crude oil is consistent with that of trapped saffron yellow petroleum inclusions. Reservoirs maintain normal pressure conditions (average P_c: 0.90).

Conclusion

In this research, multifarious paleo-fluids occurring in the sandstone reservoir of the Shahejie Formation provide information to pursue the pressure–temperature–time–composition (*P–T–t–X*). According to the previously mentioned results, the following conclusions can be reached:

1) Based on *in situ* Raman characteristic peak observations, fluorescence spectrum analysis, and microthermometry measurements, the fluid charging sequence of fluids in two types of reservoirs with different pressure states in Dongpu Sag is determined. The combination of the T_h throwing-dot method and buried and thermal models can be used to constrain the gas or oil accumulation times. In well H-83 of step I (high overpressure reservoir), saffron yellow petroleum inclusions of low maturation accumulated in the early Oligoene (T_h interval: 110.0–130.0°C). CH_4 and CO_2 fluid accumulated at ~24–21 Ma (density of CH_4 gas inclusions: 0.1772–0.1785 g/cm^3; density of CO_2 gas inclusions: 0.608–0.665 g/cm^3). Late generated oil (pale blue petroleum inclusions) with high maturation accumulated at ~12–0 Ma (T_h interval: 150.0–160.0°C). In wells Q-6, Q-11, and Q-12 of step II (normal pressure reservoir), saffron yellow petroleum inclusions accumulated at ~33–30 Ma, and after the uplift and denudation of the Dongying movement, the source rocks were buried deep again. Secondary oil generation accumulated at 4–0 Ma (T_h interval: 115.0–125.0°C). Low-abundance pale blue petroleum inclusions and high-abundance CH_4 and CO_2 gas inclusions are observed, which accumulated at ~28–20 Ma (density of CH_4 gas inclusions: 0.1010–0.1339 g/cm^3; density of CO_2 gas inclusions: 0.450–0.612 g/cm^3).
2) The recovery of paleo-pressure of CO_2 and CH_4 gas inclusions by Raman quantitative analysis and the minimum trapped pressure of oil inclusions were

determined. Both types of oil reservoirs existed in the early Oligocene under medium-overpressure conditions (P_c: 1.25–1.28). In the middle Oligocene, the Dongying movement resulted in different degrees of uplift and denudation in the two types of reservoirs, causing the reservoir to change to different pressure preservation conditions. Step I involved late oil generation in the late Miocene, and the maturity simulation was basically the same as the maturity of the pale blue petroleum inclusions. The pore pressure of the reservoir is approximately 1.67, which is under high-overpressure conditions. Because of the degradation and oxidation of crude oil in the early stage of step II, the fault destroys the reservoir and produces a large amount of CO_2 and CH_4 gas inclusions (P_c: ~1.20). The oil reservoir approaches normal pressure conditions. With the reburial of the Es_3 Formation, step II entered the middle stage of oil generation again (R_o%: 0.5–0.7). The maturity of late crude oil is consistent with that of trapped saffron yellow petroleum inclusions. Reservoirs maintain normal pressure conditions (average P_c: 0.90).

Data availability statement

The original contributions presented in the study are included in the article/Supplementary Material; further inquiries can be directed to the corresponding author.

Author contributions

YT: conceptualization, methodology, software, investigation, and writing—original draft. YW: Data processing and chart drawing. RW: validation, formal analysis, and visualization. YH: review and editing. YX: provided core and data. ZC: Review. TX: validation, formal analysis, and review and editing. TW: review and editing. HL: review and editing. All authors reviewed the article.

Funding

This paper was funded by the State Key Laboratory of Organic Geochemistry (Grant No. SKLOG202016), the Open Fund of the State Key Laboratory of Oil and Gas Reservoir Geology and Exploitation (Chengdu University of Technology) (Grant No. PLC20210206), the Joint Fund for Enterprise Innovation and Development (Grant No. U20B6001), and the National Natural Science Foundation of China (detection of phenylpolycyclic aromatic hydrocarbons and its petroleum geochemical significance) (Grant No. 41972148).

Acknowledgments

We thank the editor and reviewer for their constructive comments.

Conflict of interest

TX was employed by the SINOPEC Zhongyuan Oilfield Company.

The remaining authors declare that the research was conducted in the absence of any commercial or financial relationships that could be construed as a potential conflict of interest.

Publisher's note

References

Azbej, T., Severs, M. J., Rusk, B. G., and Bodnar, R. J. (2007). *In situ* quantitative analysis of individual H_2O–CO_2 fluid inclusions by laser Raman spectroscopy. *Chem. Geol.* 237, 255–263. doi:10.1016/j.chemgeo.2006.06.025

Baumgartner, M., and Bakker, R. J. (2009). Raman spectroscopy of pure H_2O and NaCl-H_2O containing synthetic fluid inclusions in quartz—A study of polarization effects. *Mineral. Pet.* 95, 1–15. doi:10.1007/s00710-008-0028-z

Becker, S. P., Fall, A., and Bodnar, R. J. (2008). Synthetic fluid inclusions. XVII. PVTX properties of high salinity H_2O-NaCl solutions (> 30 wt% NaCl): Application to fluid inclusions that homogenize by halite disappearance from porphyry copper and other hydrothermal ore deposits. *Econ. Geol.* 103, 539–554. doi:10.2113/gsecongeo.103.3.539

Bodnar, R. J. (1993). Revised equation and table for determining the freezing point depression of H_2O-NaCl solutions. *Geochim. Cosmochim. Acta* 57, 683–684. doi:10.1016/0016-7037(93)90378-a

Burke, E. A. J. (2001). Raman microspectrometry of fluid inclusions. *Lithos* 55, 139–158. doi:10.1016/s0024-4937(00)00043-8

Burruss, R. C. (1987). Diagenetic palaeotemperatures from aqueous fluid inclusions: Re-equilibration of inclusions in carbonate cements by burial heating. *Mineral. Mag.* 51, 477–481. doi:10.1180/minmag.1987.051.362.02

Burruss, R. C. (1991). *Practical aspects of fluorescence microscopy of petroleum fluid inclusions*. Oklahoma, United States: SEPM.

Caumon, M.-C., Robert, P., Laverret, E., Tarantola, A., Randi, A., Pironon, J., et al. (2014). Determination of methane content in NaCl–H_2O fluid inclusions by Raman spectroscopy. Calibration and application to the external part of the Central Alps (Switzerland). *Chem. Geol.* 378–379, 52–61. doi:10.1016/j.chemgeo.2014.03.016

Caumon, M.-C., Tarantola, A., and Mosser-Ruck, R. (2015). Raman spectra of water in fluid inclusions: I. Effect of host mineral birefringence on salinity measurement. *J. Raman Spectrosc.* 46, 969–976. doi:10.1002/jrs.4708

Chang, Y.-J., and Huang, W.-L. (2008). Simulation of the fluorescence evolution of "live" oils from kerogens in a diamond anvil cell: Application to inclusion oils in terms of maturity and source. *Geochim. Cosmochim. Acta* 72, 3771–3787. doi:10.1016/j.gca.2008.05.041

Diamond, L. W. (2001). Review of the systematics of CO_2-H_2O fluid inclusions. *Lithos* 55, 69–99. doi:10.1016/s0024-4937(00)00039-6

Dickinson, G. (1953). Geological aspects of abnormal reservoir pressures in Gulf Coast Louisiana. *AAPG Bull.* 37, 410–432.

Duan, Z., and Mao, S. (2006). A thermodynamic model for calculating methane solubility, density and gas phase composition of methane-bearing aqueous fluids from 273 to 523K and from 1 to 2000bar. *Geochim. Cosmochim. Acta* 70, 3369–3386. doi:10.1016/j.gca.2006.03.018

Duan, Z., Møller, N., and Weare, J. H. (2003). Equations of state for the NaCl-H_2O-CH_4 system and the NaCl-H_2O-CO_2-CH_4 system : Phase equilibria and volumetric properties above 573 k. *Geochim. Cosmochim. Acta* 67, 671–680. doi:10.1016/s0016-7037(02)01226-7

Duan, Z., and Sun, R. (2003). An improved model calculating CO_2 solubility in pure water and aqueous NaCl solutions from 273 to 533 K and from 0 to 2000 bar. *Chem. Geol.* 193, 257–271. doi:10.1016/s0009-2541(02)00263-2

Dubessy, J., Buschaert, S., Lamb, W., Pironon, J., and Thiéry, R. (2001). Methane-bearing aqueous fluid inclusions: Raman analysis, thermodynamic modelling and application to petroleum basins. *Chem. Geol.* 173, 193–205. doi:10.1016/s0009-2541(00)00275-8

Dubessy, J., Caumon, M. C., Rull, F., and Sharma, S. (2012). Instrumentation in Raman spectroscopy: Elementary theory and practice. *Eur. Mineral. Union Notes Mineral.* 12, 83–172.

Dubessy, J., Poty, B., and Ramboz, C. (1989). Advances in COHNS fluid geochemistry based on micro-Raman spectrometric analysis of fluid inclusions. *Eur. J. Mineral.* 1, 517–534. doi:10.1127/ejm/1/4/0517

Evans, M. A. (1995). Fluid inclusions in veins from the Middle Devonian shales: A record of deformation conditions and fluid evolution in the Appalachian Plateau. *Geol. Soc. Am. Bull.* 107, 327–339.

Fabre, D., and Couty, R. (1986). Investigation on the density effects in the Raman-spectrum of methane up to 3, 000 bar-application to the determination of pressure in fluid inclusions trapped in minerals. *COMPTES RENDUS Acad. Sci. Ser. II* 303, 1305–1308.

Gao, J., He, S., Zhao, J., and Yi, J. (2017). Geothermometry and geobarometry of overpressured lower Paleozoic gas shales in the Jiaoshiba field, Central China: Insight from fluid inclusions in fracture cements. *Mar. Pet. Geol.* 83, 124–139. doi:10.1016/j.marpetgeo.2017.02.018

Gao, Z., Fan, Y., Xuan, Q., and Zheng, G. (2020). A review of shale pore structure evolution characteristics with increasing thermal maturities. *Adv. Geo-Energy Res.* 4 (4), 247–259. doi:10.46690/ager.2020.03.03

Gay, A., Lopez, M., Berndt, C., and Seranne, M. (2007). Geological controls on focused fluid flow associated with seafloor seeps in the Lower Congo Basin. *Mar. Geol.* 244, 68–92. doi:10.1016/j.margeo.2007.06.003

Goldstein, R. H. (2001). Fluid inclusions in sedimentary and diagenetic systems. *Lithos* 55, 159–193. doi:10.1016/s0024-4937(00)00044-x

Goldstein, R. H. (2003). Petrographic analysis of fluid inclusions. *Fluid Incl. Anal. Interpret.* 32, 9–53.

Goldstein, R. H. (1986). Reequilibration of fluid inclusions in low-temperature calcium-carbonate cement. *Geol.* 14, 792–795. doi:10.1130/0091-7613(1986)14<792:rofiil>2.0.co;2

Guillaume, D., Teinturier, S., Dubessy, J., and Pironon, J. (2003). Calibration of methane analysis by Raman spectroscopy in H_2O–NaCl–CH_4 fluid inclusions. *Chem. Geol.* 194, 41–49. doi:10.1016/s0009-2541(02)00270-x

Guo, H., Wang, Z., Wang, B., Zhang, Y., Meng, H., and Sui, H. (2022). Molecular dynamics simulations of oil recovery from dolomite slit nanopores enhanced by CO_2 and N_2 injection. *Adv. Geo-Energy Res.* 6 (6), 306–313. doi:10.46690/ager.2022.04.05

Guo, H., Ying, C., Hu, Q., Lu, W., Ou, W., and Geng, L. (2014). Quantitative Raman spectroscopic investigation of geo-fluids high-pressure phase equilibria: Part I. Accurate calibration and determination of CO_2 solubility in water from 273.15 to 573.15 K and from 10 to 120 MPa. *Fluid Phase Equilibria* 382, 70–79. doi:10.1016/j.fluid.2014.08.032

Guo, X., He, S., Liu, K., and Zheng, L. (2011). Quantitative estimation of overpressure caused by oil generation in petroliferous basins. *Org. Geochem.* 42, 1343–1350. doi:10.1016/j.orggeochem.2011.08.017

Haszeldine, R. S., Samson, I. M., and Cornford, C. (1984). Dating diagenesis in a petroleum basin, a new fluid inclusion method. *Nature* 307, 354–357. doi:10.1038/307354a0

Head, I. M., Larter, S. R., Gray, N. D., Sherry, A., Adams, J. J., Aitken, C. M., et al. (2010). Hydrocarbon degradation in petroleum reservoirs. *Handb. Hydrocarb. Lipid Microbiol.* 2010, 3097–3109.

Horsfield, B., and McLimans, R. K. (1984). Geothermometry and geochemistry of aqueous and oil-bearing fluid inclusions from Fateh Field, Dubai. *Org. Geochem.* 6, 733–740. doi:10.1016/0146-6380(84)90094-9

Huang, Y., Tarantola, A., Wang, W., Caumon, M.-C., Pironon, J., Lu, W., et al. (2018). Charge history of CO_2 in Lishui sag, East China Sea basin: Evidence from quantitative Raman analysis of CO_2-bearing fluid inclusions. *Mar. Pet. Geol.* 98, 50–65. doi:10.1016/j.marpetgeo.2018.07.030

Hurai, V. (2010). Fluid inclusion geobarometry: Pressure corrections for immiscible H_2O–CH_4 and H_2O-CO_2 fluids. *Chem. Geol.* 278, 201–211. doi:10.1016/j.chemgeo.2010.09.014

Kawakami, Y., Yamamoto, J., and Kagi, H. (2003). Micro-Raman densimeter for CO_2 inclusions in mantle-derived minerals. *Appl. Spectrosc.* 57, 1333–1339. doi:10.1366/000370203322554473

Law, B. E., and Spencer, C. W. (1998). *Memoir 70, chapter 1: Abnormal pressure in hydrocarbon environments*. Oklahoma, United States: AAPG.

Lecumberri-Sanchez, P., Steele-MacInnis, M., and Bodnar, R. J. (2012). A numerical model to estimate trapping conditions of fluid inclusions that homogenize by halite disappearance. *Geochim. Cosmochim. Acta* 92, 14–22. doi:10.1016/j.gca.2012.05.044

Li, H., Tang, H. M., Qin, Q. R., Zhou, J. L., Qin, Z. J., Fan, C. H., et al. (2019). Characteristics, formation periods and genetic mechanisms of tectonic fractures in the tight gas sandstones reservoir: A case study of Xujiahe Formation in YB area, Sichuan Basin, China. *J. Pet. Sci. Eng.* 178, 723–735. doi:10.1016/j.petrol.2019.04.007

Li, H., Zhou, J. L., Mou, X. Y., Guo, H. X., Wang, X. X., An, H. Y., et al. (2022). Pore structure and fractal characteristics of the marine shale of the Longmaxi Formation in the Changning area, Southern Sichuan Basin, China. *Front. Earth Sci.* 10, 1018274. doi:10.3389/feart.2022.1018274

Li, R. F., Chen, L. Q., Li, Y. J., and Song, N. (2010). The thermal history reconstruction and hydrocarbon accumulation period discrimination of Gaoyou depression in Subei Basin. *Earth Sci. Front.* 17, 151–159.

Liu, D., Xiao, X., Tian, H., Min, Y., Zhou, Q., Cheng, P., et al. (2013). Sample maturation calculated using Raman spectroscopic parameters for solid organics: Methodology and geological applications. *Chin. Sci. Bull.* 58, 1285–1298. doi:10.1007/s11434-012-5535-y

Liu, J., Liu, T., Jiang, Y., Wan, T., and Liu, R. (2019). Distribution, origin, and evolution of overpressure in the Shahejie Formation of northern Dongpu depression, Bohai Bay Basin, China. *J. Pet. Sci. Eng.* 181, 106219. doi:10.1016/j.petrol.2019.106219

Lu, W., Chou, I.-M., Burruss, R. C., and Song, Y. (2007). A unified equation for calculating methane vapor pressures in the CH_4–H_2O system with measured Raman shifts. *Geochim. Cosmochim. Acta* 71, 3969–3978. doi:10.1016/j.gca.2007.06.004

Luo, Y., Liu, H., Zhao, Y., Wang, Y., Zhang, J., and Lü, X. (2016). Reevaluation of the origin of overpressure in the inter-salt shale-oil reservoir in Liutun Sag, Dongpu Depression, China. *J. Pet. Sci. Eng.* 146, 1092–1100. doi:10.1016/j.petrol.2016.08.011

Mao, S., Hu, J., Zhang, D., and Li, Y. (2013). Thermodynamic modeling of ternary CH_2-H_2O-NaCl fluid inclusions. *Chem. Geol.* 335, 128–135. doi:10.1016/j.chemgeo.2012.11.003

Mclimans, R. K. (1987). The application of fluid inclusions to migration of oil and diagenesis in petroleum reservoirs. *Appl. Geochem.* 2, 585–603. doi:10.1016/0883-2927(87)90011-4

Munz, I. A. (2001). Petroleum inclusions in sedimentary basins: Systematics, analytical methods and applications. *Lithos* 55, 195–212. doi:10.1016/s0024-4937(00)00045-1

Munz, I. A., Wangen, M., Girard, J.-P., Lacharpagne, J.-C., and Johansen, H. (2004). Pressure–temperature–time–composition (P–T–t–X) constraints of multiple petroleum charges in the Hild field, Norwegian North Sea. *Mar. Pet. Geol.* 21, 1043–1060. doi:10.1016/j.marpetgeo.2004.05.006

Osborne, M., and Haszeldine, S. (1993). Evidence for resetting of fluid inclusion temperatures from quartz cements in oilfields. *Mar. Pet. Geol.* 10, 271–278. doi:10.1016/0264-8172(93)90109-6

Ou, W., Guo, H., Lu, W., Wu, X., and Chou, I.-M. (2015). A re-evaluation of the effects of temperature and NaCl concentration on quantitative Raman spectroscopic measurements of dissolved CH_4 in NaCl aqueous solutions: Application to fluid inclusion analysis. *Chem. Geol.* 417, 1–10. doi:10.1016/j.chemgeo.2015.09.018

Parry, W. T., and Bruhn, R. L. (1990). Fluid pressure transients on seismogenic normal faults. *Tectonophysics* 179, 335–344. doi:10.1016/0040-1951(90)90299-n

Peng, D. Y., and Robinson, D. B. (1960). A new two-constant equation of state. *Minerva Ginecol.* 12, 3069–3078.

Ping, H., Chen, H., and Thiéry, R. (2013). Thermodynamic modeling of petroleum inclusions: Composition modeling and prediction of the trapping pressure of crude oils. *Fluid Phase Equilibria* 346, 33–44. doi:10.1016/j.fluid.2013.02.016

Ping, H., Chen, H., Zhai, P., Junzhang, Z., and Simon, C. G. (2019). Petroleum charge history in the Baiyun depression and Panyu lower uplift in the Pearl River Mouth Basin, northern South China Sea: Constraints from integration of organic geochemical and fluid inclusion data. *Am. Assoc. Pet. Geol. Bull.* 103, 1401–1442. doi:10.1306/11151817369

Pironon, J., and Bourdet, J. (2008). Petroleum and aqueous inclusions from deeply buried reservoirs: Experimental simulations and consequences for overpressure estimates. *Geochim. Cosmochim. Acta* 72, 4916–4928. doi:10.1016/j.gca.2008.07.019

Pironon, J., Grimmer, J. O. W., Teinturier, S., Guillaume, D., and Dubessy, J. (2003). Dissolved methane in water: Temperature effect on Raman quantification in fluid inclusions. *J. Geochem. Explor.* 78–79, 111–115. doi:10.1016/s0375-6742(03)00136-5

Pironon, J. (1990). Synthesis of hydrocarbon fluid inclusions at low temperature. *Am. Mineral.* 75, 226–229.

Revesz, K., Coplen, T. B., Baedecker, M. J., Glynn, P. D., and Hult, M. (1995). Methane production and consumption monitored by stable H and C isotope ratios at a crude oil spill site, Bemidji, Minnesota. *Appl. Geochem.* 10, 505–516. doi:10.1016/0883-2927(95)00021-6

Roedder, E. (1984). *Fluid inclusions*. Chantilly, VA: Mineralogical Society of America.

Rosso, K. M., and Bodnar, R. J. (1995). Microthermometric and Raman spectroscopic detection limits of CO_2 in fluid inclusions and the Raman spectroscopic characterization of CO_2. *Geochim. Cosmochim. Acta* 59, 3961–3975. doi:10.1016/0016-7037(95)94441-h

Saimd, T., and Ali, M. (2006). A comparative study of the Rare Earth Element (REE) distributions within the Lower Cretaceous dolomites and limestones of Central Tunisia. *Sedimentology* 32, 897–907. doi:10.1111/j.1365-3091.1985.tb00739.x

Seitz, J. C., Pasteris, J. D., and Chou, I. M. (1993). Raman spectroscopic characterization of gas mixtures; I, Quantitative composition and pressure determination of CH_4, N_2 and their mixtures. *Am. J. Sci.* 293, 297–321. doi:10.2475/ajs.293.4.297

Seitz, J. C., Pasteris, J. D., and Chou, I. M. (1996). Raman spectroscopic characterization of gas mixtures; II, Quantitative composition and pressure determination of the CO_2-CH_4 system. *Am. J. Sci.* 296, 577–600. doi:10.2475/ajs.296.6.577

Song, F., Ye, J., and Shen, C. (2010). Hydrocarbon filling history in the western slope belt of Dongpu depression. *Nat. Gas. Geosci.* 21, 264–269.

Thiery, R., Pironon, J., Walgenwitz, F., and Montel, F. (2000). PIT (petroleum inclusion thermodynamic): A new modeling tool for the characterization of hydrocarbon fluid inclusions from volumetric and microthermometric measurements. *J. Geochem. Explor.* 69, 701–704. doi:10.1016/s0375-6742(00)00085-6

Tingay, M. R., Hillis, R. R., Swarbrick, R. E., Morley, C. K., and Damit, A. R. (2009). Origin of overpressure and pore-pressure prediction in the Baram province, Brunei. *Am. Assoc. Pet. Geol. Bull.* 93, 51–74. doi:10.1306/08080808016

Van den Kerkhof, A. M., and Hein, U. F. (2001). Fluid inclusion petrography. *Lithos* 55, 27–47. doi:10.1016/s0024-4937(00)00037-2

Wang, R., Ding, W., Zhang, Y., Wang, Z., Wang, X., He, J., et al. (2016a). Analysis of developmental characteristics and dominant factors of fractures in Lower Cambrian marine shale reservoirs: A case study of Niutitang Formation in Cen'gong block, southern China. *J. Petroleum Sci. Eng.* 138, 31–49. doi:10.1016/j.petrol.2015.12.004

Wang, R., Gu, Y., Ding, W., Gong, D., Yin, S., Wang, X., et al. (2016b). Characteristics and dominant controlling factors of organic-rich marine shales with high thermal maturity: A case study of the Lower Cambrian Niutitang Formation in the Cen'gong block, southern China. *J. Nat. Gas Sci. Eng.* 33, 81–96. doi:10.1016/j.jngse.2016.05.009

Wang, W., Caumon, M.-C., Tarantola, A., Pironon, J., Lu, W., and Huang, Y. (2019). Raman spectroscopic densimeter for pure CO_2 and CO_2-H_2O-NaCl fluid systems over a wide PT range up to 360° C and 50 MPa. *Chem. Geol.* 528, 119281. doi:10.1016/j.chemgeo.2019.119281

Wang, X., Chou, I. M., Hu, W., Burruss, R. C., Sun, Q., and Song, Y. (2011). Raman spectroscopic measurements of CO_2 density: Experimental calibration with high-pressure optical cell (HPOC) and fused silica capillary capsule (FSCC) with application to fluid inclusion observations. *Geochim. Cosmochim. Acta* 75, 4080–4093. doi:10.1016/j.gca.2011.04.028

Weibull, W., Mienert, J., Bünz, S., and Hustoft, S. (2010). Fluid migration directions inferred from gradient of time surfaces of the sub seabed. *Mar. Pet. Geol.* 27, 1898–1909. doi:10.1016/j.marpetgeo.2010.07.014

Wilkins, R. W. T., Boudou, R., Sherwood, N., and Xiao, X. (2014). Thermal maturity evaluation from inertinites by Raman spectroscopy: The 'RaMM' technique. *Int. J. Coal Geol.* 128–129, 143–152. doi:10.1016/j.coal.2014.03.006

Wilkins, R. W. T., Sherwood, N., and Li, Z. (2018). RaMM (Raman maturity method) study of samples used in an interlaboratory exercise on a standard test method for determination of vitrinite reflectance on dispersed organic matter in rocks. *Mar. Pet. Geol.* 91, 236–250. doi:10.1016/j.marpetgeo.2017.12.030

Wilkins, R. W. T., Wang, M., Gan, H., and Li, Z. (2015). A RaMM study of thermal maturity of dispersed organic matter in marine source rocks. *Int. J. Coal Geol.* 150–151, 252–264. doi:10.1016/j.coal.2015.09.007

Wu, J., and Ye, J. (2009). Fluid history analysis in the western slope belt of Dongpu Sag. *Geol. Sci. Technol. Inf.* 28, 66–70.

Zhang, J., Qiao, S., Lu, W., Hu, Q., Chen, S., and Liu, Y. (2016). An equation for determining methane densities in fluid inclusions with Raman shifts. *J. Geochem. Explor.* 171, 20–28. doi:10.1016/j.gexplo.2015.12.003

Zozulya, A. A., Diddams, S. A., and Clement, T. S. (1998). Investigations of nonlinear femtosecond pulse propagation with the inclusion of Raman, shock, and third-order phase effects. *Phys. Rev. A* 58, 3303–3310. doi:10.1103/physreva.58.3303

Zuo, Y. H., Ye, B., Wu, W., Zhang, Y., Ma, W., Tang, S., et al. (2017). Present temperature field and Cenozoic thermal history in the Dongpu depression, Bohai Bay Basin, north China. *Mar. Pet. Geol.* 88, 696–711. doi:10.1016/j.marpetgeo.2017.08.037

frontiers | Frontiers in Earth Science

TYPE Original Research
PUBLISHED 13 January 2023
DOI 10.3389/feart.2022.1061211

OPEN ACCESS

EDITED BY
Shuai Yin,
Xi'an Shiyou University, China

REVIEWED BY
Caifang Wu,
China University of Mining and Technology, China
Mengdi Sun,
Northeast Petroleum University, China

*CORRESPONDENCE
Yifan Gu,
xnsygyf@126.com

SPECIALTY SECTION
This article was submitted to Structural Geology and Tectonics, a section of the journal Frontiers in Earth Science

RECEIVED 04 October 2022
ACCEPTED 27 December 2022
PUBLISHED 13 January 2023

CITATION
Cai G, Gu Y, Xiong X, Li X, Sun X, Ni J, Jiang Y, Fu Y and Ou F (2023), Reservoir characteristics and pore fluid evaluation of Shan 2^3 Submember transitional shale, eastern Ordos Basin, China: Insights from NMR experiments.
Front. Earth Sci. 10:1061211.
doi: 10.3389/feart.2022.1061211

Reservoir characteristics and pore fluid evaluation of Shan 2^3 Submember transitional shale, eastern Ordos Basin, China: Insights from NMR experiments

Guangyin Cai[1,2,3], Yifan Gu[1,2,3]*, Xianyue Xiong[4], Xingtao Li[4], Xiongwei Sun[4], Jia Ni[5], Yuqiang Jiang[1,2,3], Yonghong Fu[1,2,3] and Fang Ou[6]

[1]School of Geoscience and Technology, Southwest Petroleum University, Chengdu, China, [2]The Unconventional Reservoir Evaluation Department, PetroChina Key Laboratory of Unconventional Oil and Gas Resources, Chengdu, China, [3]Sichuan Collaborative Innovation Center for Shale Gas Resources and Environment, Chengdu, China, [4]PetroChina Coalbed Methane Company, Beijing, China, [5]Shale Gas Research Institute, PetroChina Southwest Oil and Gas Field Company, Chengdu, China, [6]Chongqing Gas Field, PetroChina Southwest Oil and Gas Field Company, Chongqing, China

The Lower Permian Shanxi Formation in the Eastern Ordos Basin is a set of transitional shale, and it is also a key target for shale gas exploration in China. Three sets of organic-rich transitional shale intervals (Lower shale, Middle shale and Upper shale) developed in Shan 2^3 Submember of Shanxi Formation. Based on TOC test, X-diffraction, porosity, *in-situ* gas content experiment and NMR experiments with gradient centrifugation and drying temperature, the reservoir characteristics and pore fluid distribution of the three sets of organic-rich transitional shale are studied. The results show that: 1) The Middle and Lower shales have higher TOC content, brittleness index and gas content, reflecting better reservoir quality, while the Upper shales have lower gas content and fracturing ability. The total gas content of shale in the Middle and Lower shales is high, and the lost gas and desorbed gas account for 80% of the total gas content. 2) The Middle shale has the highest movable water content (32.58%), while the Lower shale has the highest capillary bound water content (57.52%). In general, the capillary bound water content of marine-continental transitional shale in the Shan 2^3 Submember of the study area is high, ranging from 39.96% to 57.52%. 3) Based on pore fluid flow capacity, shale pores are divided into movable pores, bound pores and immovable pores. The Middle shale and the Lower shale have high movable pores, with the porosity ratio up to 27%, and the lower limit of exploitable pore size is 10 nm. The movable pore content of upper shale is 25%, and the lower limit of pore size is 12.6 nm. It is suggested that the Lower and Middle shales have more development potential under the associated development technology.

KEYWORDS

transitional shale, pore structure, fluid evaluation, upper permian, Shan 2^3 Submember, Ordos Basin

Introduction

Marine-continental transitional facies shale is an important field of unconventional oil and gas exploration in China, which accounts for 25% of shale gas resources in China (Kuang et al., 2020). It has a wide distribution area and great resource potential (Yang et al., 2017). However, the exploration, development and geological evaluation of marine-continental transitional facies shale gas are still in the initial stage and require further improvement (Zhang et al., 2018; Dong et al., 2021). The nanoscale pore structure has been identified as one of the most important mechanisms to affect hydrocarbon recovery from unconventional shale reservoirs (Chen et al., 2018; Han et al., 2021). Understanding nanoscale pore structure and its controlling factors is beneficial for shale reservoir evaluation. A large number of pore structure studies have been carried out on marine shale and found that nanoscale pore structure is strongly affected by mineral composition and organic matter abundance (Li et al., 2016; Jia et al., 2020). However, due to the huge difference in sediment composition, mineral composition and organic matter abundance between transitional shale and marine shale (Jia et al., 2020; Wang et al., 2022), the previous results of marine shale cannot be directly applied to transitional shale. The existence of pore water in shale reservoir will affect the adsorption capacity and flow capacity of shale gas to a great extent, which brings some difficulties to the evaluation of gas reservoir resources and the prediction of productivity (Zhang et al., 2022a; Xi et al., 2022). Therefore, the research on the prediction shale gas adsorption capacity and flow capacity under the condition of reservoir water cut is of great significance to the formulation of gas field development plan and the evaluation of development potential (Li et al., 2018). Therefore, it is of great significance for exploration evaluation and development plan-making to clarify different pore fluid characteristics. However, previous studies on transitional facies shale focus on the characteristics of shale gas reservoirs such as TOC content, mineral composition, pore type and gas content (Li et al., 2019). Meanwhile, many studies have been carried out on the sedimentary environment, sedimentary model and pore structure of transitional facies shale (Xi et al., 2017; Liu et al., 2018; Luo et al., 2018; Xi et al., 2018; Wang et al., 2022), but systematic studies on pore fluid of shale pore system is rare. In this study, the effective pore size distribution is determined by dividing the fluid types in the pores, and the systematic evaluation of the transitional shale pores in the study area is realized, which also provides a new idea for the effectiveness evaluation of transitional shale reservoirs.

Geological setting

The Ordos Basin is a typical craton basin in the western part of the North China Block (Figure 1A), and the basin area is about 370,000 km^2 (Zhang et al., 2021). The Ordos Basin comprises of six structural units, including Tianhuan Depression, Western Fold-Thrust Belt, Yimeng Uplift, Jinxi Flexural Fold Belt, Shenbei Slope and Weibei Uplift (Gu et al., 2022).

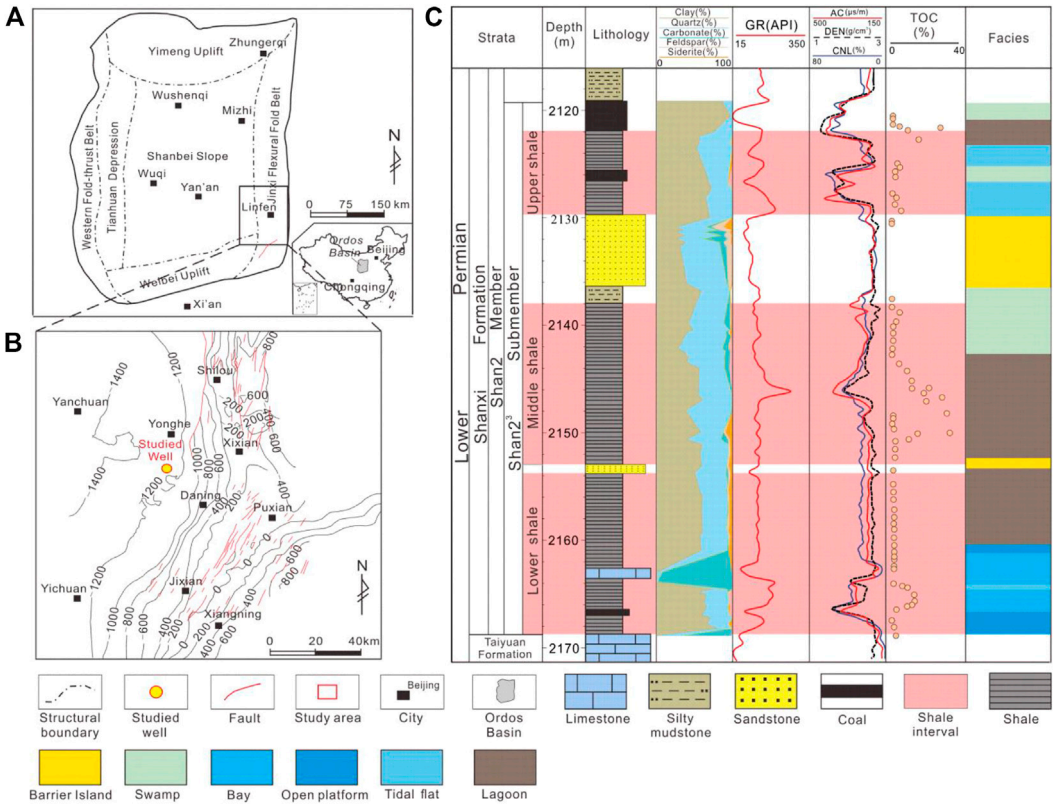

FIGURE 1
(A) Location of study area, North China. **(B)** Distribution map showing the burial depth of Shan 2^3 Submember transitional shale. **(C)** Vertical distribution of Shan 2^3 Submember transitional shale in the studied well (Facies is modified according to Zhang et al., 2021).

The study area, with an area of 4.5×10^4 km^2, is located in the Southeastern Ordos Basin, and the studied well is located in Central part of the study area (Figure 1B). From Late Carboniferous to Early Permian Shanxi Formation period, the Ordos Basin enters the subsidence period, and a large area of transgression occurs, which is dominated by marine-continental transitional facies deposits, forming thick organic-rich marine-continental transitional shale (Chen et al., 2011; Wu et al., 2021). Until the Middle Permian Shihezi period, the Ordos Basin entered continental sedimentary evolution stage (Figure 1C).

The Shanxi Formation consist of Shan 1 Member and Shan 2 Member, and Shan 2 Member consist of three submembers: Shan 2^1, Shan 2^2 and Shan 2^3. During the sedimentary period of Shanxi Formation, the sedimentary environment in the study area changed rapidly due to the frequent changes in sea level, which mainly formed the Bay facies, Lagoon facies, Tidal flat facies, Swamp facies and Delta facies. The thick organic-riched black shales deposited in Bays and Lagoons are the main intervals for the breakthrough of marine-continental transitional shales in China (Zhang et al., 2021; Gu et al., 2022). Three sets of transitional shale developed in Shan 2^3 Submember: Lower shale, Middle shale and Upper shale (Figure 1C). Organic rich shale intervals are developed in the middle shale and the lower shale, which are formed in Lagoon and Bay facies respectively.

Samples and methods

A total of seventy-nine shale samples were obtained from the Shan 2^3 Submember of studied well in the Eastern Ordos Basin. TOC of all samples, mineral composition of thirty-three samples, porosity testing of 16 samples, and *in-situ* gas content of fourteen samples have been collected to characterize the macro-characteristics of the shale reservoir. Four shale samples were selected to carry out NMR tests under different centrifugation and drying conditions to characterize the fluid occurrence characteristics.

The four plug samples were first dried at 110°C for 24 h to remove residual moisture in the samples. After 12 h of vacuum degassing, the samples were saturated with high-purity distilled water at a pressure of 25 MPa for 2 days. After the saturation was completed, the sample was taken out, and the NMR T_2 spectrum was tested after standing in the saturated fluid for 12 h. In order to reflect the occurrence characteristics of different types of fluids, two groups of parallel plug samples saturated with water were treated with different centrifugation speeds and drying temperatures, and nuclear magnetic resonance tests were performed after each centrifugation and drying. The centrifugation time of each sample is fixed at 30 min, and the drying time is fixed at 24 h.

The NMR test parameters are as follows: the echo interval (TE) is .055 ms, the number of echoes is 12,000, the cumulative sampling times (NS) is 64 times, and the waiting time (TW) is 4,000 ms. The experimental instrument is the NMRC012V nuclear magnetic resonance instrument produced by Suzhou Niumag Company, China.

Results and discussion

Macroscopic characteristics

Organic matter and thermal maturity

The TOC content of the Shan 2^3 transitional shale of the studied well is unstable in the vertical direction, and the TOC content has obvious changes (Figure 2). The TOC content of the Lower shale and the Middle shale varies widely. The TOC content of the Lower shale ranges from .32% to 26.6%, with an average of 3.37%, and the TOC content of the Middle shale ranges from .07% to 43.9%, with an average of 6.87%. The range of TOC content in the Upper shale is narrow and the content is low, ranging from .97% to 4.11%, with an average of 2.3% (Table 1). The average vitrinite reflectance of the Upper, Middle and Lower shales is 2.4, 2.73 and 2.46, respectively, all exceeding 2.0, indicating that the shale has entered the dry gas generation stage (Zhang et al., 2022b; Zhang et al., 2022c). Although the organic matter type of transitional shale is mainly type III, the rich organic matter content and high thermal maturity make it still have high hydrocarbon generation capacity (Qiu et al., 2021).

Mineral composition

Mineral composition affects the adsorption capacity of shale reservoirs (Fan et al., 2020; Fan et al., 2022; Li et al., 2022). Brittle minerals also determine the transformability of shale to a certain extent, so mineral composition is important for shale gas exploration and development (Ross and Marc Bustin, 2009). The mineral composition of Shan 2^3 transitional shale is mainly quartz and clay, more than 90%, in addition to a small amount of carbonate minerals, pyrite and siderite (Figure 2). The quartz content of the Middle shale is the highest, ranging from 29.3% to 59.7%, with an average of 46.8%. The quartz content of the Upper shale and the Lower shale is narrow, ranging from 25.1% to 47.0% (average 31.7%) and 31.7%–37.3% (average 34.4%), respectively. Most of the samples have high clay content. The clay content of the Middle shale is distributed from 28.8% to 60.6%, with an average of 44.2%, while the average clay mineral content of the Upper and Lower shale is 63.9% and 58.9%, respectively. The average content of quartz minerals in these three sets of shale is less than 50%, and the content of clay is high, which reflects that the overall fracturing ability of the transitional shale in Shan 2^3 is low.

The brittleness index calculation formula commonly used in shale in North America is: brittleness index = quartz/(quartz + calcite + clay mineral) × 100% (Yu et al., 2020; Li, 2022). Due to the complex mineral composition of transitional shale, the modified brittleness index calculation formula is adopted: brittleness index = (quartz + calcite + feldspar)/(quartz + calcite + feldspar + clay mineral). The brittleness index of the Middle shale is the highest, ranging from 35.28 to 69.8, with an average of 52.3, reflecting the relatively strong ability of fracturing. The brittleness index of the lower shale is between 18.09 and 47.44, with an average of 35.1, but there is a limestone interlayer in the lower shale. Considering the fracability of limestone, the lower shale still has a strong ability to be fractured. The brittleness index of the Upper shale is 2.26–68.12, with an average of 33.12, and the fracability is poor.

Porosity

Porosity is the main index to evaluate the storage capacity of shale reservoirs. The average porosity of the three sets of shale in this study is small. The average porosity of the Middle and Lower shale is 2.34% and 2.04% respectively, and the Upper shale porosity is low, with an average of 1.87%. The porosity of most samples is less than 2%, but the porosity of shale in the high TOC range is up to 4% (Figure 2), with strong self-generation and self-storage capacity.

Assessment of *in-situ* gas content

The *in-situ* total gas content of the Upper, Middle and Lower shales is distributed in .4–1.57 m^3/t (average .99 m^3/t), .7–2.22 m^3/t

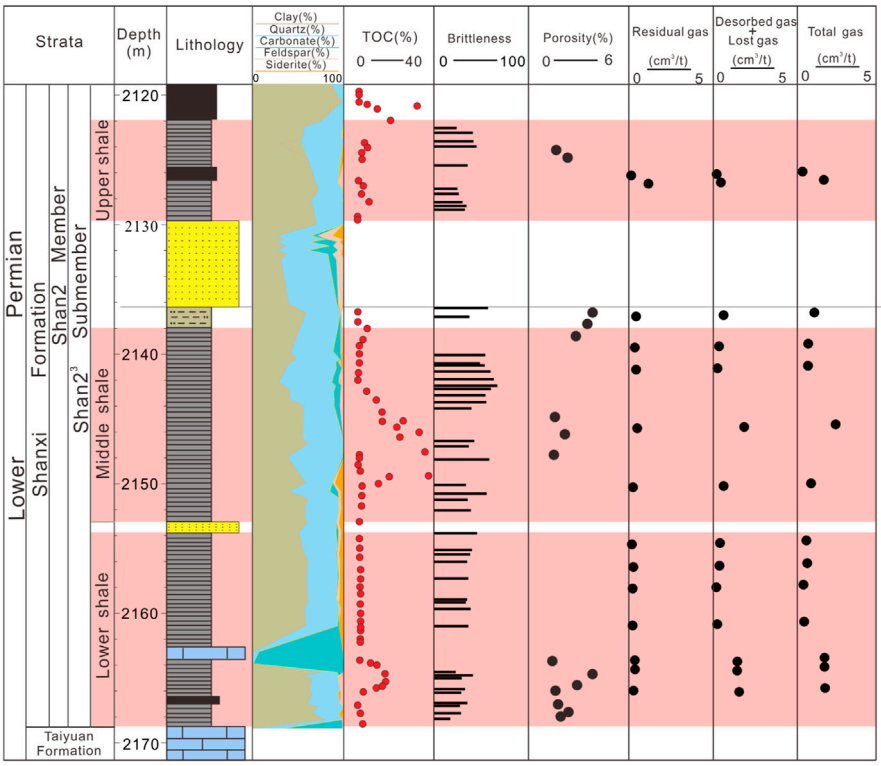

Note: Brittleness=(ω Quartz+ω Feldspar+ω carbonate minerals)/(ω Quartz+ω Feldspar+ω carbonate minerals+ω clay). ω is the corresponding mineral content.

FIGURE 2
Vertical variability of TOC, mineral composition, brittleness, porosity and gas content of studied well.

TABLE 1 Shale organic geochemical and main mineral composition characteristics.

Location	TOC/%	Ro	Quartz/%	Clay/%
Upper shale	.97–4.11 (2.3)	2.4	25.1–47.0 (36.5)	53.0–74.9 (63.9)
Middle shale	.07–43.9 (6.87)	2.73	29.3–59.7 (46.8)	28.8–60.6 (44.2)
Lower shale	.32–26.6 (3.37)	2.46	31.7–37.3 (34.4)	55.4–1.4 (58.9)

(average 1.11 m^3/t), .45–1.64 m^3/t (average 1.01 m^3/t), respectively (Figure 2). In general, the contents of residual gas, lost gas and desorbed gas in the Middle shale are distributed in .16–.33 m^3/t (average .29 m^3/t), .2–.65 m^3/t (average .38 m^3/t), .27–1.19 m^3/t (average .43 m^3/t). The contents of residual gas, lost gas and desorbed gas in the Upper shale are distributed in .06–1.01 m^3/t (average .54 m^3/t), .22–.53 m^3/t (average .38 m^3/t), .11–.69 m^3/t (average .4 m^3/t). The contents of residual gas, lost gas and desorbed gas in the Lower shale are distributed in .1–.31 m^3/t (average .2 m^3/t), .12–.41 m^3/t (average .28 m^3/t), .19–1.05 m^3/t (average .54 m^3/t). Residual gas, lost gas, desorbed gas content ratio and comparative analysis can qualitatively reflect the relative effective porosity and permeability, and to a certain extent, reflect the reservoir quality (Ghosh et al., 2022). The total gas content of the Middle and Lower shale is high, and the content of lost gas and desorbed gas accounts for 80% of the total gas content, reflecting the high reservoir quality.

Pore fluid evaluation

Movable fluid distribution

The NMR T_2 spectra of 4 samples in saturated water showed three peaks, with the main peak of the upper shale less than .1 m and the main peak of the lower shale and central shale at .2 m (Figure 3). The second peak of the Upper shale is distributed in 1–10 ms, and the third peak is distributed in 100–1,000 ms. The second and third peaks of the Middle and Lower shale are distributed in 2–20 ms and 20–1,000 ms, respectively, indicating that the Middle and Lower shale have larger pore size distribution. All samples show that the first peak signal is the highest, and its porosity component accounts for more than 70% of the total porosity, indicating that the small pores of shale are more developed, and there are a small number of large pores and microfractures.

Compared with the NMR T_2 spectrum of saturated water, the centrifuged NMR T_2 spectrum helps to analyze the flow and distribution of fluids in rock pores, thus distinguishing between movable and bound fluids. Figure 3 is the nuclear magnetic resonance T_2 spectrum of saturated water samples after centrifugation at different speeds. With the increase of centrifugal speed, the main peak of NMR T_2 spectrum of each sample changed little, but the long relaxation peaks decreased obviously. When the centrifugal speed increased to 4,000 rpm, the NMR porosity decreased by an average of nearly 2% (Figure 4). The change of NMR T_2 spectrum is the most obvious, and the long relaxation peak of each sample basically disappears, reflecting that the water in macropores or

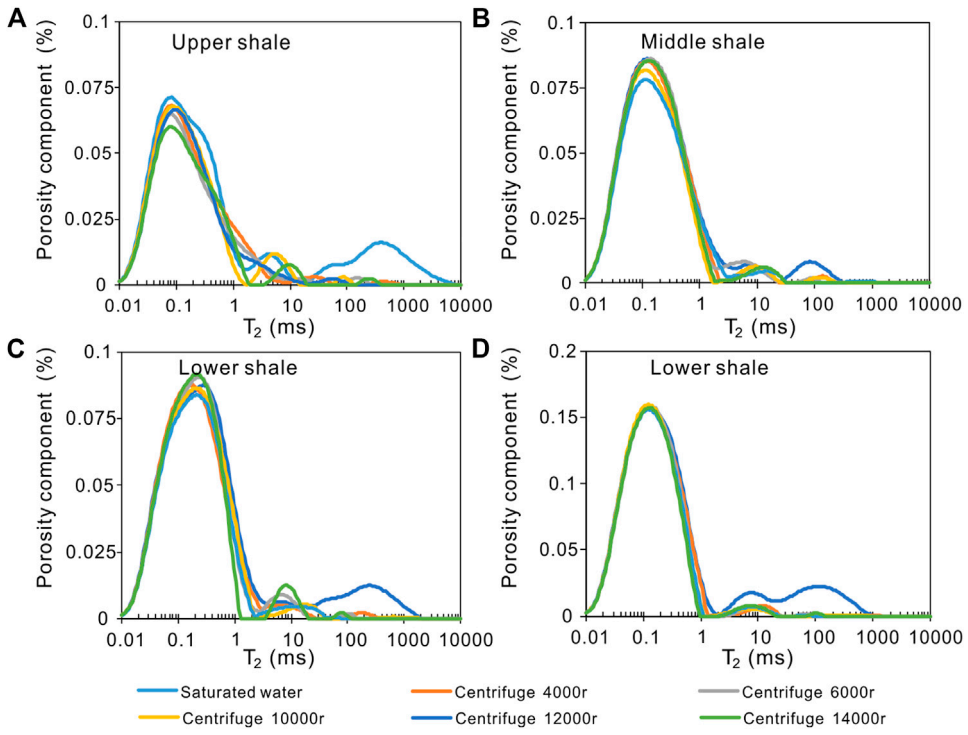

FIGURE 3
NMR T_2 spectra of Shan 2^3 Submember transitional shale under different centrifugation conditions.

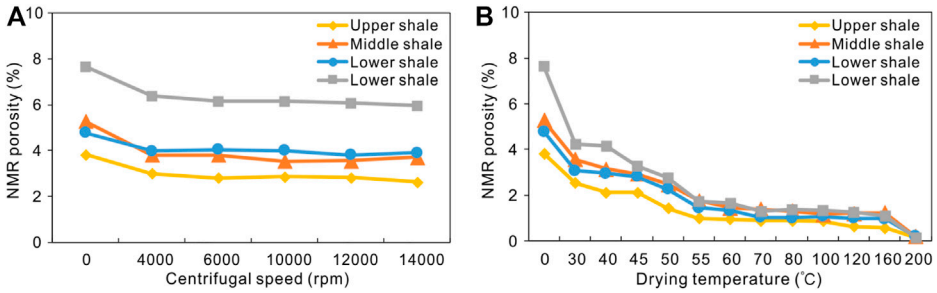

FIGURE 4
NMR porosity changes of Shan 2^3 Submember transitional shale under different centrifugation and drying conditions.

microfractures is discharged from pores under the action of centrifugal force. As the centrifugal speed continues to increase, when the centrifugal speed reaches 12,000 rpm, the second peak begins to decrease slightly, and the porosity decreases by an average of .2%. After the centrifugal speed increased to 14,000 rpm, NMR T_2 spectrum and NMR porosity did not change, at this time the water in the macropores or micro-cracks is basically discharged. Centrifugal process, movable water is preferentially discharged, but a large amount of water remains in the pores, in addition to the Upper shale, other samples NMR porosity of more than 4%.

Testamanti and Rezaee (2017) proposed that centrifugation can only remove the easily flowing water in macropores and microfractures. Centrifugal experiments cannot provide sufficient capillary pressure to remove the flowing water in the matrix. Therefore, Testamanti and Rezaee (2017) proposed to obtain capillary bound water and clay bound water content in shale by variable temperature drying. With the increase of drying temperature, the NMR porosity of shale samples has a significant linear relationship with the rising temperature, and it has segmentation, and the slopes of the three sections are obviously different (Figure 4B). Because the minimum capillary force required to expel different types of fluid is very different, the slope changes significantly when the type of fluid being drained changes. The first stage is the evaporation of movable water at a relatively large rate, and the temperature threshold is 40°C. The second stage is the evaporation of capillary bound water at a uniform speed, and the

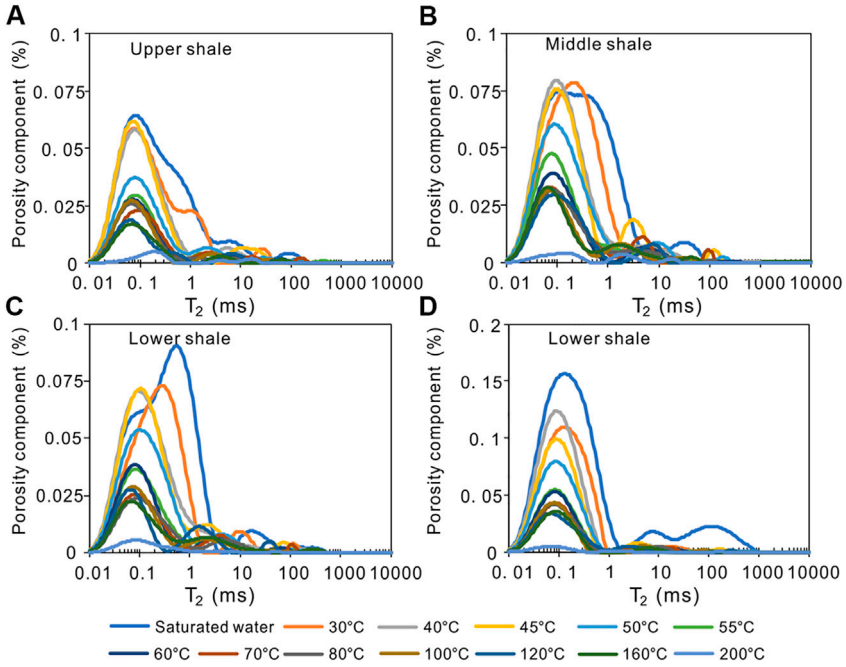

FIGURE 5
NMR T_2 spectra of Shan2[3] Submember transitional shale at different drying temperatures.

temperature threshold is 60°C; the third stage is when the temperature is higher (more than 160°C), the clay bound water in the pore begins to evaporate (Figure 4B).

Figure 5 shows the T_2 spectrum changes of saturated water samples at different drying temperatures. With the increase of drying temperature, the T_2 spectrum of all samples first showed that the long relaxation peak disappeared, then the short relaxation peak decreased, and the main peak shifted to the left obviously. Finally, the T_2 spectrum of all samples showed a single peak with a main peak of .1 ms. When the drying temperature reaches 40°C, the long relaxation peaks of all samples basically disappear, which is consistent with the centrifugal process, and the movable water in the macropores and microcracks discharges the rock. The NMR porosity after drying at 40°C is 1% lower than that after centrifugation. This may be because the drying process enhances the mobility of water molecules, so the water in the pores of the second peak migrates to the macropores, so the water loss is slightly more. When the drying temperature increased to 60°C, the NMR porosity of each sample decreased significantly. The NMR porosity of the four saturated water samples decreased by an average of 4% (Figure 4B), and the capillary bound water evaporated until it was completely lost. When the drying temperature exceeds 160°C, the NMR porosity decreases rapidly again, and the clay bound water begins to evaporate.

NMR experiments based on high-speed centrifugation and drying at gradient temperatures are an effective method for classifying pore fluid types and determining the relative content of mobile and bound fluids (Testamanti and Rezaee, 2017). The water loss in the sample after centrifugation at 14,000 rpm is movable water. After drying at 60°C, the capillary bound water in the matrix pores is also basically removed. The water loss in the sample after drying at 160°C can be approximated as clay bound water. The remaining signal is derived from the unremoved matrix signal. The calculation formulas of various types of fluids are as follows:

$$S_1 = \int_{T_{c1}}^{T_{2max}} dT_2 \Big/ \int_{T_{2min}}^{T_{2max}} dT_2 \quad (1)$$

$$S_2 = \int_{T_{c2}}^{T_{c1}} dT_2 \Big/ \int_{T_{2min}}^{T_{2max}} dT_2 \quad (2)$$

$$S_3 = \int_{T_{c3}}^{T_{c2}} dT_2 \Big/ \int_{T_{2min}}^{T_{2max}} dT_2 \quad (3)$$

$$S_4 = \int_{T_{2min}}^{T_{c3}} dT_2 \Big/ \int_{T_{2min}}^{T_{2max}} dT_2 \quad (4)$$

S_1, S_2, S_3 and S_4 are movable water saturation, capillary bound water saturation, clay bound water saturation and matrix content respectively. T_{c1}, T_{c2}, and T_{c3} are the cutoff values between movable water and capillary bound water, between capillary bound water and clay bound water, and between clay bound water and base signal, respectively. The method for determining the T_2 cutoff value of shale samples is shown in Figure 6. First, the T_2 spectrum of four states was obtained, namely saturated water, 14,000 rpm centrifugation, 60°C drying and 200°C drying. Then the T_2 spectrum is converted into the cumulative spectrum of NMR porosity and displayed in the same map. The T_{c1}, T_{c2} and T_{c3} are determined by the projection process.

Table 2 shows T_2 cut-off values for four samples and calculated saturation for different types of fluids. After comparing different fluid saturations, it is suggested that the most abundant shale fluid is capillary bound water, which is 39.96%–57.52%. This part of the fluid needs good fracturing effect to be exploited. The movable water has strong flowing ability and low mining difficulty, and its content is distributed in 20.46%–32.58%. Among the three sets of shale, the Middle shale has the highest movable water content of 32.58% and the lowest capillary bound water content of 39.96%. The Lower shale has

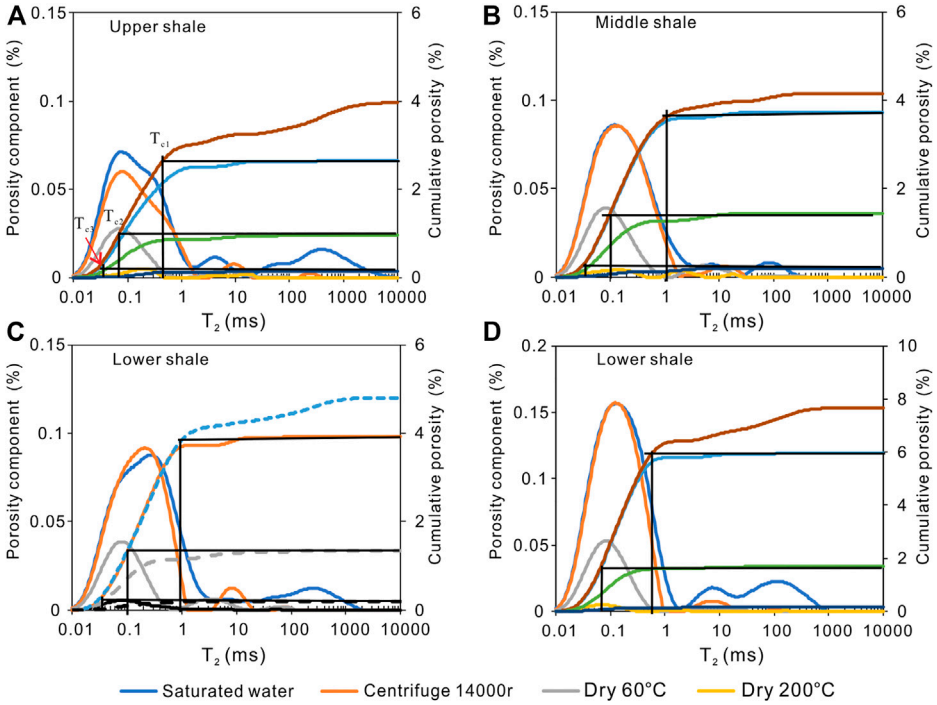

FIGURE 6
NMR $T_{2cutoff}$ values of Shan 2^3 Submember transitional shale for different fluid types.

TABLE 2 Statistics of different fluid types contents and $T_{2cutoff}$.

Sample	T_{c1} (ms)	T_{c2} (ms)	T_{c3} (ms)	S1 (%)	S2 (%)	S3 (%)	S4 (%)
Upper shale	.5	.07	.04	26.30	48.96	20.83	3.91
Middle shale	1	0.1	.04	32.58	39.96	23.67	3.79
Lower shale	1	0.1	.04	20.46	51.77	23.59	4.18
Lower shale	.6	.07	.04	20.52	57.52	20.00	1.96

TABLE 3 Statistics of different pore types contents and lower limit of pore size.

Sample	r_{c1} (nm)	r_{c2} (nm)	r_{c3} (nm)	Moveable pore (%)	Bound pore (%)	Immoveable pore (%)
Upper shale	90	12.6	7.2	25.00	42.93	32.07
Middle shale	100	10	4	27.27	40.72	32.01
Lower shale	100	10	4	27.35	52.61	20.04
Lower shale	90	10.5	6	23.53	53.73	22.75

the highest capillary bound water content (maximum 57.52%), but the movable water content is low, with an average of 20.52%.

Pore system evaluation

There is a certain positive correlation between T_2 time and shale pore size, and the full pore size distribution of rock samples can be characterized by nuclear magnetic resonance experiment (Chen et al., 2021). According to the method (Chen et al., 2021), the NMR relaxation rate of each sample can be obtained by comparing the full pore size distribution curve of shale with the T_2 spectrum, and then the T_{c1}, T_{c2}, and T_{c3} of all samples are converted to the corresponding pore sizes r_{c1}, r_{c2}, and r_{c3}, respectively (Table 3).

Under formation conditions, the space occupied by clay bound water cannot be filled by gas, so T_{c2} can be used as the minimum pore size limit for shale gas development. The lower limit of pore diameter of Middle shale and Lower shale is 10 nm, and the lower limit of pore

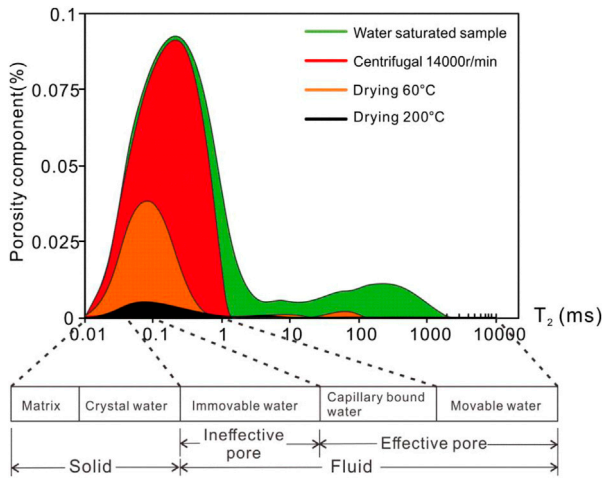

FIGURE 7
Pore fluid distribution characteristics and pore type classification of transitional shale.

diameter of Upper shale is 12.6 nm. According to the occurrence characteristics of fluid and the possible difficulty of mining, shale pores can be divided into movable pores, bound pores and immovable pores (Figure 7). The results show that the Middle shale and the Lower shale have high movable pores, and the proportion of pores can reach 27%, while that in the Upper shale is lower, which is 25%. In addition, the total content of movable pores and bound pores in the Lower shale is the highest, which is 78.61% (Table 3). It is suggested that the Lower and Middle shales may have more development potential under the associated development technology.

Conclusion

(1) Three sets of organic-rich transitional shale intervals (Lower shale, Middle shale and Upper shale) developed in Shan 2^3 Submember of Shanxi Formation. The average TOC content of the Middle shale and the Lower shale is 6.87% and 3.37% respectively, the average porosity is 2.34% and 2.04% respectively, and the average total gas content is 1.11 and 1.01 m^3/t respectively. The reservoir quality is better than that of the Upper shale. The average vitrinite reflectance results all belong to the dry gas generation stage.

(2) NMR experiments with high speed centrifugation and gradual temperature drying are effective methods to classify pore fluid types and determine the relative content of movable fluid and bound fluid. The Middle shale has the highest movable water content (32.58%) and the lowest capillary bound water content (39.96%). The Lower shale has the highest capillary bound water content, up to 57.52%.

(3) Based on the flow capacity of pore fluid, shale pores are divided into movable pores, bound pores and immovable pores, so as to realize the systematic evaluation of the pores of sea land transitional shale in the study area. The results show that the Middle shale and the Lower shale have high movable pores, and the proportion of pores can reach 27%. In addition, the total content of movable pores and bound pores in the Lower shale is the highest, which is 78.61%. The movable pores in the Upper shale is lower, which is 25%. It is suggested that the Lower and Middle shales may have more development potential under the associated development technology.

Data availability statement

The raw data supporting the conclusion of this article will be made available by the authors, without undue reservation.

Author contributions

GC contributed as the major author of the article. XX, XL, and XS conceived the project. JN, YG, FO, and YF collected the samples. YJ analyzed the samples. All authors contributed to the article and approved the submitted version.

Funding

This study was funded by the Science and Technology Cooperation Project of the CNPC-SWPU Innovation Alliance (Grant No. 2020CX030101).

Conflict of interest

Authors XX, XL, and XS were employed by PetroChina Coalbed Methane Company. Authors JN and FO were employed by PetroChina Southwest Oil and Gas field Company.

The remaining authors declare that the research was conducted in the absence of any commercial or financial relationships that could be construed as a potential conflict of interest.

Publisher's note

All claims expressed in this article are solely those of the authors and do not necessarily represent those of their affiliated organizations, or those of the publisher, the editors and the reviewers. Any product that may be evaluated in this article, or claim that may be made by its manufacturer, is not guaranteed or endorsed by the publisher.

References

Chen, D., Zhang, J., Wang, X., Lan, B., Li, Z., and Liu, T. (2018). Characteristics of lacustrine shale reservoir and its effect on methane adsorption capacity in fuxin basin. *Energy & Fuels* 32 (11), 11105–11117. doi:10.1021/acs.energyfuels.8b01683

Chen, H., Li, J., Zhang, C., Cheng, L., and Cheng, L. (2011). Discussion of sedimentary environment and its geological enlightenment of Shanxi Formation in Ordos Basin. *Acta Petrol. Sin.* 27 (8), 2213–2229.

Chen, Y., Jiang, C., Leung, J. Y., Wojtanowicz, A. K., and Zhang, D. (2021). Multiscale characterization of shale pore-fracture system: Geological controls on gas transport and pore size classification in shale reservoirs. *J. Petroleum Sci. Eng.* 202, 108442. doi:10.1016/j.petrol.2021.108442

Dong, D., Qiu, Z., Zhang, L., Li, S., Zhang, Q., Li, X., et al. (2021). Progress on sedimentology of transitional facies shales and new discoveries of shale gas. *Acta Sedimentol. Sin.* 39 (1), 28–44. doi:10.14027/j.issn.1000-0550.2021.002

Fan, C., Li, H., Qin, Q., He, S., and Zhong, C. (2020). Geological conditions and exploration potential of shale gas reservoir in Wufeng and Longmaxi Formation of southeastern Sichuan Basin, China. *J. Petroleum Sci. Eng.* 191, 107138. doi:10.1016/j.petrol.2020.107138

Fan, C., Xie, H., Li, H., Zhao, S., Shi, X., Liu, J., et al. (2022). Complicated fault characterization and its influence on shale gas preservation in the southern margin of the Sichuan Basin, China. *Lithosphere* 2022, 8035106. doi:10.2113/2022/8035106

Ghosh, K. K., Das, K., Bhattacharyya, S., and Ramteke, C. P. (2022). Characterization of shale gas reservoir of lower gondwana litho-assemblage at mohuda sub-basin, jharia coalfield, Jharkhand, India. *J. Nat. Gas Sci. Eng.* 97, 104316. doi:10.1016/j.jngse.2021.104316

Gu, Y., Li, X., Qi, L., Li, S., Jiang, Y., Fu, Y., et al. (2022). Sedimentology and geochemistry of the lower permian Shanxi Formation Shan 2^3 submember transitional shale, eastern Ordos Basin, north China. *Front. Earth Sci.* 10, 859845. doi:10.3389/feart.2022.859845

Han, H., Dai, J., Guo, C., Zhong, N., Pang, P., Ding, Z., et al. (2021). Pore characteristics and factors controlling lacustrine shales from the upper cretaceous qingshankou formation of the songliao basin, Northeast China: A study combining SEM, low-temperature gas adsorption and MICP experiments. *Acta Geol. Sin. Engl. Ed.* 95 (2), 585–601. doi:10.1111/1755-6724.14419

Jia, A., Hu, D., He, S., Guo, X., Hou, Y., Wang, T., et al. (2020). Variations of pore structure in organic-rich shales with different lithofacies from the jiangdong Block, fuling shale gas field, SW China: Insights into gas storage and pore evolution. *Energy & Fuels* 34, 12457–12475. doi:10.1021/acs.energyfuels.0c02529

Kuang, L., Dong, D., He, W., Wen, S., Sun, S., Li, S., et al. (2020). Geological characteristics and development potential of transitional shale gas in the east margin of the Ordos Basin, NW China. *Petroleum Explor. Dev.* 47 (3), 471–482. doi:10.1016/S1876-3804(20)60066-0

Li, H. (2022). Research progress on evaluation methods and factors influencing shale brittleness: A review. *Energy Rep.* 8, 4344–4358. doi:10.1016/j.egyr.2022.03.120

Li, J., Chen, Z., Li, X., Wang, X., Wu, K., Feng, D., et al. (2018). A quantitative research of water distribution characteristics inside shale and clay nanopores. *Sci. Sin. Tech.* 48, 1219–1233. doi:10.1360/N092017-00137

Li, J., Li, H., Yang, C., Wu, Y., Gao, Z., and Jiang, S. (2022). Geological characteristics and controlling factors of deep shale gas enrichment of the Wufeng-Longmaxi Formation in the southern Sichuan Basin, China. *Lithosphere* 2022 (Special 12), 4737801. doi:10.2113/2022/4737801

Li, Y., Yang, J., Pan, Z., Meng, S., Wang, K., and Niu, X. (2019). Unconventional natural gas accumulations in stacked deposits: A discussion of upper paleozoic coal-bearing strata in the east margin of the Ordos Basin, China. *Acta Geol. Sin. Engl. Ed.* 93 (1), 111–129. doi:10.1111/1755-6724.13767

Liang, Q., Tian, J., Zhang, X., Sun, X., and Yang, C. (2020). Elemental geochemical characteristics of lower—middle permian mudstones in taikang uplift, southern north China basin: Implications for the four-paleo conditions. *Geosciences J.* 24 (1), 17–33. doi:10.1007/s12303-019-0008-9

Liang, Q., Zhang, X., Tian, J., Sun, X., and Chang, H. (2018). Geological and geochemical characteristics of marine-continental transitional shale from the lower permian taiyuan formation, taikang uplift, southern north China basin. *Mar. Petroleum Geol.* 98, 229–242. doi:10.1016/j.marpetgeo.2018.08.027

Liu, S., Wu, C., Li, T., and Wang, H. (2018). Multiple geochemical proxies controlling the organic matter accumulation of the marine-continental transitional shale: A case study of the upper permian longtan formation, Western guizhou, China. *J. Nat. Gas Sci. Eng.* 56, 152–165. doi:10.1016/j.jngse.2018.06.007

Luo, W., Hou, M., Liu, X., Huang, S., Chao, H., Zhang, R., et al. (2018). Geological and geochemical characteristics of marine-continental transitional shale from the Upper Permian Longtan formation, Northwestern Guizhou, China. *Mar. Petroleum Geol.* 89, 58–67. doi:10.1016/j.marpetgeo.2017.06.029

Qiu, Z., Song, D., Zhang, L., Zhang, Q., Zhao, Q., Wang, Y., et al. (2021). The geochemical and pore characteristics of a typical marine–continental transitional gas shale: A case study of the permian Shanxi Formation on the eastern margin of the Ordos Basin. *Energy Rep.* 7, 3726–3736. doi:10.1016/j.egyr.2021.06.056

Ross, D. J. K., and Marc Bustin, R. (2009). The importance of shale composition and pore structure upon gas storage potential of shale gas reservoirs. *Mar. Petroleum Geol.* 26, 916–927. doi:10.1016/j.marpetgeo.2008.06.004

Testamanti, M. N., and Rezaee, R. (2017). Determination of NMR T2 cut-off for clay bound water in shales: A case study of carynginia formation, perth basin, western Australia. *J. Petroleum Sci. Eng.* 149, 497–503. doi:10.1016/j.petrol.2016.10.066

Wang, Z., Guo, B., Jiang, C., Qi, L., Jiang, Y., Gu, Y., et al. (2022). Nanoscale pore characteristics of the lower permian Shanxi Formation transitional facies shale, eastern Ordos Basin, north China. *Front. Earth Sci.* 10, 842955. doi:10.3389/feart.2022.842955

Wu, J., Wang, H., Shi, Z., Wang, Q., Zhao, Q., Dong, D., et al. (2021). Favorable lithofacies types and Genesis of marine-continental transitional black shale: A case study of permian Shanxi Formation in the eastern margin of Ordos Basin, NW China. *Petroleum Explor. Dev.* 48 (6), 1315–1328. doi:10.1016/S1876-3804(21)60289-6

Xi, Z., Tang, S., Wang, J., Yang, G., and Li, L. (2018200). Formation and development of pore structure in marine-continental transitional shale from northern China across a maturation gradient: Insights from gas adsorption and mercury intrusion. *Int. J. Coal Geol.* 200, 87–102. doi:10.1016/j.coal.2018.10.005

Xi, Z., Tang, S., Zhang, S., Lash, G. G., and Ye, Y. (2022). Controls of marine shale gas accumulation in the eastern periphery of the Sichuan Basin, South China. *Int. J. Coal Geol.* 251, 103939. doi:10.1016/j.coal.2022.103939

Xi, Z., Tang, S., Zhang, S., and Sun, K. (2017). Pore structure characteristics of marine–continental transitional shale: A case study in the qinshui basin, China. *Energy & Fuels* 31, 7854–7866. doi:10.1021/acs.energyfuels.7b00911

Yang, C., Zhang, J., Tang, X., Ding, J., Zhao, Q., Dang, W., et al. (2017). Comparative study on micro-pore structure of marine, terrestrial, and transitional shales in key areas, China. *Int. J. Coal Geol.* 171, 76–92. doi:10.1016/j.coal.2016.12.001

Yu, K., Gan, Y., Ju, Y., and Shao, C. (2020). Influence of sedimentary environment on the brittleness of coal-bearing shale: Evidence from geochemistry and micropetrology. *J. Petroleum Sci. Eng.* 185, 106603. doi:10.1016/j.petrol.2019.106603

Zhang, J., Li, X., Zhang, X., Zhang, M., Cong, G., Zhang, G., et al. (2018). Geochemical and geological characterization of marine-continental transitional shales from Longtan Formation in Yangtze area, South China. *Mar. Petroleum Geol.* 96, 1–15. doi:10.1016/j.marpetgeo.2018.05.020

Zhang, K., Jiang, S., Zhao, R., Wang, P., Jia, C., and Song, Y. (2022c). Connectivity of organic matter pores in the Lower Silurian Longmaxi Formation shale, Sichuan Basin, Southern China: Analyses from helium ion microscope and focused ion beam scanning electron microscope. *Geol. J.* 57, 1912–1924. doi:10.1002/gj.4387

Zhang, K., Jiang, Z., Song, Y., Jia, C., Yuan, X., Wang, X., et al. (2022a). Quantitative characterization for pore connectivity, pore wettability, and shale oil mobility of terrestrial shale with different lithofacies-A case study of the Jurassic Lianggaoshan Formation in the Southeast Sichuan Basin of the Upper Yangtze Region in Southern China. *Front. Earth Sci.* 10, 864189. doi:10.3389/feart.2022.864189

Zhang, K., Song, Y., Jia, C., Jiang, Z., Han, F., Wang, P., et al. (2022b). Formation mechanism of the sealing capacity of the roof and floor strata of marine organic-rich shale and shale itself, and its influence on the characteristics of shale gas and organic matter pore development. *Mar. Petroleum Geol.* 140, 105647. doi:10.1016/j.marpetgeo.2022.105647

Zhang, L., Dong, D., Qiu, Z., Wu, C., Zhang, Q., Wang, Y., et al. (2021). Sedimentology and geochemistry of Carboniferous-Permian marine-continental transitional shales in the eastern Ordos Basin, North China. *Palaeogeogr. Palaeoclimatol. Palaeoecol.* 571 (1-3), 110389. doi:10.1016/j.palaeo.2021.110389

frontiers | Frontiers in Earth Science

TYPE Original Research
PUBLISHED 16 January 2023
DOI 10.3389/feart.2022.1046489

OPEN ACCESS

EDITED BY
Hu Li,
Southwest Petroleum University, China

REVIEWED BY
Jingzhe Guo,
Northwest University, China
Delu Li,
Xi'an University of Science and Technology, China

*CORRESPONDENCE
Xiangliang Qiu,
1037548722@qq.com
Chengqian Tan,
1098364810@qq.com

SPECIALTY SECTION
This article was submitted to Structural Geology and Tectonics, a section of the journal Frontiers in Earth Science

RECEIVED 16 September 2022
ACCEPTED 24 October 2022
PUBLISHED 16 January 2023

CITATION
Qiu X, Ding L, Liu J, Yan Z, Bao Y and Tan C (2023), Quantitative evaluation of reservoir quality of tight oil sandstones in chang 7 member of Ordos Basin. *Front. Earth Sci.* 10:1046489. doi: 10.3389/feart.2022.1046489

Quantitative evaluation of reservoir quality of tight oil sandstones in chang 7 member of Ordos Basin

Xiangliang Qiu[1]*, Li Ding[2], Junkai Liu[3], Zhandong Yan[4], Yanxin Bao[4] and Chengqian Tan[5]*

[1]Xi'an Shiyou University, School of Petroleum Engineering, Xi'an, China, [2]PetroChina Changqing Oilfield Shale Oil Development Branch, Qingyang, China, [3]The Fifth Oil Production Plant of Petrochina Changqing Oil Field Company, Xi'an, China, [4]The Seventh Oil Production Plant of PetroChina Changqing Oilfield Company, Qingyang, China, [5]Xi'an Shiyou University, School of Earth Science and Engineering, Xi'an, China

In order to establish a quantitative evaluation system for reservoir quality suitable for tight oil sandstones, in this study, taking the Chang 7 Member in the Maling area of the Ordos Basin as an example, the nuclear magnetic resonance, clay mineral analysis, high pressure mercury injection analysis and logging interpretation technology have been used to carry out a comprehensive evaluation of the pore structures, sand body structures and oil-bearing properties of tight oil sandstone reservoirs. The results show that the pseudo-capillary pressure curves transformed by the NMR T_2 spectra are consistent with the capillary pressure curves measured by the core experiments. This method can be used for accurate characterization of the pore structures of the reservoir. The pore structure parameters calculated based on the pseudo-capillary pressure curves can accurately reflect the pore structures of the reservoirs such as micropores-thin throats and complex tortuosity. At the same time, the smoothness feature of conventional logging curves is used to evaluate the sand body structures and heterogeneity of the reservoir, and the apparent energy storage coefficient is introduced to quantitatively evaluate the oil-bearing properties of tight oil reservoirs. The evaluation results are in good agreement with the actual production situation. The larger the apparent energy storage coefficient, the higher the initial output of the oil wells. The evaluation results of the reservoir quality of the tight oil sandstones constructed in this paper are highly consistent with the production status, so the method has broad application prospects.

KEYWORDS

tight oil sandstone, reservoir quality, nuclear magnetic resonance, pore structure, oil-bearing properties

1 Introduction

At present, tight oil, which enjoys the reputation of "black gold" in the world oil industry, has become a new bright spot in the exploration and development of unconventional oil and gas. The United States and Canada have made breakthroughs in the key technical fields of tight oil development (Yao et al., 2013; Han et al., 2019; Li Y. et al., 2021; Lai et al., 2022a). China has abundant tight oil resources, which are mainly distributed in the Bohai Bay Basin, the Ordos Basin and the Sichuan Basin. Considerable geological reserves of tight oil resources represent that tight oil has broad development prospects. In recent years, many scholars around the world have achieved a lot of results in tight oil exploration and development. For example, Yang et al., (Zhang et al., 2018) redefined it according to the actual situation of different tight oil reservoirs; Zou et al. and Fu et al.(Jia et al., 2016; Jia et al., 2016; Yang et al., 2019) conducted a systematic study on the accumulation type, development characteristics and formation mechanism of tight oil in China; Zou et al. (2013), Li et al. (2019), Li et al. (2022) conducted an in-depth analysis of the accumulation conditions of tight oil, and determined the main controlling factors of hydrocarbon accumulations. In the evaluation of reservoir quality of tight oil sandstones, the difficulties in logging interpretation are mainly reflected in the following two aspects: (1) The geological and petrophysical characteristics of tight oil reservoirs are complex, but the resolution ability of conventional logging series is low and the amount of information is insufficient. Therefore, it is urgent to carry out new logging techniques, new method tests and optimization of logging parameter series; (2) The current logging evaluation of tight oil sandstone reservoirs basically follows the idea of low permeability reservoirs, and its adaptability is obviously insufficient. Therefore, the logging evaluation contents, methods and standards of reservoir quality need to be evaluated (Yao et al., 2013; Zou et al., 2013; Neves et al., 2019; Hassane et al., 2021; Zhang et al., 2020).

Generally, the pore structure of reservoir rocks is the main factor affecting the storage capacity of reservoir fluids (oil, gas, water) and the efficiency of oil and gas recovery (Jia et al., 2016; Iferobia et al., 2019; Yang et al., 2019; Zhu et al., 2019; Li J. et al., 2022). The pore structures of the Chang 7 reservoir in the Ordos Basin is characterized by fine pore throats, complex tortuosity, high capillary pressure, and complex rock and mineral components. The reservoir

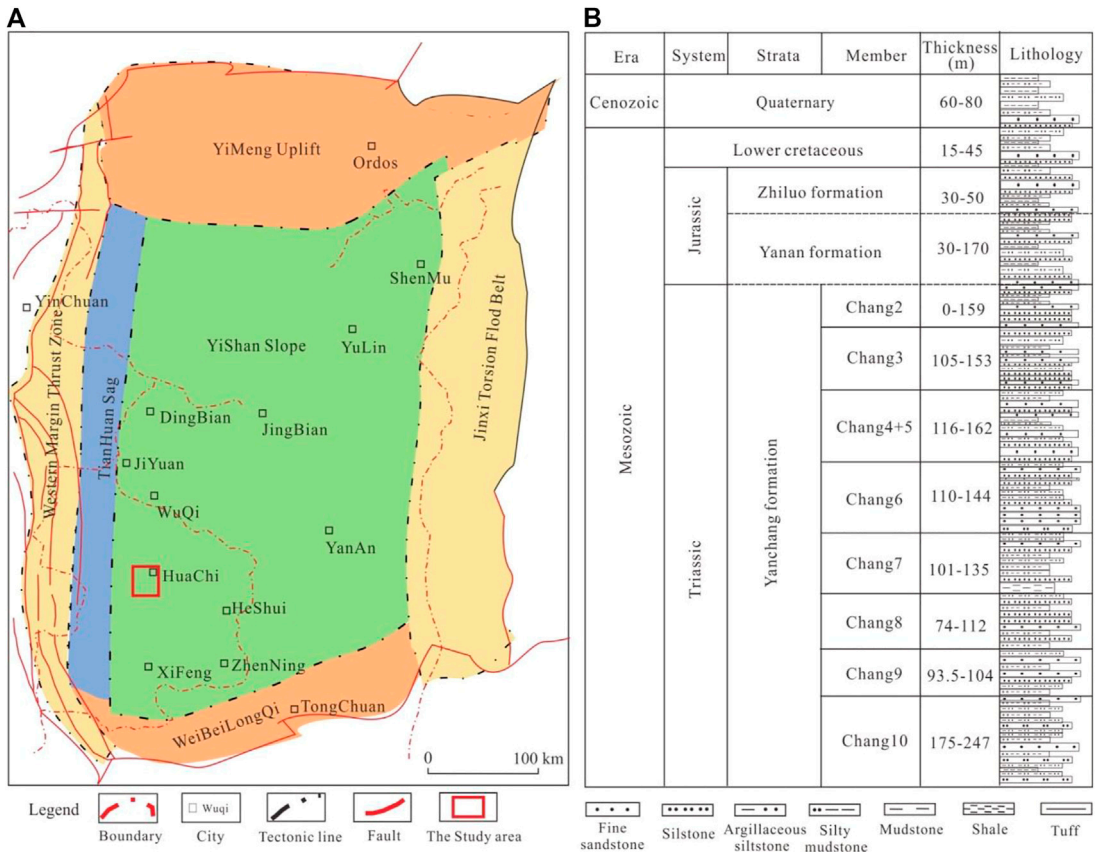

FIGURE 1
Location of study area **(A)** and division of stratigraphic units of Yanchang Formation **(B)**.

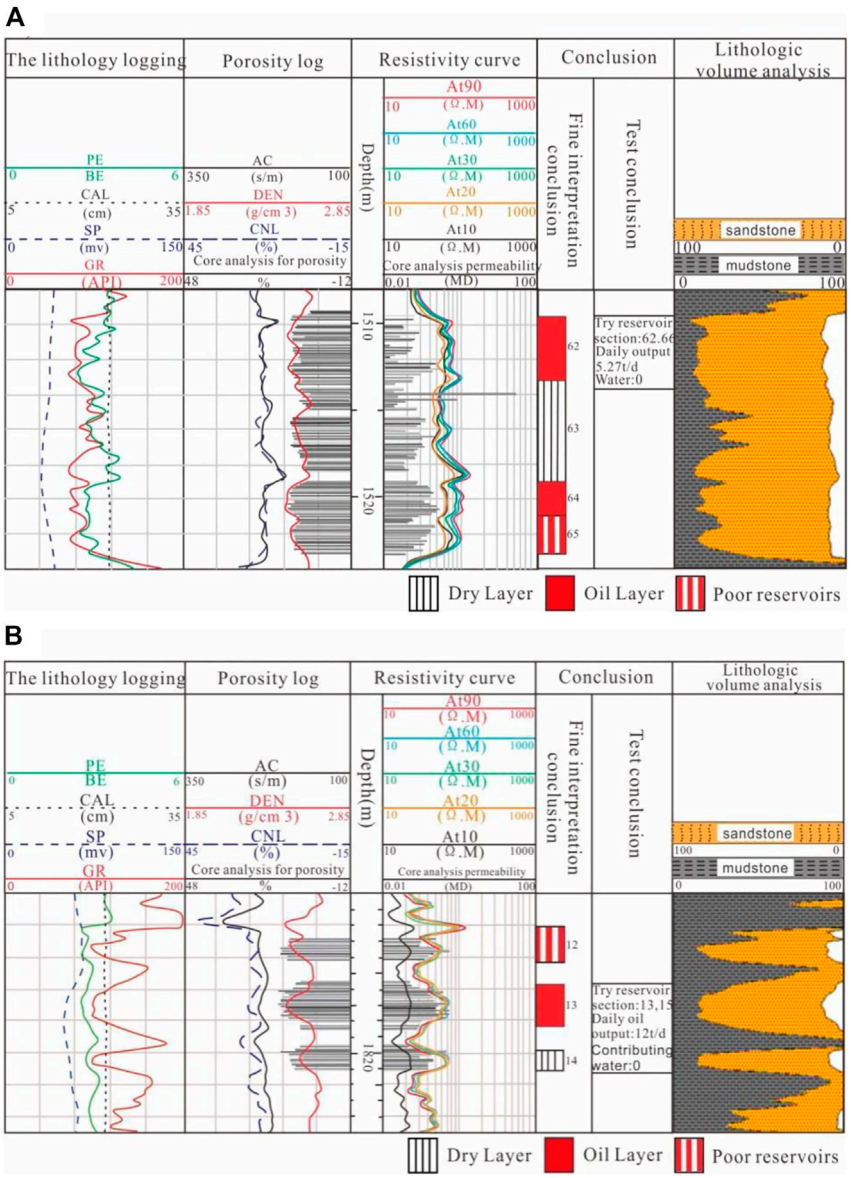

FIGURE 2
(A) Blocky sand body structure and its logging curve characteristics; **(B)** Interbedded sand body structure and its logging curve characteristics.

space is mainly secondary dissolved pores. Rock composition, pore type, pore size, fracture development and the matching relationship between these parameters are important factors for whether a tight oil reservoir can become an effective reservoir. How to define the main controlling factors of reservoir quality on the basis of petrophysical research is an important content of logging evaluation of tight sandstone reservoirs (Zhang et al., 2018; Li et al., 2019; Fan et al., 2022; Li H. et al., 2022; Li, 2022; Lu et al., 2022). Therefore, in this paper, the evaluation of rock composition and pore structures is selected as the core of reservoir quality evaluation. This research is of great significance for the rational and efficient development of tight oil sandstone reservoirs.

2 Geological background

The Maling area of the Ordos Basin is located in the northwest of the Qingcheng area. Its tectonic structure is located in the east of the Tianhuan Depression and the west of the Yishan Slope (Figure 1). Multiple sets of

source-reservoir-caprock assemblages developed in the Upper Triassic Yanchang Formation. According to the sedimentary cycle, the Yanchang Formation is divided into 10 oil layers from the Chang 10 to Chang 1 Members from bottom to top. The sedimentary evolution of the Yanchang Formation has experienced the whole process of formation, development, prosperity, decline and extinction. It belongs to a complete set of continental fluvial-delta-lake sedimentary system. Among them, during the depositional period of the Chang 7 Member, the basin entered the maximum lake flooding period, which was also the peak period of lake thermal fluid activity. The prosperity of lake algae and plankton laid the material foundation for the deposition of organic-rich shale. At this time, semi-deep lake-deep lake facies thick dark mudstone and black shale (Zhangjiatan shale) developed in the basin. The average porosity of shale reservoirs is 7.8%, and the average permeability is 0.08×10^{-3} μm^2. The Chang 7 Member of the basin is subdivided into three sub-members, that is, the Chang 7_1, Chang 7_2 and Chang 7_3 sub-members, from top to bottom. The object of this study is the tight sandstone reservoirs of the Chang 7_1 and Chang 7_2 sub-members in the upper Chang 7 Member of the Maling area, the gravity flow sand bodies are relatively developed interbeded with the source rocks. The near-source high-pressure charging of oil and gas makes the gravity flow sandstone thin interlayers have high oil saturation (Jia et al., 2016; Zhang et al., 2018; Yang et al., 2019). Such sand bodies are the main targets for large-scale exploration and development of tight oil.

Organic laminae are developed in the black shale of the Chang 7 Member in the Ordos Basin, and their total organic carbon (TOC) content ranges from 6.0% to 26.0%, with an average of 13.8%. The TOC content of dark mudstone ranges from 2.0% to 6.0%, with an average of 3.75%. In addition, the silty mudstone and siltstone associated with black shale and dark mudstone also have certain hydrocarbon generation and expulsion capabilities. Their TOC content is 0.5%–2.8%. According to the evaluation standard of source rocks, medium-good source rocks are well developed in the Chang 7 Member. Overall, the Chang 7 organic-rich shale series has good hydrocarbon-generating capacities.

3 Material and methods

In this study, samples from 15 wells (with an average burial depth of 2082 m) were selected for experimental research. The experimental items include clay mineral X-diffraction, high-pressure mercury intrusion and nuclear magnetic resonance experiments. Among them, the X-ray diffraction analysis and detection of clay minerals is based on "X-diffraction Analysis Method of Clay Minerals and Common Non-clay Minerals in Sedimentary Rocks" SY/T5163-2010, and the experimental instrument is X-ray diffraction analyzer Ultima IV. The high-pressure mercury intrusion experiment adopts the standard of "Determination of Rock Capillary Pressure Curve" SY/T5346-2005, and the experimental instrument is an AutoPore IV9505 mercury intrusion instrument. The experimental temperature was 22 °C and the humidity was 0%. The experimental instrument used for nuclear magnetic resonance is a core nuclear magnetic analyzer, the instrument number is Micro-MR02, and the experimental environment is 25°C and 97.6 KPa.

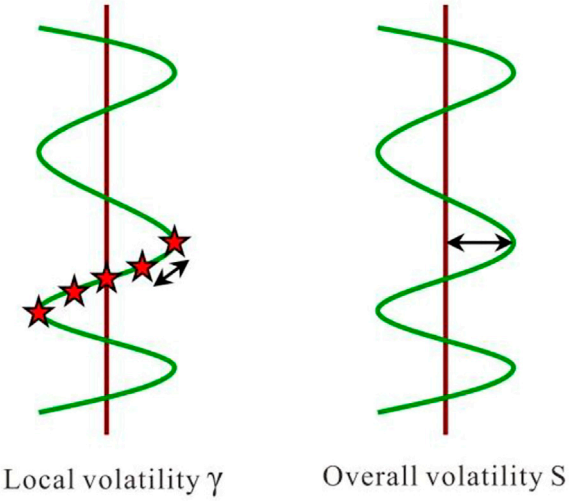

FIGURE 3
Schematic diagram of logging curve fluctuation.

3.1 Experimental principles and methods

1) X-ray diffraction of clay minerals

X-rays are light waves with very short wavelengths and have strong penetrating power. When X-rays are injected into the lattice of clay minerals, diffraction will occur. Different clay minerals and lattices have different structures and will produce different diffraction patterns. The X-ray diffraction analysis of clay minerals is based on the fact that different clay minerals have different crystal structures, and utilizes the layered structure of clay minerals and the principle of X-ray diffraction (Nikolaev et al., 2019; Si et al., 2020; Li Z. P. et al., 2021). From the diffraction peaks, the interplanar spacing is calculated, and then different mineral types are judged.

2) High pressure mercury intrusion experiments

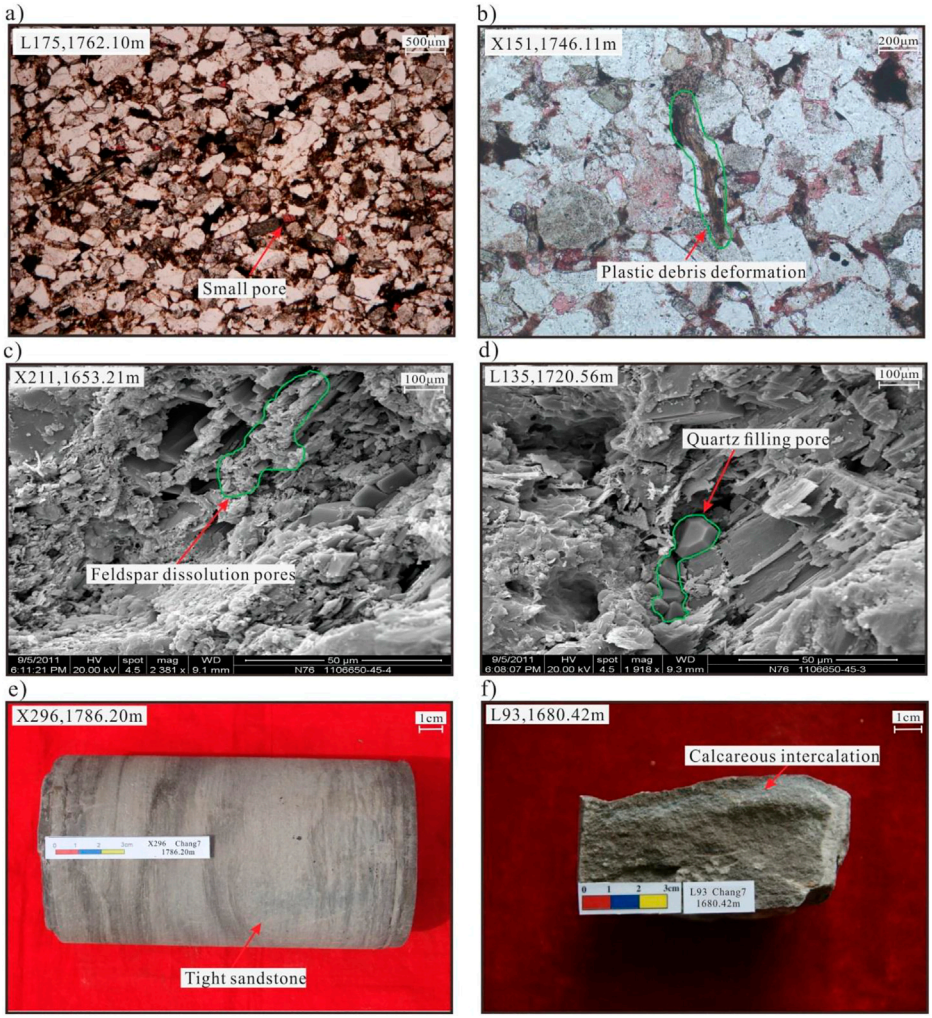

FIGURE 4
Microscopic pore structure characteristics of typical well cores. **(A)** Well L175, 1762.10 m; **(B)** Well X151, 1746.11 m; **(C)** Well 211, 1653.21 m; **(D)** Well L135, 1720.56 m; **(E)** Well X296, 1786.20 m; **(F)** Well L93, 1680.42 m.

An AutoPore IV 9505 mercury porosimeter was used to perform high pressure mercury porosimetry. Under a given pressure, the mercury at room temperature is pressed into the pores of the rock sample, and the contact surface between the capillary and the mercury will generate a capillary force in the opposite direction to the external pressure, thereby preventing the mercury from entering the capillary. When the pressure increases above the capillary force, the mercury will continue to penetrate the pores (Li C. L. et al., 2015; Pecanha et al., 2019). Therefore, a pressure value applied from the outside can be used to measure the size of the corresponding pores. The mercury injection process is a dynamic equilibrium process. The injection pressure is approximately equal to the capillary pressure, and the corresponding capillary radius is the pore throat radius. The volume of mercury entering the pores is the volume of the pores connected by the throats. By continuously changing the mercury injection pressure, a complete capillary pressure curve can be obtained. When the mercury injection pressure increases from P_1 to P_2, the corresponding pore size decreases from r1 to r2, and the mercury injection amount at this stage is the corresponding pore volume between the two pore sizes. When the mercury injection pressure increases continuously, the mercury injection amount of different pore size can be measured.

3) NMR experiments

NMR analysis is based on the principle of the magnetism of the hydrogen nucleus itself and its interaction with an external magnetic field. Furthermore, the NMR relaxation signal

TABLE 1 Pore types and pore structure parameters of reservoirs in the Chang 7 Member in the study area.

Member		Chang 71	Chang 72	Total
Pore combination (%)	Intergranular pores	0.51	0.52	0.52
	Feldspar dissolved pores	0.82	0.88	0.85
	Intergranular dissolved pores	0.07	0.11	0.09
	Detrital dissolved pores	0.11	0.19	0.15
	Microcracks	0.06	0.04	0.05
	Surface porosity	1.56	1.74	1.66
Pore structure parameters	Displacement pressure (MPa)	3.52	3.29	3.41
	Median radius (μm)	0.067	0.055	0.060
	Sorting factor	1.13	1.17	1.15
	Coefficient of variation	1.94	4.45	3.29
	Mercury removal efficiency (%)	24.9	23.8	24.4

intensities and relaxation rates in the pore fluids of the rock samples were measured and the T_2 spectra were constructed (Wu et al., 2015; Sun et al., 2015; Zhou et al., 2016). This technique is used to study the pore structures and fluid distribution inside the rock. The strength of the NMR signal depends on the total amount of pore fluids in the sample, and it reflects the porosity of saturated rock samples. However, the length of the T_2 relaxation time mainly depends on the force of the rock surface on the pore fluids. The larger the force, the shorter the T_2 relaxation time, and it reflects the relaxation characteristics of the fluids on the surface of the pores or in the pores. The smaller the force, the longer the T_2 relaxation time, and it reflects the relaxation characteristics of the fluids in the large pores. The difference in T2 relaxation time between movable water and irreducible water is used to detect the content and occurrence of irreducible and movable water in the rock samples.

A core NMR analyzer was used to carry out NMR experiments. The specific experimental steps and methods were as follows: (1) Drilling a standard core with a diameter of 25.4 mm from a full-diameter core; (2) The standard core after oil washing is then dried; (3) Measuring the gas permeability of the standard core; (4) After vacuuming, the core is saturated with simulated formation water; (5) Calculation of core porosity; (6) Nuclear magnetic resonance T_2 spectrum tests.

3.2 Well logging interpretation techniques

Sandy debris flow, turbidite and slump turbidite are developed in the Chang 7 reservoir in the study area. Therefore, the Chang 7 tight sandstones have strong heterogeneity. Complex sand body structures include massive sand bodies, sand-mud interbeds, and thin sand layers (mainly in oil shale). Based on a large number of field observations, it is found that there is a good correspondence between the sand body structure and heterogeneity of the Chang 7 Member and the logging curves (Figure 2). Therefore, conventional well logs are usually selected to characterize the sand body structure and heterogeneity of the reservoir.

The magnitudes of the logging curves can reflect changes in sediment characteristics such as sediment particle size, sorting and shale content. Moreover, the smoothness of the logs is also closely related to the energy of the depositional environment. The parameters extracted from the logging curves can quantitatively analyze the reservoir sedimentary characteristics and sand body structures.

The smoothness of the curves reflects the duration of sediment modification by the hydrodynamic environment, and can be represented by the root of variance variance G_S. In order to find N_{th} and G_S, the difference sequence a_2-a_1, a_3-a_2, ..., a_n-a_{n-1} must be constructed first. The number of difference series

TABLE 2 Statistical results of reservoir coefficient in the Chang 7 Member of the study area.

Area	Apparent Energy Storage Coefficient			Initial Production	
	Minimum	Maximum	Average	Daily Oil Production (t/d)	Water Content (%)
Northern	2.0	36.3	15.8	9.54	21.8
Central	3.2	30.1	12.9	7.68	34.2
Southern	3.1	25.8	12.4	6.54	31.0

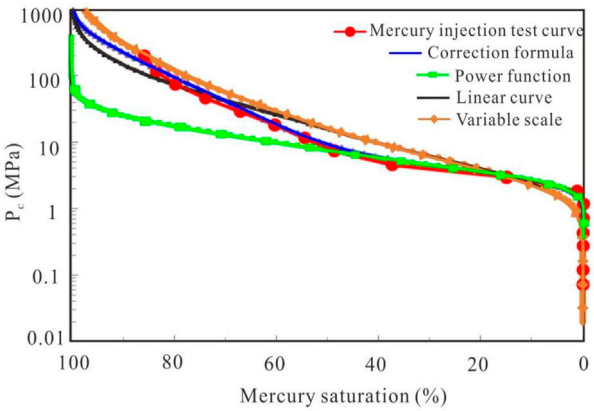

FIGURE 5
Comparison of capillary pressure curves converted by different methods.

L can reflect the number of sawtooth, and the variance S_2 can reflect the overall volatility of the data:

$$N_{th} = \frac{L}{h} \tag{1}$$

$$S^2 = \frac{1}{N}\sum_{i=1}^{n}(x_i + \bar{x})^2 \tag{2}$$

In order to reflect the size and number of sawtooth as a parameter, the variogram $\gamma(h)$ in geostatistics is introduced. It reflects the degree of change of regionalized variables within a certain distance in a certain direction, and can reflect the randomness and structure of regionalized variables. The calculation formula is as follows:

$$\gamma(h) = \frac{1}{2N(h)}\sum_{i=1}^{N(h)}(a_i - a_{i+h})^2 \tag{3}$$

In the formula, h is the separation distance between the two sample spaces; $N(h)$ is the number of data pairs (a_i, a_{i+h}) with an interval of h; a_i and a_{i+h} are the measured values of the regional variable a at spatial positions i and $i+h$, respectively [i=1,2,. . .,$N(h)$]. The variogram reflects the magnitude of the local volatility of the data.

Since the variogram reflects the local volatility of the data, and S_2 reflects the overall volatility of the data, they are combined to construct the variance root GS. In this way, it can comprehensively reflect the overall fluctuation size of the curve segment and the number and size of sawtooth, and then reflect the smoothness of the curve data. Its calculation formula is as follows:

$$GS = \sqrt{\gamma(1) + \gamma(2) + \cdots\gamma(h) + S^2} \tag{4}$$

For the logging curves, since their intervals are equal, in general, a value is measured every 0.125 m. Since the local volatility is to be reflected, the smaller h is, the better. In order to ensure the accuracy, h=1, 2. Then the above formula simplifies to:

$$GS = \sqrt{\gamma(1) + \gamma(2) + S^2} \tag{5}$$

Among them, the smaller the GS, the smoother the curve, the smaller the curve volatility, and the closer the sand body is to the block shape; on the contrary, the larger the GS, the less smooth the curve and the greater the volatility of the curve, the closer the sand body shape is to the interbedded sand-mud combination (Figure 3).

The tight oil reservoirs of the Chang 7 Member in the Ordos Basin are formed by the near-source supply. The more homogeneous the reservoir, the better the physical property, the higher the degree of oil and gas charging, the better the oil-bearing properties of the reservoir. The shape of the logging curves can reflect the deposition environment and the reservoir spot spots. The overall amplitude change index S reflects the change of mud content of reservoir and indirectly reflects the sand body structures. Moreover, the local variation function γ can reflect the heterogeneity of the reservoir. Combined application of S and γ can be used to identify the smoothness of the logging curves, furthermore, it is a comprehensive reflection of sand body structures and reservoir heterogeneity.

Through the analysis, it is found that the smoothness of the logging curves can well characterize the sand body structures. Therefore, the smoothness of the curve can be used to construct a comprehensive parameter that characterizes the sand body structure and the oil-bearing heterogeneity of the reservoir. Therefore, in this study, the curve smoothing function G_S was used to construct the logging characterization parameter P_{ss} of the sand body structures and the oil-bearing heterogeneity parameter P_{pa} of the reservoir. They are defined as follows:

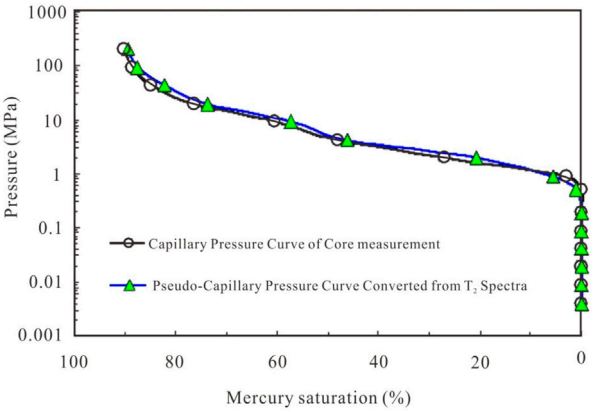

FIGURE 6
Comparison of pseudo-capillary pressure curves converted from NMR T_2 spectra.

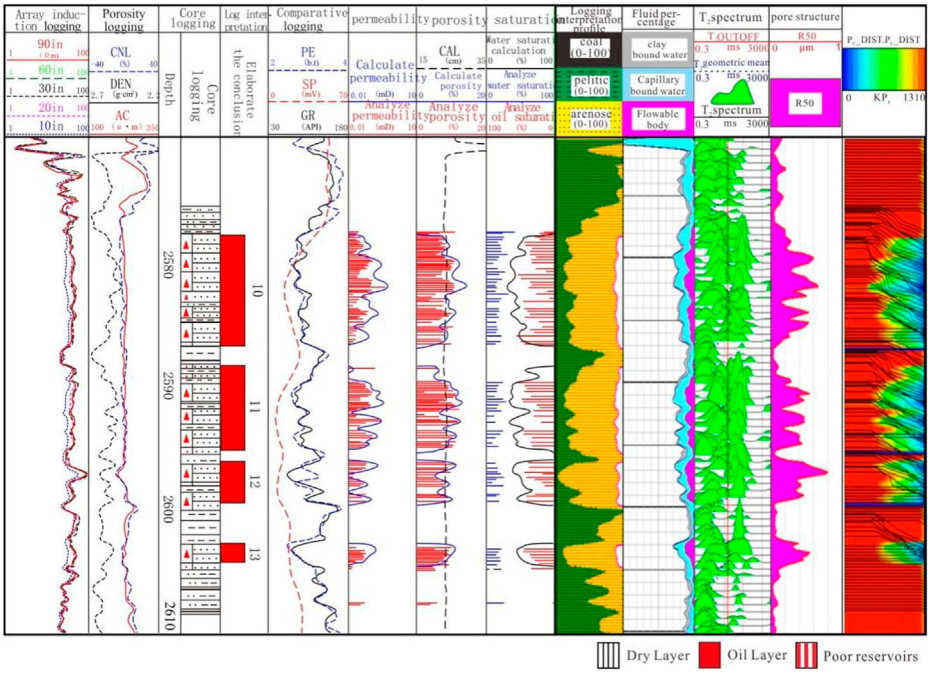

FIGURE 7
Interpretation results of pore structures from nuclear magnetic logging in the target layer of Well L38.

$$P_{ss} = GS(GR) \cdot V_{sh} \tag{6}$$

$$P_{pa} = \frac{\sum_{i=1}^{n} H_i \cdot \varnothing_i \cdot S_{oi}}{GS(DEN)} \tag{7}$$

3.3 NMR logging technology

At present, the use of nuclear magnetic resonance logging to characterize the internal structures of pores is a commonly used method. The distribution of the nuclear magnetic resonance T_2 spectrum can represent the pore size distribution. In the laboratory, mercury intrusion experiments are also often used to extract pore-throat parameters as well (Sun et al., 2015; Er et al., 2016). Previous studies have shown that the T_2 spectral distribution is similar to the pore size distribution curves obtained by mercury intrusion. Therefore, the T_2 distribution curves are converted into mercury intrusion curves, thereby realizing the quantitative characterization of the pore structures. The NMR logging instrument used in this paper is Schlumberger CMR type, and the integrated NMR logging data processing system (HERS1.5) is used for NMR data processing and analysis.

CMR is a Schlumberger stick-well nuclear magnetic resonance logging tool, which generally adopts dual-frequency measurement, one for the bound fluid signal and the other for the standard echo group signal. The data processing steps measured by CMR are as follows: data loading→echo generation→T_2 spectrum inversion and splicing→reservoir parameter calculation→oil, gas and water analysis→pore structure analysis. Among them, the first two steps belong to the data preprocessing module, and the last four steps are the inversion interpretation module.

4 Results

4.1 Reservoir pore structures

The tight oil reservoirs of the Chang 7 Member in the Maling area are mainly distributed in the Chang 7_1 and Chang 7_2 sub-members (Li et al., 2017; Guo et al., 2018). The reservoirs in the study area have poor physical properties. The porosity is mainly distributed in 6.0–10.0%, with an average porosity of 8.3%, and the permeability is concentrated in 0.05–0.20mD, with an average permeability of 0.13mD. It is a typical tight sandstone reservoir. The main pore type of the reservoirs is feldspar dissolved pores, while the primary pores are not developed. Obvious plastic cuttings deformation can be seen in the local sandstones (Figure 4A, Figure 4B); euhedral quartz crystals are observed to fill the remaining pore space in some intervals, resulting in a large reduction of reservoir pores (Figure 4C, Figure 4D).

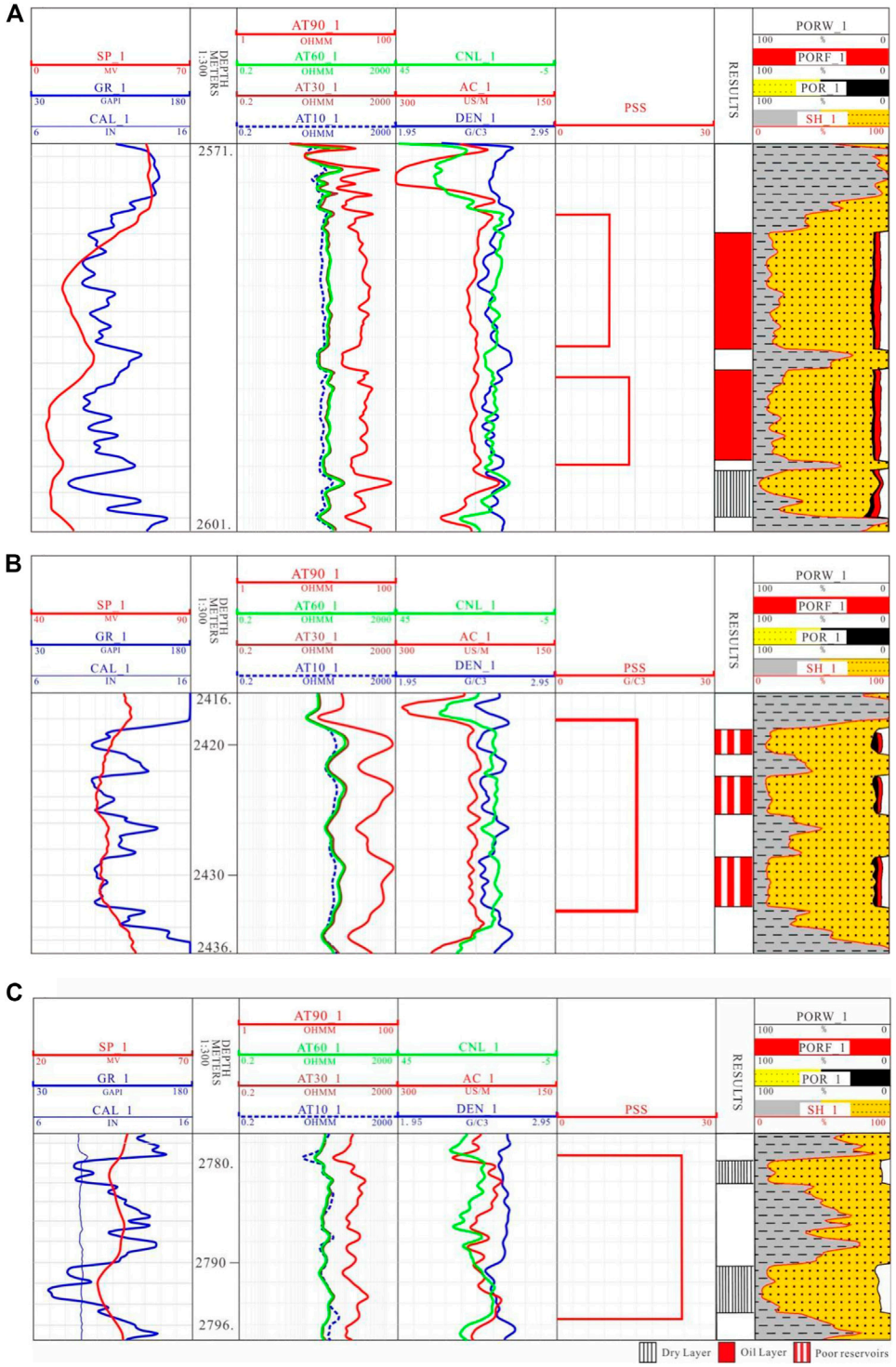

FIGURE 8
Evaluation of the classification of tight oil layers in typical wells in the study area. **(A)** Well L38; **(B)** Well B35; **(C)** Well L82.

The surface porosity of the Chang 7 Members is relatively low, with an average value of 1.66%. The pore throat radius in the target sandstones is small and the sorting is poor. The average median radius is 0.060 μm, and its pore structure belongs to the small-pore micro-throat type (as shown in Figure 4 and Table 1).

The NMR T_2 spectral distribution curves are similar to the pore size distribution curves of the mercury intrusion tests, both of which can reflect the microscopic pore structure characteristics of the reservoir. The Chang 7 reservoir in the study area has small pore throats, complex tortuosity, high capillary pressure, and the pore structures of the reservoir is very complex. The modified formula of the power function can convert the NMR T_2 spectrum into pseudo-capillary pressure curves. The capillary pressure reflects the nonlinear relationship between the pore throat radius distribution and the NMR T_2 spectrum. In this paper, the modified formula of the power function is used to convert the T_2 spectrum of the NMR experiment into the pseudo-capillary pressure curves, namely:

$$P_c = \frac{E}{T_2 D} \times \left(1 + \frac{A}{(B \times T_2 + 1)^c}\right) \tag{8}$$

where P_c is capillary pressure, MPa; E is echo interval, ms; D is self-diffusion coefficient, μm^2/ms; B is fluid free relaxation time, ms; A is pore surface area, cm^2; c is conversion coefficient; T_2 is volume (free) relaxation time of fluids, ms.

12 sandstone samples were collected from the Chang 7 tight oil reservoir in the study area, they are used to carried out the high-pressure mercury injection and nuclear magnetic resonance experiments. The pseudo-capillary pressure curves were transformed by the NMR T_2 spectrum and the high-pressure mercury injection test curves. It is found that the transformation curves of 10 samples are consistent with the test curves. The results show that the pseudo-capillary pressure curves transformed by NMR T_2 spectrum can be used to accurately characterize the pore structures of reservoir. For example, the S1 sample has a porosity of 7.9% and a permeability of 0.08 mD. Different methods of NMR conversion of pseudo-capillary pressure curves were used for conversion, and the results are shown in Figure 5. The linear transformation method uses the NMR T_2 spectrum data with linear scale values to carry out a reverse accumulation calculation, and then the NMR capillary pressure curves can be obtained. It can be seen from Figure 5 that the error of the linear transformation method is relatively large. The pseudo-capillary pressure in the core can be accurately measured by the power function calibration method (Eq. 9). However, for the tight sandstone reservoir with complex pore structures, the large pore part corresponds well, and the small pore part has a large error. The conversion results of the variable scale method (Eq. 10) is quite different from the measured capillary pressure mercury intrusion curves. In addition, the pseudo-capillary pressure curves transformed by the modified formula proposed in this study can well reflect the pore structure characteristics of the rock, and they are in good agreement with the experimental mercury intrusion curves.

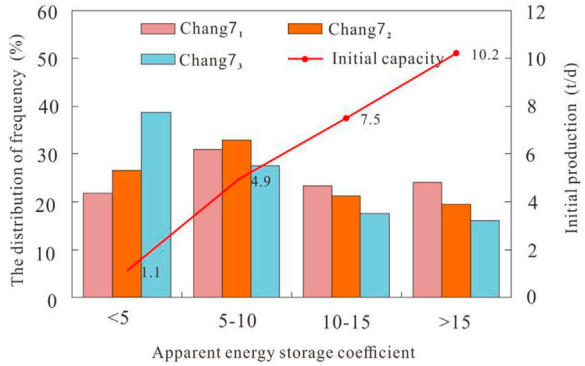

FIGURE 9
Relationship between apparent energy storage coefficient and initial production of the target layer.

$$P_c = a_1 \left(\frac{1}{T_2}\right)^{b_1} \tag{9}$$

$$P_C = \frac{1}{T_2} * \left(1 + \frac{A}{(B \times T_2 + 1)^c}\right) * \frac{D}{K} \tag{10}$$

where P_c is capillary pressure, MPa; a_1 and b_1 are reservoir pore conversion coefficient; K is permeability, mD; D is self-diffusion coefficient, μm^2/ms; B is fluid free relaxation time, ms; A is pore surface area, cm^2; c is conversion coefficient; T_2 is volume (free) relaxation time of fluids, ms.

In this paper, the oil-bearing effect correction of NMR logging is carried out based on petrophysical experiment calibration. NMR logs were used to invert capillary pressure curves, and the calculated pore parameters were reliable. It can be seen from Figure 6 that the pseudo-capillary pressure curves transformed from the nuclear magnetic resonance T_2 spectrum can well reflect the pore structure characteristics of the rock. Moreover, the constructed curves are in good agreement with the capillary pressure curves measured by the core experiments.

4.2 Evaluation of oil-bearing properties

The oil-bearing distribution of the reservoirs in the study area is uneven, and some tight sandstone reservoirs with strong calcareous cementation have poor oil-bearing properties (Li Z. et al., 2015; Xiang et al., 2015; Han et al., 2019). For tight sandstone reservoirs, due to the influence of reservoir lithology, the results of physical property and heterogeneity,

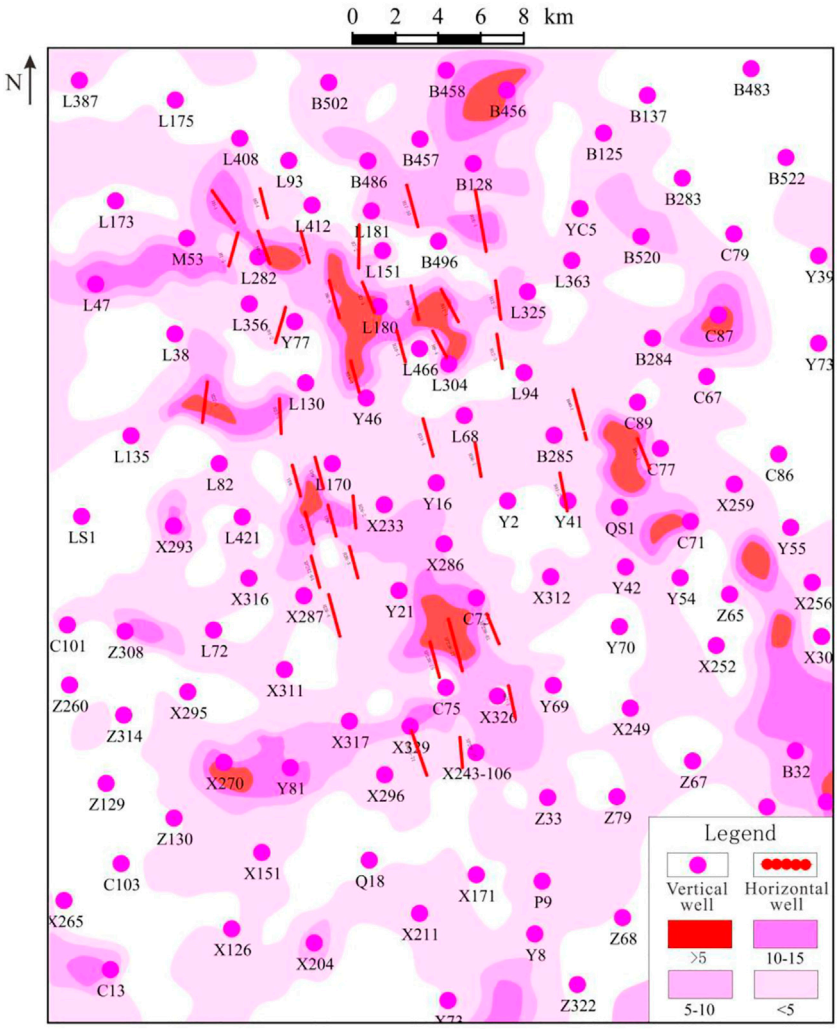

FIGURE 10
Distribution of apparent energy storage coefficient of Chang 7 Member in West 233 area.

oil saturation calculated by conventional logging cannot accurately characterize the reservoir oil bearing properties, and the lack of NMR logging data in the study area cannot reflect the plane distribution of oil. Therefore, the apparent energy storage coefficient Y is introduced in this paper to quantitatively characterize the oil bearing properties in the reservoir. The oil-bearing index R_I can eliminate the influence of reservoir lithology, physical properties, and formation water changes on resistivity, and highlight the oil-bearing characteristics. Therefore, this parameter can directly reflect the oil content of the reservoir instead of oil saturation. The reservoir porosity reflects the accommodating space of the reservoir fluid, and the product of it and the effective thickness of the reservoir reflects the macroscopic volume of the reservoir. Therefore, the apparent energy storage coefficient Y is constructed to comprehensively characterize the oil content of the reservoir, and the formula is as follows:

$$R_I = \frac{R_t \cdot \phi^m}{aR_W} \tag{11}$$

$$Y = H \times \phi \times R_I \tag{12}$$

In the formula, R_t is the formation resistivity, Ω·m; ϕ is the reservoir porosity, reflecting the fluid storage space of the reservoir, %; a is the lithology coefficient; m is the cementation index; R_w is the formation water resistivity, Ω·m; Y is the apparent energy storage coefficient; H is the effective thickness of the reservoir, and the product of it and the porosity reflects the macroscopic volume of the reservoir, m; RI is the apparent resistivity increase rate, which can reflect the oil content of the reservoir.

5 Case analysis

5.1 Evaluation of reservoir pore structures

Based on the calibration of petrophysical experiments, the modified formula of the power function is used to convert the T_2 spectra of the NMR experiments into pseudo-capillary pressure curves. Thus, quantitative evaluation parameters of reservoir pore structures (such as pore throat radius R_{50}) are calculated. These parameters are used to correct for oil effects. Figure 7 shows the interpretation results of the pore structures of the Chang 7_1 tight sandstones in the Well L38 based on NMR logging. As shown in Figure 7, the pore structure parameters calculated using the pseudo-capillary pressure curves are in good agreement with the experimental test data. The constructed curves can well reflect the small pore throats and complex tortuosity of the reservoirs in the study area.

5.2 Evaluation of oil-bearing properties of reservoirs

The oil content of reservoirs can be comprehensively evaluated by the paeameters P_{ss} and $P_{pa.}$ They are used to construct the logging characterization parameter of the sand body structures and the oil-bearing properties by the curve smoothing function G_S. The smaller the P_{ss} value, the weaker the reservoir heterogeneity, the larger the P_{pa} value, the smaller the reservoir heterogeneity, and the better the oil content. The method was used to evaluate the oil content of 25 wells in the study area with the oil tests and production data, and the evaluation results of 21 wells were consistent with the actual production situation. It is more reliable to evaluate the oil content of tight sandstone reservoir using the parameters P_{ss} and P_{pa}. Figure 8 shows an example of the calculation of the structural parameters of the sand bodies in Wells L38, B35 and L82. Among them, the first track is the natural potential and natural gamma curves; the second track is the resistivity curve; the third track is the acoustic wave time difference and density curves; the fourth track is the structural parameter results of the sand bodies calculated using the curve smoothness function; the fifth track is the oil test and interpretation results; the sixth track is the profile of sand and mudstone. The gamma logging curve in Well L38 has a slightly dentated medium-amplitude box shape, which represents a massive sand body with good homogeneity. The average value of P_{ss} is 11.5, while that of P_{pa} is 3.14, the oil heterogeneity of the reservoir is small, and the logging interpretation result is an oil layer. This set of sand body has good oil content, and its daily oil production during the oil testing is 20.9 t/d (Figure 8A). The natural gamma curve in Well B35 has a tooth bell-shaped and finger-shaped features, which represents the interbedded sand-mud structure and poor homogeneity. The reservoir has poor physical property and strong oil heterogeneity, the value of P_{ss} is 15.2, while that of P_{pa} is 1.43, and it can be interpreted as poor oil reservoir. This set of sand bodies has low oil saturation, and its daily oil production during oil testing is 6.46 t/d (Figure 8B). According to the calculated results of sand body structure parameters and oil-bearing parameters, the smoothness of Well L38 is obviously better than that of Well B35. According to the evaluation results of logging parameters and the actual production situation, the sand body structure and oil content of the reservoir in Well L38 are better than those in Well B35. Figure 8C shows the calculation results of the structural parameters of the sand bodies in Well L82. The reservoir sand bodies in Well L82 have poor quality and strong heterogeneity. The oil test results show that the sandstone reservoir in Well L82 contains no oil.

At the same time, according to the statistical analysis of the apparent energy storage coefficient in the study area and the initial production of oil wells, it is found that they have a good positive correlation. That is, the larger the apparent energy storage coefficient, the higher the initial production of the oil wells (Figure 9). Therefore, the apparent energy storage coefficient Y is used to comprehensively evaluate the oil and gas-bearing properties of the reservoir.

According to the planar distribution of the apparent energy storage coefficient of the Chang 7 reservoir in the Maling X233 area (Figure 10), the apparent energy storage coefficient in the central and northern parts of the study area is relatively large, and the value of the energy storage coefficient is mainly concentrated above 10, while that of the local areas can reach more than 15. Combined with the actual production statistics (Table 2), the larger the apparent energy storage coefficient, the higher the initial production capacity of the oil production well. For production wells with apparent energy storage coefficient greater than 15, the average initial daily oil production reached 10.2 t/d.

6 Conclusion

1) In this study, taking the Chang 7 Member in the Maling area of the Ordos Basin as an example, the nuclear magnetic resonance, clay mineral analysis, high pressure mercury injection analysis and logging interpretation technology have been used to carry out a comprehensive evaluation of the pore structures, sand body structures and oil-bearing properties of tight oil sandstone reservoirs.
2) The pseudo-capillary pressure curves transformed by the NMR T2 spectra are consistent with the capillary pressure curves measured by the core experiments. This method can be used for accurate characterization of the pore structures of the reservoir. The pore structure parameters calculated based on the pseudo-capillary pressure curves can accurately reflect the pore structures of the reservoirs such as micropores-thin throats and complex tortuosity.
3) The parameters Pss and Ppa constructed by the logging curve smoothness function GS were used to quantitatively characterize the sand body structures and oil-bearing heterogeneity of tight oil reservoir. And the apparent energy storage coefficient is introduced to quantitatively evaluate the oil-bearing properties of tight oil reservoirs. The evaluation results are in good agreement with the actual production situation. The larger

the apparent energy storage factor, the higher the initial production of the oil wells.

Data availability statement

The original contributions presented in the study are included in the article/supplementary material, further inquiries can be directed to the corresponding authors.

Author contributions

XQ and CT are responsible for the idea and writing of this paper and LD, JL, ZY and YB are responsible for the data interpretation.

Funding

This study was supported by the Project (2019–18315) of the PetroChina Changqing Oilfield Exploration and Development Research Institute and the Project (42072173) of the National Natural Science Foundation of China).

Conflict of interest

Author LD was employed by the PetroChina Changqing Oilfield Shale Oil Development Branch, author JL was employed by the Fifth Oil Production Plant of Petrochina Changqing Oil Field Company, and authors ZY and YB were employed by the Seventh Oil Production Plant of PetroChina Changqing Oilfield Company.

The remaining author declare that the research was conducted in the absence of any commercial or financial relationships that could be construed as a potential conflict of interest.

Publisher's note

All claims expressed in this article are solely those of the authors and do not necessarily represent those of their affiliated organizations, or those of the publisher, the editors and the reviewers. Any product that may be evaluated in this article, or claim that may be made by its manufacturer, is not guaranteed or endorsed by the publisher.

References

Er, C., Li, Y., Zhao, J., Wang, R., Bai, Z., and Han, Q. (2016). Pore formation and occurrence in the organic-rich shales of the triassic chang-7 member, Yanchang Formation, Ordos Basin, China. *J. Nat. Gas Geoscience* 1, 435–444. doi:10.1016/j.jnggs.2016.11.013

Fan, C. H., Xie, H. B., Li, H., Zhao, S. X., Shi, X. C., Liu, J. F., et al. (2022). Complicated fault characterization and its influence on shale gas preservation in the southern margin of the Sichuan Basin, China. *Lithosphere* 2022, 8035106. doi:10.2113/2022/8035106

Guo, H., He, R., Jia, W., Peng, P., Lei, Y., Luo, X., et al. (2018). Pore characteristics of lacustrine shale within the oil window in the upper triassic Yanchang Formation, southeastern Ordos Basin, China. *Mar. Petroleum Geol.* 91, 279–296. doi:10.1016/j.marpetgeo.2018.01.013

Han, H., Pang, P., Li, Z., Shi, P., Guo, C., Liu, Y., et al. (2019). Controls of organic and inorganic compositions on pore structure of lacustrine shales of Chang 7 member from Triassic Yan Chang Formation in the Ordos Basin, China. *Mar. Petroleum Geol.* 100, 270–284. doi:10.1016/j.marpetgeo.2018.10.038

Hassane, A., Ehirim, C. N., and Dagogo, T. (2021). Rock physics diagnostic of Eocene Sokor-1 reservoir in Termit subbasin, Niger. *J. Pet. Explor. Prod. Technol.* 11, 3361–3371. doi:10.1007/s13202-021-01259-2

Iferobia, C. C., and Ahmad, M. (2020). A review on the experimental techniques and applications in the geomechanical evaluation of shale gas reservoirs. *J. Nat. gas Sci. Eng.* 74, 103090. doi:10.1016/j.jngse.2019.103090

Jia, C., Zou, C., Li, J., Li, D., and Zheng, M. (2016). Evaluation criteria, major types, characteristics and resource prospects of tight oil in China. *Petroleum Res.* 1 (1), 1–9. doi:10.1016/S2096-2495(17)30026-1

Lai, J., Wang, G., Fan, Q., Pang, X., Li, H., Zhao, F., et al. (2022). Geophysical well-log evaluation in the era of unconventional hydrocarbon resources: A review on current status and prospects. *Surv. Geophys.* 43, 913–957. doi:10.1007/s10712-022-09705-4

Li, C. L., Li, C. X., Hou, Y., Shi, Y., Wang, C., Hu, F., et al. (2015b). Well logging evaluation of triassic Chang 7 member tight reservoirs, Yanchang Formation, Ordos Basin, NW China. *Petroleum Explor. Dev.* 42, 667–673. doi:10.1016/S1876-3804(15)30061-6

Li, H. (2022). Research progress on evaluation methods and factors influencing shale brittleness: A review. *Energy Rep.* 8, 4344–4358. doi:10.1016/j.egyr.2022.03.120

Li, H., Tang, H. M., Qin, Q. R., Zhou, J. L., Qin, Z. J., Fan, C. H., et al. (2019). Characteristics, formation periods and genetic mechanisms of tectonic fractures in the tight gas sandstones reservoir: A case study of xujiahe formation in YB area, sichuan basin, China. *J. Pet. Sci. Eng.* 178, 723–735. doi:10.1016/j.petrol.2019.04.007

Li, H., Zhou, J. L., Mou, X. Y., Guo, H. X., Wang, X. X., An, H. Y., et al. (2022b). Pore structure and fractal characteristics of the marine shale of the longmaxi formation in the changning area, southern sichuan basin, China. *Front. Earth Sci. (Lausanne).* 10, 1018274. doi:10.3389/feart.2022.1018274

Li, J., Li, H., Yang, C., Wu, Y. J., Gao, Z., and Jiang, S. L. (2022a). Geological characteristics and controlling factors of deep shale gas enrichment of the Wufeng-Longmaxi Formation in the southern Sichuan Basin, China. *Lithosphere* 2022, 4737801. doi:10.2113/2022/4737801

Li, P., Zheng, M., Bi, H., Wu, S., and Wang, X. (2017). Pore throat structure and fractal characteristics of tight oil sandstone: A case study in the Ordos Basin, China. *J. Petroleum Sci. Eng.* 149, 665–674. doi:10.1016/j.petrol.2016.11.015

Li, Y., Niu, D., Zhang, Y., Wu, H., Fu, H., and Wang, Z. (2021a). Microscopic pore-throat grading evaluation in a tight oil reservoir using machine learning: A case study of the fuyu oil layer in bayanchagan area, songliao basin central depression. *Earth Sci. Inf.* 14, 601–617. doi:10.1007/s12145-021-00594-6

Li, Z. P., Gao, C. Q., Zhao, B., Guan, Y., and Liu, J. Y. (2021b). Application of nuclear magnetic resonance logging in the low-resistivity reservoir-Taking the XP area as an example. *Interpretation* 8, T885–T893. doi:10.1190/INT-2019-0179.1

Li, Z., Qu, X., Liu, W., Lei, Q., Sun, H., and He, Y. (2015a). Development modes of triassic Yanchang Formation Chang 7 member tight oil in Ordos Basin, NW China. *Petroleum Explor. Dev.* 42, 241–246. doi:10.1016/S1876-3804(15)30011-2

Lu, S. F., Li, J. Q., Xiao, D. S., Xue, H. T., Zhang, P. F., Li, J. J., et al. (2022). Research progress of microscopic pore-throat classification and grading evaluation of shale reservoirs: A minireview. *Energy fuels.* 36, 4677–4690. doi:10.1021/acs.energyfuels.2c00431

Neves, L. F., Guedes, C. C. F., and Vesely, F. F. (2019). Facies, petrophysical and geochemical properties of gravity-flow deposits in reservoir analogs from the Itarare Group (late Carboniferous), Parana Basin, Brazil. *Mar. petroleum Geol.* 110, 717–736. doi:10.1016/j.marpetgeo.2019.07.038

Nikolaev, M. Y., and Kazak, A. V. (2019). Liquid saturation evaluation in organic-rich unconventional reservoirs: A comprehensive review. *Earth-science Rev.* 194, 327–349. doi:10.1016/j.earscirev.2019.05.012

Pecanha, A. A., Lupinacci, W. M., Ferreira, D. J. A., and Freire, A. F. M. (2019). A workflow for reservoir characterization applied to presalt coquinas from the Linguado Field, Campos Basin, Brazil. *J. petroleum Sci. Eng.* 183, 106451. doi:10.1016/j.petrol.2019.106451

Si, Z., Lin, F., Liu, D., Kong, X., Yin, Q., and Zhuang, D. (2020). Research on well logging evaluation method of igneous reservoir in Nanpu No.5 structure. *Energy Sources Part A Recovery Util. Environ. Eff.*, 1–13. doi:10.1080/15567036.2020.1798565

Sun, L., Tuo, J., Zhang, M., Wu, H., Wang, Z., and Zheng, Y. (2015). Formation and development of the pore structure in Chang 7 member oil-shale from Ordos Basin during organic matter evolution induced by hydrous pyrolysis. *Fuel* 158, 549–557. doi:10.1016/j.fuel.2015.05.061

Wu, S., Zhu, R., Cui, J. G., Cui, J. W., Bai, B., Zhang, X., et al. (2015). Characteristics of lacustrine shale porosity evolution, triassic Chang 7 member, Ordos Basin, NW China. *Petroleum Explor. Dev.* 42, 185–195. doi:10.1016/S1876-3804(15)30005-7

Xiang, J., Liu, J., and Li, X. (2015). Investigation of pore structure and fractal characteristics of organic-rich Yanchang formation shale in central China by nitrogen adsorption/desorption analysis. *J. Nat. Gas Sci. Eng.* 22, 62–72. doi:10.1016/j.jngse.2014.11.020

Yang, Z., Zou, C., Wu, S., Lin, S., Pan, S., Niu, X., et al. (2019). Formation, distribution and resource potential of the "sweet areas (sections)" of continental shale oil in China. *Mar. Petroleum Geol.* 102, 48–60. doi:10.1016/j.marpetgeo.2018.11.049

Yao, J., Deng, X., Zhao, Y., Han, T., Chu, M., and Pang, J. (2013). Characteristics of tight oil in triassic Yanchang Formation, Ordos Basin. *Petroleum Explor. Dev.* 40 (2), 161–169. doi:10.1016/S1876-3804(13)60019-1

Zhang, B., Shan, B., Zhao, Y., and Zhang, L. (2020). Review of formation and gas characteristics in shale gas reservoirs. *Energies* 5427, 5427. doi:10.3390/en13205427

Zhang, Y., Zeng, J., Dai, Z., Hari, V., Xiao, T., Ma, Y., et al. (2018). Experimental investigation on oil migration and accumulation in tight sandstones. *J. Petroleum Sci. Eng.* 160, 267–275. doi:10.1016/j.petrol.2017.10.049

Zhou, Z., Wang, G., Ran, Y., Lai, J., Cui, Y., and Zhao, X. (2016). A logging identification method of tight oil reservoir lithology and lithofacies: A case from Chang7 member of triassic Yanchang Formation in heshui area, Ordos Basin, NW China. *Petroleum Explor. Dev.* 43, 65–73. doi:10.1016/S1876-3804(16)30007-6

Zhu, P., Zhu, Z., Zhang, Y., Sun, L., Dong, Y., Li, Z., et al. (2019). Quantitative evaluation of low-permeability gas reservoirs based on an improved fuzzy-gray method. *Arab. J. Geosci.* 3, 80. doi:10.1007/s12517-019-4231-5

Zou, C., Yang, Z., Cui, J., Zhu, R., Hou, L., Tao, S., et al. (2013). Formation mechanism, geological characteristics and development strategy of nonmarine shale oil in China. *Petroleum Explor. Dev.* 40 (1), 15–27. doi:10.1016/S1876-3804(13)60002-6

frontiers | Frontiers in Earth Science

TYPE Original Research
PUBLISHED 17 January 2023
DOI 10.3389/feart.2022.1023844

OPEN ACCESS

EDITED BY
Wenlong Ding,
China University of Geosciences, China

REVIEWED BY
Jianguo Zhang,
China University of Geosciences, China
Xinghua Wang,
SINOPEC Petroleum Exploration and Production Research Institute, China
Ahmed E. Radwan,
Jagiellonian University, Poland

*CORRESPONDENCE
Chaohui Ji,
jichaohui33@163.com,
980648386@qq.com

SPECIALTY SECTION
This article was submitted to Structural Geology and Tectonics, a section of the journal Frontiers in Earth Science

RECEIVED 20 August 2022
ACCEPTED 31 October 2022
PUBLISHED 17 January 2023

CITATION
Ji C, Xue C, Sun M, Li X and Wang L (2023), Reservoir properties and hydrocarbon enrichment law of Chang 1 oil layer group in Yanchang Formation, Wanhua area, Ordos Basin. *Front. Earth Sci.* 10:1023844. doi: 10.3389/feart.2022.1023844

Reservoir properties and hydrocarbon enrichment law of Chang 1 oil layer group in Yanchang Formation, Wanhua area, Ordos Basin

Chaohui Ji[1]*, Chengwei Xue[2], Min Sun[1], Xiang Li[2] and Li Wang[1]

[1]Shaanxi Yanchang Petroleum (Group) Corp. Ltd., Nanniwan Oil Production Plant, Yan'an, Shaanxi, China, [2]The Fifth Oil Production Plant of Petrochina Changqing Oil Field Company, Xi'an, Shaanxi, China

Evaluation of tight oil reservoir properties is of great significance to the exploration of oil and gas in tight reservoirs. The Chang 1 Member of the Yanchang Formation in the Wanhua Area, Ordos Basin is a new exploration stratum for tight sandstone oil. The lack of understanding of reservoir characteristics and crude oil enrichment rules has seriously restricted the efficient development of oil and gas resources in this stratum. In this study, the reservoir characteristics of the Chang 1 Member in the Wanhua area and the effects of superimposed sand bodies, structures and paleogeomorphology on accumulation of hydrocarbons were systematically studied. The Chang 1 sandstone is a typical ultra-low porosity-ultra-low permeability reservoir, and it has experienced destructive diagenesis of mechanical compaction, pressure solution and cementation, and constructive diagenesis of dissolution. Strong pressure solution caused the secondary enlargement of quartz and feldspar and the formation of patchy dense mosaic structures. The target layer has experienced argillaceous, siliceous and carbonate cementations. Moreover, the sandstone reservoir in the Chang 1 Member also experienced strong dissolution, and it is the main factor for the formation of secondary pores and the improvement of reservoir physical properties. The study also found that the main types of pores in the Chang 1 Member are intergranular dissolved pores and remaining intergranular pores. Superimposed sand bodies, nose-shaped uplifts, dominant facies and eroded paleo-highlands have significant effects on the hydrocarbon accumulation. Based on this study, it was found that the migration and accumulation mode of hydrocarbons in the Chang 1 reservoir belongs to the ladder-like climbing migration + structural ridge accumulation type. In addition, sand body thickness is an important controlling factor for the hydrocarbon accumulation. At present, the discovered crude oil in the Chang 1 Member is always distributed in the areas with thick sand bodies (>20 m), and most of the sand bodies have a thickness in the range of 25–40 m, and the effective thickness is in the range of 2–6 m. In addition, the eroded highlands are the highest topographic units, they are favorable areas for the large-scale accumulation of oil and gas.

KEYWORDS

Yanchang formation, reservoir properties, hydrocarbon accumulation, pore structure, sandstone thickness

1 Introduction

Continental tight sandstone oil is an important type of unconventional oil and gas resource (Li et al., 2012; Huang et al., 2019; Asante-Okyere et al., 2021). The core of the study of unconventional tight oil and gas reservoirs is the study of the microscopic characteristics of the reservoir and the law of hydrocarbon enrichment (Zhang et al., 2014; Liao et al., 2020; Cui and Radwan., 2022; Jiang et al., 2022; Zhang et al., 2022). With the rapid decline of China's conventional oil and gas reserves, the importance of the exploration and development of unconventional oil and gas resources has become increasingly prominent. As we know, the efficient production of continental tight oil in the Ordos Basin relies on the application of horizontal well + volume fracturing technology. Improving the drilling encounter rate of oil layers is one of the core issues of drilling and evaluation of horizontal wells (Sun et al., 2013; Radwan., 2020; Yin et al., 2020; Zhang et al., 2020). At present, the prediction methods for the "sweet spots" of clastic tight oil reservoirs are all based on the controlling factors of reservoir properties. Therefore, it is of great significance to clarify the petrology, pore types, diagenesis, and physical properties of tight oil reservoirs for the successful exploration of "sweet spots" in tight sandstone reservoirs (Sun et al., 2014; Bukar et al., 2021; Katz et al., 2021).

In recent years, with the large-scale development of relatively high-quality reservoirs in tight oil reservoirs, the growth of oil and gas reserves has become difficult. Then, the efficient development of ultra-low permeability tight oil reservoirs with poor physical properties has become a new hot spot for the growth of oil and gas reserves. The current exploration level of the Chang 1 Member of the Yanchang Formation in Wanhua area is low. At present, only 25 development wells and 16 exploration wells were drilled in the study area. It has been found that fine sandstones developed in the middle part of the river channel has good oil and gas display. However, the influencing factors of hydrocarbon distribution in the Chang 1 Member have not been determined. Therefore, fine evaluation of the properties of the tight reservoirs in the Chang 1 Member is of great significance to the increase of oil and gas reserves and productivity in this area. In this study, the reservoir characteristics of the Chang 1 Member in the Wanhua area and the effects of superimposed sand bodies, structures and paleogeomorphology on the hydrocarbon accumulation were systematically studied. This research can provide scientific guidance for formulating an efficient development strategy for the Chang 1 Member in the future.

2 Geological background

The study area is located in the Wanhua area of Nanniwan Oilfield in the Ordos Basin. The Nanniwan Oilfield is located in the Baota District, Yan'an City, Shaanxi Province. It spans 9 townships including Guanyu, Linzhen, Madongchuan, Nanniwan, Pine Forest, Wanhua, Zaoyuan, Heyuping and Liqu. The Wanhua area is 16 km long from north to south, 25 km wide from east to west, and covers an area of about 400 km^2 (Figure 1). Regionally, the study area is located in the southeastern part of the Yishan Slope in the Ordos Basin (Figure 1). This area is a gentle monocline sloping westward, and the formation dip is 0.5° to 1°. A series of low-amplitude nose-like uplifts dipping from east to west are developed on the slope. The superimposed areas of these nose-shaped uplifts and thick sand bodies indicate favorable areas for hydrocarbon enrichment.

The Chang 1 Member of the Upper Triassic Yanchang Formation in this area is the exploration target. Drilling revealed that continental freshwater lake delta deposits are developed in the Yanchang Formation. The stratigraphic sequences of the Yanchang Formation include a set of interbeds of gray-green, gray-black mudstone, argillaceous siltstone and gray-green, gray-white medium-fine feldspar sandstone. As the study area was eroded by the Ganshan Ancient River in the Jurassic period, the Chang 1 oil layer group was eroded to different degrees. The residual thickness of the Chang 1 oil layer group in the Yanchang Formation in this area varies greatly, and its thickness ranges from 25 to 90 m. (Figure 2)

3 Databases and methods

Core observations, physical property tests, thin section and scanning electron microscope observations were carried out on the wells of Nan 141, Nan 116, Nan 117, Nan 128, Xi 41, and Xi 63 in the study area. These wells are all exploratory wells, and the samples are all sandstone collected from the river channel.

The data used in this paper are from physical property, thin section, scanning electron microscope experiments and logging data. Among them, the physical property test adopts the overburden porosimeter CMS-300, and the test standard is SY/T 5336-2006. First, the samples were processed into small columns measuring 2.5 cm in diameter and 5 cm in diameter. Then, the samples were washed and dried for 2 h. High-pressure nitrogen gas is used to apply confining pressures. The test gas source is high purity helium. Then, the CMS300 rock autoanalyzer's power and gas source were switched on to

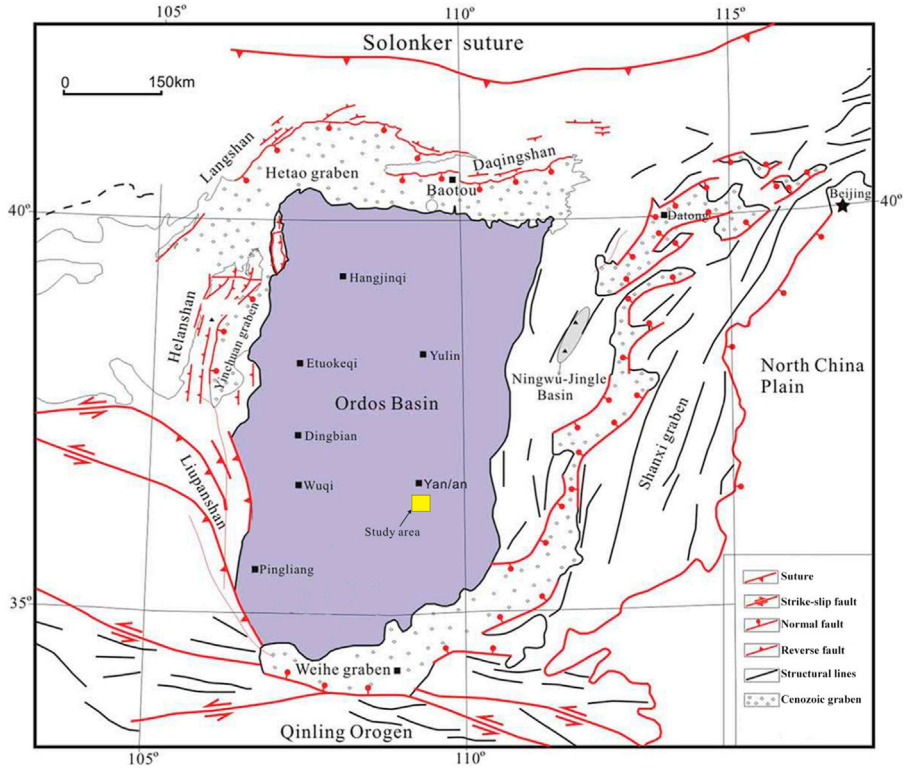

FIGURE 1
Location of the Wanhua area in the Ordos Basin (modified after Li et al., 2016).

automatically measure the porosity and permeability of the samples. The measurements are based on the Boyle's law (porosity) and the Darcy's law for unsteady flows (permeability). The accuracy of CMS300 is higher than 2,412.9 Pa-cm^3/min.

Thin section experiments are performed using a LEICA 4M research microscope and the test standard is SYT 5368-2016 (Li et al., 2012). The experimental temperature is 20°C and the relative humidity is 20%. Scanning electron microscope observations adopt a Tescan field emission electron microscope MAIA-3, and the test standard is GB/T 20307-2006. Based on the observations of thin section and scanning electron microscope of the Chang 1 Member in the study area, the petrology, pore types, and diagenesis of tight oil reservoirs have been systematically studied (Wang and Yang., 2017).

Single well logging data are used for stratigraphic divisions and sand body identifications (Li et al., 2012). On the basis of sand body identification, the effective thickness of sand bodies is also determined. There are argillaceous rocks or tight impermeable layers inside the oil layer, which have no effect on the acquisition of industrial oil flows and are deducted from the effective thickness. The argillaceous interlayers show low micro-electrode resistance value, no obvious amplitude difference, low concave resistivity, spontaneous potential and natural gamma values of abnormal amplitude return on the electrical measurement curves (Wang and Yang., 2017). The thickness of the physical property interlayers on the electrical measurement curves is lower than the effective thickness standard, and the micro-resistivity curves are close to overlap. The calcareous interlayers show high resistivity values, high peak bayonet-like microelectrodes, returning spontaneous potentials, and reduced acoustic wave time differences on logs. According to the resolution of the logging series, the effective thickness is higher than 0.4 m, and the critical thickness of the interlayers is higher than 0.2 m.

4 Results

4.1 Types of sedimentary facies

The sandstones in the Chang 1 Member in the study area are mainly light gray and gray-white, and a small proportion are light brown, gray-brown and yellow-green (Figures 3A,B). These sandstones are river channel deposits. However, mudstone,

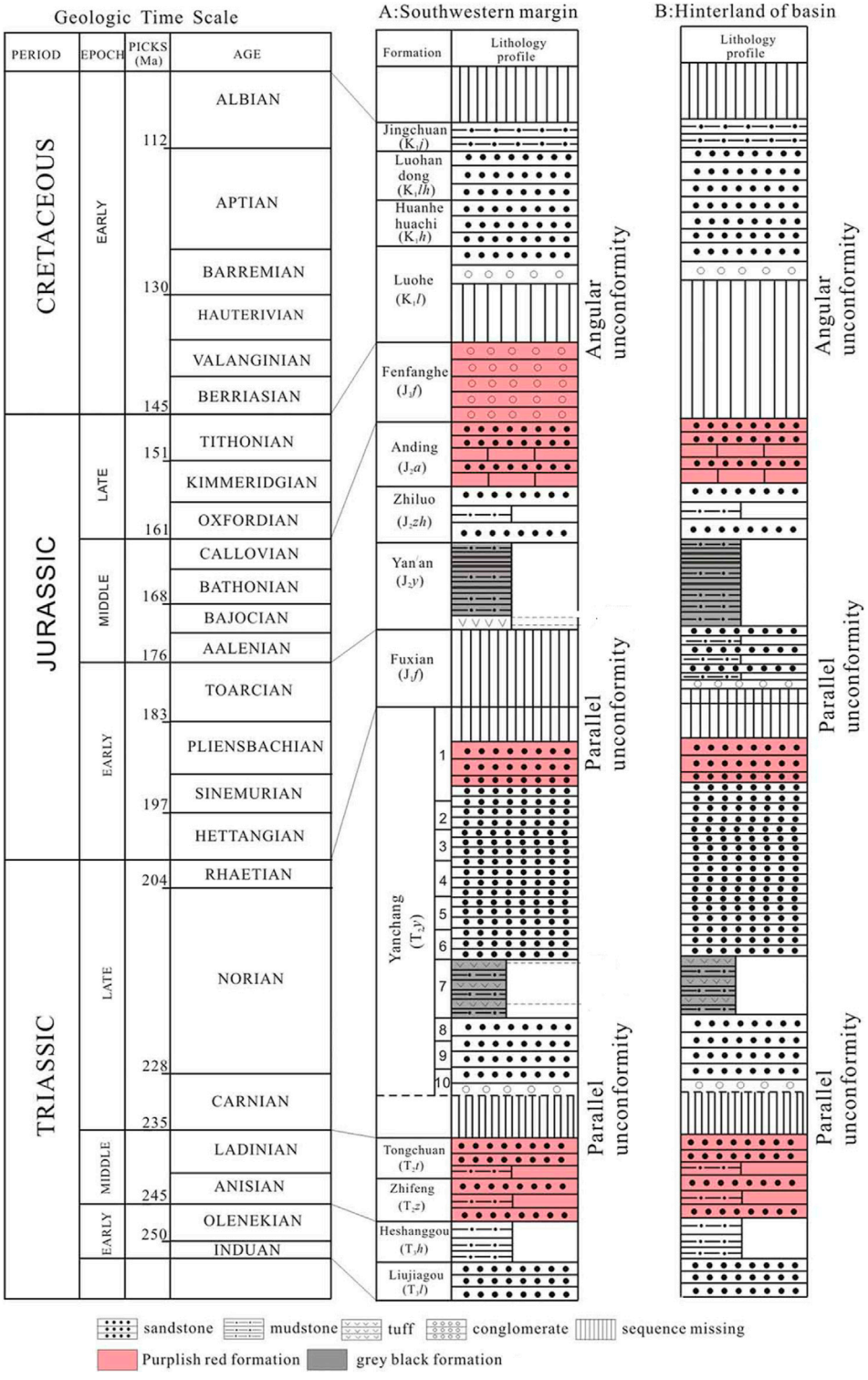

FIGURE 2
Division of stratigraphic units in the Ordos Basin (modified after Li et al., 2016). **(A)** The southwestern margin of the Ordos Basin; **(B)** Hinterland of the Ordos Basins.

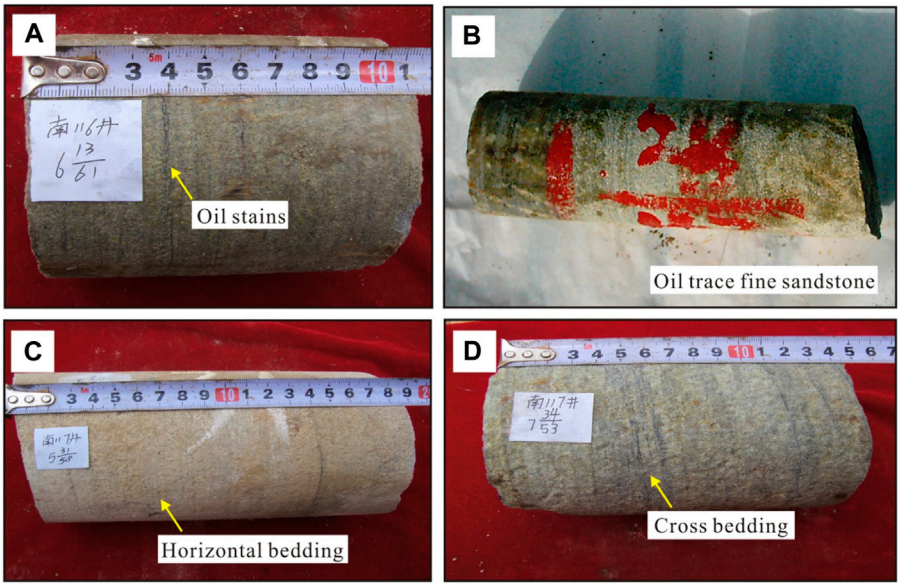

FIGURE 3
Core images of the Chang 1 Member sandstones in the study area. **(A)** Light gray oil traced fine sandstone, Well Nan116, 711.96–712.06 m; **(B)** Gray oil trace fine sandstone, Well Xi63, 726.31–726.57 m; **(C)** Parallel bedding, Well Nan117, light gray fine sandstone, 714.26–714.44 m; **(D)** Cross bedding, Well Nan117, light gray fine sandstone, 734.49–734.63 m.

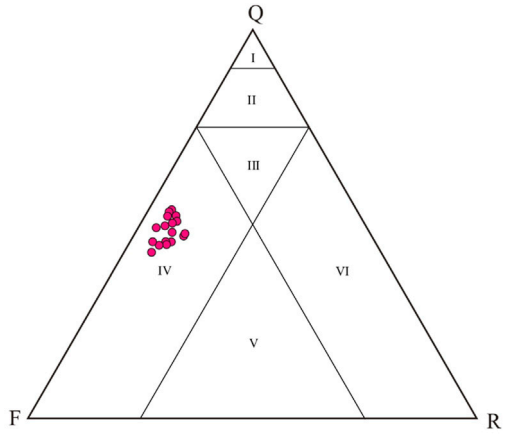

I: Pure quartz sandstone; II: Quartz sandstone;
III: Sub-feldspar lithic sandstone/Sub-lithic feldspar sandstone
IV: Feldspar sandstone; V: Feldspar detrital sandstone/−detrital feldspar sandstone; VI: detrital sandstone

FIGURE 4
Lithological classification of the Chang 1 Member sandstone.

argillaceous siltstone and silty mudstone are mostly dark gray, black and gray-black, reflecting inter-channel or inter-distributary bay deposits.

The sedimentary structures in clastic rocks are the direct reflection of the sedimentary environment and hydrodynamic conditions in the rock. Parallel and cross beddings are widely developed in the Chang 1 Member sandstones in the study area (Figures 3C,D). Horizontal beddings are rectilinear and usually parallel to the bedding. It is a common type of bedding found in argillaceous rocks. Further, it reflects the deposition of suspended matter in a low-fluid form in a low-energy environments (e.g., inter-fluvial depressions, lacustrine and swamp environments). However, parallel beddings generally occur in rapids and high-energy environments, such as river channels, and often coexist with large cross beddings. In addition, cross-beddings can occur in sedimentary environments such as water distributary channels and delta front estuarine bars (Liu et al., 2009; Wang and Yang., 2017). The Chang 1 Member of the study area belongs to meandering river facies and is divided into distributary channel (channel retention, sand bar) and interdistributary channel, and floodplain microfacies. The skeleton sand bodies are sandy deposits developed in the middle part of the river channel (Figure 3).

4.2 Reservoir petrological characteristics

The lithology of the Chang 1 reservoir in this area is mainly sandy fine-grained feldspar sandstone. As shown in Figure 4, the different samples have similar petrological characteristics. The main mineral components of the Chang 1 sandstones are quartz, accounting for 42.0%–53.0%, with an average of 47.55%; the second is feldspar, accounting for 40.0%–50.0%, with an average

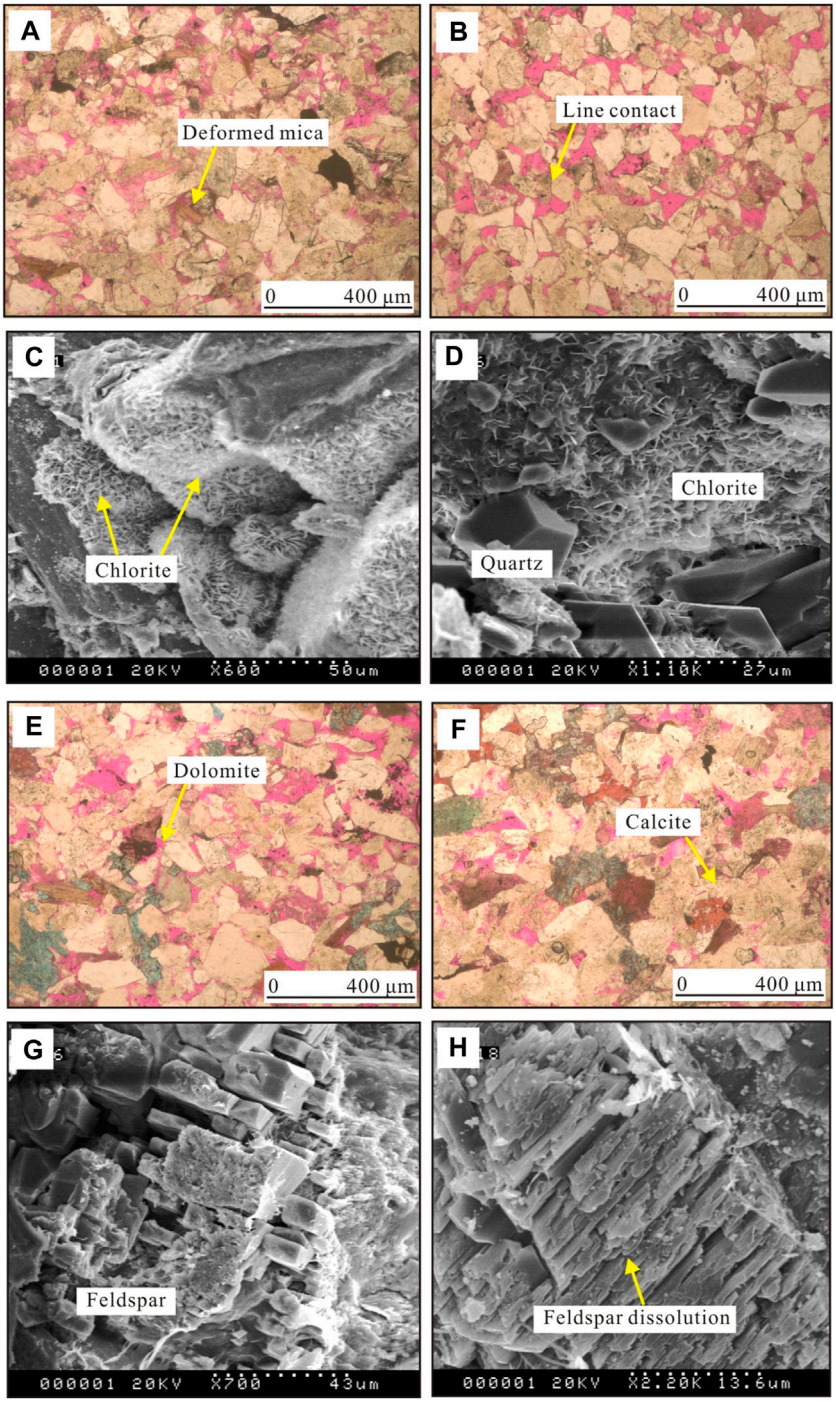

FIGURE 5
Microstructural characteristics of the Chang 1 Member sandstone in the study area. **(A)** Deformed sheet mica, Well Nan141; **(B)** Mosaic and linear contact particles, Well Nan128; **(C)** Chlorite cementation, Well Nan141, 521.97–522.07 m; **(D)** Quartz-filled and chlorite-cemented intergranular pores, Well Nan128, 715.83–715.93 m; **(E)** Dolomite and ankerite cements with grain structures are filled in the intergranular pores, Well Nan128, 725.18–725.28 m; **(F)** Calcite and ankerite cements with grain structures are filled between particles, Well Xi41, 500.89–500.99 m; **(G)** Feldspar dissolution, Well Nan128, 715.83–715.93 m; **(H)** Feldspar dissolution, Well Xi41, 500.89–500.99 m.

of 43.95%; the content of debris is between 4.0% and 11.0%, with an average of 7%; in addition, the content of mica varies little, ranging from 1.0% to 3.0%, with an average of 1.3%. The debris components in the samples are mainly metamorphic rock debris, followed by igneous rock debris and a small amount of sedimentary rock debris.

The content of interstitials in the Chang 1 Member reservoirs in this area ranges from 2.0% to 18.0%, with an average of 8.2%; the main components of cements are ankerite, turbidite, dolomite and calcite, and their average contents are 4.05%, 1.4%, 1%, 0.625%, and 0.5%, respectively; and the matrix are mainly mud components, and the average content is 1.4%.

In addition, the sandstones of the Chang 1 Member in this area have relatively uniform clastic particles, and the main particle size between 0.15 and 0.35 mm accounts for more than 85% of all samples; the particles mainly have medium sorting, followed by good sorting; the particles have sub-edge-sub-circular roundness; the grains are in point or point-line contact; and pore type and film-pore type cementations are mainly developed.

For the relation between sedimentary facies and reservoir petrological characteristics, it is found that fine sandstones are mainly developed in the middle section of the river channel, and fine-siltstones are developed in the flanks of the river channel.

4.3 Diagenesis

The Chang 1 sandstone of the Yanchang Formation in the study area is a typical ultra-low porosity-ultra-low permeability reservoir, and its diagenetic process is very complicated. In the process of burial diagenesis, various diagenesis have certain effects on the primary pores or preservation or destruction of sandstone and the development of secondary pores. It has experienced destructive diagenesis such as mechanical compaction, pressure solution and cementation, and has experienced constructive diagenesis such as dissolution (Li et al., 2016;).

4.3.1 Compaction and pressure solution

Mechanical compaction runs through the entire process of burial diagenetic stage, and is one of the main reasons for the reduction of sandstone porosity (Nabawy et al., 2022). The compaction-pressure-dissolution effect experienced by the Chang 1 sandstone reservoir is very strong. Compaction rotates, orients, deforms the detrital particles, and mechanical fracture occurs in rigid particles. Moreover, line, surface, asperity and suture contacts appeared in the detritus particles under pressure. For example, the bending deformation of mudstone debris and mica is even squeezed into the intergranular pores to form a false matrix. In particular, mica deformed by strong compaction can block pores and throats (Figure 5). In the later stage of compaction, the main clay mineral in the feldspar sandstones, the chlorite film, is precipitated. Chlorite is attached to the surface of detrital particles in the form of films or combs and blocks pores and throats (Wang et al., 2019; Su et al., 2022). Thin-section analysis shows that sandstones with high content of plastic particles such as mica and mudstone debris are significantly affected by mechanical compaction, and their surface porosities are generally low (El-Gendy et al., 2022).

As the overburden pressure increases, the compaction effect is gradually replaced by the pressure solution. Furthermore, the inter-particles contact changes from linear contact to concave-convex contact and mosaic cementation. Then, the secondary growth of feldspar and quartz leads to the reduction of the primary intergranular pores and the throat radius. Ultimately, the permeability of tight reservoirs is greatly reduced. Overall, the pressure-dissolution of the tight sandstone in the target layer resulted in the secondary increase of quartz and feldspar, and a large number of patchy dense mosaic structures could be observed under the microscope (Figures 5A,B). The porosity of the Chang 1 sandstones was greatly lost due to compaction and solution. The remaining porosity of the reservoir is only about half of the original porosity. Compaction is the main reason for the sharp decrease of rock porosity. The original porosity of the target layer is calculated according to the original porosity model of unconsolidated sandstone proposed by Beard (Wang and Yang., 2017), which is 25%.

4.3.2 Cementation

The cements in the target sandstones mainly include authigenic clay minerals, carbonate minerals, authigenic quartz feldspar and turbidite. The main types of cementation include calcite cementation, chlorite film and chlorite filling cementation, overgrowth of quartz and feldspar. They are precipitated between the detrital particles, or appear in the form of secondary particle enlargement, or in the form of mutual metasomatism and metasomatic detrital particles.

4.3.2.1 Argillaceous cementation

The argillaceous cementation is mainly clay mineral cementation, including authigenic clay minerals and a small amount of terrigenous clay (Abdel-Fattah et al., 2022). Terrigenous clay minerals mainly occur in the early diagenetic stage and are common in siltstone; while the composition of authigenic clay minerals is quite simple, which is common in medium and fine sandstones.

Under the microscope, argillaceous usually fills the intergranular pores in the form of thin films, micrites and scales. Clay cements include chlorite, kaolinite, illite, and imon mixed layer. Among them, the chlorite film is the main cement in the early diagenetic A-stage sandstone. From the X-ray diffraction test results (Table 1), the Chang 1 Member has the highest content of chlorite, followed by kaolinite, illite, and imon mixed layer.

The formation of chlorite is caused by the combination of biotite and feldspar in terrigenous debris after weathering. It was found that the chloriteization of biotite debris in the target layer is very significant. The rich content of mica debris is the main reason for the good development of chlorite film. Moreover,

TABLE 1 Statistical results of X-diffraction data of clay minerals in the target sandstones.

Horizon	Sample	I	K	C	I/S	S%
		Illite (%)	Kaolinite (%)	Chlorite (%)	Imon mixed layer (%)	Interlayer ratio
Chang 1	20	5	13	77	5	11

Notes: I-illite; K-kaolinite; C-chlorite; I/S-Imon mixed layer.

under the microscope, it can be seen that a yellow film is formed around the detrital particles, which grows perpendicular to the detrital wall and has different degrees of metasomatism to the detrital particles. Most chlorites are attached to the grain surface in leaf-like or "pompom-like" aggregates (Figures 5C,D), and the content of chlorite aggregates in the medium and fine sandstones is less than that in siltstones.

In the early stage of diagenesis, the chlorite film can effectively inhibit the regrowth or secondary enlargement of quartz, feldspar, *etc.*, and a large number of primary pores are retained (Figures 5C,D). At the same time, the covering of chlorite film on the particle surface leads to the reduction of the pore throat radius. The thickness of the chlorite films in the target layer is 0–20 μm, which causes the pores and throats to be blocked, and the permeability of the sandstone is reduced. At the same time, the development of a large number of micropores complicates the pore structures inside the sandstone (Figures 5C,D).

Kaolinite is the product of feldspar weathering. They generally appear as pseudo-hexagonal wafers under the microscope, while their aggregates usually exist in the form of book pages or worms. The content of kaolinite in the authigenic clay minerals in the target layer is relatively high (Table 1). In addition, the illite cements can be observed to grow on the pore walls in a bridging form, which results in a significant reduction in rock porosity and permeability.

4.3.2.2 Siliceous cementation

The secondary growth of quartz is formed by the coaxial growth of dissolved SiO_2 in the pore water on the surface of the detrital quartz. Early secondary enlarged quartz formed before or during compaction. The quartz overgrowth is mainly controlled by the limitation of the size of the growth space (Khan et al., 2020). It can surround the entire detrital quartz, or distributed only in local quartz grains. Therefore, secondary quartz usually exists in the form of enlarged edges or fills the pores. Type I secondary enlarged quartz is dispersed on the pore surface in the form of point-like aggregates. Type II secondary enlarged quartz has a more continuous distribution on the pore surface. Type II secondary quartz is mainly developed in the target layer.

4.3.2.3 Carbonate cementation

The carbonate cements in the target layer include ankerite, calcite, and iron-bearing calcite cements, among which ankerite cements are the main ones (Figures 5E,F). The calcite cements are divided into early and late stages. Among them, the early calcite cements are not as common as the late ferrocalcite cements under the microscope. In the early calcite-cemented detrital grains, only a very small amount of detrital quartz experienced secondary enlargement at the edges. In the target layer, late-stage calcite cementation is common, which is typically characterized by pore filling and is irregularly distributed among the clastic particles.

4.3.3 Dissolution

According to this study, the dissolution in the Chang 1 Member reservoir is strong, and the dissolution is the main factor for the formation of secondary pores and the improvement of reservoir storage properties and permeability. Dissolution in the target layer occurred in the late stage of diagenesis. At this time, the organic matter is in the low-mature to mature stage, and the organic matter in the source rock begins to decarboxylate and release CO_2. When these substances enter the pore fluids, they make the formation water acidic. This type of acidic fluid, rich in organic and inorganic acids, is the main driving force for the dissolution of reservoir detrital components (Haile et al., 2018; Liu et al., 2020). Overall, the intergranular and intragranular dissolved pores formed by dissolution are the most important secondary storage spaces of feldspar sandstones in this area (Figures 5G,H).

According to the observations of the cast thin section and scanning electron microscope in this area, a large number of dissolution-type secondary pores were formed in the sandstones during the middle diagenetic stage, and the pore structures of the sandstone reservoir were effectively improved. Through the analysis of the development characteristics of microscopic mineral components, the Chang 1 Member in the study area has gone through the syngeneic stage→early diagenetic stage→intermediate diagenetic stage A. It is in the middle diagenetic stage A now.

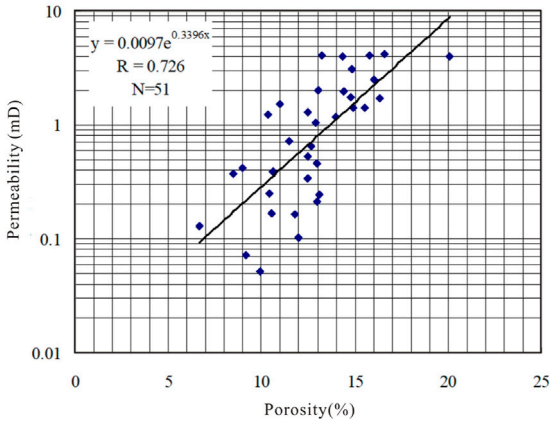

FIGURE 6
Relationship between porosity and permeability of sandstone in the Chang 1 Member of the study area.

4.4 Physical characteristics

According to the statistical results of the physical property data of 51 samples in the area, the porosity of the Chang 1 reservoir is distributed between 6.6% and 20.1%, with an average value of 12.5%. The permeability of the samples is distributed between 0.05 and 26.9 mD, with an average of 2.4 mD. There is an obvious positive correlation between the porosity and permeability of the Chang 1 reservoir in the study area (Figure 6).

The main sedimentary microfacies types of the target layer include distributary channel, estuary bar, interdistributary bay and floodplain. The relationship between sedimentary microfacies and reservoir porosity is compared, and the results are shown in Figure 7. According to statistics, the distribution intervals of the average porosity of the distributary channel, estuary bar, interdistributary bay and floodplain facies are 10%–17%, 12.5%–20%, 6.7%–10%, and less than 7%, respectively. Their average values are 14.2%, 14.9%, 8.6%, and 5.5%, respectively.

4.5 Pore types

In this study, the surface ratios of the samples were obtained from thin section tests. The LEICA 4M research microscope was used to automatically scan the micrographs of the samples. Then, the surface ratio of the samples was calculated. According to the observation and statistics of the cast thin section and electron microscope scanning of the target sandstone, the main types of pores developed in the sandstone of the Chang 1 Member are intergranular dissolved pores and residual intergranular pores (Figure 8). There are 100 samples in total.

The dissolved pores in the target layer are mainly intergranular and feldspar dissolved pores. Intergranular dissolution pores are pores formed by the dissolution of interstitials (clay, carbonate minerals) and the edges of clastic particles such as feldspar and debris. Part of the primary pores were recovered and enlarged or some new secondary pores were formed. Statistics show that the intergranular dissolution pores in the Chang 1 Member reservoir in the study area account for 66.7%–91.7% of the total surface porosity, with an average of 82.9%. Dissolution greatly improves the physical properties of the reservoir.

Residual intergranular pores refer to the pores remaining after the primary intergranular pores have been subjected to mechanical compaction or secondary quartz enlargement. The

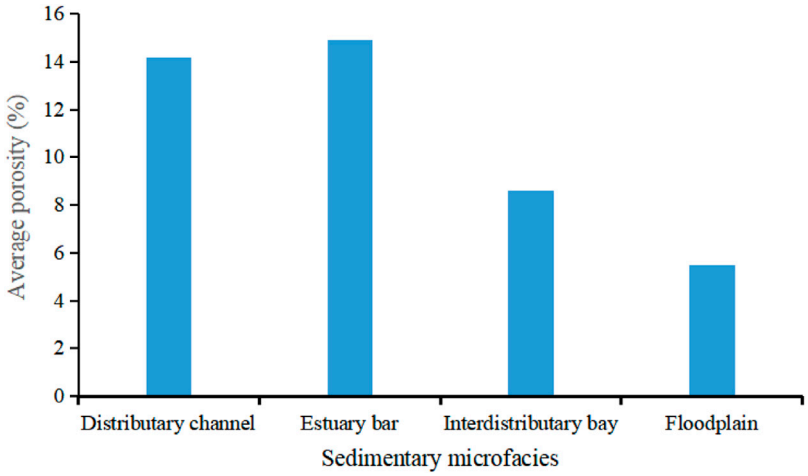

FIGURE 7
Histogram of average porosity distribution of different sedimentary microfacies.

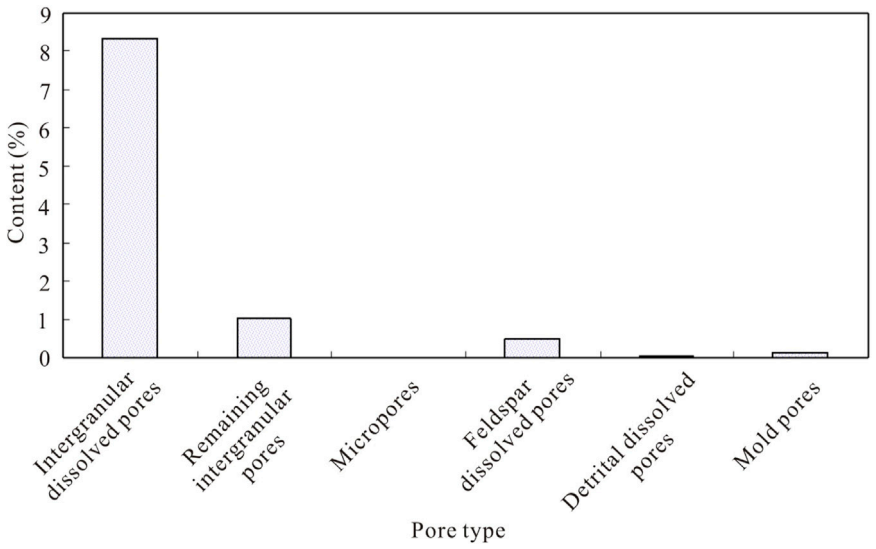

FIGURE 8
Pore types and proportions in the Chang 1 Member sandstone in the study area.

intergranular pores in the Chang 1 reservoir group in the study area are an important type of pores. They account for 5.0%–24.0% of the total surface porosity, with an average of 10.3%.

5 Discussion

The distribution of crude oil in tight reservoirs is actually the result of the coupling of various geological elements (Enayati-Bidgoli and Saemi., 2019). This study believes that the accumulation of hydrocarbons in the Chang 1 Member is mainly affected by factors of superimposed sand bodies, nose-like structures, sand body thickness, and eroded paleogeomorphology.

5.1 Effects of superimposed sand bodies and fractures on hydrocarbon migration

The oil and gas from the Chang 7 source layer in the oil-generating center in the southwest migrated under the action of buoyancy and capillary force when migrating along the lipophilic residual path network in contact with oil for a long time. Through the effective migration channels in the transport layer, the hydrocarbons migrate upward in a stepwise manner along the main fluid flow direction. When hydrocarbons encounter the top caprock and there is good shielding conditions in its updip direction, hydrocarbons can accumulate on a large scale (Figure 9). Large-scale vertical fractures mainly developed in the Chang 1 Member, and the longitudinal extension of these fractures can reach tens of meters (Figure 9). For the nose-like fold structures, oil and gas first accumulated linearly along the structural ridges where the fracture system was well developed, and then gradually accumulated outward along the areas with good physical properties and low capillary resistance. Finally, a strip-shaped hydrocarbon enrichment belt extending along the axis of the nose-like fold belt is formed on the plane. Based on this study, it is believed that the hydrocarbon migration and accumulation mode of the Chang 1 reservoir belongs to the ladder-like climbing migration + structural ridge accumulation type (Figure 10).

The Ordos Basin is a craton basin, and tectonic activities in the Mesozoic strata are not active. In the past, structural geologists believed that the Yishan Slope in the Ordos Basin was free of any faults and fractures. However, with the in-depth study of a large number of low-amplitude structures in the Ordos Basin, it has been found that the Mesozoic strata of the Yishan Slope have multiple active records of tectonic activities, and a large number of fractures have been discovered.

The study area is located in the southeastern part of the Yishan Slope, the first-level structural unit of the Ordos Basin. In the thin section observations, some micro-fractures were found in the sandstones of the Chang 1 Member (Figure 11). Sand bodies with relatively developed fractures are also important channels for hydrocarbon migration.

5.2 Effects of nose-like uplifts on hydrocarbon accumulation

The residual thickness of the Chang 1 oil layer group in the study area varies greatly, ranging from 25 to 90 m, and its

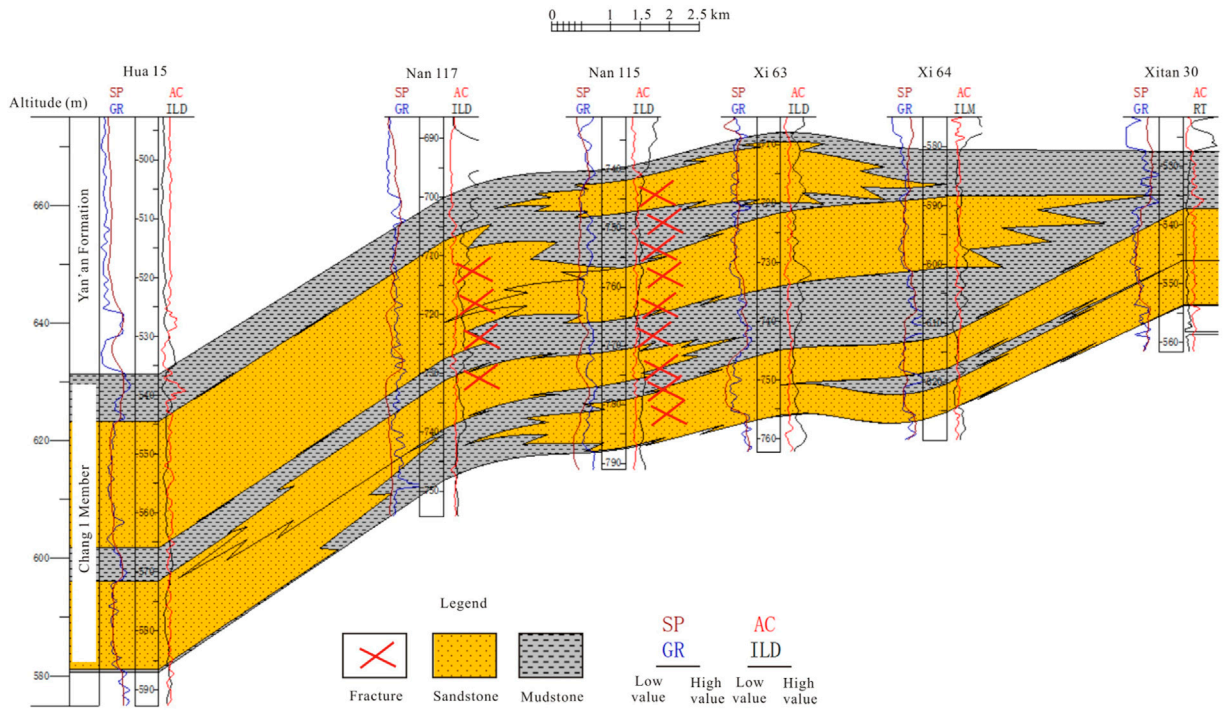

FIGURE 9
Sand body profile of connecting wells in Chang 1 Member of the study area. SP stands for spontaneous potential; GR stands for natural gamma; AC stands for acoustic time difference; ILD stands for deep lateral resistivity; ILM stands for medium induced resistivity; RT stands for true resistivity.

distribution direction is NW-SE. Due to the uneven distribution of sand and mudstone in the formation, the Chang 1 oil layer group is prone to differential compaction. Furthermore, the nose-like structures are relatively developed. On the regional west-dipping monoclinic structural background, the NW-SE or nearly EW-striking nose-like uplifts play a very important role in controlling the accumulation of crude oil in the Chang 1 Member. The discovered oil enrichment areas in the Chang 1 Member are all located in the nose-shaped uplifts with large structural amplitude and long extension distance. That is, the oil reservoir is located in the nose-shaped uplifts in the line of Well Xitan27-3 ~ Well Xitan7 ~ Well Nan127 ~ Well Nan128 ~ Well Xi63. Its structure undulates about 10–40 m, spreads about 5 km wide, and extends about 9.5 km in length. The nose-shaped uplifts are well developed in the top structure of the main sand bodies of the oil reservoir group. In addition, the oil reservoir is mainly distributed along the axial structural ridges of the nose-shaped uplifts. The main reason is that, on the one hand, the fractures formed at the axis of the nose-like fold are favorable for oil and gas migration; on the other hand, there are differences in the hydrocarbon accumulation capacity of different structural units such as monoclinic, nose-like uplift and structural high point. In the case of consistent oil and gas migration, oil and gas molecules will choose the shortest path (ie, the vertical contour direction) when they migrate upwards through buoyancy (Wang et al., 2021). Therefore, in general, the hydrocarbon accumulation capacity of different structural units such as monoclinic, nose-like uplift, and structural high point will change from weak to strong (Figure 12).

In conclusion, the Chang 1 reservoir in the study area is obviously controlled by the nose-like structures. The nose-like structure is an important factor for the accumulation and high production of oil and gas in the Chang 1 oil layer group in the study area.

5.3 Effects of dominant facies and eroded paleo-highlands on hydrocarbon accumulation

Sand body thickness is an important controlling factor for large-scale hydrocarbon accumulation (Zhang et al., 2017; Yin et al., 2020). At present, the discovered oil layers in the Chang 1 Member are all distributed in the areas with sand body thickness greater than 20 m. Most of the sand bodies have a thickness of 25–40 m, and the corresponding effective thickness is in the range of 2–6 m (Figure 13). In addition, the crude oil in Chang 1 Member is distributed in the area with sandstone ratio greater than 0.5. The sand bodies in these areas are thicker and have better physical properties, and the connectivity between the sand bodies is better as well. The good connectivity of sand

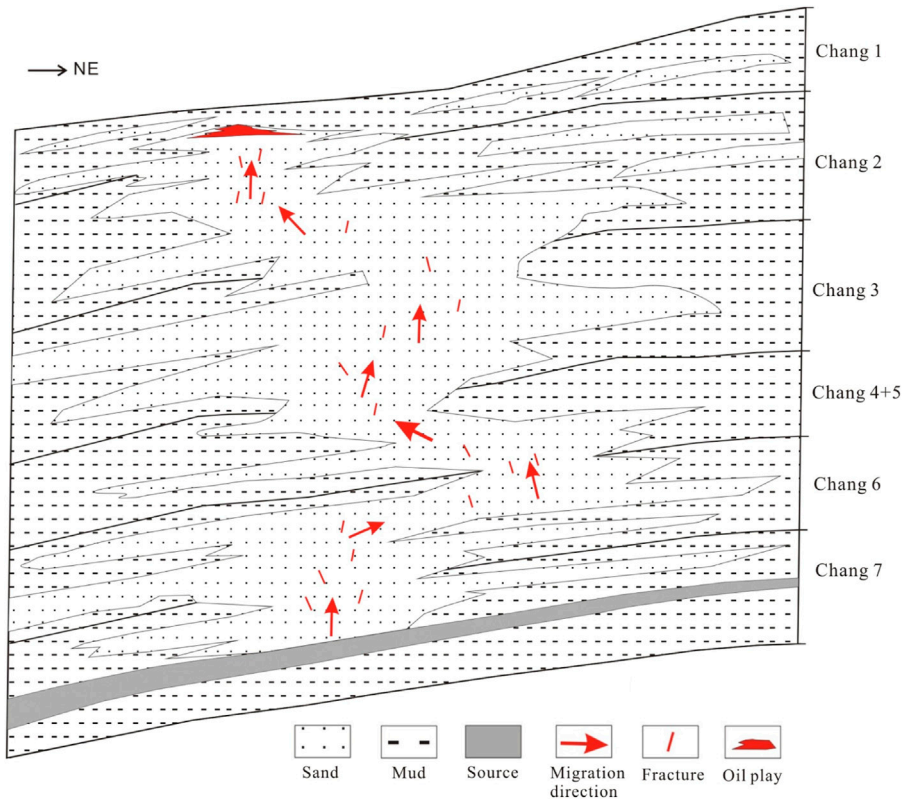

FIGURE 10
Hydrocarbon migration model of the Yanchang Formation in the study area. The superimposed sand bodies and fractures constitute channels for long-term continuous migration of hydrocarbons.

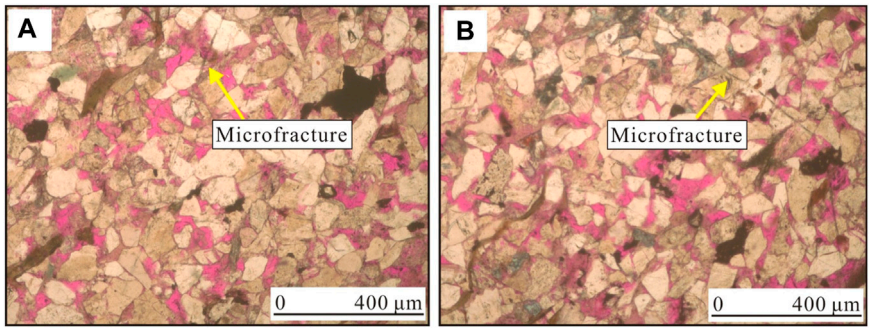

FIGURE 11
Development characteristics of micro-fractures in sandstone of the Chang 1 Member in the study area. Well Nan 141. **(A)** 521.97 m; **(B)** 522.07 m.

bodies ensures good migration channels, so that oil can accumulate in the upper part of the Chang 1 Member where there are good shielding conditions. The river channel sedimentary areas with sandstone ratio greater than 0.5 is the dominant facies areas of the Chang 1 oil layer group in the study area.

The eroded highlands are the topographical units with the highest topography. The study area is located in the east of the

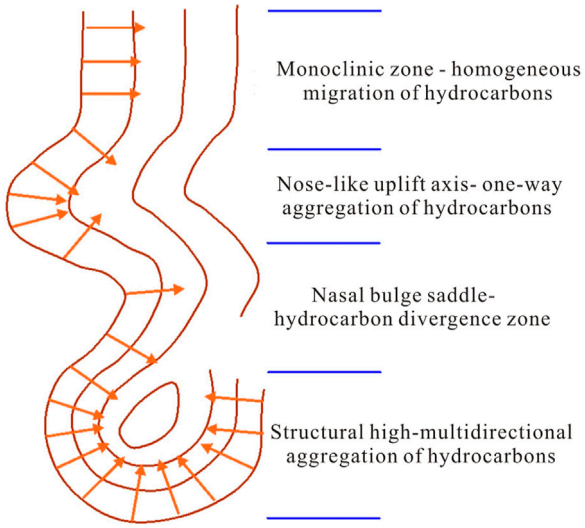

FIGURE 12
Schematic diagram of hydrocarbon migration in different structural units of the Yanchang Formation.

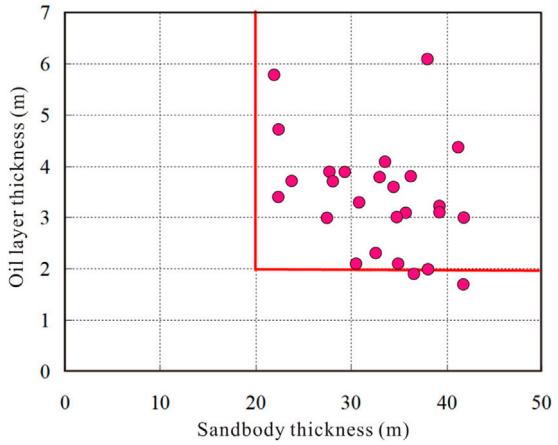

FIGURE 13
Relationship between sandstone thickness and effective thickness of the Chang 1 Member in the study area.

Ganshan ancient river. The flow direction of the Ganshan ancient river is from west to east, so that the upper strata of the Yanchang Formation are less eroded in the east of the ancient river than in the west. The residual formation thickness of the Chang 1 oil layer group in the study area is 25–90 m, so the thickness varies greatly. The distribution direction of the isopachous sand bodies is mainly in NW-SE striking, and the local striking is in NEE-SW and nearly SN directions. It reflects that the main channel of the Ganshan Ancient River in the study area is northwest-southeast.

Previous studies believed that paleotopography had an important influence on the distribution of oil and gas under the erosion surface. The paleogeomorphic units with higher topography are the main areas for oil and gas enrichment. Therefore, the eroded highlands, slope areas and residual hills are the best places for hydrocarbon accumulation in the upper strata of the Yanchang Formation. This study found that the superimposed position of dominant facies and eroded residual hills is more conducive to the accumulation of crude oil in the Chang 1 Member of the study area.

6 Conclusion

1) The Chang 1 Member sandstone in the Wanhua area is a typical ultra-low porosity-ultra-low permeability reservoir. The strong pressure solution caused secondary enlargement of quartz and feldspar and the formation of patchy dense mosaic structures. The original porosity of the target layer is 25%. Statistics show that the intergranular dissolution pores in the Chang 1 Member reservoir in the study area account for 66.7%–91.7% of the total surface porosity, with an average of 82.9%. Meanwhile, the intergranular pores account for 5.0%–24.0% of the total surface porosity, with an average of 10.3%. Dissolution is the main factor for the formation of secondary pores and the improvement of reservoir physical properties.
2) Superimposed sand bodies, nose-shaped uplifts, dominant facies and eroded paleo-highlands have significant effects on the hydrocarbon accumulation. The hydrocarbon migration and accumulation mode of the Chang 1 reservoir belongs to the ladder-like climbing migration + structural ridge accumulation type. In addition, sand body thickness is an important controlling factor for the hydrocarbon accumulation.

(3) At present, the discovered crude oil in the Chang 1 Member is distributed in the areas with thick sand bodies (>20 m), and most of the sand bodies have a thickness in the range of 25–40 m, and the effective thickness is in the range of 2–6 m. In addition, the eroded highlands are the highest topographic units, they are favorable areas for the large-scale accumulation of oil and gas.

Data availability statement

The original contributions presented in the study are included in the article/Supplementary Material, further inquiries can be directed to the corresponding author.

Author contributions

CJ is responsible for the idea and writing of this paper, and CX, MS, XL, and LW are responsible for the experiments and analysis.

Conflict of interest

Authors CJ, MS, and LW were employed by the company Shaanxi Yanchang Petroleum (Group) Corp. Ltd. and authors CX and XL were employed by the Fifth Oil Production Plant of Petrochina Changqing Oil Field Company.

Publisher's note

All claims expressed in this article are solely those of the authors and do not necessarily represent those of their affiliated organizations, or those of the publisher, the editors and the reviewers. Any product that may be evaluated in this article, or claim that may be made by its manufacturer, is not guaranteed or endorsed by the publisher.

References

Abdel-Fattah, M., Sen, S., Abuzied, S., Abioui, M., Radwan, A., and Benssaou, M. (2022). Facies analysis and petrophysical investigation of the late miocene abu madi sandstones gas reservoirs from offshore baltim east field (nile delta, Egypt). *Mar. Petroleum Geol.* 137. doi:10.1016/j.marpetgeo.2021.105501105501

Asante-Okyere, S., Ziggah, Y. Y., and Marfo, S. A. (2021). Improved total organic carbon convolutional neural network model based on mineralogy and geophysical well log data. *Unconv. Resour.* 1, 1–8. doi:10.1016/j.uncres.2021.04.001

Bukar, M., Worden, R., Bukar, S., and Shell, P. (2021). Diagenesis and its controls on reservoir quality of the Tambar oil field, Norwegian North Sea. *Energy Geosci.* 2 (1), 10–31. doi:10.1016/j.engeos.2020.07.002

Cui, X., and Radwan, A. E. (2022). Coupling relationship between current *in-situ* stress and natural fractures of continental tight sandstone oil reservoirs. *Interpretation* 10 (3), SF9–SF21. doi:10.1190/INT-2021-0200.1

El-Gendy, N., Radwan, A. E., Waziry, M., Dodd, T., and Barakat, M. (2022). An integrated sedimentological, rock typing, image logs, and artificial neural networks analysis for reservoir quality assessment of the heterogeneous fluvial-deltaic Messinian Abu Madi reservoirs, Salma field, onshore East Nile Delta, Egypt. *Mar. Petroleum Geol.* 145. doi:10.1016/j.marpetgeo.2022.105910105910

Enayati-Bidgoli, A., and Saemi, E. (2019). Effects of late diagenesis on primary reservoir quality of a quartz arenite unit: A case study from the lower cretaceous successions of SW Iran. *Pet. Sci.* 16 (2), 267–284. doi:10.1007/s12182-019-0306-x

Haile, B. G., Klausen, T. G., Czarniecka, U., Xi, K., Jahren, J., and Hellevang, H. (2018). How are diagenesis and reservoir quality linked to depositional facies? A deltaic succession, edgeøya, svalbard. *Mar. Petroleum Geol.* 92, 519–546.

Huang, Y. G., Chen, Z. Q., Wignall, P. B., Grasby, S. E., Zhao, L. S., Wang, X. D., et al. (2019). Biotic responses to volatile volcanism and environmental stresses over the Guadalupian-Lopingian (Permian) transition. *Geology* 47, 175–178. doi:10.1130/G45283.1

Jiang, W., Zhang, P., Li, D., Li, Z., Wang, J., Duan, Y., et al. (2022). Reservoir characteristics and gas production potential of deep coalbed methane: Insights from the No. 15 coal seam in shouyang block, Qinshui Basin, China. *Unconv. Resour.* 2, 12–20. doi:10.1016/j.uncres.2022.06.001

Katz, B., Gao, L., Little, J., and Zhao, Y. R. (2021). Geology still matters – unconventional petroleum system disappointments and failures. *Unconv. Resour.* 1, 18–38. doi:10.1016/j.uncres.2021.12.001

Khan, E. U., Saleem, M., Naseem, A. A., Ahmad, W., Yaseen, M., and Khan, T. U. (2020). Microfacies analysis, diagenetic overprints, geochemistry, and reservoir quality of the jurassic samanasuk. Formation at the kahi section, nizampur basin, NW himalayas, Pakistan. *Carbonates Evaporites* 35 (3), 95–96. doi:10.1007/s13146-020-00622-4

Li, S. H., Fang, G. Q., Yang, J. L., Liao, J. B., and Fan, J. M. (2012). Origin of ultra-low permeability reservoirs in Ordos Basin and its significance. *Lithol. Reserv.* 24 (6), 32–37. doi:10.3969/j.issn.1673-8926.2012.06.008

Li, Z., Xi, S., Feng, S., and Liu, X. (2016). 150 million year history of north China craton disruption preserved in mesozoic sediments of the Ordos Basin. *Int. Geol. Rev.* 58 (11), 1417–1442. doi:10.1080/00206814.2016.1166351

Liao, J. B., Xi, A. H., Liang, S. J., Zhou, X. P., Li, Z. Y., Di, J., et al. (2020). Genetic mechanisms of deep-water massive sandstones in continental lake basins and their significance in micro–nano reservoir storage systems: A case study of the Yanchang Formation in the Ordos Basin. *Nanotechnol. Rev.* 9, 489–503. doi:10.1515/ntrev-2020-0040

Liu, B., Yang, Y., Li, J., Chi, Y., Li, J., and Fu, X. (2020). Stress sensitivity of tight reservoirs and its effect on oil saturation: A case study of lower cretaceous tight clastic reservoirs in the hailar basin, northeast China. *J. Petroleum Sci. Eng.* 184. doi:10.1016/j.petrol.2019.106484106484

Liu, C., Zhao, H., and Sun, Y. (2009). Tectonic background of Ordos Basin and its controlling role for basin evolution and energy mineral deposits. *Energy Explor. Exploitation* 27 (1), 15–27. doi:10.1260/014459809788708219

Nabawy, B., Abudeif, A., Masoud, M., and Radwan, A. (2022). An integrated workflow for petrophysical characterization, microfacies analysis, and diagenetic attributes of the Lower Jurassic type section in northeastern Africa margin: Implications for subsurface gas prospection. *Mar. Petroleum Geol.* 140. doi:10.1016/j.marpetgeo.2022.105678105678

Radwan, A. E. (2022). "Chapter Two - three-dimensional gas property geological modeling and simulation," in *Sustainable geoscience for natural gas sub-surface systems*. Editors D. A. Wood and J. Cai (Elsevier), 29–45. Chapter 2 in. doi:10.1016/B978-0-323-85465-8.00011-X

Su, Y., Zha, M., Jiang, L., Ding, X., Qu, J., Jin, J., et al. (2022). Pore structure and fluid distribution of tight sandstone by the combined use of SEM, MICP and X-ray micro-CT. *J. Petroleum Sci. Eng.* 208, 109241–109245. doi:10.1016/j.petrol.2021.109241

Sun, Y., Chen, C., and Ma, S. Z. (2013). Hydrocarbon migration mechanism and accumulation models of the fuyu oil layer in southern fuxin uplift, songliao basin. *Geol. Rev.* 59 (3), 501–509.

Sun, Y., Zhang, J. Y., and Ma, S. Z. (2014). Analysis of high-resolution sequence stratigraphy of Fuyu oil layer in the southern Fuxin Uplift. *Geol. Rev.* 3, 473–480.

Wang, A., Zhong, D. K., Zhu, H. H., Guo, L., Zheng, X., Jiang, Y., et al. (2019). Depositional and diagenetic controls on the reservoir quality of Upper Triassic Chang-7 tight oil sandstones, southwestern Ordos basin, China. *Geosci. J.* 23 (3), 471–488.

Wang, J., Fu, Y., Yan, Z., Fu, J., Xie, J., Li, K., et al. (2021). Influence of sedimentation and diagenesis on reservoir physical properties: A case study of the funing formation, subei basin, eastern China. *Front. Earth Sci.* 45, 892–908. doi:10.1007/s11707-020-0836-y

Wang, Z., and Yang, G. Q. (2017). Some research hot spots of tight oil and gas reservoir. *Chin. foreign energy* 16 (8), 37–42.

Yin, S., Dong, Li., Yang, Xia., and Wang, R. (2020). Experimental investigation of the petrophysical properties, minerals, elements and pore structures in tight sandstones. *J. Nat. Gas Sci. Eng.* 76 (1), 1–14. doi:10.1016/j.jngse.2020.103189

Zhang, B., Shen, B., and Zhang, J. (2020). Experimental study of edge-opened cracks propagation in rock-like materials. *J. Min. Strata Control Eng.* 2 (3). doi:10.13532/j.jmsce.cn10-1638/td.20200313.001033035

Zhang, Q., Wu, X., Radwan, A. E., Wang, B., Wang, K., Tian, H., et al. (2022). Diagenesis of continental tight sandstone and its control on reservoir quality: A case study of the quan 3 member of the cretaceous quantou formation, fuxin uplift, songliao basin. *Mar. Petroleum Geol.* 145. doi:10.1016/j.marpetgeo.2022.105883105883

Zhang, Q., Zhu, X. M., Steel, R. J., Wang, G., and Ji, H. (2014). Fluid inclusions and their application in hydrocarbon history and genesis. *Petroleum Sci. Technol.* 32, 2911–2920. doi:10.1080/10916466.2014.933976

Zhang, Y., Bao, Z., Zhao, Y., Jiang, L., and Gong, F. (2017). Diagenesis and its controls on reservoir properties and hydrocarbon potential in tight sandstone: A case study from the upper triassic Chang 7 oil group of Yanchang Formation, Ordos Basin, China. *Arab. J. Geosci.* 10 (11), 234–240. doi:10.1007/s12517-017-3023-z

frontiers | Frontiers in Earth Science

TYPE Original Research
PUBLISHED 20 January 2023
DOI 10.3389/feart.2022.1059838

OPEN ACCESS

EDITED BY
Wenlong Ding,
China University of Geosciences, China

REVIEWED BY
Xiaoping Liu,
China University of Petroleum, Beijing, China
Chin Yik Lin,
University of Malaya, Malaysia

*CORRESPONDENCE
Haizhou Qu,
quhaizhou@swpu.edu.cn

SPECIALTY SECTION
This article was submitted to Structural Geology and Tectonics, a section of the journal Frontiers in Earth Science

RECEIVED 02 October 2022
ACCEPTED 21 November 2022
PUBLISHED 20 January 2023

CITATION
Zou B, Qu H, Zhao R, Zhang L, Zhang Y, Ma Z, Zhang X, Huang Q, Mo Q, An H and Pei Y (2023), Diagenesis of the first member of Canglangpu Formation of the Cambrian Terreneuvian in northern part of the central Sichuan Basin and its influence on porosity.
Front. Earth Sci. 10:1059838.
doi: 10.3389/feart.2022.1059838

Diagenesis of the first member of Canglangpu Formation of the Cambrian Terreneuvian in northern part of the central Sichuan Basin and its influence on porosity

Bing Zou[1,2], Haizhou Qu[1,2]*, Rongrong Zhao[3], Lianjin Zhang[4], Yu Zhang[3], Zike Ma[4], Xingyu Zhang[1,2], Qinyang Huang[1,2], Qianwen Mo[3], Hongyi An[3] and Yu Pei[5]

[1]State Key Laboratory of Oil and Gas Reservoir Geology and Exploitation, Southwest Petroleum University, Chengdu, China, [2]School of Geoscience and Technology, Southwest Petroleum University, Chengdu, China, [3]Exploration Department of PetroChina Southwest Oil and Gasfield Company, Chengdu, China, [4]Central Sichuan Oil and Gas Mine of PetroChina Southwest Oil and Gas Field Company, Suining, China, [5]Geological Exploration & Development Research Institute, CNPC Chuanqing Drilling Engineering Company Limited, Chengdu, China

In this paper, taking the first Member of the Canglangpu Formation of the Cambrian Terreneuvian in the northern central Sichuan Basin as an example, the diagenesis and its influence on porosity are systemically studied based on the observations and identifications of cores, casts and cathodoluminescence thin sections. The results show that the rock types of the first member of Canglangpu Formation are various, including mixed rocks, carbonate rocks and clastic rocks. The specific lithology is dominated by sand-bearing oolitic dolomite, sandy oolitic dolomite, sparry oolotic dolomite and fine-grained detrital sandstone. At the same time, the Cang 1 Member has experienced five types of diagenetic environments, including seawater, meteoric water, evaporative seawater, shallow burial, and medium-deep burial diagenetic environments. Moreover, the main diagenetic processes under different diagenetic environments include cementation, dissolution, compaction, chemical compaction, dolomitization and structural fractures. According to the analysis, fabric-selective dissolution in meteoric water diagenetic environment, dolomitization in evaporative seawater environment, and non-fabric-selective dissolution, dolomitization and structural fractures in buried diagenetic environment are beneficial to the development of pores. However, cementation, compaction and chemical compaction in medium and deep burial environments, are unfavorable for the development of pores.

KEYWORDS

diagenesis, Terreneuvian, Cambrian, the first member of Canglangpu Formation, Northern part of the Central Sichuan Basin

1 Introduction

The Central Sichuan Paleo-uplift controls the process of hydrocarbon accumulation in the Sinian-Cambrian Terreneuvian in the Sichuan Basin. At present, the exploration horizons in this area are mainly concentrated in the Sinian Dengying Formation and the Cambrian Terreneuvian Longwangmiao Formation, and there are few studies on other horizons. Until Well JT1 in the northern part of the central Sichuan Basin encountered thick dolomite in the Cang 1 Member, and industrial gas flow of 51.62 × 10^4 m^3/d was obtained (Yue et al., 2020), proving that the Canglangpu Formation has great hydrocarbon exploration potential. According to previous studies, shelf, coastal, platform, tidal flat, slop and delta facies are developed in the Cang 1 Member in the study area (Peng et al., 2020; Yan et al., 2020; Ma et al., 2021; Li et al., 2021a; Wang et al., 2022). Influenced by the Kangdian Ancient Continent in the west and the Chengguan complex rock masses in the northwest part, a set of "mixed sediments" of interbedded terrigenous clasts and carbonate rocks were deposited in the Cang 1 Member of the Canglangpu Formation (Yan et al., 2020). In a broad sense, mixed sediments refer to the mixing of terrigenous clastic and carbonate components in the same rock layer and the mixing of interbedded clastic and carbonate rocks (Zhang and Ye, 1989; Sha, 2001; Li et al., 2021b). At present, many previous studies have been carried out on the lithology identification, sedimentary facies, sequence stratigraphy and reservoir properties of the Canglangpu Formation in the study area (Wang et al., 2018; Peng et al., 2020; Wen et al., 2020; Yan et al., 2020; Li et al., 2021a; Dong et al., 2021; Ma et al., 2021; Yan et al., 2021; Li et al., 2022a; Wang et al., 2022), but there is no report on the diagenesis of the Cang 1 Member of the Canglangpu Formation and its influence on porosity. Thus, this paper will study the diagenesis of the Cang 1 Member of the Canglangpu Formation and its influence on porosity.

2 Geological background

The Sichuan Basin lies within the Middle and Upper Yangtze Craton and is a sedimentary basin bounded by folds and faults. The study area is located in the northern part of the central

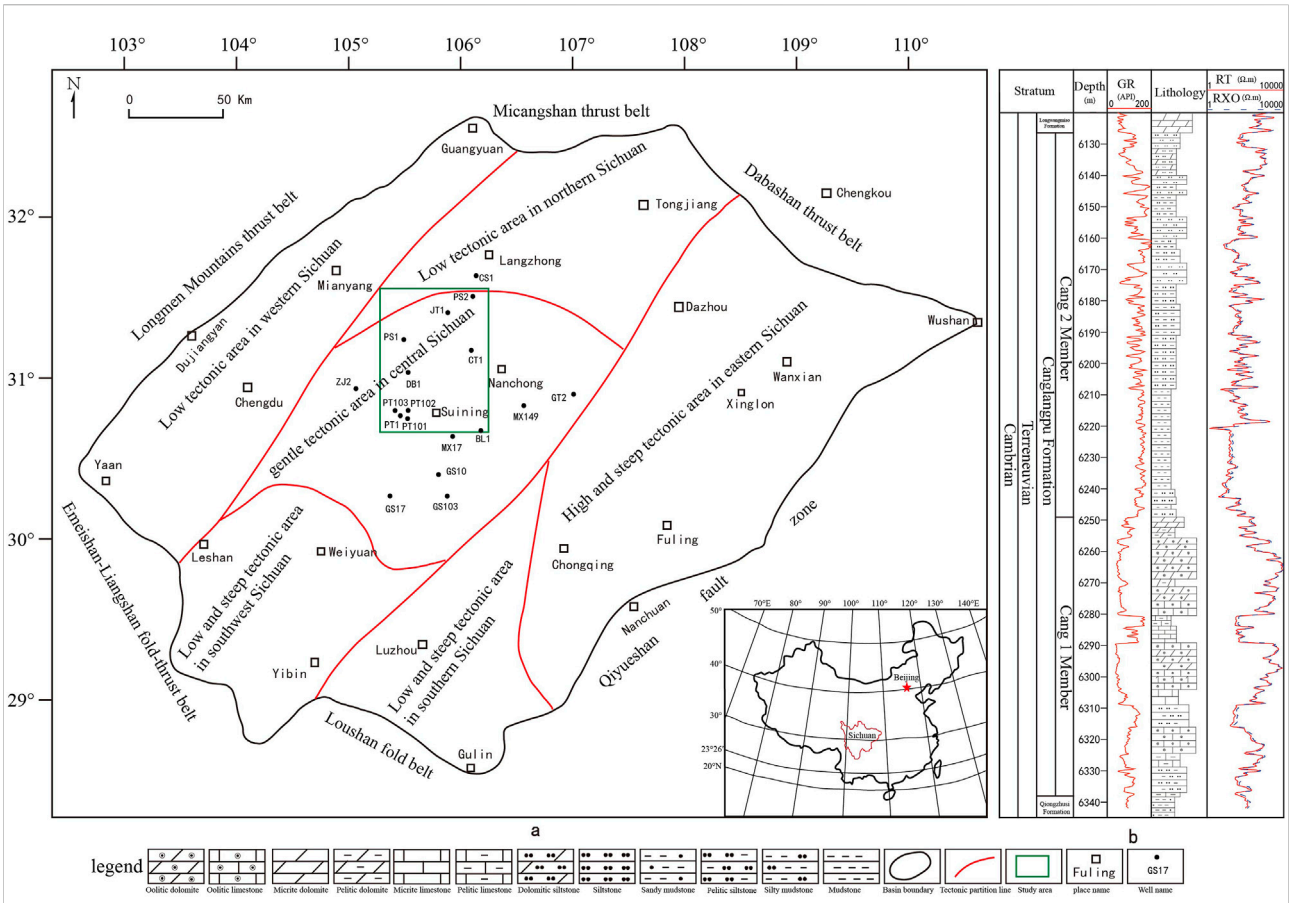

FIGURE 1
Location and comprehensive stratigraphic histogram of the study area. **(A)** Structural unit division of the Sichuan Basin (modified from Reference Hu et al., 2021); **(B)** Lithologic histogram of the Canglangpu Formation in Well CT1. GR: natural gamma ray; Rt: true formation resistivity; Rxo: flushed zone formation resistivity.

Sichuan Basin. It is located in the gentle tectonic zone of the central Sichuan Basin (Figure 1A) (Hu et al., 2021). The Canglangpu Formation is called "lower red bed" (Wang et al., 2014). According to its lithologic types and lithologic assemblages, the Canglangpu Formation can be divided into the Cang 1 and Cang 2 Members. During the Cang 1 Member period, the clastic and carbonate rocks were mainly developed on the west side of the Deyang-Anyue Rift Trough, while the carbonate rocks were mainly developed on the east side. During the Cang 2 Member period, the rifting trough was filled up, and clastic rocks were mainly deposited (Yan et al., 2020) (Figure 1B).

3 Samples and methods

Cores from Wells CT1, PS1, PS2, PT101 and DB1 in the study area are selected for core observations. 10% HCl was used to identify calcite and dolomite in the cores. At the same time, a total of 147 thin sections were prepared from cores that sampled uniformly from five Wells (CT1, PS1, PS2, PT101 and DB1). Alizarin red S and potassium ferricyanide were used to stain thin sections, and an EISS microscope (model: AXIO Scope. A1) was used to distinguish dolomite, calcite, ferric dolomite, and ferric calcite. Observations and identifications of lithology and analysis of the diagenetic process of the Cang 1 Member are the basis of the restoration of diagenetic processes. Then, 21 thin sections with well-developed cements were selected from 147 thin sections. The lithology mainly includes sand-bearing oolitic dolomite, sandy oolitic dolomite, sparry oolitic dolomite, sparry oolitic limestone and fine-grained lithic sandstone. Cathodoluminescence microscope (model: CL 8200 MK5) was used. When the voltage was 9–11 V, the exposure time was adjusted to about 3 s. The luminescence characteristics of various rock components were observed, and the stages of cements were distinguished. Combined with the characteristics of diagenesis, the diagenetic stage, diagenetic environment and diagenetic sequence were divided.

4 Results

4.1 Petrological features

The rock types of the target layer are mainly include mixed rocks, carbonate rocks and clastic rocks.

4.1.1 Mixed rocks

At present, the classification of mixed rocks has not been unified. Its classification scheme was first proposed by Mount (1984), and four end members of terrigenous clasts, dissimilar grains, stucco and argillaceous clay were selected to classify peperite. After that, Zhang (2000) defined mixed sediments with a carbonate content of 5%–95% and terrigenous clastic content of 5%–95% as peperite; Dong et al., 2007 classified rocks containing both terrigenous clasts and carbonate components as mixed rocks (0% < terrigenous clastic content <100%, 0% < carbonate content <100%); Yang and Sha, 1990 classified mixed sediments with carbonate composition >25% and terrigenous clast >10% as mixed rocks.

In this paper, Zhang's classification scheme of mixed rocks, that widely adopted by researchers, is used. That is, mixed sediments with carbonate content of 5%–95% and terrigenous clastic content of 5%–95%, called peperite. The mixed rocks types of the target layer in the study area mainly include sand-bearing oolitic dolomite, sandy oolitic dolomite and a small amount of sand-bearing oolitic limestone and sandy oolitic limestone.

Sand-bearing (sandy) oolitic dolomite: The terrigenous clastic particles are mainly sand-grade quartz, detritus, and a very small amount of feldspar. The particle size is 0.05–0.6 mm, and concentrated in 0.1–0.25 mm, and fine sand is dominant. The particles are sub-angular-sub-round with moderate roundness. In addition, the oolites have a particle size of 0.3–1 mm and are concentrated at 0.5–1 mm. Strong dolomitization occurs inside the oolites, and the powder-fine-grained metasomatic dolomite grains are usually in point contacts or line contacts (Figures 2A,B).

Sand-bearing (sandy) oolitic limestone: The terrigenous clastic particles are mainly terrigenous quartz and lithic debris. Its particle size is distributed in 0.05–0.3 mm, and concentrated in 0.1–0.25 mm. Fine sand is predominant, and the particles are sub-angular-sub-round with moderate roundness. In addition, the particle size distribution of oolites is 0.15–0.6 mm, and concentrated in 0.3–0.5 mm. The oolites are dominated by radial oolis, with a small amount of epidermal and oval oolites (Figure 2C).

4.1.2 Carbonate rocks

The carbonate rocks have a terrigenous clastic content less than 5% and a carbonate content more than 95%. Moreover, they are mainly composed of sparry oolitic dolomite and a small amount of sparry oolitic limestone, silty crystalline dolomite and limestone-dolomite transition rocks.

Sparry oolitic dolomite: The particles are mainly oolitic, with small amounts of terrigenous detritus (such as quartz and rock debris) and biodetritus (such as crinoids and trilobites). Among them, the content of terrigenous clasts and bioclasts are both less than 5%. In addition, there are also a small amount of sand clasts locally. The particle size distribution of the oolites is 0.3–1 mm, and they are concentrated at 0.5–1 mm. Strong dolomitization occurs inside the oolites, and polycrystalline or residual oolites are easily found (Figures 2D,E). In addition, small amounts of crinoids stems and trilobite fragments were seen as cores of oolites or as separate granules. Among them, the stems of crinoids usually have a lath-like shape, and they have a single-

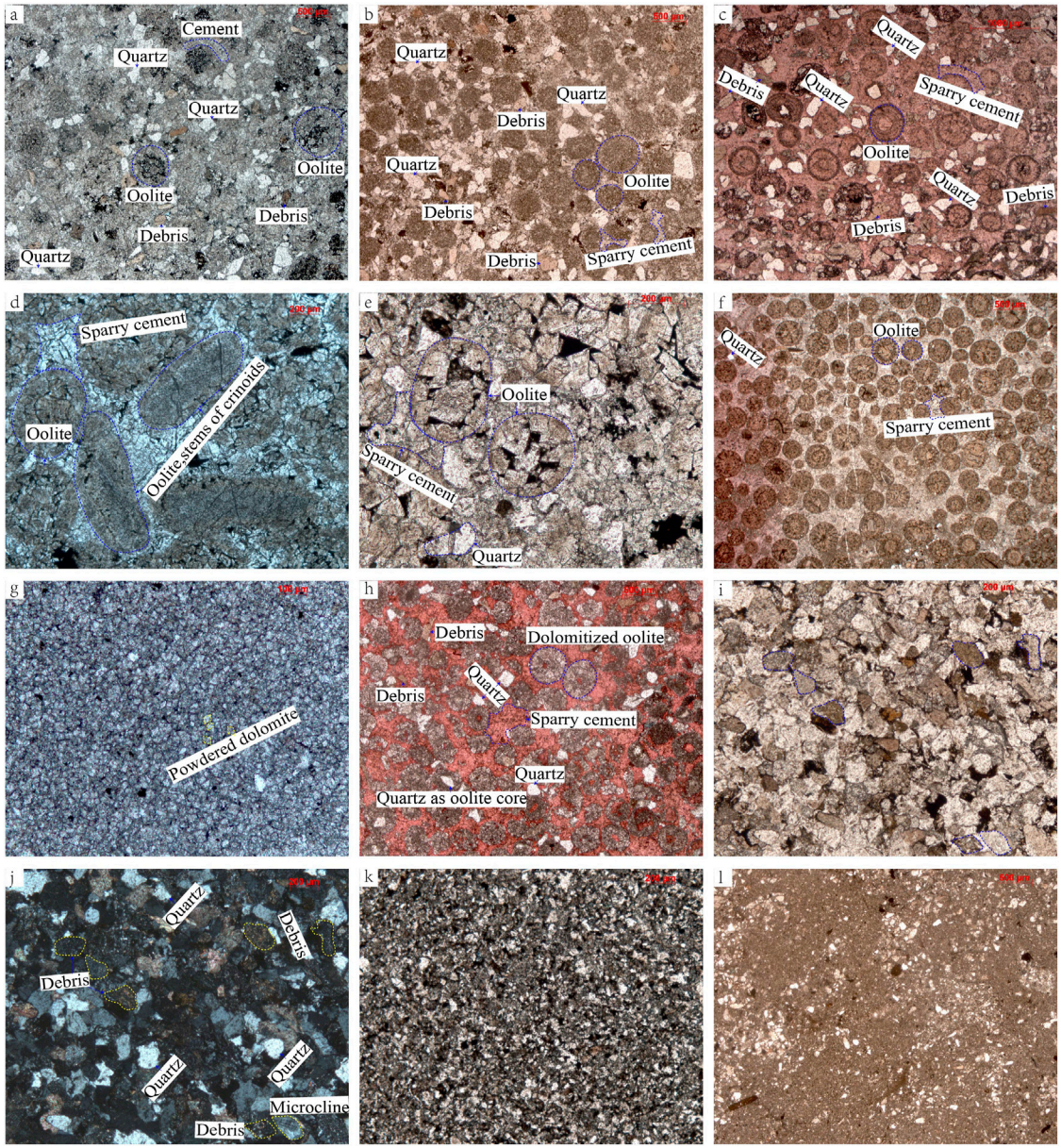

FIGURE 2
Microscopic structural features of the rock in the target layer. **(A)** Sand-bearing oolitic dolomite, Well DB1, 5942.7 m, single polarized, dyed cast thin section; **(B)** Sandy oolitic dolomite, Well PS1, 6784.21 m, single polarized light, dyed cast thin section; **(C)** Sand-bearing limestone, Well CT1, 6299.5 m, single polarized light, dyed cast thin section; **(D)** Sparry oolitic dolomite, Crinoid stems can be seen occasionally, Well DB1, 5915.7 m, single polarized, dyed cast thin section; **(E)** Sparry oolitic dolomite, Well CT1, 6273.18 m, single polarized light, dyed cast thin section; **(F)** Sparry oolitic limestone, Well CT1, 6301.31 m, single polarized light, dyed cast thin section; **(G)** powder dolomite, Well PS1, 6779.41 m, single polarized, dyed cast thin section; **(H)** Dolomite oolitic limestone, Well PS2, 7303.88 m, single polarized light, dyed cast thin section; **(I)** Fine-grained detrital sandstone, Well PT101, 5024.38m, single polarized light, dyed cast thin section; **(J)** Cross-polarized light image of sample i; **(K)** Siltstone, Well PS1, 6777.82 m, single polarized light, dyed cast thin section; **(L)** Silt mudstone, Well DB1, 5950.7 m, single polarized light, dyed cast thin section.

structure (Figure 2D); whereas, trilobites have a curved morphology and a wavy extinction structure.

Sparry oolitic limestone: The grains are mainly oolites, followed by a small amount of terrigenous quartz and detritus, the content of which is less than 5%. The particle size of the oolites is 0.2–1.5 mm, and the distribution is concentrated at 0.5–1 mm. Oolites are mostly spherical, while a few are oval. Oolites are mainly normal oolites with a core thickness greater than that of the concentric layers. A small number are epidermal oolite with a core thickness smaller than

TABLE 1 Rock characteristic of the first member of Canglangpu Formation.

Lithology	Characteristics of terrigenous detritus					Characteristics of carbonate components			
	Terrigenous particles			Argillaceous content (%)	Dolomite content (%)	Calcite content (%)	Oolite		
	Conten (%)	Main particle size (mm)	Sorting and rounding				Main types	Main particle size (mm)	Crystal content (%)
Sand-bearing (sandy) oolitic dolite	5–25 (25–50)	0.1–0.25	Well, moderate	0	5–95	0	Polycrystalline oolite, Residual oolitic	0.5–1	0
Sand-bearing (sandy) oolitic limestone	5–25 (25–51)	0.1–0.26	Well, moderate	0	0	5–95	Radial oolitic	0.3–0.5	0
Sparry oolitic dolomite	0–5	/	/	0	90–100	0–5	Radial oolitic	0.5–1	0
Sparry oolitic limestone	0–5	/	/	0	0–5	90–100	radioactive oolitic	0.5–1	0
Powder crystal dolomite	0–5	/	/	0–5	90–100	0	/	/	90–100
Dolomitic oolitic limestone	0–5	/	/	0	25–50	45–75	Polycrystalline oolite, Residual oolitic	0.2–0.5	0
Lime oolitic dolomite	0–5	/	/	0	45–75	25–50	Polycrystalline oolite, Residual oolitic	0.2–0.5	0
Fine grained lithic sandstone	90–100	0.1–0.25	well、moderate	0–10	/	/	/	/	/
Siltstone	90–100	0.01–0.1	/	0–10	/	/	/	/	/
Silty mudstone	25–50	0.01–0.1	/	50–75	/	/	/	/	/

the concentric layers and oval oolis with an oval shape. In addition, cracks are developed on the surface of the oolites (Figure 2F).

Powder dolomite: The grain size distribution is in the range of 0.005–0.1 mm, and the grains are mainly composed of powder crystal-grade dolomite. Moreover, the grains mostly have rhombic or square morphologies (Figure 2G).

Dolomitic oolitic limestone (Limestone oolitic dolomite): Dolomitization occurs inside the oolites, while there is weak dolomitization between the oolites. The oolites after dolomitization are mostly polycrystalline oolites composed of multiple powder-fine-grained dolomite crystals. In addition, a small number of oolites without dolomitization were mostly normal oolites (Figure 2H).

4.1.3 Clastic rocks

It refers to clastic rocks with terrigenous clastic content greater than 95% and carbonate content less than 5%. The main lithologies include fine-grained detrital sandstone and a small amount of siltstone and silty mudstone.

Fine-grained detrital sandstone: The detrital grains are mainly terrigenous quartz and detritus, with a very small amount of feldspar grains. Among them, the content of terrigenous quartz is 50%–60%, and the content of debris is 30%–50%. The particle size of the debris particles is 0.05–0.5 mm, and the content of the debris particles with a particle size in the range of 0.1–0.25 mm accounts for 80% of the total particle size. In addition, the particles of fine-grained detrital sandstones were mostly sub-angular-sub-round with moderate roundness (Figures 2I,J).

Siltstone: The detrital grains are mainly composed of silt-grade terrigenous quartz and detritus. The particle size is mainly distributed in 0.01–0.1 mm. Moreover, the particle size of a small amount of terrigenous quartz is larger than 0.1 mm, but its proportion is less than 10%. The silt fraction had good sorting and poor roundness (Figure 2K).

Silty mudstone: The detrital particles are mainly silt-grade terrigenous quartz and lithic debris, and their content is between 25% and 50%. The particle size is mainly 0.005–0.1 mm. In addition, its matrix is mainly brown terrigenous mud, and the content is usually between 50% and 75% (Figure 2L).

Through microscopic observation of the above lithology, the microscopic characteristics of each lithology are summarized in detail (Table 1), including the content of carbonate components

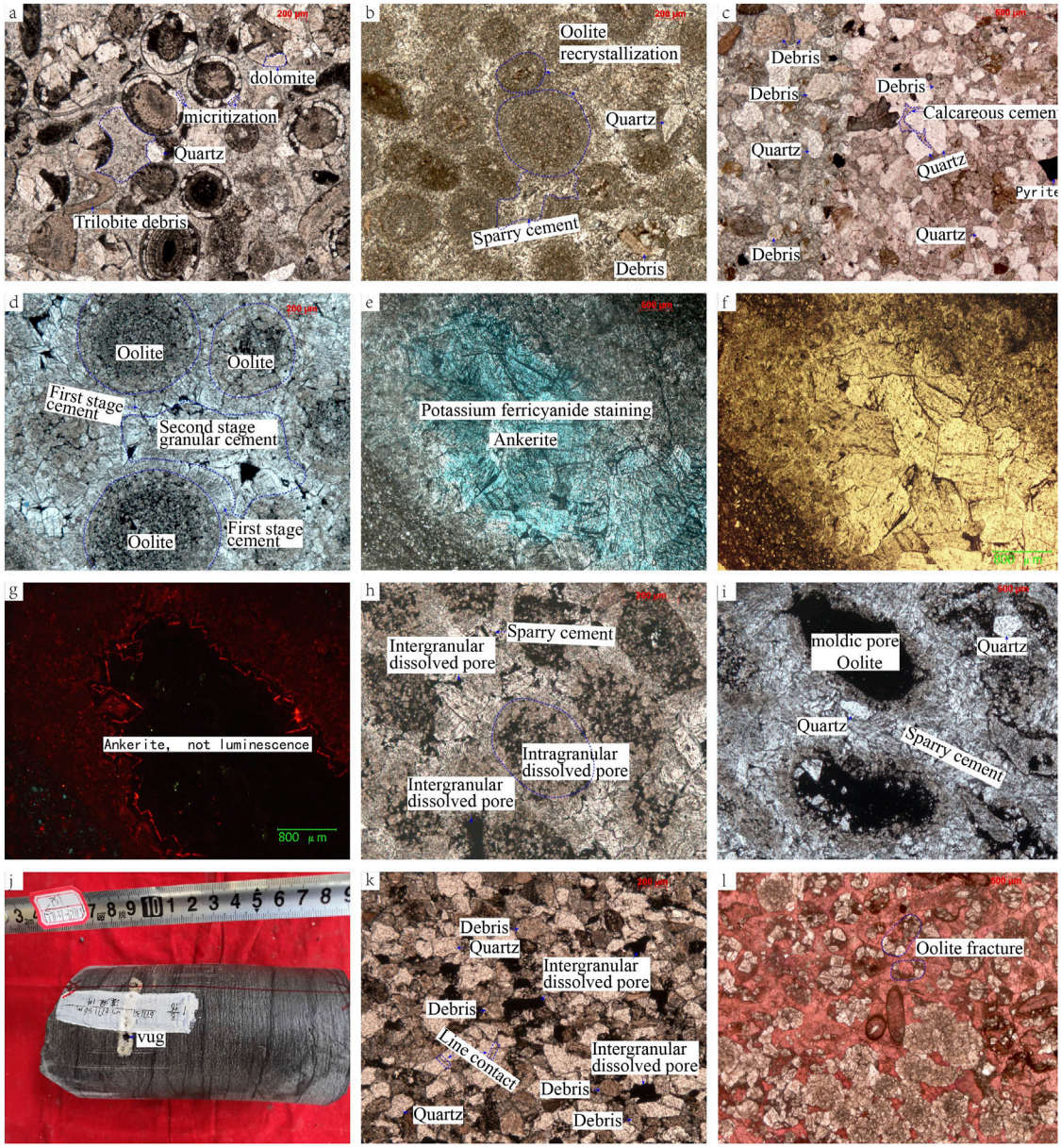

FIGURE 3
Developmental characteristics of typical diagenesisin the study area. **(A)** Micritic sleeves formed by micritization. Dolomite sparry oolitic limestone, Well CT1, 6275.63 m, single polarized light, dyed cast thin section; **(B)** Weak recrystallization occurs inside the oolites. Sparry oolitic dolomite, well PT101, 5018.1 m, single polarized light, dyed cast thin section; **(C)** Calcareous cementation at the edges of quartz grains. Calcareous fine-grained detrital sandstone, Well PT101, 5023.14 m, single polarized light, dyed cast thin section; **(D)** Horse tooth-like cement and granular cement. Sparry oolitic dolomite, Well DB1, 5938.9 m, single polarized light, dyed cast thin section; **(E)** The second phase of ankerite cement. Argillaceous silty dolomite, Well DB1, 5951.7 m, single polarized light, potassium ferricyanide dyed thin section; **(F)** Unstained thin section of sample e; **(G)** Cathodoluminescence image of sample e, the second phase ankerite cement does not emit light; **(H)** Intergranular dissolution (yellow arrows) and intragranular dissolution pores (red arrows) formed by dissolution. Sparry oolitic dolomite, CT1 well, 6264.53 m, single polarized light, dyed cast thin section; **(I)** Mold pores formed by dissolution. Sparry oolitic dolomite, Well CT1, 6268.9 m, single polarized light, dyed cast thin section; **(J)** Pores formed by dissolution, and they are mostly half filled with calcite. Gray sand-bearing oolitic dolomite, Well PS1, 6771.31–6771.56 m, core photo; **(K)** Intergranular pores formed by dissolution. Fine-grained detrital sandstone, Well DB1, 5913.45 m, single polarized light, dyed cast thin section; **(L)** Oolitic broken dolomitic oolitic limestone. Well CT1, 6285.76 m, single polarized, dyed cast thin section.

and terrigenous clastic components, the sorting, rounding and particle size of terrigenous clastic particles, and the type and particle size of oolites.

4.2 Diagenesis process

4.2.1 Diagenesis types and characteristics

According to the microscopic observation results, the diagenesis types of the Cang 1 Member of the Canglangpu Formation in the study area include micritization, recrystallization, cementation, dissolution, compaction, chemical compaction, dolomitization and structural fractures (Zhu, 2014).

Micrization refers to the phenomenon that the edges of carbonate particles are drilled by perforating algae and then filled with micritic calcite (Flügel and Munnecke, 2010). Micritization is weak in the Cang 1 Member of the Canglangpu Formation in the study area. Micritic sleeves formed by micritization are found only in local oolitic limestones. They are usually distributed along the edges of oolitic (Figure 3A).

Recrystallization usually occurs in the internal oolitic of sparry oolitic dolomites and the crystalline dolomite. After recrystallization, the grain size of micrystalline dolomite becomes larger. Furthermore, the micrystalline dolomite is transformed into powder - fine dolomite. Among them, powdery dolomite is dominant (Figure 3B).

The cementation in target clastic rocks is mainly characterized by the circumferential cementation of calcite around terrigenous quartz, lithic debris and feldspar particles (Figure 3C). However, in mixed rocks and carbonate rocks, the cementation mainly develops between oolitic, and the diameter of cementation gradually increases from the edge of oolitic to the pore center. Therefore, the cements are formed at different stages. The first stage was dominated by the horse teeth cements, ctenoid cement and the second stage was dominated by the granular cements (Figure 3D). The second stage of the cement is dyed blue by potassium ferricyanide solution, indicating that the mineral is ankerite, so that the cathode luminescence is not luminescent (Figures 3E–G). The dissolution is significant in the oolitic dolomites (including sparry oolitic dolomites, sand-bearing oolitic dolomites and sandy oolitic dolomites) and fine-grained lithic sandstones in the Cang 1 Member. Intergranular dissolution pores, intra-granular dissolution pores in oolitic dolomites, mold pores and a small number of dissolution caves are developed among oolitic dolomites (Figures 3H–J), while intergranular dissolution pores are developed among detrital particles in fine-grained lithic sandstone, and intra-granular dissolution pores are not developed (Figure 3K). The dissolution of the Cang 1 Member is divided into two stages, include the selective dissolution of fabrics in the meteoric water diagenetic environment and the non-selective dissolution of fabrics in the buried diagenetic environment. In the former, a large number of intergranular dissolved pores, ingranular dissolved pores and a small number of mold pores are formed, while in the latter, a large number of new dissolved pores are formed under the further expansion dissolution of early dissolved pores.

It is found that the compaction is weak in the target carbonate rocks (sparry oolitic dolomite/limestone) and mixed rocks [sand-bearing (sandy) oolitic dolomite]. The (detrital) particles usually show no contact or line contact with each other (Figures 3A,B). However, in clastic rocks (fine-grained lithic sandstone), compaction is strong. Line contact is dominant among the debris particles, followed by point contact and concave-convex contact (Figure 3K). In addition, compaction in the Cang 1 Member also caused ruptures and semi-directional arrangement of oolitic and detrital particles (quartz and debris components) (Figure 3L).

With the increase of compaction, the overburden pressure increases, and the solubility at the contact point of the (detrital) particles increases. Further, chemical compaction occurs, which is manifested as chemical compaction fructures or concave-convex contacts between debris particles (Figures 4A,B).

Strong dolomitization can be observed under the microscope in the Cang 1 Member of the study area. Calcite is mostly metasomatized by dolomite. For example, oolites composed of calcite are usually metasomatized by dolomite and converted to polycrystalline oolites (Figure 4C). By cathodoluminescence observations, it is found that dolomitization of the target layer can be divided into two stages: the first stage occurs in the quasi syngenesis-early stage. Keith and weber (1964) combined C and O isotopes on the basis of Epstein et al., 1953 and Lu (1986) to obtain the empirical formula of paleo-salinity: $Z=2.048 \times (\delta^{13}C+50) + 0.498 \times (\delta^{18}O+50)$. At the same time, on the basis of Urey (1947) and Craig (1965), Keith and Weber (1964) also obtained the empirical formula of paleo-water temperature of Cambrian carbonate rocks: $t=16.9–4.2 (\delta^{18}O + 0.22)+0.13 (\delta^{18}O + 0.22)^2$. After that, Ma et al., 2022 through the C and O isotope values of the samples in the study area and the above two empirical formulas, it is concluded that the sedimentary period of the first member of the Canglangpu Formation in the study area is hot and the water salinity is high (Tables 2, 3). Lin et al., 2014 and Gu (2020) also found that the palaeoclimate environment in the early Cambrian was hot and dry, which was conducive to the penecontemporaneous dolomitization (capillary concentration or evaporation pump). Combined with the luminescence characteristics of dolomite in the cathodoluminescence thin section, it is found that most of the oolites and the first-stage cements are dim luminescence (Figure 4F), which once again confirms that the first stage dolomitization mainly occurs in the penecontemporaneous period. In addition, the second stage dolomitization mainly occurred in the middle-late stage, which is burial

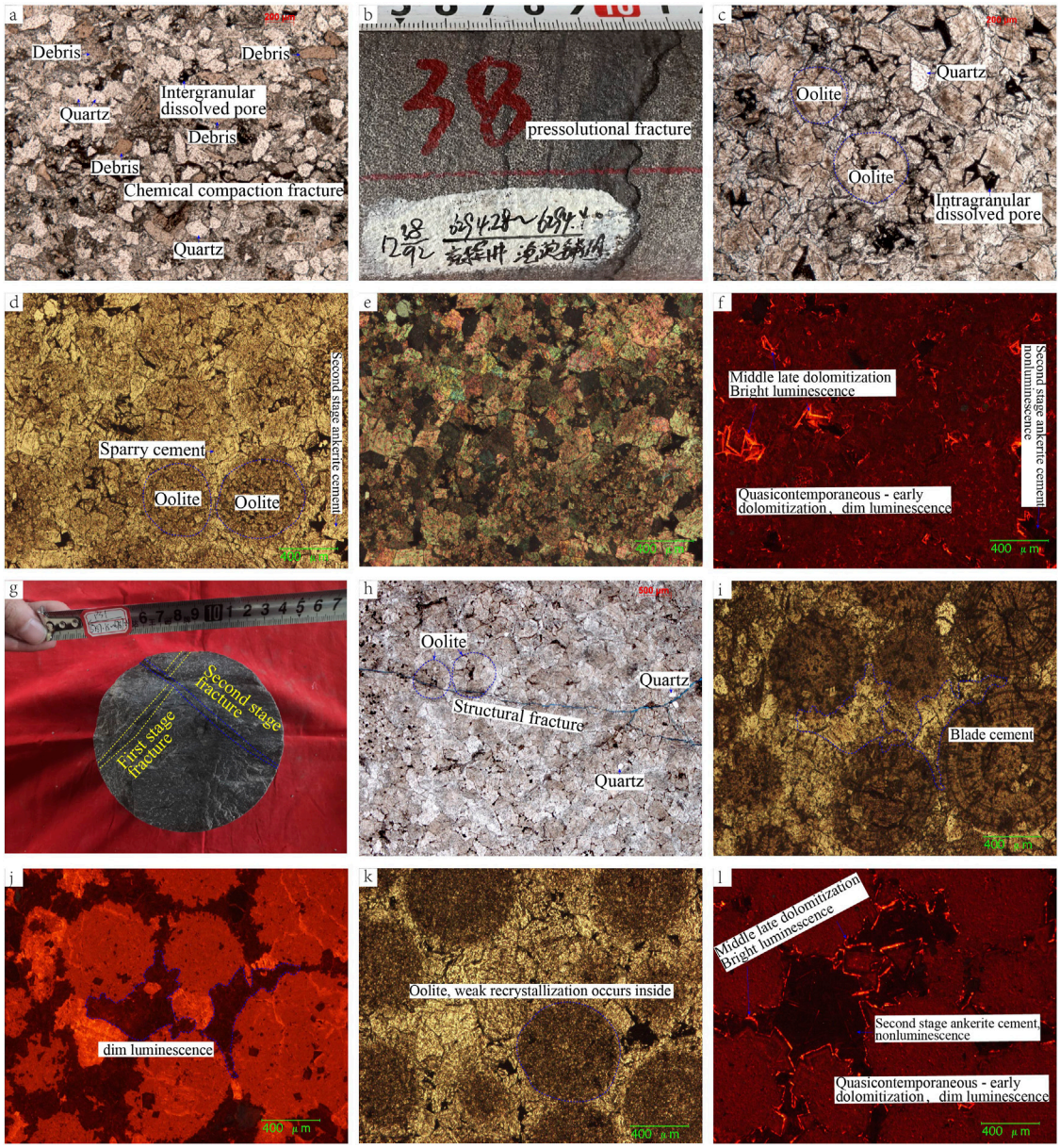

FIGURE 4
Macro and micro features of typical diagenesis observed in the target layer. **(A)** Chemical compaction fracture fully filled with asphalt, fine-grained detrital sandstone, Well PS1, 6783.72 m, single polarized light, dyed cast thin section; **(B)** Chemical compaction fracture fully filled with asphalt, gray sparry oolitic dolomite, 6294.28–6294.40 m, core photo; **(C)** Polycrystalline oolites formed by dolomitization, residual oolitic dolomite, Well CT1, 6273.74 m, single polarized light, dyed cast thin section; **(D)** Sparry oolitic dolomite, Well DB1, 5945.5 m, single polarized light, dyed cast thin section; **(E)** Orthogonal polarized light image of sample d; **(F)** Cathodoluminescence image of sample e; **(G)** The structural dissolution fractures of the first phase are cut by the structural dissolution fractures of the second phase. Gray sand-bearing oolitic dolomite, Well PS1, 6787.15–6787.24 m, core photo; **(H)** Unfilled structural dissolution fractures. Sparry residual oolitic dolomite, Well DB1, 5947.5 m, single polarized light, dyed cast thin section; **(I)** Horses tooth-like cement in seawater diagenetic environment, and its cathodoluminescence characteristic is dim luminescence. Sparry oolitic limestone, Well CT1, 6279.94 m, single polarized light, dyed cast thin section; **(J)** Cathodoluminescence image of sample i; **(K)** Recrystallization in an meteoric water diagenetic environment, and its cathodoluminescence is dim luminescence. Sparry oolitic dolomite, Well DB1, 5944.45 m, single polarized light, dyed cast thin section; **(L)** Cathodoluminescence image of sample k.

dolomitization, mainly developed at the edge of the first stage cement, and the cathode luminescence of metasomatic dolomite is strong (Figure 4F).

The Canglangpu Formation in the study area was in a stable sedimentary stage from the beginning of deposition to the early Devonian. However, during the Early Devonian-Early Permian

10.3389/feart.2022.1059838

TABLE 2 Contents of carbon and oxygen isotopes in the first member of Canglangpu Formation of the Cambrian Terreneuvian in well JT1, central Sichuan Basin (Ma at el., 2022).

Sample No	Lithology	Isotope	
		δ13CV-PDB	δ18OV-PDB
70–6960 m	Powder crystal dolomite	−2.4	−7.7
71–6961 m	Powder crystal dolomite	−0.7	−5.9
72–6962 m	Powder crystal dolomite	−1	−6.3
73–6963 m	Powder crystal dolomite	−3.1	−9.3
74–6964 m	Powder crystal dolomite	−1.6	−6.3
75–6965 m	Powder crystal dolomite	−1.3	−5.9
76–6966 m	Powder crystal dolomite	−3.4	−9.3
77–6967 m	Mudstone	−2.5	−8.8
78–6968 m	Oolitic dolomite	−2.9	−8.9
79–6969 m	Calcareous mudstone	−0.7	−6.5
80–6970 m	Powder crystal dolomite	−1.1	−7.1
81–6971 m	Powder crystal dolomite	−0.6	−6.9
82–6972 m	Powder crystal dolomite	−0.4	−6.2
83–6973 m	Argillaceous dolomite	−0.8	−6.9
85–6975 m	Powder crystal dolomite	−0.9	−7.1
86–6976 m	Powder crystal dolomite	−1.4	−7.1
87–6977 m	Argillaceous dolomite	−0.7	−7.2
88–6978 m	Argillaceous dolomite	−1.3	−7.8
89–6979 m	Argillaceous dolomite	−0.9	−7.5
90–6980 m	Argillaceous dolomite	−1	−8.1
91–6981 m	Powder crystal dolomite	−0.8	−7.3
93–6983 m	Oolitic dolomite	−0.9	−7.6
94–6984 m	Oolitic dolomite	−0.8	−7.4
1–6985 m	Oolitic dolomite	−0.6	−6.9
3–6987 m	Oolitic dolomite	−0.6	−7
4–6988 m	Oolitic dolomite	−0.8	−7
5–6989 m	Oolitic dolomite	−0.8	−7.3
6–6990 m	Oolitic dolomite	−1.6	−8.6
7–6991 m	Oolitic dolomite	−1.8	−7.7
8–6992 m	Oolitic dolomite	−1.1	−7.4
10–6994 m	Calcareous mudstone	−1.9	−9.6
11–6995 m	Calcareous mudstone	−2	−9.5
12–6996 m	Argillaceous limestone	−1.8	−9.9
13–6997 m	Argillaceous limestone	−0.9	−8.5
17–7001 m	Oolitic limestone	−1.7	−9.7
18–7002 m	Oolitic limestone	−1.9	−9.1
19–7003 m	Oolitic limestone	−1.5	−8.4
20–7004 m	Oolitic limestone	−2.1	−9.8
21–7005 m	Oolitic limestone	−1.5	−8.9
23–7007 m	Oolitic limestone	−1.3	−9.2
24–7008 m	Oolitic limestone	−1.4	−9.5
25–7009 m	Oolitic limestone	−1.2	−10
38–7022 m	Oolitic limestone	−0.9	−10
40–7024 m	Oolitic limestone	−1.4	−9.2
41–7025 m	Sandy limestone	−1.3	−8.4

(Continued on following page)

TABLE 2 (*Continued*) Contents of carbon and oxygen isotopes in the first member of Canglangpu Formation of the Cambrian Terreneuvian in well JT1, central Sichuan Basin (Ma at el., 2022).

Sample No	Lithology	Isotope	
		δ13CV-PDB	δ18OV-PDB
42–7026 m	Sandy limestone	−1.5	−9.3
43–7027 m	Sandy limestone	−1.5	−8.2
44–7028 m	Sandy limestone	−2.1	−9
46–7030 m	Sandy limestone	−1.6	−8.8
48–7032 m	Sandy limestone	−2.1	−9.2
50–7034 m	Sandy limestone	−1.4	−9
52–7036 m	Sandy limestone	−2.1	−9.5
53–7037 m	Oolitic limestone	−1.5	−8.7
55–7039 m	Oolitic limestone	−2.1	−10

periods, due to the influence of the Hercynian Movement, strong tectonic uplift occurred in the central Sichuan region, and a large number of fractures were formed in the rocks. After the Cretaceous, the margin of the basin was continuously compressed into the basin by the Yanshanian and Himalayan Movements, and the strata were continuously folded and uplifted. Continuous tectonic activities are the direct cause of the formation of fractures in rocks (Mei, 2015; Wang, 2016; Li et al., 2019; Li, 2022b; Li J. et al., 2022c; Li H. et al., 2022d). The structural fractures of the target layer mainly occurred in the Hercynian and Yanshanian-Himalayan periods. Fractures generated during the Yanshanian-Himalayan period cut the fractures generated during the Hercynian period (Figure 4G). Moreover, the fractures experienced strong dissolution at the later stage of deposition, and then the structural dissolution fractures were formed. This kind of structural dissolution fractures are mostly filled with asphalt, dolomite and pyrite, and a small amount is not filled (Figures 4G,H).

4.2.2 Diagenetic environment and stages

Diagenetic environment refers to the physical and chemical conditions that cause changes in the properties of sediments and early sedimentary rocks (Zhou and Zhang, 1993). According to the properties and occurrence states of diagenetic fluids (pore water), the diagenetic environments of the Cang 1 Member can be divided into seawater diagenetic environment, meteoric water diagenetic environment, evaporative seawater diagenetic environment and buried diagenetic environment (Moore, 1989; Zhou et al., 1993). According to the luminous characteristics of each component in the cathodoluminescent thin section of the study area, the types and characteristics of diagenesis, it is found that the first member of Canglangpu Formation has experienced seawater diagenetic environment, meteoric water diagenetic environment, evaporation seawater diagenetic environment and burial diagenetic environment. The diagenetic stages include syngenetic stage, quasi syngenetic stage, early diagenetic stage and middle-late diagenetic stage.

4.2.2.1 Seawater diagenetic environment (syngenetic stage)

The seawater diagenetic environment is the early external environment of marine carbonate rocks after deposition (Hang, 2010). Typical diagenetic types in seawater diagenetic environments include micritization, equithick fibrous ring-edge cementation, disorderly needle-like cementation, bladed cementation and fibrous calcite cementation, etc. (Huang., 2010; Qiang., 1998). A large number of horse tooth cements and slight micritic sleeve were formed in the Cang 1 Member under seawater diagenetic conditions (Figure 3A). And its cathodoluminescence tests showed dim luminescence (Figures 4I,J).

4.2.2.2 Meteoric water diagenetic environment (quasi-syngenetic stage)

The meteoric water diagenetic environment refers to the mixed environment between the surface and freshwater and seawater (Huang, 2010). In meteoric water environment, the pores are filled with atmospheric water and air. The pore fluid is rich in CO_2 and has strong solubility. The selective dissolution of the fabric promotes the formation of dissolved pores and mold pores. At the same time, strong cementation leads to the formation of crescentic and gravity cementation. The target layer mainly showed weak recrystallization (Figure 3D) and selective dissolution of the fabric in the meteoric water diagenetic environment. The former showed dim luminescence under the cathodoluminescence tests (Figures 4K,L), while the latter showed the formation of a large number of intragranular dissolved pore and a small number of mold pores (Figures 3H,I).

10.3389/feart.2022.1059838

TABLE 3 Date of paleotemperature and paleo-salinity of the first member of Canglangpu Formation of the Cambrian Terreneuvian from well JT1 in central Sichuan Basin (Ma at el., 2022).

Sample No	Paleo-salinity index Z	Uncorrected paleo-salinity S/‰	Corrected paleo-salinity S/‰	Paleo-water temperature/°C
70–6960 m	119	27.1	34.1	18.9
71–6961 m	123	28.9	35.9	11.6
72–6962 m	122	28.5	35.5	13.1
73–6963 m	116	25.5	32.5	26.2
74–6964 m	121	28.5	35.5	13.1
75–6965 m	122	28.9	35.9	11.6
76–6966 m	116	25.5	32.5	26.2
77–6967 m	118	26	33	23.9
78–6968 m	117	25.9	32.9	24.3
79–6969 m	123	28.3	35.3	13.9
80–6970 m	122	27.7	34.7	16.4
81–6971 m	123	27.9	34.9	15.6
82–6972 m	123	28.6	35.6	12.8
83–6973 m	122	27.9	34.9	15.6
85–6975 m	122	27.7	34.7	16.4
86–6976 m	121	27.7	34.7	16.4
87–6977 m	122	27.6	34.6	16.8
88–6978 m	121	27	34	19.4
89–6979 m	122	27.3	34.3	18.1
90–6980 m	121	26.7	33.7	20.7
91–6981 m	122	27.5	34.5	17.2
93–6983 m	122	27.2	34.2	18.5
94–6984 m	122	27.4	34.4	17.7
1–6985 m	123	27.9	34.9	15.6
3–6987 m	123	27.8	34.8	16
4–6988 m	122	27.8	34.8	16
5–6989 m	122	27.5	34.5	17.2
6–6990 m	120	26.2	33.2	22.9
7–6991 m	120	27.1	34.1	18.9
8–6992 m	121	27.4	34.4	17.7
10–6994 m	119	25.2	32.2	27.6
11–6995 m	118	25.3	32.3	27.2
12–6996 m	119	24.9	31.9	29.1
13–6997 m	121	26.3	33.3	22.5
17–7001 m	119	25.1	32.1	28.1
18–7002 m	119	25.7	32.7	25.3
19–7003 m	120	26.4	33.4	22
20–7004 m	118	25	32	28.6
21–7005 m	120	25.9	32.9	24.3
23–7007 m	120	25.6	32.6	25.7
24–7008 m	120	25.3	32.3	27.2
25–7009 m	120	24.8	31.8	29.6
38–7022 m	120	24.8	31.8	29.6
40–7024 m	120	25.6	32.6	25.7
41–7025 m	120	26.4	33.4	22
42–7026 m	120	25.5	32.5	26.2

(Continued on following page)

TABLE 3 (*Continued*) Date of paleotemperature and paleo-salinity of the first member of Canglangpu Formation of the Cambrian Terreneuvian from well JT1 in central Sichuan Basin (Ma at el., 2022).

Sample No	Paleo-salinity index Z	Uncorrected paleo-salinity S/‰	Corrected paleo-salinity S/‰	Paleo-water temperature/°C
43–7027 m	120	26.6	33.6	21.1
44–7028 m	119	25.8	32.8	24.8
46–7030 m	120	26	33	23.9
48–7032 m	118	25.6	32.6	25.7
50–7034 m	120	25.8	32.8	24.8
52–7036 m	118	25.3	32.3	27.2
53–7037 m	120	26.1	33.1	23.4
55–7039 m	118	24.8	31.8	29.6

4.2.2.3 Evaporative seawater diagenetic environment (quasi-syngenetic stage)

Evaporative seawater diagenetic environment refers to the environment with dry climate and strong evaporation. The early Canglangpu Formation was deposited in an arid and hot paleoclimatic environment (Lin et al., 2014; Gu, 2020). In this environment, calcite is metasomatized by dolomite, and the metasomatized dolomite has dim luminescence under the cathodoluminescence tests (Figures 4F,L).

4.2.2.4 Shallow burial diagenetic environment (early diagenetic stage)

The temperature and pressure in the shallow buried diagenetic environment are close to the surface conditions, and the diagenetic fluids are mainly atmospheric water, seawater and mixed water between them (Huang, 2010). Usually, the diagenetic temperature is lower than 85°C, and the rock is mainly affected by mechanical compaction. Under the overburden load condition, the rock particles will be broken and deformed, and there will be concave-convex contact between the particles (Figure 3L).

4.2.2.5 Medium-deep burial diagenetic stage (middle-late diagenetic stage)

In middle-deep buried diagenetic environments, diagenetic fluids are not directly affected by atmospheric water and sea water, and free oxygen almost does not exist. When carbonate rocks are in medium-deep burial environment, chemical compaction occurs (Huang, 2010). Chemical compaction fractures can be observed for the Cang1 Member in a medium-deep burial diagenetic environment (Figures 4A,B). In addition, two stages of cementation were observed. Strong dolomitization occurred at the edge of the first-stage cement, which manifested as strong luminescence under cathodic luminescence (Figures 4F,L). However, the second stage is the granular cementation of ankerite, which shows no luminescence (Figures 3E–G).

5 Discussion

5.1 Analysis of diagenetic sequence

The Canglangpu Formation conformable contact with the lower Qiongzhusi and the overlying Longwangmiao Formations. Therefore, the burial history of the Qiongzhusi Formation was similar to that of the Canglangpu Formation (Figure 5).

It can be seen from Figure 5 that both the Canglangpu and Qiongzhusi Formations experienced five sedimentary evolution stages, including three settlement-sedimentation stages and two uplift stages. They are stable settlement-sedimentation, stable uplift, rapid settlement-sedimentation, rapid settlement-sedimentation and rapid uplift, respectively. Therefore, from the early Canglangpu Formation to the early Devonian, the Canglangpu Formation was continuously deposited to a buried depth of 2000 m. After that, tectonic uplift occurred, and by the late Carboniferous, the average buried depth was only 800 m. Subsequently, the burial depth of the Canglangpu Formation increased continuously, and another uplift occurred in the early to middle Cenozoic, but the whole Canglangpu Formation was still in a deep burial environment.

According to the types and characteristics of diagenesis, regional tectonic setting, diagenetic environment analysis and burial history construction of the Cang1 Member in the study area, it is believed that the Cang 1 Member in the study area has experienced three major diagenetic stages, include syngeneic and quasi-syngeneic diagenetic stage, early diagenetic stage and middle-late diagenetic stage (Figure 5). According to Figure 5, tectonic uplift occurred in the Canglangpu Formation in the early Devonian and early Cenozoic, but the strata were not uplifted to the surface, so they did not undergo the epigenetic stage. The constructed diagenetic sequence of the Cang1 Member in the study area is shown in Figure 6.

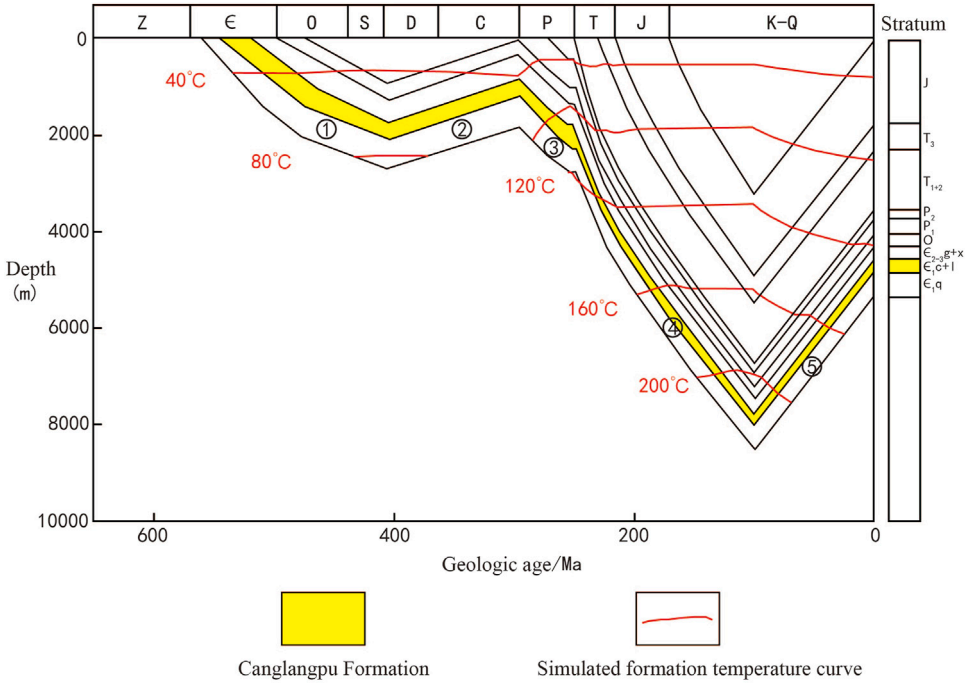

FIGURE 5
Burial history of the Qiongzhusi Formation in Well GS 17 in the Central Sichuan Paleo-uplift (modified from reference Yang et al., 2020). ①: The first stable settlement-sedimentation period; ②: The first stable uplift period; ③: The second rapid settlement-sedimentation period; ④: The third rapid settlement-sedimentation period; ⑤ The second rapid uplift period.

5.2 Influence of diagenesis on pore development

For old strata with complex geological development history, the fundamental factor affecting porosity is no longer the original sedimentary structure, but the modification of diagenesis in the late sedimentary period (Shi et al., 2010). The diagenesis of the first member of Canglangpu Formation in the study area plays a key role in the development of pores, includes diagenesis that facilitates pore development, preservation and diagenesis that reduces surface porosity.

5.2.1 Diagenesis that facilitates to pore development and preservation

Diagenesis beneficial to pore development and preservation in the study area mainly includes Structural fracture, dissolution, dolomitization and the first stage cementation.

Structural fracture: Influenced by the Hercynian, Yanshanian and Himalayan Movements, a large number of tectonic fractures occurred in the Cang 1 Member of the Canglangpu Formation in the study area (Mei, 2015; Wang, 2016). Structural fractures are conducive to the flow of acidic formation water, promote dissolution, expand the original pores and form new dissolution pores. At the same time, when acidic formation water flows through structural fractures, the fractures will also be widened by dissolution, forming structural dissolution fractures, which is more conducive to the development of rock pores. Thus, the more developed the structural dissolution fractures, the more favorable the development of pores (Figure 7).

Dissolution: In the quasi-syngenetic meteoric water diagenetic environment, the selective dissolution of the fabric results in the formation of a large number of intra-granular dissolved pores, intergranular dissolved pores, and mold pores. Furthermore, under the background of the formation of a large number of dissolution pores in the quasi-syngenesis period, acidic fluids and hydrothermal fluids in the burial period can flow better and react adequately with rocks. At this time, the pore size of the early dissolved pores is expanded, and some new intergranular dissolved pores, intra-granular dissolved pores and vugs are formed.

Dolomitization: The early Canglangpu Formation was deposited in an arid and hot paleoclimatic environment (Lin et al., 2014; Gu, 2020). Intense dolomitization results in a large amount of calcite metasomatized by dolomite to form dolomite, calcite dolomite and dolomitic limestone. After entering the burial stage, the dolomite formed by early dolomitization has stronger compressive resistance during the burial process, and the original and the secondary dissolution pores formed in the early stage can

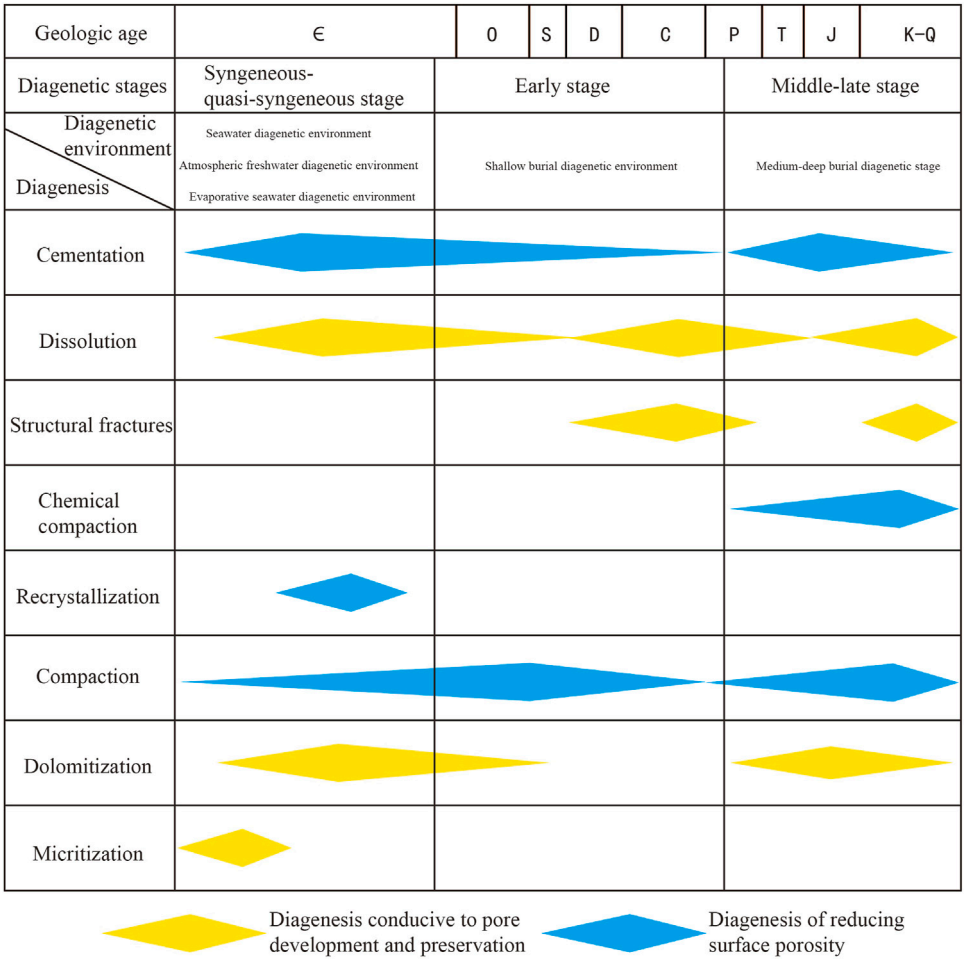

FIGURE 6
Construction results of the diagenetic sequence of the Cang 1 Member of the Canglangpu Formation.

be well protected. With the increase of burial depth, when the burial depth is more than 2000 m (the average burial depth of the Cang1 Member in the study area is more than 5000 m), burial dolomitization will cause the decrease of solid phase volume and the increase of pore size (Joachim et al., 1994; Huang, 2010; Zhou et al., 2015; Xie et al., 2018). It can be found from Figure 7 that the oolitic dolomite at the middle and upper part of the coring section (6262–6275 m) is completely dolomitized, calcite is completely metasomatized by dolomite, and its pores are relatively developed as a whole; However, the oolitic dolomite at 6288–6301 m in the middle and lower part is not completely dolomitized, containing a certain calcite, and its pores are poorly developed as a whole (Figure 7).

The first stage of cementation: in the submarine diagenesis environment and the meteoric water diagenesis environment, the drusy cement, the dentate cement and the leaf-like cement can support the pores (Shun, 2021) and have a certain protective effect on the pores. In summary, structural fracture, dissolution, dolomitization and first-stage cementation can not only protect pre-pores and form new secondary pores, but also improve pore throats and promote pore development (Figures 8A–C).

Supplement: the degree of compaction is reflected by the particle contact relationship, 0–1 indicates that the particles are mainly non-contact with a small amount of point contact; 1-2 indicates that the particles are mainly in point contact with a small amount of line contact; more than or equal to 2 indicates that the particles are mainly in line contact with a small amount of suture contact. GR: natural gamma ray; Rt: true formation resistivity; Rxo: flushed zone formation resistivity.

5.2.2 Diagenesis that reduces surface porosity

The diagenesis of reducing pore surface porosity in the study area mainly includes the second stage cementation, compaction and chemical compaction.

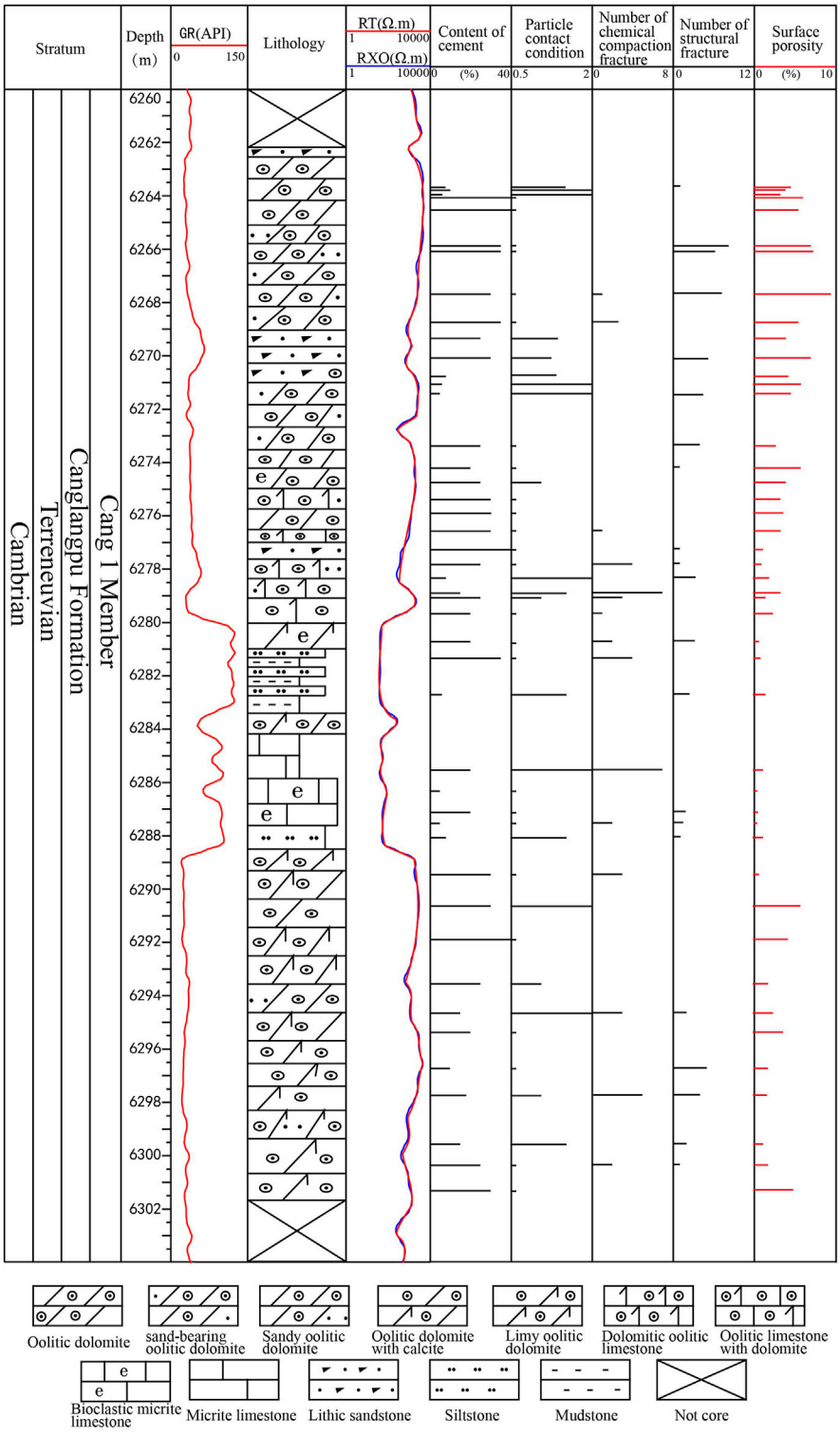

FIGURE 7
Histogram of diagenesis in coring section of well CT1.

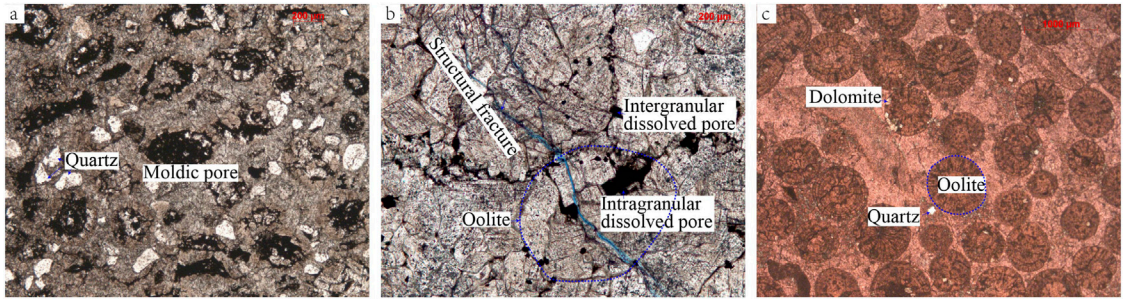

FIGURE 8
Effect of diagenesis on pore development. **(A)** Strong dolomitization and dissolution, and weak compaction. Sparry oolitic dolomite, Well CT1, 6266.42 m, single polarized light, dyed cast thin section; **(B)** Strong structural fracture and dolomitization, and pores are relatively developed. Sparry oolitic dolomite, Well DB1, 5947.5 m, single polarized light, dyed cast thin section; **(C)** Extremely underdeveloped pores, due to strong cementation, weak dolomitization, dissolution, and structural rupture. Sparry oolitic limestone, Well Chongtan 1, 6279.94 m, single polarized light, dyed cast thin section.

Second stage cementation: it is mainly granular ankerite cementation in the burial period. With the progress of the second stage cementation, the content of cement increases continuously, so that the pores are gradually filled, and the pore size of the pores is gradually reduced or even fully filled, which is not conducive to the development of pores.

Compaction: the compaction in the study area is mainly controlled by two aspects. One is the overlying pressure exerted by the overlying sediments, and the other is the properties of the sediments themselves, including the composition of the sediments, the content, sorting, and rounding of rigid particles. The (detrital) particles in the target layer in the study area are mainly include oolitic, quartz and rock debris, which have relatively little protective effect on the rock pores. The pressure exerted by overlying sediments is a key factor affecting the development of pores in the study area. With the increase of burial depth and overburden pressure, the pore size gradually decreases or even disappears, which is not conducive to the development of the rock pores. Thus, the compaction of rock is enhanced and the development of rock pores is weakened (Figure 7).

Chemical compaction: the chemical compaction of the target layer in the study area occurred on the basis of strong compaction. It can further destroy the pores and eventually lead to the reduction of the pore size inside the rocks.

Based on this study, the second stage cementation, compaction and chemical compaction are not conducive to the development of pores. Therefore, a weak diagenetic coupling of cementation, compaction and chemical compaction is favorable for the development of pores (Figures 8A–C).

6 Conclusion

(1) In this paper, taking the Cang 1 Member of the Canglangpu Formation of the Cambrian Terreneuvian in the north part of the central Sichuan Basin as an example, the diagenesis and its influence on pores are systemically studied based on the observations and identifications of cores, cast and cathodoluminescence thin sections.

(2) The rock types of the Cang 1 Member of the Canglangpu Formation are mainly include sand-bearing oolitic dolomite, sandy oolitic dolomite, sparry oolitic dolomite and fine-grained lithic sandstone. At the same time, the Cang 1 Member of the Canglangpu Formation in the study area has experienced five types of diagenetic environments, including seawater, meteoric water, evaporative seawater, shallow burial, and medium-deep burial diagenetic environments.

(3) The main diagenetic processes under different diagenetic environment conditions are cementation, dissolution, compaction, chemical compaction, dolomitization and structural fractures. According to the analysis, fabric-selective dissolution in meteoric water diagenetic environment, dolomitization in evaporative seawater environment, the first stage cementation in submarine diagenetic environment and meteoric water diagenetic environment, such as drusy cementation, dentate cementation, leaf-like cementation and non-fabric-selective dissolution, dolomitization and structural fractures in buried diagenetic environment is beneficial to the development of the pores. However, the second stage cementation, compaction and chemical compactionin medium-deep burial environments, are unfavorable for the development of the pores.

Data availability statement

The original contributions presented in the study are included in the article/Supplementary Material; further inquiries can be directed to the corresponding author.

Author contributions

BZ and HQ are responsible for the idea and writing of this paper, XZ and QH are responsible for the data sorting, RZ, LZ, YZ, ZM, QM, and HA are responsible for sample collection.

Funding

This research was financially supported by the National Natural Science Foundation of China (41702163, 41702122) and the Science and Technology Cooperation Project of the CNPC-SWPU Innovation Alliance (No. 2020CX010301).

Conflict of interest

The authors RZ, YZ, QM, and HA were employed by the company Exploration Department of PetroChina Southwest Oil and Gasfield Company. The authors LZ and ZM were employed by the company Central Sichuan Oil and Gas Mine of PetroChina Southwest Oil and Gas Field Company. The author YP was employed by CNPC Chuanqing Drilling Engineering Company Limited.

The remaining authors declare that the research was conducted in the absence of any commercial or financial relationships that could be construed as a potential conflict of interest.

Publisher's note

References

Craig, H. (1965). The measurement of oxygen isotope paleotemperatures.Stable isotopes in oceanographic studies and Paleotemperatures.Piza:consiglio nazionale delle richerche. *Lab. Geol. Nucl.* 3, 23.

Dong, G., Chen, H., and He, Y. (2007). Some problems on the study of the mixed siliciclastic-carbonate sediments. *Adv. Earth Sci.* 22 (9), 931–939.

Dong, T., Li, X., and Peng, C. (2021). "Reservoir pre-diction of the cambrian Canglangpu Formation in the xichongarea of central and northern sichuan," in Proceedings of the Geophysical Exploration Technology Seminar of China Petroleum Society, Chengdu, China, September 27, 2021, 768–771. doi:10.26914/c.cnkihy.2021.014594

Epstein, S., Buchsbaum, R., Lowenstam, H., and Urey, H. C. (1953). Revised carbonate-water isotopic temperature scale. *Geol. Soc. Am. Bull.* 64 (11), 1315–1326. doi:10.1130/0016-7606(1953)64[1315:RCITS]2.0.CO;2

Flügel, E., and Munnecke, A. (2010). *Microfacies of carbonate rocks: Analysis, interpretation and application*. Berlin, Germany: Springer, 1–5. ISBN:978-3-642-03795-5.

Gu, Z. (2020). *Sedimentary characteristics and petroleum geological significance of Cambrian gypsum salt rocks in Sichuan basin and its surrounding areas*. Jingzhou, China: Yangtze University. doi:10.26981/d.cnki.gjhsc.2020.000593

Hu, D., Wang, L., and Huang, R. (2021). Petroleum exploration history and enlightenment in Sichuan Basin: A case study on sinopec exploration areas. *Xinjiang Pet. Geol.* 42 (3), 283–290. doi:10.7657/XJPG20210304

Huang, S. (2010). *Carbonate diagenesis*. Beijing, China: Geologyical Publishing House, 1–4. ISBN:978-7-116-06938-1.

Joachim, E., Amthor, E. W., and Mountjoy, H. G. (1994). Machel. Regional-scale porosity and permeability variations in Upper Devonian Leduc buildups; implications for reservoir development and prediction in carbonates. *GeoScienceWorld* 78 (10). doi:10.1306/A25FF215-171B-11D7-8645000102C1865D

Keith, M., and Weber, J. (1964). Carbon and oxygen isotopic composition of selected limestones and fossils. *Geochim. Cosmochim. Acta* 28, 1787–1816. doi:10.1016/0016-7037(64)90022-5

Li, H. (2022b). Research progress on evaluation methods and factors influencing shale brittleness: A review. *Energy Rep.* 8, 4344–4358. doi:10.1016/j.egyr.2022.03.120

Li, H., Tang, H. M., Qin, Q. R., Zhou, J. L., Qin, Z. J., Fan, C. H., et al. (2019). Characteristics, formation periods and genetic mechanisms of tectonic fractures in the tight gas sandstones reservoir: A case study of xujiahe Formation in YB area, Sichuan Basin, China. *J. Pet. Sci. Eng.* 178, 723–735. doi:10.1016/j.petrol.2019.04.007

Li, H., Zhou, J. L., Mou, X. Y., Guo, H. X., Wang, X. X., An, H. Y., et al. (2022d). Pore structure and fractal characteristics of the marine shale of the longmaxi Formation in the changning area, southern Sichuan Basin, China. *Front. Earth Sci.* 10, 1018274. doi:10.3389/feart.2022.1018274

Li, J., Li, H., Yang, C., Wu, Y. J., Gao, Z., and Jiang, S. L. (2022c). Geological characteristics and controlling factors of deep shale gas enrichment of the Wufeng-Longmaxi Formation in the southern Sichuan Basin, China. *Lithosphere* 2022, 4737801. doi:10.2113/2022/4737801

Lin, L., Hao, Q., and Yu, Y. (2014). Development characteristics and sealing effectiveness of Lower Cambrian gypsum rock in Sichuan Basin. *Acta Petrol. Sin.* 30 (3), 718–726.

Li, Q., Bao, Z., and Xiao, Y. (2021b). Research advances and prospect of mixed deposition. *Acta Sedimentol. Sin.* 39 (1), 153–167. doi:10.14027/j.issn.1000-0550.2020.140

Li, S., Jiang, P., and Liu, L. (2022a). Seismic response characteristics and distribution law of carbonate shoals of Cang-langpu Formation in Gaoshiti-Moxi area, Sichuan Basin. *Lithol. Reserv.* 34 (4), 22–31. doi:10.12108/yxyqc.20220403

Li, Y., Chen, Y., and Yan, W. (2021a). Research on sedimentary evolution characteristics of cambrian Canglangpu formation, Sichuan Basin. *Nat. Gas. Geosci.* 32 (9), 1334–1346. doi:10.11764/j.issn.1672-1926.2021.03.010

Lu, W. (1986). *Stable isotope geochemistry*. Sichuan Chengdu, China: Chengdu Institute of Geology Press, 1–334.

Ma, S., Xie, W., and Yang, W. (2021). Lithofacies and paleogeography of the lower Canglangpu Formation of the lower cambrian in Sichuan Basin and its periphery. *Nat. Gas. Geosci.* 32 (9), 1324–1333. doi:10.11764/j.issn.1672-1926.2021.03.011

Ma, T., He, Y., and Zhu, L. (2022). Carbon and oxygen isotope characteristics of lower Canglangpu Formation of lower cambrian in central sichuan and the geological significance. *J. Chengdu Univ. Technol. Technol. Ed.* 1–17.

Mei, Q. (2015). *Tec-tonic evolution and formation mechanism of Leshan-Longnüsi paleo-uplift, Sichuan Basin*. Beijing, China): Beijing:China University of Geosciences, 1–4.

Moore, C. H. (1989). *Carbonate diagenesis and porosity*. Amsterdam, Netherlands: Elsevier, 45–47. ISBN: 0-444-87415-1.

Mount, J. F. (1984). Mixing of siliciclastic and carbonate sediments in shallow shelf environments. *Geol.* 12 (7), 432–435. doi:10.1130/0091-7613(1984)12<432:mosacs>2.0.co;2

Peng, J., Chu, J., and Chen, Y. (2020). Sedimentary characteristics of lower cambrian Canglangpu Formation in GaoshitiMoxi area, Sichuan Basin. *Lithol. Reserv.* 32 (4), 12–22. doi:10.12108/yxyqc.20200402

Qiang, Z. (1998). *Carbonate reservoir geology*. DongYing, China: Petroleum University Publishing House, 18–23. ISBN:7-5636-1130-4.

Sha, Q. (2001). Discussion on mixing deposit and Hunji rock. *J. Palaeogeogr.* 3 (3), 63–66.

Shi, G., Tian, J., and Wu, Y. (2010). Lower Paleozoic Carbonate diagenesis feature and controlling over reservoirs in southern North China. *Geol. Sci. Technol. Inf.* 29 (2), 10–15.

Shun, Y. (2021). *Diagenesis characteristics of jurassic reservoir and its influence on reservoir in moxizhuang yongjin area, junggar basin*. Kirkland, DC: Northwest University, 1–5. doi:10.27405/d.cnki.gxbdu.2021.001052

Urey, H. (1947). The thermodynamic properties of isotopic substances. *J. Chem. Soc.*, 562–581. doi:10.1039/JR9470000562

Wang, C. (2016). *The study on structure feature of Longwangmiao Formation in gaoshiti-moxi area, Sichuan Basin*. Chengdu, China: Chengdu University of Technology, 23–25.

Wang, L., Su, S., and Ma, Z. (2022). Sedimentary characteristics of cambrian Canglangpu Formation in central SichuanBasin. *Lithol. Reserv.* 34 (6), 19–31. doi:10.12108/yxyqc.20220602

Wang, W., Fan, Y., and Lai, Q. (2018). A new understanding ofdolomite distribution in the Lower Cambrian Canglangpu for mation of Sichuan Basin: Implication for petroleum geology. *Nat. Gas Explor. Dev.* 41 (1), 1–7. doi:10.12055/gaskk.issn.1673-3177.2018.01.001

Wang, Z., Jiang, H., Wang, T., Lu, W., Gu, Z., Xu, A., et al. (2014). Paleo-geomorphology formed during Tongwan tectonization in Sichuan Basin and its significance for hydrocarbon accumulation. *Petroleum Explor. Dev.* 41 (3), 338–345. doi:10.1016/s1876-3804(14)60038-0

Wen, J., Peng, J., and Chen, Y. (2020). Study on sequencestratigraphy of Canglangpu Formation in the central-northernSichuan asin. *Fault-Block Oil Gas Field* 27 (4), 424–431. doi:10.6056/dkyqt202004004

Xie, X., Ye, M., and Xu, C. (2018). High quality reservoirs characteristics and forming mechanisms of mixed siliciclastic-carbonate sediments in the bozhong sag, bohai bay basin. *Earth Sci.* 43 (10), 3526–3539. doi:10.3799/dqkx.2018.277

Yan, W., Luo, B., Zhou, G., Chen, Y., Zhong, Y., Li, K., et al. (2021). Natural gas geology andexploration direction of the Cambrian lower Canglangpu memberin central Sichuan paleo-uplift, Sichuan Basin, SW China. *Petroleum Explor. Dev.* 48 (2), 337–353. doi:10.1016/s1876-3804(21)60027-7

Yan, W., Zhong, Y., and Zhou, G. (2020). Lithofacies paleo geography features of the Lower Cambrian Canglangpu Formationin Sichuan Basin and their control on reservoir development. *Nat. Gas Explor. Dev.* 43 (4), 22–32. doi:10.12055/gaskk.issn.1673-3177.2020.04.003

Yang, C., and Sha, Q. (1990). Sedimentary environmentof the Middle Devonian Qujing Formation, Qujing, Yunnan province:A kind of mixing sedimentation of terrigenous clastics andcarbonate. *Acta Sedimentol. Sin.* 8 (2), 59–66.

Yang, C., Wen, L., and Wang, T. (2020). Timing of hydrocarbon accumulation for paleo-oil reservoirs in anyue gas field in chuanzhong uplift. *Oil Gas Geol.* 41 (3), 492–502. doi:10.11743/ogg20200306

Yue, H., Zhao, L., and Yang, Y. (2020). Great discovery of oiland gas exploration in cambrian Canglangpu Formation of the Sichuan Basin and its implications. *Nat. Gas. Ind.* 40 (11), 11–18. doi:10.3787/j.issn.1000-0976.2020.11.002

Zhang, J., and Ye, H. (1989). A study on carbonate and siliciclastic mixed sediments. *J. Chengdu Univ. Technol.* 16 (2), 87–92.

Zhang, X. (2000). Classification and origin of mixosed mentite. *Geol. Sci. Technol. Inf.* 19 (4), 31–34.

Zhou, J., Xu, C., Yao, G., Yang, G., Zhang, J., Hao, Y., et al. (2015). Genesis and evolution of lower cambrian Longwangmiao Formation reservoirs, Sichuan Basin, SW China. *Petroleum Explor. Dev.* 42 (2), 175–184. doi:10.1016/s1876-3804(15)30004-5

Zhou, S., and Zhang, X. (1993). Diagenetic environment and pore evolution of carbonate rocks. *Oil & Gas. Geol.* 14 (3), 215–222+261.

Zhu, X. (2014). *Sedimentary petrology*. Fourth Edition. BeiJing, China: Petroleum Industry Publishing House, 56–59. ISBN:978-7-5021-6755-4.

frontiers | Frontiers in Earth Science

TYPE Original Research
PUBLISHED 23 January 2023
DOI 10.3389/feart.2022.1064808

OPEN ACCESS

EDITED BY
Shuai Yin,
Xi'an Shiyou University, China

REVIEWED BY
Qin Zhang,
China University of Petroleum, Beijing, China
Jishun Pan,
North China University of Water Conservancy and Electric Power, China

*CORRESPONDENCE
Zhiqiang Shi,
szqcdut12@126.com

SPECIALTY SECTION
This article was submitted to Structural Geology and Tectonics, a section of the journal Frontiers in Earth Science

RECEIVED 08 October 2022
ACCEPTED 29 November 2022
PUBLISHED 23 January 2023

CITATION
Li X, Shi Z, Han L and Hu X (2023), Geochemical characteristics of hydrogen, oxygen, carbon isotopes and REE of cenozoic dolomites in Well Xike 1, Xisha Islands, South China sea and the significance for dolomitization in island-reef areas.
Front. Earth Sci. 10:1064808.
doi: 10.3389/feart.2022.1064808

Geochemical characteristics of hydrogen, oxygen, carbon isotopes and REE of cenozoic dolomites in Well Xike 1, Xisha Islands, South China sea and the significance for dolomitization in island-reef areas

Xiaoyu Li[1,2], Zhiqiang Shi[1]*, Lu Han[1] and Xiaolong Hu[1]

[1]State Key Laboratory of Oil and Gas Reservoir Geology and Exploitation, Chengdu University of Technology, Chengdu, Sichuan, China, [2]Institute of Multipurpose Utilization of Mineral Resources, Chinese Academy of Geological Sciences, Chengdu, Sichuan, China

Due to the special tectonic background and complex geological evolution characteristics of the South China Sea, reef dolomite reservoirs (sush as Well Xike 1) are widely developed. Based on the drilling core data of Well Xike 1, the structure and geochemical characteristics of dolomite reservoirs, including carbon, oxygen, hydrogen isotopes and REE were systematically studied using geochemical and petrological methods. It is found that the geochemical characteristics of REE show that the main diagenetic environment of dolomites is a low-temperature alkaline semi open oxidation environment; the carbon and oxygen isotopes of the dolomites are generally lack of correlation, the δD value is significantly lower than the hydrogen isotope value of seawater. Meanwhile, the oxygen isotope value of deep dolomites is negatively biased, which may be due to the increase or decrease of pore water temperature caused by deep thermal convection that related to the regional tectonic movements of the South China Sea. The $\delta^{18}O$ value is also consistent with the geological reality of increasing saddle dolomite content in deep dolomites. The distribution of the $\delta^{13}C$ value indicates that the dolomite inherited the carbon of the original limestone during dolomitization, while the characteristic of the δD value shows that it may be affected by the mixing of atmospheric precipitation and concentrated seawater in the quasi contemporaneous period. Based on the comprehensive analysis of the geochemical characteristics of the Well Xike 1, it is considered that the higher diagenetic temperature could be an important factor leading to the huge differences between the diagenetic model of deep and shallow dolomites. The geochemical characteristics of the shallow dolomites show that it is mainly reflux infiltration dolomitization under the micro evaporation and concentration sea water environments, while the deep dolomite is transformed by the hot water fluids in the epigenetic diagenetic evolution stage.

KEYWORDS
isotope, REE, cenozoic carbonate, dolomite, island dolomitization, South China sea

1 Introduction

Deceptively simple dolomites [$CaMg(CO_3)_2$] are common carbonate rocks throughout the geological records, especially in the Precambrian strata, whereas there are few dolomites in the Holocene strata and the modern natural environment rocks. However, due to the incomplete understanding of its genetic mechanism, there is great uncertainty in the prediction of dolomite distribution (Braithwaite et al., 2004). Modern sea water is oversaturated with dolomites, but the main carbonate minerals precipitated are aragonite, in addition, it has been realized that the direct precipitation reaction of dolomite is bound by kinetic factors (Land., 1998; Arvidson et al., 1999). The dolomitization, therefore, was once considered to be the only way to form dolomites. In recent years, the introduction of microbial dolomite (Mazzullo, 2000; Sánchez-Román et al., 2008; Bontognali et al., 2010; You et al., 2011; Petrash et al., 2017) has provided an additional perspective for geologists to understand the formation of dolomites, and several models of dolomitization related to microbial action are proposed, such as sulfate reduction (Vasconcelos et al., 1995, 1997; Li and Liu., 2013), methane oxidation (Aloisi et al., 2000; Kenward et al., 2009), methanogenesis (Roberts et al., 2004) and biological involvement (Sánchez-Román et al., 2008; Roberts et al., 2013; Petrash et al., 2017).

Coral reefs are composed of different types and complex structures of fixed benthic and *in situ* carbonate formations (Riding Robert, 2002). About 60% of the world's oil and gas reserves are distributed in Great Reef oil and gas fields (Arthur and Schlanger, 1979). Coral reef dolomitization model is also a new research direction that cannot be ignored. Budd (1997) believes that the island reef dolomite provides a favorable support for understanding the genetic mechanism of dolomite- island reef dolomite was originally a poorly ordered, microcrystalline structure, rich in calcium and oxygen isotopes (^{18}O) deposited quasi contemporaneously. In normal or evaporated (concentrated) seawater environment, and in the process of diagenetic evolution, the buried (epigenetic) dolomite inherited and different from quasi syngenetic dolomite is formed through a series of diagenesis such as dolomite recrystallization. The geochemical characteristics of island-reef dolomite are Ca rich and with low Sr, Fe and Mn contents. The Sr isotopic age results of many island-reef dolomites show that there is a relatively synchronous dolomitization time in the world, global ocean currents, climate and other related factors are related to the island-reef dolomitization.

Although predecessors have carried out different degrees of research on the petrological and geochemical characteristics of dolomites in Well Xike 1, they have hardly involved the change characteristics of hydrogen isotopes and rare earth elements. In order to explore the genesis of shallow, middle and deep dolomites and the diagenetic model of island-reef dolomites, in this study, taking the Well Xike 1 in Xisha area, South China Sea (Figure 1) as an example, the characteristics of isotopes and the change laws of earth elements of the shallow and middle-deep dolomites were systemically studied. Combined with the petrological characteristics, sedimentary tectonic background and global temperature changes of dolomites, the dolomitization model of the Well Xike 1 island reef is proposed.

2 Geological setting

The South China Sea, located in the southeastern Eurasian Plate (Taylor et al., 1983; Briais et al., 1993; Qiu et al., 2001; Yan et al., 2001; Lu et al., 2014), is one of the biggest marginal seas in the western Pacific Ocean. It is close to the junction part of two super convergence zones, the Tethys and the Pacific Rims (Wang P et al., 2010; D'Hondt S et al., 2012). The Xisha Island area is located in the transitional zone between the continental and oceanic crusts. The South China Sea has special geographical location, complex tectonic environment and submarine landform, which also determines the diversity of the reef systems (Xu H et al., 2015). Cenozoic carbonate reefs are well developed in the South China Sea, while Neogene dolomites are widely distributed in the Xisha Islands. Many geologists have proposed several dolomitization models to explain their genesis and dolomitization process. For example, Shi (2016) pointed out that the main patterns of dolomitization of the islands and reefs of Well Xike 1 can be explained by the infiltration and return flow model and buried diagenetic model.

Since the 1970s, several coring wells have been drilled on the small islands in the Xisha area (Figure 1), such as Wells Xiyong-1, 2, Xichen-1, Xishi-1and Xike-1 (Wei et al., 2007; Bi et al., 2018; Wang et al., 2018). Three sets of dolomites in the lower Miocene, middle-upper Miocene and upper Miocene in the interval from 0 m to 800 m deep in the Well Xichen-1 are divided. Zhai et al. (2015) divided 5 sets of dolomites in the middle Miocene, upper Miocene in the 0–700 m depth interval of Xike-1. The development of the Xisha Islands reefs (Riding Rober, 2002) are distributed almost throughout the Neogene.

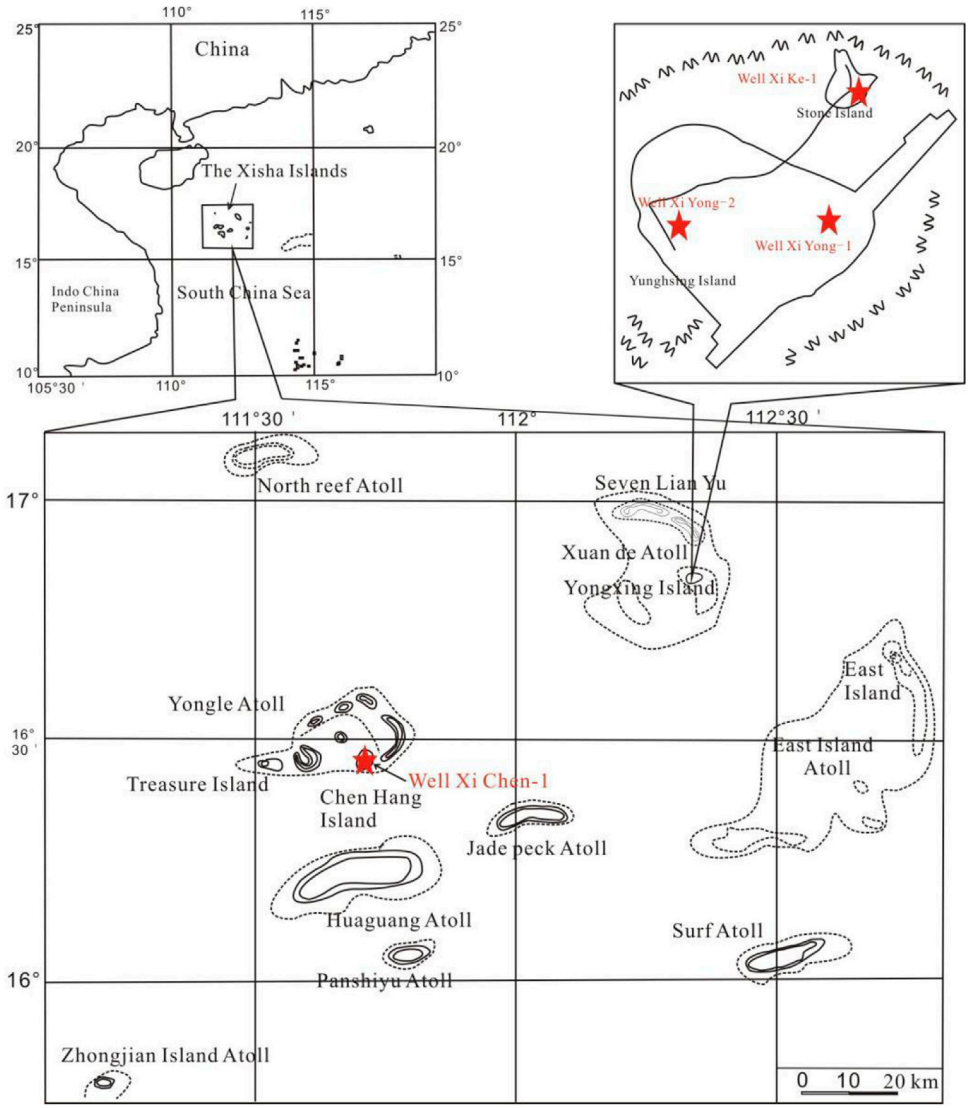

FIGURE 1
Geographic location map of Well Xike 1.

Well Xike 1 can be divided into the Sanya Formation (Lower Miocene), the Meishan Formation (Middle Miocene), the Huangliu Formation (Upper Miocene), the Yinggehai Formation (Pliocene) and the Ledong Formation (Quaternary) from bottom to top (Shi et al, 2016). There are seven thick dolomites (the thickness of thick dolomite is more than 15 m and the dolomite content is more than 75%) in the cores of 0–1257.52 m in Well Xike 1, including one in the Pliocene, three in the early Miocene, two in the Middle Miocene and one in the late Miocene. The thickness of dolomites varies (the thickest is 163 m and the thinnest is 15 m). In order to explore the spatial variation relationship of dolomites, the dolomite layers of the Well Xike 1 are divided into three categories: shallow, middle and deep dolomite. The formation thickness and content of dolomite are shown in Table 1.The dolomite layer with thickness <600 m is shallow dolomite (layers 1, 2 and 3, with a total thickness of 203 m), the middle dolomite is buried within 600–1000 m (layers 4, 5 and 6, with a total thickness of 79 m), and the deep dolomite is buried >1000 m (layer 7, with a thickness of 155 m). Thick dolomitic limestone and limestone are developed in the middle and deep layers, most of which are crystalline dolomites. Under the microscope, dolomite usually has fog core and bright edge structures, and the crystallinity of dolomite crystal tends to be better with the increase of the buried depth.

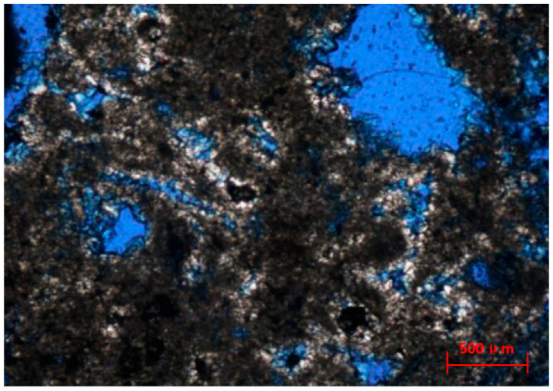

FIGURE 2
Petrological characteristics of shallow dolomite sample. Microcrystalline bioclastic dolomite at the top (288.91 m) of the second member of the Yinggehai Formation. The echinoderm bioclastic in the middle of the photo is completely dolomitized, with a diagonal length of 1.6 mm (1N).

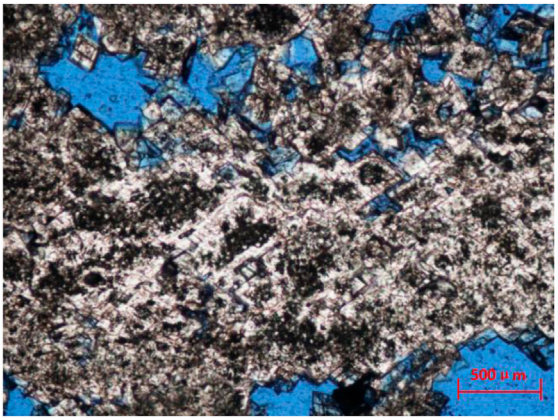

FIGURE 3
Petrological characteristics of middle dolomites. The powdery residual coral dolomites in the first member of the Meishan Formation (628.86 m) have experienced excessive dolomitization, and the content of "fog-bright edge" powdery dolomites is high, with a diagonal length of 1.6 mm (1N).

3 Methods and materials

3.1 Materials

The cores of the well Xike 1 was observed and the dolomite samples were collected at different depths. More than 200 fresh carbonate samples, including dolomite samples and a small amount of limestone samples, were collected by drilling cores. All samples are immediately stored in plastic bags to reduce pollution and oxidation. At the institute of sedimentary geology, Chengdu university of technology, 160 carbonate samples were observed by a polarizing microscope. Fifty-one dolomite samples of different layers were selected to analyze the contents of carbon, oxygen, hydrogen isotopes and REE.

3.2 Methods

An Leica polarizing microscope (Leica-Dmrx) was used for optical microscopic identifications, and the thin sections of dolomite cores were observed by transmission light. In addition, this paper also selected some samples for cathodoluminescence, which was completed on the basis of identification and statistics of stained cast thin sections. The instrument used was a CL8200MK5 cathodoluminescence instrument (equipped with Leica polarizing microscope) of the exploration and Development Research Institute of Sinopec Southwest Oil and Gas Company. Considering the comparability of samples, all samples adopted the same test conditions, i.e., beam voltage of 15.8 kv and beam current of 304 μA. The exposure duration is 1.8 s.

Carbon and oxygen isotope analysis is mainly completed by a MAT-253 isotope mass spectrometer of the Nanjing Institute of Geology and Paleontology, Chinese Academy of Sciences. Kiel IV Carbonate Device sample preparation system is used. Reference standard: GBW-04405. It is based on DZ/T0184.17-1997 "Phosphoric acid method for determination of carbon and oxygen isotopes in carbonate minerals or rocks." Analysis accuracy: The standard deviations of the measured values of $\delta^{13}C$ (PDB) and $\delta^{18}O$ (PDB) are less than 0.040‰ and 0.080‰.

Hydrogen isotopic analyses were conducted on the fluid inclusions hosted in the mineral particles (dolomite). Samples were first degassed of labile volatiles by heating under vacuum to 150°C for 3 h. Water was released by heating the samples to approximately 500°Cby means of an induction furnace. Water was converted to hydrogen by passage over heated zinc powder at 400°C (Friedman, 1953), and the hydrogen was analyzed with a MAT-252 mass spectrometer. The analyses of standard water samples suggest a precision for δD of ±3‰ (1σ). The hydrogen isotopic analyses were performed at the Analytical Laboratory of Beijing Research Institute of Uranium Geology (ALBRIUG).

REE concentrations were determined at the Key Laboratory of Marine Geology and Environment, Institute of Oceanology, Chinese Academy of Sciences. About 40 mg of each sample was first digested with 0.6 ml HNO_3 and 2 ml HF in a Teflon beaker. After standing with seal-capping for 2 h, the beaker was placed on a hotplate at about 150°C for 24 h. A 0.25 ml $HClO_4$ was added to the residue, and it again was heated to near dryness in an open-top beaker on a hotplate at about 150°C. The residue was redissolved with 1 ml HNO_3+1 ml H_2O and sealed again, and it remained on a hotplate at about 120°C for an additional 12 h. The residue was diluted by 1% HNO_3 solution to produce a volume of

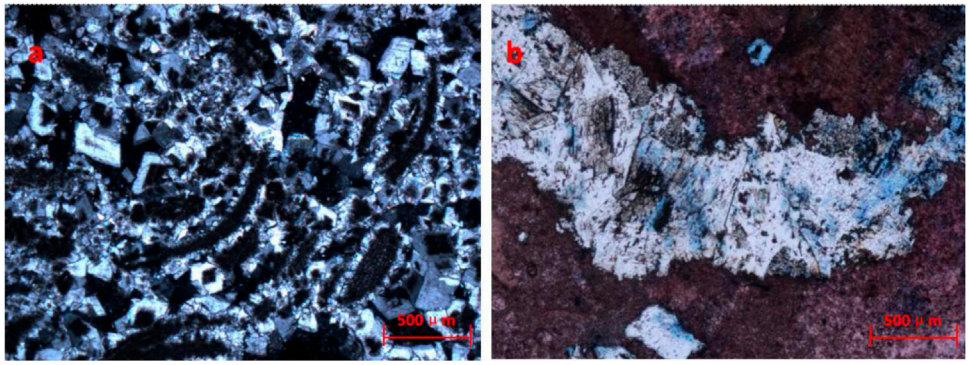

FIGURE 4
Petrological characteristics of deep dolomites. **(A)** microscopic characteristics of bright edge of dolomite fog center, 1170.42 m, diagonal length of 1.6 mm (XN); **(B)** medium and coarse-grained saddle dolomite is filled in the limestone fracture. The dolomite can see fog center and bright edge, single polarization, 1239.42 m (1N); From the overall trend, cement dolomites and excessive dolomitized fog-bright edge dolomites are widely distributed in Well Xike 1. The greater the burial depth, the greater the dolomite content, and the number of dolomite crystals increases with the increase of burial depth. In addition, the order degrees of dolomites in the Well Xike 1 range from 0.4355 to 0.6000, and generally increases with the increase of the burial depth (Shi et al., 2016). The change of dolomite content from shallow to deep layers reflects the self adjustment process of dolomite structures from recrystallization to ideal composition in the process of burial-diagenesis.

40 g, and it was subsequently analyzed by ICP-MS to determine the REEs in the sample solution.

4 Results

4.1 Petrological characteristics of dolomite

From the core observations, the crystal diameter of dolomite increases with the increase of depth, and the proportion of crystal dolomite in the rock increases with the increase of depth, in the form of yellowish brown sugar.

4.1.1 Shallow dolomite (0–600 m)

The dolomites in the second member of the Yinggehai Formation are micrite powder dolomites, and the crystal diameters are mostly less than 50 um. Common red algae structures can be seen. The dolomites of the Huangliu Formation are usually microcrystalline silty dolomites. In the second member of the Huangliu Formation below 462 m depth, the diameters of the dolomite crystal formed are large, so the content of the silty dolomite is great. For most of the silty dolomites and micritic (micro) dolomites, there have residual reef textures, grain textures or original matrix silty textures (Figure 2).

4.1.2 Middle dolomite (600–1000 m)

The middle dolomites are mainly composed of powder crystal - fine crystal dolomites. The dolomite crystals are semi automorphic automorphic crystals. Fog-bright edge dolomites are developed in the dolomites of the layers 4, 5 and 6, and bioclastic (foraminifera, echinoderms and algae clumps) components are developed in varying degrees. Some bioclastic components has residual structures (but the preservation of original components is worse than that of the shallow dolomites). By observing the core samples, it can be found that in the 620–646.5 m interval, the color is mainly light grayish white - light grayish yellow—grayish yellow and white. A large number of white marly filled insect pores, mold pores, cracks, etc., with obvious debris fillings; through scanning electron microscope observations, it is mainly fine and powder crystals, showing euhedral—semi euhedral shapes. There are obvious intergranular pores between the crystals. Corrosion is developed in some depths, and solution pores on the crystal surface can be observed. The fillings are mainly powder crystal fine-grained dolomites. Under the microscope, it is observed as flat crystal plane, euhedral semi euhedral. The crystals are in multi-faceted contacts or dense mosaic contacts, and it is difficult to find point contacts. In addition, argillaceous dolomites with poor crystal shapes and small crystals can be found, and the grains have complex curved surfaces with complementary shapes (Figure 3).

4.1.3 Deep dolomite (>1000 m)

The underlying stratum of the Meishan Formation is the first member of the Sanya Formation. The main lithology is grayish white dolomites, maroon dolomites and earthy yellow dolomites. Most dolomites have good permeability and have developed a large number of macropores (Figure 4). Deep dolomites have over-developed dolomitization, and dolomites are characterized by fog-bright edges. Compared with the

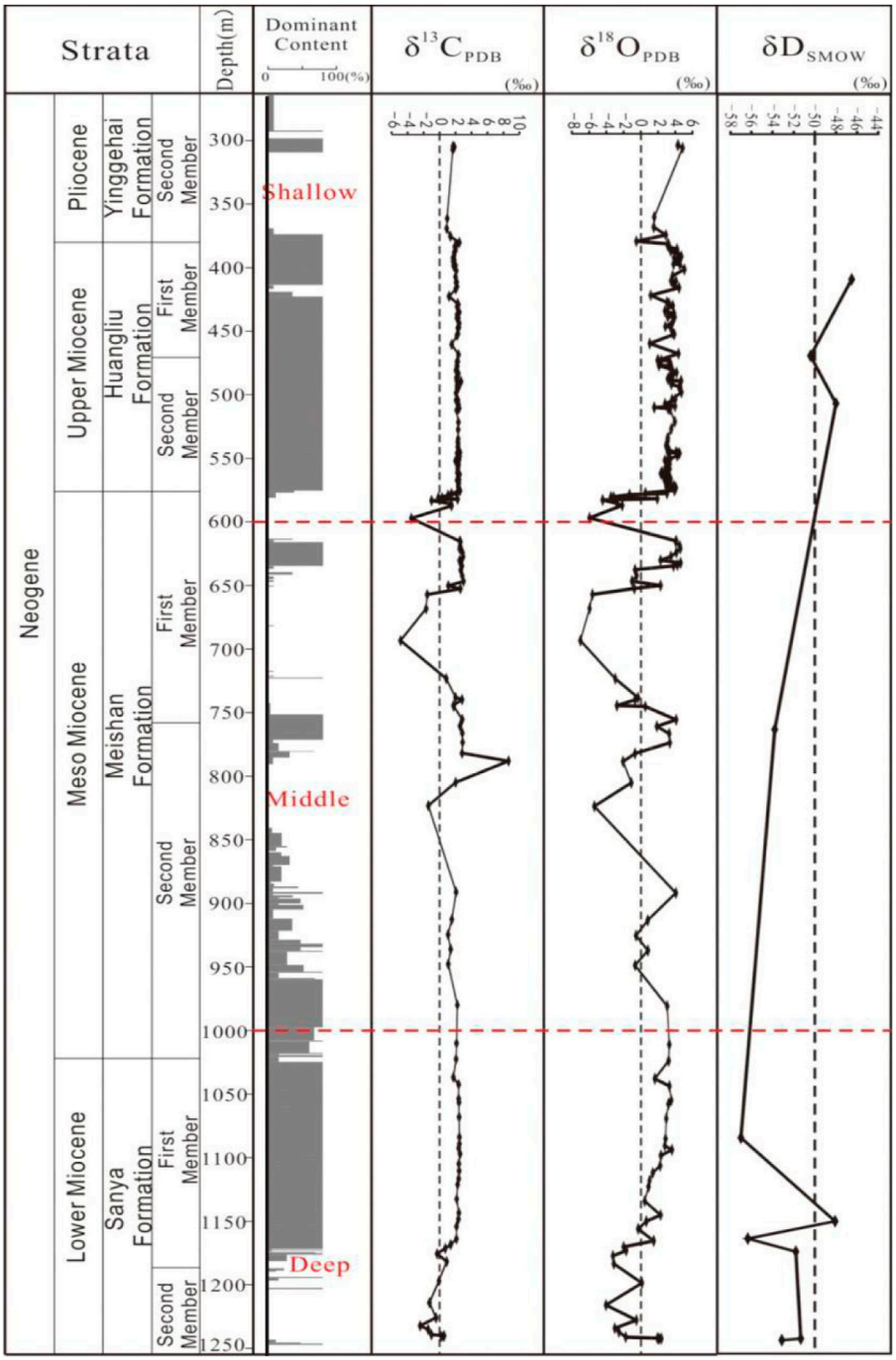

FIGURE 5
Distribution of dolomites, carbon, oxygen and hydrogen isotopes in Well Xike 1 [Data source: partial data of carbon and oxygen isotopes are from Shi et al. (2016)].

cemented dolomites, it can be found that the pore water medium formed by them has the same geological conditions and periods. Compared with the cemented dolomite, the "bright edge" of the fog-bright edge has the same composition. Under the cathodoluminescence, the optical characteristics of them are similar. In the second member of the Sanya Formation, the saddle dolomites with medium coarse crystal are more common, and the crystallization degree of crystals will gradually increase with the increase of buried depth.

TABLE 1 Formation thickness and content of dolomite in Well Xike 1.

Dolomite layer	Number	Well depth (m)	Thickness (m)	Formation age	Dolomite content (%)
Shallow	1	288.91–303.14	14.2	Pliocene series	90.90
	2	371.35–412.89	41.5	Upper-Miocen	91.50
	3	415.12–578.61	163.5	First segment of Meishan team in Middle-Miocen	92.40
Middle	4	614.94–637.14	22.2	First segment of Meishan team in Middle-Miocen	75.85
	5	759.91–775.33	15.4	Second segment of Meishan team in Middle-Miocen	93.90
	6	972.06–1018.21	38.15	Second segment of Meishan team in Middle-Miocen	61.70
Deep	7	1032.49–1187.57	155	Lower-Miocen	82.50

In addition, the deep dolomites also have experienced excessive dolomitization: in the Sanya Formation, the saddle dolomites in the limestones are commonly replaced by calcites along the cleavages. The dolomite crystal is large, the crystal plane is curved, and has wavy extinction. The fluid inclusions in 82 dolomite samples with a depth of more than 1064 m tested by Shi et al. (2016) have a homogenization temperature of 129.5°C–268.5°C and an average value of 184.6°C. It is speculated that the paleofluid temperature was high when it was formed. The saddle dolomites formed at higher temperature are prone to de dolomitization after the thermal fluids (upwelling due to tectonic action) subsides. In general, The dolomites in the lower part of the Sanya Formation and Mei-2 Member seldom undergo "decloudization", indicating that the dolomite lattice under the excessive dolomitization is relatively stable, so it is not easy to be replaced by calcite.

4.2 Carbon and oxygen isotopes

The geochemical characteristics of dolomites are an important information carrier for the genesis and formation mechanism of dolomites. The enrichment and loss, migration and preservation of elements are not only the records of sedimentary environments, but also an important calibration of geological processes (Hong H, 2004; Ni S et al., 2009; Hu Zuowei, 2010). For carbon, oxygen and hydrogen isotopes, carbon isotopes, they are mainly used to study paleotemperature, salinity and fluid properties, and hydrogen isotopes are mainly used to trace fluid properties in combination with the covariance law of oxygen isotopes (Craig, 1961; Holser, 1979; Richard, 2013).

The carbon and oxygen isotopes of 51 carbonate rock samples were analyzed in Well Xike 1. Kaufman et al. found that in order to ensure the effectiveness of data, the value of $\delta^{18}O$ cannot be less than −10‰, and Mn/Sr <10 can be used as a basis to determine whether the carbon isotope maintains the original composition (Kaufman A J et al., 1995).

4.2.1 Carbon and oxygen isotopes of shallow dolomite

In Well Xike 1, 13 shallow dolomite samples, 10 middle dolomite samples and 28 deep dolomite samples are selected. The carbon and oxygen isotope statistics are shown in Table 2. It can be seen that the $\delta^{18}O$ values are greater than −10‰. According to Kaufman's theory, the data validity can be guaranteed.

The carbon and oxygen isotopes of shallow dolomite samples have the following characteristics:

There are great differences of $\delta^{13}C$ and $\delta^{18}O$ values between dolomite-rich samples and calcite-rich samples, and ^{18}O and ^{13}C values in dolomites are significantly higher than those in limestones. Of dolomite samples, $\delta^{18}O$ value varies from 1.79‰ to 5.589‰, with an average of 3.33‰; $\delta^{13}C$ value varies from 1.56‰ to 4.33‰, with an average of 2.61‰ (Figure 5). There is no obvious correlation between carbon and oxygen isotopes (Figure 6). Of shallow dolomite samples from Well Xike 1, the $\delta^{13}C_{PBD}$ value is close to the present value and is in the global range of normal Neogene marine carbonates synthesized by Budd (1997) $\delta^{13}C$ value, and the Mn/Sr variation range of shallow dolomites is 0.167–0.316. The color of carbon isotope in shallow dolomites indicates that it inherits the carbon in the original limestone.

4.2.2 Carbon and oxygen isotopes of middle dolomite

The correlation between carbon and oxygen isotopes is not good. Through sorting and statistics of 10 groups of dolomite data, The average value of $\delta^{13}C$ is 2.39‰, ranging from 0.52‰ to 3.14‰; the average value of $\delta^{18}O$ is 1.883‰, ranging from 0.891‰ to 2.675‰. According to the statistical data, its carbon isotope value is close to the value of modern marine carbonate deposition, which is also in line with the global standard of normal Neogene marine carbonates synthesized by Budd (1997) $\delta^{13}C$ range, and its Mn/Sr variation range is 0.07–0.31. The marine color of its carbon isotope is also shown, which indicates that it inherited the carbon of the original limestone in the process of dolomitization.

TABLE 2 Carbon and oxygen isotopes of dolomite in well Xike 1.

Sample	Number of samples	[a]$\delta^{13}C_{PDB}$/‰	[a]$\delta^{18}O_{PDB}$/‰
Shallow dolomite of well Xike 1	13	1.56–4.33/2.615	1.79–5.589/3.331
Middle dolomite of well Xike 1	10	0.52–3.145/2.390	0.891–2.675/1.883
Deep dolomite of well Xike 1	28	−1.99–3.62/2.198	−1.99–3.435/1.881 (1182.5 and 1185.5 m, $\delta^{18}O$ −1.99 and −1.70)

[a]Note: The carbon and oxygen isotope values of shallow, middle and deep dolomites in Well Xike 1 are shown as the distribution interval/average value of test results.

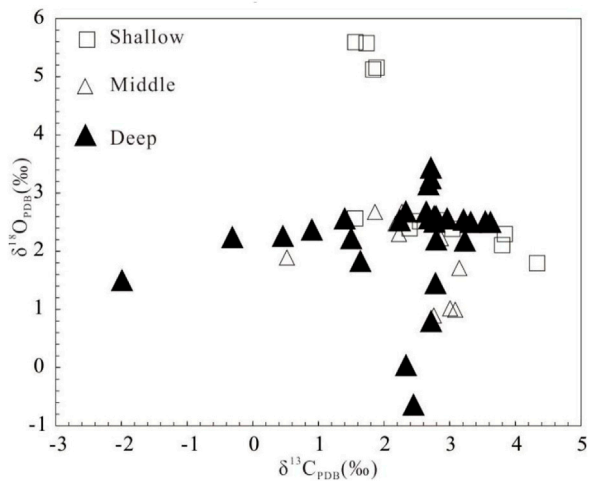

FIGURE 6
Correlation diagram of carbon and oxygen isotopes of shallow, middle and deep dolomites in Well Xike 1.

4.2.3 Carbon and oxygen isotopes of deep dolomite

In deep dolomite samples, as shown in Figure 6, the correlation between the carbon and oxygen isotopes is not good. Through sorting and statistics of 28 groups of dolomite data in deep layer, it can be found that, the average value of $\delta^{13}C$ is 2.245‰, ranging from −1.99‰ to 3.62‰, while the average value of $\delta^{18}O$ is 2.20‰, ranging from −0.639‰ to 3.435‰. According to the statistical data, the carbon isotope value is close to the value of modern marine carbonate deposition, slightly lower than the value of shallow and middle dolomite, which is also in line with the global standard of normal Neogene marine carbonates synthesized by Budd (1997) $\delta^{13}C$ range, and its Mn/Sr variation range is 0.11–0.67. The marine color of its carbon isotope is also shown, which indicates that the carbon of the original limestone was inherited in the process of dolomitization.

In terms of the average value of oxygen isotope, the deep layer is 1.449‰ lower than the shallow layer, close to the value of middle dolomite (about 0.002‰), and the sedimentary value of dolomite rich samples is relatively similar to that of limestone. It can be seen from Table 2 that this situation is particularly prominent in the Sanya formation, which also indirectly indicates that there is a great difference between dolomite and shallow layer in terms of Genesis.

While at 1182.5 and 1185.5 m, the $\delta^{18}O$ value has negative bias (respectively −1.99‰ and −1.70‰), and it is positively correlated with $\delta^{13}C$ value (1.5‰ and 0.82‰ respectively). It is generally believed that rainwater and underground fresh water are rich in light oxygen isotopes and carbon isotopes, which make it $\delta^{18}O$ and $\delta^{13}C$ presents a large negative value (Wei Xi, 2006 ab). The carbon and oxygen isotope characteristics at this place indicate that there is no obvious rain water or underground fresh water leaching environment in the deep dolomite during diagenetic evolution.

Deep dolomite $\delta^{18}O$ has a negative bias trend, $\delta^{18}O$ is a function of temperature and salinity (which can reflect the properties of diagenetic fluids) and is more sensitive to temperature to some extent (Huang, 2010), $\delta^{18}O$ value will decrease with the increase of pore water temperature, so the rise of formation water temperature caused by deep thermal convection will have a direct impact on the formation of some dolomites, which is consistent with the geological reality of the increase of saddle dolomite content in the deep part of well Xike 1. Huang et al. (2015) believed that saddle-shaped dolomite is an important diagenetic mineral in sedimentary rocks and is widely distributed in hydrothermal and other relatively high temperature diagenetic environments. For this reason, it is also commonly used as a semi-quantitative geological thermometer and indicator mineral for certain special fluids.

4.3 Hydrogen isotope

Hydrogen isotope test is carried out for dolomites in different layers of well Xike 1. The analysis results are shown in Table 3:

It can be seen from the analysis results that among the three samples in the shallow dolomites (579.26 m shallow), The maximum value of δD is −46.7‰ and the minimum value is −50.3‰; in the middle and deep dolomite interval (770.05–1257.4 m well section), the maximum value of δD is −48.1‰ and the minimum value is −57.0‰.

TABLE 3 Test results of hydrogen isotopes of dolomites in Well Xike 1.

Dolomite layer	Well depth/m	Lithology	δD_{smow} (‰)
Shallow	409.8	White dolomite	−46.7
	470.1–470.62	Fine crystalline dolomite	−50.3
	509.5	White fine silty dolomite	−48
Middle	770.05	Fine crystalline dolomite	−53.9
Deep	1095	White grain dolomite	−57
	1162.45	White grain dolomite	−48.1
	1176.55	Brown sandy dolomite	−56.5
	1187.15	Brown fine-grained dolomite	−51.9
	1256.15	Maroon hydrothermal dolomite	−51.4
	1257.4	Ferruginous dolomite	−53.1

4.4 REE data

The detailed REE element parameters of shallow, middle and deep dolomite samples from the Well Xike 1 are shown in Table 4. The REE distribution model of seawater standardized by PAAS is mainly characterized by negative Ce anomaly and relative enrichment of heavy rare earths (Zhang J et al., 1996). After PAAS standardization, the REE test results of shallow, middle and deep dolomite samples in Well Xike 1 (a total of 20 samples) show that the samples of dolomites in different layers have good similarities with the PAAS distribution curve of modern seawater, which are highlighted by LREE loss, negative Ce anomaly and positive Y anomaly (Figures 7, 8).

5 Discussions

Diagenetic environment and diagenesis affect $\delta^{13}C$ and $\delta^{18}O$ values (Peng et al., 2006). Moreover, carbon and oxygen isotopes are also controlled by temperature and salinity, which can well reflect the changes of paleotemperature and paleosalinity in the diagenetic environment of dolomites. For hydrogen isotope, there is a certain linear relationship between δD and $\delta^{18}O$ values. In addition, the hydrogen isotope can also be used to judge the relationship between surface water and groundwater (Craig, 1961; Holser, 1979; Richard, 2013).

5.1 Analysis of carbon and oxygen isotopes

5.1.1 Analysis of carbon and oxygen isotopic characteristics of shallow dolomites

Analysis of 13 shallow dolomite samples from Well Xike 1 shows that the $\delta^{18}O$ value is higher than the limestone of the formation produced by these dolomites by varying degrees. The research data of Fouke (1994) show that the dolomites formed in the Miocene Pliocene sea water has the value of $\delta^{18}O$ that significantly higher than that of calcite.

From the experimental results of the determination of $\delta^{18}O$ fractionation coefficient of carbonate water, it can be seen that when Ca is replaced by Mg, the $\delta^{18}O$ fractionation coefficient will increase. The experimental results of high magnesium calcite also show that when $MgCO_3$ increases by 1 mol, $\delta^{18}O$ will increase by 0.06‰ (Tarutani et al., 1969) and 0.17‰ (Jiménez-López et al., 2004). Analyzing the theoretical calculations and experimental results of calcite and dolomite coprecipitation, it can be found that when mg increases by 1%, the $\delta^{18}O$ value will increase by 0.05–0.14‰ (Fritz et al., 1970; Schmidt et al., 2005; Vasconcelos et al., 2005; Chacko et al., 2008). It is precisely because there is a certain difference in $\delta^{18}O$ values between calcite and synsedimentary dolomites. This phenomenon can reasonably explain the $\delta^{18}O$ of dolomite-rich samples in Well Xike 1 is positive relative to contemporaneous sedimentary limestones.

In Well Xike 1, when the Mg content in dolomites increases by 1%, the $\delta^{18}O$ value increases by 0.29‰, which shows that the formation process of dolomites not only includes its own fractionation effect in mineralogy, but also other external factors, thus resulting in the increase of $\delta^{18}O$ value.

The $\delta^{18}O$ value increases with the decrease of the paleo ocean temperature. The Well Xike 1 atoll was formed during the relatively cold period from the end of Miocene to the beginning of Pliocene. According to the sample test results, the average $\delta^{18}O$ value is about 3.33‰, which is slightly higher than the average $\delta^{18}O$ value range (2.0‰–3.5‰) of tertiary island reef dolomites formed by normal seawater in Pacific Ocean and Caribbean Sea according to Budd (1997). From this point of view, the global low temperature is not the dominant factor among the relevant factors leading to the positive value of $\delta^{18}O$.

TABLE 4 Rare earth element parameters of shallow, middle and deep dolomites (ug/g).

Dolomite layer		Well depth/m	La	Ce	Pr	Nd	Sm	Eu	Gd	Tb
Shallow	1	292.7	0.642	0.646	0.120	0.598	0.129	0.029	0.161	0.028
		295.5	0.770	0.683	0.144	0.659	0.140	0.036	0.186	0.035
		303.5	0.826	0.980	0.166	0.716	0.168	0.040	0.197	0.031
Middle	4	602.9	1.06	0.893	0.184	0.786	0.204	0.050	0.235	0.040
	5	759.90	0.700	0.670	0.140	0.600	0.130	0.040	0.160	0.030
		762.55	0.400	0.330	0.080	0.400	0.120	0.030	0.120	0.020
		768.30	0.700	0.510	0.130	0.600	0.170	0.040	0.180	0.030
		775.70	1.500	0.960	0.270	1.200	0.340	0.080	0.370	0.060
	6	974.20	0.900	0.710	0.190	0.800	0.240	0.060	0.280	0.040
		985.90	0.600	0.410	0.120	0.500	0.140	0.030	0.200	0.030
		1001.1	0.825	0.672	0.153	0.712	0.178	0.068	0.221	0.033
		1004.10	0.871	0.749	0.156	0.728	0.180	0.044	0.224	0.036
		1017.55	0.949	0.795	0.169	0.755	0.168	0.041	0.213	0.038
Deep	7	1046.25	2.178	2.134	0.437	1.853	0.478	0.110	0.552	0.087
		1062.60	1.613	1.264	0.273	1.227	0.290	0.071	0.394	0.065
		1086.50	1.072	0.764	0.186	0.844	0.212	0.053	0.248	0.040
		1089.45	1.106	1.333	0.202	0.809	0.191	0.044	0.215	0.035
		1098.30	1.706	2.162	0.319	1.405	0.369	0.088	0.425	0.064
		1120.00	0.601	0.473	0.099	0.440	0.106	0.026	0.130	0.023
		1149.00	0.779	0.588	0.125	0.550	0.135	0.029	0.150	0.026
Dolomite layer		Well depth/m	Dy	Ho	Er	Tm	Yb	Lu	Sc	Y
Shallow	1	292.7	0.166	0.037	0.110	0.015	0.078	0.014	0.474	1.42
		295.5	0.192	0.046	0.120	0.019	0.094	0.014	0.536	1.73
		303.5	0.187	0.043	0.102	0.018	0.093	0.014	0.632	1.52
Middle	4	602.9	0.221	0.046	0.118	0.014	0.082	0.010	0.725	2.36
	5	759.90	0.160	0.030	0.070	0.010	0.060	0.010	0.2	1.2
		762.55	0.110	0.020	0.050	0.010	0.040	0.010	0.1	0.9
		768.30	0.170	0.030	0.080	0.010	0.060	0.010	0.2	1.4
		775.70	0.330	0.060	0.150	0.020	0.110	0.020	0.2	3.0
	6	974.20	0.250	0.050	0.140	0.020	0.130	0.020	0.2	2.3
		985.90	0.170	0.030	0.070	0.010	0.060	0.010	0.1	1.6
		1001.1	0.192	0.043	0.112	0.014	0.077	0.012	0.563	1.89
		1004.10	0.211	0.045	0.106	0.014	0.084	0.012	0.473	1.82
		1017.55	0.190	0.044	0.111	0.015	0.076	0.010	0.422	1.90
Deep	7	1046.25	0.502	0.122	0.285	0.041	0.211	0.028	0.620	4.94
		1062.60	0.393	0.091	0.228	0.033	0.181	0.029	0.646	4.70

(Continued on following page)

TABLE 4 (*Continued*) **Rare earth element parameters of shallow, middle and deep dolomites (ug/g).**

Dolomite layer		Well depth/m	La	Ce	Pr	Nd	Sm	Eu	Gd	Tb
		1086.50	0.228	0.055	0.145	0.021	0.107	0.015	0.530	2.64
		1089.45	0.197	0.045	0.103	0.014	0.087	0.013	0.699	1.83
		1098.30	0.383	0.089	0.229	0.028	0.150	0.020	0.708	3.77
		1120.00	0.126	0.030	0.069	0.009	0.049	0.007	0.479	1.31
		1149.00	0.141	0.030	0.077	0.010	0.051	0.006	0.479	1.40

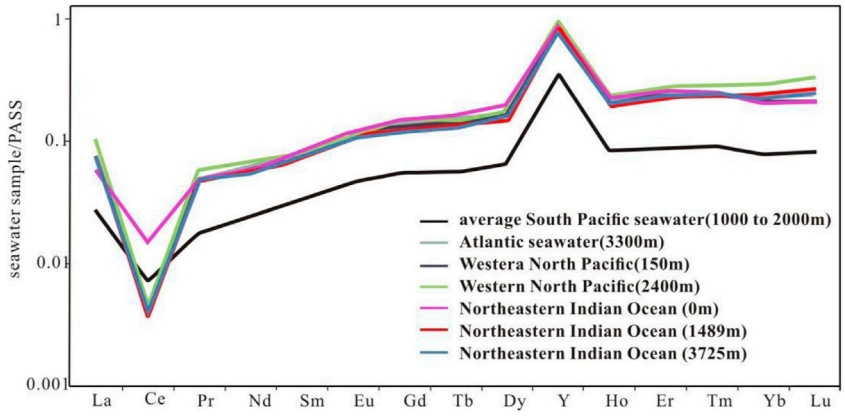

FIGURE 7
Distribution curves of REE in modern seawater (Wang et al., 2017; Wang et al., 2018).

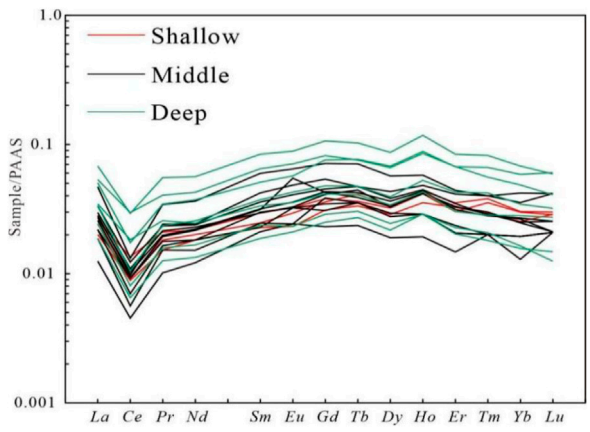

FIGURE 8
Distribution curves of REE in shallow, middle and deep limestones and dolomite samples of Well Xike 1.

The $\delta^{18}O_{(PDB)}$ value of the modern marine carbonate deposits is about 0‰, and the seawater is concentrated after evaporation, which makes the increase of the $\delta^{18}O$ value (Huang, 2010). Sibley (1990) believes that if the salinity of sedimentary medium exceeds the normal seawater during the formation process, the $\delta^{18}O$ value of sediments will exceed 2‰. The fluids formed by dolomites has slightly higher salinity than the sea water, but it can be found by analyzing the carbonate sequence of the Well Xike 1 that there is no gypsum layer with volumetric significance, which also shows that the salinity of fluids is insufficient compared with the required saturation of gypsum. Therefore, the judgment that the dolomite forming fluids is micro evaporation concentrated seawater can be implemented by using the $\delta^{18}O$ value.

5.1.2 Analysis of carbon and oxygen isotopic characteristics of middle and deep dolomites

The average value of $\delta^{18}O$ of middle buried dolomites is 1.448‰, which is lower than that of the shallow dolomites (Secend Member of the Meishan Formation), and it is only 0.002‰ lower than that of deep dolomites. There may be two reasons:

(1) There is a large change in magnesium oxide content in the 10 groups of dolomite samples, resulting in a high

TABLE 5 Dolomites of different genesis and $\delta^{13}C$, $\delta^{18}O$ and Z value of shallow, middle and deep dolomites of Well Xike 1.

Sample	$\delta^{13}C_{PDB}$/‰	$\delta^{18}O_{PDB}$/‰	Z	[a]Data sources
Dolomite in concentrated brine environment	2	3.8	133.3	Holail et al. (1988)
Dorag dolostone	−10~3	−5~5	104.3–135.9	Friedman et al. (1990)
Hydrothermal dolomite	−1.2~−16.8	−4.7~−12.0	86.9–122.5	Friedman et al. (1990)
Marine carbonatite	2.08	−0.002	131.6	Friedman et al. (1990)
Miocene Pliocene dolomite in Well Xichen 1	0.80–3.16/2.24	0.56–5.23/2.56	133.2	Wei Xi et al. (2005)
Shallow buried dolomite of Well Xike 1	1.56–4.33/2.615	1.79–5.589/3.331	131.77–136.30	This text
Middle buried dolomite of Well Xike 1	0.52–3.145/2.390	0.891–2.675/1.883	129.31–134.59	This text
Deep dolomite of Well Xike 1	−1.99–3.62/2.198	−1.99–3.435/1.881	123.97–135.80	This text

[a]Note: the carbon and oxygen isotope values of shallow, middle and deep dolomite in well Xike 1 are displayed as value interval/average value.

proportion of limestone containing dolomites and limestone dolomites. This phenomenon is particularly prominent in the Secend member of the Meishan Formation. There are great differences in the chemical composition, which will also have a certain impact on the $\delta^{18}O$ and carbon isotope values of the middle buried dolomites.

(2) There may be similar genesis between the middle and deep buried dolomites, which leads to the similarity of the $\delta^{13}C$ and $\delta^{18}O$ values.

In terms of the average value of $\delta^{18}O$, the deep layer is 1.448‰ lower than the shallow layer, and it is close to the value of middle buried dolomites. Moreover, the sedimentary value of dolomiterich samples is relatively similar to that of limestones. It can be seen from Table 2 that this situation is particularly prominent in the Sanya Formation, which also indicates that there is a great difference between dolomites and shallow layer in terms of genesis. The $\delta^{18}O$ value will decrease with the increase of pore water temperature (Hu et al., 2010). Therefore, the increase of formation water temperature will have a direct impact on the formation of dolomites, which is consistent with the geological reality of the increase of saddle dolomite content in the deep part of the Well Xike 1 (e.g., buried depth greater than 1100 m).

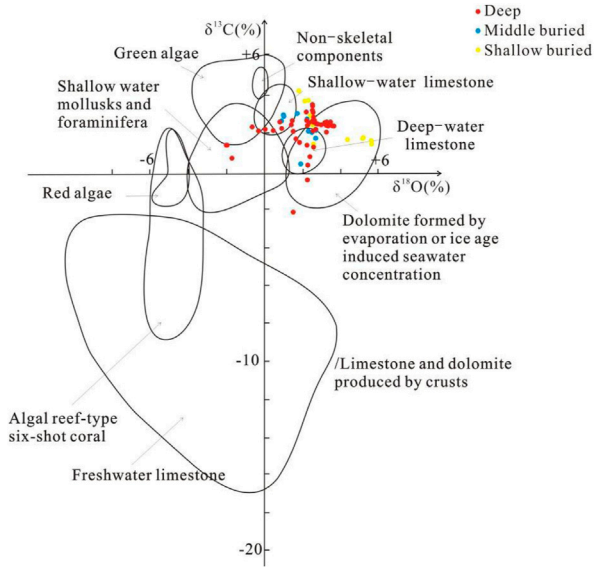

FIGURE 9
Distribution of $\delta^{13}C$ and $\delta^{18}O$ values in different types of marine carbonate rocks (modified according to Milliman, 1978).

5.1.3 Diagenetic environment of carbon and oxygen isotope reaction in dolomites

5.1.3.1 Comparison of diagenetic environments of dolomites of different genesis

The $\delta^{18}O$ value is a function of temperature and salinity, which can reflect the nature of diagenetic fluid to a certain extent (Huang, 2010). According to the paleosalinity calculation formula proposed by Keith et al. (1964),

$$Z = 2.048\left(\delta^{13}C + 50\right) + 0.498\left(\delta^{18}O + 50\right) \quad (1)$$

If the Z value is less than 120, it means that it is a continental diagenetic environment, and if the Z value is greater than 120, it means that it is a marine diagenetic environment. The Z values of shallow buried to deep dolomites in Well Xike 1 are calculated by the carbon and oxygen isotope values.

The statistical results of $\delta^{13}C$, $\delta^{18}O$ isotopic and Z values of dolomites of different origins are shown in Table 5.

The Z value of shallow, middle buried and deep dolomites exceeds 120, so it can be judged that they are formed in a marine environment. According to the statistics and comparison between the measured carbon and oxygen isotope values and the calculated Z values of different types of carbonate rocks, it is found that the variation range of

TABLE 6 Hydrogen isotopic composition of deep seawater.

Ocean	[a]δD/‰	[a]δ^{18}O/‰	Salinity/‰
Arctic Ocean	+2.2 ± 1.0	—	—
Norwegian Sea	+2.2 ± 0.7	—	—
North Atlantic	+1.2 ± 0.8	0.12	34.93
South Atlantic	+1.8 ± 0.6	—	—
Pacific	+1.1 ± 0.4	−0.17	34.692
Central Antarctic sea	+0.9 ± 0.8	−0.21	34.7
Antarctic Circle	−1.7 ± 0.8	−0.3~−0.2	34.69
Antarctic Ocean Bottom Water	—	−0.45	34.65
Indian ocean	—	−0.18	34.71

[a]Data source: hydrogen isotope according to Tian et al. (2016); Oxygen isotope according to Craig (1965).

carbon and oxygen isotopes and Z value of the shallow dolomites of Wells Xike 1 and Xichen 1 are similar (while the Z value of the middle and deep dolomites is slightly lower), and the quasi syngenetic dolomites related to the concentrated seawater is equivalent. This also indicates that the shallow dolomites of the Wells Xike 1 and Xichen 1 have similar genesis. However, the variation range of the carbon and oxygen isotopes and the decrease of the Z value of deep dolomites are closer to the saddle dolomites that related to hydrothermal activity. It indicates that the genesis of deep dolomites is different from that of the shallow dolomites.

5.1.3.2 Comparison of δ^{13}C and δ^{18}O discrimination diagrams of carbonate in different marine environments

δ^{13}C and δ^{18}O values of the shallow, middle and deep dolomites of Well Xike 1 are put into the δ^{13}C and δ^{18}O discrimination diagram of carbonate rocks in different marine environments (Milliman, 1978), the results are shown as follows (Figure 9):

For shallow buried dolomite, the δ^{18}O value varies from 1.79‰ to 5.589‰, with an average value of 3.33‰; the δ^{13}C value varies from 1.56‰ to 4.33‰, and the average value is 2.61‰. Except that some points fall in the freshwater limestone area, most of the δ^{13}C and δ^{18}O values fall in and near the dolomite areas formed by seawater concentrations (dolomites formed by seawater concentration caused by evaporation or ice age), indicating that dolomitization occurs in the period of seawater concentration and salinization.

For the middle buried dolomites, the δ^{13}C value varies from 0.52‰ to 3.14‰, with an average value of 2.39‰, while the δ^{18}O value varies from 0.891‰ to 2.675‰, with an average value of 1.883‰. For the deep dolomites, the δ^{13}C value varies from −1.99‰ to 3.62‰, with an average of 2.198‰, while the δ^{18}O value varies from −1.99‰ to 3.435‰, with an average of 1.881‰. The genesis of the middle and deep buried dolomites is quite different from that of the shallow buried dolomites.

5.2 Diagenetic environment of hydrogen isotope reaction

(1) The hydrogen and oxygen isotopes of the present seawater are relatively stable. The fluctuation range of the δD value is 4‰, and that of the oxygen isotope value is 0.3‰ (Tian et al., 2016). The hydrogen isotopic composition of deep seawater are shown in Table 6.

(2) The molecules containing light isotopes are easy to vaporize, which leads to a wide range of hydrogen and oxygen isotope values on the surface of seawater. Generally, there are hydrogen and oxygen isotopes on the surface of seawater $\delta D = M\ \delta^{18}O$. When the ratio of seawater evaporation to precipitation increases, the value of M will decrease. According to the statistical data (Tian et al., 2016), the *m* values of the North Pacific and the Red Sea are 7.5 and 0.6, respectively.

(3) The evaporation process not only causes changes in δD and δ^{18}O, but also lead to changes in seawater salinity, so δD and δ^{18}O are in direct proportion to salinity. For example, in the Red Sea, the salinity of surface water, intermediate water and deep water changes from 41‰ to 34‰, while the δ^{18}O will also change correspondingly, from 1.9‰ to 0.6‰, δD is reduced from +10‰ to +4‰ (Craig, 1965).

(4) It is found that δD value in atmospheric water is related to altitude, temperature and climate humidity during precipitation (Dansgaard, 1964). There is a certain linear correlation between δD and δ^{18}O values, which can be used

TABLE 7 Statistics of REE parameters of shallow, middle and deep dolomites.

Dolomite layer		∑REE (μg/g)	∑LREE (μg/g)	∑HREE (μg/g)	LREE/HREE	[a]δEu	[a]δCe
Shallow	Minimum	2.773	2.163	0.610	3.451	0.862	0.442
	Maximum	3.579	2.896	0.705	4.235	0.970	0.573
	Average value	3.163	2.497	0.666	3.744	0.930	0.506
Middle	Minimum	1.740	1.360	0.380	3.103	0.767	0.324
	Maximum	5.470	4.350	1.120	4.302	1.484	0.463
	Average value	3.325	2.623	0.701	3.746	1.044	0.395
Deep	Minimum	2.188	1.746	0.442	3.347	0.887	0.366
	Maximum	9.018	7.190	1.829	5.204	1.003	0.632
	Average value	5.125	4.106	1.019	4.133	0.942	0.471
Modern seawater (Kawabe et al., 1998)		11.646	7.790	3.856	2.020	0.965	0.131
Modern seawater carbonate rocks in eastern China (Yan et al., 1997)		25.500	22.760	2.740	8.306	1.123	0.921
Upper crust (Taylor et al., 1985)		146.370	132.480	13.890	9.537	0.993	1.008

[a]Note: the sample is standardized by PAAS (Taylor and McLennan, 1985). The calculation formula of each abnormal value is: δEu = EuN/(0.5Sm + 0.5Gd) N; δCe=CeN/(0.5La + 0.5Pr) N.

to judge the relationship between surface water and groundwater (Craig, 1961; Holser, 1979; Richard, 2013).

The δD and $\delta^{18}O$ values of fluids from each source are (Kyser et al., 1984; Zhang et al., 1993; Wang et al., 2011):

Magmatic water: δD −50‰~−80‰; $\delta^{18}O$+6‰~+8‰;

Present seawater: δD 0‰;

Atmospheric water (rainwater): δD −350‰~+50‰; $\delta^{18}O$ −44‰~+10‰;

Among the three samples in the shallow buried dolomites (below 579.26 m), The maximum value of δD is −46.7‰, the minimum value is −50.3‰, and the average value is −48.3‰; while in the middle and deep buried dolomite interval (770.05–1257.4 m well section), the maximum value of δD is −48.1‰, the minimum value is −57.0‰, and the average value is 53.1‰. It can be seen that no matter whether it is shallow, middle or deep dolomites, the δD value is obviously less than the hydrogen isotope value of seawater, and is similar to that of limestone. In Well Xike 1, the average hydrogen isotope value of limestone is −55.67‰ (Yin He, 2020). Richard (2013) believes that the surface fluid δD value is −40‰ ~ −70‰, it reflects that the diagenetic environment of dolomites is mainly near surface environment. While the hydrogen isotope composition in atmospheric precipitation varies greatly, the δD value ranges from −350‰~ + 50‰. It is speculated that the dolomite may have been affected by the mixing of atmospheric precipitation and concentrated seawater during the quasi syngenetic period. However, Bi et al. (2018) thinks that the small hydrogen isotope value of the Well Xike 1 may also be related to the decomposition of organic matter.

5.3 Analysis of REE data

The statistical results of REE parameters of the shallow, middle and deep dolomites are shown in Table 7. Compared with the continental crust (Taylor et al., 1985) and carbonate rocks in eastern China (Yan M et al., 1997), the dolomites in layer 7 of Well Xike 1 shows a typical low total rare earth (∑REE) -with an average value of 3.928 μg/g, the ΣREE values of most samples range from 1.74 μg/g to 5.47 μg/g, only a few samples showed high values, but none of them exceeded 100 μg/g. The distribution range of ΣREE indicates marine carbonate rocks (Qing et al., 1994). It can be seen from this feature that no other provenance is mixed into dolomites. In terms of light rare earth content, the average is 3.123 μg/g, and the ∑LREE value ranges from 1.746 μg/g to 7.190 μg/g. In terms of heavy rare earth content, the average value of light rare earth content is 0.805 μg/g, the ∑HREE value ranges from 0.380 μg/g to 1.829 μg/g. On the whole, the REE characteristics of the 7-layer dolomites are basically similar, indicating that there is a relatively similar environment in the diagenetic process.

In the redox environment, the multivalent state characteristics of Ce and Eu will show sensitive changes. Calcium and magnesium ions (Ca^{2+} and Mg^{2+}) in the lattice structures of dolomites can be replaced by rare earth elements. In the oxidation environment, Ce and Eu in dolomites are relatively less. This is because Ce and Eu ions can be trivalent in the

oxidation environment, so they are difficult to replace divalent calcium and magnesium ions in the lattice of dolomites, which are easier to be extracted and exist in the fluids. Under low temperature and alkaline environment, Eu changes from trivalent state to divalent state, which is easier to dissolve and thus is migrated and depleted. According to the analysis of the measured sample data of dolomites in well Xike 1, the dolomite δCe negative anomaly is the lowest, and the δEu values of some dolomites have different negative anomaly characteristics from carbonate rocks in the eastern China, indicating that marine derived fluids are involved in the whole diagenetic process (including dolomitization) or that the diagenesis of dolomites is mainly affected by marine derived fluids. In dolomites the negative anomaly of δCe value reflects its diagenesis in the semi open environment of partial oxidation, while the diagenetic environment corresponding to the negative δEu value anomaly is low temperature and alkaline conditions.

The degree of Eu negative anomaly in shallow dolomite is slightly higher than that in other dolomites, indicating that it may have a lower ambient temperature during its formation-the oxygen isotope characteristics of foraminifera observed in ODP184 voyage sampling core also reflect the seawater cooling event in the South China Sea in the late Pliocene, which may be the reason for the lower diagenetic ambient temperature of shallow dolomite (Li Jianru et al., 2004).

5.4 Sedimentary tectonic setting and paleoclimate in Xisha area

In the South China Sea, in the early Miocene of about 5 Ma, there was obvious magmatic activities in the residual expansion center of the southwest basin (Meng L et al., 2014). From the late Miocene, the Dongsha Movement appeared in the northern South China Sea, and its activity stopped at the end of late Miocene/early morning Miocene (5.5 Ma) (Lin et al., 2009; Zhao et al., 2012). The large-scale dolomites in Wells Xike 1 and Xichen 1 is formed below the Miocene/Pliocene boundary.

The global paleoclimate background of dolomite deposits in Well Xike-1 during the Late Miocene-Pliocene is characterized by gradual cooling. In the middle and late Miocene, the global climate became significantly cooler, marine productivity increased sharply, and organic carbon buried rapidly, which further led to the decrease of bottom water temperature, and eventually led to the expansion and permanent formation of the Antarctic ice sheet at the end of the Miocene (Zachos et al., 2001; Lu and Chen, 2006).

From the end of the Miocene to the early Pliocene, the global climate fluctuated dramatically, experiencing several cooling (about 6.15–5.8 Ma in the Late Miocene), the latest in the Miocene to the Early Pliocene (about 5.7–5.46 Ma), warming (about 5.8–5.7 Ma in the Late Miocene), 5.46–4.9 Ma in the Early Pliocene (Hodell et al., 1986), and 4.6 Ma in the Early Pliocene. Therefore, from the late Miocene to the early Pliocene, the global climate is not always cold, but during the warming period, the ice sheet melts, the sea level rises, and the hydrothermal activity of the seabed is more active than that of the cooling period.

Due to the tectonic movement around 5.5 Ma, the thermal convection generated by deep thermal fluids migration is likely to affect the deposited Huangliu formation sediments. The mineral structures of dolomites in Well Xike 1 generally shows that the mineral structures of dolomites is relatively better in the first member of the Meishan Formation (576.5–758.4 m) with relatively low degree of dolomitization. The reason may be that the temperature of the diagenetic fluids is relatively high (the homogenization temperature of 82 dolomite fluid inclusions below 1064 m well depth tested by Shi et al. (2016) is 129.5°C–268.5°C, with an average of 184.6°C). When the buried depth increases gradually, the proportion of over dolomitized fog-bright edge dolomite and cement dolomite increases significantly.

5.5 Comparison of research results between Wells Xichen 1 and Xike 1

Wells Xichen 1 and Xike 1 have similar dolomite mineral types, including bright crystal cement, various mud crystal fossils, mud crystal debris and mud crystal particles (Wei et al., 2008a; Wei et al., 2008b; Wei et al., 2008c). Dolomite accounts for the majority of dolomites in Well Xichen 1, with a volume fraction of more than 91.1%, up to 100%. From these data, it can be seen that there are relatively loose carbonate rocks in the dolomitization process, which can be fully contacted with water and rock, and can last for a long time to dolomitize.

Among the three sections of dolomites in Well Xichen 1, both the $\delta^{13}C$ and $\delta^{18}O$ values are positive numbers. Among them, the average value of $\delta^{13}C$ is 2.24‰, and the average value of $\delta^{18}O$ is 2.56‰ (Wei et al., 2008a; Wei et al., 2008b; Wei et al., 2008c), and Wei et al. (2006a, 2006b) think that there is no obvious rainwater or underground fresh water leaching environment during the formation and evolution of dolomites in Well Xichen 1. However, if the dolomites in Well Xichen 1 undergoes alteration of lithogenic and hydrothermal fluids (Wei et al., 2006ab; Wei et al., 2007) during the evolution of metagenetic rocks, the carbon and oxygen isotopes (especially oxygen isotopes) of rocks may change, and the existing test values can not fully represent the characteristics of the original sedimentary environment. Wei et al. (2008a), Wei et al. (2008b), and Wei et al. (2008c) measured the fluid inclusions of authigenic bright dolomite minerals in rock pores or fractures. The results show that the fluid homogenization temperature during inclusion capture is 102.5–296°C, with an average of 156.3°C. The salinity ranged from 0.55 to 6.25%, with an average of 3.75%. The salinity slightly higher than that of the modern seawater reflects the fluid characteristics of dolomitization of brackish

water or of medium salinity. The temperature measurement results of the inclusions are similar to the test results of Wells Sike 1 by Shi et al. (2016), which reflects that the similar diagenetic environments.

From the regional tectonic background, during the tectonic movement in the Xisha area in the late Miocene, the thermal convection caused by the upwelling of thermal fluids may have an impact on the deposited sediments of the Huangliu Formation, and the impact on the carbonate rocks of the Sanya Formation is more significant and extensive. High temperature is a necessary thermodynamic condition for the formation of dolomites (Machel, 2004; Huang, 2010). Therefore, the thermal fluids in this period undoubtedly promoted the occurrence of percolation and dolomitization. According to the research on dolomite structure, mineral composition, isotopic characteristics, inclusion type and characteristics of Well Xichen 1, it is shown that the hot water fluids played a role in the evolution process of carbonate rocks in the Xisha Islands. Under magmatism, the hydrothermal fluids can get enough heat, while the formation water and hydrothermal fluids have similar compositions, and dolomites are transformed by diagenetic fluids and hydrothermal fluids of imestone reservoirs.

Other scholars also systematically analyzed the $\delta^{13}C$ and $\delta^{18}O$ values of Well Xichen 1, and discussed the diagenetic model of dolomites of well Xichen 1 (Xisha Islands):

Previous studies suggested that that the δ18O value of dolomitse in Well xichen-1 is 2‰–5‰ higher than that of non-dolomitic rocks, and the $\delta^{13}C$ value is 3‰ higher than that of the non-dolomitic rocks. It is believed that this feature of enrichment of oxygen carbon heavy isotopes is a strong evidence of the increase of seawater salinity beyond the normal seawater. Some studies believe that the values of $\delta^{18}O$ of dolomite in Well Xichen 1 are normal, which cannot explain that the diagenetic medium has salinity anomaly higher than sea water, but the $\delta^{13}C$ value of the Xisha dolomites is too high and the $\delta^{13}C$ value of the symbiotic calcites is too light. The dolomite in Well Xichen can be explained by the mechanism of mixed water dolomitization (He and Zhang, 1990). Combined with the test results of inclusions, some studies thought that dolomites in Well xichen-1 show the characteristics of high temperature and salinity, and it is likely to be affected by hydrothermal activities when it is formed (Zhao, 2010).

6 Conclusion

(1) The geochemical characteristics of REE in reef dolomite reservoirs in Well Xike 1 show that the main diagenetic environment of dolomite is low-temperature alkaline semi open oxidation environment; the carbon and oxygen isotopes of the dolomite are generally lack of correlation, δD is significantly lower than the hydrogen isotope value of seawater. Meanwhile, the oxygen isotope value of deep dolomites is negatively biased, which may be due to the increase or decrease of pore water temperature caused by deep thermal convection that related to the regional tectonic movements of the South China Sea.

(2) The $\delta^{18}O$ value is also consistent with the geological reality of increasing saddle dolomite content in deep dolomites. The distribution of $\delta^{13}C$ value indicates that the dolomite inherited the carbon of the original limestone during dolomitization, while the characteristic of δD value shows that it may be affected by the mixing of atmospheric precipitation and concentrated seawater in the quasi contemporaneous period.

(3) Based on the comprehensive analysis of the geochemical characteristics of the Well Xike 1, it is considered that the higher diagenetic temperature could be an important factor leading to the huge differences between the diagenetic model of deep and shallow dolomites.

(4) The geochemical characteristics of the shallow dolomites show that it is mainly reflux infiltration dolomitization under the micro evaporation and concentration sea water environments, while the deep dolomite is transformed by the hot water fluids in the epigenetic diagenetic evolution stage (Vasconcelos and McKenzie, 1997; Wei et al., 2006a; Wei, 2006b; Wei et al., 2008a; Wei et al., 2008b; Huang et al., 2009; Wang R. et al., 2018; Wang Z. et al., 2018).

Data availability statement

The original contributions presented in the study are included in the article/supplementary material, further inquiries can be directed to the corresponding author.

Author contributions

XL and ZS are responsible for the idea of this paper and LH and XH are responsible for the experiments.

Conflict of interest

The authors declare that the research was conducted in the absence of any commercial or financial relationships that could be construed as a potential conflict of interest.

Publisher's note

References

Aloisi, G., Pierre, C., Rouchy, J., Foucher, J. P., and Woodside, J. (2000). Methane-related authigenic carbonates of eastern mediterranean sea mud volcanoes and their possible relation to gas hydrate destabilisation. *Earth Planet. Sci. Lett.* 184 (1), 321–338. doi:10.1016/S0012-821X(00)00322-8

Arthur, M. A., and Schlanger, S. O. (1979). Cretaceous "oceanic anoxic events" as causal factors in development of reef-reservoired giant oil fields. *Am. Assoc. Pet. Geol. Bull.* 63 (6), 870–885. doi:10.1306/2F91848C-16CE-11D7-8645000102C1865D

Arvidson, R. S., and Mackenzie, F. T. (1999). The dolomite prob-lem: Control of precipitation kinetics by temperature and sat-uration state. *Am. J. Sci.* 299 (4), 257–288. doi:10.2475/ajs.299.4.257

Bi, D. J., Zhai, S. K., Zhang, D. J., Liu, X. F., Liu, X. Y., Jiang, L. J., et al. (2018). Constraints of fluid inclusions and C, O isotopic compositions on the origin of the dolomites in the Xisha Islands, South China Sea. *Chem. Geol.* 493, 504–517. doi:10.1016/j.chemgeo.2018.07.005

Bontognali, T. R., Vasconcelos, C., Warthmann, R. J., Bernasconi, S. M., Dupraz, C., Strohmenger, C. J., et al. (2010). Dolomite formation within microbial mats in the coastal sabkha of Abu Dhabi (United Arab E-mirates). *Sedimentology* 57 (3), 824–844. doi:10.1111/j.1365-3091.2009.01121.x

Braithwaite, C. J. R., Rizzi, G., and Darke, G. (2004). The geometry and petrogenesis of dolomite hydrocarbon reservoirs: Introduction. *Geol. Soc. Lond. Spec. Publ.* 235 (1), 1–6. doi:10.1144/GSL.SP.2004.235.01.01

Briais, A., Patriat, P., and Tapponnier, P. (1993). Updated interpretation of magnetic anomalies and seafloor spreading stages in the South China Sea: Implications for the Tertiary tectonics of Southeast Asia. *J. Geophys. Res.* 98 (B4), 6299–6328. doi:10.1029/92JB02280

Budd, D. A. (1997). Cenozoic dolomites of carbonate islands: Their attributes and origin. *Earth-Science Rev.* 42, 1–47. doi:10.1016/S0012-8252(96)00051-7

Chacko, T., and Deines, P. (2008). Theoretical calculation of oxygen isotope fractionation factors in carbonate systems. *Geochimica Cosmochimica Acta* 72 (15), 3642–3660. doi:10.1016/j.gca.2008.06.001

Craig, H., and Gordon, L. I. (1965). "Deuterium and oxygen-18 variations in the ocean and marine atmosphere," in *Proceedings of the conference on stable isotopes in oceanographic studies and paleotemperatures*. Editor E. Tongiorgi (Lower Hutt, New Zealand: Laboratory of Geology and Nuclear Science), 9–130.

Craig, H. (1961). Isotopic variations in meteoric waters. *Science* 133 (3465), 1702–1703. doi:10.1126/science.133.3465.1702

D'Hondt, S., Inagaki, F., and Alvarez, Z. (2012). *IODP expedition 329: Life and habitability beneath the seafloor of the South pacific gyre dolomitization of Neogene seroe domi formation coral reef limestones on curaçao, Netherlands antilles*. Hague, Netherlands: Publications Foundation for Scientific Research in the Caribbean Region, 197–198. doi:10.2204/iodp.sd.15.01.2013

Dansgaard, W. (1964). Stable isotopes in precipitation. *Tellus* 16 (4), 436–468. doi:10.3402/tellusa.v16i4.8993

Fouke, B. W. (1994). *Deposition, diagenesis and dolomitization of Neogene seroe domi formation coral reef limestones on curacao*. Netherlands Antilles: Publications Foundation for scientific research in the Caribbean region.ISBN: 9074624030

Friedman, G. M., Ghosh, S. K., and Urschel, S. (1990). "Petrophysical characteristics related to depositional environments and diagenetic overprint: A case study of the san andres formation, mabee field, west Texas," in *Geologic and engineering approaches in evaluation of San Andres/Grayburg hydrocarbon reservoirs—Permian Basin*. Editor D. G. Bebout and P. M. Harris (Austin, Texas: Bureau of Economic Geology, The University of Texas at Austin), 125–144.

Friedman, I. (1953). Deuterium content of natural waters and other substances. *Geochimica cosmochimica acta* 4 (1-2), 89–103. doi:10.1016/0016-7037(53)90066-0

Fritz, P., and Smith, D. G. W. (1970). The isotopic composition of secondary dolomites. *Geochimica Cosmochimica Acta* 34 (11), 1161–1173. doi:10.1016/0016-7037(70)90056-6

Hodell, D. A., and Kennett, J. P. (1986). Late miocene–early Pliocene stratigraphy and paleoceanography of the South atlantic and southwest pacific oceans: A synthesis. *Paleoceanography* 1 (3), 285–311. doi:10.1029/PA001i003p00285

Holail, H., Lohmann, K. C., and Sanderson, I. (1988). Dolomitization and dedolomitization of upper cretaceous carbonates: Bahariya oasis, Egypt. *Spec. Publ.* 43, 191–207. doi:10.2110/pec.88.43.0191

Holser, W. T., Kaplan, I. R., Sakai, H., and Zak, I. (1979). Isotope geochemistry of oxygen in the sedimentary sulfate cycle. *Chem. Geol.* 25 (1-2), 1–17. doi:10.1016/0009-2541(79)90079-2

Hong, H., Su-ping, P., and Long-yi, S. (2004). Trace elements and sedimentary settings of Cambrian-Ordovician carbonates in Bachu area, Tarim Basin. *Xinjiang Pet. Geol.* 25 (6), 631. doi:10.3969/j.issn.1001-3873.2004.06.015

Hu, Z. W., Huang, S. J., and Huang, K. K. (2010a). Preservative evaluation of coeval seawater information for the Triassic marine carbonate rocks in the Huaying Mountain, eastern Sichuan. *Geol. China* 37 (5), 1374–1382. doi:10.3724/SP.J.1011.2010.01081

Hu, Z. W., Huang, S. J., Li, M. Z., Zang, X. H., Xu, E. S., and Liu, T. (2010b). Preliminary application of the dolomite-calcite oxygen isotope thermometer in studying the origin of dolomite in Feixianguan Formation, Northeast Sichuan, China. *J. ChengDu Univ. Technol. Sci. Techonlogy Ed.* 39 (1), 1–9. doi:10.3969/j.issn.1671-9727.2012.01.001

Huang, Sijing (2010). *Carbonate diagenesis*. Beijing, China: Geological Publishing House.ISBN.978-7-116-06938-1

Huang, S. J., Hu, Z. W., Zhong, Y. J., Huang, K. K., and Li, X. N. (2015). Saddledolomitein Permian—triassiccarbonaterocksand sandstones of Sichuan Basin: petrology, formation temperatureand palaeofluids. *Journal of Chengdu University of Technology (Science and Technology Edition)* 42 doi:10.3969/j.issn.1671-9727.2015.02.01

Huang, S. J., Huang, K. K., and Zhang, X. H. (2009). Chemical thermodynamics foundation of retrograde solubility for carbonate: Solution media related to CO_2. *J. Chengdu Univ. Technol. Sci. Technol. Ed.* 36 (5), 457–464. doi:10.3969/j.issn.1671-9727.2009.05.001

Jiménez-López, C., Romanek, C. S., Huertas, F. J., Ohmoto, H., and Caballero, E. (2004). Oxygen isotope fractionation in synthetic magnesian calcite. *Geochimica Cosmochimica Acta* 68 (16), 3367–3377. doi:10.1016/j.gca.2003.11.033

Kaufman, A. J., and Knoll, A. H. (1995). Neoproterozoic variations in the C-isotopic composition of seawater: Stratigraphic and biogeochemical implications. *Precambrian Res.* 73 (1-4), 27–49. doi:10.1016/0301-9268(94)00070-8

Kawabe, I., Toriumi, T., Ohta, A., and Miura, N. (1998). Monoisotopic REE abundances in seawater and the origin of seawater tetrad effect. *Geochem. J.* 32 (4), 213–229. doi:10.2343/geochemj.32.213

Keith, M. L., and Weber, J. N. (1964). Carbon and oxygen isotopic composition of selected limestones and fossils. *Geochim. Cosmochim. Acta* 28 (10-11), 1787–1816. doi:10.1016/0016-7037(64)90022-5

Kenward, P., Goldstein, R., Gonzalez, L., and Roberts, J. (2009). Precipitation of low-temperature dolomite from an anaerobic microbial consortium:The role of methanogenic Archaea. *Geobiology* 7 (5), 556–565. doi:10.1111/j.1472-4669.2009.00210.x

Kyser, T. K., and O'Neil, J. R. (1984). Hydrogen isotope systematics of submarine basalts. *Geochimica Cosmochimica Acta* 48 (10), 2123–2133. doi:10.1016/0016-7037(84)90392-2

Land, L. S. (1998). Failure to precipitate dolomite at 25°C from di-lute solution despite 1000-fold oversaturation after 32 years. *Aquat. Geochem.* 4 (3), 361–368. doi:10.1023/A:1009688315854

Li, H., and Liu, Y. (2013). Dolomite problem" and research of ancient lacustrine dolostones. *Acta Sedimentol. Sin.* 3 (2), 302–315. doi:10.14027/j.cnki.cjxb.2013.02.017

Li, J., and Wang, G. P. (2004). Late Pliocene changs of upper ocean structure in the southern south China sea. *Mar. Geol. Quat. Geol.* doi:10.16562/j.cnki.0256-1492.2004.04.010

Lin, C., and Chu, F. (2009). On tectonic movement in the South China sea during the cenozoic. *Acta Oceanol. Sin.* 28 (1), 25–36. doi:10.1061/41042(349)25

Lu, C. L., Zhang, G. C., Yao, Y. J., and Wu, S. G. (2014). Tectonic evolution of the wanan basin, southwestern south China sea. *Acta Geol. Sin. - Engl. Ed.* 88 (4), 1120–1130. doi:10.1111/1755-6724.12277

Lu, J., and Chen, M. H. (2006). Global climate events since Cenozoic. *J. Trop. Oceanogr.* 25 (6), 72–79. doi:10.3969/j.issn.1009-5470.2006.06.013

Machel, H. G. (2004). Concepts and models of dolomitization: A critical reappraisal. *Geol. Soc. Lond. Spec. Publ.* 235 (1), 7–63. doi:10.1144/GSL.SP.2004.235.01.02

Mazzullo, S. J. (2000). Organogenic dolomitization in peritidal to deep-sea sediments. *J. Sediment. Res.* 70 (1), 10–23. doi:10.1306/2DC408F9-0E47-11D7-8643000102C1865D

Meng, L., and Zhang, J. (2014). The magmatic activity mechanism of the fossil spreading center in the Southwest sub-basin, South China Sea. *Sci. China Earth Sci.* 57 (7), 1653–1663. doi:10.1007/s11430-013-4788-x

Milliman, J. D. (1978). "Modern sediment carbonate," in *Marine carbonate, translated by institute of GeoloChinese Academy of sciences* (Beijing, China: Geological Publishing House), 1. (in Chinese).

Ni, S., Ju, Y., Hou, Q., Wang, S., Liu, Q., Wu, Y., et al. (2009). Enrichment of heavy metal elements and their adsorption on iron oxides during carbonate rock weathering process. *Prog. Nat. Sci.* 19 (9), 1133–1139. doi:10.1016/j.pnsc.2009.01.008

Peng, R. M., Zhai, Y. S., Wang, Z. G., Han, X. F., Qin, J. W., Wang, J. P., et al. (2006). Characteristics and exploration of submarine sedex deposits in the Langshan-Zhaertai ore concentration area, Inner Mongolia. *Mineral. Deposits* 25 (S1), 221–224. doi:10.16111/j.0258-7106.2006.s1.058

Petrash, D. A., Bialik, O. M., Bontognali, T. R. R., Vasconcelos, C., Roberts, J. A., McKenzie, J. A., et al. (2017). Mi-crobially catalyzed dolomite formation: From near-surface to burial. *Earth-Science Rev.* 171, 558–582. doi:10.1016/j.earscirev.2017.06.015

Qing, H., and Mountjoy, E. W. (1994). formation of coarsely crystalline, hydrothermal dolomite reservoirs in the presquile barrier, western Canada sedimentary basin. *Am. Assoc. Pet. Geol. Bull.* 78 (1), 55–77. doi:10.1306/BDFF9014-1718-11D7-8645000102C1865D

Qiu, X., Ye, S., Wu, S., Shi, X., Zhou, D., Xia, K., et al. (2001). Crustal structure across the Xisha trough, northwestern south China sea. *Tectonophysics* 341, 179–193. doi:10.1016/S0040-1951(01)00222-0

Richard, A., Boulvais, P., Mercadier, J., Boiron, M. C., Cathelineau, M., Cuney, M., et al. (2013). From evaporated seawater to uranium-mineralizing brines: Isotopic and trace element study of quartz–dolomite veins in the Athabasca system. *Geochimica Cosmochimica Acta* 113, 38–59. doi:10.1016/j.gca.2013.03.009

Riding, R. (2002). Structure and composition of organic reefs and carbonate mud mounds: Concepts and categories. *Earth-Science Rev.* 58 (1-2), 163–231. doi:10.1016/S0012-8252(01)00089-7

Roberts, J. A., Kenward, P. A., Fowle, D. A., Goldstein, R. H., Gonzalez, L. A., and Moore, D. S. (2013). Surface chemistry allows for abiotic precipitation of dolomite at low temperature. *Proc. Natl. Acad. Sci. U. S. A.* 110 (36), 14540–14545. doi:10.1073/pnas.1305403110

Roberts, J., Bennett, P., González, L., Macpherson, G., and Milliken, K. L. (2004). Micro-bial precipitation of dolomite in methanogenic groundwater. *Geol.* 32 (4), 277. doi:10.1130/G20246.2

Sánchez-Román, M., Vasconcelos, C., Schmid, T., Dittrich, M., Mc, K., Zenobi, R., et al. (2008). Aerobic microbial dolomite at the nanometer scale: Implications for the geologic record. *Geol.* 36 (11), 879–882. doi:10.1130/G25013A.1

Schmidt, M., Xeflide, S., Botz, R., and Mann, S. (2005). Oxygen isotope fractionation during synthesis of CaMg-carbonate and implications for sedimentary dolomite formation. *Geochimica Cosmochimica Acta* 69, 4665–4674. doi:10.1016/j.gca.2005.06.025

Shi, Z. Q., Xie, Y. H., and Liu, L. (2016). *South China Sea-Reservoir Characteristics and Diagenetic Evolution (in Chinese)*, 147. Wuhan, China: China University of Geosciences Press–167. 978-7-5625-3975-9.

Sibley, D. F. (1990). Unstable to stable transformations during dolomitization. *J. Geol.* 98 (5), 739–748. doi:10.1086/629437

Tarutani, T., Clayton, R. N., and Mayeda, T. K. (1969). The effect of polymorphism and magnesium substitution on oxygen isotope fractionation between calcium carbonate and water. *Geochimica Cosmochimica Acta* 33 (8), 987–996. doi:10.1016/0016-7037(69)90108-2

Taylor, B., and Hayes, D. E. (1983). Origin and history of the South China Sea basin, 27. *Washington DC American Geophysical Union Geophysical Monograph Series*, 23–56. doi:10.1029/GM027p0023

Taylor, S. R., and McLennan, S. M. (1985). *The continental crust: Its composition and evolution*. Oxford, England: Blackwell Scientific Publications, 312. doi:10.1017/S0016756800032167

Tian, J. C., and Zhang, X. (2016). *Sedimentary geochemistry*, 114-115. BeiJing: Geological Publishing House. 978-7-116-09646-2.

Tian, Q., Prange, M., and Merkel, U. (2016). Precipitation and temperature changes in the major Chinese river basins during 1957–2013 and links to sea surface temperature. *J. Hydrology* 536, 208–221. doi:10.1016/j.jhydrol.2016.02.048

Vasconcelos, C., McKenzie, J. A., Bernasconi, S., Grujic, D., and Tiens, A. J. (1995). Microbial mediation as a possible mechanism for natural dolomite formation at low temperatures. *Nature* 377 (6546), 220–222. doi:10.1038/377220a0

Vasconcelos, C., and McKenzie, J. A. (1997). Microbial mediation of modern dolomite precipitation and diagenesis under anoxic conditions (Lagoa Vermelha, Rio de Janeiro, Brazil). *J. Sediment. Res.* 67 (3), 378–390. doi:10.1306/D4268577-2B26-11D7-8648000102C1865D

Vasconcelos, C., Mckenzie, J. A., Warthmann, R., and Bernasconi, S. M. (2005). Calibration of the $\delta^{18}O$ paleothermometer for dolomite precipitated in microbial cultures and natural environments. *Geol.* 33, 317–320. doi:10.1130/G20992.1

Wang, L., Lei, S., and Jia, L. (2011). The application of fluid inclusion in the study of mineral deposit. *Gold Sci. Technol.* 19 (4), 25–30. doi:10.3969/j.issn.1005-2518.2011.04.005

Wang, P., Tian, J., and Lourens, L. J. (2010). Obscuring of long eccentricity cyclicity in Pleistocene oceanic carbon isotope records. *Earth Planet. Sci. Lett.* 290 (3-4), 319–330. doi:10.1016/j.epsl.2009.12.028

Wang, R., Yu, K., Jones, B., Wang, Y., Zhao, J., Feng, Y., et al. (2018a). Evolution and development of Miocene "island dolostones" on Xisha islands, south China sea. *Mar. Geol.* 406, 142–158. doi:10.1016/j.margeo.2018.09.006

Wang, Z., Huang, K., Zhang, D., Liu, X., Luo, W., and You, L. (2017). Rare Earth element and yttrium (REY) geochemistry of cenozoic carbonates on the xuande atoll of the Xisha archipelago, the South China sea: Implications of the impact of dolomitization on REY. *Geochem. J.* 51 (6), 507–523. doi:10.2343/geochemj.2.0487

Wang, Z., Huang, K., Zhang, D., You, L., Liu, X., and Luo, W. (2018b). Maturation of neogene dolomite from xuande atoll of Xisha archipelago, the South China Sea. *Mar. Petroleum Geol.* 92, 51–64. doi:10.1016/j.marpetgeo.2018.02.016

Wei, X., Deng, J., and Xie, W. (2005). Constraints on biogenetic reef for mation during evolution of the South China Sea and exploration potential analysis. *Earth Sci. Front.* 12 (3), 245–252. doi:10.3321/j.issn:1005-2321.2005.03.026

Wei, X. (2006b). "*Forming condition of Late-Cenozoic reef facies Carbonate rocks in Xisha sea area and their oil and gas exploration potential*,". PhD Thesis (Beijing, China: China University of Geosciences).

Wei, X., Jia, C. Z., and Meng, W. G. (2008b). Discussion on biogenetic reef distribution and hydrocarbon exploration direction in Xisha sea area since neogene. *Oil Geophys. Prospect.* 43 (3), 308–315. (in Chi-nese with English Abstract). doi:10.3321/j.issn:1000-7210.2008.03.013

Wei, X., Jia, C. Z., and Meng, W. G. (2008c). Dolomitization characteristics of carbonate rock in Xisha islands and its formation: A case study of well xichen-1. *J. Jilin Univ. (Earth Sci. Ed.* 38 (2), 217–224. doi:10.13278/j.cnki.jjuese.2008.02.006

Wei, X., Jia, C. Z., Meng, W. G., and Xiong, X. H. (2008a). Biogenetic reefs and its petrological characteristics of well Xichen 1, Xisha sea area, China. *Geol. Bull. China* 27 (11), 1933–1938. doi:10.3969/j.issn.1671-2552.2008.11.024

Wei, X., Jia, C. Z., Meng, W. G., and Zhang, F. L. (2007). Mineral content and geochemistry characteristics of carbonate rock in well No. Xichen-1 and geological significance. *Acta Petrol. Sin.* 23 (11), 3015–3025. (in Chinese with English abstract). doi:10.3969/j.issn.1000-0569.2007.11.031

Wei, X., Zhu, Y. J., and Yin, J. H. (2006a). Constrains and growing trend of biological reef in South China Sea Basin. *Special Oil Gas Reservoirs* 13 (1), 10–15. doi:10.3969/j.issn.1006-6535.2006.01.003

Xu, H., Zhao, X., Eberli, G. P., Liu, X., Zhu, Y., Cai, Y., et al. (2015). Biogenic carbonate formation and sedimentation in the Xisha islands: Evidences from living halimeda. *Acta Oceanol. Sin.* 34 (4), 62–73. doi:10.1007/s13131-015-0584-0

Yan, M., Chi, Q., Gu, T., and Wang, C. (1997). Chemical composition of upper crust in eastern China. *Sci. China Ser. D-Earth. Sci.* 40 (5), 530–539. doi:10.1007/BF02877620

Yan, P., Zhou, D., and Liu, Z. (2001). A crustal structure profile across the northern continental margin of the South China Sea. *Tectonophysics* 338, 1–21. doi:10.1016/S0040-1951(01)00062-2

Yin, H. (2020). MA thesis. Chengdu: Chengdu University of technology.*Dolomite Genesis of Miocene Meishan Formation in the well xike-1*, Xisha area, south China sea

You, X., Sun, S., and Zhu, J. (2011). Progress in the study of microbial dolomite model. *Earth Sci. Front.* 18 (4), 52–64. doi:10.11743/ogg20200119

Zachos, J., Pagani, M., Sloan, L., Thomas, E., and Billups, K. (2001). Trends, rhythms, and aber-rations in global climate 65 ma to present. *Science* 292, 686–693. doi:10.1126/science.1059412

Zhai, S. (2015). A preliminary study on the lithic resource utilization mode of the Mount Dagudui Site in Xiangfen County, Shanxi. *Chin. Archaeol.* 15 (1), 87–92. doi:10.1515/char-2015-0009

Zhang, J., and Nozaki, Y. (1996). Rare Earth elements and yttrium in seawater: ICP-MS determinations in the east caroline, coral sea, and south Fiji basins of the Western south Pacific ocean. *Geochimica Cosmochimica Acta* 60 (23), 4631–4644. doi:10.1016/S0016-7037(96)00276-1

Zhang, W., and Chen, Z. (1993). *The geology of fluid inclusion*. Wuhan: China University of Geosciences Press, 156.(in Chinese). ISBN: 7-5625-0885-2

Zhao, Q. (2010). *PhD thesis*. Qingdao, China: Chinese Academy of Sciences, 158. (in Chinese with English abstract).*The sedimentary research about reef carbonate in Xisha Islands Waters*

Zhao, S., Wu, S., and Shi, H. (2012). Structures and dynamic mechanism related to the Dongsha movement at the northern margin of South China Sea. *Prog. Geophys.* 27 (3), 1008–1019. doi:10.6038/j.issn.1004-2903.2012.03.022

frontiers | Frontiers in Earth Science

TYPE Original Research
PUBLISHED 23 January 2023
DOI 10.3389/feart.2022.1055541

OPEN ACCESS

EDITED BY
Shuai Yin,
Xi'an Shiyou University, China

REVIEWED BY
Caifang Wu,
China University of Mining and Technology, China
Jintong Liang,
Chengdu University of Technology, China

*CORRESPONDENCE
Zhanlei Wang,
28142547@qq.com

SPECIALTY SECTION
This article was submitted to Structural Geology and Tectonics, a section of the journal Frontiers in Earth Science

RECEIVED 27 September 2022
ACCEPTED 22 November 2022
PUBLISHED 23 January 2023

CITATION
Zhou Y, Wang Z, Hu D, Wei Z, Wei X, Liu R, Wang D and Jiang Y (2023), Nanoscale pore characteristics of the Jurassic Dongyuemiao member lacustrine shale, Eastern Sichuan Basin, SW China: Insights from SEM, NMR, LTNA, and MICP experiments. *Front. Earth Sci.* 10:1055541. doi: 10.3389/feart.2022.1055541

Nanoscale pore characteristics of the Jurassic Dongyuemiao member lacustrine shale, Eastern Sichuan Basin, SW China: Insights from SEM, NMR, LTNA, and MICP experiments

Yadong Zhou[1,2,3], Zhanlei Wang[1,2,3]*, Dongfeng Hu[4], Zhihong Wei[4], Xiangfeng Wei[4], Ruobing Liu[4], Daojun Wang[4] and Yuqiang Jiang[1,2,3]

[1]School of Geosciences and Technology, Southwest Petroleum University, Chengdu, China, [2]The Unconventional Reservoir Evaluation Department, PetroChina Key Laboratory of Unconventional Oil and Gas Resources, Chengdu, China, [3]Collaborative Innovation Center of Shale Gas Resources and Environment, Chengdu, China, [4]Sinopec Exploration Company, Chengdu, China

The Jurassic Dongyuemiao Member is the most promising target for lacustrine shale gas exploration in Sichuan Basin. By integrating SEM, NMR, LTNA, and MICP experiments, and other basic measurements, the nanoscale pore category and structure and the corresponding controlling factors of Dongyuemiao lacustrine shale in Eastern Sichuan Basin are studied. The results denote that organic pores comprise primary pores within plant debris and secondary pores within bitumen. Inorganic pores are composed of intraparticle pores within calcite particles, intercrystalline pores between pyrite crystals, and interparticle pores between different minerals. The 4th Section lacustrine shale of Dongyuemiao Member has the best pore structure, exhibiting high organic pore proportion, large amounts of gas adsorption, and parallel plate-shaped pore morphology. Micropores (<2 nm) are the main contributors of the pore volume and surface area of Dongyuemiao lacustrine shale. Moreover, the enrichment of organic matter positively affects the formation of micropores and has no influence on the mesopore–macropore (>2 nm). Quartz does not significantly affect the nanoscale pore formation. The intraparticle pores within calcite particles constitute part of mesopore–macropore but not micropores. Clay minerals are conducive to the formation of micropores but play a negative role in the formation of mesopore–macropore.

KEYWORDS

nanoscale pore, dongyuemiao member, lacustrine shale, pore-size distribution, controlling factors, shale lithofacies

1 Introduction

Organic-rich shale can be deposited in following sedimentary environments: deep shelf, semi-deep to deep lacustrine, estuary bay, and lagoon environment (Zou et al., 2019; Gu et al., 2022a; Gu et al., 2022b; Qiu and He, 2022). In the world, North America has achieved the greatest success in marine shale exploration, followed by China (Zhang et al., 2020a; Zhang et al., 2020b). Several trillion cubic meters-scale shale gas fields, such as Weiyuan, Changning, and Jiaoshiba, have been successively built around the Sichuan Basin to date (Fan et al., 2020; Zhang et al., 2022a; Zhang et al., 2022b; Zhang et al., 2022c; Fan et al., 2022). However, the successful cases of shale gas exploration and development in China are limited to the Silurian marine shale in the Sichuan Basin and its surrounding areas (Zhang et al., 2019; Li, 2022; Li et al., 2022). With the advancement of exploration and development, alternative shale gas exploration targets need to be found (Shu et al., 2021; Sun et al., 2022; Wang et al., 2022). To date, studies on the exploration potential of lacustrine shale gas have been conducted in the Jurassic Da'anzhai Member of Sichuan Basin, Triassic Yanchang Formation in Ordos Basin, Shahejie Formation of Bohai Bay Basin, Cretaceous Shahai and Jiufotang Formation in Fuxin Basin, and the Cretaceous Qingshankou Formation of Songliao Basin (Chen et al., 2018). Results have shown that the organic matter maturity of lacustrine shale is generally low, and the R_o value is mainly in the range of 0.6%–1.1% (Wang et al., 2015; Yang and Zou, 2019), which is mostly in the oil generation stage. Inorganic pores are well-developed, but organic pores are not developed due to low maturity and oil-prone kerogens (Xu et al., 2017; Chen et al., 2018; Han et al., 2021). The organic matter maturity of the Jurassic Dongyuemiao Member lacustrine shale in Sichuan Basin is relatively high. In terms of organic matter maturity, the lacustrine shale in Dongyuemiao Member has been in a stage of high maturity evolution, which is conducive to the development of organic pores (Shu et al., 2021; Liu et al., 2021). In 2018, lacustrine shale gas reservoirs of the Dongyuemiao Member were discovered through Well FY10HF in Eastern Sichuan Basin. However, few studies have been conducted on pore development in Dongyuemiao Member, and thus, its development is poorly understood. Liu et al. (2021) proposed that in the Dongyuemiao lacustrine shale of Northern Sichuan, only inorganic pores are developed and organic pores are not basically developed. However, Shu et al. (2021) proposed contrasting views, proposing that the pore types of shale in the Dongyuemiao shale are diverse and that inorganic pores, organic pores, and fractures are all developed.

The nanoscale pore structure has been identified as one of the most important mechanisms to affect hydrocarbon recovery from unconventional shale reservoirs (Chen et al., 2018; Han et al., 2021; Wang et al., 2022). Understanding nanoscale pore structure and its controlling factors is beneficial for shale reservoir evaluation. A large number of pore structure studies have been carried out on marine shale and found that nanoscale pore structure is strongly affected by mineral composition and organic matter abundance (Li et al., 2016; Jia et al., 2020). However, due to the huge difference in sediment composition, mineral composition and organic matter abundance between lacustrine shale and marine shale (Yang et al., 2019; Li et al., 2021; Wei et al., 2021), the previous results of marine shale cannot be directly applied to lacustrine shale.

Scanning electron microscopy (SEM), Mercury injection capillary pressure (MICP), low-temperature N2 adsorption (LTNA), and nuclear magnetic resonance (NMR) have been widely used to illustrate pore structure parameters and their controlling factors. The above mentioned methods are employed in this study to 1) reveal the dominant reservoir space type of the Dongyuemiao lacustrine shale reservoir, 2) demonstrate the pore structure of the Dongyuemiao lacustrine shale reservoir, and 3) quantitatively discuss the correlation between different parameters and then reveal the main factors controlling the pore structure.

2 Geological setting

Sichuan Basin is a typical craton basin in the western part of the Upper Yangtze Block (Figure 1A), and the basin area is about 260,000 km^2. The study area, with an area of 4.2×10^3 km^2, is located in the Eastern Sichuan Basin (Figure 1B). In the Early-Middle Jurassic, most areas of the Sichuan Basin were dominated by shore-shallow lake, semi-deep lake and deep lake facies, and they experienced four lake transgressions during this period. Organic-rich shale is thought to develop in semi-deep lake and deep lake facies controlled by anoxic condition (Shu et al., 2021; Peng et al., 2022). From the bottom to the top, four sets of organic-rich shales are formed in the Zhenzhuchong Member, Dongyuemiao Member, Da'anzhai Member, and Lianggaoshan 2nd Member, respectively. The Dongyuemiao Member comprises three submembers: 1st Submember, 2nd Submember, and 3rd Submember. The 1st Submember can be subdivided into four sections: 1st, 2nd, 3rd, and 4th Sections (Figure 1C). Except for the 2nd Submember, the other intervals mainly constitute shale. The total organic carbon content (TOC) of shale is mainly distributed in the range of 0.5%–2.0%, and the average value of TOC is greater than 1% (Liu et al., 2021). The organic matter type of the shale is mainly Type II and locally developed Type III, and the vitrinite reflectance (R_o) is mostly greater than 1.2%. Thus, it has entered the stage of high maturity evolution and is dominated by gas generation.

3 Sample and method

A total of 120 core samples of Dongyuemiao Member lacustrine shale were collected from studied wells for thin-section analysis, X-ray diffraction and TOC measurement. The experimental test site is the SINOPEC Wuxi Research

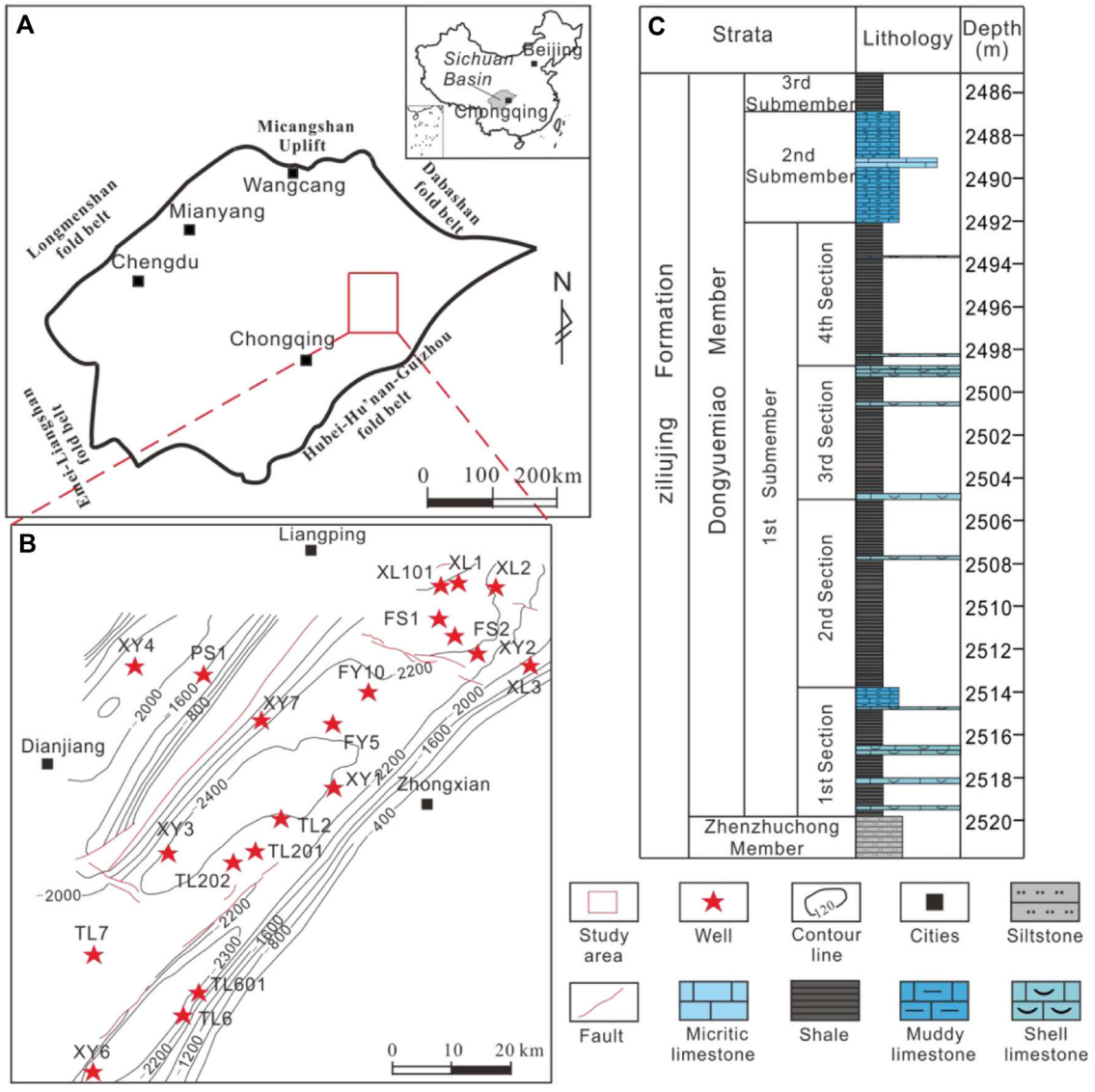

FIGURE 1
(A) Location of the study area in Eastern Sichuan Basin. **(B)** Distribution map showing the burial depth of Jurassic Dongyuemiao Member and studied wells. **(C)** Generalized stratigraphy of Jurassic Dongyuemiao Member in the study area.

Institute of Petroleum Geology. The whole-rock and clay mineral X-ray diffraction measurement was carried out using a German Bruker D8 Advance X-ray diffractometer. TOC measurement was carried out through a LECO CS230 Series Carbon and Sulfur Analyzer. NMR analysis was performed on 24 core-plug shale samples in both the dry and saturated fluid states (including n-dodecane and brine) using a c12-010V low-field NMR device manufactured at the Collaborative Innovation Center of Shale Gas Resources and Environment in Chengdu. Mercury intrusion was measured using a Quantachrome Poremaster. Samples were prepared with an approximate size of 20 × 20 mm^2 and weighed out to 10–20 g, and then, the samples were dried at 110°C for at least 24 h under vacuum in an oven. The Mercury injection pressure ranged from 0 to 215 Mpa in this experiment. The remaining samples were divided into three parts for maceral identification after kerogen extraction, SEM, and LTNA. For LTNA, the samples were crushed into 60–80 mesh, dried in an oven at 110°C for 12 h, and then placed in an Autosorb-IQ3 specific surface and a pore size distribution analyzer (Cantor Company, United States). The pretreatment was completed by degassing at 110°C for 12 h in the vacuum condition, and then nitrogen carbon adsorption was carried out. After the

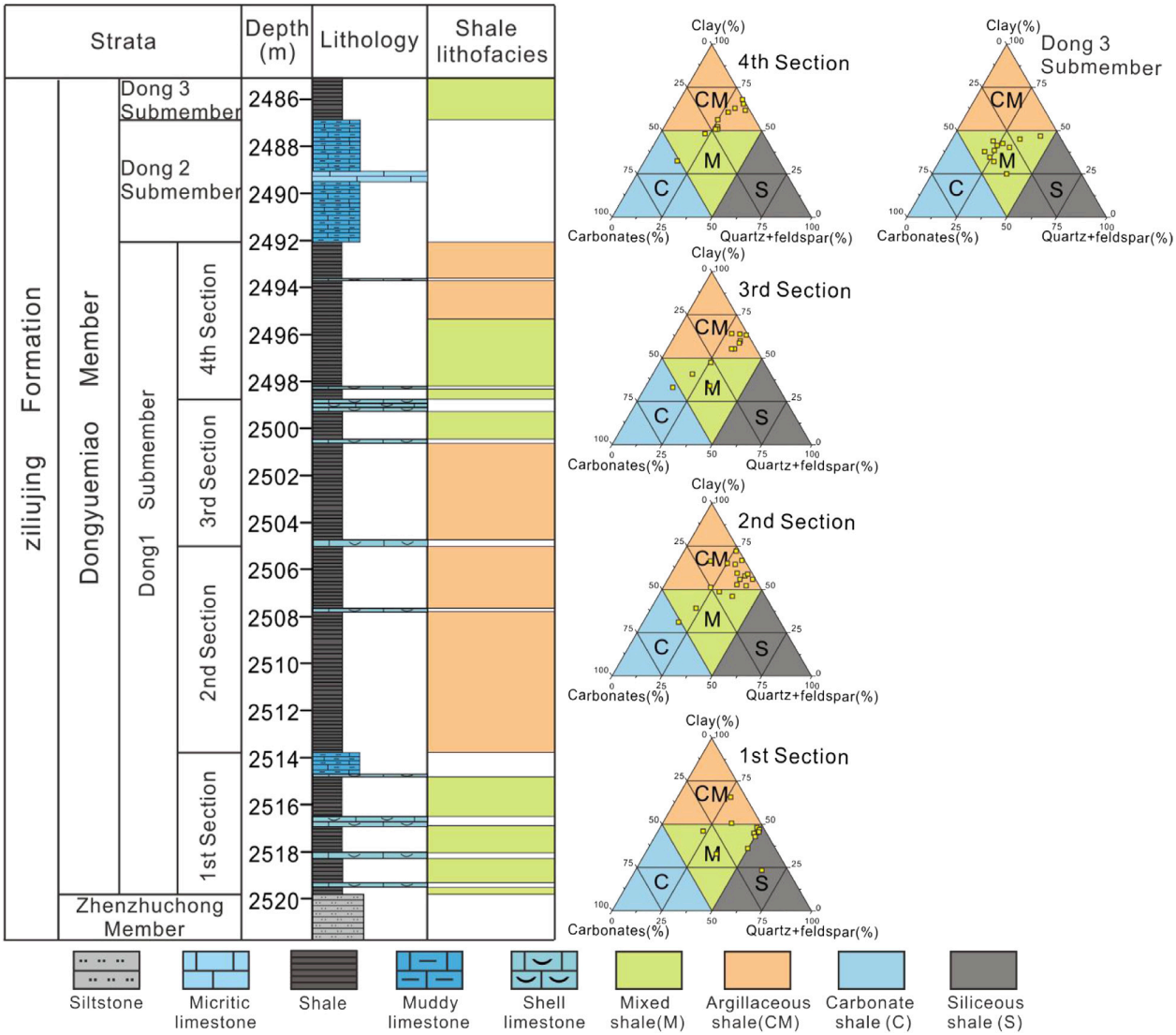

FIGURE 2
Shale lithofacies classification and vertical distribution of the Jurassic Dongyuemiao lacustrine shale in Eastern Sichuan Basin (based on Well XY4).

experiment, the Brunauer–Emmett–Teller (BET) model was used to calculate the specific surface area, and the Barrett–Joyner–Halenda (BJH) model was employed to obtain the pore size distribution and volume. The reservoir space classification is based on schemes proposed by Loucks et al. (2012). The pore size was divided into three categories according to the pore size classification scheme (Rouquerol et al., 1994), namely micropores (<2 nm), mesopores (2nm–50 nm), and macropores (>50 nm). Hysteresis loops were observed at the relative pressure (P/P_O) of about 0.5 in the adsorption–desorption curves, signifying the presence of great differences in the pore size and pore morphology among shale samples that cause such adsorption behaviors at this pressure. This relative pressure was set as the threshold to divide the samples into two groups (Wang et al., 2022). The first group with P/P_O=0-0.5 is subjected to the monolayer-multilayer adsorption process controlled by van der Waals force, while the second group with P/P_O=0.5-1.0 experiences the capillary condensation adsorption process controlled by surface tension (Sun et al., 2015; Wang et al., 2015). Herein, the Frenkel–Halsey–Hill model is used to separately determine the fractal dimensions of these two groups of samples, which are denoted as D_2 and D_1 for the first and second groups, respectively.

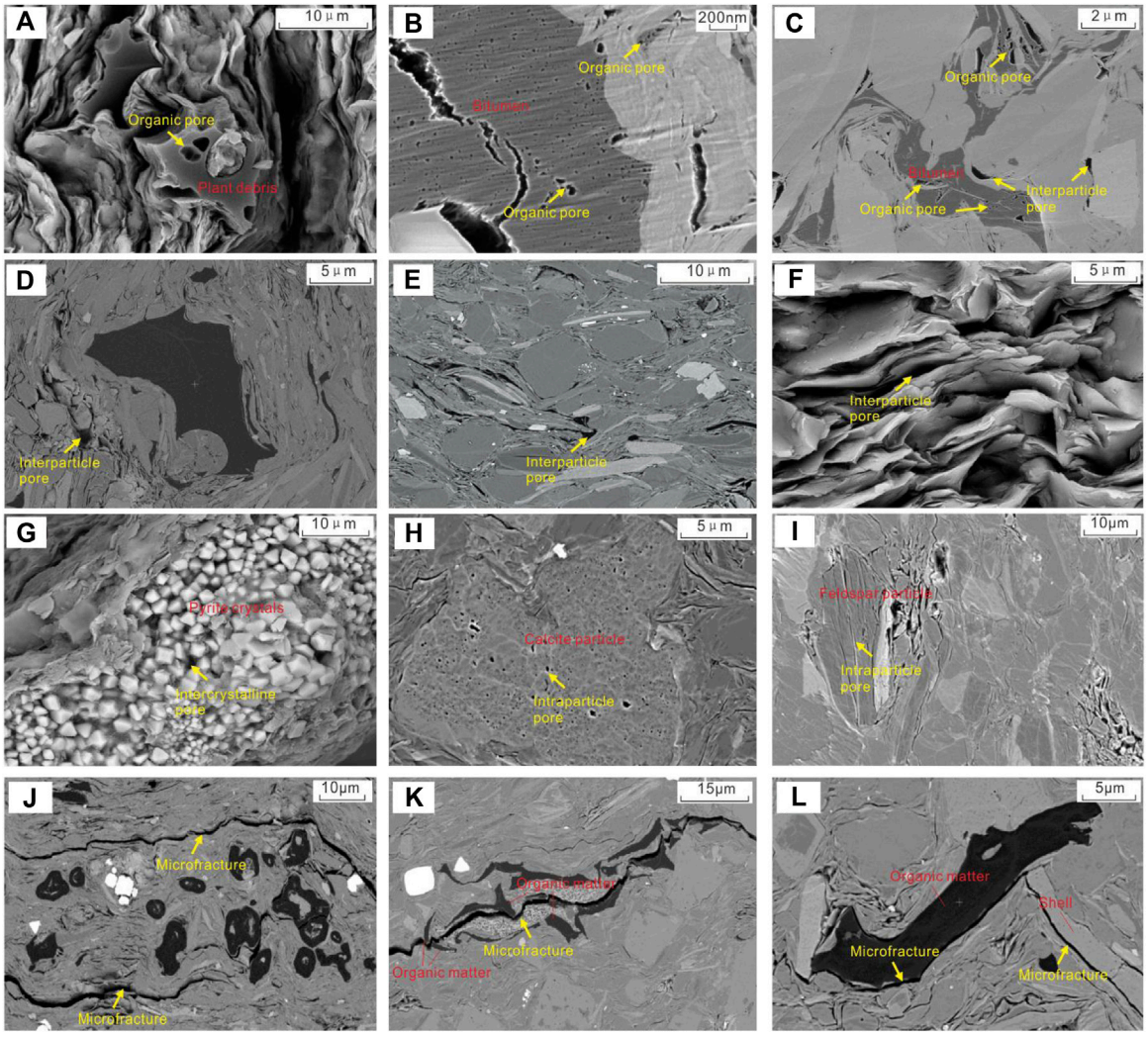

FIGURE 3
FE-SEM images of reservoir spaces in the Jurassic Dongyuemiao lacustrine shale in Eastern Sichuan Basin. **(A)** Primary organic pore in plant debris, Well XY3, 2959 m; **(B)** Abundant organic pore in bitumen, Well FY10, 2,766.46 m; **(C)** Organic pore between bitumen and mineral particles, Well FY10, 2,800.97 m; **(D)** Interparticle pores between mineral particles, Well TL601, 2,743.5 m; **(E)** Interparticle pores between mineral particles, Well TL601, 2,755.13 m; **(F)** Interparticle pores between clay mineral, Well XY3, 2,953.22 m; **(G)** Intercrystalline pores between pyrite crystals, Well XY3, 2,935.1 m; **(H)** Abundant intraparticle pores in calcite particle, Well TL601, 2,731.58 m; **(I)** Intraparticle pores in feldspar particle, Well TL601, 2,728.05 m; **(J)** Microfracture, Well TL601, 2,750.21 m; **(K)** Microfracture dislocating organic matter, Well TL601, 2,731.58m; **(L)** Microfractures around organic matter and mineral particles, Well TL601, 2,731.58 m.

4 Results

4.1 Lithofacies classification

Based on previous lithofacies classification schemes (Jia et al., 2020), the clay, carbonate, and silicon (quartz and feldspar) mineral contents of each shale sample were plotted onto a ternary diagram (Figure 2). The contents of clay minerals, siliceous minerals (quartz + feldspar) and carbonate minerals are regarded as three end-members to divide the mineral lithofacies: argillaceous shale lithofacies (CM) with clay mineral mass fraction >50%; mixed shale lithofacies (M) with clay minerals, siliceous minerals and carbonate minerals <50%. According to the classification results, the 1st and 2nd Sections are composed of mixed shale lithofacies (M) and argillaceous shale lithofacies (CM). In comparison, the 3rd Section predominantly constitutes argillaceous shale lithofacies (CM). While the bottom-to-top lithofacies of the 4th Section is mixed shale lithofacies (M) and argillaceous shale lithofacies (CM) (Figure 2).

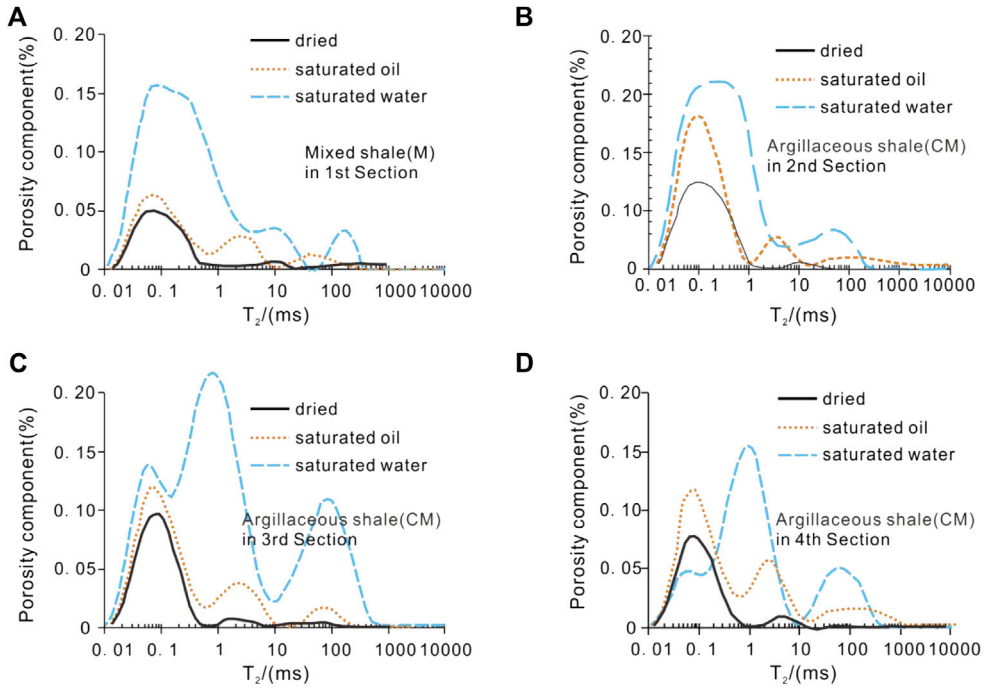

FIGURE 4
NMR T_2 spectra of different shale lithofacies under different states for the Jurassic Dongyuemiao lacustrine shale in Eastern Sichuan Basin.

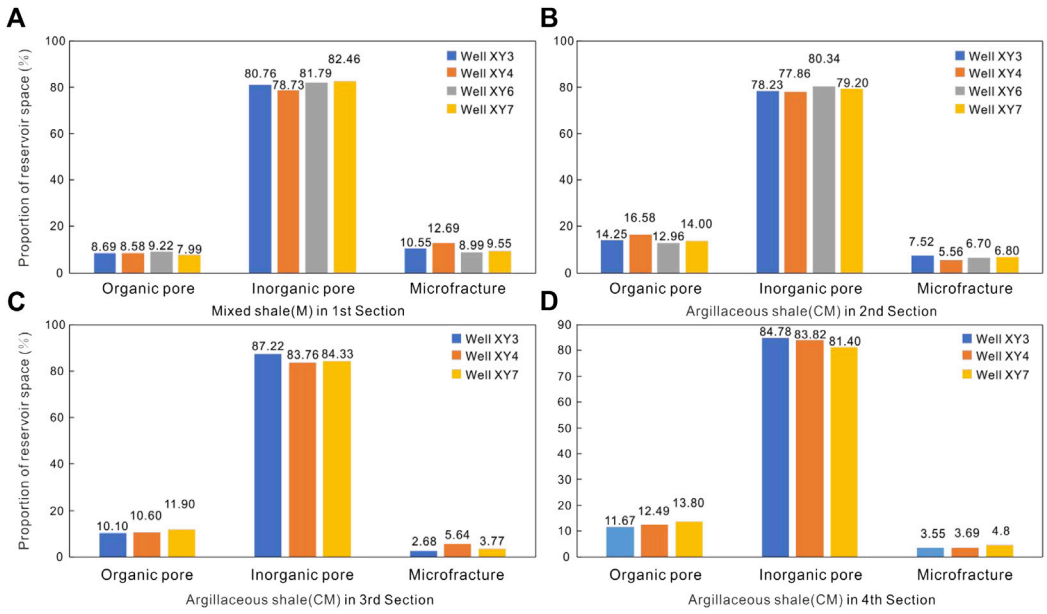

FIGURE 5
Histogram showing proportion of reservoir spaces in different shale lithofacies for the Jurassic Dongyuemiao lacustrine shale in Eastern Sichuan Basin.

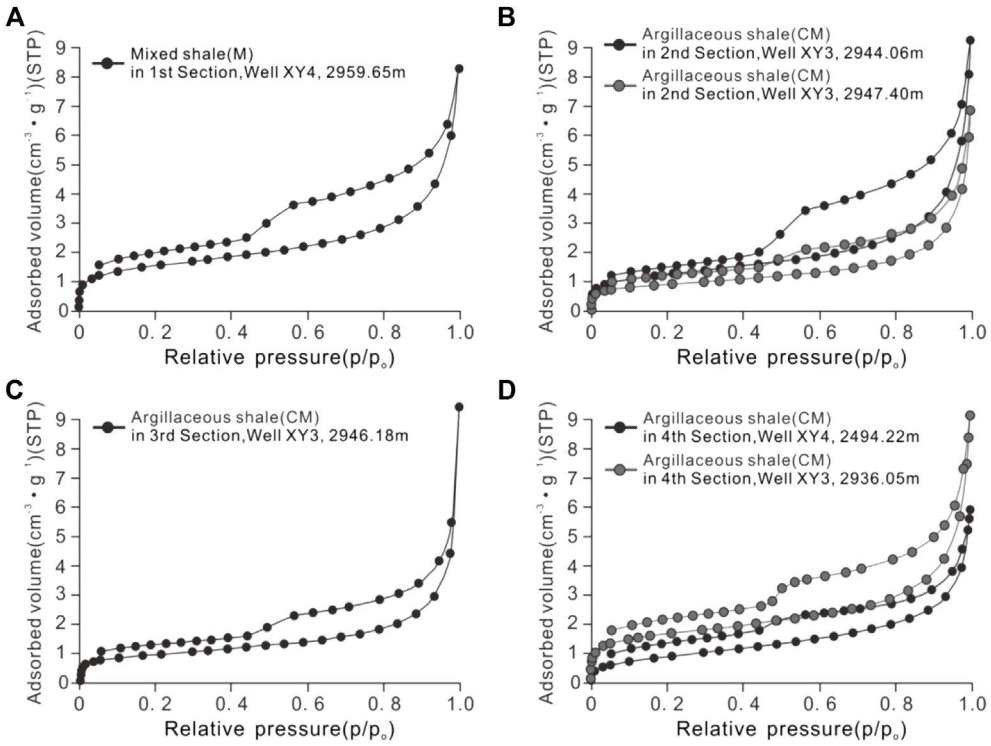

FIGURE 6
The LTNA characteristics of different shale lithofacies for the Jurassic Dongyuemiao lacustrine shale in Eastern Sichuan Basin.

4.2 Reservoir space morphology and proportion

4.2.1 Organic pores

The organic matter of Dongyuemiao lacustrine shale is in the high maturity stage (R_o = ~1.64%). A small number of primary organic pores can be observed inside the plant debris (Figure 3A). Numerous nanoscale organic pores can be observed inside the bitumen (Figure 3B). As an important part of shale pore system, organic pores within bitumen are formed in the process of shale hydrocarbon generation and evolution, which are the traces of shale gas generation diffusion and accumulation. Additionally, organic pores are observed between bitumen and its surrounding mineral particles (Figure 3C). Such organic pores are formed by the shrinkage of organic matter itself after hydrocarbon expulsion.

4.2.2 Interparticle and intercrystalline pores

The migration of sediments in the paleoenvironment will yield considerable micro sedimentary structures, and incomplete cementation between various particles will afford interparticle pores (Han et al., 2013). The interparticle pores of Dongyuemiao lacustrine shale mainly exist between different mineral particles (Figure 3D), such as clay minerals (Figure 3E), quartz, pyrite, and siderite. The size of interparticle pores is controlled by the size of mineral particles and the degree of compaction (Figure 3F). The larger the mineral particles, the larger the interparticle pores, and the greater the buried depth, the less the interparticle pores. In addition to interparticle pores, a large number of interparticle pores develop between pyrite crystals (Figure 3G). However, since the content of pyrite is generally less than 5%, the development frequency of interparticle pores is very low.

4.2.3 Intraparticle pores

The intraparticle pores of Dongyuemiao lacustrine shale mainly formed due to the dissolution of calcite and feldspar particles (Figure 3H). Intraparticle pores are well developed within each calcite and feldspar particle (Figure 3I). In terms of the pore size, the intraparticle pores of Dongyuemiao lacustrine shale belong to the mesopore–macropore, but the development frequency of such pores is generally low.

4.2.4 Microfracture

The microfractures developed in the Dongyuemiao lacustrine shale can be classified as structural or non-structural microfractures. Structural fractures are usually characterized by a stable extension direction with few branches and a large length (Figure 3J). Locally, the

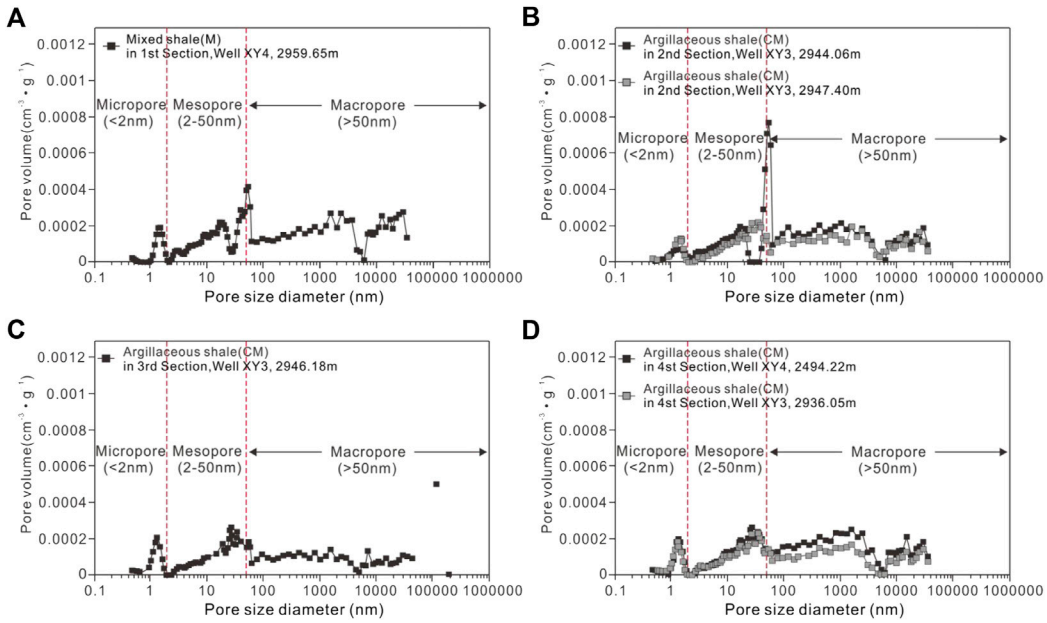

FIGURE 7
Pore-size distribution of different shale lithofacies with MICP and LTNA for the Jurassic Dongyuemiao lacustrine shale in Eastern Sichuan Basin.

microfracture dislocates the organic matter or mineral particles (Figure 3K). In comparison, non-structural fractures have the characteristics of short extension around the edges of the organic matter or the other mineral particles including the shell (Figure 3L).

4.2.5 Proportion of different reservoir spaces

Organic pores are generally lipophilic, while inorganic pores are mostly hydrophilic (Tinni et al., 2014; Li et al., 2016). Accordingly, NMR experiments were conducted under water- and oil-saturated conditions, respectively, to observe the signal characteristics on the transverse relaxation time (T_2) distribution spectra of the two types of pores. The presence of three peaks in the T_2 spectra of lipophilic pores indicates three types of organic pores: volumetrically dominant small pores with short T_2, large pores with long T_2, and microfracture developed in organic matter (Figure 4). Based on the above theoretical understanding, Fu et al. (2021) proposed a method for calculating the proportion of organic and inorganic pores based on the wettability of shale pores.

The calculation results show that the NMR T_2 spectrum of the 1st Section mixed argillaceous shale (M) at saturated oil exhibits doublet characteristics, and the amplitude of the T_2 spectrum at saturated oil is low. The average proportion of organic pores is only 8%, and that of inorganic pores is about 81%. The NMR T_2 spectrum of 2nd Section argillaceous shale (CM) at saturated oil is singlet, the amplitude of the T_2 spectrum at saturated oil is high, and the average proportion of organic pores is more than 14%. The T_2 spectrum of the 3rd Section argillaceous shale (CM) at saturated oil exhibits a singlet shape. The amplitude of the T_2 spectrum at saturated oil is high, but that of saturated water is much higher than that of saturated oil; therefore, the proportion of organic pores is only about 10%. The NMR T_2 spectrum of the 4th Section argillaceous shale (CM) at saturated oil exhibits singlet characteristics, and the average proportion of organic pores exceeds 12% (Figure 5).

4.3 Pore structure quantitative characteristics

4.3.1 N_2 adsorption-desorption isotherms and pore geometry

According to the IUPAC isothermal adsorption curve classification (Thommes et al., 2015), the hysteresis loops of the 1st Section mixed shale (M) are similar to the H4 type (Figure 6A). Furthermore, the adsorption curve is slow near the saturated vapor pressure, reflecting a small amount of gas adsorption, and slit-shaped pores are developed within this section. Hysteresis loops of the 2nd Section argillaceous shale (CM) exhibit the morphologies of both H3 and H4 (Figure 6B), and the gas adsorption amount is small. However, the desorption curves of some samples are steep near the median pressure, forming a wide hysteresis loop, indicating the development of parallel plate-shaped pores. Hysteresis loops of the 3rd Section argillaceous shale (CM) are similar to the H4 type (Figure 6C), and the adsorption curve is slow

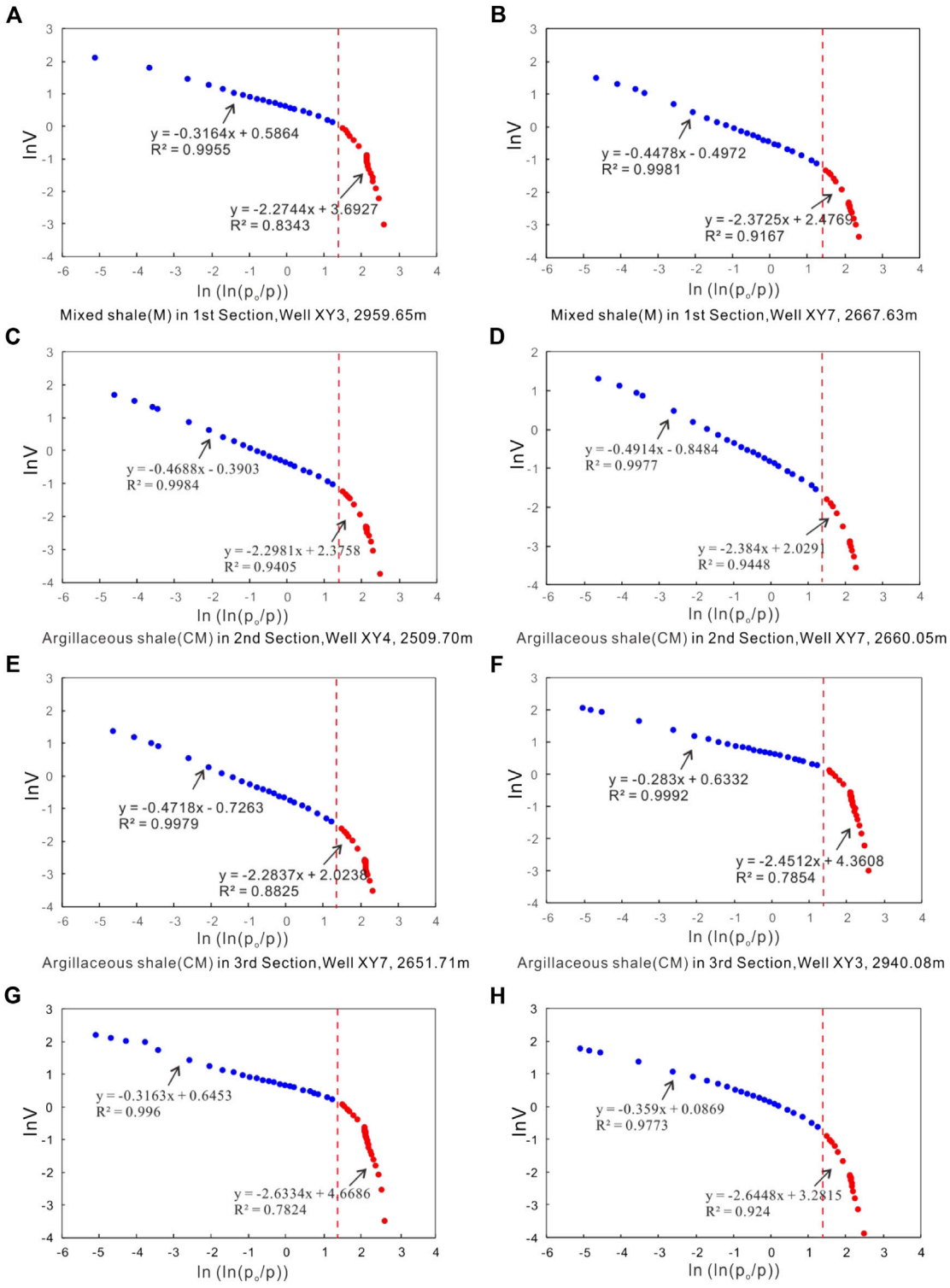

FIGURE 8
Schematic diagram of fractal fitting of shale samples with different lithofacies for the Jurassic Dongyuemiao lacustrine shale in Eastern Sichuan Basin.

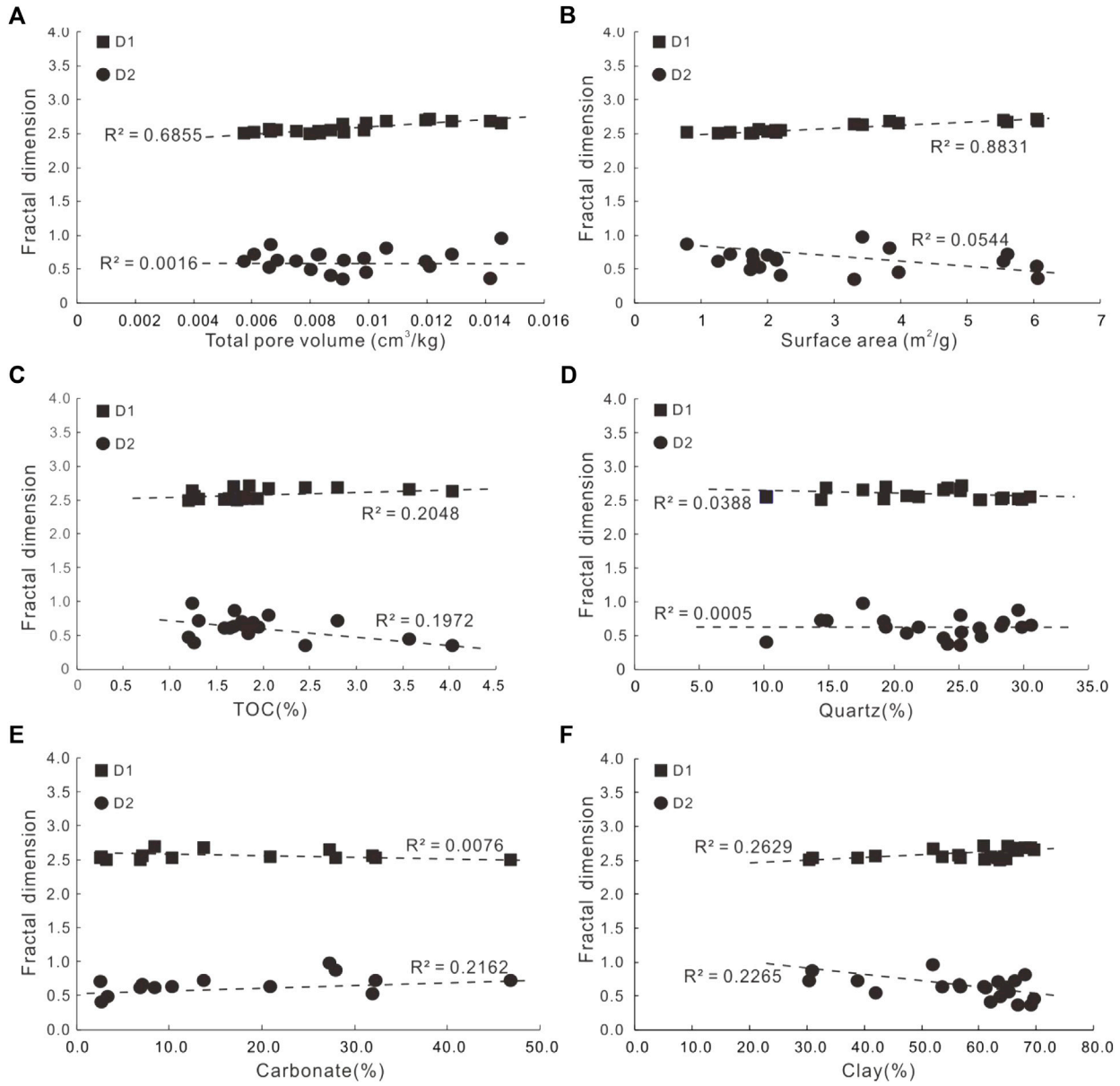

FIGURE 9
Correlations between fractal dimensions, total pore volume, surface area, TOC, quartz content, carbonate content and clay content for the Jurassic Dongyuemiao lacustrine shale in Eastern Sichuan Basin.

near the saturated vapor pressure, suggesting that the gas adsorption amount is small and that the pores are dominated by slit-shaped pores. The hysteresis loops of the 4th Section argillaceous shale (CM) are similar to the H3 type (Figure 6D), and the adsorption curve is steep near the saturated vapor pressure, suggesting a large amount of gas adsorption. The corresponding desorption curve is relatively flat at the median pressure, forming relatively wide hysteresis loops. This suggests that the pores are dominated by parallel plate-shaped pores.

4.3.2 Surface area and pore volume

The SA of the Dongyuemiao lacustrine shale samples were calculated according to the BET model. The SA range of the 1st Section mixed shale (M) is between 0.78 and 5.60 m2/g and that of the 2nd Section argillaceous shale (CM) is between 1.25 and 3.83 m2/g. The SA range of the 3rd Section argillaceous shale (CM) is between 1.43 and 6.04 m2/g and that of the 4th Section argillaceous shale (CM) is between 1.87 and 6.05 m2/g.

The PV of the Dongyuemiao lacustrine shale samples range from 5.73 to 14.54 cm^3/kg, with an average of 9.35 cm^3/kg. The average PV of the 1st Section mixed shale (M) and 3rd Section argillaceous shale (CM) was lower than that of the 2nd Section argillaceous shale (CM) and 4th Section argillaceous shale (CM).

4.3.3 Pore-size distribution

The PSD was characterized by integrating MICP and LTNA experiments. The results show that although the curve morphologies of different samples exhibit slightly differences, the distribution ranges of the pore peaks are similar. The PSD curves of the 2nd, 3rd, and 4th Section argillaceous shale (CM) are characterized by four peaks: 1–2 nm, 20–50 nm, 1,000–1,200 nm, and 10,000–12000 nm (Figure 7).

5 Discussion

In this study, the main controlling factors of pore structure are discussed by correlating fractal dimension with reservoir and pore structure parameters. The surface fractal dimension is denoted as D_1 for relative N_2 pressure $P/P_o > 0.5$ with capillary condensation and surface fractal dimension is denoted as D_2 for $P/P_o < 0.5$ with mono- and multi-layer adsorption (Figure 8).

For lacustrine shale samples, the fractal dimension D_1 represents the development degree of micropores. D_1 is generally larger than D_2 and is closer to 3, suggesting that the pore structure heterogeneity of mesopore-macropore is stronger than that of micropore. A clear positive correlation exists between D_1 and PV as well as SA (Figures 9A,B), indicating that the micropores within the Dongyuemiao lacustrine shale are the main contributors of PV and SA. The correlation between D_1 and TOC is slightly positive, suggesting that the enrichment of organic matter positively affects micropore formation (Figure 9C). Moreover, the enrichment of organic matter does not influence the mesopore–macropore development. Due to the low content of quartz in Dongyuemiao, which is mainly detrital quartz, it does not significantly affect the formation of micropores and mesopore–macropore (Figure 9D). A slight positive correlation exists between D_2 and carbonate content, indicating that intraparticle pores within calcite particles constitute part of mesopore–macropore but not micropores (Figure 9E). Clay minerals are conducive to micropore formation (Figure 9F), but play a negative role in mesopore–macropore formation due to the filling of clay minerals in the mesopore–macropore (Figure 3).

6 Conclusion

1) The 1st and 2nd Sections of Jurassic Dongyuemiao lacustrine shale in Eastern Sichuan Basin are composed of mixed shale lithofacies (M) and argillaceous shale lithofacies (CM). In comparison, the predominant lithofacies of the 3rd Section is argillaceous shale lithofacies (CM). Moreover, the 4th Section constitutes mixed shale lithofacies (M) and argillaceous shale lithofacies (CM).
2) Organic pores (primary pores within plant debris and secondary pores within bitumen), inorganic pores (interparticle pore, intercrystalline pore, and intraparticle pore), and microfractures are present in the Jurassic Dongyuemiao lacustrine shale of Eastern Sichuan Basin. The average proportion of organic pores is higher in the 2nd and 4th Sections, exceeding 12%. The 4th Section, characterized by high organic pore proportion, large amounts of gas adsorption, and parallel plate-shaped pore morphology, exhibits the best pore structure.
3) The micropores within the Dongyuemiao lacustrine shale are the main contributors of PV and SA. The enrichment of organic matter positively affects micropore formation but has no influence on mesopore–macropore development. Additionally, quartz does not significantly affect the formation of nanoscale pores. Intraparticle pores within calcite particles constitute part of mesopore–macropore but not micropores. Clay minerals are conducive to micropore formation but play a negative role in mesopore–macropore development.

Data availability statement

The raw data supporting the conclusion of this article will be made available by the authors, without undue reservation.

Author contributions

YZ contributed as the major author of the article. DH and ZW conceived the project. ZW and XW collected the samples. RL, DW, and YJ analyzed the samples. All authors contributed to the article and approved the submitted version.

Funding

This study was financially supported by the National Natural Science Foundation of China (Grant No. 42272171), National Science and Technology Major Project (Grant No. 2017ZX05036) and Sinopec "Ten Dragons" Technology Project (Grant No. P21078-1).

Conflict of interest

Authors DH, ZW, XW, RL, and DW were employed by Sinopec Exploration Company. The authors YZ, ZW and YJ were employed by PetroChina Key Laboratory of Unconventional Oil and Gas Resources.

The remaining authors declare that the research was conducted in the absence of any commercial or financial relationships that could be construed as a potential conflict of interest.

Publisher's note

References

Chen, D., Zhang, J., Wang, X., Lan, B., Li, Z., and Liu, T. (2018). Characteristics of lacustrine shale reservoir and its effect on methane adsorption capacity in fuxin basin. *Energy* 32 (11), 11105–11117. doi:10.1021/acs.energyfuels.8b01683

Fan, C., Li, H., Qin, Q., He, S., and Zhong, C. (2020). Geological conditions and exploration potential of shale gas reservoir in Wufeng and Longmaxi Formation of southeastern Sichuan Basin, China. *J. Petroleum Sci. Eng.* 191, 107138. doi:10.1016/j.petrol.2020.107138

Fan, C., Xie, H., Li, H., Zhao, S., Shi, X., Liu, J., et al. (2022). Complicated fault characterization and its influence on shale gas preservation in the southern margin of the Sichuan Basin, China. *Lithosphere* 2022, 8035106. doi:10.2113/2022/8035106

Fu, Y., Jiang, Y., Dong, D., Hu, Q., Lei, Z., Peng, H., et al. (2021). Microscopic pore-fracture configuration and gas-filled mechanism of shale reservoirs in the Western chongqing area, Sichuan Basin, China. *Petroleum Explor. Dev.* 48 (5), 1063–1076. doi:10.1016/S1876-3804(21)60091-5

Gu, Y., Hu, D., Wei, Z., Liu, R., Hao, J., Han, J., et al. (2022b). Sedimentology and geochemistry of the upper permian linghao formation marine shale, central nanpanjiang basin, SW China. *Front. Earth Sci. (Lausanne).* 10, 914426. doi:10.3389/feart.2022.914426

Gu, Y., Li, X., Qi, L., Li, S., Jiang, Y., Fu, Y., et al. (2022a). Sedimentology and geochemistry of the lower permian shanxi formation Shan 2^3 submember transitional shale, eastern Ordos Basin, North China. *Front. Earth Sci. (Lausanne).* 10, 859845. doi:10.3389/feart.2022.859845

Han, H., Dai, J., Guo, C., Zhong, N., Pang, P., Ding, Z., et al. (2021). Pore characteristics and factors controlling lacustrine shales from the upper cretaceous Qingshankou Formation of the Songliao Basin, northeast China: A study combining SEM, low-temperature gas adsorption and MICP experiments. *Acta Geol. sinica-. Engl. Ed.* 95 (2), 585–601. doi:10.1111/1755-6724.14419

Han, S., Zhang, J., Brian, H., Jiang, S., Li, W., Chen, Q., et al. (2013). Pore types and characteristics of shale gas reservoir: A case study of lower paleozoic shale in southeast chongqing. *Earth Sci. Front.* 20 (3), 247–253.

Jia, A., Hu, D., He, S., Guo, X., Hou, Y., Wang, T., et al. (2020). Variations of pore structure in organic-rich shales with different lithofacies from the jiangdong Block, fuling shale gas field, SW China: Insights into gas storage and pore evolution. *Energy* 34, 12457–12475. doi:10.1021/acs.energyfuels.0c02529

Li, H. (2022). Research progress on evaluation methods and factors influencing shale brittleness: A review. *Energy Rep.* 8, 4344–4358. doi:10.1016/j.egyr.2022.03.120

Li, J., Jin, W., Wang, L., Wu, Q., Lu, J., and Hao, S. (2016). Quantitative evaluation of organic and inorganic pore size distribution by NMR: A case from the silurian longmaxi formation gas shale in fuling area, Sichuan Basin. *Oil Gas Geol.* 37 (1), 129–134. doi:10.11743/ogg20160118

Li, J., Li, H., Yang, C., Wu, Y., Gao, Z., and Jiang, S. (2022). Geological characteristics and controlling factors of deep shale gas enrichment of the Wufeng-Longmaxi Formation in the southern Sichuan Basin, China. *Lithosphere* 2022, 4737801. doi:10.2113/2022/4737801

Li, P., Liu, Z., Nie, H., Liang, X., Li, Q., and Wang, P. (2021). Heterogeneity characteristics of lacustrine shale oil reservoir under the control of lithofacies: A case study of the Dongyuemiao member of jurassic ziliujing formation, Sichuan Basin. *Front. Earth Sci. (Lausanne).* 9, 736544. doi:10.3389/feart.2021.736544

Liu, Z., Hu, Z., Liu, G., Liu, Z., Liu, H., Hao, J., et al. (2021). Pore characteristics and controlling factors of continental shale reservoirs in the Lower Jurassic Ziliujing Formation, northeastern Sichuan Basin. *Oil Gas Geol.* 42 (1), 136–145. doi:10.11743/ogg20210112

Loucks, R. G., Reed, R. M., Ruppel, S. C., and Hammes, U. (2012). Spectrum of pore types and networks in mudrocks and a descriptive classification for matrix-related mudrock pores. *Am. Assoc. Pet. Geol. Bull.* 96 (6), 1071–1098. doi:10.1306/08171111061

Peng, J., Hu, Z., Feng, D., and Wang, Q. (2022). Sedimentology and sequence stratigraphy of lacustrine deep-water fine-grained sedimentary rocks: The lower jurassic Dongyuemiao Formation in the Sichuan Basin, western China. *Mar. Petroleum Geol.* 146, 105933. doi:10.1016/j.marpetgeo.2022.105933

Qiu, Z., and He, J. (2022). Depositional environment changes and organic matter accumulation of Pliensbachian-Toarcian lacustrine shales in the Sichuan basin, SW China. *J. Asian Earth Sci.* 232, 105035. doi:10.1016/j.jseaes.2021.105035

Rouquerol, J., Avnir, D., Fairbridge, C. W., Everett, D. H., Haynes, J. H., Pernicone, N., et al. (1994). Recommendations for the characterization of porous solids (Technical Report). *Pure Appl. Chem.* 66, 1739–1758. doi:10.1351/pac199466081739

Shu, Y., Bao, H., Zheng, Y., Chen, M., Lu, Y., Liu, H., et al. (2021). Lithofacies types, assemblage characteristics, and sedimentary evolution model of lacustrine shale in Dongyuemiao Formation of Fuxing Area. *Front. Earth Sci. (Lausanne).* 9, 772581. doi:10.3389/feart.2021.772581

Shu, Z., Zhou, L., Li, X., Liu, H., Zeng, Y., Xie, H., et al. (2021). Geological characteristics of gas condensate reservoirs and their exploration and development prospect in the Jurassic continental shale of the Dongyuemiao Member of Ziliujing Formation, Fuxing area, eastern Sichuan Basin. *Oil Gas Geol.* 42 (1), 212–223. doi:10.11743/ogg20210118

Sun, W., Feng, Y., Jiang, C., and Chu, W. (2015). Fractal characterization and methane adsorption features of coal particles taken from shallow and deep coalmine layers. *Fuel* 155, 7–13. doi:10.1016/j.fuel.2015.03.083

Sun, Y., Jiang, Y., Xiong, X., Li, X., Li, S., Qiu, Z., et al. (2022). Lithofacies and sedimentary environment evolution of the $Shan_2^3$ Submember transitional shale of the Shanxi Formation in the Danilng-Jixian area, eastern Ordos Basin. *Coal Geol. Explor.* 50 (9), 104–114. doi:10.12363/issn.1001-1986.21.12.0821

Thommes, M., Kaneko, K., Neimark, A. V., Olivier, J. P., Rodriguez-Reinoso, F., Rouquerol, J., et al. (2015). Physisorption of gases, with special reference to the evaluation of surface area and pore size distribution (IUPAC Technical Report). *Pure Appl. Chem.* 87, 1051–1069. doi:10.1515/pac-2014-1117

Tinni, A., Odusina, E., and Sulucamain, I. (2014). "NMR response of brine, oil, and methane in organic rich shales," in SPE USA Unconventional Resources Conference: The Woodlands, Texas, USA, 1-3 April 2013, 98–106.

Wang, M., Xue, H., Tian, S., Wilkins, R. W. T., and Wang, Z. (2015). Fractal characteristics of upper cretaceous lacustrine shale from the Songliao Basin, NE China. *Mar. Petroleum Geol.* 67, 144–153. doi:10.1016/j.marpetgeo.2015.05.011

Wang, Z., Guo, B., Jiang, C., Qi, L., Jiang, Y., Gu, Y., et al. (2022). Nanoscale pore characteristics of the lower permian shanxi formation transitional facies shale, eastern Ordos Basin, North China. *Front. Earth Sci. (Lausanne).* 10, 842955. doi:10.3389/feart.2022.842955

Wei, G., Wang, W., Feng, L., Tan, X., Yu, C., Zhang, H., et al. (2021). Geological characteristics and exploration prospect of black shale in the Dongyuemiao member of lower jurassic, the eastern Sichuan Basin, China. *Front. Earth Sci. (Lausanne).* 9, 765568. doi:10.3389/feart.2021.765568

Xu, Q., Liu, B., Ma, Y., Song, X., Wang, Y., and Chen, Z. (2017). Geological and geochemical characterization of lacustrine shale: A case study of the jurassic Da'anzhai member shale in the central Sichuan Basin, southwest China. *J. Nat. Gas Sci. Eng.* 47, 124–139. doi:10.1016/j.jngse.2017.09.008

Yang, R., Hu, Q., Yi, J., Zhang, B., He, S., Guo, X., et al. (2019). The effects of mineral composition, TOC content and pore structure on spontaneous imbibition in Lower Jurassic Dongyuemiao shale reservoirs. *Mar. Petroleum Geol.* 109, 268–278. doi:10.1016/j.marpetgeo.2019.06.003

Yang, Z., and Zou, C. (2019). Exploring petroleum inside source kitchen": Connotation and prospects of source rock oil and gas. *Petroleum Explor. Dev.* 46 (1), 181–193. doi:10.1016/S1876-3804(19)30018-7

Zhang, K., Jia, C., Song, Y., Jiang, S., Jiang, Z., Wen, M., et al. (2020a). Analysis of lower cambrian shale gas composition, source and accumulation pattern in different tectonic backgrounds: A case study of weiyuan Block in the upper Yangtze region and xiuwu basin in the lower Yangtze region. *Fuel* 263, 115978. doi:10.1016/j.fuel.2019.115978

Zhang, K., Jiang, Z., Song, Y., Jia, C., Yuan, X., Wang, X., et al. (2022a). Quantitative characterization for pore connectivity, pore wettability, and shale oil mobility of terrestrial shale with different lithofacies-A case study of the Jurassic Lianggaoshan Formation in the Southeast Sichuan Basin of the Upper Yangtze Region in Southern China. *Front. Earth Sci. (Lausanne).* 10, 864189. doi:10.3389/feart.2022.864189

Zhang, K., Peng, J., Liu, W., Li, B., Xia, Q., Cheng, S., et al. (2020b). The role of deep geofluids in the enrichment of sedimentary organic matter: A case study of the late ordovician-early silurian in the upper Yangtze region and early cambrian in the lower Yangtze region, south China. *Geofluids* 2020, 1–12. doi:10.1155/2020/8868638

Zhang, K., Song, Y., Jia, C., Jiang, Z., Han, F., Wang, P., et al. (2022b). Formation mechanism of the sealing capacity of the roof and floor strata of marine organic-rich shale and shale itself, and its influence on the characteristics of shale gas and organic matter pore development. *Mar. Petroleum Geol.* 140, 105647. doi:10.1016/j.marpetgeo.2022.105647

Zhang, K., Song, Y., Jiang, S., Jiang, Z., Jia, C., Huang, Y., et al. (2019). Mechanism analysis of organic matter enrichment in different sedimentary backgrounds: A case study of the lower cambrian and the upper ordovician-lower silurian, in Yangtze region. *Mar. Petroleum Geol.* 99, 488–497. doi:10.1016/j.marpetgeo.2018.10.044

Zhang, K., Song, Y., Jiang, Z., Yuan, X., Wang, X., Han, F., et al. (2022c). Research on the occurrence state of methane molecules in post-mature marine shales-A case analysis of the Lower Silurian Longmaxi Formation shales of the upper Yangtze region in Southern China. *Front. Earth Sci.* 10, 864279. doi:10.3389/feart.2022.864279

Zou, C., Zhu, R., Chen, Z., Ogg, J. G., Wu, S., Dong, D., et al. (2019). Organic-matter-rich shales of China. *Earth. Sci. Rev.* 189, 51–78. doi:10.1016/j.earscirev.2018.12.002

Frontiers in Earth Science

Investigates the processes operating within the major spheres of our planet

Advances our understanding across the earth sciences, providing a theoretical background for better use of our planet's resources and equipping us to face major environmental challenges.

Discover the latest Research Topics

See more →

Frontiers

Avenue du Tribunal-Fédéral 34
1005 Lausanne, Switzerland
frontiersin.org

Contact us

+41 (0)21 510 17 00
frontiersin.org/about/contact